Invasive dynamics for a predator–prey system with Allee effect in both populations and a special emphasis on predator mortality

Sourav Rana, Amiya Ranjan Bhowmick, and Tridip Sardar

View Online   Export Citation   CrossMark

ARTICLES YOU MAY BE INTERESTED IN

Diffusion-induced regular and chaotic patterns in a ratio-dependent predator–prey model with fear factor and prey refuge
Chaos: An Interdisciplinary Journal of Nonlinear Science **31**, 033128 (2021); https://doi.org/10.1063/5.0035130

Dynamics of advectively coupled Van der Pol equations chain
Chaos: An Interdisciplinary Journal of Nonlinear Science **31**, 033147 (2021); https://doi.org/10.1063/5.0040689

Using machine learning to predict statistical properties of non-stationary dynamical processes: System climate,regime transitions, and the effect of stochasticity
Chaos: An Interdisciplinary Journal of Nonlinear Science **31**, 033149 (2021); https://doi.org/10.1063/5.0042598

Invasive dynamics for a predator–prey system with Allee effect in both populations and a special emphasis on predator mortality

Sourav Rana,[1] (ID) Amiya Ranjan Bhowmick,[2] (ID) and Tridip Sardar[3,a] (ID)

AFFILIATIONS

[1] Department of Statistics, Visva-Bharati University, Santiniketan 731235, India
[2] Department of Mathematics, Institute of Chemical Technology, Mumbai 400019, India
[3] Department of Mathematics, Dinabandhu Andrews College, Kolkata 700084, India

[a] Author to whom correspondence should be addressed: tridipiitk@gmail.com

ABSTRACT

We considered a non-linear predator–prey model with an Allee effect on both populations on a two spatial dimension reaction-diffusion setup. Special importance to predator mortality was given as it may be often controlled through human-made harvesting processes. The local dynamics of the model was studied through boundedness, equilibrium, and stability analysis. An extensive numerical stability analysis was performed and found that bi-stability is not possible for the non-spatial model. By analyzing the spatial model, we found the condition for successful invasion and the persistence region of the species based on the predator Allee effect and its mortality parameter. Four different dynamics in this region of the parameter space are mainly explored. First, the Allee effect on both populations leads to various new types of species spread. Second, for a high value of per-capita growth rate, two completely new spreads (e.g., sun surface, colonial) have been found depending on the Allee effect parameter. Third, the Allee coefficient on the predator population leads to spatiotemporal chaos via a patchy spread for both linear and quadratic mortality rates. Finally, a more rigorous analysis is performed to study the chaotic nature of the system within the whole persistence domain. We have studied the possibility of chaos through temporal variation in different invasion regions. Furthermore, the chaotic fluctuation is studied through the sensitivity of initial conditions and by investigating the dominant Lyapunov exponent value.

Published under license by AIP Publishing. https://doi.org/10.1063/5.0035566

The present paper deals with the invasive dynamics of a spatial predator–prey model with an Allee effect on both populations. In particular, there is a strong Allee effect on the prey population and a weak Allee effect on the predator population, as plenty of ecological evidence supports the existence of these phenomena. Empirical evidence of the Allee effect has been reported in many natural populations, including plants, insects, marine invertebrates, birds, and mammals. We have given a special emphasis on predator mortality as it is often controlled through human-made harvesting activities. Most agricultural pest-control strategies describe the eradication of invasive species, where eradication refers to the total elimination of a species from a geographical area. Eradication of some species is often done by manual removal of plants, spraying of pesticides, or by some other mechanisms, as it is already an established fact that one of the processes
that can cause the extinction of low-density populations is the Allee effect, and the population that we are trying to eradicate may have a critical threshold below which they will be eventually extinct (strong Allee effect). This also may provide some economically feasible solutions for management actions in pest control as complete eradication may not often be feasible. Therefore, it is important to study the invasive dynamics when the prey, as well as the predator population, is also subject to the Allee effect. The proposed model is highly non-linear and has the potential to explain the natural system from a new perspective. In the first phase, we have studied the non-spatial model as it is the initial step to explore the complexity of the model. The positivity, boundedness, and local stability have been studied analytically as well as numerically. We observed that it is possible to find two interior equilibria for the model, although the numerical stability

analysis result shows that bi-stability is not possible. We have drawn persistence regions for the species using the long-term dynamics of the reaction-diffusion model. The respective numerical techniques have been discussed in this paper. The study mainly concentrated on these regions, and based on various parts of the persistence region, we have addressed four ecological issues. (i) Spatial spread: the previous study based on the Allee effect on the prey population reveals mainly three kinds of spreading scenarios: circular wavefront, ring front, and patchy spread. However, in the presence of the Allee effect on both populations, we have found five types of spreading: circular wavefront, ring front, double ring front that ultimately breaks into a patchy spread after a certain time, sun surface spread, and patchy spread behind a thick ring front. (ii) The spatial spread in the presence of quadratic mortality: The invasion dynamics concerning quadratic mortality leads to a special type of colonial pattern with three holes surrounded by species density. This spread is completely new and has not been reported before. (iii) The Allee effect leads to a double ring wavefront and ultimately exhibits spatiotemporal chaos. Also, spatiotemporal chaos via patchy spread for both linear and quadratic mortality rates were observed. (iv) A more rigorous analysis has been performed to study the chaotic nature of the system within the whole persistence region. We have studied the possibility of chaos through temporal variation in different invasion regions. Furthermore, chaotic fluctuation was studied through the sensitivity of initial conditions and by the dominant Lyapunov exponent value.

I. INTRODUCTION

Biological invasion is an important field of study that attracts considerable attention from both theoretical and field ecologists.[1–4] There is ample evidence that exotic species can cause serious ecological and economic harm.[5] Invasive species eat, compete, and hybridize with local species often to the detriment of the natives. Invasion can result in the loss of native species and the loss of ecosystem services such as water filtration, soil stabilization, and pest control. Invasive species log waterways, impede navigation, destroy homes, and kill livestock and fisheries.[5] A recent study was performed based on the control of invasive species using the optimal control theory technique.[6]

In general, most agricultural pests are non-indigenous, and many human diseases can be classified as non-native.[7] Non-indigenous species must pass through at least three stages before they can inflict ecological or economic harm (see Fig. 1).[3] All non-native species originally began as individuals that were picked up from their native range, transported to a new area, and released into the wild (see Transport, Fig. 1). These individuals must then establish a self-sustaining population within their new non-native range or else the population dies out (see Establishment, Fig. 1). An established non-native population may then grow in abundance and expand its geographic range or else may remain small in numbers and local in distribution (see Spread, Fig. 1). Typically, it is only when the non-native population is widespread and abundant that it will cause some sort of ecological or economic harm and thus earn the name "invasive."
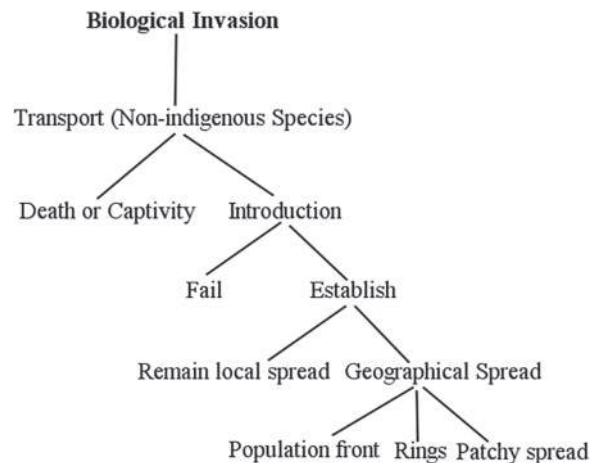

FIG. 1. Invasion process model depicting the discrete stages an invasive species passes through as well as alternative outcomes at each stage.

There are quite a few theoretical approaches that have been developed in this area of study, and considerable progress has been made during the last two decades.[8–13] Mathematically, these models are described by reaction-diffusion equations whose properties depend on the type of population growth function. Most of the early studies assumed logistic equations on population growth; however, in recent times, modification of the growth equations has been observed to include the impact of the Allee effect,[14,15] because the Allee effect was shown to affect virtually all aspects of species interactions in space and time.[16–18] The Allee effect is a density-mediated drop in a population's intrinsic growth rate at low densities.[16,19] In many cases, this reduction may lead to the existence of a critical density or size below which the population growth rate becomes negative, known as the "strong" Allee effect.

Empirical evidence of the Allee effect has been reported in many natural populations, including plants,[20] insects,[21] marine invertebrates,[22] birds, and mammals.[23] Theoretical studies predict that Allee effects in an invader can cause longer lag times, slower spread, and decreased probability of establishment.[24] Under some circumstances, Allee effects can cause different spatial distributions, including a halt to range over expansion, and in an invasive species, it may affect optimal control strategies and costs. The research of phytoplankton and zooplankton total biomass shows that the Allee effect can lead to chaotic temporal oscillation even when the species spatial distribution is pretty regular.[25] In the work by Alharbi and Petrovskii,[26] considered a reaction-diffusion model with a modification based on the effect of dispersal corridors and stepping stones. They concluded that the Allee effect, stepping stone size, and location play a vital role in the species establishment. Recently, the impact of the Allee effect on species invasion has been studied by many researchers. Kohnke and Malchow[27] considered a two-species model with the strong Allee effect on both the populations and studied the impact of an infectious disease through analytical and numerical techniques. They concluded that depending on the impact of competition, the model dynamics either slow
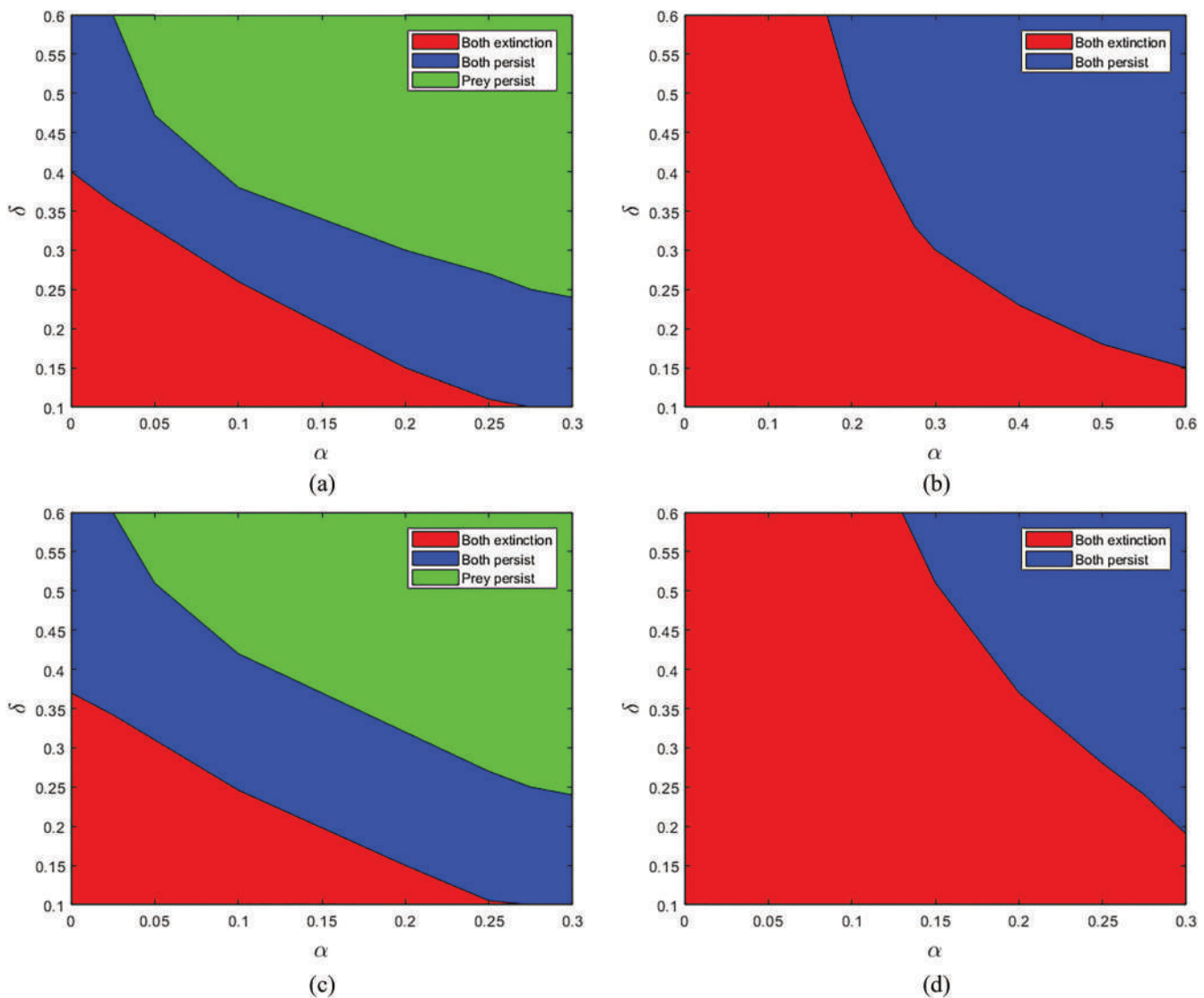
FIG. 2. Persistence region for $\gamma = 3$, $\alpha_1 = 0.2$ has been drawn in (a) and (b), and the region for $\gamma = 4.5$, $\alpha_1 = 0.2$ has been drawn in (c) and (d). The green region is the persistence for only the prey population, the red region is for the extinction of both species, and the blue region is for the persistence of both species.

down the invasion front or exhibit various complex phenomena like coexistence, oscillation, and spatiotemporal chaos. McDermott and Finnoff[28] studied the spread of invasive species with the Allee effect from a completely different point of view. The authors incorporated human interference in their study and discussed its importance on species invasion. In the paper by Manna and Banerjee,[29] they studied a two species reaction-diffusion model with the additive Allee effect on the prey population. They explored various stationary, non-stationary, and invasive patterns and revealed that the strong Allee effect plays a significant role in species invasion.

Existing research on the Allee effect in invasive population dynamics mainly emphasizes the scenario when the prey population

is subject to the Allee effect. There are some instances that predators can also affect the prey in a positive way. Positive effects of predators on preys can take on many forms, including the ability of predators to mineralize nutrients, which limit prey or prey resources, to "transport" prey to places where intra-specific prey competition is lower (e.g., granivore dispersing seeds) or to alter prey behavior.[30] Mathematical modeling reveal that predators could experience the Allee effect through such kind of positive effect. In addition, also many predators are considered K-strategists, and it is easier for them to experience the Allee effect.[31–33] For instance, most agricultural pest-control strategies describe the eradication of invasive species, where eradication refers to the total elimination of a species from

a geographical area. Eradication of some species is often done by manual removal of plants, spraying of pesticides, or some other mechanisms. As we have already mentioned, one of the processes that can cause the extinction of low-density populations is the Allee effect, and the population that we are trying to eradicate may have a critical threshold below which they will be eventually extinct (the strong Allee effect). This also may provide some economically feasible solutions for management actions in pest control as complete eradication may not be possible repeatedly.[18,34] Considering these evidences, it is important to study the invasive dynamics when the predator population is also subject to the Allee effect.[35]

In this paper, we consider a two-dimensional reaction-diffusion model for studying various invasion scenarios when both prey and predator populations are subject to the Allee effect. Specifically, in the mathematical model we considered, the prey growth is damped by the strong Allee effect and predator growth is dominated by the weak Allee effect due to difficulties in finding mates at low density. In particular, the following issues are considered:

1. How does the Allee threshold affect the persistence of the species/populations?
2. The difference in the type of spread when the Allee effect is present in both prey and predator populations compare to the scenario when only the prey population is subject to the Allee effect.[24]
3. Invasion dynamics with quadratic mortality (density-dependent per-capita mortality rate) of the predator and its comparison with the case when linear mortality of the predator is considered.
4. Changes in the invasion regimes for different values of Allee coefficients of the predator. Is there any spatial chaos or spatiotemporal chaos?
5. Study the chaotic nature of different invasion regimes.

The different sections of the paper are organized as follows: In Sec. II, we present the formulations of the mathematical model. In Sec. III, we study some preliminary analyses of our model such as local dynamics and stability of the system. Invasion thresholds for interacting species are discussed in Sec. IV. In Sec. V, we study various invasion regimes that depend on the mortality rate of the predator population. Section VI deals with the existence of chaos in different invasion regimes. Finally, we discuss our results and conclude our findings in Sec. VII.

II. MATHEMATICAL MODEL

We consider a $2D$ predator–prey interaction in a homogeneous environment described by a reaction-diffusion system,[36–39]

$$\frac{\partial H}{\partial T} = D_1 \left(\frac{\partial^2 H}{\partial X^2} + \frac{\partial^2 H}{\partial Y^2} \right) + F(H) - f(H,P),$$

$$\frac{\partial P}{\partial T} = D_2 \left(\frac{\partial^2 P}{\partial X^2} + \frac{\partial^2 P}{\partial Y^2} \right) + g(H,P) - MP^n. \tag{1}$$

Here, $H = H(X,Y,T)$ and $P = P(X,Y,T)$ are densities of the prey and the predator, respectively, at moment T and position (X,Y). The function $F(H)$ represents the intrinsic growth rate of the prey that is

damped by the strong Allee effect. The form $f(H,P)$ describes predation and $g(H,P)$ is predator growth, which is affected by the Allee effect due to difficulty in finding a mate, and the term MP^n stands for predator mortality, where we consider n either 1 (density independent) or 2 (density dependent). D_1 and D_2 are diffusion coefficients of the prey and the predator, respectively. We assume the predation term to be governed by a Holling type-I functional response (linear mass action law) and is described as follows:

$$f(H,P) = HP. \tag{2}$$

We assume that the prey population is subject to the strong Allee effect that can be described by the following term:[14]

$$F(H) = \left(\frac{4\omega}{(K-H_0)^2} \right) H (H-H_0) (K-H), \tag{3}$$

where K is the prey carrying capacity, ω is the maximum per capita growth rate, and H_0 quantifies the intensity of the Allee effect, and therefore, it is called "strong" if $0 < H_0 < K$, i.e., the growth rate becomes negative for $H < H_0$, and "weak" if $-K < H_0 \leq 0$.[9,10] For $H_0 \leq -K$, the Allee effect disappears.[14]

We assume that the predator growth rate is damped by the weak Allee effect, which can be parameterized as follows:[18,33]

$$g(H,P) = \beta H P \left(\frac{P}{P+A} \right), \tag{4}$$

where $\frac{P}{P+A}$ is the term for the Allee effect and $A > 0$ can be defined as "Allee effect coefficients." The larger the A is, the stronger the Allee effect will be, and the slower the per capita growth rate of the predator, i.e., per capita growth rate of the predator population is reduced from βH to $\beta H \left(\frac{P}{P+A} \right)$, in particular, at low density of the predator.[33] For example, many predators can be regarded as K-strategists, and it may be easier for them to exhibit an Allee effect.[32]

Equation (1) contains a large number of parameters, which makes a numerical investigation very difficult. However, by choosing appropriate scales for the variables, the number of parameters can be reduced. Considering dimensionless variables $u = \frac{H}{K}$, $v = \frac{P}{\beta K}$, $t = aT$, $x = \left(\frac{a}{D1} \right)^{1/2} X$, $y = \left(\frac{a}{D1} \right)^{1/2} Y$, and $a = \beta K$,[38] we arrived at the following system:

$$\frac{\partial u}{\partial t} = \left(\frac{\partial^2 u}{\partial x^2} + \frac{\partial^2 u}{\partial y^2} \right) + \gamma u (u - \alpha_1)(1-u) - uv,$$

$$\frac{\partial v}{\partial t} = \rho_d \left(\frac{\partial^2 v}{\partial x^2} + \frac{\partial^2 v}{\partial y^2} \right) + \frac{uv^2}{v+\alpha} - \delta v^n, \tag{5}$$

where dimensionless parameters are as follows: $\alpha = \frac{A}{\beta K}$, $\alpha_1 = \frac{H_0}{K}$, $\delta = \frac{M}{a}$, $\gamma = \frac{4\omega}{a \left(1 - \frac{H_0}{K}\right)^2}$, and $\rho_d = \frac{D_2}{D_1}$. Thus, the behavior of u and v depend on five dimensionless combinations of the original parameters rather than each of them separately. Biological invasion usually starts when the number of individuals of an exotic species is locally brought into a given ecosystem; thus, a relevant initial distribution should be considered in a finite domain.[24] We consider initial

conditions of Eq. (5) in the following form:

$$u(x, y, 0) = u_0, \quad \text{for} \quad \left(\frac{x - x_1}{R_1}\right)^2 + \left(\frac{y - y_1}{R_1}\right)^2 \leq 1,$$

$$= 0, \quad \text{otherwise} \tag{6}$$

$$v(x, y, 0) = v_0, \quad \text{for} \quad \left(\frac{x - x_2}{R_2}\right)^2 + \left(\frac{y - y_2}{R_2}\right)^2 \leq 1,$$

$$= 0, \quad \text{otherwise} \tag{7}$$

where u_0 and v_0 are initial population densities and R_1 and R_2 are radii of the initial invaded area. Initial conditions (6) and (7) also correspond to the problem of biological control; soon after the introduction of an exotic species, a predator species is introduced intentionally in an attempt to slow down or stop its spread.[10,40]

Equation (5) with the initial conditions (6) and (7) is solved in the domain $-L < x < L$ and $-L < y < L$ using a fully implicit finite difference method.[41–44] The steps of the numerical mesh were chosen as $\Delta x = 1$ and $\Delta t = 1$. The zero-flux boundary condition was used at the boundaries, and the radius L is chosen large enough in order to make the impact of the boundaries as small as possible during the simulation time. We have taken $R_1^2 = 30, R_2^2 = 25, 2L = 200$, and $x_1 = 100, y_1 = 101, x_2 = 95, y_2 = 95, u_0 = 1$, and $v_0 = 0.6$. A detailed description of the parameters and the spatiotemporal model solving the numerical protocol is presented in Table I. However,

before going to any further investigation of the above spatial model, we will first study the non-spatial dynamics of system (5).

III. MODEL ANALYSIS

A. Local dynamics

In this section, we will briefly discuss the local dynamics of model (5) without diffusion. The non-spatial version of model (5) is

$$\frac{du}{dt} = \gamma u (u - \alpha_1)(1 - u) - uv,$$

$$\frac{dv}{dt} = \frac{uv^2}{v + \alpha} - \delta v^n. \tag{8}$$

Lemma III.1. *Every solution for model* (8) *exists in the interval* $[0, \infty)$ *with* $u(t), v(t) > 0$, *for all* $t \geq 0$.

Proof. As $\gamma u (u - \alpha_1)(1 - u) - uv$ and $\frac{uv^2}{v + \alpha} - \delta v^n$ are completely continuous and locally Lipschitzian on $C^1(\mathbb{R}_+^2)$, the solution $[u(t), v(t)]$ for model (8) exists and is unique on $(0, \xi)$, where $0 < \xi \leq \infty$.[45] So from system (8), we have

$$u(t) = u(0) \exp\left[\int_0^t \gamma (u(z) - \alpha_1)(1 - u(z)) \, dz - \int_0^t v(z) \, dz\right] \geq 0$$

TABLE I. Description and values of parameters used to solve the model (8) with initial conditions (6) and (7). The model is solved in the domain of length $2L$. The zero flux boundary conditions are used at the boundaries. The model solving the numerical protocol and the simulation method is also described at the last row of the table.

Parameters	Description		
ω	Per capita growth rate of prey		
K	Prey carrying capacity		
H_0	Prey Allee effect coefficient		
β	Per capita growth rate of predator		
A	Predator Allee effect coefficient		
D_1	Prey diffusion coefficient		
D_2	Predator diffusion coefficient		
M	Predator mortality rate		
Parameters for simulation		Value	Reference
α	Dimensionless parameter	$[0, 0.6]$	
α_1	Dimensionless parameter	0.2	35
δ	Dimensionless parameter	$[0.1, 0.6]$	
γ	Dimensionless parameter	3	24
ρ_d	Dimensionless parameter	1	24
(x_1, y_1)	Center of initial invaded area of prey	(100, 101)	
(x_2, y_2)	Center of initial invaded area of predator	(95, 95)	
R_1^2	Square of radius of initial invaded area of prey	30	
R_2^2	Square of radius of initial invaded area of predator	25	
$2L$	Length of the square boundary	200	
u_0	Initial prey population density	1	
v_0	Initial predator population density	0.6	
n	Type of predator mortality	1, 2	
Numerical protocol	Simulation method		Reference
Fully implicit finite difference method	Multigrid solver		41–44

and

$$v(t) = v(0) \exp\left[\int_0^t \frac{u(z)v(z)}{v(z)+\alpha}\, dz - \delta \int_0^t v(z)^{n-1}\, dz\right] \geq 0.$$

Therefore, it completes the proof. □

Lemma III.2. *All the solutions for model* (8) *are uniformly bounded in* $\mathbb{R}_+^2$.

Proof. We define $w = u + v$.

Calculating the time derivative of w along the solution to (8), we obtain

$$\frac{dw}{dt} = \frac{du}{dt} + \frac{dv}{dt} \Rightarrow \frac{dw}{dt} \leq \gamma u(u - \alpha_1)(1 - u) - uv + \frac{uv^2}{v+\alpha} - \delta v^n$$

$$\leq \gamma u(u - \alpha_1)(1 - u) - \delta v^n \Rightarrow \frac{dw}{dt}$$

$$\leq \gamma u(1 - u) - \delta v^n \quad \text{for } \alpha_1 \in (0, 1),$$

i.e., the strong Allee effect.

It implies, $\frac{dw}{dt} + \eta w \leq u(\gamma + \eta - \gamma u) + \eta v - \delta v^n$.

For linear mortality, i.e., $n = 1$, $\frac{dw}{dt} + \eta w \leq u(\gamma + \eta - \gamma u) + (\eta - \delta)v \leq l$, where $\eta < \delta$ and $l = \frac{(\gamma+\eta)^2}{4\gamma}$.

Therefore, $0 < w \leq e^{-\eta t}(w(0) - \frac{l}{\eta}) + \frac{l}{\eta}$.

As $t \to \infty$, $w(t) \to \frac{l}{\eta}$, i.e., $w(t) \leq \frac{l}{\eta}$, since $\sup_{t\to\infty} w(t) = \frac{l}{\eta}$.

Again, for quadratic mortality, i.e., $n = 2$, $\frac{dw}{dt} + \eta w \leq u(\gamma + \eta - \gamma u) + \eta v - \delta v^2 \leq l + m$, where $l = \frac{(\gamma+\eta)^2}{4\gamma}$ and $m = \frac{\eta^2}{4\delta}$.

Therefore, $0 < w \leq e^{-\eta t}(w(0) - \frac{l+m}{\eta}) + \frac{l+m}{\eta}$.

As $t \to \infty$, $w(t) \to \frac{l+m}{\eta}$, i.e., $w(t) \leq \frac{l+m}{\eta}$, since $\sup_{t\to\infty} w(t) = \frac{l+m}{\eta}$.

So the non-spatial system (8) is uniformly bounded for both linear and quadratic mortalities. □

Model (8) with linear mortality rates (i.e., $n = 1$) has equilibrium points $E_0(0,0)$, $E_1(\alpha_1, 0)$, $E_2(1, 0)$, and $E^*(u^*, v^*)$, where $v^* = \frac{\alpha\delta}{u^* - \delta}$ and u^* are the positive roots of the equation $\gamma(u - \alpha_1)(u - \delta)(1 - u) - \alpha\delta = 0$. The interior equilibrium exists if $\max\{\alpha_1, \delta\} < u^* < 1$.

Model (8) with quadratic mortality rates (i.e., $n = 2$) has equilibrium points $E_0(0,0)$, $E_1(\alpha_1, 0)$, $E_2(1, 0)$, and $E^*(u^*, v^*)$, where $v^* = \frac{u^*}{\delta} - \alpha$ and u^* are the positive roots of the equation $\gamma\delta(u - \alpha_1)(1 - u) - (u - \alpha\delta) = 0$. The interior equilibrium exists if $\max\{\alpha_1, \alpha\delta\} < u^* < 1$.

For both linear and quadratic mortality rates, the expression for equilibrium shows that it is possible for double interior equilibrium. Now we will try to explore for any possible bi-stability phenomena. Moreover, as our focus of this paper is to study the impact of the Allee effect and mortality on the population, so we will analytically study the interior equilibrium $E^*(u^*, v^*)$ for both linear and quadratic mortality cases as it contains both Allee and mortality parameters.

Lemma III.3. *System* (8) *around* $E^*(u^*, v^*)$ *is locally asymptotically stable for both linear and quadratic mortality cases if* $\operatorname{tr}(J(E^*)) < 0$ *and* $\det(J(E^*)) > 0$, *where* $J(E^*) = \begin{pmatrix} J_{11} & J_{12} \\ J_{21} & J_{22} \end{pmatrix}$ *and* $J_{11}, J_{12}, J_{21}, J_{22}$ *are given in Eq.* (9).

Proof. The Jacobian matrix $J(E^*)$ is

$$J(E^*) = \begin{pmatrix} \gamma u^*(1 + \alpha_1 - 2u^*) & -u^* \\ \frac{v^{*2}}{v^*+\alpha} & \delta(1 - n)v^{*n-1} + \frac{\alpha u^* v^*}{(v^*+\alpha)^2} \end{pmatrix}$$

$$= \begin{pmatrix} J_{11} & J_{12} \\ J_{21} & J_{22} \end{pmatrix}.$$

Here,

$$J_{11} = \gamma u^*(1 + \alpha_1 - 2u^*),$$
$$J_{12} = -u^*,$$
$$J_{21} = \frac{v^{*2}}{v^*+\alpha}, \tag{9}$$
$$J_{22} = \delta(1 - n)v^{*n-1} + \frac{\alpha u^* v^*}{(v^*+\alpha)^2}.$$

The corresponding characteristic equation is $\lambda^2 - \operatorname{tr}(J(E^*))\lambda + \det(J(E^*)) = 0$ of the Jacobian matrix $J(E^*)$. Now by the Routh–Hurwitz criteria, the equilibrium E^* is locally asymptotically stable if $\operatorname{tr}(J(E^*)) < 0$ and $\det(J(E^*)) > 0$. □

We analytically performed the stability analysis of the interior equilibrium E^* and numerically explored the nature of the roots of the characteristic equation to determine different stabilities or instabilities of the equilibrium. A detailed numerical result in terms of stability is shown in Table II. We also have drawn several phase portrait (with vector field) illustrations. Various possibilities of equilibrium and their states are discussed for both the linear and quadratic mortality cases. In Fig. 3(f), the linear mortality rate (i.e., $n = 1$) was taken, and fixed parameters are $\alpha = 0.3$, $\alpha_1 = 0.2$, $\gamma = 3$, and $\delta = 0.46$. We found the equilibrium points $E_0(0,0)$ as a nodal sink, $E_1(0.2, 0)$ as a saddle, and $E_2(1, 0)$ as a nodal sink. We have also added the vector field in Fig. 3(f) to understand the flow around the equilibrium point. Similarly, we vary other parameters and perform the numerical stability analysis of model (8). The results are pointed out in Table II with corresponding figures [Figs. 5(g)–5(h), 7(g), 8(g), 9(g), and 10(g)]. It has been observed that there is no evidence of bi-stability phenomena for the non-spatial model. From Table II, it is clear that bi-stability cannot be possible for system (8) as one interior equilibrium is always unstable. However, when space is taken into account, the dynamics of system (8) becomes essentially different. Here, we have discussed the impact of the predator Allee effect and mortality simultaneously on the persistence and extinction of the species.

B. Stability

In this section, we will analyze the stability of the interior equilibrium (u^*, v^*) for the spatial model (5). Model (5) can be rewritten as

$$\begin{aligned} \frac{\partial W}{\partial t} &= H(W) + D\nabla^2 W, & (x,y) \in \Omega, \, t > 0, \\ \frac{\partial W}{\partial n} &= 0, & (x,y) \in \partial\Omega, \, t > 0, \\ W(x,y,0) &= (u_0(x,y), v_0(x,y))^T, & (x,y) \in \Omega, \end{aligned} \tag{10}$$

where $W = (u, v)^T$, $D = \operatorname{diag}(1, \rho_d)$, $H(W) = [\gamma u(u - \alpha_1)(1 - u) - uv, \frac{uv^2}{v+\alpha} - \delta v^n]^T$, $u_0(x,y) = u(x,y,0)$, and $v_0(x,y) = v(x,y,0)$.

TABLE II. Numerical stability analysis of model (8) for different sets of parameter values as described in the corresponding figures. N.A. stands for the equilibrium points where linear stability analysis is not applicable.

Equilibrium	Mortality	Dynamics	Figure
$E_0(0,0)$, $E_1(0.2,0)$, $E_2(1,0)$	Linear	E_0:Nodal sink, E_1:Saddle E_2:Nodal sink	3(f)
$E_0(0,0)$, $E_1(0.2,0)$, $E_2(1,0)$, $E_1^*(0.491\,05, 0.444\,39)$ $E_2^*(0.988\,98, 0.026\,088)$	Linear	E_0:Nodal sink, E_1:Saddle E_2:Nodal sink, E_1^* : Spiral source E_2^* : Saddle	5(g)
$E_0(0,0)$, $E_1(0.2,0)$, $E_2(1,0)$, $E_1^*(0.475\,36, 0.4334)$	Quadratic	E_0:N.A., E_1:N.A. E_2:Nodal sink, E_1^* : Spiral source	5(h)
$E_0(0,0)$, $E_1(0.2,0)$, $E_2(1,0)$, $E_1^*(0.516\,21, 0.688\,41)$ $E_2^*(0.957\,96, 0.143\,38)$	Linear	E_0:Nodal sink, E_1:Saddle E_2:Nodal sink, E_1^* : Spiral source E_2^* : Saddle	7(g)
$E_0(0,0)$, $E_1(0.2,0)$, $E_2(1,0)$, $E_1^*(0.432\,34, 0.593\,51)$ $E_2^*(0.982\,86, 0.060\,37)$	Linear	E_0:Nodal sink, E_1:Saddle E_2:Nodal sink, E_1^* : Spiral source E_2^* : Saddle	8(g)
$E_0(0,0)$, $E_1(0.2,0)$, $E_2(1,0)$, $E_1^*(0.535\,64, 0.701\,36)$ $E_2^*(0.985\,43, 0.0515)$	Linear	E_0:Nodal sink, E_1:Saddle E_2:Nodal sink, E_1^* : Spiral source E_2^* : Saddle	9(g)
$E_0(0,0)$, $E_1(0.2,0)$, $E_2(1,0)$, $E_1^*(0.239\,69, 0.135\,81)$ $E_2^*(0.556\,27, 0.711\,39)$	Quadratic	E_0:N.A., E_1:N.A. E_2:Saddle, E_1^* : Saddle E_2^* : Spiral sink	10(g)

Let $0 = \mu_0 < \mu_1 < \mu_2 < \cdots$ be the eigenvalues of the operator $-\nabla^2$ on Ω with the zero-flux boundary conditions and $E(\mu_i)$ be the eigenspace corresponding to μ_i in $C^1(\overline{\Omega})$. Let $X = \{W \in [C^1(\overline{\Omega})]^2 | \frac{\partial W}{\partial n} = 0 \text{ on } \partial\Omega\}$, $\{\phi_{ij} | j = 1, \ldots, \dim E(\mu_i)\}$ be an orthonormal basis of $E(\mu_i)$, and $X_{ij} = \{\xi\phi_{ij} | \xi \in \mathbb{R}^2\}$, then $X = \bigoplus_{i=1}^{\infty} X_i$, where $X_i = \bigoplus_{i=1}^{\dim E(\mu_i)} X_{ij}$.

Theorem III.4. *If the relations $\frac{\alpha}{(v^*+\alpha)^2} < \frac{1}{u^*v^*}[2\gamma u^{*2} + \delta(n-1)v^{*n-1} - \gamma(1+\alpha_1)u^*]$ and $\gamma u^*[1 + \alpha_1 - 2u^*][1 - n + \frac{\alpha}{v^*+\alpha}] + v^* > 0$ satisfy with the first eigenvalue μ_1 subject to the zero-flux boundary conditions satisfies $\mu_1 > \max\{0, [\gamma u^*(1+\alpha_1 - 2u^*)] + [\delta(1-n)v^{*n-1} + \frac{\alpha u^* v^*}{(v^*+\alpha)^2}]/\rho_d\}$, then the interior equilibrium $E^*(u^*, v^*)$ of model (5) is uniformly asymptotically stable.*

Proof. Let $\Phi_1 = D\nabla^2 + J_{E^*}$. The linearization of (5) at the equilibrium $E^*(u^*, v^*)$ is $W_t = \Phi_1 W$. For each $i \geq 1$, X_i is invariant under the operator Φ_1 and λ is an eigenvalue of Φ_1 on X_i if and only if it is an eigenvalue of the matrix $-\mu_i D + J_{E^*}$. The characteristic polynomial of $-\mu_i D + J_{E^*}$ is given by

$$\psi_i(\lambda) = \lambda^2 + [(1+\rho_d)\mu_i - \text{tr}(J_{E^*})]\lambda$$
$$+ [\rho_d \mu_i^2 - (J_{11}\rho_d + J_{22})\mu_i + \det(J_{E^*})]$$
$$= \lambda^2 + \text{tr}(J_\mu)\lambda + \det(J_\mu). \quad (11)$$

Now if the given conditions are satisfied, then $\text{tr}(J_{E^*}) < 0$ and $\det(J_{E^*}) > 0$. Taking $\mu_1 > \max\{0, [\gamma u^*(1+\alpha_1 - 2u^*)] + [\delta(1-n)v^{*n-1} + \frac{\alpha u^* v^*}{(v^*+\alpha)^2}]/\rho_d\}$, one can show that $\text{tr}(J_{\mu_i}) > 0$, $\det(J_{\mu_i}) > 0$ for all $i \geq 1$.

Therefore, the eigenvalues of the matrix $-\mu_i D + J_{E^*}$ have negative real parts. It, thus, follows from the Routh–Hurwitz criterion

that, for each $i \geq 1$, the two roots λ_{i1} and λ_{i2} of $\psi_i(\lambda) = 0$ all have negative real parts. In the following, we prove that there exists $\delta_1 > 0$ such that $Re\{\lambda_{i1}\} \leq -\delta_1$, $Re\{\lambda_{i2}\} \leq -\delta_1$. Let $\lambda = \mu_i \xi$, then $\psi_i(\lambda) = \mu_i^2\xi^2 + \text{tr}(J_\mu)\mu_i\xi + \det(J_\mu) \triangleq \widetilde{\psi}_i(\lambda)$ since $\mu_i \to \infty$ as $i \to \infty$, it follows that $\lim_{i\to\infty} \frac{\widetilde{\psi}_i(\lambda)}{\mu_i^2} = \xi^2 + (1+\rho_d)\xi + \rho_d$.

By the Routh–Hurwitz criterion, it follows that the two roots ξ_1, ξ_2 of $\widetilde{\psi}_i(\lambda) = 0$ have negative real parts. Thus, there exists a positive constant $\widetilde{d} = \min\{1, \rho_d\}$, such that $Re\{\xi_1\}$, $Re\{\xi_2\} \leq -\widetilde{d}$. By continuity, we see that there exists i_0 such that two roots ξ_{i2}, ξ_{i2} of $\widetilde{\psi}_i(\lambda) = 0$ satisfy $Re\{\xi_{i1}\} \leq -\widetilde{d}/2$, $Re\{\xi_{i2}\} \leq -\widetilde{d}/2$, for all $i \geq i_0$. In turn, $Re\{\lambda_{i1}\}$, $Re\{\lambda_{i2}\} \leq -\mu_i\widetilde{d}/2 \leq \widetilde{d}/2$, for all $i \geq i_0$. Let $-\widetilde{\delta}_1 = \max_{1\leq i\leq i_0}\{Re\{\lambda_{i1}\}, Re\{\lambda_{i2}\}\}$. Then, $\widetilde{\delta}_1 > 0$ and $Re\{\lambda_{i1}\} \leq -\delta_1$, $Re\{\lambda_{i2}\} \leq -\delta_1$ hold for $\delta_1 = \min\{\widetilde{\delta}, \widetilde{d}/2\}$.

Consequently, the spectrum of Φ_1 which consists of eigenvalue lies in $\{Re\lambda \leq -\delta\}$. Therefore, we obtain that the positive constant steady state solution $E^*(u^*, v^*)$ of model (5) is uniformly asymptotically stable.[46] $\square$

IV. INVASION THRESHOLDS FOR INTERACTING SPECIES

An immediate consequence after the introduction of a nonindigenous species is that under what conditions the species can persist in the new environment. In the simplest model, a population without an Allee effect will grow from any initial density until it reaches a stable equilibrium, its carrying capacity.[9] However, models with a strong Allee effect have a zero stable equilibrium point and a non-zero unstable equilibrium point that acts as a threshold. Therefore, if the initial density of the prey is
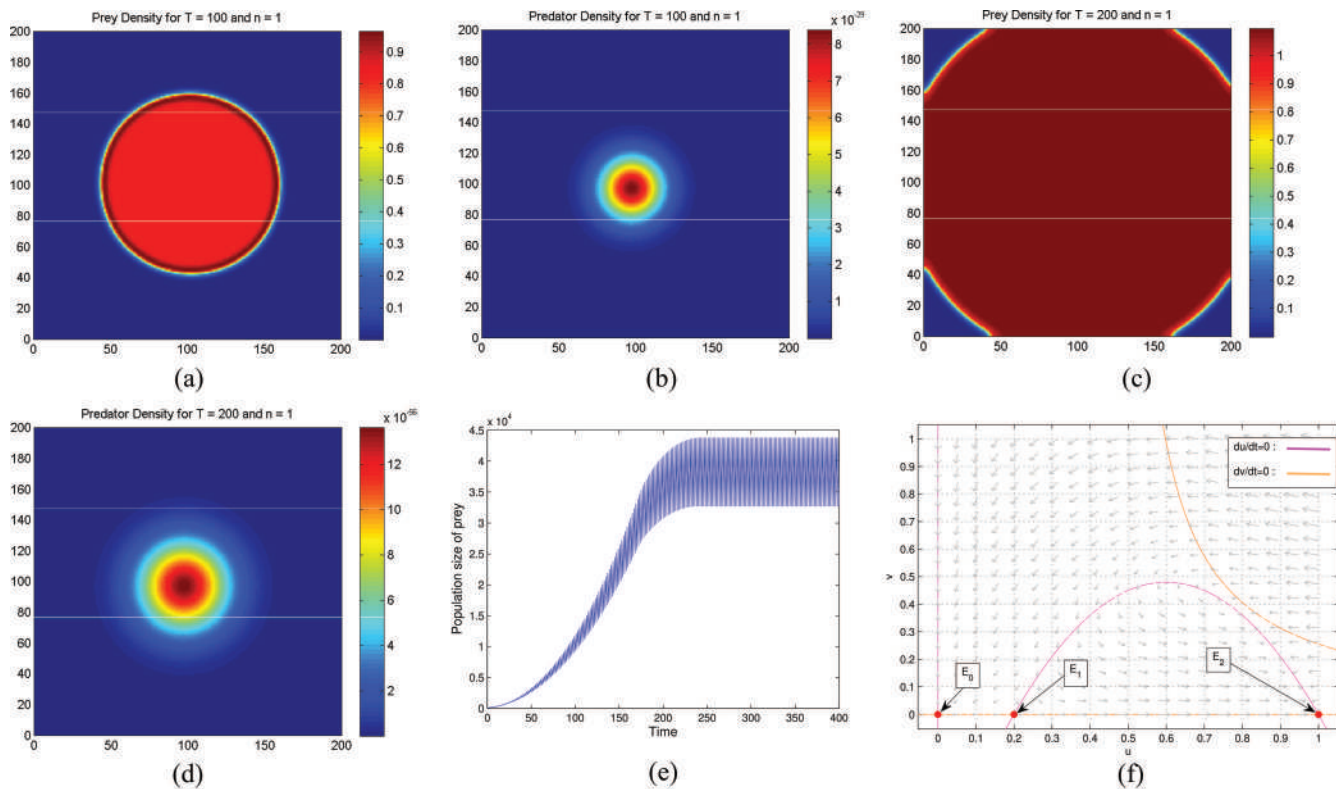
FIG. 3. Snapshots of species density distribution over the *XY* plane obtained at different time points (a)–(d) for parameter values $\gamma = 3$, $\alpha_1 = 0.2$, $\alpha = 0.3$, $\delta = 0.46$, $\rho_d = 1$, and $n = 1$. The density color bar suggests the distribution of various densities of species over the region. Here, the predator population goes to extinction and the prey population spreads over the whole region. (e) and (f) represent the respective temporal variation and the local dynamics.

lower than the threshold value, the prey population declines to extinction.[15,24] However, we do not consider any alternative food resource; thus, if the prey population becomes extinct so is the predator. Thus, the required condition for invasion to be successful is that $\alpha_1 < u_0$. Also, the initial prey population size u_0 should be greater than the initial predator population size v_0 for a successful invasion.

There is another threshold caused by the strong Allee effect in the prey, which is the minimum invaded area covered by initial population size, below which the population goes extinct, i.e., invasion failure occurs. This threshold exists in models without the Allee effect but is increased by the addition of Allee dynamics.[47,48] For single species models, this threshold has been demonstrated analytically and for critical Allee effects, in reaction-diffusion models in both one and two dimensions,[14,49,50] in integro-difference models,[8] and is supported by results from a simulation model of fruit flies.[51] The results imply that invasion might not succeed if there is insufficient habitat, i.e., if the area available is smaller than the spatial threshold.[49] However, for interacting species models in two dimensions, an analytical solution is hardly an option; thus, we numerically demonstrate the initial threshold area above which both the prey and predator populations persist. We find that the initial invaded area of the prey

should be greater than the initial invaded area of the predator for persistence of the species.

It should be emphasized that the conditions we have mentioned here are mainly based on the initial population size and initial invaded area of the prey and predator population. However, these conditions may not be a sufficient condition for successful invasion of a species. We show in Sec. V that successful invasion also depends on some parametric combinations that need to satisfy certain threshold values.

V. DIFFERENT INVASION REGIMES WITH LINEAR/QUADRATIC MORTALITY RATE OF PREDATOR

System (5) depends on a large number of parameters; therefore, its detailed numerical investigation in the whole parameter space is almost impossible. Instead, we first choose one or two controlling parameters and analyze the invasion dynamics subject to its variation. In the present paper, we have taken the predator Allee effect and predator mortality as the key parameters. We want to emphasize the impact of the Allee effect in predator on invasion dynamics of both prey and predator populations. Moreover, predator mortality can be considered as a controlling parameter because, in a
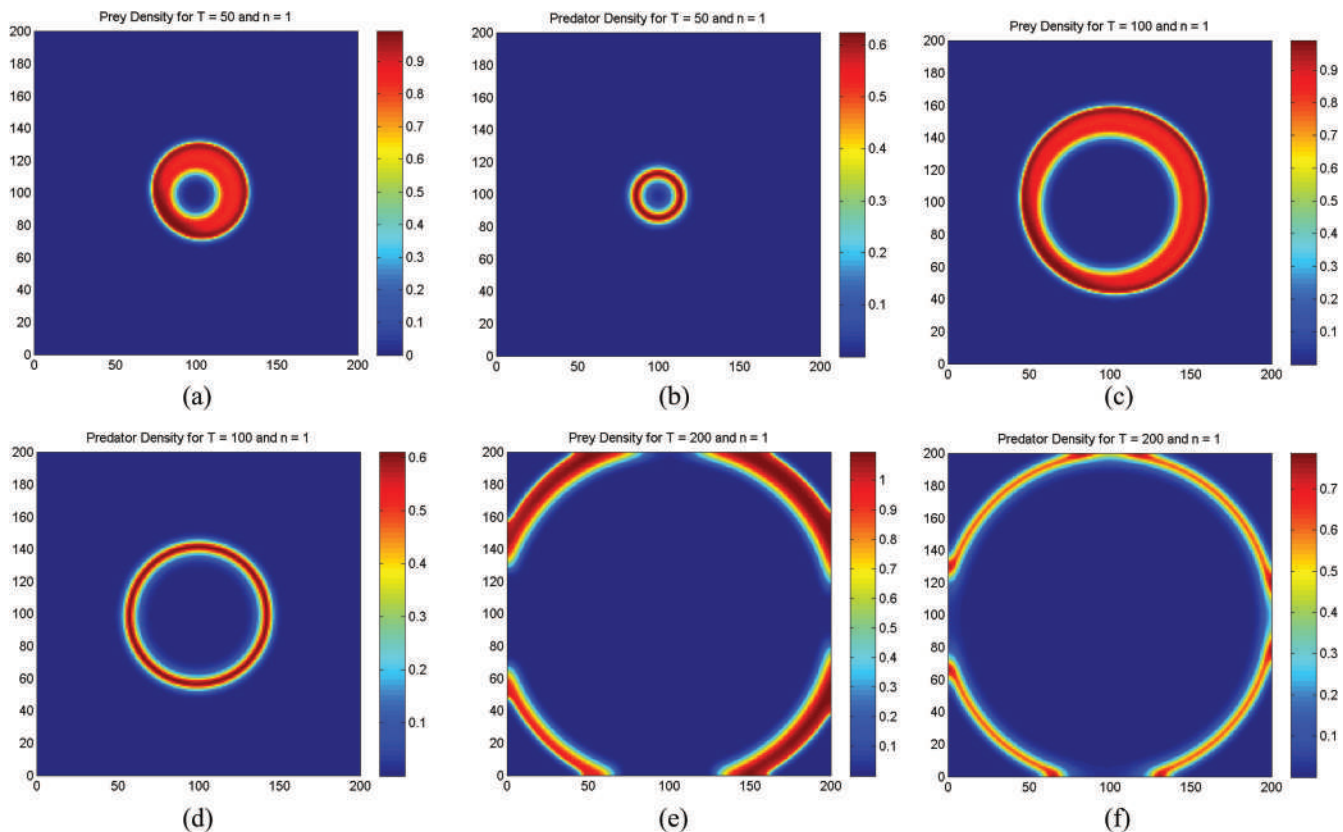
FIG. 4. Snapshots of species density distribution over the *XY* plane obtained at different time points (a)–(f) for parameter values $\gamma = 3$; $\alpha_1 = 0.2$, $\alpha = 0.1$, $\delta = 0.37$, $\rho_d = 1$, and $n = 1$. The density color bar suggests the distribution of various densities of species over the region. Here, both the populations coexist and spread through a ring format.

real ecosystem, the rate of predator mortality can be relatively easily controlled using additional harvesting.[24] We numerically simulated the spatial model and computed the whole parameter region for α and δ to identify the different regions of persistence. We have illustrated the persistence region for linear and quadratic mortality rates [see Figs. 2(a) and 2(b)] for a low value of maximum per capita growth rate. In Fig. 2, the three colors represent the persistence of both the populations (blue region), the persistence of only the prey population (green region), and the extinction of both the populations (red region). A similar diagram illustrated the persistence region for linear and quadratic mortality rates [see Figs. 2(c) and 2(d)] for a high value of maximum per capita growth rate. The persistence regions for α and δ have been drawn for a certain combination of (α, δ) (see Fig. 2). For each combination, we have simulated the spatial system up to a long time and compare the spatial average density of the prey and the predator with a small threshold value. In the α–δ plane, the points are colored red when both prey and predator populations lie below that threshold, green when only the predator population lies below the threshold, and blue when both the populations lie above the threshold.

A. Low value of maximum per capita growth rate

1. Different types of mortality

- **Case I: *Linear mortality rate.*** Results of our computer simulation show that with the linear mortality rate of the predator and with the Allee effect in both the prey and the predator exhibit a different kind of invasion regimes. We have taken four different sets of parameter values from different regions of Fig. 2(a) with initial conditions given by (6) and (7). Here, we have fixed the parameter values $\alpha_1 = 0.2$, $\gamma = 3$, and $\rho_d = 1$ and vary the predator Allee coefficient (α) and mortality rate (δ) to study the possible impact of them on invasion dynamics of the prey and predator. To draw the species density distribution, we first considered that the parameters $\alpha = 0.3$ and $\delta = 0.46$ are from the green region of Fig. 2(a). Here, Figs. 3(a) and 3(b) depict the density distribution over the *XY* plane obtained at time point $t = 100$ for the prey and predator, respectively. Similarly, Figs. 3(c) and 3(d) depict the density distribution over the *XY* plane obtained at time point $t = 200$ for the prey and predator, respectively. We observed that the predator population goes extinct and the prey population
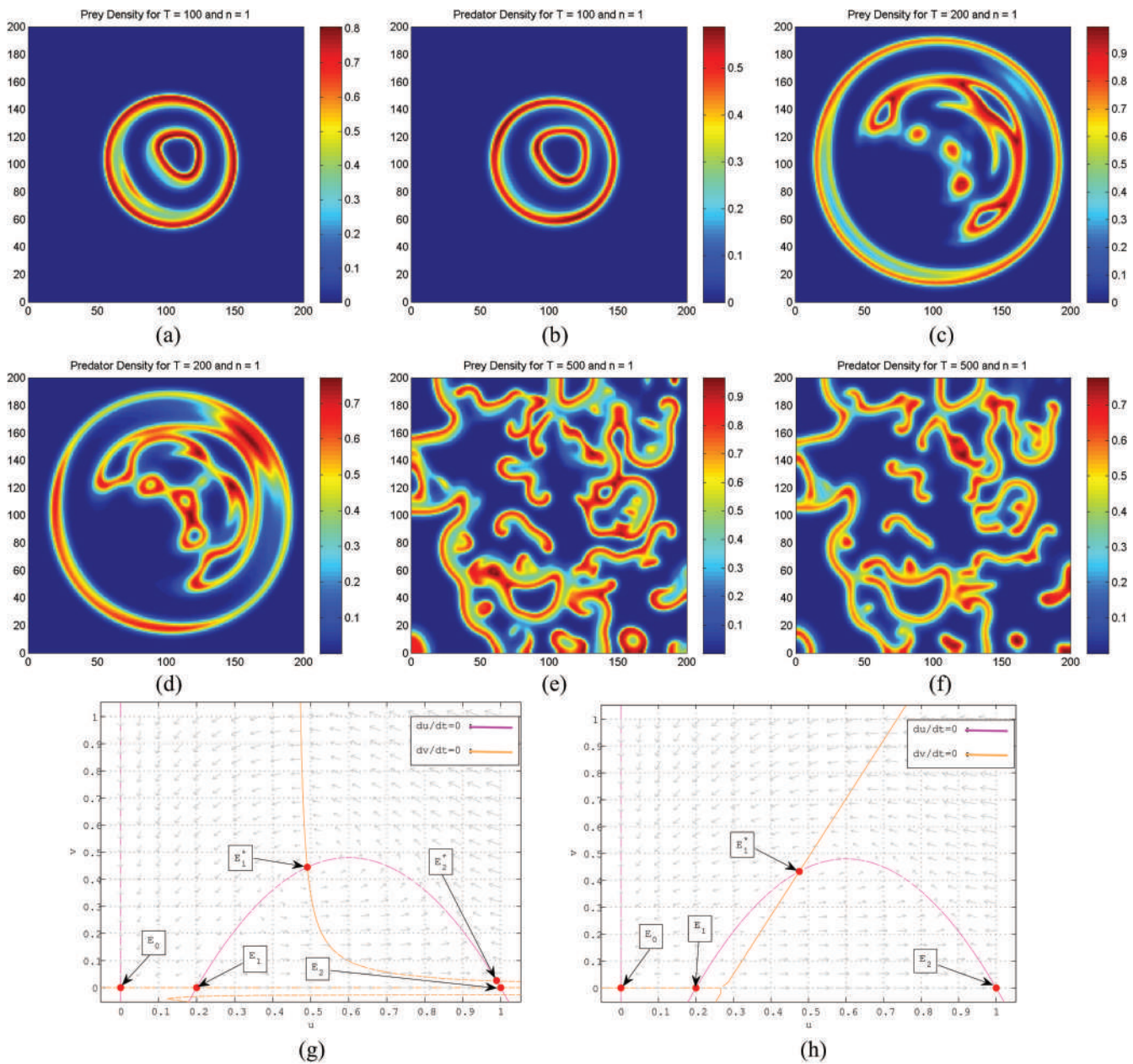
FIG. 5. Snapshots of species density distribution over the XY plane obtained at different time points (a)–(f) for parameter values $\gamma = 3$, $\alpha_1 = 0.2$, $\alpha = 0.03$, $\delta = 0.46$, $\rho_d = 1$, and $n = 1$. The density color bar suggests the distribution of various densities of species over the region. Here, both the populations initially spread through double ring format and ultimately show patchy spread. (g) represents the respective local dynamics and (h) represents the local dynamics for $\alpha = 0.6$ and $n = 2$.

becomes abundant with the regular spatial invasion structure. Next, we considered $\alpha = 0.1$ and $\delta = 0.37$ and observed that the density distribution of prey over space exhibits propagation of circular wavefront as time progresses, and this annulus region formed a ring-type circular wavefront traveling/expanding from

the place of the species initial conditions (see Fig. 4). Predator density distribution over the domain exhibits a ring-type circular wave, though they are not identically similar. In this case, the species are absent both in front of the front and behind the front. However, from an ecological perspective, this type of

system dynamics is paradoxical (see Ref. 24). In Fig. 5, we consider $\alpha = 0.03$ and $\delta = 0.46$, i.e., from the region where both populations persist. At the early stage of the system dynamics (e.g., $t = 100$), the species distribution over the space exhibits a double ring pattern [see Figs. 5(a) and 5(b)]; as time progress at $t = 200$, the outer ring moves to the whole domain and the inner ring exhibits some more complex behavior [see Figs. 5(c) and 5(d)]. Now as time progress at $T = 300$, the species distribution over the whole domain exhibits irregular dynamics of separate patches [see Figs. 5(e) and 5(f)], which are not stationary, i.e., they change their position over time (due to evasion-pursuit mechanisms[38]), merge, disappear, and produce new patches. This behavior has not been observed before for the case when the Allee effect was incorporated in the prey population only.[15,24] Note that, since we considered the diffusion coefficients of the prey and predator are the same, so patterns cannot arise because of Turing instability[36,52] and should be ascribed to another mechanism.[53,54] For all the above-mentioned figures, the parameter values except α and δ are same as Fig. 3 with the initial conditions (6) and (7). An important point we observed is that the parameter set at which the patchy behavior occurred is not unique. Although we have not shown here for some different combinations of parameter values (e.g., $\alpha = 0.05$, $\delta = 0.46$), the patchy invasion can be observed. Moreover, the patchy invasion can be seen on some parameter combinations of α and δ within the blue region (not shown here) of Fig. 2(a).

- **Case II: *Quadratic mortality rate.*** If the abundance of the predator is quite rich, then density-dependent effects start to play an important role. For instance, the effect of stress, diseases, over-crowding, and intra-specific competition among the predators causes quadratic mortality rates.[55,56] To include this factor in our model, we will study the invasion dynamics of the prey and predator with a quadratic mortality rate in the predator (i.e., $n = 2$). For the successful invasion of species with a quadratic mortality term, one of the most important factors is species introduction, i.e., initial condition. As in our earlier numerical findings with linear mortality term and in this case, the initial condition for successful species invasion is that the initial invaded area of the prey should have greater than the initial invaded area of the predator and also the initial prey size should have greater than Allee threshold. We have performed the simulation and realized that the presence of quadratic mortality drastically changes the persistence region [see Fig. 2(b)] compared to the linear case. The only prey existence region (green) disappears, the extinction region (red) expands, and the co-existence region (blue) changes. A high value of the predator Allee coefficient (α) leads to the co-existence of both species. A typical parameter set has been chosen ($\alpha = 0.6, \delta = 0.46$) to observe the density distribution over the XY plane obtained for the prey and predator (figure not shown here). Here, the density distribution of prey and predator over space exhibits a ring-type circular wavefront, similar to Fig. 4 but with a bigger ring thickness. We do not consider any alternative food resource in our model for the predator so if the prey population becomes extinct so is the predator. We also studied the density distribution for the whole parameter range of Fig. 2(b) and did not find any kind of irregular behavior in invasion dynamics, which was the case in linear mortality.

2. Temporal analysis

When an exotic species invades some new regions outside their native place, its population size gradually increases with time. If $U(t)$ and $V(t)$ are the respective population size of the prey and predator population at time t, respectively, then $U(t)$ and $V(t)$ can be calculated by the following relation:

$$U(t) = \int_0^L \int_0^L u(x,y,t)\, dy\, dx,$$

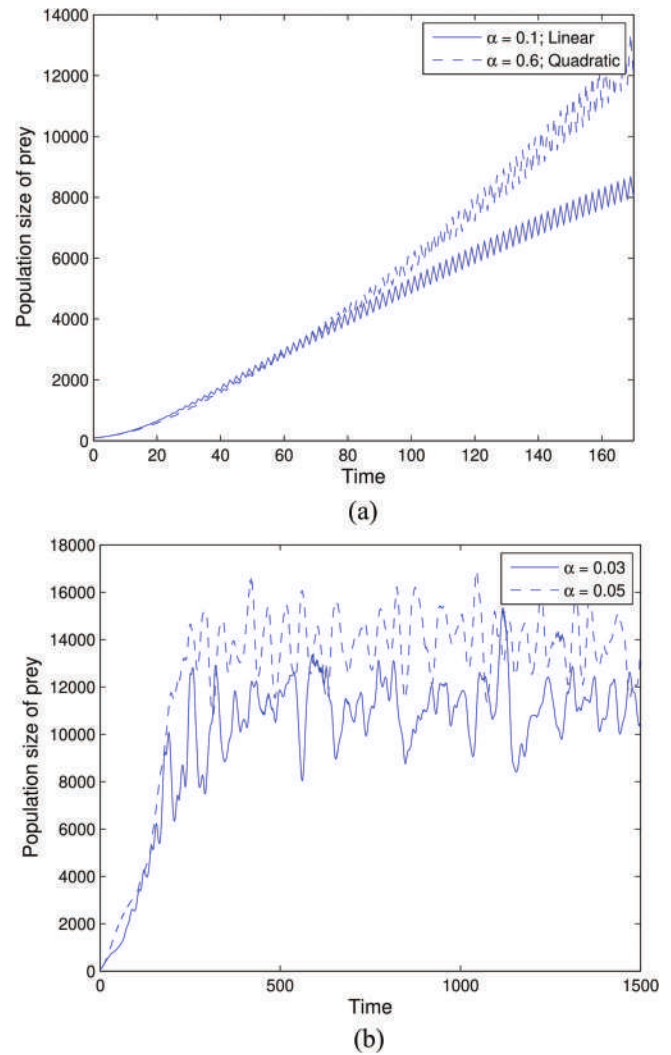$$V(t) = \int_0^L \int_0^L v(x,y,t)\, dy\, dx. \tag{12}$$

FIG. 6. Temporal variation of prey population size for different invasion scenarios: (a) corresponding to continuous traveling wave front with no spatiotemporal complexity in the wake, solid curve corresponds to Fig. 4 and dashed curve corresponds to $\alpha = 0.6$ (species density distribution is not shown); (b) corresponding to spatiotemporal complexity and patchy behavior, i.e., Fig. 5 corresponds to solid and dashed curves for $\alpha = 0.05$ (species density distribution is not shown).
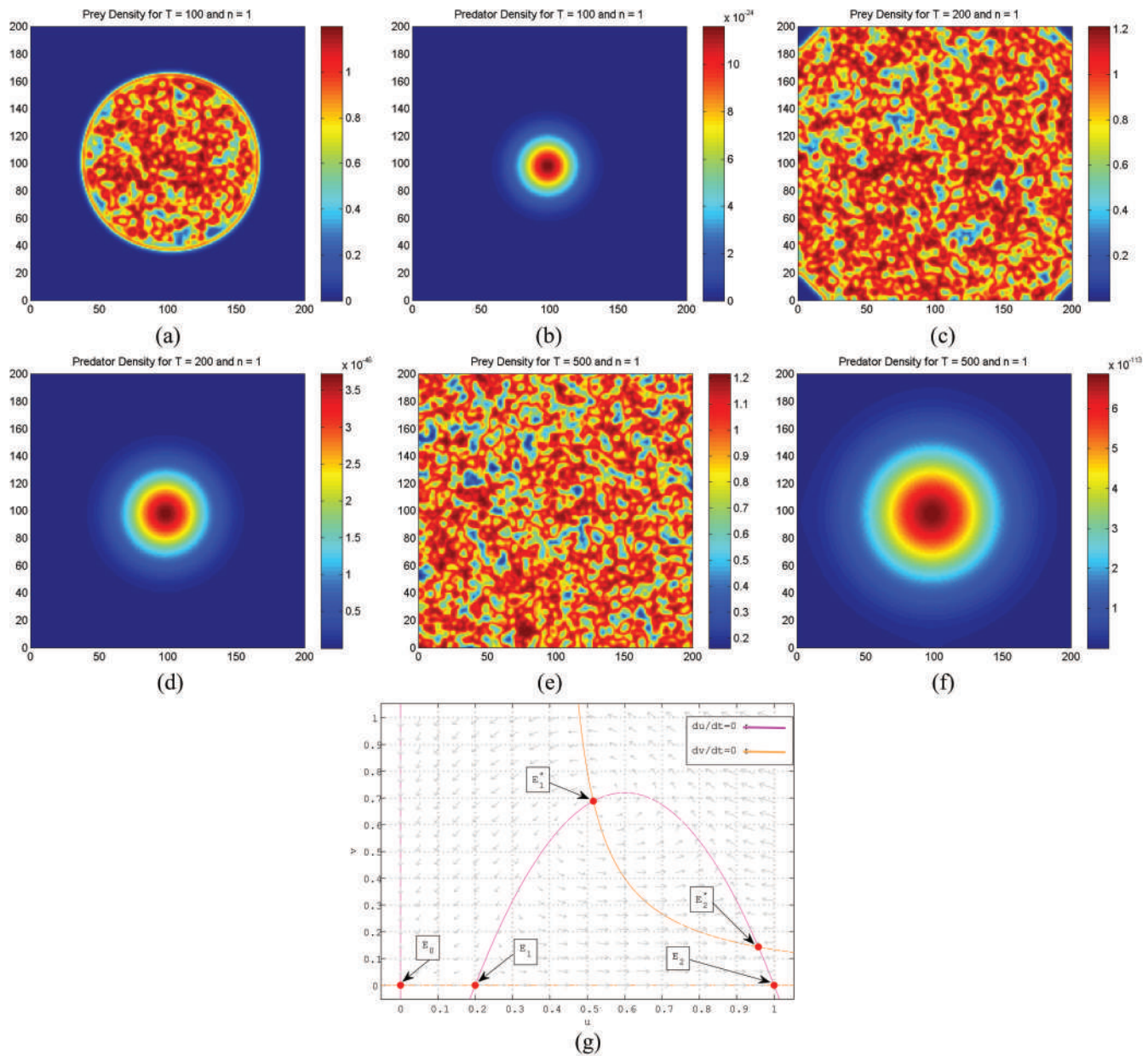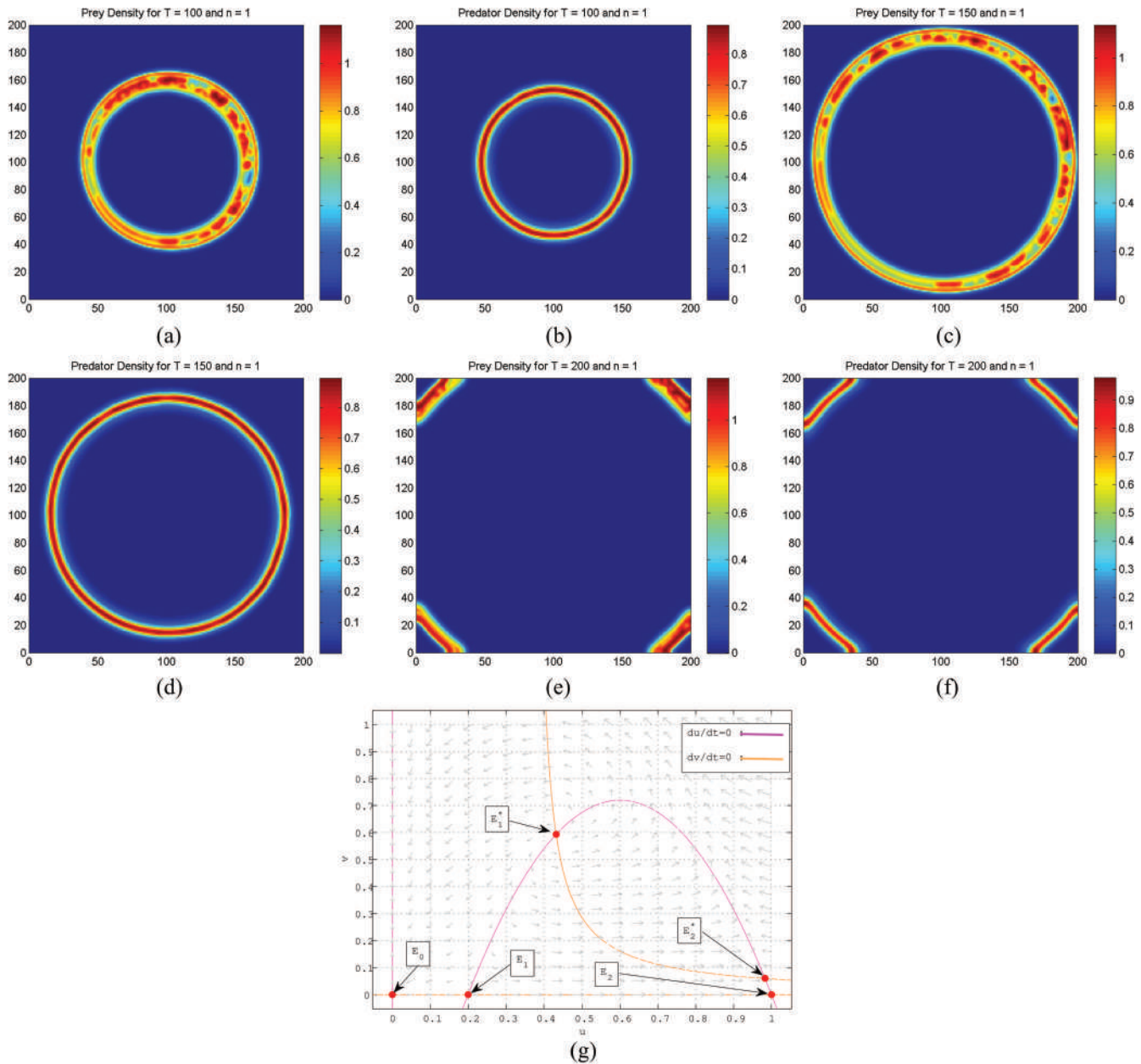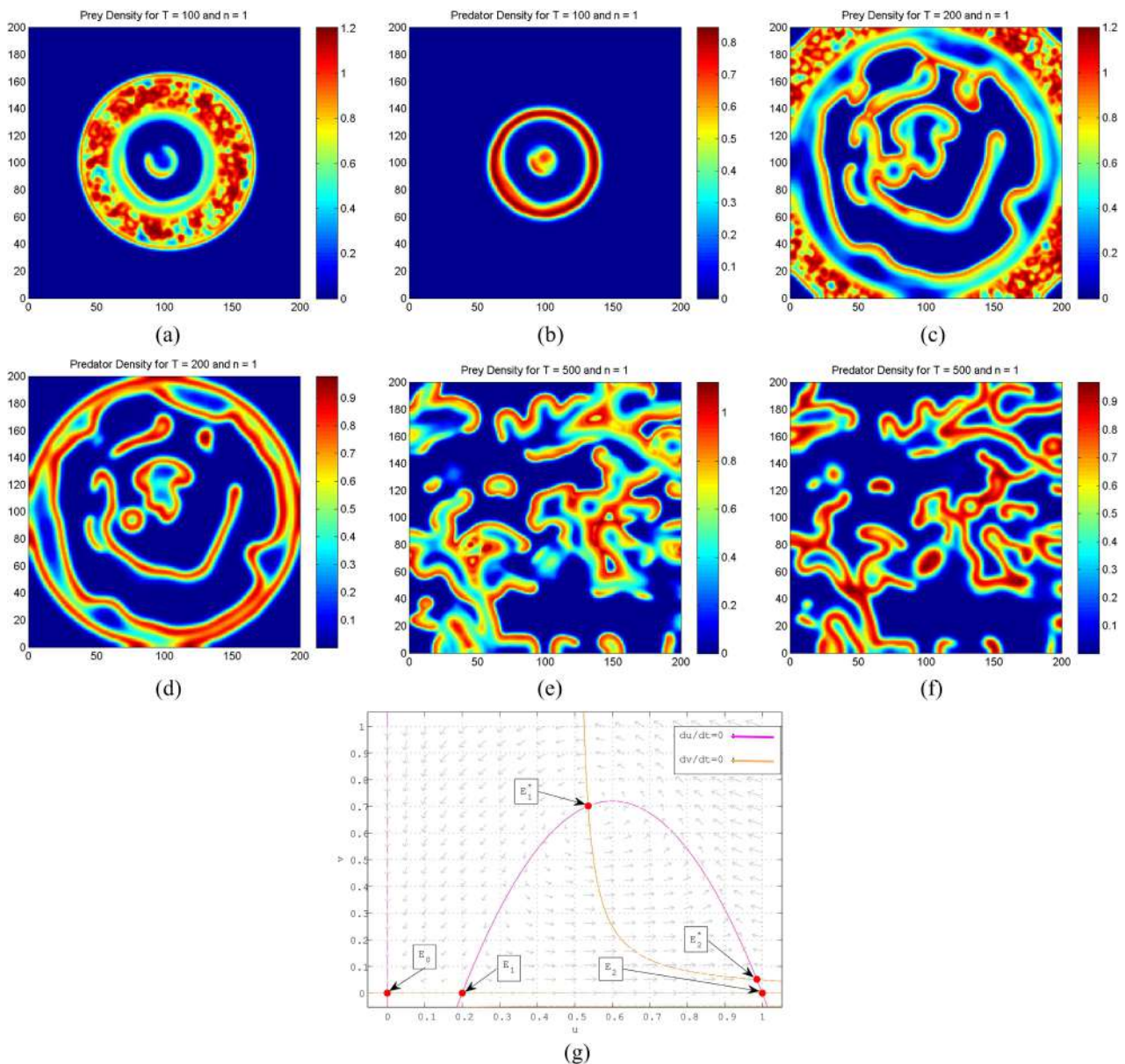
FIG. 7. Snapshots of species density distribution over the XY plane obtained at different time points (a)–(f) for parameter values $\gamma = 4.5$, $\alpha_1 = 0.2$, $\alpha = 0.2$, $\delta = 0.4$, $\rho_d = 1$, and $n = 1$. Density color bar suggests the distribution of various densities of species over the region. Here, the predator population goes to extinction and prey population abundant on the whole region through a "sun surface" like spread. (g) represents the respective local dynamics.

We have drawn the temporal variation of the prey population [see Fig. 3(e)] corresponding to the spatial distribution of Fig. 3 and did not observe any spatiotemporal complexity. The trajectory of $U(t)$ obtained corresponding to the invasion through smooth continuous wavefront with no spatiotemporal complexity in the wake

[see Fig. 6(a)], the solid curve obtained for $\alpha = 0.1$ with linear mortality rate (see Fig. 4) and the dashed curve obtained for $\alpha = 0.6$ with quadratic mortality (species density distribution not shown). Moreover, Fig. 6(b) corresponds to the regime obtained when spatiotemporal oscillation in the wake of the front and patchiness is
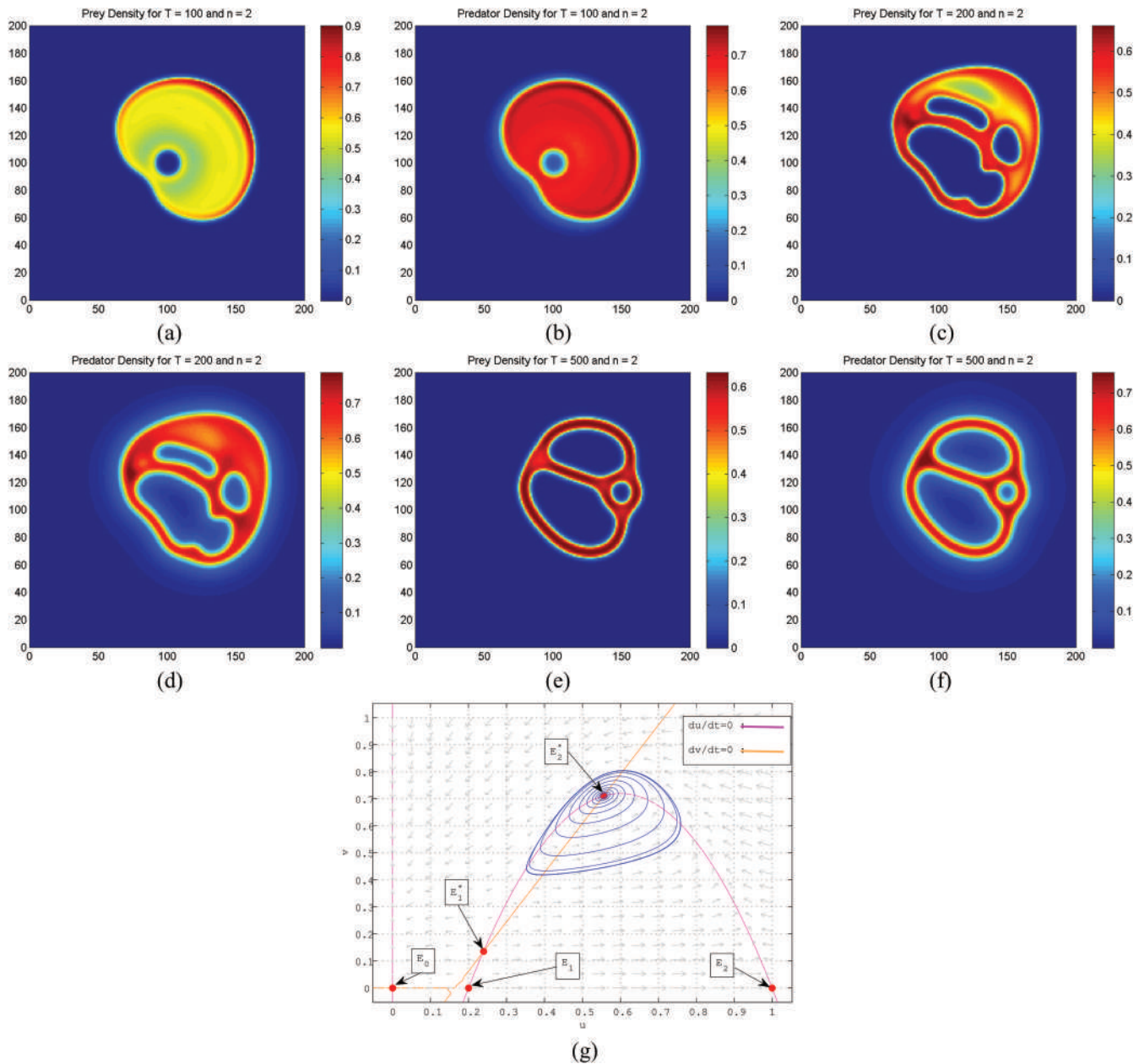
FIG. 8. Snapshots of species density distribution over the XY plane obtained at different time points (a)–(f) for parameter values $\gamma = 4.5$, $\alpha_1 = 0.2$, $\alpha = 0.1$, $\delta = 0.37$, $\rho_d = 1$, and $n = 1$. The density color bar suggests the distribution of various densities of species over the region. Here, both the populations spread through a ring wave. Figure 8(g) represents the respective local dynamics.

present, the solid curve is obtained for $\alpha = 0.03$ (see Fig. 5) and dashed curve is obtained for $\alpha = 0.05$. Figure 6(b) suggests that not only the spatial distribution of population density exhibits irregularity but also the population sizes experience irregular temporal fluctuations. A detailed study on this type of irregularities has been performed in Sec. VI.

B. High value of maximum per capita growth rate

1. Different types of mortality

- **Case I:** *Linear mortality rate*
  We have numerically simulated our proposed model and observed that, with the linear mortality rate of predator and with

FIG. 9. Snapshots of species density distribution over the XY plane obtained at different time points (a)–(f) for parameter values $\gamma = 4.5$, $\alpha_1 = 0.2$, $\alpha = 0.05$, $\delta = 0.5$, $\rho_d = 1$, and $n = 1$. The density color bar suggests the distribution of various densities of species over the region. Here, both the populations show complex behavior. (g) represents the respective local dynamics.

the Allee effect, both the prey and predator exhibit a different kind of invasion regimes. We have taken three different sets of parameter values from a different region of Fig. 2(c) with initial conditions given by (6) and (7). Here, the fixed parameters are $\alpha_1 = 0.2$, $\gamma = 4.5$, and $\rho_d = 1$. Finally, the predator Allee coefficient (α), and the mortality rate (δ) were varied to study invasion dynamics of both the prey and the predator populations.

The species distributions studied in this section are completely new compared to Sec. V A. To the best of our knowledge, these type of figures are unique (except the ring wavefront) and were not discovered in previous studies. In Fig. 7, we consider the parameters $\alpha = 0.2$ and $\delta = 0.4$ from the green region of Fig. 2(c). Figures 7(a) and 7(b) depict the density distribution over the XY plane obtained at time point $t = 100$ for the prey and

FIG. 10. Snapshots of species density distribution over the *XY* plane obtained at different time points (a)–(f) for parameter values $\gamma = 4.5$, $\alpha_1 = 0.2$, $\alpha = 0.3$, $\delta = 0.55$, $\rho_d = 1$, and $n = 2$. The density color bar suggests the distribution of various densities of species over the region. Here, both the populations coexist in a colonial form. (g) represents the respective local dynamics.

predator populations, respectively. Similarly, Figs. 7(c) and 7(d) depict the density distribution over the *XY* plane obtained at time point $t = 200$ for the prey and predator, respectively, and so on. Therefore, we can say that the predator population goes extinct and the prey population becomes abundant with a special

type of spatial invasion structure that looks like the "surface of the sun." For $\alpha = 0.1$ and $\delta = 0.37$, the density distribution of the prey over space exhibits propagation of circular wavefront as time progresses, and this annulus region formed a ring-type circular wavefront traveling/expanding from the place of the

species initial conditions (see Fig. 8). Predator density distribution over the domain exhibits similar behavior. In this case, the species are absent in both front and behind the wave, which is a paradoxical scenario from the ecological perspective. In Fig. 9, we consider $\alpha = 0.05$ and $\delta = 0.5$, i.e., from the region where both the populations persist [see Fig. 2(c)]. At the early stage of the system dynamics (say, $t = 100$), the species distribution over the space exhibits a double ring pattern; as time progress at $t = 200$, the inner ring moves to the whole domain and the outer ring exhibits some more complex behavior. Now as time progress at $T = 500$, the species distribution over the whole domain exhibits irregular dynamics of separate patches in a non-stationary manner, and these merge, disappear, and produce new patches. It is worth mentioning that the species distributions presented here are not due to Turing instability as we have considered the equal values of diffusion coefficients, and consequently, the patterns are obtained here through a non-Turing mechanism. For all the above-mentioned figures, the parameter values except α and δ are same as Fig. 7 with the initial conditions (6) and (7). An important point to be emphasized here is that the parameter set at which patchy behavior occurred is not unique. Moreover, the patchy invasion can be seen on some parameter combinations of α and δ within the blue region (not shown here) of Fig. 2(c).

- **Case II:** *Quadratic mortality rate*
  For quadratic mortality, the persistence region changes drastically [see Fig. 2(d)] compared to the linear case. The only prey existence region (green) disappears, the extinction region (red) expands, and the co-existence region (blue) gets smaller. A high value of the predator Allee coefficient (α) leads to the co-existence of both species. A typical parameter set has been chosen ($\alpha = 0.3, \delta = 0.55$) to demonstrate the density distribution over the XY plane obtained for the prey and predator in Fig. 10. The left column corresponds to prey density distribution at different time points, and the right column is for predator density distribution. Figures 10(a), 10(c), and 10(e) depict the prey density distribution in the XY plane corresponding to the time points $t = 100, 200,$ and 500, respectively. Figures 10(b), 10(d), and 10(f) depict the predator density distribution in XY plane corresponding to the time points $t = 100, 200,$ and 500, respectively. Here, the density distribution of the prey and predator over space exhibit a "three-hole colony type" form, and it is completely a new structure we have observed in our study.

2. Temporal dynamics

Figure 11 shows that the population size of the prey is calculated at different time points [$U(t)$] for parameter values corresponding to different invasion regimes. Figure 11(a) suggests that not only the spatial distribution of population density exhibits irregularity but also for the population sizes experience irregular temporal fluctuations, and Fig. 11(b) corresponds to continuous traveling wavefront with a complex spatiotemporal structure. Figure 12(a) corresponds to the regime obtained when patchiness is present, and Fig. 12(b) corresponds to fixed territorial distribution with a new type of spatiotemporal distribution.
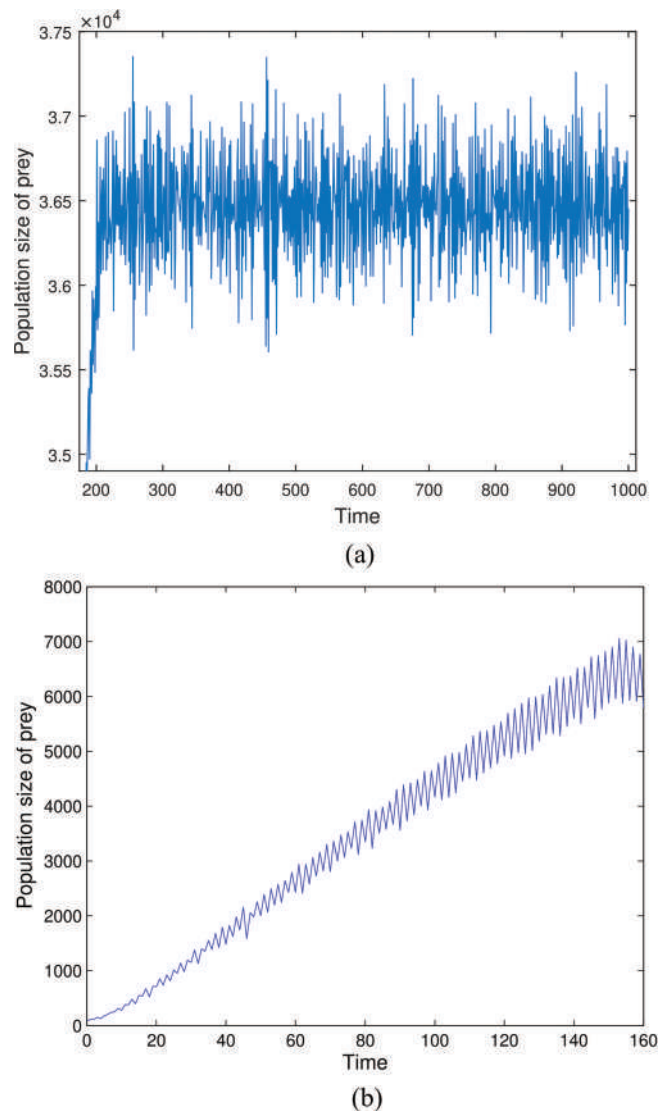

FIG. 11. Temporal variation of prey population size for different invasion scenarios: (a) corresponding to spatiotemporal complexity, i.e., Fig. 7; (b) Continuous traveling wave front with no spatiotemporal complexity, i.e., Fig. 8.

VI. EXISTENCE OF CHAOS IN DIFFERENT INVASION REGIMES

Asymmetrical temporal fluctuations of the population size obtained for low per capita growth rate with $\alpha = 0.03$ and $\alpha = 0.05$ [see Fig. 6(b)] seem to indicate that system dynamics is chaotic. Similar chaotic behavior is found for a high per capita growth rate with $\alpha = 0.2$ and $\alpha = 0.05$ [see Figs. 11(a) and 12(a)]. We also verified that the corresponding homogeneous system, i.e., Eq. (5) without diffusion terms, cannot exhibit behavior more complex than periodic (see Sec. III A). Thus, chaos in the behavior of the system,
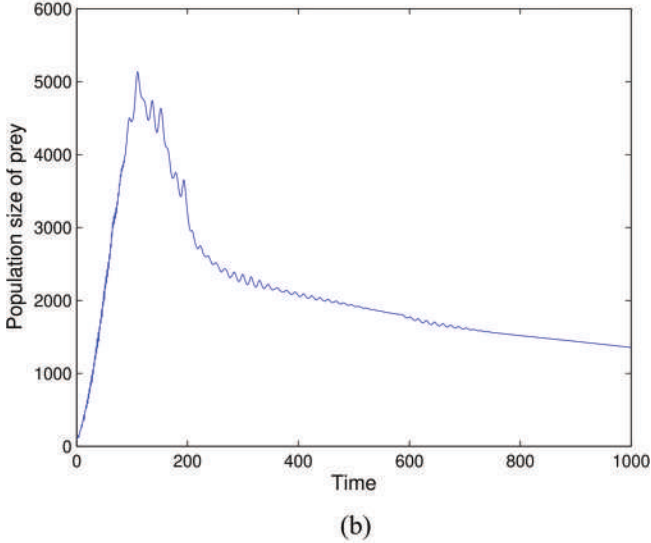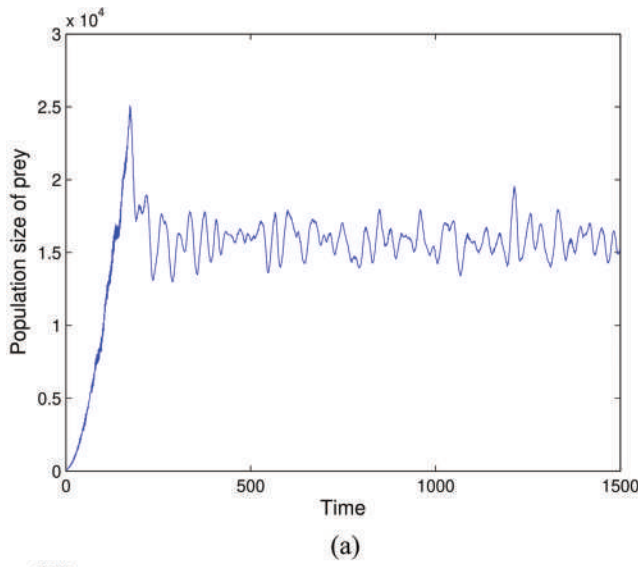
FIG. 12. Temporal variation of prey population size for different invasion scenarios: (a) corresponding to spatiotemporal complexity and patchy behavior, i.e., Fig. 9; (b) corresponding to continuous traveling wave front with no spatiotemporal complexity in the wake corresponds to Fig. 10.
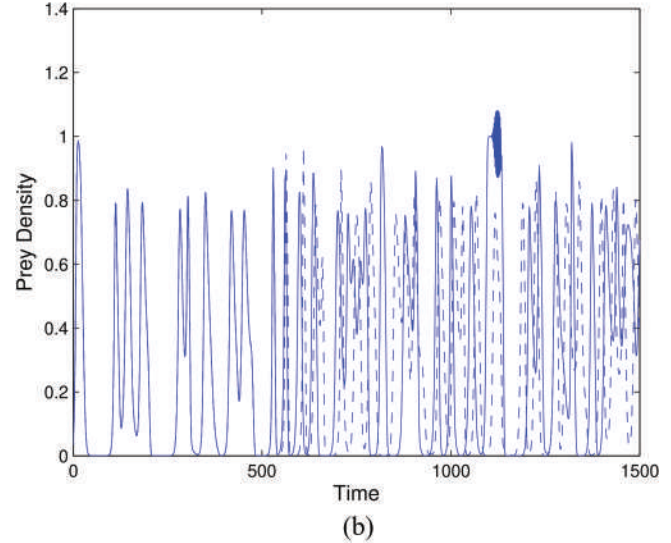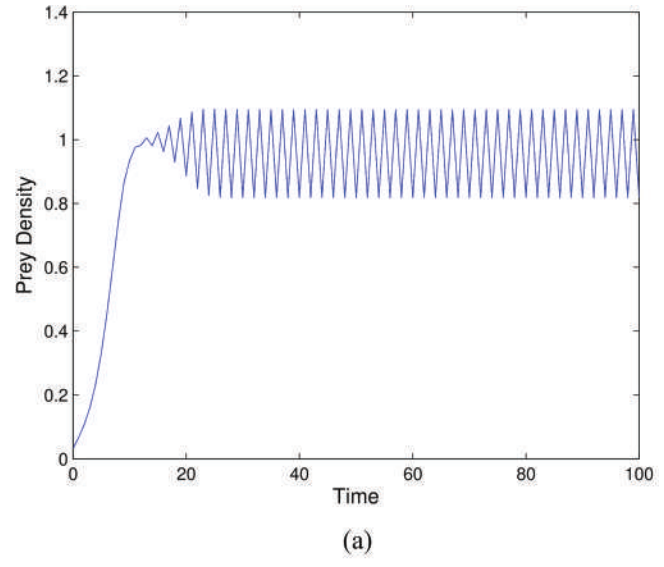

FIG. 13. Temporal oscillations of prey density at a fixed point $(100, 110)$ in the XY plane, subject to a small perturbation of the initial conditions, solid curve for the undisturbed system and dashed curve for the perturbed system; parameter values are (a) same as Fig. 3 and (b) same as Fig. 5.

i.e., Eq. (5), is a result of the system dynamics in space; this type of chaotic behavior is known as spatiotemporal chaos.[57–59] Irregularity in the system dynamics does not always correspond to chaotic dynamics and a more careful analysis is needed. Essentially, one of the basic properties of deterministic chaos is its sensitivity to the initial conditions so that the distance between the solutions corresponding to perturbed and unperturbed initial conditions grow with time.[60]

In order to check the above properties for different regimes obtained at various values of α, we varied the initial conditions (6)

and (7). Figure 13 shows the prey density over time for the unperturbed system (solid line) and the perturbed system (dashed line) obtained at a fixed point $(100, 110)$ in the XY plane. Two different sets of parameter values are taken for Fig. 13: (a) same as Fig. 3 and (b) same as Fig. 5. The perturbed system was obtained from the unperturbed system by multiplying u_0 and v_0 in Eqs. (6) and (7) to the factor $1.000\,01$. It is readily seen that for the regime (a) there is a negligible difference between the two solutions, and for the regime (b) up to $T = 550$, the difference between the two solutions is very small; however, for $T > 550$, the difference grows rapidly. In
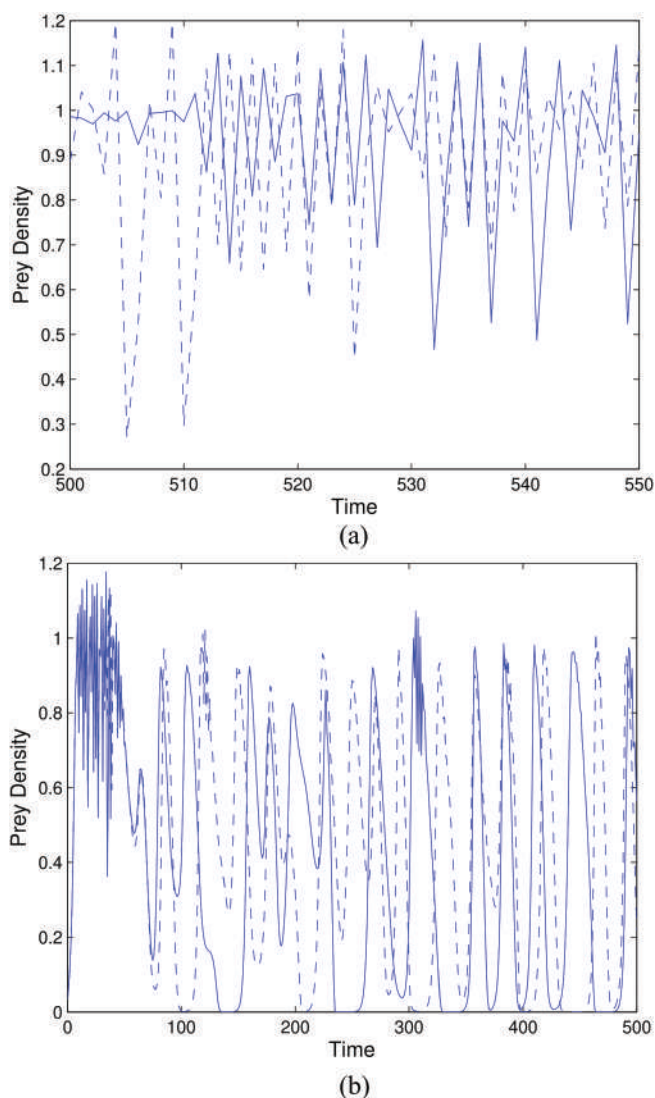
FIG. 14. Temporal oscillations of prey density at a fixed point (100, 110) in the *XY* plane, subject to a small perturbation of the initial conditions, solid curve for the undisturbed system and dashed curve for the perturbed system; parameter values are (a) same as Fig. 7 and (b) same as Fig. 9.
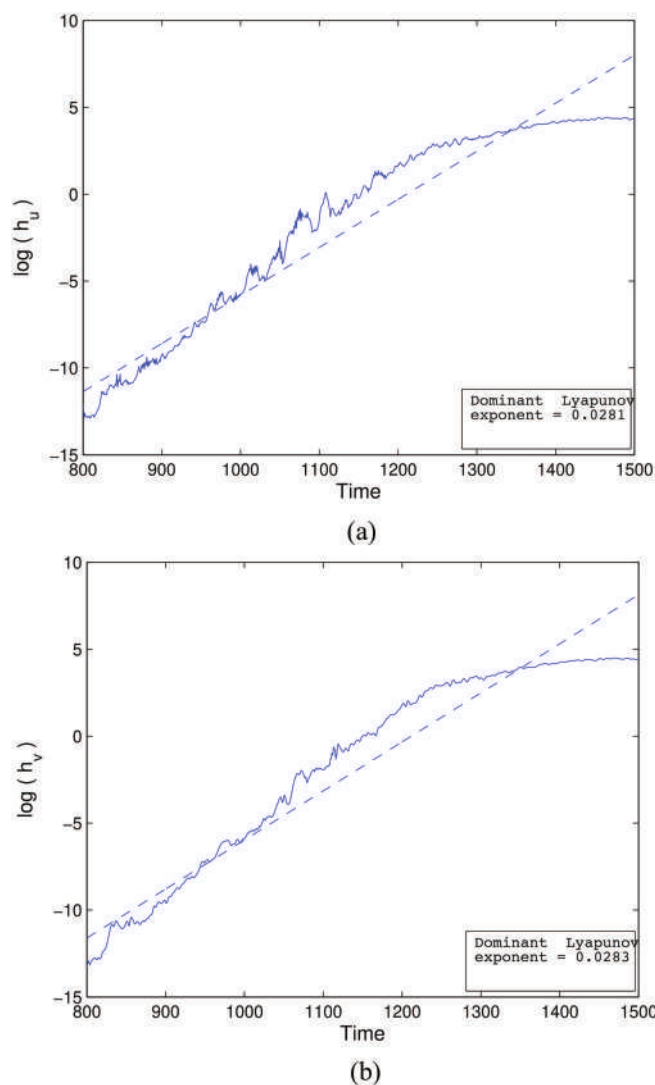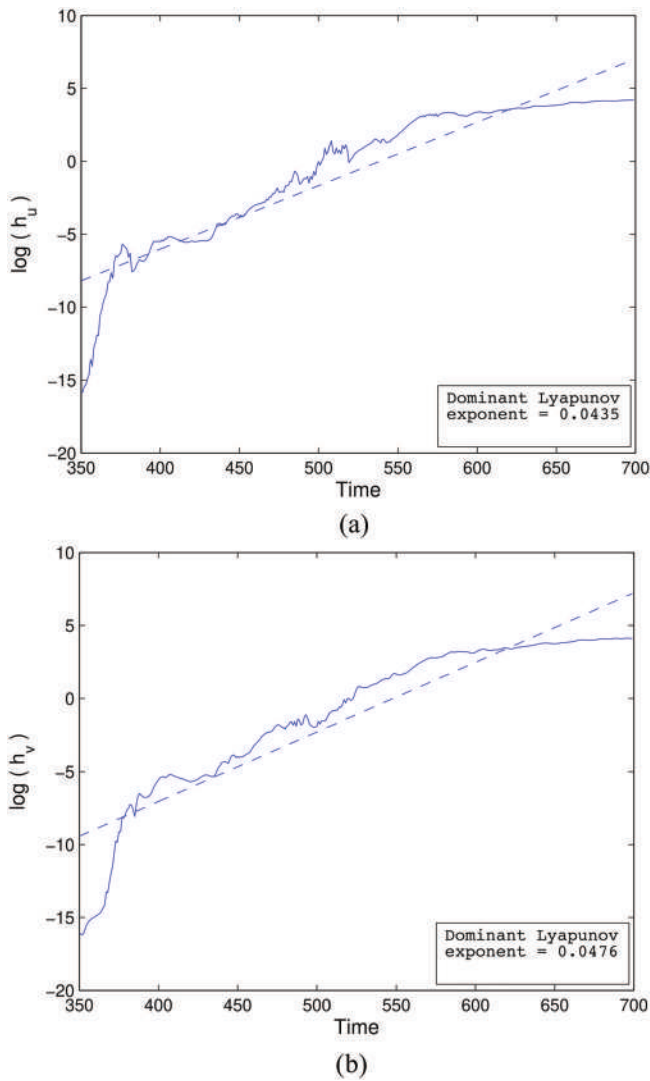

FIG. 15. Discrepancies (a) $h_u(t)$ and (b) $h_v(t)$ between two initially closed system trajectories. Parameter values are same as Fig. 5, i.e., when spatiotemporal oscillations in the wake of the expanding form.

Figs. 14(a) and 14(b), we have simulated the similar figure corresponding to the complex diagram (Figs. 7 and 9) and observed that the difference between the two solutions are significantly large. Similar results were also obtained for perturbation of other parameters and other positions in space (not shown here).

A more compact definition of deterministic chaos, however, requires the difference between the undisturbed and disturbed system with respect to the initial condition not just to be increasing but increasing exponentially. There are a number of methods available in the literature to calculate the dominant Lyapunov exponent

$\lambda_{\max}$.[61,62] In this paper, we have estimated the dominant Lyapunov exponent based on this definition.

In order to take into consideration both dynamical variables, i.e., the prey and predator densities, and also to take into consideration the spatial aspect, we analyze the behavior of the following two values:

$$h_u(t) = \| u\left(x, y, t\right) - u_1\left(x, y, t\right) \|,$$
$$h_v(t) = \| v\left(x, y, t\right) - v_1\left(x, y, t\right) \|, \tag{13}$$

FIG. 16. Discrepancies (a) $h_u(t)$ and (b) $h_v(t)$ between two initially closed system trajectories. Parameter values are same as Fig. 9, i.e., when regimes of patchy invasion.

where

$$\| u \| = \left(\int_0^L \int_0^L u^2(x, y) \, dy \, dx \right)^{1/2}. \qquad (14)$$

Analysis of the system sensitivity to phase perturbation only can be done when system dynamics are stationary. Until the species invade the whole region, the system dynamics apparently transient (see Figs. 6 and 11). Thus to estimate the dominant Lyapunov exponent, the system dynamics was studied for the post-invasion stage, i.e., for $t > t_{inv}$, where t_{inv} is the time that takes species to spread whole domain. For the parameters of Figs. 5, 7, and 9, the values of t_{inv} are approximately 322, 296, and 174, respectively.
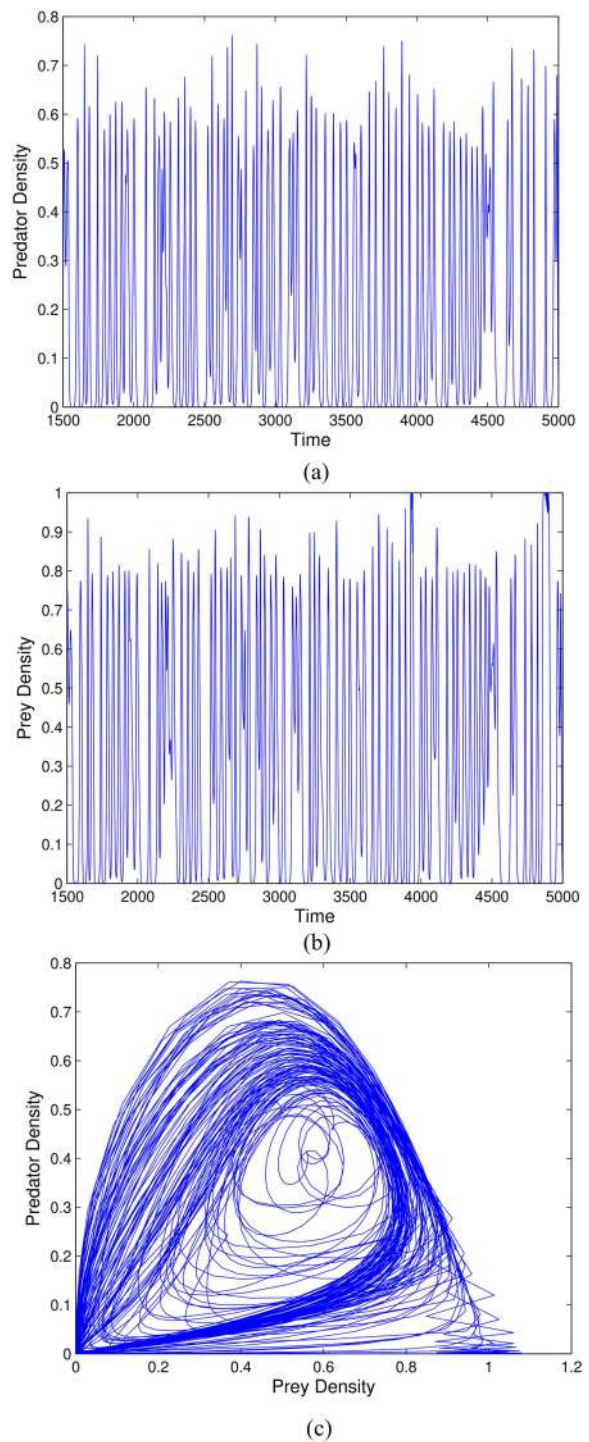
FIG. 17. Dynamics of the population densities calculated in a fixed point $(100, 110)$ in the XY plane. (a) Density of prey vs time, (b) density of predator vs time, and (c) local phase plane of the system, where the parameter values are same as in Fig. 5.

We considered the following method to estimate the dominant Lyapunov exponent. At any time $t_0 > t_{inv}$ a small perturbation is added to the system given by[24]

$$
\begin{aligned}
u_1(x, y, t_0) &= u(x, y, t_0) \left(1 + \varepsilon \cos \left[\frac{2\pi (x + y)}{L_0} \right] \right. \\
&\quad \left. - \varepsilon \cos \left[\frac{2\pi (x - y)}{L_0} \right] \right) \\
v_1(x, y, t_0) &= v(x, y, t_0) \left(1 + \varepsilon \sin \left[\frac{2\pi (x + y)}{L_0} \right] \right. \\
&\quad \left. - -\varepsilon \sin \left[\frac{2\pi (x - y)}{L_0} \right] \right)
\end{aligned}
\tag{15}
$$

The deviations h_u and h_v have been calculated using the dynamical variables u, v, u_1, and v_1 with initial conditions (15). Figure 15 shows $\ln(h_u)$ and $\ln(h_v)$ vs time calculated $\varepsilon = 10^{-9}$, $t_0 = 322$, and $L_0 = 100$ and for the same parameter as Fig. 5. The straight lines are approximated using least squares line approximation. From Figs. 15 and 16, it is clear that the absolute distance between the perturbed and unperturbed solutions grow exponentially with time (up to small fluctuations). Slope of the straight lines gives an estimate of dominant Lyapunov exponent, which came out to be $\lambda_{\max} = 0.0281 and 0.0283$ for the prey and predator dynamics, respectively. Similarly, Fig. 16 shows $\ln(h_u)$ and $\ln(h_v)$ vs time calculated $\varepsilon = 10^{-9}$, $t_0 = 174$, and $L_0 = 100$ and for the same parameter as Fig. 9. The dominant Lyapunov exponent in this case is estimated as $\lambda_{\max} = 0.0435 and 0.0476$ for prey and predator dynamics, respectively. Here, the value of the dominant Lyapunov exponent being positive indicates that Figs. 5 and 9 possess chaotic dynamics. A similar chaotic dynamics has also been observed for Fig. 7. We also calculate the density of prey and predator at a fixed point $(100, 110)$ and determine the corresponding phase portrait of the prey and predator at that particular point in the XY plane (see Fig. 17) parameter values are same as Fig. 5, and apparent irregularity suggests the existence of deterministic chaos. A similar irregular phase diagram (not shown here) suggests the existence of deterministic chaos for Fig. 9.

VII. DISCUSSION AND CONCLUSION

The biological invasion has several stages before the establishment of a new population to their non-native range. They move outside their non-native range through transportation, and after establishment, they go through the important stage known as the geographical spread. The non-native species range is formed by means of two phenomena: one is dispersal and the other is reproduction. Species mainly reproduce and, after some time, the young species move away from their parents and try to establish themselves in a non-native species range. Sometimes there are few adults present in the group of the dispersing population.[63] However, invasive species may cause damage to the native species.

In the present paper, we have addressed the invasion dynamics of a predator–prey system through reaction-diffusion equations. First, we performed an extensive numerical simulation and found

the persistence region for both prey and predator populations. The persistence region for the system in the presence of a linear mortality rate possesses mainly three types of scenarios: persistence of both populations, the persistence of only the prey population, and extinction of both populations, whereas for the quadratic mortality rate the persistence region changes to two scenarios: persistence of both populations and extinction of both populations. This persistence region gives an overview of the whole system dynamics with respect to the predator Allee effect and mortality. The blue region corresponds to the successful invasion of the predator population. Therefore, we can say that the predator Allee effect is a crucial factor for species persistence as well as successful invasion for linear mortality cases. We also observed that if the predator population goes through quadratic mortality, it is impossible for them to invade and persist with the prey population without the Allee effect. Second, the presence of the predator Allee effect leads to different types of spreading scenarios; some of them are completely new and not observed before. A previous study[24] based on the Allee effect on the prey population reveals mainly three kinds of spreading scenarios: circular wavefront, ring front, and patchy spread. However, in the presence of the Allee effect on both populations, we have found five types of spreading: circular wavefront, ring front, double ring front ultimately breaks into patchy spread after a certain time, sun surface spread, and patchy spread behind a thick ring front. A diagrammatic representation of these five types of spread on the (α, δ) plane has been displayed in Fig. 18. Here, we have mentioned the parametric regions for each type of spread. These two figures show how much the five types of spread are expected to depend on the current choice of (α, δ). As we have analyzed all the choices of (α, δ) and identified various types of spreading regions, it implies that the spreads are robust. It implies that the predator Allee effect has a potential impact on the system spatiotemporal dynamics. Third, the invasion dynamics with respect to quadratic mortality leads to a special type of colonial pattern with three holes surrounded by species density. Fourth, the Allee effect leads to a double ring wavefront and ultimately exhibits spatiotemporal chaos. A new type of spatial dynamics (it looks like "sun surface") occurs with respect to the Allee effect for a high value of per capita growth rate. We also observed a dense ring of species spatial pattern and after the wavefront propagates through the spatial boundary the patchy chaotic dynamics observed. We have found that several patchy, as well as irregular, spreads ultimately lead to chaotic fluctuations. These irregular chaotic fluctuations have been studied through varying initial conditions as well as by computing Lyapunov coefficients. The patchy invasion occurred over the whole spatial domain, and the simulation based on average density shows that chaotic dynamics are present. Here, the patterns are not formed due to Turing instability as the diffusivities of the species are equal. For non-Turing pattern formation, effective analytical methods are yet to be developed, and results are usually obtained by means of computer simulations.[64] In general, the predator–prey interactions shape the geometry of the ecological patchiness and the properties of the system's spatiotemporal dynamics.[64] Moreover, it is possible that the chaotic spatiotemporal population oscillations are triggered by the traveling front.[64] A similar idea was discussed by Lee et al.[65] that the spatiotemporal patterns may be produced by the interaction of propagating fronts. We also want to emphasize that in Fig. 7, the prey population has some kind
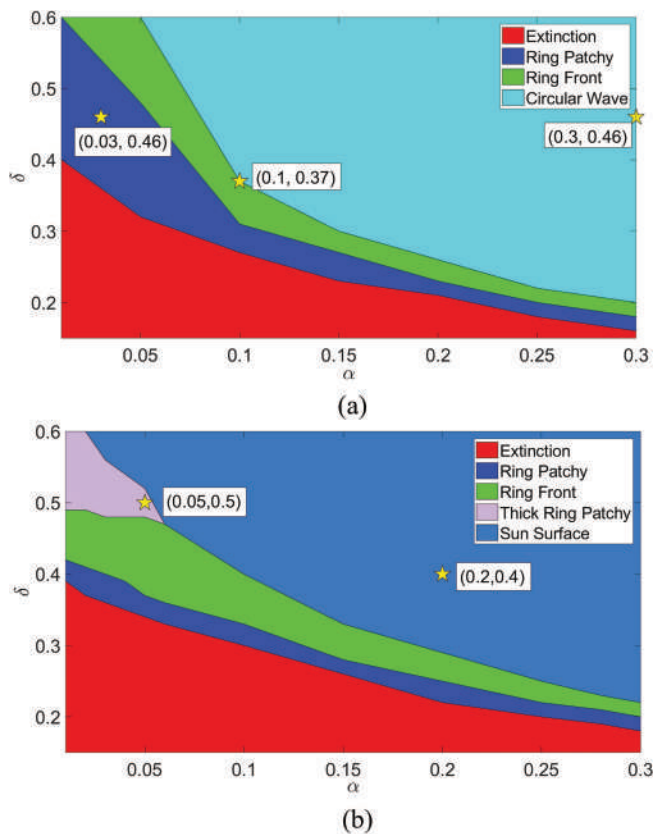
FIG. 18. The distribution of five types of spread in the (α, δ) plane. Different color regions denote the occurrence of a particular spread for the combination of (α, δ). (a) Low value of γ shows three types of spread and (b) high value of γ shows two new types of spread.

of complex dynamics and the predator population goes to extinction. Although initially the predator population has a contribution to the overall dynamics of the system, as time goes by the predator population becomes smaller and ultimately goes to extinction. In the invasion process, it is also possible that the predator population cannot establish themselves as an invasive species and goes to extinction. In that case, the prey population spreads in the entire domain although there are several other factors that may influence their spread, such as the Allee effect, density dependence, and intraspecific competition.[66] It is to be noted that pattern formation is possible for interacting species dynamics even if only one species has spatial movement.[67] It is also possible for a single species reaction-diffusion system.[68]

According to the authors' knowledge, methods based on the exponential dependence on initial conditions and the computation of dominant Lyapunov exponents are very popular to detect chaos in a dynamical system. However, there are several other promising methods available in the literature to detect chaos. The detection of chaos through the power spectra of the system was discussed by

Pascual.[57] A statistical computational procedure based on a comparison of the prediction power of linear and nonlinear models of the Volterra–Wiener form was studied by Barahona and Poon.[69] Recently, Toker *et al.*[70] discussed the "chaos decision tree algorithm" and showed that it performs with very high accuracy across a wide variety of both real and simulated systems, even in the presence of relatively high levels of measurement noise. However, to study the dynamics of a random point over time within the spatial domain, we have selected a point in the *XY* plane and studied its dynamics over time. The time series and phase plot both show a very fluctuating and irregular pattern indicating the chaotic dynamics. Therefore, we can say that the predator Allee effect is a crucial factor for the persistence of both populations as well as for successful invasion.

AUTHORS' CONTRIBUTIONS

S.R., A.R.B., and T.S. designed and performed the research and wrote the paper.

ACKNOWLEDGMENTS

DATA AVAILABILITY

The data that support the findings of this study are available within the article.

REFERENCES

[1]C. S. Elton, *The Ecology of Invasions by Animals and Plants* (Methuen, London, 1958).
[2]J. A. Drake, H. A. Mooney, F. di Castri, R. H. Groves, F. J. Kruger, M. Rejmanek, and M. Williamson, *Biological Invasions: A Global Perspective* (John Wiley, New York, 1989).
[3]N. Shigesada and K. Kawasaki, *Biological Invasions: Theory and Practice* (Oxford University Press, Oxford, 1996).
[4]K. Grayson and D. Johnson, "Novel insights on population and range edge dynamics using an unparalleled spatiotemporal record of species invasion," J. Anim. Ecol. **87**, 581–593 (2017).
[5]H. A. Mooney, R. N. Mack, J. A. McNeely, L. E. Neville, P. J. Schei, and J. K. Waage, *Invasive Alien Species: A New Synthesis* (Island Press, Washington, DC, 2005).
[6]C. Baker, F. Diele, D. Lacitignola, C. Marangi, and A. Martiradonna, "Optimal control of invasive species through a dynamical systems approach," Nonlinear Anal.: Real World Appl. **49**, 45–70 (2019).
[7]D. Pimentel, *Techniques for Reducing Pesticide Use: Economic and Environmental Benefits* (John Wiley and Sons, Chichester, 1997).
[8]M. Kot, M. A. Lewis, and P. Van den Driessche, "Dispersal data and the spread of invading organisms," Ecology **77**, 2027–2042 (1996).
[9]M. H. Wang and M. Kot, "Speeds of invasion in a model with strong or weak Allee effects," Math. Biosci. **171**, 83–97 (2001).
[10]M. R. Owen and M. A. Lewis, "How predation can slow, stop or reverse a prey invasion," Bull. Math. Biol. **63**, 655–684 (2001).
[11]A. Giometto, A. Rinaldo, F. Carrara, and F. Altermatt, "Emerging predictable features of replicated biological invasion fronts," Proc. Natl. Acad. Sci. U.S.A. **111**, 297–301 (2014).
[12]M. Bonneau, F. Johnson, and C. Romagosa, "Spatially explicit control of invasive species using a reaction-diffusion model," Ecol. Modell. **337**, 15–24 (2016).
[13]W. Wang, J. Shi, and J. Wang, "Persistence and extinction of population in reaction-diffusion-advection model with strong Allee effect growth," J. Math. Biol. **78**, 2093–2140 (2019).

[14]M. Lewis and P. Kareiva, "Allee dynamics and the spread of invading organisms," Theor. Popul. Biol. **43**, 141–158 (1993).

[15]S. V. Petrovskii, A. Morozov, and E. Venturino, "Allee effects makes possible patchy invasion in a predator-prey system," Ecol. Lett. **5**, 345–352 (2002).

[16]W. C. Allee, *Animal Aggregations, A Study in General Sociology* (The University of Chicago Press, Chicago, IL, 1931).

[17]A. A. Berryman and P. Kindlmann, *Population Systems: A General Introduction* (Springer, 2008).

[18]B. Dennis, "Allee effects: Population growth, critical density and the chance of extinction," Nat. Resour. Model. **3**, 481–538 (1989).

[19]H. T. Odum and W. C. Allee, "A note on the stable point of populations showing both intraspecific cooperation and disoperation," Ecology **35**, 95–97 (1954).

[20]M. Groom, "Allee effects limit population viability of an annual plant," Am. Nat. **151**, 487–496 (1998).

[21]M. Kuussaari, I. Saccheri, M. Camara, and I. Hanski, "Allee effect and population dynamics in the glanville fritillary butterfly," Oikos **82**, 384–392 (1998).

[22]A. Stoner and M. Ray-Culp, "Evidence for Allee effects in an over-harvested marine gastropod: Density dependent mating and egg production," Mar. Ecol. Prog. Ser. **202**, 297–302 (2000).

[23]F. Courchamp, B. Grenfell, and T. Clutton-Brock, "Impact of natural enemies on obligately cooperative breeders," Oikos **91**, 311–322 (2000).

[24]A. Morozov, S. Petroveskii, and B.-L. Li, "Spatiotemporal complexity of patchy invasion in a predator-prey system with the Allee effect," J. Theor. Biol. **238**, 18–35 (2006).

[25]A. Medvinsky, S. Petrovskii, I. Tikhonova, H. Malchow, and B. Li, "Spatiotemporal complexity of plankton and fish dynamics," SIAM Rev. **44**, 311–370 (2002).

[26]W. Alharbi and S. Petrovskii, "Effect of complex landscape geometry on the invasive species spread: Invasion with stepping stones," J. Theor. Biol. **464**, 85–97 (2019).

[27]M. Kohnke and H. Malchow, "Disease-induced chaos, coexistence, oscillations, and invasion failure in a competition-model with strong Allee effect," Math. Biosci. **317**, 108267 (2019).

[28]S. McDermott and D. Finnoff, "Impact of repeated human introductions and the Allee effect on invasive species spread," Ecol. Modell. **329**, 100–111 (2016).

[29]K. Manna and M. Banerjee, "Stationary, non-stationary and invasive patterns for a prey-predator system with additive Allee effect in prey growth," Ecol. Complex. **36**, 206–217 (2018).

[30]C. Brown, H. Ferris, S. Fu, and R. Plant, "Modeling direct positive feedback between predators and prey," Theor. Popul. Biol. **65**, 143–152 (2004).

[31]R. Sussman and P. Garber, "A new interpretation of the social organization and mating system of the Callitrichidae," Int. J. Primatol. **8**, 73–92 (1987).

[32]R. P. Freckleton, "Biological control as a learning process," Trends Ecol. Evol. **15**, 263–264 (2000).

[33]S.-R. Zhou, Y.-F. Liu, and G. Wang, "The stability of prey-predator systems subject to the Allee effects," Theor. Popul. Biol. **67**, 23–31 (2005).

[34]A. Liebhold and J. Bascompte, "The Allee effect, stochastic dynamics and eradication of alien species," Ecol. Lett. **6**, 133–140 (2003).

[35]R. K. Upadhyay, N. Kumari, and V. Rai, "Wave phenomena and edge of chaos in a diffusive predator-prey system under Allee effect," Differ. Equ. Dyn. Syst. **17**, 301–317 (2009).

[36]L. A. Segel and J. L. Jackson, "Dissipative structure: An explanation and an ecological example," J. Theor. Biol. **37**, 545–59 (1972).

[37]R. M. Nisbet and W. S. C. Gurney, *Modelling Fluctuating Populations* (John Wiley & Sons Inc., New York, 1982).

[38]J. Murray, *Mathematical Biology* (Springer, Berlin, 1989).

[39]E. E. Holmes, M. A. Lewis, J. E. Banks, and R. R. Veit, "Partial differential equations in ecology: Spatial interactions and population dynamics," Ecology **75**, 17–29 (1994).

[40]W. F. Fagan and J. G. Bishop, "Trophic interactions during primary succession: Herbivores slow a plant reinvasion at Mount St. Helens," Am. Nat. **155**, 238–251 (2000).

[41]M. Garvie, "Finite difference schemes for reaction-diffusion equations modeling predator-prey interactions in matlab," Bull. Math. Biol. **69**, 931–956 (2007).

[42]J. Bramble, *Multigrid Methods* (Longman Scientific & Technical, Essex, 1993).

[43]J. C. Strikwerda, *Finite Difference Schemes and Partial Differential Equations* (SIAM, 2004).

[44]C. Chiu, *A Multigrid Method for Solving Reaction-diffusion Systems* (Chapman and Hall, 2000).

[45]J. K. Hale, *Theory of Functional Differential Equations* (Springer, New York, 1971).

[46]D. Henry, *Geometric Theory of Semilinear Parabolic Equations*, Lecture Notes in Mathematics (Springer-Verlag, Berlin, 1981).

[47]R. Lande, "Extinction thresholds in demographic models of territorial populations," Am. Nat. **130**, 624–635 (1987).

[48]P. Amarasekare, "Allee effects in metapopulation dynamics," Am. Nat. **152**, 298–302 (1998).

[49]E. Bradford and J. R. Philip, "Stability of steady distributions of asocial populations dispersing in one dimension," J. Theor. Biol. **29**, 27–33 (1970).

[50]T. K. Soboleva, P. R. Shorten, A. B. Pleasants, and A. Rae, "Qualitative theory of the spread of a new gene into a resident population," Ecol. Model. **163**, 33–44 (2003).

[51]R. Etienne, B. Wertheim, L. Hemerik, P. Schneider, and J. Powell, "The interaction between dispersal, the Allee effect and scramble competition affects population dynamics," Ecol. Model. **148**, 153–168 (2002).

[52]S. A. Levin and L. A. Segel, "An hypothesis for the origin of planktonic patchiness," Nature **259**, 659 (1976).

[53]A. B. Medvinsky, S. V. Petrovskii, D. A. Tikhonov, I. A. Tikhonova, G. R. Ivanitsky, E. Venturino, and H. Malchow, "Biological factors underlying regularity and chaos in aquatic ecosystems: Simple models of complex dynamics," J. Biosci. **26**, 77–108 (2001).

[54]S. V. Petroveskii and H. Malchow, "Wave of chaos: New mechanism of pattern formation in spatiotemporal population dynamics," Theor. Popul. Biol. **59**, 157–174 (2001).

[55]A. Edwards and A. Yool, "The role of higher predation in Plankton population models," J. Plankton Res. **22**, 1085–1112 (2000).

[56]M. Baurmann, T. Gross, and U. Feudel, "Instabilities in spatially extended predator-prey systems: Spatio-temporal patterns in the neighborhood of turing-Hopf bifurcations," J. Theor. Biol. **245**, 220–229 (2007).

[57]M. Pascual, "Diffusion induced chaos in a spatial predator-prey system," Proc. R. Soc. Lond. B **251**, 1–7 (1993).

[58]J. A. Sherratt, M. A. Lewis, and A. C. Fowler, "Ecological chaos in the wake of invasion," Proc. Natl. Acad. Sci. U.S.A. **92**, 2524–2528 (1995).

[59]S. V. Petroveskii and H. Malchow, "A minimal model of pattern formation in a prey-predator system," Math. Comput. Model. **29**, 49–63 (1999).

[60]A. Nayfeh and B. Balachandran, *Applied Nonlinear Dynamics* (Wiley, New York, 1995).

[61]H. Kantz and T. Schreiber, *Nonlinear Time Series Analysis* (Cambridge University Press, Cambridge, 1997).

[62]A. Wolf, J. Swift, H. Swinney, and J. Vastano, "Determining Lyapunov exponents from a time series," Physica **16**, 285 (1985).

[63]J. Lockwood, M. Hoopes, and M. Marchetti, *Invasion Ecology* (Blackwell Publishing, 2007).

[64]H. Malchow, S. Petrovskii, and E. Venturino, *Spatiotemporal Patterns in Ecology and Epidemiology: Theory, Models, and Simulation* (Chapman and Hall, 2007).

[65]K. Lee, M. McCormick, Q. Ouyang, and H. Swinney, "Pattern formation by interacting chemical fronts," Science **261**, 192–194 (1993).

[66]S. Pal, S. Petrovskii, S. Ghorai, and M. Banerjee, "Spatiotemporal pattern formation in 2d prey-predator system with nonlocal intraspecific competition," Commun. Nonlinear Sci. Numer. Simulat. **93**, 105478 (2021).

[67]B. Ermentrout and M. Lewis, "Pattern formation in systems with one spatially distributed species," Bull. Math. Biol. **59**, 533–549 (1997).

[68]S. Paul, S. Ghosh, and D. Ray, "Reaction-diffusion systems with fluctuating diffusivity; spatio-temporal chaos and phase separation," J. Statist. Mech. Theory Exp. **3**, 033205 (2018).

[69]M. Barahona and C. Poon, "Detection of nonlinear dynamics in short, noisy time series," Nature **381**, 215–217 (1996).

[70]D. Toker, F. Sommer, and M. D'Esposito, "A simple method for detecting chaos in nature," Commun. Biol. **3**, 11 (2020).

Source details

Feedback >   Compare sources >

Chaos

Scopus coverage years: from 1991 to Present

Publisher: American Institute of Physics

ISSN: 1054-1500   E-ISSN: 1089-7682

Subject area: (Mathematics: Mathematical Physics) (Mathematics: Applied Mathematics) (Physics and Astronomy: Statistical and Nonlinear Physics)
(Physics and Astronomy: General Physics and Astronomy)

Source type: Journal

View all documents >   Set document alert   💾 Save to source list

CiteScore 2022   ⓘ
5.9

SJR 2022   ⓘ
0.820

SNIP 2022   ⓘ
1.127

CiteScore   CiteScore rank & trend   Scopus content coverage

Journal Pre-proof

Assessment of Lockdown Effect in Some States and Overall India: A Predictive Mathematical Study on COVID-19 Outbreak

Tridip Sardar, Sk Shahid Nadim, Sourav Rana, Joydev Chattopadhyay
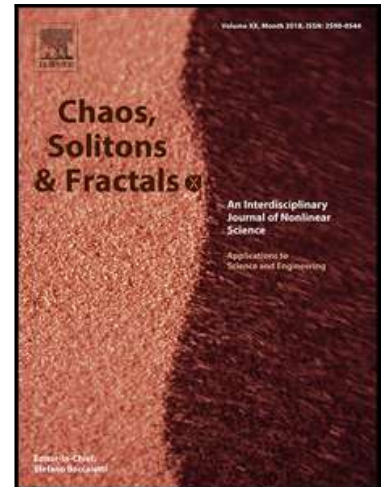
Please cite this article as: Tridip Sardar, Sk Shahid Nadim, Sourav Rana, Joydev Chattopadhyay, Assessment of Lockdown Effect in Some States and Overall India: A Predictive Mathematical Study on COVID-19 Outbreak, *Chaos, Solitons and Fractals* (2020), doi: https://doi.org/10.1016/j.chaos.2020.110078

Highlights

- A new mathematical model on COVID-19 that incorporates lockdown effect

- Several model parameters as well as the basic reproduction number are estimated

- We provide ensemble model forecast under five different lockdown scenarios

- Correlation between important parameters with the lockdown effect are derived

- Combining all the results, we proposed an effective lockdown policy

1

Assessment of Lockdown Effect in Some States and Overall India: A Predictive Mathematical Study on COVID-19 Outbreak

Tridip Sardar [1a], Sk Shahid Nadim[b], Sourav Rana[c], Joydev Chattopadhyay[b]

[a]*Department of Mathematics, Dinabandhu Andrews College, Kolkata, India*
[b]*Agricultural and Ecological Research Unit, Indian Statistical Institute, Kolkata, India*
[c]*Department of Statistics, Visva-Bharati University, Santiniketan, West Bengal, India*

Abstract

In the absence of neither an effective treatment or vaccine and with an incomplete understanding of the epidemiological cycle, Govt. has implemented a nationwide lockdown to reduce COVID-19 transmission in India. To study the effect of social distancing measure, we considered a new mathematical model on COVID-19 that incorporates lockdown effect. By validating our model to the data on notified cases from five different states and overall India, we estimated several epidemiologically important parameters as well as the basic reproduction number (R_0). Combining the mechanistic mathematical model with different statistical forecast models, we projected notified cases in the six locations for the period May 17, 2020, till May 31, 2020. A global sensitivity analysis is carried out to determine the correlation of two epidemiologically measurable parameters on the lockdown effect and also on R_0. Our result suggests that lockdown will be effective in those locations where a higher percentage of symptomatic infection exists in the population. Furthermore, a large scale COVID-19 mass testing is required to reduce community infection. Ensemble model forecast suggested a high rise in the COVID-19 notified cases in most of the locations in the coming days. Furthermore, the trend of the effective reproduction number (R_t) during the projection period indicates if the lockdown measures are completely removed after May 17, 2020, a high spike in notified cases may be seen in those locations. Finally, combining our results, we provided an effective lockdown policy to reduce future COVID-19 transmission in India.

Keywords: COVID-19; Mathematical model; Lockdown effect; Outbreak containment policy

1. Introduction

As of May 15, 2020, 4593395 cases and 306376 deaths from 2019 novel coronavirus disease (COVID-19), caused by severe acute respiratory syndrome coronavirus 2 (SARS-CoV-2), were recorded worldwide [1]. Coronaviruses are enveloped non-segmented positive-

---

[1]Corresponding author. Email: tridipiitk@gmail.com

14 sense RNA viruses that belongto the Coronaviridae family and the order Nidovirales, and
15 are widely distributed among humans and other mammals [2]. The novel coronavirus,
16 COVID-19 started in mainland China, with a geographical emphasis at Wuhan, the capi-
17 tal city of Hubei province [3] and has widely spread all over the world. Many of the initial
18 cases were usually introduced to the wholesale Huanan seafood market, which also traded
19 live animals. Clinical trials of hospitalized patients found that patients exhibit symptoms
20 consistent with viral pneumonia at the onset of COVID-19, most commonly fever, cough,
21 sore throat and fatigue [4]. Some patients reported changes in their ground-glass lungs;
22 normal or lower than average white lymphocyte blood cell counts and platelet counts;
23 hypoxemia; and deranged liver and kidney function. Most were said to be geographically
24 related to the wholesale market of Huanan seafood [5]. Severe outbreaks occur in USA
25 (1457593 cases), Spain (272646 cases), Russia (262843 cases), UK (236711 cases), Italy
26 (223885) and so many countries and the disease continues to spread globally. This has
27 been declared a pandemic by the World Health Organization. It is the third zoonotic
28 human coronavirus that has arisen in the present century, after the 2002 severe acute
29 respiratory syndrome coronavirus (SARS-CoV), which spread to 37 countries and the
30 2012 Middle East respiratory syndrome coronavirus (MERS-CoV), which spread to 27
31 countries.

32 The 2019 pandemic novel coronavirus was first confirmed in India on January 30, 2020,
33 in the state of Kerala. A total of 82087 confirmed cases and 2648 deaths in the country
34 have been reported as of May 15, 2020 [6]. The Indian government has introduced social
35 distance as a precaution to avoid the possibility of a large-scale population movement
36 that can accelerate the spread of the disease. India government implemented a 14-hour
37 voluntary public curfew on 22 March 2020. Furthermore, the Prime Minister of India
38 also ordered a nationwide lockdown at midnight on March 24, 2020 to slow the spread
39 of COVID-19. Despite no vaccine, social distancing has identified as the most commonly
40 used prevention and control strategy [7]. The purpose of these initiatives is the restriction
41 of social interaction in workplaces, schools, and other public spheres, except for essential
42 public services such as fire, police, hospitals. No doubt the spread of this virus outbreak
43 has seriously disrupted the life, economy and health of citizens. This is a great concern
44 for everyone how long this scenario will last and when the disease will be controlled.

45 Mathematical modeling based on system of differential equations may provide a com-
46 prehensive mechanism for the dynamics of a disease transmission [8]. Several modeling
47 studies have already been performed for the COVID-19 outbreak [9; 10; 11; 12; 13]. Based
48 on data collected from December 31, 2019 till January 28, 2020, Wu et al [13] developed
49 a susceptible exposed infectious recovered model (SEIR) to clarify the transmission dy-
50 namics and projected national and global spread of disease. They also calculated around
51 2.68 is the basic reproductive number for COVID-19. Tang et al [12] proposed a compart-

2

mental deterministic model that would combine the clinical development of the disease, the epidemiological status of the patient and the measures for intervention. Researchers found that the amount of control reproduction number may be as high as 6.47, and that methods of intervention including intensive touch tracing followed by quarantine and isolation would effectively minimize COVID cases [12]. For the basic reproductive number, Read et al. reported a value of 3.1 based on the data fitting of an SEIR model, using an assumption of Poisson-distributed daily time increments [14]. A report by Cambridge University has indicated that India's countrywide three-week lockdown would not be adequate to prevent a resurgence of the new coronavirus epidemic that could bounce back in months and cause thousands of infections [15]. They suggested that two or three lockdowns can extend the slowdown longer with five-day breaks in between or a single 49-day lockdown. Data-driven mathematical modeling plays a key role in disease prevention, planning for future outbreaks and determining the effectiveness of control. Several data-driven modeling experiments have been performed in various regions [12; 16]. Currently, there are very limited works that studied the impact of lockdown on COVID-19 transmission dynamics in India.

In the present manuscript, we proposed a new mathematical model for COVID-19 that incorporates the lockdown effect. We also considered variability in transmission between symptomatic and asymptomatic populations with former being a fast spreader of the disease. Analyzing COVID-19 daily notified cases from five affected states (Maharashtra, Delhi, Tamil Nadu, Gujarat and Punjab) and from overall India, we studied the effect of social distancing measures implemented by the Govt. on notified cases reduction in those regions. We also estimates the basic reproduction numbers (R_0) for these six locations. Using a post-processing BMA technique, we ensemble our COVID-19 mathematical model with different statistical forecast model to obtain a projection of notified cases in those six locations for the period May 17, 2020 till May 31, 2020. A global sensitivity analysis is carried out to determine the correlation of two epidemiologically measurable parameters on lockdown effect and also on R_0. Finally to determine the COVID-19 transmission trend during the projection period (May 17, 2020 till May 31, 2020), we estimate the effective reproduction number (R_t) for the mentioned six locations.

2. Method

Based on the development and epidemiological characteristics of COVID-19, a SEIR type model is more appropriate to study the dynamics of this current pandemic [17; 18; 8]. The model we developed in this paper is based on the interaction of seven mutually exclusive sub-classes namely, Susceptible (S), Lockdown (L), Exposed (E), Asymptomatic (A), Symptomatic (I), Hospitalized (C), and Recovered (R).

Susceptible population (S) increased due to constant recruitment rate Π_H and those

89 individuals coming back from lockdown compartment after the lockdown period $\frac{1}{\omega}$. Popu-
90 lation in the susceptible class decreased due to new infection in contact with symptomatic
91 and asymptomatic infected population, natural death and also a fraction of the suscep-
92 tible individuals become home-quarantine due to lockdown at a rate l. We also assumed
93 variability in disease transmission in asymptomatic and symptomatic population with
94 later being a fast spreader of infection with a variability factor ($0 \le \rho \le 1$) [19; 20].

95 Lockdown population (L) increased by those susceptible who are home-quarantined
96 during the lockdown period $\frac{1}{\omega}$, at a rate l. Population under lockdown is decreased due
97 to natural death and those individuals who become susceptible again after the lockdown
98 period $\frac{1}{\omega}$. For simplicity, we assume ideal lockdown scenario $i.e.$ all population under
99 lockdown maintained proper social distancing and do not contribute to new infection.

100 Population in the exposed compartment (E) increased by new infection coming from
101 susceptible compartment. A fraction κ of the exposed individuals become symptomatic
102 infected and remaining fraction ($1-\kappa$) become asymptomatic infected after the disease
103 incubation period $\frac{1}{\sigma}$. Exposed population also decreased due to natural death at a rate
104 μ.

105 Asymptomatic infected compartment (A) increased due to a fraction ($1-\kappa$) of infec-
106 tion coming from exposed compartment. Since, asymptomatic COVID-19 cases are hard
107 to detect therefore, we assume that asymptomatic infection are not notified. Population
108 in this compartment is decreased due to natural recovery and deaths at a rate γ_1 and μ,
109 respectively.

110 Population in the symptomatic infected compartment (I) increased due to a fraction
111 κ of infection coming from exposed compartment after the incubation period $\frac{1}{\sigma}$. This
112 compartment decreased due to natural recovery at a rate γ_2, natural death at a rate μ
113 and those infected population who are notified & hospitalized at a rate τ.

114 Notified & hospitalized infected population (C) increased due to influx of infection
115 coming from symptomatic infected class at a rate τ. This population decreased due to
116 natural death at a rate μ, disease related deaths at a rate δ, and recovery from COVID-19
117 at a rate γ_3. We assume that population of this compartment do not mix with the general
118 population in the community $i.e.$ this compartment do not contribute in the COVID-19
119 transmission.

120 Finally, recovered population (R) increased due to influx of individuals coming from
121 asymptomatic (A), symptomatic (I), and notified & hospitalized individuals (C) at a
122 rate γ_1, γ_2, and γ_3, respectively. As we are analyzing this study in a shorter time frame
123 therefore, we assume definitive immunity $i.e.$ recovered population do not contribute to
124 new COVID-19 infection. Thus recovered population decreased due to natural death at
125 a rate μ.

4

126 Based on the above assumptions the system of equations that represent COVID-19
127 transmission with and without lockdown are provided below:

128 **Model without lock-down**

$$
\begin{aligned}
\frac{dS}{dt} &= \Pi_H - \frac{\beta_1 IS}{(N-C)} - \frac{\rho\beta_1 AS}{(N-C)} - \mu S \\
\frac{dE}{dt} &= \frac{\beta_1 IS}{(N-C)} + \frac{\rho\beta_1 AS}{(N-C)} - (\mu+\sigma)E, \\
\frac{dA}{dt} &= (1-\kappa)\sigma E - (\gamma_1+\mu)A, \\
\frac{dI}{dt} &= \kappa\sigma E - (\gamma_2+\tau+\mu)I, \\
\frac{dC}{dt} &= \tau I - (\delta+\gamma_3+\mu)C, \\
\frac{dR}{dt} &= \gamma_1 A + \gamma_2 I + \gamma_3 C - \mu R,
\end{aligned}
\tag{2.1}
$$

129 **Model with lock-down**

$$
\begin{aligned}
\frac{dS}{dt} &= \Pi_H + \omega L - \frac{\beta_1 IS}{(N-L-C)} - \frac{\rho\beta_1 AS}{(N-L-C)} - \mu S - lS \\
\frac{dL}{dt} &= lS - (\mu+\omega)L, \\
\frac{dE}{dt} &= \frac{\beta_1 IS}{(N-L-C)} + \frac{\rho\beta_1 AS}{(N-L-C)} - (\mu+\sigma)E, \\
\frac{dA}{dt} &= (1-\kappa)\sigma E - (\gamma_1+\mu)A, \\
\frac{dI}{dt} &= \kappa\sigma E - (\gamma_2+\tau+\mu)I, \\
\frac{dC}{dt} &= \tau I - (\delta+\gamma_3+\mu)C, \\
\frac{dR}{dt} &= \gamma_1 A + \gamma_2 I + \gamma_3 C - \mu R.
\end{aligned}
\tag{2.2}
$$

130 A diagram of our model is provided in Fig 1. Information of our model parameters is
131 provided in Table 1.

132 **Mathematical properties of the model**

133 We studied the positivity and boundedness of solution of the model (2.1) (see supple-
134 mentary appendix). The system (2.1) demonstrates two equilibria, that is, the disease-
135 free equilibrium and an unique endemic equilibrium (see supplementary appendix). The

5

disease-free state is locally asymptotically stable whenever the corresponding basic reproduction number (R_0) is less than unity (see supplementary appendix). By using a nonlinear Lyapunov function, it is also seen that the disease-free equilibrium is globally asymptotically stable whenever $R_0 < 1$ (see supplementary appendix). In addition, the model (2.1) has an unique endemic equilibrium if R_0 exceeds unity. Furthermore, using the central manifold theory, the local stability of the endemic equilibrium is established whenever $R_0 > 1$ (see supplementary appendix).

Data

Daily COVID-19 reported cases from Maharashtra (MH), Delhi (DL), Tamil Nadu (TN), Gujarat (GJ), Punjab (PJ) and whole India (IND) for the time period March 14, 2020 till May 3, 2020 are considered for our study. These five states are deeply affected by current COVID-19 outbreak in India [6]. Daily COVID-19 notified cases were collected from [6]. Demographic data of the different locations are taken from [21; 22].

Estimation procedure

Several important epidemiological parameters (see Table 1) of our mathematical model (2.2) are estimated using COVID-19 daily reported cases from the mentioned six locations. Total time duration of lockdown implemented by Govt. is 54 days starting from March 25, 2020 till May 17, 2020. Time-series data of daily COVID-19 cases in our study for the locations MH, DL, TN, GJ, PJ, and IND, respectively contains both with and without lockdown effect. Therefore, a combination of our mathematical models (2.1)& (2.2) (with and without lockdown) are used for calibration. From our models (2.1)& (2.2), new COVID-19 notified cases during the ith time interval $[t_i, t_i + \Delta t_i]$ is

$$H_i(\hat{\theta}) = \tau \int_{t_i}^{t_i + \Delta t_i} I(\xi, \hat{\theta}) \ d\xi, \tag{2.3}$$

where, Δt_i is the time step length and $\hat{\theta}$ is the set of unknown parameters of the models (2.1)& (2.2) that are estimated. Then K observation from the data and from the models (2.1)& (2.2) are $\{D_1, D_2, ..., D_K\}$ and $\{H_1(\hat{\theta}), H_2(\hat{\theta}), ..., H_K(\hat{\theta})\}$, respectively. Therefore, we constructed the sum of squares function [23] as:

$$SS(\hat{\theta}) = \sum_{i=1}^{K} \left[D_i - H_i(\hat{\theta}) \right]^2, \tag{2.4}$$

MATLAB based nonlinear least square solver $fmincon$ is used to fit simulated and observed daily COVID-19 notified cases for the mentioned states and the whole country. Delayed Rejection Adaptive Metropolis [24] (DRAM) algorithm is used to sample the 95% confidence region. An elaboration of this model fitting technique is provided in [25].

6

Statistical forecast models and the ensemble model

COVID-19 mathematical model we developed in this study may be efficient in capturing the transmission dynamics. However, as solution of the mathematical model is always smooth therefore, our model may not be able to replicate the fluctuations occurring in daily time-series data. Moreover, forecast of future COVID-19 cases based on a single mathematical model may not be very reliable approach. For this purpose, we used two statistical forecast models namely, Auto-regressive Integrated Moving Average (ARIMA); and ARMA errors, Trend and Seasonal components (TBATS) respectively. A Hybrid statistical model (HYBRID) based on the combination of ARIMA and TBATS is also used during forecast. Calibration of three statistical forecast models (ARIMA, TBATS and HYBRID) using COVID-19 daily notified cases from MH, DL, TN, GJ, PJ, and IND, respectively during March 14, 2020 till May 3, 2020, are done using the R package 'forecastHybrid' [26]. Each individuals models (ARIMA and TBATS) are first fitted to the aforesaid time-series data and then we combined each models with weightage based on in sample error to obtain the HYBRID model [26]. Prediction skill of the each three statistical forecast model (ARIMA, TBATS and HYBRID) are tested on the daily COVID-19 notified cases during May 4, 2020 till May 8, 2020 for each of the six locations (see supplementary Table S2). Based on the prediction skill (see supplementary Table S2), the best statistical forecast model is ensemble with our COVID-19 mathematical models (2.1) and (2.2). A post-processing BMA technique based on 'DRAM' algorithm [24] is used to determine the weightage (see supplementary Table S3 and Fig S6 to Fig S11) to combine the best statistical model with the COVID-19 mathematical models (2.1) and (2.2).

Disease forecasting under different lockdown scenario

Govt. have implemented lockdown all over India on March 25, 2020 and it will continue till May 17, 2020. The short and medium scale industries are largely affected by the lockdown [27; 28]. To partially recover the economy, Govt. of India continuously relaxing the lockdown rules from April 20, 2020 [29; 30; 31]. To forecast COVID-19 cases for the period May 17, 2020 till May 31, 2020, for the six locations (MH, DL, TN, GJ, PJ and IND) based on the Govt. strategy, we considered following scenarios:

Forecast based on current lockdown rate: We have estimated the average lockdown rate for our COVID-19 mathematical model (see Table 1 and Table 2). Using this lockdown rate and using other parameters (estimated and known) of our mathematical models (2.1) & (2.2), we forecast COVID-19 notified cases during May 17, 2020 till May 31, 2020 for the locations MH, DL, TN, GJ, PJ, and IND, respectively. Finally, forecast based on our mathematical model is ensemble with the result based on the best statistical forecast model for a location mentioned earlier.

7

203 Forecast based on 15% reduction in current lockdown rate: We followed same proce-
204 dure as the previous scenario with 15% decrement in the estimate of lockdown rate (see
205 Table 1 and Table 2) to obtained the forecast during the mentioned time period.

206 Forecast based on 20% reduction in current lockdown rate: we followed the same
207 procedure as previous two scenarios with 20% decrement in the estimate of lockdown rate
208 (see Table 1 and Table 2) to obtained the forecast during the mentioned time period.

209 Forecast based on 30% reduction in current lockdown rate: we followed the same
210 procedure as previous three scenarios with 30% decrement in the estimate of lockdown
211 rate (see Table 1 and Table 2) to obtain the forecast during the mentioned time period.

212 Forecast based on no lockdown: Continue as earlier and assuming lockdown is lifted
213 after May 17, 2020, we forecast COVID-19 notified cases during May 17, 2020 till May
214 31, 2020, for the six mentioned locations.

215 ### *Estimation of the basic and the effective reproduction number*

216 Since we assumed that population under the lockdown do not contact with the in-
217 fection from the community therefore the basic reproduction number (R_0) [32] for our
218 mathematical model with and without lockdown (see Fig 1 and supplementary method)
219 are same and its expression is provided below:

$$R_0 = \frac{\beta_1 \kappa \sigma}{(\mu + \sigma)(\gamma_2 + \tau + \mu)} + \frac{\rho \beta_1 (1 - \kappa) \sigma}{(\mu + \sigma)(\gamma_1 + \mu)}.$$

220 The effective reproductive number (R_t) is defined as the expected number of secondary
221 infection per infectious in a population made up of both susceptible and non-susceptible
222 hosts [33]. If $R_t > 1$, the number of new cases will increase, for $R_t = 1$, the disease
223 become endemic, and when $R_t < 1$ there will be a decline in new cases.

224 Following [33], the expression of R_t is given as follows:

$$R_t = R_0 \times \hat{s},$$

225 where, $\hat{s}$ is the fraction of the host population that is susceptible.

226 R_0 can easily be estimated by plugin the sample values of the unknown parameters
227 (see Table 2) of the model without lockdown (2.1) in the expressions of R_0.

228 Following procedure is adapted to estimate R_t during May 17, 2020 till May 31, 2020
229 under two lockdown scenarios:

230 • Using current estimate of the lockdown rate and different parameters of our mathe-
231   matical model (see Table 1 and Table 2), we estimate $\hat{s}$ and R_t during May 17, 2020
232   till May 31, 2020, for the locations MH, DL, TN, GJ, PJ and IND, respectively.

8

233 • Using different parameters (see Table 1 and Table 2) of our mathematical model with-

234 out lockdown (2.1), we estimated $\hat{s}$ and R_t during May 17, 2020 till May 31, 2020

235 for the mentioned six locations.

Sensitivity analysis and effective lockdown strategy

237 To determine an effective lockdown policy in those six locations (MH, DL, TN, GJ, PJ

238 and IND) will require some correlation between lockdown effect with some epidemiolog-

239 ically measurable parameters of our mathematical model (see Fig 1). There are several

240 important parameters of our mathematical model (see Table 1) and among them there

241 are two parameters that are measurable namely, κ: fraction of new infected that become

242 symptomatic (COVID-19 testing will provide an accurate estimate) and τ: Average no-

243 tification & hospitalization rate of symptomatic COVID-19 infection (this parameter is

244 proportional to the number of COVID-19 testing). Lockdown effect is measured as the

245 difference between the total number of cases projected by our ensemble model with and

246 without lockdown. A global sensitivity analysis [34] is performed to determine the effect

247 of the mentioned two parameters on the lockdown effect and on the basic reproduction

248 number (R_0). Using Latin Hyper cube sampling (LHS), we draw 1000 samples for κ and

249 τ, respectively from their respective ranges (see Table 1). Partial rank correlation and

250 its corresponding p-value are examined to determine the relation between two mentioned

251 parameters with the lockdown effect and R_0, respectively.

3. Results and discussion

253 Three models (mathematical, statistical forecast and ensemble) fitting to daily COVID-

254 19 notified cases during March 14, 2020 till May 3, 2020, for Maharashtra (MH), Delhi

255 (DL), Tamil Nadu (TN), Gujarat (GJ), Punjab (PJ), and India (IND) is depicted in

256 Fig 2. Among the three statistical forecast models (ARIMA, TBATS and HYBRID), the

257 ARIMA model performed better on the test prediction data (May 4, 2020 till May 8,

258 2020) of DL and GJ (see supplementary Table S2). Whereas, the TBATS model provide

259 better result in compare to other two models for the test prediction data (May 4, 2020

260 till May 8, 2020) of PJ (see supplementary Table S2). For the remaining three locations

261 (MH, TN and IND), the HYBRID model provide the best result (see supplementary Ta-

262 ble S2) on the test prediction data (May 4, 2020 till May 8, 2020). The ensemble model,

263 which is a combination of our COVID-19 mathematical models (2.1) & (2.2) and the best

264 statistical forecast model (region specific), is performed well in capturing COVID-19 daily

265 time-series data trend in all the six locations. Posterior distribution of the weights at

266 which we combine our COVID-19 mathematical model with the best statistical forecast

267 model in the six different locations are provided in supplementary method (see Fig S6 to

268 Fig S11 and Table S3).

9

₂₆₉ In MH, DL, and GJ, the estimate of the symptomatic influx fraction (κ) suggest
₂₇₀ that low percentage (about 11% to 20%) of symptomatic infected in the population (see
₂₇₁ Table 2). However, in TN and PJ, relatively higher percentage (about 82% to 88%) of
₂₇₂ symptomatic infection is found (see Table 2). In overall India, our estimate shows that
₂₇₃ currently about 62% of new infection are symptomatic (see Table 2). Except for GJ, in
₂₇₄ other five locations, estimate of the transmission rate (β_1) are found to be in same scale
₂₇₅ (see Table 2). Relatively higher value of β_1 is found in Gujrat (see Table 2). Low value
₂₇₆ of the transmission variability factor (ρ) indicates most of the community infection in
₂₇₇ GJ are due to contact with the symptomatic infected population. As in GJ, the value of
₂₇₈ κ is found to be small (about 11%) therefore, relatively smaller symptomatic population
₂₇₉ producing most of the infection in GJ. This indicate that there may be a possibility of
₂₈₀ existence of super-spreaders among the symptomatic infected in GJ. This observation
₂₈₁ is agree with a recent survey result in GJ [35]. Except for PJ, in other five locations,
₂₈₂ the estimates of ρ (below 50%) are found to be low (see Table 2). This indicates small
₂₈₃ contribution of the asymptomatic infected population towards the new infection produced
₂₈₄ in MH, DL, TN, GJ and IND, respectively. Estimate of the lockdown rate in the five
₂₈₅ states (MH, DL, TN, GJ and PJ) suggest that around 50% to 88% of the total susceptible
₂₈₆ population are successfully home quarantined during the lockdown period (see Table 2).
₂₈₇ Thus, lockdown is overall successful in those five states. However, this is not the case for
₂₈₈ overall India, our estimate suggest that about 11% of the total susceptible population in
₂₈₉ India maintained proper social distancing during the lockdown period (see Table 2).

₂₉₀ Our estimate of the basic reproduction number (R_0) (see Table 3), in the six locations
₂₉₁ found to be in good agreement of the world-wide estimate provided by WHO [36]. We
₂₉₂ performed a global sensitivity analysis of two epidemiologically measurable parameters
₂₉₃ of our mathematical model (see Fig 1) namely κ: fraction of new infected that become
₂₉₄ symptomatic and τ: Average notification & hospitalization rate of symptomatic COVID-
₂₉₅ 19 infection, on R_0. Partial rank correlation and its corresponding p-value (see Fig 3)
₂₉₆ suggest that τ has a negative correlation on R_0. Thus, more testing will isolate more
₂₉₇ infection from the community and therefore may reduce the COVID-19 community trans-
₂₉₈ mission. Furthermore, high positive correlation of κ with R_0 (see Fig 3) indicates the
₂₉₉ possibility of high COVID-19 transmission in those areas where population have higher
₃₀₀ percentage of symptomatic infection.

₃₀₁ Ensemble model forecast of notified COVID-19 cases between May 17, 2020 till May
₃₀₂ 31, 2020 (see Table 4, Fig. 4, and Fig S1 to Fig S10 in supplementary appendix) indicate
₃₀₃ that in the coming few days, a high increment in the COVID-19 notified cases may be
₃₀₄ observed in MH, DL, TN, GJ, PJ, and IND. Furthermore, our ensemble model prediction
₃₀₅ during the mentioned period suggest that around 117645 to 128379 cases may occurred
₃₀₆ in overall India (see Table 4). These numbers are much higher than the total cumulative

307 cases between March 2, 2020 till May 15, 2020, in whole India.

308 A global sensitivity analysis of κ and τ on the lockdown effect suggest that both of
309 these parameters have high positive correlation with the lockdown effect in all the six
310 locations (see Fig. 5). Therefore, lockdown will be effective in those region where higher
311 percentage of symptomatic infection is found in the population and also larger COVID-19
312 mass testing will be required to isolate the cases.

313 To measure the COVID-19 transmission trend during May 17, 2020 till May 31, 2020,
314 we estimated the effective reproduction number (R_t) during the mentioned period for
315 MH, DL, TN, GJ, PJ and IND, respectively (see Fig. 6). Our result suggest that, a
316 decreasing trend in new notified COVID-19 cases $(R_t < 1)$ may be seen after May 31,
317 2020 if current lockdown measures (see Table 2) are maintained in DL, TN and PJ,
318 respectively. Furthermore, if social distancing measures are removed after May 17, 2020,
319 we may see a rise in the daily COVID-19 cases in all of the six locations (see Fig. 6).

4. Conclusion

321 Up to May 15, 2020, total number of reported COVID-19 cases and deaths in India
322 are **81794** and **2649**, respectively [6]. This tally rises with few thousand new notified
323 cases every day reported from different locations in India [6]. Currently, there is no
324 treatment or vaccine available for COVID-19. Therefore, only measure to control the
325 outbreak may be home quarantined (lockdown) a larger percentage of susceptible pop-
326 ulation. However, this disease control strategy may have some negative impact on the
327 economy. Therefore, it is utmost important to determine an effective lockdown policy
328 that may reduce COVID-19 transmission in the community as well as save the Indian
329 economy from drowning. This policy may be found by studying the dynamics and pre-
330 diction of a mechanistic mathematical model for COVID-19 transmission and testing the
331 results in real life situation.

332 In this present study, we consider a new mathematical model on COVID-19 transmis-
333 sion that incorporates the lockdown effect (see Fig 1). In our models (2.1) & (2.2), we
334 also considered transmission variability between symptomatic and asymptomatic popu-
335 lation with former being a fast spreader of the disease. Using daily time-series data of
336 notified COVID-19 cases from five states (Maharashtra, Delhi, Tamil Nadu, Gujarat and
337 Punjab) and overall India, we studied the effect of lockdown measures on the reduction
338 of notified cases in those regions. Our result suggest that lockdown will be effective in
339 those locations where higher percentage of symptomatic infection exist in the popula-
340 tion. Furthermore, a large scale COVID-19 mass testing is required to reduce community
341 infection in those locations. Using a post-processing BMA technique, we ensemble the
342 prediction of our mathematical model with the results obtained from different statistical
343 forecast model. Our ensemble model forecast of COVID-19 daily notified cases during

11

May 17, 2020 till May 31, 2020, suggested a very high rise in the COVID-19 notified cases in the mentioned time duration in most of the locations. Furthermore, estimation of the effective reproduction number (R_t) during the mentioned time duration indicates if the lockdown measures are completely removed after May 17, 2020, in those locations, a high spike in COVID-19 notified cases may be seen during the mentioned forecasting period. We provide a suggestion for the Indian Govt. and policy makers to acquire the following steps for effective containment of COVID-19 transmission:

1. Perform a survey to find the percentage of symptomatic infection in different states and regions.

2. Focus implementing extensive lockdown in those locations only where the percentage of symptomatic infection is high.

3. Provide relaxation in lockdown in other locations for some time. This process will increase the percentage of symptomatic infection.

4. Repeat step-2, when a region has a sufficient percentage of symptomatic infection.

There are some drawback in our study and may be modified in future. We assume that lockdown population (L) and notified & hospitalized infection (C) do not mix with the general population in the community. However, there are numerous evidences where disease transmitted from the hospital and from home confined individuals [37]. We shall leave these challenges for our future objectives.

Conflict of interests

The authors declare that they have no conflicts of interest.

Acknowledgments

375 India, New Delhi.

376

References

[1] "Coronavirus COVID-19 Global Cases by the Center for Systems Science and Engineering.." `https://gisanddata.maps.arcgis.com/apps/opsdashboard/index.html#/bda7594740fd40299423467b48e9ecf6`, 2020. Retrieved : 2020-04-02.

[2] D. D. Richman, R. J. Whitley, and F. G. Hayden, *Clinical virology.* John Wiley & Sons, 2016.

[3] C. Wang, P. W. Horby, F. G. Hayden, and G. F. Gao, "A novel coronavirus outbreak of global health concern," *The Lancet*, vol. 395, no. 10223, pp. 470–473, 2020.

[4] "Centers for disease control and prevention: 2019 novel coronavirus.." `https://www.cdc.gov/coronavirus/2019-ncov`, 2020. Retrieved : 2020-03-10.

[5] "Wuhan wet market closes amid pneumonia outbreak." `https://www.chinadaily.com.cn/a/202001/01/WS5e0c6a49a310cf3e35581e30.html`, 2019. Retrieved : 2020-03-04.

[6] "India COVID-19 Tracker." `https://www.covid19india.org/`, 2020. Retrieved : 2020-04-03.

[7] N. Ferguson, D. Laydon, G. Nedjati Gilani, N. Imai, K. Ainslie, M. Baguelin, S. Bhatia, A. Boonyasiri, Z. Cucunuba Perez, G. Cuomo-Dannenburg, *et al.*, "Report 9: Impact of non-pharmaceutical interventions (npis) to reduce covid19 mortality and healthcare demand," 2020.

[8] T. Sardar, I. Ghosh, X. Rodó, and J. Chattopadhyay, "A realistic two-strain model for mers-cov infection uncovers the high risk for epidemic propagation," *PLOS Neglected Tropical Diseases*, vol. 14, no. 2, p. e0008065, 2020.

[9] B. Tang, N. L. Bragazzi, Q. Li, S. Tang, Y. Xiao, and J. Wu, "An updated estimation of the risk of transmission of the novel coronavirus (2019-ncov)," *Infectious Disease Modelling*, vol. 5, pp. 248–255, 2020.

[10] B. J. Quilty, S. Clifford, *et al.*, "Effectiveness of airport screening at detecting travellers infected with novel coronavirus (2019-ncov)," *Eurosurveillance*, vol. 25, no. 5, 2020.

[11] M. Shen, Z. Peng, Y. Xiao, and L. Zhang, "Modelling the epidemic trend of the 2019 novel coronavirus outbreak in china," *bioRxiv*, 2020.

[12] B. Tang, X. Wang, Q. Li, N. L. Bragazzi, S. Tang, Y. Xiao, and J. Wu, "Estimation of the transmission risk of the 2019-nCoV and its implication for public health interventions," *Journal of Clinical Medicine*, vol. 9, no. 2, p. 462, 2020.

[13] J. T. Wu, K. Leung, and G. M. Leung, "Nowcasting and forecasting the potential domestic and international spread of the 2019-ncov outbreak originating in wuhan, china: a modelling study," *The Lancet*, vol. 395, no. 10225, pp. 689–697, 2020.

[14] J. M. Read, J. R. Bridgen, D. A. Cummings, A. Ho, and C. P. Jewell, "Novel coronavirus 2019-ncov: early estimation of epidemiological parameters and epidemic predictions," *MedRxiv*, 2020.

[15] R. Singh and R. Adhikari, "Age-structured impact of social distancing on the covid-19 epidemic in india," *arXiv preprint arXiv:2003.12055*, 2020.

[16] T. Chen, J. Rui, Q. Wang, Z. Zhao, J.-A. Cui, and L. Yin, "A mathematical model for simulating the transmission of wuhan novel coronavirus," *bioRxiv*, 2020.

[17] A. J. Kucharski, T. W. Russell, C. Diamond, Y. Liu, J. Edmunds, S. Funk, R. M. Eggo, F. Sun, M. Jit, J. D. Munday, *et al.*, "Early dynamics of transmission and control of COVID-19: a mathematical modelling study," *The Lancet Infectious Diseases*, 2020.

[18] L. Peng, W. Yang, D. Zhang, C. Zhuge, and L. Hong, "Epidemic analysis of covid-19 in china by dynamical modeling," *arXiv preprint arXiv:2002.06563*, 2020.

[19] A. B. Gumel, S. Ruan, T. Day, J. Watmough, F. Brauer, P. Van den Driessche, D. Gabrielson, C. Bowman, M. E. Alexander, S. Ardal, *et al.*, "Modelling strategies for controlling sars outbreaks," *Proceedings of the Royal Society of London. Series B: Biological Sciences*, vol. 271, no. 1554, pp. 2223–2232, 2004.

[20] S. Mandal, T. Bhatnagar, N. Arinaminpathy, A. Agarwal, A. Chowdhury, M. Murhekar, R. R. Gangakhedkar, and S. Sarkar, "Prudent public health intervention strategies to control the coronavirus disease 2019 transmission in india: A mathematical model-based approach," *The Indian journal of medical research*, vol. 151, no. 2-3, p. 190, 2020.

[21] "Statewise population data.." http://statisticstimes.com/demographics/population-of-indian-states.php, 2019. Retrieved : 2020-04-05.

[22] "Life expectancy at birth.." https://niti.gov.in/content/life-expectancy, 2019. Retrieved : 2020-04-05.

[23] T. Sardar, S. Mukhopadhyay, A. R. Bhowmick, and J. Chattopadhyay, "An optimal cost effectiveness study on Zimbabwe cholera seasonal data from 2008–2011," *PLoS One*, vol. 8, no. 12, p. e81231, 2013.

[24] H. Haario, M. Laine, A. Mira, and E. Saksman, "Dram: efficient adaptive mcmc," *Statistics and computing*, vol. 16, no. 4, pp. 339–354, 2006.

[25] T. Sardar and B. Saha, "Mathematical analysis of a power-law form time dependent vector-borne disease transmission model," *Mathematical biosciences*, vol. 288, pp. 109–123, 2017.

[26] D. Shaub and P. Ellis, *forecastHybrid: Convenient Functions for Ensemble Time Series Forecasts*, 2020. https://gitlab.com/dashaub/forecastHybrid, https://github.com/ellisp/forecastHybrid.

[27] "World's biggest lockdown may have cost Rs 7-8 lakh crore to Indian economy." `https://economictimes.indiatimes.com/news/economy/finance/worlds-biggest-lockdown-may-have-cost-rs-7-8-lakh-crore-to-indian-economy/articleshow/75123004.cms?from=mdr`, 2020. Published on: 2020-04-13.

[28] "Coronavirus: 5 Indian sectors that need urgent help as virus ravages economy." `https://www.indiatoday.in/business/story/coronavirus-5-indian-sectors-that-need-urgent-help-as-virus-ravages-economy-1670`, 2020. Published on: 2020-04-24.

[29] "Red, orange, green zones may come up during extended lockdown." `https://economictimes.indiatimes.com/news/politics-and-nation/red-orange-green-zones-may-come-up-during-extended-lockdown/articleshow/75101054.cms?from=mdr`, 2020. Published on: 2020-04-14.

[30] "COVID-19 lockdown relaxation: Full list of activities allowed from april 20: details." `https://www.financialexpress.com/lifestyle/covid-19-lockdown-relaxation-full-list-of-activities-allowed-from-april-20-detail/1933136/`, 2020. Published on: 2020-04-19.

[31] "Coronavirus lockdown — railways to restart passenger services in phased manner." `https://www.thehindu.com/news/national/coronavirus-lockdown-railways-to-resume-select-passenger-train-services-from-may-article31551514.ece`, 2020. Published on: 2020-05-10.

[32] P. Van den Driessche and J. Watmough, "Reproduction numbers and sub-threshold endemic equilibria for compartmental models of disease transmission," *Mathematical biosciences*, vol. 180, no. 1-2, pp. 29–48, 2002.

[33] K. J. Rothman, S. Greenland, and T. L. Lash, *Modern epidemiology.* Lippincott Williams & Wilkins, 2008.

[34] S. Marino, I. B. Hogue, C. J. Ray, and D. E. Kirschner, "A methodology for performing global uncertainty and sensitivity analysis in systems biology," *Journal of theoretical biology*, vol. 254, no. 1, pp. 178–196, 2008.

[35] "334 coronavirus "super-spreaders" found in ahmedabad: Officials." `https://www.ndtv.com/ahmedabad-news/coronavirus-india-334-covid-19-super-spreaders-found-in-ahmedabad-gujarat-officia` 2020. Published on: 2020-05-10.

[36] Y. Liu, A. A. Gayle, A. Wilder-Smith, and J. Rocklöv, "The reproductive number of COVID-19 is higher compared to SARS coronavirus," *Journal of travel medicine*, 2020.

[37] "19 Doctors, 38 Nurses Among 480 Infected With Coronavirus In AIIMS." `https://www.ndtv.com/delhi-news/coronavirus-19-doctors-38-nurses-among-480-infected-in-aiims-2240563`, 2020. Published on: 2020-06-04.

[38] "What the cms told pm modi during consultations over covid-19." `https://timesofindia.indiatimes.com/india/what-the-cms-told-pm-modi-during-consultations-over-covid-19/articleshow/75677731.cms`, 2020. Published on: 2020-05-11.

[39] X. Yang, L. Chen, and J. Chen, "Permanence and positive periodic solution for the single-species nonautonomous delay diffusive models," *Computers & Mathematics with Applications*, vol. 32, no. 4, pp. 109–116, 1996.

[40] H. W. Hethcote, "The mathematics of infectious diseases," *SIAM review*, vol. 42, no. 4, pp. 599–653, 2000.

[41] R. M. Anderson and R. M. May, "Population biology of infectious diseases: Part i," *Nature*, vol. 280, no. 5721, pp. 361–367, 1979.

[42] R. M. Anderson, B. Anderson, and R. M. May, *Infectious diseases of humans: dynamics and control.* Oxford university press, 1992.

[43] J. P. LaSalle, *The stability of dynamical systems*, vol. 25. Siam, 1976.

[44] H. L. Smith and P. Waltman, *The theory of the chemostat: dynamics of microbial competition*, vol. 13. Cambridge university press, 1995.

17

[45] C. Castillo-Chavez and B. Song, "Dynamical models of tuberculosis and their applications," *Mathematical Biosciences & Engineering*, vol. 1, no. 2, p. 361, 2004.
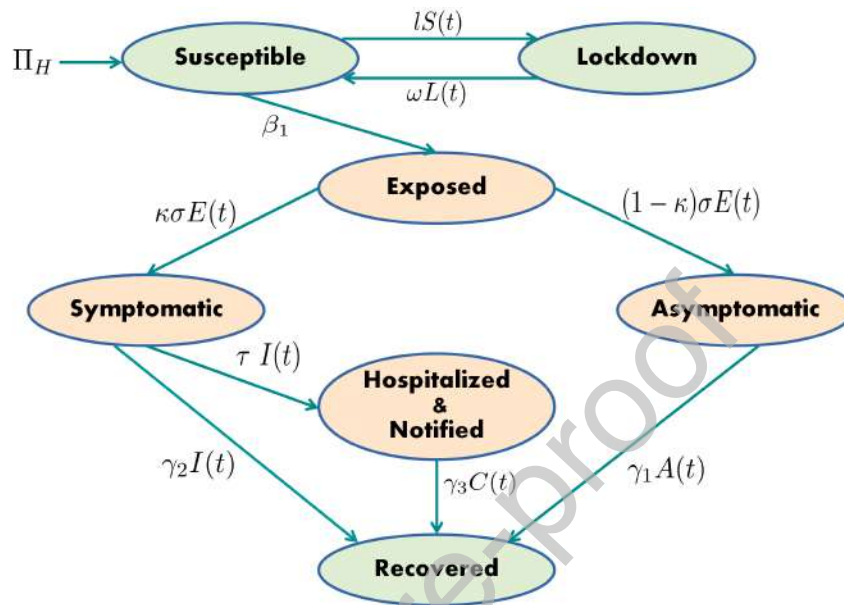
Figures

Figure 1: Flow diagram of the mathematical model with lockdown. Epidemiological information of different parameters shown in the above figure are provided in Table 1.
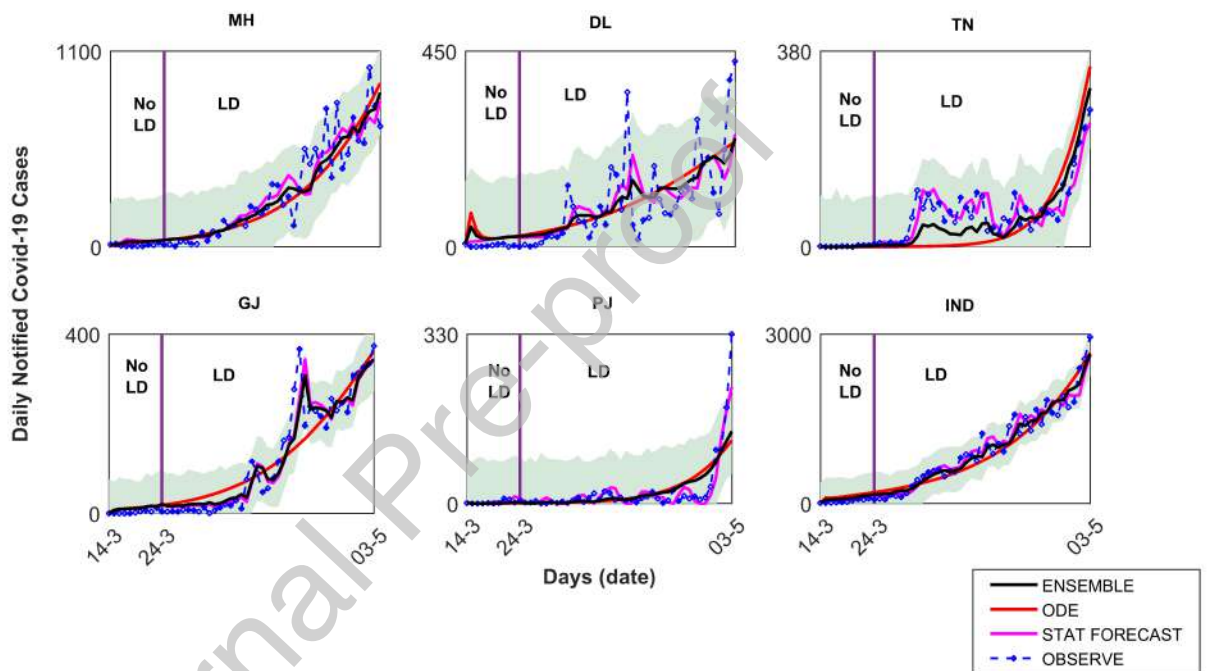
Figure 2: Three models (mechanistic mathematical model, statistical forecast model and ensemble model) fitting to daily notified COVID-19 cases from five different states and overall India for the period March 14, 2020 till May 3, 2020. Respective subscript are MH: Maharashtra, DL: Delhi, TN: Tamil Nadu, GJ: Gujarat, PJ: Punjab, and IND: India. Here **LD** denotes lockdown period and **No LD** indicate the period before lockdown implementation. Statistical forecast model for different locations are ARIMA (DL and GJ), TBATS (PJ) and HYBRID (MH, TN and IND), respectively. Lockdown effect is only considered for the mechanistic mathematical model and consequently in the ensemble model. Shaded area indicate the 95% confidence region.
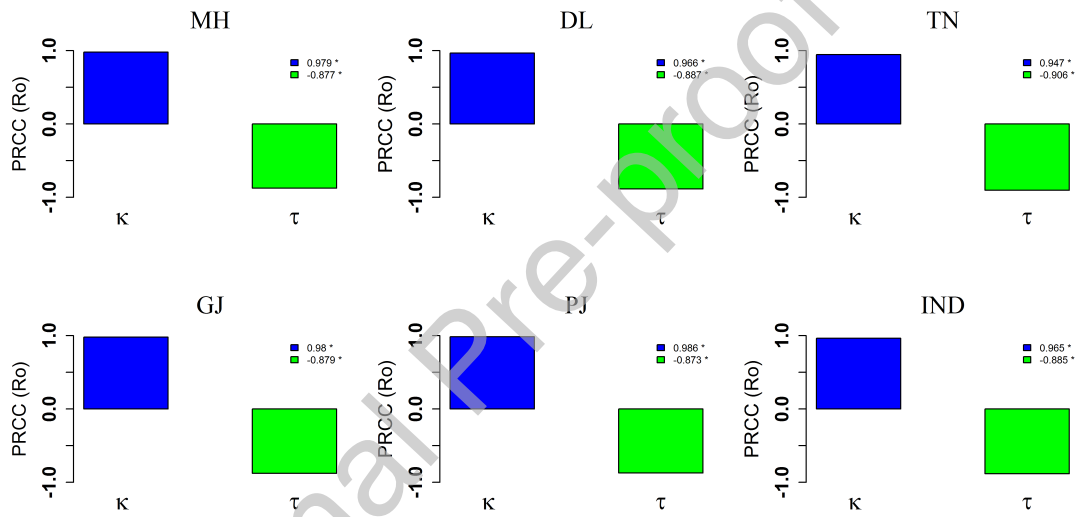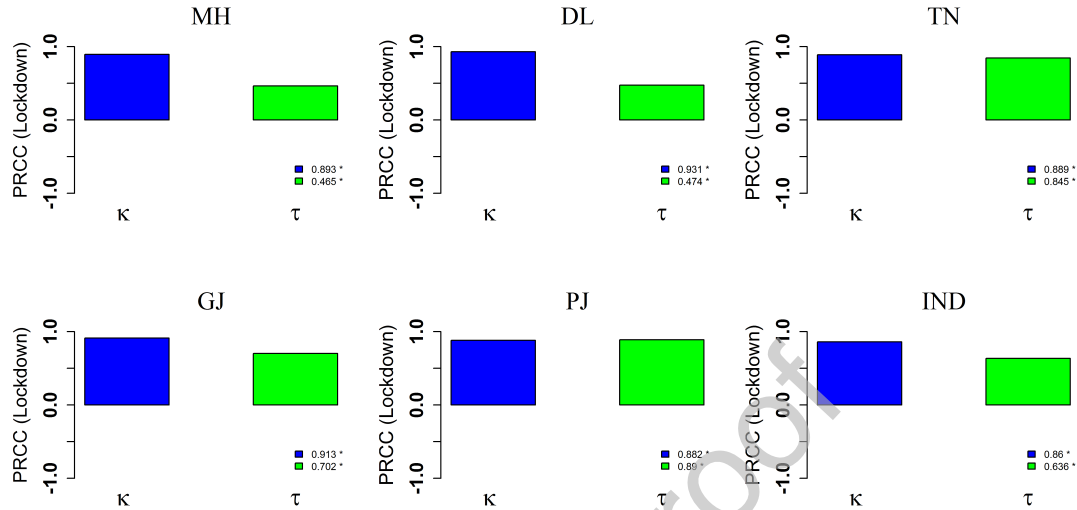
Figure 3: Global sensitivity analysis of two epidemiologically measurable parameters namely κ: fraction of new infected that become symptomatic and τ: average notification & hospitalization rate of symptomatic COVID-19 infection, on R_0. The subscripts MH, DL, TN, GJ, PJ and IND, respectively are same as Fig 2.

21

India (IND)
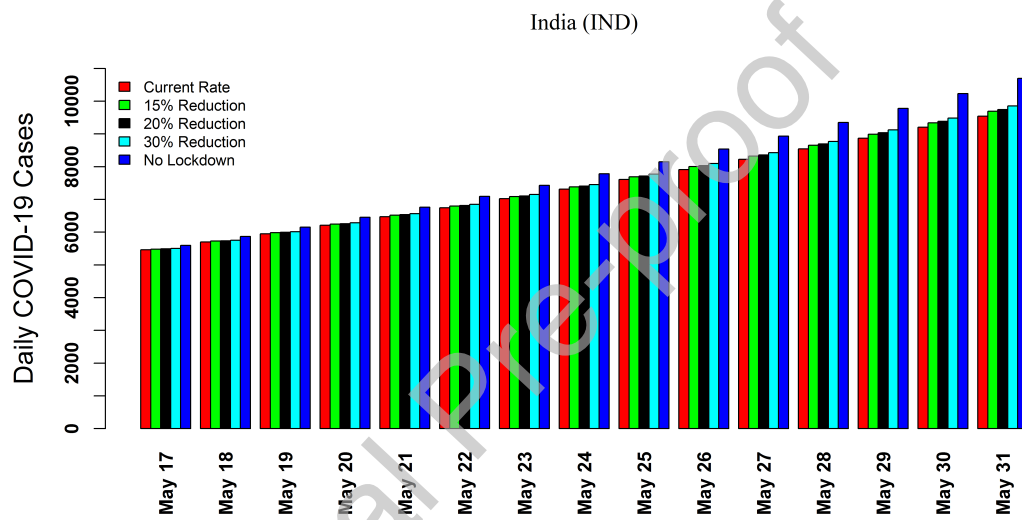
Figure 4: Ensemble model forecast for the daily notified COVID-19 cases in India during May 17, 2020 till May 31, 2020, under five different social distancing measure. Various legends are **Current Rate**: daily notified case projection using the estimated value of the lockdown rate (see Table 2), **15% Reduction**: daily notified case projection using 15% reduction in the estimated value of the lockdown rate (see Table 2), **20% Reduction**: daily notified case projection using 20% reduction in the estimated value of the lockdown rate (see Table 2), **30% Reduction**: daily notified case projection using 30% reduction in the estimated value of the lockdown rate (see Table 2), and **No lockdown**: daily notified case projection based on no lockdown scenario, respectively.

22

Figure 5: Global sensitivity analysis of two epidemiologically measurable parameters namely κ: fraction of new infected that become symptomatic and τ: average notification & hospitalization rate of symptomatic COVID-19 infection, on the lockdown effect. The effect of lockdown is measured as the difference between the total number of cases projected by our ensemble model with and without lockdown scenario during May 17, 2020 till May 31, 2020. The subscripts MH, DL, TN, GJ, PJ and IND, respectively are same as Fig 2.
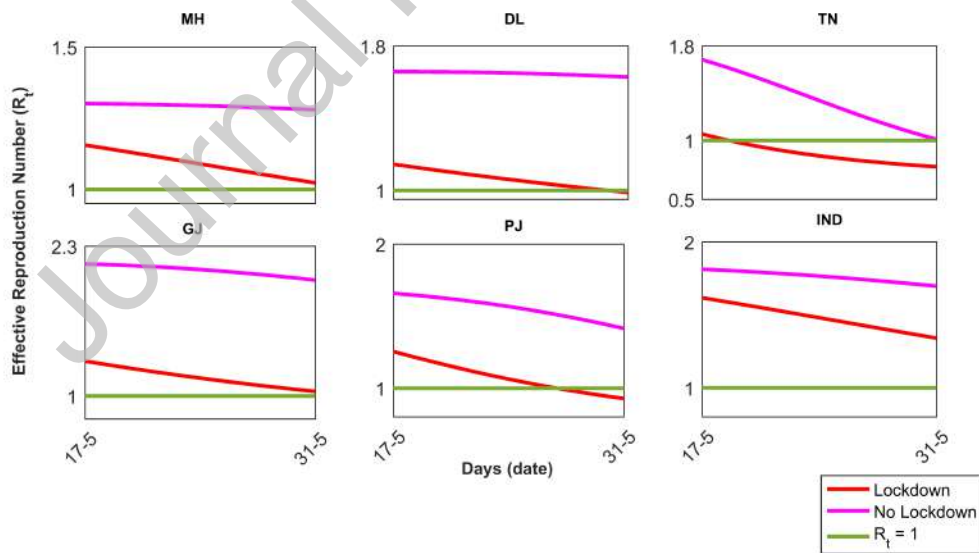
Figure 6: Effective reproduction number (R_t) for the period May 17, 2020 till May 31, 2020, in MH, DL, TN, GJ, PJ and IND, respectively. The subscripts MH, DL, TN, GJ, PJ and IND, respectively are same as Fig 2.

23

510

Tables

Table 1: Parameters with their respective epidemiological explanation for the mechanistic mathematical model (see Fig 1) for COVID-19.

Parameters	Epidemiological Meaning	Ranges	Reference
N	Total population	Varies over different region	[21]
$\Pi_H = \mu \times N$	Average recruitment rate	Varies over different region	–
$\dfrac{1}{\mu}$	Average life expectancy at birth	Varies over states	[22]
β_1	Transmission rate of symptomatic infected	$(0 - 200)\ day^{-1}$	Estimated
ρ	Reduction in COVID-19 transmission for Asymptomatic infected	$0 - 1$	Estimated
$\dfrac{1}{\sigma}$	COVID-19 incubation period	$(2 - 14)\ days$	Estimated
κ	Fraction of exposed population that become symptomatic infected	$0 - 1$	Estimated
γ_1	Recovery rate for asymptomatic infected	$(\gamma_3 - 1)\ day^{-1}$	Estimated
γ_2	Recovery rate for symptomatic infected	$(\gamma_3 - 1)\ day^{-1}$	Estimated
τ	Average notification & hospitalization rate of symptomatic infection	$(0 - 1)\ day^{-1}$	Estimated
δ	Average case fatality rate	Varies over states	[6]
γ_3	Average recovery rate for COVID-19 hospitalized & notified infection	Varies over states	[6]
l	Average lockdown rate	$(0 - 1)\ day^{-1}$	Estimated
$\dfrac{1}{\omega}$	lockdown period	54 days	[38]

25

Table 2: Estimated parameter values of the mechanistic mathematical model (see Fig 1). Respective row subscripts are same as Fig. 2. All data are given in the format **Estimate (95% CI)**.

Location	β_1	ρ	σ	κ	γ_1	γ_2	$\tau \times 100$	$l \times 100$
MH	5.58	0.015	0.39	0.20	0.63	0.69	24.36	57.84
	$(2.62-9.79)$	$(0.01-0.15)$	$(0.07-0.45)$	$(0.11-0.53)$	$(0.27-0.99)$	$(0.22-0.98)$	$(11.34-93.53)$	$(11.77-86.19)$
DL	5.93	0.13	0.11	0.16	0.99	0.47	37.86	87.03
	$(0.78-6.30)$	$(0.02-0.82)$	$(0.07-0.47)$	$(0.11-0.93)$	$(0.31-0.99)$	$(0.33-0.98)$	$(12.48-98.27)$	$(11.25-87.11)$
TN	1.47	0.37	0.30	0.88	0.84	0.60	0.56	52.16
	$(1.23-3.63)$	$(0.18-0.91)$	$(0.15-0.48)$	$(0.03-0.91)$	$(0.29-0.98)$	$(0.30-0.98)$	$(0.22-9.65)$	$(12.38-88.92)$
GJ	10.73	0.03	0.10	0.11	0.24	0.91	16.79	77.68
	$(5.96-20.53)$	$(0.002-0.15)$	$(0.07-0.20)$	$(0.10-0.15)$	$(0.21-0.98)$	$(0.66-0.99)$	$(10.10-23.56)$	$(37.15-89.36)$
PJ	1.63	0.68	0.26	0.82	0.43	0.98	2.11	48.18
	$(1.31-5.35)$	$(0.016-0.95)$	$(0.076-0.45)$	$(0.11-0.90)$	$(0.12-0.97)$	$(0.24-0.99)$	$(0.12-2.24)$	$(12.50-87.76)$
IND	2.60	0.02	0.08	0.62	0.73	0.79	0.6	10.41
	$(1.04-2.92)$	$(0.02-0.77)$	$(0.07-0.14)$	$(0.30-0.98)$	$(0.31-0.98)$	$(0.33-0.98)$	$(0.2-0.9)$	$(10.37-42.56)$

Table 3: Estimated values of the basic reproduction number (R_0) in MH, DL, TN, GJ, PJ and IND. Respective row subscripts are same as Fig 2. All data are given in the format **Estimate (95% CI)**.

Location	Basic Reproduction Number (R_0)
MH	1.3320 (1.2369−2.3053)
DL	1.7569 (1.2409−2.2392)
TN	2.2169 (1.78−5.0374)
GJ	2.3911 (1.6223−2.7436)
PJ	1.8077 (1.7342−6.3960)
IND	2.0337 (1.6645−2.3318)

27

Table 4: Ensemble model forecast of the total COVID-19 cases during May 17, 2020 till May 31, 2020 in five different states and overall India under five different lockdown scenario. Respective row subscripts are same as Fig. 2. Different lockdown scenarios are **Current Rate**: cumulative case projection using the estimated value of the lockdown rate (see Table 2), **15% Reduction**: cumulative case projection using 15% reduction in the estimated value of the lockdown rate (see Table 2), **20% Reduction**: cumulative case projection using 20% reduction in the estimated value of the lockdown rate (see Table 2), **30% Reduction**: cumulative case projection using 30% reduction in the estimated value of the lockdown rate (see Table 2), and **No lockdown**: cumulative case projection based on no lockdown scenario, respectively. All data are provided in the format **Estimate (95% CI)**.

Location	Current Rate	15% Reduction	20% Reduction	30% Reduction	No lockdown
MH	33138 (31910−34046)	34602 (34430−34730)	35144 (34983−35361)	36318 (35532−37383)	48635 (41285−58578)
DL	6247 (5857−6811)	6504 (6253−6866)	6601 (6403−6887)	6816 (6734−6933)	9623 (7535−11068)
TN	19344 (19319−21503)	20958 (20946−21975)	21598 (21591−22162)	23076 (22562−23107)	60390 (31726−62172)
GJ	8227 (8128−9039)	8414 (8273−9572)	8485 (8328−9776)	8646 (8452−10233)	11208 (10433−17549)
PJ	7427 (7128−7517)	8188 (7702−8333)	8480 (7924−8647)	9139 (8421−9354)	19715 (16406−20705)
IND	117645 (110999−122572)	119204 (111569−124863)	119740 (111765−125650)	120831 (112164−127255)	128379 (114923−138352)

Credit Author statement.pdf

Conceptualization: Tridip Sardar, Joydev Chattopadhyay.

Data curation: Tridip Sardar, Sk Shahid Nadim.

Formal analysis: Tridip Sardar, Sk Shahid Nadim, Sourav Rana.

Investigation: Tridip Sardar, Sk Shahid Nadim, Sourav Rana.

Methodology: Tridip Sardar, Sk Shahid Nadim

Software: Tridip Sardar, Sourav Rana

Supervision: Tridip Sardar, Joydev Chattopadhyay.

Validation: Tridip Sardar

Writing original draft: Tridip Sardar, Sk Shahid Nadim, Sourav Rana, Joydev Chattopadhyay.

Writing review & editing: Tridip Sardar, Sk Shahid Nadim, Sourav Rana, Joydev Chattopadhyay.

Conflict of interests

All the authors declare that they have no conflicts of interest.

Source details

Feedback 〉 Compare sources 〉

Chaos, Solitons and Fractals

Scopus coverage years: from 1991 to Present

Publisher: Elsevier

ISSN: 0960-0779   ⓘ

Subject area: (Mathematics: Mathematical Physics) (Mathematics: Applied Mathematics) (Physics and Astronomy: Statistical and Nonlinear Physics)

(Physics and Astronomy: General Physics and Astronomy)

Source type: Journal

View all documents 〉   Set document alert   🖫 Save to source list

CiteScore 2022   ⓘ
11.8

SJR 2022   ⓘ
1.393

SNIP 2022   ⓘ
1.988

CiteScore   CiteScore rank & trend   Scopus content coverage

Check for
updates

Boundary Element Modeling for Simulation and Optimization of Three-Temperature Anisotropic Micropolar Magneto-thermoviscoelastic Problems in Porous Smart Structures Using NURBS and Genetic Algorithm

M. A. Fahmy, et al. *[full author details at the end of the article]*

Abstract

The main objective of the present paper is to propose a new boundary element modeling technique for simulation and optimization of three-temperature micropolar magneto-thermoviscoelastic problems in anisotropic porous smart structures, where we implemented the genetic algorithm (GA), as a method of optimization based on the free form deformation (FFD) methodology to improve the performance of our proposed technique. Two numerical examples are presented herein, in order to prove that the proposed technique is able to optimize the shape of the domains with minimum computational effort. A nonuniform rational B-spline curve (NURBS) has been introduced to define the optimum boundary where it decreases the number of control points and offers a new degree of versatility in the design of various different shapes. The profiles of the items considered shall be represented by the FFD methodology. The location vectors of the FFD control points are known to be the genes, and then the chromosomes for the profiles are determined by the gene sequence. The population is made up of several chromosomes individuals, where the fitness functions of individuals are assessed using BEM. The numerical results are depicted graphical forms to show the effects of viscosity and magnetic fields on the three temperatures, displacement components, microrotation components, pore pressure, electric potential, and thermal stress components. The validity, accuracy, and computational efficiency of the proposed BEM technique were demonstrated by comparing our BEM-obtained results with the corresponding results of normal mode analysis method (NMAM), finite difference method (FDM), and finite element method (FEM).

Keywords Anisotropic · Boundary element modeling · Genetic algorithm · Micropolar magneto-thermoviscoelasticity · Porous smart structures · Simulation and optimization

⌥ Springer

Nomenclature

$\alpha, \bar{\alpha}, \bar{\bar{\alpha}}, \breve{\alpha}$	Micropolar constants
β_{ij}	Stress–temperature coefficients, N/K m^2
δ_{ij}	Kronecker delta ($i, j = 1, 2$)
ε_{ij}	Strain tensor
ε_{ijk}	Alternate tensor
ϵ_{ij}	Micro-strain tensor
θ	Thermodynamic temperature, K
λ	Tractions, Pa
μ_0	Magnetic permeability (G/Oe)
ϑ_0	Viscoelastic relaxation time, s
ϖ	Weights of control points
ρ	Density $\left(\text{kg} \cdot \text{m}^{-3}\right)$
σ_{ij}	Force stress tensor, Pa
σ_0	Reference stress
τ	Time, s
τ_0, τ_1, τ_2	Relaxation times, s
φ_{ij}	Maxwell's stress tensor
ω_i	Microrotation $\left(\text{rad} \cdot \text{s}^{-1}\right)$
Φ	Electric potential, V
ϕ	Porosity
Ω	Angular velocity $\left(\text{rad} \cdot \text{s}^{-1}\right)$
$\aleph : = \left(1 + \vartheta_0 \frac{\partial}{\partial \tau}\right)$	Viscoelastic constant
$C_{v\alpha}$	Specific heat capacity $(\text{J/kg} \cdot \text{K})$
C_{ijkl}	Constant elastic moduli, GPa
D_i	Electric displacement, m
E_i	Electric field vector (V/m)
e	$= \varepsilon_{kk} = \epsilon_{kk}$ dilatation
$\mathbb{e}_{lij}$	Piezoelectric tensor
F_i	Mass force vector, N
$\mathbb{f}_{il}$	Permittivity tensor (F/m)
H_i	Magnetic field vector, Oe
$\tilde{h}$	Perturbed magnetic field $\left(\text{N/A}^2\right)$
J	Micro-inertia coefficient
$\mathbb{J}$	Current density vector $\left(\text{A/m}^2\right)$
$\mathbb{K}_\alpha$	Thermal conductivity (W/K m)
M_i	Mass couple vector
m_{ij}	Couple stress tensor, Pa
$N_{i,o}(t)$	Basis functions of order o
P_i	Control points
p	Pore pressure, Pa
T_α	Temperature functions, K
u_i	Displacement vector, m
$\mathbb{W}_{\text{ei}}$	Electron–ion energy coefficient, J
$\mathbb{W}_{\text{er}}$	Electron–phonon energy coefficient, J

1 Introduction

Nowadays, the development of smart structures will undoubtedly be actually the most essential task in several fields of science and technology such as bio-engineering, information science, aerospace engineering, microelectronics, computer science, medical treatment, energy, safety engineering, transportation, life science, military technologies, robotics, and vibration/shape control. Therefore, several applications and industries have been developed to give the increasing importance to the field of smart structures research.

The classical thermoelasticity (CTE) theory proposed by Duhamel [1] and Neuman [2] has two deficiencies: The first deficiency is that the equation of heat conduction related to this theory does not involve any elastic terms, which shows up opposite to the reality that elastic changes create thermal impacts. The second deficiency is that the equation of heat conduction is of a parabolic form, predicting infinite speeds of proliferation of heat waves opposite to physical perceptions. Biot [3] has developed the classical coupled thermoelasticity (CCTE) theory to address the first deficiency in CTE. Lord and Shulman (L–S) [4] developed the extended thermoelasticity (ETE) theory, where the Fourier's law is replaced by the Maxwell–Cattaneo law. This theory is also known as the theory of generalized thermoelasticity with one relaxation time. Green and Lindsay (G–L) [5] proposed the temperature-rate-dependent thermoelasticity (TRDTE) theory taking into consideration two relaxation times that relate the stress and entropy to the temperature. Green and Naghdi (G–N) [6, 7] proposed three linear generalized thermoelasticity theories which are denoted as GN theories of type I, II, and III. Model I is based on Fourier's law of heat conduction, model II deals with thermoelastic behavior without energy dissipation, and model III deals with thermoelastic interaction with energy dissipation. Hetnarski and Ignaczak (H–I) [8] introduced the low-temperature thermoelasticity model which is characterized by a system of nonlinear field equations in which both the free energy and the heat flux depend on the temperature, the strain tensor, and elastic heat flow. Tzou [9, 10] introduced the dual phase-lag (DPL) heat conduction model that includes two time (phase) lags of heat flux and temperature gradient in Fourier law of heat conduction in order to take into consideration the phonons–electrons interactions. The DPL heat conduction model is extended to the dual-phase-lag thermoelasticity (DPLTE) [11, 12]. Roychoudhuri [13] has recently introduced a three-phase-lag thermoelastic model that takes into account the phase-lag of heat flux, phase-lag of temperature gradient, and phase-lag of thermal displacement gradient. In the three-phase-lag model, the constitutive variable is the thermal displacement gradient, whereas in the conventional thermoelasticity theory, the constitutive variable is the temperature gradient. This more general model can be reduced to the previous models as special cases.

Chen and Gurtin [14] introduced the two-temperatures heat conduction theory in deformable bodies, which depends on the conductive temperature and thermodynamic temperature. Youssef [15] investigated this theory in the context of the generalized theory of thermoelasticity. Fahmy [16] developed the time-domain

dual reciprocity boundary element technique for solving optimization problems in the context of two-temperature generalized magneto-thermoelasticity. Fahmy [17] used the boundary element model to place the basics of three-temperature theory in the thermoelasticity field under the influence of multiple fields. The linear theory of elasticity which describes the mechanical behavior of the solid materials can not represent the behavior of polymers and elastomers. Therefore, the linear theory of micropolar elasticity [18] has been developed to describe the mechanical behavior of such materials. Then, Eringen [19] extended it to micropolar thermoelasticity. These different theories and models of micropolar elasticity and thermoelasticity have attracted much research attention from many researchers, among of them are research in [20–34].

Since the temperature fields are always an initial step in thermoelastic computations where the stresses are strongly affected by accuracy of heat transfer calculations. Hence we discuss the nonlinear three-temperature radiative heat conduction formulation which guarantees the accuracy of the solution of the considered problem. The energy conservation can be further approximated by three nonlinear time-dependent radiative heat conduction equations coupled with each other by exchanging energy from phonon to electron at first and then transmitting energy from electron to ion later.

One can find that the time consumption during solution of the whole system of the considered general and complex problem due to the energy equation. Hence, improved efficient numerical methods to solve the energy equation are needed. Due to its strong nonlinearity and discontinuity, the numerical solution and simulation of such problems are often very difficult and need the development of new approaches. It is necessary and critical to develop appropriate highly accurate numerical schemes and to design energy-efficient algorithms for the corresponding discrete system. Fortunately, we can decouple the radiation poro-visco-elastodynamics equations into the 3-T radiative heat conduction equations, which are described by the coupled radiation diffusion equations of electron, ion and phonon temperatures and poro-visco-elastodynamics governing equation with preserving main and essential properties.

The boundary element method (BEM) was implemented successfully for solving a wide class of engineering and industrial applications due to its straightforwardness, effectiveness, and ease of execution [35–60]. The boundary element formulation of the micropolar thermoelasticity was introduced by Sladek and Sladek [61–63] and developed by Huang and Liang [64].

Evolutionary computation has received significant attention for determining optimal solutions to industrial and engineering problems [65–67]. Due to advantages of the genetic algorithm such as reaching an optimum solution, even in the presence of complex shapes and reducing computational cost of finding optimum solution. The GA can deal with the multi-objective problems easily and we don't need to calculate the sensitivities.

The main aim of the present article is to propose a new boundary element modeling technique for simulation and optimization three-temperature anisotropic micropolar magneto-thermoviscoelastic problems in porous smart structures, where we used two-dimensional three-temperature (2D 3-T) nonlinear

time-dependent radiative heat conduction equations coupled with electron, ion and phonon temperatures and implemented the genetic algorithm (GA), as an optimization method based on free form deformation (FFD) technique, the nonuniform rational B-spline curve (NURBS) was used to model optimized boundary. The numerical results of the considered problem are presented graphically to show the effects of viscosity and magnetic fields on the three temperatures, displacement components, microrotation components, pore pressure, electric potential and thermal stress components. For comparison purposes with other methods which are special cases of our general and complex study, we considered the one-dimensional case of the current problem. The validity, efficiency and accuracy of our proposed BEM technique were confirmed by comparing our BEM-obtained results with the corresponding results of NMAM, FDM and FEM.

2 Formulation of the Problem

With reference to a rectangular Cartesian system (x_1, x_2, x_3) shown in Fig. 1, we consider an anisotropic micropolar porous smart structure with a configuration $R = \left\{ 0 < x_1 < \underline{\alpha}, \, 0 < x_2 < \underline{\beta}, \, 0 < x_3 < \underline{\gamma} \right\}$ bounded by a closed surface S, and S_i $(i = 1, 2, 3, 4, 5, 6, 7, 8)$ denotes subsets of S such that $S_1 + S_2 = S_3 + S_4 = S_5 + S_6 = S_7 + S_8 = S$.

According to Lukaszewicz [21] who introduced the governing equations of micropolar fluids in the context of elasticity and Eringen [22] who introduced the governing equations of magnetohydrodynamics piezoelectricity of micropolar viscous fluids, the governing equations of Eringen can be combined with the three-temperature radiative heat conduction theory [17] to obtain the governing equations for the three-temperature micropolar magneto-thermoviscoelastic
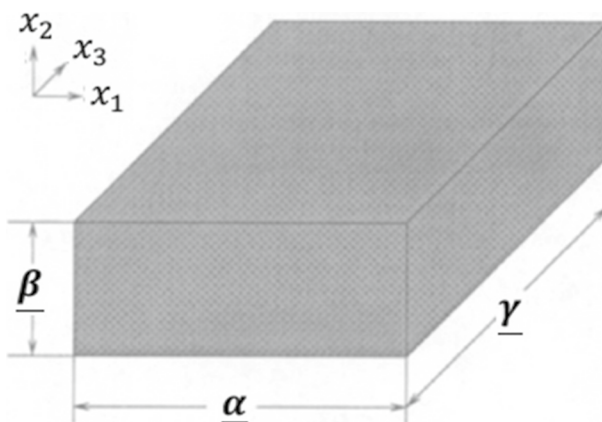
Fig. 1 Computational domain of the considered problem

problems in the context of anisotropic porous smart structures which can be written in non-dimensionless form as follows

$$\sigma_{ij,j} + \varphi_{ij,j} + \rho F_i = \rho \ddot{u}_i + \phi \rho_{\mathcal{F}} \ddot{v}_i \tag{1}$$

$$m_{ij,j} + \varepsilon_{ijk}\sigma_{jk} + \rho M_i = J\rho \ddot{\omega}_i \tag{2}$$

$$D_{i,i} = 0 \tag{3}$$

$$\dot{\zeta} + q_{i,i} = \mathbb{C} \tag{4}$$

where

$$\sigma_{ij} = C_{ijkl} \aleph \, e\delta_{ij} - A\delta_{ij}p + \breve{\alpha}\left(u_{j,i} - \varepsilon_{ijk}\omega_k\right) - \mathbb{e}_{lij}E_l - \beta_{ij}\,\theta \tag{5}$$

$$C_{ijkl} = C_{klij} = C_{jikl}, \; \beta_{ij} = \beta_{ji}$$

$$\varphi_{ij} = \mu_0\left(\tilde{h}_i H_j + \tilde{h}_j H_i - \delta_{ji}\left(\tilde{h}_k H_k\right)\right) \tag{6}$$

$$m_{ij} = \alpha\,\omega_{k,k}\,\delta_{ij} + \bar{\alpha}\,\omega_{i,j} + \bar{\bar{\alpha}}\,\omega_{j,i} \tag{7}$$

$$D_i = e_{ijk}\varepsilon_{jk} + \mathbb{f}_{ik}E_k \tag{8}$$

$$\zeta = Au_{k,k} + \frac{\phi^2}{R}p \tag{9}$$

$$q_i = -\bar{k}\left(p_{,i} + \rho_{\mathcal{F}}\ddot{u}_i + \frac{\rho_0 + \phi\rho_{\mathcal{F}}}{\phi}\ddot{v}_i\right) \tag{10}$$

$$\epsilon_{ij} = \varepsilon_{ij} - \varepsilon_{ijk}\left(r_k - \omega_k\right), \quad \varepsilon_{ij} = \frac{1}{2}\left(u_{i,j} + u_{j,i}\right), \quad E_l = -\Phi_l, \quad r_i = \frac{1}{2}\varepsilon_{ikl}u_{l,k} \tag{11}$$

The three-temperature radiation heat transfer equations can be expressed as

$$C_{ve}\frac{\partial T_e(r,\tau)}{\partial \tau} - \frac{1}{\rho}\nabla\left[\mathbb{K}_e \nabla T_e(r,\tau)\right] = -\mathbb{W}_{ei}\left(T_e - T_i\right) - \mathbb{W}_{er}\left(T_e - T_r\right) \tag{12}$$

$$C_{vi}\frac{\partial T_i(r,\tau)}{\partial \tau} - \frac{1}{\rho}\nabla\left[\mathbb{K}_i \nabla T_i(r,\tau)\right] = \mathbb{W}_{ei}\left(T_e - T_i\right) \tag{13}$$

$$C_{vr}\frac{\partial T_r(r,\tau)}{\partial \tau} - \frac{1}{\rho}\nabla\left[\mathbb{K}_r\nabla T_r(r,\tau)\right] = \mathbb{W}_{er}\left(T_e - T_r\right) \tag{14}$$

In which $C_{v\alpha} = \begin{cases} c_e & \alpha = e \\ c_i & \alpha = i \\ c_r T_r^3 & \alpha = r \end{cases}$ and $\mathbb{K}_{\alpha} = \begin{cases} \mathbb{A}_e T_e^{5/2} & \alpha = e \\ \mathbb{A}_i T_i^{5/2} & \alpha = i \\ \mathbb{A}_r T^{3+\mathbb{B}} & \alpha = r \end{cases}$ where we consid-

ered that $\theta = T_e + T_i + T_r$, T_e, T_i and T_r are temperature functions of electron, ion and phonon, respectively, $0 \leq \tau \leq T_{\max}$, $\mathbb{K}_{\alpha} = \mathbb{K}_{\alpha}(\rho, T_{\alpha})(\alpha = e, i, r)$ are heat conductive coefficients of electron, ion and phonon, respectively, ρ is the material density which is constant inside each subdomain, energy exchanging coefficients are $\mathbb{W}_{ei} = \rho\mathbb{A}_{ei}T_e^{-2/3}$ and $\mathbb{W}_{er} = \rho\mathbb{A}_{er}T_e^{-1/2}$, $c_{\alpha}(\alpha = e, i, r)$ are constants, $\mathbb{A}_{\alpha}(\alpha = e, i, r)$. The proposed solution algorithm of the considered problem is described in Fig. 2.

3 BEM Modeling for Temperature Field

The two-dimensional three-temperature (2D-3T) radiative heat conduction Eqs. 12–14 can be expressed as follows

$$\nabla\left[\mathbb{K}_{\alpha}\nabla T_{\alpha}(r,\tau)\right] + \overline{\mathbb{W}}(r,\tau) = c_{\alpha}\rho\delta_1\frac{\partial T_{\alpha}(r,\tau)}{\partial \tau} \tag{15}$$

where

$$\overline{\mathbb{W}}(r,\tau) = \begin{cases} -\rho\mathbb{W}_{ei}\left(T_e - T_i\right) - \rho\mathbb{W}_{er}\left(T_e - T_r\right), & \alpha = e, \delta_1 = 1 \\ \rho\mathbb{W}_{ei}\left(T_e - T_i\right), & \alpha = i, \delta_1 = 1 \\ \rho\mathbb{W}_{er}\left(T_e - T_r\right), & \alpha = r, \delta_1 = T_r^3 \end{cases}$$

The unit mass total energy is given by

$$P = P_e + P_i + P_r, \quad P_e = c_e T_e, \quad P_i = c_i T_i, \quad P_r = \frac{1}{4}c_r T_r^4 \tag{16}$$

The considered conditions can be composed as

$$T_{\alpha}(x, y, 0) = T_{\alpha}^0(x, y) = g_1(x, \tau) \tag{17a}$$

$$\mathbb{K}_{\alpha}\frac{\partial T_{\alpha}}{\partial n}\bigg|_{\Gamma_1} = 0, \alpha = e, i, \quad T_r|_{\Gamma_1} = g_2(x, \tau) \tag{17b}$$

$$\mathbb{K}_{\alpha}\frac{\partial T_{\alpha}}{\partial n}\bigg|_{\Gamma_2} = 0, \quad \alpha = e, i, r \tag{17c}$$

By using the fundamental solution that satisfies the following differential equation
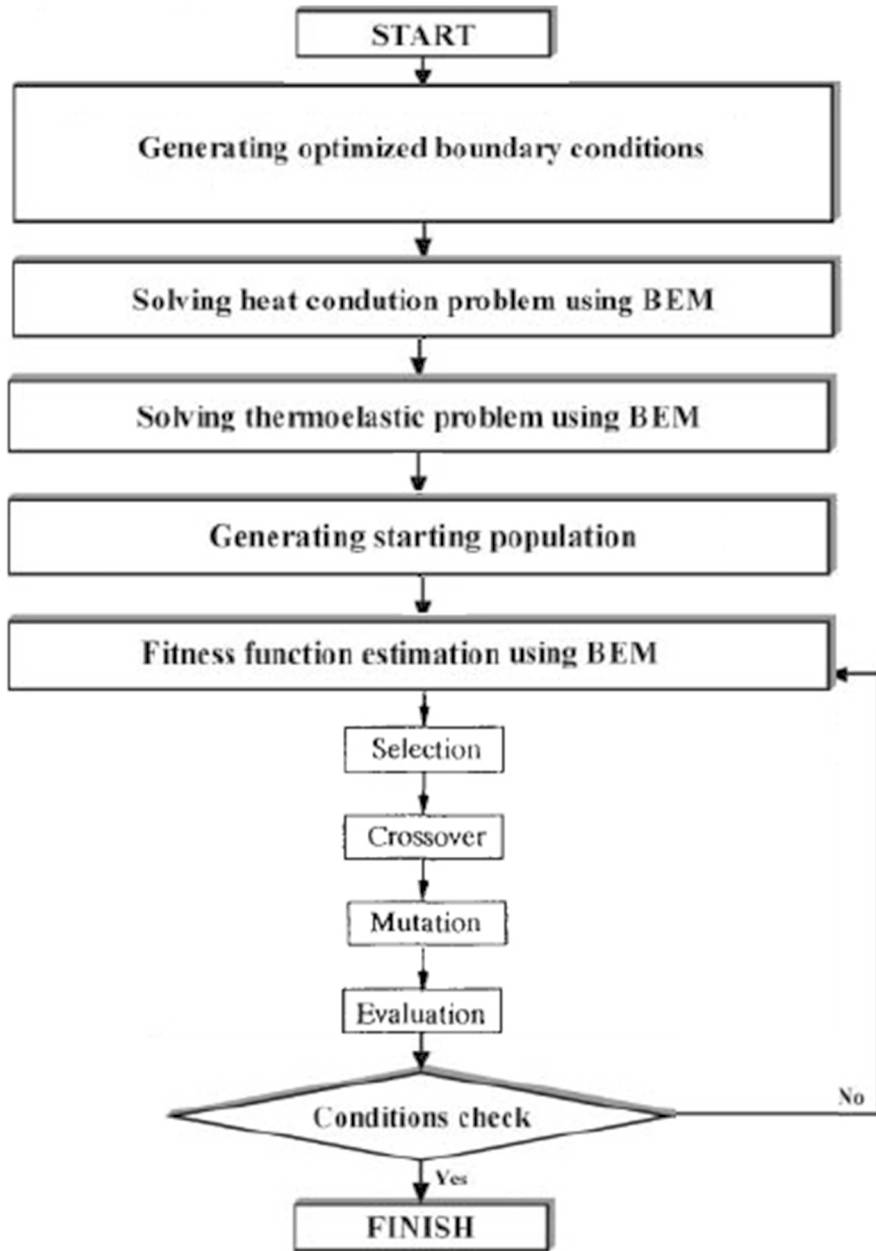
Fig. 2 Algorithm of solution of the considered problem

$$D\nabla^2 T_\alpha + \frac{\partial T_\alpha^*}{\partial n} = -\delta(r - p_i)\delta(\tau - r), \quad D = \frac{\mathbb{K}_\alpha}{\rho c} \tag{18}$$

where p_i are singular points.

The direct formulation of the integral equation corresponding to transient heat conduction can be obtained by employing the dual reciprocity boundary element method of Fahmy [17] as follows

$$CT_\alpha = \frac{D}{\mathbb{K}_\alpha} \int_O^\tau \int_S \left[T_\alpha q^* - T_\alpha^* q \right] dS d\tau + \frac{D}{\mathbb{K}_\alpha} \int_O^\tau \int_R b T_\alpha^* dR d\tau + \int_R T_\alpha^i T_\alpha^* \Big|_{\tau=0} dR \tag{19}$$

which can be expressed as follows

$$CT_\alpha = \int_S \left[T_\alpha q^* - T_\alpha^* q \right] dS - \int_R \frac{\mathbb{K}_\alpha}{D} \frac{\partial T_\alpha^*}{\partial \tau} T_\alpha dR \tag{20}$$

To transform the domain integral in (20) to the boundary, we suppose that time temperature derivative can be approximated in terms of known functions $f^j(r)$ and unknown coefficients $a^j(\tau)$ as follows

$$\frac{\partial T_\alpha}{\partial \tau} \cong \sum_{j=1}^N f^j(r)^j a^j(\tau) \tag{21}$$

Now, we assume that $\hat{T}_\alpha^j$ is a solution of

$$\nabla^2 \hat{T}_\alpha^j = f^j \tag{22}$$

Thus, Eq. 20 results in the following form

$$CT = \int_S \left[T_\alpha q^* - T_\alpha^* q \right] dS + \sum_{j=1}^N a^j(\tau) D^{-1} \left(C\hat{T}_\alpha^j - \int_S \left[T_\alpha^j q^* - \hat{q}^j T_\alpha^* \right] dS \right) \tag{23}$$

where

$$\hat{q}^j = -\mathbb{K}_\alpha \frac{\partial \hat{T}_\alpha^j}{\partial n} \tag{24}$$

and

$$a^j(\tau) = \sum_{i=1}^N f_{ji}^{-1} \frac{\partial T(r_i, \tau)}{\partial \tau} \tag{25}$$

ere f_{ji}^{-1} are defined as [34]

$$\{F\}_{ji} = f^j(r_i) \tag{26}$$

By applying the BEM discretization scheme to Eq. 23 and using Eq. 25, we obtain the following set of ordinary differential equations

$$C\dot{T}_\alpha + HT_\alpha = GQ \tag{27}$$

The diffusion matrix can be defined as

$$C = -\left[H\hat{T}_\alpha - G\hat{Q}\right]F^{-1}D^{-1} \tag{28}$$

with

$$\{\hat{T}\}_{ij} = \hat{T}^j(x_i) \tag{29}$$

$$\{\hat{Q}\}_{ij} = \hat{q}^j(x_i) \tag{30}$$

Now, we interpolate the functions T_α and q as

$$T_\alpha = (1-\theta)T_\alpha^m + \theta T_\alpha^{m+1} \tag{31}$$

$$q = (1-\theta)q^m + \theta q^{m+1} \tag{32}$$

where $0 \leq \theta = \frac{\tau - \tau^m}{\tau^{m+1} - \tau^m} \leq 1$.

By applying differentiation of Eq. 33 with respect to τ get

$$\dot{T}_\alpha = \frac{dT_\alpha}{d\theta}\frac{d\theta}{d\tau} = \frac{T_\alpha^{m+1} - T_\alpha^m}{\tau^{m+1} - \tau^m} = \frac{T_\alpha^{m+1} - T_\alpha^m}{\Delta\tau^m} \tag{33}$$

Substitution of Eqs. 33–35 into Eq. 27, yields

$$\left(\frac{C}{\Delta\tau^m} + \theta H\right)T_\alpha^{m+1} - \theta GQ^{m+1} = \left(\frac{C}{\Delta\tau^m} - (1-\theta)H\right)T_\alpha^m + (1-\theta)GQ^m \tag{34}$$

which can be written as

$$\mathbb{a}\mathsf{X} = \mathbb{b} \tag{35}$$

The successive over-relaxation (SOR) method requires less memory in comparison with the Jacobi and Gauss–Seidel iterative methods [35], so it was efficiently implemented to solve the resulting linear algebraic systems.

4 BEM Modeling for Displacement Field

By applying the weighted residual method to Eqs. 1–4, we obtain

$$\int_R \left(\sigma_{ij,j} + U_i\right)u_i^* dR = 0 \tag{36}$$

$$\int_R \left(m_{ij,j} + \varepsilon_{ijk}\sigma_{jk} + V_i\right)\omega_i^* dR = 0 \tag{37}$$

$$\int_R \left(D_{,i}\right)\Phi_i^* dR = 0 \tag{38}$$

$$\int_R \left(q_{,i} + \dot{\zeta}_i - \mathbb{C}_i\right)p_i^* dR = 0 \tag{39}$$

where u_i^*, ω_i^*, Φ_i^* and p_i^* are weighting functions, $U_i = \varphi_{ij,j} + \rho F_i - \rho \ddot{u}_i - \phi\rho_{\mathcal{F}}\dot{v}_i$ and $V_i = \rho\left(M_i - J\ddot{\omega}_i\right)$.

Now, we consider the following boundary conditions

$$u_i = \bar{u}_i \text{ on } S_1 \tag{40a}$$

$$\lambda_i = \sigma_{ij}n_j = \bar{\lambda}_i \text{ on } S_2 \tag{40b}$$

$$\omega_i = \bar{\omega}_i \text{ on } S_3 \tag{40c}$$

$$\mu_i = m_{ij}n_j = \bar{\mu}_i \text{ on } S_4 \tag{40d}$$

$$\Phi = \bar{\Phi} \text{ on } S_5 \tag{40e}$$

$$Q = \frac{\partial\Phi}{\partial n} = \bar{Q} \text{ on } S_6 \tag{40f}$$

$$p = \bar{p} \text{ on } S_7 \tag{40g}$$

$$L = \frac{\partial p}{\partial n} = \bar{L} \text{ on } S_8 \tag{40h}$$

By applying integration by parts to Eqs. 36–39, we get

$$-\int_R \sigma_{ij}u_{i,j}^* dR + \int_R U_i u_i^* dR = -\int_{S_2} \lambda_i u_i^* dS \tag{41}$$

$$-\int_R m_{ij}\omega_{i,j}^* dR + \int_R \varepsilon_{ijk}\sigma_{jk}\omega_i^* dR + \int_R V_i\omega_i^* dR = -\int_{S_4} \mu_i\omega_i^* dS \tag{42}$$

$$-\int_R D\Phi_{i,i}^* dR == -\int_{S_6} Q_i\Phi_i^* dS \tag{43}$$

$$-\int_R q\mathrm{p}_{i,i}^* dR + \int_R \dot\zeta_i \mathrm{p}_i^* dR - \int_R \mathbb{C}_i \mathrm{p}_i^* dR = -\int_{S_8} L_i \mathrm{p}_i^* dS \tag{44}$$

On the basis of Huang and Liang [64], we obtain

$$-\int_R \sigma_{ij,j} u_i^* dR + \int_R (m_{ij,j} + \varepsilon_{ijk}\sigma_{jk})\omega_i^* dR + \int_R U_i u_i^* dR$$
$$+\int_R V_i \omega_i^* dR - \int_R D\Phi_{i,i}^* dR - \int_R q\mathrm{p}_{i,i}^* dR + \int_R \dot\zeta_i \mathrm{p}_i^* dR - \int_R \mathbb{C}_i \mathrm{p}_i^* dR = \int_{S_1} \left(\lambda_i - \overline\lambda_i\right) u_i^* dS + \int_{S_1}\left(\overline u_i - u_i\right)\lambda_i^* dS$$
$$+\int_{S_4}\left(\mu_i - \overline\mu_i\right)\omega_i^* dS + \int_{S_3}\left(\overline\omega_i - \omega_i\right)\mu_i^* dS + \int_{S_6}\left(Q_i - \overline Q_i\right)\Phi_i^* dS + \int_{S_5}\left(\overline\Phi_i - \Phi_i\right)Q_i^* dS + \int_{S_8}\left(L_i - \overline L_i\right)\mathrm{p}_i^* dS + \int_{S_7}\left(\overline{\mathrm{p}}_i - \mathrm{p}_i\right)L_i^* dS \tag{45}$$

By applying integration by parts to (45), we obtain

$$-\int_R \sigma_{ij}\varepsilon_{ij}^* dR - \int_R m_{ij,j}\omega_{i,j}^* dR + \int_R U_i u_i^* dR + \int_R V_i \omega_i^* dR - \int_R D\Phi_{i,i}^* dR$$
$$-\int_R q\mathrm{p}_{i,i}^* dR + \int_R \dot\zeta_i \mathrm{p}_i^* dR - \int_R \mathbb{C}_i \mathrm{p}_i^* dR = -\int_{S_2}\overline\lambda_i u_i^* dS - \int_{S_1}\lambda_i u_i^* dS + \int_{S_1}\left(\overline u_i - u_i\right)\lambda_i^* dS - \int_{S_4}\overline\mu_i\omega_i^* dS - \int_{S_3}\mu\omega_i^* dS$$
$$+\int_{S_3}\left(\overline\omega_i - \omega_i\right)\mu_i^* dS - \int_{S_6}\overline Q_i\Phi_i^* dS - \int_{S_5} Q_i\Phi_i^* dS + \int_{S_5}\left(\overline\Phi_i - \Phi_i\right)Q_i^* dS - \int_{S_8}\overline L_i \mathrm{p}_i^* dS - \int_{S_8} L_i \mathrm{p}_i^* dS + \int_{S_7}\left(\overline{\mathrm{p}}_i - \mathrm{p}_i\right)L_i^* dS \tag{46}$$

Based on Eringen [68], we can write

$$\sigma_{ij} = \mathbb{A}_{ijkl}\varepsilon_{kl}, m_{ij} = \mathbb{B}_{ijkl}\omega_{k,l} \text{ where } \mathbb{A}_{ijkl} = \mathbb{A}_{klij} \text{ and } \mathbb{B}_{ijkl} = \mathbb{B}_{klij} \tag{47}$$

Hence, Eq. 46 can be expressed as

$$-\int_R \sigma_{ij}^*\varepsilon_{ij} dR - \int_R m_{ij,j}^*\omega_{i,j} dR + \int_R U_i u_i^* dR + \int_R V_i \omega_i^* dR - \int_R D\Phi_{i,i}^* dR$$
$$-\int_R q\mathrm{p}_{i,i}^* dR + \int_R \dot\zeta_i \mathrm{p}_i^* dR - \int_R \mathbb{C}_i \mathrm{p}_i^* dR = -\int_{S_2}\overline\lambda_i u_i^* dS - \int_{S_1}\lambda_i u_i^* dS$$
$$+\int_{S_1}\left(\overline u_i - u_i\right)\lambda_i^* dS - \int_{S_4}\overline\mu_i\omega_i^* dS - \int_{S_3}\mu_i\omega_i^* dS + \int_{S_3}\left(\overline\omega_i - \omega_i\right)\mu_i^* dS$$
$$-\int_{S_6}\overline Q_i\Phi_i^* dS - \int_{S_5} Q_i\Phi_i^* dS + \int_{S_5}\left(\overline\Phi_i - \Phi_i\right)Q_i^* dS - \int_{S_8}\overline L_i \mathrm{p}_i^* dS$$
$$-\int_{S_8} L_i \mathrm{p}_i^* dS + \int_{S_7}\left(\overline{\mathrm{p}}_i - \mathrm{p}_i\right)L_i^* dS \tag{48}$$

Using integration by parts again for the left-hand side of (48) and using boundary conditions, we obtain

$$
\int_R \sigma_{ij,j}^* u_i dR + \int_R \left(m_{ij,j}^* + \varepsilon_{ijk}\sigma_{jk}^* \right)\omega_i dR
$$
$$
= -\int_S u_i^* \lambda_i dS - \int_S \omega_i^* \mu_i dS
$$
$$
= -\int_S \Phi_i^* Q_i dS - \int_S p_i^* L_i dS + \int_S \lambda_i^* u_i dS + \int_S \mu_i^* \omega_i dS
$$
$$
+ \int_S Q_i^* \Phi_i dS + \int_S L_i^* p_i dS
$$

(49)

The obtained weighting functions for a point load $U_i = \Delta^n$ and $V_i = 0$ along the unit vector direction e_l were first used as follows:

$$
\sigma_{lj,j}^* + \Delta^n e_l = 0
$$

(50)

$$
m_{ij,j}^* + \varepsilon_{ijk}\sigma_{jk}^* = 0
$$

(51)

The fundamental solution of Dragos [69] may be written as

$$
u_i^* = u_{li}^* e_l, \ \omega_i^* = \omega_{li}^* e_l, \ \Phi_i^* = \Phi_{li}^* e_l, \ p_i^* = p_{li}^* e_l, \ \lambda_i^* = \lambda_{li}^* e_l, \ \mu_i^* = \mu_{li}^* e_l, \ Q_i^* = Q_{li}^* e_l, \ L_i^* = L_{li}^* e_l
$$

(52)

The obtained weighting functions for a point load $U_i = 0$ and $V_i = \Delta^n$ along the unit vector direction e_l were next used as follows:

$$
\sigma_{ij,j}^{**} = 0
$$

(53)

$$
m_{lj,j}^{**} + \varepsilon_{ljk}\sigma_{jk}^{**} + \Delta^n e_l = 0
$$

(54)

Based on Dragos [69] the fundamental solution may be expressed as

$$
u_i^* = u_{li}^{**} e_l, \ \omega_i^* = \omega_{li}^{**} e_l, \ \Phi_i^* = \Phi_{li}^{**} e_l,
$$
$$
p_i^* = p_{li}^{**} e_l, \ \lambda_i^* = \lambda_{li}^{**} e_l \ \mu_i^* = \mu_{li}^{**} e_l, \ Q_i^* = Q_{li}^{**} e_l, \ L_i^* = L_{li}^{**} e_l
$$

(55)

By applying the above two sets of weighting functions to (49) we have

$$
C_{li}^n u_i^n = -\int_S \lambda_{li}^* u_i dS - \int_S \mu_{li}^* \omega_i dS - \int_S Q_{li}^* \Phi_i dS
$$
$$
-\int_S L_{li}^* p_i dS + \int_S u_{li}^* \lambda_i dS + \int_S \omega_{li}^* \mu_i dS + \int_S \Phi_{li}^* Q_i dS + \int_S p_{li}^* L_i dS
$$

(56)

$$C_{li}^n \omega_i^n = - \int_S \lambda_{li}^{**} u_i dS - \int_S \mu_{li}^{**} \omega_i dS - \int_S Q_{li}^{**} \Phi_i dS$$

$$- \int_S \mathrm{L}_{li}^{**} p_i dS + \int_S u_{li}^{**} \lambda_i dS + \int_S \omega_{li}^{**} \mu_i dS \omega_{li}^{**} \mu_i dS + \int_S \Phi_{li}^{**} Q_i dS + \int_S p_{li}^{**} \mathrm{L}_i dS \tag{57}$$

Thus, we can write

$$C^n \mathbb{q}^n = - \int_S \mathbb{p}^* \, \mathbb{q} \, dS + \int_S \mathbb{q}^* \, \mathbb{p} \, dS + \int_S \mathbb{d}^* \, \Phi \, dS + \int_S \mathbb{f}^* \, \frac{\partial \Phi}{\partial n} \, dS$$

$$+ \int_S \mathbb{a}^* \, p \, dS + \int_S \mathbb{b}^* \, \frac{\partial p}{\partial n} \, dS \tag{58}$$

where

$$C^n = \begin{bmatrix} C_{11} & C_{12} \\ C_{21} & C_{22} \end{bmatrix}, \mathbb{q}^* = \begin{bmatrix} u_{11}^* & u_{12}^* & \omega_{13}^* \\ u_{21}^* & u_{22}^* & \omega_{23}^* \\ u_{31}^{**} & u_{32}^{**} & \omega_{33}^{**} \end{bmatrix}, \mathbb{p}^* = \begin{bmatrix} \lambda_{11}^* & \lambda_{12}^* & \mu_{13}^* \\ \lambda_{21}^* & \lambda_{22}^* & \mu_{23}^* \\ \lambda_{31}^{**} & \lambda_{32}^{**} & \mu_{33}^{**} \end{bmatrix}$$

$$\mathbb{q} = \begin{bmatrix} u_1 \\ u_2 \\ \omega_3 \end{bmatrix}, \mathbb{p} = \begin{bmatrix} \lambda_1 \\ \lambda_2 \\ \mu_3 \end{bmatrix}, \mathbb{d}^* = \begin{bmatrix} \mathbb{d}_1^* \\ \mathbb{d}_2^* \\ 0 \end{bmatrix}, \mathbb{f}^* = \begin{bmatrix} \mathbb{f}_1^* \\ \mathbb{f}_2^* \\ 0 \end{bmatrix}, \mathbb{a}^* = \begin{bmatrix} \mathbb{a}_1^* \\ \mathbb{a}_2^* \\ 0 \end{bmatrix}, \mathbb{b}^* = \begin{bmatrix} \mathbb{b}_1^* \\ \mathbb{b}_2^* \\ 0 \end{bmatrix}$$

Now, we introduce the following functions.

$$\mathbb{q} = \psi \, \mathbb{q}^j, \mathbb{p} = \psi \, \mathbb{p}^j, \Phi = \psi_0 \, \Phi^j, \frac{\partial \Phi}{\partial n} = \psi_0 \left(\frac{\partial \Phi}{\partial n} \right)^j, p = \psi_0 \, p^j, \frac{\partial p}{\partial n} = \psi_0 \left(\frac{\partial p}{\partial n} \right)^j \tag{59}$$

By applying (59) to (58), we have.

$$C^n \mathbb{q}^n = \sum_{j=1}^{N_e} \left[- \int_{\Gamma_j} \mathbb{p}^* \psi \, d\Gamma \right] \mathbb{q}^j + \sum_{j=1}^{N_e} \left[\int_{\Gamma_j} \mathbb{q}^* \psi \, d\Gamma \right] \mathbb{p}^j + \sum_{j=1}^{N_e} \left[\int_{\Gamma_j} \mathbb{d}^* \psi_0 \, d\Gamma \right] \Phi^j$$

$$+ \sum_{j=1}^{N_e} \left[\int_{\Gamma_j} \mathbb{f}^* \psi_0 \, d\Gamma \right] \left(\frac{\partial \Phi}{\partial n} \right)^j + \sum_{j=1}^{N_e} \left[\int_{\Gamma_j} \mathbb{a}^* \psi_0 \, d\Gamma \right] p^j \tag{60}$$

$$+ \sum_{j=1}^{N_e} \left[\int_{\Gamma_j} \mathbb{b}^* \psi_0 \, d\Gamma \right] \left(\frac{\partial p}{\partial n} \right)^j$$

which may be expressed as

$$C^i \mathbb{q}^i = -\sum_{j=1}^{N_e} \hat{\mathbb{H}}^{ij} \mathbb{q}^j + \sum_{j=1}^{N_e} \hat{\mathbb{G}}^{ij} \mathbb{p}^j + \sum_{j=1}^{N_e} \hat{\mathbb{D}}^{ij} \Phi^j + \sum_{j=1}^{N_e} \hat{\mathbb{F}}^{ij} \left(\frac{\partial \Phi}{\partial n}\right)^j$$

$$+ \sum_{j=1}^{N_e} \hat{\mathbb{a}}^{ij} p^j + \sum_{j=1}^{N_e} \hat{\mathbb{b}}^{ij} \left(\frac{\partial p}{\partial n}\right)^j \tag{61}$$

where

$$\mathbb{H}^{ij} = \begin{cases} \hat{\mathbb{H}}^{ij} & \text{if } i \neq j \\ \hat{\mathbb{H}}^{ij} + C^i & \text{if } i = j \end{cases} \tag{62}$$

Therefore, Eq. (61) may be written as

$$\sum_{j=1}^{N_e} \mathbb{H}^{ij} \mathbb{q}^j = \sum_{j=1}^{N_e} \hat{\mathbb{G}}^{ij} \mathbb{p}^j + \sum_{j=1}^{N_e} \hat{\mathbb{D}}^{ij} \Phi^j + \sum_{j=1}^{N_e} \hat{\mathbb{F}}^{ij} \left(\frac{\partial \Phi}{\partial n}\right)^j + \sum_{j=1}^{N_e} \hat{\mathbb{a}}^{ij} p^j + \sum_{j=1}^{N_e} \hat{\mathbb{b}}^{ij} \left(\frac{\partial p}{\partial n}\right)^j \tag{63}$$

which can be expressed as

$$\mathbb{H}\mathbb{Q} = \mathbb{G}\mathbb{P} + \mathbb{D}\Theta + \mathbb{F}\mathbb{S} + \mathbb{a}\mathbb{i} + \mathbb{b}\mathbb{j} \tag{64}$$

the vector $\mathbb{Q}$ represents all the values of displacements and microrotations, the vector $\mathbb{P}$ represents all the tractions and couple stress vector, the vector Θ represents all the values of electric potential, the vector $\mathbb{S}$ represents all the values of electric potential gradients, the vector $\mathbb{i}$ represents all the values of pore pressure and the vector $\mathbb{j}$ represents all the values of pore pressure gradients before applying boundary conditions.

Now, we can write (64) as follows

$$\mathbb{A}\mathbb{X} = \mathbb{B} \tag{65}$$

We apply successive over-relaxation (SOR) as described in Golub and Van Loan [70] to solve the system (65) and obtain all boundary values.

5 Evolutionary shape optimization of micropolar smart structures

During the optimisation of smart systems, two requirements can be applied.

I. The minimum global compliance:

$$\mathcal{F} = \frac{1}{2} \int_S (\lambda \cdot u) dS \tag{66}$$

where λ is the tractions, u is the field of boundary displacements.

II. The minimum boundary equivalent stresses

$$\mathcal{F} = \int_S \left(\frac{\sigma_{ij}}{\sigma_0} \right)^n dS \tag{67}$$

In which σ_{ij} are equivalent stresses on the boundary, σ_0 is a reference stress and n is a natural number.

In order to obtain the optimal temperature boundary conditions, we apply the following functional

$$\mathcal{F} = \int_S \left(\frac{u}{u_0} \right)^n dS \tag{68}$$

where u is a boundary displacement and u_0 is a reference displacement.

Now, we use the following functional to determine the inner boundary

$$\mathcal{F} = \delta \sum_{k=1}^M \left(u^k - \hat{u}^k \right) + \eta \sum_{l=1}^N \left(\theta^l - \hat{\theta}^l \right) \tag{69}$$

where $\hat{u}^k$ and $\hat{\theta}^l$ are measured values of displacements and temperatures, u^k and θ^l are computed values of displacements and temperatures in boundary points k and l, respectively, δ and η are weight coefficients, M, N are numbers of sensors.
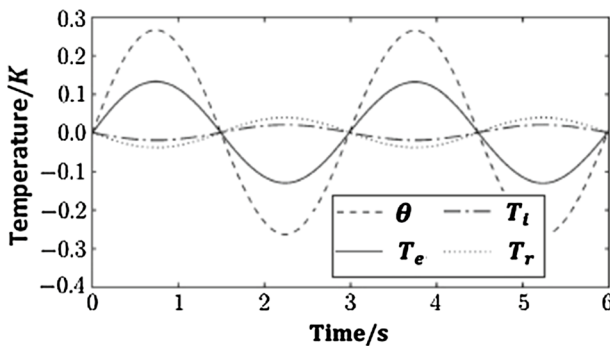
Fig. 3 Variation of the three temperatures T_e, T_i, T_r and considered temperature θ with the time τ
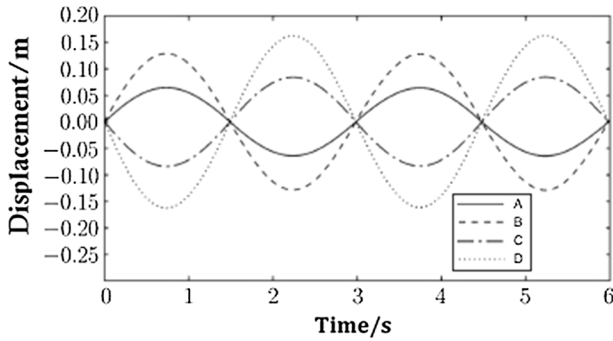
Fig. 4 Variation of the displacement $\mathbf{u}_1$ with the time τ
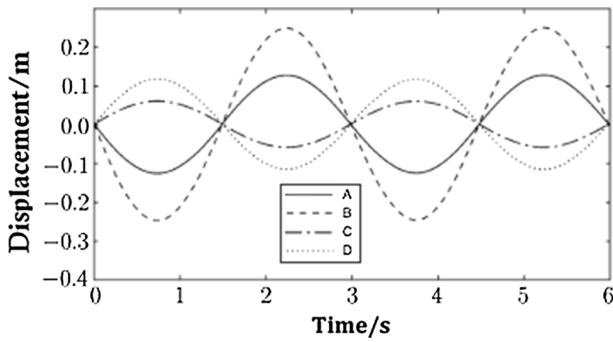
Fig. 5 Variation of the displacement $\mathbf{u}_2$ with the time τ
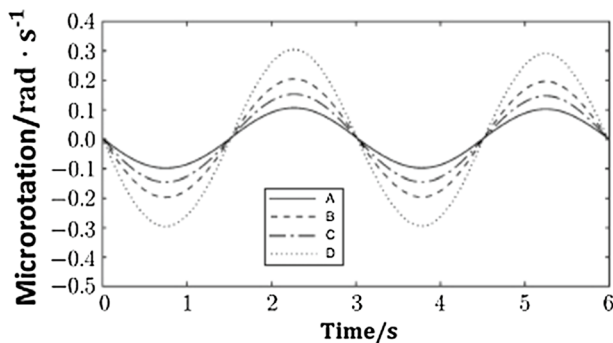
Fig. 6 Variation of the microrotation $\boldsymbol{\omega}_1$ with the time τ

6 Numerical Results and Discussions

The proposed technique implemented in the present paper should be applicable to a wide range of three-temperature micropolar magneto-thermoviscoelastic problems in anisotropic porous smart structures. All the physical parameters satisfy
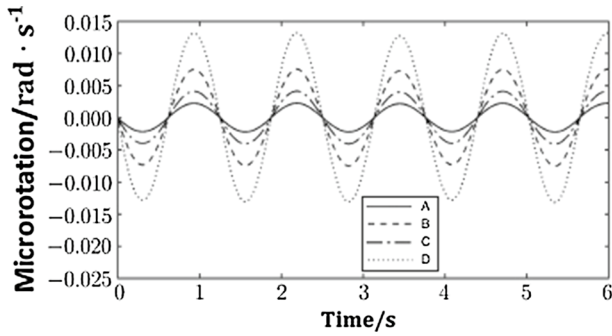
Fig. 7 Variation of the microrotation ω_2 with the time τ
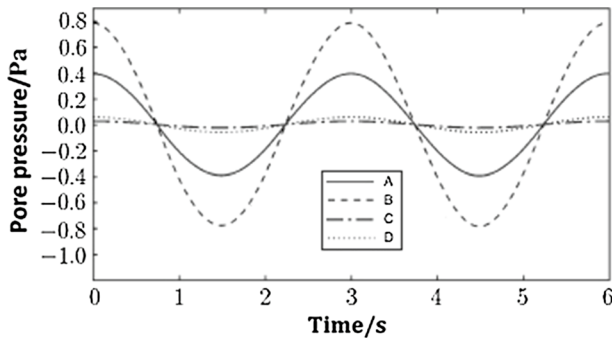
Fig. 8 Variation of the pore pressure **p** with the time τ
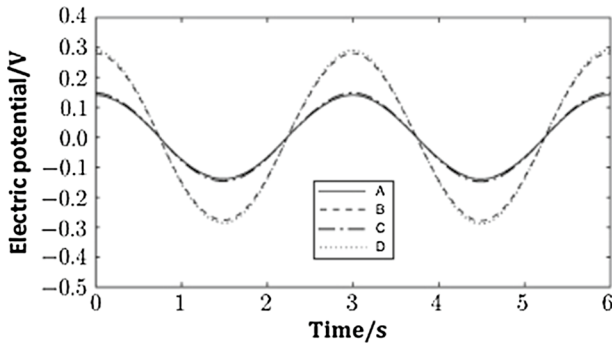
Fig. 9 Variation of the electric potential Φ with the time τ

the initial and boundary conditions. The validity, accuracy and efficiency of our model has been enhanced by using NURBS to reduce the iteration number and computation time.
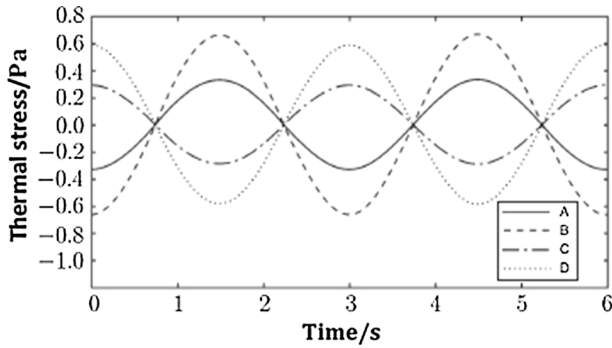
Fig. 10 Variation of the thermal stress σ_{11} with the time τ
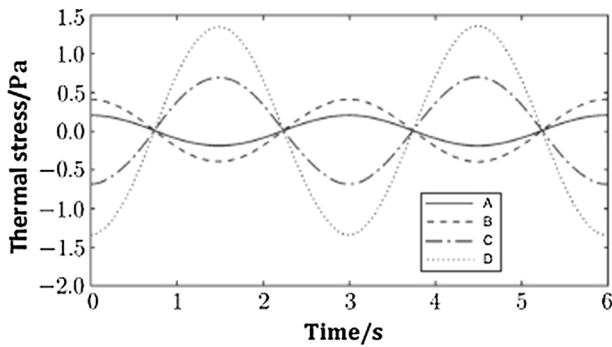
Fig. 11 Variation of the thermal stress σ_{12} with the time τ
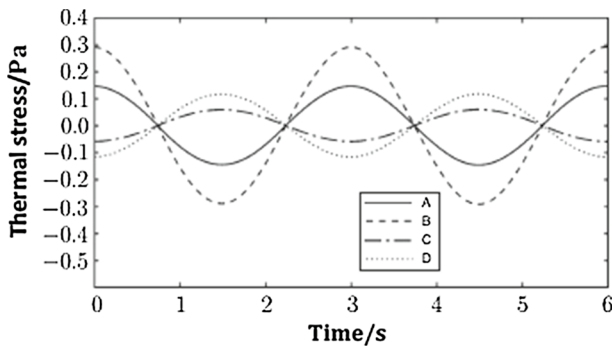
Fig. 12 Variation of the thermal stress σ_{22} with the time τ

In order to compute the effect of the viscosity and magnetic fields on the displacement components, microrotation components, pore pressure and electric potential in an anisotropic micropolar magneto-thermoviscoelastic porous smart structures, a comparison of the results is presented graphically for the

Fig. 13 Optimized smart structure for example 1, where all dimensions given in the figure are in centimeters
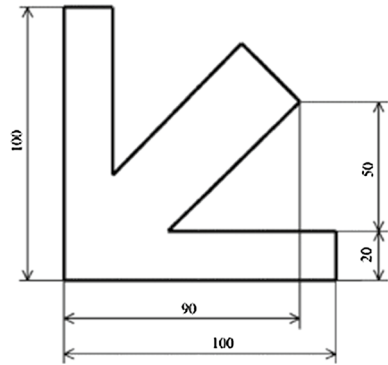
following different cases: the solid line denoted by "A" represents the solution in the absence of viscosity effect ($\aleph = 1$) and in the absence of magnetic effect ($\mu_0 = 0$), the dashed line denoted by "B" represents the solution in the absence of viscosity effect ($\aleph = 1$) and in the presence of magnetic effect ($\mu_0 = 0.5$), the dashed-dotted line denoted by "C" represents the solution in the presence of viscosity effect ($\aleph \neq 1$) and in the absence of magnetic effect ($\mu_0 = 0$), and the dotted denoted by "D" represents the solution in the presence of viscosity effect ($\aleph \neq 1$) and in the presence of magnetic effect ($\mu_0 = 0.5$).

Figure 3 shows the variations of the three temperatures T_e, T_i, T_r and considered temperature θ with the time τ.

Figures 4 and 5 show the variation of the displacement components u_1 and u_2 with the time τ. It can be shown from these figures that the viscosity and magnetic fields have strong effects on the displacement components.

Figures 6 and 7 show the variation of the microrotation components ω_1 and ω_2 with the time τ. It can be seen from these figures the viscosity and magnetic fields have strong effect on the microrotation components.

Figure 8 shows the variation of the pore pressure with the time τ. It can be seen from this figure viscosity has a significant effect on pore pressure p but the magnetic field has a weak effect on pore pressure.

Figure 9 shows the variation of the electric potential with the time τ. It can be noted from this figure that the viscosity and magnetic fields have weak effect on the electric potential.

Table 1 Genetic parameters used by the algorithm for Example 1

Population size	200
Number of generations	100
Selection scheme	RSSWR
Crossover scheme	Uniform crossover
Mutation scheme	Normal
Other operators	Elitism
Crossover probability	0.8
Mutation probability	0.005
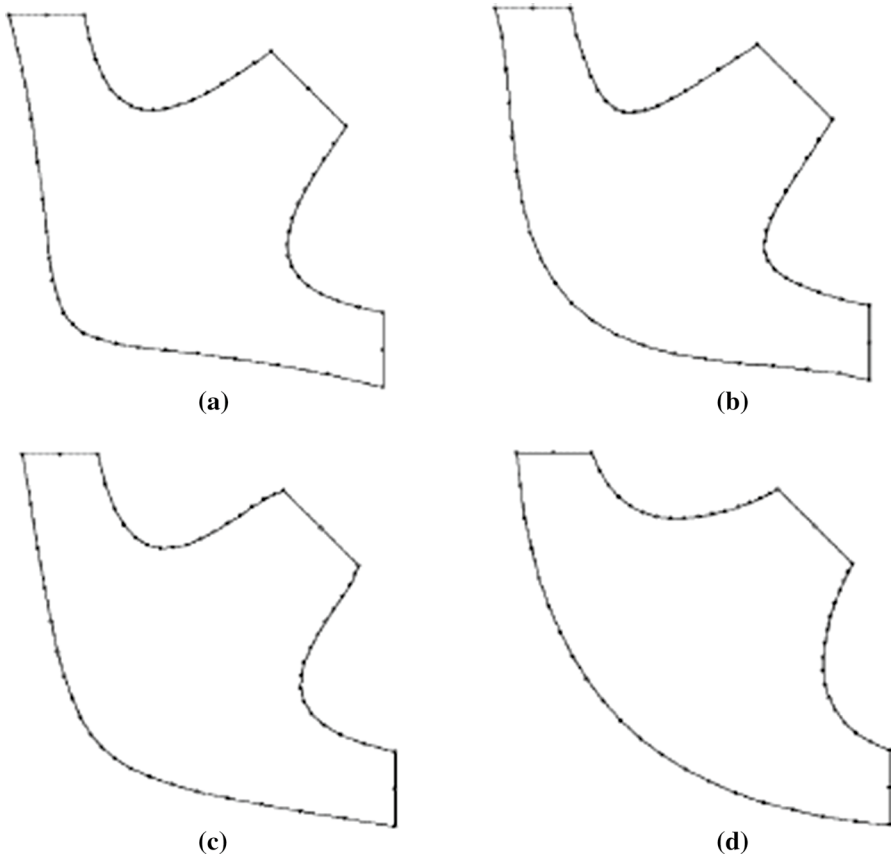
Fig. 14 The optimal shape of smart structure for example 1 for (a) $\theta=0$ K, (b) $\theta=100$ K, (c) $\theta=200$ K, and (d) $\theta=300$ K
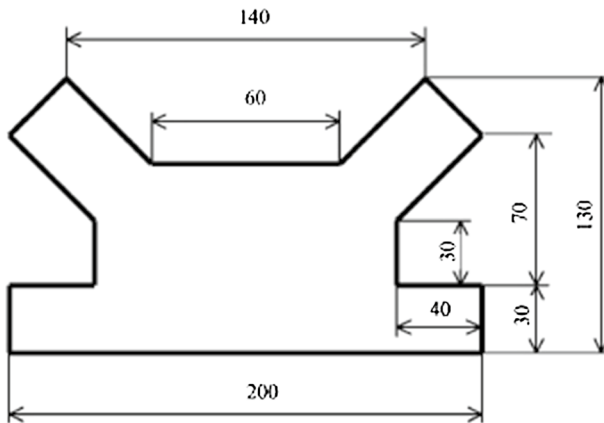
Fig. 15 Optimized smart structure for example 2, where all dimensions given in the figure are in centimeters

Table 2 Genetic parameters used by the algorithm for Example 2	Population size	100
	Number of generations	50
	Selection scheme	RSSWR
	Crossover scheme	Uniform crossover
	Mutation scheme	Normal
	Other operators	Elitism
	Crossover probability	1.0
	Mutation probability	0.02
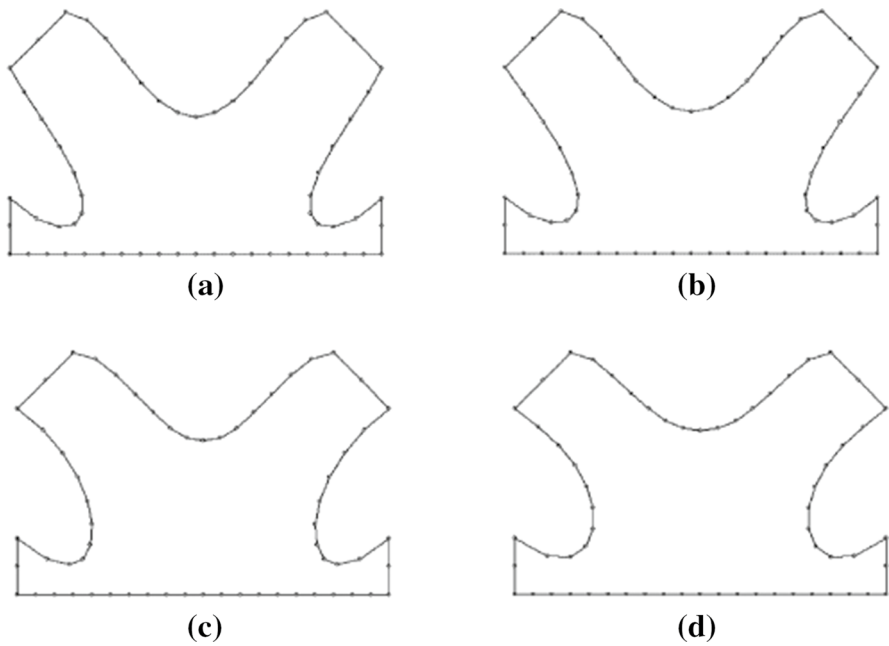
Fig. 16 The optimal shape of smart structure for example 2 for (a) $\theta = 0$ K, (b) $\theta = 100$ K, (c) $\theta = 200$ K, and (d) $\theta = 300$ K

Figures 10, 11, and 12 show the variations of the thermal stresses σ_{11}, σ_{12} and σ_{22} with the time τ. It can be shown from these figures that the viscosity and magnetic fields have significant effects on the thermal stresses.

Two numerical examples are presented herein, in order to prove that the proposed technique is able to optimize the shape of the domains with minimum computational effort.

A nonuniform rational B-spline curve (NURBS) can be described as follows

$$C(t) = \frac{\sum_{i=0}^{n} N_{i,o}(t)\varpi_i P_i}{\sum_{i=0}^{n} N_{i,o}(t)\varpi_i} \tag{70}$$
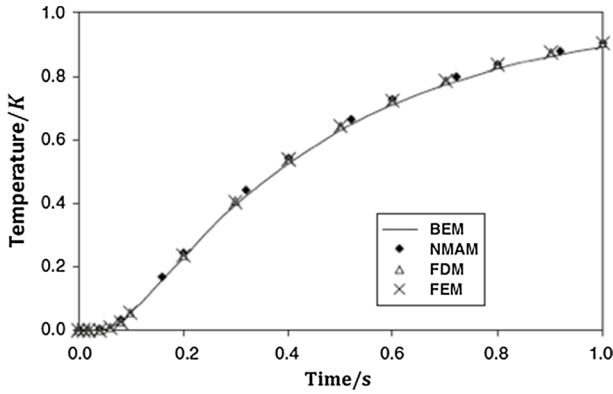
Fig. 17 Variation of the considered temperature θ with the time τ
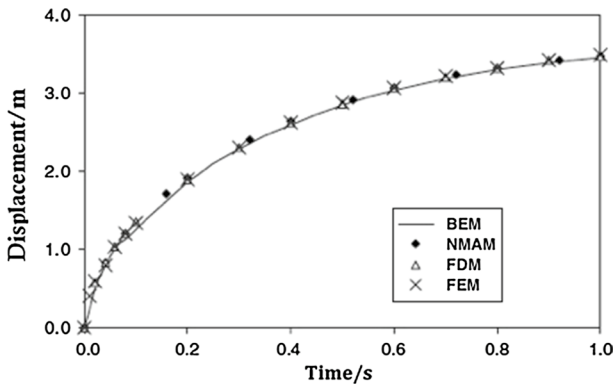
Fig. 18 Variation of the displacement u_1 with the time τ
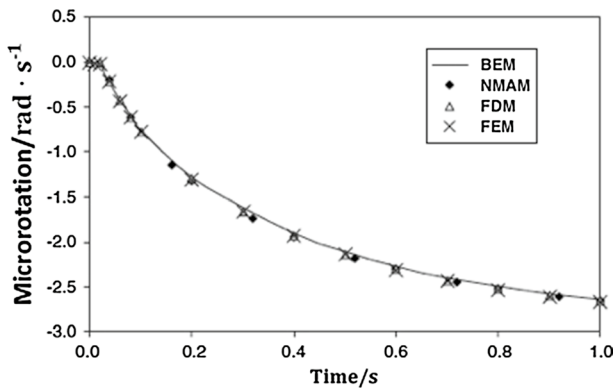
Fig. 19 Variation of the microrotation ω_1 with the time τ
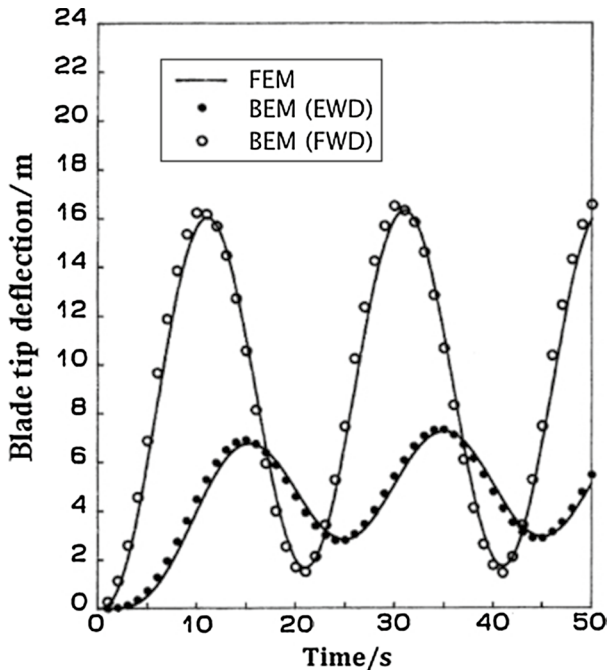
Fig. 20 Blade tip deflections for 75 m/s

Example 1 A shape optimization of the micropolar smart structure presented in Fig. 13 is considered. NURBS was used to model optimized boundary. The fitness function is given by (66) with constrains on the upper bound of the volume of the micropolar smart structure.

Table 1 contains evolutionary parameters which were applied as in Cerrolazaa et al. [60]. The optimal shape of the micropolar smart structure for different values of temperature θ is presented in Fig. 14.

Example 2. A shape optimization of the micropolar smart structure presented in Fig. 15 is considered. NURBS has been used to model optimized boundary. The fitness function is given by (67) with constrains on the upper bound of the volume of the micropolar smart structure.

Table 2 contains evolutionary parameters which were applied as in Cerrolazaa et al. [60]. The optimal shape of the micropolar smart structure for different values of temperature θ is presented in Fig. 16.

Due to nature of the considered problem, either analytical or numerical solutions are very difficult to obtain in general and as far as we know, there are no analytical or numerical solutions in the literature for the considered problem. But some literatures may be considered as special cases from our BEM results. Therefore, we compare

our one-temperature results with some previously known from the literature. In the special case under consideration, the results are plotted in Figs. 17, 18 and 19. The validity, accuracy and efficiency of the proposed methodology was demonstrated by comparing our one-temperature BEM results with those obtained using the normal mode analysis method (NMAM) [71], FDM [72] and FEM [73]. It is noticed from these results that the BEM are in excellent agreement with the NMAM, FDM and FEM.

In order to validate the BEM numerical simulations, we considered the same standstill case for wind turbine structure of Jonkman et al. [74]. The results of this case are presented graphically in Fig. 20, it can be noted, that the proposed BEM results for edgewise deflection (EWD) and flapwise deflection (FWD) are in an excellent agreement with the finite element results of simulation with COMSOL multiphysics software.

7 Conclusion

The study of the numerical results and figures helps us to make some final remarks:

(1) The research of the present study has received considerable attention due to its practical applications in several fields such as plasma physics, petroleum and mineral prospecting, geophysics, geomechanics, earthquake engineering, nuclear reactors, space vehicles, aircraft, materials science, fiber-optic communication, fluid mechanics, oceanology, automobile industries and other industrial applications

(2) The domain methods include the simulation of the entire geometry, including the surrounding area. But BEM just needs to solve the unknowns on the boundary. Therefore, BEM solves problems with more efficiency and accuracy than domain methods and reduces the computational costs of its solver.

(3) The genetic algorithm (GA) has been implemented as an optimization method based on free form deformation (FFD) technique and using NURBS to the shape optimization of the anisotropic micropolar magneto-thermoviscoelastic porous smart structures.

(4) For closed or open boundary problem BEM users need only to deal with real geometry boundaries. The considered problem is associated with open boundary structures problems. For these open boundary structures problems, FDM and FEM use artificial boundaries, which are far away from the real structure. Also, these artificial boundaries are also becoming a big challenge for FDM users and FEM users. So, BEM becomes the best method for the considered problem.

(5) The presence of viscosity and magnetic fields in the current study play a significant role in all the physical quantities and their design sensitivities during optimization.

(6) All the field variables satisfy the initial and boundary conditions.

(7) The validity and accuracy of the proposed BEM technique was verified by comparing obtained results of our current general research with the corresponding

normal mode analysis method (NMAM), FDM and FEM, it is noted that the BEM results are in excellent agreement with the FDM and FEM results, and therefore our results thus confirm the accuracy of BEM technique.

(8) The fluid–structure coupled simulations are performed to validate the proposed BEM simulations.

(9) From the research that has been performed, it is possible to conclude that the proposed BEM technique is effective and stable for time-domain problems in micropolar magneto-thermoviscoelasticity.

(10) Current numerical results for our complex and general problem may provide interesting information for computer scientists and engineers, geotechnical, geothermal engineers and material science researchers as well as for those working on the creation of micropolar magneto-thermoviscoelastic structures.

(11) It can be concluded from this paper that Some well-known micropolar thermoelasticity theories such as micropolar porothermoelasticity, micropolar magnetothermoelasticity and micropolar thermoviscoelasticity can be combined with the three-temperature radiative heat conduction theory to describe the deformation of anisotropic multi-material smart structures and nano structures.

References

1. J. Duhamel, Journal de l'École polytechnique **15**, 1–57 (1837)
2. F. Neumann, *Vorlesungen Uber Die Theorie Der Elasticitat* (Brestau, Meyer, 1885).
3. M. Biot, J. Appl. Phys. **27**, 249–253 (1956)
4. H.W. Lord, Y. Shulman, J. Mech. Phys. Solids **15**, 299–309 (1967)
5. A.E. Green, K.A. Lindsay, J. Elast. **2**, 1–7 (1972)
6. A.E. Green, P.M. Naghdi, J. Therm. Stresses **15**, 253–264 (1992)
7. A.E. Green, P.M. Naghdi, J. Elast. **31**, 189–208 (1993)
8. R.B. Hetnarski, J. Ignaczak, Int. J. Eng. Sci. **34**, 1767–1787 (1996)
9. D.Y. Tzou, ASME Journal of Heat Transfer. **117**, 8–16 (1995)
10. D.Y. Tzou, Int. J. Heat Mass Transf. **38**, 3231–3240 (1995)
11. D.Y. Tzou, *Macro-to Microscale Heat Transfer: The Lagging Behavior* (Taylor & Francis, New York, 1997).
12. D.S. Chandrasekharaiah, Appl. Mech. Rev. **51**, 705–729 (1998)
13. S.K. Roy Choudhuri, J. Thermal Stress. **30**, 231–238 (2007)
14. P.J. Chen, M.E. Gurtin, Zeitschrift für angewandte Mathematik und Physik ZAMP **19**, 614–627 (1968)
15. H. Youssef, IMA J. Appl. Math. **71**, 383–390 (2006)
16. M.A. Fahmy, J. Therm. Stress. **41**, 119–138 (2018)
17. M.A. Fahmy, Eng. Anal. Boundary Elem. **108**, 192–200 (2019)
18. A.C. Eringen, E.S. Suhubi, Int. J. Eng. Sci. **2**, 189–203 (1964)
19. A.C. Eringen, *Foundations of Micropolar Thermoelasticity* (Springer-Verlag, Wien GMBH, 1970).
20. M.A. Ezzat, M.I. Othman, A.S. El-Karamany, Int. J. Eng. Sci. **40**, 283–302 (2002)
21. G. Lukaszewicz, *Micropolar Fluids: Theory and Applications* (Birkhäuser, Switzerland, 1999).
22. A.C. Eringen, *Microcontinuum Field Theories: I. Foundations and Solids* (Springer, Berlin, 2012).
23. Kh. Lotfy, Waves in Random and Complex Media (2019). https://doi.org/10.1080/17455030.2019.1566680

24. Kh. Lotfy, Sci. Rep. **9**, 3319 (2019)
25. A.E. Abouelregal, W.W. Mohammed, Math. Methods Appl. Sci. (2020). https://doi.org/10.1002/mma.6764
26. A.E. Abouelregal, Eur. Phys. J. Plus **135**, 263 (2020)
27. S. Shaw, M.I.A. Othman, Appl. Math. Model. **67**, 605–620 (2019)
28. S. Shaw, M. I. A. Othman, Waves in Random and Complex Media. 2020. https://doi.org/10.1080/17455030.2020.1788747
29. S. Mondal, P. Pal, M. Kanoria, Acta Mech. **230**, 179–199 (2019)
30. S. Mondal, Comput. Math. Model. **31**, 256–276 (2020)
31. I.V. Kudinov, V.A. Kudinov, T.E. Gavrilova, Int. J. Heat Mass Transf. **138**, 326–334 (2019)
32. I.V. Kudinov, A.V. Eremin, V.A. Kudinov, A.I. Dovgallo, V.V. Zhukov, Int. J. Solids Struct. **200–201**, 231–241 (2020)
33. M.A. Ezzat, Int. J. Eng. Sci. **42**, 1503–1519 (2004)
34. M.A. Ezzat, A.S. El-Karamany, A.A. El-Bary, J. Electromagn. Waves Appl. **29**, 1018–1031 (2015)
35. A.M. Abd-Alla, M.A. Fahmy, T.M. El-Shahat, Arch. Appl. Mech. **78**, 135–148 (2008)
36. M.A. Fahmy, Numer. Heat Transfer A Appl. **53**, 1001–1011 (2008)
37. M.A. Fahmy, T.M. El-Shahat, Arch. Appl. Mech. **78**, 431–442 (2008)
38. M.A. Fahmy, Int. J. Appl. Mech. **3**, 1–24 (2011)
39. M.A. Fahmy, Eng. Anal. Boundary Elem. **36**, 335–345 (2012)
40. M.A. Fahmy, Appl. Math. Model. **36**, 4565–4578 (2012)
41. M.A. Fahmy, Simul. Sci. Comput. **3**, 1250002 (2012)
42. M.A. Fahmy, ASME J. Appl. Mech. **79**, 1015 (2012)
43. M.A. Fahmy, J. Eng. Phys. Thermophys. **85**, 950–958 (2012)
44. M.A. Fahmy, Numer Heat Transfer A Appl. **61**, 547–564 (2012)
45. M.A. Fahmy, Eng. Anal. Boundary Elem. **37**, 107–115 (2013)
46. M.A. Fahmy, J. Therm. Stresses **36**, 1–20 (2013)
47. M.A. Fahmy, Numer. Heat Transfer A Appl. **63**, 713–733 (2013)
48. M.A. Fahmy, Latin Am. J. Solids Struct. **11**, 386–409 (2014)
49. M.A. Fahmy, Math. Comput. Simul.. **66**, 193–205 (2019)
50. M.A. Fahmy, Eng. Anal. Boundary Elem. **101**, 156–164 (2019)
51. M.A. Fahmy, Numer. Heat Transfer A Appl. **75**, 616–626 (2019)
52. M.A. Fahmy, Arab. J. Sci. Eng. **44**, 1671–1684 (2019)
53. M.A. Fahmy, Int. J. Appl. Mech. **12**, 2050027 (2020)
54. M.A. Fahmy, Arab. J. Basic Appl. Sci. **27**, 1–12 (2020)
55. F. Ebrahimi, *Mechanics of Functionally Graded Materials and Structures*, 1st edn. (IntechOpen, London, 2019).
56. M.A. Fahmy, Int. J. Appl. Mech. **10**, 1850108 (2018)
57. A. Sadollah, T.S. Sinha (eds.), *Recent Trends in Computational Intelligence*, 1st edn. (IntechOpen, London, 2020)
58. M.A. Fahmy, Eng. Anal. Boundary Elem. **87**, 27–35 (2018)
59. R. Koprowski, *Fractal Analysis*, 1st edn. (IntechOpen, London, 2020).
60. M. Cerrolazaa, W. Annicchiaricoa, M. Martinezb, Eng. Anal. Boundary Elem. **24**, 427–440 (2000)
61. V. Sladek, J. Sladek, Eng. Anal. **2**, 40–50 (1985)
62. V. Sladek, J. Sladek, Eng. Anal. **2**, 81–91 (1985)
63. V. Sladek, J. Sladek, Eng. Anal. **2**, 155–162 (1985)
64. F.Y. Huang, K.Z. Liang, Eng. Anal. Boundary Elem. **17**, 19–26 (1996)
65. D.E. Goldberg, *Genetic Algorithms in Search, Optimization and Machine Learning* (Addison-Wesley Longman Publishing Co., Boston, 1989).
66. D.B. Fogel, *Evolutionary Computation: Toward a New Philosophy of Machine Intelligence* (Wiley-IEEE Press, New York, 2005).
67. D.S. Weile, E. Michielssen, IEEE Trans. Antennas Propag. **45**, 343–353 (1997)
68. A. C. Eringen, in Fracture, ed. By H. Liebowitz, (Academic Press, New York, 1968), pp. 621–729
69. L. Dragos, Int. J. Eng. Sci. **22**, 265–275 (1984)
70. G.H. Golub, C.F. Van Loan, *Matrix Computations*, 3rd edn. (North Oxford Academic, Oxford, 1983).
71. S. Deswal, B.S. Punia, K.K. Kalkal, Multidiscip. Model. Mater. Struct. **14**, 102–124 (2018)
72. E. Pazera, J. Jędrysiak, Compos. Struct. **202**, 296–303 (2018)
73. Q.L. Xiong, X.G. Tian, Latin Am. J. Solids Struct. **12**, 2562–2580 (2015)

74. J. Jonkman, S. Butterfield, W. Musial and G. Scott, Definition of a 5-MW reference wind turbine for offshore system development, Technical Report NREL/TP-500-38060, (2009)

Affiliations

M. A. Fahmy[1,2] ⓘD · **S. Shaw[3]** · **S. Mondal[4]** · **A. E. Abouelregal[5,6]** · **Kh. Lotfy[7,8]** · **I. A. Kudinov[9]** · **A. H. Soliman[10]**

✉ M. A. Fahmy
maselim@uqu.edu.sa; mohamed_fahmy@ci.suez.edu.eg

[1] Department of Mathematics, Jamoum University College, Umm Al-Qura University, Jamoum, Makkah, 25371, Saudi Arabia

[2] Department of Basic Sciences, Faculty of Computers and Informatics, Suez Canal University, El Salam District, New Campus, 4.5 Km, Ring Road, Ismailia 41522, Egypt

[3] Department of Mathematics, Indian Institute of Engineering Science and Technology, Shibpur, India

[4] Department of Mathematics, Basirhat College, Kolkata, Basirhat, West Bengal 743412, India

[5] Department of Mathematics, Faculty of Science, Mansoura University, Mansoura 35516, Egypt

[6] Department of Mathematics, College of Science and Arts, Jouf University, Al-Qurayyat 72388, Saudi Arabia

[7] Department of Mathematics, Faculty of Science, Zagazig University, Zagazig 44519, Egypt

[8] Department of Mathematics, College of Science, Taibah University, Al-Madinah, Saudi Arabia

[9] Department of Heat Engineering and Hydromechanics Theoretical Foundations, Samara State Technical University, Samara 443100, Russia

[10] Department of Mathematics, Faculty of Women for Arts, Science and Education, Ain Shams University, Cairo 11757, Egypt

Source details

Feedback ›   Compare sources ›

International Journal of Thermophysics

Scopus coverage years: from 1980 to Present

Publisher: Springer Nature

ISSN: 0195-928X   E-ISSN: 1572-9567

Subject area: (Physics and Astronomy: Condensed Matter Physics)

Source type: Journal

[View all documents ›]   [Set document alert]   💾 Save to source list

CiteScore 2022   ⓘ
3.4

SJR 2022   ⓘ
0.394

SNIP 2022   ⓘ
0.804

CiteScore   CiteScore rank & trend   Scopus content coverage
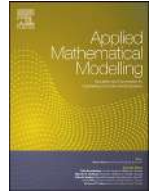
Extensional and flexural modes of Rayleigh–Lamb wave in an orthotropic thermoelastic layer lying over a viscoelastic half-space

Soumen Shaw[a], Mohamed I.A. Othman[b,*]

[a] Department of Mathematics, Indian Institute of Engineering Science and Technology, Shibpur, India
[b] Department of Mathematics, Faculty of Science, Zagazig University, Zagazig, Egypt

ARTICLE INFO

ABSTRACT

In this article the characteristics of the extensional and flexural modes, propagating in a thermoelastic orthotropic layer lying over a viscoelastic half-space, are analyzed. The complete analysis is carried out in the framework of a thermodynamically consistent hyperbolic type heat conduction model without energy dissipation. The normal-mode-analysis is adopted and a general form of dispersive equation is derived for an anisotropic thermoelastic layered medium. A prominent distinction with the isotropic elastic solids is observed in the symmetric as well as anti-symmetric modes of dispersion curves. In turn, such deformation reshapes the wave propagation while the deformation stiffening changes significantly the phase velocities of the wave till the acoustic radiation stresses are balanced by elastic stresses in the current configuration of the hyperelastic medium.

1. Introduction

Seismology is the study of earthquake and seismic wave that tells about the structure of Earth and a detail information about the earthquake environmental effects. The science of seismology aims simultaneously to know the infrastructure of the Earth's interior with the help of seismic wave phenomena and to study the nature of earthquake sources with ultimate goal of mitigating and eventually controlling the phenomena. If the Earth rapidly displaced at some point and the energy, imparted into the Earth's surface by the source of the distortion, can be transmitted in the form of elastic waves.

There are two types of surface waves exist, while analyzing the seismic waves, propagating on land: Rayleigh and Love waves. The first once described mathematically by Lord Rayleigh, while it was Prof. Love who, in 1911, described the kind of waves that were then named after him. Rayleigh wave is a type of surface wave that travels along the surface of solids. They can be produced in materials in many ways, such as by a localized impact or by piezo-electric transduction, and are frequently used in non-destructive testing for detailing defects. Rayleigh waves are part of the seismic waves that are produced on the Earth by earthquakes. When guided in layers they are referred to as Lamb waves, Rayleigh–Lamb waves. The problems of propagation of Love waves in the anisotropic and non-homogeneous medium have of great practical importance. They are not only helpful in investigating the internal structure of Earth but also are very helpful to explore the natural resources buried inside the Earth's surface. These waves are propagated when the solid medium near the surface

---

has non-homogeneous elastic properties. In Love-type waves, there is no particle motion in the vertical plane but particle motion takes place in the horizontal plane only and it is transverse to the direction of propagation. A detailed study on seismology and plate tectonics can be found from the book of Shearer [1]. Manna et al. [2] investigated the propagation of Love wave in a piezoelectric layer overlying an inhomogeneous elastic half-space. Seismic waves in heterogeneous layer lying over an initially stressed heterogeneous half-space was studied by Kundu et al. [3]. Wave transport for a scalar model of the Love waves observed by Bal and Ryzhik [4]. The Influence of anisotropy on the Love waves in a self-reinforced medium had obtained by Pradhan et al. [5].

Characteristics analysis of waves in elastic plates is one of the classical problems of continuum mechanics. An extensive theoretical and experimental set of data are available in the literature on the properties of plate vibrations, particularly for elastic plates with traction free faces. Every technique implemented in the literature offers its own unique advantages in detecting certain types of defects [6–8]. Especially, Lamb waves are a form of elastic perturbations that can propagate in a solid plate with free boundaries; there are two types of polarised waves such as Extensional or Flexural waves and Shear-horizontal waves [9]. The temperature changes due to the elastic deformation cannot be ignored; therefore it is required to determine the thermal and mechanical fields in the body concurrently.

In the last decade, the wave propagation in elastic and thermoelastic plate structures has received more attention due to its numerous engineering applications [10,11]. Gevorgyan [12] studied the thermoelastic wave propagation in a transversely isotropic heat-conducting as well as non-heat conducting elastic materials. the asymptotic expansion of the frequency equation for wave motion in a thermoelastic plate generated by the thermoelastic Rayleigh-Lamb equation does not give a adequate approximation. On account of non-linearity, it is hard to accomplish accurate resolution of lamb waves in an anisotropic media mathematically.

Thermoelasticity is the coupling between the strain and temperature fields. Based on the irreversible thermodynamic processes, Biot discovered the governing equations of thermo-elastic conductivity. Later on, during last few decades, several researchers proposed numerous generalizations to get rid-off various shortcomings. Among them we can mention the works of Lord and Shulman, Green and Lindsay, Green and Naghdi and Chandrasekhariah (for details see the monograph of Ignaczak and Ostoja-Starzewski [13] and the Refs. therein).

Anisotropy (basically orthotropy) of the solid is an accoutrement on the propagation of lamb waves, which is a determining challenge and to be analysed. Here, an attempt is made to consider the consequences of anisotropy on the propagation of extensional and flexural waves. It is applicable for the assortment of engineering materials and its applications at several thermo-mechanical environment.

An visco-elastic orthotropic thermoelastic medium is a considerable issue for the feasibility of thorough appliance in miscellaneous classifications that are applied in science and technology, especially in geophysics. In consideration of accurately representing the underground propagation of seismic waves, their processing, and interpolation, a media model is preferred that represents an anisotropic characteristic of composition and viscoelastic properties for the numeral computation and determination of wave field [14–19].

2. Mathematical modelling of the problem

In the model used in this study guided waves propagate along an infinite layer of finite thickness lying over an infinite soil medium (in larger scale). Continuity of displacements and stresses is imposed at the interface between the layer and the soil. The dispersion of the guided wave is due to geometrical effects and leakage of energy to the embedding medium. The soil is assumed to behave as an elastic solid material since the guided waves introduce only small strain perturbations.

The guided wave can be modelled by imposing surface boundary conditions on the equations of motion. However this approach introduces the dispersion phenomenon; that is the velocity of propagation of the guided wave along the plate being a function of frequency or equivalently wave length.

2.1. Problem formulation

In this paper, an orthotropic layer of finite thickness h lying over a visco-elastic half-space (as shown in Fig. 1), is considered. The interface of these two media is considered as $z = 0$, whereas $z = -h$ is the free surface. Here z axis is directed vertically downward and x axis is assumed in the direction of the wave propagation.

Consequently, the displacement components can be taken in the following form: $u_i = u_i(x, z, t)$, $v_i = 0$ and $w_i = w_i(x, z, t)$; $(i = 1, 2)$. $i = 1$ denotes for upper layer medium and $i = 2$ stands for the lower vis-elastic half-space. T_i represents the temperature of the medium above the reference temperature.

2.2. Boundary conditions

We consider an incompressible thermoelastic body which, when undeformed and unstressed and in the absence of thermal fields, occupies the reference configuration, denoted B_r, with boundary ∂B_r. It is then subject to a static deformation due to the combined action of a thermal fields and mechanical surface and body forces. The deformed configuration is denoted B, which has boundary ∂B. The two configuration are related by a deformation function χ which maps a point X in B_r to $x = \chi(X)$ in B. The deformation gradient tensor $F = Grad\,\chi$ satisfies the incompressibility constraint $J \equiv det\,F = 1$,
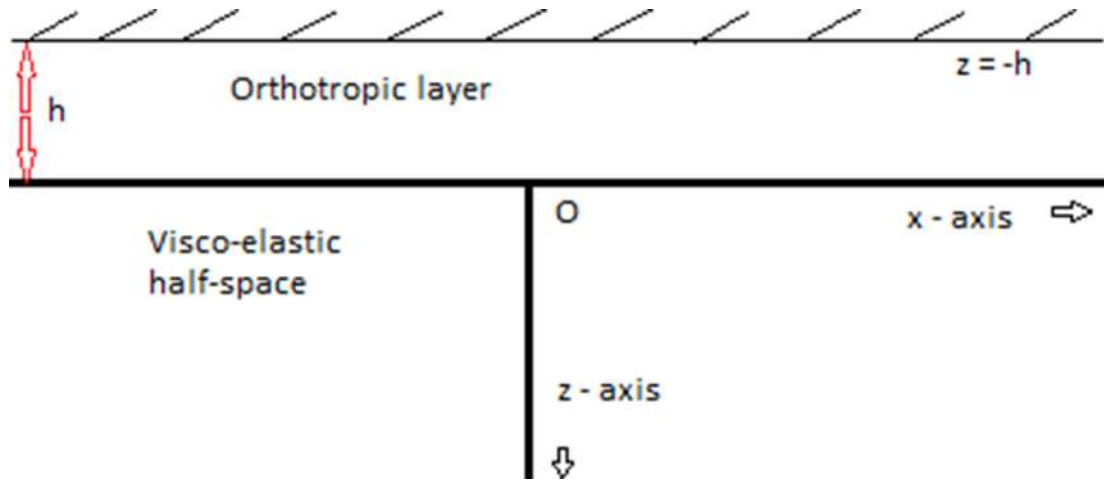
Fig. 1. Schematic diagram of the problem.

where *Grad* is the gradient operator with respect to *X*. It is further assumed that the material is electrically non-conducting and there is no electric field. Outside the material, which has been taken as vacuum (although a magnetizable, polarizable medium could also be considered).

It is assumed that the top surface of the orthotropic layer $z = -h$ is free from any traction and is isothermal. Therefore, at $z = -h$, the following conditions must hold:

$$
\begin{aligned}
&(i) \quad (\tau_{zz})_1 = 0 \\
&(ii) \quad (\tau_{xz})_1 = 0 \\
&(iii) \quad (T_1)_{,z} = 0
\end{aligned}
\tag{1}
$$

Moreover, the boundary conditions existing at the interface $z = 0$ must be specified. Two conditions are of particular interest in practical situations. The first is the case where two media are bounded together. Under such conditions, continuity of displacement and stress across the interface is required. Thus, for a bounded interface, we have

$$
\begin{aligned}
&(i) \quad (\tau_{xz})_1 = (\tau_{xz})_2 \\
&(ii) \quad w_1 = w_2 \\
&(iii) \quad T_1 = T_2
\end{aligned}
\tag{2}
$$

The last case is of particular interest in ultrasonics, where transducers used to launch and receive waves into and from a solid are often coupled by an oil or grease film to the media.

3. Governing equations

3.1. Orthotropic layered medium

The dynamic equations for the thermoelastic orthotropic layer in absence of body forces and heat sources are given by

$$
\begin{aligned}
\frac{\partial (\tau_{xx})_1}{\partial x} + \frac{\partial (\tau_{xz})_1}{\partial z} &= \rho_1 \frac{\partial^2 u_1}{\partial^2 t} \\
\frac{\partial (\tau_{xz})_1}{\partial x} + \frac{\partial (\tau_{zz})_1}{\partial z} &= \rho_1 \frac{\partial^2 w_1}{\partial^2 t}
\end{aligned}
\tag{3}
$$

Heat conduction equation without energy dissipation is as follows:

$$
K_1^* \frac{\partial^2 T_1}{\partial^2 x} + K_3^* \frac{\partial^2 T_1}{\partial^2 z} = \rho_1 C_e \frac{\partial^2 T_1}{\partial^2 t} + T_0 \frac{\partial^2}{\partial^2 t} \left[\beta_1 \frac{\partial u_1}{\partial x} + \beta_3 \frac{\partial w_1}{\partial z} \right]
\tag{4}
$$

where $(\tau_{ij})_1$ are the stress tensor, $\beta_i \quad (i = 1, 3)$ represent the thermal moduli, ρ_1 is the mass density, $K_i^* \quad (i = 1, 3)$ are the material's constant characteristics of the elastic solid, C_e is the specific heat at constant strain. T_1 is the absolute temperature above the reference temperature T_0 such that $\frac{T_1}{T_0} << 1$.

The constitutive relations for thermoelastic-orthotropic solids are given by

$$
\begin{aligned}
(\tau_{xx})_1 &= c_{11} e_{xx} + c_{13} e_{zz} - \beta_1 T_1 \\
(\tau_{zz})_1 &= c_{13} e_{xx} + c_{33} e_{zz} - \beta_3 T_1 \\
(\tau_{xz})_1 &= 2 c_{55} e_{xz}
\end{aligned}
\tag{5}
$$

in which c_{ij} are the material's elastic moduli and the strain-displacement relations can be expressed as

$$e_{xx} = \frac{\partial u_1}{\partial x}, \quad e_{zz} = \frac{\partial w_1}{\partial z}, \quad e_{xz} = \frac{1}{2}\left(\frac{\partial u_1}{\partial z} + \frac{\partial w_1}{\partial x}\right)$$ (6)

With the help of Eqs. (5) and (6), the equations of motion (3) and coupled heat Eq. (4) can be recast in the following manner:

$$c_{11}\frac{\partial^2 u_1}{\partial x^2} + c_{55}\frac{\partial^2 u_1}{\partial z^2} + \left(c_{13} + c_{55}\right)\frac{\partial^2 w_1}{\partial x \partial z} - \beta_1\frac{\partial T_1}{\partial x} = \rho_1\frac{\partial^2 u_1}{\partial t^2}$$ (7)

$$\left(c_{13} + c_{55}\right)\frac{\partial^2 u_1}{\partial x \partial z} + c_{55}\frac{\partial^2 w_1}{\partial x^2} + c_{33}\frac{\partial^2 w_1}{\partial z^2} - \beta_3\frac{\partial T_1}{\partial z} = \rho_1\frac{\partial^2 w_1}{\partial t^2}$$ (8)

$$K_1^*\frac{\partial^2 T_1}{\partial^2 x} + K_3^*\frac{\partial^2 T_1}{\partial^2 z} = \rho_1 C_e\frac{\partial^2 T_1}{\partial^2 t} + T_0\frac{\partial^2}{\partial^2 t}\left[\beta_1\frac{\partial u_1}{\partial x} + \beta_3\frac{\partial w_1}{\partial z}\right]$$ (9)

Eqs. (7) and (8) control the propagation of Rayleigh–Lamb type waves coupled with the heat conduction Eq. (9).

In order to solve the governing equations, without loss of any generality, the displacement components u_1 and w_1 can be expressed in terms of two displacement potential functions ϕ and ψ as

$$u_1 = \frac{\partial \phi}{\partial x} - \frac{\partial \psi}{\partial z}, \quad w_1 = \frac{\partial \phi}{\partial z} + \frac{\partial \psi}{\partial x}$$ (10)

Therefore, the displacement potential functions ϕ and ψ should satisfy the following set of equations simultaneously;

$$c_{11}\frac{\partial^2 \phi}{\partial x^2} + \left(c_{13} + 2c_{55}\right)\frac{\partial^2 \phi}{\partial z^2} - \beta_1 T_1 = \rho_1\frac{\partial^2 \phi}{\partial t^2}$$ (11)

$$\left(c_{11} - c_{55} - c_{13}\right)\frac{\partial^2 \psi}{\partial x^2} + c_{55}\frac{\partial^2 \psi}{\partial z^2} = \rho_1\frac{\partial^2 \psi}{\partial t^2}$$ (12)

$$\left(c_{13} + 2c_{55}\right)\frac{\partial^2 \phi}{\partial x^2} + c_{33}\frac{\partial^2 \phi}{\partial z^2} - \beta_3 T_1 = \rho_1\frac{\partial^2 \phi}{\partial t^2}$$ (13)

$$\left(c_{33} - c_{55} - c_{13}\right)\frac{\partial^2 \psi}{\partial z^2} + c_{55}\frac{\partial^2 \psi}{\partial x^2} = \rho_1\frac{\partial^2 \psi}{\partial t^2}$$ (14)

$$K_1^*\frac{\partial^2 T_1}{\partial^2 x} + K_3^*\frac{\partial^2 T_1}{\partial^2 z} = \rho_1 C_e\frac{\partial^2 T_1}{\partial^2 t} + T_0\frac{\partial^2}{\partial^2 t}\left[\beta_1\left(\frac{\partial^2 \phi}{\partial x^2} - \frac{\partial^2 \psi}{\partial x \partial z}\right) + \beta_3\left(\frac{\partial^2 \phi}{\partial z^2} + \frac{\partial^2 \psi}{\partial x \partial z}\right)\right]$$ (15)

In this article, we have solved the problem under the conditions that the material moduli satisfy the following conditions: $c_{11}c_{33} = \left(c_{13} + 2c_{55}\right)^2$, $\left(c_{13} + 2c_{55}\right)\beta_1 = c_{11}\beta_3$ and $2\left(c_{13} + 2c_{55}\right) = \left(c_{11} + 2c_{33}\right)$.

Eqs. (11) and (12) are equivalent to Eqs. (13) and (14), respectively, subject to the above conditions.

Solutions of Eqs. (11), (14) and (15) can be taken in the following manner:

$$\psi(x, z, t) = \left(A_2 \sin \lambda_2 z + B_2 \cos \lambda_2 z\right) exp\left[ik(x - ct)\right]$$

$$\phi(x, z, t) = \sum_{r=1,3}\left(A_i \sin \lambda_r z + B_i \cos \lambda_r z\right) exp\left[ik(x - ct)\right] + E\left(A_2 \cos \lambda_2 z - B_2 \sin \lambda_2 z\right) exp\left[ik(x - ct)\right]$$

$$T_1(x, z, t) = \sum_{r=1,3} d_r\left(A_i \sin \lambda_i z + B_i \cos \lambda_i z\right) exp\left[ik(x - ct)\right] + E d_2\left(A_2 \cos \lambda_2 z - B_2 \sin \lambda_2 z\right) exp\left[ik(x - ct)\right]$$ (16)

The expression for stresses and strains in terms of potential functions are given by

$$\left(\tau_{xx}\right)_1 = c_{11}\frac{\partial^2 \phi}{\partial x^2} + c_{13}\frac{\partial^2 \phi}{\partial z^2} + (c_{13} - c_{11})\frac{\partial^2 \psi}{\partial x \partial z} - \beta_1 T_1,$$

$$\left(\tau_{zz}\right)_1 = c_{13}\frac{\partial^2 \phi}{\partial x^2} + c_{33}\frac{\partial^2 \phi}{\partial z^2} + (c_{33} - c_{13})\frac{\partial^2 \psi}{\partial x \partial z} - \beta_3 T_1,$$

$$\left(\tau_{xz}\right)_1 = c_{55}\left(2\frac{\partial^2 \phi}{\partial x \partial z} + \frac{\partial^2 \psi}{\partial x^2} - \frac{\partial^2 \psi}{\partial z^2}\right),$$

$$e_{xx} = \frac{\partial^2 \phi}{\partial x^2} - \frac{\partial^2 \psi}{\partial x \partial z}, \quad e_{zz} = \frac{\partial^2 \phi}{\partial z^2} + \frac{\partial^2 \psi}{\partial x \partial z}, \quad e_{xz} = \frac{1}{2}\left(2\frac{\partial^2 \phi}{\partial x \partial z} + \frac{\partial^2 \psi}{\partial x^2} - \frac{\partial^2 \psi}{\partial z^2}\right)$$

where

$$E = ic^2 k^3 T_0 \frac{\beta_1(\beta_1 - \beta_3)\lambda_2}{P\lambda_2^4 + Q\lambda_2^2 + R} \text{ and } d_r = \frac{k^2(\rho_1 c^2 - c_{11}) - \lambda_r^2(c_{13} + 2c_{55})}{\beta_1} \quad (r = 1, 2, 3) \text{ with}$$

$$P = K_3^*(c_{13} + 2c_{55})$$

$$Q = k^2\left[K_3^*(\rho_1 c^2 - c_{11}) + (c_{13} + 2c_{55})(\rho_1 C_e c^2 - K_1^*) + T_0 \beta_1 \beta_3 c^2\right]$$

$$R = k^4\left[(\rho_1 c^2 - c_{11})(\rho_1 C_e c^2 - K_1^*) - T_0 \beta_1^2 c^2\right]$$

λ_r^2 $(r = 1, 3)$ are the roots of the equations: $P\lambda^4 + Q\lambda^2 + R = 0$ and $\lambda_2^2 = k^2 \frac{\rho_1 c^2 - c_{55}}{c_{33} - c_{55} - c_{13}}$.

3.2. Lower visco-elastic half-space

Visco-elastic materials, such as amorphous polymers, semi-crystalline polymers, bio-polymers and even the living tissue and cells, can be modelled in order to determine their stress and strain or force and displacement interactions as well as their temporal dependencies. These models, which include the Maxwell model, the Kelvin–Voigt model, and the Standard Linear Solid Model, are used to predict a material's response under different loading conditions. Visco-elastic behaviour has elastic and viscous components modelled as linear combinations of springs and dashpots, respectively. Each model differs in the arrangement of these elements, and all of these visco-elastic models can be equivalently modelled as electrical circuits. In an equivalent electrical circuit, stress is represented by voltage, and strain rate by current. The elastic modulus of a spring is analogous to a circuit's capacitance (it stores energy) and the viscosity of a dashpot to a circuit's resistance (it dissipates energy). In this present study, to characterize the visco-elastic behaviour of the abdomen half-space, we consider the Kelvin–Voigt model of linear visco-elasticity theory.

In absence of body forces and heat sources, the equations of motion for the lower visco-elastic half-space are given by

$$(\lambda^* + \mu^*)\nabla(\nabla.\mathbf{u}) + \mu^*\nabla^2\mathbf{u} - \beta^*\nabla T_2 = \rho_2\ddot{\mathbf{u}} \tag{17}$$

Heat conduction equation without energy dissipation for visco-elastic half-spaces is

$$K^*\nabla^2 T_2 = \frac{\partial^2}{\partial t^2}\left[\rho_2 C_E T_2 + \beta^* T_0 e\right] \tag{18}$$

in which

$\lambda^* = \lambda\left(1 + \alpha_0 \frac{\partial}{\partial t}\right)$, $\mu^* = \mu\left(1 + \alpha_1 \frac{\partial}{\partial t}\right)$, $\beta^* = \beta_e\left(1 + \beta_0 \frac{\partial}{\partial t}\right)$, $\beta_e = (3\lambda + 2\mu)\alpha_t$, $\beta_0 = (3\lambda\alpha_0 + 2\mu\alpha_1)/\beta_e$, where λ, μ are the Lame' constants, α_0, α_1 are visco-elastic relaxation parameters, α_t is the coefficient of linear thermal expansion, K^* is the material constant characteristic of the elastic solid, ρ_2 is the mass density, C_E represents the specific heat at constant strain and T_2 denotes the absolute temperature with respect to the reference body temperature T_0.

Here we use two displacement potential functions Φ and Ψ to express the displacement components u_2 and w_2 for the visco-elastic half-space as follows:

$$u_2 = \frac{\partial \Phi}{\partial x} - \frac{\partial \Psi}{\partial z}, \quad w_2 = \frac{\partial \Phi}{\partial z} + \frac{\partial \Psi}{\partial x} \tag{19}$$

Therefore, from Eqs. (17) and (18) we obtain

$$(\lambda^* + 2\mu^*)\nabla^2\Phi - \beta^* T_2 - \rho_2\ddot{\Phi} = 0 \tag{20}$$

$$\mu^*\nabla^2\Psi - \rho_2\ddot{\Psi} = 0 \tag{21}$$

$$\left(K^*\nabla^2 - \rho_2 C_E \frac{\partial^2}{\partial t^2}\right)T_2 - \beta^* T_0\nabla^2\Phi = 0 \tag{22}$$

In which ∇^2 denotes the Laplacian operator.

4. Wave propagation

4.1. Thermoelastic medium

On the basis of the above equations and boundary conditions we now study Rayleigh–Lamb type wave propagation in the x direction. We consider harmonic solutions of the form

$$\Psi = D_2 exp\Big[-m_2 + ik(x - ct)\Big]$$

$$\Phi = \sum_{r=1,3} C_r exp\Big[-m_r + ik(x - ct)\Big]$$

$$T_2 = \sum_{r=1,3} L_r C_r exp\Big[-m_r + ik(x - ct)\Big] \tag{23}$$

with the condition $Re(m_r) > 0$ for the wave to decay away from the surface of the half-space. Here $i = \sqrt{-1}$, k is the wave number, c is the wave speed.

In which,

$$L_r = \frac{1}{\beta^*}\Big[c^2 k^2 \big(\rho_2 - (\lambda^* + 2\mu^*)a_r^2\big)\Big]$$

$$m_2^2 = k^2\Big(1 - \frac{c^2 \rho_2}{\mu^*}\Big)$$

$$m_r^2 = k^2\Big(1 - a_r^2 \frac{c^2 \rho_2}{\lambda^* + 2\mu^*}\Big); \quad r = 1, 3$$

$$a_r^2 = \frac{-\Delta \pm \sqrt{\Delta^2 - 4C_E k^*(\lambda^* + 2\mu^*)}}{2k^*}$$

$$and \quad \Delta = k^* + C_E(\lambda^* + 2\mu^*) - \beta^{*2} T_0 \tag{24}$$

The solution (16) represents plane waves propagating back and forth within the layer. The solution (23) gives a wave that retains its energy close to the interface.

Substituting of (16) and (24) into the constitutive relations (10) and (19) and using the continuity conditions (2) yields

$$A_2 = D_2$$

$$C_1 = \frac{m_3(d_1 B_1 + d_3 B_3) + (Ed_2 m_3 + L_3(m^2 + k^2))A_2}{L_1 m_3 - m_1 L_3}$$

$$C_3 = \frac{m_1(d_1 B_1 + d_3 B_2) + (Ed_2 m_1 + L_1(m^2 + k^2))A_2}{m_1 L_3 - m_3 L_1} \tag{25}$$

which are satisfied non-trivially and defining the wave speed $c = \omega/k$ we have three equations for extensional wave propagation

$$\big(-c_{11}k^2 - c_{13}\lambda_1^2 - \beta_1 d_1\big)B_1 \cos\lambda_1 \ h + \{(c_{11}k^2 + c_{13}\lambda_2^2)E - (c_{11} - c_{13})ik\lambda_2 + \beta_1 d_2 E\}A_2 \cos\lambda_2 \ h$$
$$+ \big(-c_{11}k^2 - c_{13}\lambda_3^2 - \beta_1 d_3\big)B_3 \cos\lambda_3 h = 0 \tag{26}$$

$$2ik\lambda_1 B_1 \sin\lambda_1 \ h + \{-2ik\lambda_2 E + (\lambda_2^2 - k^2)\}A_2 \sin\lambda_2 \ h + 2ik\lambda_3 B_3 \sin\lambda_3 \ h = 0 \tag{27}$$

$$d_1 B_1 \cos\lambda_1 \ h + d_2 E A_2 \cos\lambda_2 \ h + d_3 B_3 \cos\lambda_3 \ h = 0 \tag{28}$$

and we have another set of three equations for flexural wave as follows

$$\big(c_{11}k^2 + c_{13}\lambda_1^2 + \beta_1 d_1\big)A_1 \sin\lambda_1 \ h + \{-(c_{11}k^2 + c_{13}\lambda_2^2)E + (c_{11} - c_{13})ik\lambda_2 - \beta_1 d_2 E\}B_2 \sin\lambda_2 \ h$$
$$+ \big(c_{11}k^2 + c_{13}\lambda_3^2 + \beta_1 d_3\big)A_3 \sin\lambda_3 h = 0 \tag{29}$$

$$2ik\lambda_1 A_1 \cos\lambda_1 \ h + \{-2ik\lambda_2 E + (\lambda_2^2 - k^2)\}B_2 \cos\lambda_2 \ h + 2ik\lambda_3 A_3 \cos\lambda_3 \ h = 0 \tag{30}$$

$$d_1 A_1 \sin\lambda_1 \ h - d_2 E B_2 \sin\lambda_2 \ h + d_3 A_3 \cos\lambda_3 \ h = 0 \tag{31}$$

For non-trivial solutions for A_r and B_r, the determinant of coefficients must vanish, which yields the dispersive equation of extensional as well as flexural waves in the layered medium, which we write compactly as

$$\big(c_{11}k^2 + c_{13}\lambda_1\lambda_3 + \beta_1 d_3\big)\lambda_1\Big[\frac{tan\lambda_1 h}{tan\lambda_2 h}\Big]^{\pm 1} + \big(c_{11}k^2 + c_{13}\lambda_1\lambda_3 + \beta_1 d_1\big)\lambda_3\Big[\frac{tan\lambda_3 h}{tan\lambda_2 h}\Big]^{\pm 1}$$

$$+ \Big[\big(c_{11}k^2 + c_{13}\lambda_2^2 + \beta_1 d_2\big) - ik\lambda_2 \frac{c_{11} - c_{13}}{E}\Big]\Big\{\lambda_1 \frac{d_3}{d_2}\Big[\frac{tan\lambda_1 h}{tan\lambda_2 h}\Big]^{\pm 1} - \lambda_3 \frac{d_1}{d_2}\Big[\frac{tan\lambda_3 h}{tan\lambda_2 h}\Big]^{\pm 1}\Big\}$$

$$= \Big(\frac{\lambda_2}{d_2} - i\frac{\lambda_2^2 - k^2}{2kEd_2}\Big)\Big[c_{11}k^2(d_1 - d_3) - c_{13}(d_3\lambda_1^2 - d_1\lambda_3^2)\Big] \tag{32}$$

where positive exponent represents the extensional waves and negative exponent stands for the flexure waves propagating through the layered medium.

Post-shock oscillations refer to the spurious oscillations that occur behind the shock fronts. Front-shock oscillations refer to the spurious oscillations that occur in front of the discontinuities. By post-shock oscillations, it is meant to refer to deleterious oscillations trailing the stress waves and/or velocity discontinuities. It is well established that post-shock oscillations are triggered by the mismatch of the physics of wave propagation speed across the adjacent. It is hoped that the analysis will shed some light on practical problems such as the performance of pipe isolators and the effect of attached structural discontinuities. In the flexural mode (Fig. 3), it is significant that the velocity is vanishing for the long phase. This is the large wavelength limit, in which the frequency of our wave is just the frequency of the particles by themselves. Imagine the whole row of particles all moving back and forth in perfect synchronization. Equivalently, you can imagine making the coupling between the particles tend towards zero, which will put us in the same regime. Now all of the particles move back and forth in perfect synchronization, so if you try to follow the motion of a "wave crest", it will appear to move at an arbitrarily fast speed, approaching infinity in the limit that our wavelength goes to infinity and all of the particles are truly synchronized (they all have the same phase). Additionally, if we consider this as the limit of vanishing coupling, it makes sense that the group velocity should vanish, as the group velocity gives us the velocity at which a disturbance moves through our system. If the particle's coupling is arbitrarily small, and you jostled one of them, that disturbance would move arbitrarily slowly to the other particles.

4.2. Pure elastic case

We now take the thermal field to vanish in order to reduce our results to the purely elastic case. For this purpose we take $T_1 = T_2 = 0$, $C_e = 0$, $C_E = 0$, $\beta_1 = \beta_3 = 0$, $\beta^* = 0$. Under this specialization, the governing equations (11)–(15) and (20)–(22) become

$$c_{11}\frac{\partial^2 \phi}{\partial x^2} + \left(c_{13} + 2c_{55}\right)\frac{\partial^2 \phi}{\partial z^2} - \rho_1 \ddot{\phi} = 0,$$

$$\left(c_{33} - c_{55} - c_{13}\right)\frac{\partial^2 \psi}{\partial z^2} + c_{55}\frac{\partial^2 \psi}{\partial x^2} - \rho_1 \ddot{\psi} = 0, \tag{33}$$

$$\left(\lambda^* + 2\mu^*\right)\nabla^2 \Phi - \rho_2 \ddot{\Phi} = 0,$$
$$\mu^* \nabla^2 \Psi - \rho_2 \ddot{\Psi} = 0, \tag{34}$$

in the layer and half-space, respectively. The relations (16) and (24) become

$$E = 0,$$
$$Q = k^2\left[\left(\rho_1 c^2 - c_{11}\right)K_3^* - K_1^*\left(c_{13} + 2c_{55}\right)\right],$$
$$R = k^4 K_1^*\left(c_{11} - \rho_1 c^2\right), \tag{35}$$

consequently, the equation $P\lambda^4 + Q\lambda^2 + R = 0$ reduces to

$$\left(K_3^* \lambda^2 - k^2 K_1^*\right)\left\{\left(c_{13} + 2c_{55}\right)\lambda^2 + \left(\rho_1 c^2 - c_{11}\right)k^2\right\} = 0 \tag{36}$$

and

$$m_1^2 = 0, \quad m_3^2 = k^2\left(1 - \frac{\rho_2 c^2}{\lambda^* + 2\mu^*}\right) \tag{37}$$

For this simplification, the secular Eq. (32) become

$$\left[2k^2 \lambda_2\left(c_{11} - c_{13}\right)\right]\left\{\lambda_1\left[\frac{\tan\lambda_1 h}{\tan\lambda_2 h}\right]^{\pm 1} - \lambda_3 \frac{d_1}{d_3}\left[\frac{\tan\lambda_3 h}{\tan\lambda_2 h}\right]^{\pm 1}\right\}$$
$$= \left(\lambda_2^2 - k^2\right)\left[c_{11}k^2\left(\frac{d_1}{d_3} - 1\right) - c_{13}\left(\lambda_1^2 - \frac{d_1}{d_3}\lambda_3^2\right)\right] \tag{38}$$

where $\lambda_r > 0$ and it is to be noted that to qualify for a surface wave the inequality $\rho_1 c^2 < c_{11}$ must be satisfied and that there are no real solutions for the wave speed if $\lambda^2 < 0$. Thus,

$$c_{55}/\rho_1 < c^2 < \mu^*/\rho_2 \tag{39}$$

The first factor of Eq. (36) i.e. $\left(K_3^* \lambda^2 - k^2 K_1^*\right) = 0$ does not corresponds any wave, so without any loss of generality, we may discard λ_1 and Eq. (38) become

$$\left[\frac{\tan\lambda_3 h}{\tan\lambda_2 h}\right]^{\pm 1} = \frac{\left(\lambda_2^2 - k^2\right)\left[c_{11}k^2 - c_{13}\lambda_3^2\right]}{2k^2 \lambda_2 \lambda_3\left(c_{11} - c_{13}\right)} \tag{40}$$
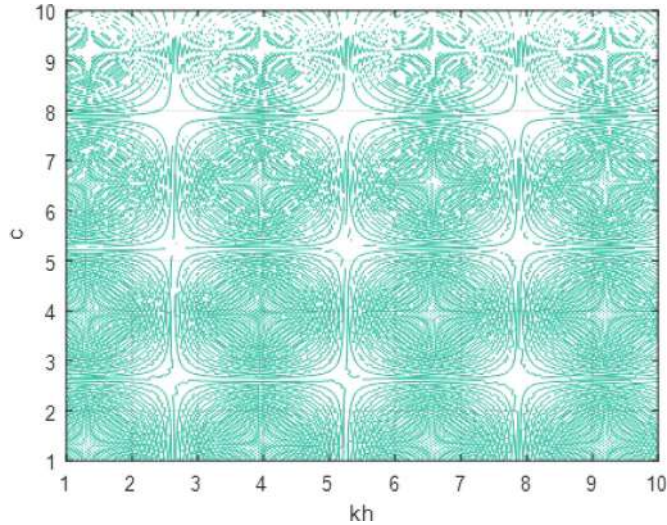
Fig. 2. Phase velocity profile for extensional wave propagation.

4.2.1. Special cases

(i) For the isotropic linear elastic case: $c_{11} = c_{33} = \lambda + 2\mu$, $c_{55} = \mu$, $c_{13} = \lambda$, where λ and μ are the Lame's elastic parameters.

Then the secular Eq. (38) reduces to

$$\left[\frac{tankh\sqrt{1 - \frac{c^2}{c_1^2}}}{tankh\sqrt{\frac{c^2}{c_2^2} - 1}} \right]^{\pm 1} = \frac{\left(\frac{c^2}{c_2^2} - 2 \right)\left[2 + \left(\frac{c_1^2}{c_2^2} - 2 \right)\frac{c^2}{c_1^2} \right]}{4\sqrt{1 - \frac{c^2}{c_1^2}}\sqrt{\frac{c^2}{c_2^2} - 1}} \tag{41}$$

In which, $c_1^2 = \frac{\lambda + 2\mu}{\rho_1}$, $c_2^2 = \frac{\mu}{\rho_1}$.

This equation, known as the Rayleigh–Lamb equation in wave propagation, was already discussed by Shaw and Mukhopadhyay [20].

(ii) Lame Mode:

For convenience of writing $\lambda^2 = k$, we obtain the following frequency equation,

$$c = c_1 \sqrt{1 - \frac{n^2 \pi^2}{4k^2 h^2}} \quad n = 0, 1, 2, \dots. \tag{42}$$

which is the Lame modes, a spacial class of exact solution, first identified by Lame. $n = 0$, or an even value of $n = 2m, m \in N$ yield the Lame mode of extensioal wave. Whereas, corresponding to an odd value of $n = 2m + 1, m \in N$ give the Lame mode of flexural wave.

Velocity profiles are observed as contour plots in thermoelastic orthotropic medium (Figs. 2 and 3). In purely elastic medium, the modes of velocity profile are observed in Figs. 4 and 5. The Lame modes of the Torsional as well as Flexural waves are distinguished in Figs. 6 and 7. For numerical computation purpose the relevant parameters for cobalt type material is considered, as the orthotropic material, as follows [19]:

$c_{11} = 3.07 \times 10^{11} \text{Nm}^{-2}; c_{13} = 1.027 \times 10^{11} \text{Nm}^{-2}; c_{33} = 3.581 \times 10^{1} 1 \text{Nm}^{-2} c_{55} = 1.510 \times 10^{11} \text{Nm}^{-2};$
$\beta_1 = 7.04 \times 10^6 \text{Nm}^{-2}; \beta_3 = 6.90 \times 10^6 \text{Nm}^{-2}; K_1 = 69 \text{Wm}^{-1} \text{deg}^{-1}; K_3 = 69 \text{Wm}^{-1} \text{deg}^{-1};$
$K_1^* = 13.1 \text{ Wm}^{-1} \text{deg}^{-1}; K_3^* = 15.4 \text{ Wm}^{-1} \text{deg}^{-1} s; \rho = 1660 \text{Kg m}^{-3}$

5. Attenuation measurements

Fig. 8 represents the measurement of attenuation for flexural mode and Fig. 9 represents the extensional mode of wave propagation. The attenuation of the flexural mode is found to be larger than that of the extensional mode.

6. Near surface wave-fields

The wave field can be described for any monotone plane wave propagating in a homogeneous acoustic medium by the Helmholtz equation:

$$(\nabla^2 - k^2)F = 0 \tag{43}$$
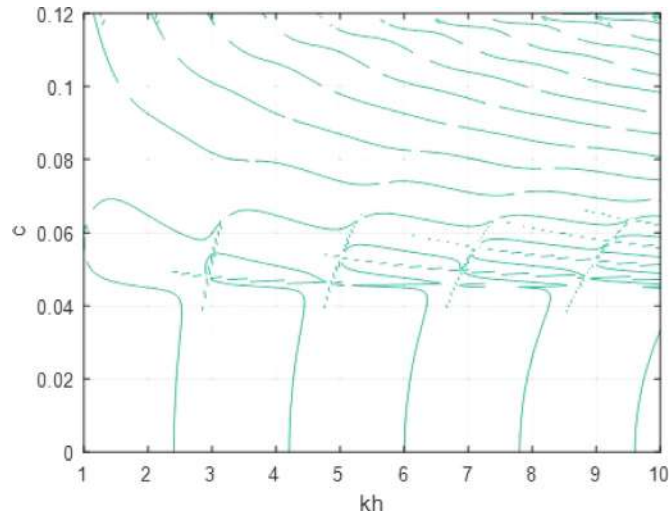
Fig. 3. Phase velocity profile for flexural wave propagation.
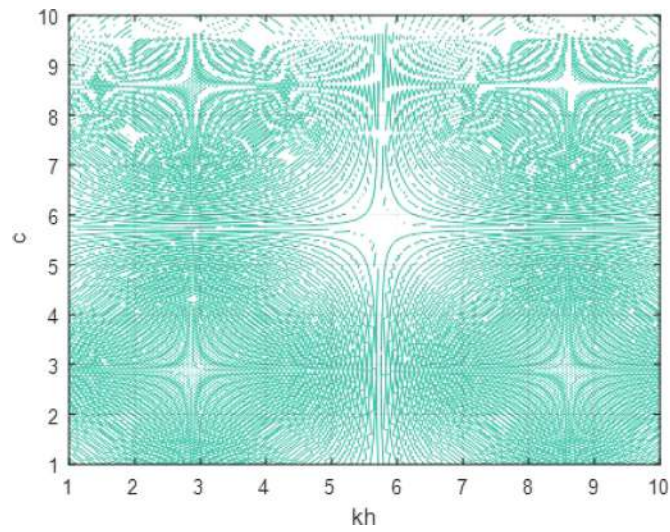
Fig. 4. Phase velocity profile in isotropic body for extensional wave propagation.
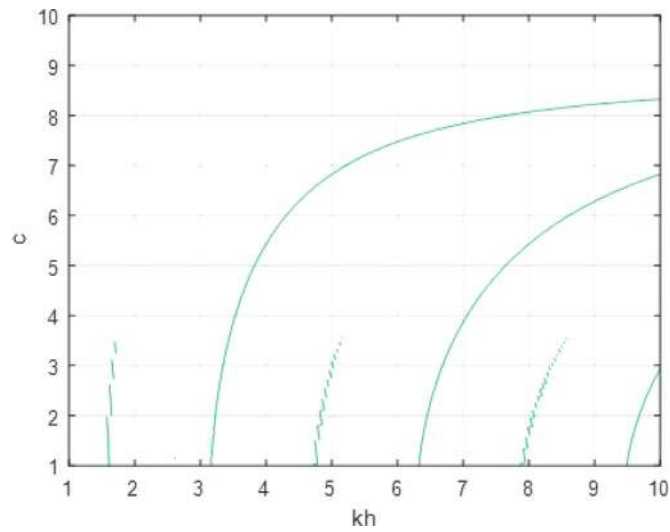
Fig. 5. Phase velocity profile in isotropic body for flexural wave propagation.
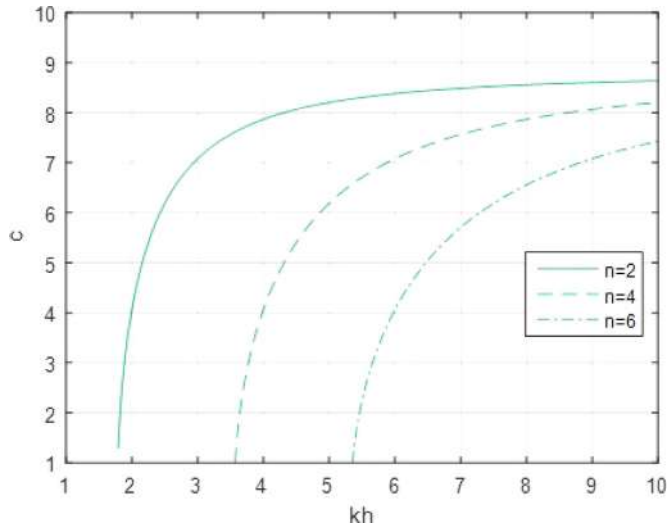
Fig. 6. Velocity profile in Lamb mode for extensional wave propagation.
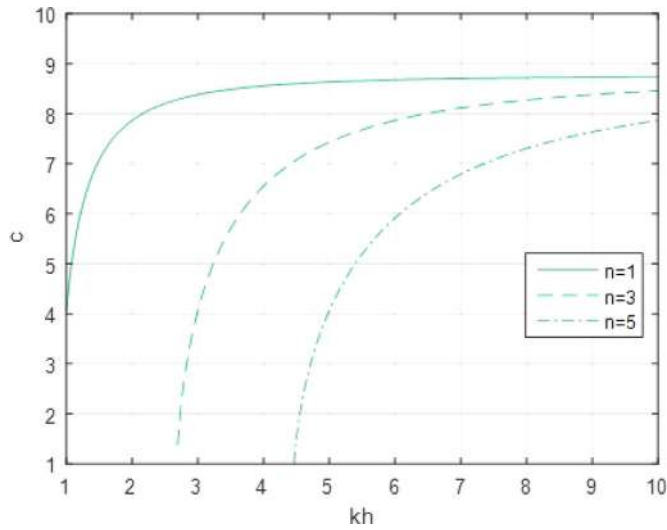
Fig. 7. Velocity profile in Lamb mode for flexural wave propagation.

where $lnF = a(x) + i\phi(x)$ represents one dimensional wavefield propagation along the x-direction; $a(x)$ and $\phi(x)$ are amplitude and phase, respectively. k is the structure wave number which relates to continuous wavefields as:

$$k^2 = -F^{-1}\nabla^2 F \tag{44}$$

Whereas, the dynamic wavenumber vector ω is obtained by calculating the negative spatial gradient of the wavefield's phase

$$\omega = -\nabla(Im(lnF)) = -\nabla\phi \tag{45}$$

It is obvious that $\omega = |\omega|$ is generally different from structure wavenumber k, but each can be converted into the other when the distribution of amplitudes around the observation point is known

$$k^2 = \omega^2 - (\nabla a)^2 - \nabla^2 a \tag{46}$$

Then the structure phase velocity c is calculated by the modified classical equation with an amplitude-correction term ϕ_a as

$$c = \frac{2\pi}{T\sqrt{\|\nabla\phi\|^2 - \phi_a}} \tag{47}$$

where T is the period of the wave near the surface.
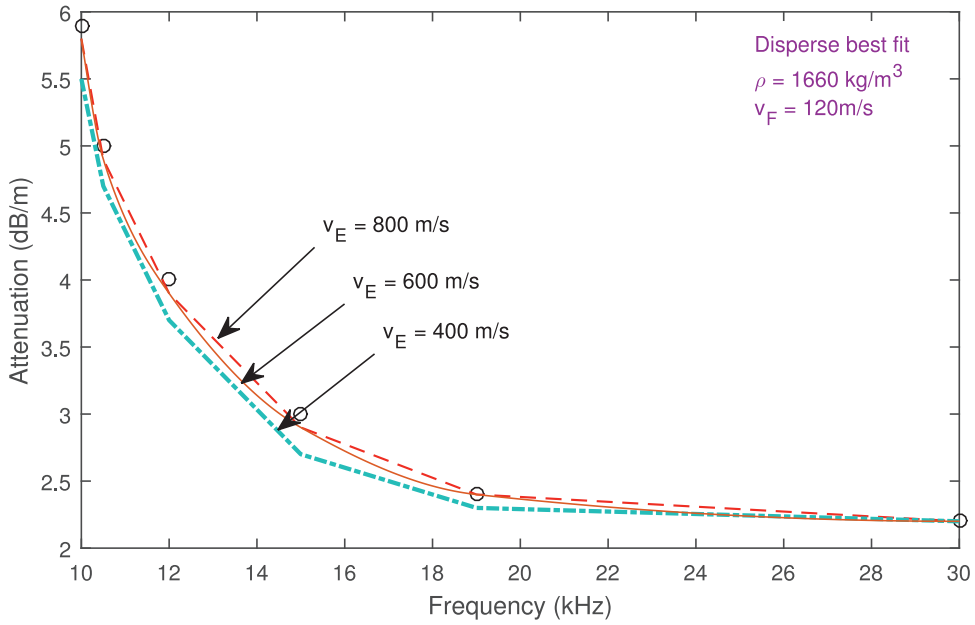
Fig. 8. Attenuation measurements as a function of frequency and Disperse simulation fits for flexural wave propagation.
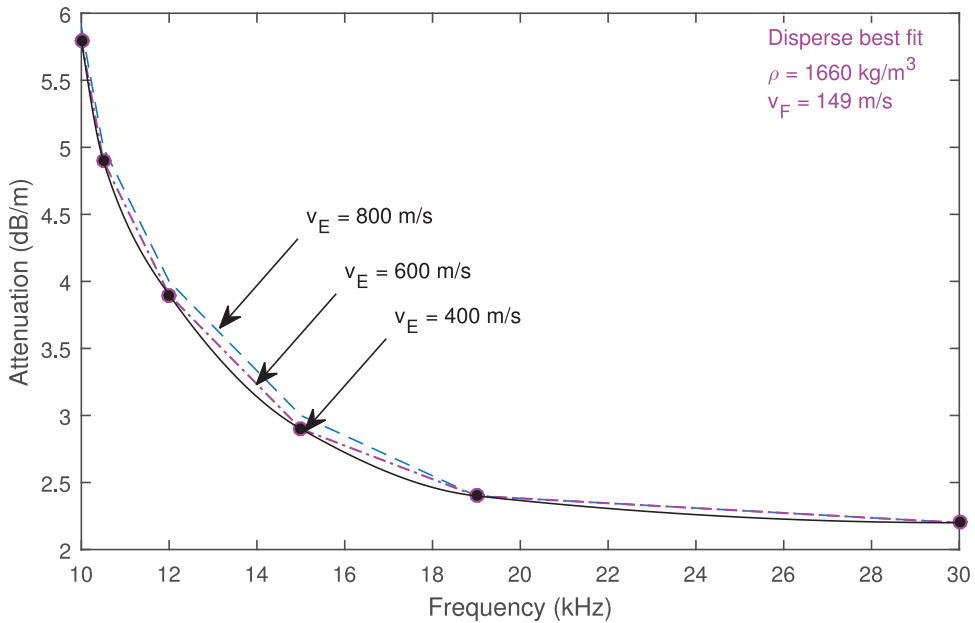
Fig. 9. Attenuation measurements as a function of frequency and Disperse simulation fits for extensional wave propagation.

7. Application to a hyperelastic type material

Two opposing waves with identical amplitude and frequency induce a standing-wave field in the thin layer. Due to acoustic momentum flux transfer between adjacent material particles, the ultrasonic wave propagation in the hyperelastic medium can give rise to acoustic radiation forces. At sufficiently high frequencies, the hyperelastic medium bar negligible dynamical shear stress, thus behaving like a fluid in so far as the propagation of ultrasonic wave is of concern.

A focused ultrasonic wave can generate acoustic radiation forces that are sufficiently large to deform hyperelastic media [21]. Correspondingly, the radiation force can be expressed in the following second order tensor as:

$$\langle \mathbf{T} \rangle = \mid \frac{\langle p^2 \rangle}{2\rho_a c_a^2} - \frac{\rho_a \langle \mathbf{u}.\mathbf{u} \rangle}{2} \mid \mathbf{I} + \rho_a \langle \mathbf{u} \otimes \mathbf{u} \rangle \tag{48}$$

where p is acoustic pressure, $\mathbf{u}$ is particle velocity vector, $\mathbf{I}$ is identity matrix, ρ_a and c_a are material density and acoustic speed, respectively, $\mathbf{T}$ is momentum flux tensor, and $\langle\mathbf{T}\rangle = \left(\omega/2\pi\right)\int_0^{2\pi/\omega}\mathbf{T}dt$, ω being angular frequency.

The deformation actuated by ultrasonic wave propagation can be characterised by using the acousto-mechanical model of hyperelastic media together with the non linear elastic theory. The acousto-mechanical Cauchy stress can be written as:

$$\sigma = \frac{F}{J}\frac{\partial W(F)}{\partial F} - \left[\frac{\langle p^2\rangle}{2\rho_a c_a^2} - \frac{\rho_a\langle\mathbf{u.u}\rangle}{2}\right]\mathbf{I} - \rho_a\langle\mathbf{u}\otimes\mathbf{u}\rangle \tag{49}$$

where $W(F)$ is the Helmholtz free energy function of hyperelastic medium. $\mathbf{F} = \frac{\partial\mathbf{x}}{\partial\mathbf{X}}$ is the deformation gradient, $\mathbf{x}$ and $\mathbf{X}$ being the position vectors in reference and current configuration, respectively, and $J = det(F)$ is the Jacobian determinant of deformation gradient.

When load is applied and then removed, general materials show elastic behaviour returning to its original state within the range where the relationship between load and deformation is linear. However, rubber-like materials show hyperelastic characteristics representing elastic behaviour in the range of large deformation showing non linear relationship between load and deformation. In general, the behaviour of rubber-like materials can be represented as a strain energy density function.

7.1. Gent model

This model is applicable to describe the non linear elastic behaviour of the hyperelastic medium. The Gent is capable of accounting for the effect of deformation stiffening in the medium, expressed as,

$$W(F) = -\frac{\mu J_m}{2}ln\left(1 - \frac{I_c - 3}{J_m}\right) - \mu lnJ + \left(\frac{k}{2} - \frac{\mu}{2} - \frac{\mu}{J_m}\right)(J - 1)^2 \tag{50}$$

where μ is the initial shear modulus.

7.2. The ogden model

We consider a generalization of the strain energy function for the thermoelastic case which is a light modification of the one used by Ogden and given by

$$W(e_1, e_2, e_3) = \sum_{i=0}^{n}(e_1^{\alpha_i} + e_2^{\alpha_i} + e_3^{\alpha_i} - 3) \tag{51}$$

where μ_i and α_i are experimentally determined material constants.

7.3. The Mooney–Rivlin model

$$W = C_1(I_c - 3) + C_2(II_c - 3) \tag{52}$$

This model can be viewed as special case of Ogden model since setting $n = 2, \alpha_1 = 2, \alpha_2 = -2$ in the Ogden model, and using the incompressibility constraint $e_1^2 e_2^2 e_3^2 = 1$ gives

$$W = \frac{\mu_1}{2}(I_c - 3) - \frac{\mu_2}{2}(II_c - 3) \tag{53}$$

7.4. Neo-Hooken model

The neo-Hooken energy function is special case of Mooney–Rivlin model, wherein $C_2 = 0$, giving

$$W = C_1(I_c - 3) \tag{54}$$

It is useful as a model of non linear elasticity within the small-strain range.

8. Conclusion

Guided Wave Testing(GWT) is one of the most powerful methods of inspection of pipelines and has been successfully employed for over a decade in a variety of applications in the petrochemical, power and nuclear industries. The method employs ultrasonic signals guided by the inspected structure and offers the possibility of rapid screening over long lengths of pipework for the detection of corrosion and other defects.

In this paper, we discussed the propagation of torsional and flexural waves in an anisotropic layered medium lying over a semi-infinite viscoelastic medium described by the hyperbolic type generalized theory of heat conduction. In particular, Lame Mode of wave propagation is illustrated in the due course of the study.

Velocity profile of the wave propagation are described by contour plots. Due to the considered thermal effects more concentrated polygons are observed. Consequently, the modes of wave propagation are increased for torsional as well as flexure waves in layered medium. Then, we analyzed the stress free boundary condition in order to provide some general remarks concerning a particular thermochemical model without energy dissipation. In purely elastic medium, waves are propagating smoothly in compared with the thermodynamic framework and the wavelengths are also increased. The result is that this model appears to be consistent with the expected behavior of a pressure wave as it propagates within a large artery. Finally, we provided an analytic description of the wave propagation in the hyperelastic medium and the behavior of the response function for both the scenarios.

Supplementary material

Supplementary material associated with this article can be found, in the online version, at 10.1016/j.apm.2020.03.029

References

[1] P.M. Shearer, Introduction to Seismology, second ed., Cambridge University Press, UK, 2009.
[2] S. Manna, S. Kundu, S. Gupta, Love wave propagation in a piezoelectric layer overlying an inhomogeneous elastic half-space, J. Vib. Control. 21 (13) (2013) 2553–2568.
[3] S. Kundu, S. Gupta, S. Manna, Propagation of g-type seismic waves in heterogeneous layer lying over an initially stressed heterogeneous half-space, Appl. Math. Comput. 234 (2014) 1–12.
[4] G. Bal, L. Ryzhik, Wave transport for a scalar model of the love waves, Wave Motion 36 (2002) 49–66.
[5] A. Pradhan, S.K. Samal, N.C. Mahanti, The influence of anisotropy on the love waves in a self-reinforced medium, Tamkang J. Sci. Eng. 6 (3) (2003) 173–178.
[6] A. Galvagni, P. Cawley, The reflection of guided waves from simple supports in pipes, J. Acoust. Soc. Am. 129 (4) (2001) 1869–1880.
[7] T. Vogt, M. Lowe, P. Cawley, Cure monitoring using ultrasonic guided waves in wires, J. Acoust. Soc. Am. 114 (3) (2003) 1303–1313.
[8] J.N. Sharma, M.I.A. Othman, Effect of rotation on generalized thermo-viscoelastic Rayleigh–Lamb waves, Int. J. Solid. Struct. 44 (2007) 4243–4255.
[9] J.N. Sharma, P.K. Sharma, S.K. Rana, Extensional wave motion in homogenous isotropic thermoelastic plate by using asymptotic method, Appl. Math. Model. 35 (1) (2011) 317–327.
[10] K.L. Verma, Thermoelastic wave propagation in laminated composite plates, Appl. Comput. Mech. 6 (2012) 197–208.
[11] J. Yu, B. Wu, C. He, Guided thermoelastic wave propagation in layered plates without energy dissipation, Acta Mech. Solida Sin. 24 (2) (2011) 205–215.
[12] R.S. Gevorgyan, Asymptotic solution of coupled dynamic problems of thermoelasticity for isotropic plates, J. Appl. Math. Mech. 72 (2008) 87–91.
[13] J. Ignaczak, M. Ostoja-Starzewski, Thermoelasticity with Finite Wave Speeds, Oxford University Press Inc., New York, 2010.
[14] Y.Q. Song, Y.C. Zhang, H.Y. Xu, B.H. Lu, Magneto-thermoviscoelastic wave propagation at the interface between two micropolar viscoelastic media, Appl. Math. Comput. 176 (2006) 785–802.
[15] O. Gültekin, G. Sommer, G. Holzapfel, An orthotropic viscoelastic model for the passive myocardium: continuum basis and numerical treatment, Comput. Method. Biomech. 19 (15) (2016) 1647–1664.
[16] R. Kumar, T. Kansal, Rayleigh- lamb waves in transversely isotropic thermoelastic diffusive layer, Int. J. Thermophys. 30 (2) (2009) 710–733.
[17] A. Chattopadhyay, S. Gupta, V.K. Sharma, P. Kumari, Propagation of g type seismic waves in viscoelastic medium, Int. J. Appl. Math. Mech. 6 (9) (2010) 63–75.
[18] V. Sharma, S. Kumar, Dispersion of SH waves in a viscoelastic layer imperfectly bonded with a couple stress substrate, J. Theor. Appl. Mech. 55 (2) (2017) 535–546.
[19] S. Shaw, M.I.A. Othman, Characteristics of Rayleigh wave propagating in orthotropic magneto-thermoelastic half-space: an eigen function expansion method, Appl. Math. Model. 67 (2019) 605–620.
[20] S. Shaw, B. Mukhopadhyay, Thermo elastic waves with thermal relaxation in isotropic micropolar plate, Sadhana 36 (2011) 209–221.
[21] P.A. Kelly, Mechanics Lecture Notes: An Introduction to Solid Mechanics, Part-III, University of Auckland, 2015, pp. 372–385.

Source details

Feedback ⟩   Compare sources ⟩

Applied Mathematical Modelling

Scopus coverage years: from 1976 to Present

Publisher: Elsevier

ISSN: 0307-904X

Subject area: (Mathematics: Applied Mathematics) (Mathematics: Modeling and Simulation)

Source type: Journal

View all documents ⟩   Set document alert   💾 Save to source list

CiteScore 2022   ⓘ
9.4

SJR 2022   ⓘ
1.080

SNIP 2022   ⓘ
1.743

CiteScore   CiteScore rank & trend   Scopus content coverage

Journal Pre-proof

Memory-dependent generalized thermoelasticity with finite wave speeds

Indranil Sarkar, Santanu Banerjee, Soumen Shaw

Please cite this article as: Sarkar, I., Banerjee, S., Shaw, S., Memory-dependent generalized thermoelasticity with finite wave speeds, *Mechanics of Materials* (2020), doi: https://doi.org/10.1016/j.mechmat.2020.103655.

This is a PDF file of an article that has undergone enhancements after acceptance, such as the addition of a cover page and metadata, and formatting for readability, but it is not yet the definitive version of record. This version will undergo additional copyediting, typesetting and review before it is published in its final form, but we are providing this version to give early visibility of the article. Please note that, during the production process, errors may be discovered which could affect the content, and all legal disclaimers that apply to the journal pertain.

Memory-dependent generalized thermoelasticity with finite wave speeds

Authors and affiliation:

Indranil Sarkar, Santanu Banerjee and Soumen Shaw*

Department of Mathematics

Indian Institute of Engineering Science and Technology, Shibpur,

Howrah-711103, India.

*Corresponding author. Email: shaw_soumen@rediffmail.com

Memory-dependent generalized thermoelasticity with finite wave speeds

ABSTRACT

The present article deals with the question: how time dependent non-locality influence the domain of dependency of thermal signals in solids? In order to establish the hypothesis "domain of influence" in an isotropic medium, based on the temperature-rate dependent thermoelasticity (TRDTE) theory, a thermodynamic consistent model is formulated by incorporating memory-dependent derivative (MDD). Firstly, the domain of influence theorem is established followed by a domain of dependence inequality and it certifies that for a finite time $t > 0$ a solution of a given thermo-dynamical problem, corresponding to the data defined in a bounded support, vanishes outside a suitably defined bounded domain $\mathscr{D}^*(t)$. It physically interprets that an initial perturbation of a bounded thermo-elastic domain generates thermal signals which for any $t > 0$ can not occupy the whole space, i.e. it propagates with a finite speed. Finally, a two-dimensional thermoelastic problem in the isotropic medium is considered for a supporting visualization of the domain of influence theorem of the memory-dependent generalized thermoelasticity theory.

Introduction

The thermoelasticity theory deals with the interaction between the mechanical and thermal field variables in the deformable bodies. Owing to the parabolic nature of the heat conduction equation in the classical dynamic thermoelasticity theory [1], based on the Fourier's heat conduction law, the impact of thermomechanical loading on an isotropic and homogeneous body comes to instantaneously at all points of the body from the point of application. In the case of coupled thermoelastic problems, it describes that the impact of thermomechanical loading influences the magnitude and pattern of the displacements, stresses and temperature distribution instantaneously everywhere in the solution domain. Physically it means that the thermal signals occupy the whole space for any time $t > 0$ i.e. the thermal signals propagate with infinite speed. This behavior is inconsistent with the heat transfer mechanism and contradicts physical phenomena. In order to overcome the mathematical inconsistency connected with the infinite speed propagation for the thermal signals, generalized thermoelasticity theories involving finite speed propagation for the thermal signals have been developed in the literature by several researchers. The problems of heat transfer mechanism involving finite speed propagation for the thermal signals in thermoelastic materials have received a great deal of attention over the last five decades and a broad survey regarding this area is given by Chandrasekharaiah [2, 3]. The leading hyperbolic or generalized thermoelasticity theories in the literature are the extended thermoelasticity (ETE) theory with single relaxation time parameter proposed by Lord-Shulman [4] and that the temperature-rate dependent thermoelasticity (TRDTE) theory with two different relaxation time parameters by Green-lindsay [5], the thermoelasticity models GN-I, II, III by Green-Naghdi [6–8], the dual-phase-lag (DPL) model by Tzou [9], the three-phase-lag model by Roy Choudhuri [10] etc.

The recent decade is a revolution in terms of modelling thermoelasticity problems using memory-dependent derivative (MDD) tool. The reason behind the requirement of a new form of derivative has come into play because Engineers have understood that the next state of physical system not only depends upon the present state, but also upon all of its historical states. Thus the presence of a memory factor is required on describing and analysing physical problems involving elastic bodies. Wang and Li [11] has introduced

the concept of memory-dependent derivative (MDD) by surpassing the fractional order derivative. Memory response in the generalized thermoelasticity for the Lord-Shulman (L-S) model has been first investigated by Yu et al. [12]. A number of papers have been devoted in the literature by several researchers [13–24] from the theoretical and the applied aspects. The strength evaluation, the damage tolerance and the thermal durability of an elastic material require measurements of thermophysical quantities like stress and temperature variation within the material. The generalized thermoelasticity models together with the kernel function and time-delay parameter with regards to memory-dependent derivative (MDD) provides convergent, specific and moderate solution for the thermophysical quantities with respect to the space variables in diverse field of thermoelasticity including Mechanical and engineering sciences like-nuclear reactor design, viscoelasticity, construction engineering, geophysics, earthquake science etc.

"A domain of influence theorem" is one of the prime results in generalized thermo-elasticity theories and the finite speed propagation of the thermal signals in these theories is mathematically justified. The deformation of a material in the presence of thermomechanical loading and the hyperbolicity of the heat conduction theory are well described by the idea of domain of influence. Nunziato and Cowin [25] primarily proposed the the idea of domain of influence. Later on several researchers have contributed in this direction and the contributions are cited from the following references [26–31].

In the present article, a novel mathematical model (Green-Lindsay model with MDD) is formulated in order to prove the domain of influence theorem. The theorem is proved by following thermodynamic consistency of the model and a domain of dependence inequality. Also, a two dimensional problem is considered for a supporting visualization of the domain of influence theorem.

Mathematical formulation of the model

Let $\mathscr{D}$ denote a bounded regular region in the physical space $\mathbb{R}^3$, occupied by a homogeneous, isotropic, thermoelastic body, whose piecewise smooth boundary and the closure are denoted by $\partial\mathscr{D}$ and $\bar{\mathscr{D}}$ respectively. The body is referred to a fixed system of rectangular Cartesian axes $Ox_i(i = 1, 2, 3)$. The Greek subscript and the Latin indices range over

$(1, 2, 3)$ and $(1, 2)$ respectively and usual summation over repeated subscripts is employed throughout the paper. The comma followed by a subscript and superposed dot denote partial differentiation with respect to time and the corresponding Cartesian co-ordinate respectively. The basic governing equations for the linear theory of generalized thermoelasticity under Green-Lindsay (GL) model with memory-dependent derivative (MDD) are mathematically formulated as follows:

The kinematic relation:

$$e_{ij} = \frac{(u_{i,j} + u_{j,i})}{2},$$ (1)

The Hooke's law:

$$\sigma_{ij} = \lambda e \delta_{ij} + 2\mu e_{ij} - \gamma(\theta + \nu D_\omega \theta)\delta_{ij},$$ (2)

The equation of motion:

$$\sigma_{ij,j} + \rho f_i = \rho \ddot{u}_i, \ \sigma_{ij} = \sigma_{ji},$$ (3)

The heat conduction equation under Green-Lindsay model with MDD:

$$k\theta_{,ii} = \rho c_e (1 + \tau D_\omega)\dot{\theta} + \gamma \theta_0 \dot{e} - \rho Q$$ (4)

where, the memory-dependent derivative operator D_ω operating on a differentiable function $f(t)$ in association with the the time-delay parameter $\omega(\omega > 0)$ and the differentiable kernel function $K(t-\xi)$ with respect to its arguments t and ξ $[0 < K(t-\xi) \leq 1]$, over the delayed interval $[t - \omega, t]$ is defined [11] as

$$D_\omega f(t) = \frac{1}{\omega} \int_{t-\omega}^{t} K(t - \xi) f'(\xi) d\xi.$$ (5)

To depict material's memory response, the time-delay parameter and the kernel function are selected according to the application environment of the physical problem. Moreover, the kernel function plays a significant role in order to describe the degree of the past time $t - \omega$ on the present time t of the physical problem. For a precribed real number ξ, the kernel $K(t, \xi)$ is a fixed function, while different processes need different kernel functions to reflect their memory effect. Several researchers [14,19,32] investigated memory response by choosing the kernel functions as 1, $1 - \frac{t-\xi}{\omega}$, $(1 - \frac{t-\xi}{\omega})^2$ etc.

4

In the above equations, ν and τ represents the relaxation times, λ, μ are the Lame's constants, α_t is the coefficient of linear thermal expansion, $\theta = T - \theta_0$ is the temperature deviation from the reference temperature θ_0, T is the absolute temperature, u_i are the components of the displacement vector, e is the cubic dilatation, e_{ij} are the components of the strain tensor, σ_{ij} are the components of the stress tensor, k is the thermal conductivity, f_i are the components of the external body force per unit mass, $\gamma = (3\lambda + 2\mu)\alpha_t$, ρ is the mass density, c_e is the specific heat at constant strain, Q is the external heat source per unit mass, δ_{ij} is the Kronecker's symbol.

Now, for a fixed time $\tau^* > 0$, the thermoelastic problem with memory-dependent derivative (MDD) (1)-(4) satisfies the initial conditions:

$$u_i(x,0) = u_i^0(x), \; \dot{u}_i(x,0) = u_i^1(x), \; \theta(x,0) = \theta^0(x) \quad \text{for } x \in \bar{\mathscr{D}} \tag{6}$$

and the boundary conditions:

$$u_i = \bar{u}_i \text{ on } \partial\mathscr{D}_1 \times [0,\tau^*),$$
$$\sigma_{ij}n_j = \bar{\sigma}_i \text{ on } \partial\mathscr{D}_1^c \times [0,\tau^*),$$
$$\theta = \bar{\theta} \text{ on } \partial\mathscr{D}_2 \times [0,\tau^*),$$
$$q = q_i n_i = \bar{q} \text{ on } \partial\mathscr{D}_2^c \times [0,\tau^*), \tag{7}$$

where, the components of the unit outward normal to the boundary $\partial\mathscr{D}$. are denoted by n_i. Also, $\{\partial\mathscr{D}_1, \partial\mathscr{D}_1^c\}$ and $\{\partial\mathscr{D}_2, \partial\mathscr{D}_2^c\}$ denote the two partitions of the boundary $\partial\mathscr{D}$ such that

$$\partial\mathscr{D}_1 \cup \partial\mathscr{D}_1^c = \partial\mathscr{D}_2 \cup \partial\mathscr{D}_2^c = \partial\mathscr{D},$$
$$\partial\mathscr{D}_1 \cap \partial\mathscr{D}_1^c = \partial\mathscr{D}_2 \cap \partial\mathscr{D}_2^c = \Phi,$$

where Φ denotes the empty set.

Throughout the paper it is assumed that

$$\theta_0 > 0, \; \rho > 0, \; \alpha_t > 0, \; k > 0, \; c_e > 0, \; \lambda > 0, \; \mu > 0, \; \nu \geq \tau > 0. \tag{8}$$

Let the thermoelastic mixed initial-boundary value problem of the present model consists solution (u_i, θ) in the domain $\Gamma_0 = \mathscr{D} \times [0,\tau^*)$ subject to the conditions (6)-(7) for all $(x,t) \in \Gamma_0$.

5

Lemma 1

For any scalar function f defined on $\bar{\mathscr{D}}$, the following inequality holds: $\dot{f}D_\omega f \geq 0$.

Proof.

Case I: Let $D_\omega f \geq 0$ for all ω ($\omega > 0$) and K ($0 < K \leq 1$) in the definition (5). Then, in particular for $K = 1$ and making $\omega \to 0$, we have from the definition (5) that $\dot{f} \geq 0$ and hence $\dot{f}D_\omega f \geq 0$.

Case II: Let $D_\omega f \leq 0$ for all ω ($\omega > 0$) and K ($0 < K \leq 1$) in the definition (5). Then, in particular for $K = 1$ and making $\omega \to 0$, we have from the definition (5) that $\dot{f} \leq 0$ and hence $\dot{f}D_\omega f \geq 0$.

Thus, the Lemma 1 is proved by following the Case I and Case II.

Thermodynamic consistency of the model

This section is mainly devoted to the derivation of the constitutive equations of the proposed model from the balance laws or conservation laws of continuum mechanics or thermodynamics and it is regarded as the thermodynamic consistency of the present model.

The deformation of a material body is characterized by the kinematic relation (1) and the equation of motion with the symmetric property of the stress tensor (3), are derived from the balance laws of linear momentum and angular momentum [33].

In the present model, the principle of energy conservation or the first law of thermodynamics for the domain $\mathscr{D}$ is in the following form:

$$\frac{d}{dt}\int_{\mathscr{D}}[\rho\dot{u}_i\dot{u}_i + U]dV = \int_{\mathscr{D}}\rho f_i\dot{u}_i dV + \int_{\partial\mathscr{D}}[\sigma_{ij}\dot{u}_i - q_i]n_i dA + \int_{\mathscr{D}}\rho Q dV, \tag{9}$$

where U is the internal energy of the body.

With the help of the Eq. (3) and the divergence theorem, we get from (9) that

$$\dot{U} = \sigma_{ij}\dot{e}_{ij} - q_{i,i} + \rho Q. \tag{10}$$

The second law of thermodynamics for the present model is given below [34]

$$\rho\dot{\eta} \geq -(\frac{q_i}{\phi})_{,i} + \frac{\rho Q}{\phi}, \tag{11}$$

where η is the entropy density of the body, $\phi = \phi(T, T^*) > 0$ and $T^* = D_\omega T$, thus ϕ is a scalar function of two independent variables of T and T^*. Physically ϕ interprets the

6

generalized temperature corresponding to the current thermoelasticity model [35].

According to Green and Laws [34], we introduce the generalized free energy function of the model as

$$\psi = U - \rho\eta\phi, \tag{12}$$

from which

$$\dot{\psi} = \dot{U} - \rho\dot{\eta}\phi - \rho\eta\dot{\phi}. \tag{13}$$

Then, the relations (10)-(11) in terms of the functions ϕ and ψ takes the following form:

$$\dot{\psi} + \rho\dot{\eta}\phi + \rho\eta\dot{\phi} = \sigma_{ij}\dot{e}_{ij} - q_{i,i} + \rho Q, \tag{14}$$

$$\dot{\psi} + \rho\eta\dot{\phi} - \sigma_{ij}\dot{e}_{ij} + \frac{q_i\phi_{,i}}{\phi} \le 0. \tag{15}$$

Now, we extend the domain of ψ by taking $\psi = \psi(e_{ij}, T, T^*)$.

From this, we get

$$\dot{\psi} = \frac{\partial\psi}{\partial e_{ij}}\dot{e}_{ij} + \frac{\partial\psi}{\partial T}\dot{T} + \frac{\partial\psi}{\partial T^*}\dot{T}^*. \tag{16}$$

And also, the derivatives of ϕ are also expressed as

$$\dot{\phi} = \frac{\partial\phi}{\partial T}\dot{T} + \frac{\partial\phi}{\partial T^*}\dot{T}^*, \tag{17}$$

$$\phi_{,i} = \frac{\partial\phi}{\partial T}T_{,i} + \frac{\partial\phi}{\partial T^*}T^*_{,i}. \tag{18}$$

With the help of the relations (16)-(18), the relations (14)-(15) are reduced as

$$\left(\frac{\partial\psi}{\partial e_{ij}} - \sigma_{ij}\right)\dot{e}_{ij} + \left(\frac{\partial\psi}{\partial T} + \rho\eta\frac{\partial\phi}{\partial T}\right)\dot{T} + \left(\frac{\partial\psi}{\partial T^*} + \rho\eta\frac{\partial\phi}{\partial T^*}\right)\dot{T}^* + \rho\dot{\eta}\phi = -q_{i,i} + \rho Q, \tag{19}$$

and

$$\left(\frac{\partial\psi}{\partial e_{ij}} - \sigma_{ij}\right)\dot{e}_{ij} + \left(\frac{\partial\psi}{\partial T} + \rho\eta\frac{\partial\phi}{\partial T}\right)\dot{T} + \left(\frac{\partial\psi}{\partial T^*} + \rho\eta\frac{\partial\phi}{\partial T^*}\right)\dot{T}^* + \frac{q_i}{\phi}\left(\frac{\partial\phi}{\partial T}T_{,i} + \frac{\partial\phi}{\partial T^*}T^*_{,i}\right) \le 0. \tag{20}$$

Now, we postulate that the constitutive equations are in the following forms

$$\sigma_{ij} = \frac{\partial\psi}{\partial e_{ij}}, \tag{21}$$

$$\frac{\partial\psi}{\partial T^*} + \rho\eta\frac{\partial\phi}{\partial T^*} = 0. \tag{22}$$

7

Then, the relations (19)-(20) reduces to

$$(\frac{\partial \psi}{\partial T} + \rho \eta \frac{\partial \phi}{\partial T})\dot{T} + \rho \dot{\eta} \phi = -q_{i,i} + \rho Q, \tag{23}$$

and

$$(\frac{\partial \psi}{\partial T} + \rho \eta \frac{\partial \phi}{\partial T})\dot{T} + \frac{q_i}{\phi}(\frac{\partial \phi}{\partial T}T_{,i} + \frac{\partial \phi}{\partial T^*}T^*_{,i}) \leq 0. \tag{24}$$

We will now prove that for a linear thermoelastic body (23) and (24) hold true if

$$\phi = \theta_0 + \theta + \nu D_\omega \theta, \tag{25}$$

$$\psi = \mu e_{ij}e_{ij} + \frac{\lambda}{2}e^2 - \gamma e(\theta + \nu D_\omega \theta) - \frac{\rho c_e}{2\theta_0}\theta^2 - \frac{\rho c_e}{\theta_0}\nu\theta D_\omega \theta - \frac{\rho c_e}{2\theta_0}\nu\tau(D_\omega \theta)^2, \tag{26}$$

where

$$\theta = T - \theta_0, \tag{27}$$

$$0 < \tau \leq \nu, \tag{28}$$

and

$$\theta_{,i}(D_\omega \theta)_{,i} \geq 0. \tag{29}$$

In the present linear thermoelasticity theory, it is considered that

$$|\frac{\theta}{\theta_0}| << 1 \text{ as well as } |\frac{\theta + \nu D_\omega \theta}{\theta_0}| << 1. \tag{30}$$

With the help of the Eqs. (25)-(26), we obtain

$$\frac{\partial \phi}{\partial T} = 1, \ \frac{\partial \phi}{\partial T^*} = \nu, \tag{31}$$

$$\frac{\partial \psi}{\partial T} = -\gamma e - \frac{\rho c_e}{\theta_0}(\theta + \nu D_\omega \theta), \tag{32}$$

$$\frac{\partial \psi}{\partial T^*} = \nu[-\gamma e - \frac{\rho c_e}{\theta_0}(\theta + \tau D_\omega \theta)], \tag{33}$$

$$\frac{\partial \psi}{\partial e_{ij}} = 2\mu e_{ij} + \lambda e\delta_{ij} - \gamma(\theta + \nu D_\omega \theta)\delta_{ij}. \tag{34}$$

Using the relations (21) and (34), we obtain

$$\sigma_{ij} = \lambda e\delta_{ij} + 2\mu e_{ij} - \gamma(\theta + \nu D_\omega \theta)\delta_{ij}. \tag{35}$$

Thus, the Hooke's law (2) is derived.

In view of the Eqs. (22), (31) and (33), we obtain

$$\rho\theta_0\eta = \gamma\theta_0 e + \rho c_e(\theta + \tau D_\omega \theta). \tag{36}$$

8

Again, using the Eqs. (25), (31), (32) in (23) and disregarding the terms proportional to $\theta D_\omega \theta$, $\theta \dot{\theta}$, $\dot{\theta} D_\omega \theta$, $\theta D_\omega \dot{\theta}$, $D_\omega \theta D_\omega \dot{\theta}$, $\dot{e}\theta$ and $\dot{e}D_\omega \theta$ as small relative to those proportional to $\dot{e}$, $\dot{\theta}$ and $D_\omega \dot{\theta}$, we obtain the following linear form of energy balance as

$$\rho \theta_0 \dot{\eta} = -q_{i,i} + \rho Q. \tag{37}$$

Eliminating η from the Eqs. (36) and (37), we obtain

$$- q_{i,i} + \rho Q = \gamma \theta_0 \dot{e} + \rho c_e (1 + \tau D_\omega)\dot{\theta}. \tag{38}$$

In order to prove the validity of the dissipation inequality (24), we first observe that

$$\frac{1}{\phi} = \frac{1}{\theta_0}\Big[1 + \frac{\theta + \nu D_\omega \theta}{\theta_0}\Big]^{-1}. \tag{39}$$

Based on the assumption (30), binomial expansion in the relation (39) and neglecting the term $\frac{\theta + \nu D_\omega \theta}{\theta_0}$ and its higher order, we obtain

$$\frac{1}{\phi} \approx \frac{1}{\theta_0}. \tag{40}$$

which interprets that for $\phi > 1$, the values of the function rapidly tends to the reference temperature θ_0.

Using the Eqs. (31)-(32), (36) and (40) in the relation (24), we obtain

$$\frac{\rho c_e}{\theta_0}(\nu - \tau)\dot{\theta} D_\omega \theta - \frac{q_i}{\theta_0}[\theta_{,i} + \nu(D_\omega \theta)_{,i}] \geq 0. \tag{41}$$

Now, we introduce

$$q_i = -k\theta_{,i}. \tag{42}$$

Then, with the help of the Lemma 1 and the relations (8), (29) and (42), the inequality (41) is obviously satisfied.

Eliminating q_i from the Eqs. (38) and (42), we obtain

$$k\theta_{,ii} = \rho c_e (1 + \tau D_\omega)\dot{\theta} + \gamma \theta_0 \dot{e} - \rho Q. \tag{43}$$

Thus, the heat conduction equation under Green-Lindsay model with MDD (4) is derived.

9

Domain of Influence

Let us denote the set $\mathscr{D}(t)$ by the points $x \in \bar{\mathscr{D}}$ having the following properties:

i. for $x \in \mathscr{D}$, $u_i^0 \neq 0$ or $u_i^1 \neq 0$ or $\theta^0 \neq 0$ or $\exists\, t^* \in [0, t]$ such that $f_i(x, t^*) \neq 0$ or $Q(x, t^*) \neq 0$,

ii. for $x \in \partial \mathscr{D}_1$, $\exists\, t^* \in [0, t]$ such that $\bar{u}_i(x, t^*) \neq 0$,

iii. for $x \in \partial \mathscr{D}_1^c$, $\exists\, t^* \in [0, t]$ such that $\bar{\sigma}_i(x, t^*) \neq 0$,

iv. for $x \in \partial \mathscr{D}_2$, $\exists\, t^* \in [0, t]$ such that $\bar{\theta}(x, t^*) \neq 0$,

v. for $x \in \partial \mathscr{D}_2^c$, $\exists\, t^* \in [0, t]$ such that $\bar{q}(x, t^*) \neq 0$.

Now, the domain of influence of the present problem at an instant t is defined as:

$$\mathscr{D}^*(t) = \{x \in \bar{\mathscr{D}} : \mathscr{D}(t) \cap \mathscr{S}(x_0, ct) \neq \Phi\} \tag{44}$$

where Φ is the empty set and $\mathscr{S}(x_0, ct)$ is the open ball in the Euclidean 3D space $\mathbb{R}^3$ centered at x_0 with radius ct.

The constant c is a positive constant of velocity dimension such that

$$\frac{9\lambda^2}{2\mu\rho} + \frac{6\mu}{\rho} + \frac{2\nu\theta_0\gamma^2}{\tau\rho^2 c_e} \leq c_1^2, \quad \frac{k}{\tau\rho c_e} \leq c_2^2$$

and

$$c \geq \max\{c_1, c_2\} \tag{45}$$

In order to prove the domain of influence theorem, we introduce a smooth non-decreasing function $\mathscr{W}_\varepsilon(z)$ as

$$\mathscr{W}_\varepsilon(z) = \begin{cases} 0, & \text{if } z \in (-\infty, 0] \\ 1, & \text{if } z \in [\varepsilon, \infty) \end{cases} \tag{46}$$

for sufficiently small $\varepsilon > 0$.

For $0 \leq \zeta \leq t$, we define an useful function $\mathscr{H}(x, \zeta)$ with the help of the above function $\mathscr{W}_\varepsilon(z)$ as follows:

$$\mathscr{H} : \mathscr{D} \times [0, t] \to \mathbb{R}, \text{ such that } \mathscr{H}(x, \zeta) = \mathscr{W}_\varepsilon\left(\frac{\mathsf{R} - r}{c} + t - \zeta\right). \tag{47}$$

10

Here, $\mathsf{R} > 0$, $t > 0$ are fixed constants, $r = |x - x_0|$, x_0 is an arbitrary fixed point and $c > 0$ is the velocity of the thermal signals defined by (45).

It is obvious that $\mathscr{H}(x, \zeta)$ is a smooth function on $\mathscr{D} \times [0, t]$ and it vanishes outside the set Σ, which is defined by

$$\Sigma = \bigcup_{\zeta \in [0, t]} \mathscr{S}[x_0, \mathsf{R} + c(t - \zeta)].$$

The open ball $\mathscr{S}(x_0, d)$ is defined as

$$\mathscr{S}(x_0, d) = \{x \in \mathbb{R}^3 : |x - x_0| < d\}.$$

Now, we define the functions $\mathscr{U}(x, \zeta)$ as

$$\mathscr{U}(x, \zeta) = \frac{1}{2}\left[\rho \dot{u}_i \dot{u}_i + \lambda e^2 + 2\mu e_{ij} e_{ij} + \frac{\rho c_e}{\theta_0}(\theta + \tau D_\omega \theta)^2 + \frac{\rho c_e}{\theta_0}\tau(\nu - \tau)(D_\omega \theta)^2\right](x, \zeta), \quad (48)$$

Lemma 2.

For any two positive real numbers ν and τ such that $\nu \geq \tau$, the scalar valued function f, defined on $\bar{\mathscr{D}}$, satisfies the following inequality:

$$(f + \nu D_\omega f)^2 \leq (\frac{\nu}{\tau})[(f + \tau D_\omega f)^2 + \tau(\nu - \tau)(D_\omega f)^2].$$

Proof.

We consider the following expression

$$g = (\frac{\nu}{\tau})[(f + \tau D_\omega f)^2 + \tau(\nu - \tau)(D_\omega f)^2] - (f + \nu D_\omega f)^2.$$

Straight forward calculations give $g = (\frac{\nu - \tau}{\tau})f^2 \geq 0$ and this proves the Lemma 2.

Lemma 3

Let A_{ij}, h and y_i denote the components of a symmetric tensor, a scalar quantity and the components of a vector respectively, $(x) = (x_i) \in \mathbb{R}^3$, $|x| = r$ and $i, j = 1, 2, 3$, then for

11

any arbitrary parameter $p' > 0$, the following inequalities hold:

(i) $\frac{A_{ij}x_i y_j}{r} \leq \frac{1}{2}[p'A_{ij}A_{ij} + \frac{1}{p'}y_i y_i]$, (dim $p' = \frac{\dim y_i}{\dim A_{ij}}$).

Proof.

$$
\begin{aligned}
\frac{A_{ij}x_i y_j}{r} &= \frac{A_{11}x_1 y_1}{r} + \frac{A_{12}x_1 y_2}{r} + \frac{A_{13}x_1 y_3}{r} \\
&+ \frac{A_{21}x_2 y_1}{r} + \frac{A_{22}x_2 y_2}{r} + \frac{A_{23}x_2 y_3}{r} \\
&+ \frac{A_{31}x_3 y_1}{r} + \frac{A_{32}x_3 y_2}{r} + \frac{A_{33}x_3 y_3}{r}.
\end{aligned}
\tag{49}
$$

Now, for any arbitrary parameter $p' > 0$ the arithmetic-geometric mean inequality

$$
ab \leq \frac{1}{2}[p'a^2 + \frac{1}{p'}b^2], \ (\dim p' = \frac{\dim b}{\dim a})
$$

of each term in (46) yields the following relation

$$
\begin{aligned}
\frac{A_{ij}x_i y_j}{r} &\leq \frac{1}{2}[(p'A_{11}^2 + \frac{1}{p'}\frac{x_1^2}{r^2}y_1^2) + (p'A_{12}^2 + \frac{1}{p'}\frac{x_1^2}{r^2}y_2^2) + (p'A_{13}^2 + \frac{1}{p'}\frac{x_1^2}{r^2}y_3^2) \\
&+ (p'A_{21}^2 + \frac{1}{p'}\frac{x_2^2}{r^2}y_1^2) + (p'A_{22}^2 + \frac{1}{p'}\frac{x_2^2}{r^2}y_2^2) + (p'A_{23}^2 + \frac{1}{p'}\frac{x_2^2}{r^2}y_3^2) \\
&+ (p'A_{31}^2 + \frac{1}{p'}\frac{x_3^2}{r^2}y_1^2) + (p'A_{32}^2 + \frac{1}{p'}\frac{x_3^2}{r^2}y_2^2) + (p'A_{33}^2 + \frac{1}{p'}\frac{x_3^2}{r^2}y_3^2)].
\end{aligned}
\tag{50}
$$

Then, (50) proves the Lemma 3(i) as $|x| = \sqrt{x_1^2 + x_2^2 + x_3^2} = r$.

(ii) $\frac{hx_i y_i}{r} \leq \frac{1}{2}[p'h^2 + \frac{1}{p'}y_i y_i]$, (dim $p' = \frac{\dim y_i}{\dim h}$).

Proof.

$$
\frac{hx_i y_i}{r} = \frac{hx_1 y_1}{r} + \frac{hx_2 y_2}{r} + \frac{hx_3 y_3}{r}.
\tag{51}
$$

Similarly, following the way as in (i) we obtain from (51) that

$$
\frac{hx_i y_i}{r} \leq \frac{1}{2}[(p'\frac{h^2 x_1^2}{r^2} + \frac{1}{p'}y_1^2) + (p'\frac{h^2 x_2^2}{r^2} + \frac{1}{p'}y_2^2) + (p'\frac{h^2 x_3^2}{r^2} + \frac{1}{p'}y_3^2)]
\tag{52}
$$

Then, (52) proves the Lemma 3(ii) as $|x| = \sqrt{x_1^2 + x_2^2 + x_3^2} = r$.

Lemma 4.

$|\mathscr{H}_{,j}\sigma_{ij}\dot{u}_i - \frac{\mathscr{H}_{,i}(\theta + \nu D_\omega \theta)q_i}{\theta_0}| \leq \mathscr{W}'\left[\mathscr{U}(x,\zeta) + \frac{2\nu k}{\theta_0}\theta_{,i}\theta_{,i}\right].$

Proof.

Since, $\mathscr{H}_{,j} = \frac{\partial H}{\partial r} \frac{\partial r}{\partial x_j} = -\frac{1}{c} \mathscr{W}_{\varepsilon}' \frac{x_j}{r}$,

we have,

$$
|\mathscr{H}_{,j} \sigma_{ij} \dot{u}_i - \frac{\mathscr{H}_{,i}(\theta + \nu D_\omega \theta) q_i}{T_0}|
$$
$$
= | -\frac{1}{c} \mathscr{W}_{\varepsilon}' \frac{x_j}{r} \sigma_{ij} \dot{u}_i + \frac{1}{c} \mathscr{W}_{\varepsilon}' \frac{x_i}{r} \frac{(\theta + \nu D_\omega \theta) q_i}{\theta_0}|
$$
$$
\leq \frac{1}{c} \mathscr{W}_{\varepsilon}' \frac{1}{r} \big[|\lambda e x_i \dot{u}_i + 2\mu e_{ij} x_j \dot{u}_i - \gamma(\theta + \nu D_\omega \theta) x_i \dot{u}_i| + |\frac{(\theta + \nu D_\omega \theta) x_i q_i}{\theta_0}| \big]
$$

With suitable choice of the parameter $p' = \frac{2\mu c}{9\lambda}, \frac{c}{3}, \frac{\rho c_e c \tau}{2\theta_0 \gamma \nu}, \frac{k}{2\nu c}$ and using Lemma-1, Lemma-3 the above relation yields,

$$
|\mathscr{H}_{,j} \sigma_{ij} \dot{u}_i - \frac{\mathscr{H}_{,i}(\theta + \nu D_\omega \theta) q_i}{\theta_0}|
$$
$$
\leq \frac{1}{2} \mathscr{W}_{\varepsilon}' \Big[\Big(\frac{2}{9} \mu e^2 + c^{-2} \frac{9\lambda^2}{2\mu \rho} \rho \dot{u}_i \dot{u}_i \Big) + \Big(\frac{2}{3} \mu e_{ij} e_{ij} + c^{-2} \frac{6\mu}{\rho} \rho \dot{u}_i \dot{u}_i \Big) + \Big\{ \frac{1}{2} \frac{\rho c_e}{\theta_0} (\theta + \tau D_\omega \theta)^2
$$
$$
+ \frac{1}{2} \frac{\rho c_e}{\theta_0} \tau(\nu - \tau)(D_\omega \theta)^2 + \frac{2\nu \theta_0 \gamma^2}{\tau \rho^2 c_e} c^{-2} \rho \dot{u}_i \dot{u}_i \Big\} + \Big\{ \frac{1}{2} \frac{\rho c_e}{\theta_0} (\theta + \tau D_\omega \theta)^2
$$
$$
+ \frac{1}{2} \frac{\rho c_e}{\theta_0} \tau(\nu - \tau)(D_\omega \theta)^2 \Big\} \Big\{ \frac{4\nu k \theta_{,i} \theta_{,i}}{\rho c_e[(\theta + \tau D_\omega \theta)^2 + \tau(\nu - \tau)(D_\omega \theta)^2]} + \frac{kc^{-2}}{\rho c_e \tau} \Big\} \Big]
$$
$$
\leq \mathscr{W}' \Big[\mathscr{U}(x, \zeta) + \frac{2\nu k}{\theta_0} \theta_{,i} \theta_{,i} \Big]
$$

where the constant c is given by the inequality (45).

Theorem 1 (Domain of dependence inequality).

Let the the solution of the system of Eqs. (1)-(4) is (u_i, θ) in the presence of the initial conditions (6) and the boundary conditions (7) with the inequality (45), then for any $\mathsf{R} > 0, t > 0$ and $x_0 \in \mathscr{D}$, the following inequality holds:

13

$$\int_{\mathscr{D}(x_0,\mathsf{R})} \mathscr{U}(x,t)d\mathscr{D} + \frac{\rho c_e}{\theta_0}(\nu - \tau)\int_0^t d\zeta \int_{\mathscr{D}[x_0,\mathsf{R}+c(t-\zeta)]} \dot{\theta}D_\omega\theta d\mathscr{D}$$

$$+\frac{1}{\theta_0}\int_0^t d\zeta \int_{\mathscr{D}[x_0,\mathsf{R}+c(t-\zeta)]}[k\theta_{,i}\theta_{,i} + \nu k\theta_{,i}(D_\omega\theta)_{,i}]d\mathscr{D}$$

$$\leq \int_{\mathscr{D}(x_0,\mathsf{R}+ct)} \mathscr{U}(x,0)d\mathscr{D} + \int_0^t d\zeta \int_{\mathscr{D}[x_0,\mathsf{R}+c(t-\zeta)]} \rho[f_i\dot{u}_i + \frac{Q(\theta+\nu D_\omega\theta)}{\theta_0}]d\mathscr{D}$$

$$+\int_0^t d\zeta \int_{\partial\mathscr{D}[x_0,\mathsf{R}+c(t-\zeta)]}[\bar{\sigma}_i\dot{u}_i - \frac{\bar{q}\theta + \nu D_\omega\theta)}{\theta_0}]dA$$

where $\mathscr{D}(x_0,d) = \{x \in \mathscr{D} : |x - x_0| < d\}$, $\partial\mathscr{D}(x_0,d) = \{x \in \partial\mathscr{D} : |x - x_0| = d\}$.

Proof :

For any $(x,\zeta) \in \mathscr{D} \times [0,t]$, multiplying the Eq. (3) by $\mathscr{H}\dot{u}_i$ and using the relation $(\mathscr{H}\sigma_{ij}\dot{u}_i)_{,j} = \mathscr{H}_{,j}\sigma_{ij}\dot{u}_i + \mathscr{H}\sigma_{ij,j}\dot{u}_i + \mathscr{H}\sigma_{ij}\dot{u}_{i,j}$, one can deduce that

$$\frac{1}{2}\mathscr{H}\frac{d}{dt}(\rho\dot{u}_i\dot{u}_i) = \rho\mathscr{H}f_i\dot{u}_i + (\mathscr{H}\sigma_{ij}\dot{u}_i)_{,j} - \mathscr{H}_{,j}\sigma_{ij}\dot{u}_i - [\lambda e\delta_{ij} + 2\mu e_{ij} - \gamma(\theta + \nu D_\omega\theta)\delta_{ij}]\mathscr{H}\dot{u}_{i,j}.$$
(53)

Again, multiplying the Eq. (4) by $\frac{1}{\theta_0}(\theta + \nu D_\omega\theta)\mathscr{H} = \frac{1}{\theta_0}[(\theta + \tau D_\omega\theta) + (\nu - \tau)D_\omega\theta]\mathscr{H}$ and using the relation $(\mathscr{H}\theta q_i)_{,i} = \mathscr{H}_{,i}\theta q_i + \mathscr{H}\theta_{,i}q_i + \mathscr{H}\theta q_{i,i}$, we obtain

$$\frac{1}{2}\mathscr{H}\frac{d}{dt}\Big[\frac{\rho c_e}{\theta_0}(\theta + \tau D_\omega\theta)^2 + \frac{\rho c_e}{\theta_0}\tau(\nu - \tau)(D_\omega\theta)^2\Big] + \frac{\rho c_e}{\theta_0}(\nu - \tau)\dot{\theta}(D_\omega\theta)\mathscr{H} = \frac{\rho Q(\theta + \nu D_\omega\theta)}{\theta_0}\mathscr{H}$$

$$-\frac{1}{\theta_0}\Big\{[(\theta + \nu D_\omega\theta)q_i\mathscr{H}]_{,i} - (\theta + \nu D_\omega\theta)q_i\mathscr{H}_{,i} - q_i(\theta + \nu D_\omega\theta)_{,i}\mathscr{H}\Big\} - \gamma\mathscr{H}\theta\dot{e}(\theta + \nu D_\omega\theta).$$
(54)

Adding the Eqs.(53) and (54), we get

$$\frac{1}{2}\mathscr{H}\frac{d}{dt}\Big[\rho\dot{u}_i\dot{u}_i + \frac{\rho c_e}{\theta_0}(\theta + \tau D_\omega\theta)^2 + \frac{\rho c_e}{\theta_0}\tau(\nu - \tau)(D_\omega\theta)^2\Big] + \frac{\rho c_e}{\theta_0}(\nu - \tau)\dot{\theta}D_\omega\theta\mathscr{H}$$

$$+\frac{k\theta_{,i}(\theta + \nu D_\omega\theta)_{,i}}{\theta_0}\mathscr{H} = \Big[f_i\dot{u}_i + \frac{Q(\theta + \nu D_\omega\theta)}{\theta_0}\Big]\rho\mathscr{H} + \Big[\Big\{\sigma_{ij}\dot{u}_i - \frac{(\theta + \nu D_\omega\theta)q_j}{\theta_0}\Big\}\mathscr{H}\Big]_{,j}$$

$$-(\lambda e\dot{e} + 2\mu e_{ij}\dot{e}_{ij})\mathscr{H} - \mathscr{H}_{,j}\sigma_{ij}\dot{u}_i + \frac{(\theta + \nu D_\omega\theta)q_i}{\theta_0}\mathscr{H}_{,i}.$$
(55)

The Eq. (55) can be rewritten as

14

$$\frac{1}{2}\mathscr{H}\frac{d}{dt}[\rho\dot{u}_i\dot{u}_i + \lambda e^2 + 2\mu e_{ij}e_{ij} + \frac{\rho c_e}{\theta_0}(\theta + \tau D_\omega\theta)^2 + \frac{\rho c_e}{\theta_0}\tau(\nu - \tau)(D_\omega\theta)^2]$$
$$+ \frac{\rho c_e}{\theta_0}(\nu - \tau)\dot{\theta}D_\omega\theta\mathscr{H} + \frac{[\theta_{,i}\theta_{,i} + \nu\theta_{,i}(D_\omega\theta)_{,i}]}{\theta_0}k\mathscr{H} = [f_i\dot{u}_i + \frac{Q(\theta + \nu D_\omega\theta)}{\theta_0}]\rho\mathscr{H}$$
$$+ [(\sigma_{ij}\dot{u}_i - \frac{(\theta + \nu D_\omega\theta)q_j}{\theta_0})\mathscr{H}]_{,j} - \mathscr{H}_{,j}\sigma_{ij}\dot{u}_i + \frac{(\theta + \nu D_\omega\theta)q_i}{\theta_0}\mathscr{H}_{,i}. \tag{56}$$

or,

$$\mathscr{H}\dot{\mathscr{U}}(x,\zeta) + \frac{\rho c_e}{\theta_0}(\nu - \tau)\dot{\theta}(D_\omega\theta)\mathscr{H} + \frac{[\theta_{,i} + \nu(D_\omega\theta)_{,i}]\theta_{,i}}{\theta_0}k\mathscr{H} = [f_i\dot{u}_i + \frac{Q(\theta + \nu D_\omega\theta)}{\theta_0}]\rho\mathscr{H}$$
$$+ [(\sigma_{ij}\dot{u}_i - \frac{(\theta + \nu D_\omega\theta)q_j}{\theta_0})\mathscr{H}]_{,j} - \mathscr{H}_{,j}\sigma_{ij}\dot{u}_i + \frac{(\theta + \nu D_\omega\theta)q_i}{\theta_0}\mathscr{H}_{,i} \tag{57}$$

which leads to,

$$\int_{\mathscr{D}}\mathscr{H}\mathscr{U}(x,t)d\mathscr{D} + \frac{\rho c_e}{\theta_0}(\nu - \tau)\int_0^t d\zeta\int_{\mathscr{D}}\mathscr{H}\dot{\theta}(D_\omega\theta)d\mathscr{D} + \frac{1}{\theta_0}\int_0^t d\zeta\int_{\mathscr{D}}k[\theta_{,i} + \nu(D_\omega\theta)_{,i}]\theta_{,i}\mathscr{H}d\mathscr{D}$$
$$= \int_{\mathscr{D}}\mathscr{H}\mathscr{U}(x,0)d\mathscr{D} + \int_0^t d\zeta\int_{\mathscr{D}}[f_i\dot{u}_i + \frac{Q(\theta + \nu D_\omega\theta)}{\theta_0}]\rho\mathscr{H}d\mathscr{D} + \int_0^t d\zeta\int_{\partial\mathscr{D}}[\bar{\sigma}_i\dot{u}_i - \frac{\bar{q}(\theta + \nu D_\omega\theta)}{\theta_0}]\mathscr{H}dA$$
$$+ \int_0^t d\zeta\int_{\mathscr{D}}\dot{\mathscr{H}}\mathscr{U}(x,\zeta)d\mathscr{D} - \int_0^t d\zeta\int_{\mathscr{D}}(\mathscr{H}_{,j}\sigma_{ij}\dot{u}_i - \frac{(\theta + \nu D_\omega\theta)q_i}{\theta_0})\mathscr{H}_{,i}d\mathscr{D}. \tag{58}$$

Now, using the Lemma-4, we obtain

$$\int_0^t d\zeta\int_{\mathscr{D}}\dot{\mathscr{H}}\mathscr{U}(x,\zeta)d\mathscr{D} - \int_0^t d\zeta\int_{\mathscr{D}}(\mathscr{H}_{,j}\sigma_{ij}\dot{u}_i - \frac{\mathscr{H}_{,i}(\theta + \nu D_\omega\theta)q_i}{\theta_0})d\mathscr{D} - \frac{1}{\theta_0}\int_0^t d\zeta\int_{\mathscr{D}}\mathscr{H}k\theta_{,i}\theta_{,i}d\mathscr{D}$$
$$\leq \frac{1}{\theta_0}\int_0^t d\zeta\int_{\mathscr{D}}k\theta_{,i}\theta_{,i}\Big(2\nu\mathscr{W}' - \mathscr{H}\Big)d\mathscr{D} \leq 0. \tag{59}$$

Note: This also gives an idea about an upper bound of the parameter ν i.e. $\nu \leq (\mathscr{H}/2\mathscr{W}')$.
With the help of the inequality (59), the equation (58) yields

$$\int_{\mathscr{D}}\mathscr{H}\mathscr{U}(x,t)d\mathscr{D} + \frac{\rho c_e}{\theta_0}(\nu - \tau)\int_0^t d\zeta\int_{\mathscr{D}}\mathscr{H}\dot{\theta}D_\omega\theta d\mathscr{D} + \frac{1}{\theta_0}\int_0^t d\zeta\int_{\mathscr{D}}k\nu(D_\omega\theta)_{,i}\theta_{,i}\mathscr{H}d\mathscr{D}$$
$$\leq \int_{\mathscr{D}}\mathscr{H}\mathscr{U}(x,0)d\mathscr{D} + \int_0^t d\zeta\int_{\mathscr{D}}\Big[f_i\dot{u}_i + \frac{Q(\theta + \nu D_\omega\theta)}{\theta_0}\Big]\rho\mathscr{H}d\mathscr{D} + \int_0^t d\zeta\int_{\partial\mathscr{D}}[\bar{\sigma}_i\dot{u}_i - \frac{\bar{q}\theta + \nu D_\omega\theta)}{\theta_0}]\mathscr{H}dA \tag{60}$$

Making $\varepsilon \to 0$ in the above relation, we see that $\mathscr{H}$ approaches boundedly to the characteristic function of Σ and hence the Theorem-1.

15

Theorem 2 (Domain of influence theorem).

If the system of Eqs. (1)-(4) a solution (u_i, θ) subjected to the conditions (6)-(7), then

$$u_i = \theta = 0 \text{ on } \{\bar{\mathscr{D}} \setminus \mathscr{D}^*(t)\} \times [0, t].$$

Proof : To prove the Theorem 2 we proceed as follows:

Let $(x_0, t^*) \in \{\bar{\mathscr{D}} \setminus \mathscr{D}^*(t)\} \times [0, t]$, an arbitrary fixed point.

Then, by using the Theorem 1(Domain of dependence inequality) with $t = t^*$ and $\mathsf{R} = c(t - t^*)$, we obtain

$$
\int_{\mathscr{D}[x_0, c(t-t^*)]} \mathscr{U}(x, t^*) d\mathscr{D} + \frac{\rho c_e}{\theta_0}(\nu - \tau) \int_0^t d\zeta \int_{\mathscr{D}[x_0, c(t-\zeta)]} \dot{\theta} D_\omega \theta d\mathscr{D}
$$
$$
+ \frac{1}{\theta_0} \int_0^{t^*} d\zeta \int_{\mathscr{D}[x_0, c(t-\zeta)]} k\nu(D_\omega \theta)_{,i} \theta_{,i} dV \leq \int_{\mathscr{D}(x_0, ct)} \mathscr{U}(x, 0) d\mathscr{D}
$$
$$
+ \int_0^{t^*} d\zeta \int_{\mathscr{D}[x_0, c(t-\zeta)]} \rho[f_i u_i + \frac{Q(\theta + \nu D_\omega \theta)}{\theta_0}] d\mathscr{D} + \int_0^{t^*} d\zeta \int_{\partial\mathscr{D}[x_0, c(t-\zeta)]} [\bar{\sigma}_i \dot{u}_i - \frac{\bar{q}(\theta + \nu D_\omega)\theta}{\theta_0}] dA.
$$
(61)

Since, $x_0 \in \{\bar{\mathscr{D}} \setminus \mathscr{D}^*(t)\} \times [0, t]$, we have $x \in \mathscr{D}(x_0, ct) \Rightarrow x \notin \mathscr{D}(t)$ and hence

$$\int_{\mathscr{D}(x_0, ct)} \mathscr{U}(x, 0) d\mathscr{D} = 0. \tag{62}$$

Again, since $\mathscr{D}[x, c(t - \zeta)] \subseteq \mathscr{D}(x_0, ct)$, we also obtain

$$\int_0^{t^*} d\zeta \int_{\mathscr{D}[x_0, c(t-\zeta)]} \rho[f_i u_i + \frac{Q(\theta + \nu D_\omega \theta)}{T_0}] d\mathscr{D} = 0, \tag{63}$$

and

$$\int_0^{t^*} d\zeta \int_{\partial\mathscr{D}[x_0, c(t-\zeta)]} [\bar{\sigma}_i \dot{u}_i - \frac{\bar{q}(\theta + \nu D_\omega \theta)}{T_0}] dA = 0. \tag{64}$$

Now, with the help of the inequality (29), the Lemma 1 and the relations (62)-(64), we obtain from (61) that

$$\int_{\mathscr{D}[x_0, c(t-t^*)]} \mathscr{U}(x, t^*) d\mathscr{D} \leq 0. \tag{65}$$

The definition of $\mathscr{U}$ implies that

$$\dot{u}_i(x_0, t^*) = \theta(x_0, t^*) = 0 \tag{66}$$

16

for all $(x_0, t^*) \in \{\bar{\mathscr{D}} \setminus \mathscr{D}^*(t)\} \times [0, t]$.

Finally, since $u_i(x_0, 0) = 0$ for all $x_0 \in \{\bar{\mathscr{D}} \setminus \mathscr{D}^*(t)\} \times [0, t]$, we deduce that

$$u_i(x_0, t^*) = \theta(x_0, t^*) = 0 \text{ for all } (x_0, t^*) \in \{\bar{\mathscr{D}} \setminus \mathscr{D}^*(t)\} \times [0, t].$$

Thus, the proof of the theorem is complete.

Special cases:

(i) For $K(t-\xi) = 1$ and $\omega \longrightarrow 0$, the present thermoelasticity theory reduces to temperature-rate dependent thermoelasticity theory with finite speed propagation [5].

(ii) For $\nu = \tau = 0$, the present thermoelasticity theory reduces to classical coupled thermoelasticity theory with infinite speed propagation [1].

Application

We consider a two dimensional elastic body in the xy-plane such that $-\infty < x < \infty$ and $0 \leq y < \infty$. An external heat source is present at some point upon the x-axis. The entire x-axis is assumed to be the boundary of the plate under consideration. The coupled governing equations without external body forces and external heat sources per unit mass are obtained as,

$$\begin{aligned}
\mu \nabla^2 u + (\lambda + \mu) \frac{\partial e}{\partial x} - \gamma (1 + \nu D_\omega) \frac{\partial \theta}{\partial x} &= \rho \ddot{u} \\
\mu \nabla^2 v + (\lambda + \mu) \frac{\partial e}{\partial y} - \gamma (1 + \nu D_\omega) \frac{\partial \theta}{\partial y} &= \rho \ddot{v}
\end{aligned} \tag{67}$$

$$k \nabla^2 \theta = \rho c_e (1 + \tau D_\omega) \dot{\theta} + \gamma \theta_0 \frac{\partial}{\partial t} \left(\frac{\partial u}{\partial x} + \frac{\partial v}{\partial y} \right) \tag{68}$$

where $e = e_{xx} + e_{yy} = \frac{\partial u}{\partial x} + \frac{\partial v}{\partial y}$.

Applying the non-dimensional transformations

$$\left(x', y', u', v'\right) = v_1 \varsigma \left(x, y, u, v\right), \quad \left(\nu', \tau', t'\right) = v_1^2 \varsigma \left(\nu, \tau, t\right), \quad \theta' = \frac{\gamma}{\lambda + 2\mu} \theta$$

where $v_1^2 = \frac{\lambda + 2\mu}{\rho}, \quad \varsigma = \frac{\rho c_e}{k}$.

we obtain,

$$\frac{\partial^2 u}{\partial x^2} + \frac{\partial^2 u}{\partial y^2} + \beta \frac{\partial}{\partial x}\left(\frac{\partial u}{\partial x} + \frac{\partial v}{\partial y}\right) - \beta\left(1 + \nu D_\omega\right)\frac{\partial \theta}{\partial x} = \beta \ddot{u}$$

$$\frac{\partial^2 v}{\partial x^2} + \frac{\partial^2 v}{\partial y^2} + \beta \frac{\partial}{\partial y}\left(\frac{\partial u}{\partial x} + \frac{\partial v}{\partial y}\right) - \beta\left(1 + \nu D_\omega\right)\frac{\partial \theta}{\partial y} = \beta \ddot{v} \tag{69}$$

$$\frac{\partial^2 \theta}{\partial x^2} + \frac{\partial^2 \theta}{\partial y^2} = \left(1 + \tau D_\omega\right)\dot{\theta} + \varepsilon\left(\frac{\partial u}{\partial x} + \frac{\partial v}{\partial y}\right) \tag{70}$$

where $\beta = \frac{\lambda + 2\mu}{\mu}$ and $\varepsilon = \frac{\gamma^2 \theta_0}{\rho c_e(\lambda + 2\mu)}$ is the thermoelastic coupling factor.

Initial and boundary conditions

The initial conditions of the problem are given by,

$$u(x,y,0) = \dot{u}(x,y,0) = v(x,y,0) = \dot{v}(x,y,0) = \theta(x,y,0) = \dot{\theta}(x,y,0) = 0 \tag{71}$$

$$\sigma_{xx}(x,y,0) = \sigma_{yy}(x,y,0) = \sigma_{yx}(x,y,0) = \sigma_{xy}(x,y,0) = 0 \tag{72}$$

The boundary condition is considered as,

$$u(x,0,t) = v(x,0,t) = 0$$

$$\theta(x,0,t) = f(x,t) \tag{73}$$

Equations in integral transform domain

Ezzat and his co-workers [32] proposed another form of the memory kernel,

$$K(t-\xi) = 1 - \frac{2b}{\omega}(t-\xi) + \frac{a^2(t-\xi)^2}{\omega^2} \tag{74}$$

where ω is the time delay and a, b are the parameters to be chosen.

Laplace transform of a function containing the MDD would have been a challenging task in our succeeding discussion. Thus, Laplace transform of any function $f(t)$ with first order MDD is provided here,

$$L\left[D_\omega f(t)\right] = \frac{\overline{f}(s)}{\omega}\left(\left(1 - \frac{2b}{\omega s} + \frac{2a^2}{\omega^2 s^2}\right) - exp\left(-\omega s\right)\left(1 - 2b^2 + a^2 + \frac{2\left(a^2 - b\right)}{\omega s} + \frac{2a^2}{\omega^2 s^2}\right)\right) \tag{75}$$

18

If the kernel function in MDD is constant i.e. when $K(t,p) = 1$ then,

$$L\left[D_\omega f(t)\right] = \frac{1}{\omega}\left(1 - exp\left(-\omega s\right)\right)\overline{f}(x,s) \tag{76}$$

where $\overline{f}(x,s)$ denotes the Laplace transform of $f(x,t)$ and $f(x, t-\omega) = 0$ for $t < \omega$.

Applying Laplace transform defined by the relation

$$\overline{f}(x,y,s) = L\left[f(x,y,t)\right] = \int_0^\infty exp\left(-st\right)f(x,y,s)dt$$

followed by Fourier transform defined by

$$\overline{f}^*(p,y,s) = F\left[\overline{f}(x,y,s)\right] = \frac{1}{\sqrt{2\pi}}\int_{-\infty}^\infty exp\left(-ipx\right)\overline{f}(x,y,s)dx$$

on Eq.(69) and Eq.(70) we get,

$$\frac{d^2\overline{u}^*}{dy^2} = \left(p^2 + \beta p^2 + \beta s^2\right)\overline{u}^* + \beta s_1 ip\overline{\theta}^* - \beta ip\frac{d\overline{v}^*}{dy} \tag{77}$$

$$\frac{d^2\overline{v}^*}{dy^2} = \frac{1}{1+\beta}\left[\left(p^2 + \beta s^2\right)\overline{v}^* - \beta ip\frac{d\overline{u}^*}{dy} + \beta s_1\frac{d\overline{\theta}^*}{dy}\right] \tag{78}$$

$$\frac{d^2\overline{\theta}^*}{dy^2} = \varepsilon ip\overline{u}^* + \left(p^2 + s_3 s\right)\overline{\theta}^* + \varepsilon\frac{d\overline{v}^*}{dy} \tag{79}$$

Eq.(77), Eq.(78) and Eq.(79) can be written in matrix from as follows,

$$\frac{d\widetilde{U}(p,y,s)}{dy} = \widetilde{A}(p,s)\widetilde{U}(p,y,s) \tag{80}$$

where,

$$\overline{U} = \left[\overline{u}^* \quad \overline{v}^* \quad \overline{\theta}^* \quad \frac{d\overline{u}^*}{dy} \quad \frac{d\overline{v}^*}{dy} \quad \frac{d\overline{\theta}^*}{dy}\right]^T$$

and

$$\widetilde{A} = \begin{bmatrix} O & I \\ P & Q \end{bmatrix}$$

19

in which,

$$O = \begin{bmatrix} 0 & 0 & 0 \\ 0 & 0 & 0 \\ 0 & 0 & 0 \end{bmatrix}, I = \begin{bmatrix} 1 & 0 & 0 \\ 0 & 1 & 0 \\ 0 & 0 & 1 \end{bmatrix}, P = \begin{bmatrix} m_{41} & 0 & m_{43} \\ 0 & m_{52} & 0 \\ m_{61} & 0 & m_{63} \end{bmatrix}, Q = \begin{bmatrix} 0 & m_{45} & 0 \\ m_{54} & 0 & m_{56} \\ 0 & m_{65} & 0 \end{bmatrix}$$

Here,

$$m_{41} = p^2 + \beta p^2 + \beta s^2, m_{43} = \beta s_1 ip, m_{45} = -\beta ip, m_{52} = \frac{p^2 + \beta s^2}{1 + \beta},$$

$$m_{54} = \frac{-\beta ip}{1 + \beta}, m_{56} = \frac{\beta s_1}{1 + \beta}, m_{61} = \varepsilon ip, m_{63} = p^2 + s_3 s, m_{65} = \varepsilon \tag{81}$$

where,

$$s_1 = 1 + \nu \xi$$

$$s_3 = 1 + \tau \xi$$

$$\xi = \frac{1}{\omega} \left(\left(1 - \frac{2b}{\omega s} + \frac{2a^2}{\omega^2 s^2} \right) - exp\left(-\omega s \right) \left(1 - 2b^2 + a^2 + \frac{2\left(a^2 - b \right)}{\omega s} + \frac{2a^2}{\omega^2 s^2} \right) \right)$$

Solution of the vector matrix differential equation

The characteristic equation of the matrix $\widetilde{A}(p, s)$ can be written as:

$$\lambda^6 - t_1 \lambda^4 + t_2 \lambda^2 - t_3 = 0 \tag{82}$$

where,

$$t_1 = m_{65} m_{56} + m_{45} m_{54} + m_{63} + m_{52} + m_{41},$$

$$t_2 = m_{45} m_{54} m_{63} - m_{43} m_{54} m_{65} + m_{41} m_{65} m_{56}$$

$$-m_{45} m_{61} m_{56} + m_{52} m_{63} + m_{41} m_{63} + m_{41} m_{52} - m_{61} m_{43}, \tag{83}$$

$$t_3 = m_{41} m_{63} m_{52} - m_{43} m_{61} m_{52}$$

We assume the eigen values of the matrix $\widetilde{A}(p, s)$ to be $\pm\lambda_1$, $\pm\lambda_2$ and $\pm\lambda_3$ which are given by,

$$\lambda_1 = \sqrt{\frac{1}{3}\left(2k\,sin\,q + t_1\right)}$$

$$\lambda_2 = \sqrt{\frac{1}{3}\left[t_1 - k\left(\sqrt{3}\,cos\,q + sin\,q\right)\right]} \qquad (84)$$

$$\lambda_3 = \sqrt{\frac{1}{3}\left[t_1 + k\left(\sqrt{3}\,cos\,q - sin\,q\right)\right]}$$

where,

$$k = \sqrt{t_1^2 - 3t_2}, \quad q = \frac{sin^{-1}r}{3}, \quad r = \frac{2t_1^3 - 9t_1t_2 + 27t_3}{2k^3} \qquad (85)$$

The right eigen vector $\widetilde{X} = \begin{bmatrix} X_1 & X_2 & X_3 & X_4 & X_5 & X_6 \end{bmatrix}^T$ corresponding to the eigen value λ is calculated as:

$$\widetilde{X} = \begin{bmatrix} \lambda^2\left(m_{45}m_{56} + m_{43}\right) - m_{43}m_{52} \\ \lambda^3 m_{56} + \lambda\left(m_{54}m_{43} - m_{41}m_{56}\right) \\ \lambda^4 - \lambda^2\left(m_{41} + m_{52} + m_{45}m_{54}\right) + m_{41}m_{52} \\ \lambda^3\left(m_{45}m_{56} + m_{43}\right) - \lambda m_{43}m_{52} \\ \lambda^4 m_{56} + \lambda^2\left(m_{54}m_{43} - m_{41}m_{56}\right) \\ \lambda^5 - \lambda^3\left(m_{41} + m_{52} + m_{45}m_{54}\right) + \lambda m_{41}m_{52} \end{bmatrix} \qquad (86)$$

Thus from Eq.(86), the right eigen vectors $\widetilde{X}_i$ corresponding to the eigen values $\lambda = \pm\lambda_i$ are given by,

$$\widetilde{X}_1 = \widetilde{X}\big|_{\lambda=\lambda_1}, \ \ \widetilde{X}_2 = \widetilde{X}\big|_{\lambda=-\lambda_1}, \ \ \widetilde{X}_3 = \widetilde{X}\big|_{\lambda=\lambda_2}, \ \ \widetilde{X}_4 = \widetilde{X}\big|_{\lambda=-\lambda_2}, \ \ \widetilde{X}_5 = \widetilde{X}\big|_{\lambda=\lambda_3}, \ \ \widetilde{X}_6 = \widetilde{X}\big|_{\lambda=-\lambda_3}$$
$$(87)$$

Assuming the regularity conditions at infinity (ie. $\overline{u}^*, \overline{v}^*, \overline{\theta}^*, \dfrac{d\overline{u}^*}{dy}, \dfrac{d\overline{v}^*}{dy}, \dfrac{d\overline{\theta}^*}{dy} \longrightarrow 0$ as $y \to \infty$) the solution of Eq.(80) can be expressed as follows:

$$\widetilde{U}(p,y,s) = C_1\widetilde{X}_2 exp(-\lambda_1 y) + C_2\widetilde{X}_4 exp(-\lambda_2 y) + C_3\widetilde{X}_6 exp(-\lambda_3 y) \qquad (88)$$

where $y > 0$.

Hence the field functions can be expressed as follows:

$$\overline{u}^* = \sum_{i=0}^{3} C_i\Lambda_i exp(-\lambda_i y) \qquad (89)$$

21

$$\overline{v}^* = \sum_{i=0}^{3} C_i \Lambda_i' exp(-\lambda_i y) \tag{90}$$

$$\overline{\theta}^* = \sum_{i=0}^{3} C_i \Lambda_i'' exp(-\lambda_i y) \tag{91}$$

Applying Eq.(73) upon Eqs.(89)-(91) we obtain the expressions for C_i $(i = 1, 2, 3)$ as follows,

$$
\begin{aligned}
C_1 &= \frac{\overline{f}^*}{\Lambda} \left(\Lambda_2 \Lambda_3' - \Lambda_2' \Lambda_3 \right) \\
C_2 &= \frac{\overline{f}^*}{\Lambda} \left(\Lambda_3 \Lambda_1' - \Lambda_3' \Lambda_1 \right) \\
C_3 &= \frac{\overline{f}^*}{\Lambda} \left(\Lambda_1 \Lambda_2' - \Lambda_1' \Lambda_2 \right)
\end{aligned}
\tag{92}
$$

where,

$$
\begin{aligned}
\Lambda_i &= \lambda_i^2 \left(m_{45} m_{56} + m_{43} \right) - m_{43} m_{52} \\
\Lambda_i' &= \lambda_i^3 m_{56} + \lambda_i \left(m_{54} m_{43} - m_{41} m_{56} \right) \\
\Lambda_i'' &= \lambda_i^4 - \lambda_i^2 \left(m_{41} + m_{52} + m_{45} m_{54} \right) + m_{41} m_{52}
\end{aligned}
\tag{93}
$$

and,

$$
\Lambda = \begin{vmatrix} \Lambda_1 & \Lambda_2 & \Lambda_3 \\ \Lambda_1' & \Lambda_2' & \Lambda_3' \\ \Lambda_1'' & \Lambda_2'' & \Lambda_3'' \end{vmatrix}
\tag{94}
$$

Suppose a constant step up temperature is applied along the x-axis, then the function $f(x, t)$ in Eq.(73) can be taken as $Q_0 H(x) H(t)$.

For this the solution in transformed domain will be given by Eqs.(89)-(91), where

$$
\begin{aligned}
C_1 &= \frac{Q_0}{2s\Lambda} \left(\delta(p) - \frac{i}{\pi p} \right) \left(\Lambda_2 \Lambda_3' - \Lambda_2' \Lambda_3 \right) \\
C_2 &= \frac{Q_0}{2s\Lambda} \left(\delta(p) - \frac{i}{\pi p} \right) \left(\Lambda_3 \Lambda_1' - \Lambda_3' \Lambda_1 \right) \\
C_3 &= \frac{Q_0}{2s\Lambda} \left(\delta(p) - \frac{i}{\pi p} \right) \left(\Lambda_1 \Lambda_2' - \Lambda_1' \Lambda_2 \right)
\end{aligned}
\tag{95}
$$

Numerical results and discussion

In order to illustrate the theories discussed in the article, we consider the inverse fourier transform of the Eqs.(89)-(91) in view of Eq.(95), followed by the inverse laplace transform.

Since it is complicated to determine the inverse laplace transform of the above mentioned equations analytically, we employ the algorithm for numerical inversion given by Honig and Hirdes [36]. For the purpose of numerical computation in the space-time domain, we choose the parameters of a copper-like material where the values of the physical constants are as follows (for detail see Banerjee et al. [22]):

$$\lambda = 7.76 \times 10^{10} N/m^2, \quad \mu = 3.86 \times 10^{10} N/m^2, \quad \varepsilon = 0.0168, \quad \tau = 1, \quad \nu = 5, \quad Q_0 = 1$$

The numerical computations were carried out comparing the displacements u, v and temperature θ along the y-axis considering time delays $\omega = 0.01$ (Figs.1-3) and $\omega = 0.05$ (Figs.4-6). We considered three different set of values for the memory dependent parameters a and b (see the figures). The most important phenomena observed in each of the graphs that the solution of the thermoelastic problem of the present model in the presence of MDD is restricted in a bounded region and beyond this region the solution is identically zero. This means that thermal signals according to the novel generalized thermoelasticity theory with MDD shows the behavior of the finite speeds of wave propagation and hence provides a supporting visualization to the overall theory of the domain of influence theorem of the present thermoelasticity theory.
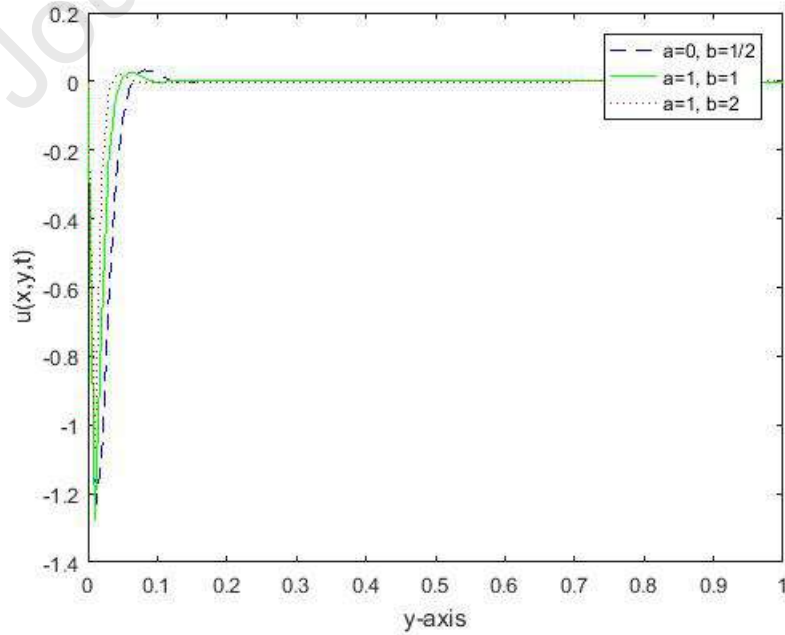
Fig. 1 Displacement u along the y-axis for different values of a and b in context of MDD,
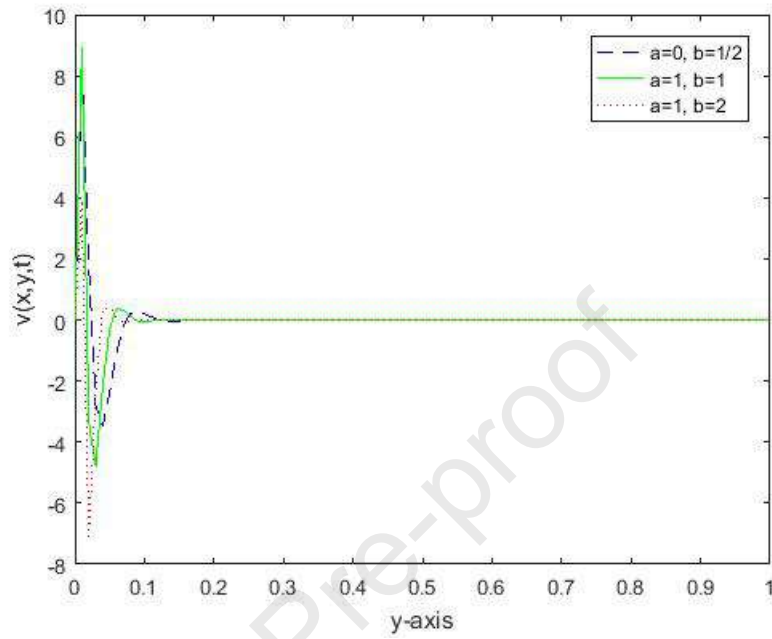
considering $\omega = 0.01$.

Fig. 2 Displacement v along the y-axis for different values of a and b in context of MDD, considering $\omega = 0.01$.

Fig. 3 Temperature θ along the y-axis for different values of a and b in context of MDD, considering $\omega = 0.01$.

24
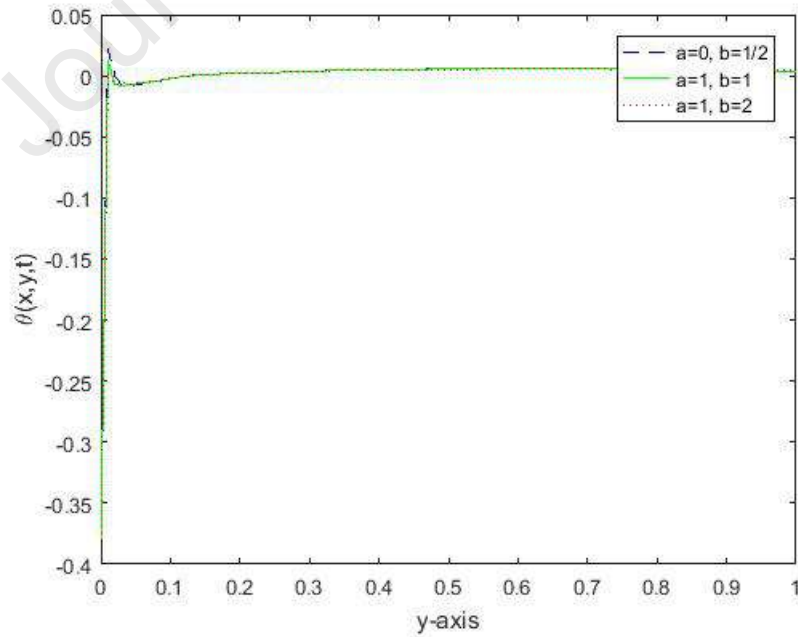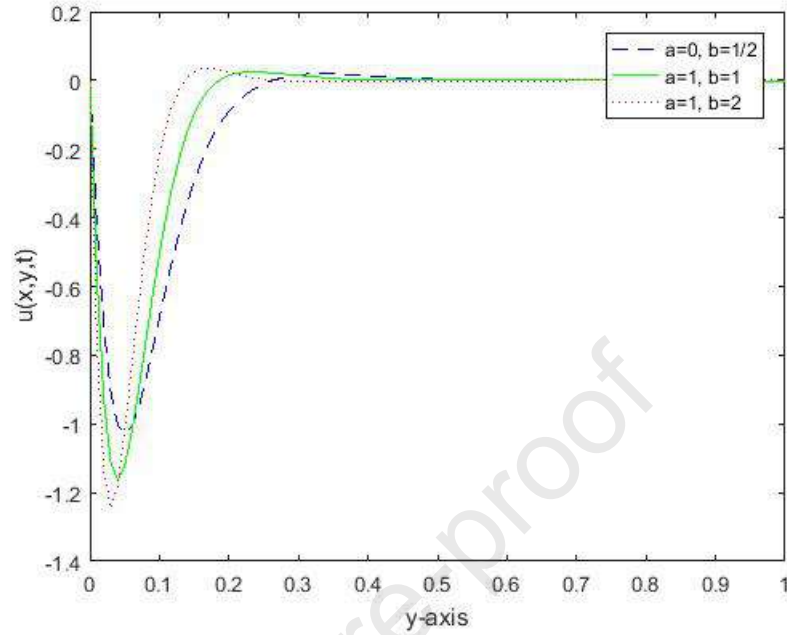
Fig. 4 Displacement u along the y-axis for different values of a and b in context of MDD, considering $\omega = 0.05$.
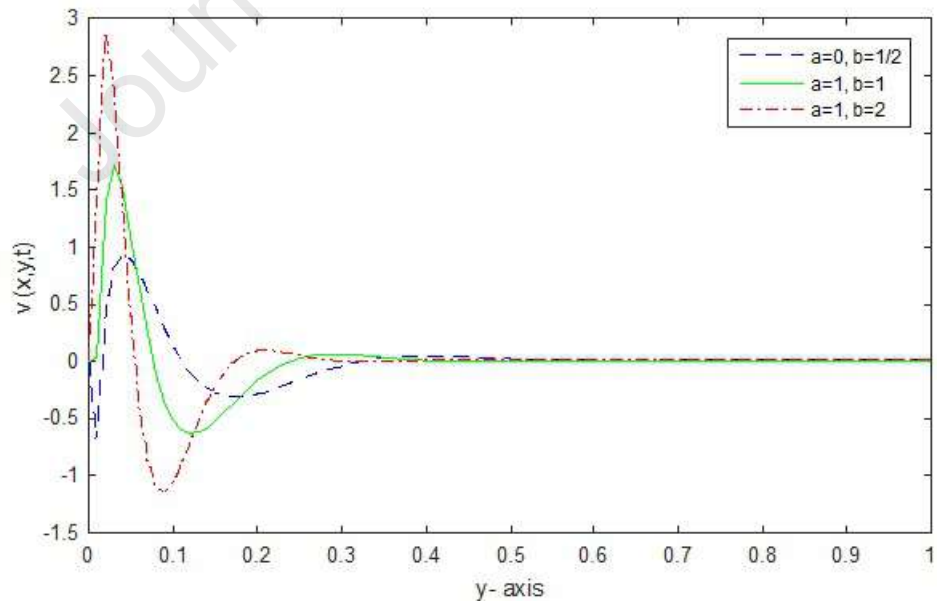
Fig. 5 Displacement v along the y-axis for different values of a and b in context of MDD, considering $\omega = 0.05$.

25
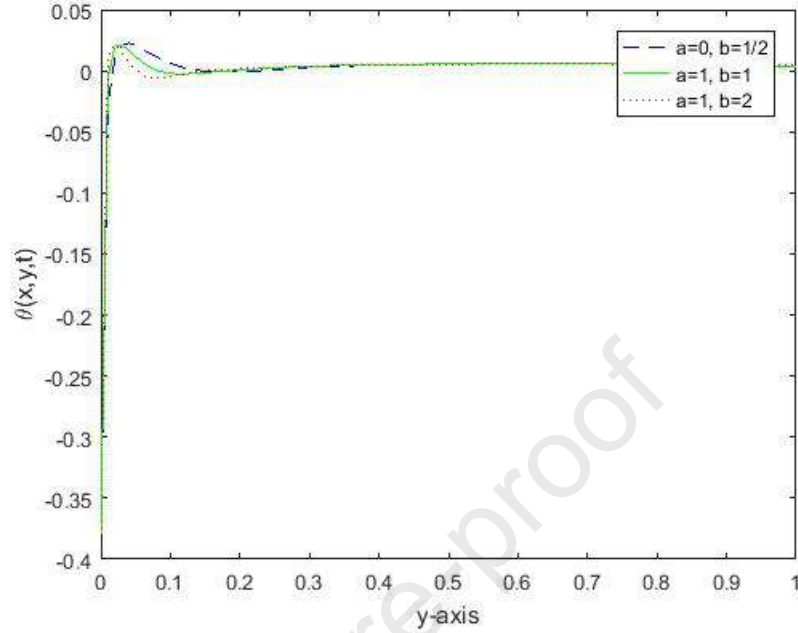
Fig. 6 Temperature θ along the y-axis for different values of a and b in context of MDD, considering $\omega = 0.05$.

Conclusions and possible future perspectives

The following remarkable points and possible future perspectives are obtained from theoretical analysis and numerical simulation of the present article:

- The thermodynamic consistency of the temperature-rate dependent thermoelasticity (TRDTE) theory with memory is established.

- In order to prove the finite propagation speed of the thermal signals of the present model, a domain of influence theorem is established.

- In the limiting case of the present model $\nu = \tau \to 0$, consequently the definition of c implies that $c \to \infty$ i.e. thermal signals propagate with infinite speed. This result is well expected since the present model reduces to the classical thermoelasticity theory.

- The analysis is considered for homogeneous and isotropic materials. Based on appropriate hypotheses upon the material coefficients, the results can also be extended to the class of anisotropic and inhomogeneous materials.

26

- Thermoelasticity theories with second sound in the presence of memory-dependent derivative (MDD) have seen a wide range of applications in both theoretical and applied viewpoints in recent years. However, a better understanding of the mechanism of memory effect on multiphysical responses of advanced materials is yet required, specifically in the industrial applications. According to the necessity of the physical problem, appropriate choices of the kernel function and the time-delay of MDD show their advantages in dealing with damping in various oscillatory systems as well as transient, time-dependent thermal wave effect due to various types of heating [37–40]. Memory-dependent heat conduction theories are ideal to capture the history of heat conduction and its impact on the thermo-mechanical responses of advanced materials and provides a more accurate prediction of the integrity of structures under high-strain rate mechanical deformation as well as thermal shocks.

References

[1] M. A. Biot, Thermoelasticity and irreversible thermodynamics, J. Appl. Phys. 27 (3) (1956) 240–253.

[2] D. S. Chandrasekharaiah, Thermoelasticity with second sound: A review, Applied Mechanics Reviews 39 (1986) 355–376.

[3] D. S. Chandrasekharaiah, Hyperbolic thermoelasticity: A review of recent literature, Applied Mechanics Reviews 51 (1998) 705–729.

[4] H. W. Lord, Y. Shulman, A generalized dynamical theory of thermoelasticity, Journal of the Mechanics and Physics of Solids 15 (5) (1967) 299–309.

[5] A. E. Green, K. A. Lindsay, Thermoelasticity, Journal of Elasticity 2 (1) (1972) 1–7.

[6] A. E. Green, P. Naghdi, A re-examination of the basic postulates of thermomechanics, Proceedings of the Royal Society of London. Series A: Mathematical and Physical Sciences 432 (1991) 171–194.

[7] A. E. Green, P. M. Naghdi, On undamped heat waves in an elastic solid, Journal of Thermal Stresses 15 (2) (1992) 253–264.

[8] A. E. Green, P. M. Naghdi, Thermoelasticity without energy dissipation, Journal of Elasticity 31 (3) (1993) 189–208.

[9] D. Y. Tzou, A unified field approach for heat conduction from macro- to micro-scales, Journal of Heat Transfer 117 (1) (1995) 8–16.

[10] S. K. R. Choudhuri, On a thermoelastic three-phase-lag model, Journal of Thermal Stresses 30 (3) (2007) 231–238.

[11] J.-L. Wang, H.-F. Li, Surpassing the fractional derivative: Concept of the memory-dependent derivative, Computers and Mathematics with Applications 62 (3) (2011) 1562–1567.

[12] Y.-J. Yu, W. Hu, X. Tian, A novel generalized thermoelasticity model based on memory-dependent derivative, International Journal of Engineering Science 81 (2014) 123–134.

[13] S. Shaw, B. Mukhopadhyay, A discontinuity analysis of generalized thermoelasticity theory with memory-dependent derivatives, Acta Mechanica 228 (7) (2017) 2675–2689.

[14] S. Shaw, Theory of generalized thermoelasticity with memory-dependent derivatives, Journal of Engineering Mechanics 145 (3) (2019) 04019003.

[15] B. Singh, S. P. (Sarkar), K. Barman, Thermoelastic interaction in the semi-infinite solid medium due to three-phase-lag effect involving memory-dependent derivative, Journal of Thermal Stresses 42 (7) (2019) 874–889.

[16] I. Sarkar, B. Mukhopadhyay, Thermo-viscoelastic interaction under dual-phase-lag model with memory-dependent derivative, Waves in Random and Complex Media`doi: 10.1080/17455030.2020.1736733`.

[17] A. S. El-Karamany, M. A. Ezzat, Modified fourier's law with time-delay and kernel function: Application in thermoelasticity, Journal of Thermal Stresses 38 (7) (2015) 811–834.

[18] M. A. Ezzat, A. S. El-Karamany, A. A. El-Bary, On dual-phase-lag thermoelasticity theory with memory-dependent derivative, Mechanics of Advanced Materials and Structures 24 (11) (2017) 908–916.

[19] M. A. Ezzat, A. El-Karamany, A. El-Bary, Modeling of memory-dependent derivative in generalized thermoelasticity, The European Physical Journal Plus 131 (10) (2016) 372.

[20] A. El-Karamany, M. A. Ezzat, Thermoelastic diffusion with memory-dependent derivative, Journal of Thermal Stresses 39 (9) (2016) 1035–1050.

[21] Y. Li, T. He, A generalized thermoelastic diffusion problem with memory-dependent derivative, Mathematics and Mechanics of Solids 24 (5) (2019) 1438–1462.

[22] S. Banerjee, S. Shaw, B. Mukhopadhyay, Memory response on thermal wave propagation emanating from a cavity in an unbounded elastic solid, Journal of Thermal Stresses 42 (2) (2019) 294–311.

[23] S. Banerjee, S. Shaw, B. Mukhopadhyay, Memory response on thermoelastic deformation in a solid half-space with a cylindrical hole, Mechanics Based Design of Structures and Machines (2019) 1–23.

[24] I. Sarkar, B. Mukhopadhyay, On energy, uniqueness theorems and variational principle for generalized thermoelasticity with memory-dependent derivative, International Journal of Heat and Mass Transfer 149 (2020) 119112.

[25] J. W. Nunziato, S. C. Cowin, A nonlinear theory of elastic materials with voids, Archive for Rational Mechanics and Analysis 72 (2) (1979) 175–201.

[26] B. Carbonaro, R. Russo, Energy inequalities and the domain of influence theorem in classical elastodynamics, Journal of Elasticity 14 (2) (1984) 163–174.

[27] J. Ignaczak, B. Carbonaro, R. Russo, Domain of influence theorem in thermoelastic1ty with one relaxation time, Journal of Thermal Stresses 9 (1) (1986) 79–91.

[28] I. Sarkar, B. Mukhopadhyay, A domain of influence theorem for generalized thermoelasticity with memory-dependent derivative, Journal of Thermal Stresses 42 (11) (2019) 1447–1457.

[29] S. Mukhopadhyay, S. Kothari, R. Kumar, A domain of influence theorem for thermoelasticity with dual phase-lags, Journal of Thermal Stresses 34 (9) (2011) 923–933.

[30] R. S. Dhaliwal, J. Wang, Domain of influence theorem in the theory of elastic materials with voids, International Journal of Engineering Science 32 (11) (1994) 1823–1828.

[31] M. Marin, A domain of influence theorem for microstretch elastic materials, Nonlinear Analysis: Real World Applications 11 (5) (2010) 3446 – 3452.

[32] M. Ezzat, A. El-Karamany, A. El-Bary, Generalized thermo-viscoelasticity with memory-dependent derivatives, International Journal of Mechanical Sciences 89 (2014) 470–475.

[33] D. S. Chandrasekharaiah, L. Debnath, Continuum Mechanics, Elsevier Inc., 1994.

[34] A. E. Green, N. Laws, On the entropy production inequality, Arch. Ration. Mech. Anal. 45 (1) (1972) 17–53.

[35] D. T. Haimo, Generalized temperature functions, Duke Math. J. 33 (2) (1966) 305–322. doi:10.1215/S0012-7094-66-03335-7.
URL https://doi.org/10.1215/S0012-7094-66-03335-7

[36] H. G., H. U., A method for the numerical inversion of laplace transforms, Journal of Computational and Applied Mathematics 10 (1984) 113–132.

[37] S. Shaw, A thermodynamic analysis of an enhanced theory of heat conduction model: Extended influence of finite strain and heat flux, International Journal of Engineering Science 152 (2020) 103277. doi:https://doi.org/10.1016/j.ijengsci.2020.103277.
URL http://www.sciencedirect.com/science/article/pii/S0020722520300653

[38] S. Kant, S. Mukhopadhyay, An investigation on responses of thermoelastic interactions in a generalized thermoelasticity with memory-dependent derivatives inside a thick plate, Mathematics and Mechanics of Solids 24 (8) (2019) 2392–2409.

[39] S. Mondal, P. Pal, M. Kanoria, Transient response in a thermoelastic half-space solid due to a laser pulse under three theories with memory-dependent derivative, Acta Mech. 230 (2019) 179–199.

[40] A. Al-Jamel, M. F. Al-Jamal, A. El-Karamany, A memory-dependent derivative model for damping in oscillatory systems, Journal of Vibration and Control 24 (11) (2018) 2221–2229. doi:10.1177/1077546316681907.

Highlights

- Based on the temperature rate-dependent thermoelasticity theory the stability of the thermal signals in solids is analyzed with memory
- A domain of influence theorem of the model is proved
- A two dimensional problem is considered for the overall visualization of the domain of influence theorem

To

The Editor-in-Chief,

Mechanics of Materials.

Dear Sir,

We are herewith submitting one of my recent articles entitled "A unifying energy approach for stability analysis of thermal signals in solids with memory" towards your journal for the consideration of its publication.

We declare that there is no conflict of interest with any individual/ group/ organization in any extent.

Thanks & regards

Dr. Soumen Shaw (corresponding author)

Mr. Indranil Sarkar

Mr. Santanu Banerjee

IIEST, Shibpur, INDIA.

Source details

Feedback >   Compare sources >

Mechanics of Materials

Scopus coverage years: from 1982 to Present

Publisher: Elsevier

ISSN: 0167-6636

Subject area: (Physics and Astronomy: Instrumentation)   (Engineering: Mechanics of Materials)   (Materials Science: General Materials Science)

Source type: Journal

View all documents >   Set document alert   💾 Save to source list

CiteScore 2022   ⓘ
6.7

SJR 2022   ⓘ
0.884

SNIP 2022   ⓘ
1.271

CiteScore   CiteScore rank & trend   Scopus content coverage

THE EUROPEAN
PHYSICAL JOURNAL PLUS

Non-Gaussian laser pulse response on photo-thermoelastic interactions in a silicon plate under the light of memory-dependent thermoelasticity theory

Santanu Banerjee[a], Soumen Shaw, Basudeb Mukhopadhyay

Department of Mathematics, Indian Institute of Engineering Science and Technology, Shibpur, West Bengal, India

Abstract In the present article, the wave propagation in a homogeneous semi-infinite silicon plate through photo-thermal process has been comparatively studied under the light of memory-dependent thermoelasticity theories with thermal relaxations. Without neglecting the coupling between the plasma and thermoelastic waves that photo-generated through intensity modulated beam of non-Gaussian laser pulse, a two-dimensional semiconducting medium having homogeneity in thermal and elastic properties is considered. The analytical solutions were observed in the domain of Laplace–Fourier transform by the method of eigenvalues approach. Finally, suitable graphical discussions and conclusions are presented with respect to varied thermal relaxation times.

1 Introduction

Analysing the after effects of an incident laser beam upon an elastic body is carried out by the photo-thermal modelling of the experiment. This leads to the excitation of short elastic pulses in the body, which is of noted interest for engineers due to its application in several fields involving a semiconducting material. Of late, the investigation of the photo-thermoelastic effects of a laser strike upon a semiconducting material with a band gap energy E_g becomes of interest to scientists and mathematicians when the laser beam's photo-energy E is higher than E_g. This incident is followed by an electron excitement where an electron travels the valence band to an energy level of $E - E_g$, which is above the conduction band edge. Pairs of electron–hole plasma are formed, which is followed by a recombination process. The diffusion behaviour controls the plasma density which is similar to the heat flow process of the thermal source. Hence, a modulated plasma density along with the thermal wave arises, when a laser beam is incident upon the material's surface. This wave obviously produces a local strain and stress upon the material.

The conventional theory of thermoelasticity based upon the Fourier's law of heat conduction has several flaws. The parabolic nature of that theory predicted infinite propagation speeds for thermal waves, which were absurd. In the year 1967, Lord and Shulmann [1] introduced a generalized theory of thermoelasticity by replacing the parabolic model with a

---

[a] e-mail: santanubandopadhyay@gmail.com (corresponding author)

Springer

hyperbolic model. The Fourier's classical law of heat conduction was replaced by a new law which contained one thermal relaxation time parameter connected to the heat flux vector. This new law contains the heat flux vector as well as its time derivative. In 1972, Green and Lindsay [2] proposed their generalization to the theory of thermoelasticity. They not only modified the heat conduction equation, but also the equation of motion by introducing two relaxation time parameters. In their theory, the Duhamel–Neumann relationships and the entropy relation were modified by introducing two relaxation times that relate the stress and entropy to the temperature rate.

During the last decade, the modelling of thermoelastic problems viewed the requirement of using new derivative tools. Mathematicians argued the reason behind the requirement of a new form of derivative by reasoning that the next state of physical system not only depends upon the present state, but also upon all of its historical states. Thus, the presence of a memory factor is required to describe and analyse a physical problem involving elastic bodies. Wang and Li [3] introduced the concept of memory-dependent derivatives (MDD) in the beginning of the past decade. The MDDs are local, as well as they exhibit a memory recalling nature too. Thus, the incorporation of MDDs served useful to many thermoelastic problems. In some recent works, several authors investigated the effect of MDD upon thermoelastic and their allied systems [4–12].

In recent times, the effect of laser pulsed heating upon thermoelastic bodies is being under constant study. In this regard, the work of Abbas and Marin [13] which showed that increasing the relaxation time reduces the magnitudes of the field variables when studied under the light of laser pulsed heat source. Also to mention that photo-thermal behaviour upon elastic bodies is becoming an interesting field of study for researchers. Due to the plasma wave's depth difference, the thermal and elastic waves are produced that in turn produces periodic heat and mechanical scatterings. These effects of photo-thermoelastic deformations upon a semiconducting medium with a coupled mathematical system containing thermoelastic and plasma equations have been recently studied and analysed by various researchers [14–17]. In the present paper, we studied coupled systems of plasma and thermoelastic models based upon the modifications of the Lord–Shulman type and Green–Lindsay type models with memory. Comparative investigations are carried out analysing the photo-thermoelastic interactions of a non-Gaussian laser pulse upon a silicon plate with respect to varied thermal relaxation times. The analytical solutions are expressed in the Laplace and Fourier transformed domains, adopting the eigenvalue approach. The numerical computations are carried out for a silicon-like semiconducting material by inverting the transformed equations, and the outcomes are represented graphically.

2 Mathematical model

The photo-thermoelastic theory is mainly based upon the coupled equations of elastic, plasma and thermal waves having variables of plasma carrier density n and temperature distribution θ along with the components of elastic displacement u_i and stress σ_{ij}. We shall consider the discussion restricted to a homogeneous, elastic and isotropic material.

The equation of motion as formulated by Nowacki [18] is

$$\sigma_{ij,j} = \rho \ddot{u}_i \tag{1}$$

The plasma-coupled modified Hooke–Duhamel–Neumann law is given by [14,15]

$$\sigma_{ij} = \mu \left(u_{i,j} + u_{j,i} \right) + \left(\lambda u_{k,k} - \gamma_n N - \gamma_t \theta \right) \delta_{ij} \tag{2}$$

and the memory-dependent plasma-coupled Hooke–Duhamel–Neumann law with a thermal relaxation time is

$$\sigma_{ij} = \mu \left(u_{i,j} + u_{j,i} \right) + \left(\lambda u_{k,k} - \gamma_n N - \gamma_t \left(1 + \nu D_\omega \right) \theta \right) \delta_{ij} \tag{3}$$

Using Eqs. (1) and (2), we obtain the modified displacement equation of motion without thermal relaxation time

$$(\lambda + \mu) u_{j,ij} + \mu u_{i,jj} - \gamma_n N_{,i} - \gamma_t \theta_{,i} = \rho \ddot{u}_i \tag{4}$$

and by using Eqs. (1) and (3), we obtain the memory-dependent displacement equation of motion with a thermal relaxation time

$$(\lambda + \mu) u_{j,ij} + \mu u_{i,jj} - \gamma_n N_{,i} - \gamma_t \left(1 + \nu D_\omega \right) \theta_{,i} = \rho \ddot{u}_i \tag{5}$$

The coupling between plasma and thermoelastic waves is provided by the equation

$$D_e N_{,jj} - \dot{N} - \frac{N}{\tau_0} + \delta \frac{\theta}{\tau_0} = 0 \tag{6}$$

Owing to the coupling between the plasma and the heat conduction equation [19,20], the memory-dependent Lord–Shulman type plasma-heat conduction equation can be written as:

$$K\theta_{,jj} + \frac{E_g}{\tau_0} N = (1 + \tau D_\omega) \left(\rho c_e \dot{\theta} + \gamma_t \theta_0 \dot{u}_{j,j} \right) \tag{7}$$

and the memory-dependent Green–Lindsay type plasma-heat conduction equation in coupled form is

$$K\theta_{,jj} + \frac{E_g}{\tau_0} N = \rho c_e \left(1 + \tau D_\omega \right) \dot{\theta} + \gamma_t \theta_0 \dot{u}_{j,j} \tag{8}$$

Relations (2), (4), (6) and (7) form the constitutive equations for a memory-dependent extended photo-thermoelasticity (EPTE) theory (with one thermal relaxation time parameter); and the relations (3), (5), (6) and (8) form the constitutive equations for a memory-dependent temperature-rate-dependent photo-thermoelasticity (TRDPTE) theory (with two thermal relaxation time parameters).

Here $N = n - n_0$ (n_0 is the equilibrium carrier density), θ_0 is the reference temperature, ρ is the medium density, λ and μ are Lame's constants, $\gamma_n = (3\lambda + 2\mu) d_n$ (d_n is the coefficient of electronic deformation), $\gamma_t = (3\lambda + 2\mu) \alpha_t$ (α_t is the coefficient of linear thermal expansion), τ and ν are the thermal relaxation times (for semiconductors $10^{-12}s \leq \tau, \nu \leq 10^{-10}s$), D_e is the coefficient of carrier diffusion, τ_0 is the photo-generated carrier lifetime, $\delta = \frac{\partial n_0}{\partial \theta}$ is the thermal activation coupling factor, E_g is the semiconductor energy gap, K is the thermal conductivity, c_e is the specific heat at constant strain, ω is the time delay (see "Appendix").

3 Application

Consider a two-dimensional silicon plate in the xy-plane such that $-\infty < x < \infty$ and $0 \leq y < \infty$. The entire x-axis is assumed to be the boundary of the plate under consideration. A non-Gaussian laser pulse (see "Appendix") is applied, which may be scaled to any point upon the boundary of the plate. The components of the photo-thermoelastic variables in the silicon medium are defined as $N(x, y, t), \theta(x, y, t), \mathbf{u}(u, v, 0), u(x, y, 0)$ and $v(x, y, 0)$ (Fig. 1).
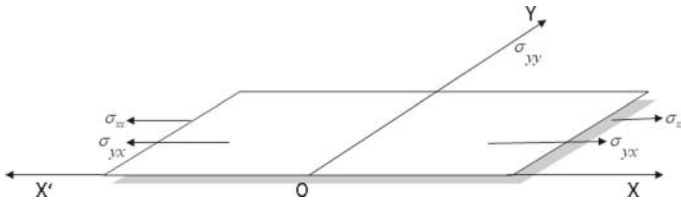
Fig. 1 A schematic illustration of the silicon plate

Initial conditions are considered as

$$u(x, y, 0) = v(x, y, 0) = N(x, y, 0) = \theta(x, y, 0) = 0 \tag{9}$$

$$\dot{u}(x, y, 0) = \dot{v}(x, y, 0) = \dot{N}(x, y, 0) = \dot{\theta}(x, y, 0) = 0 \tag{10}$$

$$\sigma_{xx}(x, y, 0) = \sigma_{yy}(x, y, 0) = \sigma_{yx}(x, y, 0) = 0 \tag{11}$$

Here we consider the line of applied laser pulse as the x-axis and the origin is taken at the middle point of the applicable region of the laser pulse. More specifically, the laser pulse is applied in the region $-L < x < L$ and there is no other stresses on the boundary. Hence, the boundary conditions are as follows:

$$\sigma_{yy}(x, 0, t) = \sigma_{yx}(x, 0, t) = 0 \tag{12}$$

$$\theta(x, 0, t) = \theta_0 H(L - |x|) L_P(t) \tag{13}$$

The flux of the carrier density at the boundary is considered as:

$$D_e \frac{\partial N}{\partial y}\bigg|_{(x,0,t)} = s_0 N \tag{14}$$

where $H(L - |x|)$ is the Heaviside function, $L_P(t)$ is the non-Gaussian laser pulse function (see "Appendix") and s_0 is the velocity of surface re-combinations.

4 Memory-dependent EPTE model

From Eqs. (2), (4), (6) and (7), the constitutive equations in two-dimensional form are expressed as:

$$(\lambda + 2\mu) \frac{\partial^2 u}{\partial x^2} + (\lambda + \mu) \frac{\partial^2 v}{\partial x \partial y} + \mu \frac{\partial^2 u}{\partial y^2} - \gamma_n \frac{\partial N}{\partial x} - \gamma_t \frac{\partial \theta}{\partial x} = \rho \frac{\partial^2 u}{\partial t^2} \tag{15}$$

$$(\lambda + 2\mu) \frac{\partial^2 v}{\partial y^2} + (\lambda + \mu) \frac{\partial^2 u}{\partial x \partial y} + \mu \frac{\partial^2 v}{\partial x^2} - \gamma_n \frac{\partial N}{\partial y} - \gamma_t \frac{\partial \theta}{\partial y} = \rho \frac{\partial^2 v}{\partial t^2} \tag{16}$$

$$D_e \left(\frac{\partial^2 N}{\partial x^2} + \frac{\partial^2 N}{\partial y^2} \right) - \frac{N}{\tau_0} + \delta \frac{\theta}{\tau_0} = \frac{\partial N}{\partial t} \tag{17}$$

$$K \left(\frac{\partial^2 \theta}{\partial x^2} + \frac{\partial^2 \theta}{\partial y^2} \right) = -\frac{E_g}{\tau_0} N + (1 + \tau D_\omega) \left[\rho c_e \frac{\partial \theta}{\partial t} + \gamma_t \theta_0 \frac{\partial}{\partial t} \left(\frac{\partial u}{\partial x} + \frac{\partial v}{\partial y} \right) \right] \tag{18}$$

$$\sigma_{xx} = (\lambda + 2\mu) \frac{\partial u}{\partial x} + \lambda \frac{\partial v}{\partial y} - \gamma_n N - \gamma_t \theta \tag{19}$$

$$\sigma_{yy} = (\lambda + 2\mu) \frac{\partial v}{\partial y} + \lambda \frac{\partial u}{\partial x} - \gamma_n N - \gamma_t \theta \tag{20}$$

$$\sigma_{yx} = \sigma_{xy} = \mu \left(\frac{\partial u}{\partial y} + \frac{\partial v}{\partial x} \right) \tag{21}$$

For convenience, the following non-dimensional transformations are considered:

$$\left(x', y', u', v' \right) = c\eta \left(x, y, u, v \right), \quad \left(v', \tau', \tau'_0, t' \right) = c^2 \eta \left(v, \tau, \tau_0, t \right),$$
$$N' = \frac{N}{n_0}, \quad \theta' = \frac{\theta}{\theta_0}, \quad \sigma'_{ij} = \frac{\sigma_{ij}}{\mu} \tag{22}$$

where $c^2 = \frac{\lambda + 2\mu}{\rho}$, $\eta = \frac{\rho c_e}{K}$.

Applying the above non-dimensional transformations upon Eqs. (15)–(21), we obtain

$$\frac{\partial^2 u}{\partial x^2} + \alpha_1 \frac{\partial^2 v}{\partial x \partial y} + \alpha_2 \frac{\partial^2 u}{\partial y^2} - \beta_n \frac{\partial N}{\partial x} - \beta_t \frac{\partial \theta}{\partial x} = \frac{\partial^2 u}{\partial t^2} \tag{23}$$

$$\frac{\partial^2 v}{\partial y^2} + \alpha_1 \frac{\partial^2 u}{\partial x \partial y} + \alpha_2 \frac{\partial^2 v}{\partial x^2} - \beta_n \frac{\partial N}{\partial y} - \beta_t \frac{\partial \theta}{\partial y} = \frac{\partial^2 v}{\partial t^2} \tag{24}$$

$$\frac{\partial^2 N}{\partial x^2} + \frac{\partial^2 N}{\partial y^2} = \alpha \left(\frac{\partial N}{\partial t} + \frac{N}{\tau_0} \right) - \beta \frac{\theta}{\tau_0} \tag{25}$$

$$\frac{\partial^2 \theta}{\partial x^2} + \frac{\partial^2 \theta}{\partial y^2} = -\varepsilon_2 \frac{N}{\tau_0} + (1 + \tau D_\omega) \left[\frac{\partial \theta}{\partial t} + \varepsilon_1 \frac{\partial}{\partial t} \left(\frac{\partial u}{\partial x} + \frac{\partial v}{\partial y} \right) \right] \tag{26}$$

$$\sigma_{xx} = \frac{\partial u}{\partial x} + \alpha_3 \frac{\partial v}{\partial y} - \beta_n N - \beta_t \theta \tag{27}$$

$$\sigma_{yy} = \frac{\partial v}{\partial y} + \alpha_3 \frac{\partial u}{\partial x} - \beta_n N - \beta_t \theta \tag{28}$$

$$\sigma_{yx} = \sigma_{xy} = \alpha_2 \left(\frac{\partial u}{\partial y} + \frac{\partial v}{\partial x} \right) \tag{29}$$

where $\alpha_1 = \frac{\lambda + \mu}{\lambda + 2\mu}$, $\alpha_2 = \frac{\mu}{\lambda + 2\mu}$, $\alpha_3 = \frac{\lambda}{\lambda + 2\mu}$, $\beta_n = \frac{n_0 \gamma_n}{\lambda + 2\mu}$, $\beta_t = \frac{\theta_0 \gamma_t}{\lambda + 2\mu}$, $\beta = \frac{\delta \theta_0}{n_0 \eta D_e}$, $\alpha = \frac{1}{\eta D_e}$, $\varepsilon_1 = \frac{\gamma_t}{\rho c_e}$ and $\varepsilon_2 = \frac{E_g n_0}{\eta K \theta_0}$ are the plasma-thermoelastic coupling factors.

4.1 Equations in Laplace–Fourier transform domain

Applying Laplace transform defined by the relation

$$\overline{f}(x, y, s) = L\left[f(x, y, t) \right] = \int_0^\infty \exp\left(-st\right) f(x, y, s) \mathrm{d}t$$

followed by Fourier transform defined by

$$\overline{f}^*(p, y, s) = F\left[\overline{f}(x, y, s) \right] = \frac{1}{\sqrt{2\pi}} \int_{-\infty}^\infty \exp\left(-ipx\right) \overline{f}(x, y, s) \mathrm{d}x$$

on Eqs. (23) and (29), we get

$$\frac{\mathrm{d}^2 \overline{u}^*}{\mathrm{d}y^2} = \frac{s^2 + p^2}{\alpha_2} \overline{u}^* + \frac{ip\beta_n}{\alpha_2} \overline{N}^* + \frac{ip\beta_t}{\alpha_2} \overline{\theta}^* - \frac{ip\alpha_1}{\alpha_2} \frac{\mathrm{d}\overline{v}^*}{\mathrm{d}y} \tag{30}$$

$$\frac{\mathrm{d}^2 \overline{v}^*}{\mathrm{d}y^2} = \left(s^2 + p^2 \alpha_2 \right) \overline{v}^* - ip\alpha_1 \frac{\mathrm{d}\overline{u}^*}{\mathrm{d}y} + \beta_n \frac{\mathrm{d}\overline{N}^*}{\mathrm{d}y} + \beta_t \frac{\mathrm{d}\overline{\theta}^*}{\mathrm{d}y} \tag{31}$$

$$\frac{\mathrm{d}^2 \overline{N}^*}{\mathrm{d}y^2} = \left(\alpha s + \frac{\alpha}{\tau_0} + p^2 \right) \overline{N}^* - \frac{\beta}{\tau_0} \overline{\theta}^* \tag{32}$$

$$\frac{d^2\overline{\theta}^*}{dy^2} = ips_2s\varepsilon_1\overline{u}^* - \frac{\varepsilon_2}{\tau_0}\overline{N}^* + \left(s_2s + p^2\right)\overline{\theta}^* + s_2s\varepsilon_1\frac{d\overline{v}^*}{dy} \tag{33}$$

$$\overline{\sigma}_{xx}^* = ip\overline{u}^* + \alpha_3\frac{d\overline{v}^*}{dy} - \beta_n\overline{N}^* - \beta_t\overline{\theta}^* \tag{34}$$

$$\overline{\sigma}_{yy}^* = ip\alpha_3\overline{u}^* + \frac{d\overline{v}^*}{dy} - \beta_n\overline{N}^* - \beta_t\overline{\theta}^* \tag{35}$$

$$\overline{\sigma}_{yx}^* = \overline{\sigma}_{xy}^* = \alpha_2\left(\frac{d\overline{u}^*}{dy} + ip\overline{v}^*\right) \tag{36}$$

where

$$s_2 = 1 + \tau\xi$$

and

$$\xi = \frac{1}{\omega}\left(\left(1 - \frac{2b}{\omega s} + \frac{2a^2}{\omega^2 s^2}\right) - \exp\left(-\omega s\right)\left(1 - 2b^2 + a^2 + \frac{2\left(a^2 - b\right)}{\omega s} + \frac{2a^2}{\omega^2 s^2}\right)\right)$$

Equations (30), (31), (32) and (33) can be written in vector-matrix form as follows:

$$\frac{d\widetilde{U}(p, y, s)}{dy} = \widetilde{A}(p, s)\widetilde{U}(p, y, s) \tag{37}$$

where

$$\overline{U} = \left[\overline{v}^* \ \overline{u}^* \ \overline{N}^* \ \overline{\theta}^* \ \frac{d\overline{v}^*}{dy} \ \frac{d\overline{u}^*}{dy} \ \frac{d\overline{N}^*}{dy} \ \frac{d\overline{\theta}^*}{dy}\right]^T$$

and

$$\widetilde{A} = \begin{bmatrix} O & I \\ P & Q \end{bmatrix}$$

in which

$$O = \begin{bmatrix} 0 & 0 & 0 & 0 \\ 0 & 0 & 0 & 0 \\ 0 & 0 & 0 & 0 \\ 0 & 0 & 0 & 0 \end{bmatrix}, I = \begin{bmatrix} 1 & 0 & 0 & 0 \\ 0 & 1 & 0 & 0 \\ 0 & 0 & 1 & 0 \\ 0 & 0 & 0 & 1 \end{bmatrix}$$

,

$$P = \begin{bmatrix} a_{51} & 0 & 0 & 0 \\ 0 & a_{62} & a_{63} & a_{64} \\ 0 & 0 & a_{73} & a_{74} \\ 0 & a_{82} & a_{83} & a_{84} \end{bmatrix}, Q = \begin{bmatrix} 0 & a_{56} & a_{57} & a_{58} \\ a_{65} & 0 & 0 & 0 \\ 0 & 0 & 0 & 0 \\ a_{85} & 0 & 0 & 0 \end{bmatrix}$$

Here

$$a_{51} = s^2 + p^2\alpha_2, a_{56} = -\alpha_1 ip, a_{57} = \beta_n, a_{58} = \beta_t, a_{62} = \frac{s^2 + p^2}{\alpha_2}, a_{63} = \frac{ip\beta_n}{\alpha_2},$$

$$a_{64} = \frac{ip\beta_t}{\alpha_2}, a_{65} = -\frac{ip\alpha_1}{\alpha_2}, a_{73} = \alpha\left(s + \frac{1}{\tau_0}\right) + p^2, a_{74} = -\frac{\beta}{\tau_0}, a_{82} = ips_2s\varepsilon_1, \tag{38}$$

$$a_{83} = -\frac{\varepsilon_2}{\tau_0}, a_{84} = s_2s + p^2, a_{85} = \varepsilon_1 s_2 s$$

5 Memory-dependent TRDPTE model

From Eqs. (3), (5), (6) and (8), the constitutive equations for the theory with two thermal relaxation times are expressed as:

$$(\lambda + 2\mu)\frac{\partial^2 u}{\partial x^2} + (\lambda + \mu)\frac{\partial^2 v}{\partial x \partial y} + \mu\frac{\partial^2 u}{\partial y^2} - \gamma_n\frac{\partial N}{\partial x} - \gamma_t(1 + vD_\omega)\frac{\partial \theta}{\partial x} = \rho\frac{\partial^2 u}{\partial t^2} \quad (39)$$

$$(\lambda + 2\mu)\frac{\partial^2 v}{\partial y^2} + (\lambda + \mu)\frac{\partial^2 u}{\partial x \partial y} + \mu\frac{\partial^2 v}{\partial x^2} - \gamma_n\frac{\partial N}{\partial y} - \gamma_t(1 + vD_\omega)\frac{\partial \theta}{\partial y} = \rho\frac{\partial^2 v}{\partial t^2} \quad (40)$$

$$D_e\left(\frac{\partial^2 N}{\partial x^2} + \frac{\partial^2 N}{\partial y^2}\right) - \frac{N}{\tau_0} + \delta\frac{\theta}{\tau_0} = \frac{\partial N}{\partial t} \quad (41)$$

$$K\left(\frac{\partial^2 \theta}{\partial x^2} + \frac{\partial^2 \theta}{\partial y^2}\right) = -\frac{E_g}{\tau_0}N + \rho c_e(1 + \tau D_\omega)\frac{\partial \theta}{\partial t} + \gamma_t\theta_0\frac{\partial}{\partial t}\left(\frac{\partial u}{\partial x} + \frac{\partial v}{\partial y}\right) \quad (42)$$

$$\sigma_{xx} = (\lambda + 2\mu)\frac{\partial u}{\partial x} + \lambda\frac{\partial v}{\partial y} - \gamma_n N - \gamma_t(1 + vD\omega)\theta \quad (43)$$

$$\sigma_{yy} = (\lambda + 2\mu)\frac{\partial v}{\partial y} + \lambda\frac{\partial u}{\partial x} - \gamma_n N - \gamma_t(1 + vD\omega)\theta \quad (44)$$

$$\sigma_{yx} = \sigma_{xy} = \mu\left(\frac{\partial u}{\partial y} + \frac{\partial v}{\partial x}\right) \quad (45)$$

Applying the non-dimensional transformations (22) upon Eq. (39)-Eq. (45), we obtain

$$\frac{\partial^2 u}{\partial x^2} + \alpha_1\frac{\partial^2 v}{\partial x \partial y} + \alpha_2\frac{\partial^2 u}{\partial y^2} - \beta_n\frac{\partial N}{\partial x} - \beta_t(1 + vD_\omega)\frac{\partial \theta}{\partial x} = \frac{\partial^2 u}{\partial t^2} \quad (46)$$

$$\frac{\partial^2 v}{\partial y^2} + \alpha_1\frac{\partial^2 u}{\partial x \partial y} + \alpha_2\frac{\partial^2 v}{\partial x^2} - \beta_n\frac{\partial N}{\partial y} - \beta_t(1 + vD_\omega)\frac{\partial \theta}{\partial y} = \frac{\partial^2 v}{\partial t^2} \quad (47)$$

$$\frac{\partial^2 N}{\partial x^2} + \frac{\partial^2 N}{\partial y^2} = \alpha\left(\frac{\partial N}{\partial t} + \frac{N}{\tau_0}\right) - \beta\frac{\theta}{\tau_0} \quad (48)$$

$$\frac{\partial^2 \theta}{\partial x^2} + \frac{\partial^2 \theta}{\partial y^2} = -\varepsilon_2\frac{N}{\tau_0} + (1 + \tau D_\omega)\frac{\partial \theta}{\partial t} + \varepsilon_1\frac{\partial}{\partial t}\left(\frac{\partial u}{\partial x} + \frac{\partial v}{\partial y}\right) \quad (49)$$

$$\sigma_{xx} = \frac{\partial u}{\partial x} + \alpha_3\frac{\partial v}{\partial y} - \beta_n N - \beta_t(1 + vD_\omega)\theta \quad (50)$$

$$\sigma_{yy} = \frac{\partial v}{\partial y} + \alpha_3\frac{\partial u}{\partial x} - \beta_n N - \beta_t(1 + vD_\omega)\theta \quad (51)$$

$$\sigma_{yx} = \sigma_{xy} = \alpha_2\left(\frac{\partial u}{\partial y} + \frac{\partial v}{\partial x}\right) \quad (52)$$

where $\alpha_1 = \frac{\lambda + \mu}{\lambda + 2\mu}$, $\alpha_2 = \frac{\mu}{\lambda + 2\mu}$, $\alpha_3 = \frac{\lambda}{\lambda + 2\mu}$, $\beta_n = \frac{n_0\gamma_n}{\lambda + 2\mu}$, $\beta_t = \frac{\theta_0\gamma_t}{\lambda + 2\mu}$, $\beta = \frac{\delta\theta_0}{n_0\eta D_e}$, $\alpha = \frac{1}{\eta D_e}$, $\varepsilon_1 = \frac{\gamma_t}{\rho c_e}$ and $\varepsilon_2 = \frac{E_g n_0}{\eta K \theta_0}$ are the plasma-thermoelastic coupling factors.

5.1 Equations in integral transform domain

Applying Laplace transform followed by Fourier transform up on Eqs. (46) and (52), we obtain

$$\frac{d^2 \overline{u}^*}{dy^2} = \frac{s^2 + p^2}{\alpha_2}\overline{u}^* + \frac{ip\beta_n}{\alpha_2}\overline{N}^* + \frac{ip\beta_t s_1}{\alpha_2}\overline{\theta}^* - \frac{ip\alpha_1}{\alpha_2}\frac{d\overline{v}^*}{dy} \quad (53)$$

$$\frac{\mathrm{d}^2\overline{v}^*}{\mathrm{d}y^2} = \left(s^2 + p^2\alpha_2\right)\overline{v}^* - ip\alpha_1\frac{\mathrm{d}\overline{u}^*}{\mathrm{d}y} + \beta_n\frac{\mathrm{d}\overline{N}^*}{\mathrm{d}y} + \beta_t s_1\frac{\mathrm{d}\overline{\theta}^*}{\mathrm{d}y} \tag{54}$$

$$\frac{\mathrm{d}^2\overline{N}^*}{\mathrm{d}y^2} = \left(\alpha s + \frac{\alpha}{\tau_0} + p^2\right)\overline{N}^* - \frac{\beta}{\tau_0}\overline{\theta}^* \tag{55}$$

$$\frac{\mathrm{d}^2\overline{\theta}^*}{\mathrm{d}y^2} = ips\varepsilon_1\overline{u}^* + \left(s_2 s + p^2\right)\overline{\theta}^* - \frac{\varepsilon_2}{\tau_0}\overline{N}^* + s\varepsilon_1\frac{\mathrm{d}\overline{v}^*}{\mathrm{d}y} \tag{56}$$

$$\overline{\sigma}^*_{xx} = ip\overline{u}^* + \alpha_3\frac{\mathrm{d}\overline{v}^*}{\mathrm{d}y} - \beta_n\overline{N}^* - \beta_t s_1\overline{\theta}^* \tag{57}$$

$$\overline{\sigma}^*_{yy} = ip\alpha_3\overline{u}^* + \frac{\mathrm{d}\overline{v}^*}{\mathrm{d}y} - \beta_n\overline{N}^* - \beta_t s_1\overline{\theta}^* \tag{58}$$

$$\overline{\sigma}^*_{yx} = \overline{\sigma}^*_{xy} = \alpha_2\left(\frac{\mathrm{d}\overline{u}^*}{\mathrm{d}y} + ip\overline{v}^*\right) \tag{59}$$

where

$$s_1 = 1 + \nu\xi$$
$$s_2 = 1 + \tau\xi$$

and

$$\xi = \frac{1}{\omega}\left(\left(1 - \frac{2b}{\omega s} + \frac{2a^2}{\omega^2 s^2}\right) - \exp\left(-\omega s\right)\left(1 - 2b^2 + a^2 + \frac{2\left(a^2 - b\right)}{\omega s} + \frac{2a^2}{\omega^2 s^2}\right)\right)$$

Equation (53), Eq. (54), Eq. (55) and Eq. (56) can also be represented in a vector-matrix differential equation form as shown in Eq. (37).

Here the expressions for the elements in matrices P and Q are given by

$$a_{51} = s^2 + p^2\alpha_2, a_{56} = -\alpha_1 ip, a_{57} = \beta_n, a_{58} = \beta_t s_1, a_{62} = \frac{s^2 + p^2}{\alpha_2}, a_{63} = \frac{ip\beta_n}{\alpha_2},$$

$$a_{64} = \frac{ip\beta_t s_1}{\alpha_2}, a_{65} = -\frac{ip\alpha_1}{\alpha_2}, a_{73} = \alpha\left(s + \frac{1}{\tau_0}\right) + p^2, a_{74} = -\frac{\beta}{\tau_0}, a_{82} = ips\varepsilon_1 \tag{60}$$

$$a_{83} = -\frac{\varepsilon_2}{\tau_0}, a_{84} = s_2 s + p^2, a_{85} = \varepsilon_1 s$$

6 Solution of the vector matrix differential equations

The characteristic equation of the matrix $\widetilde{A}(p, s)$ can be written as:

$$m^8 - t_1 m^6 + t_2 m^4 + t_3 m^2 + t_4 = 0 \tag{61}$$

where

$t_1 = a_{51} + a_{84} + a_{58}a_{85} + a_{62} + a_{56}a_{65} + a_{73},$

$t_2 = a_{56}a_{65}a_{84} + a_{51}a_{62} - a_{58}a_{65}a_{82} - a_{64}a_{82} + a_{51}a_{73} + a_{62}a_{73} + a_{56}a_{65}a_{73} - a_{74}a_{83}$
$\qquad + a_{51}a_{84} + a_{62}a_{84} + a_{73}a_{84} + a_{58}a_{62}a_{85} + a_{58}a_{73}a_{85} - a_{57}a_{74}a_{85} - a_{56}a_{64}a_{85},$

$t_3 = a_{56}a_{65}a_{74}a_{83} + a_{58}a_{65}a_{73}a_{82} + a_{57}a_{62}a_{74}a_{85} + a_{64}a_{73}a_{82} - a_{51}a_{62}a_{73} + a_{51}a_{64}a_{82}$
$\qquad - a_{63}a_{74}a_{82} - a_{57}a_{65}a_{74}a_{82} + a_{51}a_{74}a_{83} + a_{62}a_{74}a_{83} - a_{51}a_{62}a_{84}$

$$- a_{51}a_{73}a_{84} - a_{62}a_{73}a_{84} - a_{56}a_{65}a_{73}a_{84} - a_{58}a_{62}a_{73}a_{85} + a_{56}a_{64}a_{73}a_{85}$$
$$- a_{56}a_{63}a_{74}a_{85},$$
$$t_4 = a_{51}a_{63}a_{74}a_{82} + a_{51}a_{62}a_{73}a_{84} - a_{51}a_{64}a_{73}a_{82} - a_{51}a_{62}a_{74}a_{83} \tag{62}$$

Assuming the eigenvalues of the matrix $\widetilde{A}(p, s)$ to be $\pm m_1, \pm m_2, \pm m_3$ and $\pm m_4$, we obtain

$$m_1 = \left[\frac{-\left(w_1 - \frac{t_1}{2}\right) + \sqrt{\left(w_1 - \frac{t_1}{2}\right)^2 - 4\left(l + w_2\right)}}{2} \right]^{\frac{1}{2}}$$

$$m_2 = \left[\frac{-\left(w_1 - \frac{t_1}{2}\right) - \sqrt{\left(w_1 - \frac{t_1}{2}\right)^2 - 4\left(l + w_2\right)}}{2} \right]^{\frac{1}{2}}$$

$$m_3 = \left[\frac{\left(w_1 + \frac{t_1}{2}\right) + \sqrt{\left(w_1 + \frac{t_1}{2}\right)^2 - 4\left(l - w_2\right)}}{2} \right]^{\frac{1}{2}} \tag{63}$$

$$m_4 = \left[\frac{\left(w_1 + \frac{t_1}{2}\right) - \sqrt{\left(w_1 + \frac{t_1}{2}\right)^2 - 4\left(l - w_2\right)}}{2} \right]^{\frac{1}{2}}$$

where

$$l = w_3 - \frac{w_4}{w_3} + \frac{t_2}{6}, \quad w_1 = \frac{1}{2}\sqrt{t_1^2 + 8l - 4t_2}, \quad w_2 = \sqrt{l^2 - t_4},$$

$$w_3 = \left[\frac{1}{2}\left(-w_5 + \sqrt{w_5^2 + 4w_4^3} \right) \right]^{\frac{1}{3}}, \quad w_4 = -\frac{1}{3}\left(\frac{t_1 t_3}{4} + t_4 + \frac{t_2^2}{12} \right), \tag{64}$$

$$w_5 = -\frac{1}{2}\left[\frac{t_2}{3}\left(\frac{t_1 t_3}{4} + t_4 \right) + \frac{t_2^3}{54} + \frac{t_3^2}{4} + \frac{t_1^2 t_4}{4} - t_2 t_4 \right]$$

The corresponding eigenvectors $\widetilde{X}_i$ ($i = 1(1)4$) are provided by

$$\widetilde{X}_1 = \widetilde{X}\big|_{m=m_1}, \quad \widetilde{X}_2 = \widetilde{X}\big|_{m=-m_1}, \quad \widetilde{X}_3 = \widetilde{X}\big|_{m=m_2}, \quad \widetilde{X}_4 = \widetilde{X}\big|_{m=-m_2},$$
$$\widetilde{X}_5 = \widetilde{X}\big|_{m=m_3}, \quad \widetilde{X}_6 = \widetilde{X}\big|_{m=-m_3} \quad \widetilde{X}_7 = \widetilde{X}\big|_{m=m_4}, \quad \widetilde{X}_8 = \widetilde{X}\big|_{m=-m_4} \tag{65}$$

where

$$\widetilde{X} = \begin{bmatrix} m^2 a_{58}(-(a_{58}(m^2 - a_{62}) + a_{56}a_{64})(m^2 - a_{73}) - (a_{57}(m^2 - a_{62}) + a_{56}a_{63})a_{74}) \\ -ma_{58}(((m^2 - a_{51})a_{64} + m^2 a_{58}a_{65})(m^2 - a_{73}) + ((m^2 - a_{51})a_{63} + m^2 a_{57}a_{65})a_{74}) \\ ma_{58}(-(m^2 - a_{51})(m^2 - a_{62}) + m^2 a_{56}a_{65})a_{74} \\ -ma_{58}((m^2 - a_{51})(m^2 - a_{62}) - m^2 a_{56}a_{65})(m^2 - a_{73}) \\ m(m^2 a_{58}(-(a_{58}(m^2 - a_{62}) + a_{56}a_{64})(m^2 - a_{73}) - (a_{57}(m^2 - a_{62}) + a_{56}a_{63})a_{74})) \\ m(-ma_{58}(((m^2 - a_{51})a_{64} + m^2 a_{58}a_{65})(m^2 - a_{73}) + ((m^2 - a_{51})a_{63} + m^2 a_{57}a_{65})a_{74})) \\ m(ma_{58}(-(m^2 - a_{51})(m^2 - a_{62}) + m^2 a_{56}a_{65})a_{74}) \\ m(-ma_{58}((m^2 - a_{51})(m^2 - a_{62}) - m^2 a_{56}a_{65})(m^2 - a_{73})) \end{bmatrix} \tag{66}$$

Assuming the regularity conditions at infinity (ie. $\overline{u}^*, \overline{v}^*, \overline{N}^*, \overline{\theta}^*, \dfrac{d\overline{u}^*}{dy}, \dfrac{d\overline{v}^*}{dy}, \dfrac{d\overline{N}^*}{dy}, \dfrac{d\overline{\theta}^*}{dy}$ $\longrightarrow 0$ as $y \to \infty$), the solution of Eq. (37) can be expressed as follows:

$$
\begin{aligned}
\widetilde{U}(p, y, s) &= C_1 \widetilde{X}_2 \exp(-m_1 y) + C_2 \widetilde{X}_4 \exp(-m_2 y) \\
&\quad + C_3 \widetilde{X}_6 \exp(-m_3 y) + C_4 \widetilde{X}_8 \exp(-m_4 y)
\end{aligned}
\tag{67}
$$

where $y > 0$. Hence, the field functions can be expressed as follows:

$$
\overline{u}^* = \sum_{i=1}^{4} C_i \Lambda_i^{(0)} \exp(-m_i y)
\tag{68}
$$

$$
\overline{v}^* = \sum_{i=1}^{4} C_i \Lambda_i^{(1)} \exp(-m_i y)
\tag{69}
$$

$$
\overline{\theta}^* = \sum_{i=1}^{4} C_i \Lambda_i^{(2)} \exp(-m_i y)
\tag{70}
$$

$$
\overline{N}^* = \sum_{i=1}^{4} C_i \Lambda_i^{(3)} \exp(-m_i y)
\tag{71}
$$

where

$$
\begin{aligned}
\Lambda_i^{(0)} &= -m_i a_{58}(((m_i^2 - a_{51})a_{64} + m_i^2 a_{58} a_{65})(m_i^2 - a_{73}) + ((m_i^2 - a_{51})a_{63} \\
&\quad + m_i^2 a_{57} a_{65})a_{74}) \\
\Lambda_i^{(1)} &= m_i^2 a_{58}(-(a_{58}(m_i^2 - a_{62}) + a_{56} a_{64})(m_i^2 - a_{73}) - (a_{57}(m_i^2 - a_{62}) + a_{56} a_{63})a_{74}) \\
\Lambda_i^{(2)} &= -m_i a_{58}((m_i^2 - a_{51})(m_i^2 - a_{62}) - m_i^2 a_{56} a_{65})(m_i^2 - a_{73}) \\
\Lambda_i^{(3)} &= m_i a_{58}(-(m_i^2 - a_{51})(m_i^2 - a_{62}) + m_i^2 a_{56} a_{65})a_{74}
\end{aligned}
\tag{72}
$$

Eventually from Eqs. (34), (35) and (36), we obtain

$$
\overline{\sigma}_{xx}^* = \sum_{i=1}^{4} C_i \left(ip\Lambda_i^{(0)} - m_i \alpha_3 \Lambda_i^{(1)} - \beta_t \Lambda_i^{(2)} - \beta_n \Lambda_i^{(3)} \right) \exp(-m_i y)
\tag{73}
$$

$$
\overline{\sigma}_{yy}^* = \sum_{i=1}^{4} C_i \left(ip\alpha_3 \Lambda_i^{(0)} - m_i \Lambda_i^{(1)} - \beta_t \Lambda_i^{(2)} - \beta_n \Lambda_i^{(3)} \right) \exp(-m_i y)
\tag{74}
$$

$$
\overline{\sigma}_{yx}^* = \overline{\sigma}_{xy}^* = \sum_{i=1}^{4} C_i \alpha_2 \left(-m_i \Lambda_i^{(0)} + ip\Lambda_i^{(1)} \right) \exp(-m_i y)
\tag{75}
$$

Applying the boundary conditions upon Eqs. (68)–(71), we obtain the expressions for C_i $(i = 1(1)4)$ are as follows:

$$
C_1 = \frac{\Delta_1}{\Delta} \quad , \quad C_2 = \frac{\Delta_2}{\Delta} \quad , \quad C_3 = \frac{\Delta_3}{\Delta} \quad , \quad C_4 = \frac{\Delta_4}{\Delta}
\tag{76}
$$
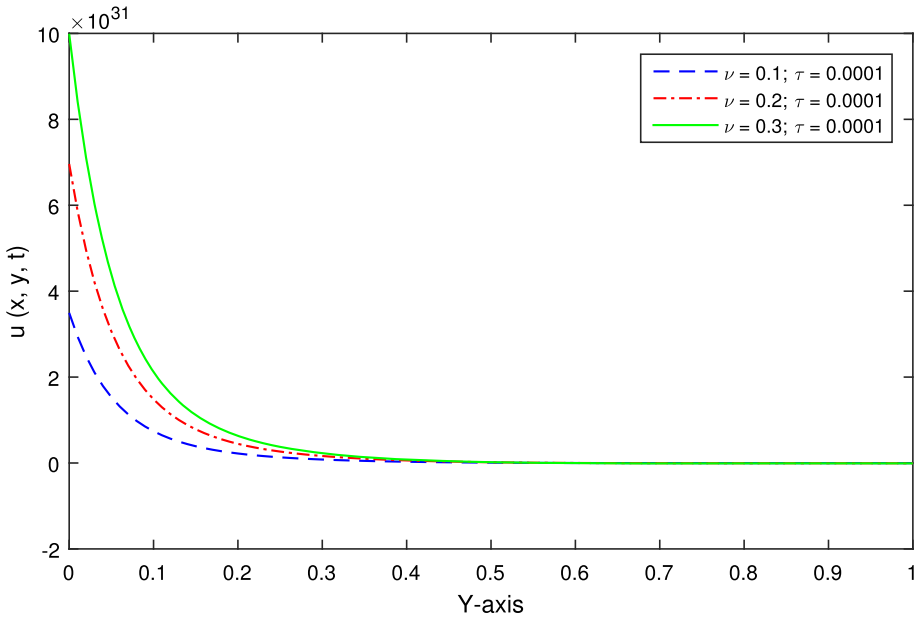
Fig. 2 The variations of horizontal displacement u versus y in TRDPTE model

where

$$\Delta_1 = \begin{vmatrix} 0 & \Lambda_2^{(0)} & \Lambda_3^{(0)} & \Lambda_4^{(0)} \\ 0 & \Lambda_2^{(1)} & \Lambda_3^{(1)} & \Lambda_4^{(1)} \\ \zeta & \Lambda_2^{(2)} & \Lambda_3^{(2)} & \Lambda_4^{(2)} \\ 1 & \Lambda_2^{(3)} & \Lambda_3^{(3)} & \Lambda_4^{(3)} \end{vmatrix}, \Delta_2 = \begin{vmatrix} \Lambda_1^{(0)} & 0 & \Lambda_3^{(0)} & \Lambda_4^{(0)} \\ \Lambda_1^{(1)} & 0 & \Lambda_3^{(1)} & \Lambda_4^{(1)} \\ \Lambda_1^{(2)} & \zeta & \Lambda_3^{(2)} & \Lambda_4^{(2)} \\ \Lambda_1^{(3)} & 1 & \Lambda_3^{(3)} & \Lambda_4^{(3)} \end{vmatrix},$$

$$\Delta_3 = \begin{vmatrix} \Lambda_1^{(0)} & \Lambda_2^{(0)} & 0 & \Lambda_4^{(0)} \\ \Lambda_1^{(1)} & \Lambda_2^{(1)} & 0 & \Lambda_4^{(1)} \\ \Lambda_1^{(2)} & \Lambda_2^{(2)} & \zeta & \Lambda_4^{(2)} \\ \Lambda_1^{(3)} & \Lambda_2^{(3)} & 1 & \Lambda_4^{(3)} \end{vmatrix}, \Delta_4 = \begin{vmatrix} \Lambda_1^{(0)} & \Lambda_2^{(0)} & \Lambda_3^{(0)} & 0 \\ \Lambda_1^{(1)} & \Lambda_2^{(1)} & \Lambda_3^{(1)} & 0 \\ \Lambda_1^{(2)} & \Lambda_2^{(2)} & \Lambda_3^{(2)} & \zeta \\ \Lambda_1^{(3)} & \Lambda_2^{(3)} & \Lambda_3^{(3)} & 1 \end{vmatrix}, \quad (77)$$

$$\Delta = \begin{vmatrix} \Lambda_1^{(0)} & \Lambda_2^{(0)} & \Lambda_3^{(0)} & \Lambda_4^{(0)} \\ \Lambda_1^{(1)} & \Lambda_2^{(1)} & \Lambda_3^{(1)} & \Lambda_4^{(1)} \\ \Lambda_1^{(2)} & \Lambda_2^{(2)} & \Lambda_3^{(2)} & \Lambda_4^{(2)} \\ \Lambda_1^{(3)} & \Lambda_2^{(3)} & \Lambda_3^{(3)} & \Lambda_4^{(3)} \end{vmatrix}$$

and $\zeta = \sqrt{\dfrac{2}{\pi}} \dfrac{\varepsilon_4 L_0 sin(Lp)}{Lp(\varepsilon_4 + st_p)^2}$

where $\varepsilon_4 = \dfrac{1}{\eta c^2}$.
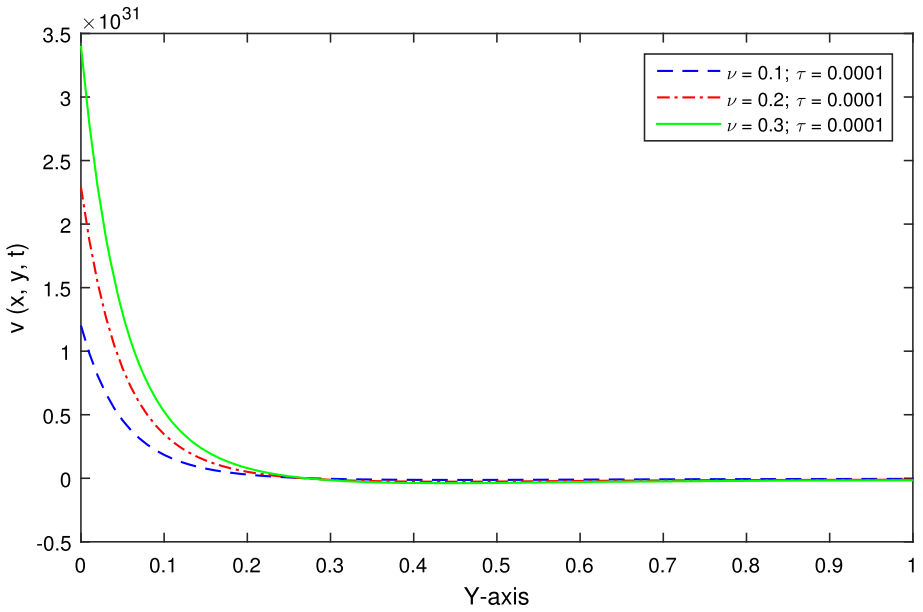
Fig. 3 The variations of vertical displacement v versus y in TRDPTE model
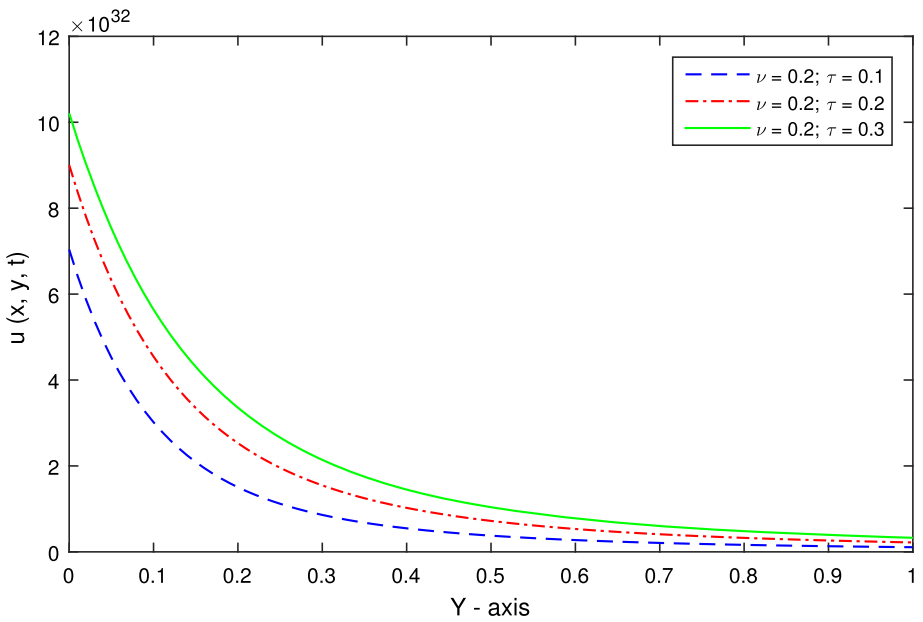
Fig. 4 The variations of horizontal displacement u versus y in TRDPTE model
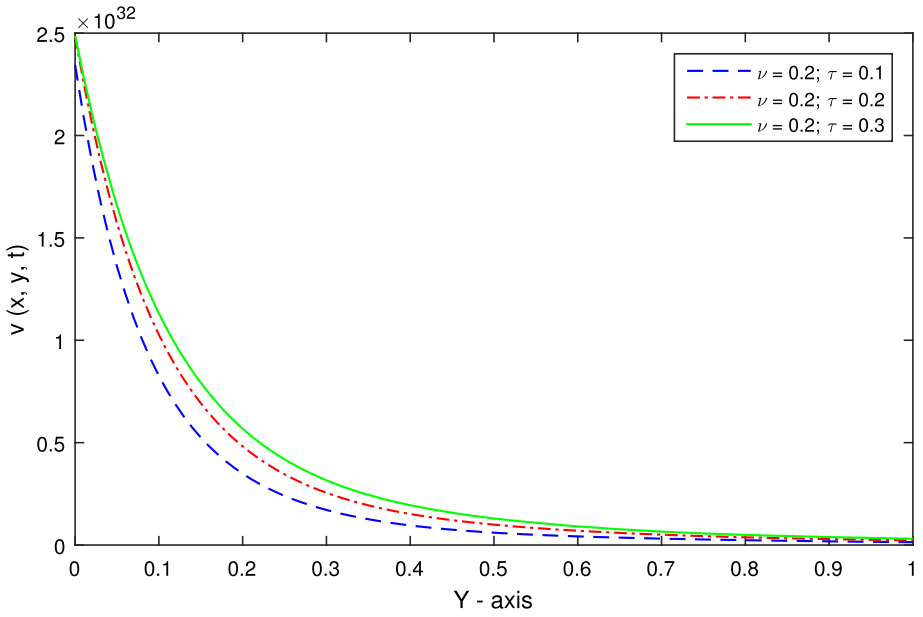
Fig. 5 The variations of vertical displacement v versus y in TRDPTE model
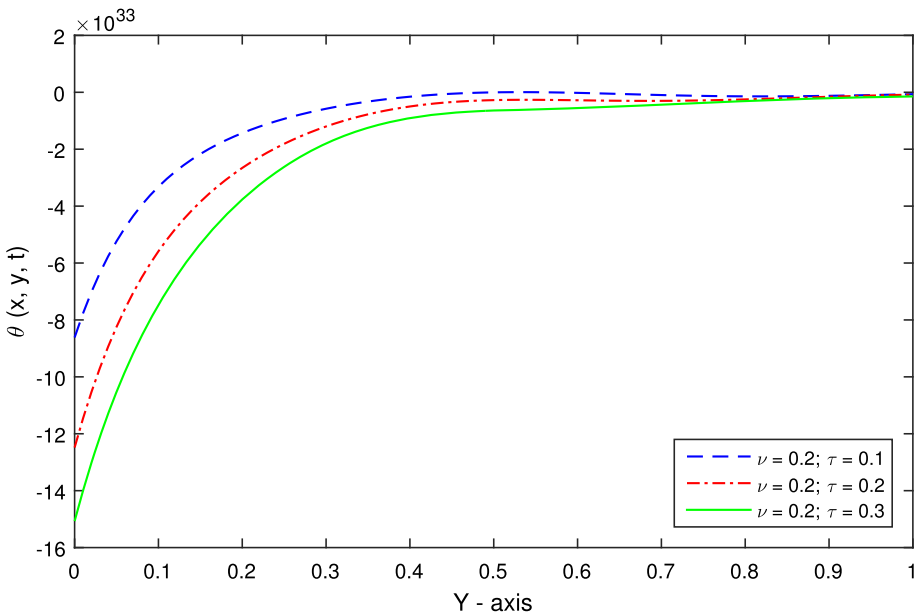
Fig. 6 The variations of temperature θ versus y in TRDPTE model
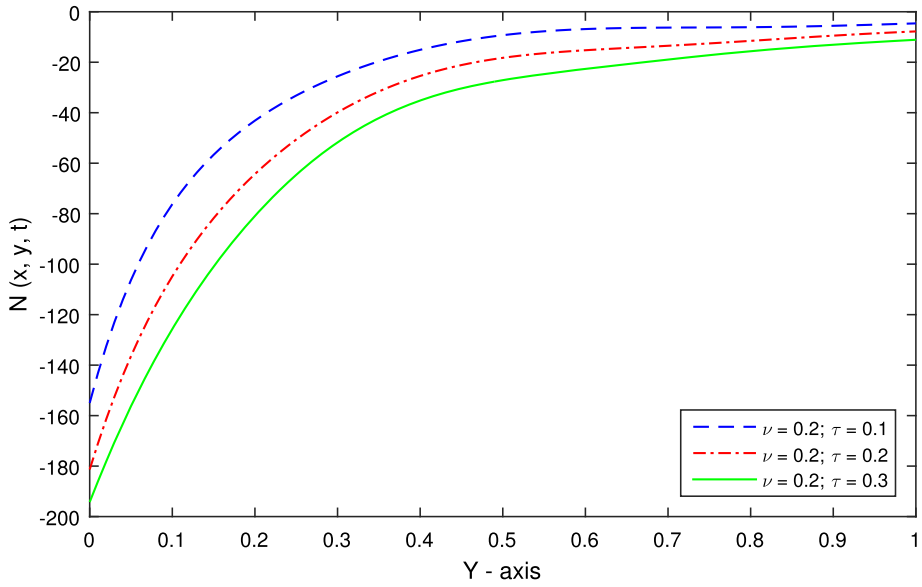
Fig. 7 The variations of carrier density N versus y in TRDPTE model
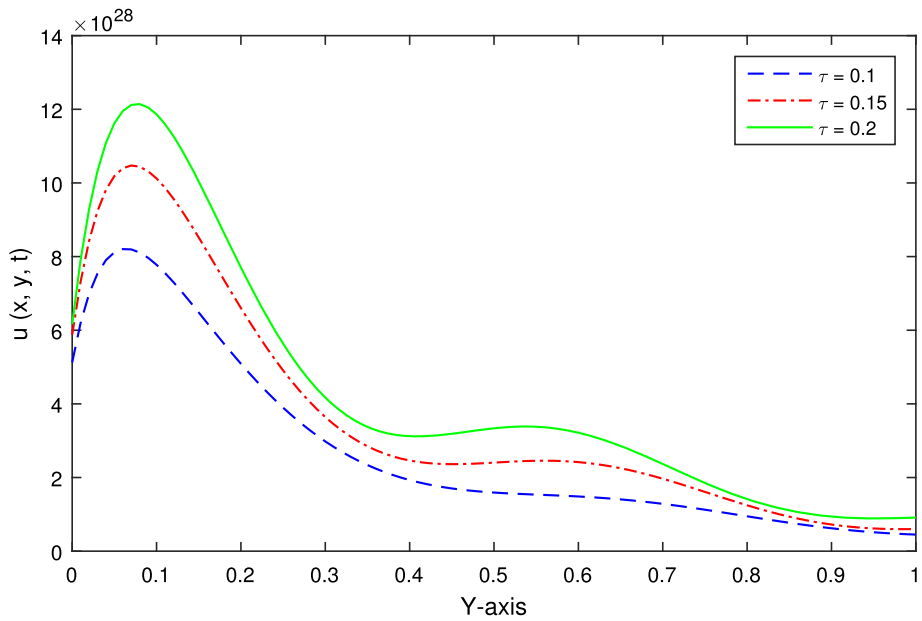
Fig. 8 The variations of horizontal displacement u versus y in EPTE model
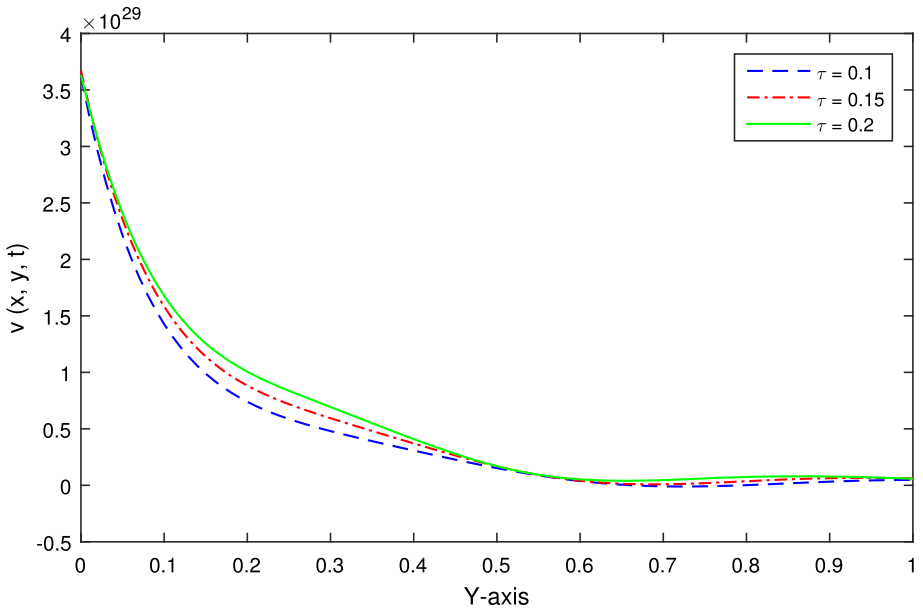
Fig. 9 The variations of vertical displacement v versus y in EPTE model
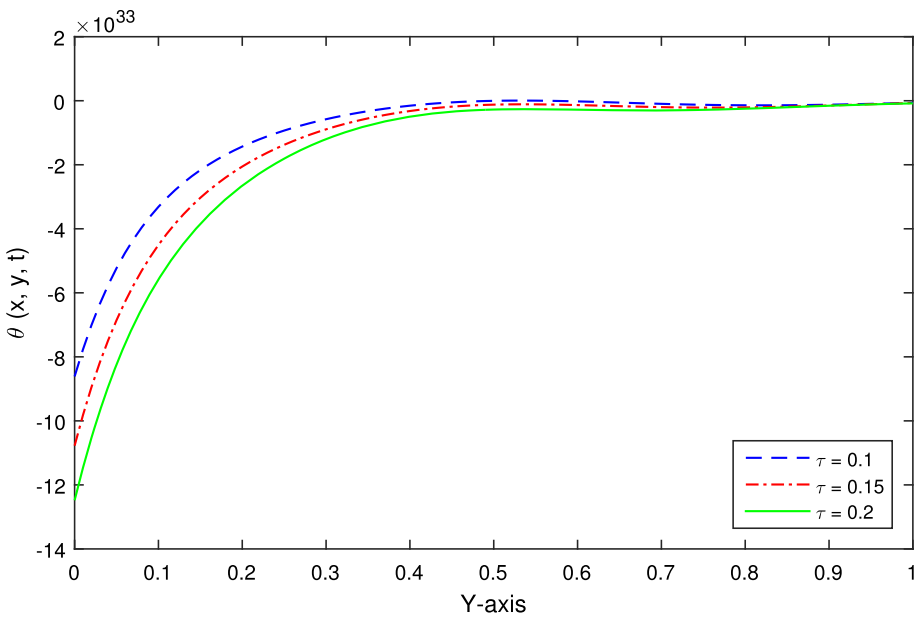
Fig. 10 The variations of temperature θ versus y in EPTE model
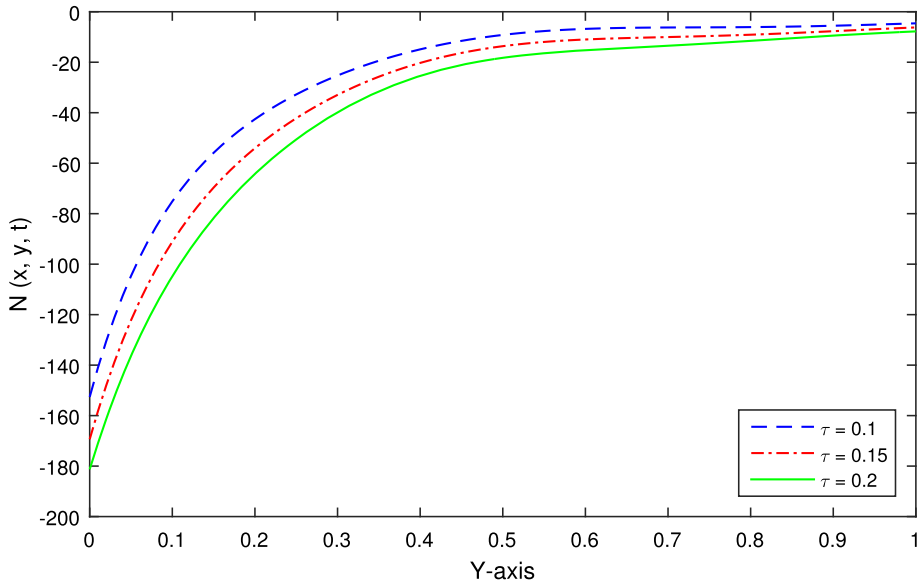
Fig. 11 The variations of carrier density N versus y in EPTE model

7 Numerical results and discussion

In order to illustrate the theories discussed in the article, we consider the inverse Fourier transform of Eqs. (68)–(71) and (73)–(75), followed by the inverse Laplace transform. Since it is complicated to determine the inverse Laplace transform of the above-mentioned equations analytically, we employ the algorithm for numerical inversion given by Honig and Hirdes [21]. For the purpose of numerical computation in the space-time domain, we choose the parameters of a silicon plate where the values of the physical constants are as follows [22]:

$$\lambda = 3.64 \times 10^{10} \text{ N/m}^2, \quad \mu = 5.46 \times 10^{10} \text{ N/m}^2, \quad \tau_0 = 5 \times 10^{-5} \text{ s}, \quad \theta_0 = 300 \text{ K}$$

$$c_e = 695 \text{ J/kg/K}, \quad E_g = 1.11 \text{ eV}, \quad s_0 = 2 \text{ m/s}, \quad E = 2.33 \text{ eV}, \quad D_e = 2.5 \times 10^{-3} \text{ m}^2/\text{s}$$

$$\alpha_t = 3 \times 10^{-6} \text{ K}^{-1}, \quad \rho = 2330 \text{ kg/m}^3, \quad n_0 = 10^{20} \text{ m}^{-3}, \quad d_n = -9 \times 10^{-31} \text{ m}^3$$

Based up on the above data set, Figs. 2, 3, 4, 5, 6, 7, 8, 9, 10 and 11 represent the numerically computed physical quantities at different values of relaxation times with respect to the distance y for $x = 0.05$ and $t = 0.01$. The boundary parameters are taken as $L_0 = 3$, $t_p = 0.1$ and $L = 1$. Numerical computations are carried out to study the effects of thermal relaxation times in the variations of temperature, carrier density and distributions of displacement along the y-axis in the context memory-dependent photo-thermal theories for memory parameters $a = 1, b = 0$. The variations of horizontal displacement u along y for the TRDPTE model are shown in Figs. 2 and 4. It is observed that u attains maximum value at the point $x = 0.05$ upon x-axis where the non-Gaussian laser beam was applied and it gradually decreases to zero as we move along the positive y-axis. Figures 3 and 5 show the variations of vertical displacement v with respect to the distance y in TRDPTE model. It was noticed that the vertical displacement shows an ultimate positive value at a the location where boundary condition was applied and then, it progressively decreases to zero. From Fig. 6, it was noted that for the TRDPTE model, the temperature graph shows a nearly monotonically increasing

curve till it gradually flattens to zero. A similar nature for the carrier density N, is observed from Fig. 7, where it started with an minimum negative value which gradually rose before converging to zero.

Figures 8, 9, 10 and 11 depict the numerical computations for the effects of the thermal relaxation time τ in the variations of temperature, carrier density and distributions of displacement along the y-axis in the context memory-dependent EPTE theory. It is observed form Fig. 8 that the variations in horizontal displacement u steeply increase along the positive direction of y-axis where it attains a peak in near vicinity of the boundary and then it gradually decreases with a wavy pattern. Figure 9 shows that the vertical displacement v starts off with its maximum value at $x = 0.05$ upon the boundary and henceforth monotonically decreases to zero. Figures 10 and 11 suggest that both variations of temperature and carrier density have a steep rise from the point of application of boundary conditions, finally graduating towards zero. From the variations of θ, it clearly indicates the finite nature of thermal waves' propagation since each time the curves nullify to zero along the vertical axis.

8 Conclusive remarks

This article investigated the effects of thermal relaxation times in two generalized models of plasma and thermoelastic waves under the light of memory-dependent derivatives, in a two-dimensional semi-infinite semiconductor plane.

1. It was noticed from the graphical results of the memory-dependent TRDPTE model that there is a direct proportional correspondence between horizontal and vertical displacements, and the thermal relaxation times in terms of their values.
2. For the TRDPTE model, τ plays a vital role in temperature and carrier density distribution along the vertical direction. For a narrow beamed boundary condition like non-Gaussian laser pulse, the relaxation time ν shares a negligible role for temperature and carrier density distribution when compared with the other relaxation time τ.
3. The variations of temperature and carrier density for the TRDPTE model share an inverse proportionate relation with the finite build up time for the onset of heat flow τ, along the y-axis.
4. In the theory with one thermal relaxation time (EPTE model), the horizontal displacement component attains its maximum at a distance away from the boundary of application of the laser pulse, and eventually, it diminishes to zero as we move away vertically from the boundary.
5. For the EPTE model, an increase in thermal relaxation time τ shows an increase in both horizontal and vertical displacement components.
6. Similar to the TRDPTE model, the EPTE model also suggests that an increase in thermal relaxation time can lower the temperature and carrier density variations along the vertical axis in the 2D plate.

Hence, as expected, it can be found from this study that the thermal relaxation times have a major impact on the values of all the physical quantities. Further, the outcomes obtained in this article may also prove useful to cater the memory inclusion needs for designing various semiconducting materials.

9 Appendix

9.1 Memory-dependent derivatives

Wang and Li [3] defined memory-dependent derivatives (MDDs) in an integral form with a kernel function on a slipping interval as follows:

$$D_\omega^{(1)} f(x, t) = \frac{1}{\omega} \int_{t-\omega}^{t} k(t - \xi) \frac{\partial f(x, \xi)}{\partial \xi} \partial \xi \tag{78}$$

where ω is the time delay and $K(t - \omega)$ is the kernel function.

The kernel function should be chosen in such a way such that the magnitude of MDD should be smaller than that of the common partial derivative, and for that the bounds of the kernel should be $0 \leq k(t - \xi) \leq 1$ for $\xi \in [t - \omega, t]$. This is done to educe the memory effect better than others. The time delay $\omega(> 0)$ should always be chosen in such a manner, that the material's thermodynamical behaviour can be understood more properly.

It is to note that in case $k(t - \xi) = 1$ we shall obtain

$$D_\omega^{(1)} f(x, t) = \frac{1}{\omega} \int_{t-\omega}^{t} \frac{\partial f(x, \xi)}{\partial \xi} \partial \xi = \frac{f(x, t) - f(x, t - \omega)}{\omega}$$

This implies that as $\omega \to 0$, MDD tends to common partial derivative of first order. The kernel shows a monotone nature with $K = 0$ for the past time $t - \xi$ and $K = 1$ for the present time t.

During the year 2017, Ezzat and his co-workers [6] have proposed a form of the memory kernel, which is as follows:

$$k(t - p) = 1 - \frac{2b}{\omega} (t - p) + \frac{a^2 (t - p)^2}{\omega^2} \tag{79}$$

a and b are the parameters, the values of which are to be chosen.

The Laplace transform of a function containing the MDD with a kernel of the form (79) is:

$$L[D_\omega f(t)] = \frac{\overline{f}(s)}{\omega} \left(\left(1 - \frac{2b}{\omega s} + \frac{2a^2}{\omega^2 s^2} \right) \right.$$
$$\left. - \exp(-\omega s) \left(1 - 2b^2 + a^2 + \frac{2(a^2 - b)}{\omega s} + \frac{2a^2}{\omega^2 s^2} \right) \right) \tag{80}$$

If the kernel function $k(t, p) = 1$, then

$$L[D_\omega f(t)] = \frac{1}{\omega} (1 - \exp(-\omega s)) \overline{f}(s) \tag{81}$$

where $\overline{f}(s)$ denotes the Laplace transform of $f(t)$ and $f(t - \omega) = 0$ for $t < \omega$.

9.2 Non-Gaussian laser pulse function

The temporal profile of a non-Gaussian laser pulse is defined as

$$L_P(t) = \frac{L_0}{t_p^2} t e^{-\frac{t}{t_p}} \tag{82}$$

Fig. 12 The temporal profile of
the laser power L_P/L_0
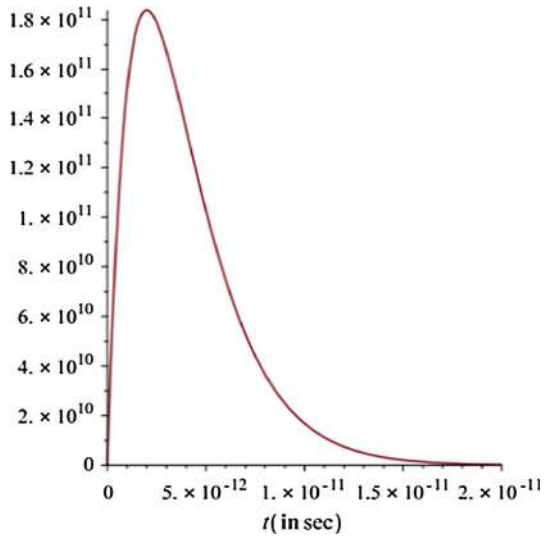
where L_0 is the laser intensity that is defined as the total energy carried by a laser pulse per
unit area of the laser beam, and t_p is the characteristic time of the laser pulse which may also
be referred as the time duration of the laser pulse.

The function has the property

$$\int_0^\infty L_P(t)\, \mathrm{d}t = 1 \tag{83}$$

and

$$\max_{\forall t} [L_P(t)] = L_P(t_p) \tag{84}$$

The following figure provides the temporal profile of the laser power L_P/L_0, by considering
$tp = 2p$ s (Fig. 12).

The Laplace transform of Eq. (82) can be easily obtained by using the first shifting property
of the transform.

The Laplace transform followed by the Fourier transform of the non-Gaussian laser pulse
function is obtained as:

$$\overline{L}^*(t) = \frac{L_0 \delta(p)}{(1 + st_p)^2} \tag{85}$$

References

1. H.W. Lord, Y. Shulman, A generalized dynamical theory of thermoelasticity. J. Mech. Phys. Solids **15**(5), 299–309 (1967)
2. A.E. Green, K.A. Lindsay, Thermoelasticity. J. Elast. **2**(1), 1–7 (1972)
3. J.-L. Wang, H.-F. Li, Surpassing the fractional derivative: concept of the memory-dependent derivative. Comput. Math. Appl. **62**(3), 1562–1567 (2011)
4. M.A. Ezzat, A. El-Karamany, A. El-Bary, Modeling of memory-dependent derivative in generalized thermoelasticity. The European Physical Journal Plus **131**(10), 372 (2016)
5. A. El-Karamany, M.A. Ezzat, Thermoelastic diffusion with memory-dependent derivative. J. Therm. Stresses **39**(9), 1035–1050 (2016)

6. M.A. Ezzat, A.S. El-Karamany, A.A. El-Bary, On dual-phase-lag thermoelasticity theory with memory-dependent derivative. Mech. Adv. Mater. Struct. **24**(11), 908–916 (2017)

7. S. Shaw, B. Mukhopadhyay, A discontinuity analysis of generalized thermoelasticity theory with memory-dependent derivatives. Acta Mech. **228**(7), 2675–2689 (2017)

8. S. Shaw, Theory of generalized thermoelasticity with memory-dependent derivatives. J. Eng. Mech. **145**(3), 04019003 (2019)

9. Y. Li, T. He, A generalized thermoelastic diffusion problem with memory-dependent derivative. Math. Mech. Solids **24**(5), 1438–1462 (2019)

10. S. Banerjee, S. Shaw, B. Mukhopadhyay, Memory response on thermal wave propagation emanating from a cavity in an unbounded elastic solid. J. Therm. Stresses **42**(2), 294–311 (2019)

11. S. Banerjee, S. Shaw, B. Mukhopadhyay, Memory response on thermoelastic deformation in a solid half-space with a cylindrical hole. Mech. Based Des. Struct. Mach. (2019) https://doi.org/10.1080/15397734.2019.1686989

12. S. Banerjee, S. Shaw, B. Mukhopadhyay, Thermal memory response in magneto-thermoelastic medium having long cylindrical cavity. WSEAS Transactions on Circuits and Systems **19**(1), 1–12 (2020)

13. I.A. Abbas, M. Marin, Analytical solution of thermoelastic interaction in a half-space by pulsed laser heating. Physica E-Low-Dimen. Syst. Nanostruct. **87**, 254–260 (2017)

14. A. Hobiny, I. Abbas, Analytical solutions of photo-thermo-elastic waves in a non-homogenous semiconducting material. Results Phys. **10**, 385–390 (2018)

15. F.S. Alzahrani, I.A. Abbas, Photo-thermoelastic interactions in a 2d semiconducting medium. Eur. Phys. J. Plus **133**, 1–17 (2018)

16. F.S. Alzahrani, I.A. Abbas, Photo-thermoelastic interactions in a 2d semiconducting medium. Results Phys. **15**, 505 (2018)

17. A. Hobiny, I. Abbas, Generalized thermoelastic interaction in a two-dimensional porous medium under dual phase lag model. Int. J. Numer. Methods Heat Fluid Flow **30**, 4865–4881 (2020)

18. W. Nowacki, *Thermoelasticity* (Pergamon Press, Oxford, 1986)

19. D.M. Todorovic, Plasma, thermal, and elastic waves in semiconductors. Rev. Sci. Instrum. **74**, 582–585 (2003)

20. D.M. Todorovic, Plasmaelastic and thermoelastic waves in semiconductors. J. Phys. IV **125**, 551–555 (2005)

21. G. Honig, U. Hirdes, A method for the numerical inversion of laplace transforms. J. Comput. Appl. Math. **10**, 113–132 (1984)

22. Y. Song, D.M. Todorovic, B. Cretin, P. Vairac, J. Xu, J. Bai, Bending of semiconducting cantilevers under photothermal excitation. Int. J. Thermophys. **35**, 305–319 (2014)

Source details

Feedback ›   Compare sources ›

European Physical Journal Plus

Scopus coverage years: from 2011 to Present

Publisher: Springer Nature

ISSN: 2190-5444

Subject area: (Chemical Engineering: Fluid Flow and Transfer Processes)   (Physics and Astronomy: General Physics and Astronomy)

Source type: Journal

View all documents ›   Set document alert   💾 Save to source list

CiteScore 2022   ⓘ
4.9

SJR 2022   ⓘ
0.548

SNIP 2022   ⓘ
0.979

CiteScore   CiteScore rank & trend   Scopus content coverage

Computational analysis on the influence of damping in solid body deformation during thermoelastic mass diffusion

Soumen Shaw & Mohamed I. A. Othman

Taylor & Francis
Taylor & Francis Group

Check for updates

Computational analysis on the influence of damping in solid body deformation during thermoelastic mass diffusion

Soumen Shaw[a] and Mohamed I. A. Othman [b]

[a]Department of mathematics, Indian Institute of Engineering Science and Technology, Shibpur, Howrah, India; [b]Department of Mathematics, Faculty of Science, Zagazig University, Zagazig, Egypt

ABSTRACT

In the present study, the identification of thermodynamic damping is investigated on mass diffusion in the solid body deformation due to the heat emanating from a cavity into the medium. The governing equations have come into the possession of mechanics of continuous medium by employing the D'Alembert's principle, non-classical heat conduction theory, conservation of energy and the theory of 'non-Fickian' mass diffusion. In the framework of spherical symmetry, displacement, radial stresses as well as temperature distributions is distinguished for different measures of time delay. The expression of the field functions are obtained in terms of modified Bessel's functions in the Laplace transform domain. A compatible form of discretization and numerical computational technique of inverse Laplace transformation is analyzed. In order to estimate the nature of the displacements, stresses and temperature distributions in the physical domain, an efficient approximate numerical inverse Laplace transform technique is adopted. The effect of mass diffusion (MD) on the thermoelastic deformation is analyzed meticulously for the various speed of revolution, diffusive relaxation time, thermal time delay and those are categorically compared with the existing results reported in the literature. Moreover, the present study can be comprehensively applied to the anisotropic medium, with or without energy dissipation.

Nomenclature:

α_t	Coefficients of linear thermal expansion a: Radius of the spherical cavity,
α_c	Coefficients of diffusion expansion b: Measures of diffusive effects,
λ, μ	Lame' constants c: Measures of thermodiffusion effects,
ρ	Mass density c_E: Specific heat at constant strain,
τ	Diffusion relaxation time D: Diffusion coefficient,
τ_0	Thermal relaxation time e_{ij}: Components of the strain tensor,
Ω	Angular velocity k: Coefficient of thermal conductivity
σ_{ij}	Components of the stress tensor, T: Absolute temperature,
T_0	Uniform reference temperature of the medium

CONTACT Mohamed I. A. Othman ✉ m_i_a_othman@yahoo.com

P	Chemical potential
u_r	Radial component of the displacement vector
(r, θ, φ)	Spherical polar coordinate system.
C	Concentration of the diffusive material in the elastic body.

1. Introduction

The theory of elasticity in the ambiance of thermal field was well acquainted with Duhamel [1] and Neumann [2]. Over the decades, the manifestations of heat sources/ thermal fields of the theory of elasticity are observed. To a certain extent, the strain and stresses generated in the medium must be influenced by the existing thermal effect. This thermo-mechanical process is termed as thermoelasticity. Initially, the manifestation of the thermal effects in the elasticity theory was in uncoupled form. Later on, in the second half of the twentieth century, Biot [3] introduced the classical theory on thermoelasticity which was the coupled form of heat conduction and the associated elastic-deformation in the medium. It has been observed that the traditional theory of heat conduction predicts infinite speed of thermal signals when a homogeneous isotropic elastic solid is imperiled to a thermal disturbance. In the classical theory of thermoelasticity, the paradoxical behaviors of the heat propagation were due to the fact that the waveform of heat propagation was represented by a parabolic type heat conduction equation. In order to escape those discrepancies, Lord and Shulman [4] introduced a modified thermal propagation law incorporating a relaxation time (i.e. delay time) in the Fourier law of heat conduction which fallout is the finite speed of heat flow. In 1972 Green and Lindsay [5], without violating the classical law of heat conduction, incorporated two time delays in both the constitutive functions. Conferring to those theories, wave form of heat propagation is registered instead of a diffusion phenomenon. Suhubi [6] mentioned this wave form of thermal flow as 'second sound'. To apply the thermoelasticity theories including generalized heat conduction law in a wider class of heat flow problems, Green and Naghdi [7–9] have made certain basic modifications to this generalized theory and reported three different generalization of the aforementioned theory of elasticity. Dhaliwal and Sherief [10] extended the generalized theory of thermoelasticity to an anisotropic medium.

The analysis of thermoelastic mass-diffusion phenomenon is of great interest due to its numerous applications in various disciplines of geophysics and industries. Consequently, in the last decade, several research articles have been reported on theoretical and industrial aspects of thermo-diffusion (for details see Refs. [11–23]). Mass-diffusion can be described by two different approaches, an atomistic approach and a phenomenological approach. According to the atomistic approach, diffusion is considered as a result of the random walk of diffusing particles. Whereas, the phenomenological approach is based on Fick's law, according to which diffusion is the random walk of an ensemble of particles from regions of high concentration to regions of low concentration. It occurs as a result of the second law of thermodynamics, which states that the entropy or disorder of any system must always increase with time. In cell biology, diffusion is one of the essential forms of transport for necessary materials such as amino acids within the cells. Diffusion process is one of the active processes during the metabolism as well as the respiration. Diffusion is also one of the modern techniques to improve the oil extraction technology.

Thermoelastic mass-diffusion in the mechanics of continuous medium is due to the coupling of the fields of strain, temperature and mass diffusion. It is one of the transport processes that has great practical importance. A general model for a continuum solid that takes into account the coupling influence of strain, heat conduction and mass diffusion with some general assumptions was incorporated by Podstrigach [24]. Podstrigach and Pavlina [25] introduced some fundamental constitutive relations and simultaneous differential equations for thermo-diffusion process. Later on, Nowacki [26–28] put forward the theory of thermoelastic diffusion by using a coupled thermoelastic models.

Based on the aforementioned pioneer works on thermoelastic mass-diffusion, in the twentieth century, several research articles have been reported in various esteemed international journals. Among them we can mention: Shaw [29], Shaw and Mukhopadhyay [30,31], Sherief et al. [32], Li and He [33], Abouelregal [34], Davydov et al. [35], Othman et al. [36].

In this article, the generalized theory of thermoelastic diffusion is revisited and it is adopted to analyze the effect of MD in a homogeneous thermoelastic solid. We try to settle the question: in the presence of heat flow into the medium, how the influence of rotation enhances its impact over the field functions (e.g. deformation, temperature changes, the concentration of the diffusion material in the elastic body, etc.)? In addition, the effect of generalized thermoelastic diffusion over heat transfer as well as thermo-elastic deformations in a homogeneous thermally conducting elastic medium are also studied and a computational scheme is established.

2. Kinematics

In this section, measures of fundamental kinematic which will be pragmatic to quantify the motion and deformation of the mechanics of continuous medium are discussed. For further details, one may refer to the articles reported by [37–39].

Consider a continuum body occupying a region v_0 at an instant $t = 0$ in the reference frame. ∂v_0 denotes its boundary in the reference configuration with outward drawn unit normal vector $\mathbf{N}$. Position of any point in the reference frame at the instant $t = 0$ is denoted by the vector $\mathbf{X}$ and the transformed position vector of that point at time t is denoted by $\mathbf{x}$. The absolute temperature of the medium is represented by the attribute $T(\mathbf{x}, t)$ over the reference temperature T_0. The transform function $\varphi(\mathbf{x}, t)$ relates the spatial configuration with reference frame such that $\mathbf{X} = \varphi(\mathbf{x}, t)$. The deformation gradient is defined by the usual manner as:

$$F(X, t) = \frac{\partial \varphi}{\partial X}.$$

It has been assumed that the determinant of the Jacobian of the deformation gradient $J = \det F > 0$ (Figure 1).

3. Formulation and modeling the problem

A homogeneous and isotropic thermoelastic solid is considered in the context of the present investigation. It is also assumed that the temperature of the medium to be uniform.

(T_0) at $t = 0$ i.e. at the undisturbed state of the medium. As soon as the rotation is initiated into the medium, with respect to the inertial frame, with a uniform angular velocity
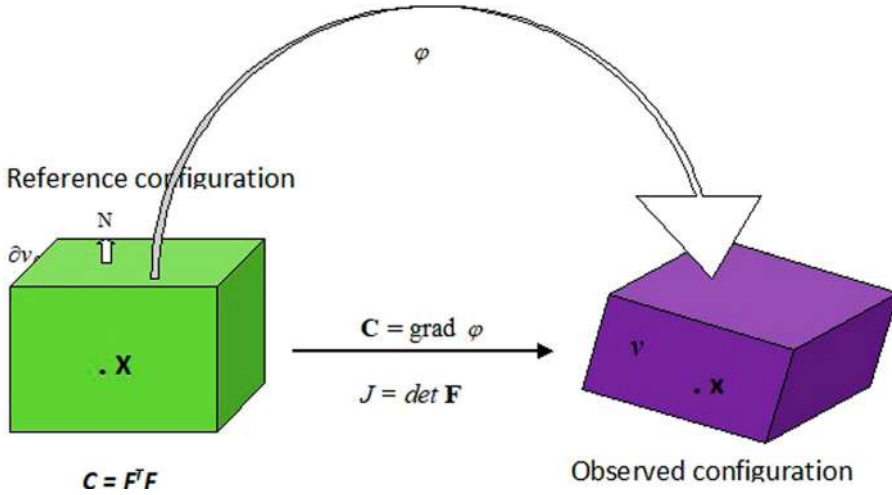
Figure 1. Motion and deformation of mechanics of continuous medium.

$\mathbf{\Omega} = \Omega\mathbf{N}$, Coriolis and Centrifugal forces come into action. Both of them are proportional to the mass of the object. The aforementioned forces are also referred as the inertial forces or pseudo forces. The former one quite small and only the horizontal component of that force have taken into consideration.

Taking into account the Coriolis and Centrifugal forces, the equations governed by the motions of the particles of the considered thermoelastic solid, in the absence of body forces and body couples, are as follows (for details see ref. [40]):

$$\sigma_{ij,j} = \rho u_{i,tt} + \rho[\{\mathbf{\Omega} \times (\mathbf{\Omega} \times \mathbf{u})\}_i + (2\mathbf{\Omega} \times \mathbf{u}_{,t})_i]. \tag{1}$$

The constitutive functions for homogeneous and isotropic thermoelastic solid with diffusion are given by (see, Sherief et al. [32]),

$$\sigma_{ij} = 2\mu e_{ij} + \delta_{ij}[\lambda e_{kk} - \beta_1(T - T_0) - \beta_2 C], \tag{2}$$

$$P = -\beta_2 e_{kk} + bC - c(T - T_0), \tag{3}$$

where $\beta_1 = (3\lambda + 2\mu)\alpha_t$, $\beta_2 = (3\lambda + 2\mu)\alpha_c$ and the entropy equation has been utilized in the derivation of equation of motion and in the generalized equation of heat conduction given bellow.

Inserting the relations (2) and (3) in the Equation (1), we get finally the required displacement equations of motion

$$\mu u_{i,jj} + (\lambda + \mu)u_{j,ij} - \beta_1 T_{,i} - \beta_2 C_{,i} = \rho u_{i,tt} + \rho[\{\mathbf{\Omega} \times (\mathbf{\Omega} \times \mathbf{u})\}_i + (2\mathbf{\Omega} \times \mathbf{u}_{,t})_i]. \tag{4}$$

Generalized heat conduction and mass diffusion equations in isotropic solid are respectively (see, Sherief et al. [32]),

$$\left(\frac{\partial}{\partial t} + \tau_0 \frac{\partial^2}{\partial t^2}\right)(\rho c_E T + T_0 \beta_1 e_{kk} + c T_0 C) = k T_{,ii}, \tag{5}$$

$$D\beta_2 e_{kk,ii} + DC T_{,ii} + \left(\frac{\partial}{\partial t} + \tau \frac{\partial^2}{\partial t^2}\right)C = Db C_{,ii}. \tag{6}$$

Here we consider an isotropic, homogeneous, infinite elastic medium which is rotating with a uniform angular velocity $\boldsymbol{\Omega}$, occupying the region $a \leq r < \infty$.

For this present analysis, the considered medium here is an unbounded thermoelastic solid and an amount of heat is emanating from a spherical cavity into the medium. We take the origin at the center of the cavity and 'a' denotes the dimensionless radius of the cavity. If initially the body is at rest in an unreformed state and has its temperature-change and temperature-rate equal to zero, then the following initial conditions must be hold: $u = \frac{\partial u}{\partial t} = \theta = \frac{\partial \theta}{\partial t} = 0$ at $t = 0$ for $r \geq a$.

For spherical symmetric interfaces, the displacement vector possesses only the radial displacement $\boldsymbol{u} = \boldsymbol{u}(r, t)$, where r is the radial distance measured from the origin (point of symmetry), and the stress tensor is determined by the radial stress σ_{rr} and the circumferential stress (hoop stress) $\sigma_{\phi\phi}$.

Consequently, the following components of the strain tensor:

$$e_{rr} = \frac{\partial u}{\partial r}, \quad e_{\phi\phi} = e_{\vartheta\vartheta} = \frac{u}{r}, \quad e_{r\phi} = e_{r\vartheta} = e_{\vartheta\phi} = 0. \tag{7}$$

The cubical dilatation:

$$e = \frac{\partial u}{\partial r} + 2\frac{u}{r}. \tag{8}$$

Due to spherical symmetry, Equatioins (2)–(6) take the following form:

$$\rho \frac{\partial^2 u}{\partial t^2} = (\lambda + 2\mu)\frac{\partial e}{\partial r} - \beta_1 \frac{\partial T}{\partial r} - \beta_2 \frac{\partial C}{\partial r} - \rho\left(\Omega^2 u + 2\Omega \frac{\partial u}{\partial t}\right), \tag{9}$$

$$k\nabla^2 T = \left(\frac{\partial}{\partial t} + \tau_0 \frac{\partial^2}{\partial t^2}\right)(\rho c_E T + T_0 \beta_1 e + c T_0 C), \tag{10}$$

$$Db\nabla^2 C = D\beta_2 \nabla^2 e + DC\nabla^2 T + \left(\frac{\partial}{\partial t} + \tau \frac{\partial^2}{\partial t^2}\right)C, \tag{11}$$

$$\sigma_{rr} = 2\mu \frac{\partial u}{\partial r} + \lambda e - \beta_1(T - T_0) - \beta_2 C, \tag{12}$$

$$e_{\phi\phi} = e_{\vartheta\vartheta} = 2\mu \frac{u}{r} + \lambda e - \beta_1(T - T_0) - \beta_2 C, \tag{13}$$

$$P = -\beta_2 e + bC - c(T - T_0), \tag{14}$$

where

$$\nabla^2 = \frac{\partial^2}{\partial r^2} + \frac{2}{r}\frac{\partial}{\partial r}.$$

Now we define the following non-dimensional variables as:

$$r^* = c_1 \eta_0 r, \quad u^* = c_1 \eta_0 u, \quad \theta = \frac{\beta_1(T - T_0)}{\lambda + 2\mu}, \quad C^* = \frac{\beta_2 C}{\lambda + 2\mu},$$

$$\Omega^* = \frac{\Omega}{c_1^2 \eta_0}, \quad \sigma_{ij}^* = \frac{\sigma_{ij}}{\lambda + 2\mu}, \quad P^* = \frac{P}{\beta_2}, \quad t^* = c_1^2 \eta_0 t, \quad \{\tau^*, \tau_0^*\} = c_1^2 \eta_0 \{\tau, \tau_0\},$$

where $c_1^2 = \frac{\lambda + 2\mu}{\rho}$ and $\eta_0 = \frac{\rho c_E}{k}$.

Introducing the non-dimensional variables into the Equations (9)–(14) and dropping the asterisks, we obtain

$$\frac{\partial^2 u}{\partial t^2} = \frac{\partial e}{\partial r} - \frac{\partial \theta}{\partial r} - \frac{\partial C}{\partial r} - \Omega^2 u - 2\Omega \frac{\partial u}{\partial t}, \tag{15}$$

$$\nabla^2 \theta = \left(\frac{\partial}{\partial t} + \tau_0 \frac{\partial^2}{\partial t^2} \right)(\theta + \varepsilon e + \varepsilon \alpha_1 C), \tag{16}$$

$$\alpha_3 \nabla^2 C = \alpha_2 \left(\frac{\partial}{\partial t} + \tau \frac{\partial^2}{\partial t^2} \right) C + \nabla^2 e + \alpha_1 \nabla^2 \theta, \tag{17}$$

$$\sigma_{rr} = e - \frac{4u}{\beta^2 r} - \theta - C, \tag{18}$$

$$\sigma_{\phi\phi} = \sigma_{\vartheta\vartheta} = \frac{2u}{\beta^2 r} + \left(1 - \frac{2}{\beta^2} \right) e - \theta - C, \tag{19}$$

$$P = \alpha_3 C - e - \alpha_1 \theta, \tag{20}$$

where $\varepsilon = \frac{T_0 \beta_1^2}{\rho^2 c_E c_1^2}, \alpha_1 = \frac{c \rho c_1^2}{\beta_1 \beta_2}, \alpha_2 = \frac{\mu}{D \eta_0}, \alpha_3 = \frac{b \rho c_1^2}{\beta_2^2}, \beta^2 = \frac{\lambda + 2\mu}{\mu}.$

4. Boundary conditions

If the thermoelastic interactions are produced by a uniform step in temperature applied to the boundary of the cavity which is held in stress-free state, then the following boundary conditions hold:

$$\sigma_{rr}(a, t) = 0, \quad \theta(a, t) = \theta_0 H(t), \quad P(a, t) = P_0 H(t), \tag{21}$$

where θ_0, P_0 are constants and $H(t)$ is the Heaviside unit step function.

5. Method of solution in Integral transform domain

We define the Laplace transform as

$$\bar{f}(x, s) = \int_0^\infty f(x, t) e^{-st} dt \tag{22}$$

Introducing this transformation into Equations (15)–(17) and using homogeneous initial conditions yields the following equations:

$$s_1^2 \bar{u} = \frac{\partial \bar{e}}{\partial r} - \frac{\partial \bar{\theta}}{\partial r} - \frac{\partial \bar{C}}{\partial r}, \tag{23}$$

$$\nabla^2 \bar{\theta} = s(1 + \tau_0 s)(\bar{\theta} + \varepsilon \bar{e} + \varepsilon \alpha_1 \bar{C}), \tag{24}$$

$$\alpha_3 \nabla^2 \bar{C} = \alpha_2 s(1 + \tau s)\bar{C} + \nabla^2 \bar{e} + \alpha_1 \nabla^2 \bar{\theta}, \tag{25}$$

where

$$s_1^2 = s^2 + \Omega^2 + 2\Omega s, \quad \nabla^2 \equiv \frac{\partial^2}{\partial r^2} + \frac{2}{r} \frac{\partial}{\partial r}.$$

Operating $\frac{\partial}{\partial r} + \frac{2}{r}$ on Equation (23) yields,

$$(\nabla^2 - s_1^2)\bar{e} = \nabla^2\bar{\theta} + \nabla^2\bar{C}. \tag{26}$$

Now, from Equations (24)–(26), we obtain

$$(\nabla^6 - a_1\nabla^4 + a_2\nabla^2 - a_3)\{\bar{e}, \bar{\theta}, \bar{C}\} = 0, \tag{27}$$

where

$$a_1 = \frac{1}{\alpha_3 - 1}[\{\varepsilon(\alpha_3 + 2\alpha_1 + \alpha_1^2) - 1 + \alpha_3\}$$
$$\times \{s(1 + \tau_0 s)\} + s\alpha_2(1 + \tau s) + \alpha_3(s^2 + \Omega^2 + 2\Omega s)], \tag{28}$$

$$a_2 = \frac{1}{\alpha_3 - 1}[s^2\alpha_2(1 + \varepsilon)(1 + \tau_0 s)(1 + \tau s) + \{s(1 + \tau_0 s)(2\alpha_3 + \varepsilon\alpha_1\alpha_3 + \varepsilon\alpha_1^2) - 1\}$$
$$\times (s^2 + \Omega^2 + 2\Omega s)], \tag{29}$$

$$a_3 = \frac{1}{\alpha_3 - 1}[s^2\alpha_2(1 + \tau_0 s)(1 + \tau s)(s^2 + \Omega^2 + 2\Omega s)]. \tag{30}$$

The system of Equations (27) can be factorized as

$$(\nabla^2 - k_1^2)(\nabla^2 - k_2^2)(\nabla^2 - k_3^2)\{\bar{e}, \bar{\theta}, \bar{C}\} = 0, \tag{31}$$

where k_1, k_2 and k_3 are the roots of the characteristic equation

$$k^6 - a_1 k^4 + a_2 k^2 - a_3 = 0. \tag{32}$$

Now we take $m = k^2$, the Equation (32) reduces to

$$m^3 - a_1 m^2 + a_2 m - a_3 = 0. \tag{33}$$

From this equation one can get three values of m i.e. of k^2. If k^2 is positive and real, each value of m corresponds to a wave. The roots k_1, k_2 and k_3 are given by

$$k_1 = \sqrt{\frac{1}{3}\{2p\sin(q) + a_1\}}, \quad k_2 = \sqrt{\frac{1}{3}[a_1 - p\{\sqrt{3}\cos(q) + \sin(q)\}]},$$
$$k_3 = \sqrt{\frac{1}{3}[a_1 + p\{\sqrt{3}\cos(q) - \sin(q)\}]}, \tag{34}$$

in which

$$p = \sqrt{a_1^2 - 3a_2}, \quad q = \frac{1}{3}\sin^{-1}(w), \quad w = -\frac{1}{2p^3}(2a_1^3 - 9a_1 a_2 + 27a_3). \tag{35}$$

The solution of Equation (31) is given by

$$\bar{\theta}(r, s) = \frac{1}{\sqrt{r}}\sum_{i=1}^{3} A_i(s)K_{1/2}(k_i r), \tag{36}$$

$$\bar{e}(r, s) = \frac{1}{\sqrt{r}}\sum_{i=1}^{3} A'_i(s)K_{1/2}(k_i r), \tag{37}$$

$$\bar{C}(r, s) = \frac{1}{\sqrt{r}}\sum_{i=1}^{3} A''_i(s)K_{1/2}(k_i r), \tag{38}$$

where $K_{1/2}$ is the modified Bessel function of the second kind of order ½ and A_i, A'_i, A''_i are parameters depending only on s.

From the Equations (36)–(38) along with Equations (24) and (25), we obtain

$$A'_i(s) = \frac{k_i^4\alpha_3 - \{s(\alpha_1^2\varepsilon + \alpha_3)(1 + \tau_0 s) + \alpha_2 s(1 + \tau s)\}k_i^2 + s^2\alpha_2(1 + \tau_0 s)(1 + \tau s)}{\varepsilon s(1 + \tau_0 s)\{(\alpha_1 + \alpha_3)k_i^2 - \alpha_2 s(1 + \tau s)\}}A_i(s),$$

(39)

$$A''_i(s) = \frac{k_i^2\{k_i^2 - s(1 + \tau_0 s)(1 - \varepsilon\alpha_1)\}}{\varepsilon s(1 + \tau_0 s)\{(\alpha_1 + \alpha_3)k_i^2 - \alpha_2 s(1 + \tau s)\}}A_i(s).$$

(40)

Now we integrate both sides of Equations (36)–(38) in the interval (r, ∞) and considering the regularity condition at infinity, we obtain

$\bar{u}(r, s)$

$$= -\frac{2}{\varepsilon s s_1^2(1 + \tau_0 s)\sqrt{r}} \times \sum_{i=1}^{3} \frac{k_i^4(\alpha_3 - 1) - [s(1 + \tau_0 s)\{\varepsilon\alpha_1(2 + \alpha_1) + \alpha_3(1 + \varepsilon) - 1\}}{\{(\alpha_1 + \alpha_3)k_i^2 - \alpha_2 s(1 + \tau s)\}}$$

$$\times A_i(s)k_i K'_{1/2}(k_i r).$$

(41)

Therefore from Equations (18), (36), (37) (38) and (41) we get,

$\bar{\sigma}_{rr}(r, s)$

$$= -\frac{1}{\varepsilon s(1 + \tau_0 s)\sqrt{r}} \times \sum_{i=1}^{3} \frac{k_i^4(\alpha_3 - 1) - [s(1 + \tau_0 s)\{\varepsilon\alpha_1(2 + \alpha_1) + \alpha_3(1 + \varepsilon) - 1\}}{\{(\alpha_1 + \alpha_3)k_i^2 - \alpha_2 s(1 + \tau s)\}}$$

$$\times \left[K_{1/2} + \frac{8}{\beta^2 s_1^2 r}k_i K'_{1/2}(k_i r)\right]A_i(s),$$

(42)

$$\bar{P}(r, s) = -\frac{1}{\varepsilon s(1 + \tau_0 s)\sqrt{r}} \sum_{i=1}^{3} \frac{-[2\alpha_3 s(1 + \tau_0 s) + \alpha_2 s(1 + \tau s)]k_i^2 + \alpha_2 s^2(1 + \varepsilon\alpha_1)}{\{(\alpha_1 + \alpha_3)k_i^2 - \alpha_2 s(1 + \tau s)\}}$$

$$\times A_i(s)K_{1/2}(k_i r).$$

(43)

Now invoking the boundary conditions (21), and using the Equations (36), (42) and (42) one can determine the unknown parameters $A_j (j = 1, 2, 3)$, which yields the following set of linear equations:

$$\sum_{i=1}^{3} \frac{k_i^4(\alpha_3 - 1) - [s(1 + \tau_0 s)\{\varepsilon\alpha_1(2 + \alpha_1) + \alpha_3(1 + \varepsilon) - 1\} + \alpha_2 s(1 + \tau s)]k_i^2}{\{(\alpha_1 + \alpha_3)k_i^2 - \alpha_2 s(1 + \tau s)\}}$$

$$\times \left[K_{1/2}(k_i a) + \frac{8}{\beta^2 s_1^2 a}k_i K'_{1/2}(k_i a)\right]A_i(s) = 0,$$

(44)

$$\sum_{i=1}^{3} A_i(s)K_{1/2}(k_i a) = \frac{\theta_0 \sqrt{a}}{s}, \tag{45}$$

$$\sum_{i=1}^{3} \frac{-[2\alpha_3 s(1 + \tau_0 s) + \alpha_2 s(1 + \tau s)]k_i^2 + \alpha_2 s^2 (1 + \varepsilon\alpha_1)(1 + \tau_0 s)(1 + \tau s)}{\{(\alpha_1 + \alpha_3)k_i^2 - \alpha_2 s(1 + \tau s)\}} A_i(s)K_{1/2}(k_i a)$$
$$= P_0 \varepsilon (1 + \tau_0 s)\sqrt{a}. \tag{46}$$

Solving these Equations (24)–(26), one can obtain the parameters A_1, A_2 and A_3.

$$A_1 = \frac{\sqrt{a}}{s}\left[\frac{P_0 s \varepsilon (a_2 b_3 - a_3 b_2)(1 + \tau_0 s) - \theta_0 (a_2 c_3 - a_3 c_2)}{\Delta}\right],$$

$$A_2 = \frac{\sqrt{a}}{s}\left[\frac{P_0 s \varepsilon (a_3 b_1 - a_1 b_3)(1 + \tau_0 s) - \theta_0 (a_1 c_3 - a_3 c_1)}{\Delta}\right],$$

$$A_3 = \frac{\sqrt{a}}{s}\left[\frac{P_0 s \varepsilon (a_1 b_2 - a_2 b_1)(1 + \tau_0 s) - \theta_0 (a_1 b_3 - a_3 b_1)}{\Delta}\right],$$

in which

$$a_i = \frac{\begin{aligned}&k_i^4(\alpha_3 - 1) - [s(1 + \tau_0 s)\{\varepsilon\alpha_1(2 + \alpha_1) + \alpha_1(1 + \varepsilon) - 1\} + \alpha_2 s(1 + \tau s)]k_i^2 \\ &\qquad + s\alpha_2(1 + \varepsilon)(1 + \tau_0 s)(1 + \tau s)\end{aligned}}{(\alpha_1 + \alpha_3)k_i^2 - \alpha_2 s(1 + \tau s)}$$
$$\times \left[K_{1/2}(k_i a) + \frac{8}{\beta^2 s_1^2 a}k_i K_{1/2}(k_i a)\right],$$

$$b_i = K_{1/2}(a k_i),$$

$$c_i = \frac{\alpha_2 s^2 (1 + \varepsilon\alpha_1)(1 + \tau s)(1 + \tau_0 s) - [2\alpha_3 s(1 + \tau_0 s) + \alpha_2 s(1 + \tau s)]k_i^2}{(\alpha_1 + \alpha_3)k_i^2 - \alpha_2 s(1 + \tau s)} b_i;$$

$i = 1, 2, 3$ and $\Delta = a_1(b_2 c_3 - b_3 c_2) - a_2(c_3 b_1 - c_1 b_3) + a_3(b_1 c_2 - b_2 c_1)$.

6. Discretization and numerical computational technique of inverse Laplace transformation

Computation of the Laplace inversion numerically for all the values of $t > 0$ is a timeworn as well as formidable task. A quite a few research articles have been reported in the literature in the regard and till now it remains a challenge to the scientific computing fraternity. One may find several methodologies for the computation of this inversion technique, but most of the problems are ill-posed (for details see refs. [41−44] and the cross references therein). In order to reduce the propagation of errors, the regularization method is a one of the common approaches to overcome this ill-posedness of the problems.

Here in this section, we try to adopt a very striving and compact methodology to compute inverse Laplace transform numerically over real axis without considering the regularization approaches. At first we discretize the transform function:

$$\bar{f}(s) = L[f(t); t \to s] = \int_0^\infty f(t)e^{-st}dt. \tag{47}$$

As follows:

Here we consider, $t_k \approx \frac{\pi^2}{16N}(2k-1)^2, k = 1, 2, 3, \dots N.$ and

$$K(t_j, x, z) \approx \frac{(2s+1)^{\frac{1}{2}}}{2\sqrt{2\pi}}[e^{-st_j}e^{\sqrt{(4s^2-1)t_jx}}]\frac{1}{\sqrt{x}}e^{-sx},$$

where s is given by $s = \frac{(1+z)}{2(1-z)}.$

This Mobius transformation maps $|z| < 1$ to the half plane $\text{Re}(s) > 0$. Now, we fix the index j to 1 and use the fact that $x_1 \to 0$ as $N \to \infty$ to obtain,

$$\int_0^\infty e^{-st}f(t)dt \approx \frac{2\sqrt{2\pi}}{(2s+1)^{1/2}}\sum_{k=1}^N T_{1k}(z)\sqrt{t_k}f(t_k), \quad \text{Re}(s) > 0.$$

In which $T_{1k}(z) \approx \frac{(2s+1)^{1/2}}{2\sqrt{2\pi}}\frac{\pi}{2\sqrt{N}}e^{-st_k}.$

Thus, we obtain the quartered formula:

$$\int_0^\infty e^{-st}f(t)dt \approx \frac{\pi^2}{4N}\sum_{k=1}^N (2k-1)e^{-s\frac{\pi^2(2k-1)^2}{16N}}f(t_k), \quad \text{Re}(s) > 0, \tag{48}$$

Now we try to evaluate the above quartered at some points $0 < s_1 < s_2 < \dots < s_M$ which yield a linear system of equations. In order to obtain the inverse Laplace transformation, then we try to solve them analytically. Instead of regularization methods, here we can control the instability by choosing the number of nodes $s_k(k = 1, 2, \dots, M)$ as well as the values of N.

Now let $0 < s_1 < s_2 < \dots < s_M$ be $M < N$ nodes chosen from the s-plane. Then Equation (47) takes the matrix form

$$\bar{f}(s_j) = \sum_{k=1}^N L_{jk}f(t_k), \quad j = 1, 2, \dots, M, \tag{49}$$

where L denotes the matrix of order $M \times N$ with

$$L_{jk} = \frac{\pi^2}{4N}(2k-1)e^{-s_j\frac{\pi^2(2k-1)^2}{16N}}. \quad j = 1, 2, \dots, M; \quad k = 1, 2, \dots, N.$$

Thus,

$$(LL^T)_{jk} = \frac{2\pi}{\sqrt{N}}\sum_{l=1}^N x_l e^{-(s_j+s_k)x_l}\Delta\sigma(x_l),$$

where $\Delta\sigma(x_l) \approx \frac{\pi}{2\sqrt{N}}.$

Therefore, if $s_j \neq s_k$, LL^T is a nonsingular and rank$(L) = M$. This indicates that the linear system (5.3) can be written in the following simple form:

$Lf = \bar{f}$, has a solution, which can be found by using the right inverse $L^T(LL^T)^{-1}$, which yields

$$f = L^T(LL^T)^{-1}\bar{f}. \tag{50}$$

This is the form by which we can obtain the approximate numerical values of the inverse Laplace transform.

7. Applications

7.1. Anisotropic medium

This work can also be extended to the anisotropic materials with or without mass diffusion. We suppose that the waves are generated due to the application of a constant step in temperature on the boundary of the cavity which is held in stress-free state. Also, we consider the medium is orthotropic and the heat transfer model is due to Green-Naghdi.

The stress–strain-temperature relations, due to spherical symmetry, are (see Lekhnitskii, [45]) given by

$$\tau_{rr} = c_{33}\frac{\partial u}{\partial r} + (c_{13} + c_{23})\frac{u}{r} - \beta_r T, \tag{51}$$

$$\tau_{\theta\theta} = c_{13}\frac{\partial u}{\partial r} + (c_{11} + c_{12})\frac{u}{r} - \beta_\theta T, \tag{52}$$

$$\tau_{\varphi\varphi} = c_{23}\frac{\partial u}{\partial r} + (c_{12} + c_{22})\frac{u}{r} - \beta_\varphi T. \tag{53}$$

Heat conduction equation with energy dissipation theory of thermoelasticity is

$$\frac{1}{r^2}\frac{\partial}{\partial r}\left[r^2\left\{K^*\frac{\partial T}{\partial r} + K\frac{\partial \dot{T}}{\partial r}\right\}\right] = \frac{\partial^2}{\partial t^2}\left[\rho C_E T + T_0\left\{\beta_r\frac{\partial u}{\partial r} + (\beta_\theta + \beta_\phi)\frac{u}{r}\right\}\right]. \tag{54}$$

The stress equation of motion in the spherical polar coordinate system is

$$\frac{\partial \tau_{rr}}{\partial r} + \frac{1}{r}(2\tau_{rr} - \tau_{\theta\theta} - \tau_{\varphi\varphi}) = \rho\frac{\partial^2 u}{\partial t^2}. \tag{55}$$

As follows in the preceding sections, the non-dimensional form of the governing Equations (54) and (55) can be recast in the following form in the Laplace transform domain:

$$(M - s^2)D_1\bar{u} = M\bar{\theta}, \tag{56}$$

$$(c_p^2 L - s^2)D\bar{\theta} = \varepsilon s^2 L\bar{\theta}, \tag{57}$$

where $c_p^2 = c_T^2 + sc_k^2$, $L \equiv DD_1$, $M = D_1D$ in which $D \equiv \frac{\partial}{\partial r}$, $D_1 \equiv D + \frac{2}{r}$, $c_T^2 = \frac{K^*}{\rho C_E G^2}$, $c_k^2 = \frac{K}{a\rho C_E G}$, $G^2 = \frac{c_{33}}{\rho}$.

Under the regularity condition that $\bar{u}$ and $\bar{\theta} \to 0$ as $r \to \infty$, the general solutions of Equations (56) and (57) are given by

$$\bar{u} = \sum_{\alpha=1}^{2} A_\alpha \left(\frac{1}{r} + \frac{1}{m_\alpha r^2} \right) e^{-m_\alpha r}, \tag{58}$$

$$\bar{\theta} = \frac{1}{r} \sum_{\alpha=1}^{2} B_\alpha e^{-m_\alpha r}, \tag{59}$$

where m_α^2 with $\text{Re}(m_\alpha) > 0$ satisfy the equation $c_p^2 m^2 - s^2(c_p^2 + 1 + \varepsilon)m + s^4 = 0$, A_α and B_α are functions of s and m_α.

Now invoking the boundary conditions one can find that $B_\alpha = \frac{\varepsilon s^2 m_\alpha}{s^2 - c_p^2 m_\alpha^2} A_\alpha$ with $A_\alpha = (-1)^{\alpha+1} \frac{\Upsilon_\alpha}{\Gamma}$, in which

$$Y_\alpha = \frac{\theta_0}{m_\alpha}(c_p^2 m_\alpha^2 - s^2)[\varepsilon s^2 m_1^2 m_2^2 - (c_p^2 m_{3-\alpha}^2 - s^2)]e^{m_\alpha},$$

$$\Gamma = \varepsilon s^3[(c_p^2 m_2^2 - s^2)\Lambda_1 + (c_p^2 m_1^2 - s^2)\Lambda_2],$$

$$\Lambda_\alpha = m_\alpha^2[m_{3-\alpha}^2 + 2(1 - \eta)(1 + m_{3-\alpha}^2)], \quad \eta = \frac{c_{13} + c_{23}}{2c_{33}}.$$

Substituting the expressions for A_α, B_α and m_α we obtain $\bar{u}$ and $\bar{\theta}$ in terms of r and s. The forms of these expressions indicate that each of the displacement and thermal fields (and consequently the stress field) consist of two parts and that each part corresponds to a wave propagating with a finite speed, the wave corresponding to the first part having its speed equal to V_1 and that corresponds to the second part equal to V_2.

It has been observed that for large values of time the coupled and the generalized thermoelasticity theories give close results. The situation is reasonably different once we consider small value of time. The coupled theory predicts infinite speeds of thermal signals. This is evident from the fact that the obtained solutions are not identically zero for any value of time but fade gradually very small values at points far removed from the surface. The solutions obtained in the context of the Lord and Shulman theory, however, exhibit the behavior of finite speeds of wave propagation. For small values of time the solutions are localized in a finite region of space surrounding the surface and are identically zero outside this region. This region grows with increasing time. Its edge is the location of the wave front.

7.2. Functionally graded medium

In this case, the parameters c_{ij}, ρ, β_i, K and K^* are space dependent. Without any loss of generality, we may replace these quantities respectively by $c_{ij}f(r), \rho f(r), \beta_i f(r), K f(r)$ and $K^* f(r)$.

The material is assumed to be elastic and has an inhomogeneity in the radial direction.

Thus we may consider $f(r) = (\frac{r}{a})^n$, where n is a dimensionless parameter. The values of this parameter have a definite correlation with the material's moduli e.g.

$$n = \frac{c_{11} + 2c_{12} + c_{22} - (c_{13} + 2c_{33} + c_{23})}{c_{13} + c_{23} + c_{33}}$$

For detail see Ref. [30,46].
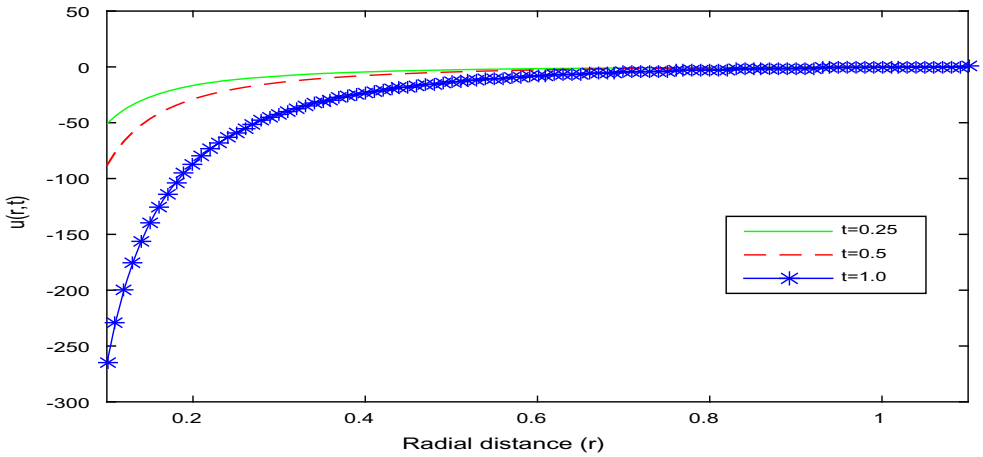
Figure 2. Variation of radial displacement with time.

8. Numerical results and discussions

In order to illustrate the theoretical developments in the preceding sections and to get the nature of the field functions in the space–time domain, we have to consider inverse Laplace transform of the Equations (41), (42) and (36). Since the roots k_α are an implicit function of transforming domain parameter s, therefore, analytical computation of inverse Laplace transform of the field functions for all values of s is a formidable task. Thus, here we have considered the aforementioned techniques for numerical inversion of Laplace transform. For this purpose, copper type material is considered whose physical data are given as follows:

$$\alpha_t = 1.78 \times 10^{-5} K^{-1}, k = 386 W/(mK), \alpha_c = 1.98 \times 10^{-4} m^3/kg, D = 0.85 \times 10^{-8} kgs/m^3,$$

$T_0 = 293K$, $c = 1.2 \times 10^4 m^2/(s^2 K)$, $b = 0.9 \times 10^6 m^5/(s^2 kg)$, $\eta_0 = 8886.73 s/m^2$, and $\tau = 0.22$, $\tau_0 = 0.03$, $P_0 = 1$, $\theta_0 = 1$, $a = 1$ (non dimensional).

For numerical computational purpose MATLAB simulation technique is adopted. The variations of non-dimensional displacement $u(r, t)$, concentration of the diffusion material in the elastic body $C(r, t)$ and temperature changes $\theta(r, t)$ with the radial distance $r = |r^* - a|$ (non-dimensional) are shown graphically in Figures 2–10 for a thermo-elastic medium with spherical cavity in presence of a uniform rotation.

We have plotted radial displacement, in Figures 2–4, as a function of non-dimensional radius for various time ($t = 0.25, 0.5, 1.0$), different uniform rotation ($\Omega = 1, 2, 3$) and for variations in the relaxation times in thermal as well as mass diffusion respectively. In Figures 5–7 respectively, we have plotted the temperature distribution for the variations of time, uniform rotation and time delay. Concentration of the diffusion material in the elastic body with respect to the radial distance from the source of heat are represented by the Figures 8–10 respectively, for the deviations of time, uniform rotation and time delay.

From the Figures 2–4, it is observed that the displacement is increasing in nature with increasing values of time in the vicinity of the heat source. The displacement profiles are converging rapidly with radial distance from the boundary of the cavity. It is also observed
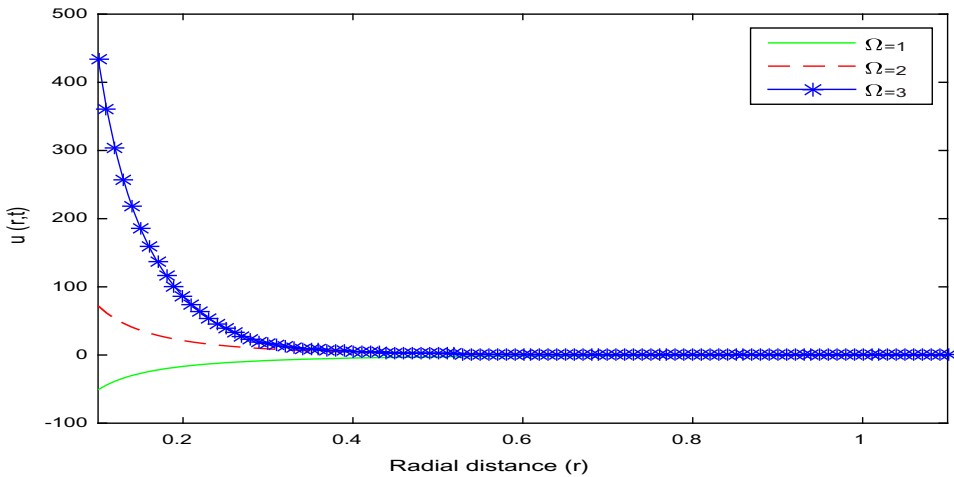
Figure 3. Variation of radial displacement with rotation.
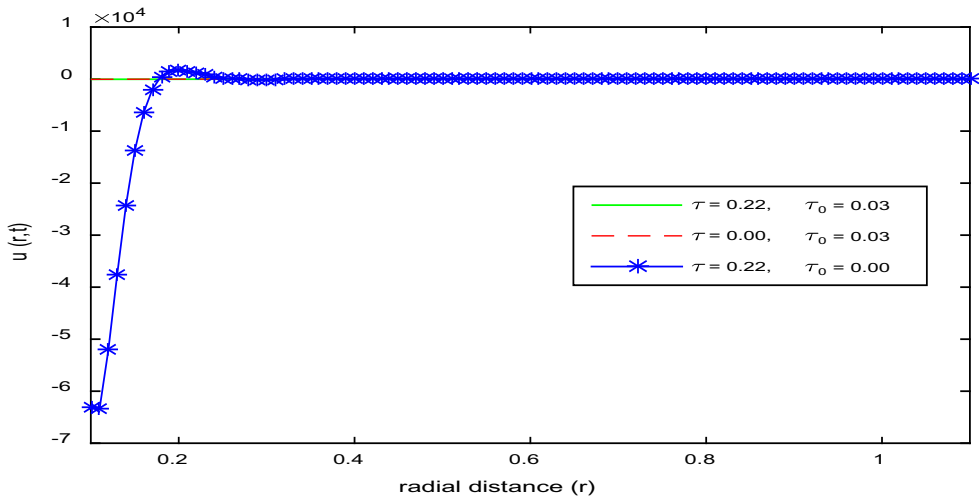
Figure 4. Variation of radial displacement with relaxation times.

that a uniform rotation could enhance the displacement near the boundary. The diffusive relaxation time is the dominating factor over the thermal time delay.

The temperature distributions with radial distance from the boundary of the cavity with respect to time variation, uniform rotation and for the different values of relaxation times are displayed in Figures 5–7. It is observed that in presence to a uniform rotation, initially temperature is decreased near the boundary, but with the increasing distance from the boundary a steady state nature is perceptibly shown. The effect of rotation over the temperature field is very much noticeable, without rotation the temperature field takes negative values, but in the presence of finite rotation the temperature fields manage to attain the positive values. In contrast, with displacement field, it is seen that, from the Figure 7, the thermal relaxation time marked its significance over temperature field.
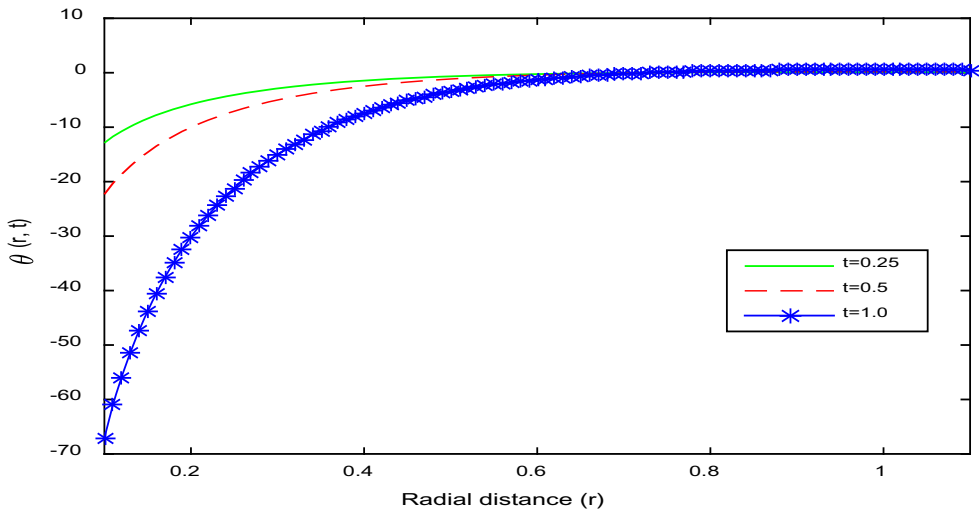
Figure 5. Variation of temperature distribution with time.
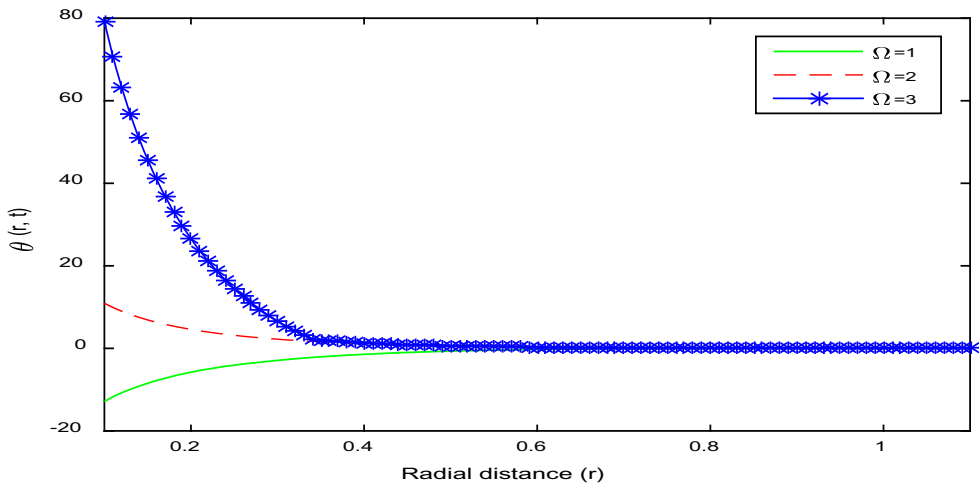
Figure 6. Variation of temperature distribution with rotation.

From the illustrated figures (Figures 5–7), it is found that near the vicinity of the cavity, the solution is markedly different. This is due to the fact that thermal waves in the coupled theory (i.e. $\tau_0 = 0$) travel with an infinite speed of propagation as opposed to a finite speed in the generalized case. On the surface of the cavity where the boundary conditions dominate the coupled theory and the generalized theories give very close results. Thus, the solution is not identically zero (though it may be very small) for some small value of time. At different instants, the non-zero region removes forward correspondingly with the passage of time. This indicates that the heat propagates as a wave with finite velocity.

From the Figures 8–10, it has been observed that the variation of the concentration of the diffusion material in the elastic body with radial distance. A uniform rotation can
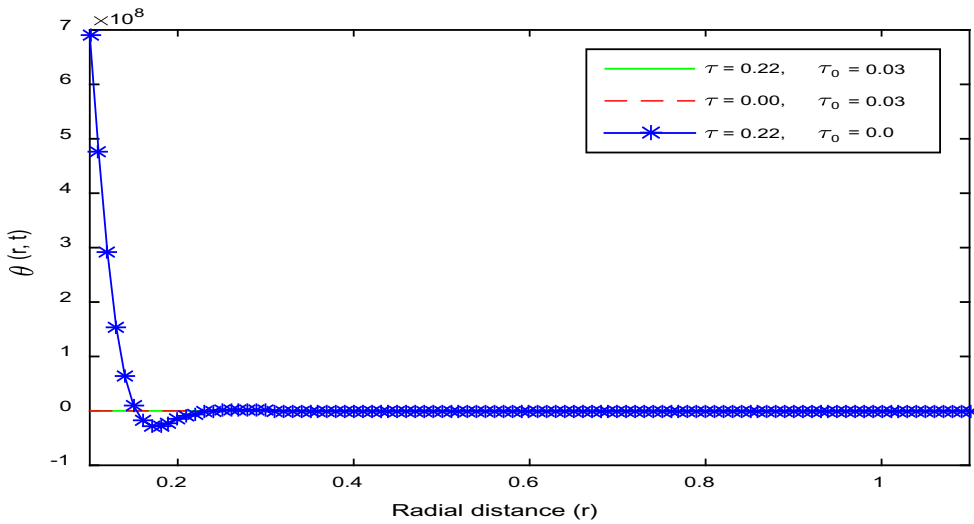
Figure 7. Variation of temperature distribution with relaxation time.
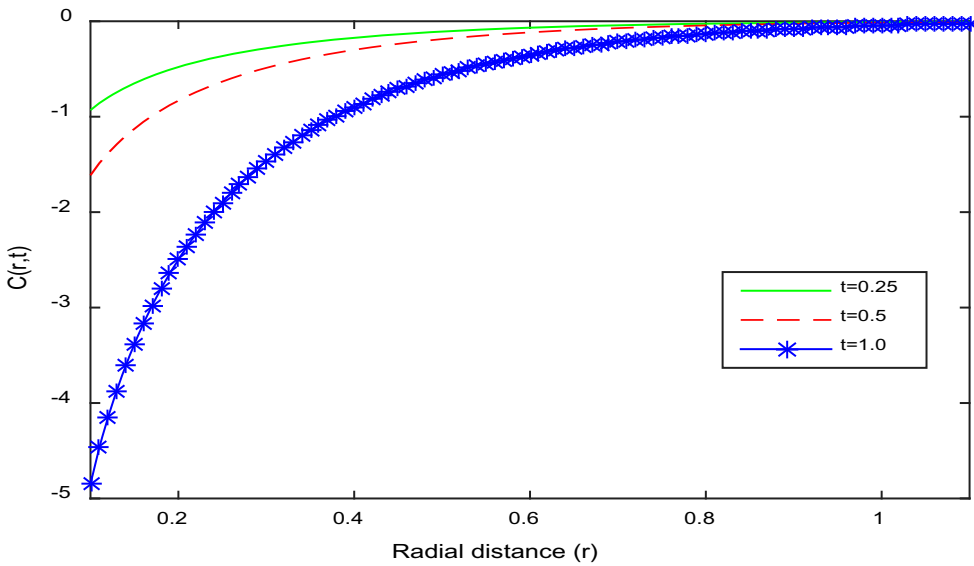
Figure 8. Variation of concentration of the diffusive material in the elastic body with time.

increase the concentration level of the diffusion material in the thermoelastic body. In addition, with increasing values of diffusion relaxation time can help to increase the diffusive concentration level.

The field functions attain their larger values with increasing elapsed time. This is due to the fact that the influences of coupling, effects thermal disturbances, arising strain and mass diffusion into the medium. Due to these coupling impacts, the thermal excitation produces
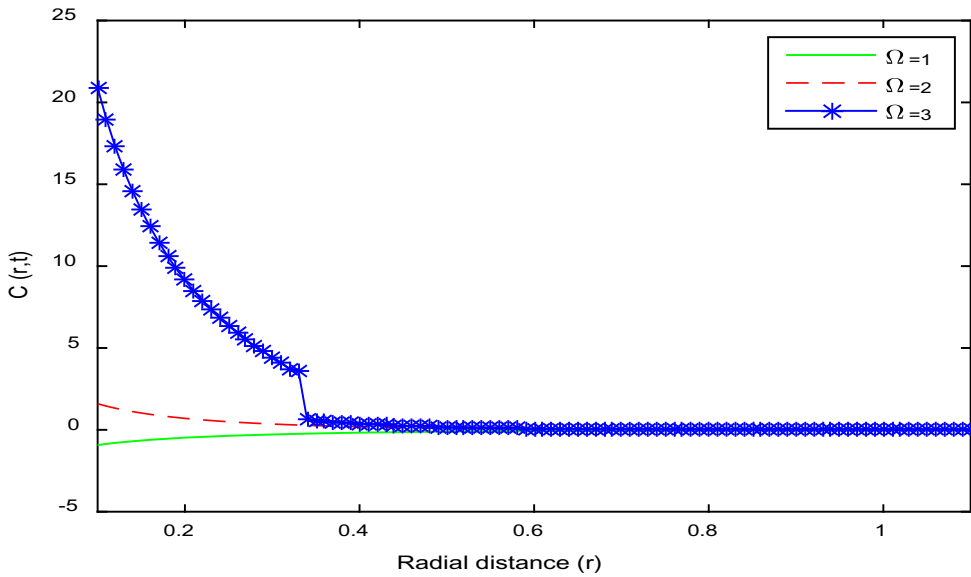
Figure 9. Variation of concentration of the diffusive material in the elastic body with rotation.
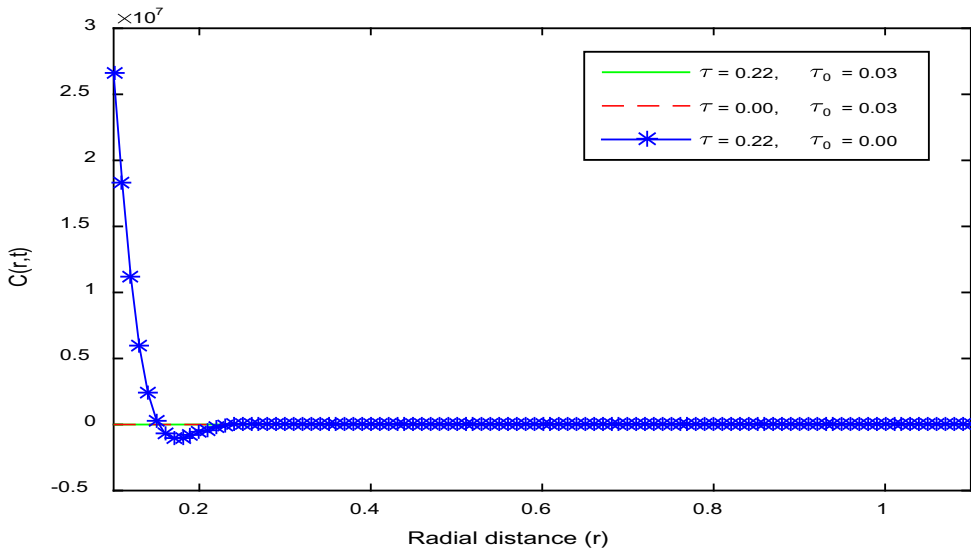
Figure 10. Variation of concentration of the diffusive material in the elastic body with relaxation time.

the supplementary responses. In fact, the more time is responsible for the exchange of thermal diffusion energy within the domain, consequently higher the values of the solutions are.

In Figures 11–13, the obtained results for the field functions (e.g. radial displacement, temperature changes and concentration of the diffusion material in the elastic body) are compared with the results of Aouadi [47]. The results show appreciable differences with those in the usual thermoelasticity theory without any rotation. Thus, rotation can enhance
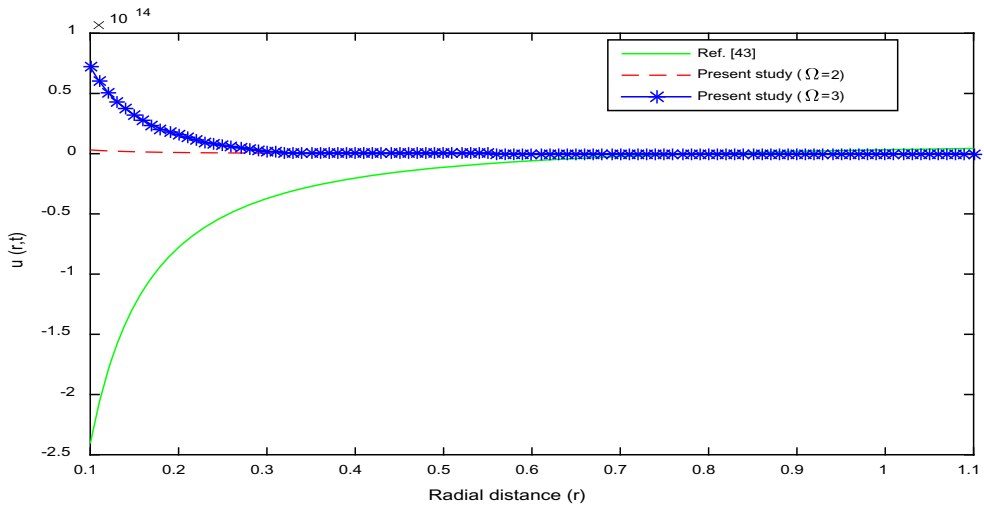
Figure 11. Comparison of radial displacements with Ref. [47].
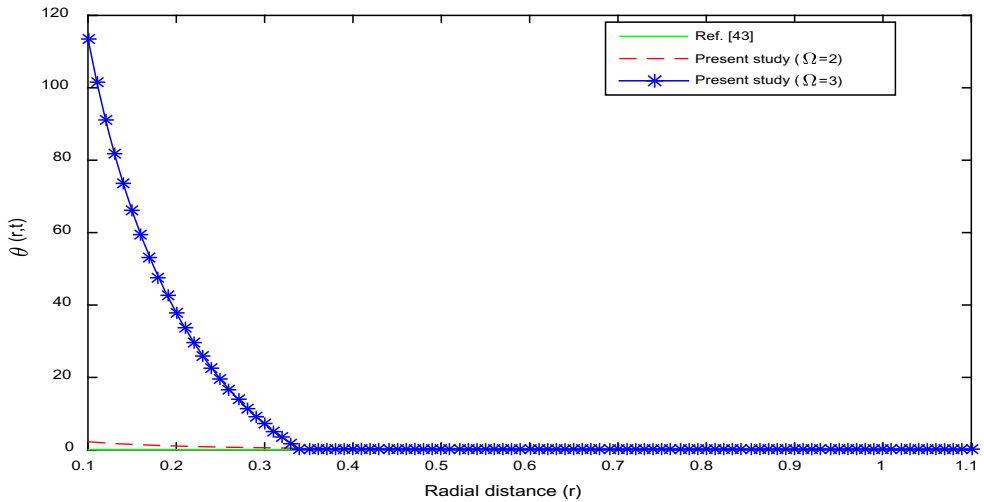
Figure 12. Comparison of temperature distribution with Ref. [47].

the thermoelastic deformation as well as the concentration of the diffusion material in an elastic body.

9. Conclusions

This article directly used, modified Bessel functions with a complex argument to study the thermo-diffusive problems of homogeneous, isotropic half-space with a cavity based on three-dimensional thermoelasticity. Due to rotation, the Coriolis and Centrifugal forces act as the cause of damping on thermoelastic diffusion. It is noticed that due to rotation the effect of thermoelastic diffusion into the medium is much less on the periphery of the cavity. Here we are concentrating on the impact of thermoelastic diffusion into the homogeneous
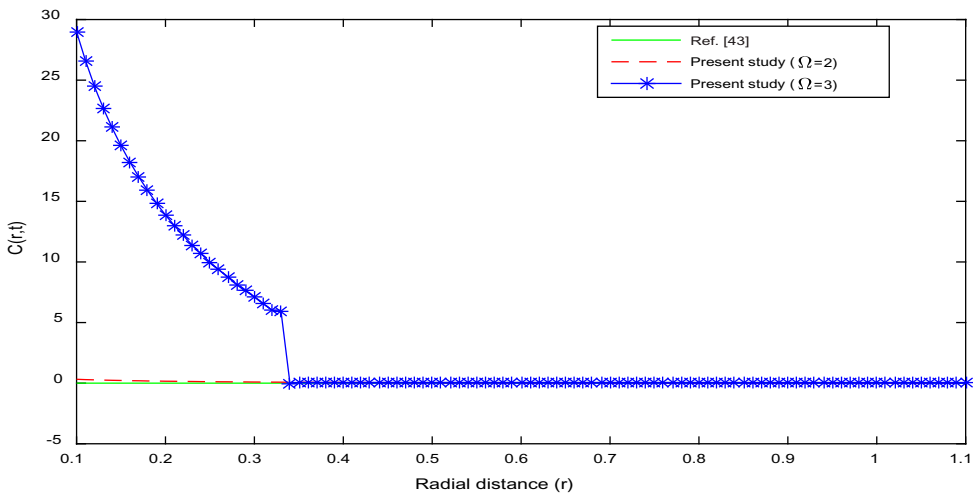
Figure 13. Comparison of concentration of the diffusive material in the elastic body with Ref. [47].

solids in very short time duration such that the influence of thermal time delay as well as diffusion relaxation time be taken into account.

With the view of theoretical analysis and numerical computation, we can conclude the following phenomena:

(1) The present article provides a detailed analysis of mass diffusion response on a thermoelastic disturbance in an unbounded elastic medium in the presence of a constant (in the form of Heaviside function) thermal load applied to the traction free boundary of the cavity.

(2) In Hyperbolic type heat conduction theory, the thermal time delay is the dominating factor over thermoelastic diffusive relaxation time.

(3) Rotation into the medium helped to enhance the thermoelastic mass diffusion in the homogeneous elastic body.

(4) The analyzed deformation and mass diffusion in the very short time interval, consequently, this investigation, though the analysis is theoretical, is a very helpful for heat flux and high-frequency domain.

(5) The theoretical analysis and computational results confirm that mass diffusion can increase the disturbance in the thermoelastic field.

(6) One can select the appropriate amount (rps) of rotation to enhance the effect of mass diffusion in the theory of hyperbolic thermoelasticity. It is encouraging that diffusion relaxation will also make sense in comparison to other thermoelastic time delay.

(7) The theoretical developments presented in this article may be useful for researchers who are working in the fields like, material science, theoretical and mathematical physics, and the development of the hyperbolic thermoelasticity theory.

Disclosure statement

No potential conflict of interest was reported by the author(s).

ORCID

Mohamed I. A. Othman ⬦ http://orcid.org/0000-0002-9577-5479

References

[1] Duhamel J. Some memoire sur les phenomenes thermomechanique. J. de L Ecole polytechnique. 1837;15:1–31.

[2] Neumann F. Vorlessungen Uber die theorie der Elasticitat. Brestau: Meyer; 1885.

[3] Biot MA. Thermoelasticity and irreversible thermo-dynamics. J Appl Phys. 1956;27:240–253. DOI:10.1063/1.1722351

[4] Lord HW, Shulman Y. A generalized dynamical theory of thermoelasticity. J Mech Phys Solids. 1967;15(5):299–309. DOI:10.1016/0022-5096(67)90024-5

[5] Green AE, Lindsay KA. Thermoelasticity. J Elast. 1972;2(1):1–7. DOI:10.1007/BF00045689

[6] Suhubi E. Thermoelastic solids in continuum physics, Vol. 2. Eringen AC, editor. New-York: Academic Press; 1975.

[7] Green AE, Naghdi PM. A re-examination of the basic postulates of thermodynamics. Porc Royal Soc London (A). 1991;432:171–194.

[8] Green AE, Naghdi PM. Thermoelasticity without energy dissipation. J Elast. 1993;31:189–208. DOI:10.1007/BF00044969

[9] Green AE, Naghdi PM. On uncoupled heat wave in an elastic solid. J Therm Stress. 1992;15:253–264.

[10] Dhaliwal RS, Sherief HH. Generalized thermoelasticity for anisotropic media. Quart Appl Math. 1980;38(1):1–8.

[11] Akoum F, Klapisz C. Influence on thermal diffusion of the inclination of a column with both ends closed. Int J Heat Mass Transfer. 1979;22(7):1147–1149. DOI:10.1016/0017-9310(79)90187-X

[12] Shaw S, Mukhopadhyay B. Thermoelastic waves with thermal diffusion in an isotropic micropolar plate. J Eng Phys Thermophys. 2015;88(5):1264–1273. doi:10.1007/s10891-015-1308-1

[13] Othman MIA, Eraki EEM. Generalized magneto-thermoelastic half-space with diffusion under initial stress using three-phase-lag model. Mech Base Design Struct Mach, Int J. 2017;45(2):145–159. DOI:10.1080/15397734.2016.1152193

[14] Sharma JN, Sharma YD, Sharma PK. On the propagation of elastothermo-diffusive surface waves in heat conducting materials. J Sound Vib. 2008;315(4):927–938. doi:10.1016/j.jsv.2008.01.011

[15] Said SM, Othman MIA. Effects of diffusion and internal heat source on a two- temperature thermoelastic medium with three-phase-lag model. Arch Thermody. 2018;39(2):15–39. DOI:10.1515/aoter-2018-0010

[16] Shaw S, Mukhopadhyay B. Theory of generalized micropolar thermoelastic diffusion. Int J Appl Math Mech. 2013;9:1–23.

[17] Marin M, Baleanu D, Vlase S. Effect of micro-temperatures for micropolar thermo- elastic bodies. Struct Eng Mech. 2017;61(3):381–387. DOI:10.12989/sem.2017.61.3.381

[18] Marin M. An uniqueness result for body with voids in linear thermoelasticity. Rendiconti di Matematica, Roma. 1997;17(7):103–113.

[19] Marin M. An evolutionary equation in thermoelasticity of dipolar bodies. J Math Phys. 1999;40(3):1391–1399. DOI:10.1063/1.532809

[20] Kaur I, Lata P. Rayleigh wave propagation in transversely isotropic magneto thermoelastic medium with three phase lag heat transfer and diffusion. Int J Mech Mater Eng. 2019;14(12):1–11. DOI:10.1186/s40712-019-0108-3

[21] Lata P, Kaur I. Thermomechanical interactions in transversely isotropic magneto- thermoelastic medium with fractional order generalized heat transfer and hall current. Arab J Basic Appl Sci. 2020;27(1):13–26. DOI:10.1080/25765299.2019.1703494

[22] Lata P, Kaur I. Thermomechanical interactions in transversely isotropic magneto- thermoelastic solid with two temperatures and without energy dissipation. Steel Comp Struct. 2019;32(6):779–793. DOI:10.12989/scs.2019.32.6.779

[23] Lata P, Kaur I. Thermomechanical interactions due to time harmonic sources in a transversely isotropic magneto thermoelastic solids with rotation. Int J Microstruct Mater Properties. 2019;14(6):549. DOI:10.1504/IJMMP.2019.103190

[24] Podstrigach YS. Differential equations of the problem of thermodiffusion in isotropic deformable solidsm. Doklady Acad Sci Ukrain SSR. 1961;2:169–172.

[25] Podstrigach YS, Pavlina VS. Differential equations of thermodynamic processes in n-component solid solutions. Soviet Mater Sci. 1966;1:259–264.

[26] Nowacki W. Dynamical problems of thermodiffusion in solids II. Biol Bull Acad Sci Tech Sci. 1974;22:129–135.

[27] Nowacki W. Problems of thermodiffusion in solids III. Bull Pol Acad Sci Tech Sci. 1974;22:257–266.

[28] Nowacki W. Dynamical problems of thermodiffusion in solids. Proc. Vib. Prob. 1974;15:105–128.

[29] Shaw S. A thermodynamic analysis of an enhanced theory of heat conduction model: extended influence of finite strain and heat flux. Int J Eng Sci. 2020;152:103277.

[30] Shaw S, Mukhopadhyay B. Periodically varying heat source response in a functionally graded microelongated medium. Appl Math Comp. 2012;218(11):6304–6313. DOI:10.1016/j.amc.2011.11.109

[31] Shaw S, Mukhopadhyay B. Theory of fractional ordered thermoelastic diffusion. The Eur Phys J Plus. 2016;131(6):183–193. DOI:10.1140/epjp/i2016-16183-6

[32] Sherief HH, Hamza FA, Saleh HA. The theory of generalized thermoelastic diffusion. Int J Eng Sci. 2004;42:591–608. DOI:10.1016/j.ijengsci.2003.05.001

[33] Li Y, He T. A generalized thermoelastic diffusion problem with memory dependent derivative. Math Mech Solids. 2019;24(5):1438–1462. DOI:10.1177/1081286518797988

[34] Abouelregal AE. Generalized mathematical novel model of thermoelastic diffusion with four phase lags and higher-order time derivative. Euro Phys J Plus. 2020;135:263. DOI:10.1140/epjp/s13360-020-00282-2

[35] Davydov SA, Zemskov AV, Akhmetova ER. Thermoelastic diffusion multi- component half-space under the effect of surface and bulk unsteady perturbations. Math Comput Appl. 2019;24(1):26. DOI:10.3390/mca24010026.

[36] Othman MIA, Atwa SY, Farouk RM. The effect of diffusion on two-dimensional problem of generalized thermoelasticity with Green-Naghdi theory. Int Commun in Heat and Mass Transfer. 2009;36(8):857–864. DOI:10.1016/j.icheatmasstransfer.2009.04.014

[37] Marin M, Chirilă A, Othman MIA. An extension of Dafermos's results for bodies with a dipolar structure. Appl Math Comp. 2019;361:680–688. DOI:10.1016/j.amc.2019.06.024

[38] Marsden JE, Hughes JR. Mathematical Foundations of elasticity. New York, Dover: Prentice Hall; 1983.

[39] Marsden JE, Ratiu T. Introduction to mechanics and symmetry. New York: Springer; 2003.

[40] Schoenberg M, Censor D. Elastic waves in rotating media. Quart Appl Math. 1973;31:115–125. Available from: https://www.jstor.org/stable/43636594

[41] Davies B, Martin B. Numerical inversion of the Laplace transform: a survey and comparison of methods. J Comp Phys. 1979;33(1):1–32. DOI:10.1016/0021-9991(79)90025-1

[42] Honig G, Hirdes U. A method for the numerical inversion of Laplace transforms. J Comp Appl Math. 1984;10(1):113–132. DOI:10.1016/0377-0427(84)90075-X

[43] Epstein CL, Schotland J. The bad truth about Laplace's transform. SIAM Rev. 2008;50:504–520.

[44] Gzyl H, Tagliani A, Milev M. Laplace transform inversion on the real line is truly ill-conditioned. Appl Math and Comp. 2013;219(18):9805–9809. DOI:10.1016/j.amc.2013.03.112

[45] Lekhnitskii SG. Theory of elasticity of an anisotropic body. Moscow: Mir; 1980.

[46] Kar A, Kanoria M. Generalized thermoelastic functionally graded orthotropic hollow sphere under thermal shock with three-phase-lag effect. Eur J Mech A/ Solids. 2009;28:757–767. DOI:10.1016/j.euromechsol.2009.01.003

[47] Aouadi M. A problem for an infinite elastic body with a spherical cavity in the theory of generalized thermoelastic diffusion. Int J Solids and Struct. 2007;44(17):5711–5722. DOI:10.1016/j.ijsolstr.2007.01.019

Source details

Feedback ›   Compare sources ›

Waves in Random and Complex Media

Formerly known as: Waves in Random Media

Scopus coverage years: from 2005 to 2023

(coverage discontinued in Scopus)

Publisher: Taylor & Francis

ISSN: 1745-5030   E-ISSN: 1745-5049

Subject area: (Engineering: General Engineering)   (Physics and Astronomy: General Physics and Astronomy)

Source type: Journal

View all documents ›   Set document alert   🖫 Save to source list

CiteScore 2022   ⓘ
6.4

SJR 2022   ⓘ
0.483

SNIP 2022   ⓘ
1.077

CiteScore   CiteScore rank & trend   Scopus content coverage

anveṣak

A bi-annual journal

Sardar Patel Institute of Economic and Social Research

Contents of the Past Issues

Vol.42 January-December 2012 No.1 & 2	
Key Note Address: Problems and Prospects	Yoginder K. Alagh
Economic Viability and Sustainability of Small Scale Farming: A Study in the Irrigated Gangetic Plains of UP	Ajit Kumar Singh
Food Security Aspects and Diversification of Demand in the Context of Gujarat	Niti Mehta
Rationalisation of Agricultural Subsidies: Study of Electricity and Fertiliser Subsidies in Karnataka and Tamil Nadu	Elumalai Kannan
Institutional Reform for Water Use Efficiency in Agriculture	Jharna Pathak
Political Economy of the Energy-Groundwater Nexus in India: Exploring Issues and Assessing Policy Options	Tushaar Shah, Mark Giordano and Aditi Mukherji
Positive and Normative Aspects of Price and the Market in Indian Agriculture-A Look at Government Policy Interventions in Food Management in an Unchanging Narrative of Traditional Agriculture	Munish Alagh
Land, Livelihoods, and State in India: Issues and Challenges	Sukhpal Singh
Sustainability of Rice Cultivation in the Kole Land of Kerala	Jeena T. Srinivasan
Growth of Paddy Production in India's North Eastern Region: A Case of Assam	Komol Singha
Determinants of Non-Farm Employment in Rural Uttar Pradesh	Vachaspati Shukla
How Sustainability Can be Ensured in Uncomfortable Nexus of Water, Agriculture and Institutions?	Dalbir Singh

Vol.41   January-June 2011   No.1

Vol.40   January-December 2010   No.1-2

Vol.39	January-June 2009	No.1
Contract Farming in Two Horticultural Crops: A Perspective	S.R. Asokan & Anita Arya	
Equity and Livelihood Issues in Watershed Development Evidences from Andhra Pradesh	U. Hemantha Kumar	
Growth of Revenue Receipts of Indian States - A Comparative Study	Himani Joshi	
Credit Cooperatives and Financial Inclusion - Evidence from India	KRamesha	
An Examination of Foreign Institutional Investment and Stock Market Returns in India: Evidence from ARDL Bounds Testing Approach	P Srinivasan & KShamBhat	
Ownership Pattern, Size and Growth of Firms in India - An analysis	Maneet Gill & Kuldip Kaur	
A Perspective on Global and Bilateral Trade Behaviour in India and China	Anjali Tandon	

Vol.38	July-December 2008	No.2
The Indian Development Perspective: Thoughts on Desirable Future Can Micro Finance Provide a Sustainable Solution for Poverty? Some Empirical Evidences from Gujarat	Yoginder K. Alagh Neha Shah	
Resource Use Efficiency: An Application to Public Owned Lands in Tamil Nadu	Rajendra T, K Palanisami & M. Jegadeesan	
The Income Elasticity of Public Expenditure in Andhra Pradesh: An Empirical Exercise	B Narayana	
Does Indian Public Sector Banks Persist Profits - A Pre and Post Reform Period Analysis	Siva Reddy Kalluru, Vijay Bhaskar Reddy M & Aranath G.	
Reforms in Public Sector Enterprises in India: A Review	P. Venkataramana	
Growth and Profitability of Acquiring Firms in India: An Analysis	Kushwinder Kaur & Kuldip Kaur	
Trade Competitiveness in ASEAN	P R Bhatt	
Book Review		
Protecting the Vulnerable Poor in India: The Role of Social Safety Nets	S P Kashyap	

Shift in the Growth of Productivity of Agricultural Crops in Andhra Pradesh: An Empirical Research	B Narayana
Area irrigated by different sources in Andhra Pradesh: An analysis of Disparities across the districts at a point of time	M Upender, AG Moss TKN Swamy & I Daisy
Estimation of Abatement cost of air pollution in Durgapur city of West Bengal	Kakali Mukhopadhyay & Souvik Bhattacharya
Growth, Immiserization and Inequality: An Inter-State analysis International Labour Organization - Its impact on labour legislation in India: A Status Paper	S Abdul gulam P Venkataramana
Rural Credit and Micro Finance in India: An analysis Women entrepreneurship in India: An Analysis Study of Interrelatedness in Indian Economy: An input output approach	Kuldip Kaur, Seema Saini DPullaRao Aditya K Patra
Book-Review	
Rural Non-Farm Employment in India-A Focus on Food for work	Tattwamasi Paltasingh

Imbalances in Development between Regions and Social Groups: Evidences from Gujarat	Niti Mehta
Assessment of Food Security Situation for Disaster Risk Management: An Analysis for the Gujarat State	Gajendra Singh and T.S.Bhogal
Role of Community Pressure in Environmental Regulation : An Empirical Analysis	Trupti Mishra
Evaluating Technical Change : An Application to Indian Sunrise Industries	Biresh K. Sahoo
Need for a Paradigm Shift in Rural Employment Policies	Anita Arya
Book-Review	
Liberalization and Urban Social Services	Niti Mehta

Vol.35   July-December 2005   No.2

The Economics of Forestry in India	Y.K. Alagh
Agro -Processing in Gujarat: Role of Contract Farming and Cooperatives	Anita Arya
Managing Water Scarcity and Rural Conflicts in India	Shy am Sunder Prasad Sharma
Environment and Population Growth in India -An Analysis	Inder Pal Kaur and Shveta Sharma
Defining Disabilities :NSSO v/s Census	Kishor Bhanushali
Role of the State in Social Sector : Some Reflections	T. Nirmala Devi
New Vistas in Entrepreneurship Development	M. S. Chhikara and Sahay
The Trade Related Intellectual Property Right (Trips) Agreement and the Developing Countries	M. Lakshmi Narasaiah
Book- Review	
Social Structure and Change: Women in Indian Society	Tattwamasi Paltasingh
The Development State in History and in the Twentieth Century	S. P. Kashyap

Vol.35   January-June 2005   No.1

Poverty among Agricultural Laborers in Tarai Region of Uttar- Pradesh and Uttaranchal : Measurement Identification and Determinants	Anil Kumar Singh, A. K. Singh and S. P .R. Chaurasia
Economics of Production and Marketing and Off-Season Vegetables in Himachal Pradesh	Y Chakrabarty Singh, R. S. Prasad and Y. S. Negi
Empirical Analysis of Health Sector HumanResource Developmentof Himachal Pradesh	Devinder Sharma
Consumption Behavior of the Elderly : The Life Cycle Hypothesis	B. C. Mehta and Karntikapor
Women Employee in the Emerging Service Sector : A Case Study	Sujatha Sony Onattu
Globalized Indian Economy : Some Reflections on Workers Mobility	Bhaskar Majumdar
Book Review	
Urbanization in India: Sociological Contribution	C. N. Ray

Irrigation Facilities and Copping Pattern in Andhra Pradesh -A Special Survey	N. Damodar Reddy
A Study on Growth and Instability of Crop Production in Andhra Pradesh : A District Level Analysis from 1971-2001	K. Pochanna
Seasonal Variability of Income and Employment of Agricultural Labour in Tarai Regions of Uttar-Pradesh and Uttaranchal	Anil Kumar Singh,A. K. Singh and S. P .R. Chaurasia
Determinants of Rural Non -Farm Employment in India-An Interstate Analysis	Kuldeep Kaur
Strategies for Reducing Inter-District Disparities in the Levels of Development in U.P.	V.S.Singh
Swaranjayanti Gram Swarojgar Yojana brought Swarna to Farmers : A Study of Ahmednagar District in Maharashtra	Shankar Chatterjee
Managing Jan Sikshan Sansthans-The Institutional Way	M. S. Chhikara
Book-Review	
Girls Schooling Womens Autonomy and Fertility Change in South Asia	Niti Mehta

Vol.32   June 2002   No.1

Some Aspects of State Government Expenditure : A Case Study of Gujarat -1980-81 to 1997-98	K.M.Parekh
Surplus Generation Process by Micro Enterprise in Non-Farm Sector in Gujarat	S.P.Kashyap, Jayshree Shah
Behavior of Area ,Production and Yield of Food grain Across States During Last Two Decades	Anita Arya, S.N.Joshi
Rural-Urban Migration and Socio Economic Change : A Case Study	Preet Mohinder Pal Singh
Demand Function for Cargo Services of Indian Airlines	Danish A Hashim
Globalization and the Growing Convergence of the World	Mukesh Puri
Nature and Causes of Inflationary Growth in Nigeria (1980-2000) : An Empirical Investigation	Ajie H.A.
Irrigation Projects Rehabilitation Problems and Ecological Crisis	Arun Prabha Choudhary, Samuel M.Mwawasi
Water Environment and Agricultural Development in India	Shyam Sunder Prasad Sharma
Book-Review	
Economic Reforms - Development and Finance (2002)	M.S.Chhikara
Rural Industrialization in Kerala: Its Dynamics and The Local Linkages	Shankar Chatterjee
Commodity Taxes in India : Directions for Reforms	Mukesh Puri

Population of Gujarat: An Overview and Perspective	P.J.Jhala
Finance of Gujarat State : An Enquiry into the Federal Finance Relations	Himmat Patel
Agricultural Development in Gujarat -Performance and Future Strategy	Arun S.Patel
Forestry and Environmental Concerns of Gujarat	Rohit Shukla
Water -A Scarce and Valuable Resource	C.C.Patel
Gujarat: 2010: Challenges in Education	Ramesh B. Shah
Employment and Human Resource Development	A.K.Pradhan,J. G.Pandya ,S.P. Gosai
Urbanization and Urban Development	G.R.Aloria
Infant Mortality Rate : Issues and Experience	Sewa Rural Team
Women's Development and Empowerment	Illaben Pathak
Liberalization in Gujarat: A Review of Recent Experience	Ravinder H.Dholakia
A Perspective on Gujarat's Development with Emphasis on Human Resources	S.P.Kashyap

Vol.30   June 2000   No.1

Vol.28   December 1998   No.2

Vol.27　　　June-December 1997　　　No.1-2

Conference Volume : Issues on Infrastructure Development in India – Guest Editor Jayshree Shah

Introduction : Issues of Infrastructure Development in India	Jayshree Shah
Status of Infrastructure in the Irrigation Sector	D.T.Buch
Irrigation Infrastructure Policy and ACRP	S.N.Joshi
Irrigation Infrastructure in India : Nature of Development and Consequences	A.S.Patel,H.P. Trivedi
Infrastructure Planning	Y.K. Alagh, Jayshree Shah, Vinod Shah
Economic Operation of the Maharashtra Power System	Rajeev K. Chaturvedi, K.Bhattacharya and Jyoti Parikh
Human Capital for Development and the Development of Human Capital in India	Jandhyala B. G. Tilak
Issues in Indian Educational Development	Surjit Singh
Total Literacy Campaign : Gujarat Experience	Gokul O.Parikh
Some Methodological Nuances in Organizing Literacy Campaign	Yoganand Shastry Chaturvedi
Development Management in Metropolitan Periphery : A Case of Western Ahmedabad	H.M. Shivanand Swamy, V.P.Bharadwaj and Turush Chandra
Spread of Infrastructure Facilities in Rural Gujarat: A Preliminary Exercise	Manjari Kashyap
New Concepts of Infrastructure Development for Industries	P.J.Divetia

Vol.26	June 1996	No.1
Regional Development in the Perspective of Allied Agricultural Activities : A Case Study of Gujarat	Pravin G.Pathak	
Growth of Agricultural Production and Productivity in Punjab 1970-73 through 1990-93: A Component Analysis	K.K.Dhindsa,Anju Sharma	
National Resource and Changing Agrarian Relations in Himachal Pradesh to Sustainable Use	Dalbir Singh	
Demand Management of Water : A Review	Ratna Reddy	
Rural Social Transformation in India : Some Thoughts	Surjit Singh	
Book-Review		
Future of Computerization in Institution of Higher Learning	Uday an K. Mandavia	
Information India 1992-93: Global View	Amita R. Patel	
Pricing Behavior in Philippine Corn Markets : Implications for Market Efficiency	Anita Arya	

Trends in Capacity Utilization : A Comparative Study Between State Public and Private Sector Manufacturing Industries and Kerala	Beena P.L.
Jari Industry : Yesterday and Today	Rohit D. Desai
Spread of Infrastructure Facilities in Rural Gujarat: A Preliminary Exercise	Manjari Kashyap
Land use and Food grain Production : An Inter-Country Comparison	S.N.Joshi
Book-Review	
Contraceptive Use and Fertility in India	Thomas Mathew
Adoption of Hybrid Maize in Zambia : Effects on Gender Roles, Food Consumption and Nutrition	S.N.Joshi
Structure and Administration of Sales Taxation in India	K.M.Parekh
Education and Value in the Mahabharata	Rohit D. Desai

Vol.25	June 1995	No.1
Agricultural Development Perspective -Gujarat	S.N.Joshi	
Organizational Efficiency and Indian Industry : A Firm Level Analysis	P. Rameshan	
Poverty Alleviation and Decentralized Rural Development in India : A Case Study In West Bengal	Surjit K Dutta, Dilip K Ghosh	
Growth and Structural Changes in Indian Economy	Anil K Yadav	
Viewpoint on the Gujarat Economy		
Gujarat: The Decisive Phase	Y.K. Alagh	
Industrial Scene in Gujarat - A Contrast of Two Patterns	S. P. Kashyap	
Emerging Water Scenario in Gujarat	G. S. Guha	
Book-Review		
Employment ,Earnings and Poverty-A Study of Rural India and Indonesia	Indira Hirway	

Vol.24   December 1994   No.2

Vol.24   June 1994   No.1

Constant Elasticity of Substitution Production Functions of Gujarat Industries : A Case Study of Factor-Use Pattern	G. Pravin Pathak
Performance on Principal Exports of India	P.C.Verma
The Impact of Price Movements of Areas Under Groundnut in North Arcot District	R. Cauvery, U. K. Sudha Nayak R.Meenakshi
An Analysis of Nigeria's Public Expenditures: 1970-1991	John C Anayanwu
Development of Banking System And Demand for Money in India : Further Results	M.S.Trivedi
Effects of Monetary Uncertainty on Rate of Inflation : Evidence from the Indian Economy	Far had Bazargan
Book-Review	
Industrial Development Policy of India	Jayshree Shah
Indian Economy in Transition : Structural Reforms	H.N.Desai

Vol.21	June 1991	No.1
Regional Cost Advantages : A Study of Gujarat Industries in a Comparative Spatial Dimension	Pravin G.Pathak	
Intertemporal Interindustry Linkage Pattern of Gujarat Manufacturing Industries	Himal Chandel	
An Analysis of Inflation and Relative Price Variability in India	R.J.Mody, B.C.Thaker	
Surplus Labor in Agriculture in the Context of Technological Change : An Analysis of Andhra Pradesh	V.Ratna Reddy	
Rural to Urban (Male) Decadal District In-Migration Model, 1971,1981 (Rajasthan)	B. C.Mehta, Anju Kohli	
Stability of Agricultural Prices in Gujarat	Anita Arya	
Irrigation and Intensity of Cropping : A Cross Section Analysis at State Level	S.S.Yadav	

Vol.18 June-December 1988 No.1-2

Vol.17   December 1987   No.2

Poverty : Concepts, Measurement and Reoriented Strategy for Its Alleviation	V.S.Singh
Changing Structure of Sectoral Distribution of Per-Capita Income in Non- Agricultural Sector in India	B.C.Thaker
VES Production Function with Neutral Technological Change -A Comparative Study of the Industrial Sectors of Gujarat State Vs All India	K.C.Soni, B.B.Jani
Comparison of Regional Input-Output Table - Rajasthan, Punjab and Haryana	K.K.Saxsena, Ira Bhatnagar
Input-Output Allocation Model for India - A Note	Arun Sen- Gupta
Returns to Scale and Elasticity of Substitution of a Few Manufacturing Industries of Assam : A Note	Mohd.Islamuddin
Book-Review	
Land Reforms in India	Rohit Shukla
Book Abstracts	
Uttar Pradesh in Statistics	Kripa Shankar
Farmer's Movement in India	M. V.Nandkarni
Economic Activities of Children	B.M.Dinesh
Panchayati Raj and The Weaker Sections	U.Gurumurty
Alternatives in Industrial Development -Sugar-cane Processing in India	H.H.De.Haan
Energy Environment in Agriculture	Somu Giriappa
Land Power and People 1981-70 Rural Elite in Transition	Rajendra Singh
Social Values and Development: Asian Perspectives	Durganand Sinha, Henry S.R.Kao
The Hour of the Fox	Roberts Anderson, Water Huber
Small Scale Enterprises in Industrial Development: The Indian Experience	Sage Publications

Vol.16 December 1986 No.2

Economics of Water Use in Dantiwada District Canal Command Area	Arun. S. Pate l, Haribhai. F. Pate l
Econometrics Models for India : A Review	Surjit Singh
Manpower Forecasting by Skills in a Perspective Planning Frame -Punjab	Autar S.Dhesi, Sunita Handa, Surjit Singh
Estimation of an Agricultural Production Function using Principal Components	C.V.Seshachalapathi, N.A.Rao
Agricultural and Economic Development in Gujarat	G.N.Joshi
Industrialization in Gujarat: An Analysis Over Time and Space	A.J. Vora

Vol.15   December 1985   No.2

The Real Balance Effect-Some Issues	K.M.Joshi, S.M.Joshi
Wage Relatives in an Open Economy - Its Economic Consequences	D.S.Pathak
The Dynamic Aspects of Power Sector and the Level of Economic Development in India	Jayshree Shah
Growth, Concentration and Efficiency, Prospects of Small Scale Industries of Gujarat	P.A.Amin
Aggregation Overtime in Distributed Lag Models	N.A.Rao

Vol.15   June 1985   No.1

The Demand Pull and Cost Push Inflation in India	P.N.Mathur
Regional Input-Output Modeling in India	Himal Singh
Estimation and Stability Tests of Some Demand for Money Functions	Paramdeep Singh
Growth Employment and Choice of Techniques- A Survey	A.M.Kadak
Underemployment Theory and Concepts in Different Work Situations -Some Issues	Joseph Abraham
Ph.D. Abstracts	

Vol.13   June 1983   No.1

Selected Papers from Seminar on Employment, Levels of living and Public Policy

Vol.10	June 1980	No.1
Regional Disparities in Rates of Growth and Productivity in Indian Agriculture : Causes and Remedies	Y.K.Alagh	
Adoption of New Seed Technology and Factors Associated with it in Gujarat	U.S.Sharma	
On a Random Coefficient General Function Form	G. V.S.N.Murty,Sukumari Murty	
Estimation and Testing of Economies of Scale in Household Consumption : An Application of Box-Cox Transformation	Naresh Shah	
Demand for Money in India : Results of an Alternative Functional Form	M.S.Trivedi	
On Estimating Net Fixed Capital Formation at Constant Prices in Registered Manufacturing Sector at State Level	Ravindra H. Dholakia,P.M.Patel	
Note on Capacity Utilization in Indian Cotton Textile Industry	Jayshree Shah	

Vol.9	June-December1979	No.1-2
Special Issue : Gujarat Economy 2001 A.D.		
Industry	P.G.Pathak	
Government Sector	Atul Sarma,K.M.Parekh	
Manpower	B.B.Patel,D.R. Veena	
Water	R. G.Nambiar	
Energy	K.K.Subrahmanian,D.R. Veena	

Vol.8	June-December1978	No.1-2
Special Issue: Gujarat Economy 2001A.D.		
Population	M.M. Gangotra	
Macro-Economic Framework	Y.K.Alagh, R.J.Mody,B.C.Thaker	
Perspective in a Consistency Frame	S.P.Kashyap	
Household Consumption	G V.S.N.Murty, Naresh Shah	
Agriculture and Animal Husbandry	Baldev Singh, U.S.Sharma	

Vol.7	June 1977	No.1
Employment Behavior in a Labor Surplus Economy in a Famine Situation: A Study of Gujarat	Rohit Shukla	
The Role of Credit in Agricultural Development: A Case Study of a Backward Indian District, Surendranagar	Baldev Singh	
Poverty, Inequality and Development: A Study of Rural Andhra Pradesh	S.A.R.Sastry	
Net Exchange Earnings, Economic Efficiency and Export Strategy: The Case of India	R. G.Nambiar	
Industrial Economy of Bangladesh and West -Bengal : Structural Comparisons with Inter-Industry Frame	Bhanwar Singh	
On a Non -Linear Expenditure System	K.N.Murty	
Incidence of Taxation on Sales of Households in Gujarat	K.B. Trivedi	

Vol.5   June-December1975   No. 1-2

Input-Output Economics	P.N.Mathur
Dynamic Inverse for Indian Economy	R.K.Koti
Leontief Capital-Output Ratios for Large Scale Manufacturing Industries, 1963	S.R.Hashim,M.M.Dadi
Incremental Machine Tool-Output Ratios for the Indian Economy	Y.K.Alagh, Jayshree Shah
A Model for Forecasting of Input-Output Coefficients An Aggregative Approach	H.Sarkar
Hicks Leontief Aggregation -Price and Quality Variants-An Empirical Exploration of Grouping of Commodities on the Basis of Hicks-Leontief Theorem of Aggregation	K.N.Prasad
Structural Decomposition of Indian Industrial Economy	R.D.Desai
A Review of Models for the Correction of Input-Output Forecast with Special Reference to the ECAFE Region	A. Ghosh,H.Sarkar and D. Chakraborty
Technology Change in Indian Economy -1953-54 to 1964-65	P .S.Shanmukham,K. V.Santhanam
Import Substitution in Indian Industry -A Case Study of Automobiles	D.U.Sastry
Input Structures of Specified Dyes Groups	S.D.Naik
Input-Output Models of Educational System with Applications to Indian Data	Shri Prakash
Inter-Industry Study of the Marathawada Region	R. G.Paithankar
Industrial Estates in Gujarat- A Preliminary Study of Linkage Patterns	S.P.Kashyap, Pravin G.Pathak, Jayshree Shah

Title	Author
Input-Output Model for Manpower Projection by Occupation and Educational Levels in Gujarat's Economy	D.R. Veena
Input Structure of the Coal Mining Industry -A Case Study on the Stability of Input Coefficients	N.Naganna
Determinants of Urban Local Expenditures-An Explorations in the Gujarat Context	Atul Sarma, K.M.Parekh, L.Tombi Singh
Some Results on the Power Regressions, with an Application to Indian Consumption Patterns	G. V. S. N. Murty, T. Suryanarayan
Econometric Models of Edible Oils Price Behavior	M.L.Jhala
Analysis of Sugar Industry-A Production Function Approach	S.S.Mehta
Estimation of the Elasticity of Substitution with the Stock of Capital from the Constant Elasticity of Substitution Production Function -An Interstate Production Study for Indian Industries	U.A.Kazi
Cotton Textiles Complex Analysis -A Preliminary Exploration	Rohit. D. Desai

Vol.4	June 1974	No.1
Growth and Productivity in Indian Industries	S.S.Mehta	
An Analysis of Selected Industries of Gujarat	R.J.Mody,P.V. George	
Cost, Size and Location of Colleges in Gujarat	D.T. Lakdawala, K.R.Shah	
Fiscal Performance of Andhra-Pradesh	S.S. Chandrashekhar	
Central Taxes in India: A Structural Analysis	K.V.Nambiar,K.C.Joshi	
A Fortran IV Computer A logarithm for Estimating a System of Non-linear Equations by Two- Stage Iterative Procedures	C. S.R.Murty, G V. S.N.Murty	
Notes: Hybrid Bajra- Cause of Breakthrough in Bajra Production in Gujarat State	Gunwant A.Patel, J.H.Pathak	
Production, Inter-Industry Use and Consumption of Edible Vegetable Oilseeds and Different Forms of Edible OilsinIndia,1951-1971	M.L.Jhala	

Reference Technology and Regional Forecasting	Y.K. Alagh, Rohit. D.
The Nature of Spatial Clusters of Indian Economy	R.Dhar
Growth Variants of a Regional Economy: Implications of Reduced Inequalities	S.P.Kashyap
A Very Skeptical Note on the Fifth Plan Approach to Solution of Economic Backwardness as Defined by the Planners	P. R. Brahmananda
Regional Planning as a Tool of Development Planning	R S.Rao, Sulbha Brahma
Formal Approaches to the Planning of Industrial Location	Nitin Desai
Delineation of Industrially Homogeneous Regions of Gujarat: Comparison of Regional Industrial Activity	Pravin G.Pathak
Acreage Response in Gujarat: An Inter-District Analysis	V.S.Misra
Note on the Study of Regional Inequalities in the levels of Living in India	D.B.Gupta
An Approach to Estimate Complete set of Demand Elasticities based on Two Stage Budgeting: With an Applications to the Patterns of Gujarat Demand	R.Radhakrishna, G.V.S.N.Murty
Pattern of Education and Economic Development: A Case Study of Gujarat	D.R. Veena
Inter-regional Migration in India	N.D.Kamle
Some Issues in Regional Planning	P. Venkatramiah
Gujarat's State Tax Revenue: Growth, Responsiveness, Determinants, and Projections	Atul Sarma, M.Govind Rao, R. Radhakrishna
The Regional Problem in India: Some Reflections on a Viable Strategy	Om Prakash Mathur
Regional Economic Policy: A Preliminary Framework	R.J.Mody

Vol.2	December 1972	No.2
Mobilization of Savings and Financial Assets	D. T. Lakdawala, R.J.Mody	
Consistent Forecasting Model of Gujarat's Economy	Y.K. Alagh, S.P.Kashyap, Rohit. D. Desai	
Technique of Cluster Formation in Regional Science	R.Radhakrishna, , G.V.S.N.Murty	
Spatial Economic Planning Models for India	D.T. Lakdawala, Y.K. Alagh, Atul Sarma	
Inventory Behavior and Efficiency of Credit Control	P.V. George	
Some Aspect of Concentration of Economic Power in Indian Manufacturing	Vinod.K. Gupta	
Manpower Utilization in Rural Maharashtra	N.D.Kamble	
Distribution and Growth of Urban Population in West Bengal	Atul Sarma, R.Radhakrishna	
West Bengal's Industrial Economy: An Analysis in Input-Output Framework	Bhanwar Singh	

Vol.2	June 1972	No.1
Gibrat' s Law and Growth of Corporations in Gujarat: A Regional Study	P.V. George	
Production Function for Gujarat Industries	Pravin G.Pathak	
Temporal Consumption Patterns of Tamil-Nadu	K.Kalirajan, G. V.S.N.Murty, B.P.Panapatte	
Determinants of Revenue in Developing Countries	K. V.Nambiar, M.Govind Rao	
Inter-Industry Wage Structure: Technology Hypothesis	T.S. Papola	
Derivation of Quadratic Type of Indifference Surfaces by Means of Linear Engel Curves	R. Radhakrishna	
Factor Structure of India's Foreign Trade	R .G.Nambiar	
On Consumption of Capital Coefficient: Linear Programming Approach	Shashikant Valavade	
Note on Capital Formation in the Central Government Sector during the Third Five Year Plan	R G.Paithankar	

Vol.1	June 1971	No.1
Growth of crop output in Gujarat: A component Analysis	V.N.Mishra	
Problems and uses of Regional Input-Output Models	Y.K.Alagh, S.P.Kashyap	
Reforms of Urban Property Taxes -A Case Study of Municipal Corporation in Gujarat	Shibshankar P. Gupta	
Regional Differentials in Industrial Wages in India	T.S. Papola	
Regional Cost Variations in Vanaspati and Edible Oil Industries in India	Y.K. Alagh, K.K.Subramanian, Rohit Desai	
Pricing Models of Edible Oil and Vanaspati Industries in India	Y.K. Alagh, K.K.Subramanian, Rohit Desai	
Commodity Taxation in India	D. T. Lakdawala, K V.Nambiar	
A Theory of the Price Level and the Rate of Interest	R.J.Mody	
Profitability and Growth of Firms: The case of Indian Chemical Industries	K.K.Subramanian, T.S. Papola	
A Note on the Level and Structure of Gujarat's Interregional Trade	Jyoti D. Thakkar	

UGC-CARE List

You searched for **"0378-4568"**. Total Journals : **1**

Search: [   ]

Sr.No.	Journal Title	Publisher	ISSN	E-ISSN	UGC-CARE coverage years	Details
1	Anvesak	Sardar Patel Institute of Economic and Social Research	0378-4568	NA	from June-2019 to Present	View

Showing 1 to 1 of 1 entries

Previous 1 Next

Home

UGC

Search

SAVITRIBAI PHULE PUNE UNIVERSITY

Catalytic potency of zeolite Y immobilized copper-2,2′-bipyridine hybrid complex in oxidation of olefins

Rajesh Bera[1] · Chandan Adhikary[2]

Abstract

A zeolite immobilized hybrid catalyst $[Cu(bpy)_2]^{2+}$NaY [bpy = 2,2′-bipyridine](**1**) was prepared by immobilizing Cu(II)-bipyridine complex onto NaY zeolite and characterized by spectral methods. X-ray powder diffraction analysis of **1** revealed that the structural integrity of the mother zeolite in the hybrid material remained intact upon immobilization of the complex. Spectroscopic studies showed that the coordination geometry of **1** undergoes a significant distortion when it is entrapped in the zeolite cavity. The catalytic oxidation of a series of alkenes was carried out with the neat and the immobilized complexes in the presence of the ecofriendly oxidant tert-BuOOH (TBHP) at an ambient condition. The catalyst exhibited excellent catalytic potency and product selectivity, with respect to the neat complex in these reactions. The activity of the immobilized catalyst remained nearly the same after several cycles, indicating the true heterogeneous nature of the catalyst.

Keywords Zeolite Y · Copper-2,2′-bipyridine · Catalysis · Oxidation · Olefins

1 Introduction

Over the last few decades, epoxidation of alkenes using peroxides as oxidants has become a captivating research area, because the epoxide products are an important class of industrial chemicals that have been used as versatile chemical intermediates [1]. Catalysts derived by immobilization of transition metal complexes in microporous or mesoporous matrices [2–4] by various means have been employed in epoxidation reactions in recent times [5–7]. The heterogenization of transition metal complexes on zeolites, mesoporous silicate materials, polymers or activated carbons, MOFs etc. is an area of flourishing research interest [8–12]. Immobilization of analogues of homogeneous catalysts in a porous solid support makes the hybrid materials industrially important, because the hybrid catalysts offer the advantage of shape selectivity and site isolation retaining

and often enhances the catalytic activity of the metal complex [13]. The catalysts prepared by immobilizing metal complexes in porous matrix have shown better catalytic efficacy in comparison to their corresponding homogeneous counterparts [14–16]. Schiff base and other Cu(II) complexes upon immobilization into microporous or mesoporous aluminosilicates are capable of catalyzing olefin epoxidations and/or oxidations [17–30]. Manganese complex of 2,2′-bipyridine, $[Mn(bpy)_2]^{2+}$, encapsulated in the supercages of zeolite X and Y can catalyze selective epoxidation of alkenes in the presence of hydrogen peroxide as oxidant [31]. Several oxidants like molecular oxygen, 30% hydrogen peroxide, sodium hypochlorite, are employed for the epoxidation of alkenes. But industrial processes still mainly count on tert-butyl-hydroperoxide (tert-BuOOH) [32]. In the industrial epoxidation like Halcon-Arco and Sumitomo processes [33–36], alkyl-hydroperoxides are applied on a large scale. The recycling of the co-product, e.g. tert-BuOOH has been convinced in the Sumitomo process. Here we report the immobilization of the Cu(II)bipyridine complex in NaY zeolite matrix, characterization of the prepared hybrid catalyst and their catalytic efficiency in certain alkene oxidation reactions in the presence of tert-BuOOH as oxidant.

✉ Chandan Adhikary
    cadhikary123@gmail.com

    Rajesh Bera
    berarajesh2010@gmail.com

1   Department of Chemistry, Dinabandhu Andrews College, Kolkata 700084, West Bengal, India

2   Department of Education, The University of Burdwan, Golapbag, Burdwan 713104, West Bengal, India

2 Experimental

2.1 Materials and method

The zeolite NaY ($SiO_2/Al_2O_3 = 5.7$) was purchased from Tosoh Company Ltd., Japan, used for immobilization. 2,2′-bipyridinewas purchased from Sigma-Aldrich. All other chemicals were of AR/GR quality.

Infrared and electronic spectra were measured on Shimadzu 8400S and Shimadzu 3101CP respectively. EPR spectra were measured on a Bruker EMX X-band EPR spectrophotometer at room temperature. Varian CP3800 gas chromatograph equipped with an FID detector quantified the catalytic reaction. The copper content of the sample was estimated on a Varian Techtron AA-575ABQ atomic absorption spectrometer. The powder X-ray diffraction (XRD) patterns of samples were recorded with a Rigaku Miniflex X-Ray diffractometer.

2.2 Synthesis of [Cu(NO₃)(2,2′-bipyridine)₂] (NO₃). H₂O

The free complex was synthesized according to the procedure reported earlier by Catalan et al. [37]. $Cu(NO_3)_2$. $3H_2O$ (1.00 g, 4.13 mmol) was dissolved in 50 ml of ethanol. 2,2′-bipyridine (1.29 g, 8.26 mmol) was added to this solution. The solution was refluxed for 30 min. Blue crystals were obtained from the cooled solution. The solid was filtered from solution and washed with cold ethanol.The complex, thus obtained was designated as CuL.

2.3 Synthesis of Cu-NaY

For incorporation of Cu(II) into zeolite matrix an aqueous solution of $Cu(NO_3)_2.3H_2O$ (0.1 g) was stirred with NaY (5 g) in suspension for 1 h. During stirring the white mass turns into blue. The solid mass then filtered and washed thoroughly with copious amount of deionized water (using soxhlet) and dried under vacuum to give a light-blue powder. The Cu–NaY zeolite thus produced was used for immobilization work.Calcination of the prepared Cu(II)-incorporated zeolite was avoided to arrest the migration of Cu(II) ions from the vicinity of the supercage.

2.4 Immobilization of 2,2′-bpy in NaY

Cu(II) ion was incorporated in the zeolite matrix using the process reported earlier. The immobilization was done by the flexible ligand method. Cu–NaY(1 g) was allowed to react with an excess of molten 2,2′-bipyridine ligand (4 g)

at 363 K for 24 h in a closed system to stimulate complex formation. On cooling, the whole mass transforms into a dark solid, which on washing with a soxhlet using CH_3CN to remove unreacted ligand produced a light-blue solid. Finally, the material was stirred with 0.01 M NaCl for 6 h to back exchange of excess uncoordinated Cu(II) with Na^+ ions. The solid product was dried under vacuum to produce light blue powder. The hybrid catalyst thus obtained will be referred as $[Cu(bpy)_2]^{2+}$–NaY (**1**).

2.5 Catalytic reactions

The catalytic reactions were carried out in a glass batch reactor, according to the following procedure. The alkene (1 g) and catalyst (50 mg) were added to 10 ml of acetonitrile in a round-bottom flask. This was then equilibrated to 70 °C in an oil bath. After addition of the tert-BuOOH (2 ml) the reaction was stirred continuously. The products of the oxidation reactions were collected at different time intervals and were identified and quantified by gas chromatography.

3 Results and discussion

3.1 X-ray powder diffraction studies of compound 1

The powder XRD pattern of the neat NaY, Cu-NaY and $[Cu(bpy)_2]^{2+}$–NaY are displayed in Fig. 1. It can be observed from Fig. 1 that, apart from a slight change in the intensity of the diffraction lines, no new crystalline patterns have appeared in the case of Cu–NaY and $[Cu(bpy)_2]^{2+}$–NaY. This indicates the crystallinity and morphology of the zeolitic matrix remained intact upon immobilization and the complex is well distributed in the nanovoids of zeolite Y [38]. The relative peak intensities of the 220, 311, and 331 reflections correspond to the locations of cations. In case of pure NaY and for Cu-NaY, the order of peak intensity is $I_{331} > > I_{220} > I_{311}$, while for the encapsulated complex, the order of peak intensity becomes $I_{331} > > I_{311} > I_{220}$. This reversal in the relative peak intensities indicates that the ion-exchanged Cu^{2+}, which substitutes the location of Na^+, undergoes rearrangement during complexation, i.e., reallocation of Cu^{2+} ion occurs [27, 39]. This observation supports that copper bipyridine complex is successfully immobilized within the supercage of NaY.

3.2 Infrared and atomic absorption spectra

FTIR spectra of the neat complex CuL, NaY and the catalyst $[Cu(bpy)_2]^{2+}$–NaY (**1**) is depicted in Fig. 2. FTIR spectra of NaY shows strong zeolite lattice bands in the range

Fig. 1 XRD pattern of the **a** NaY; **b** Cu-NaY and **c** $[Cu(bpy)_2]^{2+}$–NaY
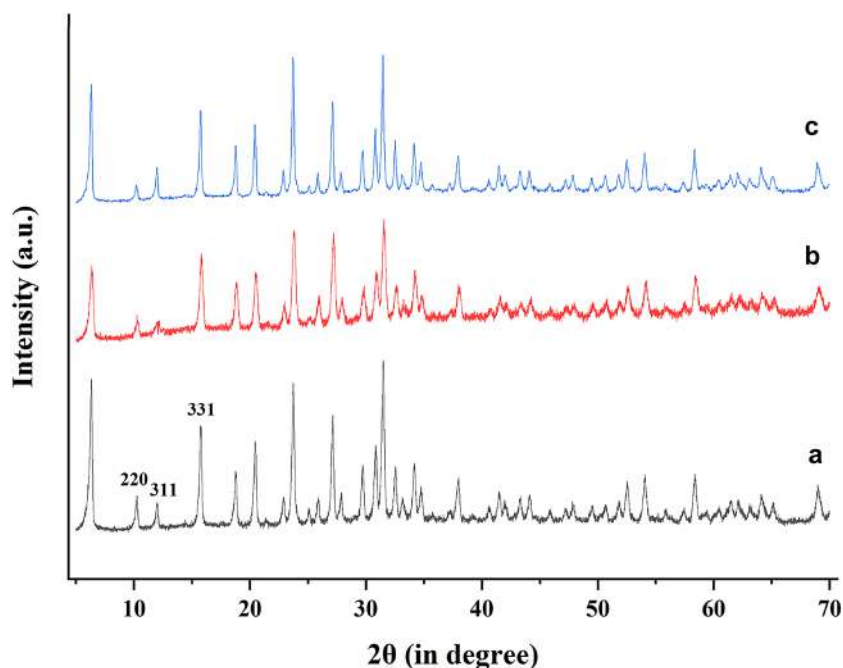
$500-1200$ cm^{-1}. The strong and broad bands in the region $1010-1045$ cm^{-1} could be attributed to the asymmetric stretching vibrations of (Si/Al)O$_4$ units. The broad bands in the regions 1638 and 3446 cm^{-1} are due to lattice water molecules and surface hydroxyl groups, respectively [27, 39]. The NaY zeolite shows characteristic bands at 580, 724, and 1023 cm^{-1} (Fig. 2b) that is attributed to T–O bending mode, symmetric stretching, and antisymmetric vibrations respectively [40]. No shift is observed upon the encapsulation of the metal complex (Fig. 2c), which further reveals that the zeolite framework remained unchanged upon the encapsulation of the complex. The IR bands of the encapsulated complex are weak because of their low concentration in the zeolite cage. The bands of water might mask some of the weak bands in the encapsulated complex. Within the range 1620–1210 cm^{-1} (the range where zeolite Y materials do not absorb), a weaker band is present at 1458 cm^{-1}, which not only confirms the formation of metal complex, but also indicate its lower concentration within zeolite Y [27]. Atomic absorption spectrometry result showed the copper content of the catalyst is *ca.* 0.46 (wt%).

3.3 UV–Vis spectra

The electronic spectra of the neat complex CuL and the catalyst $[Cu(bpy)_2]^{2+}$–NaY have been measured in solid state (Fig. 3). The peaks that appeared ca.704 and 346 nm in the case of CuL are assigned to d–d transition and charge transfer (MLCT) bands respectively. These two bands appeared at ca. 663 and 315 nm for $[Cu(bpy)_2]^{2+}$–NaY. This shows that the d-d transition band of CuL is blue-shifted in the case of $[Cu(bpy)_2]^{2+}$–NaY. The shifting of d-d band to the higher energy region demonstrates that the in-plane ligand field around the metal ion is becoming stronger upon immobilization of the complex in NaY matrix than in un-immobilized state. In case of $[Cu(bpy)_2]^{2+}$–NaY, the two higher energy bands appeared at ca. 218 and 263 nm is due to π–π^* transitions and n–π^* transition respectively. In the complex CuL, these two peaks appeared at 218 and 286 nm respectively.

3.4 EPR spectra

The EPR spectra of the neat complex CuL and the final catalyst $[Cu(bpy)_2]^{2+}$–NaY is depicted in Fig. 4. The principle g value has been calculated by usual methods. The assigned $g_\parallel$ and $g_\perp$ values of the CuL are 2.22 and 2.11 respectively, whereas for $[Cu(bpy)_2]^{2+}$–NaY, the values are found to be 2.38 and 2.12 respectively. It has been observed that for both CuL and $[Cu(bpy)_2]^{2+}$–NaY, $g_\parallel > g_\perp > 2.0023$, suggesting that the unpaired electron occupies the d$_{x^2-y^2}$ orbital, which is characteristic of a tetragonally elongated system. From this we can conclude that geometry around Cu(II) center is square planner, i.e., 2,2′-bipyridine chelates Cu(II) ion from an equatorial site only. The hyperfine coupling due to metal ion A$_{Cu}$ (^{63}Cu, I = 3/2) was well-resolved in the present case and $A_\parallel$ value is calculated to be 188G. Immobilization of CuL in NaY matrix has a significant effect on both
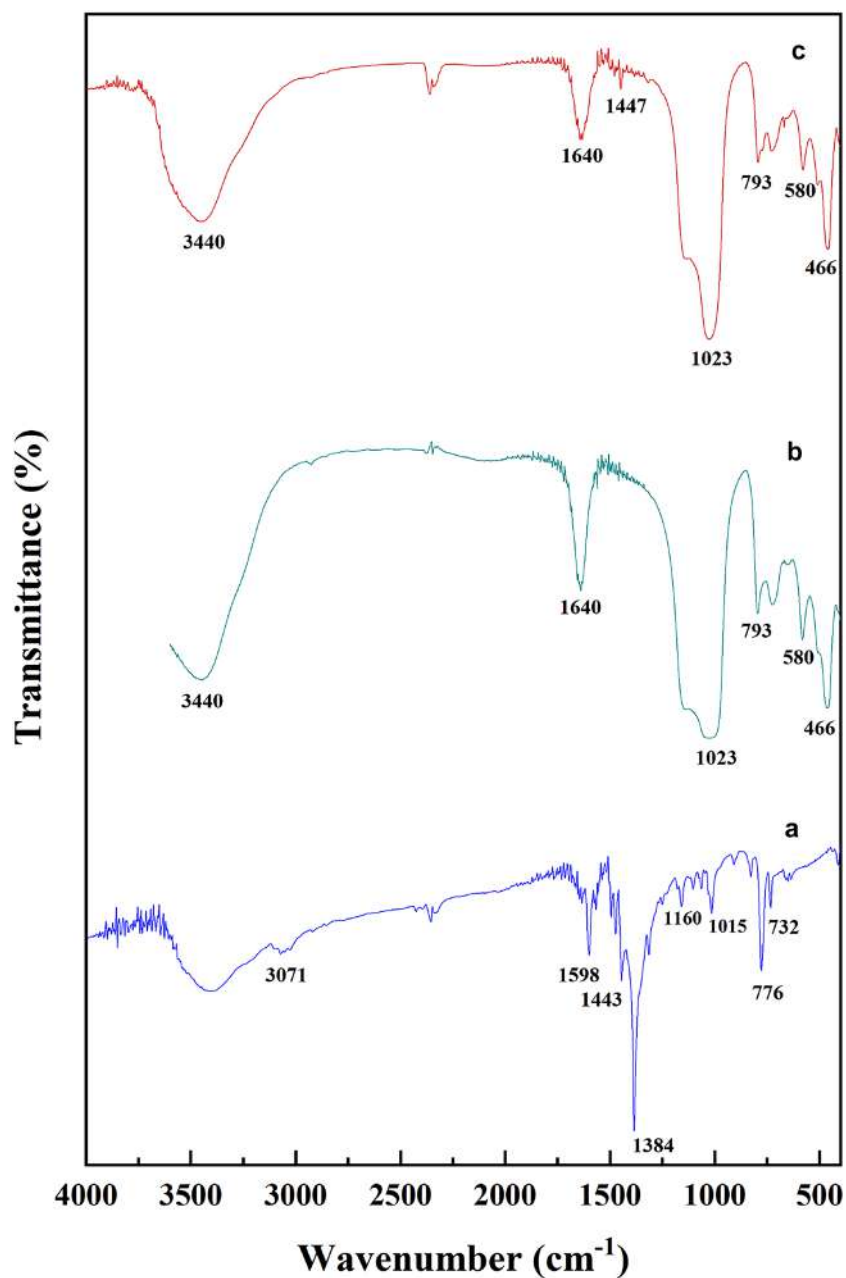
$g_\parallel$ and $g_\perp$ values. It is evident from the EPR spectrum that the $g_\parallel$ value is higher in the catalyst in comparison to the corresponding value in free complex. This means the neat complex on immobilization suffers a considerable amount of distortion around the metal–ligand environment. As a result the in-plane ligand field around Cu(II) ion is increased in the catalyst. Consequently, the d–d transition band of the complex moiety is also shifted to the shorter wavelength region which is in accord to the UV–Vis spectra observed.

3.5 Catalytic reactions

The oxidation of both aliphatic and aromatic alkenes was carried out. The results of the reactions are given in Table 1. The hybrid catalyst showed better catalytic activity and
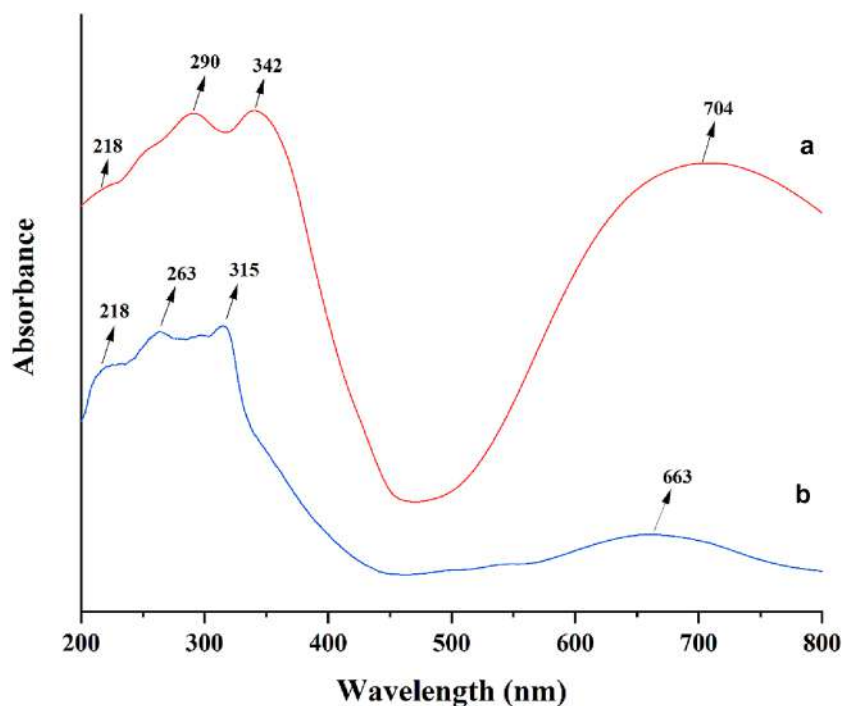
product selectivity than the neat complex in acetonitrile. The oxidation of styrene with tert-BuOOH gives styrene oxide in 42% yield (epoxide selectivity-57%) (Table 1) under the heterogeneous condition. Along with this, benzaldehyde and benzoic acid are also detected. Turnover frequency of ~107 for the epoxide production was attained in 24 h. The free CuL complex showed 55% conversion of styrene, but the yield of styrene oxide is very low with only 36% selectivity. The heterogeneous oxidation of cyclohexene showed an excellent conversion~99%, but cyclohexene oxide was not the major product of this reaction. Cyclohexene oxide was produced in 42% yield with only moderate selectivity (42%). Apart from cyclohexene-oxide, cyclohex-2-en-1-ol and cyclohex-2-en-1-one were also generated (57%), since its active allylic C–H site could also be activated in the process of oxidation. Oxidation of cyclohexene in homogeneous condition by CuL shows slightly lower conversion (85%). Here also selectivity of cyclohexene oxide is only 35%. Bulkier cycloalkenes like norbornene has been effectively converted selectively to exo-epoxynorbornane (conversion 99%, selectivity 100%) in heterogeneous condition. But in homogeneous condition, although selectivity of exo-epoxynorbornane is 100%, conversion is very low (57%). The oxidation of cyclooctene proceeds smoothly when catalyzed by [Cu(bpy)$_2$]$^{2+}$–NaY, showing excellent conversion of 81%,

where the selectivity of cyclooctene oxide was 77%. Along with this, cyclooctane-1,2-diol (19%) was also generated. In homogeneous condition, the conversion and selectivity were lower (conversion 76%, cyclooctene oxide selectivity 70%). To test the leaching of copper from the catalyst during the reaction, the reaction mixture was filtered out hot after the reaction is over and was subjected to atomic absorption spectroscopic analysis. The analyses show copper was absent in the filtrate. The filtrate mixture also did not show any catalytic activity towards oxidation reactions. Therefore, it is concluded that copper is not leaching out from the catalyst during oxidation. The [Cu(bpy)$_2$]$^{2+}$–NaY catalyst has been recovered from the reaction mixture and has been reused successively three times under the same reaction conditions. After each reaction, the catalyst has been washed with acetonitrile. The solid catalyst has been recovered by filtration after each reaction and has been washed thoroughly with acetonitrile. The recovered catalyst showed almost the same catalytic activity for norbornene epoxidation reaction by tert-BuOOH in every run: first run, norbornene conversion=98%; second run, norbornene conversion=99%; third run, norbornene conversion=98%. No induction period was observed in all the reactions (Fig. 5). The Cu(II) binds the peroxo-group on treatment with peroxides to form the precatalyst containing LxCu–OOH (where L=ligand), which

are capable of transferring the oxo-functionality to the organic substrates to produce the oxidized products [41]. It is our assumption that a similar kind of mechanism may be operative in this case. The excellent catalytic potency of the encapsulated catalyst may be due to the formation of facile and reversible intermediate species [20]. The coordination environment around Cu(II) is easily approachable for an external ligand. As a result, tert-BuOOH occupies enough space to bind copper in the intermediate stages of the catalytic cycle. The lower catalytic activity of the homogeneous catalyst (CuL) with respect to the zeolite Y encapsulated one may be imputed to the degradation of the homogeneous catalyst [30].

4 Conclusions

The immobilization of the copper bipyridine complex within zeolite Y was done using a flexible ligand method. It was well characterized by various physicochemical and spectral methods. The catalyst showed high catalytic efficiency towards the oxidation of alkenes using tert-BuOOH as oxidant. The encapsulated catalyst can be recovered and reused without loss of much catalytic activity which makes them superior to the homogeneous counterpart.

Fig. 4 EPR spectra of **a** CuL and **b** $[Cu(bpy)_2]^{2+}$–NaY

Table 1 Catalytic oxidation of olefins catalysed by $[Cu(bpy)_2]^{2+}$–NaY and CuL in acetonitrile media

Catalyst	Substrate	Conversion (wt%)	%Yield of products[a]		TOF[e] (h^{-1})
			Epoxide	Others	
$[Cu(bpy)_2]^{2+}$–NaY	Styrene	74	42	32[b]	57
	Cyclohexene	99	42	57[c]	65
	Cyclooctene	81	62	19	58
	Norbornene	99	99[d]	–	107
CuL	Styrene	55	20	35[b]	–
	Cyclohexene	85	30	55[c]	–
	Cyclooctene	76	53	23	–
	Norbornene	57	57[d]	–	–

Reaction condition: alkenes (1 g); Cu(bpy)-NaY (50 mg); CuL (2 mg); *tert*-BuOOH (2 ml); acetonitrile (10 ml) and temperature 343 k (24 h data)

[a]Products are identified and quantified by GC

[b]Benzaldehyde

[c]Cyclohex-2-en-1-ol and and cyclohex-2-en-1-one was formed

[d]Exo-epoxynorbornane

[e]Turn Over Frequency = moles converted/moles of active site/time. The products of the epoxidation reactions were collected at different time intervals and were identified and quantified by Varian CP3800 gas chromatograph equipped with an FID detector and a CP-Sil 8 CB capillary column

Fig. 5 Reaction profile for the oxidation of olefins with tert-BuOOH in the presence of $[Cu(bpy)_2]^{2+}$–NaY

Compliance with ethical standards

Conflict of interest No potential conflict of interest was reported by the authors.

References

1. W. Gerhartz, Y.S. Yamamoto, L. Kandy, J.F. Rounsaville, G. Schulz, *Ullmann's Encyclopedia of Industrial Chemistry*, vol. A9, 5th edn. (Wiley, Weinheim, 1987), p. 531
2. J.M. Thomas, Angew. Chem. Int. Ed. Engl. **38**, 3588 (1999)
3. M. Pillinger, I.S. Gonçalves, A.D. Lopes, J. Madureira, P. Ferreira, A.A. Valente, T.M. Santos, J. Rocha, J.F.S. Menezes, L.D. Carlos, J. Chem. Soc. Dalton Trans. (2001). https://doi.org/10.1039/B101152I
4. G.J. Kim, S.H. Kim, Catal. Lett. **57**, 139 (1999)
5. F. Bedioui, Coord. Chem. Rev. **144**, 39 (1995)
6. M. Silva, C. Freire, B.D. Castro, J.L. Figueiredo, J. Mol. Catal. A: Chem. **258**, 327 (2006)
7. P. Karandikar, M. Agashe, K. Vijayamohanan, A.J. Chandwadkar, Appl. Catal. A: Gen. **257**, 133 (2004)
8. C.E. Song, S.E. Lee, Chem. Rev. **102**, 3495 (2002)
9. A.R. Silva, M.M.A. Freitas, C. Freire, B. de Castro, J.L. Figueiredo, Langmuir **18**, 8017 (2002)
10. H. Zhang, S. Xiang, C. Li, Chem. Commun. (2005). https://doi.org/10.1039/B417041E
11. P. McMorn, G.J. Hutchings, Chem. Soc. Rev. **33**, 108 (2004)
12. A. Sakthivel, W. Sun, G. Raudaschl-Sieber, A.S.T. Chiang, M. Hanzlik, F.E. Kühn, Catal. Commun. **7**, 302 (2006)
13. A. Corma, Catal. Rev. **46**, 369 (2004)
14. K.J. Balkus Jr., M. Eissa, R. Levedo, J. Am. Chem. Soc. **117**, 10753 (1995)
15. I.F.J. Vankelecom, D. Tas, R.F. Parton, V.V. de Vyver, P.A. Jacobs, Angew. Chem. Int. Ed. Engl. **35**, 1346 (1996)
16. S. Koner, Chem. Commun. (1998). https://doi.org/10.1039/A707681I
17. B. Dutta, S. Jana, R. Bera, P.K. Saha, S. Koner, Appl. Catal. A: Gen. **318**, 89 (2007)
18. P.K. Saha, B. Dutta, S. Jana, R. Bera, S. Saha, K. Okamoto, S. Koner, Polyhedron **26**, 563 (2007)
19. M.R. Maurya, C. Haldar, S. Behl, N. Kamatham, F. Avecilla, J. Coord. Chem. **64**, 2995 (2011)

20. M.R. Maurya, P. Saini, C. Haldar, A.K. Chandrakar, S. Chand, J. Coord. Chem. **65**, 2903 (2012)

21. V.K. Bansal, P.P. Thankachan, R. Prasad, Appl. Catal. A: Gen. **381**, 8 (2010)

22. S.J. Kulkarni, C.N. Rohitha, N. Narender, A. Koeckritz, J. Porous Mater. **17**, 321 (2010)

23. M. Salavati-Niasari, J. Mol. Catal. A:Chem. **283**, 120 (2008)

24. M.R. Maurya, A.K. Chandrakar, S. Chand, J. Mol. Catal. A: Chem. **263**, 227 (2007)

25. M.R. Maurya, A.K. Chandrakar, S. Chand, J. Mol. Catal. A: Chem. **274**, 192 (2007)

26. A. Baneai, B. Rezazadeh, J. Coord. Chem. **66**, 2129 (2013)

27. D.R. Godhani, H.D. Nakum, D.K. Parmar, J.P. Mehta, N.C. Desai, Inorg. Chem. Comm. **72**, 105 (2016)

28. S. Jana, B. Dutta, R. Bera, S. Koner, Langmuir **23**, 2492 (2007)

29. B. Shi, H. Yu, S. Gao, L. Zhang, Y. Liu, K. Huang, Microporous Mesoporous Mater. **294**, 109890 (2020)

30. S. Rayati, E. Khodaei, M. Jafarian, J. Coord. Chem. **70**, 2736 (2017)

31. P.P. Knops-Gerrits, D.E. De Vos, F. Thibault-Starzyk, P.A. Jacobs, Nature **369**, 543 (1994)

32. J.M. Brégeault, Dalton Trans. (2003). https://doi.org/10.1039/B303073N

33. L.F. Veiros, Â. Prazeres, P.J. Costa, C.C. Romão, F.E. Kühn, M.J. Calhorda, Dalton Trans. (2006). https://doi.org/10.1039/B515484G

34. M.N. Sheng, G.J. Zajaczek, ARCOBr. Patent 1.136.923 (1968)

35. J.H. Kollar, US Patent 3.350.422 (1967)

36. J.H. Kollar, US Patent 3.351.635 (1967)

37. K.J. Catalan, S. Jackson, J.D. Zubkowski, Polyhedron **14**, 2165 (1995)

38. W.H. Quayle, J.H. Lunsford, Inorg. Chem. **21**, 97 (1982)

39. K.K. Bania, G.V. Karunakar, K. Goutham, R.C. Deka, Inorg. Chem. **52**, 8017 (2013)

40. W. Jin, Y. Fan, B. Jia, J. Fan, R.L. Ma, J. Mol. Catal. A: Chem. **249**, 23 (2006)

41. E.I. Solomon, P. Chen, M. Metz, S.-K. Lee, A.E. Palner, Angew. Chem. Int. Ed. **40**, 4570 (2001)

Publisher's Note Springer Nature remains neutral with regard to jurisdictional claims in published maps and institutional affiliations.

Source details

Feedback >   Compare sources >

Journal of Porous Materials

Scopus coverage years: from 1995 to Present

Publisher: Springer Nature

ISSN: 1380-2224   E-ISSN: 1573-4854

Subject area: (Engineering: Mechanical Engineering)   (Engineering: Mechanics of Materials)   (Materials Science: General Materials Science)

Source type: Journal

View all documents >   Set document alert   💾 Save to source list

CiteScore 2022   ⓘ
4.5

SJR 2022   ⓘ
0.448

SNIP 2022   ⓘ
0.526

CiteScore   CiteScore rank & trend   Scopus content coverage

Double end-on azido derivative of a tridentate (NNO) Schiff base dimeric copper(II) complex: synthesis, X-ray structure, magnetic property and catalytic effectiveness

Habibar Chowdhury , Rajesh Bera , Corrado Rizzoli & Chandan Adhikary

View supplementary material ⬚

Published online: 23 Oct 2020.

Submit your article to this journal ⬚

Article views: 8

View related articles ⬚

View Crossmark data ⬚

Check for updates

Double end-on azido derivative of a tridentate (NNO) Schiff base dimeric copper(II) complex: synthesis, X-ray structure, magnetic property and catalytic effectiveness

Habibar Chowdhury[a], Rajesh Bera[b], Corrado Rizzoli[c] (ID) and Chandan Adhikary[d]

[a]Department of Chemistry, Kabi Nazrul College, Murarai, West Bengal, India; [b]Department of Chemistry, Dinabandhu Andrews College, Kolkata, West Bengal, India; [c]Departimento di Scienze Chimiche, della Vita e della Sostenibilità Ambientale, Parma, Italy; [d]Department of Education, The University of Burdwan, Burdwan, West Bengal, India

ABSTRACT

A dimeric copper(II) complex, bis{(2-[1-(aminoethylimino)ethyl]-phenoxo}-di-$\mu_{1,1}$-azido-dicopper(II), $[Cu_2(L)_2(\mu_{2-1,1}-N_3)_2]$ (**1**) [L = 2-[1-(aminoethylimino)ethyl]-phenoxo ion], has been isolated using a self-assembly reaction using a 1:1:1 molar ratio of $Cu(NO_3)_2 \cdot 3H_2O$, HL and NaN_3 in methanol at room temperature and characterized through X-ray diffraction analysis and spectroscopic studies. X-ray structural analysis reveals that **1** consists of two distinct dinuclear molecular units, where each copper(II) center in the individual dinuclear unit adopts a distorted square pyramidal geometry with a CuN_4O chromophore ligated through a tridentate (NNO) Schiff base and two N atoms of two different bridging azides in $\mu_{1,1}$-mode. Two Cu(II) centers are linked through double $\mu_{2-1,1}-N_3$ bridges to form the dinuclear unit $[Cu_2(L)_2(\mu_{2-1,1}-N_3)_2]$. In the crystalline state, the dinuclear units in **1** are associated through weak intermolecular N-H···O hydrogen bonds to afford a 2-D sheet structure viewed along the crystallographic *a*-axis. The small magnitude of the antiferromagnetic interaction ($J = -0.45 \, cm^{-1}$) is a result of the long Cu···Cu separation (3.205(2) Å). The catalytic efficacy of **1** was studied in a series of solvents for the epoxidation of alkenes using *tert*-butylhydroperoxide (TBHP) as an efficient oxidant under mild conditions.

CONTACT Chandan Adhikary ✉ cadhikary123@gmail.com 🖃 Department of Education, The University of Burdwan, Golapbag, Burdwan 713104, West Bengal, India

Supplemental data for this article is available online at at 10.1080/00958972.2020.1836360
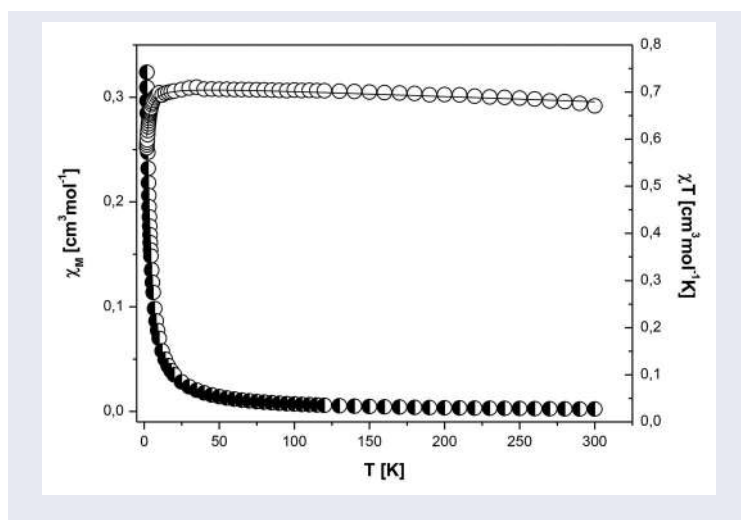
1. Introduction

Copper(II) complexes with different nuclearities and varied pseudohalide bridges have spawn great interest because of their interesting structures, catalytic and magnetic properties [1–9], and also as models for the active sites of biomolecules [10]. Of them, homoatomic azide-bridged compounds [11] with $\mu\text{-}_{1,1}$ (end-on, EO) and $\mu\text{-}_{1,3}$ (end-to-end, EE) bridging motifs show different molecular architectures and magnetic interactions [9, 12–20]. The crystalline architectures of these compounds are found to be interesting due to the variations of the nature of forces such as weak intramolecular and/or intermolecular interactions. The magnetic super-exchange pathways [9, 12–19] in these compounds depend on structural parameters, such as Cu-N and Cu….Cu distances, Cu–N–Cu angles and of course on the nature of the magnetic orbitals. This indicates that the structural parameters have great influence on the magnetic properties; thus a detailed knowledge of these parameters is essential for magneto-structural/-chemical correlations. Although the activity of Schiff base copper(II) complexes toward several oxidation reactions both in homogeneous [21–26] and heterogeneous conditions [27–31] are well documented, catalytic oxidation of alkenes involving Schiff base copper azido complexes has been scarcely reported [32–35]. Several oxidants such as molecular oxygen, 30% hydrogen peroxide and sodium hypochlorite are used for the epoxidation of alkenes. But industrial processes still mainly rely on *tert*-butyl-hydroperoxide (*tert*-BuOOH) [36]. In industrial epoxidation such as the Halcon–Arco and Sumitomo processes [37–40], alkyl-hydroperoxides are used on a large scale. The recycling of the co-product, e.g. *tert*-BuOH has been realized in the Sumitomo process. In the present endeavor, we have chosen a tridentate Schiff base (HL) (Scheme 1) to isolate one neutral dinuclear copper(II) azido complex bis{(2-[1-(aminoethylimino)ethyl]-phenoxo}-di-$\mu_{1,1}$-azido-dicopper(II), [Cu$_2$(L)$_2(\mu_{2\text{-}1,1}\text{-}N_3)_2$] (**1**) [L $=$ 2-[1-(aminoethylimino)ethyl]-phenoxo ion. Details of the synthesis, crystal structure, magnetic behavior and its catalytic
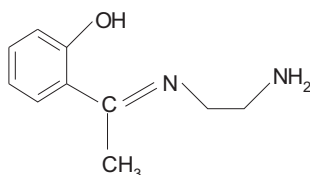
Scheme 1. Framework of Schiff base ligand (HL).

effectiveness toward epoxidation of alkenes using *tert*-BuOOH as an oxidant of this compound are presented in the following sections.

2. Experimental

2.1. Materials

High purity 1-(2-hydroxyphenyl)ethanone (Aldrich, USA), ethane-1,2-diamine (Aldrich, USA), sodium azide (E. Merck, India) and copper(II) nitrate trihydrate (Merck, India) were purchased from their respective concerns and used without purification. All other chemicals and solvents were of AR grade. The solvents used were distilled and dried before use. The synthetic reactions and work-up were done in the open air.

Caution! Transition metal azido complexes are potentially explosive especially in the presence of organic ligands. Although we have not encountered any problem during our study, yet a small amount of materials should be prepared and it should be handled with care.

2.2. Physical measurements

Elemental analyses (carbon, hydrogen and nitrogen) were performed on a Perkin-Elmer 240C elemental analyzer. The IR spectrum (KBr disc, 4000–200 cm^{-1}) was recorded using a Nicolet Magna IR 750 Series II FTIR spectrometer. Ground state absorption (in methanol) was measured with a Perkin Elmer LAMBDA EZ-301 spectrophotometer. Variable-temperature (1.8–300 K) magnetic measurements were carried out using a Quantum Design SQUID-based MPMSXL-5-type magnetometer. The palladium rod sample (Materials Research Corporation, measured purity 99.9985%) was used to calibrate the SQUID magnetometer where the superconducting magnet was normally run from 0 to 5 T field strength. Measurements were made at a magnetic field of 0.5 T. Corrections are based on subtracting the sample holder signal and contribution χ_D estimated from the Pascal constants [41]. Magnetization measurements were conducted at 2 K in the magnetic field from 0 to 5 T. X-band (9.5 GHz) EPR measurements were done on polycrystalline samples using a Bruker ElexSys E 500 spectrometer. The measurements were performed at room and liquid nitrogen temperature. The spectrometer was equipped with a NMR teslameter (ER 036TM) and an X-band frequency counter (E 41 FC). Measurement parameters were as follows: microwave power 10 mW, modulation amplitude 8 G, center field 3500 G, range 7000 G for X-band.

2.3. Synthesis and analytical data for Schiff base (HL) and [Cu$_2$(L)$_2$ ($\mu_{2-1,1}$-N$_3$)$_2$] (1)

2.3.1. Schiff base, 2-[1-(aminoethylimino)ethyl]-phenol (HL)

1-(2-Hydroxyphenyl)ethanone (0.136 g, 1.00 mmol) was refluxed (10 h) with ethane-1,2-diamine (0.060 g, 1.00 mmol) in ethanol (20 mL). After 10 h, the reaction solution was evaporated under reduced pressure to yield a gummy mass, which was dried and stored *in vacuo* over CaCl$_2$ for subsequent use (Supplementary Material Scheme S1). Yield: 0.125 g (70%). Elemental Anal. Calcd for C$_{10}$H$_{14}$N$_2$O (HL): C, 67.38; H, 7.92; N, 15.72%. Found: C, 68.10; H, 8.15; N, 14.80%. IR (KBr pellets, cm^{-1}): ν(C$=$N) 1640; ν(N-H) 3284. ^{1}H NMR (300 MHz, CDCl$_3$): (δ 2.25 (m, 6H, CH$_3$); 2.6 (t, 2H, CH$_2$); 3.6 (t, 2H, CH$_2$); 7.2 (m, 3H, aromatic).

2.3.2. Bis{(2-[1-(aminoethylimino)methyl]-phenoxo}-di-$\mu_{1,1}$-azido-dicopper(II), [Cu$_2$(L)$_2$($\mu_{2-1,1}$-N$_3$)$_2$] (1)

The tridentate Schiff base, HL (0.178 g, 1.00 mmol), in MeOH (20 mL) was added slowly to a copper(II) nitrate trihydrate (0.242 g, 1.00 mmol) solution (20 mL) in the same solvent producing an intense blue solution, which was stirred for 30 min. An aqueous solution (5 mL) of NaN$_3$ (0.065 g, 1.00 mmol) was added dropwise to the resulting mixture with continuous stirring, which gave a green solution. After filtration through a fine glass-frit, the green solution filtrate was kept in air for slow evaporation. Black rectangular crystals of **1** were deposited within a week, which were separated by filtration and dried *in vacuo* over silica gel indicator. Yield: 0.339 g (60%). Elemental Anal. Calcd for C$_{20}$H$_{26}$N$_{10}$O$_2$Cu$_2$ (**1**): C, 42.47; H, 4.63; N, 24.77%. Found: C, 42.84; H, 5.15; N, 25.08%. IR (KBr, cm^{-1}): υ_{asy}(N$_3$) 2045, 2031; $\upsilon_{bending}$(N$_3$) 635. UV–vis [DMF; λ_{max}/nm (ε_{max}/dm^3 mol^{-1} cm^{-1}]: 262, 292 (1.30 $\times$ 10^4), 382 (1.25 $\times$ 10^4), 609 (2.35 $\times$ 10^2). Λ_M (DMF, Ω^{-1} cm^2 mol^{-1}): 6.

2.4. X-ray data collection and structure refinement of [Cu$_2$(L)$_2$($\mu_{2-1,1}$-N$_3$)$_2$] (1)

A single crystal of **1** suitable for X-ray analysis was selected from those obtained by slow evaporation of a methanol solution at room temperature. Diffraction data were collected on a Bruker APEX IICCD diffractometer using graphite monochromated Mo-Kα radiation ($\lambda = 0.71073$ Å) and were used to measure cell dimensions and diffraction intensities. The ω-θ scan technique in the range to a maximum 2.7$^\circ < \theta < 25.5^\circ$ has been fixed for data collection. For the purpose of data reduction and cell refinement, the program SAINT-Plus [42] was used. Absorption correction was applied using SADABS [42]. The structure was solved by direct methods using SIR97 [43] and refined with version 2018/3 of SHELXL [44] using least squares minimization. The amine H atoms were located in a difference Fourier map and refined with $U_{iso(H)} = 1.2\,U_{eq}$(N). The N-H bond distances were restrained to be equal using the SADI command with an effective standard deviation of 0.05. Refinement of the C-bound H atoms was carried out using a riding model, with C-H $= 0.96$–0.97 Å and with $U_{iso(H)} = 1.2\,U_{eq}$(C) or 1.5 U_{eq}(C) for methyl H atoms. A large residual density peak (3.37 e Å^{-3}) in the final difference Fourier map located at 1.62 Å from atom Cu$_3$ should be considered as a residual absorption artifact due to the poor quality of the crystal ($R_{int} = 10.4\%$). The

Table 1. Crystallographic data and structure refinement parameters for 1.

Chemical formula	$C_{20}H_{26}N_{10}O_2Cu_2$
Formula mass	565.59
Crystal system	Monoclinic
Space group	$P21/c$
a (Å)	16.866(11)
b (Å)	14.881(10)
c (Å)	14.879(10)
$\alpha/°$	90
β (°)	111.562(7)
γ (°)	90
V (Å^3)	3473(4)
λ (Å)	0.71073
ρ_{calcd} (mg cm^{-3})	1.623
Z	6
T (K)	295(2)
μ (mm^{-1})	1.877
$F(000)$	1740
Crystal size (mm^3)	$0.16 \times 0.11 \times 0.06$
θ ranges (°)	1.30 to 25.25
Index ranges	$-20 \leq h \leq 20$
	$-17 \leq k \leq 17$
	$-17 \leq l \leq 12$
Reflections collected	20,852
Independent reflections	6274
T_{max} and T_{min}	0.896 and 0.769
Data/restraints/parameters	6274/15/481
R(int)	0.104
Goodness-of-fit on F^2	0.996
Final R indices [$I > 2\sigma(I)$]	$R = 0.0815$ and $wR2 = 0.2039$
R indices (all data)	$R = 0.1540$ and $wR2 = 0.2487$
Largest peak and hole (eÅ^{-3})	3.330 and -0.676

Weighting scheme: $R = \Sigma||F_o| - |F_c||/\Sigma|F_o|$, $wR = [\Sigma w(F_o^2 - F_c^2)^2/\Sigma w(F_o^2)^2]^{1/2}$, calcd $w = 1/[\sigma^2(F_o^2) + (0.1337P)^2 + 0.0000P]$ where $P = (F_o^2 + 2F_c^2)/3$.

final positional and thermal parameters are available as Supplementary Material. A summary of the crystallographic data and structure determination parameters for **1** is detailed in Table 1.

2.5. Catalytic reactions

The catalytic reactions were carried out in a glass batch reactor according to the following procedure. Substrate (10 mmol), solvent (8 mL) and catalyst (0.005 mmol) were first mixed in a round-bottom flask. The mixture was then equilibrated to 65 °C in an oil bath. After addition of tert-BuOOH (20 mmol), the mixture was stirred continuously for 24 h. The products of the oxidation reactions were collected at different time intervals and were identified and quantified by a VARIAN CP-3800 gas chromatograph equipped with an FID detector. A CP-Sil 8 CB capillary column was used for analysis of the products.

3. Results and discussion

3.1. Synthesis and physical measurements

The pentacoordinate dinuclear copper(II) complex, bis{(2-[1-(aminoethylimino)methyl]-phenoxo}-di-$\mu_{1,1}$-azido-dicopper(II), [Cu$_2$(L)$_2$(μ_2-$_{1,1}$-N$_3$)$_2$] (**1**), was obtained in a one-pot
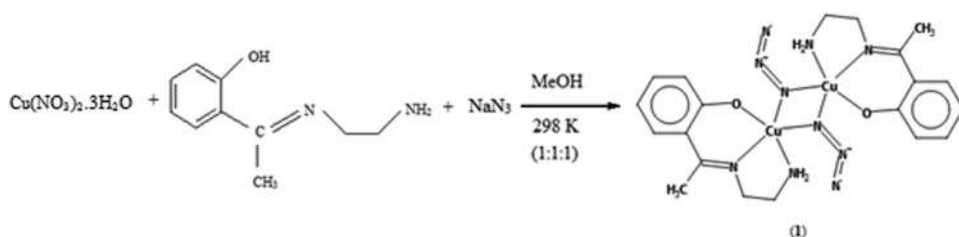
Scheme 2. Synthetic route of **1**.

reaction of a 1:1:1 molar ratio of the copper(II) nitrate trihydrate, HL [HL = 2-[1-(ami-noethylimino)ethyl]-phenol] and NaN$_3$ in MeOH solution at room temperature (Scheme 2).

Complex **1** was characterized by microanalytical (C, H and N), spectroscopic and other physico-chemical results. The microanalytical data are in good conformity with the formulation. The air stable moisture insensitive compound is stable over long periods of time in powdery and crystalline states, and is soluble in MeOH, EtOH, MeCN, DMF and DMSO, but is insoluble in water. In the IR spectrum, bands at 2045 and 2031 cm^{-1} are assigned to the asymmetric vibration of the coordinated azide group [v_{as} N$_3^-$] and the band at 635 cm^{-1} is attributed to the bending vibration of the azide group. Similar characteristic bands for azides have been observed in a number of mononuclear and polynuclear azido-bridged complexes [45]. Complex **1** displays multiple absorption bands in the 200–1100 nm range. A weak low-intensity absorption band at 609 nm is assignable to a d-d transition, consistent with the square pyramidal (sp) geometry of the copper(II) centers. The absorption band at 382 nm may be attributed to the ligand to copper(II) charge transfer transition (LMCT) [46, 47]. Additionally, two strong absorption bands at 262 and 292 nm may be assigned to a ligand-based charge transfer transitions [48].

3.2. Structural description of [Cu$_2$(L)$_2$($\mu_{2-1,1}$-N$_3$)$_2$] (1)

A single crystal X-ray diffraction study of [Cu$_2$(L)$_2$($\mu_{2-1,1}$-N$_3$)$_2$] (**1**) was made to define the coordination sphere. An ORTEP diagram and packing view of the 2-D sheet structures of **1** are shown in Figures 1 and 2, respectively. Selected bond distances and angles relevant to the coordination spheres can be found in Table 2 and non-covalent interaction parameters are given in Table 3. X-ray structural analysis reveals that **1** consists of two distinct dinuclear molecular units as [Cu^{1}Cu^2(L)$_2$($\mu_{2-1,1}$-N$_3$)$_2$] and [Cu$^3{}_2$(L)$_2$($\mu_{2-1,1}$-N$_3$)$_2$]. Each Cu(II) center in asymmetric unit adopts a distorted square pyramidal geometry [$\tau = 0.283$(Cu1)/0.227(Cu2)/0.198(Cu3)] with a CuN$_4$O chromophore [49] coordinated through two N atoms and one O atom [N1, N2,O1 in Cu^1/N9, N10,O2 in Cu^2/N11, N12,O3 in Cu^3] of a tridentate Schiff base (L) and two N atoms [N3,N6 in both Cu^1 and Cu^2/N13,N13^i in Cu^3] of two different bridging azides in $\mu_{1,1}$-mode (Figure 1) (symmetry code: (i) 1 − x, −y, 1 − z). The basal plane is ligated by N1, N2, O1 and N3 in Cu^1/N9, N10, O2 and N6 in Cu^2/N11, N12, O3 and N13 in Cu^3, whereas the apical position is occupied by N6 in Cu^1/N3 in Cu^2/N13^i in Cu^3. A considerable deviation from ideal square pyramidal geometry is seen, which is presumably
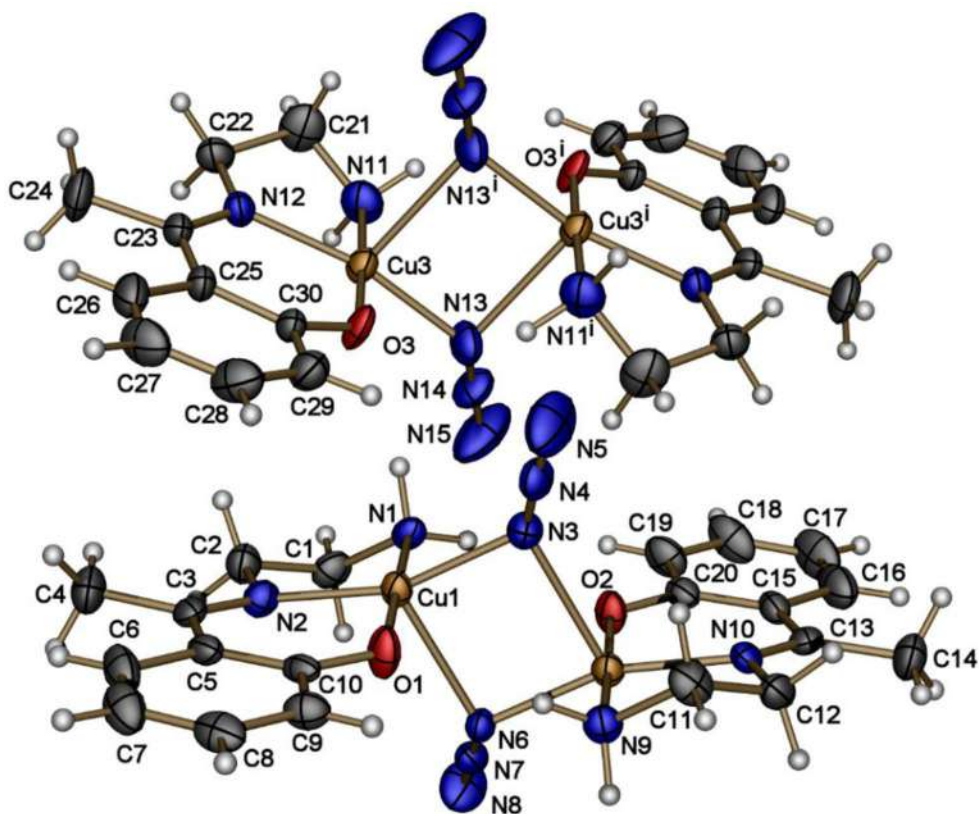
Figure 1. An ORTEP diagram of two distinct dinuclear molecular units in **1** as [Cu^{1}Cu^2(L)$_2$($\mu_{2\text{-}1,1}$-N$_3$)$_2$] and [Cu$^3_2$(L)$_2$($\mu_{2\text{-}1,1}$-N$_3$)$_2$] with displacement ellipsoids drawn at the 30% probability level. Symmetry code: (i) 1 − x, −y, 1 − z.

due to the smaller bite angles produced by the ligand [N1-Cu1-N2 85.8(3)° in Cu^1/N9-Cu2-N10 86.5(3)°/N11-Cu3-N12 85.3(3)°]. The basal plane consists of four short bond lengths [Cu1-N1: 1.991(7) Å, Cu1-N2: 1.957(7) Å, Cu1-O1: 1.873(6) Å, Cu1-N3: 2.021(8) Å in Cu^1/Cu2-N9:1.995(7) Å, Cu2-N10: 1.962(7) Å, Cu2-O2: 1.881(6) Å, Cu2-N6: 2.010(7) Å in Cu^2/Cu3-N11:1.994(9) Å, Cu3-N12: 1.996(7) Å, Cu3-O3: 1.897(6) Å, Cu3-N13: 1.999(9) Å in Cu^3] and the apical position is occupied by a longer bond [Cu1-N6: 2.414(7) Å in Cu^1/Cu2-N3: 2.448(8) Å in Cu^2/Cu3-N13^i: 2.457(9) Å in Cu^3] (Table 2). The Cu1, Cu2 and Cu3 copper(II) centers deviate 0.1370(12), 0.1221(12) and 0.1249(12) Å, respectively, from the mean basal plane. In the [Cu^{1}Cu^2(L)$_2$($\mu_{2\text{-}1,1}$-N$_3$)$_2$] unit, two Cu(II) centers (Cu^1 and Cu^2) are different in position linked and through double $\mu_{2\text{-}1,1}$-N$_3$ bridges to form a dinuclear unit, whereas in [Cu$^3_2$(L)$_2$($\mu_{2\text{-}1,1}$-N$_3$)$_2$] unit, two inversion related Cu(II) centers (Cu^3) are connected via double $\mu_{2\text{-}1,1}$-N$_3$ bridges to construct the dinuclear unit (Supplementary Material Figure S1). The Cu-N$_{azide}$-Cu bridging angles are similar [Cu1-N3-Cu2: 91.1(3)°; Cu1-N6-Cu2: 92.4(3)°; Cu3-N13-Cu3^i: 91.5(4)°]. The $\mu_{2\text{-}1,1}$-N$_3$ (end-on) bridged azides are linear, which is reflected in their angles [N3-N4-N5: 176.8(12) Å; N6-N7-N8: 179.2(10) Å; N13-N14-N15: 176.9(13) Å]. The Cu … Cu distance in the dinuclear unit is 3.205(2) Å. In the crystalline state, the dinuclear units in **1** are associated through weak intermolecular N-H⋯O hydrogen bonds to afford a 2-D sheet structure
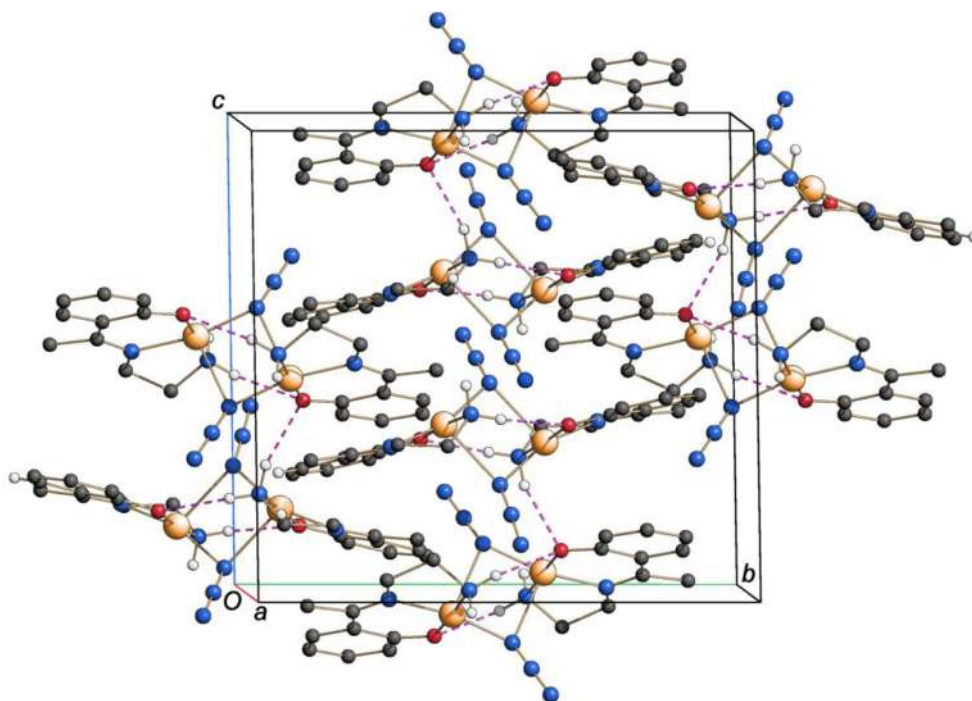
Figure 2. Packing diagram of 2-D supramolecular sheet structure in **1** through intermolecular N-H···O hydrogen bonds viewed down the *a* axis. Hydrogens not involved in hydrogen bonding (dashed lines) are omitted.

Table 2. Selected bond distances (Å) and angles (°) for **1**.

Bond distances Bond angles	Cu^1	Cu^2	Cu^3
Cu-NA (NA = N1/N9/N11)	1.991(7)	1.995(7)	1.994(9)
Cu-NB (NB = N2/N10/N12)	1.957(7)	1.962(7)	1.996(7)
Cu-OC (OC = O1/O2/O3)	1.873(6)	1.881(6)	1.897(6)
Cu-ND (ND = N3/N6/N13)	2.021(8)	2.010(7)	1.999(9)
Cu-NE (NE = N6/N3/N13^i)	2.414(7)	2.449(8)	2.457(9)
N3-N4/N6-N7/N13-N14	1.170(11)	1.218(11)	1.153(12)
N4-N5/N7-N8/N14-N15	1.132(13)	1.169(11)	1.120(13)
NA-Cu-NB	85.8(3)	86.5(3)	85.5(4)
NA-Cu-OC	176.7(3)	175.3(3)	178.4(4)
NA-Cu-ND	89.3(3)	85.0(3)	86.8(3)
NA-Cu-NE	88.5(3)	90.1(3)	94.0(4)
NB-Cu-ND	159.7(3)	161.7(3)	166.5(4)
NB-Cu-NE	110.9(3)	109.7(3)	104.8(3)
NB-Cu-OC	93.5(3)	93.6(3)	92.9(3)
ND-Cu-NE	88.6(3)	87.9(3)	88.6(4)
ND-Cu-OC	92.4(3)	90.6(3)	87.6(3)
NE-Cu-OC	88.7(3)	91.3(3)	93.5(3)
Cu1-N3-Cu2	91.1(3)	91.1(3)	–
Cu1-N6-Cu2	92.4(3)	92.4(3)	–
Cu3-N13-Cu3^i/ Cu3-N13^i-Cu3^i	–	–	91.4(4)
N3-N4-N5	176.8(12)	176.8(12)	–
N6-N7-N8	179.2(10)	179.2(10)	–
N13-N14-N15	–	–	176.9(13)

Symmetry code: (i) 1 − *x*, −*y*, 1 − *z*.

Table 3. Hydrogen bond interaction parameters (Å, °) for **1**.

D-H···A	D-H	H···A	D···A	D-H···A	Symmetry code
N1-H1N···O3	0.99(6)	2.12(6)	3.102(10)	171(5)	–
N1-H3N···O2	0.97(6)	2.34(7)	3.157(10)	140(5)	–
N9-H3N···O1	0.94(6)	2.26(7)	3.136(10)	155(5)	–
N9-H4N···O1	0.95(6)	2.37(6)	3.303(10)	166(5)	$-x, -y, -z$
N11-H5N···O3	0.96(9)	2.42(10)	3.248(13)	144(7)	$1 - x, -y, 1 - z$
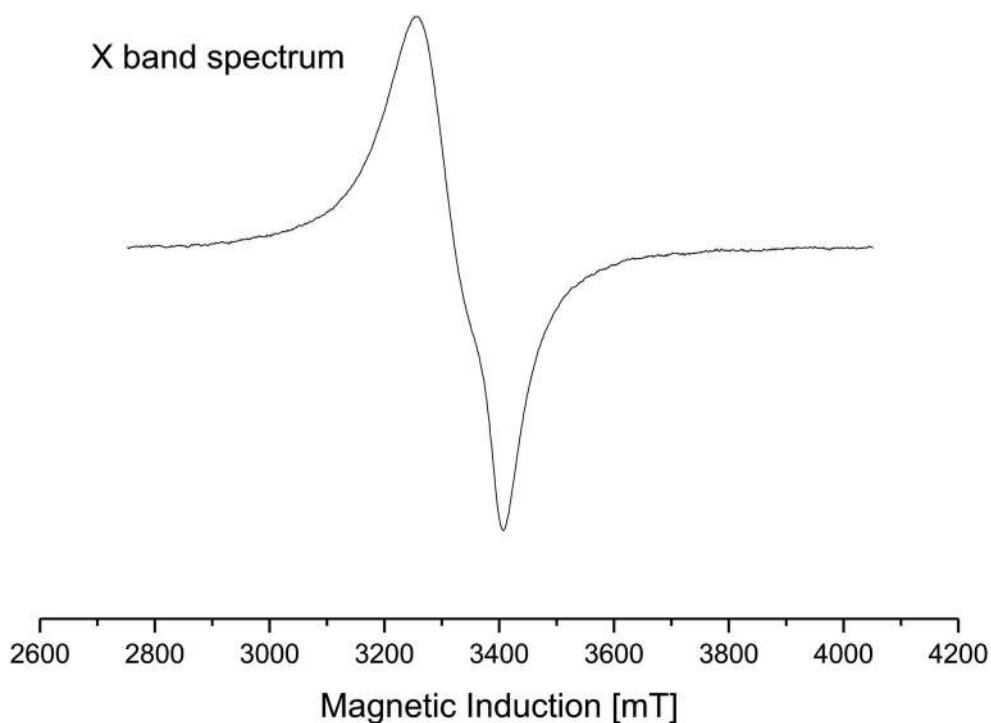
Figure 3. X-band EPR spectrum of **1** at room temperature with $g_x = 2.07$; $g_y = 2.08$, $g_z = 2.18$ ($g_{av} = 2.11$).

viewed along the crystallographic *a*-axis (Figure 2). The weak N-H···O hydrogen bonds between the O atom (O1/O2/O3) of the tridentate Schiff base (L) with H atoms (H1N/H3N/H4N/H5N) of amines (-NH$_2$) group (Table 3) are in operation to strengthen the architecture of the dinuclear unit in **1**.

3.3. EPR spectroscopy

The X-band EPR spectra of the magnetically concentrated polycrystalline samples were recorded at room and liquid nitrogen temperatures. The EPR spectrum of **1** is depicted in Figure 3. The principal *g* values have been determined by conventional methods of EPR spectra [50]. At X-band, the EPR spectrum for **1** shows an axial symmetry with an asymmetry in the perpendicular region with $g_x = 2.07$; $g_y = 2.08$; $g_z = 2.18$; $g_{av} = 2.11$ (Figure 3). This approximately axial spectrum, in view of the significant anisotropy between $g_x \sim g_y$ and g_z, indicates that copper(II) ion assumes either a square planar
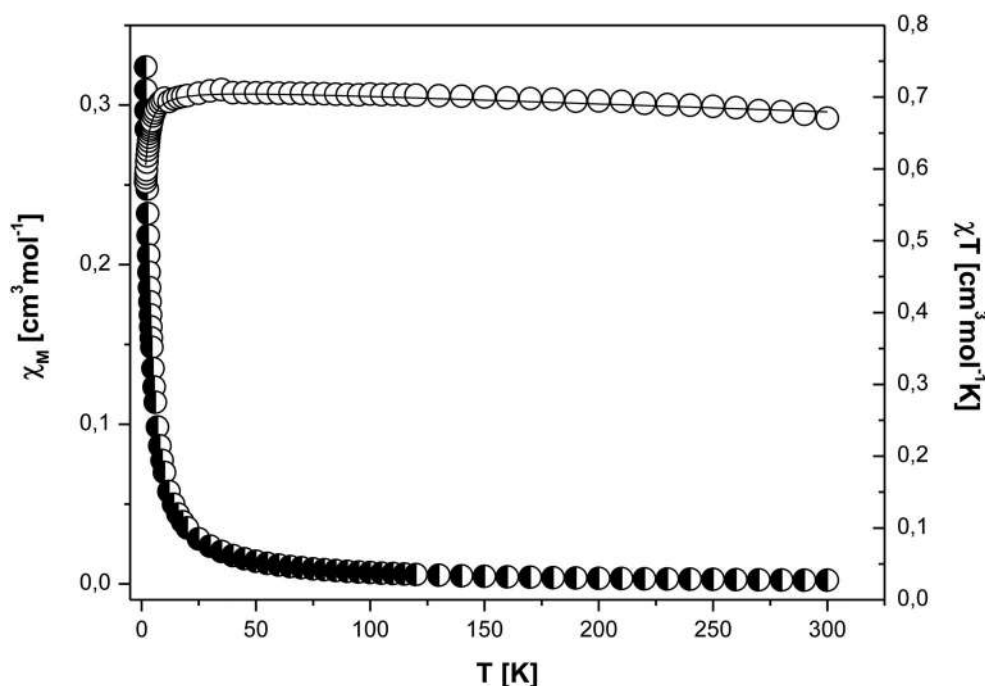
Figure 4. Thermal dependence of (○) $\chi_M T$ and (●) χ_M for **1**. The inset shows thermal dependence of inverse magnetic susceptibility. The solid line is the calculated curve using Bleaney–Bowers expression.

or a penta-coordinated geometry around it. The X-ray crystal structure shows the complex indeed displays square-pyramidal geometry.

3.4. Magnetic study

Variable-temperature magnetic susceptibility measurements of **1** have been made on a powdered monocrystalline sample in the temperature range 2–300 K under the external magnetic field of 0.5 T. Figure 4 depicts the thermal dependence of $\chi_M T$ ($\chi_M T$ vs. T) and χ_M (χ_M vs. T) for **1**. The χ values increase slowly with decrease of the temperature and a rapid increase of the molar susceptibility values is observed in the low temperature region without showing any peak. The product function $\chi_M T$ (and/or the effective magnetic moment) increases slowly on cooling from room temperature down to $T = 30$ K: $\chi_M T$ (300 K) $= 0.67\,\text{cm}^3\,\text{mol}^{-1}$ K (slightly lower than the spin-only value expected for two isolated copper(II) ions with $S = 1/2$ and $g = 2.00$), $\chi_M T$ (30 K) $= 0.72\,\text{cm}^3\,\text{mol}^{-1}$ K). Below 30 K, a rapid drop of the $\chi_M T$ product is registered until $\chi_M T$ (2 K) $= 0.57\,\text{cm}^3\,\text{mol}^{-1}$ K. This feature is characteristic of weak antiferromagnetic coupling. The magnetic data were fitted to the modified Bleaney–Bowers expression for two interacting copper(II) ions ($S = 1/2$) (Eqs. (1) and (2)) with the Hamiltonian in the form $H = -J\hat{S}_1\hat{S}_2$ (Eq. (3)) [51]

$$x_d = \frac{Ng^2\mu_B^2}{3kT}\frac{3\exp\left(\frac{J}{kT}\right)}{1 + 3\exp\left(\frac{J}{kT}\right)} \tag{1}$$

Table 4. Main structural and magnetic parameters for asymmetric double end-on ($\mu_{2\text{-}1,1}$-N$_3$) azido bridgedcomplexes.

Compound	Cu-N-Cu (°)	R (Å)	R* (Å)	Cu-Cu (Å)	τ	J (cm^{-1})	Ref.
[Cu$_2$(L)$_2$($\mu_{2\text{-}1,1}$-N$_3$)$_2$]	91.1(3), 92.4(3), 91.5(4)	2.021(8), 2.010(7), 1.999(9)	2.414(7), 2.448(8), 2.457(9)	3.205(2)	0.283, 0.227, 0.198	0.53	This work
[Cu$_2$(L)$_2$($\mu_{1,1}$-N$_3$)$_2$]	89.9	1.95	2.02	3.205	0.268	0.75	55
[Cu$_2$L$_2$(N$_3$)$_2$]	86.9	–	2.55	3.166	–	24	55
[Cu$_2$(L)(N$_3$)$_2$][ClO$_4$]$_2$	96.7	–	2.54	3.391	–	WF	55
Cu$_2$(dmterpy)$_2$(N$_3$)]$_2$(N$_3$)$_2$(NO$_3$)(H$_2$O)$_2$	117.4	1.99	2.31	3.674	–	2.9	55
[CuL^3(N$_3$)]$_2$	93.6	2.06	2.48	3.318	0.26	2.9	55
[CuL^1(N$_3$)]$_2$	90.5	1.923	2.440	3.193	0.02	−1.8	55
[Cu(dpt)(N$_3$)]$_2$(ClO$_4$)$_2$	101.0(2), 100.7(2)	2.022(4)	2.398(4)	3.314(1), 3.314(1)	0.28, 0.49	−2.9	55
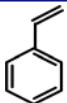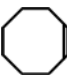
$R = $ M-N$_{azido(basal)}$; $R^* = $ M-N$_{azido(apical)}$ Å; $\tau = $ trigonality index ($\tau = 0$ infers a perfect square pyramid, $\tau = 1$ a perfect trigonal bipyramid).

$$\chi'_M = \frac{\chi_M}{1 - \left(\frac{2zJ'}{N\beta^2 g^2}\right)\chi_M} \qquad (2)$$

$$J = -\frac{(E_{HS} - E_{BS})}{(S_1 + S_2)(S_1 + S_2 + 1)} \qquad \text{[in the weak coupling limit]} \qquad (3)$$

The small J value observed, comparable with those reported for similar complexes described in the literature [52], may be explained by the fact that the magnetic orbitals are unfavorably oriented to interact. The experimental data can be matched with $J = -0.45 \text{ cm}^{-1}$, $g = 2.10$, $R = \Sigma[(\chi T)_{exp} - (\chi T)_{calc}]^2 / \Sigma[(\chi T)_{exp}]^2 = 2.53 \times 10^{-6}$. For azido-bridged binuclear copper(II) system, an unusual range of magnetic behavior is strongly dependent on two main factors: the geometry of the dimers and the $<$ Cu-N-N and Cu-N$_3$-Cu torsion angle in the bridging region. Consideration of the electronic states of weakly interacting metal centers have revealed that the bridging ligand is most effective in supporting antiferromagnetic exchange interactions between the two metal ions if the bridge has available molecular orbitals that can interact with the bonding combination of the metal's d-orbitals [53]. The antiferromagnetic contribution reduces when the environment around metal atom changes from planar to tetrahedral geometry. The coupling may be strongly antiferromagnetic when the azido bridge is in basal–basal position, in which case two $d_{x^2-y^2}$ orbitals are involved in the exchange mechanism. In the case of the examined complex, the Cu(II) ion assumes a square pyramidal coordination environment and the azido bridge adopts a basal-apical asymmetric disposition between copper ions involving $d_{x^2-y^2}$ and d_{z^2} atomic orbitals. As a result the interaction between Cu1 and Cu1′ magnetic orbitals are expected to be very weak, leading to a small exchange coupling parameter. According to literature data [54], Cu(II) dimers with double end-on asymmetric azido bridges present antiferromagnetic or ferromagnetic interaction depending not only on coordination geometry, but also of several structural parameters such as dissymmetry or asymmetry of the μ-N$_3$ bridge (the distortion on planarity described by out-of-plane displacement (Table 4) [55] Cu–Cu distance, and the nature of the other ligating centers inclusive of their fluxionality. Ferromagnetic ordering appears when the Cu-N-Cu angle is small (due to spin polarization effects) and decreases with increasing Cu-N-Cu angle up to

Table 5. Homogeneous catalytic oxidation of olefins catalyzed by [$Cu_2(L)_2(\mu_{2\text{-}1,1}\text{-}N_3)_2$] (**1**) in aceto-nitrile media.

Substrate	Reaction time (hr)	Conversion (wt%)	% yield of products	
			Epoxide	Others
	24	82	49	33a
	24	78	56	22b
	24	68	38	30c

Reaction conditions: alkenes (10 mmol); catalysts (0.005 mmol); *tert*-BuOOH (20 mmol); acetonitrile (10 mL); temperature 70 °C.
[a]Benzaldehyde and benzoic acid.
[b]Cyclooctane-1,2-diol,.
[c]Cyclohex-2-en-1-ol and cyclohex-2-en-1-one.

antiferromagnetic ordering if the bridge is large (critical angle ~104°) [55]. On the other hand, the long Cu–Cu distance reduces the overlap between the MO's bearing unpaired electrons which will result in a reduction of the magnitude of J_{AF} as evidence of ferromagnetic contributions. Temperature-dependent measurements of magnetic susceptibility reveal the occurrence of competitive exchange interactions with a net very weak ferromagnetic character. However, the elaborate hydrogen-bonding network is also able to transmit magnetic coupling [56]. Strong hydrogen bonds (Figure 2) form the next magnetic pathway between the Cu ions of neighboring dimers in the crystal network. The small magnitude of this antiferromagnetic interaction ($J = -0.45\,\text{cm}^{-1}$) is a result between the long Cu···Cu separation (3.205(2) Å). In order to explain the weakness of intramolecular interaction in **1**, two effects must be taken into account: (i) dominant intermolecular antiferromagnetic interaction ($J = -0.45\,\text{cm}^{-1}$) and (ii) the large Cu-Cu distance (3.205(2) Å), the large Cu-$N_{azido(basal)}$ distance (2.021(8) Å), smaller Cu-$N_{azido(apical)}$ distance (2.414(7) Å), the large Cu-N-Cu angle (92.4(3)°) and the large τ parameter (0.283) (Table 4). The combined effect may be attributable for the very weak nature of the magnetic character.

3.5. Catalytic activities

The catalytic activity of **1** in the epoxidation of various alkenes in homogeneous medium is summarized in Table 5. The graphical representation of different alkene conversion for **1** is shown in Figure 5. For **1**, the conversion trend of alkenes follows the order styrene > cyclooctene > cyclohexene, while the observed epoxide selectivity is cyclooctene (72%) > styrene (60%) > cyclohexene (56%). The oxidation of styrene gives styrene epoxide in 60% yield (selectivity 61%), and along with this a moderate amount of benzaldehyde and benzoic acid are also detected. Cyclooctene epoxide is produced in good yield, with high selectivity when cyclooctene reacts with *tert*-
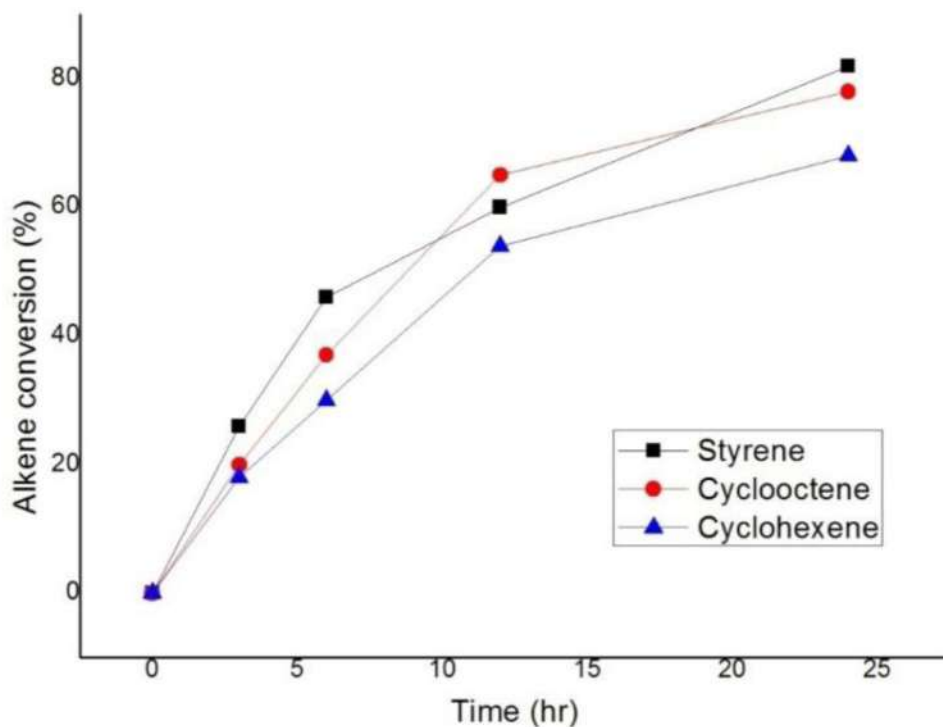
Figure 5. Reaction profile for the epoxidation of olefins with *tert*-BuOOH in the presence of **1**.

BuOOH. In addition, a small amount of cyclooctane-1,2-diol was also formed. For cyclohexene, epoxide selectivity is the least since its active allylic C-H site could also be activated in the process of oxidation. Apart from cyclohexene oxide, cyclohex-2-en-1-ol and cyclohex-2-en-1-one were also generated, owing to allylic C-H oxidation. We have studied the epoxidation of alkenes over Schiff base copper(II) azido complexes under homogeneous conditions in the recent past [35]. We have demonstrated that Schiff base copper(II) azido complexes viz., $[Cu(L^1)(N_3)],[Cu_2(L^2)_2(\mu_{2\text{-}1,1}\text{-}N_3)_2]$ $[Cu(L^2)(N_3)],[Cu(L^3)(N_3)]$ [where $HL^1 = $ 1-(*N*-5-methoxy-*ortho*-hydroxyacetophenim ino)-2,2-dimethyl-aminoethane], $HL^2 = $ 1-(*N*-ortho-hydroxyacetophenimine)-2,2-diethyl-aminoethane and $HL^3 = $ 1-(*N*-salicylideneimino)-2-(*N*,*N*-diethyl)-aminoethane] exhibit high catalytic activity in the oxidation reactions of a variety of olefins with *tert*-BuOOH in acetonitrile media. The results of the catalytic activity of these systems are compared with **1** in Table 6. From Table 6, it is evident that in similar reaction conditions, $[Cu(L^1)(N_3)]$ is more efficient catalyst than the others. This might be due to the slight variation in structural morphologies of the complexes. The decreased efficacy of **1** as well as selectivity of the reaction may be due to the absence of an electron donating group (-OMe) at the aryl ring of the Schiff base (Scheme 1). Rayati *et al.* reported that copper(II) complexes of salen-type tetradentate Schiff-bases show improved catalytic activity by introduction of *p*-electron-donating groups at the aromatic rings [26]. The effect of various reaction media on epoxidation of cyclooctene catalyzed by **1** has also been studied. A graphical representation of the relative efficacy of **1** as catalyst for the

Table 6. Comparison of catalytic efficacy of $[Cu_2(L)_2(\mu_{2-1,1}-N_3)_2]$ (1) with other reported copper(II) azido catalysts for the epoxidation of alkenes with *tert*-BuOOH in acetonitrile media.

Complex	Conversion (%)			References
	Styrene	Cyclooctene	Cyclohexene	
$[Cu(L^1)(N_3)]$	98	95	82	[15]
$[Cu_2(L^2)_2(\mu_{2-1,1}-N_3)_2]$ $[Cu(L^2)(N_3)]$	96	90	84	[15]
$[Cu(L^3)(N_3)]$	90	85	70	[15]
$[Cu_2(L)_2(\mu_{2-1,1}-N_3)_2]$	82	78	68	This work

HL^1 = 1-(*N*-5-methoxy-ortho-hydroxyacetophenimino)-2,2-dimethyl-aminoethane], HL^2 = 1-(*N*-ortho-hydroxyaceto-phenimine)-2,2-diethyl-aminoethane and HL^3 = 1-(*N*-salicylideneimino)-2-(N,N-diethyl)-aminoethane.
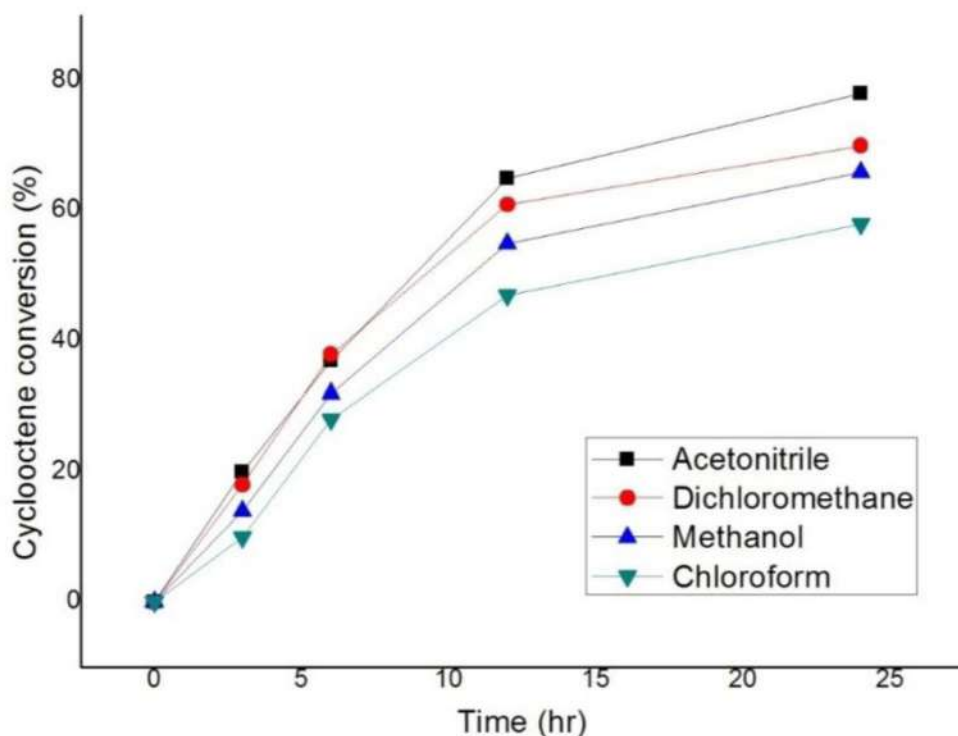
Figure 6. Reaction profile for the epoxidation of cyclooctene with *tert*-BuOOH in different solvents over **1**.

epoxidation of cyclooctene in different solvents has been given in Figure 6. From Figure 6, it is evident that the best performance of the catalyst was observed in acetonitrile medium. The catalytic efficiency follows the order acetonitrile > dichloromethane > methanol > chloroform. The facilitating factor of the epoxidation may be attributed due to optimum polarity of acetonitrile to dissolve both olefin and *tert*-BuOOH. A similar trend was found in our previous work [34, 35]. Bera *et al.* also reported the same trend in the study of epoxidation of cyclooctene catalyzed by a single end-on azido-bridged Schiff base copper(II) complex [32]. We studied the reactions of cyclooctene by varying the temperature from room temperature to 75 °C in acetonitrile to determine the optimum temperature. It was found that
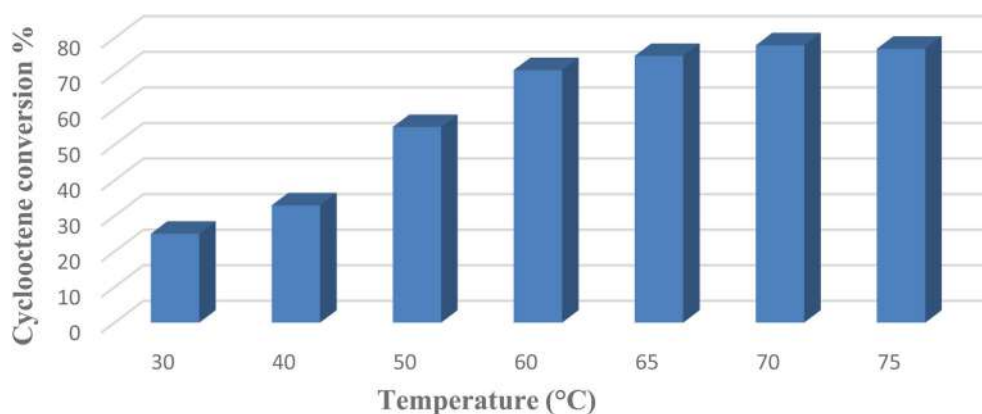
Figure 7. Comparison of catalytic efficacy of **1** at different temperatures.

maximum conversion occurs at 70 °C (Figure 7). The complex contains a five-coordinate coordinatively unsaturated Cu-center, thus the complex has been used for Lewis acid catalysis reactions under homogeneous conditions. The copper(II) binds the peroxo-group upon treatment with peroxides [41] to form the pre-catalyst containing LxCu–OOH (where L = ligand), which are capable of transferring the oxo-functionality to the organic substrates to produce the oxidized products [42, 43]. We assume that a similar kind of mechanism is operative in our case. X-ray crystal structure analysis shows the presence of five-coordinate Cu(II) in [Cu$_2$(L)$_2$($\mu_{2\text{-}1,1}$-N$_3$)$_2$] (**1**). Thus, the coordination environment around copper(II) is easily accessible for an external ligand. As a result, *tert*-BuOOH gets enough space to bind copper in the intermediate stages of the catalytic cycle.

4. Conclusion

One neutral diazido-bridged dinuclear copper(II) compound, bis{(2-[1-(aminoethylimino)methyl]-phenoxo}-di-$\mu_{1,1}$-azido-dicopper(II) (**1**), containing a tridentate Schiff base ligand has been isolated. Structural analysis reveals that each copper(II) center, with a distorted square pyramidal geometry in **1**, is linked to each other by asymmetric $\mu_{2\text{-}1,1}$-azido bridges in the square pyramid conformation. The structure of **1** is stabilized by intermolecular weak N-H···O hydrogen bond interactions forming a 2-D sheet structure. Variable-temperature magnetic susceptibility measurement shows weak intermolecular antiferromagnetic interactions among the dinuclear entities as a result between the long Cu···Cu separation. The complex exhibited excellent catalytic activity in homogeneous oxidation of alkenes. A better selectivity was found when acetonitrile was used as a solvent. The catalytic efficacy of similar copper(II) azido complexes was compared. It was found that the absence of an electron-donating group at the aryl ring of the Schiff base decreases the efficiency of the catalyst.

Disclosure statement

Acknowledgement

Funding

ORCID

Corrado Rizzoli http://orcid.org/0000-0002-4841-6123

References

[1] R.D. Willet, D. Gatteschi, O. Kahn (Eds.). *Magneto-Structural Correlations in Exchange Coupled Systems*, NATO ASI Series, Reidel, Dordrecht (1985).
[2] M.M. Turnbull, T. Sugimoto, L.K. Thompson (Eds.). *Molecular Based Magnetic Materials: Theory, Techniques and Applications*, ACS Symposium Series, Vol. 644, ACS, Washington (1996).
[3] A. Caneschi, D. Gatteschi, L. Pardi, R.S. Clusters. In *Perspectives in Coordination Chemistry*, A.F. Williams (Ed.), VCH, Weinheim, 486 (1992).
[4] J.L. Manson, A.M. Arif, J.S. Miller. *Chem. Commun.*, 1479, (1999).
[5] O. Kahn. *Comments Condens. Mater. Phys.*, **17**, 39 (1994).
[6] J.R. Long. In *Molecular Cluster Magnets in Chemistry of Nanostructured Materials*, P. Yang (Ed.), World Scientific, Hong Kong, 291 (2003).
[7] L.K. Thompson, S.K. Tandon. *Comments Inorg. Chem.*, **18**, 125 (1996).
[8] A. Escuer, G. Aromí. *Eur. J. Inorg. Chem.*, **2006**, 4721 (2006).
[9] Y.-F. Zeng, X. Hu, F.-C. Liu, X.-H. Bu. *Chem. Soc. Rev.*, **38**, 469 (2009).
[10] S. Saha, D. Mal, S. Koner, A. Bhattacherjee, P. Gütlich, S. Mondal, M. Mukherjee, K.-I. Okamoto. *Polyhedron*, **23**, 1811 (2004).
[11] S. Koner, S. Iijima, M. Watanabe, M. Sato. *J. Coord. Chem*, **56**, 103 (2003).
[12] O. Kahn. *Adv. Inorg. Chem.*, **43**, 179 (1995).
[13] R. Robson. *Aust. J. Chem.*, **23**, 2217 (1970).
[14] A. Escuer, M.A.S. Goher, F.A. Mautner, R. Vicente. *Inorg. Chem.*, **39**, 2107 (2000).
[15] W.-W. Sun, X.-B. Qian, C.-Y. Tian, E.-Q. Gao. *Inorg. Chim. Acta*, **362**, 2744 (2009).
[16] S. Sikorav, I. Bkouche-Waksman, O. Kahn. *Inorg. Chem.*, **23**, 490 (1984).
[17] B. Graham, M.T.W. Hearn, P.C. Junk, C.M. Kepert, F.E. Mabbs, B. Moubaraki, K.S. Murray, L. Spiccia. *Inorg. Chem.*, **40**, 1536 (2001).
[18] S.S. Tandon, L.K. Thompson, M.E. Manuel, J.N. Bridson. *Inorg. Chem.*, **33**, 5555 (1994).
[19] S. Youngme, T. Chotkhun, S. Leelasubcharoen, N. Chaichit, C. Pakawatchai, G.A. van Albada, J. Reedijk. *J. Reedijk. Polyhedron*, **26**, 725 (2007).
[20] J.D. Woodward, R.V. Backov, K.A. Abboud, D. Dai, H.-J. Koo, M.-H. Whangbo, M.W. Meisel, D.R. Talham. *Inorg. Chem.*, **44**, 638 (2005).
[21] G. Das, R. Shukla, S. Mandal, R. Singh, P.K. Bharadwaj, J. van Hall, K.H. Whitmire. *Inorg. Chem.*, **36**, 323 (1997).
[22] S. Zolezzi, E. Spodine, A. Decinti. *Polyhedron*, **22**, 1653 (2003).
[23] C. Adhikary, R. Bera, B. Dutta, S. Jana, G. Bocelli, A. Cantoni, S. Chaudhuri, S. Koner. *Polyhedron*, **27**, 1556 (2008).
[24] S. Bunce, R.J. Cross, L.J. Farrugia, S. Kunchandy, L.L. Meason, K.W. Muir, M.O. Donnell, R.D. Peacock, D. Stirling, S.J. Teat. *Polyhedron*, **17**, 4179 (1998).

[25] X.-H. Lu, Q.-H. Xia, H.-J. Zhan, H.-X. Yuan, C.-P. Ye, K.-X. Su, G. Xu. *J. Mol. Catal. A: Chem.*, **250**, 62 (2006).
[26] S. Rayati, S. Zakavi, M. Koliaei, A. Wojtczak, A. Kozakiewicz. *Inorg. Chem. Commun.*, 13, 203 (2010).
[27] P. Karandikar, M. Agashe, K. Vijayamohanan, A. Chandwadkar. *Appl. Catal. A: Gen.*, **257**, 133 (2004).
[28] S. Koner. *Chem. Commun.*, **5**, 593 (1998).
[29] S. Jana, B. Dutta, R. Bera, S. Koner. *Langmuir*, **23**, 2492 (2007).
[30] S. Jana, B. Dutta, R. Bera, S. Kone. *Inorg. Chem.*, **47**, 5512 (2008).
[31] R. Sen, R. Bera, A. Bhattacharjee, P. Gutlich, S. Ghosh, A.K. Mukherjee, S. Koner. *Langmuir*, **24**, 5970 (2008).
[32] R. Bera, C. Adhikary, S. Ianelli, S. Chaudhuri, S. Koner. *Polyhedron*, **29**, 2166 (2010).
[33] P. Roy, K. Dhara, M. Manassero, P. Banerjee. *Inorg. Chem. Commun.*, **11**, 265 (2008).
[34] S. Banerjee, C. Adhikary, C. Rizzoli, R. Pal. *Inorg. Chim. Acta*, **409**, 202 (2014).
[35] C. Adhikary, S. Banerjee, J. Chakraborty, S. Ianelli. *Polyhedron*, **65**, 48 (2013).
[36] L.F. Veiros, A. Prazeres, P.J. Costa, C.C. Romão, F.E. Kühn, M.J. Calhorda. *Dalton Trans.*, **11**, 1383 (2006).
[37] J.-M. Brégeault. *Dalton Trans.*, **17**, 3289 (2003).
[38] M.N. Sheng, G.J. Zajaczek. ARCO, Br. Pat., 1,136,923 (1968).
[39] J.H. Kollar. US Pat. 3,350,422 (1967).
[40] J.H. Kollar. US Pat. 3,351,635 (1967).
[41] E.A. Boudreaux, L.N. Mulay. *Theory and Applications of Molecular Paramagnetism*, Wiley-Interscience, New York (1976).
[42] Bruker APEX2 (Version 2008.1-0), *SAINT (Version 7.51A) and SADABS (Version 2007/4)*, Bruker AXS Inc., Madison, Wisconsin, USA (2008).
[43] A. Altomare, M.C. Burla, M. Camalli, G. Cascarano, C. Giacovazzo, A. Uagliardi, A.G.G. Moliterni, G. Polidori, R. Spagna. *J. Appl. Crystallogr.*, **32**, 115 (1999).
[44] G.M. Sheldrick. *Acta Crystallogr. C Struct. Chem.*, **71**, 3 (2015).
[45] K. Nakamoto. *Infrared and Raman Spectra of Inorganic and Coordination Compounds*, 5th edn., Parts A and B, Wiley, New York (1997).
[46] P. Dapporto, M. Formica, V. Fusi, L. Giorgi, M. Micheloni, P. Paoli, R. Pontellini, P. Rossi. *Inorg. Chem.*, **40**, 6186 (2001).
[47] T. Gajda, A. Jancso, S. Mikkola, H. Lonnberg, H. Sirges. *J. Chem. Soc. Dalton Trans.*, 1757 (2002).
[48] A.B.P. Lever. *Inorganic Electronic Spectroscopy*, 2nd edn., Elsevier, New York (1984).
[49] A.W. Addison, T.N. Rao, J. Reedijk, J. van Rijn, G.C. Verschoor. *J. Chem. Soc. Dalton Trans*, 1349 (1984).
[50] (a) W.T.M. Andriessen. *Inorg. Chem.*, **14**, 792 (1975);(b) B.R. McGarvey, R.L. Carlin (Eds.). *Transition Metal Chemistry*, Vol. 89, Marcel Dekker, New York (1966);(c)M.M. Roessler, E. Salvadori. *Chem. Soc. Rev.*, **47**, 2534 (2018);(d) S. Stoll, R.D. Britt. *Phys. Chem. Chem. Phys.*, **11**, 6614 (2009).
[51] (a) B. Bleaney, K.D. Bowers. *Inorg. Chem.*, 214, 1068 (2012);(b) D.L. Reger, A. Debreczeni, M. Smith, J. Jezierska, A. Ożarowski. *Inorg. Chem.*, **51**, 1068 (2012).
[52] (a) L. Gasque, V.M. Ugalde-Saldivar, I. Membrillo, J. Olguin, E. Mijangos, S. Bernes, I. Gonzales. *J. Inorg. Biochem.*, **102**, 1227 (2008);(b) A.E. Reed, L.A. Curtiss, F. Weinhold. *Chem. Rev.*, **88**, 899 (1988).
[53] E.D. Glendening, A.E. Reed, J.E. Carpenter, F. Weinhold. *NBO 3.1 Theoretical Chemistry Institute*, University of Wisconsin, Madison, WI (1996).
[54] (a) P.J. Hay, J.C. Thibeault, R. Hoffmann, *J. Am. Chem. Soc.*, **97**, 4884 (1975);(b), O. Kahn. *Molecular Magnetism*, VCH Publishers, New York (1993).
[55] C. Adhikary, S. Koner. *Coord. Chem. Rev.*, **254**, 2933(2010).
[56] (a) C. Desplanches, E. Ruiz, A. Rodriguez-Fortea, S. Alvarez. *J. Am. Chem. Soc.*, 124, 5197 (2002);(b) P. Talukder, S. Sen, S. Mitra, L. Dahlenberg, C. Desplanches, J.-P. Sutter. *Eur. J. Inorg. Chem.*, 2006, 329 (2006) ;(c) G. Mendoza-Diaz, W.L. Driessen, J. Reedijk, S. Gorter, L. Gasque, K.R. Thompson. *Inorg. Chim. Acta*, **339**, 51 (2002).

Source details

Feedback ›   Compare sources ›

Journal of Coordination Chemistry

Scopus coverage years: from 1971 to Present

Publisher: Taylor & Francis

ISSN: 0095-8972   E-ISSN: 1029-0389

Subject area: (Materials Science: Materials Chemistry)   (Chemistry: Physical and Theoretical Chemistry)

Source type: Journal

View all documents ›   Set document alert   💾 Save to source list

CiteScore 2022	ⓘ
3.0	

SJR 2022	ⓘ
0.279	

SNIP 2022	ⓘ
0.491	

CiteScore   CiteScore rank & trend   Scopus content coverage

ℹ️ Improved CiteScore methodology   ✕

A nitrate bridged one-dimensional copper(II) coordination polymer with a tridentate (NNO) Schiff base: synthesis, X-ray structure and catalytic efficacy

Habibar Chowdhury[1] · Rajesh Bera[2] · Corrado Rizzoli[3] · Chandan Adhikary[4]

Abstract

A one-dimensional Cu(II) coordination polymer of $[Cu(L)(\mu\text{-}ONO_2)]_n$ (**1**) (HL = 4-methoxy-2-[1-(methylaminoethylimino) methyl]-phenol) with bidentate bridging nitrate has been isolated and characterized by X-ray diffraction analysis and spectroscopic studies. Single crystal X-ray analysis revealed that each copper(II) center in the asymmetric unit of complex **1** adopts a distorted square pyramidal geometry with a CuN_2O_3 chromophore ligated through a tridentate Schiff base (L) with (NNO) donor sets and two O atoms of bridging nitrate ion. The adjacent copper atoms are connected by bridging nitrate (μ-ONO_2) in bidentate fashion affording a 1D coordination polymeric chain structure along the crystallographic *b*-axis. In the polymeric framework, the Cu…Cu separation is 4.3749(4) Å. The catalytic efficacy of complex **1** was studied in a series of solvents for the epoxidation of cyclooctene using *tert*-butyl-hydroperoxide (TBHP) as an efficient oxidant under mild conditions. The catalytic reaction mixture was analyzed by gas chromatography and the data indicated that the yield of the epoxidation reaction and its selectivity is maximum in acetonitrile medium.

✉ Chandan Adhikary
cadhikary123@gmail.com

Habibar Chowdhury
habibar_hs@yahoo.co.in

Rajesh Bera
berarajesh2010@gmail.com

Corrado Rizzoli
corrado.rizzoli@unipr.it

[1] Department of Chemistry, Kabi Nazrul College, Murarai, Birbhum, West Bengal 731 219, India

[2] Department of Chemistry, Dinabandhu Andrews College, Kolkata, West Bengal 700084, India

[3] Departimento di Scienze Chimiche, della Vita e della Sostenibilità Ambientale, Parco Area delle Scienze 17/A, 43124 Parma, Italy

[4] Department of Chemistry, Institute of Education (P.G.) for Women, Chandernagore, Hooghly, West Bengal 712138, India

Introduction

Coordination polymers (CPs) [1] and metal–organic frameworks (MOFs) [2] through strong metal–ligand covalent bonds [3] and multiple weak non-covalent forces [4] have attracted great attention of many research groups in the isolation of different advanced functional materials [5–9]. Single-pot synthesis [10] is an efficient synthetic approach using judiciously chosen metal ions, organic ligands and bridging units in pre-assigned molar ratios to isolate such target materials. Cu(II), a $3d^9$ ion, affords [11] a variety of geometries that may lead to significant differences in overall molecular and crystalline architectures and thereby produce different biological and catalytic activities [12]. The copper ion also finds significant use in bioinorganic chemistry [13]. A group of mono-negative NNO donor tridentate Schiff base ligands derived from the mono-condensation of diamines with carbonyl compounds (salicylaldehyde, o-hydroxyacetophenone, acetylacetone or benzoylacetone), readily react with transition metal ions and auxiliary ligands to form mono- and polynuclear complexes with varied functionalities and versatile applications. Depending on the relative position, number and nature of the donor atoms of a Schiff base, the ligand approves a favourable control over the stereochemistry of the metallic centers in homo- and heteropolynuclear compounds

Fig. 1 Different coordination motifs of the nitrate ion
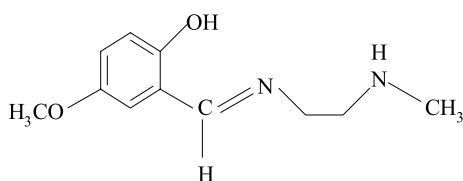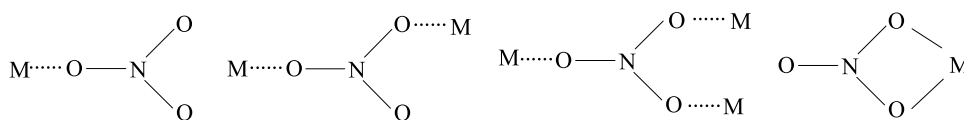
Fig. 2 Framework of tridentate (NNO) Schiff base ligand (HL)

[14]. All these opportunities make Schiff bases privileged ligands in the attempt to synthesize metal complexes having relevance to bioinorganic chemistry, catalysis, encapsulation, transport and separation processes [14]. Schiff base copper complexes can now be extensively used as active catalysts in several oxidation reactions, both in homogeneous [15–18] and heterogeneous condition [19, 20]. Nitrate ion (NO_3^-) [21] acts as monodentate, bidentate bridging and bidentate chelating ligand (Fig. 1) for the construction of supramolecular architectures. In the framework of our research efforts constituting a part of our continuing study on metal complexes of tridentate Schiff base ligands based on substituted ethylenediamines, we have chosen a tridentate Schiff base (HL) (Fig. 2) to isolate a neutral coordination polymer, $[Cu(L)(\mu\text{-}ONO_2]_n$ (1) (HL = 4-methoxy-2-[1-(methylaminoethylimino)methyl]-phenol). The structure of complex 1 has been determined by X-ray diffraction measurements and the catalytic efficacy of 1 for the epoxidation of cyclooctene, employing *tert*-butyl-hydroperoxide (TBHP) as an efficient oxidant in different solvent media, is also reported.

Experimental

Materials and method

High purity 5-Methoxysalicyladehyde (E. Merck, India), *N*-methyl ethanediamine (Aldrich, USA) and Cu(II) nitrate hexahydrate (E. Merck, India) were purchased from their respective concerns and used as received. Cyclooctene and

tert-BuOOH (70% aq.) were purchased from Aldrich and used as received. All other chemicals and solvents were AR grade. The solvents used were distilled and dried before use. The synthetic reactions and work-up were done in the open air. Microanalysis (CHN) was performed using a Perkin Elmer 240 elemental analyzer. IR spectra were recorded with a Bruker Alpha T 200140 FT-IR spectrometer. Absorption spectra were studied with a Shimadzu UV2100 UV–Vis recording spectrophotometer. GC analysis was carried out with an Agilent Technologies 6890 N network GC system equipped with a fused silica capillary column (30 m × 0.32 mm) and a FID detector.

Synthesis of Schiff base (HL)

5-Methoxysalicyladedehyde (0.15 g, 1 mmol) was refluxed (10 h) with N-methylethylenediamine (0.07 g, 1 mmol) in dehydrated alcohol (20 ml) with a little modification [22]. After 10 h the reaction solution was evaporated under reduced pressure to yield a gummy mass, which was dried and stored *in vacuo* over $CaCl_2$ for subsequent use (Scheme 1). Yield 0.28 g (80% based on amine). Elemental Anal. Calcd for $C_{11}H_{16}N_2O_2$ (HL): C, 63.4; H, 7.7; N, 13.5%. Found: C, 63.8; H, 8.2; N, 13.5%. FTIR (cm^{-1}): ν(C=N), 1632; ν(N–H), 3120.

Synthesis of [Cu(L)(μ-ONO₂)]ₙ (1)

A solution of HL (0.21 g, 1 mmol) in MeOH (5 ml) was added dropwise to a solution of Cu(II) nitrate hexahydrate (0.29 g, 1 mmol) in the same solvent (10 ml). The final deep blue solution was filtered and the supernatant liquid was kept undisturbed in open air for slow evaporation. After 5 days, a blue crystalline product of 1 was isolated by filtration, washed with dehydrated alcohol and dried *in vacuo* over silica gel. Yield 0.44 g (70% based on ligand). *Anal.* Calcd for $C_{11}H_{15}N_3O_5Cu$ (1): C 39.7; H 4.5; N 12.6%. Found: C 40.2; H 4.1; N 13.0%. FTIR (KBr/cm^{-1}): $\nu_s(NO_3)$ 1735, 1794. UV–Vis in DMF [λ_{max}, nm (ε_{max}/dm^{3}mol^{-1} cm^{-1})]: 266, 296 (1.20 × 10^4), 387 (1.15 × 10^4), 607 (2.30 × 10^2); Λ_M (DMF/ohm^{-1} cm^2 mol^{-1}):

Scheme 1 Synthetic route for Schiff base HL

Schiff base (HL)
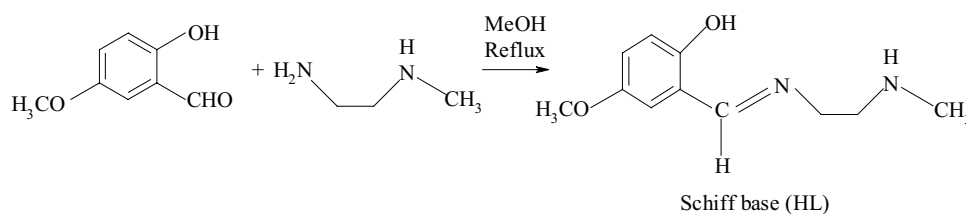
6. $\mu_{\text{eff.}}$ (B.M.) $= 1.78$. ESR (solid state): $g_{\parallel} = 2.042$; $g_{\perp} = 2.013$, $g_{\text{av}} = 2.022$; $G = 4.753$.

X-ray crystallographic analysis

A single crystal of **1** suitable for X-ray analysis was selected from those obtained by slow evaporation of a methanol solution at room temperature. Diffraction data were collected on a Bruker SMART 1000 CCD diffractometer using graphite monochromated Mo-$K\alpha$ radiation ($\lambda = 0.71073$ Å) and were used to measure cell dimensions and diffraction intensities. Data were collected using the ω–θ scan technique in the range to a maximum $2.7° < \theta < 25.5°$. For data collection, data reduction and cell refinement. the program SAINT-Plus [23] was used. The structure was solved by direct methods using SIR97 [24] and refined with version 2018/3 of SHELXL [25] using Least Squares minimisation. The model was refined. The amine H atoms were located on a difference Fourier map and refined freely. C-bound H atoms were positioned geometrically and refined using a riding model, with C–H $= 0.96$–0.97 Å and with Uiso $= 1.2$ Ueq(C) or 1.5 Ueq(C) for methyl H atoms. The final positional and thermal parameters are available as supplementary material. A summary of the crystallographic data and structure determination parameters for complex **1** is set in Table 1. Crystallographic data for the structural analysis has been deposited with the Cambridge Crystallographic Data Centre (CCDC No. 2000429 for **1**). A copy of this information can be obtained free of charge from The Director, CCDC, 12 Union Road, Cambridge, CB2 1EZ, UK (fax:+44-1223-336-033; e-mail: deposit@ccdc.cam.ac.uk or www: https://www.ccdc.cam.ac.uk).

Catalytic reactions

The catalytic reactions were carried out in a glass batch reactor, according to the following procedure. Substrate (10 mmol), solvent (8 ml) and catalyst (0.005 mmol) were first mixed in a round-bottom flask. The mixture was then equilibrated to 65 °C in an oil bath. After addition of *tert*-BuOOH (20 mmol), the mixture was stirred continuously for 24 h. The products of the oxidation reactions were collected at different time intervals and were identified and quantified by a VARIAN CP-3800 gas chromatograph equipped with an FID detector. A CP-Sil 8 CB capillary column was used for analysis of the products.

Results and discussion

Synthesis and physical measurements

A nitrate bridged 1D chain Cu(II) coordination polymer, $[\text{Cu(L)}(\mu\text{-ONO}_2)]_n$ (**1**)

Table 1 Crystallographic data and structure refinement parameters for **1**

Crystal parameters	**1**
Empirical formula	$C_{11}H_{15}N_3O_5Cu$
Formula weight	332.80
Crystal system	Monoclinic
Space group	$P\,21/n$
A (Å)	12.8738 (10)
b (Å)	7.8553 (6)
c (Å)	13.0713 (10)
α^0	90
$\beta°$	93.6188 (12)
γ^0	90
V (Å^3)	1319.23 18)
λ (Å)	0.71073
ρ_{calcd} (g cm^{-3})	1.672
Z	4
T (K)	294(2)
μ (mm^{-1})	1.676
$F(000)$	684
Crystal size (mm^3)	$0.17 \times 0.09 \times 0.08$
θ ranges (°)	2.15 to 25.25
Index ranges	$-14 \leq h \leq 15$ $-9 \leq k \leq 9$ $-15 \leq l \leq 15$
Reflections collected	8498
Independent reflections	2401
T_{max} and T_{min}	0.878 and 0.812
Data/restraints/parameters	2401/1/187
R (int)	0.025
Goodness-of-fit on F^2	1.066
Final R indices [$I > 2\sigma(I)$]	$R = 0.0275$ and wR $= 0.0734$
R indices (all data)	$R = 0.0307$ and wR $= 0.0756$
Largest peak and hole (eÅ^{-3})	0.333 and -0.186

Weighting scheme: $R = \Sigma||F_o| - |F_c||/\Sigma|F_o|$, wR $= [\Sigma w(F_o^2 - F_c^2)^2/\Sigma w(F_o^2)^2]^{1/2}$, calcd $w = 1/[\sigma^2(F_o^2) + (0.0422P)^2 + 0.5323P]$ where $P = (F_o^2 + 2F_c^2)/3$

HL $= 4$-methoxy-2-[1-(methylaminoethylimino)methyl]-phenol) has been isolated using a one-pot reaction of a 1:1 molar ratio of Cu(NO$_3$)$_2$·6H$_2$O and a Schiff base (HL) in methanol at room temperature. The typical synthesis is summarized in Eq. (1):
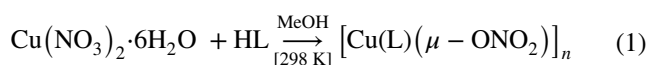
$$\text{Cu}(\text{NO}_3)_2 \cdot 6\text{H}_2\text{O} + \text{HL} \xrightarrow[\text{[298 K]}]{\text{MeOH}} [\text{Cu(L)}(\mu - \text{ONO}_2)]_n \quad (1)$$

Complex **1** was characterized by microanalytical (C, H and N), spectroscopic and other physico-chemical results. The microanalytical data are in good agreement with the formulation of the complex. The air stable moisture insensitive compound is stable over a long period of time in powder and crystalline states and is soluble in MeOH, EtOH, MeCN,
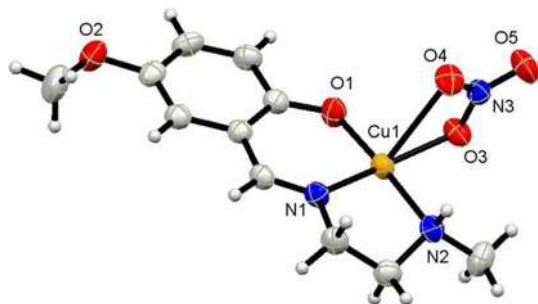
Fig. 3 An ORTEP diagram of the asymmetric unit of [Cu(L) (μ-ONO$_2$)]$_n$ (**1**) with displacement ellipsoids drawn at the 50% probability level
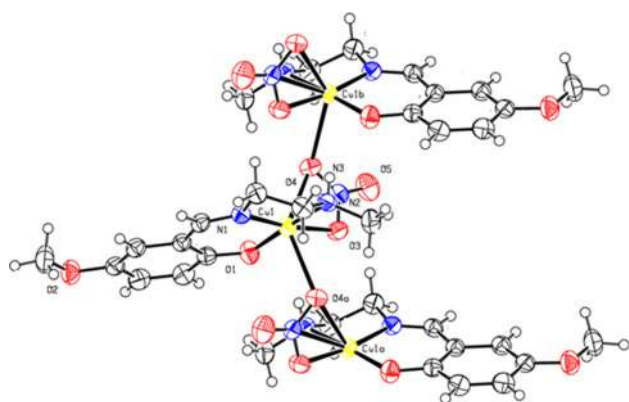
Fig. 4 Perspective view of molecular unit of **1**

DMF and DMSO, but is insoluble in water. In DMF solution, the complex **1** is a non-electrolyte as reflected from the low conductivity value (6 $\Omega^{-1}cm^2mol^{-1}$).

Crystal structure of [Cu(L)(μ-ONO$_2$)]$_n$ (1)

Single crystal X-ray diffraction study of [Cu(L)(μ-ONO$_2$)]$_n$ (**1**) was made to define the coordination sphere. An ORTEP diagram of asymmetric units, molecular unit and packing view of 1D polymeric chain structure of 1 are depicted in Figs. 3, 4 and 5, respectively. Selected bond distances and angles relevant to the coordination spheres are presented in Table 2. X-ray structural analysis reveals that each Cu(II) center in the asymmetric unit of **1** adopts a distorted square pyramidal geometry ($\tau = 0.07$) with a CuN$_2$O$_3$ chromophore [26] coordinated by two N atoms (N1, N2) and one O atom (O1) of the tridentate Schiff base ligand (L) and two O atoms (O3, O4) of the bridging nitrate (Fig. 3). A considerable deviation from ideal square pyramidal geometry is seen, which is presumably due to the smaller bite angles produced by ligand [N1–Cu1–N2 84.54(7)°] and nitrate [O3–Cu1–O4_a 79.37(6)°]. The coordination sites of the
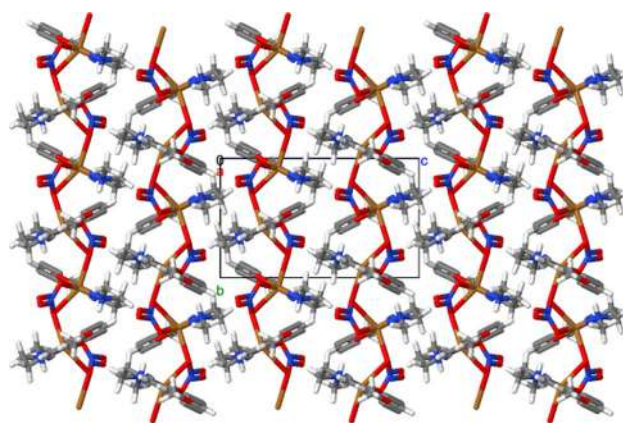
Fig. 5 Partial and complete crystal packing views of **1** showing a polymeric chain extending along *b* axis

Table 2 Selected bond distances (Å) and bond angles (°) for **1**

Bond distances			
Cu1–N1	1.9384 (17)	Cu1–O4_a	2.4319 (16)
Cu1–N2	2.0386 (19)	Cu1_b–O4	2.4319 (16)
Cu1–O1	1.9026 (15)	O3–N3	1.276 (2)
Cu1–O3	2.0531 (15)	O4–N3	1.242 (2)
Cu1–O4	2.5817 (16)	O5–N3	1.215 (2)
Bond angles			
N1–Cu1–N2	84.54 (7)	N2–Cu1–O4_a	86.94 (7)
N1–Cu1–O1	94.14 (7)	O1–Cu1–O3	89.76 (6)
N1–Cu1–O3	172.11 (7)	O1–Cu1–O4	91.72 (6)
N1–Cu1–O4	119.12 (6)	O1–Cu1–O4_a	90.05 (7)
N1–Cu1–O4_a	107.44 (7)	O3–Cu1–O4	53.81 (6)
N2–Cu1–O1	176.19 (7)	O3–Cu1–O4_a	79.37 (6)
N2–Cu1–O3	91.99 (7)	O4–Cu1–O4_a	133.12 (6)
N2–Cu1–O4	92.04 (7)	Cu1–O4–Cu1_b	121.50 (7)

Symmetry code: (a) $1/2-x$, $-1/2+y$, $1/2-z$; (b) $1/2-x$, $1/2+y$, $1/2-z$

basal plane are occupied by two N atoms (N1, N2) and one O atom of the Schiff base (L) and two O atoms (O3, O4) of bridging nitrate acting as a bidentate ligand. The bond distance of Cu1–N1$^{(amine)}$ [1.9384(17)Å] is smaller than Cu1–N2$^{(imine)}$ [2.0386(19) Å]. The three Cu–O bond lengths are different, where Cu1–O1(ligand) [1.9026(15) Å] is smallest than the other two Cu1–O3(nitrate) [2.0531(15) Å] and Cu1–O4(nitrate) [2.5817(16) Å] (Table 2). The Cu(II) center deviates 0.0314(2) Å from the N1/N2/O1/O3 mean plane. The apical position is occupied by O atom [Cu1–O4_a: 2.4319(16) Å; symmetry code: $a = 1/2-x$, $-1/2+y$, $1/2-z$] of the other bridging nitrate (Fig. 6). Complex **1** is an example of a coordination polymer containing a bidentate bridging nitrate. The adjacent copper atoms are connected by a bidentate bridging nitrate with μ-ONO$_2$ bridging mode affording a 1D polymeric chain structure (Fig. 5). The Cu1–O4–Cu1_*b*

(symmetry code: $b = ½ − x, −½ + y, ½ − z$) bridging angle is 121.49(6)°. In the polymeric framework, the Cu…Cu separation is 4.3749(4) Å.

FT-IR and electronic spectra of 1

In the FT-IR spectrum, complex **1** exhibits a band at 1794 cm^{-1} with a shoulder at 1735 cm^{-1} due to the bidentate bridging nitrate [21]. Also, the bands of weak intensity at 3062, 2945 and 2840 cm^{-1} are assigned to the C–H stretching vibrations of aromatic rings, methylene and methoxy groups, respectively [27]. In the UV–Vis spectrum, a weak low-intensity absorption band at 600 nm is assignable to *d–d* transition, consistent with the square pyramidal (sp) geometry of the Cu(II) centers [28]. The absorption band observed at 380 nm may be attributed to the ligand -to -Cu(II) charge transfer transition (LMCT) [29]. Additionally, two strong absorption bands in the region 265 and 295 nm may be assigned to ligand-based transitions.

Magnetic study and EPR spectroscopy of 1

Room-temperature solid-phase magnetic susceptibility measurement shows that compound (**1**) has a magnetic moment of 1.78 BM, which is close to the expected spin-only value. The powder EPR spectrum of complex **1** in the solid state is depicted in Fig. 6. The principal *g* values have been determined by conventional methods of EPR spectroscopy [30]. The $g_{\parallel}$ and $g_{\perp}$ values of the complex were calculated to be 2.18 and 2.08 with $g_{av} = 2.022$; $G = 4.753$. This is a typical axial spectrum in which the copper(II) ion possesses either a square planar or five-coordinate geometry. The X-ray crystal structure shows that the complex indeed displays a square-pyramidal coordination geometry.

Catalytic activities

The catalytic activity of $[Cu(L)(\mu\text{-}ONO_2)]_n$ (**1**) was studied in the epoxidation of cyclooctene with *tert*-BuOOH as an oxidant. Cyclooctene was converted to cyclooctene epoxide in

good yield with high selectivity in different solvents when catalyzed by complex **1**. The results of the catalytic epoxidation of cyclooctene are given in Table 3. As evident from Table 3, complex **1** exhibits the highest conversion of 88% with 86% epoxide selectivity. A graphical representation of the relative efficacy of complex **1** as catalyst for the epoxidation of cyclooctene in different solvents has been given in Fig. S1. In general, the catalytic efficiency in different solvents followed the order: acetonitrile > chloroform > dichloromethane > methanol. The optimum polarity of acetonitrile that is suitable to dissolve both *tert*-BuOOH and cyclooctene might be facilitating the highest catalytic activity. We studied the reactions by varying the temperature from room temperature to 75 °C in acetonitrile to determine the optimum temperature. It was found that the maximum conversion occurred at 65 °C (Fig. S2). The results of control experiments in the epoxidation of cyclooctene with *tert*-BuOOH at 65 °C are presented in Table 4. Control experiments without using catalyst failed to produce the desired product. The conversion of cyclooctene was only 4% in the absence of the catalyst. The $Cu(NO_3)_2$ salt, however, achieved a conversion of 66%, but selectivity was lower (53%). The results of reported epoxidation reactions of cyclooctene using *tert*-BuOOH as oxidant over Cu(II) Schiff base complexes under homogeneous conditions are collated in Table 5 [15–18]. We have earlier studied the oxidation reactions of a variety of olefins over Cu(II) Schiff base complexes, $[Cu(L^1)(H_2O)](ClO_4)$

Table 3 Homogeneous oxidation of cyclooctene catalyzed by the complex $[Cu(L)(\mu\text{-}ONO_2)]_n$ (**1**) at 65 °C in different solvents

Solvents	Reaction time (Hr)	Conversion (wt%)	Yield of products	
			Epoxide	Others
CH$_3$CN	24	88	86	2[a]
CH$_2$Cl$_2$	24	64	59	5[a]
CHCl$_3$	24	58	53	5[a]
CH$_3$OH	24	55	44	11[a]

Reaction conditions: Cyclooctene (10 mmol); catalysts (0.005 mmol); *tert*-BuOOH (20 mmol); acetonitrile (8 mL). [a]2-Cyclooctene-1-ol

Fig. 6 Powder EPR spectrum of the complex **1**
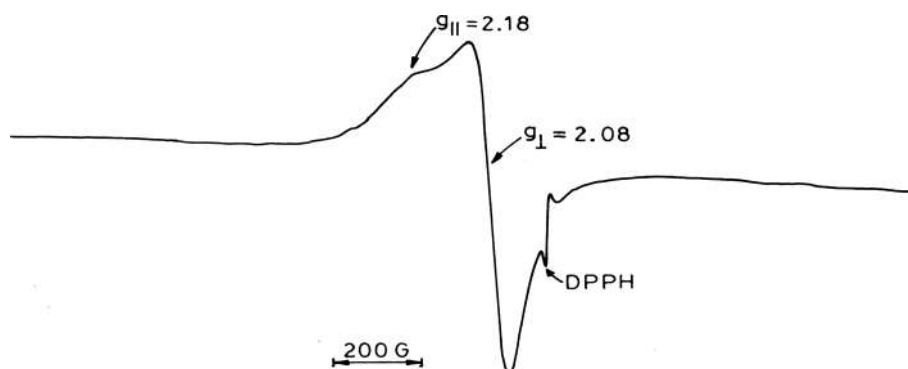
Table 4 Control experiments in epoxidation of cyclooctene with *tert*-BuOOH at 65 °C

Run	Catalyst	Conversion (wt%)	% Yield of epoxide
1	No catalyst	4	4
2	Cu(NO₃)₂	66	35
3	[Cu(L)(μ-ONO₂)]ₙ	88	86

Reaction condition: Cyclooctene (10 mmol), Catalyst (0.005 mmol), *tert*-BuOOH (20 mmol), CH₃CN (8 ml)

Table 5 Comparison of catalytic efficacy of the complex [Cu(L)(μ-ONO₂)]ₙ (**1**) with other reported copper(II) catalysts for the epoxidation of cyclooctene with *tert*-BuOOH in CH₃CN media

Complexes	Conversion (%)	Reference
[Cu(L¹)(H₂O)](ClO₄)	75	[15]
[Cu(L²)]	75	[15]
[Cu(L³)]	76	[15]
[CuL(μ -₁,₁-N₃)]ₙ	86	[16]
][Cu{salnptn(3-OMe)₂}]	70[a]	[17]
[Cu(hnaphnptn)]	70[a]	[17]
(CuLⁿ, n = 1–4)	69	[18]
Cu-MCM-41	92	[20]
CuᴵᴵC(Schiff base)Cl₂@GO-CP[b]	88	[32]
Cu-L'-Y	84	[33]
[Cu(L)(μ-ONO₂)]ₙ	88	This study

HL¹ = 1-(N-*ortho*-hydroxy-acetophenimine)-2-methyl-pyridine, H₂L² = N,N'-(2-   hydroxy-propane-1,3-diyl)-bis-salicylideneimine, H₂L³ = N,N'-(2,2-dimethyl-propane-1,3-diyl)-bis-salicylideneimine, H₂{salnptn(3-OMe)₂} = Schiff-base derived by thecondensationof2,2′-dimethylpropandiamineand2-hydroxy-3-methoxybenzaldehyde, H₂{hnaphnptn} = Schiff-basederivedbythecondensationof2,2′-dimethylpropandiamine and 2-hydroxy-1-naphthaldehyde, Schiff-base derived from the condensation of meso-1,2-diphenyl-1,2-ethylenediamine with various salicylaldehyde derivatives (x-salicylaldehyde for H₂Ln, x = H (n = 1), 5-Br (n = 2), 5-Br-3-NO2 (n = 3) and 2′-hydroxyacetophenone (n = 4).Cu(II) (Schiff base)Cl₂@GO-CP = Cu(II) Schiff base complex immobilized on Graphene oxide.   L' = 3,4,11,12-dibenzo-1,14-diaza-5,10-dioxa cyclohexadecane-1,13-diene.[a]For 8 h, [b]For5hr

(HL¹ = 1-(N-ortho-hydroxy-acetophenimine)-2-methylpyridine), [Cu(L²)] (HL² = *N,N'*-(2-hydroxy-propane-1,3-diyl)-bis-salicylideneimine),[Cu(L³)](HL³ = *N,N'*-(2,2-dimethyl-propane-1,3-diyl)-bis-salicylideneimine), which exhibit high catalytic activity with *tert*-BuOOH in different solvent media, where cyclooctene has been converted to its epoxide (conversion 76–75%, selectivity 63–56%) in acetonitrile media [15]. We have also demonstrated the epoxidation of cyclooctene using a single end-on azido bridged 1D chain Schiff-base copper(II) complex [CuL(μ₁,₁-N₃)]ₙ(HL = 1-(N-*ortho*-hydroxyacetophenimine)-2-(N-ethyl)aminoethane) as catalyst, where the highest conversion occurs also in acetonitrile

(conversion 86%, selectivity 81%) with *tert*-BuOOH as oxidant [16]. Rayati et al. reported the oxidation of cyclooctene with *tert*-BuOOH in the presence of electron-rich salen-type Schiff base copper(II) complexes, where the highest conversion was 70% after 8 hr in acetonitrile media and epoxide selectivity was 100% [17] (Table 5). Abbasi et al. studied the epoxidation of cyclooctene using a series of mononuclear and dinuclear salen-type copper(II) Schiff base complexes, where the highest conversion goes to 85%, but epoxide selectivity maximum was 67%. Along with the epoxide, the allylic oxidation product cyclooct-2-enol, and cyclooct-2-enone were also obtained [18]. However, in our present study, the conversion of cyclooctene by complex **1** displayed marked improvement with good selectivity. Cu(II) Schiff base catalysts under heterogeneous conditions have been used for epoxidation of olefins with *tert*-BuOOH in the recent past. Sakthivel et al. have reported the oxidation of cyclooctene with *tert*-BuOOH over a tetrahydro-salen Cu(II) complex grafted on iodosilane modified surfaces of MCM-41 and MCM-48, but the conversion was only 53–54% with 78–85% selectivity. However, in homogeneous condition, there was a reported 73.7% conversion and 73% selectivity [31]. Jana et al. have obtained 92% conversion of cyclooctene with 92% epoxide selectivity using a Cu(II) Schiff-base anchored MCM-41 catalyst [20]. Zarnegaryan et al. have reported that the effective conversion of cyclooctene (conversion 88%, selectivity 100%) by Cu(II) Schiff base complex immobilized on graphene nanosheets using *tert*-BuOOH in acetonitrile media, although the highest conversion (99%) occurred in dichloromethane media [32]. Banaei et al. studied the epoxidation of cyclooctene by zeolite-Y encapsulated Cu(II) complexes with 16- and 17-membered diazadioxa macrocyclic Schiff bases nanocomposite materials, where conversion goes to a highest value of 84% (selectivity up to 82%) with the formation of three by-products [33]. However, in the case of complex **1**, allylic C–H oxidation was 2–11% in different solvents. The reaction profile of the epoxidation of cyclooctene with different solvents is shown in Fig. S3. The complex contains five-coordinated coordinatively unsaturated Cu-center; thus, the complex has been used for the Lewis acidic catalysis reaction under homogeneous conditions. The Cu(II) binds the peroxo-group on treatment with peroxides [34] to form the pre-catalyst containing L*x*Cu–OOH (where L = ligand), which are capable of transferring the oxo-functionality to the organic substrates to produce the oxidized products [35]. We assume that a similar kind of mechanism is operative in our case. The probable mechanism for catalytic cycle is depicted in Scheme 2. X-ray crystal structure analysis shows the presence of five-coordinated Cu(II) in [Cu(L)(μ-ONO₂]ₙ (**1**). So, the coordination environment around Cu(II) is easily accessible for an external ligand. As a result, *tert*-BuOOH has enough space to bind copper in the intermediate stages of the catalytic cycle.

Scheme 2 Probable mechanism of catalytic cycle for olefinic epoxidation catalyzed by complex **1**
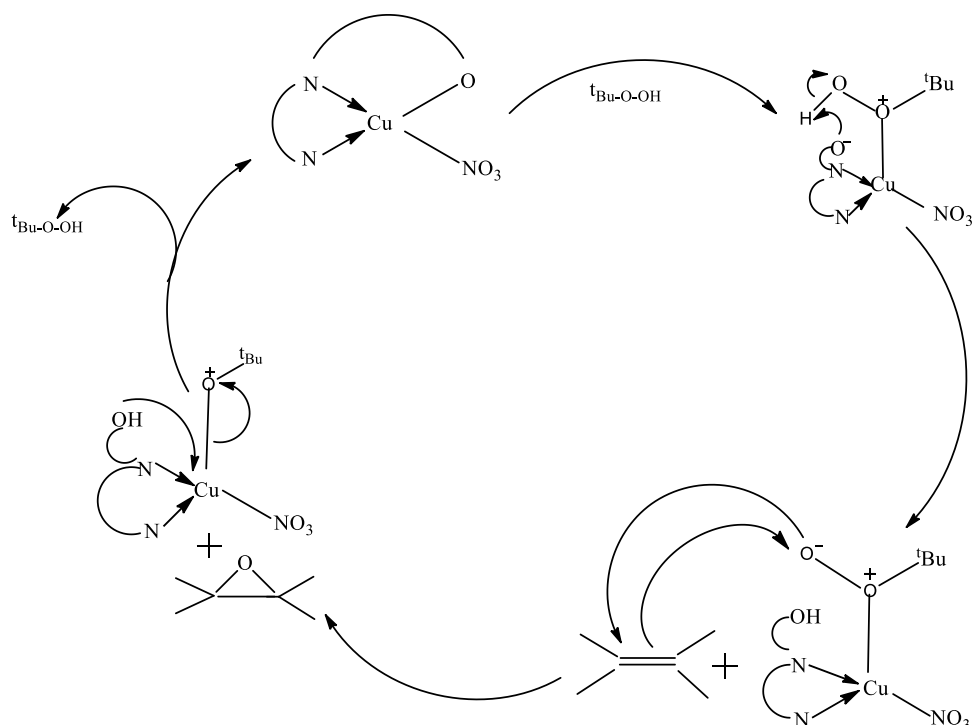
Conclusion

In summary, a neutral nitrate bridged coordination polymer **1** of Cu(II) containing a tridentate Schiff base has been isolated and characterized by single crystal X-ray diffraction. Structural analysis revealed that each Cu(II) center features a distorted square pyramidal geometry bearing a CuN_2O_3 chromophore in **1**. The adjacent copper atoms are connected by a bidentate μ-NO_3 bridge to form a one-dimensional coordination polymeric structure. Complex **1** displayed moderate catalytic efficacy in homogeneous cyclooctene epoxidation. The catalytic reaction also revealed the highest selectivity in acetonitrile medium.

Compliance with ethical standards

References

1. Wang Y, He C-T, Liu Y-J, Zhao T-Q, Lu X-M, Zhang W-X, Zhang J-P, Chen J-M (2012) Inorg Chem 51:4772
2. Ricco R, Pfeiffer C, Sumida K, Sumby CJ, Falcaro P, Furukawa S, Champness NR, Doonan CJ (2016) CrystEngComm 18:6532
3. Neidig ML, Clark DL, Martin RL (2013) Coord Chem Rev 257:394
4. Reedijk J (2013) Chem Soc Rev 42:1776
5. Tiekink ERT, Zukerman-Schpector J (2012) The importance of Pi-interactions in crystal engineering: frontiers in crystal engineering, 1st edn. Wiley, Chichester, UK
6. Ozer RR, Hinestroza JP (2015) RSC Adv 5:15198
7. Correa CC, Lopes LB, Santos LHR, Diniz R, Yoshida MI, Oliveira LFC, Machado FC (2011) Inorg Chim Acta 367:187
8. Wang ZN, Wang X, Wei SY, Wang JX, Bai FY, Xing YH, Sun LX (2015) J Chem 39:4168
9. Mottillo C, Friscic T (2015) Chem Commun 51:8924
10. Special issue on focus on self-assembly (1999) Acc Chem Res 32:4
11. Habib M, Karmakar TK, Aromi G, Ribas J, Fun H-K, Chantrapromma S, Chandra SK (2008) Inorg Chem 47:4109
12. Konar S, Dalai S, Ribas J, Drew MGB, Zangrando E, Chaudhuri NR (2004) Inorg Chim Acta 357:4208
13. Du M, Wang Q, Wang Y, Zhao X-J, Ribas J (2006) J Solid State Chem 179:3926
14. Banerjee S, Adhikary C, Rizzoli C, Pal R (2014) Inorg Chim Acta 409:202
15. Adhikary C, Bera R, Dutta B, Jana S, Bocelli G, Cantoni A, Chaudhuri S, Koner S (2008) Polyhedron 27:1556
16. Bera R, Adhikary C, Ianelli S, Chaydhuri S, Koner S (2010) Polyhedron 29:2166
17. Rayati S, Zakavi S, Koliaei M, Wojtczak A, Kozakiewicz A (2010) Inorg Chem Commun 13:203
18. Abbasi Z, Behzad M, Ghaffari A, Rudbari HA, Bruno G (2014) Inorg Chim Acta 414:78
19. Bhattacharjee A, Halder S, Ghosh K, Rizzoli C, Roy P (2017) J Chem 41:5696
20. Jana S, Dutta B, Bera R, Koner S (2007) Langmuir 23:2492
21. Aromí G, Bhaduri S, Artús P, Folting K, Christou G (2002) Inorg Chem 41:805

22. Naiya S, Giri S, Biswas S, Drew MGB (2014) Ghosh A Polyhedron 73:139
23. Bruker (2008) APEX2 (Version 2008.1-0), SAINT (Version 7.51A) and SADABS (Version 2007/4) Bruker AXS Inc. Madison, Wisconsin, USA
24. Altomare A, Burla MC, Camalli M, Cascarano G, Giacovazzo C, Uagliardi A, Moliterni AGG, Polidori G, Spagna R (1999) J Appl Cryst 32:115
25. Sheldrick GM (2015) SHELXL Acta Cryst C71:3
26. Addison AW, Rao TN, Reedjik J, van Rijn J, Verschoor CG (1984) J Chem Soc Dalton Trans 1349
27. Nakamoto K (2009) Infrared and Raman spectra of inorganic and coordination compounds, part B, 6th edn. Wiley, Jersey
28. Lever ABP (1984) Inorganic electronic spectroscopy, 2nd edn. Elsevier, New York
29. Reger DL, Debreczeni A, Smith M, Jezierska J, Ożarowski A (2012) Inorg Chem 51:1068
30. Andriessen WTM (1975) Inorg Chem 14:792
31. Sakthivel A, Sun W, Raudaschl-Sieber G, Chiang AST, Hanzlik M, Kühn FE (2006) Catal Commun 7:302
32. Zarnegaryan A, Pahlevanneshan Z, Moghadam M, Tangestaninejad S, Mirkhani V, Mohammdpoor Baltork I (2019) J Iran Chem Soc 16:747
33. Banaei A, Rezazadeh B (2013) J Coord Chem 66:2129
34. Osako T, Nagatomo S, Tachi Y, Kitagawa T, Itoh S (2002) Angew Chem Int Ed Engl 41:4325
35. Prigge ST, Eipper BA, Mains RE, Amzel LM (2004) Science 304:864

Source details

Feedback ＞   Compare sources ＞

Transition Metal Chemistry

Scopus coverage years: from 1975 to Present

Publisher: Springer Nature

ISSN: 0340-4285   E-ISSN: 1572-901X

Subject area: (Materials Science: Metals and Alloys) (Chemistry: Inorganic Chemistry) (Materials Science: Materials Chemistry)

Source type: Journal

View all documents ＞   Set document alert   💾 Save to source list

CiteScore 2022   ⓘ
4.0

SJR 2022   ⓘ
0.299

SNIP 2022   ⓘ
0.433

CiteScore   CiteScore rank & trend   Scopus content coverage

ⓘ Improved CiteScore methodology   ✕

CiteScore 2022 counts the citations received in 2019-2022 to articles, reviews, conference papers, book chapters and data

papers published in 2019-2022, and divides this by the number of publications published in 2019-2022. Learn more ＞

Catalytic Efficacy of 2,2′-Bipyridine Cobalt(II) Complex: Hydrothermal Synthesis, X-Ray Structure and Aerobic Epoxidation of Alkenes

Rajesh Bera

Department of Chemistry, Dinabandhu Andrews College, Garia, Kolkata-700084, India

Corresponding author: E-mail: berarajesh2010@gmail.com

A mononuclear cobalt(II) complex, $[Co(bpy)_2(NO_3)](NO_3)\cdot 3H_2O$ (**1**) (bpy = 2,2′-bipyridine) has been synthesized hydrothermally and the crystal structure was characterized by X-ray crystallography. Complex **1** is capable of activating aerobic oxygen at atmospheric pressure. $[Co(bpy)_2(NO_3)](NO_3)\cdot 3H_2O$ (**1**) was used as an active catalyst for the aerobic epoxidaion of various alkenes with isobutyraldehyde as co-reductant in acetonitrile medium. Complex **1** catalyzes the epoxidaion reaction efficiently, which reflected in high yield of products with desired selectivity.

Keywords: Cobalt(II), 2,2′-Bipyridine, Hydrothermal synthesis, X-ray crystallography, Epoxidation, Alkene.

INTRODUCTION

The catalytic epoxidation of alkenes is a reaction of great industrial interest given the numerous applications of epoxides as precursors in the production of valuable chemicals [1]. Conventionally, the epoxidation of alkenes is carried out by stoichiometric amount of peracids [2]. However, peracids are expensive, corrosive, non-selective for the epoxide formation, lead to the formation of undesirable products, so create a lot of waste [3]. Therefore, many alternative methodologies using single oxygen donor reagents such as $NaIO_4$, NaOCl, PhIO, RCOOOH, $KHSO_5$ and H_2O_2 have been reported for the epoxidation of alkenes. However, these methods are either expensive or not environment friendly. Another commercial manufacturing method of epoxides is the chlorohydrin process, which causes serious environmental pollution. Hence, from both economic and environmental viewpoint and to avoid co-products, the epoxidation of alkenes with O_2 or naturally cheap air over effective catalysts is a promising and attractive method.

Metal complexes catalyzed homogeneous epoxidation system could produce high yield of epoxide in presence of an aldehyde which acts as a reducing agent for the reductive activation of oxygen [4]. Many efforts have been made to seek methods of epoxidation with molecular oxygen or air [5-13]. Among all

these methods, Mukaiyama epoxidation system [8,10-13] uses metal complexes such as Ni(II), Mn(III), Co(II) or Fe(III) as the homogeneous catalysts, aldehydes or alcohols as the reductants is confirmed to be very effective. Subsequently, many metal catalysts such as manganese complex [14,15], metalloporphyrins [16-19], cobalt-containing molecular sieves [20] demonstrated highly catalytic performance for the aerobic oxidation in the presence of aldehyde.

Cobalt ions and cobalt complexes are used as catalysts for the selective oxidation of alkanes and alkylbenzenes with O_2 [21]. In the recent past, Budnik and Kochi [22] have used cobalt complexes for the epoxidation of alkenes with molecular oxygen. Using a cobalt(II) complex, the catalytic oxidation of terminal olefins, including styrene, by O_2 to the corresponding 2° ketones and 2° alcohols has been reported [23,24]. Cobalt-salen complexes were reported to show catalytic activity for epoxidation of styrene with O_2, where isobutyraldehyde was used as a sacrificial co-reductant [25]. Again, one of the major drawbacks of using metal salens in homogenous solutions is the formation of μ-oxo dimers and other polymeric species, which leads to irreversible catalyst deactivation. Iqbal *et al.* [26,27] studied various Schiff-base cobalt complexes for the epoxidation of alkenes including steroids and terpenoids in the presence of either aliphatic aldehyde or β-ketoester. Saha

et al. [28] studied the epoxidation of alkenes over a cobalt(III) Schiff-base complex in the presence of molecular oxygen using isobutyraldehyde [28]. Co(II) salen derived Jacobsen type complexes [16] were used as catalysts for aerobic asymmetric epoxidation [29]. Oxidation of monoterpenes with O_2 using $CoCl_2$ as catalyst has been reported, and it was found that allylic oxidation takes place predominantly [30]. In the presence of propionaldehyde diethyl acetal as the reducing agent, bis-(diketonato)cobalt(II) derivatives, *i.e.* Co(acac)$_2$ are active in the aerobic epoxidation of alkenes [31]. Cobalt based heterogeneous catalysts for aerobic epoxidation of alkenes are also reported in recent past [32-40].

Herein, the synthesis, characterization, X-ray single crystal structure of a new mononuclear cobalt(II) complex and its catalytic efficacy towards aerobic epoxidation of olefins in presence of isobutyraldehyde as co-reductant are reported.

EXPERIMENTAL

The chemicals *viz*. Co(NO$_3$)$_2$·6H$_2$O, styrene, cyclooctene, cyclohexene, 1-hexene, 1-octene, limonene, 2,2′-bipyridine were purchased from Aldrich and used as received. The solvents were purchased from Merck (India) and distilled before use.

Synthesis of [Co(bpy)$_2$(NO$_3$)](NO$_3$)·3H$_2$O (1): Complex [Co(bpy)$_2$(NO$_3$)](NO$_3$)·3H$_2$O (**1**) was synthesized hydrothermally. Compound **1** was grown as red block crystals in a Teflon-lined Parr acid digestion bomb. For digestion, cobalt(II) nitrate, 2,2′-bpy and aspartic acid were added in the molar ratio of 1:1:1 in 10 mL of distilled water and kept at 160 ℃ for 3 days followed by slow cooling at the rate of 5 ℃/h to room temperature. The crystals thus formed were filtered off, washed first with water and then with a small amount of ethyl alcohol and dried in air (yield 75 %, based on cobalt). Anal. calcd. (found) % for C$_{20}$H$_{22}$N$_6$O$_9$Co: C, 50.97 (50.50); H, 4.00 (4.20); N, 15.29 (15.50); Co, 10.72 (10.51). The crystal structure of [Co(2,2′-bpy)$_2$(NO$_3$)]NO$_3$·5H$_2$O has been reported previously [41], however, the synthetic procedure was different.

X-ray single crystal structure determination of 1: X-Ray diffraction data of complex **1** was collected at 293(2) K on a Bruker SMART APEX CCD X-ray diffractometer using graphite-monochromated MoKα radiation $(λ = 0.71073$ Å$)$. Determination of integrated intensities and cell refinement were performed with the SAINT [42] software package using a narrow-frame integration algorithm. An empirical absorption correction (SADABS) [43] was applied. The structure was solved by direct method and refined using full-matrix least-squares technique against F^2 with anisotropic displacement parameters for non-hydrogen atoms with the programs SHELXS-97 and SHELXL-97 [44]. All hydrogen atoms were located from difference Fourier map and treated as a suitable riding models with isotropic displacement parameters derived from their carrier atoms and were refined with isotropic thermal parameters (except for the hydrogen atoms of water molecules). A summary of crystal data and relevant refinement parameters for complex **1** is collated in Table-1. The molecular graphics softwares used were ORTEP III [45] and MERCURY 1.2.1 [46].

Catalytic epoxidation reaction: The catalytic epoxidation reactions were carried out under air in a batch reactor at 60 ℃.

TABLE-1
CRYSTALLOGRAPHIC DATA AND STRUCTURE
REFINEMENT PARAMETERS FOR COMPLEX 1

Parameters	
Chemical formula sum	C$_{20}$H$_{22}$N$_6$O$_9$Co
Chemical formula weight	549.36
Crystal system	Monoclinic
Space group	C2/c
Cell dimensions	a =10.9317(3) Å; b = 16.0118(3) Å; c = 14.4587(5) Å
β (º)	102.017(2)
V (Å^3)	2475.33(12)
Z	8
Temperature (K)	293(2)
D$_c$ (g cm^{-3})	1.571
μ (mm^{-1})	0.765
F(000)	1212
Intervals of reflection indices	-14≤h≥14, -20≤k≥20, -18≤l≥18
Reflections with [I>2σ(I)]	2863
Independent reflections	2504
Final R indices [I>2σ(I)]	R1=0.0481, wR2= 0.1366
R indices (all data)	R1=0.0545, wR2= 0.1426
Δρ$_{max}$ (e Å^{-3})	0.382
Δρ$_{min}$ (e Å^{-3})	-0.617
Goodness-of-fit on F^2	1.076

$R_1 = Σ$ ||Fo| – |Fc||/Σ|Fo, $wR_2 = [Σw(|Fo| – |Fc|)^2] / Σ[w(Fo^2)]^{½}$

Typically, a 50 mL three-neck round-bottomed flask equipped with a water condenser containing 1 g alkene in 10 mL dry acetonitrile and 2 mg of catalyst is kept in a preheated oil bath. Air was bubbled through the reaction mixture at atmospheric pressure at a flow rate of *ca*. 3.0 cm^3 min^{-1}. The reaction mixture was magnetically stirred continuously for 8 h. The products of the epoxidation reactions were collected at different time intervals and were identified and quantified by Varian CP 3800 gas chromatograph equipped with an FID detector and a CP-Sil 8 CB capillary column.

RESULTS AND DISCUSSION

X-ray structure of [Co(bpy)$_2$(NO$_3$)](NO$_3$)·3H$_2$O (1): The complex shows a cationic monomeric unit [Co(bpy)$_2$(NO$_3$)] along with three water molecules of crystallization and a discrete nitrate anion. The unique metal center (Co1) is surrounded by two bipyridyl ligand and one bidentate NO$_3^-$ ion forming a distorted octahedron. An ORTEP view with atom numbering scheme of complex **1** is shown in Fig. 1. Selected bond lengths and angles of complex **1** are given in Table-2. The basal plane of Co1 center is formed by the two nitrate oxygen atoms O2, O2* and two bipyridine nitrogen atoms N1, N1*; the axial positions are occupied by the two bipyridine nitrogen atoms N2 and N2* [where * = -x, y, ½-z]. Among the two nitrate ions, one is chelated with the Co1 center and other nitrate ion is present outside of coordination sphere, thereby balancing the charge of the Co1 center. Three water molecules are also present in the lattice without offering any hydrogen bonding. The bond lengths and bond angles are well in agreement with the reported cobalt(II) complexes [46,47].

Epoxidation reaction: Catalytic activity of the complex was investigated in the epoxidation of both cyclic and straight
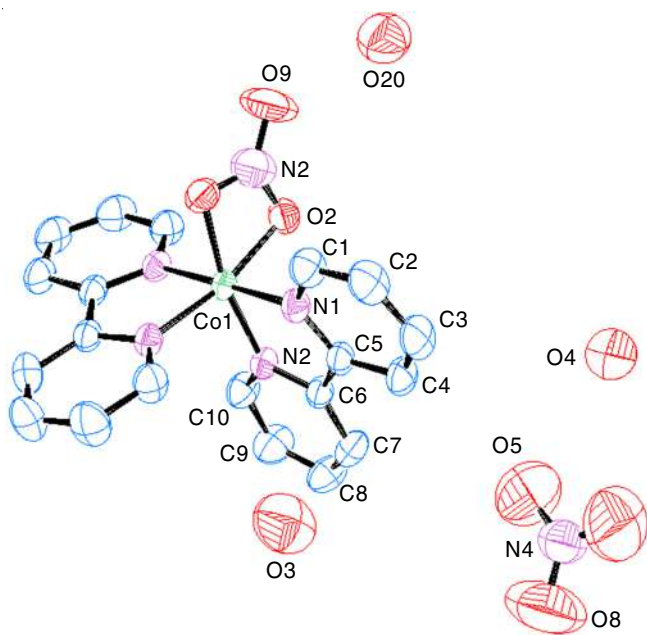
Fig. 1. ORTEP diagram of complex **1** with the atom-numbering scheme

TABLE-2
SELECTED BOND LENGTHS (Å)
AND ANGLES (°) FOR COMPLEX **1**

Bond lengths (Å)		Bond angles (°)	
Co(1)-O(2)	1.8887(19)	O(2)-Co(1)-O(2)	70.14(13)
Co(1)-N(2)	1.922(2)	O(2)-Co(1)-N(2)*	88.31(9)
Co(1)-N(1)	1.932(2)	O(2)-Co(1)-N(2)	88.31(9)
Co(1)-N(3)	2.286(4)	N(2)-Co(1)-N(2)	179.42(12)
N(2)-C(10)	1.341(4)	O(2)-Co(1)-N(1)	98.38(9)
N(1)-C(1)	1.337(3)	O(2)-Co(1)-N(1)*	167.82(9)
O(2)-N(3)	1.314(3)	N(2)-Co(1)-N(1)	96.37(9)
N(3)-O(9)	1.230(5)	N(1)-Co(1)-N(1)	93.35(12)
N(3)-O(2)	1.314(3)		

*-x, y, ½-z

chain alkenes with air. The resultant conversions, selectivities and turnover number (TONs) are given in Table-3. The reaction profile of the epoxidation of alkenes is shown in Fig. 2. The epoxidation of styrene gives styrene oxide in 76% yield (conversion 88%, selectivity 67%); along with this, benzaldehyde (yield 12%) was also detected. Turnover number of ~2347 has been attained for the epoxide production. Epoxidation of styrene with molecular oxygen over a variety of cobalt catalysts under homogeneous condition has been studied in the recent past. Kureshy *et al*. [29] studied epoxidation of styrene over Co(II) chiral Schiff-base complexes in presence of molecular oxygen using isobutyraldehyde which shows up to 45% conversion. Cobalt(II) calix[4]pyrrole complexes afforded a maximum of 68% yield of styrene oxide in presence 2-ethylbutyraldehyde/O_2 in 24h [48]. Opre *et al*. [49] reported that DMF interacts with oxygen, styrene and cobalt containing catalyst according to a complex reaction network, resulting in the formation of 49% styrene oxide with various co-products, such as *N*-formyl-*N*-methylformamide, CO_2 and dimethylamine [49]. They concluded that DMF should be considered as a "sacrificial" solvent that functions as a co-reductant in the epoxidation

TABLE-3
HOMOGENEOUS ALKENE EPOXIDATION
CATALYZED BY COMPLEX **1**[a]

Substrate	Conversion (%)	Yield of product (%)		TON[f]
		Epoxide	Others	
	88	76	16[b]	2347
	92	80	12[c]	3111
	99	99	–	2495
	67	67	–	2211
	55	48	7[d]	1361
	52	52[e]	–	1060

[a]Reaction conditions: alkenes (1 g); catalyst (2 mg); flow rate of air, 3.0 cm³min⁻¹ ; CH₃CN (10 mL); Temperature (60°C). [b]Benzaldehyde. [c]2-Cyclohexen-1-ol and 2-Cyclohexen-1-one. [d]Other unidentified product. [e]Limonene epoxide. [f]Turn Over Number = moles converted / moles of active site. The products of the epoxidation reactions were collected at different time intervals and were identified and quantified by Varian CP3800 gas chromatograph equipped with an FID detector and a CP-Sil 8 CB capillary column.
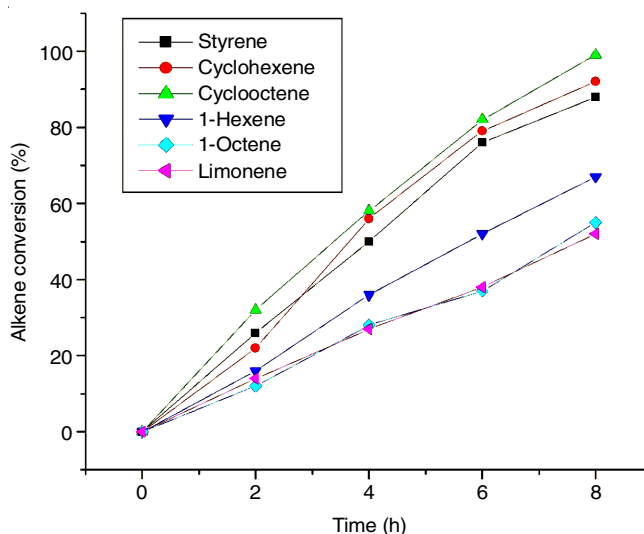
Fig. 2. Reaction profile for the aerobic epoxidation of alkenes over complex **1**

reaction. In present study, the reaction in DMF under this condition was performed but no conversion of styrene was observed. O'Neill *et al*. [50] obtained a yield of 74% styrene epoxide using *bis*(2,2,6,6-tetramethyl-3,5-heptanedionato)cobalt(II), [Co(thd)₂] under aerobic condition using pivaldehyde as sacrificial reductant.

The epoxidation of endocyclic alkene such as cyclohexene showing a conversion (92%) with 80% epoxide selectivity. Along with the epoxide, a small amount of allylic oxidation products *i.e.* 2-cyclohexen-1-ol and 2-cyclohexen-1-one are also detected. The epoxidation of cyclooctene goes smoothly, showing an excellent conversion of 99% with 100% epoxide selectivity. The linear aliphatic olefins such as 1-hexene and 1-octene converted to the corresponding 1, 2-epoxy alkanes. As shown in Table-3, the conversion of 1-hexene is 67% where epoxide was the sole product. Conversion of 1-octene was 55%, where epoxide selectivity was 87%. Along with 1,2-epoxy alkane, a small amount (7%) of other undetected side product was also obtained. It shows that the catalytic activity decreases along with length of olefin. This may due to the larger hexyl group of 1-octene connected to double bond sterically hinders it in approaching to the catalyst metal center with respect to 1-hexene which its double bond carries a smaller butyl group. Limonene undergoes a relatively slow conversion and after 8 h of reaction only 52% conversion is noticed. At that time, limonene oxide is the exclusive product. da Silva *et al*. [30] studied the oxidation of limonene with dioxygen in acetonitrile medium over $CoCl_2$ where the molar ratio of allyl oxidation and epoxidation products was nearly 1:1. However, no allylic oxidation product is noticed in epoxidation reaction catalyzed by complex **1**.

Conclusion

A new mononuclear cobalt(II) complex was hydrothermally synthesized and characterized by X-ray crystallography. The complex has shown excellent catalytic efficacy towards the aerobic epoxidation of alkenes in presence of isobutyraldehyde as co-reductant. The complex **1** is new example of cobalt based catalyst that can oxidize olefinic substrates only by bubbling air.

Supplementary material

Crystal data are available from The Director, CCDC, 12 Union Road, Cambridge, CB2 1EZ, U.K. (Fax: +44-1223-336-033; www: http://www.ccdc.cam.ac.uk or E-mail: deposit@ccdc.cam.ac.uk) upon request, quoting the deposition number CCDC 808604.

CONFLICT OF INTEREST

The authors declare that there is no conflict of interests regarding the publication of this article.

REFERENCES

1. W. Gerhartz, Y.S. Yamamoto, L. Kandy, J.F. Rounsaville and G. Schulz, Ullmann's Encyclopedia of Industrial Chemistry, Verlag Chemie; Weinheim, Germany, edn 5, vol. A9, p. 531 (1987).

2. D. Swern, Organic Peroxide, Wiley-Interscience; New York, vol. 2 (1971).
3. G.A. Barf and R.A. Sheldon, *J. Mol. Catal. A Chem.*, **102**, 23 (1995); https://doi.org/10.1016/1381-1169(95)00089-5
4. M. Hamamoto, K. Nakayama, Y. Nishiyama and Y. Ishii, *J. Org. Chem.*, **58**, 6421 (1993); https://doi.org/10.1021/jo00075a043
5. I. Tabushi and N. Koga, *J. Am. Chem. Soc.*, **101**, 6456 (1979); https://doi.org/10.1021/ja00515a063
6. D. Mansuy, M. Fontecave and J.-F. Bartoli, *J. Chem. Soc. Chem. Commun.*, 253 (1983); https://doi.org/10.1039/C39830000253
7. T. Yamada, K. Imagawa and T. Mukaiyama, *Chem. Lett.*, **21**, 2109 (1992); https://doi.org/10.1246/cl.1992.2109
8. T. Mukaiyama and T. Yamada, *Bull. Chem. Soc. Jpn.*, **68**, 17 (1995); https://doi.org/10.1246/bcsj.68.17
9. Z. Xi, H. Wang, Y. Sun, N. Zhou, G. Cao and M. Li, *J. Mol. Catal. A Chem.*, **168**, 299 (2001); https://doi.org/10.1016/S1381-1169(00)00189-8
10. T. Yamada, T. Takai, O. Rhode and T. Mukaiyama, *Chem. Lett.*, **20**, 1 (1991); https://doi.org/10.1246/cl.1991.1
11. T. Mukaiyama, T. Yamada, T. Nagata and K. Imagawa, *Chem. Lett.*, **22**, 327 (1993); https://doi.org/10.1246/cl.1993.327
12. T. Yamada, T. Takai, O. Rhode and T. Mukaiyama, *Bull. Chem. Soc. Jpn.*, **64**, 2109 (1991); https://doi.org/10.1246/bcsj.64.2109
13. T. Nagata, K. Imagawa, T. Yamada and T. Mukaiyama, *Chem. Lett.*, **23**, 1259 (1994); https://doi.org/10.1246/cl.1994.1259
14. J.Y. Qi, Y.M. Li, Z.Y. Zhou, C.M. Che, C.H. Yeung and A.S.C. Chan, *Adv. Synth. Catal.*, **347**, 45 (2005); https://doi.org/10.1002/adsc.200404224
15. K.S. Ravikumar, F. Barbier, J.-P. Bégué and D. Bonnet-Delpon, *Tetrahedron*, **54**, 7457 (1998); https://doi.org/10.1016/S0040-4020(98)00396-2
16. J. Haber, T. Mlodnicka and J. Poltowicz, *J. Mol. Catal.*, **54**, 451 (1989); https://doi.org/10.1016/0304-5102(89)80160-9
17. A.K. Mandal and J. Iqbal, *Tetrahedron*, **53**, 7641 (1997); https://doi.org/10.1016/S0040-4020(97)00431-6
18. S. Ellis and I.V. Kozhevnikov, *J. Mol. Catal. Chem.*, **187**, 227 (2002); https://doi.org/10.1016/S1381-1169(02)00274-1
19. X.-T. Zhou, Q.-H. Tang and H.-B. Ji, *Tetrahedron Lett.*, **50**, 6601 (2009); https://doi.org/10.1016/j.tetlet.2009.09.061
20. R. Raja, G. Sankar and J.M. Thomas, *Chem. Commun.*, 829 (1999); https://doi.org/10.1039/a901127g
21. R.A. Sheldon and J.K. Kochi, Metal-Catalyzed Oxidation of Organic Compounds, Academic Press: New York (1981).
22. R.A. Budnik and J.K. Kochi, *J. Org. Chem.*, **41**, 1384 (1976); https://doi.org/10.1021/jo00870a020
23. A. Zombeck, D.E. Hamilton and R.S. Drago, *J. Am. Chem. Soc.*, **104**, 6782 (1982); https://doi.org/10.1021/ja00388a051
24. D.E. Hamilton, R.S. Drago and A. Zombeck, *J. Am. Chem. Soc.*, **109**, 374 (1987); https://doi.org/10.1021/ja00236a014
25. B. Rhodes, S. Rowling, P. Tidswell, S. Woodward and S.M. Brown, *J. Mol. Catal. Chem.*, **116**, 375 (1997); https://doi.org/10.1016/S1381-1169(96)00360-3
26. T. Punniyamurthy, B. Bhatia and J. Iqbal, *J. Org. Chem.*, **59**, 850 (1994); https://doi.org/10.1021/jo00083a029
27. T. Punniyamurthy, S. Velusamy and J. Iqbal, *Chem. Rev.*, **105**, 2329 (2005); https://doi.org/10.1021/cr050523v
28. D. Saha, T. Maity, R. Bera and S. Koner, *Polyhedron*, **56**, 230 (2013); https://doi.org/10.1016/j.poly.2013.03.050
29. R.I. Kureshy, N.H. Khan, S.H.R. Abdi, A.K. Bhatt and P. Iyer, *J. Mol. Catal. Chem.*, **121**, 25 (1997); https://doi.org/10.1016/S1381-1169(96)00452-9

30. M.J. da Silva, P. Robles-Dutenhefner, L. Menini and E.V. Gusevskaya, *J. Mol. Catal. Chem.*, **201**, 71 (2003);
https://doi.org/10.1016/S1381-1169(03)00180-8

31. T. Mukaiyama, K. Yorozu, Y. Takai and T. Yamada, *Chem. Lett.*, **22**, 439 (1993);
https://doi.org/10.1246/cl.1993.439

32. S. Bhunia, S. Jana, D. Saha, B. Dutta and S. Koner, *Catal. Sci. Technol.*, **4**, 1820 (2014);
https://doi.org/10.1039/C4CY00084F

33. M.J. Beier, W. Kleist, M.T. Wharmby, R. Kissner, B. Kimmerle, P.A. Wright, J. Grunwaldt and A. Baiker, *Chem. Eur. J.*, **18**, 887 (2012);
https://doi.org/10.1002/chem.201101223

34. M. Jafarpour, H. Kargar and A. Rezaeifard, *RSC Adv.*, **6**, 79085 (2016);
https://doi.org/10.1039/C6RA16167G

35. M. Kazemnejadi, A. Shakeri, M. Nikookar, M. Mohammadi and M. Esmaeilpour, *Res. Chem. Intermed.*, **43**, 6889 (2017);
https://doi.org/10.1007/s11164-017-3027-z

36. Z. Li, S. Wu, H. Ding, D. Zheng, J. Hu, X. Wang, Q. Huo, J. Guan and Q. Kan, *New J. Chem.*, **37**, 1561 (2013);
https://doi.org/10.1039/c3nj00099k

37. B. Qi, X.-H. Lu, S.-Y. Fang, J. Lei, Y.-L. Dong, D. Zhou and Q.-H. Xia, *J. Mol. Catal. Chem.*, **334**, 44 (2011);
https://doi.org/10.1016/j.molcata.2010.10.021

38. P. Shringarpure and A. Patel, *J. Mol. Catal. Chem.*, **321**, 22 (2010);
https://doi.org/10.1016/j.molcata.2010.01.014

39. J. Sun, G. Yu, L. Liu, Z. Li, Q. Kan, Q. Huo and J. Guan, *Catal. Sci. Technol.*, **4**, 1246 (2014);
https://doi.org/10.1039/c4cy00017j

40. G. Yu, J. Sun, F. Muhammad, P. Wang and G. Zhu, *RSC Adv.*, **4**, 38804 (2014);
https://doi.org/10.1039/C4RA03746D

41. Y.-Q. Zheng and J.-L. Lin, *Z. Kristallogr. NCS*, **217**, 331 (2002);
https://doi.org/10.1524/ncrs.2002.217.1.331

42. Bruker. APEX 2, SAINT, XPREP, Bruker AXS Inc., Madison, Wisconsin, USA (2007).

43. Bruker. SADABS. Bruker AXS Inc., Madison, Wisconsin, USA (2001).

44. G.M. Sheldrick, SHELXS97 and SHELXL97, Programs for Crystal Structure Solution and Refinement, University of Göttingen, Germany (1997).

45. M.N. Burnett and C.K. Jonnson, ORTEP III, Report ORNL-6895, Oak Ridge National Laboratory, Tennessee, USA (1996).

46. I.J. Bruno, J.C. Cole, P.R. Edgington, M. Kessler, C.F. Macrae, P. McCabe, J. Pearson and R. Taylor, *Acta Crystallogr. B*, **58**, 389 (2002);
https://doi.org/10.1107/S0108768102003324

47. R. Sen, A. Bhattacharjee, P. Gütlich, Y. Miyashita, K. Okamoto and S. Koner, *Inorg. Chim. Acta*, **362**, 4663 (2009);
https://doi.org/10.1016/j.ica.2009.06.036

48. P. Buranaprasertsuk, Y. Tangsakol and W. Chavasiri, *Catal. Commun.*, **8**, 310 (2007);
https://doi.org/10.1016/j.catcom.2006.06.022

49. Z. Opre, T. Mallat and A. Baiker, *J. Catal.*, **245**, 482 (2007);
https://doi.org/10.1016/j.jcat.2006.11.018

50. P.M. O'Neill, S. Hindley, M.D. Pugh, J. Davies, P.G. Bray, B.K. Park, D.S. Kapu, S.A. Ward and P.A. Stocks, *Tetrahedron Lett.*, **44**, 8135 (2003);
https://doi.org/10.1016/j.tetlet.2003.09.033

Source details

Feedback >   Compare sources >

Asian Journal of Chemistry

Scopus coverage years: from 1996 to Present

Publisher: Asian Publication Corporation

ISSN: 0970-7077

Subject area: (Chemistry: General Chemistry)

Source type: Journal

View all documents >   Set document alert   💾 Save to source list

CiteScore 2022   ⓘ
0.9

SJR 2022   ⓘ
0.149

SNIP 2022   ⓘ
0.223

CiteScore   CiteScore rank & trend   Scopus content coverage

Applied Organometallic Chemistry WILEY

Copper(II) complexes with a benzimidazole functionalized Schiff base: Synthesis, crystal structures, and role of ancillary ions in phenoxazinone synthase activity

Prafullya Kumar Mudi[1] 🔵 | Rajani Kanta Mahato[1] 🔵 | Mayank Joshi[2] 🔵 |
Madhusudan Shit[3] 🔵 | Angshuman Roy Choudhury[2] 🔵 | Hari Sankar Das[1] 🔵 |
Bhaskar Biswas[1] 🔵

[1]Department of Chemistry, University of North Bengal, Darjeeling, India

[2]Department of Chemical Sciences, Indian Institute of Science Education and Research, Mohali, Punjab, India

[3]Department of Chemistry, Dinobandhu Andrews College, Kolkata, India

Correspondence
Bhaskar Biswas, Department of Chemistry, University of North Bengal, Darjeeling 734013, India.
Email: bhaskarbiswas@nbu.ac.in; icbbiswas@gmail.com

Funding information
Science and Engineering Research Board, Grant/Award Number: TAR/2018/000473

This research study reports the synthesis, structural characterization and phenoxazinone synthase-like activity of two structurally similar copper(II) complexes developed with a benzimidazole functionalized Schiff base (**L**). The ligand, **L**, was designed and synthesized in high yield by the reaction of *p*-methoxy benzaldehyde with *o*-phenylenediamine. The reaction of **L** with $CuCl_2$ and $Cu(NO_3)_2$ leads to the formation of two isostructural complexes, $[Cu(\mathbf{L})_2Cl_2]_2$ (**1**) and $[Cu(\mathbf{L})_2(NO_3)_2]_2$ (**2**). Single crystal X-ray structural study reveals that both the Cu(II) centre in **1** and **2** adopts a square planar geometry. An attempt has also been made to understand the role of coordinated co-ligands on the catalytic oxidation of 2-aminophenol (2-AP) to 2-amino-3*H*-phenoxazine-3-one (2-APX) in methanol. The presence of coordinated nitrate to Cu(II) ions imparts a more labile character to complex **2**, and the catalytic efficiency (k_{cat}/K_M) for complex **2** (1.50×10^7) was determined almost double compared with that of complex **1** (8.78×10^6). Electro-chemical and electrospray ionization mass spectrometry studies of **1** and **2** with 2-AP suggests that the square planar geometries of the Cu(II) centres remain the driving force to develop enzyme-substrate adducts and excellent catalytic performance of the complexes. Electrochemical and EPR spectral analysis of the reaction mixture confirm the presence of active 2-AP$^-$/2-AP$^{•-}$ redox species in the course of catalytic oxidation and suggest the radical driven oxidative coupling of 2-AP in an aerobic environment. Temperature-dependent kinetic measurements were carried out to evaluate the activation parameters (E_a, $\Delta H^{\ddagger}$, $\Delta S^{\ddagger}$), which favours the higher rate of catalytic oxidation of 2-AP for complex **2** than complex **1**.

KEYWORDS
copper(II), crystal structure, electrochemical analysis, phenoxazinone synthase activity, Schiff base

1 | INTRODUCTION

Nowadays, copper(II)-based coordination compounds represent a promising class of smart molecules with significant contributions in designing functional materials like catalytic, magnetic, optic and conducting materials.[1–8] In the biological world, copper(II) ion remains one of the most prevalent metal ions, and its compounds play significant roles in different metal-dependent proteins such as the active site in haemocyanin[9] as an oxygen carrier and perform aromatic ring oxidations in tyrosinase,[10] catechol oxidase,[11] oxygenase enzyme in quercetin 2,3-dioxygenase,[12–14] hydrogen peroxide producer in galactose and glyoxal oxidases[15–18] and methane oxidation as methane monooxygenase, pMMO.[19–21] Among the different copper-based metalloproteins and metalloenzymes in the living system, phenoxazinone synthase acts as an important metalloenzyme.[22] Phenoxazinone synthase catalyses the oxidation of 2-aminophenols to 2-aminophenoxazinone species actinomycin D, a naturally occurring antineoplastic agent, which inhibits DNA-directed RNA synthesis and is also used clinically for the treatment of certain types of cancer.[23–25]

On the other hand, benzimidazole and its derivatives are considered as a significant class of *N*-containing heterocyclic compounds because of their broad range of biological activities such as antimicrobial, antivirus, antifungals, anti-inflammatory, anticancer, antiulcer, proton pump inhibitors and anticoagulants activities.[26–37] They are also the key intermediate in many organic reactions and are used for the industrial synthesis of numerous products.[38] Therefore, various scientific groups have been engrossed in the synthesis and metallation of benzimidazoles with novel functionality to develop smart molecules with improved biomimetic and pharmacological activities that remain an urgent priority. Until to date, several methods are employed for the synthesis of different substituted benzimidazoles using either a catalyst or high temperature, which makes the process economically and environmentally less attractive.[39–42] Because copper(II) and benzimidazole play a significant role in many disciplines, it is important to study the copper–benzimidazole interaction, and chemists have made use of this interaction to build up some fascinating classes of molecules that show many interesting properties.[43–45] As a part of our interest in developing copper-based coordination compounds for mimicking the bio-inspired oxidation reactions, we report a straightforward synthesis of 1-(4-methoxybenzyl)-2-(4-methoxyphenyl)benzimidazole

(**L**) ligand under ambient conditions. To elucidate the use of such type of ligand in coordination and applied chemistry research field, we have prepared two structurally similar mononuclear copper(II) complexes with **L**, namely, $[Cu(\mathbf{L})_2Cl_2]_2$ (**1**) and $[Cu(\mathbf{L})_2(NO_3)_2]_2$ (**2**) and structurally characterized by X-ray diffraction technique with other spectroscopic methods. Attempts have also been made to illustrate the presence of ancillary ligands in the primary zone of coordination of Cu(II) centre for the oxidative catalysis of 2-aminophenol in methanol medium. Both the complexes were found to show impressive phenoxazinone synthase mimicking activity towards oxidative coupling of 2-aminophenol.

2 | EXPERIMENTAL

2.1 | Preparation of the Schiff base and dinuclear copper(II) complex

2.1.1 | Chemicals, solvents and starting materials

Highly pure *o*-phenylenediamine (Sigma Aldrich, USA), *p*-anisaldehyde (Sigma Aldrich, USA), copper(II) chloride dihydrate (Merck, India), copper(II) nitrate trihydrate (Merck, India) and *o*-aminophenol (Sigma Aldrich, USA) are purchased from the respective outlets. All the materials used in this investigation were of high purity.

2.1.2 | Synthesis of the Schiff base, L

The Schiff base ligand, **L**, was prepared following the reported procedure with slight modification.[46–48] The Schiff base was prepared by refluxing *o*-phenylenediamine (0.108 g, 1 mmol) with *p*-anisaldehyde (0.272 g, 2 mmol) in 25-ml ethanol for 6 h. The brown coloured compound was extracted from the solution and stored in vaccuo over $CaCl_2$. Yield: 0.219 g (~85.2%). Anal. Calc. for $C_{22}H_{20}N_2O_2$ (**L**): C, 76.72; H, 5.85; N, 8.13; O, 9.29; Found: C, 76.70; H, 5.80; N, 8.11; O, 9.28. IR (KBr, cm^{-1}; Figure S1): 3433 (ν_{OH}), 3058 (ν_{CH2}), 1612 ($\nu_{C=N}$); UV-vis (λ_{max}, nm; Figure S2): 258, 289, 335; ^{1}H NMR (δ ppm, 400 MHz, CDCl$_3$; Figure S3) δ = 6.844–7.847 (Ar-H, 12H), 5.386 (s, 2H), 3.786–3.852 (s, 6H), ppm. ^{13}C NMR (400 MHz, CDCl$_3$; Figure S4): 160.887 (HC=N); 159.113, 154.129, 148.89 (Ar-OCH$_3$); 136.108 (Ar-N=C); 130.706, 128.512, 127.212, 122.708, 122.497, 119.735, 114.420, 114.176, 110.394 (Ar-C).

2.1.3 | Synthesis of copper(II) complexes

A methanolic solution of $CuCl_2 \cdot 2H_2O$ (0.170 g, 1 mmol)/ $Cu(NO_3)_2 \cdot 3H_2O$ (0.241 g, 1 mmol) was mixed dropwise to dichloromethane solution of **L** (0.688 g, 2 mmol). The yellow coloured solution of the Schiff base immediately turned green for both the reactions, and the resulting solutions were further stirred for 45 min followed by filtering. The filtrate was kept for slow evaporation in an open atmosphere. After 5–7 days, microcrystalline green coloured crystals for **1** and **2** were separated, which were dried over silica gel.

Yield of **1**: 0.1310 g (∼77.0% metal salt based) Anal. calc. for $C_{44}H_{40}N_4O_4CuCl_2$: C, 64.47; H, 5.17; Cl, 8.46; Cu, 7.58; N, 6.68; O, 7.63; Found: C, 64.45; H, 5.16; Cl, 8.42; Cu, 7.54; N, 6.63; O, 7.60. IR (KBr pellet, cm^{-1}; Figure S5): 3021, 2939(ν_{CH_2}), 1620 ($\nu_{C=N}$); UV-vis (1×10^{-4} M, λ_{max} (abs), nm, MeOH; Figure S6): 286, 605.

Yield of **2**: 0.1850 g (∼76.80% metal salt based) Anal. calc. for $C_{44}H_{40}N_6O_{10}Cu$: C, 60.30; H, 4.60; Cu, 7.25; N, 9.59; O, 18.26; Found: C, 60.28; H, 4.59; Cu, 7.21; N, 9.55; O, 18.24. IR (KBr pellet, cm^{-1}; Figure S5): 3019, 2938(ν_{CH_2}), 1617($\nu_{C=N}$); UV-vis (1×10^{-4} M, λ_{max} (abs), nm, MeOH; Figure S6): 282, 611.

2.2 | Physical measurements

FT-IR spectra of the Schiff base and copper compounds were recorded using FTIR-8400S SHIMADZU spectrometer in the range of 400–3600 cm^{-1}. ^1H and ^{13}C NMR spectrum of Schiff base were obtained on a Bruker Advance 400-MHz spectrometer in $CDCl_3$ at 298 K. Steady-state absorption and other spectral data were recorded with a JASCO V-730 spectrophotometer. ESI-MS spectral measurements were performed with a Q-TOF-micro quadruple mass spectrometer. A Perkin Elmer 2400 CHN microanalyser was employed to carry out the elemental analyses of the compounds. The pH values of different solutions were measured by Labman pH meter at room temperature. X-band EPR spectral measurements for the copper complexes were done with a Magnettech GmbH MiniScope MS400 spectrometer where the microwave frequency was measured with an FC400 frequency counter.

2.3 | X-ray structural studies and refinement

A Rigaku XtaLABmini diffractometer equipped with Mercury 375R (2 × 2 bin mode) CCD detector was employed to collect X-ray diffraction data for the copper(II) complexes with graphite monochromated Mo-Kα radiation ($\lambda = 0.71073$ Å) at 100 K for **1** and at 150 K for **2** using ω scans. The data were reduced and the space group was determined using CrysAlisPro 1.171.39.35c and 1.171.39.7f.[49] The crystal structures were solved by dual space method, and the space group was redetermined using SHELXT-2015.[50] The crystallographic data were refined by full-matrix least-squares procedures using the SHELXL-2015[51] software package through OLEX2 suite.[52]

2.4 | Hirshfeld surface analysis of the copper(II) complexes

Hirshfeld surfaces[53] and 2D fingerprint plots[54] for the copper(II) complexes have been generated by Crystal Explorer 17.5[55] program package employing their X-ray diffraction data. The location of intermolecular interactions within crystal packing was examined through Hirshfeld Surface analysis. The details of Hirshfield surface analysis were described elsewhere.[53–55]

2.5 | Catalytic oxidation studies of 2-aminophenol

The catalytic oxidation of 2-aminophenol was performed by treatment of 1×10^{-4} M solution of copper(II) complexes with 1×10^{-3} M of 2-aminophenol (2-AP) solution in methanol (MeOH). The wavelength scans for the course of catalysis were monitored with a spectrophotometer for 2 h from the 300- to 700-nm wavelength range.[24]

Kinetic experiments were also carried out spectrophotometrically to comprehend the catalytic efficacy and nature of oxidation of aminophenol by the copper(II) complexes in MeOH at 298 K[56]; 0.04 mL of 1×10^{-4} M constant concentration of copper(II) complexes the solutions were mixed with 2 ml of 10-fold concentrated solution of 2-AP to attain the final concentration as 1×10^{-4} M. The catalytic conversion of 2-aminophenol to its oxidation product was examined with the variation of time at 433 nm for **1** and 430 nm for **2** (time scan) in MeOH.[57,58] The rate of catalytic oxidation based on substrate concentration was determined by following the initial rate law in triplicate. The kinetics of the catalytic oxidation reactions were carried out at different temperature to determine the activation parameters.

The product, 2-amino-3H-phenoxazine-3-one (APX) developed by catalytic oxidation of 2-AP has been extracted with column chromatographic method for both the copper(II) complexes. Neutral alumina as column

support and benzene-ethyl acetate an eluant mixture was employed in the chromatographic separation. Proton NMR spectroscopy was evidenced to check the purity of aminophenoxazinone compound (APX). ^{1}H NMR data for APX, (CDCl$_3$, 400 MHz,) δ_H: 7.61 (m, 1H), 7.45 (m, 3H), 6.46 (s, 1H), 6.37 (s, 1H), 6.25 (s, 1H).

2.6 | Detection of hydrogen peroxide in the course of catalysis

The participation of atmospheric oxygen in the oxidative coupling of 2-AP was verified from the detection of hydrogen peroxide with reported literature.[59,60] In the course of oxidation of 2-AP in MeOH, H$_2$SO$_4$ was added to attain pH 2. After a certain time, an equal volume of water was mixed to stop further oxidation. The oxidation product, phenoxazinone compound was extracted three times with DCM; 10% solution of KI (1 ml) and three drops of a 3% solution of ammonium molybdate were mixed with the aqueous layer. The development of I$_3^-$ species at λ_{max} = 353 nm was monitored through a spectrophotometer, which may be assignable to the production of hydrogen peroxide.

2.7 | Electrochemical analysis

The BASi Epsilon-EC instrument containing 0.2-M tetrabutylammonium hexafluorophosphate as supporting electrolyte was employed for carrying out electrochemical experiments in the DCM medium. The BASi platinum working electrode, platinum auxiliary electrode and Ag/AgCl reference electrode were used for all the measurements.

3 | RESULTS AND DISCUSSION

3.1 | Synthesis and structural formulation of the Schiff base (L) and copper(II) complexes

The benzimidazole functionalized ligand, **L**, was synthesized by refluxing o-phenylenediamine with p-anisaldehyde in ethanol. The copper(II) complexes were obtained by adding hydrated copper(II) chloride and nitrate salts to the ligand, **L**, in 1:2 mole ratio in MeOH-DCM under slow stirring conditions (Scheme 1). The different stoichiometric ratios between hydrated copper(II) salts and **L** were applied to divulge the mode of coordination of the benzimidazole functionalized ligand with Cu(II) ion.

However, we were unsuccessful to prepare the copper complexes with different structural compositions. Other copper(II) salts like perchlorate, bromide, acetate and sulphate were also reacted with **L** to develop the copper(II) complexes of varied dimensions and nuclearities but did not able to do so. Complexes **1** and **2** displayed good solubility in polar solvents like methanol, acetonitrile and dichloromethane. The compounds may be successfully synthesized in methanol–dichloromethane or methanol–acetonitrile medium.

3.2 | Description of crystal structures and Hirshfeld surface analysis

The X-ray structural analysis indicates that both complexes **1** and **2** crystallize in the triclinic space group P-1 and are isomorphous and isostructural, differing for the coordinating chlorine and nitrate anions in **1** and **2**,
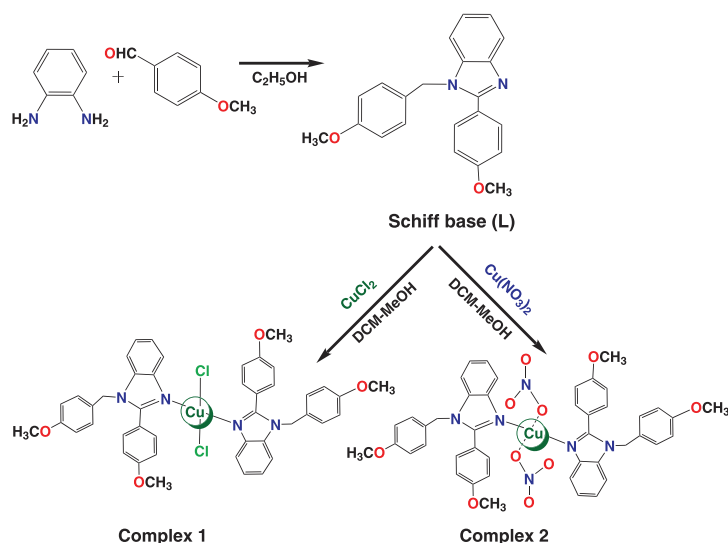
SCHEME 1 Synthesis of 1,2-disubstituted benzimidazole (**L**) and complexes **1** and **2**

respectively. Crystallographic refinement details are shown in Table 1. Selected bond lengths and bond angles for complexes **1** and **2** are tabulated in Tables S1 and S2, respectively. The ORTEP representations of complexes **1** and **2** are shown in Figures 1 and 2, respectively. The asymmetric unit of both compounds **1** and **2** comprises two half complexes located on a centre of symmetry having a slight different conformation. The metals in all cases exhibit an almost regular square planar geometry, as evidenced by the coordination bond angles close to 90° (Tables S1 and S2). The copper(II) ion in **1** is coordinated by two ligand units through the benzimidazole N atom and by two chloride ions (Figure 1), whereas in **2**, the

metal is similarly coordinated by two benzimidazole N atoms from organic ligands and by two monodentate nitrate anions (Figure 2).

The Cu–N bond lengths in all the copper(II) complexes are close comparable falling in the range 1.956 (2)–1.963(2) Å, whereas the Cu–Cl bond lengths in **1** average to 2.2837(8) Å, and Cu–O in **2** are similar, of 2.003(2) Å. The NO_3^- ligands in the two complexes of **2** have approximate coplanar atoms with the uncoordinated O5/O5' and O7/O7' atoms located above and below the coordination plane. This is also reflected by the Cu-O3-N-O5 and Cu-O7-N-O9 torsion angles close to 20° (Table S2). The monodentate coordination mode of the NO_3^- ligands in **2** is confirmed by the criteria listed in Table S3.[61] All the values, Δd, $\Delta d'$, $\Delta \theta$ and $\theta 3$ of 0.609 Å, 0.037 Å, 28.19° and 119.30°, respectively, are in the range of monodentate coordination mode (Table 2). Bond length analysis within the NO_3^- ligands show a relatively longer N–O bond length for the coordinated oxygen, of 1.265(3) and 1.273(3) Å, to be compared with the other N–O bond lengths in the range 1.237(3)–1.249 (3) Å, due to the coordination. The benzimidazole and the para-methoxyphenyl mean planes are not coplanar as indicated by the torsion angles N1–C8–C5–C4/ N4-C29-C30 in **1** and N1–C7–C8–C9/N3-C30-C27-C28 in **2** (φ) that increases from 36.7° in free **L**[66] to 46.30 and 51.34° in **1**, 48.57 and 51.34° in **2**, likely due to packing requirements. The structures of **1** and **2** are very close as evident from the identical space group and crystal system, and the unit cell dimensions exhibit a very small difference in cell axes (Table 1).

The nature of Hirshfeld surfaces of complexes **1** and **2** was analysed using d_{norm} calculation through Crystal Explorer software (Figures S7 and S8). The d_{norm} area and the area consisting of supramolecular interactions of the complexes **1** and **2** with their neighbouring units are displayed in red colour. The 2D fingerprint plots and elemental participation in %share of close interaction with others are displayed in Figures S9 and S10, respectively. In the d_{norm}, blue areas show the engagement of $\pi\cdots\pi$ interactions between phenyl centroid of the ligand, whereas the red area highlights intermolecular C–H$\cdots$O/Cl/N interactions and displays in fingerprint plots (Figures S9 and S10). It is also observed that the self-assembled supramolecular architectures for complex **1** were principally dominated by C–H$\cdots$O/Cl interactions (Figure S11), whereas the self-assembled 3D network for complex **2** was constructed by C–H$\cdots$O interactions (Figure S12). The H$\cdots$O/Cl interactions are found of moderate strength (2.42–2.56 Å; Table S4) in **1**; however, extensive but moderate to weak ranged H$\cdots$O interactions are noted in the construction of the supramolecular architecture of complex **2** (2.42–2.56 Å; Table S5).

TABLE 1 Crystallographic data and structure refinement parameters for the copper complexes

Parameters	1	2
Crystal data	2046275	2046276
Empirical formula	$C_{44}H_{40}N_4O_4Cl_2Cu$	$C_{44}H_{40}N_6O_{10}Cu$
Formula weight	823.24	876.36
T (K)	100	150
Wavelength (Å)	0.71073	0.71073
Crystal system	Triclinic	Triclinic
Space group	P-1	P-1
Unit cell dimensions		
a (Å)	9.1963(3)	9.0794(4)
b (Å)	10.0533(6)	10.2760(5)
c (Å)	21.9806(7)	22.4587(11)
α (°)	100.666(4)	79.878(4)
β (°)	90.164(3)	89.780(4)
γ (°)	102.356(4)	77.426(4)
V (Å^3)	1948.90(15)	2012.02(17)
Z	2	2
ρ (gm cm^{-3})	1.403	1.447
Absorption coefficient (mm^{-1})	0.747	0.612
F(000)	854	910
Crystal size (mm^3)	$0.1 \times 0.2 \times 0.21$	$0.18 \times 0.27 \times 0.32$
Theta range for data collection	2.5 to 32.8°.	3.1 to 27.6°.
Goodness-of-fit on F^2	1.057	1.074
Reflections collected	34,507	25,004
Independent reflections	12,780	9226
Final R indexes [$I \geq 2\sigma$ (I)]	$R_1 = 0.0650$, w$R_2 = 0.1491$	$R_1 = 0.0592$, w$R_2 = 0.1767$
Largest diff. peak/ hole/e Å^{-3}	0.90/−0.70	2.53/−0.50
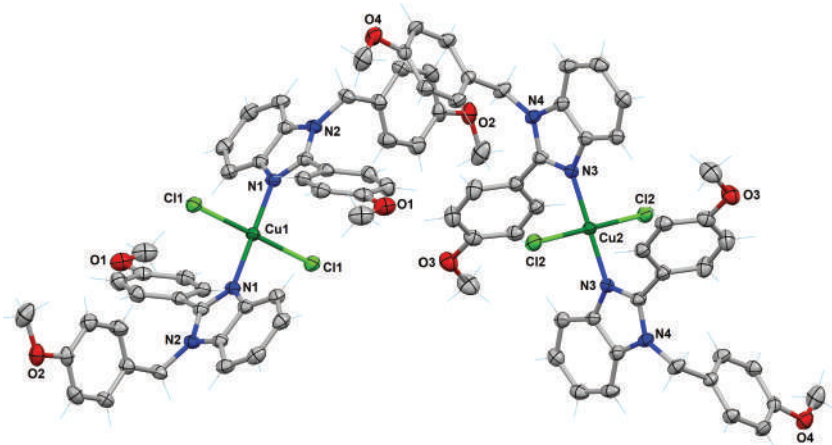
FIGURE 1 ORTEP view (thermal ellipsoid probability at 30%) of the two independent complexes of **1** located on a center of symmetry
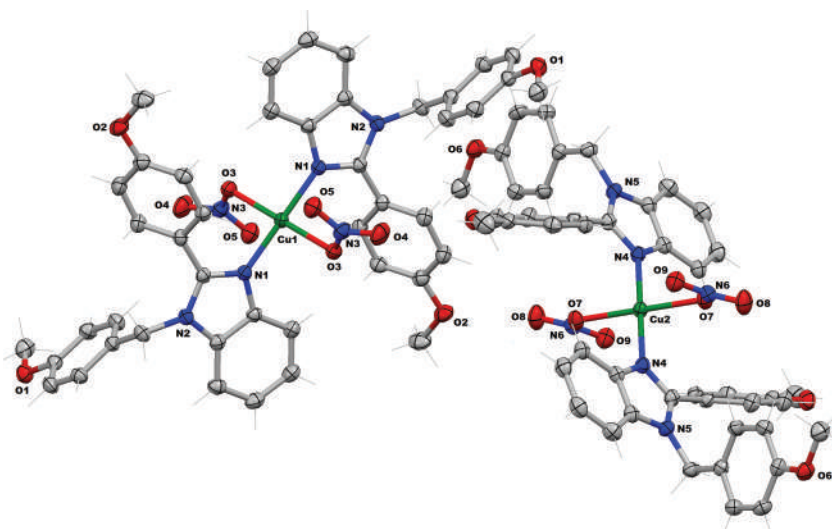
FIGURE 2 ORTEP view (thermal ellipsoid probability at 30%) of the two independent complexes of **2** located on a center of symmetry

TABLE 2 Comparison of k_{cat} (h^{-1}) values for catalytic oxidation of 2-AP by reported copper(II) compounds and copper complexes **1** and **2**

Complex	k_{cat} (h^{-1}) (solvent)	CCDC no.	Ref.
[L^{1}Cu(μ-Cl)$_2$CuL^1]	1.06×10^4 (CH$_3$OH)	1572023	Ghosh et al.[62]
[Cu$_4$(L^2)$_4$]	86.3 (CH$_3$OH)	1507035	Sagar et al.[63]
[Cu$_4$(L^3)$_4$]	340.26 (CH$_3$OH)	1507036	Sagar et al.[63]
[Cu(μ-Cl)(Phen)Cl]	1.69×10^4(CH$_3$OH)	1524680	Garai et al.[56]
[(CH$_3$CN)Cu(L$_s$)$_2$Cu]$^{2+}$	11.1 (CH$_3$OH)	1940162	Dutta et al.[64]
[Cu$_2$(L^{b1})$_3$]ClO$_4$	78.14 (CH$_3$CN)	1957033	Mudi et al.[47]
[Cu(L^{b2})$_2$]	536.4 (CH$_3$CN)	2024056	Mahato et al.[5]
[Cu(L^{b3})](H$_2$O)	5.89×10^2	1981345	Mahato and Biswas[65]
[Cu(L)$_2$Cl$_2$]$_2$ (**1**)	(CH$_3$OH) 2.31×10^4	2046275	This work
[Cu(L)$_2$(NO$_3$)$_2$]$_2$ (**2**)	(CH$_3$OH) 6.3×10^4 (CH$_3$OH)	2046276	This work

Note: L^1 = 2-(α-hydroxyethyl)benzimidazole (Hhebmz), L^2 = (E)-4-chloro-2-((thiazol-2-ylimino)methyl)phenol, L^3 = (E)-4-bromo-2-((thiazol-2-ylimino)methyl) phenol, L^{b1} = (Z)-2-methoxy-6-(((2-methoxyphenyl)imino)methyl)phenol, L^{b2} = 2-(2-methoxybenzylideneamino) phenol.

3.3 | Catalytic oxidation studies of 2-aminophenol and mechanistic inferences

The catalytic oxidation of 2-aminophenol (2-AP) was studied with the copper(II) complexes. In the course of oxidation reaction, 2-aminophenol (2-AP) was considered as a standard substrate in methanol (Scheme 2). The bio-mimics of catalytic oxidation of 2-AP were monitored with a spectrophotometer at an interval of 12 min for 2 h. It is well documented that 2-AP exhibits a single band at 267 nm. Upon addition of copper(II) complexes (1×10^{-4} M solution) to 2-AP (1×10^{-2} M solution), the appearance of new electronic bands at 433 and 430 nm with increasing intensity was observed for both **1** and **2**, respectively (Figures 3 and 4).

The development of the electronic bands at 433 and 430 nm for **1** and **2** is a signature for the production of phenoxazinone compound in solution, which is well established in the scientific literature.[67,68] Controlled experiments were also performed using 2-AP and 2-AP in the presence of benzimidazole functionalized ligand **L** separately under identical reaction conditions (Figure S13) up to 2 h; however, yields of control reactions were very little and can be ignored. The
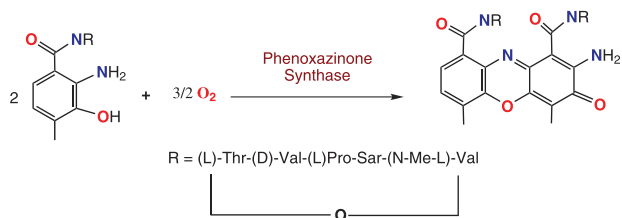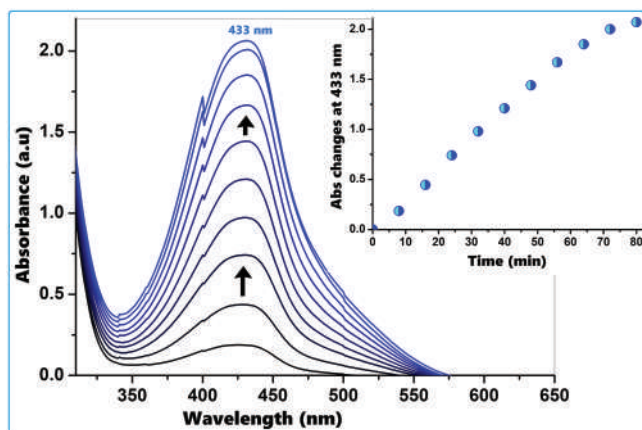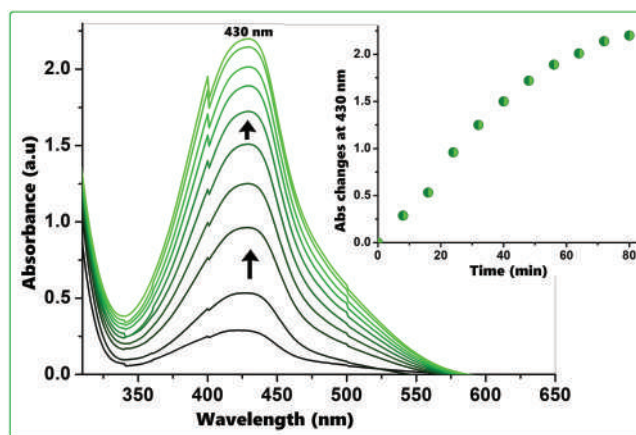
FIGURE 4 Development of a new electronic band at 430 nm after treatment of complex **2** to 2-AP in MeOH with a time interval of 8 min. Inset: time vs. absorbance plot at 430 nm

production of oxidation product in control reactions reveal that auto-oxidation of 2-AP under ambient reaction condition.

The phenoxazinone species was extracted by column chromatographic method. Neutral alumina as column support and benzene-ethyl acetate as an eluant mixture were employed for this chromatographic separation. The oxidation product was isolated in high yield ($\sim$83% and $\sim$76% for **1** and **2**). The product was principally identified by ^{1}H NMR spectroscopy.[47,56,57]

^{1}H NMR data for 2-amino-3*H*-phenoxazine-3-one (APX), (CDCl$_3$, 400 MHz), δ_H: 7.61 (m, 1H), 7.46 (m, 3H), 6.48 (s, 1H), 6.39 (s, 1H), 6.27 (s, 1H).

Kinetic studies of the catalytic oxidation of 2-AP were carried out to understand the catalytic efficacy for the copper(II) complexes. The method of initial rates was followed to unveil the nature of kinetic for this catalytic oxidation of 2-AP. The kinetics of oxidative coupling of 2-AP was monitored for the growth of oxidized products at 433 and 430 nm as a function of time (Figures S14 and S15).[65,69–71] The rate constants versus concentration of the substrate plot seem to be saturation kinetics. The values of the kinetics parameters for the oxidation of 2-AP by **1** and **2** were determined considering the Michaelis–Menten approach of enzymatic kinetics and summarized in Table 2. An attempt was also made to examine the reactivity of the synthesized copper complexes with a comparison of the kinetic parameter for other reported copper complexes.[5,47,56,59,62–64] The kinetics parameter are furnished in Table 2.

Michaelis–Menten equation is presented as follows:

$$V = \frac{V_{\max}[S]}{K_M + [S]},$$

SCHEME 2 Oxidative coupling of 2-aminophenol by phenoxazinone synthase

FIGURE 3 Generation of a new electronic band at 433 nm after addition complex **1** to 2-AP in MeOH with a time interval of 8 min. Inset: time vs. absorbance plot at 433 nm

where V indicates the reaction rate, K_M is considered as the Michaelis–Menten constant, V_{max} presents maximum reaction velocity, and $[S]$ is the substrate concentration.

The values of kinetics parameters were determined from Michaelis–Menten approach of enzymatic kinetics for **1** as V_{max} $(MS^{-1}) = 6.44 \times 10^{-4}$; $K_M = 2.63 \times 10^{-3}$ [std. error for V_{max} $(MS^{-1}) = 7.65 \times 10^{-5}$; std. error for K_M (M) $= 1.29 \times 10^{-4}$] and for **2** as V_{max} $(MS^{-1}) = 1.75 \times 10^{-3}$; $K_M = 4.18 \times 10^{-3}$ [std. error for V_{max} $(MS^{-1}) = 4.16 \times 10^{-5}$; std. error for K_M (M) $= 1.97 \times 10^{-4}$].

The turnover number (k_{cat}) for the copper(II) complexes **1** and **2** were determined as 2.31×10^4 and 6.3×10^4 h^{-1}, respectively. The catalytic efficiency (k_{cat}/K_M) for **1** and **2** towards phenoxazinone synthase activity was found high and calculated as 8.78×10^6 and 1.50×10^7. It is observed that complex **2** exhibits approximately twofold greater rate of oxidation compare to complex **1**. In the copper(II) complex **2**, the presence of coordinated nitrate with Cu(II) centre creates higher steric hindrance and leads to more lability, and as a consequence, loss of the coordinated nitrate probably occurs during the incoming approach of 2-AP towards the copper(II) centre. For complex **1**, the presence of coordinated chloride to the square plane of Cu(II) centre facilitates a more stable/inert structure compared to complex **2**. The high catalytic efficiencies of the copper(II) complexes may be explained from the perspective of easy incorporation of 2-AP through the expansion of the coordination number of copper(II) centres.

The higher rate of catalytic oxidation for complex **2** was further evaluated in terms of determination of the activation parameters obtained from Eyring equation/ Arrhenius equation through temperature-dependent kinetic measurements. To understand the thermal effect on the rate of catalytic oxidative coupling of 2-AP, kinetic experiments were carried out with both the complexes in the temperature range (283 K–303 K). During the kinetic measurement at different temperature, the concentration for both the copper complexes was kept constant at 1×10^{-3} M, whereas the concentration of 2-AP was fixed at 1×10^{-2} M. It is observed that the rate of oxidation of 2-AP increases with an increase in temperature for both the copper(II) complex catalysed reactions. The activation energy (E_a), the heat of enthalpy ($\Delta H^{\ddagger}$), and entropy change ($\Delta S^{\ddagger}$) (Table S6) were determined from the Arrhenius (Figure S16) and Eyring (Figure S17) plots. The activation energy for the complex **2** catalysed oxidation of 2-AP was found 9.67 kJ mol^{-1}, which is lower than that of complex **1** ($E_a = 25.68$ kJ mol^{-1}). Noteworthy, both the complexes exhibit negative $\Delta S^{\ddagger}$ value and recommend the formation of substrate-complex adduct at the transition state.

The redox activities of copper(II) complexes and mixtures of the complexes with 2-AP were studied by cyclic voltammetry in CH_2Cl_2. The electrochemical potential values corresponding to active species of the copper complexes with reference to ferrocenium/ ferrocene (Fc^+/Fc) couple are displayed in Table S7. The cyclic voltammograms for complexes **1** and **2** are illustrated in Figures 5 and S18. Both the copper complexes produce quite similar nature of cathodic and anodic waves in the presence and absence of 2-AP. Complexes **1** and **2** show reversible cathodic waves at -0.655 and -0.730 V, which may be assigned as imine/imine anion radical corresponding to 2e redox waves of the two C=N bonds in two benzimidazole ligands. The other cathodic peaks at -1.53 and 1.68 V for complexes **1** and **2** appear for the irreversible Cu^{2+}/Cu^+ redox couples.

The copper complexes **1** and **2** showed the presence of anodic peaks at 0.38 and $+0.52$ V, respectively. In the mixture of individual copper complexes **1** and **2** in the presence of 2-AP, the reversible cathodic wave of imine/imineanion radical shifted to -0.68 and -0.97 V, respectively. Noteworthy, the irreversible cathodic peak of Cu^{2+}/Cu^+ redox couple in **1** shifted to -1.14 V. In addition to the presence of cathodic waves, each of the
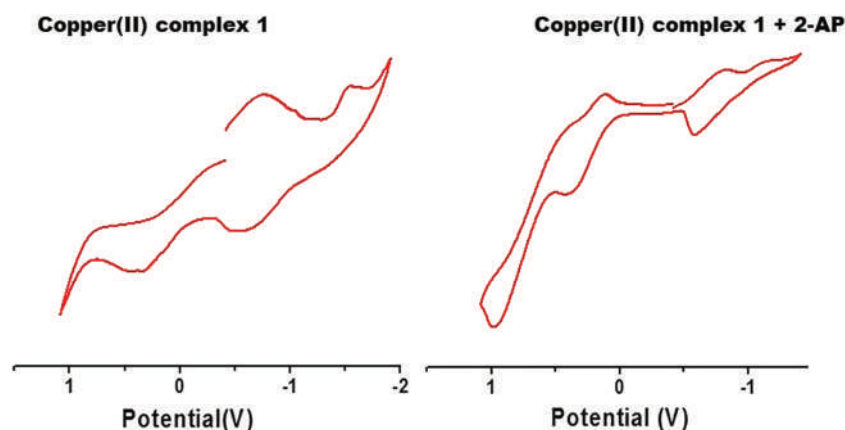
FIGURE 5 Left: Cyclic voltammogram of the copper(II) complex **1** in anhydrous DCM medium; right: cyclic voltammogram of copper(II) complex **1** in the presence of 2-AP under molecular oxygen atmosphere in anhydrous DCM in CH_2Cl_2 (0.20 M [N(n − Bu)$_4$]PF$_6$) at 295 K

copper complexes exhibits reversible anodic waves at +0.25 and +0.48 V, respectively, and suggests the development of 2-AP$^-$/2-AP$^{\bullet-}$ redox couples in the course of catalysis. An irreversible anodic peak at +0.98 V for complex **1** in the presence of 2-AP was also observed and may be attributed to the presence of 2-AP$^{\bullet-}$/2-IQ redox couple in solution. The electrode potential values observed for the development of 2-AP$^{\bullet-}$/2-IQ species in the course of catalytic oxidation of 2-AP were well corroborated with the values reported by a few previously reported copper complexes.[5,47,61]
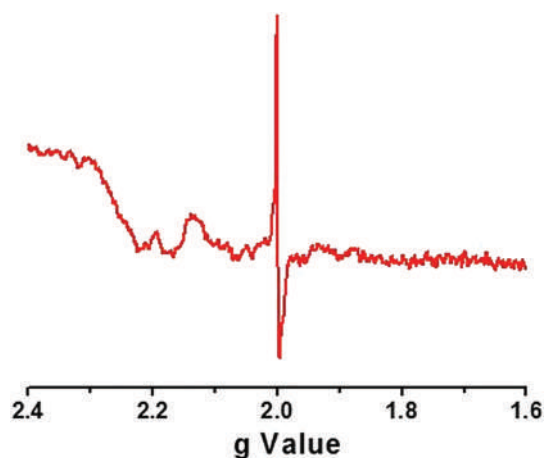
FIGURE 6 EPR spectrum of the copper(II) complex **1** in the presence of 2-AP anhydrous DCM medium

To find further insights into the mechanistic aspects of the course of catalysis, X-band EPR spectral analysis of the reaction mixture of copper complex **1** with 2-AP was carried out in DCM medium. Complex **1** produces four line hyperfine EPR spectra (Figure S19) for the presence of ^{63}Cu ($I = 3/2$), and the g value was found 2.116, which may be well correlated with the reported EPR spectra of copper(II) ion.[5,47] However, when 2-AP was added to the complex **1** solution, the hyperfine spectra was quenched and a new single-line spectra was found at $g = 2.001$, indicating the presence of iminobenzoquinone radical (Figure 6).[5]

Furthermore, electrospray ionization (ESI) mass spectra of the copper(II) complexes **1** and **2** in the presence of 2-AP were measured after mixing of 10 min to understand the labile character and the binding aspects of the copper(II) complexes with 2-AP in MeOH medium. The spectra are shown in Figures S20 and S21 for complexes **1** and **2**, respectively. It was observed that the ESI-MS of the reaction mixture for **1** (Figure S20) showed a base peak at m/z 213.27, which is attributed to the existence [(2-amino-3*H*-phenoxazine-3-ones) + H$^+$] species in solution. Furthermore, a characteristics peak at m/z 823.55 was also detected, which reveals the presence of molecular ion peak. The binding adduct between complex **1** and 2-AP, [[**1** + (2-AP)] + H$^+$] was further confirmed from the appearance of another characteristic peak at 927.41 m/z. ESI-MS spectrum of complex **2** with 2-AP (Figure S21) displayed a characteristic peak at 213.29
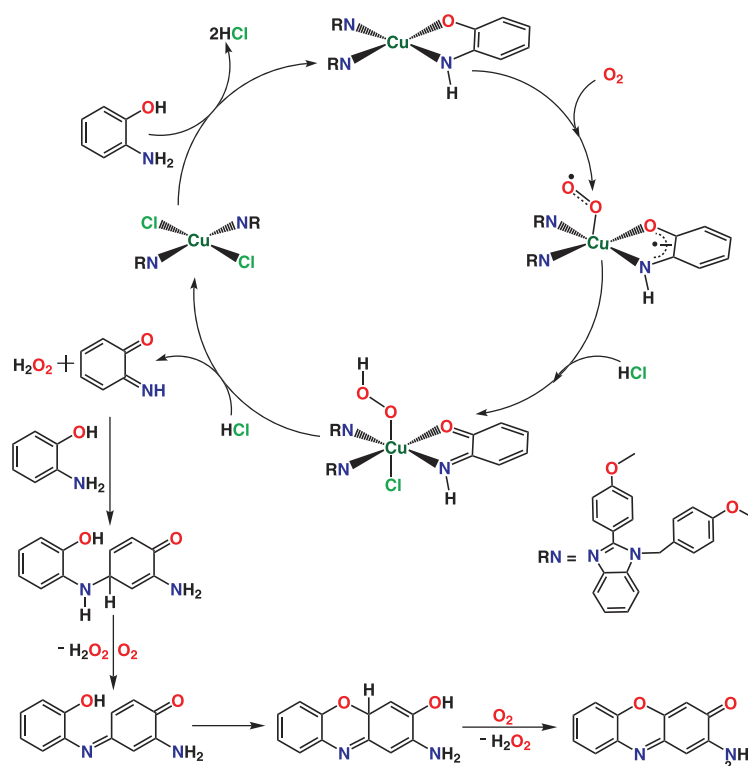
SCHEME 3 Plausible mechanistic pathway for phenoxazinone synthase activity of the copper complexes

and confirmed the development of [(2-amino-3*H*-phenoxazine-3-ones) + H$^+$] species in MeOH. The enzyme-substrate adduct for complex **2** was also ensured as [[Cu(**L**)$_2$ + (2-AP)] + H$^+$], which corroborated well with the characteristic peak at m/z 860.29 in the spectrum. However, the molecular ion peak for complex **2** was absent in the spectrum. Therefore, ESI-MS spectra for both the copper complexes suggest that both the complexes undergo the course of catalysis through the formation of the enzyme-substrate adduct. It is also recommended that complex **2** in addition to 2-AP displaced the coordinated nitrates to the solution and more lability or coordinatively unsaturation at the copper(II) centre facilitates higher catalytic performance than complex **1**. The participation of aerobic oxygen was also examined to understand the fate of O$_2$ through the detection of hydrogen peroxide in the course of catalysis. The development of hydrogen peroxide was detected with a UV-vis spectrophotometer, and the observed electronic band at 353 nm corresponds to the production of I$_3^-$ species (Figure S22)[59] and thereby confirmed the existence of hydrogen peroxide. Therefore, based on spectrophotometric, kinetics, ESI-MS spectra of the reaction mixtures, electrochemical analysis and EPR spectral measurement, the mechanistic pathways for the course of catalytic oxidation may be proposed according to Scheme 3.

4 | CONCLUSIONS

This research study reports the details of synthesis, spectroscopic and structural characterization of a newly designed substituted benzimidazole ligand and two structurally similar copper(II) complexes containing the ligand. The effect of ancillary ligands (chloride and nitrate) in the bio-mimics of phenoxazinone synthase activity has also been investigated. X-ray structural analysis exhibits that both the complex adopts a perfect square planar geometry and exists in *trans* configuration. It is observed that the catalytic efficiency (k_{cat}/K_M) for both the copper complexes was found high towards the bio-mimicking oxidation of 2-AP. k_{cat}/K_M values were determined as 8.78×10^6 and 1.50×10^7 for **1** and **2**, respectively, and it can be addressed that the catalytic oxidation efficiency is almost double that of **1**. The presence of coordinated nitrate in **2** creates steric repulsion in the square plane and makes the complex more labile, which facilitates the entrance of 2-AP to the Cu(II) centre. Electrochemical analysis for both the copper complexes in the presence of 2-AP confirms the development of AP$^-$/AP$^{\bullet-}$ redox couple in the course of oxidative coupling of 2-AP. EPR spectral analysis consolidates the existence of organic radical at $g = 2.01$ and

supports the catalytic oxidation as radical driven. The evaluated activation parameters through temperature-dependent kinetic measurements further support the higher rate of catalytic oxidation of 2-AP for complex **2**. Finally, this study leads to easy preparation of benzimidazole derivative ligand and its copper(II) complexes and explores the effect of ancillary ligands in the bio-mimetic oxidation of 2-AP through details spectroscopic, ESI-MS and electrochemical methods.

SUPPLEMENTARY DATA

Supplementary crystallographic data are available free of charge from The Director, CCDC, 12 Union Road, Cambridge, CB2 1EZ, UK (fax: +44-1223-336033; E-mail: deposit@ccdc.cam.ac.uk or through http://www.ccdc.cam.ac.uk) upon request, quoting deposition number CCDC 2046275 and 2046276 for complexes **1** and **2**, respectively. Experimental information such FT-IR, UV-vis, ^{1}H and ^{13}C NMR, supramolecular architectures, Hirshfeld surface, fingerprint plots, rate vs. [substrate] plot, bond distance and bond angle parameters and redox potential data are given here.

AUTHOR CONTRIBUTIONS
Prafullya Kumar Mudi: Conceptualization; formal analysis; investigation; methodology. **Rajani Kanta Mahato:** Conceptualization; formal analysis; investigation; methodology. **Mayank Joshi:** Methodology; validation; visualization. **Madhusudan Shit:** Formal analysis; investigation; methodology. **Angshuman Roy Choudhury:** Data curation; formal analysis; software; validation. **Hari Sankar Das:** Formal analysis; investigation; supervision. **Bhaskar Biswas:** Conceptualization; supervision.

DATA AVAILABILITY STATEMENT
The data that supports the findings of this study are available in the supporting information of this article.

ORCID
Prafullya Kumar Mudi https://orcid.org/0000-0002-3365-0961
Rajani Kanta Mahato https://orcid.org/0000-0003-0765-2979
Mayank Joshi https://orcid.org/0000-0003-2463-4967

Madhusudan Shit https://orcid.org/0000-0002-4271-4293
Angshuman Roy Choudhury https://orcid.org/0000-0002-4018-0451
Hari Sankar Das https://orcid.org/0000-0003-0036-0244
Bhaskar Biswas https://orcid.org/0000-0002-5447-9729

REFERENCES

[1] T. Shi, Y. Xu, Y. J. Zou, Z. X. Wang, *Dalton Trans.* **2019**, *48*, 11186.

[2] P. Xiao, F. Dumur, J. Zhang, J. P. Fouassier, D. Gigmes, J. Lalevée, *Macromolecules* **2014**, *47*(12), 3837.

[3] M. Mondal, S. Jana, M. G. B. Drew, A. Ghosh, *Polymer* **2020**, *204*, 122815.

[4] S. Dasgupta, G. Aullón, E. Zangrando, D. Das, *New J. Chem.* **2019**, *43*, 2501.

[5] S. Mahato, N. Meheta, K. Muddukrishnaiah, M. Joshi, P. Ghosh, M. Shit, A. R. Choudhury, B. Biswas, *Appl. Organomet. Chem.* **2020**, *34*, e5935.

[6] L. H. Abdel-Rahman, A. M. Abu-Dief, M. Shaker, S. Adam, S. K. Hamdan, *Catal. Lett.* **2016**, *146*, 1373.

[7] E. M. M. Ibrahim, L. H. Abdel-Rahman, A. M. Abu-Dief, A. Elshafaie, S. K. Hamdan, A. M. Ahmed, *Phys. Scr.* **2018**, *93*, 055801.

[8] S. I. Al-Saeedi, L. H. Abdel-Rahman, A. M. Abu-Dief, S. M. Abdel-Fatah, T. M. Alotaibi, A. Alsalme, A. Nafady, *Catalysts* **2018**, *8*, 452.

[9] K. A. Magnus, H. T. That, J. E. Carpenter, *Chem. Rev.* **1994**, *94*, 727.

[10] A. S. Ferrer, J. N. R. Lopez, F. G. Canovas, F. G. Carmona, *Biochim. Biophys. Acta* **1995**, *1*, 1247.

[11] C. Gerdemann, C. Eicken, B. Krebs, *Acc. Chem. Res.* **2002**, *35*, 183.

[12] F. Fusetti, K. H. Schröter, R. A. Steiner, P. I. van Noort, T. Pijning, H. J. Rozeboom, K. H. Kalk, M. R. Egmond, B. W. Dijkstra, *Structure* **2002**, *10*, 259.

[13] R. A. Steiner, I. M. Kooter, B. W. Dijkstra, *Biochemistry* **2002**, *41*, 7955.

[14] I. M. Kooter, R. A. Steiner, B. W. Dijkstra, P. I. van Noort, M. R. Egmund, M. Huber, *Eur. J. Biochem.* **2002**, *269*, 2971.

[15] J. W. Whittaker, *Chem. Rev.* **2003**, *103*, 2347.

[16] M. Halcrow, S. Phillips, P. Knowles, In Subcellular Biochemistry, in *Enzyme-Catalyzed Electron and Radical Transfer*, (Eds: A. Holzenburg, N. S. Scrutton) Vol. 35, Plenum, New York **2000** 183.

[17] M. M. Whittaker, P. J. Kersten, N. Nakamura, J. S. Loehr, E. S. Schweizer, J. W. Whittaker, *J. Biol. Chem.* **1996**, *271*, 681.

[18] M. M. Whittaker, P. J. Kersten, D. Cullen, J. W. Whittaker, *J. Biol. Chem.* **1999**, *274*, 36226.

[19] H. H. T. Nguyen, K. H. Nakagawa, B. Hedman, S. J. Eliot, M. E. Lidstrom, K. O. Hodgson, S. I. Chan, J. Am, *Chem. Soc.* **1996**, *118*, 12766.

[20] S. J. Elliott, D. W. Randall, R. D. Britt, S. I. Chan, *J. Am. Chem. Soc.* **1998**, *120*, 3247.

[21] R. L. Lieberman, D. B. Shrestha, P. E. Doan, B. M. Hoffman, T. L. Stemmler, A. C. Rosenzweig, *Proc. Natl. Acad. Sci.* **2003**, *100*, 3820.

[22] E. Katz, in *Biosynthesis of secondary metabolites: roles of trace metals Antibiotics II*, (Eds: D. Gottlieb, P. D. Shaw), Springer, New York **1967** 276.

[23] U. Hollstein, *Chem. Rev.* **1974**, *74*, 625.

[24] L. I. Simandi, S. Nemeth, N. Rumlis, *J. Mol. Catal.* **1987**, *42*, 357.

[25] A. Butenandt, *Angew. Chem.* **1957**, *69*, 16.

[26] T. M. Simándi, L. I. Simándi, M. Győr, A. Rockenbauer, A. Gömöry, *Dalton Trans.* **2004**, 1056.

[27] G. W. K. Cavill, P. S. Clezy, J. R. Tetaz, R. L. Werner, *Tetrahedron* **1959**, *5*, 275.

[28] J. Kaizer, R. Csonka, G. Speier, *J. Mol. Catal. A: Chem.* **2002**, *180*, 91.

[29] K. Ansari, C. Lal, *Eur. J. Med. Chem.* **2009**, *44*, 2294.

[30] R. V. Devivar, E. Kawashima, G. R. Revankar, J. M. Breitenbach, E. D. Kreske, J. C. Drach, L. B. Townsend, *J. Med. Chem.* **1994**, *37*, 2942.

[31] P. Keller, C. Müller, I. Engelhardt, E. Hiller, K. Lemuth, H. Eickhoff, K. H. Wiesmüller, A. B. Kentischer, F. Bracher, S. Rupp, *Antimicrob. Agents Chemother.* **2015**, *59*(10), 6296.

[32] A. Hussain, M. F. AlAjmi, M. T. Rehman, S. Amir, F. M. Husain, A. Alsalme, M. A. Siddiqui, A. A. AlKhedhairy, R. A. Khan, *Scientific Rep.* **2019**, *9*, 5237.

[33] A. Katiyar, J. Rai, S. Gangwar, A. K. Mohanty, A. P. Mishra, *J. Drug Discov. Dev.* **2018**, *2*, 2.

[34] M. J. Van Oosten, G. Silletti, G. Guida, V. Cirillo, E. Di Stasio, P. Carillo, P. Woodrow, A. Maggio, G. Raimondi, *Front. Recent Dev. Plant Sci.* **2017**, *8*, 1220.

[35] H. Yang, Y. Ren, X. Gao, Y. Gao, *Chem. Res. Chin. Univ.* **2016**, *32*(6), 973.

[36] L. H. A. Rahman, A. A. Abdelhamid, A. M. Abu-Dief, M. R. Shehata, M. A. Bakheet, *Journal Mol. Struct.* **2020**, *1200*, 127034.

[37] A. M. Abu-Dief, L. H. Abdel-Rahman, A. A. Abdelhamid, A. A. Marzouk, M. R. Shehata, M. A. Bakheet, O. A. Almaghrabi, A. Nafady, *Spectrochim. Acta a: Mol. Biomol. Spectros.* **2020**, *228*, 117700.

[38] P. Ghosh, A. Mandal, *Tetrahedron Lett.* **2012**, *53*, 6483.

[39] S. Paul, B. Basu, *Tetrahedron Lett.* **2012**, *53*, 4130.

[40] D. Zornik, R. M. Meudtner, T. E. Malah, C. M. Thiele, S. Hecht, *Chem. – Eur. J.* **2011**, *17*, 1473.

[41] D. Yang, D. Fokas, J. Li, L. Yu, C. M. Baldino, *Synthesis* **2005**, *2005*, 47.

[42] H. J. Lim, D. Myung, I. Y. C. Lee, M. H. Jung, *J. Comb. Chem.* **2008**, *10*, 501.

[43] G. Csire, J. Demjén, S. Timári, K. Várnagy, *Polyhedron* **2013**, *61*, 202.

[44] R. Kalarani, M. Sankarganesh, G. G. V. Kumar, M. Kalanithi, *J. Mol. Struct.* **2020**, *1206*, 127725.

[45] B. Bertrand, G. Gontard, C. Botuha, M. Salmain, *Eur. J. Inorg. Chem.* **2020**, *35*, 3370. https://doi.org/10.1002/ejic.202000717

[46] C. K. Pal, S. Mahato, M. Joshi, S. Paul, A. R. Choudhury, B. Biswas, *Inorg. Chim. Acta* **2020**, *506*, 119541.

[47] P. K. Mudi, N. Bandopadhyay, M. Joshi, M. Shit, S. Paul, A. R. Choudhury, B. Biswas, *Inorg. Chim. Acta* **2020**, *505*, 119468.

[48] S. Mahato, N. Meheta, K. Muddukrishnaiah, M. Joshi, M. Shit, A. R. Choudhury, B. Biswas, *Polyhedron* **2021**, *194*, 114933.

[49] CrysAlisPro 1.171.39.35c, **2017**, Rigaku Oxford Diffraction, Rigaku Corporation: Tokyo, Japan.

[50] G. M. Sheldrick, *Acta Cryst.* **2015**, *A71*, 3.

[51] G. M. Sheldrick, *Acta Cryst.* **2015**, *C71*, 3.

[52] O. V. Dolomanov, L. J. Bourhis, R. J. Gildea, J. A. K. Howard, H. Puschmann, *J. Appl. Crystallogr.* **2009**, *42*, 339.

[53] M. J. Turner, J. J. McKinnon, S. K. Wolff, D. J. Grimwood, P. R. Spackman, D. Jayatilaka, M. A. Spackman, Crystal Explorer17, http://hirshfeldsurface.net, **2017**.

[54] M. A. Spackman, D. Jayatilaka, *Cryst. Eng. Comm.* **2009**, *11*, 19.

[55] M. A. Spackman, J. J. McKinnon, *Cryst. Eng. Comm.* **2002**, *4*, 378.

[56] M. Garai, D. Dey, H. R. Yadav, A. R. Choudhury, M. Maji, B. Biswas, *ChemistrySelect* **2017**, *2*, 11040.

[57] S. Thakur, S. Banerjee, S. Das, S. Chattopadhyay, *New J. Chem.* **2019**, *43*, 18747.

[58] R. K. Mahato, A. K. Mahanty, S. Paul, V. Gopal, B. Perumalsamy, G. Balakrishnan, T. Ramasamy, D. Dharumadurai, B. Biswas, *J. Mol. Struct.* **2021**, *1223*, 129264.

[59] B. Chowdhury, M. Maji, B. Biswas, *J. Chem. Sci.* **2017**, *129*, 1627.

[60] C. K. Pal, S. Mahato, H. R. Yadav, M. Shit, A. R. Choudhury, B. Biswas, *Polyhedron* **2019**, *174*, 114156.

[61] G. J. Kleywegt, W. G. R. Wiesmeijer, G. J. V. Driel, W. L. Driessen, J. Reedijk, *J. Chem. Soc. Dalton Trans.* **1985**, 2177.

[62] A. K. Ghosh, A. Ali, Y. Singh, C. S. Purohit, R. Ghosh, *Inorg. Chim. Acta* **2018**, *474*, 156.

[63] S. Sagar, S. Sengupta, A. J. Mota, S. K. Chattopadhyay, A. E. Ferao, E. Riviere, W. Lewis, S. Naskar, *Dalton Trans.* **2017**, *46*, 1249.

[64] T. Dutta, S. Mirdya, P. Giri, S. Chattopadhyay, *Polyhedron* **2020**, *175*, 114164.

[65] S. Mahato, B. Biswas, *J. Indian Chem. Soc.* **2020**, *97*, 849.

[66] M. N. Manjunatha, A. G. Dikundwar, K. R. Nagasundara, *Polyhedron* **2011**, *30*, 1299.

[67] S. Ganguly, J. Mayans, A. Ghosh, *Chem. – Asian J.* **2020**, *15*, 1.

[68] S. Dutta, T. K. Ghosh, P. Mahapatra, A. Ghosh, *Inorg. Chem.* **2020**, *59*, 14989.

[69] A. Mandal, S. Dasgupta, A. Adhikary, D. Samanta, E. Zangrando, D. Das, *Dalton Trans.* **2020**, *49*, 5999.

[70] S. Pal, B. Chowdhury, M. Patra, M. Maji, B. Biswas, *Spectrochim. Acta A. Mol. Biomol. Spectros.* **2015**, *144*, 148.

[71] B. Chowdhury, B. Bhowmik, A. Sahu, M. Joshi, S. Paul, A. R. Choudhury, B. Biswas, *J. Chem. Sci.* **2018**, *130*, 161.

SUPPORTING INFORMATION

Additional supporting information may be found online in the Supporting Information section at the end of this article.

How to cite this article: Mudi PK, Mahato RK, Joshi M, et al. Copper(II) complexes with a benzimidazole functionalized Schiff base: Synthesis, crystal structures, and role of ancillary ions in phenoxazinone synthase activity. *Appl Organomet Chem.* 2021;35:e6211. https://doi.org/10.1002/aoc.6211

Source details

Feedback >   Compare sources >

Applied Organometallic Chemistry

Scopus coverage years: from 1987 to Present

Publisher: Wiley-Blackwell

ISSN: 0268-2605   E-ISSN: 1099-0739

Subject area: (Chemistry: Inorganic Chemistry)   (Chemistry: General Chemistry)

Source type: Journal

View all documents >   Set document alert   🖫 Save to source list

CiteScore 2022   ⓘ
7.3

SJR 2022   ⓘ
0.518

SNIP 2022   ⓘ
0.782

CiteScore   CiteScore rank & trend   Scopus content coverage

Journal Pre-proofs

Synthesis, Structure, Polyphenol Oxidase Mimicking and Bactericidal Activity of a Zinc-Schiff Base Complex

Shreya Mahato, Nishith Meheta, K Muddukrishnaiah, Mayank Joshi, Madhusudan Shit, Angshuman Roy Choudhury, Bhaskar Biswas

Please cite this article as: S. Mahato, N. Meheta, K. Muddukrishnaiah, M. Joshi, M. Shit, A. Roy Choudhury, B. Biswas, Synthesis, Structure, Polyphenol Oxidase Mimicking and Bactericidal Activity of a Zinc-Schiff Base Complex, *Polyhedron* (2020), doi: https://doi.org/10.1016/j.poly.2020.114933

This is a PDF file of an article that has undergone enhancements after acceptance, such as the addition of a cover page and metadata, and formatting for readability, but it is not yet the definitive version of record. This version will undergo additional copyediting, typesetting and review before it is published in its final form, but we are providing this version to give early visibility of the article. Please note that, during the production process, errors may be discovered which could affect the content, and all legal disclaimers that apply to the journal pertain.

Synthesis, Structure, Polyphenol Oxidase Mimicking and Bactericidal Activity of a Zinc-Schiff Base Complex

Shreya Mahato,[a] Nishith Meheta,[a] K Muddukrishnaiah,[b] Mayank Joshi,[c] Madhusudan Shit,[d] Angshuman Roy Choudhury,[c] and Bhaskar Biswas[a,*]

[a]*Department of Chemistry, University of North Bengal, Darjeeling-734013, India*

[b]*Department of Pharmaceutical Technology, Anna University, BIT Campus Thiruchirappalli, India*

[c]*Department of Chemical Sciences, Indian Institute of Science Education and Research, Mohali, Sector 81, Knowledge City, S. A. S. Nagar, Manauli PO, Mohali, Punjab 140306, India*

[d]*Department of Chemistry, Dinabandhu Andrews College, Kolkata 700084, India*

Focusing on the important biological functions of metallo-enzymes and metallo-therapeutics in living world, this research work demonstrates the synthesis, crystal structure, supramolecular architecture, 4-methylcatechol oxidation and bactericidal activity of an interesting zinc-Schiff base complex, $[Zn(HL)_2Cl_2]$ (**1**), [Schiff base (H**L**) = 2-(2-methoxybenzylideneamino)phenol]. Crystal structure analysis of the zinc-Schiff base reveals that zinc centre exists in a distorted tetrahedral geometry. The Schiff base adopts three donor centres, however it gets protonated to exist in a zwitter ionic form and behaves as a monodentate coordinator in **1**. This zinc-Schiff base complex has been examined towards the bio-mimetic oxidation of 4-methylcatechol (4-MC) in methanol and portrays its good efficacy with good turnover number, 1.45×10^3 h^{-1}. Electro-chemical study, electron paramagnetic resonance analysis and electrospray ionization mass spectrometry results for the zinc-Schiff base complex in presence of 4-MC ensures that the catalytic reaction undergoes through enzyme-substrate binding, and generation of radical in the course of catalysis drives the catalytic oxidation of 4-MC. Antibacterial study has also been performed against few clinical pathogens (*Bacillus* SP, *Enterococcus*, and *E.coli*). Scanning electron microscope and EDAX analysis for the pathogen with little dose of zinc complex confirms the destruction of bacterial cell membrane with 1.44% occurrence of zinc in the selected zone of inhibition area. This observation holds a great promise to develop future antibacterial agent.

*Corresponding author. E-mail: bhaskarbiswas@nbu.ac.in / icbbiswas@gmail.com

1. Introduction

In the field of coordination chemistry, Schiff base, a unique class of compounds has been emerged as a widely used chelator towards the development of metal complexes [1-7]. The newly prepared Schiff bases and their coordination compounds hold a great promise to scientific community for their novel properties in designing efficient catalysts, smart magnetic materials, important therapeutics, opto-electronic devices, bio-mimetic models and so on [8-14]. Among the different 3d elements, zinc is an indispensable bio-metal in living system which has significant functions in various biological processes [15]. Most captivatingly, zinc-Schiff-base complexes have been well recognized for their catalytic, opto-electronic and therapeutic properties [13,14,16-21]. Zinc ion in association with Schiff base exhibits diversified coordination geometries [22,23] and interesting supramolecular architectures [24]. Added to this, zinc-Schiff base complexes also provide promising potency towards the resistance of microbial activity and consider as one of the suitable candidates for the discovery of potent metallo-therapeutics [25-27].

Polyphenol oxidase (PPO) consists of a group of copper containing proteins which monitors the browning of wide range of natural fruits, vegetables, and sea-food products through the enzymatic oxidation of phenolics and lead to the development of brown pigments [28,29]. PPO catalyzes the hydroxylation of monophenol (monophenolase activity) following the subsequent oxidation of diphenol to quinones (diphenolase activity) which promptly convert to brown coloured relatively insoluble polymers (melanins) [30]. This development of brown colour catalyzed by PPO has received paramount attention in food industry as it provides significant information about nutritional quality and, thereby, produced a crucial economic impact on the food-processing industry [31]. Scientific literatures exhibit that the rate of metallo-enzyme catalysed browning of natural fruits as well as vegetables fundamentally depends on concentrations of phenolic substrate, pH, temperature, and specific activity of the PPO [28-31]. It is also well documented that catalytic oxidation of phenols actually produces biologically important *o*-quinones which exhibits facile redox reactions for its higher chemical activity. The *o*-quinone also plays various biological functions likely to

develop antibiotics, defensive secretions, and pigmentation [32]. Melanin pigment, a polymerise form of *o*-quinone protects all the living organisms from UV-light of sun [33]. In the context, with an aim to study the bactericidal activity and catalytic fate towards the bio-mimetic oxidation of 4-MC, we have designed, synthesized, and structurally characterized of an interesting zinc-Schiff base complex and studied its bactericidal and bio-mimicking activity.

2. Experimental

2.1. Preparation of the Schiff base and zinc-Schiff base complex

(a) Chemicals, solvents and starting materials

Highly pure *o*-anisidine (Sigma Aldrich, USA), salicylaldehyde (Sigma Aldrich, USA) and zinc chloride hexahydrate (Merck, India) were purchased from the respective outlets. All the chemicals and solvents were of analytical grade and used as received without further purification.

(b) *Synthesis of the Schiff base and zinc-Schiff base complex*

The synthetic details and spectroscopic characterization of this Schiff base, H**L** was recently reported by our group [34].

The zinc-Schiff base complex was synthesized by addition of solid zinc(II) chloride hexahydrate (0.244 g, 1 mmol) to aqueous-methanolic solution of H**L** (0.454 g, 2 mmol). The yellow coloured solution of Schiff base was turned to bright yellow solution. After that, the reaction mixture was kept for slow stirring for ~30 mins and set in open atmosphere for slow evaporation. Bright yellow coloured single crystals of zinc-Schiff base were separated out after 10-12 days. The crystalline compound was washed with hexane and dried over silica gel. Finally, different spectroscopic methods were employed to establish the molecular composition of zinc-Schiff base and the results are summarized as follows.

Yield of **1**: 0.415 g (~63.5% based on metal salt) Anal. Calc. for $C_{28}H_{26}N_2O_4Zn$ (**1**): C, 56.92; H, 4.44; N, 4.74; Found: C, 56.95; H, 4.41; N, 4.80. IR (KBr pellet, cm^{-1}; Fig. S1): 3571, 3488 ($\nu_{C=N}$), 1623,1609 ($\nu_{C=N}$); UV-Vis (1×10^{-4} M, λ_{max}(abs), nm, MeOH; Fig. S2): 230, 269, 344; ^{1}H NMR (δ ppm, 400 Mz, DMSO-d_6; Fig. S3) δ = 13.79 (s, 2H), 8.94 (s, 2H), 7.41-6.92 (Ar-H, 16H), 3.84 (t, 6H) ppm. ^{13}C NMR (400 MHz, DMSO-d_6; Fig. S4): 192.26 (HC=NH$^+$), 163.03, 161.22 (HC=N), 153.09 (Ar-N=C), 136.81, 133.54, 132.90, 129.74, 128. 65, 119.81,

119.64, 117.68, 117.16, 114.53, 114.53, 112.68 (Ar-C), 56.23, 55.66 (-OCH$_3$). ESI-Ms (m/z, MeOH; Fig. S5): [Zn(H**L**)(CH$_3$OH)$_2$+H], 310.14 (Theoretical m/z 310.10).

2.2. Physical measurements

FT-IR spectra of the Schiff base and zinc-Schiff base were recorded with a FTIR-8400S SHIMADZU spectrophotometer (Shimadzu, Kyoto, Japan) from 400 to 3600 cm^{-1} with KBr pellet. ^{1}H and ^{13}C NMR spectra of the Schiff base ligand (H**L**) were measured on a Bruker Advance 400 MHz spectrometer (Bruker, Massachusetts, USA) in CDCl$_3$ at 298 K. Steady-state absorption and other electronic bands were recorded with a JASCO V-730 UV-Vis spectrophotometer (Jasco, Tokyo, Japan). Electrospray ionization (ESI) mass spectrum zinc-Schiff base was recorded using a Q-tof-micro quadruple mass spectrometer. Elemental analyses were performed on a Perkin Elmer 2400 CHN microanalyser (Perkin Elmer, Waltham, USA). X-band EPR spectrum was recorded with a Magnettech GmbH MiniScope MS400 spectrometer (equipped with temperature controller TC H03, Magnettech, Berlin, Germany).

2.3. Crystal structure determination and refinement

A Rigaku XtaLABmini diffractometer equipped with Mercury 375R (2×2 bin mode) CCD detector was employed to collect the X-ray diffraction data for zinc-Schiff base. The data were collected with graphite monochromated Mo-Kα radiation (λ=0.71073 Å) at 298 K using ω scans. The data were reduced using CrysAlisPro 1.171.39.35c [35] and the space group determination was done using Olex2. The structure was resolved by dual space method using SHELXT-2015 [36] and refined by full-matrix least-squares procedures using the SHELXL-2015 [37] software package through OLEX2 suite [38]. All hydrogen atoms were geometrically fixed.

2.4. Hirshfeld surface analysis of zinc-Schiff base complex

Hirshfeld surfaces and 2D fingerprint plots for the zinc-Schiff base complex were generated employing Crystal Explorer 17.5 [39] progam to understand the involvement of intermolecular interactions in crystal packing. The function, d$_{norm}$ is used to find out the ratio of the distances of any surface point to the nearest interior (d$_i$) and exterior (d$_e$) atom and the

van der Waals radii of the atoms [40,41]. The normalized contact distance (d_{norm}) is expressed as

$$d_{norm} = \frac{d_i - r_i^{vdw}}{r_i^{vdw}} + \frac{d_e - r_e^{vdw}}{r_e^{vdw}}$$

$$...(1)$$

Where, r_e^{vdW} and r_i^{vdW} denote the corresponding van der Waals radii of atoms. The details of analysis can be obtained elsewhere [39-41].

2.5. 4-methylcatechol oxidation study

The oxidation of 4-methylcatechol (4-MC) was carried out by addition of 1×10^{-4} M solution of zinc complex with 1×10^{-2} M of 4-MC solution in methanol. The course of catalysis was performed under aerobic conditions. The wavelength scans of catalytic oxidation were monitored through a UV-Vis spectrophometer with an interval of 8 minutes for 2h from 200-700 nm [10,11,17-20,42-44].

Kinetic experiments were performed with a spectrophotometer and kinetic parameters were analysed to understand the course of 4-MC oxidation by this zinc-Schiff base in MeOH [17-20]. 0.04 mL 1×10^{-4} M of zinc-Schiff base solution was treated with 2 mL of 4-MC with a variation of its concentration from 1×10^{-3} M to 1×10^{-2} M in order to achieve the final concentration of zinc-Schiff base as 1×10^{-4} M. The catalytic conversion of 4-MC was monitored with the progress of time at 409 nm (time scan) in MeOH [42-46]. All the kinetic experiments were performed in triplicate.

The extraction of purified oxidation product of PPO has remained difficult because of irreversible binding of high phenolic content in purification steps. Different scientists showed different way of extraction for catechol oxidation product, o-quinone. Suyama and group [45] extracted the oxidation product of 4-MC as 4-methyl-o-quinone (4MQ) in treatment with *n*-butylamine under oxygen saturated environment. In general, amines preferably attack the oxidized catechols by either Michael-type addition or through formation of a Schiff base [46]. In 2018, we were successfully isolated the single crystals of 3,5-di-*tert*-butyl-o-quinone in association with the hydrogen bonded catechol in non-aqueous medium [14]. In this 4-MC oxidation, the red coloured product was isolated employing column chromatography with *n*-hexane-diethyl ether solvent mixture (9:1, v/v). The identification of the product was confirmed by a comparison of spectral data between the extracted compound and reported

compound. ^{1}H NMR data for 4-methyl-*o*-quinone, (CDCl$_3$, 400 MHz,) δ_H: 6.76 (m, 1H), 6.64 (d, 1H), 6.52 (d, 1H), 2.18 (s, 3H).

2.6. Electro-chemical analysis

BASi Epsilon-EC was employed to carry out the for cyclic voltammetric experiments in CH$_2$Cl$_2$ solutions containing 0.2 M tetrabutylammonium hexafluorophosphate as supporting electrolyte. The BASi platinum working electrode, platinum auxiliary electrode, Ag/AgCl reference electrode were used for the measurements.

2.7. Clinical bacterial cultures and culture media

The antimicrobial property of the zinc-Schiff base was examined against few clinical pathogenic bacteria like *Bacillus* SP, *Enterococcus* and *E. coli*. Clinical Microbial cultures were procured from government medical college from Tiruchirappalli, Tamil Nadu. Muller-Hinton agar media of Himedia Pvt. Bombay, India was used for the media for the microbial test. The antibacterial activity was evaluated by using the Himedia zone reader.

2.7.1. Inoculums preparation

The collected clinical pathogens, *Bacillus* SP, *Enterococcus* and *E.coli* were inoculated individually in 5 mL of sterile nutrient broth (NB) media and incubated at 37°C for 24h. Thereafter, 200 µL of the fresh culture of organisms was dispensed into 30 mL sterile nutrient broth and incubated 24 h to standardize the bacterial culture to 10^8 CFU/ml (colony forming units).

2.7.2. Agar well diffusion method (Kirby-Bauer method)

The bactericidal activity of the synthesized zinc-Schiff base compound and a standard marketed drug (Amikacin, 100 mg/2mL) was studied initially by using agar well plate method [47]. *Bacillus* SP, *Enterococcus* and *E.coli* inoculums were prepared by using sterile nutrient broth media. Mueller Hinton agar double strength media were made by autoclaving 760 mg in 100 mL. Standardized inoculums inoculate the test microorganisms on the Mueller Hinton agar plates by using sterile cotton swabs. Four 8 mm diameter agar wells were prepared using sterile cork-borer, and 100µL (50 mg/mL) zinc-Schiff base complex and Amikacin 5 µL (10 mg/mL) were placed on agar well using micropipette under aseptic conditions. Sterile water used as a negative control. Agar plates were incubated for 30 min in the refrigerator to diffuse the formulation into the agar, and finally, plates were incubated at 37° C for 24 h. Antibacterial activity was evaluated by using the Himedia zone reader.

Preparation of stock solutions for MIC

Weight of the powder (mg) =

$$\frac{\text{Volume of solution (mL)} \times \text{Concentration (mg/L)}}{\text{The potency of powder (mg/g)}}$$

2.7.3 Determination of MIC and MBC for zinc-Schiff base against clinical bacillus SP

The method of micro-dilution was used to establish the antibacterial potential of the zinc-Schiff base and respective controls. A spectrophotometer (OD595 = 0.22) equivalent to 10^8 CFU/mL was used to fix the bacterial cultures to 0.22 optical density at 595 nm. Different concentrations of zinc-Schiff base (100, 50, 25, 12.5, 6.25 mg/mL) and standard drug (50, 25, 12.5, 6.25, 3.125, 1.5625 mg/mL) were added in 2 mL MIC tubes as the respective controls. 100 µL of the zinc-Schiff base solutions were added to each MIC test tube. MIC tubes were incubated overnight at 37 °C for 24 h.

2.7.4 Antimicrobial activity of zinc-Schiff base with field emission scanning electronic microscope (FESEM) and energy dispersive X-ray analysis (EDAX)

The area showing an inhibition against the clinical *Bacillus* SP pathogen on the MHA plate was removed by cutting agar, fixed by soaking in 2 % glutaraldehyde in cacodylate buffer 0.1 M for 60 min [48]. The samples were washed with 0.1 M cacodylate buffer and added in triplicate for successive 60 min wash. Samples were placed in a freshly prepared cold cacodylate buffer for transportation into the laboratory for FE-SEM and EDAX.

3. Results and discussion

3.1. Synthesis and formulation of the Schiff base (H**L**) and zinc-Schiff base complex

The Schiff base was obtained from the condensation between salicylaldehyde with *o*-anisidine under reflux (Scheme 1). The synthetic route of zinc-Schiff base is presented in Scheme 1. The zinc complex was synthesized by portionwise addition of hydrated zinc(II) chloride to H**L** in aq.-methanol medium with slow thermal agitation on a magnetic stirrer. The mole ratio between zinc chloride and H**L** was varied to examine the variation in molecular composition, although the molecular formulation was determined as $[Zn(HL)_2Cl_2]$ for every reaction. The single crystals of zinc-Schiff base were obtained employing slow evaporation technique at room temperature. The zinc complex was soluble in methanol, chloroform etc.
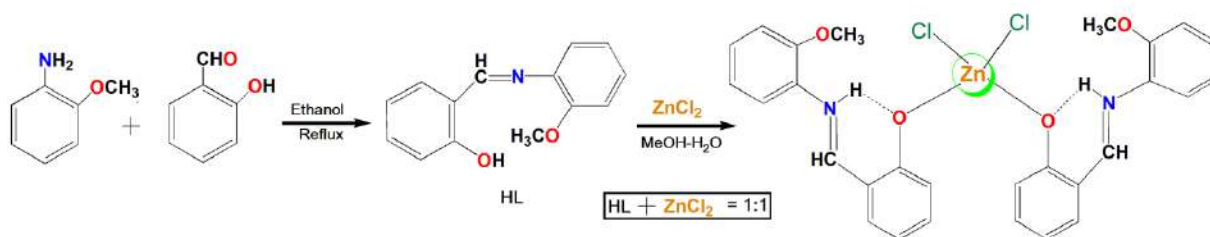
Scheme 1. Synthetic procedure of **1**

3.2. Description of crystal structure and Hirshfeld surface analysis of zinc complex

Crystal structure analysis reveals that the zinc-Schiff base complex crystallizes in a triclinic system with $P1$ space group. The thermal ellipsoids of the zinc complex are shown in Fig. 1. The crystal structure refinement parameter for this zinc-Schiff base complex is presented in Table 1. The metal centric bond distances and bond angles are presented in Table 2. The crystal structure of zinc-Schiff base complex looks very interesting in which two azomethine-Ns of the H**L** abstract two protons from phenolic-OH and lead to zwitter ionic form of the Schiff base. This phenomenon prohibits the chelation property of the Schiff base ligand and thereby H**L** behaves as a simple monodentate ligand instead of tridentate chelating ligand towards Zn(II) ion. The zinc centre in the crystal structure exists in distorted tetrahedral coordination geometry. The Schiff base may be considered as a zwitter ion since it contains equal number of positively- and negatively-charged functional groups. This zwitter ionic form of H**L** facilitates the mono-coordination of phenoxo-O to $ZnCl_2$ leading to a tetrahedral structure. Two H**L** units in association with two chlorides coordinate with Zn(II) ion to form tetracoordinate zinc complex. The methoxy group attached to phenyl ring in the Schiff base remains non-reactive in the complex formation. The formation of tetrahedral geometry was further evident from the values of metal centric bond angles [Cl1-Zn1-Cl2, 124.59(5)°; Cl1-Zn1-O2, 104.69(9)°; Cl1-Zn1-O3, 104.42(10)°; Cl2-Zn1-O2, 103.97(10)°; Cl2-Zn1-O3; 103.73(9)°; O2-Zn1-O3, 116.31(12)°]. The average bond angle value around zinc(II) centre was estimated as 109. 61° which deviates little from ideal tetrahedral geometry.

Hirshfeld surface analysis of zinc-Schiff base was carried out using d_{norm} calculation with Crystal Explorer software (Fig. S6). Red highlighted areas represent d_{norm} area as well as supramolecular interactions of **1** with its neighbouring zinc complex units. The elemental contribution of each element with % share in close interaction with others is expressed in Table S1. In the d_{norm}, blue areas are showing the engagement of $\pi \cdots \pi$ interactions between

phenyl centroid of the Schiff base while red area highlights intermolecular C-H···Cl interactions and displays in Fingerprint plots (Fig. S7). Self-assembled architecture for the zinc complex displayed important C-H···Cl interactions which help to develop a 3D supramolecular structure (Fig. S8). Moreover, π···π interactions between the phenyl centroids of the H**L** provide additional strength to the 3D architecture (Fig. S9, Table S2). Previously, a crystal structure of zinc complex [ZnLCl$_2$] containing a different Schiff base, **L** = 4-methyl-2,6-di[(S)-(+)-1-phenylethylimino methyl]phenol}was reported by Das *et al*. [24] Although we found the CIF of that structure in SI file; however we didn't find the CCDC number of the CIF in the published paper as well as in CCDC. That zinc(II) complex crystallized in orthorhombic system with $P2_12_12_1$ space group and produced supramolecular helices through C-H···Cl interaction [24]. In that case, a N,O,N type tridentate Schiff base was monoprotonated to one azomethine-N and behaves as a bidentate chelator towards Zn(II) ion. However, in our case, the Schiff base is a O,N,O-type ligand which exists in a zwitter ionic form and act as a monodentate ligand towards Zn(II) ion. The zinc complex crystallizes in triclinic system with $P1$ space group and forms a 3D architecture employing C-H···Cl and π···π interactions in the crystalline phase (Fig. S8, Fig. S9, Table S2). The reported value for C-H···Cl hydrogen bond by Das *et al*. [24] was larger (3.665 Å in length) than that of the value in the self-assembled architecture in our synthetic zinc complex. The values of C-H···Cl H-bonding are of comparable range with the reported values [49,50].

3.3. Solution behaviour of the zinc-Schiff base complex

The zinc-Schiff base shows good solubility in methanol (MeOH). The zinc complex exhibits characteristic electronic transitions at 230, 269 and 344 nm which are very close to the electronic transitions of the Schiff base (230, 270 and 346 nm). The electronic spectra for H**L** and zinc complex are displayed in Fig. S2. The electronic bands of zinc(II) complex at 230 and 269 nm are assignable to n→π* and π→π* transitions of azomethine origin [14,17-20] and the optical band at 344 nm may be attributed as intra-ligand electronic transition [17-20,51].

3.4. 4-methylcatechol oxidation study of the zinc-Schiff base complex

The catalytic oxidation of 4-methylcatechol (4-MC) was studied by addition of catalytic amount of zinc-Schiff base to 100 fold of 4-MC under aerobic atmosphere at 25°C (Scheme 2).
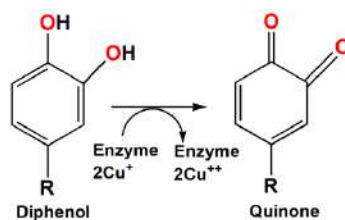
Scheme 2. Catalytic oxidation by polyphenol oxidase (PPO)

The changes of absorbance upon addition of zinc complex to 4-MC solution were observed with a UV–Vis spectrophotometer. The nature of spectral change in the course of catalysis was monitored for 1h with 8 min interval (Fig. 2). Upon addition of 1×10^{-4} M zinc-Schiff base solution to 1×10^{-3} M solution of 4-MC in MeOH, a new electronic band at 409 nm with a red shift of ~16 nm was developed. This development of the electronic band at 409 nm was a definite signature for the production of 4-methyl-*o*-benzoquinone species in solution (Fig. 2) [14,18,20,42-44]. Controlled experiment was also performed in presence of catalytic amount of H**L** under identical reaction set up. No significant changes of electronic bands have been observed for 2h in the course of catalysis. This phenomenon accounts on about the non-functional activity of H**L** in the catalytic oxidation of 4-methylcatechol.

The kinetics for the catalytic oxidation of 4-MC was studied following Michaelis–Menten model of saturation kinetics and the method of initial rates was applied to find out the kinetic parameter.

The Michaelis–Menten equation is expressed as:

$$V = \frac{V_{max}\,[\text{S}]}{K_M + [\text{S}]} \quad \ldots\ldots\ldots(2)$$

Where, V indicates the velocity of reaction (rate of the reaction), K_m expresses the Michaelis–Menten constant, V_{max} presents the maximum reaction velocity, and $[S]$ is the substrate concentration. The growth of 4-methyl-*o*-benzoquinone species was monitored at 409 nm with the function of time [14,18,20,34,35,41]. The profile of kinetics was plotted rate constants vs. substrate concentration (Fig. S10). The values of kinetics parameters were determined as $V_{max}(MS^{-1}) = 4.03 \times 10^{-3}$; $K_M = 1.38 \times 10^{-3}$ [Std. Error for V_{max} $(MS^{-1}) = 4.81 \times 10^{-4}$; Std. Error for K_m (M)$= 5.53 \times 10^{-4}$]. A comparison of K_M values towards the oxidation of 4-MC by the zinc-Schiff base as well as in natural sources is summarized in Table 3 [52,53]. The zinc-Schiff base catalyzed the oxidation of 4-MC under aerobic atmosphere with high efficacy, $k_{cat}/K_M = 1.05 \times 10^6\,h^{-1}$.

3.5. Mechanistic studies on 4-methylcatechol oxidation

The electrochemical potentials of the zinc-Schiff base in absence and presence of 4-MC were studied with cyclic voltammetry in CH_2Cl_2 at 295 K. The redox potential data referenced to ferrocenium/ferrocene (Fc^+/Fc) couple are summarized in Table S3. The cyclic voltammograms of zinc complex and its reaction mixture with 4-MC are illustrated in Fig. 3. In the cyclic voltammogram of zinc-Schiff base, two reversible anodic peaks at 0.064 V and 0.421 V were developed for the oxidation of two phenoxide ion in two Schiff base ligands which are assignable to phenoxide/phenoxide radical ($O^-/O^{\bullet-}$) redox couple in the solution. The zinc-Schiff base didn't exhibit any cathodic peak indicating the stable +2 oxidation state of zinc ion. The electrochemical potential plots of the reaction mixture of zinc complex with 4-MC exhibits one reversible anodic wave at -0.55 V and one irreversible cathodic peak at -1.33 V. The appearance of anodic peak is due to oxidation of 4-methylcatechol to 4-methyl-*o*-benzosemiquinone ($cat/sq^{\bullet-}$) and the irreversible cathodic wave is attributed to the reduction of Zn^{2+} to Zn (Zn^{2+}/Zn). Thus, electrochemical analysis ensures the active participation of zinc-Schiff base and facilitates the oxidation process of catechol to benzo-semiquinone radical formation. Therefore, zinc complex exhibits metal mediated polyphenol oxidase activity through the radical pathway.

EPR studies were further investigated to consolidate the electrochemical observations in the course of catalytic oxidation of 4-MC in CH_2Cl_2. To unveil the mechanistic insights, we have recorded the EPR spectrum of the zinc-Schiff base in presence of 4-MC in CH_2Cl_2 medium (Fig. 4). The EPR spectrum of zinc complex in presence of 4-MC at room temperature produced a characteristic signal for the development of organic radical at g ca 2.001 which strongly suggests that the course of catalysis was driven by generation of radical species (Fig. 4). The g value for oxidised 3,5-ditertbutylcatechol was previously reported as 2.0051 in 10^{-1} M Bu_4NPF_6 [14,54,55]. Scheme 3 presents the plausible mechanistic pathway for the course of catalytic oxidation of 4-MC.
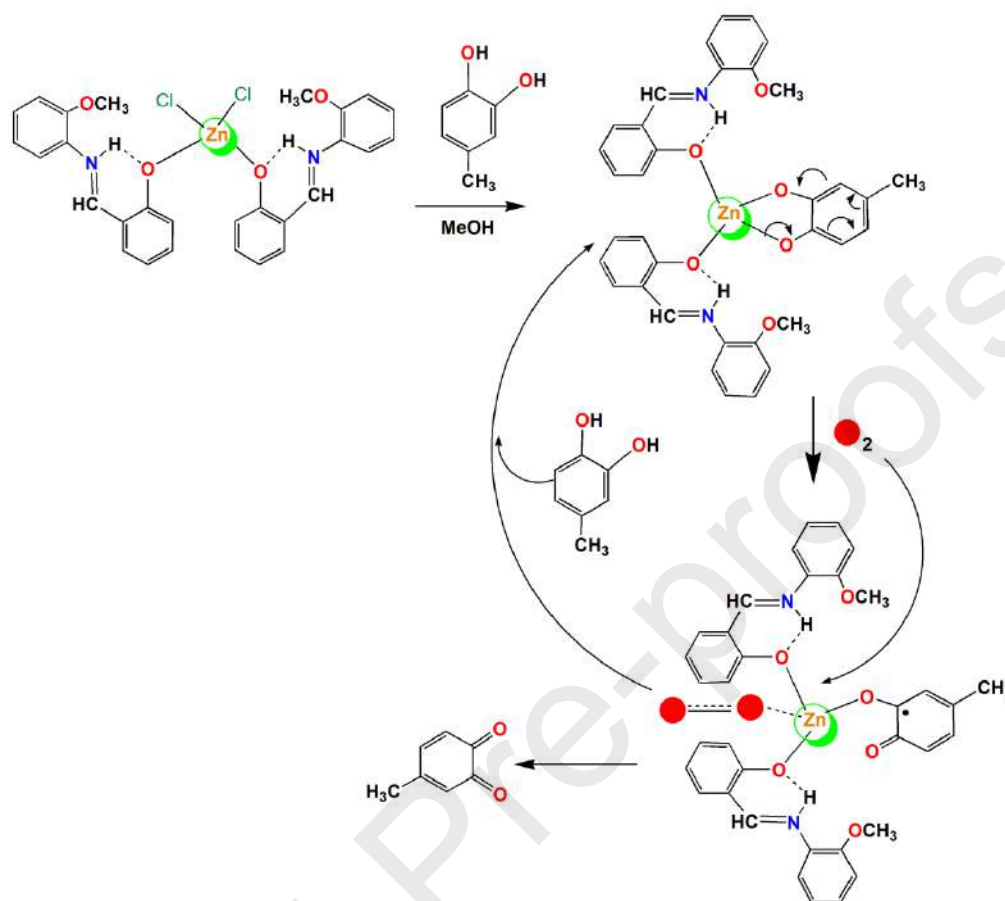
Scheme 3. Plausible mechanism for the catalytic oxidation of 4-MC

Therefore, based on the experimental outcomes of spectrophotometric titration, electrochemical analysis and electron paramagnetic measurement it may be portrayed that 4-MC initially binds with zinc-Schiff base (enzyme) complex to generate enzyme-substrate (ES) adduct with concurrent development of benzo-semiquinone radical. The zinc centre thereby supplies electron to antibonding molecular orbital of oxygen molecule to facilitate the production of *o*-benzoquinone product with returning back to ES along with the production of hydrogen peroxide. Noteworthy, if the course of 4-MC oxidation runs for longer time, there is every possibility to progress polymerisation reaction of 4-MC. To the best of our knowledge, our synthetic zinc-Schiff base complex will be the first zinc-Schiff base complex which exhibits 4-MC oxidation activity in scientific literature.

3.6. Antibacterial activity

The study of the antibacterial activity of zinc-Schiff base was initially determined by the method of well diffusion against clinical *Bacillus* SP, *Enterococcus*, and *E.coli*. The results of

the inhibition zone diameters shown in Table S4. The bactericidal efficacy of the zinc-Schiff base on *Bacillus* SP Minimum was evaluated in terms of the estimation of minimum inhibitory Concentration (MIC) and minimum bacterial concentration (MBC) (Table S5). The MIC and MBC values were obtained as 50 and 25 mg/mL respectively against *Bacillus* SP strain.

According to scientific literatures the mechanism for the destruction of cell membranes of microbial species is well established. It is experimentally proved that the generation of reactive oxygen species (ROS) remains the driving force to cause oxidative stress and leads to the damage of cell membrane and DNA. This phenomenon actually destroys microbial/bacterial species and prevents the growth of microbes effectively (Scheme 4).
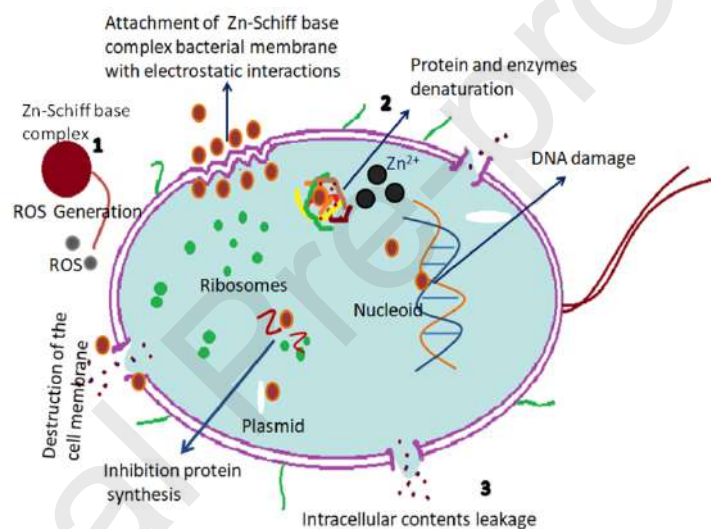
Scheme 4. Zinc-Schiff base induced cell membrane destruction mechanism for *Bacillus* SP

In the context of evaluation of bactericidal activity of this zinc-Schiff base against few pathogenic bacteria, Zn^{2+} ion interacts with the enzyme, amino acids and proteins in bacteria. The specific interaction between zinc ion and cell membrane through electrostatic forces destroy the plasma membrane and cause leakage of intracellular material (Scheme 4). Herein, zinc ion prefers stronger interactions with the amino acids and proteins in bacteria and decomposition of coordination environment of the Zn(II) ion covered by two units of Schiff bases is actually occurred. Though the Schiff base contains three donor centres and should be behaved as a tridentate chelator, however in reality the Schiff base acts as a simple monodentate ligand towards Zn(II) ion. Self-protonation of the Schiff base diminishes its chelation property and prefers stronger interactions with the amino acids / proteins in bacteria.

In our previous work, we studied the bactericidal effect of a mononuclear copper(II)-Schiff base complex containing this same Schiff base [10]. The comparison of MIC values clearly indicates that this zinc complex shows an excellent activity compared to that of the copper(II)-Schiff base complex. Previously, Keypour *et al*. and Das *et al*. synthesized different metal complexes using polydentate Schiff base ligands and studied their antibacterial effect towards different gram positive and gram negative bacteria [56,57]. Their zinc-Schiff base compounds developed good inhibition zone and MIC values against the bacterial species compared to our synthesized zinc-Schiff base complex (Table S4 and Table S5). We also studied the antibacterial effect of Amikacin under identical experimental conditions. Amikacin is a medically recommended antibiotic used for a number of bacterial infections. Truly, this zinc-Schiff base exhibits little activity compared to that of Amikacin (Table S4 and Table S5). Most strikingly, we were able to detect the presence of 1.44% zinc in the chosen zone of inhibition and it was confirmed by energy dispersive X-ray (EDAX) analysis which portrayed the area in a quantitative manner (Fig.S11). This is a rare observation in the study of bactericidal activity and portrays a real promise for the future development of antibacterial agents. Fig. 5 displays the electron microscope scan image which shows the morphological changes in the multiplication of clinical bacillus SP at zone inhibition site and a clear indication of destruction of the bacterial cell membrane.

4. Conclusions

This present study reports the synthesis, crystal structure, supramolecular architecture, bactericidal activity and bio-mimics of 4-MC oxidation of a newly developed zinc-Schiff base complex, $[Zn(HL)_2Cl_2]$. Crystal structure analysis reveals that Zn(II) centre adopts a distorted tetrahedral geometry. More captivatingly, the tridentate chelator actually exists in zwitter ionic form and behaves a monodentate ligand towards zinc ion. The zinc complex exhibits good bio-mimicking activity towards the oxidation of 4-MC with turnover number, 1.45×10^3 h^{-1}. The electrochemical potential analysis of the zinc complex in presence and absence of 4-MC ensures the production of 4-methyl-*o*-benzosemiquinone (cat/sq$^{\bullet-}$) with an active involvement of zinc(II) centre to facilitate the formation of benzo-semiquinone radical. Further, EPR studies confirm the generation of radical species in the course of catalytic oxidation of 4-MC. To the best of our knowledge, our synthetic zinc-Schiff base complex will be the first report to exhibit 4-MC oxidation activity in scientific literature. The scanning electron microscopy images indicate the destruction of bacterial cell membrane and energy dispersive X-ray

spectrum confirmed the existence of 1.44% zinc in the cell membrane. The incorporation of zinc by the bacterial cell will certainly bring some new light in designing future antimicrobial agents of good promise.

Supplementary data

Supplementary crystallographic data are available free of charge from The Director, CCDC, 12 Union Road, Cambridge, CB2 1EZ, UK (fax: +44-1223-336033; E-mail: deposit@ccdc.cam.ac.uk or www: http://www.ccdc.cam.ac.uk) upon request, quoting deposition number CCDC 2020846. Experimental information such FT-IR, UV-Vis, ^{1}H & ^{13}C NMR, ESI mass spectra, rate vs. [substrate] plot, Hirshfeld surface plot, bond distance & bond angle parameters, redox potential data etc are given here.

Acknowledgement

References

[1] K.L. Haas, K.J. Franz, Chem. Rev., 109 (2009) 4921–4960.

[2] P.G. Cozzi, Chem. Soc. Rev., 33 (2004) 410-421.

[3] W. Al Zoubi, Y.G. Ko, Appl. Organomet. Chem., 31 (2017) e3574.

[4] M. Karar, P. Paul, B. Biswas, T. Majumdar, A. Mallick, J. Chem. Phys., 152 (2020) 075102.

[5] B. Chowdhury, M. Karar, S. Paul, M. Joshi, A.R. Choudhury, B. Biswas, Sens. Actuators. B. 276 (2018) 560-566.

[6] S. Dutta, J. Mayans, A. Ghosh, Dalton Trans., 49 (2020) 1276-1291.

[7] M. Karar, S. Paul, B. Biswas, T. Majumdar, A. Mallick , Dalton Trans., 47 (2018) 7059-7069.

[8] A. Sarkar, A. Chakraborty, T. Chakraborty, S. Purkait, D. Samanta, S. Maity, D. Das, Inorg. Chem., 59 (2020) 9014–9028.

[9] M. Mondal, S. Ghosh, S. Maity, S. Giri, A. Ghosh, Inorg. Chem. Front. 7 (2020) 247-259.

[10] S. Mahato, N. Meheta, K. Muddukrishnaiah, M. Joshi, P. Ghosh, M. Shit, A.R. Choudhury, B. Biswas, Appl. Organomet. Chem., 34 (2020) e5935.

[11] P.K. Mudi, N. Bandopadhyay, M. Joshi, M. Shit, S. Paul, A.R. Choudhury, B. Biswas, Inorg. Chim. Acta, 505 (2020) 119468.

[12] A. De, D. Dey, C.K. Pal, S. Paul, B. Biswas, J. Mol. Struct. 1195 (2019) 293-301.

[13] T. Chowdhury, S. Dasgupta, S. Khatua, K. Acharya, D. Das, ACS Appl. Bio. Mater., 3 (2020) 4348–4357.

[14] S. Das, A. Sahu, M. Joshi, S. Paul, M. Shit, A.R. Choudhury, B. Biswas, ChemistrySelect, 3 (2018) 10774-10781.

[15] W.N. Lipscomb, N. Strater, Chem. Rev., 96 (1996) 2375-2433.

[16] B.L. Vallee, D.S. Auld, Acc. Chem. Res., 26 (1993) 543-551.

[17] M. Garai, A. Das, M. Joshi, S. Paul, M. Shit, A.R. Choudhury, B. Biswas, Polyhedron, 156 (2018) 223-230.

[18] D. Dey, G. Kaur, A. Ranjani, L. Gayathri, P. Chakraborty, J. Adhikary, J. Pasan, D. Dhanasekaran, A.R. Choudhury, M.A. Akbarsha, N. Kole, B. Biswas, Eur. J. Inorg. Chem., 2014 (2014) 3350-3358.

[19] D. Dey, G. Kaur, M. Patra, A.R. Choudhury, N. Kole, B. Biswas, Inorg. Chim. Acta, 421 (2014) 335-341.

[20] S. Pal, B. Chowdhury, M. Patra, M. Maji, B. Biswas, Spectrochim. Acta, Part A, 144 (2015) 148–154.

[21] C.K. Pal, S. Mahato, M. Joshi, S. Paul, A.R. Choudhury, B. Biswas, Inorg. Chim. Acta, 506 (2020) 119541.

[22] A. Erxleben. Coord. Chem. Rev. 246 (2003) 203–228.

[23] P.D. Frischmann, A.J. Gallant, J.H. Chong, M.J. MacLachlan, Inorg. Chem., 47 (2008) 101–112.

[24] M. Prabhakar, P.S. Zacharias, S.K. Das, Inorg. Chem., 44 (2005) 2585-2587.

[25] B.F. Abrahams, S.R. Batten, H. Hamit, B.F. Hoskins, R. Robson, J. Chem. Soc., Chem. Commun., (1996) 1313-1314.

[26] R.S. Joseyphus, M.S. Nair, Mycobiology, 36 (2008) 93-98.

[27] B. Biswas, M. Patra, S. Dutta, M. Ganguly, N. Kole, J. Chem. Sci. 125 (2013) 1445-1453.

[28] R. Yoruk, M.R. Marshall, J. Food Biochem., 27 (2003) 361-422.

[29] B.B. Mishra, S. Gautam, Enz. Eng., 5 (2016) 141-149.

[30] M.V. Madinez, J.R. Whitaker, Trends Food Sci. Tech., 6 (1995) 195-200.

[31] S.M. Shetty, A. Chandrashekar, Y.P. Venkatesh, Phytochemistry 72 (2011) 2275-2287.

[32] J. Borovansky, P. A. Riley, Melanins and Melanosomes, Wiley-VCH Verl Co. KGaA, Boschstr, 12, 69469 Weinheim, Germany, (2011).

[33] J. Reedijk, Bioinorganic Catalysis, 1st Ed. Marcel Dekker, New York, (1993).

[34] S. Mahato, N. Meheta, K. Muddukrishnaiah, M. Joshi, P. Ghosh, M. Shit, A.R. Choudhury, B. Biswas, Appl. Organomet. Chem. 34 (2020) e5935.

[35] CrysAlisPro 1.171.39.35c, (2017) Rigaku Oxford Diffraction, Rigaku Corporation: Tokyo, Japan.

[36] G.M. Sheldrick, SHELXT- Integrated space-group and crystal-structure determination. Acta Cryst. A, 71 (2015) 3-8.

[37] G.M. Sheldrick, Acta Cryst. C, 71 (2015) 3-8.

[38] O.V. Dolomanov, L.J. Bourhis, R.J. Gildea, J.A.K. Howard, H. Puschmann, J. Appl. Crystallogr., 42 (2009) 339-341.

[39] M.J. Turner, J.J. McKinnon, S.K. Wolff, D.J. Grimwood, P.R. Spackman, D. Jayatilaka, M.A. Spackman, Crystal Explorer, University of Western Australia, http://hirshfeldsurface.net17 (2017).

[40] M.A. Spackman, D. Jayatilaka, Hirshfeld surface analysis. CrystEngCom, 11 (2009) 19-32.

[41] S.K. Seth, V.S. Lee, J. Yana, S.M. Zain, A.C. Cunha, V.F. Ferreira, A.K. Jordao, M.C.B.V. de Souza, S.M.S.V. Wardell, J.L. Wardellf, E.R.T. Tiekink, CrystEngComm, 17 (2015) 2255-2266.

[42] J. Cabanes, F. Garcia-Canovas, F. Garcia-Carmona, Biochim. Biophys. Acta, Protein Struct. Mol. Enzymol, 914 (1987) 190-197.

[43] (a) T. Zlateva, P.Di Muro, B. Salvato, M. Beltramini. FEBS Letters., 384 (1996) 251-254; (b) C.K. Pal, S. Mahato, H.R. Yadav, M. Shit, A.R. Choudhury, B. Biswas, Polyhedron, 174 (2019) 114156; (c) D. Dey, S. Das, H.R. Yadav, A. Ranjani, L. Gyathri, S. Roy, P.S. Guin, D. Dhanasekaran, A.R. Choudhury, M.A. Akbarsha, B. Biswas, Polyhedron, 106 (2016) 106-114.

[44] (a) H.S. Mason, E.W. Peterson, Biochim. Biophys. Acta, 111 (1965) 134-146; (b) A. De, M. Garai, H.R. Yadav, A.R. Choudhury, B. Biswas, Appl. Organomet. Chem., 31 (2017) e3551; (c) B. Chowdhury, M. Maji, B. Biswas,. J. Chem. Sci., 129 (2017) 1627-1637.

[45] M. Akagawa, K. Suyama, Biochem. Biophys. Res. Commun., 281 (2001) 193-199.

[46] E. Faure, C. Falentin-Daudré, T.S. Lanero, C. Vreuls, G. Zocchi, C. Van De Weerdt, et al. Adv. Funct. Mater., 22 (2012) 5271-5282.

[47] A. Daoud, D. Malika, S. Bakari, N. Hfaiedh, K. Mnafgui, A. Kadri, N. Gharsallah. Arab. J. Chem. (2015). doi: 10.1016/j.arabjc.2015.07.014.

[48] F.M. War Nongkhlaw, S.R. Joshi, J. Microsc. Ultrastruct., 5 (2017) 132–139.

[49] V. Balamurugan, M.S. Hundal, R. Mukherjee. Eur. J. Chem., 10 (2004) 1683.

[50] (a) R. Xuan, W. Hu, Z. Yang, R. Xuan. Acta Cryst. C, 59 (2003) m112-m114; (b) D. Braga, S. M. Draper, E. Champeil, F. Grepioni, J. Organomet. Chem. 573 (1999) 73.

[51] C.K. Pal, S. Mahato, M. Joshi, S. Paul, A.R. Choudhury, B. Biswas, Inorg. Chim. Acta, 506 (2020) 119541.

[52] M. Fraignier, L. Marques, A. Fleuriet, J. Macheix. J. Agric. and Food Chem., 43 (1995) 2375–2380.

[53] Y. Jiang, X. Duan, H. Qu, Browning: Enzymatic Browning, Encyclopedia of Food and Health, 508-514 (2016), http://dx.doi.org/10.1016/B978-0-12-384947-2.00090-8.

[54] F. Hartl, Inorg. Chim. Acta, 232 (1995) 99-108.

[55] A. De, D. Dey, H.R. Yadav, M. Maji, V. Rane, R.M. Kadam, A.R. Choudhury, B. Biswas,. J. Chem. Sci., 128 (2016) 1775-1782.

[56] H. Keypour, F. Forouzandeh, S. Salehzadeh, F. Hajibabaei, S. Feizi, R. Karamian, N. Ghiasi, R. W. Gable, Polyhedron 170 (2019) 584-592.

[57] M. Das, A. Biswas, B.K. Kundu, M.A.J. Charmier, A. Mukherjee, S.M Mobin, G. Udayabhanu, S. Mukhopadhyay, Chem. Engg. J. 357 (2019) 447-457.

Table 1. Crystallographic data and structure refinement parameters for zinc-Schiff base

Parameters	1
Empirical formula	$C_{28}H_{26}Cl_2N_2O_4Zn$
Formula weight	590.78
Temperature (K)	298
Crystal system	Triclinic
Space group	P-1
a (Å)	9.2904(4)
b (Å)	10.6979(4)
c (Å)	14.9283(4)
α	94.357(3)
β	97.159(3)
γ	114.451(4)
Volume (Å^3)	1326.67(10)
Z	2
ρ (gcm^{-3})	1.479
μ (mm^{-1})	1.164
F (000)	608
R_{int}	0.083
θ ranges (º)	2.4-32.9
Number of unique reflections	9032
Total number of reflections	24064
Final R indices (R_1 and wR_2)	0.0603, 0.1919
Largest peak and hole (eA$^{°-3}$)	0.67, -0.60

Table 2. Bond angles and bond distances value of zinc-Schiff base complex

Bond distances (Å)			
Zn1-O2	1.981(3)	Zn1-Cl1	2.2344(15)
Zn1-O3	1.979(3)	Zn1-Cl2	2.2369(15)
Bond angles (°)			
Cl1-Zn1-Cl2	124.59(5)	Cl2-Zn1-O2	103.97(10)
Cl1-Zn1-O2	104.69(9)	Cl2-Zn1-O3	103.73(9)
Cl1-Zn1 -O3	104.42(10)	O2-Zn1-O3	116.31(12)

Table 3. Comparison of K_M values for catalytic oxidation of 4-MC in natural sources and by zinc-Schiff base complex (4-Methylcatechol = 4-MC)

Source	**Substrate with higher affinity**	**K_m (mM)**	**Optimum pH**	**Optimum Temperature (°C)**	**References**
Apple (cv.Amasya)	4-MC Catechol	3.1 34.0	7	15	[53]
Apricot	4-MC		5–5.5	25	[52]
Artichoke	4-MC Catechol	10.2 12.4	6	25	[53]
Banana (cv.Anamur)	Catechol	8.5	7	30	[53]
Cherry	4-MC		4.5		[52]
Cucumber	Catechol		7		[53]
Eggplant	4-MC		5–6.5		[53]
Litchi	4-MC	10	7.4	70	[53]
Longan	4-MC		6.5	35	[53]
Olive	4-MC		5.5–7.5		[53]
Peach	4-MC		5		[52]
Plum	4-MC		4–5.5		[52]
[Zn(H**L**)$_2$Cl$_2$]	4-MC	1.38×10^{-3}	5.5	27	This work
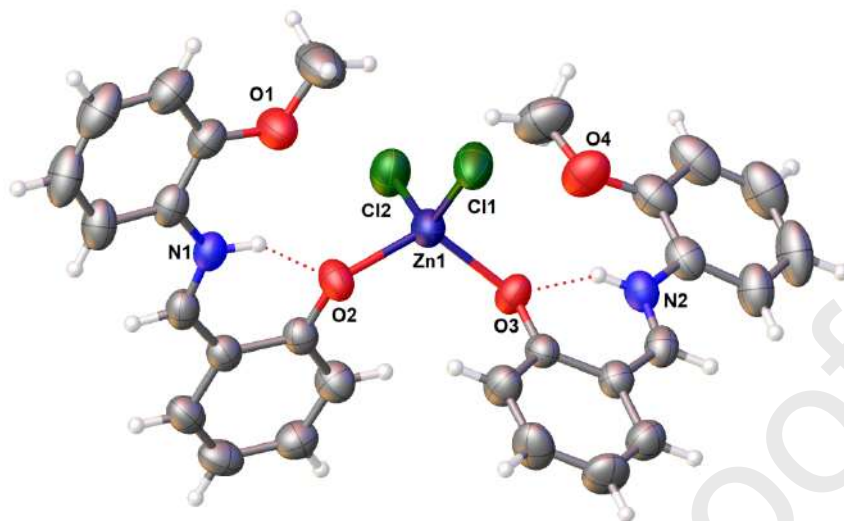
Figure 1. X-ray structure of the zinc-Schiff base complex with 30% ellipsoid probability
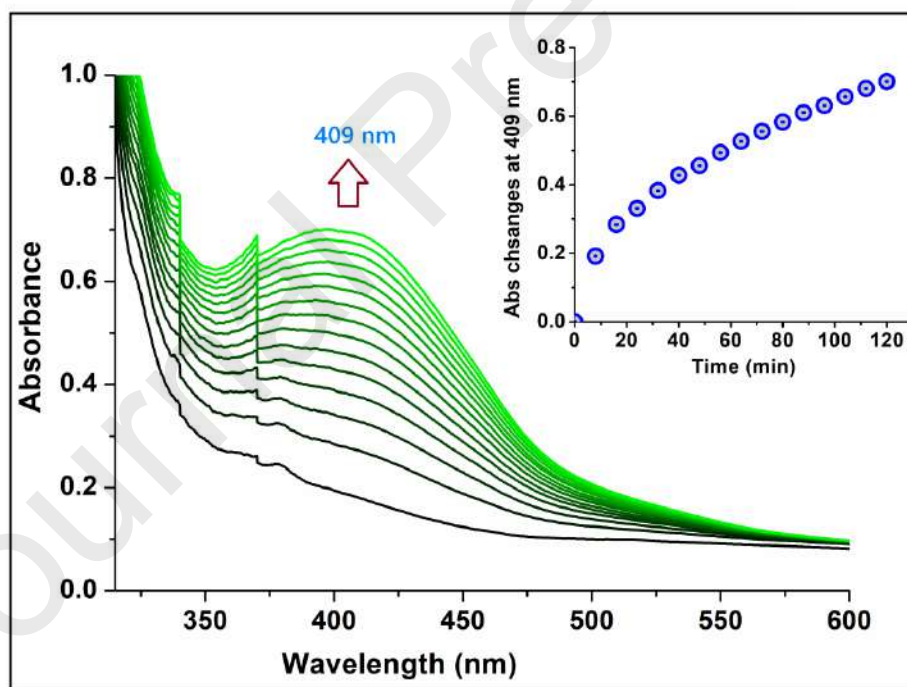
Figure 2. Rise of new electronic band at 409 nm after treatment of zinc complex to 4-MC in MeOH with a time interval of 8 mins. Inset: Time vs Absorbance plot at defined wavelength
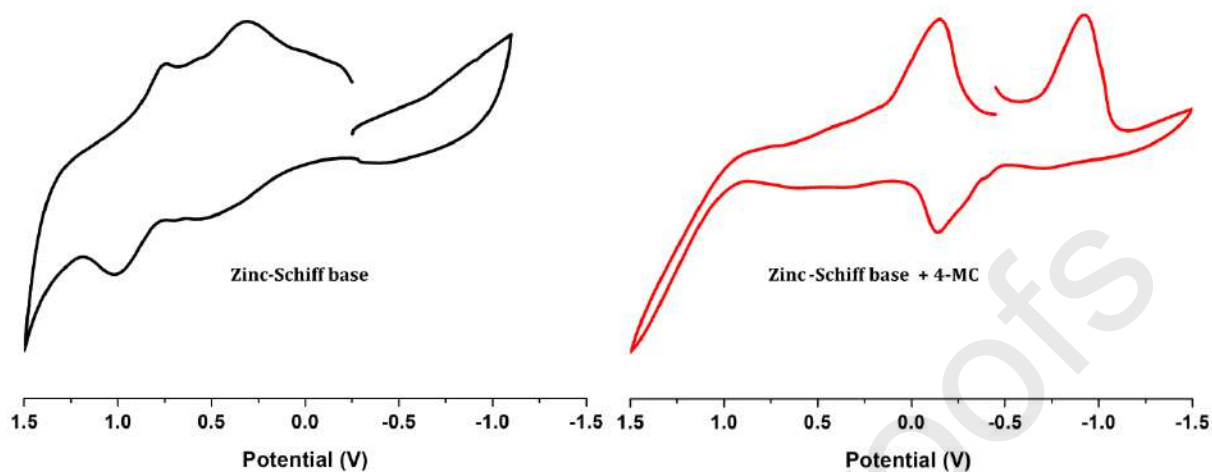
Figure 3. Left: Cyclic voltammogram of the zinc complex in anhydrous DCM medium; **Right:** Cyclic voltammogram of zinc complex in presence of 4-MC under molecular oxygen atmosphere in anhydrous DCM in CH_2Cl_2 (0.20 M [N(n−Bu)$_4$]PF$_6$) at 295 K.
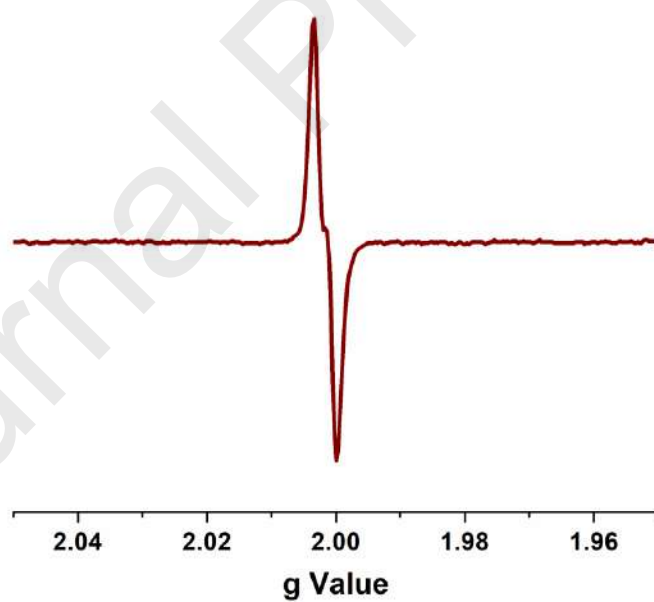
Figure 4. X-band EPR spectrum of 4-MC in presence zinc complex after 10 mins.
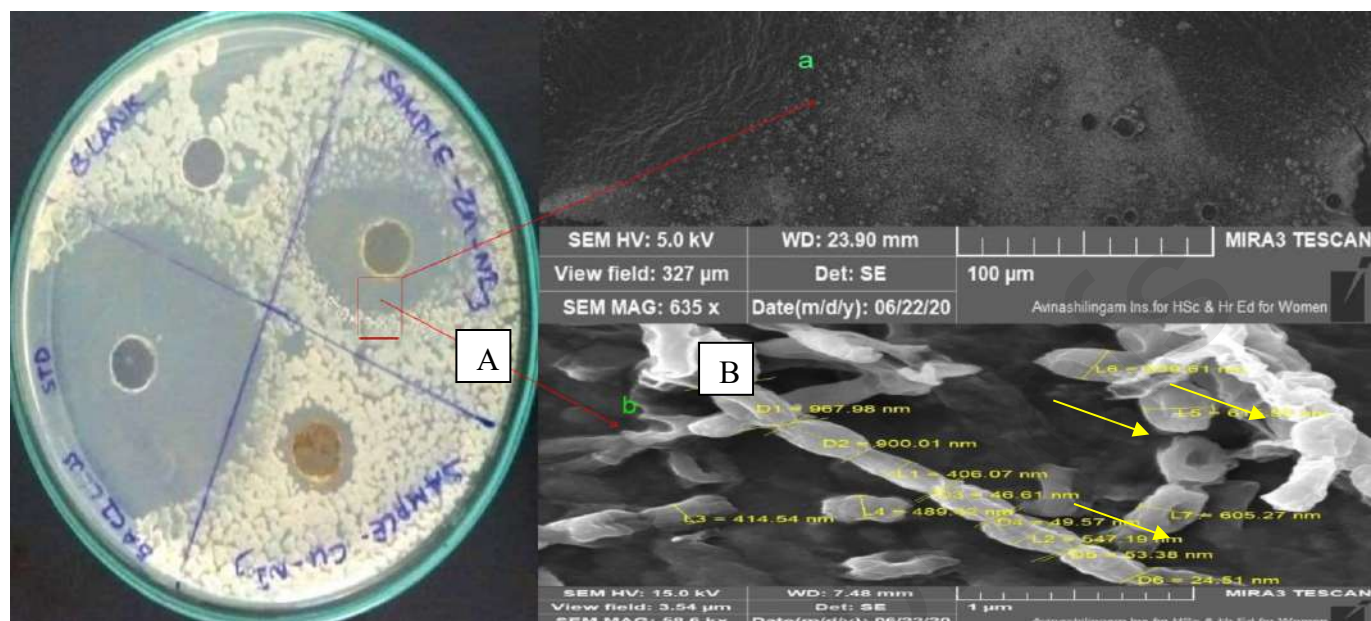
Figure 5. Electron microscope scans showing morphological changes in pathogenic bacteria. A: Zinc complex induced destruction of the bacterial cell membrane (MIC) and B: morphological change of bacterial cell (MBC)

Shreya Mahato: Conceptualization, Formal analysis, Methodology, Investigation; **Nishith Meheta**: Formal analysis, Visualization; **K Muddukrishnaiah**: Solution preparation and study for antimicrobial activity; **Mayank Joshi**: Data analysis; **Madhusudan Shit:** Electrochemical analysis; **Angshuman Roy Choudhury:** X-ray structure analysis; **Bhaskar Biswas**: Writing-Reviewing and Editing, Supervision.

Synthesis, Structure, Polyphenol Oxidase Mimicking and Bactericidal Activity of a Zinc-Schiff Base

Shreya Mahato,[a] Nishith Meheta,[a] K Muddukrishnaiah,[b] Mayank Joshi,[c] Madhusudan Shit,[d] Angshuman Roy Choudhury,[c] and Bhaskar Biswas[a,*]

<i>ᵃDepartment of Chemistry, University of North Bengal, Darjeeling-734013, India</i>

<i>ᵇDepartment of Pharmaceutical Technology, Anna University, BIT Campus Thiruchirappalli, India</i>

<i>ᶜDepartment of Chemical Sciences, Indian Institute of Science Education and Research, Mohali, Sector 81, Knowledge City, S. A. S. Nagar, Manauli PO, Mohali, Punjab 140306, India</i>

<i>ᵈDepartment of Chemistry, Dinabandhu Andrews College, Kolkata 700084, India</i>

This research work demonstrates the synthesis, crystal structure, supramolecular architecture, 4-methylcatechol oxidation and bactericidal activity of a newly designed zinc complex containing a protonated Schiff base of zwitter ion type.
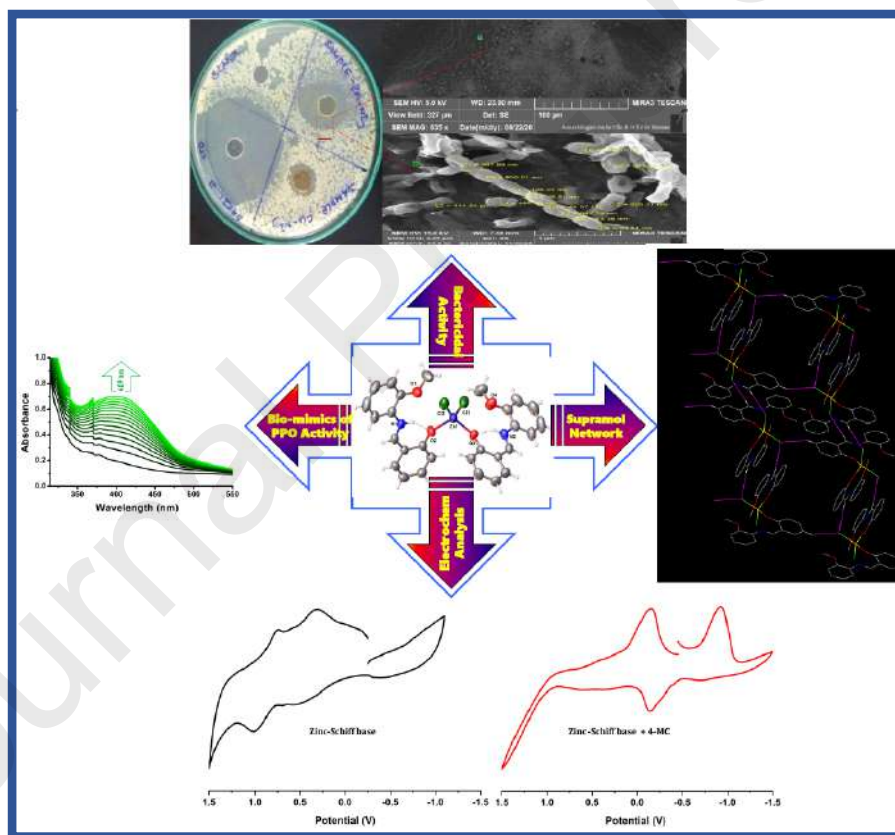
Highlights

- Synthesis and crystal structure of a tetrahedral zinc-Schiff base complex
- Schiff base gets protonated to exhibit monodentate behaviour
- The zinc complex exhibits good efficiency towards the bio-mimetic oxidation of 4-methylcatechol
- Radical driven catalytic activity has been observed.

- Shows good bactericidal activity with 1.44% presence of zinc in cell membrane of bacteria

Source details

Feedback 〉 Compare sources 〉

Polyhedron

Formerly known as: Journal of Inorganic and Nuclear Chemistry
Formerly known as: Inorganic and Nuclear Chemistry Letters

Scopus coverage years: from 1982 to Present
Publisher: Elsevier
ISSN: 0277-5387
Subject area: (Chemistry: Inorganic Chemistry)   (Materials Science: Materials Chemistry)   (Chemistry: Physical and Theoretical Chemistry)
Source type: Journal

CiteScore 2022   ⓘ
5.4

SJR 2022   ⓘ
0.400

SNIP 2022   ⓘ
0.635

View all documents 〉   Set document alert   💾 Save to source list

---

CiteScore   **CiteScore rank & trend**   Scopus content coverage

Nickel(II) di-aqua complex containing a water cluster: synthesis, X-ray structure and catecholase activity†

Madhusudan Shit,[ab] Suvendu Maity,[a] Sachinath Bera,[a] Prafullya Kumar Mudi,[c] Bhaskar Biswas,[c] Thomas Weyhermüller[d] and Prasanta Ghosh (ID) *[a]

A *trans*-diaquanickel(II) complex of the type $[(L^{2-})Ni^{II}(H_2O)_2] \cdot nH_2O$ ($1 \cdot nH_2O$) was isolated, where LH_2 is (*E*)-2-(2-((2-hydroxyphenylimino)methyl)phenoxy)acetic acid (LH_2), a tetradentate ligand. The molecular geometry of $1 \cdot nH_2O$ was confirmed by single crystal X-ray structure determination. It is observed that in the crystal, coordinated water, bulk water and ligand oxygen atoms form six membered water clusters by OH···H interactions. $1 \cdot nH_2O$ has emerged as a catalyst for the oxidation of 3,5-di-*tert*-butylcatechol to 3,5-di-*tert*-butyl-*o*-benzoquinone with a turnover number (k_{cat}) of 4.46×10^2 h^{-1} in CH_3OH. During oxidation, the coordination of catechol to the nickel(II) centre and the formation of an *o*-benzosemiquinone intermediate were confirmed by a nickel based EPR signal, ESI mass spectrometry and UV-vis spectra. $1 \cdot nH_2O$ exhibits an irreversible anodic peak at 0.83 V *versus* the Fc$^+$/Fc couple due to the phenoxyl/phenolato redox couple, authenticated by DFT calculations.

Introduction

Transition metal aqua complexes act as precursors of metal promoted organic transformations *in vivo* and *in vitro*. The usefulness of these complexes is in exploring water exchange kinetics, tuning of the acidity of the coordinated water and redox potentials of the complexes containing aqua ions, coordination catalysts, proton coupled redox reactions and epoxidation of different alkenes.[1] It should be mentioned that iron and ruthenium aqua complexes were widely used as redox catalysts for the oxidation of various organic and inorganic species.[2] In this context, several transition metal aqua complexes were synthesized and characterized; however, aqua complexes of nickel containing water clusters are very few.[3]

Theoretical and experimental studies of water clusters to elucidate the structure and characteristic features of water and ice[4] are worth performing. Water clusters have an important role to stabilize the supramolecular system both in the solid and solution state.[5] Therefore, it is necessary to understand how water molecules can influence aggregation to form supramolecular structures. The void space provided by organic ligands can accommodate discreet water molecules and help to build the metal organic framework.[6] It was reported that host water molecules present in molecular cavities, channels and layers help to form supramolecular solids through hydrogen bonding.[7]

Design of transition metal complexes that exhibit catecholase activity is significant in chemical science. One of the simplest realizations of such modelling is to introduce a poly-dentate hemilabile ligand to the metal centre or weaker co-ligands with stronger chelating ligands. In the second option, the weakly binding ligand can reversibly de-coordinate, producing vacant sites around the transition metal ion. In this investigation the same is presented as a catalyst for catechol oxidation.[8] Notably, the coordinated ligand environment also plays a key role in making an active catalyst. Aryloxyacetic acid derivatives exhibit several medicinal activities like antimycobacterial, antiinflammatory, antioxidant, antibacterial, analgesic, antisickling, antilipaemic, antiplatelet, *etc.*[9]

In this work an octahedral nickel(II) complex containing a stronger chelating ligand and two weaker water ligands has been synthesized. The particular complex isolated is $[(L^{2-})Ni^{II}(H_2O)_2] \cdot nH_2O$ ($1 \cdot nH_2O$) where L^{2-} is (*E*)-2-(2-((2-oxidophenylimino)methyl)phenoxy)acetate. From the crystal structure it is evident that the water molecules lie *trans* to each other and water

[a] Department of Chemistry, R. K. Mission Residential College, Kolkata 700103, India

[b] Department of Chemistry, Dinabandhu Andrews College, Kolkata, West Bengal, India

[c] Department of Chemistry, University of North Bengal, Darjeeling, West Bengal, India

[d] Max-Planck-Institut für Chemische Energiekonversion, Stiftstrasse 34-36 D-45470 Mülheim an der Ruhr, Germany

† Electronic supplementary information (ESI) available. CCDC 2040401. For ESI and crystallographic data in CIF or other electronic format see DOI: 10.1039/d0nj05238h
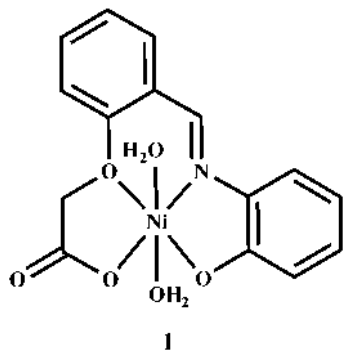
Chart 1 Geometry of **1**.

present in the bulk forms a six membered water cluster along with the ligand oxygen atoms through hydrogen bonding. $1 \cdot n H_2O$ exhibits catecholase activity with a good turnover number and it compares well with a few other nickel(II) complexes exhibiting catecholase activity.[10] The geometry of **1** is shown in Chart 1.

Experimental section

Materials and physical measurements

o-Aminophenol (AP) salicylaldehyde, chloroacetic acid, 3,5-di-$tert$-butylcatechol (3,5-DTBC) and hydrated nickel(II) acetate were purchased from commercial suppliers and used without further purification. 2-(2-Formylphenoxy)acetic acid was prepared using a reported procedure.[11] Spectroscopic grade solvents were used for spectroscopic and electrochemical measurements. The C, H, and N contents of the compounds were obtained using a PerkinElmer 2400 Series II elemental analyzer. The elemental analyses were performed after evaporating the solvents under a high vacuum. Infrared spectra of the samples were measured from 4000 to 400 cm^{-1} with KBr pellets at 295 K on a PerkinElmer Spectrum RX 1 Fourier transform infrared (FT-IR) spectrophotometer. Electrospray ionization (ESI) mass spectra were obtained using an LCMS 2020 mass spectrometer. Thermogravimetric analysis was performed on a PerkinElmer Pyris Diamond TG/DTA in the temperature range between 30 °C and 600 °C under a nitrogen atmosphere at a heating rate of 12 °C min^{-1}. Electronic absorption spectra of the solutions of the complexes were recorded on a PerkinElmer Lambda 750 spectrophotometer in the range of 3300–175 nm. Spectrophotometric titration and kinetics measurements were made with a JASCO model V-730 UV-vis spectrophotometer. The electro-analytical instrument BASi Epsilon EC was used for cyclic voltammetry experiments in acetonitrile containing 0.2 M tetrabutylammoniumhexafluorophosphate as a supporting electrolyte. A BASi platinum working electrode, platinum auxiliary electrode, and Ag/AgCl reference electrode were used for the measurements. The redox potential data were referenced to the ferrocenium/ferrocene, Fc^+/Fc, couple.

Syntheses

$[(L_1^{2-})Ni^{II}(H_2O)_2]$ (**1**). To (E)-2-(2-((2-hydroxyphenylimino)methyl) phenoxy)acetic acid (LH$_2$) (68 mg, 0.25 mmol) in a round

bottom flask, MeOH (20 mL) was added and heated at 325 K for 15 min. It was cooled at RT, filtered and collected in a beaker. To this solution a solution of hydrated Ni(OAc)$_2$ (62 mg, 0.25 mmol) in CH$_3$OH (10 mL) was added. The reaction mixture was allowed to evaporate slowly in air. After 5–7 days, crystals of **1** separated out, which were collected upon filtration and dried in air. Yield: 68 mg (∼75% with respect to nickel). Mass spectral data [electrospray ionization (ESI) positive ion, CH$_3$OH]: m/z 362 for $[1]^+$ (Fig. S1, ESI†). Elemental analysis: anal. calcd for $C_{15}H_{15}NO_6Ni$: C, 49.50; H, 4.15; N, 3.85; found: C, 48.92; H, 4.05; N, 3.80. IR/cm^{-1} (KBr): ν 3412(s), 2926(m), 1656(s), 1601(m), 1475(s), 1400(s), 1384(s), 1291(m), 1276(s), 1255(m), 1220(m), 1130(m), 1022(s), 950(m), 833(s), 754(m), 735(s) (Fig. S2, ESI†).

Single crystal X-ray structure determinations of the complexes (CCDC 2040401)†

Dark single crystals of **1** were picked up with nylon loops and mounted on a Bruker AXS Enraf-Nonius Kappa CCD diffractometer equipped with a Mo-target rotating-anode X-ray source and a graphite monochromator (Mo Kα, λ = 0.71073 Å). Final cell constants were obtained from least-squares fits of all measured reflections. Intensity data were corrected for absorption using intensities of redundant reflections. The structure was readily solved by direct methods and subsequent difference Fourier techniques. The Siemens SHELXS-97[12a] software package was used for solution, and SHELXL-97[12b] was used for the refinement and XS. Ver. 2013/1,[12c] XT. Ver. 2014/4[12d] and XL. Ver. 2014/7[12e] were used for the structure solution and refinement. All non hydrogen atoms were refined anisotropically. Hydrogen atoms were placed at the calculated positions and refined as riding atoms with isotropic displacement parameters.

Catalytic oxidation of 3,5-DTBC

The catecholase activity of **1** was studied by addition of a 1 × 10^{-4} M solution of **1** to 100 equiv. of 3,5-di-$tert$-butylcatechol (3,5-DTBC) in MeOH in air at room temperature. The absorption features of the mixture in the wavelength range of 300–800 nm at an interval of 8 min for 2 h confirm the oxidation of 3,5-DTBC. Kinetic experiments were also carried out spectrophotometrically following reported procedures.[13–15] 0.04 mL of 1 × 10^{-4} M **1** was added to 2 mL of 3,5-DTBC of a particular concentration (varying its concentration from 1 × 10^{-3} M to 1 × 10^{-2} M) to attain a final concentration of **1** of 1 × 10^{-4} M. The dependence of the rate on the concentration of 3,5-DTBC was determined by kinetic analyses and all the measurements were performed in triplicate.

Density functional theory (DFT) calculations

All calculations reported in this article were done with the Gaussian 03W[16] program package supported by GaussView 4.1. The DFT[17] calculations were performed at the level of the Becke three parameter hybrid functional with the nonlocal correlation functional of Lee–Yang–Parr (B3LYP).[18] The gas-phase geometry of **1** was optimized with a triplet spin state, while **1**$^+$ was optimized with a doublet spin state, using Pulay's Direct

Inversion[19] in the Iterative Subspace (DIIS) "tight" convergent self consistent field procedure[20] ignoring symmetry. All the calculations were performed with the LANL2DZ basis set[21] along with the corresponding effective core potential (ECP) for nickel, 6-31+G*(d,p)[22] basis set for C, O, and N atoms, and 6-31G[23] for H atoms.

Results and discussion

Syntheses and characterization

The reaction of $Ni(OAc)_2$ with LH_2 in MeOH affords $1 \cdot nH_2O$ in good yields. Details of the synthesis are outlined in the experimental section. The IR spectrum of $1 \cdot nH_2O$ displays a broader absorption band at 3412 cm^{-1} due to H_2O and a band at 1022 cm^{-1} indicates the presence of an ethereal bond in the complex. The absorption bands at 2926 cm^{-1} and 1601 cm^{-1} are attributes of the coordinated $–COO^-$ group and a band at 1656 cm^{-1} arises due to the $C{=}N$ stretching vibration.

Single crystal X-ray crystallography

The crystallographic data of $1 \cdot nH_2O$ is summarized in Table 1. $1 \cdot nH_2O$ crystallizes in the $P\bar{1}$ space group. The molecular structure of $\mathbf{1}$ in crystals and the atom labelling schemes are illustrated in Fig. 1. Selected bond parameters are summarized in Table 2. L^{2-} in this case acts as a tetra-dentate ligand and makes a NiN_2O_2 square plane and two water molecules coordinating at the axial positions form an octahedral geometry. The $Ni–H_2O$ lengths are 2.061(3) and 2.045(3) Å. The $Ni–O_{phenolato}$, $Ni–O_{acetate}$ and $Ni–O_{ether}$ bond lengths are 2.008(3), 2.033(3) and 2.097(3) Å, respectively. The increasing order of the $Ni–O$ bond lengths
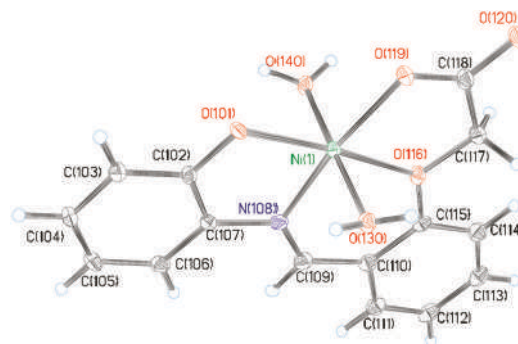
Fig. 1   Molecular geometry of $\mathbf{1} \cdot nH_2O$ in crystals (30% thermal ellipsoid, H_2O and H are omitted for clarity).

Table 2   Selected experimental and calculated bond lengths (Å) of $1 \cdot nH_2O$

Exp.		Cal.
Bonds	Length (Å)	Length (Å)
Ni(1)–O(101)	2.008(3)	2.011
Ni(1)–O(119)	2.033(3)	2.034
Ni(1)–O(116)	2.097(3)	2.137
Ni(1)–O(130)	2.061(3)	2.180
Ni(1)–O(140)	2.045(3)	2.181
Ni(1)–N(108)	2.001(3)	2.036
O(101)–C(102)	1.336(5)	1.319
N(108)–C(109)	1.277(6)	1.293
C(115)–O(116)	1.374(5)	1.377
C(118)–O(119)	1.255(5)	1.294
C(118)–O(120)	1.254(5)	1.226

predicts that the charge density over the oxygen atom decreases as phenoxide > acetate > ether where phenoxide is mono negative, acetate is delocalized mono negative and ether is neutral coordinated to the nickel(II) ion. The two C–O bonds of the acetate group are the same, authenticating that the negative charge is delocalized. The $C{=}N$ length is 1.277(6) Å.

In the crystal the coordinated water molecules make a water cluster by $OH\cdots O$ interactions. The formation of a six membered ring by $OH\cdots O$ interactions with the coordinated waters and the ligand oxygen atom is depicted in Fig. 2b and c. The infinite 1D chain formed due to the H-bonding interaction with the bulk water molecules and the coordinated water molecules is illustrated in Fig. 2d. The hydrogen bond parameters for water in $1 \cdot nH_2O$ are listed in Table S1 (ESI†). The $O140\cdots O520$ and $O520\cdots O550$ distances are 2.750 and 2.703 Å. The O550 water molecule is attached by $OH\cdots O$ interactions to the O419 acetate oxygen and the distance is 2.795 Å. O140 exhibits another $OH\cdots O$ interaction with a coordinated phenolic oxygen (O401) and the $O140\cdots O401$ distance is 2.692 Å. In the lattice aromatic $\pi\cdots\pi$ interactions have been observed (Fig. 2a) and the minimum distance between two aromatic centroids is 3.729 Å. The bulk water molecules play an important role in the formation of the stable structural architecture of $1 \cdot nH_2O$. The thermal stability of the compound was analysed by TGA analysis. The TGA is depicted in Fig. S3 (ESI†). The bulk water molecules were completely removed at 135 °C, where the

Table 1   Crystallographic data for $1 \cdot nH_2O$

Formula	$C_{15}H_{18.50}NO_{7.75}Ni$
CCDC	2040401
F_w	395.52
Crystal system	Triclinic
Crystal color	Green
Space group	$P\bar{1}$
a (Å)	12.343(2)
b (Å)	14.617(3)
c (Å)	18.348(3)
α (deg)	81.497(9)
β (deg)	89.659(8)
γ (deg)	89.249(9)
V (Å)	3273.6(10)
Z	8
T (K)	100(2)
2θ	132.24
ρ_{calcd} (g cm^{-3})	1.605
Refl. collected	74 139
Uniquerefl.	11 191
Reflection ($I > 2\sigma(I)$)	9927
$F(000)$	1644
No. of params/restr.	982/51
λ (Å)/μ (mm^{-1})	1.54178/2.114
$R_1{}^a$ [$I > 2\sigma(I)$]/GOF^b	0.0636/1.099
$wR_2{}^c$ [$I > 2\sigma(I)$]	0.1523
Residual density (e $Å^{-3}$)	1.030

^{a} Observation criterion: $R_1 = \Sigma \|F_o\| - |F_c\|/\Sigma|F_o|$. ^{b} GOF = $\{\Sigma[w(F_o{}^2 - F_c{}^2)^2]/(n - p)\}^{1/2}$. ^{c} $wR_2 = [\Sigma[w(F_o{}^2 - F_c{}^2)^2]/\Sigma[w(F_o{}^2)^2]]^{1/2}$ where $w = 1/[\sigma^2(F_o{}^2) + (aP)^2 + bP]$, $P = (F_o{}^2 + 2F_c{}^2)/3$.
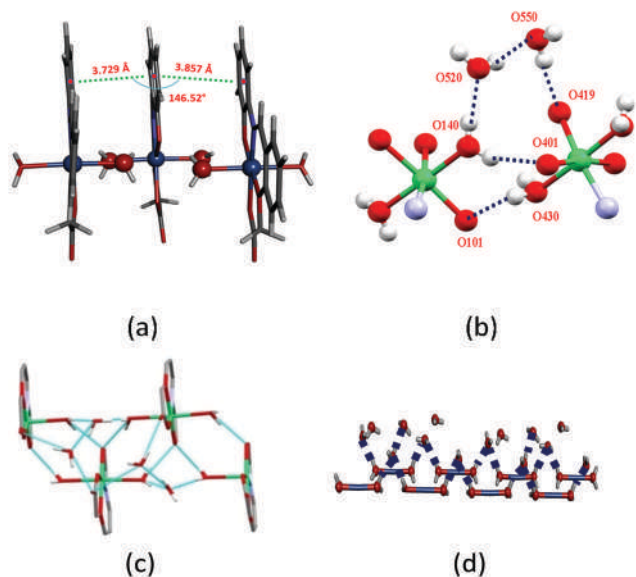
Fig. 2 (a) The $\pi\cdots\pi$ interactions within the crystal, (b) and (c) the OH$\cdots$O interactions present among the water molecules (a-axis) and (d) the linear 1D water chain of $1 \cdot n$H$_2$O along the a-axis.

removal of water molecules starts at 70 °C. The water loss of $1 \cdot n$H$_2$O was monitored by the percentage of sharp weight loss. The coordinated water molecules were removed at 240–310 °C.

Electrochemical studies

The cyclic voltammetry study of $1 \cdot n$H$_2$O in CH$_3$CN at 295 K shows that the phenoxyl/phenolato redox peak at 0.83 V (Fig. 3) referenced to the ferrocenium/ferrocene (Fc$^+$/Fc) couple is irreversible. The DFT calculations support this assignment.

Catecholase activity

The catecholase like activity of $1 \cdot n$H$_2$O was examined using 3,5-di-$tert$-butylcatechol (3,5-DTBC) as a standard substrate. 3,5-DTBC is considered as a model substrate due to it consisting of two bulky t-butyl substituents attached to an aromatic ring as well as the low reduction potential of quinone-catechol species

(Scheme 1). In general, 3,5-DTBQ is highly stable in solution and exhibits an absorption maximum at 401 nm in methanol.[24]

The oxidation of 3,5-DTBC (1×10^{-2} M) in air was followed using a 1×10^{-4} M methanolic solution of $1 \cdot n$H$_2$O. The course of catalytic oxidation was investigated by recording the UV-vis absorption spectra of the mixture at an interval of 8 min for 2 h and the change of the spectral pattern is shown in Fig. 4. It is well documented that 3,5-DTBC displays a single electronic band at 284 nm.[25] Upon addition of $1 \cdot n$H$_2$O, the intensity of this band gradually decreases concomitantly, and the appearance of a new band at $\sim$390 nm (Fig. 4) due to the 3,5-DTBQ form was recorded. The oxidation occurs through the removal of one or two water molecules from the trans position of the complex followed by coordination of one 3,5-DTBC molecule. The reaction was followed by ESI mass spectrometry in methanol and the appearance of mass peaks at m/z 546 and 564 correlates well with the formation of the o-benzosemiquinonate anion radical as an intermediate (Fig. S4, ESI†). The other peaks at m/z 586 and 791 appear due to $[(L_1{}^{2-})Ni^{II}(o\text{-benzo-}$ semiquinonate anion radical)(CH$_3$CN)] and $[(L_1{}^{2-})Ni^{II}[(o\text{-}$ benzosemiquinonate anion radical)$_2$]Na$^+$], respectively. The formation of o-benzosemiquinone as an intermediate was confirmed by cyclic voltammetry analysis also. The cyclic voltammetry of $1 \cdot n$H$_2$O was performed in the presence of 3,5-DTBC in
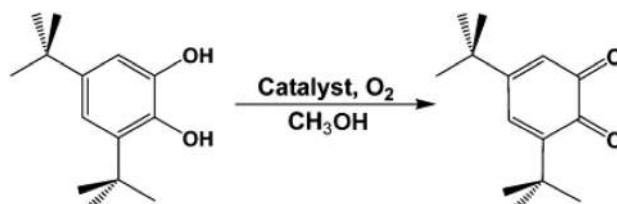
Scheme 1 Catalytic oxidation of 3,5-DTBC to 3,5-DTBQ in air-saturated methanol.

Fig. 3 Cyclic voltammogram of 1 in CH$_3$CN (0.20 M [N(n-Bu)$_4$]PF$_6$) at 295 K.
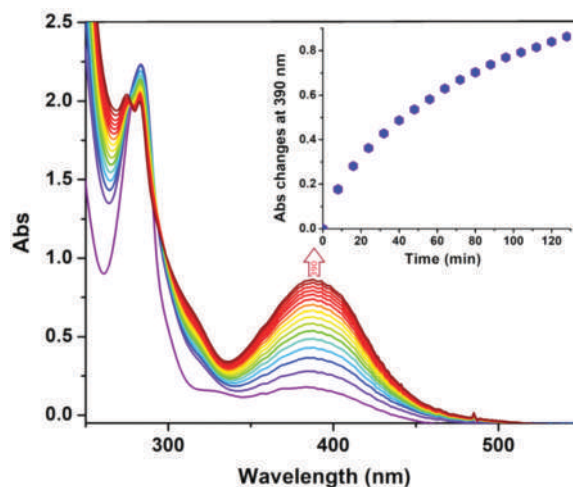
Fig. 4 Ni(II) complex mediated catalytic oxidation of 3,5-DTBC under an aerobic atmosphere in MeOH. The spectra were recorded at a time interval of 8 mins for 2 h. Inset: Time $vs.$ changes of absorbance at 390 nm.

CH$_3$CN at 295 K. The redox peak at -0.36 V (Fig. S5, ESI†) referenced to the ferrocenium/ferrocene (Fc$^+$/Fc) couple is due to reduction of the o-benzosemiquinonate anion radical to the phenolato form.

The oxidation product, 3,5-DTBQ, was extracted and separated with column chromatography using hexane–ethyl acetate as an eluent mixture. The product was identified by ^{1}H NMR spectroscopy. ^{1}H NMR (CDCl$_3$, 400 MHz) δ_H: 1.14 (s, 9H), 1.19 (s, 9H), 6.17 (d, J = 2.4 Hz, 1H), 6.83 (d, J = 2.4 Hz, 1H).

The kinetics for catalytic oxidation of 3,5-DTBC was studied to evaluate the catalytic efficiency of **1**·nH$_2$O. The method of initial rates was followed to unveil the kinetic parameter for the oxidation of 3,5-DTBC. The development of 3,5-DTBQ was monitored at 390 nm as a function of time (Fig. 5).[26] The rate constant $vs.$ substrate concentration profile disclosed the nature of the kinetics (Fig. 5). The nature of the kinetics seems to be first order kinetics, which reveals that the Michaelis–Menten model looks to be most suitable as per the following eqn (1):

$$V = \frac{V_{\max}[S]}{K_M + [S]} \quad (1)$$

where V is the rate of the reaction, K_M is the Michaelis–Menten constant, $V_{\max}$ is the maximum velocity of the reaction, and [S] is the concentration of the substrate.

The kinetic parameters were determined from the Michaelis–Menten equation as $V_{\max}$ (MS^{-1}) = 1.24 × 10^{-5}; K_M = 1.68 × 10^{-3} [std. error for $V_{\max}$ (MS^{-1}) = 1.69 × 10^{-6}; std. error for K_M (M) = 1.46 × 10^{-4}]. The turnover number (k_{cat}) was determined as 4.46 × 10^2 h^{-1}.

EPR spectroscopy

The X-band EPR spectrum of the mixture of **1**·nH$_2$O and 3,5-DTBC was recorded in CH$_2$Cl$_2$ at 120 K. No signal was recorded with the fluid solution, inferring the coupling of the organic radical with the S = 1 state of the nickel(II) ion. The frozen glass hyperfine EPR spectrum as depicted in Fig. 6 was deconvoluted into two sub spectra due to the octahedral [(L$_1^{2-}$)Ni^{II} (o-benzosemiquinonate anion radical)(H$_2$O)] ($S = \frac{1}{2}$) and square planar-radical [(L$_1^{2-}$)Ni^{II}(o-benzosemiquinonate anion radical)] ($S = \frac{1}{2}$) components. In the former the spin is centred on the

Fig. 6 X-band EPR spectra of a mixture of **1**·nH$_2$O and 3,5-DTBC in CH$_2$Cl$_2$ solution at 140 K; experimental (black) and simulated (red).

nickel ion (simulated parameters, g_1 = 2.049 (A_{Ni} = 100), g_2 = 2.029 (A_{Ni} = 50) and g_3 = 1.979 (A_{Ni} = 100 M Hz)), while the latter is an organic radical (simulated g = 2.021, A_N = 25 MHz). The study infers that the o-benzosemiquinonate anion radical coordinates to the nickel(II) ion during oxidation. However, in the presence of excess 3,5-DTBC, no EPR signal was recorded, maybe due to the coordination of the two o-benzosemiquinonate anion radicals to the nickel(II) ion resulting in an S = 0 state.

DFT calculations

DFT calculations were employed on **1** and **1**$^+$ to elucidate the electronic structures of the complex and its oxidized analogues. The gas phase geometry of **1** was optimized with a triplet spin state. The optimized geometries of **1** and **1**$^+$ are given in Fig. 7. The calculated Ni–H$_2$O, Ni–O$_{phenoxy}$, Ni–O$_{carboxy}$ and Ni–O$_{acetoxy}$ bond lengths of **1** correlate well with those obtained from the single crystal X-ray diffraction study of **1**·1.75H$_2$O.

Electronic spectra and TD DFT

The UV-vis/NIR absorption spectrum of **1**·nH$_2$O recorded in CH$_3$OH at 295 K is illustrated in Fig. S6 (ESI†). The spectral data is given in Table S2 (ESI†). The free ligand LH$_2$ absorbs strongly at 400 nm due to a ligand to ligand charge transfer (LLCT) transition (Fig. 8), which is red shifted to 430 nm in the

Fig. 5 Rate $vs.$ concentration of 3,5-DTBC plot.
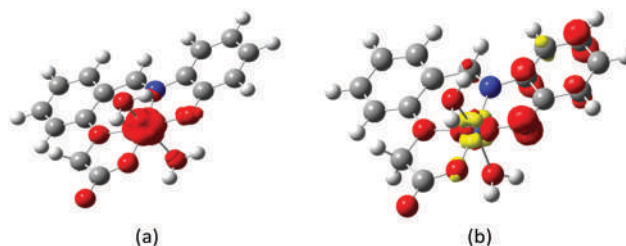
Fig. 7 Optimized geometries of (a) **1** and (b) **1**$^+$.
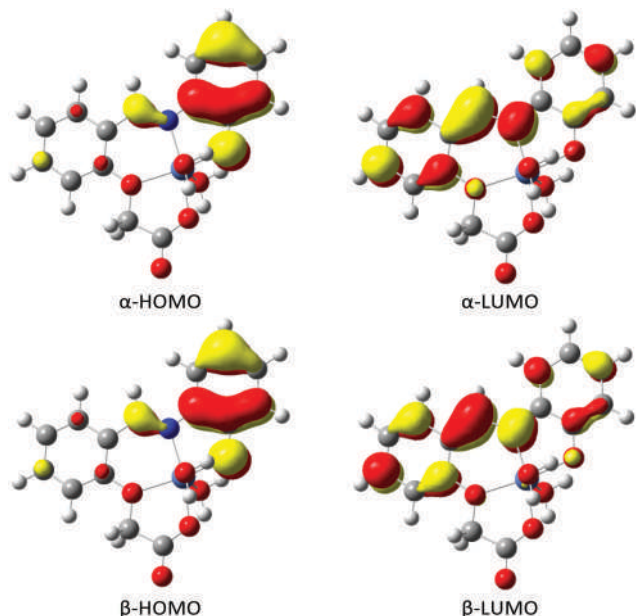
Fig. 8 Frontier molecular orbitals of **1**.

complexes, and the corresponding λ_{cal} of **1** is 459.94 nm (f = 0.25), which is due to LLCT.

Conclusions

The article discloses the synthesis and characterization of a trans di-aqua complex of nickel(II) incorporating an aryloxyacetic acid derivative. In the crystal, the existence of a water cluster has been confirmed. The water cluster due to hydrogen bonding interactions among coordinated water, bulk water molecules and oxygen atoms of the ligand is significant. The removal temperatures of the coordinated and the bulk water molecules were investigated by TGA analyses. The complex exhibits catecholase activity with a good turnover number and the formation of a coordinated *o*-benzosemiquinonate anion radical intermediate during oxidation has been confirmed by EPR spectra, ESI mass spectrometry and cyclic voltammetry. The catalytic oxidation reaction was followed by UV-vis spectroscopic analysis.

Conflicts of interest

There are no conflicts of interest to declare.

Acknowledgements

Notes and references

1 (a) E. Manrique, X. Fontrodona, M. Rodríguez and I. Romero, *Eur. J. Inorg. Chem.*, 2019, 2124–2133;

(b) K. T. Mahmudov, M. N. Kopylovich, M. Haukka, G. S. Mahmudova, E. F. Esmaeila, F. M. Chyragov and A. J. L. Pombeiro, *J. Mol. Struct.*, 2013, **1048**, 108–112; (c) Y.-M. So, K.-L. Wong, H. H. Y. Sung, I. D. Williams and W.-H. Leung, *Eur. J. Inorg. Chem.*, 2019, 2368–2374.

2 M. N. Kopylovich, T. C. O. Mac Leod, M. Haukka, G. I. Amanullayeva, K. T. Mahmudov and A. J. L. Pombeiro, *J. Inorg. Biochem.*, 2012, **115**, 72–77.

3 N. Saraei, O. Hietsoi, C. S. Mullins, A. J. Gupta, B. C. Frye, M. S. Mashuta, R. M. Buchanan and C. A. Grapperhaus, *CrystEngComm*, 2018, **20**, 7071.

4 (a) G. A. Jeffrey, *An Introduction to Hydrogen Bonding*, Oxford University Press, Oxford, UK, 1997, pp. 160–180; (b) L. Infantes and S. Motherwell, *CrystEngComm*, 2002, **4**, 454; (c) R. Ludwig, *Angew. Chem., Int. Ed.*, 2001, **40**, 1808; (d) I. Ohmine and S. Satio, *Acc. Chem. Res.*, 1999, **32**, 741; (e) W. S. Benson and E. D. Siebert, *J. Am. Chem. Soc.*, 1992, **114**, 4269; (f) K. A. Udachin and J. A. Ripmeester, *Nature*, 1999, **397**, 420; (g) A. Müller, E. Krickemeyer, H. Bögge, M. Schmidtmann, B. Botar and M. O. Talismanova, *Angew. Chem., Int. Ed.*, 2003, **42**, 2085.

5 (a) M. H. Mir and J. J. Vittal, *Angew. Chem., Int. Ed.*, 2007, **46**, 5925–5928; (b) M. H. Mir and J. J. Vittal, *Cryst. Growth Des.*, 2008, **8**, 1478–1480; (c) M. H. Mir, L. Wang, M. W. Wong and J. J. Vittal, *Chem. Commun.*, 2009, 4539–4541; (d) R. E. Dehl and C. A. Hoeve, *J. Chem. Phys.*, 1969, **50**, 324; (e) C. Migchelsen, J. C. H. Berendsen and A. J. Rupprecht, *Mol. Biol.*, 1968, **37**, 235; (f) F. Steckel and S. Szapiro, *Trans. Faraday Soc.*, 1963, **59**, 331; (g) S. D. Colson and T. H. Dunning, *Science*, 1994, **265**, 43; (h) K. Liu, J. D. Cruzan and R. J. Saykally, *Science*, 1996, **271**, 929; (i) L. J. Barbour, G. W. Orr and J. L. Atwood, *Chem. Commun.*, 2000, 859; (j) L. Infantes and S. Motherwell, *CrystEngComm*, 2002, **4**, 454–461; (k) L. Infantes, J. Chisholm and S. Motherwell, *CrystEngComm*, 2003, **5**, 480–486; (l) M. Mascal, L. Infantes and J. Chisholm, *Angew. Chem., Int. Ed.*, 2006, **45**, 32–36; (m) B. Dutta, S. R. Ghosh, A. Ray, S. Jana, C. Sinha, S. Das, A. D. Jana and M. H. Mir, *New J. Chem.*, 2020, **44**, 15857–15870; (n) F. Ahmed, J. Datta, S. Sarkar, B. Dutta, A. D. Jana, P. P. Ray and M. H. Mir, *ChemistrySelect*, 2018, **3**, 6985–6991; (o) B. Dutta, A. Hazra, A. Dey, C. Sinha, P. P. Ray, P. Banerjeeand and M. H. Mir, *Cryst. Growth Des.*, 2020, **20**(2), 765–776.

6 (a) L. H. Eddaoudi, M. M. O'Keeffe and O. M. Yaghi, *Nature*, 1999, **402**, 276–279; (b) S. S. Y. Chui, S. M. F. Lo, J. P. H. Charmant, A. G. Orpen and I. D. Williams, *Science*, 1999, **283**, 1148–1150; (c) K. S. Park, Z. Ni, A. P. Côté, J. Y. Choi, R. Huang, F. J. Uribe-Romo, H. K. Chae, M. O'Keeffe and O. M. Yaghi, *Proc. Natl. Acad. Sci. U. S. A.*, 2006, **103**, 10186–10191; (d) G. Férey, C. Mellot-Draznieks, C. Serre, F. Millange, J. Dutour, S. Surble and I. Margiolaki, *Science*, 2005, **309**, 2040–2042; (e) J. H. Cavka, S. Jakobsen, U. Olsbye, N. Guillou, C. Lamberti, S. Bordiga and K. P. Lillerud, *J. Am. Chem. Soc.*, 2008, **130**, 13850–13851.

7 (a) S. J. Brown, M. M. Olmstead and P. K. Mascharak, *Inorg. Chem.*, 1989, **28**, 3720; (b) K. Diemert, W. Kuchen, W. Poll

and F. Sandt, *Eur. J. Inorg. Chem.*, 1998, 361; (c) L. Dupont, J. Lamotte-Brasseur, O. Dideberg, H. Campsteyn, M. Vermeireand and L. Angenot, *Acta Crystallogr., Sect. B: Struct. Crystallogr. Cryst. Chem.*, 1977, **33**, 1801; (d) G. J. Kemperman, R. Gelder, F. J. Dommerholt, P. C. Raemakers-Franken, A. J. H. Klunder and B. Zwanenburg, *J. Chem. Soc., Perkin Trans. 2*, 2000, 1425; (e) J. C. Kapteyn, R. C. Montijn, E. Vink, J. Cruz, A. Llobell, J. E. Douwes, H. Shimoi, P. N. Lipke and F. M. Klis, *Glycobiology*, 1996, **6**, 337.

8 (a) M. Mondal, S. Ghosh, S. Maity, S. Giri and A. Ghosh, *Inorg. Chem. Front.*, 2020, **7**, 247; (b) A. Das, K. Bhattacharya, L. K. Das, S. Giri and A. Ghosh, *Dalton Trans.*, 2020, **49**, 3369–3371; (c) P. Mahapatra, M. G. B. Drew and A. Ghosh, *Inorg. Chem.*, 2018, **57**(14), 8338–8353; (d) A. Das, K. Bhattacharyaa, L. K. Dasc, S. Giri and A. Ghosh, *Dalton Trans.*, 2018, **47**, 9385–9399; (e) P. Mahapatra, M. G. B. Drew and A. Ghosh, *Dalton Trans.*, 2018, **47**, 13957–13971; (f) P. Chakraborty, S. Majumder, A. Jana and S. Mohanta, *Inorg. Chim. Acta*, 2014, **410**, 65–75; (g) A. Neves, L. M. Rossi, A. J. Bortoluzzi, B. Szpoganicz, C. Wiezbicki, E. Schwingel, W. Haase and S. Ostrovsky, *Inorg. Chem.*, 2002, **41**(7), 1788–1794.

9 V. Bala, Y. S. Chhonker and S. R. Hashim, *Asian J. Chem.*, 2010, **22**, 3447–3452.

10 (a) T. Ghosh, J. Adhikary, P. Chakraborty, P. K. Sukul, M. S. Jana, T. K. Mondal, E. Zangrando and D. Das, *Dalton Trans.*, 2014, **43**, 841; (b) A. Guha, K. S. Banu, S. Das, T. Chattopadhyay, R. Sanyal, E. Zangrando and D. Das, *Polyhedron*, 2013, **52**, 669–678; (c) B. Mandal, M. C. Majee, D. Mandal and R. Ganguly, *J. Mol. Struct.*, 2020, **1202**, 127340.

11 A. W. Burgstahler and L. R. Worden, *Org. Synth.*, 1973, **546**, 2512810.15227.

12 (a) G. M. Sheldrick, *ShelXS97*, Universitat Gottingen, Gottingen, Germany, 1997; (b) G. M. Sheldrick, *ShelXL97*, Universitat Gottingen, Gottingen, Germany, 1997; (c) G. M. Sheldrick, *XS. Version 2013/1*, Georg-August-Universitat Gottingen, Gottingen, Germany, 2013; (d) G. M. Sheldrick, *Acta Crystallogr., Sect. A: Found. Adv.*, 2015, **71**, 3–8; (e) G. M. Sheldrick, *Acta Crystallogr., Sect. C: Struct. Chem.*, 2015, **71**, 3–8.

13 D. Dey, G. Kaur, A. Ranjani, L. Gyathri, P. Chakraborty, J. Adhikary, J. Pasan, D. Dhanasekaran, A. R. Choudhury, M. A. Akbarsha, N. Kole and B. Biswas, *Eur. J. Inorg. Chem.*, 2014, 3350–3358.

14 D. Dey, S. Das, H. R. Yadav, A. Ranjani, L. Gyathri, S. Roy, P. S. Guin, D. Dhanasekaran, A. R. Choudhury, M. A. Akbarshaand and B. Biswas, *Polyhedron*, 2016, **106**, 106–114.

15 S. Pal, B. Chowdhury, M. Patra, M. Maji and B. Biswas, *Spectrochim. Acta, Part A*, 2015, **144**, 148–154.

16 M. J. Frisch, G. W. Trucks, H. B. Schlegel, G. E. Scuseria, M. A. Robb, J. R. Cheeseman Jr., J. A. Montgomery, T. Vreven, K. N. Kudin, J. C. Burant, J. M. Millam, S. S. Iyengar, J. Tomasi, V. Barone, B. Mennucci, M. Cossi, G. Scalmani, N. Rega, G. A. Petersson, H. Nakatsuji, M. Hada, M. Ehara, K. Toyota, R. Fukuda, J. Hasegawa, M. Ishida, T. Nakajima, Y. Honda, O. Kitao, H. Nakai, M. Klene, X. Li, J. E. Knox,

H. P. Hratchian, J. B. Cross, V. Bakken, C. Adamo, J. Jaramillo, R. Gomperts, R. E. Stratmann, O. Yazyev, J. A. Austin, R. Cammi, C. Pomelli, J. W. Ochterski, P. Y. Ayala, K. Morokuma, G. A. Voth, P. Salvador, J. J. Dannenberg, V. G. Zakrzewski, S. Dapprich, A. D. Daniels, M. C. Strain, O. Farkas, D. K. Malick, A. D. Rabuck, K. Raghavachari, J. B. Foresman, J. V. Ortiz, Q. Cui, A. G. Baboul, S. Clifford, J. Cioslowski, B. B. Stefanov, G. Liu, A. Liashenko, P. Piskorz, I. Komaromi, R. L. Martin, D. J. Fox, T. Keith, M. A. Al-Laham, C. Y. Peng, A. Nanayakkara, M. Challacombe, P. M. W. Gill, B. Johnson, W. Chen, M. W. Wong, C. Gonzalez and J. A. Pople, *Gaussian 03 (Revision E.01)*, Gaussian, Inc., Wallingford, CT, 2004.

17 (a) R. G. Parr and W. Yang, *Density Functional Theory of Atoms and Molecules*, Oxford University Press, Oxford, UK, 1989; (b) D. R. Salahub and M. C. Zerner, *The Challenge of d and f Electrons*, ACS Symposium Series 394, American Chemical Society, Washington, DC, 1989; (c) W. Kohn and L. J. Sham, *Phys. Rev.*, 1965, **140**, A1133–A1138; (d) P. Hohenberg and W. Kohn, *Phys. Rev.*, 1964, **136**, B864–B871.

18 (a) A. D. Becke, *J. Chem. Phys.*, 1993, **98**, 5648–5652; (b) B. Miehlich, A. Savin, H. Stoll and H. Preuss, *Chem. Phys. Lett.*, 1989, **157**, 200–205; (c) C. Lee, W. Yang and R. G. Parr, *Phys. Rev. B: Condens. Matter Mater. Phys.*, 1988, **37**, 785–789.

19 P. J. Pulay, *Comput. Chem.*, 1982, **3**, 556.

20 H. B. Schlegel and J. J. McDouall, in *Computational Advances in Organic Chemistry*, ed. C. Ogretir and I. G. Csizmadia, Kluwer Academic, The Netherlands, 1991, 167–185.

21 (a) P. J. Hay and W. R. Wadt, *J. Chem. Phys.*, 1985, **82**, 270–283; (b) W. R. Wadt and P. J. Hay, *J. Chem. Phys.*, 1985, **82**, 284–298; (c) P. J. Hayand and W. R. Wadt, *J. Chem. Phys.*, 1985, **82**, 299–310.

22 W. J. Hehre, R. Ditchfield and J. A. Pople, *J. Chem. Phys.*, 1972, **56**, 2257–2261.

23 (a) V. A. Rassolov, M. A. Ratner, J. A. Pople, P. C. Redfern and L. A. Curtiss, *J. Comput. Chem.*, 2001, **22**, 976–984; (b) M. M. Francl, W. J. Pietro, W. J. Hehre, J. S. Binkley, D. J. DeFrees, J. A. Pople and M. S. Gordon, *J. Chem. Phys.*, 1982, **77**, 3654–3665; (c) P. C. Hariharan and J. A. Pople, *Mol. Phys.*, 1974, **27**, 209–214; (d) P. C. Hariharan and J. A. Pople, *Theor. Chim. Acta*, 1973, **28**, 213–222; (e) W. J. Hehre, R. Ditchfield and J. A. Pople, *J. Chem. Phys.*, 1972, **56**, 2257–2261.

24 (a) L.-Z. Cai, W.-T. Chen, M.-S. Wang, G.-C. Guo and J.-S. Huang, *Inorg. Chem. Commun.*, 2004, **7**, 611–613; (b) S. Mondal, S. Bera, S. Maity and P. Ghosh, *ACS Omega*, 2018, **3**(10), 13323–13334.

25 G. Hennrich, H. Sonnenschein and U. R. Genger, *J. Am. Chem. Soc.*, 1999, **121**, 5073–5074.

26 (a) A. De, D. Dey, H. R. Yadav, M. Maji, V. Rane, R. M. Kadam, A. R. Choudhury and B. Biswas, *J. Chem. Sci.*, 2016, **128**, 1775–1782; (b) A. De, M. Garai, H. R. Yadav, A. R. Choudhury and B. Biswas, *Applied Organometallic Chemistry*, Wiley, 2017, vol. 31, p. 3551; (c) M. Garai, D. Dey, H. R. Yadav, A. R. Choudhury, M. Majiand and B. Biswas, *ChemistrySelect*, 2017, **2**, 11040–11047.

Source details

Feedback >   Compare sources >

New Journal of Chemistry

Scopus coverage years: from 1996 to Present

Publisher: Royal Society of Chemistry

ISSN: 1144-0546   E-ISSN: 1369-9261

Subject area: (Materials Science: Materials Chemistry)   (Chemistry: General Chemistry)   (Chemical Engineering: Catalysis)

Source type: Journal

View all documents >   Set document alert   💾 Save to source list

CiteScore 2022   ⓘ
5.8

SJR 2022   ⓘ
0.601

SNIP 2022   ⓘ
0.682

CiteScore   CiteScore rank & trend   Scopus content coverage

FULL PAPER

Ligand directed synthesis of a unprecedented tetragonalbipyramidal copper (II) complex and its antibacterial activity and catalytic role in oxidative dimerisation of 2-aminophenol

Shreya Mahato[1] | Nishith Meheta[1] | Muddukrishnaiah Kotakonda[2] |
Mayank Joshi[3] | Prasanta Ghosh[4] | Madhusudan Shit[5] |
Angshuman Roy Choudhury[3] | Bhaskar Biswas[1] [ORCID]

[1]Department of Chemistry, University of North Bengal, Darjeeling-734013, India

[2]Department of Pharmaceutical Technology, Anna University, BIT Campus Thiruchirappalli, India

[3]Department of Chemical Sciences, Indian Institute of Science Education and Research, Mohali, Sector 81, Knowledge City, S. A. S. Nagar, Manauli PO, Mohali, Punjab 140306, India

[4]Department of Chemistry, Narendrapur Ramakrishna Mission Residential College, Kolkata 700103, India

[5]Department of Chemistry, Dinabandhu Andrews College, Kolkata 700084, India

Correspondence
Bhaskar Biswas, Department of Chemistry, University of North Bengal, Darjeeling-734013, India.
Email: icbbiswas@gmail.com

Funding information
Science and Engineering Research Board, Grant/Award Number: TAR/2018/000473

In pursuit of the significant contribution of copper ion in different biological processes, this research work describes the synthesis, X-ray structure, Hirshfeld surface analysis, oxidative dimerization of 2-aminophenol and antibacterial activity of a newly designed copper (II)-Schiff base complex, [Cu(L)$_2$] (1), [Schiff base (HL) = 2-(2-methoxybenzylideneamino)phenol]. X-ray structural analysis of 1 reveals that the Cu (II) complex crystallizes in a cubic crystal system with Ia-3d space group. The Cu (II) centre adopts an unprecedented tetragonal bipyramidal geometry in its crystalline phase. The Schiff base behaves as a tridentate chelator and forms an innermetallic chelate of first order with Cu (II) ion. The copper (II) complex has been tested in the bio-mimics of phenaxozinone synthase activity in acetonitrile and exhibits good catalytic activity as evident from high turnover number, 536.4 h^{-1}. Electrochemical analysis exhibits the appearance of two additional peaks at −0.15 and 0.46 V for Cu (II) complex in presence of 2-AP and suggests the development of AP$^-$/AP$^{\bullet-}$ and AP$^{\bullet-}$/IQ redox couples in solution, respectively. The presence of iminobenzosemiquinone radical at g = 2.057 in the reaction mixture was confirmed by electron paramagnetic resonance and may be considered the driving force for the oxidative dimerisation of 2-AP. The existence of a peak at m/z 624.81 for Cu (II) complex in presence of 2-AP in electrospray ionization mass spectrum ensures that the catalytic oxidation proceeds through enzyme-substrate adduct formation. The copper (II) complex exhibits potential antibacterial properties against few pathogenic bacterial species like *Staphylococcus aureus*, *Enterococcus* and *Klebsiella pneumonia* and scanning electron microscope studies consolidates that destruction of bacterial cell membrane accounts on the development of antibacterial activity.

Shreya Mahato and Nishith Meheta have equal contribution.

1 | INTRODUCTION

In this modern age of science, Schiff base as polydentate chelators have been widely used in the development of coordination compounds of varied functionality.[1–3] Among the transition metal ions, copper ion has been considered as an essential metal ion in living system and it also plays significant role in designing advance functional materials.[4–7] In nature, copper ions are integrated with different bio-ligands in the functional sites of various metallo-enzymes such as catechol and galactose oxidase, phenoxazinone synthase, superoxide dismutase, lysine oxidase, N_2O reductase etc.[8–11] It pursuit of deep understanding of different biological oxidation processes in nature, synthetic coordination chemists have been stepped forward to tune electronic and geometric factors of the ligands in engineering bio-inspired coordination driven compounds.[12–15] It is well documented that the bio-inspired synthetic analogues also serve as magic catalysts in several catalytic oxidation reactions of laboratory and industrial significance.[14–16] Among the different oxidase enzymes, phenoxazinone synthase has drawn special attention[14,15] as the oxidized product, aminophenoxazinone acts as an antineoplastic agent named actinomycin D (questiomycin A) which is usually recommended in the treatment of certain types of cancer.[17–20] Furthermore, 2-aminophenoxazin-3-one and 3-aminophenoxazin-2-one compounds show potential antimicrobial, antiviral, and antitumor activities against different pathogens.[21–24] Aminophenoxazinone compounds have also been reported in different forms like Streptomyces parvulus and wood rotting fungi metabolites, oxidative coupling products of o-aminophenols with bovine erythrocyte hemolyzate, and bio-conversion products of Pseudomonas putida grown on nitroarenes.[24–28]

In light of incessant emergence for new antibiotics with potential resistance against microorganisms, it is of great importance to design novel antibiotics, which would destroy the lipoid layer as well as the cell membrane of the pathogen with high selectivity.[29,30] In this perspective, copper based coordination compounds hold a great promise to provide future alternatives to the existed antibiotics.[30,31] In the context of newly designed copper (II) complexes with high catalytic activities and potential therapeutic values, this research study deals with the synthesis, structural characterization and catalytic oxidase activity of a new copper (II)-Schiff base complex. The antibacterial property of this copper (II) complex towards different bacterial species has also been delineated.

2 | EXPERIMENTAL

2.1 | Preparation of the Schiff base and dinuclear copper (II) complex

2.1.1 | Chemicals, solvents and starting materials

Highly pure o-anisidine (Sigma Aldrich, Missouri, Texas, USA), salicylaldehyde (Sigma Aldrich, Missouri, Texas,USA) and cupric acetate monohydrate (SRL, Gurugram, Haryana, India) were purchased from the respective concerns and used as received. All other chemicals and solvents were of analytical grade and used as received without further purification.

2.1.2 | Synthesis of the Schiff base and copper (II) complex

The Schiff base, H**L** was synthesized following a reported method.[32] The Schiff base was synthesized through condensation reaction between o-anisidine (0.123 g, 1 mmol) and salicylaldehyde (0.122 g, 1 mmol) in ethanol under reflux for 8 hr. Then, the yellowish brown coloured gummy product was extracted and stored in vaccuo over $CaCl_2$ for use. Yield: 0.201 g (∼88.5%). Anal. Calc. for $C_{14}H_{13}NO_2$ (H**L**): C, 73.99; H, 5.77; N, 6.16; Found: C, 73.93; H, 5.72; N, 6.19. IR (KBr, cm^{-1}; Figure S1): 3372 (ν_{OH}), 1615, 1590 ($\nu_{C=N}$); UV–Vis (λ_{max}, nm; Figure S2): 230, 270, 346; ^{1}H NMR (δ ppm, 400 Mz, CDCl$_3$; Figure S3) δ = 13.88 (s, 1H), 8.63 (s, 1H), 7.26–6.82 (Ar-H, 7H), 3.79–3.83 (t, 3H) ppm. ^{13}C NMR (400 MHz,CDCl$_3$; Figure S4): 162.06 (HC=N); 153.03, (Ar-OH); 137.05 (Ar-N=C); 132.94, 132.05, 127.95, 127.13, 119.64, 118.46, 117.40, 115.05, (Ar-C); 77.49, 77.17, 76.85 (-OCH$_3$).

The copper (II)-Schiff base complex was prepared by drop wise addition of acetonitrile solution of Cu (OAc)$_2$ (0.199 g, 1 mmol) to the methanolic solution of H**L** (0.454 g, 2 mmol). The yellow coloured Schiff base solution was instantly turned to green coloured solution.

Thereafter, the reaction mixture was kept on a magnetic stirrer for 20 mins and kept in open atmosphere for slow evaporation. After 7–10 days, green coloured single crystals of the compound were separated out from the solution. The crystalline compound was washed with toluene and dried over silica gel. Finally, different spectroscopic analysis was carried out to determine the structural formulation of the Cu (II)-Schiff base complex. The results are summarized as follows.

Yield of **1**: 0.415 g (~63.5% based on metal salt) Anal. calc. For $C_{28}H_{24}N_2O_4Cu$ (**1**): C, 65.17; H, 4.69; N, 5.43; Found: C, 65.13; H, 4.61; N, 5.38. IR (KBr pellet, cm^{-1}; Figure S1): 1605,1585 ($\nu_{C=N}$); UV–Vis (1×10^{-4} M, λ_{max} (abs), nm, MeCN; Figure S2): 238, 283, 400.

2.2 | Physical measurements

FTIR-8400S SHIMADZU spectrometer (Shimadzu, Nakagyo-ku, Kyoto, Japan) was employed to record IR spectrum (KBr) of Schiff base and **1** in the range of 400–3,600 cm^{-1}. ^{1}H and ^{13}C NMR spectra of the ligand (H**L**) were obtained on a Bruker Advance 400 MHz spectrometer (Bruker, MA, USA) in CDCl$_3$ at 298 K. Steady-state absorption and other spectral data were recorded with a JASCO V-730 UV–Vis spectrophotometer (Jasco, Hachioji,Tokyo, Japan). Electrospray ionization (ESI) mass spectral measurements were performed with a Q-TOF-micro quadruple mass spectrometer (Waters, Milford,USA). Elemental analyses were performed on a Perkin Elmer 2400 CHN microanalyser (Perkin Elmer, Waltham, Massachusetts, USA). X-band EPR spectra were recorded on a Magnettech GmbH MiniScope MS400 spectrometer (equipped with temperature controller TC H03, Magnettech, Berlin, Germany), where the microwave frequency was measured with an FC400 frequency counter. The EPR spectrum of Cu (II) complex was simulated using Easy Spin software.

2.3 | Crystal structure determination and refinement

X-ray diffraction data of **1** were collected using a Rigaku XtaLABmini diffractometer equipped with Mercury 375R (2 × 2 bin mode) CCD detector. The data were collected with graphite monochromated Mo-Kα radiation (λ = 0.71073 Å) at 296 (2) K using ω scans. The data were reduced using CrysAlisPro 1.171.39.35c[33a] and the space group determination was done using Olex2. The structure was resolved by dual space method using SHELXT-2015[33b] and refined by full-matrix

least-squares procedures using the SHELXL-2015[33c] software package through OLEX2 suite.[33d]

2.4 | Hirshfeld surface calculations of copper (II) compound

Crystal Explorer 17.5[34a] progam package was employed to generate Hirshfeld surfaces[34b] and 2D fingerprint plots[34c] of **1** using its single crystal X-ray diffraction data. Hirshfeld Surface analysis is an important tool to study and locate intermolecular interactions within crystal packing.[34c,d] The function d$_{norm}$ is a ratio of the distances of any surface point to the nearest interior (d$_i$) and exterior (d$_e$) atom, and the van der Waals radii of the atoms.[35,36] The normalized contact distance (d$_{norm}$) could be expressed following the equation 1.

$$d_{norm} = \frac{d_i - r_i^{vdW}}{r_i^{vdW}} + \frac{d_e - r_e^{vdW}}{r_e^{vdW}} \tag{1}$$

Where, r$_e^{vdW}$ and r$_i^{vdW}$ denote the corresponding van der Waals radii of atoms. The negative value of d$_{norm}$ indicates that the sum of d$_i$ and d$_e$ is shorter than the sum of the relevant van der Waals radii, which is considered to be a closest contact and is visualized in red colour. The white colour denotes intermolecular distances close to van der Waals contacts with d$_{norm}$ equal to zero whereas contacts longer than the sum of van der Waals radii with positive d$_{norm}$ values are coloured with blue. A plot of d$_i$ versus d$_e$ is a fingerprint plot that identifies the presence of different types of intermolecular interactions.

2.5 | Aminophenol oxidation activity of copper (II) complex (1)

Aminophenol oxidation activity was studied by treating 1×10^{-4} M solution of Cu (II) complex with 1×10^{-3} M of 2-aminophenol (2-AP) solution in acetonitrile under aerobic conditions at room temperature. Absorbance vs. wavelength (wavelength scans) of the solution was monitored through spectrophometer at a regular time interval of 6 min for 1 hr in the wavelength range from 300–700 nm.[13,15]

Kinetic experiments were also carried out spectrophotometrically to specify the efficacy of catalytic oxidation of aminophenol by the Cu (II) complex in MeCN at 298 K.[13,15] 0.04 ml of the complex solution with a constant concentration of 1×10^{-4} M was added to 2 ml solution of 2-AP of a particular concentration (varying its concentration from 1×10^{-3} M to 1×10^{-2} M) to achieve the ultimate concentration as 1×10^{-4} M. The conversion

of 2-aminophenol to 2-aminophenoxazine-3-one was monitored with time at a wavelength 407 nm (time scan) in MeCN.[13,15,37,38] To determine the dependence of rate on substrate concentration, kinetic analyses were performed in triplicate.

The oxidized product was extracted by column chromatography. Neutral alumina was employed as column support and benzene-ethyl acetate solvent mixture was treated as an eluant mixture in this chromatographic separation. The purity of catalytic oxidation product of 2-AP was examined by proton NMR spectroscopy. ^{1}H NMR spectral analysis reveals to identify the final product. ^{1}H NMR data for 2-amino-3H-phenoxazine-3-one (APX), (CDCl$_3$, 400 MHz,) δ$_H$: 7.61 (m, 1H), 7.45 (m, 3H), 6.46 (s, 1H), 6.37 (s, 1H), 6.25 (s, 1H).

2.6 | Detection of presence of hydrogen peroxide in the catalytic oxidation of 2-aminophenol

The involvement of aerobic oxygen in the course of oxidative dimerization of 2-AP was examined by testing the presence of hydrogen peroxide following a reported procedure.[37,38] In the oxidation of aminophenol in MeCN, the solution was acidified with H$_2$SO$_4$ till the pH of the solution became 2. After a certain time, an equal volume of water was added to stop further oxidation. The phenoxazinone species were extracted three times with dichloromethane. 1 ml of 10% solution of KI and three drops of a 3% solution of ammonium molybdate were added to the aqueous layer. The formation of I$_3^-$ was monitored through spectrophotometer to examine the development of the characteristic I$_3^-$ band (λ$_{max}$ = 353 nm) which may be assignable to the production of hydrogen peroxide.

2.7 | Electro-chemical analysis

The electroanalytical instrument, BASi Epsilon-EC was employed for electrochemical experiments in CH$_2$Cl$_2$ solutions containing 0.2 M tetrabutylammonium hexafluorophosphate as supporting electrolyte. The BASi platinum working electrode, platinum auxiliary electrode, Ag/AgCl reference electrode were used for the measurements.

2.8 | Antimicrobial susceptibility studies

Antibacterial activity of the Cu (II) complex was tested against few clinical pathogenic bacteria by well plate and serial dilution method.

2.8.1 | Bacterial strains (clinical bacterial cultures), culture media

The antimicrobial property of the Cu (II) complex was examined against clinical *Staphylococcus aureus*, *Enterococcus* and *Klebsiella*. Microbial cultures were procured from government medical college from Tiruchirappalli, Tamil Nadu. Muller-Hinton agar media of Himedia Pvt. Bombay, India was used for the media for the microbial test. The antibacterial activity was evaluated by using the Himedia zone reader.

2.8.2 | Agar well diffusion method

The antibacterial activity of Cu (II)-Schiff base complex and a standard drug (Amikacin-100 mg/2 ml) was studied initially by using a well plate method. *Staphylococcus aureus*, *Enterococcus* and *Klebsiella pneumoniae* inoculums were prepared by using nutrient broth media. Double strength sterile Mueller Hinton agar media were prepared by autoclaving 7.6 gm in 100 ml. Inoculate the test microorganisms on the Mueller Hinton agar plates by using sterile cotton swabs. Formulations of Cu (II) complex and Amikacin were placed on agar well. Plates were incubated for 30 min at the refrigerator to diffuse the formulation into the agar plate, and finally, plates were again incubated at 37°C for 24 hr. Antibacterial activity was evaluated by using the Himedia zone reader.

2.8.3 | Determination of MIC and MBC for Cu (II) complex against clinical *Klebsiella pneumoniae*

The minimum inhibitory concentration (MIC) and minimum bactericidal concentration (MBC) was determined by selecting *Klebsiella pneumonia*. Among the three pathogenic bacteria, *Klebsiella pneumoniae* is a very well-known opportunistic pathogen that accounts for ~10% of nosocomial bacterial infections, including sepsis, pneumonia, urinary tract infections, and hepatic abscess. The organism can invade almost all part of the human body, although the most frequently affected urinary and respiratory tracts.

The method of micro-dilution was used to establish the antibacterial potential of the copper (II)-Schiff base complex and respective controls. A spectrophotometer (OD595 = 0.22) equivalent to 10^8 CFU/mL used to fix the bacterial cultures to 0.22 optical density at 595 nm. Different concentrations of Cu (II) complex and the respective controls in 2.0 ml centrifuge tubes at 37°C for

2 hr, were incubated with an inoculum of 10 μL of the above bacteria culture. Next, bacteria were diluted serially and placed 10 μL of each dilution on nutrient agar plates. Such plates were incubated overnight at 37°C, followed by a viable count of CFU bacteria.[39]

Preparation of stock solutions for MIC was done according to following equation 2.

$$= \frac{Weight\ of\ the\ powder\ (mg)}{\frac{Volume\ of\ solution\ (mL) \times Concentration\ (mg/L)}{The\ potency\ of\ powder\ (mg/g)}}$$

(2)

2.8.4 | Antimicrobial activity of Cu (II) complex using scanning electronic microscope

To examine the mode of action of Cu (II) complex on bacterial species, bacterial cultures were obtained from MIC and MBC samples and centrifuged. Thereafter, the bacterial cells were collected and sputter-coated with a thin layer of gold–palladium. The coated bacterial cells were fixed on a glass coverslip and observed under a scanning electron microscope.[40]

3 | RESULTS AND DISCUSSION

3.1 | Synthesis and formulation of the Schiff base (HL) and copper (II) complex(1)

The tridentate Schiff base was prepared by refluxing *o*-aminophenol with *o*-anisaldehyde in 1:1 mole ratio in ethanol. The synthetic route is given in Scheme 1. The Cu (II) complex was synthesized by adding copper (II) acetate to HL in 2:3 mole ratio in methanol-acetonitrile under slow stirring on magnetic stirrer. Different ratio of Cu (II) acetate and HL was also used to produce copper (II) complex of varied nuclearity, however same molecular composition,[Cu(L)₂] was observed in each cases. Replacement of copper (II) acetate by

hydrated copper (II) chloride also produced same Cu (II) complex. Single crystal form of the Cu (II) complex was obtained by slow evaporation of reaction mixture at room temperature. This Cu (II) complex is highly soluble in polar solvents like methanol, acetonitrile, chloroform etc.

3.2 | Description of crystal structure

X-ray structural analysis indicates that the Cu (II) complex crystallizes in a cubic crystal system with *I*a-3d space group. The thermal ellipsoidal plot of Cu (II) complex is shown in Figure 1. The structural refinement parameter for this Cu (II) complex is presented in Table 1. The bond angles and bond distances are given in Table 2. Two units of HL coupled with one Cu (II) ion and lead to mononuclear Cu (II) complex of inner-metallic chelate of first order. In accordance with the disposition of coordination centres around metal centre as well as M-L bond angle values, it is confirmed that the Cu (II) centre adopts an irregular six coordinate geometry. The coordination geometry of copper (II) ion is described as tetragonal bipyramidal geometry. Close inspection on coordination geometry suggests that Cu (II) centre forms a tetragonal plane based on O1,O1, N1,O2 and bipyramidal geometry appears from apical existence of two donor sites, N1 and O2.
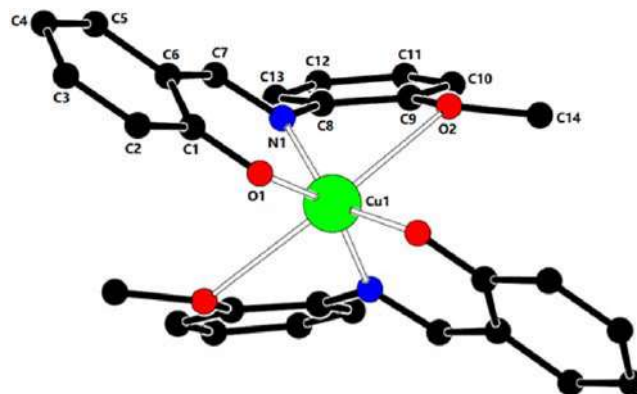
FIGURE 1 X-ray structure of the copper (II)-Schiff base complex with 30% ellipsoid probability
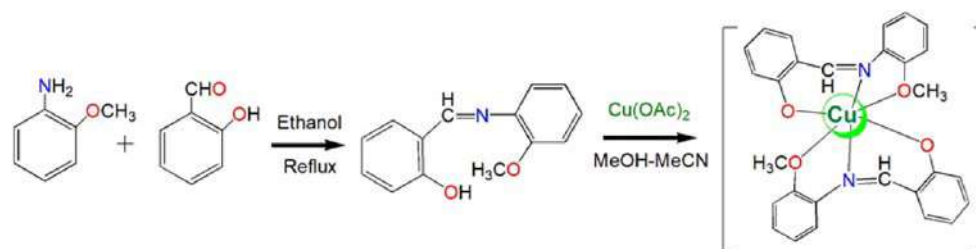
SCHEME 1 Synthetic route for the formation of 1

TABLE 1 Crystallographic data and structure refinement parameters for **1**

Parameters	1
Empirical formula	$C_{28}H_{24}N_2O_4Cu$
Formula weight	516.03
Temperature (K)	296
Crystal system	Cubic
Space group	$Ia\text{-}3d$
a (Å)	31.2952(17)
b (Å)	31.2952(17)
c (Å)	31.2952(17)
Volume (Å^3)	30,650(3)
Z	48
ρ (gcm^{-3})	1.571
μ (mm^{-1})	0.890
F (000)	12,816
R_{int}	0.179
θ ranges ($^\circ$)	2.4–32.9
Number of unique reflections	4,617
Total number of reflections	69,708
Final R indices	0.0984, 0.3585
Largest peak and hole (eA$^{\circ-3}$)	1.38, −0.34

TABLE 2 Bond angles and bond distances value of Cu (II) complex

Bond distances			
Cu1-O1	**1.903(4)**	**Cu1-O2**	**2.727(4)**
Cu1-N1	1.981(4)	Cu1-O1a	1.903(4)
Cu1-O2a	2.727(4)	Cu1-N1a	1.981(4)
Bond angles		O11-Fe2-O3	94.9(3)
O1-Cu1-O2	128.81(15)	O1-Cu1-N1	93.62(17)
N1-Cu1-O1a	88.84(18)	O1-Cu1-O2a	88.74(15)
O1-Cu1-N1a	149.01(17)	O2-Cu1-N1	65.86(14)
O1a-Cu1-O2	88.74(15)	O2-Cu1-O2a	129.91(11)
O2-Cu1-N1a	82.15(14)	O1a-Cu1-N1	149.01(17)
O2a-Cu1-N1	82.15(14)	N1-Cu1-N1a	99.77(16)
O1a-Cu1-O2a	128.81(15)	O1a-Cu1-N1a	93.62(17)
O2a-Cu1-N1a	65.86(14)		

3.3 | Hirshfeld analysis of copper (II)-Schiff base complex

Crystal Explorer software was employed to demonstrate the Hirshfeld surface of Cu (II) complex (Figure S5) over a definite d_{norm}. The surface volume is calculated as 628.31 Å^3 and surface area is determined as 491.0 Å^2. The red highlighted area shows the d_{norm} area and close non-covalent interactions of **1** with its surrounding within the 3D crystal. Percentage share of each element in close interaction with others is given in Table S1. In this d_{norm}, the blue area is showing the weak C-H···π interactions between aromatic H attached to aromatic C and aromatic rings of the ligands. Red area indicates very weak intermolecular C-H···O H-bonding between C-H of benzene ring and O of OPh/OCH$_3$. This molecule is interacted by surrounding molecules through C-H···O hydrogen bond, and C-H···π interactions as display in Fingerprint plots (Figure S6). Quantitative information of different intermolecular interactions by each pair of elements is given in Table S1.

3.4 | Solution property of the Schiff base and copper (II) complex

The electronic transitions for the Schiff base and its Cu (II) complex were recorded in acetonitrile medium (MeCN) from 200 to 900 nm at room temperature. The Schiff base, H**L** displayed electronic transitions at 230, 270 nm and 346 nm and the Cu (II) complex exhibited electronic bands at 238, 283 and 400 nm. The electronic spectra are displayed in Figure S2. Electronic bands at 230, 270 and 346 nm in the UV region for the Schiff base may be attributed to $\pi \rightarrow \pi^*$ and $n \rightarrow \pi^*$ electronic transitions.[41] The appearance of electronic bands at 238 and 283 nm may be corresponded to $\pi \rightarrow \pi^*$ and $n \rightarrow \pi^*$ electronic transitions of ligand origin[41] while the optical band at 400 nm may be assigned as phenoxo to Cu (II) ion electronic transition.[42b,c]

The electrolytic behaviour of the Cu (II) complex has been checked through measurement of molar conductivity in MeCN medium at room temperature. The molar conductance value was recorded for 1.15×10^{-3} M solution of **1** as 05 Sm^{2}mol^{-1}. The molar conductance value suggests about the non-electrolytic nature of the Cu (II) complex in MeCN medium.[43]

3.5 | Phenoxazinone synthase mimicking activity of the copper (II) complex (1)

The oxidation of 2-aminophenol (2-AP) was studied by addition of catalytic amount of copper (II) complex (1×10^{-4} M) to 2-AP (1×10^{-3} M) under aerobic atmosphere at 25°C (Scheme 2).

The changes of absorbance in the course of catalysis were monitored through a UV–Vis spectrophotometer. The wavelength scan was recorded for 1 hr with a time
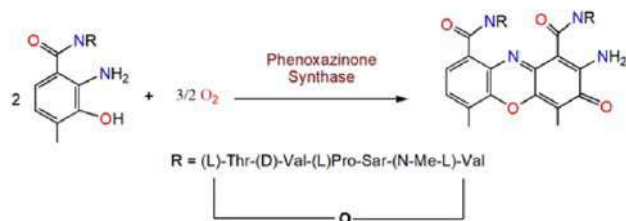
SCHEME 2 Catalytic oxidation of substituted aminophenol by phenoxazinone synthase

interval of 5 min (Figure 2). The substrate, 2-AP exhibits a characteristic single electronic transition at 267 nm in MeCN and indicates its high purity in solution. Addition of the solution of Cu (II) complex to the solution of 2-AP in MeCN, the optical band corresponding to phenoxo to Cu (II) electronic transition at 400 nm was initiated to exhibit a bathochromic shift. As a result, a new electronic band at 407 nm with
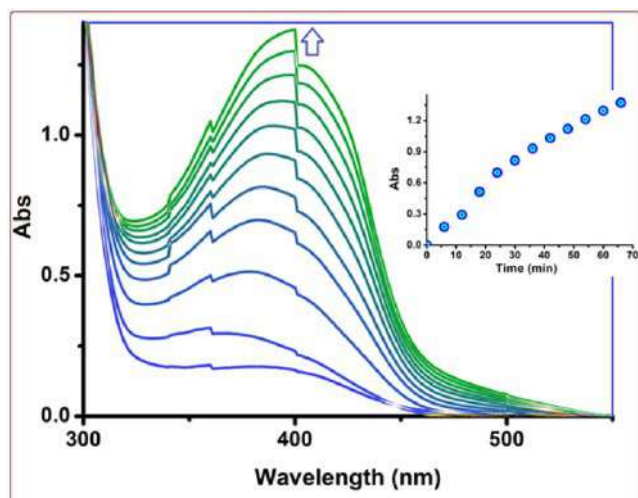
FIGURE 2 Development of new electronic band at 407 nm upon addition of Cu (II) complex to of 2-AP in MeCN. (The spectra are recorded after every 6 min). Inset: Time vs Absorbance plot at defined wavelength

increasing absorbance was developed (Figure 2). Switching of the electronic band from 400 nm to 407 nm is a definite signature for the oxidation of 2-AP in MeCN.[13,15,44] This spectrophotometric evidence may correspond to the development of aminophenoxazinone species in solution.

The kinetics for the oxidative coupling of 2-AP was also carried out to understand the catalytic efficacy of the copper (II) catalyst. The method of initial rates was followed to unveil the kinetic parameter of this oxidative dimerization of 2-AP. The growth of oxidation product was monitored at 407 nm as a function of time (Figure S7).[13,15,37,38,44] The rate constants vs. substrate concentration displayed the nature of kinetics (Figure S7). The first order saturation kinetics reveals that Michaelis–Menten model seems to be applicable in this case and may be presented according to the following equation 3:

$$V = \frac{V_{\max}[S]}{K_M + [S]} \tag{3}$$

Where, V is rate of the reaction, K_m is denoted as Michaelis–Menten constant, $V_{\max}$ is the maximum velocity of the reaction, and $[S]$ is concentration of the substrate.

The values of kinetics parameters were determined from Michaelis–Menten equation as $V_{\max}$ $(MS^{-1}) = 1.49 \times 10^{-5}$; $K_M = 9.46 \times 10^{-4}$ [Std. Error for $V_{\max}$ $(MS^{-1}) = 2.55 \times 10^{-6}$; Std. Error for K_m (M) = 1.72×10^{-5}].

A comparison of catalytic oxidation of 2-AP by this Cu (II) complex with some other reported Cu (II) complexes is tabulated in Table 3.[26c,45–47] The catalytic efficiency for the oxidative dimerization of 2-AP by this Cu (II) complex was found high as $k_{\text{cat}}/K_M = 5.67 \times 10^5$.

TABLE 3 Comparison of k_{cat} (h^{-1}) values for catalytic oxidation of 2-AP by reported copper (II) compounds and **1**

Complex	k_{cat} (h^{-1})(Solvent)	CCDC No	Ref
[L^{1}Cu(μ-Cl)$_2$CuL^1]	1,065 (CH$_3$OH)	1,572,023	[45]
	213 (CH$_3$CN)		
[Cu$_4$(L^2)$_4$]	86.3 (CH$_3$OH)	1,507,035	[46]
[Cu$_4$(L^3)$_4$]	340.26 (CH$_3$OH)	1,507,036	[46]
[Cu$_2$(L^4)$_3$]	78.14 (CH$_3$OH)	1,957,033	[26c]
[Cu(2,2′-bpy)Cl$_2$]	2.08 × 10^3(CH$_3$OH)	1,524,681	[15c]
[Cu(2,2′-bpy)$_2$(OAc)] $^+$	1.83 × 10^3 (CH$_3$OH)	1,513,638	[47]
[Cu(**L**)$_2$]	5.364 × 10^2 (CH$_3$CN)	1,957,033	This work

L^1 = 2-(a-Hydroxyethyl)benzimidazole (Hhebmz), L^2 = (E)-4-Chloro-2-((thiazol-2-ylimino)methyl)phenol, L^3 = (E)-4-Bromo-2-((thiazol-2-ylimino)methyl)phenol, L^4 = (Z)-2-methoxy-6-(((2-methoxyphenyl)imino) methyl)phenol].

Electrochemical analysis and EPR studies were vperformed to understand the catalytic behaviour of Cu (II) complex in the oxidative dimerization of 2-AP in acetonitrile medium. The cyclic voltammogram of the Cu (II) complex was recorded in dichloromethane medium at 298 K where N-tetrabutylammonium hexafluorophosphate was employed to record the electrochemical data in aerobic environment and shown in Figure 3. The Cu (II)-Schiff base complex displays one irreversible cathodic wave at −0.94 V which is assignable to electron transfer in Cu^{2+} to Cu^+ redox couple in solution phase. The active participation of copper (II) centre in catalytic oxidation of 2-AP is confirmed by measurement of redox potentials of Cu (II) complex in presence of 2-AP under identical reaction conditions.

The mixture of copper (II) complex in presence of 2-AP produces irreversible cathodic peak at −1.11 V due to Cu^{2+} to Cu^+ redox couple i.e. the peak shifted from −0.94 to −1.11 V due to co-ordination of 2- AP to the Cu^{2+} centre of the complex. Furthermore, two new peaks at −0.15 and 0.46 V appeared which were assigned to the development of $AP^-/AP^{\bullet-}$ and $AP^{\bullet-}/IQ$ redox couples. The redox potential data strongly suggests the course of 2-AP oxidation undergoes through iminobenzoquinone radical formation. To view more insights of this copper (II) complex mediated oxidative coupling of 2-AP, EPR spectra of the Cu (II) complex in presence and absence of 2-AP are recorded in MeCN and presented in Figure 4.

The EPR spectrum of copper (II) complex (**1**) with X-band frequency at room temperature in MeCN medium displays four line hyperfine spectra at g = 2.12 due to presence of ^{63}Cu nuclei with $I = 3/2$.[13,15] and the calculated EPR spectrum for the Cu (II)-Schiff base resembles very well as evident from the simulated g value, 2.1262 (Figure 4). The mixture of copper complex in presence of 2-AP is EPR silent due to antiferromagnetic coupling
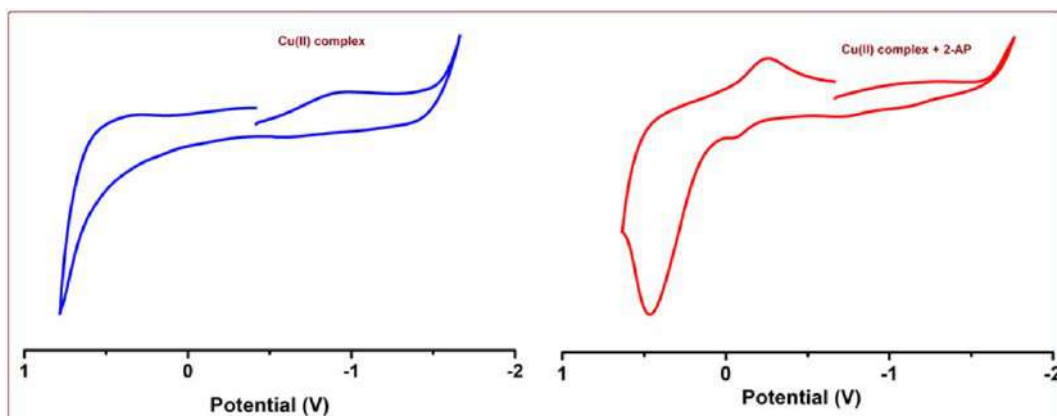
FIGURE 3 Left: Cyclic voltammogram of the Cu (II)-Schiff base complex in anhydrous DCM medium; Right: Cyclic voltammogram of Cu (II) complex in presence of 2-AP under molecular oxygen atmosphere in anhydrous DCM in CH2Cl2 (0.20 M [N(n − Bu)4]PF6) at 295 K
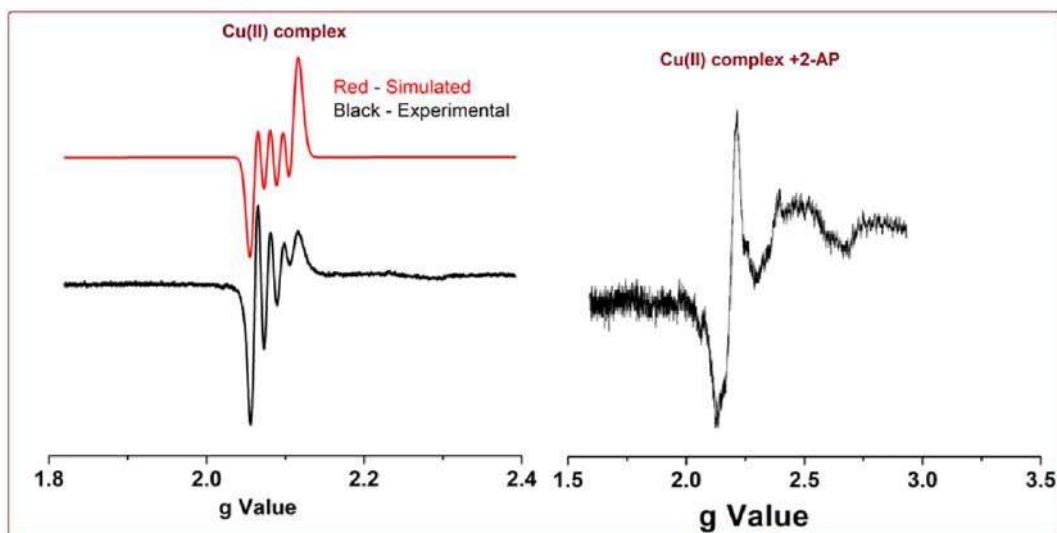
FIGURE 4 X- band EPR spectra of the copper (II)-Schiff base in presence of 2-AP after 20 min in CH3CN solution at 298 K

between $Cu^{2+}(S = 1/2)$ with iminobenzosemiquinonate anion radical. The EPR spectral analysis of the copper complex in presence of 2-AP in acetonitrile at room temperature strongly suggests the generation of radical species for the appearance of additional signal at g ca 2.057 (Figure 4). The reported g value for oxidised 2-AP radical (iminobenzoquinone) is 2.0051 in 10^{-1} M Bu_4NPF_6.[15c,26]

Furthermore, electrospray ionization (ESI) mass spectrum of the copper (II)-Schiff base complex in presence of 2-AP is recorded after mixing of 10 min to reveal the binding aspects of the copper (II) complex and 2-AP. It was observed that the ESI-Ms of the reaction mixture (Figure S8) exhibits the base peak at m/z 213.12 which is assignable to the presence of aminophenoxazinone species, [(2-amino-3H-phenoxazine-3-ones) + H+]. Appearance of another important peak at m/z 624.81 corresponds to the formation of adduct between copper (II)-Schiff base complex and 2-AP, [[1 + (2-AP)] + H+]. The experimental m/z values correlate well with the theoretical m/z values. In this context, involvement of molecular oxygen in the course of oxidation of 2-AP was tested through production of hydrogen peroxide in solution using a reported method.[37,38] No spectral band at λ_{max} 353 nm corresponds to generation of hydrogenperoxide was observed throughout the course of catalysis and ensure the presence of water as a byproduct appeared from molecular oxygen.

Previously study by P. Chaudhury and co-workers[48] presented tetracopper complex as a bio-mimetic model towards 2-AP oxidation and recommends an "on–off"

mechanism via radical generation in active participation with the metal centres favouring 6e oxidative coupling of substrate. T.P. Begley and co-workers[49] suggests the production of 2-aminophenoxazinone through a sequence of three consecutive 2e oxidation of 2-AP. The tautomerization reactions were the controlling unit in regeneration of the 2-Ap during this course of catalytic oxidation reaction. Based upon the outcomes observed by different analytical methods like electrochemical, EPR and ESI-MS, a plausible mechanism is proposed in Scheme 3. So, oxidative dimerization of 2-AP undergoes through formation of catalyst-substrate intermediate in the primary stage. Subsequently, Cu centre activates molecular oxygen to produce water as a byproduct and iminobenzosemiquinonate radical in the course of catalytic oxidation. Iminobenzosemiquinonate radical proceeds to couple with another unit of 2-AP and develop aminophenoxazinone species as a final product.

3.6 | Antibacterial activity of the cu (II)-Schiff base complex

The antibacterial activity of Cu (II) complex was assessed through the method of well diffusion against the bacteria *Staphylococcus aureus*, *Enterococcus* and *Klebsiella pneumoniae*. The results of the inhibition zone diameters shown in Table S2. The therapeutic efficiency of this Cu (II) complex was determined by calculating MIC and MBC on *Klebsiella pneumoniae* (Table S3). *MIC and MBC values were determined as 1.250 mg/ml, 0.625 mg/ml for*
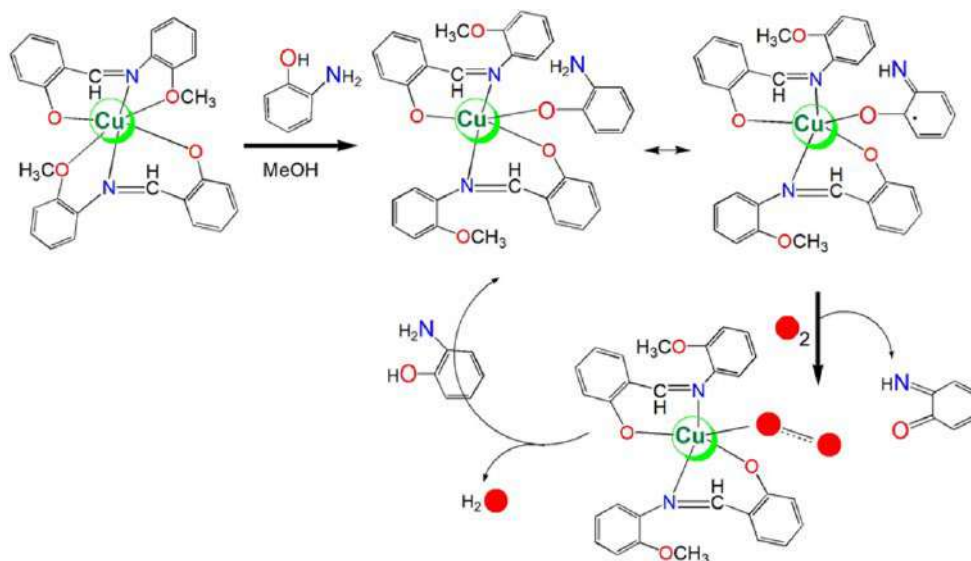
SCHEME 3 Plausible mechanism for the catalytic oxidation of 2-AP
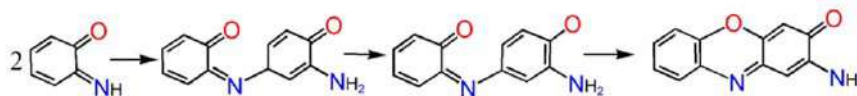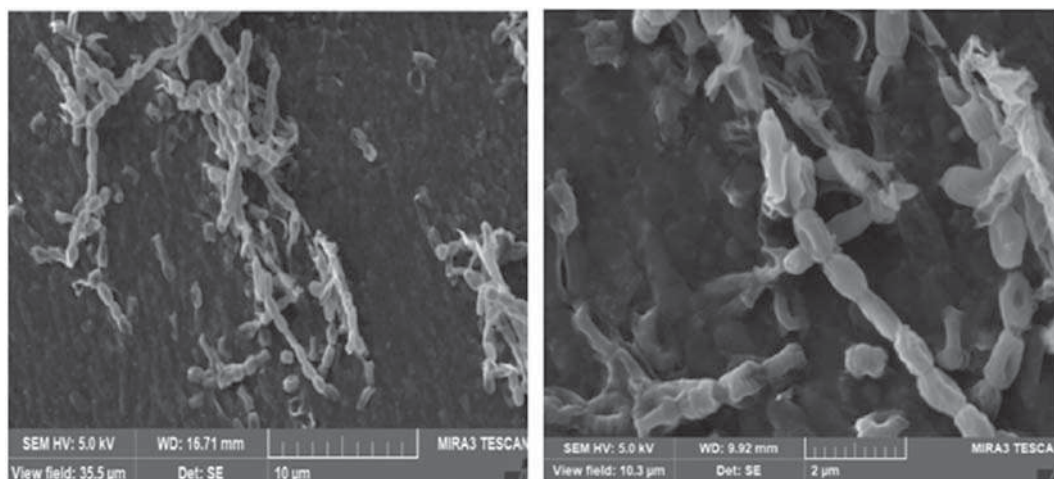
FIGURE 5 Electron microscope scans showing morphological changes in pathogenic bacteria. Destruction of the bacterial cell membrane (MIC) and B growth of bacteria (MBC)

this Cu (II)-Schiff base complex. Scientific literatures suggest that the Cu (II) complex is quite competent to inhibit the growth of pathogenic bacterial species. Aiming to explore the origin of antibacterial property for this copper (II)-Schiff base complex, a study involving the exposure of Cu (II) complex on *Klebsiella pneumoniae* was carried out employing scanning electron microscope (SEM) analysis. SEM image of the *Klebsiella pneumoniae* in presence of Cu (II) complex accounts on the change of morphology on the cell wall. The recorded SEM micrographs of *Klebsiella pneumonia* cells are shown in Figure 5.

Commonly, MBC of *Klebsiella pneumonia* was observed as typical rod-shape with smooth and intact cell walls. Although, the number of *Klebsiella pneumonia* was remarkably decreased, and cell walls became wrinkled and damaged after addition of Cu (II) complex to *Klebsiella pneumonia*.[50,51] In reality, in limited cases, such type of observations were noted and will definitely bring some hope in developing suitable therapeutic agents.

4 | CONCLUSIONS

This research study provides an overview of synthesis, X-ray structural characterization, Hirshfeld surface analysis and bio-mimetic oxidation of 2-AP as well as antibacterial activity of a newly synthesized copper (II)-Schiff base complex, [Cu(**L**)$_2$] (**1**). X-ray structure of the Cu (II) complex shows that the Cu (II) centre adopts an unprecedented tetragonal bipyramidal geometry in its crystalline phase. The copper (II) complex has been evaluated as a bio-inspired catalyst towards oxidative coupling of 2-AP in acetonitrile

and exhibits good catalytic activity with turnover number, 536.4 h^{-1}. In view of mechanistic insights, electrochemical analysis of the Cu (II) complex in presence of 2-AP was carried out and indicates the generation of AP$^-$/AP$^{\bullet-}$ and AP$^{\bullet-}$/IQ redox couple in the course of catalysis. EPR spectral analysis of the reaction mixture confirms the existence iminobenzosemiquinone radical at g = 2.057 which suggests the radical driven catalytic oxidation of 2-AP. Furthermore, ESI-MS analysis of the Cu (II) complex in presence of 2-AP ensures that the catalytic oxidation of 2-AP proceeds through the formation of enzyme-substrate adduct. Antibacterial property of the copper (II) complex has been examined against different pathogenic bacteria. Scanning electron microscope images reveal that destruction of bacterial cell membrane remains the driving force for the development of potential antibacterial properties of the copper (II)-Schiff base complex. Importantly, this Schiff base ligand can able to isolate Cu (II) ion in an intermediate coordination geometry (tetragonal bipyramidal geometry) and represents a rare example of unprecedented coordination geometry which is controlled by steric factors of the Schiff base ligand.

ORCID

Bhaskar Biswas https://orcid.org/0000-0002-5447-9729

REFERENCES

[1] Y. Ruan, X. Jia, C. Wang, W. Zhen, X. Jiang, *ACS Biomater. Sci. Eng.* **2019**, *5*, 1016.

[2] A. S. Smirnov, L. M. D. R. S. Martins, D. N. Nikolaev, R. A. Manzhos, V. V. Gurzhiy, A. G. Krivenko, K. O. Nikolaenko, A. V. Belyakov, A. V. Garabadzhiu, P. B. Davidovich, *New J. Chem.* **2019**, *43*, 188.

[3] W. Al Zoubi, Y. G. Ko, *Appl. Organomet. Chem.* **2016**, *31*, e3574.

[4] D.-D. Li, E. Yagüe, L.-Y. Wang, L.-L. Dai, Z.-B. Yang, S. Zhi, N. Zhang, X.-M. Zhao, Y.-H. Hu, *ACS Med. Chem. Lett.* **2019**, *9*, 1328.

[5] X. Li, K. Du, J. Sun, F. Feng, *ACS Appel. Bio. Mat.* **2020**, *3*, 654.

[6] M. K. Ghosh, S. Pathak, T. K. Ghorai, *ACS Omega* **2019**, *4*, 16068.

[7] Y. Fan, J. Zhang, M. Shi, D. Li, C. Lu, X. Cao, C. Peng, S. Mignani, J.-P. Majoral, X. Shi, *Nano Lett.* **2019**, *19*, 1216.

[8] E. I. Solomon, D. E. Heppner, E. M. Johnston, J. W. Ginsbach, J. Cirera, M. Qayyum, M. T. Kieber-Emmons, C. H. Kjaergaard, R. G. Hadt, L. Tian, *Chem. Rev.* **2014**, *114*, 3659.

[9] E. I. Solomon, M. J. Baldwin, M. D. Lowery, *Chem. Rev.* **1992**, *92*, 521.

[10] (a) E. I. Solomon, B. L. Hemming, D. E. Root, *Electronic Structures of Active Sites in Copper Proteins: Coupled Binuclear and Trinuclear Cluster Sites in Bioinorganic chemistry of copper*, (K. D. Karlin, Z. Tyeklár), Chapman & Hall Publishing House, New York, USA, **1993**, doi:https://doi.org/10.1007/978-94-011-6875-5

[11] C. Mukherjee, U. Pieper, E. Bothe, V. Bachler, E. Bill, T. Weyhermüller, P. Chaudhuri, *Inorg. Chem.* **2008**, *47*, 8943.

[12] (a) J.L. McLain, J. Lee, J. T. Groves, in *Biomimetic Oxidations Catalyzed by Transition Metal Complexes*, (Ed.: Meunier B.), Imperial College Press, London; (b) F. Benedini, G. Galliani, M. Nali, B. Rindone, S. Tollari, *J. Chem. Soc. Perkin Trans.* **1985**, *2*, 1963; (c) K. D. Karlin, Z. Tyeklár, A. Farooq, M. S. Haka, P. Ghosh, R. W. Cruse, Y. Gultneh, J. C. Hayes, P. J. Toscano, J. Zubieta, *Inorg. Chem.* **1991**, *31*, 1436.

[13] (a) L. I. Simándi, S. Németh, N. Rumlis, *J. Mol. Catal.* **1987**, *42*, 357; (b) Z. Szeverenyl, E. R. Mileava, L. I. Simándi, *J. Mol. Catal.* **1991**, *67*, 251; (c) G. C. Paul, K. Das, S. Maity, S. Begum, H. K. Srivastava, C. Mukherjee, *Inorg. Chem.* **2018**, *58*, 1782.

[14] (a) S. Dutta, J. Mayans, A. Ghosh, *Dalton Trans.* **2020**, *49*, 1276; (b) A. Begum, A. H. Sheikh, G. Moula, S. Sarkar, *Sci. Rep.* **2017**, *7*, 1; (c) B. Mondal, A. Dey, *Chem. Commun.* **2017**, *53*, 7707; (d) I. Ghosh, S. Banerjee, S. Paul, T. Corona, T. K. Paine, *Angew. Chem., Int. Ed.* **2019**, *58*, 12534; (e) A. Sarkar, A. Chakraborty, A. Adhikary, S. Maity, A. Mandal, D. Samanta, P. Ghosh, D. Das, *Dalton Trans.* **2019**, *48*, 14164.

[15] (a) N. C. Jana, M. Patra, P. Brandão, A. Panja, *Inorg. Chim. Acta* **2019**, *490*, 163; (b) S. Thakur, S. Banerjee, S. Das, S. Chattopadhyay, *New J. Chem.* **2019**, *43*, 18747; (c) M. Garai, D. Dey, H. R. Yadav, A. R. Choudhury, M. Maji, B. Biswas, *ChemistrySelect* **2017**, *2*, 11040; (d) A. De, M. Garai, H. R. Yadav, A. R. Choudhury, B. Biswas, *Appl. Organomet. Chem.* **2017**, *31*, e3551.

[16] (a) C. C. L. McCrory, S. Jung, I. M. Ferrer, S. M. Chatman, J. C. Peters, T. F. Jaramillo, *J. Am. Chem. Soc.* **2015**, *137*, 4347;

(b) D. Li, H. Baydoun, C. N. Verani, S. L. Brock, *J. Am. Chem. Soc.* **2016**, *138*, 4006.

[17] S. Sakaue, T. Tsubakino, Y. Nishiyama, Y. Ishii, *J. Org. Chem.* **1993**, *58*, 3633.

[18] J. Kaizer, R. Csonka, G. Speier, *J. Mol. Catal. A: Chem.* **2002**, *180*, 91.

[19] T. Horváth, J. Kaizer, G. Speier, *J. Mol. Catal. A: Chem.* **2004**, *215*, 9.

[20] M. R. Maurya, S. Sikarwar, T. Joseph, S. B. Halligudi, *J. Mol. Catal. A: Chem.* **2005**, *236*, 132.

[21] K. Anzai, K. Isono, K. Ohkuma, S. Suzuki, *J. Antibiot.* **1960**, *13*, 125.

[22] A. Iwata, T. Yamaguchi, K. Sato, R. Izumi, A. Tomoda, *Tohoku J. Exp. Med.* **2003**, *200*, 161.

[23] Y. Igarashi, K. Takagi, T. Kajiura, T. Furumai, T. Oki, *J. Antibiot.* **1998**, *51*, 915.

[24] T. Schimamoto, A. Tomoda, R. Ishida, K. Ohyashiki, *Clin. Cancer Res.* **2001**, *7*, 704.

[25] S. Shimizu, M. Suzuki, A. Tomoda, S. Arai, H. Taguchi, T. Hanawa, S. Kamiya, *Tohoku J. Exp. Med.* **2004**, *203*, 47.

[26] (a) P. Dorrestein, T. P. Begley, *Bioorg. Chem.* **2005**, *33*, 136; (b) P. Mahapatra, S. Ghosh, S. Giri, V. Rane, R. Kadam, M. G. B. Drew, A. Ghosh, *Inorg. Chem.* **2017**, *56*, 5105; (c) P. K. Mudi, N. Bandopadhyay, M. Joshi, M. Shit, S. Paul, A. R. Choudhury, B. Biswas, *Inorg. Chim. Acta* **2020**, *505*; 119468.

[27] C. Eggert, *Microbiol. Res.* **1997**, *152*, 315.

[28] M. A. Hughes, M. J. Baggs, J. Al-Dulayymi, M. S. Baird, P. A. Williams, *Appl. Environ. Microbiol.* **2002**, *68*, 4965.

[29] C. Duncan, A. R. White, *Metallomics* **2012**, *4*, 127.

[30] J. Zhang, D. Duan, J. Xu, J. Fang, *ACS Appl. Mat. Interfer.* **2018**, *10*, 33010.

[31] K. Y. Djoko, M. M. Goytia, P. S. Donnelly, M. A. Schembri, W. M. Shafer, A. G. McEwan, *Antimicrob. Agents Chemother.* **2015**, *59*, 6444.

[32] (a) M. Garai, A. Das, M. Joshi, S. Paul, M. Shit, A. R. Choudhury, B. Biswas, *Polyhedron* **2018**, *156*, 223; (b) D. Dey, G. Kaur, A. Ranjani, L. Gayathri, P. Chakraborty, J. Adhikary, J. Pasan, D. Dhanasekaran, A. R. Choudhury, M. A. Akbarsha, N. Kole, B. Biswas, *Eur. J. Inorg. Chem.* **2014**, *2014*, 3350; (c) D. Dey, G. Kaur, M. Patra, A. R. Choudhury, N. Kole, B. Biswas, *Inorg. Chim. Acta* **2014**, *421*, 335; (d) C. K. Pal, S. Mahato, M. Joshi, S. Paul, A. R. Choudhury, B. Biswas, *Inorg. Chim. Acta* **2020**, *506*, 119541.

[33] (a) CrysAlisPro 1.171.39.35c, (**2017**) Rigaku Oxford Diffraction, *Rigaku Corporation*: Tokyo, Japan; (b) G. M. Sheldrick, *Acta Cryst.* **2015**, *A71*, 3; (c) G. M. Sheldrick, *Acta Cryst.* **2015**, *C71*, 3; (d) O. V. Dolomanov, L. J. Bourhis, R. J. Gildea, J. A. K. Howard, H. Puschmann, *J. Appl. Cryst.* **2009**, *42*, 339.

[34] (a) M. J. Turner, J. J. McKinnon, S. K. Wolff, D. J. Grimwood, P. R. Spackman, D. Jayatilaka, M. A. Spackman, Crystal Explorer, University of Western Auestralia, http://hirshfeldsurface.net17 (**2017**); (b) M. A. Spackman, D. Jayatilaka, *CrystEngCom.* **2009**, *11*, 19; (c) S. K. Seth, V. S. Lee, J. Yana, S. M. Zain, A. C. Cunha, V. F. Ferreira, A. K. Jordao, M. C. B. V. de Souza, S. M. S. V. Wardell, J. L. Wardellf, E. R. T. Tiekink, *Cryst. Eng. Comm.* **2015**, *17*, 2255; (d) M. N. Ahamad, M. Kumar, A. Ansari, I. Mantasha, M. Ahmad, M. Shahid, *New J. Chem.* **2019**, *43*, 14074.

[35] (a) M. A. Spackman, D. Jayatilaka, *Cryst. Eng. Comm.* **2009**, 1119; (b) M. A. Spackman, J. J. McKinnon, *Cryst. Eng. Comm.* **2002**, *4*, 378.

[36] H. Yamatera, *Acta Chem. Scand. A* **1979**, *33*, 107.

[37] C. K. Pal, S. Mahato, H. R. Yadav, M. Shit, A. R. Choudhury, B. Biswas, *Polyhedron* **2019**, *174*, 114156.

[38] D. Dey, S. Das, H. R. Yadav, A. Ranjani, L. Gyathri, S. Roy, P. S. Guin, D. Dhanasekaran, A. R. Choudhury, M. A. Akbarsha, B. Biswas, *Polyhedron* **2016**, *106*, 106.

[39] A. Anwar, A. Masri, K. Rao, K. Rajendran, N. A. Khan, M. R. Shah, R. Siddiqui, *Sci. Rep.* **2019**, *9*, 3122.

[40] F. M. W. Nongkhlaw, S. R. Joshi, *J. Microsc. Ultrastruct.* **2017**, *5*, 132.

[41] B. Chowdhury, M. Karar, S. Paul, M. Joshi, A. R. Choudhury, B. Biswas, *Sens. Actuators, B* **2018**, *276*, 560.

[42] (a) A. De, D. Dey, H. R. Yadav, M. Maji, V. Rane, R. M. Kadam, A. R. Choudhury, B. Biswas, *J. Chem. Sci.* **2016**, *128*, 1775; (b) S. Khan, S. Herrero, R. González-Prieto, M. G. B. Drew, S. Banerjee, S. Chattopadhyay, *New J. Chem.* **2018**, *42*, 13512; (c) T. M. Rajendiran, R. Kannappan, R. Mahalakshmy, J. Rajeswari, R. Venkatesan, P. Rao, *Transition Met. Chem.* **2003**, *28*, 447.

[43] W. J. Geary, *Coord. Chem. Rev.* **1971**, *7*, 81.

[44] B. Chowdhury, B. Bhowmik, A. Sahu, M. Joshi, S. Paul, A. R. Choudhury, B. Biswas, *J. Chem. Sci* **2018**, *130*, 161.

[45] A. K. Ghosh, A. Ali, Y. Singh, C. S. Purohit, R. Ghosh, *Inorg. Chim. Acta* **2018**, *474*, 156.

[46] S. Sagar, S. Sengupta, A. J. Mota, S. K. Chattopadhyay, A. E. Ferao, E. Riviere, W. Lewis, S. Naskar, *Dalton Trans.* **2017**, *46*, 1249.

[47] B. Chowdhury, M. Maji, B. Biswas, *J. Chem. Sci.* **2017**, *129*, 1627.

[48] C. Mukherjee, T. Weyhermüller, E. Bothe, E. Rentschler, P. Chaudhuri, *Inorg. Chem.* **2007**, *46*, 9895.

[49] (a) C. E. Barry III, P. G. Nayar, T. P. Begley, *Biochemistry* **1989**, *28*, 6323; (b) C. E. Barry III, P. G. Nayar, T. P. Begley, *J. Am. Chem. Soc.* **1988**, *110*, 3333; (c) J. C. Freeman, P. G. Nayar, T. P. Begley, J. J. Villafranca, *Biochemistry* **1993**, *32*, 4826.

[50] A. Reyes-Jara, N. Cordero, J. Aguirre, M. Troncoso, G. Figueroa, *Front. Microbiol.* **2016**, *7*.

[51] H. Li, Q. Chen, J. Zhao, K. Urmila, *Sci. Rep.* **2015**, *5*.

SUPPORTING INFORMATION

Additional supporting information may be found online in the Supporting Information section at the end of this article.

Source details

Feedback >   Compare sources >

Applied Organometallic Chemistry

Scopus coverage years: from 1987 to Present

Publisher: Wiley-Blackwell

ISSN: 0268-2605   E-ISSN: 1099-0739

Subject area: (Chemistry: Inorganic Chemistry) (Chemistry: General Chemistry)

Source type: Journal

View all documents >   Set document alert   🖫 Save to source list

CiteScore 2022	ⓘ
7.3	

SJR 2022	ⓘ
0.518	

SNIP 2022	ⓘ
0.782	

CiteScore   CiteScore rank & trend   Scopus content coverage

Rhodium(III) complexes of 1-Alkyl-2-{(o-thioalkyl) phenylazo} imidazoles: synthesis, structure, spectral characterization, DNA binding study and DFT calculation

Dibakar Sardar[1] · Papia Datta[2] · Chittaranjan Sinha[3]

Abstract

The Rh(III) complexes of 1-alkyl-2-{(o-thioalkyl)phenylazo}imidazole (SRaaiNR′, **1**; R = R′ = Me (**a**); R = Me, R′ = Et (**b**); R = Et, R′ = Me (**c**); R = R′ = Et (**d**)), [Rh(SRaaiNR′)(PPh₃)Cl₂](ClO₄) (**2**) have been synthesized. The complexes have been characterized by physicochemical and spectroscopic methods. The single-crystal X-ray diffraction study authenticates the structure of [Rh(SMeaaiNEt)(PPh₃)Cl₂](ClO₄) (**2b**). The DNA binding ability of the complexes has been investigated by electronic absorption and fluorescence spectroscopic methods. Density functional theory computation technique has been used to enlighten the electronic structures and their spectral properties.

Introduction

The study of the interaction of transition metal complexes with DNA plays a significant role in the development of anticancer drugs [1–5]. Owing to the large diversity in structure, binding modes and flexible ligand exchange kinetics, metal complexes provide much scope for the design of anticancer agents [6]. The interaction of metal complexes with DNA leads to the formation of metal-DNA adducts that affects both replication and transcription of DNA and ultimately leads to the cell death [7].

The discovery of anticancer activity of cisplatin started the era of inorganic medicines in the field of cancer chemotherapy research. Inorganic medicines, mainly platinum-based drugs, have now become indispensable in chemotherapy research and cover nearly 50% of the total anticancer drugs used worldwide

[8]. In spite of the massive success, adverse side effects, lack of selectivity, rapid development of drug resistance and severe toxicity of platinum-based drugs have shifted the attention of investigation to other metals complexes. Over the last few years, a large variety of other transition metals complexes have been developed to explore their potential as anticancer drugs [9–13]. Specially, ruthenium complexes have attracted much due to their low toxicity, variable oxidation states and favorable kinetic aspects [2, 11, 14–16]. In this context, the complexes of Rh(III) and Ir(III) have been a little less attractive due to their kinetic inertness, which is mainly responsible for their poor biological activity. Recently, Rh(III) and Ir(III) complexes have drawn attention for their tunable chemical and biological properties. A number of rhodium complexes have been reported where biological activity of the complexes has been strategically improved [8, 17–19].

In this article, synthesis and characterization of Rh(III) complexes of 1-alkyl-2-{(o-thioalkyl) phenylazo}imidazoles are described. The DNA binding property of the complexes is established by spectroscopic studies, and the electronic properties are correlated with DFT calculation.

Experimental

Materials and physical measurements

RhCl₃·3H₂O was procured from Arora Matthey Limited, India. The solvents and NaClO₄ were obtained from E.

✉ Dibakar Sardar
dibakardac@gmail.com

1 Department of Chemistry, Dinabandhu Andrews College, Garia, Kolkata 700084, India

2 Department of Applied Science, RCC Institute of Information Technology, Canal South Road, Kolkata 700015, India

3 Department of Chemistry, Jadavpur University, Kolkata 700032, India

Merck, India. The ligands, 1-alkyl-2-{(*o*-thioalkyl) phenylazo} imidazoles (SRaaiNR', **1**), have been synthesized by already reported procedure [20]. In the synthesis purpose, analytical grade chemicals and freshly dried solvents [21] were used, while for spectral studies, spectroscopic grade solvents from Sigma-Aldrich were used.

> Caution! Perchlorate salts are explosive. Handling of small quantities of salt with proper care is recommended.

Elemental analysis (C, H, N) was carried out using a PerkinElmer 2400 CHN elemental analyzer. UV–Vis absorption spectra were recorded on Lambda 25 PerkinElmer. IR spectra were carried out on PerkinElmer RX-1 FTIR spectrophotometer (KBr disk). ^{1}H NMR spectra in $CDCl_3$ were recorded of Bruker 300 MHz FT-NMR spectrometers using trimethylsilane (TMS) as internal standard.

Synthesis

Synthesis of Rh(SMeaaiNMe) (PPh₃)Cl₃] (ClO₄) (2a)

$RhCl_3.3H_2O$ (130 mg, 0.494 mmol) was added to a methanol solution of 1-methyl-2-{*o*-(thiomethyl)phenylazo}imidazole (SMeaaiNMe) (115 mg, 0.494 mmol) and triphenylphosphine (130 mg, 0.494 mmol). The mixture was refluxed with stirring for 5 h and was cooled to room temperature. Then, saturated aqueous solution of $NaClO_4$ was added which separated a brown precipitate. The precipitate was filtered off, washed with methanol, dried under vacuum and subjected to chromatography. A red band was eluted with acetonitrile–toluene (1:3, v/v) which upon evaporation resulted analytically pure product **2a**. Yield was 242 mg (64%).

All other complexes were prepared by the same procedure, and the isolated yields were 60–65%. Elemental analysis, Calc. (%) for $C_{29}H_{27}N_4O_4PSCl_3Rh$ (**2a**): C, 45.34; H, 3.52; N, 7.29. Found: C, 45.28; H, 3.56; N, 7.35. UV/Vis (CH_3CN), λ_{max} (ε, M^{-1} cm^{-1}): 614 (1512), 478 (8979), 422 (17,374), 411 (17,304), 309 (28,065), 268 (42,292) nm. IR (KBr, ν/cm^{-1}): 1582 (C=N), 1392 (N=N), 1093 (ClO_4^-), 523(s), 691(s), 748(s) (PPh₃). TOF–MS: *m/z* 668.75 $(M–ClO_4^-)^+$, 632.8 ($M–ClO_4^-–Cl$), 407 ($M–ClO_4^-$-PPh₃). ^{1}H-NMR (300 MHz, $CDCl_3$), δ (ppm): 2.87 (s, 3H; S-CH₃), 4.27 (s, 3H; N-CH₃), 7.21 (s, 1H; 5-H), 7.66 (m, 2H; 9, 10-H), 7.78 (s, 1H; 4-H), 7.96 (d, *J* = 7.1 Hz, 1H; 8-H), 8.12 (d, *J* = 7.4 Hz, 1H; 11-H), 7.26–7.50 (m, 15 H; PPh₃).

Elemental analysis, Calc. (%) for $C_{30}H_{29}N_4O_4PSCl_3Rh$ (**2b**): C, 44.53; H, 3.45; N, 7.17. Found: C, 44.48; H, 3.49; N, 7.11. UV/Vis (CH_3CN), λ_{max} (ε, M^{-1} cm^{-1}): 615 (1263), 477 (8903), 421 (17,215), 412 (17,148), 311 (27,621), 269 (39,562) nm. IR (KBr, ν/cm^{-1}): 1586 (C=N); 1372 (N=N); 1097 (ClO_4^-); 527, 695, 750 (PPh₃). TOF–MS: *m/z* 682.5

$(M–ClO_4^-)^+$, 646.6 ($M–ClO_4^-–Cl$), 420.5 ($M–ClO_4^-$-PPh₃). ^{1}H-NMR (300 MHz, $CDCl_3$), δ (ppm): 1.46 (t, *J* = 7.6, 3H; N-R':-CH₃), 2.82 (s, 3H; S-CH₃), 4.27 (q, *J* = 8 Hz, 3H; N-R':-CH₂-), 7.16 (s, 1H; 5-H), 7.56 (m, 2H; 9, 10-H), 7.70 (s, 1H; 4-H), 7.90 (d, *J* = 7.0 Hz, 1H; 8-H), 8.08 (d, *J* = 7.5 Hz, 1H; 11-H), 7.26–7.50 (m, 15 H; PPh₃).

Elemental analysis, Calc. (%) for $C_{30}H_{29}N_4O_4PSCl_3Rh$ (**2c**): C, 44.53; H, 3.45; N, 7.17. Found: C, 44.45; H, 3.40; N, 7.11. UV/Vis (CH_3CN), λ_{max} (ε, M^{-1} cm^{-1}): 613 (1286), 474 (8558), 422 (15,774), 412 (15,712), 310 (25,436), 267 (42,739) nm. IR (KBr, ν/cm^{-1}): 1575 (C=N); 1386 (N=N); 1093 (ClO_4^-); 519, 696, 748 (PPh₃). TOF–MS: *m/z* 682.6 $(M–ClO_4^-)$ $^+$, 646.7 ($M–ClO_4^-$ –Cl), 420.7 ($M–ClO_4^-$-PPh₃). ^{1}H-NMR (300 MHz, $CDCl_3$), δ (ppm): 1.50 (t, *J* = 8.0, 3H; S-R:–CH₃), 3.38 (q, *J* = 8.0, 3H; S-R:–CH₂–), 4.25 (s, 3H; N-CH₃), 7.24 (s, 1H; 5-H), 7.62 (m, 2H; 9, 10-H), 7.74 (s, 1H; 4-H), 7.93 (d, *J* = 7.0 Hz, 1H; 8-H), 8.15 (d, *J* = 7.5 Hz, 1H; 11-H), 7.26–7.50 (m, 15 H; PPh₃).

Elemental analysis, Calc.(%) for $C_{31}H_{31}N_4O_4PSCl_3Rh$ (**2d**): C, 43.75; H, 3.39; N, 7.04. Found: C, 43.68; H, 3.32; N, 7.01. UV/Vis (CH_3CN), λ_{max} (ε, M^{-1} cm^{-1}): 613 (1182), 475 (10,536), 422 (18,490), 411 (18,501), 310 (30,743), 270 (44,760) nm; IR (KBr, ν/cm^{-1}): 1576 (C=N); 1385 (N=N); 1088 (ClO_4^-); 526, 698, 750 (PPh₃). TOF–MS: *m/z* 696.3 $(M–ClO_4^-)$ $^+$, 661.3 ($M–ClO_4^-–Cl$), 435.1 ($M–ClO_4^-$-PPh₃). ^{1}H-NMR ((300 MHz, $CDCl_3$), δ (ppm): 1.41 (t, *J* = 8.0, 3H; S-R:–CH₃), 1.52 (t, *J* = 8.0, 3H; N-R':–CH₃), 3.34 (q, *J* = 7.5, 3H; S-R:–CH₂–), 4.25 (q, *J* = 8.3, 3H; N-R':–CH₂–), 7.24 (s, 1H; 5-H), 7.62 (m, 2H; 9, 10-H), 7.74 (s, 1H; 4-H), 7.93 (d, *J* = 7.0 Hz, 1H; 8-H), 8.15 (d, *J* = 7.5 Hz, 1H; 11-H), 7.26–7.50 (m, 15 H; PPh₃).

X-ray diffraction study

Crystals were grown by slow diffusion of dichloromethane solution of **2b** into hexane. Crystal parameters and refined data are listed in *Supplementary material* Table.S1. The data were collected by fine focus sealed tube at 100 (2) K using graphite monochromator Bruker Smart CCD Area Detector (Mo-Kα radiation (λ = 0.71073 Å). Unit cell parameters were determined from least-squares refinement of setting angles with θ in the range $3.37 \leq \theta \leq 69.09°$. The *hkl* range is $-10 \leq h \leq 10$; $-18 \leq k \leq 18$; $-31 \leq l \leq 30$. Reflection data were recorded using the ω scan technique. Data were corrected for Lorentz polarization effects and for linear decay. Semi-empirical absorption corrections based on ψ-scans were applied. Data reduction was carried out by Bruker SAINT Program. The structure was solved by direct method using SHELXS-97 [22] and successive difference Fourier syntheses. All non-hydrogen atoms were refined anisotropically. The hydrogen atoms were fixed geometrically and refined using the riding model. All calculations were

carried out using SHELXL-97 [22], ORTEP-32 [23] and PLATON-99 [24] programs.

Crystallographic data for the structural analysis have been deposited in the Cambridge Crystallographic Data Centre, and the depository number is CCDC-1998671. Copies of this information may be obtained free of charge from the Director, CCDC, 12 Union Road, Cambridge, CB2 1FZ, UK (email: deposit@ccdc.cam.ac.uk or http://www.ccdc.cam.ac.uk).

Computational methods

All computations have been performed using the Gaussian 09 program package [25]. The Becke's three-parameter hybrid exchange functional and the Lee–Yang–Parr nonlocal correlation functional (B3LYP) have been used during computation [26]. Elements except iridium have been assigned a 6-31G basis set in our calculations. For iridium, the Los Alamos effective core potential plus double zeta (LanL2DZ) basis set has been employed [27]. The geometric structure of the complex **2b** in the ground state (S_0) has been fully optimized at the B3LYP level. Geometry optimization has been carried out from the geometry obtained from the crystal structure without any symmetry constraints. During optimization, vibrational frequencies were calculated to ensure that optimized geometries represented local minima. Using the respective optimized S_0 geometries, we employed time-dependent density functional theory (TDDFT) at the B3LYP level to predict their electronic absorptions characteristics [28].

DNA binding study

Preparation of stock solutions

The stock solutions of complexes (2 mM) were prepared in acetone-free methanol and diluted with Tris-HCl buffer to get the required concentration before each set of experiments.

The solution of calf thymus (CT) DNA (Bangalore Genei, India) was prepared in 5 mM Tris-HCl/50 mM NaCl buffer (pH 7.2) using deionised and sonicated HPLC grade water. The CT DNA used in the experiments was sufficiently free from protein (UV absorption ratio $A_{260nm}/A_{280nm} \sim 1.9$). The DNA concentration was determined with the help of its extinction coefficient, ε of 6600 M^{-1} cm^{-1} at 260 nm. The prepared stock solution of DNA was stored at 4 °C and used within 4 days.

Ethidium bromide (EB) dust (Sigma-Aldrich, USA) was dissolved in double distilled water at a concentration of 1 mM. Stored stocks (at 4 °C in the dark) were diluted freshly before each experiment.

Absorption spectroscopic studies of the complexes in presence of CT DNA

Absorption spectroscopic studies were done on PerkinElmer, lambda-25 spectrophotometer. The interaction between the metal complexes and CT DNA was observed by adding increasing concentrations of DNA (2 μM to 20 μM) to a fixed concentration of complex (40 μM) and by adding increasing concentrations of complex (2–20 μM) to fixed concentration of DNA (100 μM). After each addition, the DNA and complex mixtures were incubated at room temperature for 15 min and scanned from 290 to 700 nm. The self-absorption of DNA was eliminated in each set of experiments. Modified Benesi–Hildebrand plot was used for the determination of ground-state binding constant between the complexes and CT DNA [29]. The binding constant "K" was determined by using the following relation:

$$A_0/\Delta A = A_0/\Delta A_{max} + (A_0/\Delta A_{max})X1/KX1/L_t$$

where $\Delta A = A_0 - A$, ΔA_{max} = maximum change in reduced absorbance, A_0 = maximum absorbance of receptor molecules (without any ligand), A = reduced absorbances of the receptor molecules (in presence of ligand), and L_t = ligand concentration.

Fluorescence spectroscopic studies of the complexes with EB bound DNA

Fluorescence spectroscopic studies of EB bound CT DNA with varying concentrations of the complexes (0–100 μM) were done by using by LS 55 PerkinElmer spectrofluorimeter at room temperature (298 K). The EB bound CT DNA was prepared freshly before each experiment by treating with 10^{-5} M DNA solution with 10^{-5} M of EB solution, and it was incubated for 30 min. The experiments were carried out with gradual addition of the complexes (10 μM) into EB bound DNA mixture and incubated for 15 min, and the fluorescence spectra were taken. The excitation wavelength was 500 nm, and the emission spectra were scanned from 510 to 750 nm.

The study is based on the competitive binding of the complex to DNA by replacing EB from EB bound DNA, and this is observed by the quenching of the fluorescence intensity. The fluorescence quenching of EB bound DNA is expressed by the Stern–Volmer equation [30, 31]

$$I_0/I = 1 + K_{SV}[Q] = 1 + kq\tau_0[Q]$$

where I_0 and I are the fluorescence intensities of BSA in the absence and in the presence of the metal complex (quencher), respectively, K_{SV} is the Stern–Volmer quenching constant, $[Q]$ is the concentration of the quencher, kq is the quenching rate constant of the biomolecule, and τ_0 is

the average lifetime of the molecule in the absence of the quencher. A linear I_0/I versus $[Q]$ plot indicates that a single type of quenching mechanism is involved, either static or dynamic, while a deviation from linearity suggests a mixed quenching mechanism [32].

Results and discussion

Synthesis and formulation

The ligands, 1-alkyl-2-{(o-thioalkyl)phenylazo}imidazoles (SRaaiNR′, **2**; R = R′ = Me (**a**); R = Me, R′ = Et (**b**); R = Et, R′ = Me (**c**); R = R′ = Et (**d**)), are *N,N′,S*-tridentate ligands where *N,N′* and *S* refer to imidazole-*N*, azo-*N* and thioalkyl (SR)-*S* donor centers, respectively (Scheme 1). The reaction of RhCl$_3$ with 1-alkyl-2-{(o-thioalkyl)phenylazo}imidazole (SRaaiNR′, **1**) and PPh$_3$ in ethanol under refluxing condition results a red solution which upon addition of a saturated aqueous solution of NaClO$_4$ (Scheme 1) separates a red precipitate having a composition of [Rh(SRaaiNR/)(PPh$_3$)Cl$_2$](ClO$_4$) (**2**). The composition of the complexes is consistent with the microanalytical data. The structural confirmation has been done by single-crystal X-ray diffraction in one representative case. The complexes are diamagnetic, which indicates the + 3 oxidation state of the metal.

Molecular structure of [Rh(SMeaaiNEt)(PPh$_3$)Cl$_2$] (ClO$_4$) (2b)

The structural characterization of [Rh(SMeaaiNEt)(PPh$_3$) Cl$_2$](ClO$_4$) (**2b**) was carried out by a single-crystal X-ray diffraction study. The molecular structure is shown in Fig. 1. The relevant bond parameters are listed in Table 1. The six-coordinated Rh(III) center has a distorted octahedral geometry, and it is surrounded by two Cl, one PPh$_3$ and one SMeaaiNEt ligand which acts as *N,N′,S*-tridentate

chelator. The ligand forms two adjacent five-membered chelate rings with bite angles N(4)–Rh(1)–N(2), 78.1 (3)° and N(4)–Rh(1)–S(1), 85.4 (2)°. The two chlorines are cis to each other and the bond angle Cl(1)–Rh(1)–Cl(3) is 89.64 (9)°. The Rh–Cl bond [Rh–Cl(2), 2.402 (2) Å] trans to PPh$_3$ is longer than that of cis [Rh–Cl(1), 2.334 (3) Å] establishing the presence trans effect of PPh$_3$ [33]. The Rh–N(azo) length [Rh–N(3), 1.993 (7) Å] is shorter than the Rh–N(imidazole) lengths [Rh–N(1), 2.047 (6) Å] which may be due to better *π*-accepting ability of N(azo) center. This N=N distance, 1.267 (9), is closer to the free ligand bond length (1.258 (5) Å) [20]. This bond parameter comparison explains the presence of better d(Rh) → π*(azo) donation in [Rh(SMeaaiNEt)Cl$_3$] (**3b**) which may be due to thioether-S
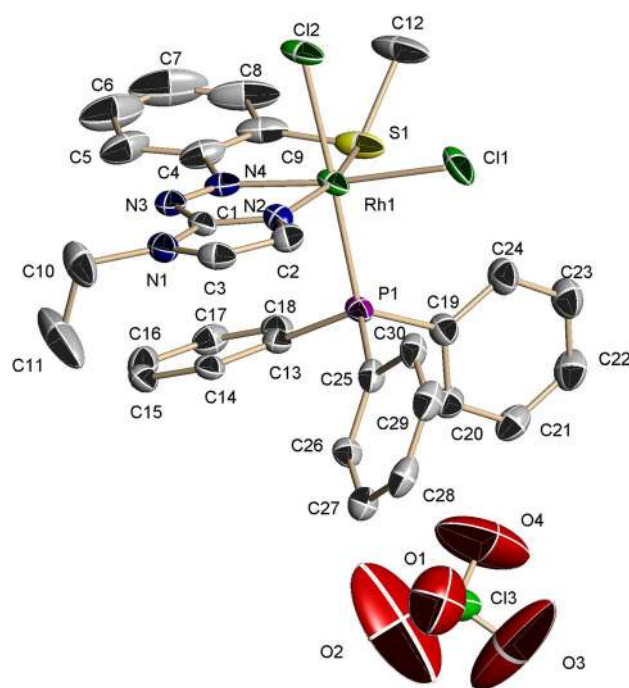
Fig. 1 ORTEP diagram of [Rh(SMeaaiNEt) (PPh$_3$)Cl$_2$](ClO$_4$) (**2b**)

Scheme 1 Ligands and the complexes

1, SRaaiNR′

R = R′= Me (SMeaaiNMe) (a)
R = Me, R′= Et (SMeaaiNEt) (b)
R = Et, R′ = Me (SEtaaiNMe) (c)
R = R′=Et (SEtaaiNEt) (d)

2, [Rh(SRaaiNR′)(PPh$_3$)Cl$_2$](ClO$_4$)
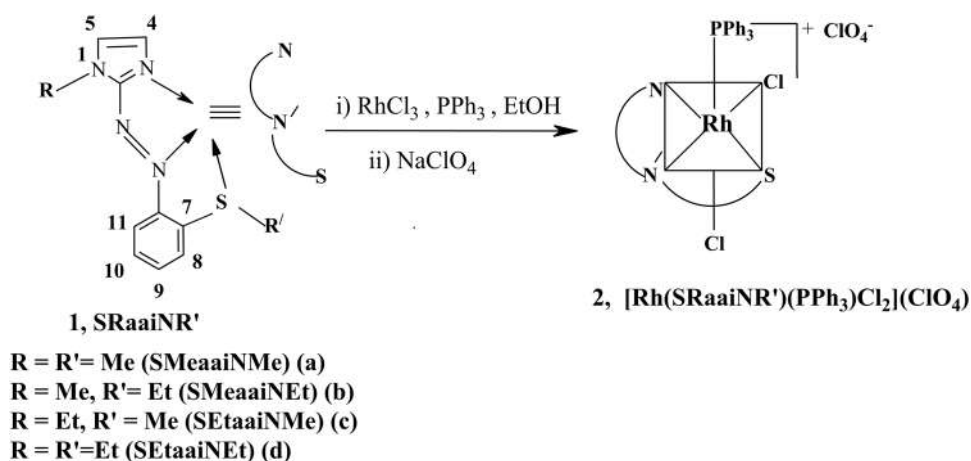
Table 1 Selected bond lengths (Å) and angles (°) for the complex [Rh(SMeaaiNEt)(PPh$_3$)Cl$_2$]ClO$_4$ (**2b**) (experimental from X-ray and theoretical from DFT calculation)

Bond length(Å)	Experimental value	Theoretical value	Bond angle (°)	Experimental value	Theoretical value
Rh(1)–N(2)	2.047 (6)	2.081	N(4)–Rh(1)–N(2)	78.1 (3)	77.7
Rh(1)–N(4)	1.993 (7)	2.028	N(4)–Rh(1)–S(1)	85.4 (2)	85.5
Rh(1)–S(1)	2.307 (2)	2.371	N(2)–Rh(1)–S(1)	163.5 (2)	163.2
Rh(1)–P(1)	2.3201 (19)	2.403	N(4)–Rh(1)–P(1)	95.24 (18)	97.3
Rh(1)–Cl (1)	2.334 (3)	2.392	N(2)–Rh(1)–P(1)	91.28 (18)	90.9
Rh(1)–Cl (2)	2.402 (2)	2.450	S(1)–Rh(1)–P(1)	88.86 (8)	92.1
N(3)–N(4)	1.267 (9)	1.275	N(4)–Rh(1)–Cl(1)	172.91 (18)	171.6
			N(2)–Rh(1)–Cl(1)	99.9 (2)	102.3
			S(1)–Rh(1)–Cl(1)	96.62 (12)	94.1
			P(1)–Rh(1)–Cl(1)	91.60 (8)	91.0
			N(4)–Rh(1)–Cl(2)	83.47 (19)	82.0
			N(2)–Rh(1)–Cl(2)	87.08 (18)	85.0
			Cl(1)–Rh(1)–Cl(2)	89.64 (9)	88.4

coordination to Rh(III). The optimized structure of complex **2b** is also generated theoretically using the DFT computation technique. The bonding parameters of calculated structure show good agreement with the experimental bonding parameters (Table 1).

Spectral characterization

The IR spectra of the complexes show the stretching vibrations bands for azo, i.e., ν (N=N), and imine, i.e., ν (C=N) in the regions 1372–1386 cm^{-1} and 1575–1592 cm^{-1}, respectively, and these frequencies significantly shift to lower values compared to free ligand (*Supplementary Material* Fig.S1) [20]. The appearance of these bands at the lower values indicates the coordination of ligand (SRaaiNR′) to the metal center through azo and imine nitrogens. The presence of ClO$_4$$^-$ is verified by a strong band in the region 1088–1097 cm^{-1} along with a weak band at around 620 cm^{-1}. The spectra also exhibit three characteristics of strong bands around 750, 695 and 525 cm^{-1} for coordinated PPh$_3$ ligand.

The mass fragmentations by ESI–MS (positive ion) of the complexes show expected fragmentation pattern. The mass spectra of the complexes recorded the (M–ClO$_4$$^-$)$^+$ ion peak as the base peak (*Supplementary material* Fig.S2).

The ^{1}H-NMR spectra of the complexes in CDCl$_3$ recorded the downfield shifting of proton signals compared to free ligand data [20], and this may be the outcome of the electron-withdrawing effect of the coordinated Rh(III). The maximum downfield shifting was observed in case of the imidazole proton 4-H which suffers maximum shifting of 0.7–0.8 ppm compared to the free ligand position and appears as a broad singlet at 7.75–7.85 ppm. The imidazole

proton, 5-H, experiences ~ 0.05–0.20 ppm downfield shift and also appears as a broad singlet. The resonances of the phenyl protons of triphenylphosphine were observed as multiplets at 7.20–7.50 ppm. The representative spectra of the complexes are shown in *Supplementary material* Fig.S3.

The absorption spectra of the complexes in acetonitrile show several absorptions bands in the wavelength region 250–700 nm (Fig. 2). All the complexes show two high intense transitions (ε ~ 10^4 M^{-1} cm^{-1}) at ~ 411 nm and ~ 422 nm along with a shoulder at ~ 475 nm (ε ~ 10^3 M^{-1} cm^{-1}). The spectra of the complexes also show one weak transition (ε ~ 10^2 M^{-1} cm^{-1}) at ~ 615 nm in the visible region and one high intense transition (ε ~ 10^4 M^{-1} cm^{-1}) at ~ 285 nm in the UV region. The high energy transitions (< 400 nm) region may be regarded as ligand-centered transitions, and the transitions in the visible region (> 400 nm) may be assigned as MLCT (metal-to-ligand charge transfer) transitions because these transitions are not present in free ligands. These assignments of absorption bands are further explained by TDDFT calculations.

DFT calculation and electronic structure

The DFT computation of the complex **2b** has been performed with the optimized geometry to correlate the electronic structure with the observed electronic spectra. The theoretical bond parameters show close agreement with the experimental values (Table 1). The energy and the composition of some selected molecular orbitals are given in *Supplementary material* Tables 2, and surface plots of some frontier orbitals are shown in Fig. 3. The energies of HOMO and LUMO are − 8.89 eV and − 6.29 eV, respectively. The occupied frontier orbitals HOMO, H-1, H-2 and H-3 are mainly constituted (51–81%) by chlorine $p\pi$ orbitals with
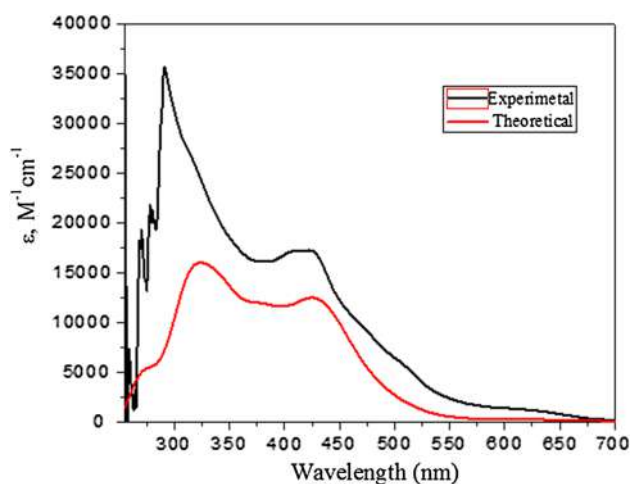
Fig. 2 Experimental and theoretical UV–visible spectra of [Rh(SMeaaiNEt)(PPh$_3$)Cl$_2$](ClO$_4$)(**2b**)

little contributions from PPh$_3$ and metal d-orbitals, while in case of H-4 and H-5, about 90% contribution come from PPh$_3$. The LUMO is almost delocalized on ligand π^* orbitals (94%). The LUMO + 1 is constituted by metal (Rh, 42%) and PPh$_3$ (23%), while LUMO + 2 is carrying 49% metal and 25% (**4b**) ligand contribution.

The TDDFT calculations were performed to gain an insight about the nature of electronic transitions and to explain the electronic spectra. The experimental spectra of **2b** correlate well with the theoretical spectra

(Fig. 2). Selected list of excited energies and transitions of [Rh(SMeaaiNEt)(PPh$_3$)Cl$_2$]ClO$_4$ (**2b**) obtained from TDDFT calculation in the gas phase are given in *Supplementary material* Table S3. The experimental spectrum shows a transition at 615 nm which appears at 606 nm in theoretical spectrum and is mainly due to the transitions from HOMO-1, HOMO-2 and HOMO→LUMO and can be regarded as admixture of chloride-to-ligand (LLCT: Cl→Azo, Im), PPh$_3$-to-ligand (LLCT: PPh$_3$→Azo, Im), and metal-to-ligand (MLCT: Rh→Azo) charge transfer transitions. Similarly, the bands observed within 400–500 nm are assigned to the mixture of multiple transitions originated from LLCT [Cl→Azo, Im], LLCT [PPh$_3$→Azo, Im], MLCT [Rh→Azo], etc. The other transitions at shorter wavelengths are mixture of mainly PPh$_3$-to-metal (LMCT), intra-PPh$_3$ (ILCT), intraligand (ILCT), PPh$_3$-to-chloride (LLCT) charge transfer transitions.

DNA interaction study of the complexes

Absorption spectroscopic studies

The interaction of the complexes with CT DNA was studied by observing the changes in UV–Vis absorption spectra. Any change in absorption spectra that occurs due to the mixing of DNA and complex molecules is the direct evidence of interaction between them [34]. Upon addition of increasing concentrations of complexes to fixed concentration of CT DNA (100 µM), the absorption of DNA at

Fig. 3 Surface plots of some frontier orbitals of [Rh(SMeaaiNEt) (PPh$_3$)Cl$_2$] ClO$_4$ (**2b**)

HOMO	HOMO - 1	HOMO - 2
E = -8.9 eV Rh, 5%; Cl, 75%; Ligand, 19%	E = -9.1 eV Rh, 14%; Cl, 76%	E = -9.14 eV Rh, 12%; Cl, 81%
LUMO	**LUMO + 1**	**LUMO + 2**
E = - 6.29 eV Rh, 4%; Ligand: 93%	E = - 5.1 eV Rh, 42%; PPh$_3$, 21%; Cl, 14%	E = - 4.8 eV Rh, 49%; Ligand, 23%

260 nm was decreased successively and the reverse course of action, i.e., addition of increasing concentrations of CT DNA to fixed concentration of complexes, recorded a steady decrease in absorption with a slight redshift (Figs. 4, 5 and *Supplementary material* Fig.S4-5). Such changes in absorbance clearly indicate the existence of some specific interaction between the complex and DNA molecules. To compare the binding ability of the complexes, we have calculated the ground-state binding constant (K_b) between the complexes and DNA at the absorption maximum of DNA by using modified Benesi–Hildebrand (BH) plot (Figs. 4, 5 and *Supplementary material* Fig.S4-5) and the binding constants are 7.08×10^4 M^{-1} (**2a**), 5.296×10^4 (**2b**), 4.655×10^4 (**2c**) and 3.44×10^5 (**2d**). The observed binding constants (K_b)

revealed that the complex **2a** binds strongly with CT DNA than the other complexes.

Fluorescence quenching studies

To further ensure the interaction between DNA and complex molecules, we studied the ability of the complexes to displace ethidium bromide (EB) from EB bound DNA. Interestingly, either DNA or EB does not have fluorescence property alone, but being a fluorescence probe, EB emits intense fluorescent light in the presence of DNA due to its strong intercalation between adjacent base pairs. The fluorescence spectroscopic studies showed that the addition of increasing concentration of complexes to a DNA solution previously treated with EB caused quenching in fluorescence intensity. The fluorescence quenching of EB bound DNA upon successive addition of complexes follows the
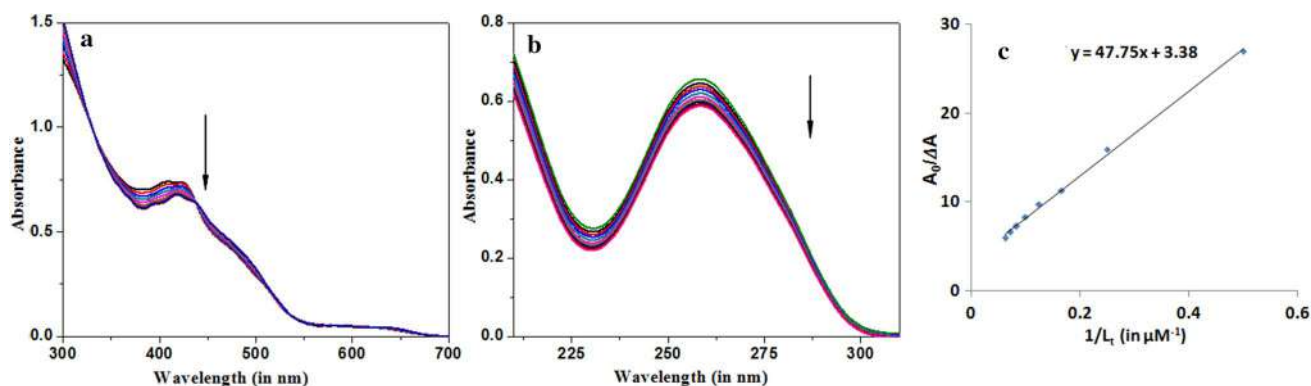
Fig. 4 a Absorption spectroscopic study of 40 µM complex **2a** with increasing concentrations of CT DNA (0, 1, 2, 4, 6, 8, 10, 12, 14, 16, 18 and 20 µM), respectively. **b** Absorption spectroscopic study of CT DNA (100 µM) with increasing concentrations of complex **2a** (0, 2, 4, 6, 8, 10, 12, 14, 16, 18 and 20 µM), respectively. **c** Modified Benesi–Hildebrand plot for the determination of ground-state binding constant between CT DNA and rhodium complex **2a**
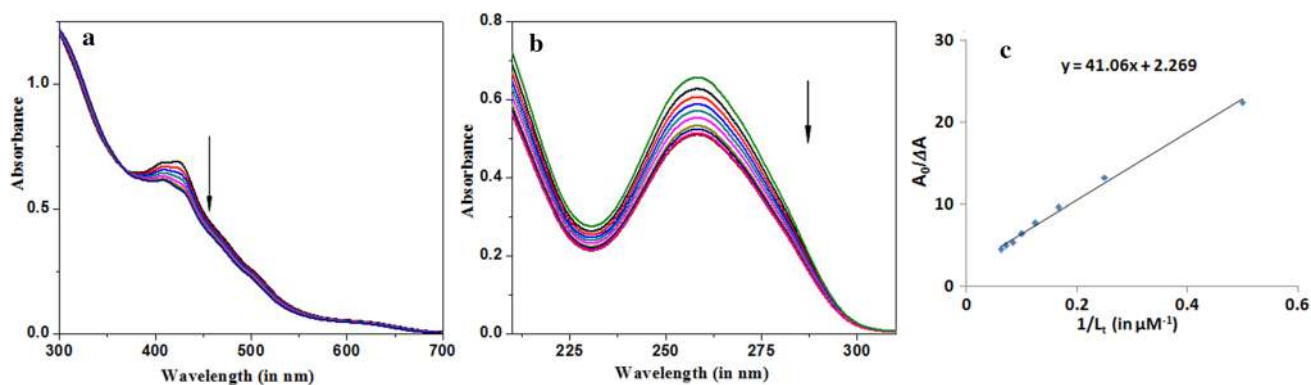
Fig. 5 a Absorption spectroscopic study of 40 µM complex **2b** with increasing concentrations of CT DNA (0, 1, 2, 4, 6, 8, 10, 12, 14, 16, 18 and 20 µM), respectively. **b** Absorption spectroscopic study of CT DNA (100 µM) with increasing concentrations of complex **2b** (0, 2, 4, 6, 8, 10, 12, 14, 16, 18 and 20 µM), respectively. **c** Modified Benesi–Hildebrand plot for the determination of ground-state binding constant between CT DNA and rhodium complex **2b**
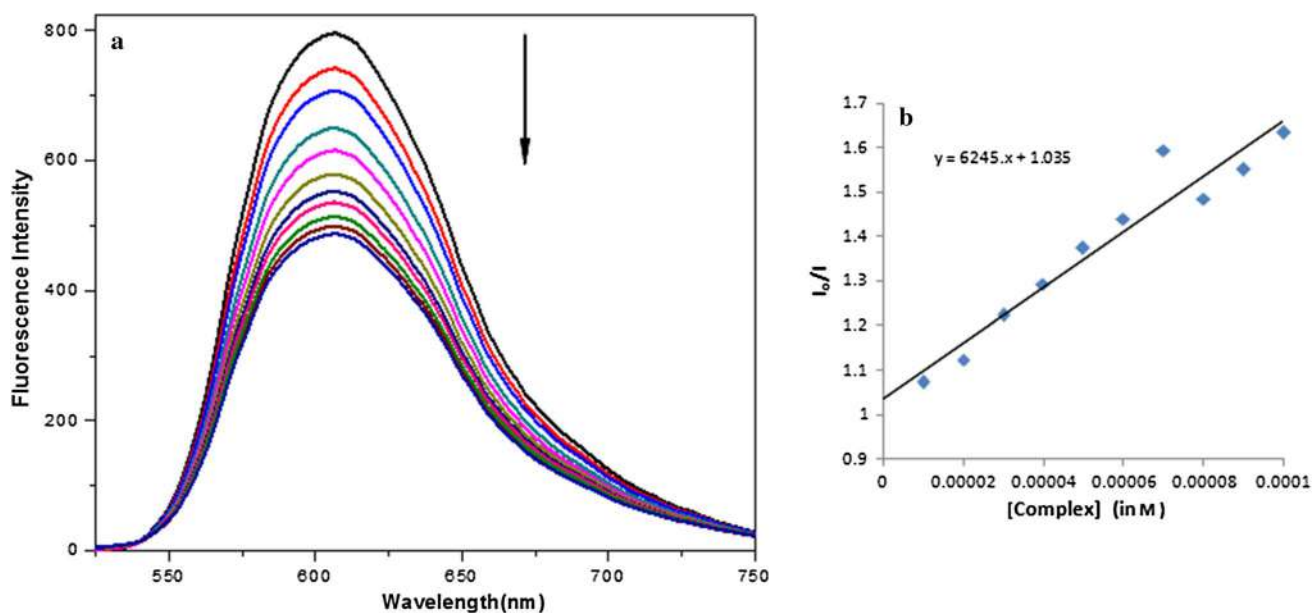
Fig. 6 **a** Fluorescence spectroscopic study of EB bound DNA with increasing concentrations of complex, 2**b** (0, 10, 20, 30 40, 50, 60, 70, 80, 90 and 100 µM), respectively. **b** Stern–Volmer plot for complex **2b**

classic linear Stern–Volmer equation (Figs. 6, 7 and *supplementary material* Fig.S6-7). The Stern–Volmer quenching constants (K_{sv}) obtained from the slope of the plot [Q] versus I_0/I are 1.194×10^4 M^{-1} (**2a**), 6.245×10^3 M^{-1} (**2b**), 8.661×10^3 M^{-1} (**2c**) and 5.521×10^3 M^{-1} (**2d**). These values indicate the strong interaction of the complexes and with

the DNA [35]. The apparent binding constants (K_{app}) were also calculated from the equation $K_{EB}[EB] = K_{app}[complex]$, where $K_{EB} = 1.0 \times 10^7$ M^{-1}, [EB] = 50 µM, and [complex] is the concentration that causes a 50% quenching of the initial EB fluorescence [35]. The K_{app} values of the complexes are 5.7×10^5 (**2a**), 3.23×10^5 (**2b**), 4.17×10^5 (**2c**) and 5.7×10^5
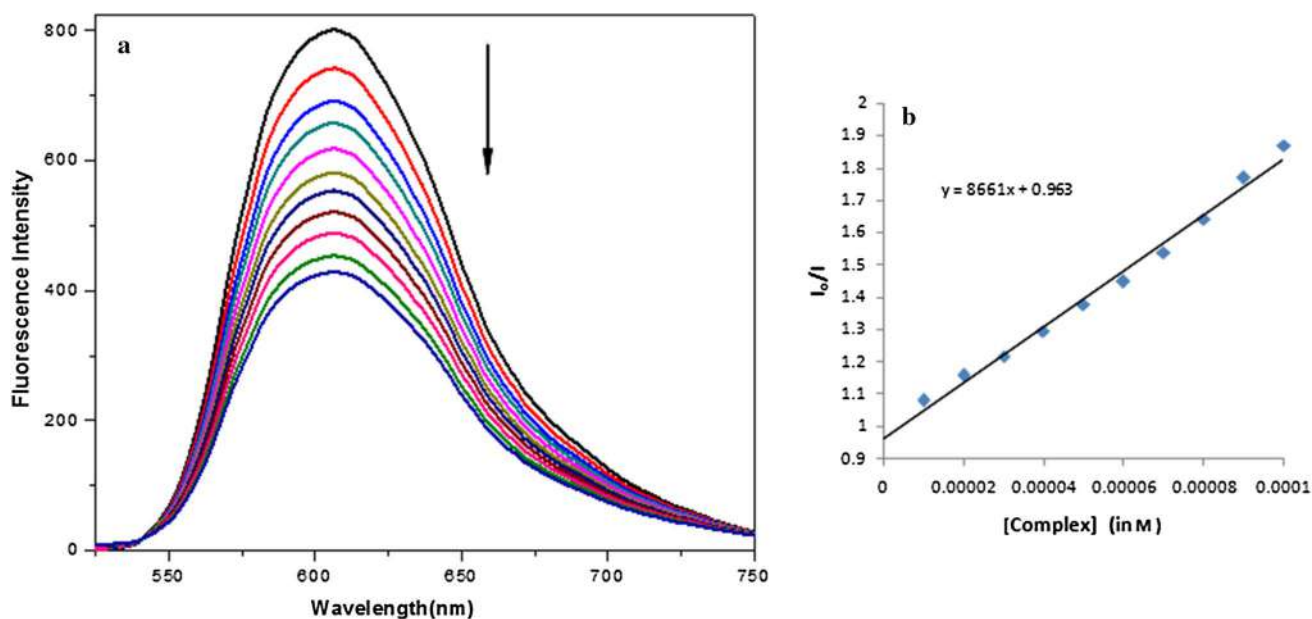
Fig. 7 **a** Fluorescence spectroscopic study of EB bound DNA with increasing concentrations of complex. **2c** (0, 10, 20, 30 40, 50, 60, 70, 80, 90 and 100 µM), respectively. **b** Stern–Volmer plot for complex **2c**

(**2d**) which also suggest that the interaction of complexes with DNA is strong [35].

Conclusion

This article describes the synthesis, characterization and DNA binding ability of four Rh(III) complexes of 1-alkyl-2-{(*o*-thioalkyl)phenylazo}imidazoles. Density functional theory (DFT) study well interprets the electronic structure and the spectral properties of complex **2b**. The DNA binding study by absorption and fluorescence spectroscopic methods explain the DNA binding ability of the complexes. The complex **2a** binds most strongly, while the least binding ability was observed in case of complex **2d**. The similar studies Ir(III) complexes are in progress.

Compliance with ethical standards

Conflict of interest There are no conflicts to declare.

References

1. Yousefi R, Aghevlian S, Mokhtari F, Samouei H, Rashidi M, Nabavizadeh SM, Tavaf Z, Pouryasin Z, Niazi A, Faghihi R (2012) Appl Biochem Biotech 167(4):861–872
2. Kostova I (2006) Curr Med Chem 13(9):1085–1107
3. Muhammad N, Sadia N, Zhu C, Luo C, Guo Z, Wang X (2017) Chem Comm 53(72):9971–9974
4. Nagaj J, Kołkowska P, Bykowska A, Komarnicka UK, Kyzioł A, Jeżowska-Bojczuk M (2015) Med Chem Res 24:115–123
5. Heydari M, Moghadam ME, Tarlani A, Farhangian H (2017) Appl Biochem Biotech 182(1):110–127
6. Gasser G, Ott I, Metzler-Nolte N (2011) J Med Chem 54(1):3–25
7. Johnstone TC, Suntharalingam K, Lippard SJ (2016) Chem Rev 116(5):436–3486
8. Mukhopadhyay S, Gupta RK, Paitandi RP, Rana NK, Sharma G, Koch B, Rana LK, Hundal MS, Pandey DS (2015) Organometallics 34(18):4491–4506
9. Patel M, Chhasatia M, Bhatt B (2011) Med Chem Res 20(2):220–230
10. Arthi P, Shobana S, Srinivasan P, Mitu L, Rahiman AK (2015) Spectrochim Acta A 143:49–58
11. Kostrhunova H, Florian J, Novakova O, Peacock AFA, Sadler PJ, Brabec V (2008) J Med Chem 51:3635–3643
12. Cutillas N, Yellol GS, de Haro C, Vicente C, Rodríguez V, Ruiz J (2013) Coord Chem Rev 257:2784–2797
13. Sathyadevi P, Krishnamoorthy P, Butorac RR, Cowley AH, Dharmaraj N (2012) Metallomics 4:498–511
14. Aird RE, Cummings J, Ritchie AA, Muir M, Morris RE, Chen H, Sadler PJ, Jodrell DI (2002) Br J Cancer 86:1652–1657
15. Loughrey BT, Healy PC, Parsons PG, Williams ML (2008) Inorg Chem 47:8589–8591
16. Mendoza-Ferri MG, Hartinger CG, Mendoza MA, Groessl M, Egger AE, Eichinger RE, Mangrum JB, Farrell NP, Maruszak M, Bednarski PJ (2009) J Med Chem 52:916–925
17. Petrini A, Pettinari R, Marchetti F, Pettinari C, Therrien B, Galindo AN, Scopelliti R, Riedel T, Dyson PJ (2017) Inorg Chem 56:13600–13612
18. Payne R, Govender P, Therrien B, Clavel CM, Dyson PJ, Smith GS (2013) J Organomet Chem 729:20–27
19. Almodares Z, Lucas SJ, Crossley BD, Basri AM, Pask CM, Hebden AJ, Phillips RM, McGowan PC (2014) Inorg Chem 53:727–736
20. Banerjee D, Ray U, Jasimuddin S, Liou J-C, Lu T-H, Sinha C (2006) Polyhedron 25:1299–1306
21. Vogel AI, Tatchell AR, Furnis BS, Hannaford AJ, Smith PWG (1996) A text book of practical organic chemistry, 5th edn. Prentice Hall, Upper Saddle River
22. Sheldrick GM (1997) SHELXS-97. Program for the solution of crystal structure. University of Gottingen, Gottingen
23. Farrugia LJ (1997) ORTEP-3 for windows. J Appl Cryst 30:565
24. Spek AL (1999) PLATON. Molecular Geometry Program, University of Utrecht, Utrecht
25. Schlegel HB et al (2009) Gaussian 09, Revision A.02, Gaussian, Inc., Wallingford
26. Lee C, Yang W, Parr RG (1988) Phys Rev B 37:785–789
27. Hay PJ, Wadt WR (1985) J Chem Phys 82:270–283
28. EMSL, basis set library available http://www.emsl.pnl.gov/forms/basisform.html
29. Benesi HA, Hildebrand JH (1949) J Am Chem Soc 71:2703–2707
30. Lakowicz JR (1999) Principles of fluorescence spectroscopy, 2nd edn. Kluwer Academic/Plenum Publishers, New York
31. Valeur B (2001) Molecular fluorescence. Principles and applications. Wiley, Weinheim
32. Eftink MR, Ghiron CA (1981) Fluorescence quenching studies with proteins. Anal Biochem 114:199–227
33. Sardar D, Datta P, Saha R, Raghavaiah P, Sinha C (2013) J Organomet Chem 732:109–115
34. Pyle AM, Rehmann JP, Meshoyrer R, Kumar CV, Turro NJ, Barton JK (1989) J Am Chem Soc 111:3051–3058
35. García-Giménez JL, González-Álvarez M, Liu-González Malva, Macías B, Joaquín Borrás J, Alzuet G (2009) J Inorg Biochem 103:923–934

Source details

Feedback >   Compare sources >

Transition Metal Chemistry

Scopus coverage years: from 1975 to Present

Publisher: Springer Nature

ISSN: 0340-4285   E-ISSN: 1572-901X

Subject area: (Materials Science: Metals and Alloys)   (Chemistry: Inorganic Chemistry)   (Materials Science: Materials Chemistry)

Source type: Journal

[View all documents >]   [Set document alert]   💾 Save to source list

CiteScore 2022 ⓘ
4.0

SJR 2022 ⓘ
0.299

SNIP 2022 ⓘ
0.433

CiteScore   CiteScore rank & trend   Scopus content coverage

Synthesis, structure elucidation and dft study of a new thiazole–pyridine anchored nnn donor and it's cobalt(II) complex: In-vitro antitumor activity against U937 cancer cells, dna binding property and molecular docking study

Pradip Bera [a,†], Abhishek Aher [b], Paula Brandao [c], Sunil Kumar Manna [b], Indranil Bhattacharyya [a], Chandana Pramanik [a,‡], Basudev Mandal [a,§], Satyabrata Das [d], Pulakesh Bera [a,*]

[a] Post Graduate Department of Chemistry, Panskura Banamali College (Autonomous)(Vidyasagar University), Panskura R.S, Midnapore (East), West Bengal, India–721152
[b] Centre for DNA Fingerprinting & Diagonostics (CDFD), Hyderabad, Telengana–500 039, India
[c] Department of Chemistry, CICECO, University of Aveiro, 3810−193 Aveiro, Portugal
[d] Department of Chemistry, CMR Institute of Technology, Bangalore, Karnataka – 560037, India

ARTICLE INFO

ABSTRACT

The reaction between 4-(2-bromoacetyl)benzonitrile and 2-benzoylpyridine thiosemicarbazone produces a tridentate NNN ligand, 4-(2-(2-(phenyl(pyridine-2-yl)methylene)hydrazinyl)thiazole-4-yl)benzonitrile (**ppytbH**). The ligand constructs an octahedral complex with composition $[Co(ppytbH)_2](ClO_4)_2.3(H_2O)$ (**1**) when reacted with cobalt(II) perchlorate salt in acetonitrile methanol (1:1) solution. The structures of **ppytbH** and **1** have been established by single X-ray crystallography, spectroscopic (^{1}H NMR, IR, UV-Visible and fluorescence), thermal and electrochemical methods. The chemical reactivity and HOMO–LUMO energy of the compounds have been calculated using Density Functional Theory (DFT). The compounds **ppytbH** and **1** exhibit potential anticancer activity against U937 human monocytic cells and IC50 values are found 12.76 ± 0.75 and 12.83 ± 1.37 µM, respectively. The fluorescence and molecular docking study interpret the intercalative DNA binding mode with the titled molecules.

© 2020 Published by Elsevier B.V.

1. Introduction

Cancer is a group of diseases involving abnormal cells division and uncontrollable cell growth which cause ultimate death of the human population and notably causes of more than 10 million deaths worldwide in a year [1]. High throughput research has been initiated worldwide to erase the fatal disease. The development of more safe and selective anticancer drugs is a challenging task to the synthetic chemists. Generally, heterocyclic compounds have significant role in pharmacology. Over 35 years, various NN, NS donor ligands and their metal complexes have been discovered as anticancer agents [2,3]. Among them, the thiazole scaffold is widely distributed in the natural products and bioactive molecules including anticancer drugs. In view of unique physicochemical and biological properties, it has been used as a privileged scaffold in the drug design. Thiazole derivatives with N, S donor atoms play significant interactions with biomolecules [4–6]. Many natural and synthetic thiazole derivatives have been discovered as promising candidates for anticancer drugs. Among natural thiazole derivatives, the thiamine pyrophosphate involves in many cellular processes of living system [7]. Largazole isolated from the marine cyanobacterium *Symploca* sp., exhibited remarkable antiproliferative effects and acted as potent inhibitor of the metal dependent histone deacetylase [8,9]. Vitamin B1 (thiamine) and cystothiazole A are isolated from myxobacterium culture broth of *Cystobacter fuscus* and possess potent antifungal activity against large range of fungi including *Candida albicans* [10]. The thiazole containing WS75624 B is isolated from the fermentation broth of *Scharothrix*

sp. and used as potent hypertensive agents [11]. Dabrafenib and Dasatinib are the example of substituted thiazole anchored pyrimidine compounds showing selected anticancer drug with tyrosine kinase inhibitory activities [12,13].

Recent review reflects that several pyridine anchored thiazole compounds have excellent pharmacological profiles. Elshaflu et al. have been reported the potential antitumor activity of pyridinyl thiazole compounds against human breast adenocarcinoma (MCF-7) cell line [14]. Chimenti et al. demonstrated the selective and reversible oxidase inhibitors property of acetyl pyridine-2-thiazolyl hydrazone towards human monoamine (hMAO-B) [15]. Cardoso et al. have been synthesized several 2-(pyridin-2-yl)−1, 3-thiazoles derivatives for the treatment of Chagas disease which is caused by the protozoan parasite *Trypanosoma cruzi* (*T. cruzi*) [16]. Silva et al. reported the synthesis and potential anticancer activity of 2- (pyridin-2-yl)−1,3-thiazoles derivatives against HL-60 (leukemia), MCF-7 (breast adenocarcinoma), HepG2 (hepatocellular carcinoma) and NCI-H292 (lung carcinoma) cells [17]. Neonicotinoids and pyridine thiazole derivatives have been established as safe and high target specific antitumor [18]. In view of the important structural features of thiazole in the cancer treatment, we have explored the synthesis and characterization of different thiazole anchored compounds for their biological activities that reflected in the recent publications [19,20]. Essential trace element like cobalt is found to be a relatively nontoxic essential trace element in human metabolism and become major component of vitamin B12 (cobalamin) and other co-enzymes [21–23]. Due to relatively high human tolerance of cobalt and less toxic than noble metals like platinum etc., research has been initiated with cobalt containing compounds as alternative to platinum based anticancer drug [24,25].

Here in, we report the synthesis and characterization of a pyridinyl thiazole ligand namely, 4-(2-(2-(phenyl(pyridine-2-yl)methylene)hydrazinyl)thiazol-4-yl)benzonitrile (**ppytbH**) and its Co(II) complex, [Co(ppytbH)$_2$](ClO$_4$)$_2$ (**1**), to evaluate the anticancer activity against U-937 human monocytic cells.

2. Experimental

2.1. Materials and instrumentations

Thiosemicarbazide (99%), 2-benzoylpyridine (99%) and 4-(2-bromoacetyl)benzonitrile, ethidium bromide, CT–DNA, Tris–buffer and PBS were obtained from Sigma Aldrich Chemical Company. Cobalt(II) perchlorate hexahydrate was obtained from Merck chemical company. All the associated reagents and solvents involved in the preparation of ligand, complexes and biological assay were collected from best grade available and used without further purification.

A Perkin Elmer Lambda 35 spectrophotometer with wavelength range 200–800 nm was used to evaluate UV–Vis absorption spectra of the ligand and complex at room temperature. Samples were dissolve in DMSO solvents for UV–Vis experiment and concentration of the sample was taken in the order 10^{-5} (M). Perkin Elmer Fluorescence Spectrometer LS 45 was used to study the fluorescence properties both ligand and complexes. FT-Infrared spectra of the samples were recorded in the range 4000–500 cm^{-1} using a Perkin Elmer Spectrum Spectrophotometer using KBr plate. ^{1}H NMR and ^{13}C NMR spectra of the ligand was collected in CDCl$_3$ solvent using JEOL JNM-ECZ 400S/L1 400 MHz NMR spectrometer. The elemental analysis (C, H and N) both the ligand and complexes were performed using FISONS EA-1108 CHN analyzer. The thermal analyses were carried out using a Perkin Elmer Thermal Analyzer TGA4000 instrument at a constant heating rate 10 or 20 °C/min under nitrogen atmosphere. The electrochemical measurements were carried out using a CHI 620D electrochemical analyser. Single crystal X-ray diffraction data for ligand and complex were collected with monochromatic Mo-Kα radiation (λ = 0.71073 Å) on a Bruker Kappa Apex-II diffractometer, equipped with a CCD area detector at low temperatures. Several scans in φ and ω directions were made to increase the number of redundant reflections and were averaged during the refinement cycles. Data processing for all the complexes were performed using Bruker Apex-II suite. Reflections were then corrected for absorption, inter-frame scaling, and other systematic errors with SADABS [26]. All the structures were solved by the direct methods and all non-hydrogen atoms were refined anisotropically by the full-matrix least squares based on F2 using the SHELXL-2014 [27]. The hydrogen atoms were treated isotropically using a riding model with their isotropic displacement parameters depending on the parent atoms.

2.2. Synthesis

2.2.1. Synthesis of ligand 4-(2-(2-(phenyl(pyridine-2-yl)methylene)hydrazinyl)thiazol-4-yl)benzonitrile (**ppytbH**)

The ligand (**ppytbH**) was prepared by the condensation of 4-(2-bromoacetyl)benzonitrile and 2-(phenyl(pyridin-2-yl)methylene)hydrazine-1-carbothioamide with modified Hantzsch reaction (Scheme 1). According to the method, methanolic solution of 4-(2-bromoacetyl)benzonitrile (10 mmol, 2.245 g) was added drop wise in to the methanol acetonitrile (1:1) mixture solution (20 mL) of 2-(phenyl(pyridin-2-yl)methylene)hydrazine-1-carbothioamide (10 mmol, 2.56 g) with constant stirring at RT. The color of the solution change yellow to deep orange. The reaction mixture is refluxed in water bath for 3 h in presence of perchloric acid (1 mL). Deep orange precipitate was obtained which was filtered off and washed with aqueous methanol. The crude product is recrystallized from methanol and acetonitrile (1:1) mixture. Deep orange transparent rod shape crystals were obtained on slow evaporation. Yield: 5.124 g (73.79%). Decomposition temperature is 170 °C. Anal. Calculation for C$_{22}$H$_{18}$N$_5$O$_5$SCl (%) C, 52.81; H, 3.60; N, 14.00; Found C, 52.76; H, 3.57; N, 14.16. IR (KBr pellets, cm^{-1}): $\nu_{(N-H)}$ 3326, $\nu_{(nitrile-C≡N)}$ 2200, $\nu_{(thiazole\ ring-\ C\ =\ N)}$ 1524, $\nu_{(aromatic\ -C\ =\ C)}$ 1247, $\nu_{(C-S)}$ 764, $\nu_{(perchlorate\ Cl-O)}$ 687. ^{1}H NMR (CDCl$_3$), δ (in ppm) (Fig. S1): 11.649 (s, 1H at N3), 8.672 (s, 1H at C1), 8.37 (s, 1H at C3), 7.97 (d, 1H at C4, J = 8.4 Hz), 7.87 (d, 2H at C17, J = 8.4 Hz), 7.71 (d, 2H at C18, J = 8.0 Hz), 7.66 (d, 1H at C3, J = 8.0 Hz), 7.43–7.37 (m, 2H at C8–C12), 7.29 (m,1H), 7.26–720 (m, 2H) and 7.17–7.08 (m, 1H at C14). ^{13}C NMR (CDCl$_3$), δ (in ppm) (Fig. S2): 148.5 (2C), 139.04, 129.67 (s, C7), 129.33 (3C), 129.14 (2C), 128.7, 127.5, 127.3 (2C), 126.9 (2C), 126.46 (2C), 126.12, 124.96, 122.65 and 101.88.

2.2.2. Synthesis of **1**

A methanolic solution (10 mL) of Co(ClO$_4$)$_2$•6H$_2$O (0.75 g, 3.0 mmol) was added drop by drop to the solution of methanol and acetonitrile solvent (1:1) of **ppytbH** (1.143 g, 3.0 mmol). The resulting solution was starred at 100 °C for one hour. The orange color of the solution changed to deep wine red on prolonged heating. Then mixture was further refluxed in water bath for 3 h. The reaction mixture is filtered and kept in open air. Reddish brown rod shaped single crystals were separated out from the solution upon standing the solution at room temperature for several days. The preparation of **1** is represented in Scheme 1. Yield– 0.45 g (68%) (with respect to metal salt). Anal. Calculation for C$_{44}$H$_{36}$Cl$_2$N$_{10}$CoO$_{11}$S$_2$: C, 51.77; H, 2.96; N, 13.72%. Found C, 49.12; H, 3.34; N, 13.02%. IR (KBr pellets, in cm^{-1}): $\nu_{(N-H)}$ 3398, $\nu_{(thiazole\ ring\ C\ =\ N)}$ 1578, $\nu_{(nitrile\ C≡N)}$ 2197, $\nu_{(hydrazine\ -N-N)}$ 1392, $\nu_{(thiazole\ ring\ C\ =\ S)}$ 824, $\nu_{(perchlorate\ Cl-O)}$ 681. Several attempts have been made to synthesize the complexes with other metals of first transition series but all were unsuccessful.

2.3. Characterization techniques

2.3.1. DFT calculation

HOMO and LUMO orbital plot and energy calculation were performed using the self-consistent field "tight" option of the Orca _4_0_1_2_win64_msmpi 81 program to ensure sufficiently well converged values for the state energies. The basic set and correlation function were used according to our previous report [28].

2.3.2. Cell lines and cell culture

Human histiocytic lymphoma (U-937) cells were obtained from ATCC (American Type Culture Collection) [Manassas, Virginia, USA]. Cells were cultured in Dulbecco's Modified Eagle Medium (DMEM) with high glucose, supplemented with 10% fetal bovine serum, penicillin (100 U/ml), and streptomycin (100 μg/mL). Cells were free from mycoplasma contamination.

2.3.3. Cytotoxicity assay

U-937 cells (5×10^3 in 100 μL seeded in 96-well plate), incubated in 5% CO_2 incubator at 37 °C were treated with **ppyztbH** and **1** at different concentrations ranging from 0.75 to 100 μM in triplicates for 72 h. Doxorubicin (1 μM) treated cells was considered as positive control. After treatments, cells were incubated with 10 μL of MTT dye [(3-(4,5-Dimethylthiazol-2-yl)−2,5-diphenyltetrazolium bromide)] in each well from the stock solution (4 mg/mL prepared in PBS) in dark for 3 h. Then, 100 μL of MTT lysis buffer (20% SDS and 50% DMF at 1:1 ratio) was added in each well and incubated overnight in the orbital shaker (200 rpm) in dark. Absorbance was taken at 595 nm using BIO-RAD iMark Microplate Reader and Microplate Analyst software. Cytotoxicity assay was performed and the percentage of cell death was plotted and IC_{50} values were calculated using Graph Pad Prism 6 [28].

2.3.4. Caspase 3 activity

The basis of the assay was the aminomethylcoumarin (AMC)-derived substrate Z-DEVD-AMC which is weakly fluorescent in UV range but upon proteolytic cleavage by caspase 3 gives bright, blue fluorescence at excitation/emission maxima ~342/441 nm. Doxorubicin (1 μM) was used as positive control. Therefore, the amount of AMC produced is equal to the number of apoptotic cells in the test sample. The caspase 3 activity of the test compounds were evaluated as reported previously [29,30].

2.3.5. LDH release assay

LDH is a cytosolic enzyme released into culture supernatant upon induction of necrosis in the cells. U-937 cells (2×10^6) were taken per well of a 6-well plate and incubated for 30 min at 37 °C in 5% CO_2 incubator followed by treatment of **ppyztbH** and **1** with the concentrations of IC50 and double of IC50 values. After incubating for 12 h and 24 h, cells were centrifuged at 9000 rpm, 4 °C for 5 min to collect supernatant. To 20 μl of supernatant from each sample, 100 μL of LDH Mix (2.8 ml of 0.2 M Tris–HCl, pH 7.3 + 0.1 mL of 6.6 mM NADH + 0.1 mL of 30 mM sodium pyruvate) was added and absorbance was recorded at 340 nm at 25 °C till 30 min, at every 5 min interval using Spectramax M5 by Molecular Devices and Softmax Pro 7.0 software. This was performed in triplicates and the obtained data was analyzed to calculate percentage LDH release, plotted as bar graph. The absorbance obtained from the supernatant, collected from cells treated with 1% Triton X-100 was considered as 100% [28].

2.3.6. PARP cleavage

U-937 cells seeded in 6-well plate 30 min prior to treat were treated with **ppyztbH** and **1** at concentration of 20 μm and 40 μm for 24 h. Treated cells were pelleted down by spinning at 14,000 rpm for 5 min and the supernatant was discarded. The pellet was washed thrice with cold PBS buffer and excess of PBS was aspirated. The pellet was re-suspended in Tris- HCl lysis buffer pH 7.6 added with 1% protease inhibitor cocktail to prepare whole cell lysate. Briefly, mixture was cooled on ice for 15 min followed by vortexing for 30 s and intermittent cooling for 45 s for 30 min to lyse the cells. Then, whole cell lysate was centrifuged at high speed to collect supernatant and protein concentration in supernatant was calculated with Bradford protein estimation protocol. The 100 μg of protein was used to check the PARP cleavage using cleaved PARP (Asp214) primary antibody (Cat: D64E10) on Western blot. The GAPDH was probed as gel loading control. Western blots were observed under UVITEC Chemidoc (Cambridge) and given result was analysed with UVITEC NineAliance software.

2.3.7. Live and dead assay

U-937 cells seeded in 6 plate were treated with 20 μM of **ppytbH** and **1** overnight at 37 °C. Following day, cells were collected by centrifugation and washed with chilled PBS three times. Washed cells were stained with 5 μM calcein-AM [4′,5′-bis{N,N-bis(carboxymethyl)aminomethyl}fluorescein acetoxymethyl ester] and propidium iodide (PI). The calcin-AM probes live cells, whereas PI binds to dead cells. The stained cells were counted under Olympus IX73 Fluorescent Microscope to quantify percentage live and dead cells [31,32].

2.3.8. Effect of synthetic compounds on isolated PBMCs

Peripheral blood mononuclear cells (PBMCs) were isolated from human blood with Ficoll-paque (Histopaque-1077) density gradient centrifugation method as mentioned before. Briefly, blood was withdrawn in EDTA vial and diluted with PBS followed by layering over chilled histopaque-1077 (1.077 density). It was centrifuged at $400 \times g$ for 30 min and PBMCs formed a buffy layer above histopaque. This layer was collected to centrifuge again and washed with PBS thrice. Finally, PBMCs were re-suspended in RPMI media for culture. The isolated PBMCs were stained with typan blue dye to quantify their viability and purity. About 98% of cells are viable and 95% cells are pure mononuclear cells. Five thousand PBMCs were seeded 96 well plate followed by treating of compounds with the concentrations of IC50 and double the IC50 for 24 h. After treatment, MTT assay was performed as described before.

2.3.9. Docking study

The molecular docking was carried out using AUTODOCK 4.0 software as accomplished by the graphical user interface AUTODOCK TOOLS 4.0 (AD4.1_bound.dat). The macro cyclic receptor was choosing as PDB formed of three dimensional x–ray crystals structure of a CT-DNA. The graphical user interface AUTODOCK TOOLS was devoted to setup the protein: water molecule was deleted from the crystal of protein, only polar hydrogen were added, computed gasteigers charge was calculated as –25.9962 and non polar hydrogen were merged to carbon atom. Complexes 3D structures were saved in PDB format with the aid of the program MERCURY. The AUTODOCK TOOLS program was used to make docking input file. A grid box size for complex **ppytbH** and **1** were $30 \times 26 \times 72$ and $50 \times 34 \times 64$ respectively with grid spacing 1 Å. Both receptor and complex are save pdbqt format. Distances-dependent functions of the dielectric constant are used for the calculation of the energetic map. Ten runs are generated by using Lamarckian genetic algorithm searches. Default settings are used with maximum number 2.5×10^6 energy evaluations, an initial population of 50 randomly placed individuals [33,34]. Final docking is run with autogrid4.exe and autodock4.exe function to generate glg and dlg files respectively. The graphical interactions picture were found using YASARA software.
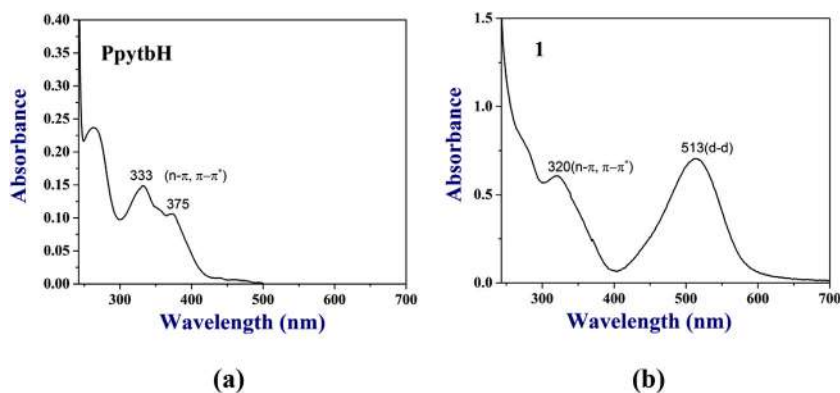
Fig. 1. UV–Vis spectra of **ppytbH** (a) and **1** (b).
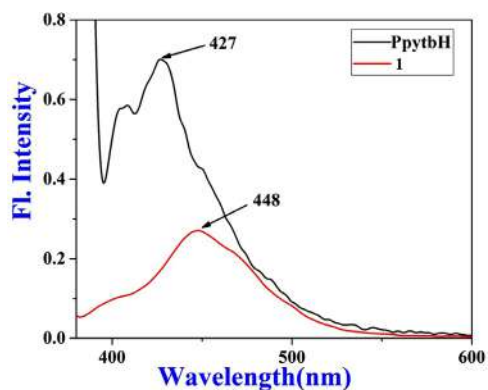
Fig. 2. Emission spectra of **ppytbH** and **1**.
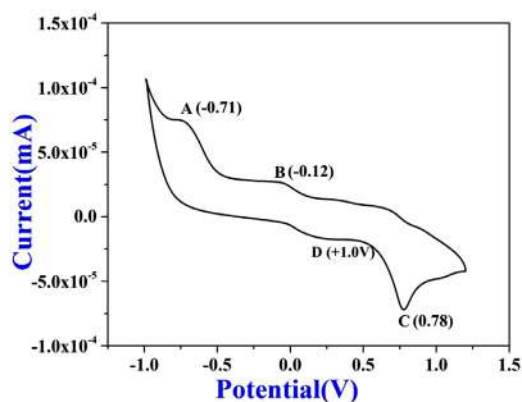
Fig. 3. Cyclic voltammogram of **ppytbH** in acetonitrile solvent containing tetrabutyl-ammonium perchlorate as a supporting electrolyte at scan rate 100 mV/s.

Fig. 4. Cyclic voltammogram of **1** in acetonitrile solvent containing tetrabutyl-ammonium perchlorate as a supporting electrolyte at scan rate 100 mV/s.
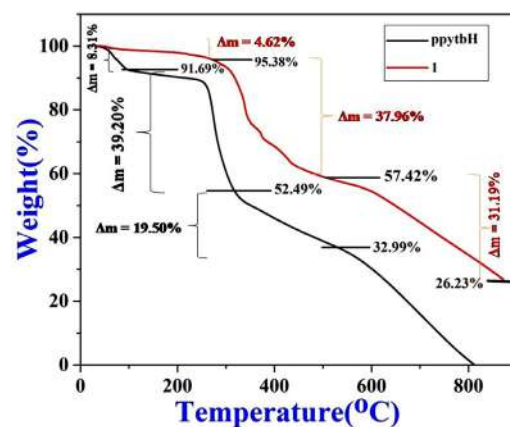
Fig. 5. Thermogravimetry plot of **ppytbH** and **1**.

3. Results and discussion

The ligand, 4-(2-(2-(phenyl(pyridine-2-yl)methylene)hydrazinyl)thiazole-4-yl)benzonitrile (**ppytbH**) is synthesized by the reaction of 2-(1-(pyrazin-2-yl)ethylidene)hydrazine-1-carbothioamide and 4-(2-bromoacetyl)benzonitrile in methanol acetonitrile mixed solvent following Hantzsch's reaction [16]. The orange product is reacted with perchloric acids to get block shaped orange color single crystals of perchlorate salt (Scheme 1). The reaction of **ppytbH** with $Co(ClO_4)_2 \cdot 6H_2O$ in mixed solvent methanol and acetonitrile (1:1) furnished reddish brown rod shape single crystals of complex [Co(ppytbH)₂] (ClO₄)₂ (**1**) (Scheme 1).

3.1. Spectroscopic study

3.1.1. NMR study of *ppytbH*

The structure of the ligand **ppytbH** is assured by NMR Spectroscopy, FT-IR and X–ray crystallography. The ^{1}H–NMR experiment is performed in CDCl₃. The signals obtained in the ^{1}H NMR spectrum of **ppytbH** are in good agreement with the expected structure as shown in Figure S1. The signal at δ 11.649 ppm can be assigned for benzoyl pyridyl hydrazone (–NH) proton. The single peak observed at δ 8.672 ppm indicates the proton attached with C1 atom. Another single peak found at δ 8.376 ppm is attributed to the proton at C3. The doublet peak observed at δ 7.96 ppm may be due the presence of proton at C4. Another doublet peak
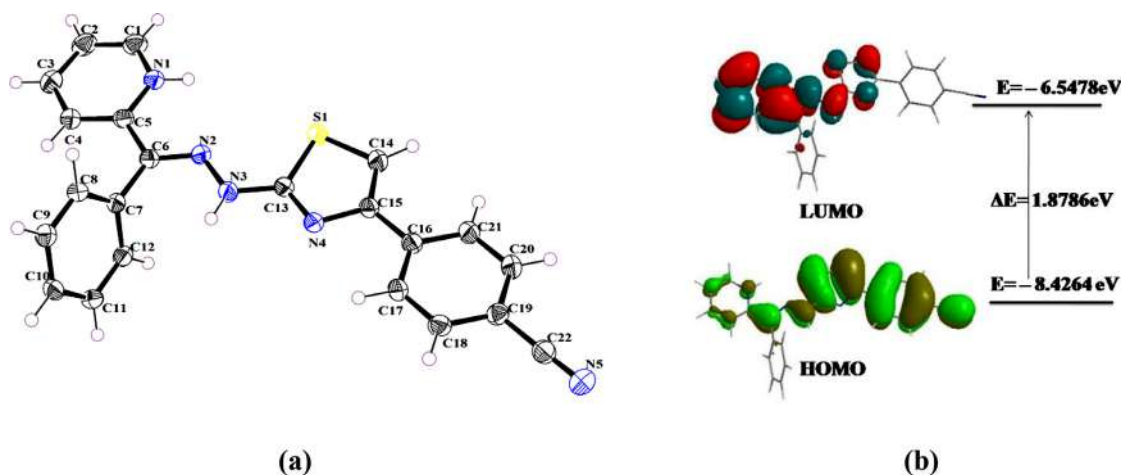
Fig. 6. Molecular structure of **ppytbH** shows the atom numbering scheme. Ellipsoids are drawn at the 50% probability level (a).HOMO and LUMO energy level diagram of **ppytbH** (b).
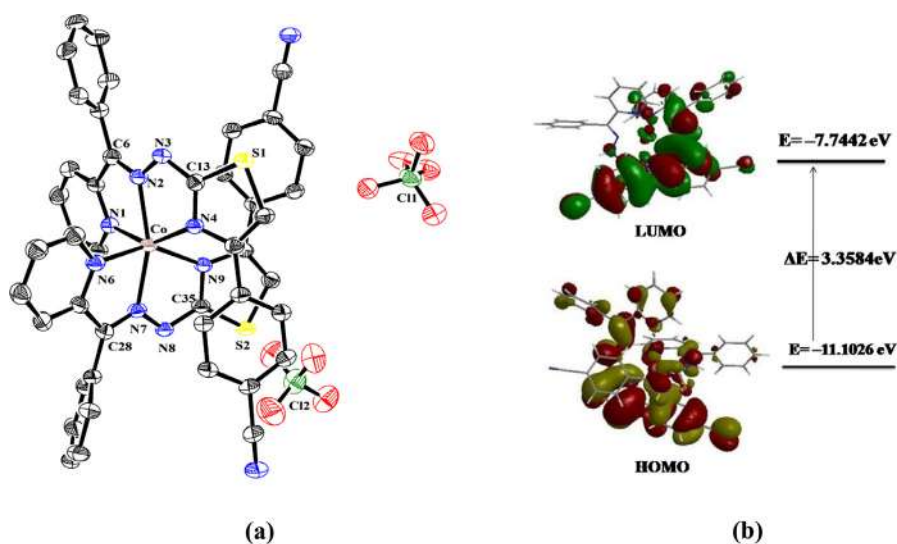
Fig. 7. Molecular structure of **1** showing the atom numbering scheme. Ellipsoids are drawn at the 50% probability level (a). HOMO and LUMO molecular orbital picture of **1** in (**b**).

at δ 7.87 ppm counts two protons and can be the protons attached with C21 and C17. The doublet peak at δ 7.71 also counts two protons that can be attached to C18 and C20 with J value 8.0 Hz. The doublet at δ 7.66 ppm corresponds to a single proton and this can be assigned to the proton attached to C3. The multiplet at δ 7.43–7.37 ppm can be assigned for the protons attached to C8–C12. Two multiplets in the region δ 7.29 and 7.17 ppm represent one proton while the multiplet at 7.26–7.20 ppm corresponds two protons. The upfield peak at δ 7.17 ppm for a single proton may correspond to proton attached to C14. No peak was found in the low field region δ 3.0 to 3.5 ppm corresponding to CH$_2$ proton of azo form of ligand, which signifies that the ligand does not show any dynamic isomerism in CDCl$_3$. The ^{13}C NMR spectrum of ppytbH consists fourteen peaks in the region of aromatic carbon atoms except the solvent peak at δ 74 ppm (Fig. S2). Mostly deshielded carbons in the thiazole ring (C13 and C15) can be assigned to the peak at δ 148.5 ppm while the peaks at δ 129.7 and 129.3 ppm can be assigned for two adjacent carbon atoms (C1 and C5) to nitrogen atoms in pyridine ring of ppyztbH. The azomethine carbon (C6) and cyanide carbon (C22) peak are also expected in the aromatic carbon region and can be assigned to the peaks at δ 139.0 and 122.65 ppm, respectively.

3.1.2. FT-IR study of the **ppytbH** and **1**

The IR spectra of ligand and complex are performed in solid state with KBr pellet. Ligand (**ppytbH**) displays low intense broad band at 3326 cm^{-1} indicates the presence of and hydrazone (–NH) bond (Fig. S3). High intense sharp band at 2200 cm^{-1} attributed to the presence of nitrile (–C≡N) group in the ligand moiety. The observed peak at 1524 cm^{-1} is due to the vibration of $C = N$ bond (thiazole ring). Low intense peaks at 1272 and 764 cm^{-1} indicate the stretching vibration frequency of –N–N and –$C = S$ (thiazole ring) bonds, respectively. Another peak is found at 687 cm^{-1} which implies Cl–O stretching vibration [35,36]. Complex **1** shows low intense broad band at 3326 cm^{-1} for (–NH) bond are remain unchanged in coordination environment around Co(II) (Fig. S4). Another stretching vibration peaks are found at 2197 cm^{-1} for $\nu_{(C≡N)}$, 1578 cm^{-1} for $\nu_{(C = N)}$, 1392 cm^{-1} for $\nu_{(C = C)}$, 805 cm^{-1} for $\nu_{(C = S)}$ of thiazole ring and 681 cm^{-1} for $\nu_{(Cl-O)}$ of perchlorate. The IR peaks with appropriate assignment of **ppytbH** and **1** are summarized in Table S1. The FT-IR peak of the ligand when compared to the peaks in complex, the point of attachments is established. The vibrational frequency of $C = N$ bond shifted to the higher frequency range on complex by 54 cm^{-1} due to bonding through azomethine nitrogen. The frequency of $C = S$ also shifted
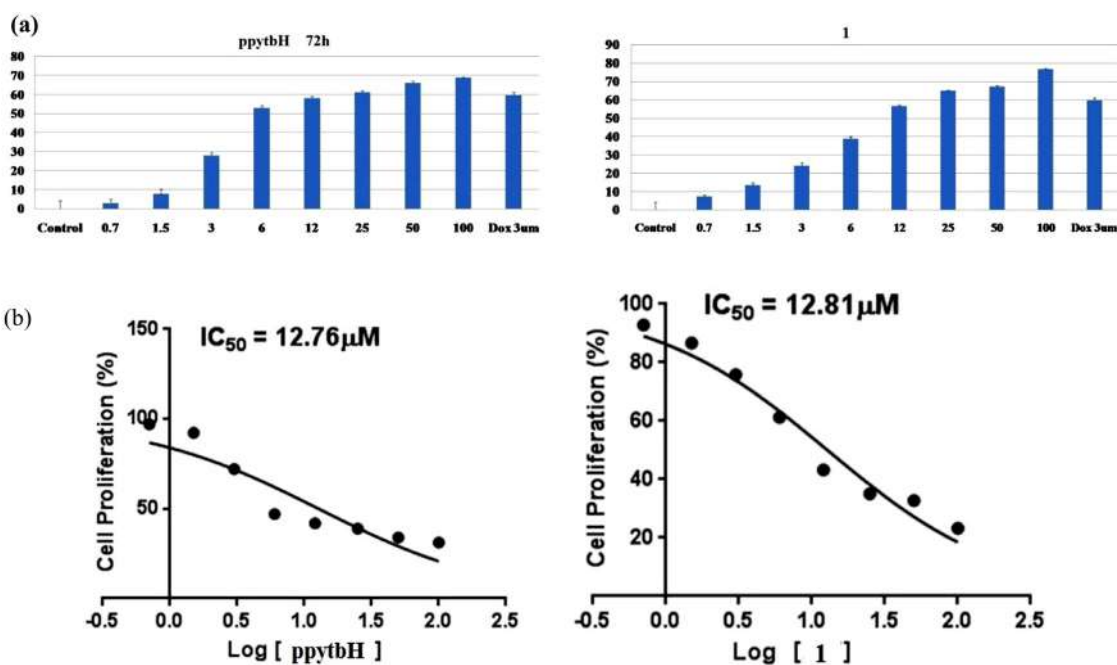
Fig. 8. Effect of compounds on cytotoxicity of U-937 cells. U-937 cells (5000 cell/well of 96-Well plate) are treated with different concentrations of ligand (**ppytbH**) and its derivatives **1** for 72 h in triplicate. MTT cell viability was assayed. Mean cell death from triplicate samples were calculated in percentage, considering untreated cell death is 0% and indicated in graph (**A**). U-937 cells are treated as shown above for 72 h with different concentrations of **ppytbH** and **1** and MTT assay was done and percentage of cell viability was plotted in group (**B**). Data were transformed, normalized and IC50 values were calculated using Graph pad Prism. Data represents mean of the three independent experiments.
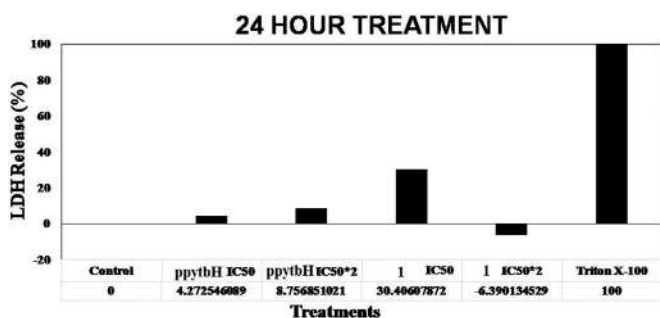
Fig. 9. Effect of compounds on cytolysis. U-937 cells are treated with IC50 value of **ppytbH** and **1** for 24 h of treatment. LDH release is plotted as percentage against triton X-100, which is considered as 100% and untreated cells' value is considered as 0%.

Fig. 10. Caspase activity upon treatment with **ppytbH** and **1**. U-937 cells (1×10^6) are treated with 40 μm of each compound at 37 °C for 24 h. The cell lysate is incubated with fluorescent substrate Z-DEVD–AMC (supplied with kit) in 96-well plate for 20 min, 40 min and 60 min. Then, fluorescence intensity is measured at excitation λ_{ex}= 342 using Spectramax M5 by Molecular Devices and Softmax pro 7.0 software. Doxorubicin (1 μM) is used as positive control.

to higher frequency range on complexation which explains the co-ordination of N-atom.

3.1.3. UV–visible spectral study **ppytbH** and **1**

The electronic spectra of the **ppytbH** and **1** are given in Fig. 1(a) and (b), respectively and the spectral data are giving in the Table S2. The absorption band of **ppytbH** at 333 nm and 375 nm arise due to intra–ligand π–π^* and n–π^* transitions in azomethane and thiazole ring [37,38]. Complex **1** shows two distinct absorption bands at 513 nm and 320 nm which can be assigned to the $^4T_{1g}(F) \rightarrow {}^4T_{2g}(F)$ (ν_1) and $^4T_1g(F) \rightarrow 4T_{1g}(P)$ (ν_3) electronic transition, respectively; which are conceived distorted octahedral high spin Co(II) complex in presence of ligand field environment [39–41]. The broad band at 513 nm can be assigned to the combination of $^4T_{1g}(F) \rightarrow {}^4T_{2g}(F)$ (ν_1) and $^4T_1g(F) \rightarrow 4T_{1g}(P)$ (ν_3) transitions for a distorted octahedral Co(II) complex [42]. The peak at 320 nm in the spectrum is due to the n–π^* and π–π^* transition in ligand part.

Fig. 11. Cleavage of PARP upon treatment with **ppytbH** and **1**. U-937 cells (2×10^6/mL) were treated with 25 μM concentrations of **ppytbH** and **1** for 24 h. Whole cell lysate was run on Western blot and probed against cleaved PARP antibody. Doxorubicin (3 μM) treated cells was used as positive control.
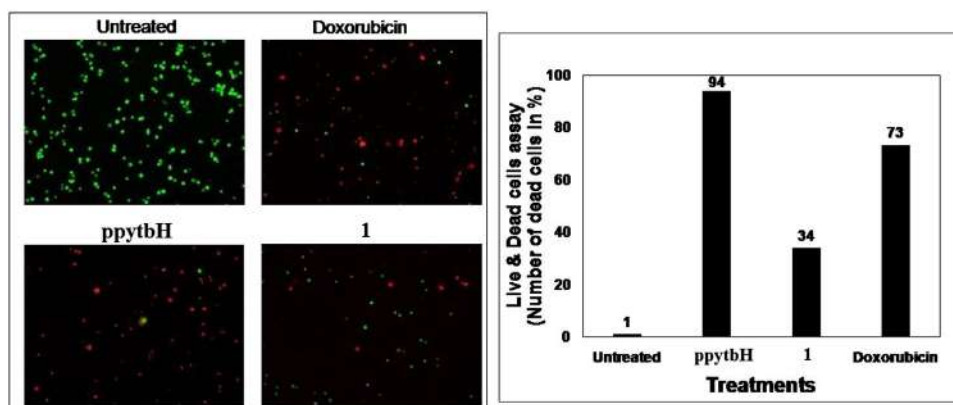
Fig. 12. Live and dead cells upon treatment with **ppytbH** and **1**. U-937 cells (1×10^6) were treated with **ppytbH** or its derivative **1** (20 μM each) and doxorubicin (2 μM) for 24 h. Live and Dead assay was carried out after staining the cells with Calcein AM and PI. The cells were visualized under florescence microscopy (A) and the number of red cells (as dead) are indicated in percentage (B).
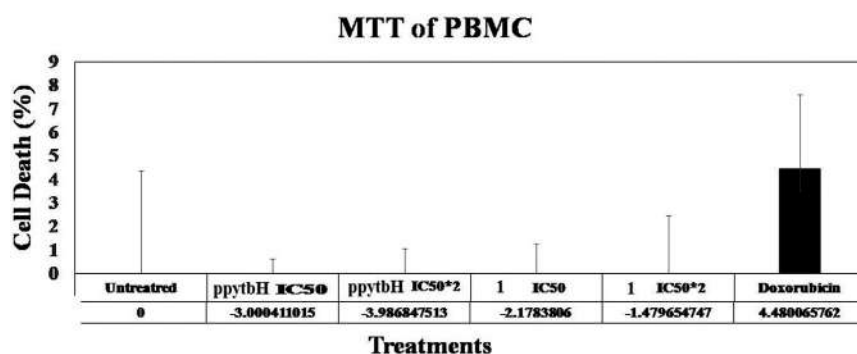
Fig. 13. Cytotoxic effect of **ppytbH** and **1** on PBMC. PBMC (10^4 cells/well) are treated in triplicate with the concentrations of IC50 and twice of it (IC50×2) of each for 24 h. MTT assay was done and cell death is calculated, considering untreated cells' value as 0%.

3.1.4. Fluorescence spectroscopy study

The fluorescence spectral properties of **ppytbH** and **1** are studies in methanol solution at room temperature. No emissions bands are observed if an excitation wavelength resembles to the lowest energy absorption are applied. Both the compounds show strong emission band. The emission maxima are observed at 427 and 448 nm for **ppytbH** and **1**, respectively as shown in Fig. 2 [43]. The emission wavelength both **ppytbH** and **1** show a positive shift of about 28 to 57 nm compared to those of excitation maxima Table S2.

3.1.5. Cyclovoltammetric study

Biological activity, metabolic properties, chemical and electrochemical reaction of organic ligand and its metal complex depends on its redox properties. The electrochemical behavior of the compound attests the potent anticancer efficacy against U-937 (human monocytic cells). The cyclovoltametry study of **ppytbH** and **1** has been performed in dry acetonitrile using supporting electrolyte, tetra butyl ammonium perchlorate (0.1 M) at room temperature. In electrochemical experiment, 0.1 M concentration of electrolyte is used. As can be shown in Fig. 3, the ligand reduces at –0.71 V (A) and –1.5 V (B) and the corresponding reverse oxidation processes are observed at +0.10 V (D) and +0.78 V (C).

The CV of **1** in Fig. 4 shows two reduction potential peaks at 0.68 V (A1) and 0.90 V (A2) versus Ag/AgCl in saturated KCl, indicating that the Co(II) is reduced to Co(I) and then the Co(I) is reduced to Co(0), respectively while in reverse process two oxidation potential peaks observed at 0.78 V (C1) and 1.0 V (C2) im-

plying Co(1)→Co(II) and Co(0)→Co(I), respectively. Both the ligand and complex shows quasi reversible behavior.

3.1.6. Thermogravimetry analysis of **ppytbH** and **1**

The thermal stability, purity and composition of a compound can be qualitatively estimated by TGA analysis. Thermogravimetry analysis curve of **ppytbH** consists three distinguishable decomposition steps (Fig. 5). The first step of weight loss in the temperature range 30–110 °C comprises the loss of moisture and one mole of water of crystallization which accounts 8.31% of total mass (calcd. 3.65%). The difference between the estimated value and calculated value is due to moisture content of the sample. The second step is a sharp mass loss of cyanobenzothiazole unit which is equivalent to 39.2% of total mass (calcd. 40%) in the temperature range 250–300 °C. The removal of perchlorate ion happens in the third step of decomposition with a mass loss equivalent to 19.5% (calcd. 20.18%) in the temperature range 300–600 °C. High temperature is required to remove perchlorate ion because it is attached through a strong ionic bond in the molecule. In the last step of decomposition (600–800 °C), nitrogen gas and residual organics evaporate completely without keeping any residue. The decomposition steps of **ppytbH** are represented in scheme 2. TG plot of **1** reveals that the molecule releases three moles of water of crystallization on heating at 250 °C, which is equivalent to the weight 4.62% (calcd. 5.02%) (Fig. 5). The results suggests that the water molecules are strongly attached through hydrogen bonds. The prominent weight loss is observed above 250 °C as indicated in the second step of scheme 3. In this decomposition step (250–600 °C), one unit of
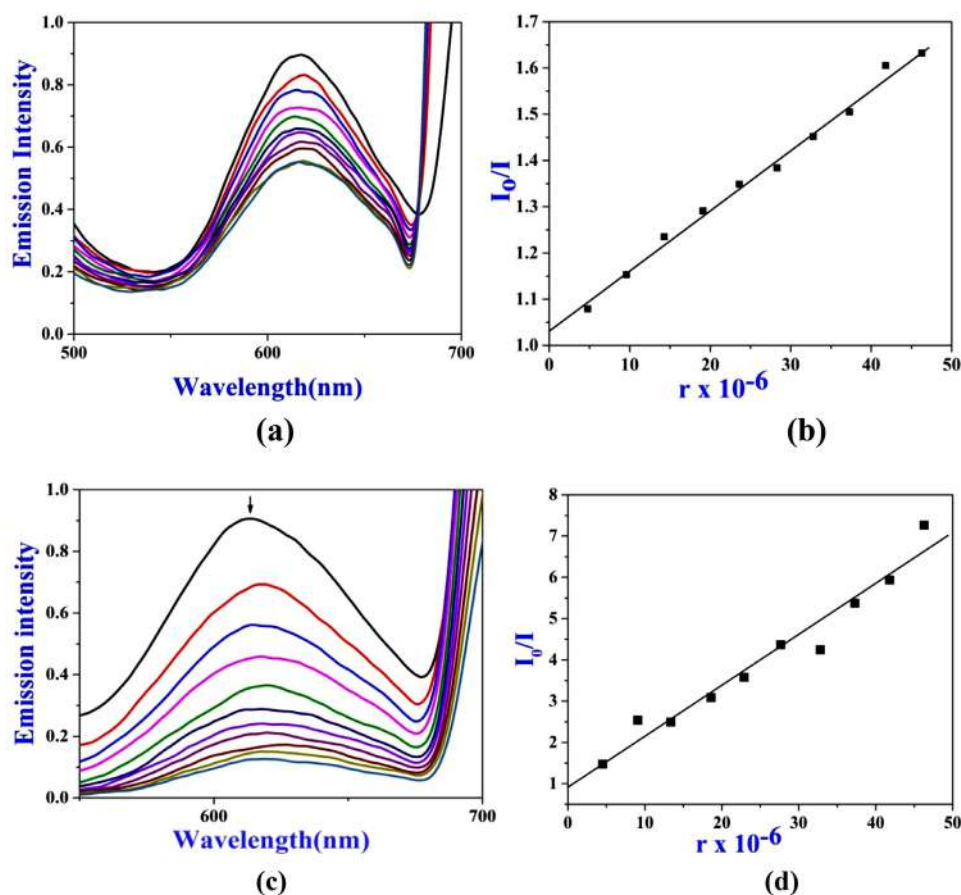
Fig. 14. Fluorescence quenching curves of EB bound to DNA by **ppytbH (a)** and **1(c)** ([complex] $= 0$–46.8×10^{-6} M). The arrow indicates the intensity quenching with [compound]. Plot of I_0/I vs. [compound] for **ppytbH (b)** and **1 (d)** ($\lambda_{em} = 610$ nm).
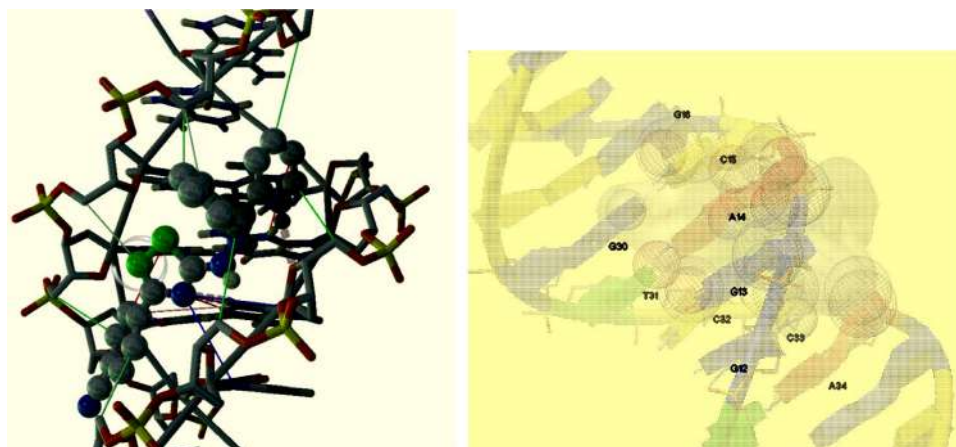
Fig. 15. Hydrophobic and hydrogen bond interaction of **ppytbH** with CT–DNA. The DNA is shown in surface. Ligand is shown in ball stick model.

cyanobenzothiazole azo of each associated ligand is lost which accounts about 37.96% of the total mass and the loss is very close to the calculated value (37.21%). The third step of decomposition of **1** is attributed to the loss of two moles of ClO_4^- and two moles of N_2 leading to formation of P. The estimated amount for this process is found 31.19% (calcd. 31.91%). The complex (P) needs temperature above 800 °C to decompose into cobalt residue. The probable decomposition steps are illustrated in the scheme 3. The thermogravimetry analysis of **ppytbH** and **1** attest the result of crystallography.

3.1.7. X-ray crystallography description of the **ppytbH** and **1**

X-ray crystallography structure of the **ppytbH** and **1** are given in Figs. 6 and 7, respectively. All crystallography parameters, bond distance and bond angle are given in the Table S3–S5. The unit cell of **ppytbH** contains one unit of perchlorate and one unit of water of crystallization. Hydrogen bonding is observed between water and perchlorate ion. The O100 and H10a atom in water molecule formed intermolecular hydrogen bonds with H1a attached with pyridyl nitrogen at distance 2.10 Å and O14 of perchlorate ion with distance 2.10 and 2.00 Å, respectively (Fig. S5). The pyridyl
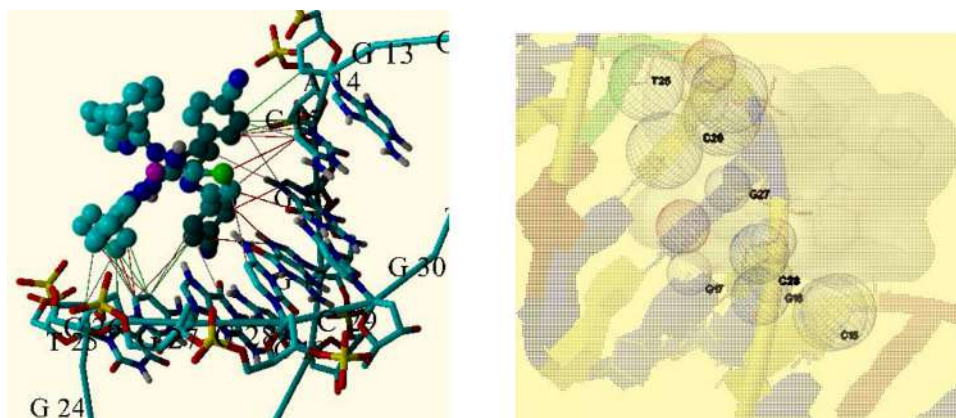
Fig. 16. Hydrophobic interaction of **1** with CT–DNA. The DNA is shown in surface. Ligand is shown in ball stick model.
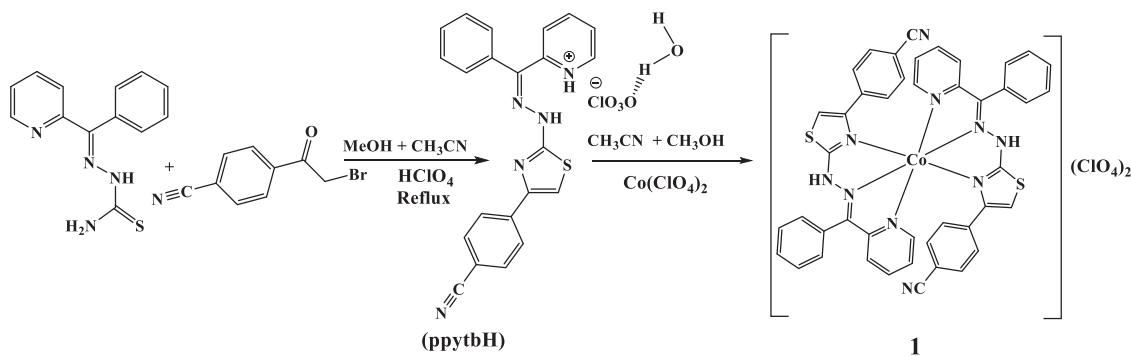
Scheme 1. Synthesis of **ppytbH** and its cobalt(II) complex.
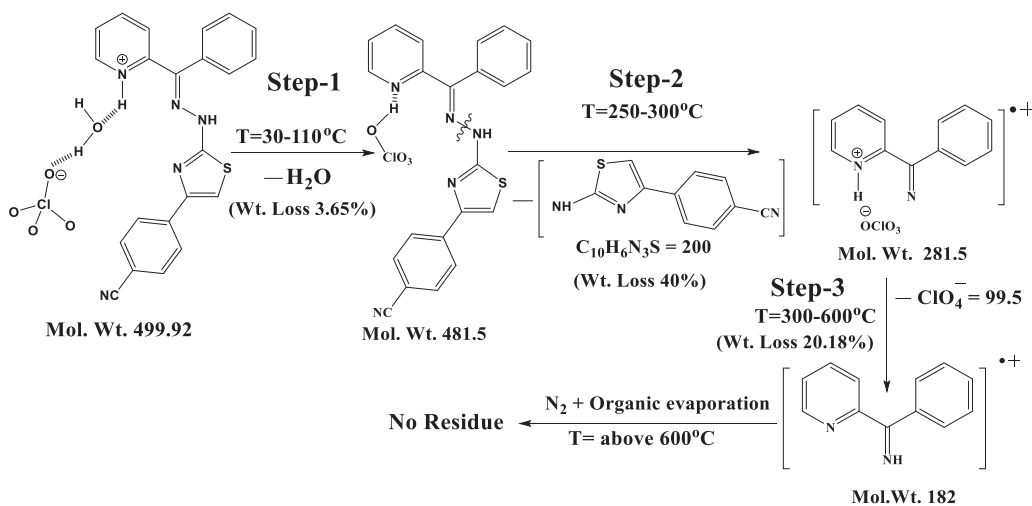
Scheme 2. Fragmentation of **ppytbH**.

and phenyl ring are oriented in space perpendicularly to minimize steric repulsion. The dihedral angle between pyridine and phenyl ring is 53.23°. The DFT study of **ppytbH** evaluates the HOMO and LUMO orbital picture as given in Fig. 6(b). The thiazole unit of ligand contributed more in HOMO than LUMO. The energy gap between HOMO and LUMO is estimated 1.8786 eV.

The crystallography data shows that complex **1** is a monoclinic crystal system with space group P 21/c. The **ppytbH** behaves as neutral tridentate NNN donor during complexation with cobalt(II). The coordination environment around cobalt displays distorted octahedral geometry with two *cis* pyridinyl nitrogen, two *cis* thiazole nitrogen and two *trans* azomethine nitrogen atoms. The two lig-

ands are perpendicularly oriented in *mer* configuration. In asymmetric unit, the perchlorate ion (ClO_4^-) that present outside of the coordination zone satisfies the primary charge of the central cobalt. The pyridyl nitrogen (N1 and N6) and thiazolyl nitrogen (N4 and N9) of ligand occupied the equatorial positions of the octahedron in such a way that pyridyl nitrogens and thiazolyl nitrogens are *cis* to each other (Fig. 7) but both the nitrogen atoms are configured *trans* to the nitrogen atom of thiazole ring in the same direction making a ring. The central cobalt atom is placed by 0.33 Å above from the equatorial plane. Two axial Co–N2 (2.10 Å) and Co–N7 (2.07 Å) bonds are found shorter than equatorial bonds (Co–N4, 2.132 Å; Co–N1, 2.142 Å; Co–N6, 2.143 Å and Co–N9, 2.157 Å

Scheme 3. Fragmentation of **1**.
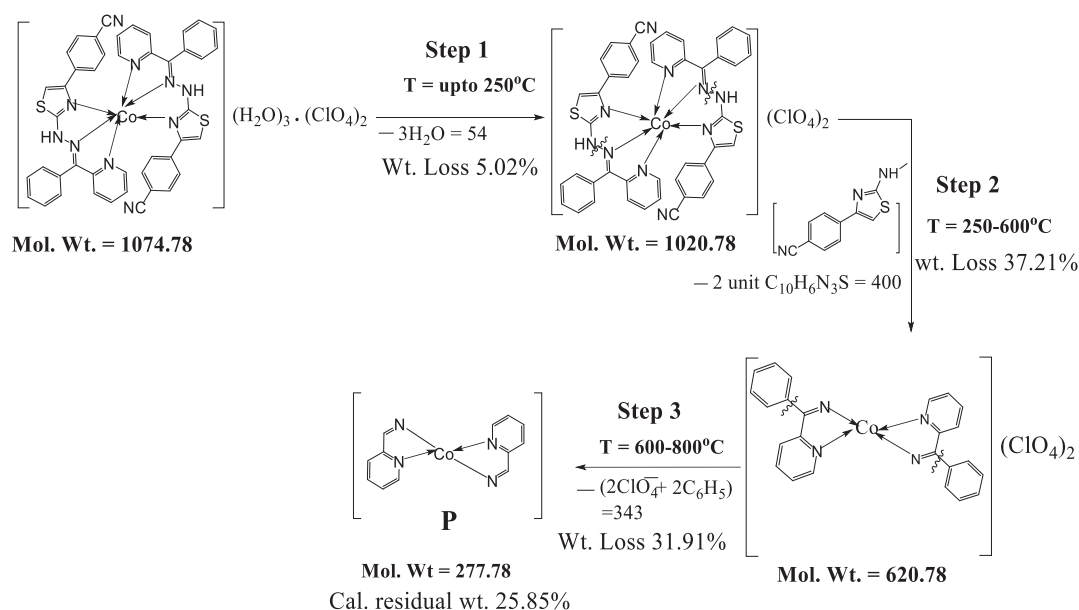
Table 1
Calculated E_H, E_L, energy band gap (E_H-E_L), chemical potential (μ), electronegativity (χ), global hardness (η), global softness(S) and global electrophilicity index (ω) for **ppytbH** and **1**.

Compound	HOMO (eV)	LUMO (eV)	(E_L-E_H) eV	X (eV)	M (eV)	H (eV)	S (eV)−1	$\omega = \mu^2 /2\,\eta$
ppytbH	−8.4264	−6.5478	1.876	7.4871	−7.4871	1.876	0.5330	14.9404
1	−11.1036	−7.8827	3.584	9.4931	−9.4931	3.584	0.2790	12.5723

(Table S4). The N4CoN7 and N9CoN2 bond angle are 119.33° and 117.69°, respectively which are larger than the idealized bond angle 90°. Consequently, the axial bond angle N2CoN7 is found to be 162.48° instead 180°. The above bond distances and bond angles parameter of **1** attributed to a strong distortion (z–in) in the molecule of low spin Co(II) ($d^7=t_{2g}^6\ e_g^1$). The complex is stabilised through intermolecular hydrogen bonding with hydrogen bond distance 1.96 Å along b axis (Table S6). The supramolecular chain is formed by H–bonding and π–π stacking interaction. The π–π stacking is obtained between thiazole ring and phenyl ring at a distance 3.83 Å (Fig. S6). HOMO and LUMO picture of **1** (Fig. 7b) implies that the participation of metal orbitals is less in the formation of HOMO and LUMO compared to ligand orbital contribution. Calculated energy difference between HOMO and LUMO is found 3.3584 eV. The bond value sum (BVS) calculation is also indicative of oxidation state +II for the cobalt (Table S7) [44].

3.1.8. Chemical reactivity of *ppytbH* and *1*

HOMO and **LUMO** energy gap of **ppytbH** (Fig. 6b) and **1** (Fig. 7b) are 1.876 and 3.584 eV, respectively. Chemical reactivity of organic and inorganic compounds has been successfully predicted with DFT based descriptors like electronic chemical potential (μ), chemical hardness (η), chemical softness (σ), absolute electronegativity (χ) and electrophilicity index (ω) [45]. All the values are given in the Table 1. At the outset, anticancer agents bind to sulfur-rich biomolecules generating intermediates which regarded as 'drug reservoirs' [45,46]. Chemical hardness of a compound is calculated with the equation η (hardness) = ($E_{LUMO} - E_{HOMO}$), which correlates the stability and reactivity of the chemical species. Chemical softness is the reverse property of chemical hardness and represented as S (softness) = $1/\eta$. Higher the value of

HOMO-LUMO energy difference higher will be hardness and lower of its reactivity [47].

The values of hardness and softness indicate that **ppytbH** is the softest among the compounds under discussion and it has high tendency to accept electron. The higher electronic chemical potential (μ) [$\mu = -\chi = -\frac{1}{2}$ ($E_{LUMO} + E_{HOMO}$), where χ denotes global electronegativity] imparts more reactiveness to the species. The trend of μ values is consistent with the S (softness). The softness of **ppytbH** is higher value of μ. Global electrophilicity index (ω) measures the tendency/receptivity of complex to achieve an additional electronic charge from the environment [where $\omega = \mu^2/2\eta = \chi/2\eta$] [48]. Electrophilicity index values interpret that **ppytbH** is more electrophilic and will be more reactive species towards DNA base pair than **1** [49]. Generally the cytotoxicity of a compound depends on the structural features. The ligand (**ppytbH**) has nearly planar structure and it is sterically less hindered. It might be interacted easily the double stranded helix of DNA compare to bulky **1**.

3.4. Biological activity

3.4.1. Cytotoxicity assay of *ppytbH* and *1*

U-937 human monocytic cells are used to determine the anticancer properties of the compounds under investigation. The ligand **ppytbH** shows better cytotoxic effect against U937 human monocytic cell line than metal complex. The IC50 values are 12.76 ± 0.75 μM and 12.81 ± 1.37 μM for **ppytbH** and **1**, respectively as shown in Fig. 8a and 8b. The cytotoxicity of a compound depends on the structure, electronic environment, redox behavior, lability, coordination environment and oxidation state. The structural changes influence some interesting biological functions which may help to understand the structure-activity relationship. Further

Table 2
Different interaction energy of **ppytbH** and **1** with CT–DNA are giving in Kcal/mol.

Compound	vdW+H bond + dissolving energy ($\Delta G_{vdW+hb+desolv}$)	Electrostatic energy (ΔG_{elec})	Total internal energy (ΔG_{total})	Torsional free energy (ΔG_{tor})	Unbound system's energy (ΔG_{unb})	Binding free Energy ($\Delta Gbinding$)
ppytbH	– 8.63	– 0.15	– 1.63	+1.49	– 1.63	– 7.13
1	– 5.58	– 0.01	– 4.72	+1.19	– 4.72	– 4.39

optimization in the structure of the compound can be manipulated on the basis of the result to make it most effective one.

3.4.2. LDH release assay of *ppytbH* and *1*

LDH assay of the compounds is employed to differentiate apoptotic (programmed cell death) activity to necrotic activity [50]. We observed that these compounds exert cytotoxicity in tumor cells. Lactate dehydrogenase (LDH) enzyme, marker of cytoplasm leakage due to necrosis, is assayed to elucidate the physiological pathway followed by compounds to explain their action on cells. U-937 cells are treated with the compounds **ppytbH** and **1** at respective IC$_{50}$ value to release of LDH. The amount of LDH release was quantified after 24 h post-treatment. The **ppytbH** and **1** have shown 6.6% and 35.2% LDH release at the concentration of IC$_{50}$ values, respectively. The **ppytbH** has shown 10.2% LDH release at double IC50 value whereas **1** has not shown any LDH release at double IC50 values at 24 h treatment (Fig. 9). These data suggest that **ppytbH** and **1** might follow the apoptotic mode of cell death, not necrosis significantly.

3.4.3. Caspase 3 activity of *ppytbH* and *1*

The EnzChek^{TM} Caspase-3 Activity Assay Kit is a fluorescent probe that identified the activity of caspase-3 in cell lysates [39,40]. The apoptotic mode of cell death is confirmed by using EnzChek^{TM} Caspase-3 Assay Kit #1. The basis for the Caspase-3 assay is the aminomethyl coumarin (AMC)-derived substrate Z-DEVD-AMC, which is a weak fluorescent in UV range but proteolytic cleavage by caspase 3 gives bright and blue fluorescence at emission maxima 441 nm (λ_{ex}=342 nm). Therefore, the amount of AMC produced is equal to the number of apoptotic cells in the test sample. The lysate of U-937 cells treated with **ppytbH** and **1** show Caspase 3 activity at 20 min and the Caspase 3 activity is pronounced with time. Both the compounds **ppytbH** and **1** show caspase 3 activity, even after 20, 40 and 60 min of incubation (Fig. 10). Both LDH release and Caspase 3 assay cumulatively suggest **ppytbH** and **1** exhibit an apoptotic mode of cell death but an apoptotic mode of cell death of **ppytbH** is slightly higher than **1**.

3.4.4. PARP cleavage in western blotted method

Poly (ADP-ribose) polymerase (PARP) is a high abundant nuclear enzyme which involved in the DNA repair process. The activation of the specified apoptosis family of proteases Caspases results in cleavage of PARP. The cleavage produces C-terminal 89 kDa fragment which is detected by western blot. The occurrence of an apoptotic mode of cell death is further validated employing in vitro PARP cleavage (Fig. 11). Apoptosis nature of **ppytbH** is further supported by the appearance of band of cleaved PARP at 89 kDa at a concentration of 25 μM. The non-appearance of the corresponding bands for **1** reveals it's less potent than **ppytbH**. So it can be concluded that **ppytbH** shows potent antitumor activity than **1** following apoptosis mode of cell death mechanism [51]. This fact is also attested by the low level of LDH release assay of **ppytbH**. It is interesting to note that metal derivative (**1**) shows the base level of LDH release but do not show any sign of PARP cleavage.

3.4.5. Live and dead cell assay

U-937 cells are treated with 20 μM of each compound by incubating at 37 °C in 5% CO$_2$ incubator for overnight. The cells are treated with 1 μM of doxorubicin which is used as control. Cells are washed thrice with PBS and stained with 5 μM calcein-AM fluoresce in acetoxy methyl ester along with propidium iodide to assess the live and dead cell population in the treated cells. As can be shown in Fig. 12(A), calcein-AM stained green cells are live where propidium iodide stained red color cells are dead. The stained cells are observed under Olympus IX73 Fluorescent Microscope [52,53]. The data show that almost 94% cells are dead upon treatment with **ppytbH** whereas, 34% by **1** at 20 μM concentration (Fig. 12B). The above result implies **ppytbH** is more reactive than its cobalt(II) complex.

3.5. Peripheral blood mononuclear cell assay of *ppytbH* and *1*

The concentrations of IC50 and twice of it for **ppytbH** and **1** were used to determine the cytotoxicity on primary cells (PBMC). The both **ppytbH** and **1** did not show any cell death effect towards PBMCs (Fig. 13). This result suggests that both compounds are non-toxic to cells as these are not inducing cell death in PBMC indicating the use of **ppytbH** and **1** as potential anticancer agent as safe molecules against tumor cells.

3.5.1. DNA-Binding study with fluorescence method using etbr indicator

Fluorescence measurement is useful method to ascertain the interactions of DNA base pair with the compounds under investigation. The interaction of the compounds with DNA is monitored using fluorescence probe ethidium bromide, because of its strong intercalation nature with DNA [54]. EB emits instant fluorescence at about 617 nm in presence of DNA in 50 mM Tris–HCl buffer solution (pH=7.4). The characteristics fluorescence of EB is quenched by the addition of drug molecule due to the reduction of binding sites between EB and DNA [55,56]. As shown in Fig. 14, the fluorescence is quenched with the concentration of the tested molecules. Stern-Volmer equation is applied to determine the relative binding properties of **ppytbH** and **1** from the slope of the straight line obtained from the plot of fluorescence intensity versus concentration of compound [57]. The apparent binding constant is obtained from the equation $K_{app}\times[\text{compound}]_{50}=K_{EB}\times[EB]$, where K_{app} is the apparent binding constant of the complex studied, [compound]$_{50}$ is the concentration of the molecule at 50% quenching of DNA-bound EB emission intensity, K_{EB} is the binding constant of EB (where K_{EB}=1.0×10^7 M^{-1}) at concentration 2.96 μM (EB) [57]. The apparent binding constant of **ppytbH** and **1** are estimated with value 0.60×10^7 and 0.20×10^7 M^{-1}, respectively at room temperature. The estimated Kapp values are very close to the binding constant for the classical intercalators or metallointercalators (10^7 M^{-1}) [58]. It can be concluded that the ligand and complex are good intercalator to the base pair of CT-DNA [59].

3.6. Docking study with ct–dna

Energetically most favourable conformation of dock poses for **ppytbH** and **1** are given in Fig. 15 and 16 and different interac-

tion energy of **ppytbH** and **1** with DNA are giving in Table 2. It is found that the free binding energy of **ppytbH** (– 7.13 Kcal/mol) is more negative than **1** (– 4.23 Kcal/mol). The planar **ppytbH** can easily interact with the empty cavities and base pair receptors of the double standard helix of DNA [60,61]. The interactions mainly hydrophobic type which acted between electronic charge of the tested small molecules with base pair of G16, C15, Al14, G30, T31, G13, C32, G12, C33 and A34 for **ppytbH** and T26, C10, G27, G17, C23, G13 and C15 for **1**. The docking result suggests that **ppytbH** is more reactive than **1**. Therefore, it can be concluded the theoretical study corroborates to the biological evaluation studies like MTT assay, LDH release assay, PARP cleavage, caspase 3 activity, Live and dead cell assay and PBMC assay of the molecules under discussion.

4. Conclusion

A novel thiazolyl pyridine ligand, namely 4-(2-(2-(phenyl (pyridine-2-yl)methylene)hydrazinyl)thiazole-4-yl)benzonitrile (**pp ytbH**) and its mononuclear cobalt(II) complex (**1**) have been synthesized and characterized by various spectroscopic and X-ray crystallographic methods. Both **ppytbH** and **1** exerted high level of in vitro cytotoxicity against U-937 human histiocytic lymphoma cells with IC_{50} values 12.76 and 12.81 μM, respectively. The apoptosis modes of cell death of the compounds are confirmed by caspase 3 activity study, PI-stained red cells' number (Live and Dead assay), and PARP cleavage assay. However, both compounds did not show significant cytolysis (LDH release upon treatment) and compare to compound **ppytbH** and **1** did not show any cytoplasmic leakage suggesting this group of compounds are safe for their activity to exert cell death effect and for further use as cancer therapeutics. The compounds do not show any cytotoxicity against peripheral blood mononuclear cell (PBMC) which suggests that these are non-effective to primary cells indicating no side-effect as therapeutics. The apparent fluorescence binding constant ($K_{app} \approx 10^7$ M^{-1}) and free binding energy (ΔG = –7.13 Kcal/mole for **ppytbH** and –4.39 Kcal/mol for **1**) suggest intercalative binding mode of the molecules with CT DNA. Having property of electron acceptor, the **ppytbH** is more electrophilic in nature compare to **1**. Besides these, due to planar and less sterically hindered conformation of **ppytbH** than **1**, it can interact with the biological molecules, including DNA and proteins more comfortably. This might help to interfere the cell signaling cascades that required for cell growth especially in tumor cells. Tumor cells are more affected due to the high metabolic activity and it uptake the materials from the surroundings is more that required for rapid proliferation, compare to primary cells. The pronounced cell death was observed in tumor cells, but not the primary cells, like PBMC. Overall, the new thiazolyl pyridine class of compounds, especially more planer compound **ppytbH** have the upper hand to cut the life line of tumor cells which needs to be tested in vivo before going for clinical trial as future anti-cancer therapeutics. Synthesis of novel and new derivatives of thiazolyl pyridine will open a new avenue on further exploration.

Declaration of Competing Interest

The authors declare that they have no known competing financial interests or personal relationships that could have appeared to influence the work reported in this paper.

It is to be declared that there is no conflict of interest.

Acknowledgement

Supplementary material

Supplementary material associated with this article can be found, in the online version, at doi:10.1016/j.molstruc.2020.129015.

References

[1] S. Ramos-Inza, C. Aydillo, C. Sanmartín, D. Plano, Thiazole Moiety, An Interesting Scaffold for Developing New Antitumoral Compounds, Heterocycles–Synthesis and Biological Activities (2019).

[2] M.C. Heffern, N. Yamamoto, R.J. Holbrook, A.L. Eckermann, T.J. Meade, Cobalt derivatives as promising therapeutic agent, Current Opinion Chem. Bio. 17 (2013) 189–196.

[3] C.R. Munteanu, K. Suntharalingam, Advances in cobalt complexes as anticancer agents, Dalton Trans. 44 (2015) 13796–13808.

[4] A. Bhardwaj, A Review on Azole Derivatives as Potent Anticancer Agents, International Journal of Chem. Tech. Research 11 (2018) 154–175.

[5] Y. Hu, Molecular scaffolds with high propensity to form multi-target activity cliffs, J. Chem. Inf. Model 50 (2010) 500–510.

[6] M.E. Welsch, S.A. Snyder, B.R. Stockwell, Privileged scaffolds for library design and drug discovery, Current Opinion Chem. Biol. 14 (2010) 347–361.

[7] S. Kumar, M.T. Patil, R. Kataria, D.B. Salunke, Thiazole: A privileged Scaffold in Drug Discovery, Chapter in Chemical Biology & Drug Design, 2016.

[8] E. Cole, D.P. Dowling, M.A. Boone, A.J. Phillips, D.W. Christianson, Structural Basis of the Antiproliferative Activity of Largazole, a Depsipeptide Inhibitor of the Histone Deacetylases Kathryn, J. Am. Chem. Soc. 133 (2011) 12474–12477.

[9] A.A. Bowers, N. West, T.L. Newkirk, A.E. Troutman-Youngman, S.L. Schreiber, O. Wiest, J.E. Bradner, R.M. Williams, Synthesis and Histone Deacetylase Inhibitory Activity of Largazole Analogs: alteration of the Zinc-Binding Domain and Macrocyclic Scaffold, Org. Lett. 11 (6) (2009) 1301–1304.

[10] M. Vinicius, N.D. Souza, Synthesis and biological activity of natural thiazoles: an important class of heterocyclic compounds, Journal of Sulfur Chemistry 26 (2005) 429–449.

[11] Y. Tsuruni, H. Ueda, K. Hayashi, S. Takase, M. Nishikawa, S. Kiyoto, M.O. kuhara, WS75624 A and B, New Endothelin Converting Enzyme Inhibitors Isolated from Saccharothrix sp. No. 75624, J. Antibiotics 48 (1995) 1073–1075.

[12] A. Puszkiel, G. Noé, A. Bellesoeur, N. Kramkimel, M.N. Paludetto, A. Thomass—choemann, M. Vidal, F. Goldwasser, E. Chatelut, B. Blenchet, Clinical Pharmacokinetics and Pharmacodynamics of Dabrafenib, Clin. Pharmacokinet. 58 (4) (2019) 451–467.

[13] G.M. Keating, Dasatinib: a review in chronic myeloid leukaemia and Ph+ acute lymphoblastic leukaemia, Drugs 77 (2017) 85–96.

[14] H. Elshaflu, S. Bjelogrlic, C.D. Muller, R.T. Todorovic, M. Rodic, M. Marinkovic, N.R. Filipovic, Co(III) complex with (E)-2-(2-(pyridine-2-ylmethylene)hydrazinyl)-4-(4-tolyl)-1,3-thiazole: structure and activity against 2-D and 3-D cancer cell models, J. Coord. Chem. 69 (2016) 3354–3363.

[15] P. Chimenti, A. Petzer, S. Carradori, M.D. Ascenzio, R. Silvestri, S. Alcaro, F. Ortuso, J.P. Petzer, D. Seccia, Exploring 4-substituted-2-thiazolylhydrazones from 2-, 3-, and 4- acetylpyridine as selective and reversible hMAO-B inhibitors, Eur J Med Chem 62 (2013) 221–227.

[16] M.V. de Oliveira Cardoso, L.R.P. de Siqueira, E.B. da Silva, L.B. Costa, M.Z. Hernandes, M.M. Rabello, R.S. Ferreira, L.F. da Cruz, D.R. Magalh–aes Moreira, V.R.A. Pereira, M.C.A.B. de Castro, P.V. Bernhardt, A.C. Lima Leite, 2-Pyridyl thiazoles as novel anti-Trypanosoma cruzi agents: structural design, synthesis and pharmacological evaluation, Eur J Med Chem 86 (2014) 48–59.

[17] T.D.S. Silva, L.M. Bomfim, A.C.B.C. Rodrigues, C.B.S.Sales R.B.Dias, C.A.G. Rocha, M.B.P. Soares, D.P. Bezerra, M.V.O. Cardoso, A.C.L. Leite, G.C.G. Militão, Anti-liver cancer activity in vitro and in vivo induced by 2-pyridyl 2,3-thiazole derivatives, Toxicol. Appl. Pharmacol. 329 (2017) 212–223.

[18] C. Lamberth, J. Dinges (Eds.), Bioactive Heterocyclic compounds class: Agrochemicals Wiley-vchverleg GmbH & co, 2012.

[19] P. Bera, P. Brandão, G. Mondal, A. Santra, A. Jana, R. Babu Mokhamatam, S.K. Manna, T.K. Mandal, P. Bera, An unusual iminoacylation of 2-amino pyridyl thiazole: synthesis, X-ray crystallography and DFT study of copper(II) amidine complexes and their cytotoxicity, DNA binding and cleavage study, Polyhedron 159 (2019) 436–445.

[20] P. Bera, P. Brandão, G. Mondal, H. Jana, A. Jana, A. Santra, P. Bera, Synthesis of a new pyridinyl thiazole ligand with hydrazone moiety and its cobalt (III) complex: x-ray crystallography, in vitro evaluation of antibacterial activity, Polyhedron 134 (2017) 230–237.

[21] M.T. Chhabria, S. Patel, P. Modi, P.S. Brahmkshatriya, Thiazole: a Review on Chemistry, Synthesis and Therapeutic Importance of its Derivatives, Curr. Topi. Medici. Chem. 16 (2016) 2841–2862.

[22] D. Lison, in: Handbook On the Toxicology of Metals, 3rd Edition, Academic Press, Burlington, 2007, pp. 511–552.

[23] A. Sigel, H. Sigel, R.K.O. Sigel, in: Interrelations Between Essential Metal Ions and Human Diseases, Part of the Metal Ions in Life Sciences Book Series, 13, Springer, Netherlands, 2013, pp. 295–320. (MILS, volume 13).

[24] C.R. Munteanu, K. Suntharalingam, Advances in Cobalt Complexes as Anticancer Agents, Dalton Trans. 44 (2015) 13796–13808.

[25] G. Vellaiswamy, S. Ramaswamy, Co(II) complexes of 4-((3-ethoxy-2-hydroxyb enzylidene)amino) -N-(thiazol-2-yl)benzene sulphonamide and 4-((pyridin-2-ylmethylene)amino)-N-(thiazol-2-tl) benzene sulfonamide: synthesis, Fluorescence Properties and Anticancer Activity, J Fluoresc 27 (2017) 1559–1565.

[26] G.M. Sheldrick, SADABS, University of Göttingen, Germany, 1996.

[27] G.M. Sheldrick, SHELXL-97, Crystal Structure Refinement Program, University of Göttingen, 1997.

[28] P. Bera, A. Aher, P. Brandao, S.K. Manna, G. Mondal, A. Jana, A. Santra, H. Jana, P. Bera, Induced apoptosis against U937 cancer cells by Fe(II), Co(III) and Ni(II) complexes with a pyrazine-thiazole ligand: synthesis, structure and biological evaluation, Polyhedron 182 (2020) 114503.

[29] L.F. Lincz, Deciphering the apoptotic pathway: all roads lead to death, Immunol. Cell Biol. 76 (1998) 1–19.

[30] P. Villa, S.H. Kaufmann, W.C. Earnshaw, Caspases and caspase inhibitors, Trends Biochem Sci 22 (1997) 388.

[31] T.B. Bal, D. Dutta, A. Duthie, B.G.M. Rocha, M.F.C.G. de Silva, S. Saurav, S.K. Manna, Synthesis, structural snapshots, solution redox properties and cytotoxic performance of designated ferrocene scaffolds appended with organistannyl(IV) benzoate en route for human hepatic carcinoma, Organometallics 37 (18) (2018) 2961–2979.

[32] T.B. Bal, P. Kehie, A. Duthie, N. Guchait, N. Raviprakash, R.B. Mokhamatam, S.K. Manna, N. Armata, M. Scopellite, R. Wang, U. Englert, Synthesis, photophysical properties and structures of organotin Schiff base utilizing aromatic amino acid from the chiral pool and evaluation of the biological perspective of a triphenyltin compound, J. Inorg. Biochem. 168 (2017) 76–89.

[33] R. Huey, G.M. Morris, A.J. Olson, D.S. Goodsell, A semi empirical free energy force field with charge-based desolvation, Computational Chemistry 28 (2007) 1145–1152.

[34] K. Sudeepa, N. Narsimha, B. Aparna, S. Sreekanth, A.V. Aparna, M. Ravi, J. Mohmed, C.S. Devi, Synthesis, spectral characterization, antimicrobial, DNA interactions and molecular modelling studies of metal complexes of 1, 3-benzothiazole carbohydrazone, J. Chem. Sci. 130 (2018) 52.

[35] C.R. Munteanu, K. Suntharalingam, Advances in Cobalt Complexes as Anticancer Agents, Dalton Trans 44 (2015) 13796–13808.

[36] A. Eskandari, A. Kundu, C. Lu, S. Ghosh, K. Suntharalingam, Synthesis, characterization, and cytotoxic properties of mono- and di-nuclear cobalt(II)-polypyridyl complexes, Dalton Trans 47 (2018) 5755–5763.

[37] G. Vellaiswamy, S. Ramaswamy, Co(II) Complexes of 4-((3-ethoxy -2-hydroxybenzylidene)amino) -N-(thiazol-2-yl)benzenesulphonamide and 4-((pyridin-2-ylmethylene)amino)-N-(thiazol-2-yl) benzenesulfonamide: synthesis, Fluorescence Properties and Anticancer Activity, J Fluoresc 27 (2017) 1559–1565.

[38] M.A. Neelakantan, S.S. Marriappan, J. Dharmaraja, T. Jeyakumar, K. Muthukumaran, X.R.D. Spectral, SEM and biological activities of transition metal complexes of polydentate ligands containing thiazole moiety, Spectrochimica Acta Part A 71 (2008) 628–635.

[39] M. Sobiesiak, T. Muzioł, M. Rozalski, U. Krajewska, E. Budziszd, Ni(II) and Cu(II) complexes with phenylthiazole and thiosemicarbazone-derived ligands: synthesis, structure and cytotoxic effects, New J. Chem. 38 (2014) 5349–5361.

[40] B.P. Baranwal, T. Gupta, Synthesis and Physico-Chemical Studies on Iron(II,III,III) and Cobalt(II) Thiocarboxylates, Synthesis and Reactivity in Inorganic and Metal-Organic Chemistry 34 (2004) 1737–1754.

[41] B. Kayal, Z.K. Yılmaz, O. Şahin, B. Aslim, Ü. Tükenmez, B. Ülküseven, Structural analysis and biological functionalities of iron(III) and manganese(III)–thiosemicarbazone complexes: in vitro anti-proliferative activity on human cancer cells, DNA binding and cleavage studies, Journal of Biological Inorganic Chemistry 24 (2019) 365–376.

[42] G.B. Bagihalli, P.G. Avaji, S.A. Patil, P.S. Badami, Synthesis, spectral characterization, in vitro antibacterial, antifungal and cytotoxic activities of Co(II), Ni(II) and Cu(II) complexes with 1,2,4-triazole Schiff bases, Euro. J. Med. Chem. 43 (2008) 2639–2649.

[43] M. Gulcan, Y. Karataş, S. Işık, G. Öztürk, E. Akbş, E. Şahin, Transition Metal, Complexes of a Novel Symmetrical Benzothiazole-Based Ligand: synthesis, Spectral/Structural Characterization and Fluorescence Properties, J Fluorescence 24 (2014) 1679–1686.

[44] H.H. Thorp, Bond valence sum analysis of metal-ligand lengths in metalloenzymes and model complexes, Inorg 31 (1992) 1585–1588.

[45] I. Mitra, S. Mukherjee, V.P. Reddy, B. Misini, P. Das, S. Dasgupta, W. Linert, S.C. Moi, Synthesis, biological evaluation, substitution behaviour and DFT study of Pd(II) complexes incorporating benzimidazole derivative, New. J. Chem. 42 (2018) 2574–2589.

[46] Y. Onda, Y. Masuda, M. Yoshida, T. Do, Conformation-Based Design and Synthesis of Apratoxin A Mimetics Modified at the α,β-Unsaturated Thiazoline Moiety, J. Med. Chem. 60 (2017) 6751–6765.

[47] P.K. Chattaraj, B. Maiti, HSAB Principle Applied to the Time Evolution of Chemical Reactions, J. Am. Chem. Soc. 125 (2003) 2705–2710.

[48] Zhong-Lu You, Yong-Ming Cui, Yu-Ping Ma, C. Wang, Xiao-Shuang Zhou, K. Li, Synthesis, characterization and urease inhibitory activity of oxovanadium(V) complexes with similar Schiff bases, Inorg. Chem. Comm. 14 (2011) 636–640.

[49] D.R. Roy, U. Sarkar, P.K. Chattaraj, A. Mitra, J. Padmanabhan, R. Parthasa, V. Subramanian, S. Van Damme, P. Bultinck, Analyzing toxicity through electrophilicity, Mol. Divers. 10 (2006) 119–131.

[50] L. Parhamifar, H. Andersen, S.M. Moghimi, Lactate Dehydrogenase Assay for Assessment of Polycation Cytotoxicity, Nanotechnology for Nucleic Acid Delivery 1943 (2019) 291–299.

[51] J.D.F. Wadsworth, S. Joiner, A.F. Hill, T.A. Campbell, M. Desbruslais, P.J. Luthert, J. Collinge, Tissue distribution of protease resistant prion protein in variant CJD using a highly sensitive immuno-blotting assay, The Lancet 358 (2001) 171–180.

[52] K. Ou, S. Mertsch, S. Theodoropoulou, J. Wu, J. Liu, D.A. Copland, L.M. Scott, A.D. Dick, S. Schrader, L. Liu, Müller, Cells Stabilize Microvasculature through Hypoxic Preconditioning, Cell Physiol Biochem 52 (2019) 668–680.

[53] H. Cherif, D.G. Bisson, P. Jarzem, M. Weber, J.A. Ouellet, L. Haglund, Curcumin and o-Vanillin Exhibit Evidence of Senolytic Activity in Human IVD Cells In Vitro, J. Clin. Med. 8 (2019) 433–440.

[54] N. Shahabadi, M. Hakimi, T. Morovati, N. Fatahi, DNA binding affinity of a macrocyclic copper(II) complex: spectroscopic and molecular docking studies, Nucleosides Nucleotides and Nucleic acids 36 (2017) 497–510.

[55] B.C. Baguley, M.L. Bret, Quenching of DNA-ethidium fluorescence by amsacrine and other antitumor agents: a possible electron-transfer effect, Biochemistry 23 (1984) 937–943.

[56] R.F. Pasternack, M. Caccam, B. Keogh, T.A. Stephenson, A.P. Williams, E.J. Gibbs, Long-range fluorescence quenching of ethidium ion by cationic porphyrins in the presence of DNA, J. Am. Chem. Soc. 113 (1991) 6835–6840.

[57] M.R. Eftink, C.A. Ghiron, Fluorescence quenching studies with proteins, Anal. Biochem 114 (1981) 199–227.

[58] M. Cory, D.D. McKee, J. Kagan, D.W. Henry, J.A. Miller, Design, synthesis, and DNA binding properties of bifunctional intercalators. Comparison of polymethylene and diphenyl ether chains connecting phenanthridine, J. Am. Chem. Soc. 107 (1985) 2528–2536.

[59] J.R. Lakowicz, Fluorescence spectroscopic investigations of the dynamic properties of proteins, membranes and nucleic acids, J. Biochem. Biophys. Methods 2 (1980) 91–119.

[60] Z. Zhao, J. Zhang, S. Zhi, W. Song, J. Zhao, Novel binuclear and trinuclear metal (II) complexes: DNA interactions and in vitro anticancer activity through apoptosis, J. Inorg. Biochem. 197 (2019) 110696.

[61] Md.S. Hossain, P.K. Roy, R. Ali, C.M. Zakaria, Md. K.E.-Zahan, Selected Pharmacological Applications of 1st Row Transition Metal Complexes: a review work, Clinical Medicine Research 6 (2017) 177–190.

Source details

Feedback ›   Compare sources ›

Journal of Molecular Structure

Scopus coverage years: from 1967 to Present

Publisher: Elsevier

ISSN: 0022-2860

Subject area: (Chemistry: Inorganic Chemistry) (Chemistry: Analytical Chemistry) (Chemistry: Spectroscopy) (Chemistry: Organic Chemistry)

Source type: Journal

View all documents ›   Set document alert   💾 Save to source list

CiteScore 2022 ⓘ
6.0

SJR 2022 ⓘ
0.482

SNIP 2022 ⓘ
0.954

CiteScore   CiteScore rank & trend   Scopus content coverage

ZINC ENRICHMENT IN MAIZE GROWN IN SOIL DRESSED WITH NEEM FERTILIZER

[1]Rupa Chakraborty, [2]Anish Pyne

[1]Assistant Professor, [2]Research Student
[1]Department of Botany,
[1]Dinabandhu Andrews College, Kolkata-84, India.

Abstract: A large part of reclaimed wetland in the Eastern fringe of Kolkata is being used for maize farming. Fertilizers are frequently being added to the soil by maize growers in order to obtain better yield as well as to improve the soil quality in many cases. In this study, effect of supplementation of urea and neem fertilizer in wetland soil on zinc uptake by maize leaves and grains were investigated, as maize is one of the staple crops consumed by all irrespective of economic standards in our country and also throughout the world.

Key words: Maize, Neem fertilizer, Urea, Wetland, Zinc, Immunity, Anti-Oxidant.

I. INTRODUCTION:-

India is an agro-based country. As until 2018, agriculture employed more than 50% of the Indian work force and contributed 17–18% to country's GDP. Across seasons, varieties of crops are grown throughout the country going in accordance with the quality of the soil, fertilizers and other allied factors. Quality of the soil, where a particular crop is grown plays a very crucial role in deciding not only the yield but also the nutritional index of the crop itself. This depends on a number of factors like the ability of the soil to make essential nutrients available to the crops, aeration, percentage of heavy metals in the soil etc. The number of heavy metals found in any soil plays a pivotal role in estimating the quality of the soil. Heavy metals like copper, zinc and arsenic can prove to decisive weather a particular soil can be used for farming or not. The use of fertilizers for better yield of crops are a must nowadays given the demand and supply ratio throughout the country and even in the export relations abroad.

The wetland located in the Eastern fringe of Kolkata is famous for dumping wastes. At the same time, these wetlands are also being used for agricultural purposes. Maize is a very important crop due to its nutritional values (Nuss and Tanumihardjo, 2010) and also because it acts as an important raw material in several industrial applications. Maize farming is a popular practice in these wetland areas. Maize farmers supply different fertilizers in their field regularly for better yield. Urea is frequently being used by maize growers as it is an inexpensive form of nitrogen fertilizer. In addition to it, farmers are now using organic fertilizers in their field also.

Several studies have confirmed the presence of different heavy metals in wetland soil (Chattopadhyay et al., 2002; Khatun et al., 2016; Dutta et al., 2016). Zinc, a heavy metal, also found to be present in the wetland soil (Das et al., 2014), proves to be a very important one for human body as it has anti-oxidant properties and acts both as a co-factor for enzymes like carbonic anhydrase and inhibitor for enzymes like NADPH Oxidase. At the same time, excessive concentrations of zinc can lead to unwanted toxicity in the body. Maize plant is a significant accumulator of zinc (Lu et al., 2015). During the present investigation, a field experiment was conducted to study the effect of supplementation of urea and neem fertilizer in wetland soil on zinc uptake by maize leaves and grains. Our study is based on the effect of some fertilizers in supplementing the uptake of heavy metal (in our case, zinc). The study was carried forward with the following objectives:-

- To improve the yield of maize, an inexpensive staple crop available to all irrespective of socio-economic standards in an eco-friendly manner
- To test whether the incorporation of organic fertilizers increase the zinc uptake in maize plants, which is a natural accumulator of zinc.
- To exploit the anti-oxidant property of zinc at a non-toxic concentration which helps us to reduce oxidative stress and boost our immunity, which is the need of the hour.

II. Materials and Methods:

2.1. Growing plants in the field:

Three plots (33 sq. m each) were selected in reclaimed wetland in the eastern fringe of Kolkata (Latitude - 22.572645, Longitude - 88.363892). One plot was used as control while the other two were used for urea and neem fertilizer treatment separately. Maize seeds (Cv. MSF 56) were disinfected with 0.1% HgCl2 solution for 5 minutes , washed thoroughly with sterile distilled water , soaked in water for overnight and then sown in rows (60- 75 cm apart) in the field (wetland soil).

2.2. Supplementation of urea and neem fertilizer in the soil:

Maize seeds (Cv. MSF 56) sown in wetland soil was supplemented with urea and neem fertilizer at the rate of 150 and 500kg / ha respectively. Leaves and cobs of 88 old day plants were collected and the amount of zinc was estimated.

2.3. Estimation of zinc:

Zinc content in the sample was estimated using Atomic Absorption Spectrophotometer

(Perkin Elmer 2380).

III.   Results:-

3.1. Effect of supplementation of urea and neem fertilizer (Neem shield) on zinc uptake by maize leaves

The results of Zinc uptake by leaves of maize plants (Cv. MSF 56) are given in Table 1.

Table 1. Effect of supplementation of urea and neem fertilizer (Neem shield) on zinc uptake by maize leaves

Treatment		Average zinc content (µg /g dry wt.) in leaves
Untreated (control)		13.93 ± 0.467
Treated (fertilizer)	Urea	12.97 ± 0.467
	Neem fertilizer	34.50 ± 0.467

Results show that addition of neem fertilizer to wetland soil increased zinc uptake significantly by maize leaves when it is compared to untreated set and urea treatment too. In case of neem fertilizer treatment, 147.66 % enhancement in zinc uptake was noticed in relation to control. A decrease (6.89 %) in zinc uptake has been noted in case of urea treatment when it is compared to untreated control set.

3.2. Effect of supplementation of urea and neem fertilizer (Neem shield) on zinc uptake by maize grains

The results of zinc uptake by cobs of treated maize plants (Cv. MSF 56) are given in Table 2.

Table 2. Effect of supplementation of urea and neem fertilizer on zinc uptake by maize grains

Treatment		Average zinc content (µg /g dry wt.) in grains
Untreated (control)		10.13 ± 0.467
Treated (fertilizer)	Urea	26.50 ± 0.467
	Neem fertilizer	27.30 ± 0.467

Results reveal that addition of fertilizer to wetland soil enhanced zinc uptake by maize grains. Urea and neem fertilizer treatment showed 161.6 % and 169.49 % increase in zinc uptake respectively. Supplementation of neem fertilizer showed a slight increase in zinc uptake in comparison to urea.

IV.   Discussions:-

Maize plant is responsive to zinc sources (Ruffo et al. 2016). Lu et al., 2015 also proved that presence of heavy metal in the soil resulted in the accumulation of heavy metal content specially zinc in maize plant. A great effect of nitrogen fertilizer on zinc absorption by winter wheat has been established by Zhao et al, 2016. They showed that nitrogen application increased total Zn accumulations and Zn concentrations of each plant part of winter wheat. Furthermore, it was also noted that appropriate N application increased Zn content in grains. The results obtained from our study shows the increase in the amount of zinc uptake via supplementation with fertilizers as nitrogen sources which automatically uplifts the nutritional value of these cobs as the anti-oxidant property of zinc allows reduction of oxidative stress in our body and builds up immunity which is the need of the hour amidst the deadly pandemic situation the world is stuck in today. These advantages acquired from zinc can be extracted from the maize grown in fertilized soil and owing to the fact that maize is an inexpensive staple crop consumed all around the world irrespective of the socio-economic status of people employed in varied sectors, this study can be our key to boost immunity in such a handy way amidst the COVID-19 crisis. The concentration of zinc accumulated in both the maize leaves and cobs, are well below the toxicity level but provides us with the added advantage that can be accumulated from zinc uptake whose mechanism is well explained by Gupta et al., 2016.

V.   Conclusion:

Present experiment indicates that supplementation of fertilizer (urea and neem fertilizer) in wetland soil plays an important role in zinc uptake by maize plants. Addition of neem fertilizer showed higher increase in zinc uptake in both maize leaves and grains (cobs) when it was compared to untreated control set which boosted the nutritional index of the maize and hence may lead to the improvement of the socio-economic status of the maize farmers.

VI.   Acknowledgement

VII.   References:

[1] Das, D. K. Bandopadhyay, P. K. Jee, A. Karmakar. "Geochemistry of sediments and water with a health risk assessment of heavy metal contaminated vegetables grown in Dhapa, a waste disposal site in Kolkata, India". World Review of Science Technology and Sustainable Development. 11(3/4): pp 248 – 268, 2014. DOI: 10.1504/WRSTSD.2014.066817

[2] Khatun , S. Pal , A. K. Mukherjee , P. Samanta1, S. Mondal , D. Kole , P. Chandra , A. R. Ghosh. "Evaluation of metal contamination and phytoremediation potential of aquatic macrophytes of East Kolkata Wetlands, India" .Environmental Health and Toxicology, Vol.31, Article ID: e2016021, 7 pages. 2016 https://doi.org/10.5620/eht.e2016021 eISSN: 2233-6567

[3] Chattopadhyay, A. Chatterjee, S. K. Mukhopadhyay . "Bioaccumulation of metals in the East Calcutta wetland ecosystem". Aquatic Ecosystem Health & Management, 5(2): pp 191-203, 2002.

[4] E. T. Nuss, S. A. Tanumihardjo." Maize: a paramount staple crop in the context of global nutrition". Compr. Rev. Food Sci. F. 9, pp 417–436. 2010. doi: 10.1111/j.1541-4337.2010.00117.x

[5] J. Dutta, A. Saha, A. Mitra. "Impact of acidification on heavy metal levels in a bheri of East Kolkata Wetlands (EKW), a Ramsar Site in the Indian sub-continent". Int. J. Adv. Res. Biol. Sci. 3(11): pp154-159, 2016. DOI: http://dx.doi.org/10.22192/ijarbs.2016.03.11.018

[6] M. Ruffo,   R. Olson, I. Daverede." Maize yield response to zinc sources and effectiveness of diagnostic indicators". Communications in Soil Science and Plant Analysis .47 (2):pp. 137–41. 2016 doi:10.1080/00103624.2015.1108433.

[7] Y. Lu, H. Yao, D. Shan, Y. Jiang, S. Zhang, and J. Yang. "Heavy Metal Residues in Soil and Accumulation in Maize at Long-Term Wastewater Irrigation Area in Tongliao, China".   Journal of Chemistry. vol. 2015, Article ID 628280, 9 pages, 2015. https://doi.org/10.1155/2015/628280.

[8] P. Zhao,F.Yang,F. Sui,Q. Wang & H. Liu."Effect of nitrogen fertilizers on zinc absorption and translocation in winter wheat"Journal of Plant Nutrition .39 (9) : pp. 1311-1318.2016 https://doi.org/10.1080/01904167.2015.1106560

[9] Gupta, N., Ram, H. & Kumar, B. Mechanism of Zinc absorption in plants: uptake, transport, translocation and accumulation. Rev Environ Sci Biotechnol 15, 89–109 (2016). https://doi.org/10.1007/s11157-016-9390-1

[10] Zou CQ, Zhang YQ, Rashid A, Ram H, Savasli E, Arisoy RZ, Ortiz-Monasterio I, Simunj S, Wang ZH, Sohu V, Hassan M et al (2012) Biofortification of wheat with zinc through zinc fertilization in seven countries. Plant Soil 361:119–130

[11] Vymazal J, Brezinova T (2015) Heavy metals in plants in constructed and natural wetlands: concentration, accumulation and seasonality. Water Sci Tecchnol 71:268–276

Effect of Foliar Spray of Fungicides on Development of Leaf Blight Disease of Maize (*Zea mays* L.)

Rupa Chakraborty

Department of Botany,
Dinabandhu Andrews College, Garia, South 24 Parganas, Kolkata - 700 084, West Bengal, India

A B S T R A C T

A large part of reclaimed wetland in the Eastern fringe of Kolkata is being used for maize farming. Fungicides are frequently being used by maize growers. Leaf blight is a common disease of maize in this area which is caused by *Exserohilum turcicum*. Inhibited growth response of the pathogen was noted *in-vitro* when fungicides namely Chlorothalonil and Mancozeb were added the basal medium. Field experiment showed that the foliar spray of those two fungicides significantly controlled the disease intensity of maize leaf blight. Mancozeb was found to be most effective at 100 and 1500 µg/ml for selected and recommended doses respectively in field condition.

Key words: Wetland, maize, Leaf blight disease, *Exserohilum turcicum* , Fungicide, Bioassay

The vast tract of reclaimed wetland located in the eastern fringe of Kolkata is of tremendous importance to the dwellers of the city. The area has been acted as a municipal waste recycling ground in the backyard of the city and immensely contributing to the harmonious development of the people living in this fringe. At the same time, this wetland is also being utilized for agricultural purposes. Maize is a very important crop regarding its nutrition (Nuss and Tanumihardjo 2010) and also very significant raw material in several industrial applications. Maize farming is a popular practice in this wetland area. Because of the reclaimed nature of the wetland soil, infection of the crop plants is quite probable. Maize is susceptible to several foliar fungal spot and blight diseases (Balint-Kurti and Johal 2009, White 1999). On the basis of the distribution of pathogenic organisms in the wetland area, *Exserohilum turcicum* is one of the major pathogens causing leaf blight disease of maize (Chakraborty and Purkayastha 1999). It causes serious problems in terms of leaf damage, and severe loss of grain yield (Wise 2011, Mueller and Wise 2013). Farmers are regularly applying fungicides to their corn fields for disease management and yield enhancement. A great risk is there involving residue-borne disease-driven yield loss in maize; it leads to greater interest in foliar fungicides (Wise and Mueller 2011). Chlorothalonil (tetrachloroisophthalonitrile) and Mancozeb (manganese ethylene bisdithiocarbarmate with zinc salt) are popular fungicides which are frequently being used by crop growers. In this investigation, two aforesaid fungicides have been applied to study their individual effect on growth response of *E. turcicum* as well as on the development of leaf blight disease of maize.

MATERIALS AND METHODS

Growing of plants in the field

One plot (33 m^2 each) was selected in reclaimed wetland in the eastern fringe of Kolkata. Maize seeds (cv. MSF 56) were disinfected with 0.1% HgCl$_2$ solution for 5 minutes, washed thoroughly with sterile distilled water, soaked in water for overnight and then sown in rows (60- 75 cm apart) in the field (reclaimed wetland soil).

Isolation and identification of causal organism of leaf blight disease of maize

Infected maize leaves with characteristic spots (oblong to "cigar" shaped) were collected from the field. Small

*Corresponding author: Rupa Chakraborty, Assistant Professor, Department of Botany, Dinabandhu Andrews College, Garia, South 24 Parganas, Kolkata - 700 084, West Bengal

e-mail: drrupachakraborty@gmail.com | **Contact:** +91- 9903176267

pieces of infected leaves were disinfected with 0.1% HgCl₂, washed thrice with sterile distilled water and transferred aseptically to potato-dextrose-agar (PDA) slants. After 12 days, the cultures were examined, described and identified as *Exserohilum turcicum.*

Fungal culture

The culture of *E. turcicum was* maintained at 4°C and also at room temperature (30-32°C). Subculturing was done at regular interval of time. To obtain spores in culture, Malt-dextrose-peptone-agar (agar -25g, malt extract -20g, dextrose -20g, peptone -1g, distilled water -1L) medium was used. Since the number of spores gradually decreased in culture after 4-5 subculturing, infected plants were also maintained in the field for obtaining sporulating culture by fresh isolation of organism.

Assessment of mycelial growth in liquid media

Basal medium was prepared, dispensed in flasks (50 ml / 250 ml flask), plugged with non-absorbent cotton and sterilized in autoclave. After inoculation, the flasks were incubated for a desired period (8 days). At the end of the incubation period, the mycelia were collected, dried at 60°C for 96h, cooled and weighed.

The composition of basal medium was as follows:

Dextrose - 20g　　　　　　　　　Asparagine - 2 g
KH₂PO₄ - 1 g　　　　　　　　　MgSO₄,7H₂O - 0.5 g
Distilled water - 1 L　　　　　　　pH - 5.6

Preparation of fungicide solution

Two fungicides namely Chlorothalonil (tetrachloroisophthalonitrile 75%) and Mancozeb (manganese ethylene bisdithiocarbarmate with zinc salt 80 %) were used. Sterile distilled water was added for this purpose. Stock solutions were prepared on the basis of formulations and dilutions were made accordingly. A thin paste was made first which was mixed well with required volume of water.

Bioassay of fungicides

The basal medium (above mentioned) supplemented with 1.5% CaCO₃ was autoclaved for 20 min at 1 atm. pressure (Steinberg 1935) to remove the trace element contaminants. After standing overnight, the clear solution was taken and supplemented separately with different conc. (1, 10, 50 and 100 μg/ml) of fungicides. Flasks were inoculated with the test organism i.e. *E. turcicum* (one agar block with 4-day-old mycelia / flask) and incubated for 8 days at room temperature (30 ± 1°C). At the end of the incubation period, the mycelia were collected, dried at 60°C for 96h, cooled and weighed. Control set (basal medium without any fungicide) was maintained in each case.

Foliar spray with fungicides (Chlorothalonil and Mancozeb)

Fungicide solutions for both Cholorothalonil and Mancozeb were prepared separately as already described. For Cholorothalonil, 100 and 1000 μg / ml concentrations were applied as selected and recommended doses respectively. These doses differed in case of Mancozeb which were 100 and 1500 μg/ml for selected and recommended doses respectively. Each concentration was applied as foliar spray in inoculated and non- inoculated plants. Foliar spray was carried out twice at an interval of 48h before inoculation (first spray on 56-day old plants and second spray on 58-day old plants). Approximately 50 to 100 ml of fungicide solution was used per plant.

Inoculation technique and assessment of disease intensity

Disinfected maize seeds were sown in rows (60-75 cm apart) and plants in the rows were spaced at 20-25 cm in the reclaimed wetland soil. Two leaves of each of ten treated and ten untreated plants (60-day-old) were inoculated at random with spore suspension (1×10⁶ spores/ml) of *E. turcicum* by automizer and covered with moist polythene bags for 48h and then removed.

Disease intensity was measured after 7,14, 21 and 28 days following inoculation (Chakraborty and Purkayastha 1999). The spots were graded into 4 size groups according to the length of the spot viz. < 2 mm; <5 mm; 5-10 mm and >10 mm with respective values of 0.01, 0.1, 0.2 and 0.4. The total number of spots of each size group was multiplied by respective value. The total score was divided by the total number of leaves inoculated. Disease index was calculated as follows:

$$\frac{\text{D.I.}}{\text{Leaf}} = \frac{\text{Total score}}{\text{No. of leaves inoculated}}$$

Control leaves were sprayed with sterile distilled water instead of spore suspension.

RESULTS AND DISCUSSION

Bioassay of fungicides

Sterilized basal medium was taken, trace metal contaminants were removed and was supplemented separately with different conc. (1, 10, 50, 100 μg/ml) of Cholorothalonil and Mancozeb. Flasks were inoculated with the test organism i.e. *E. turcicum* following the procedure as stated in Materials and Methods. Control (basal medium without fungicides) was maintained in each case.

Table 1 Effect of fungicides (Chlorothalonil and Mancozeb) on mycelial growth of *E. turcicum*

Concentration (μg/ml)	Mycelial dry wt. (mg) with S.E.	
	Chlorothalonil treatment	Mancozeb treatment
Control (Basal medium)	159.16 ± 4.69	170.30 ± 3.42
1	103.81 ± 0.63	158.56 ± 4.29
10	92.77 ± 0.52	145.46 ± 0.74
50	5.72 ± 0.82	122.91 ± 0.79
100	2.54 ± 1.48	104.07 ± 1.30

Average of 5 replicates / treatment;　　Initial pH - 5.6
Incubation time - 8 days;　　　　Temperature - 30 ± 1° C

Results in (Table 1, Fig 1) show that mycelial growth was decreased with increasing concentration of fungicides in both cases. Chlorothalonil was found to be more effective. It causes about 98% growth inhibition at 100 μg/ml level whereas 39% reduction in mycelial growth was observed in

case of Mancozeb treatment at same concentration. In another research, similar fungistatic response of fungicides was noted in case of *E. turcicum* grown in vitro. In that experiment, Chlorothalonil and Mancozeb in addition to other fungicides were used and showed 100% inhibition in fungal growth (Wathaneeyawech *et al*. 2015).
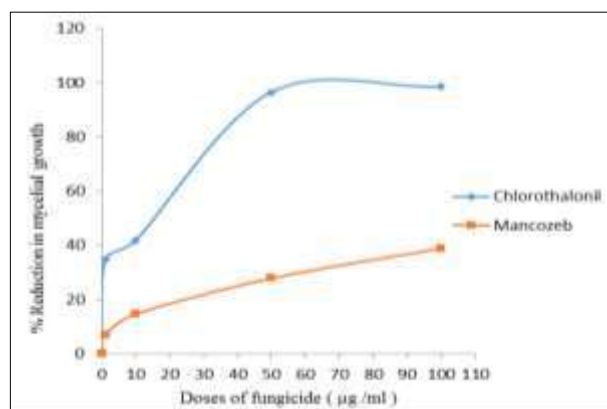
Average of 5 replicates / treatment
Initial pH - 5.6
Incubation time - 8 days
Temperature - 30 ± 1°C

Fig 1 Effect of fungicides (Chlorothalonil and Mancozeb) on percent reduction of mycelial growth in E. *turcicum*
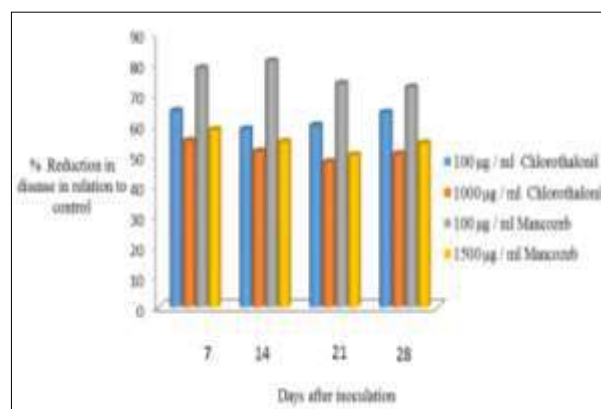
Age of the plant - 60 days (at the time of inoculation)
Age of culture - 15 days ;   20 leaves / treatment (foliar spray)
Temperature - 24.4-32°C
Relative humidity: Maximum - 98.5%; Minimum - 47%

Fig 2 Effect of foliar spray of fungicides (Chlorothalonil and Mancozeb) on percent reduction in disease intensity in relation to control in maize

Effect of foliar spray of fungicides (Cholorothalonil and Mancozeb) on development of leaf blight disease of maize
    Two leaves of each of ten treated and untreated plants were inoculated and disease intensity was measured following the steps as already described in Materials and Methods. Results are summarized in (Table 2, Fig 2).

Table 2 Effect of foliar spray of fungicides (Chlorothalonil and Mancozeb) on development of leaf blight disease of maize

Treatment		Conc (µg/ml)	Disease Index / Leaf (days after inoculation)			
			7 days	14 days	21 days	28 days
Untreated	Non-inoculated	0	0	0	0	0
	Inoculated	0	34.48±2.75	65.36±0.97	82.32±1.73	92.86±2.34
Treated (Chlotothalonil)	Non-inoculated	100*	0	0	0	0
	Inoculated	100	22.18±0.42	38.14±3.85	49.06±2.14	59.24±1.42
	Non -inoculated	1000**	0	0	0	0
	Inoculated	1000	18.80±3.22	33.36±1.35	39.16±0.76	46.58±4.24
Treated (Mancozeb)	Non -inoculated	100*	0	0	0	0
	Inoculated	100	27.02±2.18	52.70±0.78	60.34±3.52	66.98±2.26
	Non -inoculated	1500**	0	0	0	0
	Inoculated	1500	20.04±0.64	35.40±1.36	41.04±3.46	49.92±0.74

*Selected dose
Age of the plant - 60 days (at the time of inoculation)
20 leaves / treatment (foliar spray)
Relative humidity: Maximum - 98.5%

**Recommended dose
Age of culture - 15 days
Temperature - 24.4 - 32°C
Minimum - 47%

    Results indicate that foliar spray of fungicides could effectively control leaf blight disease in maize grown in wetland soil. Leaf blight is a major threat in maize field. Present investigation involves control of leaf blight of maize in the backdrop of hot, humid wetland environment. Addition of both fungicides (Cholorothalonil and Mancozeb) separately reduced the mycelial growth of *Exerohilum turcicum* in-vitro. Chlorothalonil was more effective as it showed nearly 98% decrease in growth than Mancozeb which achieved 39% reduction at the concentration of 100 µg/ml (Fig 1). The same compounds i.e. Chlorothalonil and Mancozeb when sprayed to the leaves of maize plant in field and the disease assessment was carried out, it showed 50% and 54% reduction respectively at their recommended doses (Fig 2). In the field trial, Mancozeb was found to be little more efficient in controlling disease intensity. The development of this disease is largely dependent on different environmental factors like soil factor, humidity, temperature which is not yet thoroughly investigated. Even the role of different biotic factors is also not ruled out (Yehouda and Yigel 1995). In-vitro condition exhibited more sensitivity of the pathogen

towards Cholorothalonil whereas the reverse response i.e. Mancozeb was found to be more effective in field condition. This could be due to the photo sensitivity of organochlorine nature of Chlorothalonil which lost its efficacy in intense light (Wallace *et al*. 2010, Monadjemi *et al*. 2011) in the field after foliar spray. On the contrary, Mancozeb being an inorganic compound, retained its stability as a foliar spray. Kolkata wetland is reclaimed because of dumping of municipal wastes; the soil may contain different components and is thoroughly heterogeneous in nature. Microorganisms present in rhizosphere and phyllosphere region are continuously interacting with the plant interfering disease development.

Efficacy of fungicides to manage foliar diseases in corn has been evaluated by several researchers (Shelby *et al*. 2018, Mallowa *et al*. 2015, Wise and Mueller 2011), including corn leaf blight (Blandino *et al*. 2012). It was observed that spraying fungicides prior to inoculation of pathogen could reduce disease intensity (Sommat 2000, Abebe and Singburaudom 2006, Wathaneeyawech *et al*. 2015). A number of factors like environmental conditions, stage of development, susceptibility of the cultivar, presence of inoculum and disease severity are important to make foliar spray of fungicide successful for disease management. The results of present work clearly indicate that spraying fungicides (Chlorothalonil and Mancozeb) before inoculation could successively control leaf blight disease of maize in wetland environment.

Present investigation concludes that fungicides (Chlorothalonil and Mancozeb) could inhibit mycelial growth of *Exserohilum turcicum* significantly when added in basal medium in laboratory. To control leaf blight disease of maize crops grown in Kolkata wetland environment, foliar spray of those fungicides before the appearance of disease symptoms is strongly recommended. In addition to this foliar spray of fungicides, biological and mechanical measures such as natural predators, crop rotations, hybrid seed selection and tillage practices should be taken into considerations (not investigated in this study) to maximize the outcome of disease management.

LITERATURE CITED

Abebe D and Singburaudom N. 2006. Morphology, culture, and pathogenicity variation of *Exserohilum turcicum* (Pass) leonard and suggs isolates in maize (*Zea mays* L.). *Kasetsart Journal* **40**: 341-352.

Balint Kurti P J and Johal G. 2009. *Maize Disease Resistance. In: Handbook of Maize*. Springer Science and Business Media. pp 229-250.

Blandino M, Galeazzi M, Savoia W and Reyneri A. 2012. Timing of azoxystrobin + propiconazole application on maize to control Northern corn leaf blight and maximize grain yield. *Field Crops Research*. **139**: 20–29.

Chakraborty R and Purkayastha R P. 1999. Heavy metal and disease susceptibility of maize. *Indian Phytopthology* **52**(4): 381-384.

Mallowa S O, Esker P D, Paul P A, Bradley C A, Chapara V R and Conley S P. 2015. Effect of maize hybrid and foliar fungicides on yield under low foliar disease severity conditions. *Phytopathology* **105**: 1080-1089.

Monadjemi S, El Roz M, Richard C and Ter Halle A. 2011. Photoreduction of chlorothalonil fungicide on plant leaf models. *Environmental Science and Technology* **45**: 9582-9589.

Mueller D and Wise K. 2013. Corn disease loss estimates from the United States and Ontario, Canada – 2013. Purdue Extension. BP-96-13-W.

Nuss E T and Tanumihardjo S A. 2010. Maize: A paramount staple crop in the context of global nutrition. *Comparative Review of Food Science* **9**: 417-436.

Shelby R J, Villamil M B, Ames K A and Bradley C A. 2018. Effects of Pyraclostrobin foliar fungicide corn hybrid, and harvest timing on stalk health of corn. *Crop for Turf Management* **4**: 180006.

Sommat T. 2000. *Chemical Control for Plant Diseases*. Department of Plant Pathology. Faculty of Agriculture, Kasetsart University, Bangkok. pp 371.

Steinberg R A. 1935. Nutrient solution purification for removal of heavy metals in the deficiency investigations with *A. niger*. *Journal of Agricultural Research* **51**: 413.

Wallace D F, Hand L H and Oliver R G. 2010. The role of indirect photolysis in limiting the persistence of crop protection products in surface waters. *Environmental Toxicology and Chemistry* **29**(3): 575-581.

Wathaneeyawech S, Kirdsiri K, Sirithunya P and Smitamana P. 2015. Efficacies of some fungicides and antagonists in controlling northern corn leaf blight disease. *Journal of Agricultural Technology* **11**: 925-936.

White D G. 1999. *Compendium of Corn Diseases*. 3rd Edition. American Phytopathological Society, St. Paul, MN.

Wise K and Mueller D. 2011. Are fungicides no longer just for fungi? An analysis of foliar fungicide use in corn. *APSnet Features*. doi:10.1094/APSnetFeature-2011-0531

Wise K. 2011. *Diseases of Corn: Northern Corn Leaf Blight*. Purdue University Extension Publication. Purdue University.

Yehouda L and Yigal C. 1983. Biotic and environmental factors affected infection of sweet corn with *Exerohilum turcicum*. *Phytopathology* **73**(5): 722-725.

UGC-CARE List

SAVITRIBAI PHULE PUNE UNIVERSITY

Home

○ UGC

🔍 Search ‹

UGC-CARE List

You searched for **"0976-1675"**. Total Journals : **1**

Search: [   ]

Sr.No.	Journal Title	Publisher	ISSN	E-ISSN	UGC-CARE coverage years	Details
1	Research Journal of Agricultural Sciences- An International Journal	Centre for Advanced Research in Agricultural Sciences	0976-1675	2249-4538	from September-2019 to Present	View

Showing 1 to 1 of 1 entries

Previous | 1 | Next

Review

Comparative review on left-handed Z-DNA

Reetabrita Roy[1,†], Pallab Chakraborty[2,†], Arindam Chatterjee[3], Joy Sarkar[4,*]

[1]Department of Zoology, Acharya Prafulla Chandra College, New Barrakpur, Kolkata, 700131 West Bengal, India,
[2]Department of Botany, Acharya Prafulla Chandra College, New Barrakpur, Kolkata, 700131 West Bengal, India,
[3]Department of Zoology, University of Calcutta, 700019 Kolkata, India, [4]Department of Botany, Dinabandhu Andrews College, Garia, Kolkata, 700084 West Bengal, India

TABLE OF CONTENTS

1. Abstract

Being polymorphic, deoxyribonucleic acid is worthy of raise a variety of structure like right-handed B to left-handed Z conformation. In left-handed contour of DNA consecutive nucleotides substitute between syn-arrangement and anti-arrangement, through the chain. 2D gel electrophoresis comprising d(PCpG)n of topo isomers of a plasmid inserts d(pCpG)n, in this 'n' ranges among 8 to 21, indicate the change of B-Z DNA. The high denseness of salt is required for conversion of B configuration d(CG)n toward Z configuration. The rate of B to Z transition is measured by "Cytosine Analogues" and "Fluorescence Spectroscopy". h-ZαADAR1 that a Z-DNA's binding domain, binds and stabilizes one part in Z configuration and therefore the remaining half in B deoxyribonucleic acid configuration. At halfway point, it creates B-Z junction. "Stacking" is the main reason for the B-Z DNA junction construction. Upregulation of ADAM-12, related with Z-DNA is said to a cause for cancer, arthritis, and hypertrophy. Z-DNA forming sequence (ZFS) conjointly generates massive - scale deletion in cells from mammals.

2. Introduction

In 1979, a left-handed crystal deoxyribonucleic acid structure was published, which convey a unique zigzag, sugar-phosphate backbone, it's named as Z conformation of deoxyribonucleic acid (Z-DNA) and it's all biological relevance had yet to be established [1, 2]. It was already known that normal right-handed B conformation can assume a diverse number of configurations, under certain torsional stress [3]. Z configuration exists in high energy state than the common B-DNA configuration. This conformation has negative super helicity which soothes the structure. In contrast to B form with anti-conformation, in Z-DNA convey anti-conformation and syn-conformations alternately by rotating around glycosyl bonds, along with the chain [4]. Under bound condition non-B-DNA structure like cruciform, triplex, hairpin, etc. are formed by collapsible monotonous DNA sequence. This unusual structure has effects on several biological progressions [5]. Super helicity is the most significant inducer for Z contour in usual DNA. Non-super helical, natural DNA holds practically no Z-DNA, but other hand the same DNA under extreme negative super helicity, as in "form V" may have as much as 35–40% of its sequence in Z arrangement [6]. Except for Z-DNA, X-ray fiber diffraction outlines were framed and

Table 1. Comparable information between A-DNA, B-DNA, Z-DNA [2, 9].

Parameter	A-DNA	B-DNA	Z-DNA
Helix sense	Right-handed	Right-handed	Left-handed
Axial raise [in Armstrong]	2.55	3.4	3.7
Helix pitch	28°	34°	35°
Base pair tilt	20°	-6°	7°
Rotation per residues	33°	36°	-30°
Diameter of helix [in angstrom]	23	20	18
Glycosidic bond configuration	Anti	Anti	Anti
da, dT, dC, dG	Anti	Anti	Syn
Inserted phosphate phosphate distance [in Armstrong]	5.9	7.0	7.0
da, dT, dC, dG	5.9	7.0	5.9
Suger pucker	C3'-endo	C2'-endo	C2'-endo
da, dT, dC, dG	C3'-endo	C2'-endo	C3'-endo

differentiates several conformations of DNA. Most DNA enters the A-DNA conformation which's per turn contain 11 bp through right-handed helix [7]. The single-crystal method resolute the complementary structure, oligo deoxy nucleosides, d(GGTATACG) and d(IODO-CCGG) [7, 8] (Table 1).

Existence of B-Z transition and Z-DNA is further deep-rooted by the specific ZBP discovery [10]. *In vitro*, Z-DNA was postulated for identification of proteins that bind with it in a structure-precise manner, act as a cis-element and aid in biological development. RNA Double Strand adenosine deaminase 1 is a type of the ZBP [11]. This ADAR1 has a Zα domain capable of transform B into Z conformation and create the junction [12, 13]. Formation of Z-DNA is induced by a unique sequence motif. Sometimes, it presents frequently adjacent with the start site of transcription and induce the transcription [14–16]. The junction between B-Z is formed with the help of ZBP. Formation of this portion carries out flipping over of bases, stacking of bases, and infringement of one base pair [17]. In another study also verified that normal B form also transfers into Z form by elevation of salt of aggregation [18, 19]. In humans, Z-DNA first came into consideration through the autoimmune disease Lupus erythematosus [20]. Z-DNA formation sequence (ZFS) is found to be associated with immune retorts and infection genome uncertainty. The Z configuration is also evidenced to be linked with large scale deletion in the cells of mammals [21, 22]. It also controls the genes transcription regulation of c-myc and CRH of human [23, 24].

3. Z-DNA structure

The optical investigation originally proposed the Z-DNA. The result of the experiment exhibited that a 4 mL NaCl solution contains a polymer which consists of discontinuous cytosine and guanine residue and formed a nearly inverted circular dichroism gamut [25]. Until 1979, the invention of Z-DNA remained unknown. Orig-

inal atomic steadfastness exposed that it was not the same right-handed B-DNA which was invented by James D. Watson & H.C. Crick in 1953. Despite that, this new left-handed helical structure named as Z deoxyribonucleic acid. This Z form consists of extremely immunogenic antibodies to recognize the configuration, unlike B form of DNA [26]. There have some familiar features of B form with the d(Cg)$_3$ system. The antiparallel double-helical structure holds Watson-Crick base pairing between the base of Guanine and Cytosine. The left-handed helicity oligomers have six base pairs with significant regularity. Balance correlated hexamers stack on one other so closely in an endless polymer of alternating cytosine guanine residues sequence [2].

Various conformational topographies differ the Z-DNA from the B-DNA (Fig. 1). The double-helical Hexanucleoside Penta Phosphate molecules allied with the crystal. Crystal of Z arrangement contains discontinuous cytosine and guanine residues'-DNA is dinucleotide while B-DNA is mononucleotide with anti-configuration. All deoxycytidine has anti-configuration whereas all the deoxyguanosine has anti syn-configuration.

In Z arrangement the base pair is lifted from the center, so the guanine imidazole ring is originated at the edge, but in case of B-DNA those bases are at the center. In B configuration 34Å pitch with 10.5 bp is present where Z configuration convey 44.6Å pitch with 12 bp per turn [9]. Six levels of base pairing have been seen in the d(Cg)$_3$ structure because of C1 base pair with G12, G2, C11 and so on. Z-DNA is not slanted with each other straight, but they remain linked to a literal translation of 7Å relative to each other so that it can shear the appearance from one another with a little rotation throughout the chain. Despite being stacked on other bases the guanine is loaded upon the oxygen atoms of prior deoxyribose residues. The backbone of sugar-phosphate is constant for both the Z form and B form. In B configuration the minor-grooves are above the base pairs. But in Z form minor-grooves exist below the base pair [2].
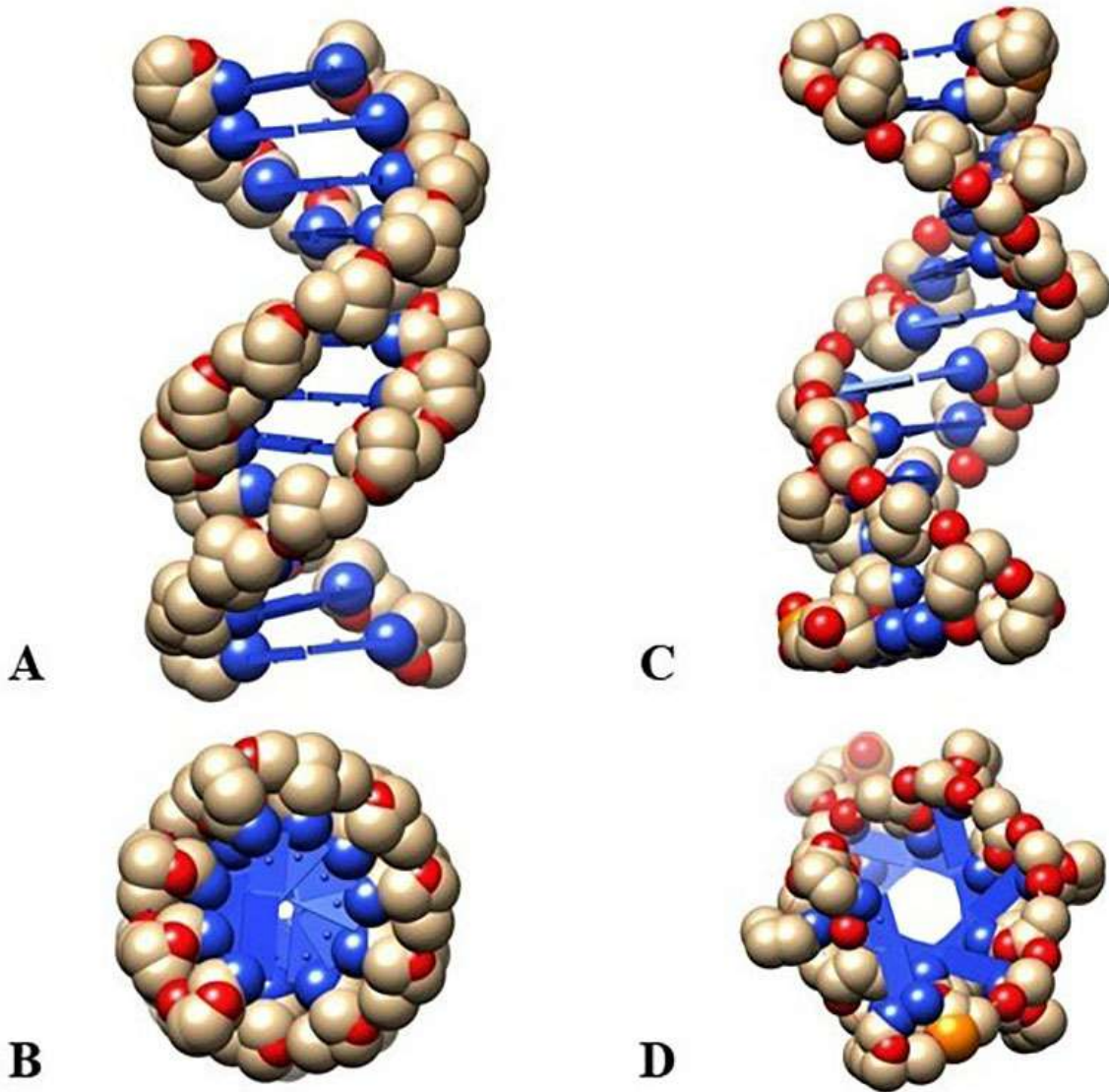
Fig. 1. Evaluation of the structure between Z and B-DNA configuration. (A, B) Z-DNA configuration showing left-handed elongated spiral with a lateral view and a polar view. (C, D) B-DNA configuration showing right-handed elongated spiral with a lateral view and a polar view.

4. B-DNA to Z-DNA transition

Earliest Harvey model is used for examining B-Z transition. This model defines the procedure which is engrossed by another longitudinal DNA conscious models. Base pairs opening was another early observed mechanism regarding this model before the Wang model. At the present portrait of Zipper Model demonstrated that Z-DNA contains high energy joint that grows through the DNA polymer until the full B-Z trans polymer gets transferred into Z-DNA. Though there are some problems in the model because it does not disclose many vibrant structural details, so it has limited applications in thermodynamics. There are several facts regarding the transition of B-Z such as the high concentration of salt in the solution which balance the Z-DNA due to massive reduction in electrostatic repulsion in the pillar of phosphate. Negative helicity of deoxyribonu-cleic acid needs energy that can also uncoil B form to configure the Z form. Z-DNA can also be stabilized by transcription.

Maruyama and colleague establish the B-DNA to Z-DNA transition communed by a method called "cationic graft copolymer" where the Poly (L-lysine)-graft dextran (PLL-g-Dex), begins with two-step method including the creation of a clear intermediate [27]. Amid DNA phosphate group electrostatic repulsion reduce by the cationic backbone of the copolymer and the transition is a result of these 2 factors. The most plausible Z form created negative supercoiling, utilizing B-DNA occurs during several metabolisms like Transcription and replication processes [28]. For reducing the transition stress, unusual such DNA as Z-DNA is formed [6, 29]. Lee *et al.* (1992) used "Magnetic-tweezers" and FRET combinedly to examine at molecule level of negative supercoiling [30]. Mag-

netic tweezers are a very useful technique for investigating wind/unwinding procedure of twisted DNA through precisely controlling infinite tension [28, 31]. Therefore, B-Z change can be active by tiny negative super helicity and approximately one Pico Newton Tension. This outcome suggests that in tension Z arrangement is formed more easily *in vivo* [32]. Methanol, Ethanol, Ethylene Glycol (Dehydrating agent) balance the Z-DNA configuration. Due to adjacent clustering counteractions all over the DNA, though more strong ionic properties, thus it provides additional mutually repelling phosphate groups [6]. Antibodies and ZBP can bind the Z form of DNA selectively. This conformation has triggering capability. The Qu group had been reported that Alzheimer amyloid protein brings about the Z-B transition. Forming the Z-form is correlated with Alzheimer's disease [33, 34]. Bae *et al.* analyzed to transition from B-Z conformational change occurs by Z-DNA binding protein unravel the detailed binding machinery and whether the protein industriously initiates Z-DNA's or passively traps transitionally performed Z form. Therefore, it proved that the conformational selection mechanism stabilized the Z-DNAs by alternating the "induced fit" mechanism. A chemical modification also stabilizes Z-DNA transformation [4]. Bulky group's introduction precise in a certain base also steady the growth of Z arrangement by increasing static hindrance.

5. B-DNA and Z-DNA hybrid junction

Double-stranded adenosine deaminase RNA is an enzyme of the deaminase family which edited the appearance of the ds-mRNA by converting adenosine to inosine and creating diversity between RNA and Protein [11]. It is noted as a naturally stirring protein with obvious specificity for methylated and hemi-brominated DNA contains discontinuous deoxy guanosine-deoxycytidine residues [13]. ADAR1 carry two binding motifs for Z-DNA, $Z\alpha$ and $Z\beta$ [11].

A few numbers of investigations were completed to show the interface between the solution of DNA and $Z\alpha$ ADAR1 domain. If the DNA solution is interacting with dodecamer $(d(CG)_6)$ it produces the B-DNA circular-dichroism spectrum. When $Z\alpha$ ADAR1 is mixed into the solution the spectrum progressively altered, which mirrored Z conformation. This demonstrated that the $Z\alpha$ domain is equipped for alleviating the dodecamer in the Z configuration. Brownian motion or Pedesis is the reason for this twist of dodecamer fragment. After this conformational change, DNA binds with the $Z\alpha$ domain to prevent the reappearance of B-DNA conformation [12, 13].

Kim *et al.* in 2005 developed a DNA duplex with 15 bp and with two hanging nucleotides [17]. This DNA duplex is co-crystallized with the $Z\alpha$ADAR1 domain (amino acids 140-202). So, Z-DNA is tightly bound with the binding domain of Z DNA, h-$Z\alpha$ADAR1. After the binding,

it stabilizes one half in the Z configuration and remaining part in B form. In the centre portion, a B-Z junction is created [17]. At this DNA duplex, eight bases stabilized with normal Z-DNA conformation [2]. The remaining six bases are maintaining the typical B conformation [35]. On the link point, A-T bases are disrupted from each other and make a sharp turn, which obliged an inversion in the way of the backbone. This creates a bent at the intersection point of B-Z DNA. The disrupted A, T bases adopted anti-conformation. Base A is extended out from the helix and T is slanted analogous to the spiral. But first base-pair from the Z-DNA after the junction creates a long rise distance which clearly showed the stacked A-T the bases within the B-DNA conformation. Stacking is the main stabilizing factor for the junction, and it is proved that one bp extruding by breaking can cause reversion of the handedness of the duplex. Other than A-T bases, it is equally possible for other G-C bases to be extruded [17]. Thermodynamic examinations of the melting of oligomers holding the junction show that the edifice of the hybrid junction from B-DNA declines the melting free energy by 0.5 kcal/mol [36]. This B-Z configurational change and syn-conformation of both bases are done by base 'flipping over'. A torsional strain breaks and causes base extrusion. This extruded base is allowed to flip over and reorganization the bp, which creates a ZIP-like movement in two direction. This movement for the limitation of the ZFS with an extruded base at the intersection. Base-pair disruption, expulsion, and reconstruction are lengthening the Z-DNA segment through an additional negative torsional strain of chromatin [17].

Another investigation also proved that B-Z DNA junction can be produced by oligomeric sequences in the aqueous solution at 3 M or high salt concentration. The 5.5 M NaCl with a 95 mM combination induces the A-T sequence into the Z-DNA conformation [18]. This study re-establishes that when $NiCl_2$ is added in the salt solution, it creates a striking change in Raman Spectra, indicating A-T bases are adopting the Z conformation [19].

6. Z-DNA in human disease

In living body, Z-DNA can form and role as a dynamic component in various genome's metabolic courses under certain biological circumstances [21]. Z-DNA is used in many precise activators or repressors enrolment for directive gene countenance, genome uncertainty control [22]. Another study proved that in cells of mammal's ZFS fetch genetic uncertainty. Repair mechanism can proceed with the Z-DNA development in the mammal's body, which creates a large genomic alteration. These sorts of changes are relevant to the breakage and translocation near ZFS in human lymphoma and leukaemia [9]. In humans, Z-DNA links with the transcription of the c-myc genes, which means when the Z-DNA development is turned off the cell gives a signal as a result, c-myc transcrip-

tion also starts to down-regulate [23]. In the same way, Z-DNA development is also associated with the corticotropin-releasing hormone (CRH) gene transcription [37]. On the other hand, the human body also shows the activation of the Nrf2 gene which is relevant to the HO-1 gene's promoter, which allied with Z-DNA development [24]. A few numbers of immunoglobulin-related genes (example-ETV6) are enriched by the Z-DNA sequence. But in blood cancer, these genes are related to translocation of the chromosome [22]. Interferonopathies disease like Aicardi-Goutières Syndrome is caused by Mutation, which reduces p150 Z-binding with impaired enzymatic activity. This is induced by dsRNAs and most commonly these dsRNAs derive from Alu retroelement. The Z-DNA and Z-RNA both are essential for limiting Alu retroelement intrusion of primate genomes [38]. Z-DNA provides a base for therapeutically reducing the chances of Arthritis, Cancer, and cardiac hypertrophy. This role is believed to be arbitrated by the downregulation of ADAM-12. It was observed that ADAM-12 protein expression is raised when there are pieces evidence of arthritis, cancer, and cardiac hypertrophy. Whereas ADAM-12 expression level Is exceptionally low in certain adult tissue. The regulation of ADAM-12 is related to the highly conserved region containing a stretch of dinucleotide repeat sequence and known as negative regulatory element (NRE), which serves as a repressor of ADAM-12 expression. There is a certain Z-DNA binding protein-like MeCP2. It modulates the ADAM-12 repression by recruiting NF1 transcriptional factors. Loss of ZFS leads to a low level of MeCP2 which results in metastatic breast cancer [22, 39]. Apart from this, HIF1α induced Z-DNA development in the microsatellite of slc11a1 gene promoter. It was also perceived to control its definite allele expression in patients of rheumatoid arthritis, tuberculosis [40]. Z-DNA also has an immunogenic character and it can prevent systemic lupus erythematosus. But in the patient's sera of these diseases, some anti-Z-DNA antibody are found. Two kinds of antibody are found, first-one responsible for denaturation of both B and Z form and second-one is Z-DNA specific [20, 41]. Z arrangement also induce conformation instability by acting as a site for cancer-related genes like scl, bcl2, and c-myc [9]. B-Z junction is a site where CAG trinucleotide repeat instability happened. X fragile chromosome and skeletal dysplasia associated with CGG repeats and GAC trinucleotides repeat respectively [42–44]. In a study, typical left-handed Z-DNA was originated in brains of severe AD affected patients. Similarly, the moderately affected patients showed the existence of B-Z intermediate conformation in their brain DNA. Immunohistochemical data has proved that the total amount of Z form is one-seventh than B arrangements in human's genome [45, 46]. It was also observed that some genes, related to Alzheimer's like presenilin-1, presenilin-2, APOE (Apolipoprotein E), etc. are overexpressed in patients and has an important appeal in Alzheimer's pathogenesis. Z-DNA existing in the brains of Alzheimer's patients are far more vulnerable to hydroxyl radical-induced damage of DNA, in comparison to A-DNAs or B-DNAs. This was due to the occurrence of more exposed bases and patients with severe Alzheimer's showed the existence of both Z-DNA and damaged DNA of similar types [47]. This finding has again been confirmed from another study which showed that Z-DNA became sensitive to hydrolytic enzyme DNase I, on incubation with Aβ protein for a certain period [34]. This results in alteration of Z arrangement back into normal B form. These transition of Z form to normal B form is verified as quicker process when an interaction of Aβ is made, in the existence of ethylene glycol also [48].

7. Conclusions

Z-DNA is a double-helical structure that preserves antiparallel backbone of sugar-phosphate chains with Watson Crick pairing. Despite that, it has a contour which is fundamentally dissimilar from B configuration of DNA. Two-dimensional Gel Electrophoresis offers us a powerful method to examine the super helicity-induced physical revolution in the DNA. Besides this, B-Z conversion is also designated here. One of a reasons for transition is a cause of free unfavourable energy. Affected advances are unrestricted from the uniting effect of genomics, human genetics, biophysics, and molecular studies on non-B-DNA configurations through mutation causing agents, intricate in Genetic diseases. Autoimmune processes may be suspected in all clinical conditions where specific anti-Z-DNA antibodies are found, but for further investigation, larger population is wanted to prove such an immunological hypothesis. Future prominence will challenge to tune the acceptance of the non-B-DNA configurations at a definite location of genes to correlate this behavior extra thoroughly with the generation reposition terminuses. Also, the analysis to recognize the kind of non-B-DNA structures that obtain certain sort of mutations and the fascinated enzyme on the evolution of therapeutics, to ameliorate the disturbing corollaries of these disorders.

8. Author contributions

9. Ethics approval and consent to participate

The work reported here in the manuscript is original and free from any plagiarism. All the data in the article are real and authentic. All the co-authors have read and agree to publish all the items listed above.

10. Acknowledgment

Reetabrita Roy and Pallab Chakraborty contributed equally to this article.

11. Funding

We don't have any funding support from any organizational or institutional level. On behalf of all listed authors, the corresponding author declares that there is not any sort of financial and non-financial conflict of interest in the subject materials mentioned in this manuscript.

12. Conflict of interest

The authors declare no conflict of interest.

13. References

[1] de Rosa M, de Sanctis D, Rosario AL, Archer M, Rich A, Athanasiadis A, *et al*. Crystal structure of a junction between two Z-DNA helices. Proceedings of the National Academy of Sciences of the United States of America. 2010; 107: 9088–9092.

[2] Wang AH, Quigley GJ, Kolpak FJ, Crawford JL, van Boom JH, van der Marel G, *et al*. Molecular structure of a left-handed double helical DNA fragment at atomic resolution. Nature. 1979; 282: 680–686.

[3] Kohwi-Shigematsu T, Manes T, Kohwi Y. Unusual conformational effect exerted by Z-DNA upon its neighboring sequences. Proceedings of the National Academy of Sciences of the United States of America. 1987; 84: 2223–2227.

[4] Rich A, Zhang S. Z-DNA: the long road to biological function. Nature Reviews Genetics. 2003; 4: 566–572.

[5] Choi J, Majima T. Conformational changes of non-B DNA. Chemical Society Reviews. 2011; 40: 5893–5909.

[6] Johnston BH. Generation and detection of Z-DNA. Methods in Enzymology. 1992; 211: 127–158.

[7] Heinemann U, Alings C, Hahn M. Crystallographic studies of DNA helix structure. Biophysical Chemistry. 1994; 50: 157–167.

[8] Cruz P, Bubienko E, Borer PN. A model for base overlap in RNA. Nature. 1982; 298: 198–200.

[9] Rich A, Nordheim A, Wang AHJ. The chemistry and biology of left-handed Z-DNA. Annual Review of Biochemistry. 1984; 53: 791–846.

[10] Kimura T, Kawai K, Fujitsuka M, Majima T. Detection of the G-quadruplex-TMPyP4 complex by 2-aminopurine modified human telomeric DNA. Chemical Communications. 2006; 4: 401–402.

[11] Wang G, Vasquez KM. Z-DNA, an active element in the genome. Frontiers in Bioscience. 2007; 12: 4424–4438.

[12] Kim Y, Lowenhaupt K, Maas S, Herbert A, Schwartz T, Rich A. The zab domain of the human RNA editing enzyme ADAR1 recognizes Z-DNA when surrounded by B-DNA. Journal of Biological Chemistry. 2000; 275: 26828–26833.

[13] Berger I, Winston W, Manoharan R, Schwartz T, Alfken J, Kim Y, *et al*. Spectroscopic characterization of a DNA-binding domain, Zα, from the editing enzyme, dsRNA adenosine deaminase: evidence for left-handed Z-DNA in the Zα-DNA Complex. Biochemistry. 1998; 37: 13313–13321.

[14] Champ PC, Maurice S, Vargason JM, Camp T, Ho PS. Distributions of Z-DNA and nuclear factor I in human chromosome 22: a model for coupled transcriptional regulation. Nucleic Acids Research. 2004; 32: 6501–6510.

[15] Liu R, Liu H, Chen X, Kirby M, Brown PO, Zhao K. Regulation of CSF1 promoter by the SWI/SNF-like BAF complex. Cell. 2001; 106: 309–318.

[16] Oh D, Kim Y, Rich A. Z-DNA-binding proteins can act as potent effectors of gene expression *in vivo*. Proceedings of the National Academy of Sciences. 2002; 99: 16666–16671.

[17] Ha SC, Lowenhaupt K, Rich A, Kim Y, Kim KK. Crystal structure of a junction between B-DNA and Z-DNA reveals two extruded bases. Nature. 2005; 437: 1183–1186.

[18] Ridoux JP, Liquier J, Taillandier E. Raman spectroscopy of Z-form poly[d(a-T)].poly[d(a-T)]. Biochemistry. 1988; 27: 3874–3878.

[19] Dai Z, Thomas GA, Evertsz E, Peticolas WL. The length of a junction between the B and Z conformations in DNA is three base pairs or less. Biochemistry. 1989; 28: 6991–6996.

[20] Lafer EM, Valle RP, Möller A, Nordheim A, Schur PH, Rich A, *et al*. Z-DNA-specific antibodies in human systemic lupus erythematosus. Journal of Clinical Investigation. 1983; 71: 314–321.

[21] Kha DT, Wang G, Natrajan N, Harrison L, Vasquez KM. Pathways for double-strand break repair in genetically unstable Z-DNA-forming sequences. Journal of Molecular Biology. 2010; 398: 471–480.

[22] Ravichandran S, Subramani VK, Kim KK. Z-DNA in the genome: from structure to disease. Biophysical Reviews. 2019; 11: 383–387.

[23] Wittig B, Wölfl S, Dorbic T, Vahrson W, Rich A. Transcription of human c-myc in permeabilized nuclei is associated with formation of Z-DNA in three discrete regions of the gene. EMBO Journal. 1992; 11: 4653–4663.

[24] Maruyama A, Mimura J, Harada N, Itoh K. Nrf2 activation is associated with Z-DNA formation in the human HO-1 promoter. Nucleic Acids Research. 2013; 41: 5223–5234.

[25] Herbert A, Rich A. Left-handed Z-DNA: structure and function. Structural biology and functional genomics. Genetica. 1999; 106: 37–47.

[26] Lafer EM, Möller A, Nordheim A, Stollar BD, Rich A. Antibodies specific for left-handed Z-DNA. Proceedings of the National Academy of Sciences of the United States of America. 1981; 78: 3546–3550.

[27] Shimada N, Kano A, Maruyama A. Design of cationic graft copolymers as a potential inducer of B-Z transition. Nucleic Acids Symposium Series. 2009; 53: 251–252.

[28] Yang X, Li Z, Polyakova T, Dejneka A, Zablotskii V, Zhang X. Effect of static magnetic field on DNA synthesis: the interplay between DNA chirality and magnetic field left-right asymmetry. FASEB BioAdvances. 2020; 2: 254–263.

[29] Murchie AI, Lilley DM. Supercoiled DNA and cruciform structures. Methods in Enzymology. 1992; 211: 158–180.

[30] Lee S, Kwak C, Shim J, Kim J, Choi S, Kim HF, *et al*. A cellular model of memory reconsolidation involves reactivation-induced destabilization and restabilization at the sensorimotor synapse in Aplysia. Proceedings of the National Academy of Sciences of the United States of America. 2012; 109: 14200–14205.

[31] Strick TR, Allemand JF, Bensimon D, Bensimon A, Croquette V. The elasticity of a single supercoiled DNA molecule. Science. 1996; 271: 1835–1837.

[32] Sanford DG, Stollar BD. Assay of anti-DNA antibodies. Methods in Enzymology. 1992; 212: 355–371.

[33] Breslow JL, Ross D, McPherson J, Williams H, Kurnit D, Nussbaum AL, *et al*. Isolation and characterization of cDNA clones for human apolipoprotein A-I. Proceedings of the National Academy of Sciences of the United States of America. 1982; 79: 6861–6865.

[34] Geng J, Zhao C, Ren J, Qu X. Alzheimer's disease amyloid beta converting left-handed Z-DNA back to right-handed B-form. Chemical Communications. 2010; 46: 7187–7189.

[35] Herbert A, Lowenhaupt K, Spitzner J, Rich A. Chicken double-stranded RNA adenosine deaminase has apparent specificity for Z-DNA. Proceedings of the National Academy of Sciences of the United States of America. 1995; 92: 7550–7554.

[36] Sheardy RD, Levine N, Marotta S, Suh D, Chaires JB. A thermodynamic investigation of the melting of B-Z junction forming DNA oligomers. Biochemistry. 1994; 33: 1385–1391.

[37] Wölfl S, Martinez C, Rich A, Majzoub JA. Transcription of the human corticotropin-releasing hormone gene in NPLC cells is correlated with Z-DNA formation. Proceedings of the National Academy of Sciences of the United States of America. 1996; 93: 3664–3668.

[38] Herbert A. Z-DNA and Z-RNA in human disease. Communications Biology. 2019; 2: 7.

[39] Ray BK, Dhar S, Shakya A, Ray A. Z-DNA-forming silencer in the first exon regulates human ADAM-12 gene expression. Proceedings of the National Academy of Sciences of the United States of America. 2011; 108: 103–108.

[40] Bayele HK, Peyssonnaux C, Giatromanolaki A, Arrais-Silva WW, Mohamed HS, Collins H, *et al*. HIF-1 regulates heritable variation and allele expression phenotypes of the macrophage immune response gene SLC11a1 from a Z-DNA forming microsatellite. Blood. 2007; 110: 3039–3048.

[41] Allinquant B, Malfoy B, Schuller E, Leng M. Presence of Z-DNA specific antibodies in Crohn's disease, polyradiculoneuritis and amyotrophic lateral sclerosis. Clinical and Experimental Immunology. 1984; 58: 29–36.

[42] Khan N, Kolimi N, Rathinavelan T. Twisting right to left: A…A mismatch in a CAG trinucleotide repeat overexpansion provokes left-handed Z-DNA conformation. PLoS Computational Biology. 2015; 11: e1004162.

[43] Vorlíčková M, Kejnovská I, Tumová M, Kypr J. Conformational properties of DNA fragments containing GAC trinucleotide repeats associated with skeletal displasias. European Biophysics Journal. 2001; 30: 179–185.

[44] Renčiuk D, Kypr J, Vorlíčková M. CGG repeats associated with fragile X chromosome form left-handed Z-DNA structure. Biopolymers. 2011; 95: 174–181.

[45] Soyer-Gobillard MO, Géraud ML, Coulaud D, Barray M, Théveny B, Révet B, *et al*. Location of B- and Z-DNA in the chromosomes of a primitive eukaryote dinoflagellate. Journal of Cell Biology. 1990; 111: 293–304.

[46] Gagna CE, Lambert WC, Kuo HR, Farnsworth PN. Localization of B-DNA and Z-DNA in terminally differentiating fiber cells in the adult lens. Journal of Histochemistry and Cytochemistry. 1997; 45: 1511–1521.

[47] Michalik V, Spotheim Maurizot M, Charlier M. Calculation of hydroxyl radical attack on different forms of DNA. Journal of Biomolecular Structure & Dynamics. 1995; 13: 565–575.

[48] Zacharias W, Larson JE, Klysik J, Stirdivant SM, Wells RD. Conditions which cause the right-handed to left-handed DNA conformational transitions. Evidence for several types of left-handed DNA structures in solution. Journal of Biological Chemistry. 1982; 257: 2775–2782.

Send correspondence to: Joy Sarkar, Department of Botany, Dinabandhu Andrews College, Garia, Kolkata, 700084 West Bengal, India, E-mail: jsarkar80@gmail.com
[†] These authors contributed equally.

Source details

Feedback >   Compare sources >

Frontiers in Bioscience - Landmark

See also: Frontiers in Bioscience - Elite

Open Access   ⓘ

Scopus coverage years: from 1996 to Present

Publisher: IMR Press Limited

ISSN: 2768-6701   E-ISSN: 2768-6698

Subject area: (Immunology and Microbiology: General Immunology and Microbiology)

(Biochemistry, Genetics and Molecular Biology: General Biochemistry, Genetics and Molecular Biology)

Source type: Journal

View all documents >   Set document alert   💾 Save to source list

---

CiteScore 2022   ⓘ
3.4

SJR 2022   ⓘ
0.583

SNIP 2022   ⓘ
0.607

CiteScore   CiteScore rank & trend   Scopus content coverage

A COMPARATIVE STUDY BETWEEN THE FIRST AND SECOND WAVES OF WORLD THREATENING COVID-19 DISEASE

Article *in* European Journal of Translational and Clinical Medicine · November 2020

2 authors:

Tanmay Ghosh
Dinabandhu Andrews College university of calcutta
77 PUBLICATIONS   214 CITATIONS

SEE PROFILE

Mohan Kumar Biswas
Visva Bharati University
118 PUBLICATIONS   525 CITATIONS

SEE PROFILE

A COMPARATIVE STUDY BETWEEN THE FIRST AND SECOND WAVES OF WORLD THREATENING COVID-19 DISEASE

[1]Tanmay Ghosh, [2]Dr. Mohan Kumar Biswas*

[1]Department of Microbiology, Dinabandhu Andrews College,
Baishnabghata, South 24 Parganas, Kolkata –
700084, West Bengal, India.
[2]Department of Plant Pathology, PalliSiksha Bhavana Visva -Bharti,
Sriniketan, Birbhum, West Bengal
[First Author –
tanmay.tanmay.ghosh780@gmail.com
*Corresponding Author –
mohankumar.biswas@visva-bharati.ac.in]

Abstract:

The global pandemic caused by severe acute respiratory syndrome (Corona virus disease - COVID-19) is the major concern of mankind now. The tiny virus has wiped out million of lives and changed the total economic scenario of world. The present review is formulated with a view to study and analyse the epidemics of first and second wave of COVID-19 in relation to its effects on human health. The infection pattern has been changed and many countries have witnessed higher number of people infected in the second wave than the first one. The result of stimulation suggests that the second wave may occur in the mid July 2020 to the last week of December 2020. One of the main problems in managing the COVID-19 epidemic crisis in second wave is its effects on human health and disease syndrome as compared to the first wave of COVID-19 and also the technical and calculated capabilities of nations. According to scientists, 18 mutations in 7 genes have been observed as a result of mutation and the new variant has been named B.1.617. The pair of spike genes has been linked to amino acid deletion and the ability to evade vaccines. As a result, he is entering the receptor faster and infection is spreading rapidly. Corona virus enters the human body through this spike protein. In India RT-PCR tests are targeted at three genomic sequences of viruses. Only if three different genomic sequences match then there will be a positive report.

Key-words: Genomic sequence, Mutation, Virus, Microbiology, COVID-19, Pathology, Biology.

Introduction:

The World threatening COVID-19 disease is sweeping throughout the World. Second wave of COVID-19 daily case numbers have exploded since last October 2020 in India. Rising of daily COVID-19 cases has worstly impact on people. The scenario is getting awfull day by day due to people's carelessness, limited availability of vaccine etc. Many researcher's analysis that the major country U.S. and Europe, including the proposed method, model and results, published discretion responses and limited additions may create the effects of the second wave and of corona virus (COVID-19) epidemics on the human health is more effect than the first one. And result indicated that the regulations were effective in increasing the number dates from the beginning of mid-June in several countries to July mid-week in the others.
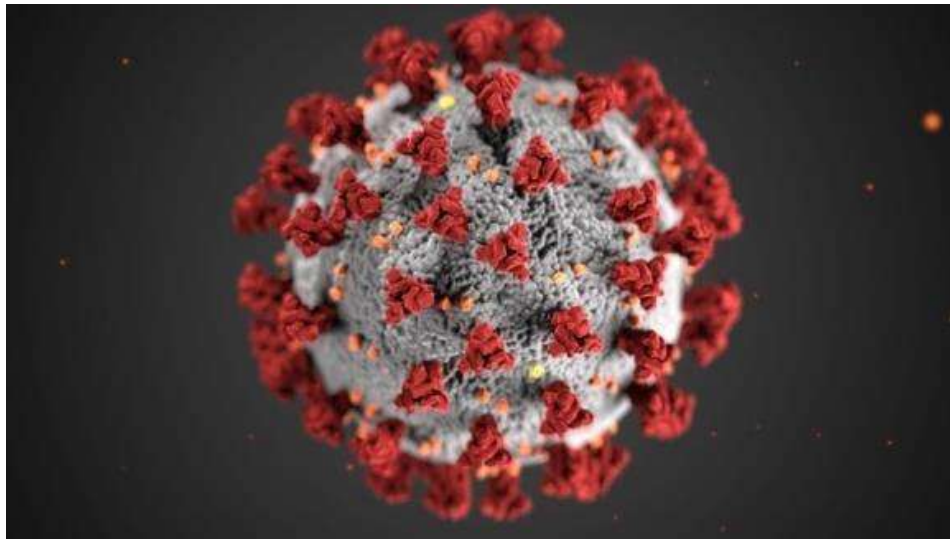
Fig: COVID-19
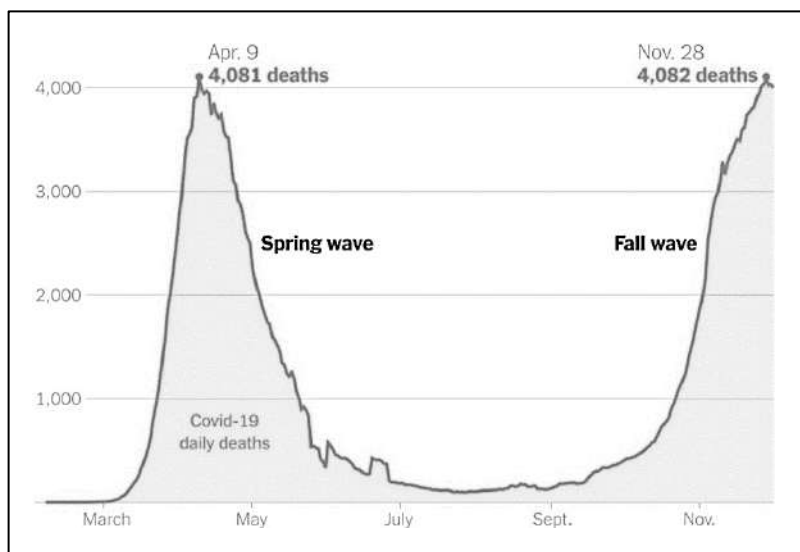
Fig: The first and second wave named as spring and fall wave in Europe

The European countries results continue to relax from 30 to 55% and if the actual trend countries if not checked there could be a significant 2nd wave that is longer lasting than the previous waves. The United States, various number of cases has already peaked for the next time, an expanded version of it, the model conceive that the transmission of infection may now be similar after the first wave. 2nd wave of COVID-19 diseases flooded in India from last week of October 2020. These cases peak is rises on daily basis. A study by an American University has warned expected optimum peak at mid December 2020.

The major differences between the properties of the two first and second waves are generally obscure. The human population examinations because of technical and calculated capabilities of nations, among them are the identification and diagnosis of non-symptomatic people and gently symptomatic people. There have been a lot of improvement in the six months and it is through that the frequency of infections in the early stages of the epidemic was a lot of higher than reported. Be that as it may, a more precise correlation of the first and second wave can be concentrated through the investigation of patients for which the illnesses was affirmed by (reverse transcriptase polymerase chain reaction) RT- PCR and extreme manifestation. According to WHO creates a virus and its own replica or multiple replicas which is called mutation. The three most risky variations are US (B.1.1.1.7 variant), South Africa (B.1.1. 351) and Brazil (B.1.1.1.28.2.1 variant). Double mutation variant first known as cross conversion. According to the researchers 18 mutations in 7

genes have been observed as a result of mutation. As a result, the virus has become more powerful. Kalyani National institute of biomedical genomics has discovered a new genome sequence for this virus. This new variant has been named B.1.617. Another triple mutation was also found that was named as B.1.618. Changes in spike protein are usually observed here. The first appearance of this variant was found on 25 October. A genomic sequencing in March showed that the presence of this variant in the COVID samples are increasing. The corona virus also contains glycoprotein, a type of S1 and S2. S1 contains a lot of amino acids of which 69 to 70 are amino acids. As a result, he does not have to make two amino acids. As a result, he enters the receptor faster than his old incarnation. As a result, the infection is spreading rapidly. According to scientists this is probably the reason why the South African AstraZeneca or COVISHIELD vaccine has not been effective. A very harmful second wave of the COVID-19, the world class pandemic has attacked India very hard. Approximately 2lakhsinfections are reported in the country India. Many states are grappling with the shortage of medical oxygen, the antiviral Remdesivir, hospital beds and vaccines. ICMR, the top medical research body of India has put the data to us that states about the comparison between the hospitalization of first and second wave of COVID-19 pandemic. The data is clearly putting light upon the evidence of the younger population getting more probable to get infected in the waves of COVID-19.More and more asymptomatic people are been admitted to the hospitals in the second wave. It was stated by the ICMR has done interim analysis.
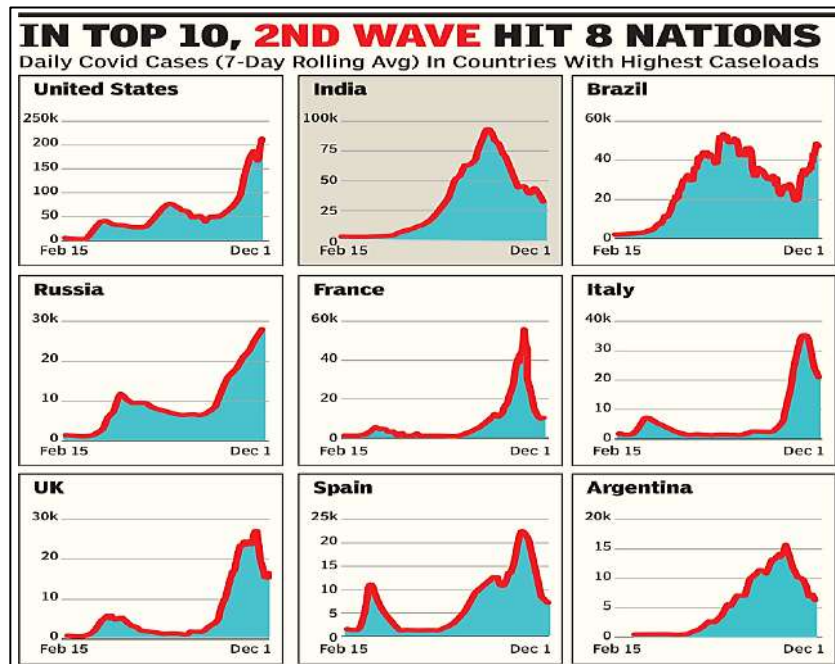
Fig: Cases of corona virus 2nd wave worldwide

➢ Colombia with 10th highest Covid Case hold, has been several mini waves after 1st big wave started abating in August.

➢ In top 10, only India & Argentina have escaped a 2nd wave so far.

Age	COVID 19 patients in first wave	Covid19 patients in second wave
0 to 19 year old	4.9	5.8
20 to 24 year old	23.9	25.5
After 30 year old	30	32

Table: Age wise break up of younger COVID-19 patients compared between first and second wave.
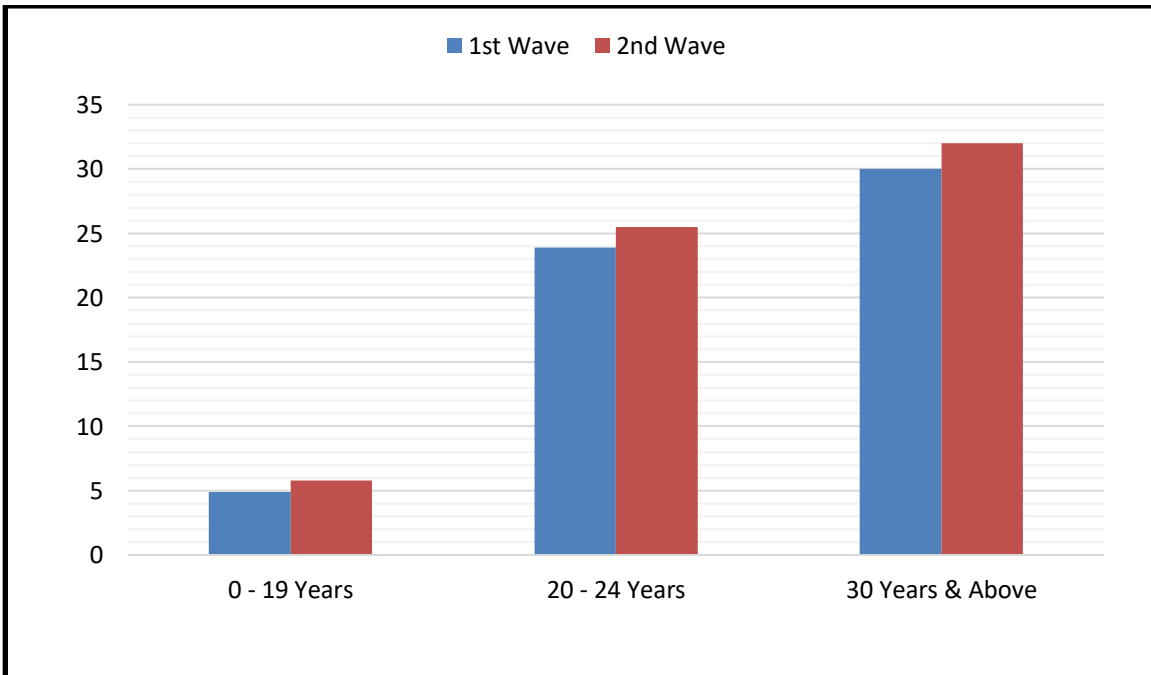
Graph: Age wise break up of younger COVID-19 patients compared between first and second wave.

It shows that the older population continues to be more vulnerable to Covid – 19 in the second wave while a marginal increase is recorded in the number of young people testing positive the virus.

Materials and Methods:

- **First wave of and second wave of COVID comparison based on mortality:**

  Low paces of contrast were found for the rushes of Corona virus dependent on the mortality. Both have high paces of death overall. Be that as it may, the mortality outline of India has seen a very distinction for this situation alongside numerous blistering environment nations. This is said by the specialist in charges of National Corona virus the board system unit of India. It was discovered that there's the relative expansion in breathing issues to individuals over 60 years in the primary wave which stays still unaltered in the subsequent wave. In any case, the primary contrast was found in the cases for individuals fewer than 20. The disease rates among more youthful patients are barely higher. Contrasted with first wave (4.2% youngsters contaminated) the subsequent wave is feeling to be exceptionally cataclysmic with 5.8% individuals tainted. For the contamination of mid age individuals as 20-40 years of age the main wave is 25.5% where the current wave is having lower pace of disease in mid age individuals of 23.7%.

  From the information of a segment of hospitalized patients from the first and second wave, Director-General, Indian Council of Medical Research (ICMR) said 44% of indicative patients introduced 'windedness' in the subsequent wave (October – December 2020) contrasted with 41% in the principal wave (Sept.- Nov.'20).

  The side effects related with the infection of COVID are for the most part coughing, chills, joint agony, and quick breathing weakness. Both first and second wave have comparable manifestations however there are varieties as well. 6,642 patients were dissected in the main wave however and in the subsequent wave, just 1,405 were broke down.

  Of 6, 650 conceded patients from September-November a year ago, 9.6% capitulated though from March-April, 9.7% of a gathering of 351died from the infection.

  Specialists have confronted the huge contrast in the patient needed to have mechanical ventilation because of the illness.

The subsequent wave — aside from a precarious ascent in Covid cases — has been portrayed by phenomenal interest for clinical evaluation oxygen prompting serious deficiencies. Dr. Bhargava said the unexpected flood may have set off alarm and an interest for more oxygen. "This is information from clinic settings thus we don't yet have the foggiest idea what's setting off the interest from outside these settings," he said at an internet meeting.

Dr. V.K. Paul seats upon the enabled bunch on inoculations and COVID the board (NEGVAC). He said there was no distinction in mortality, in the first and second wave, in those 40 and under. "There is no overall extra/abundance hazard of more youthful turning out to be COVID positive," he said.

On drug convention for treatment, Dr. Randeep Guleria focused on that none of the antiviral medications Remdesivir, Fapiravir just as gaining strength plasma had any settled advantage in relieving the illness. Other medicine the utilization of the steroids like dexamethasone, tocilizumab too had restricted utilize particularly in examples of basically sick patients who were encountered an invulnerable framework over-response, called a cytokine storm.

"Steroids, Tocilizumab, Remdesivir these are to be given, if need be, at the ideal time. Giving a mixed drink of medications (solo) can be deadly. Remdesivir is valuable in moderate ailment and to treat abatement in oxygen immersion yet has a restricted job. Whenever given too soon, dexamethasone (Steroid) is hurtful and Tocilizumab is just valuable during a cytokine storm," he added.

- **General difference between the waves of corona virus:**

In the second flood of Covid-19 this year, the more seasoned populace keeps on being more powerless while just a minor increment has been recorded in the quantity of more youthful individuals testing positive for COVID, said Indian Council of Medical Research (ICMR) chief general, Dr. Balram Bhargava on Monday.

Almost a half year after the pinnacle of the main wave in September 2020, COVID cases in India indeed began ascending from the primary seven day stretch of March flagging the appearance of the second rush of the pandemic in the country.

Doing an examination of the first and the second influx of Covid-19 that hit India in mid 2020 and end 2020 separately, the ICMR DG said that there is no significant change in the manner diverse age bunches have been influenced by Covid-19 in the two waves.

"More than 70% patients in the two waves are over 40 years of age, just possibly higher extent of more youthful patients," Bhargava said dependent on the investigation of 1,885 patients in the subsequent waves and 7,600 patients in the primary wave.

In light of ICMR's investigation, Bhargava said in the subsequent waves, a higher extent of asymptomatic patients have been recorded. Tending to the media, he said there is no distinction in passing's between the first and second wave among hospitalized patients. In the subsequent wave, while the oxygen necessity is higher, ventilator prerequisite isn't high, said Bhargava. Bhargava advanced that wastage of oxygen should not occur and it ought to be think. NITI Aayog part (wellbeing) VK Paul said: "basically there is no distinction" in age correlation of patients in the first and second wave. Paul added that Remdesivirshould be utilized on hospitalized patients in moderate phases of disease on oxygen and it isn't to be utilized in home settings.
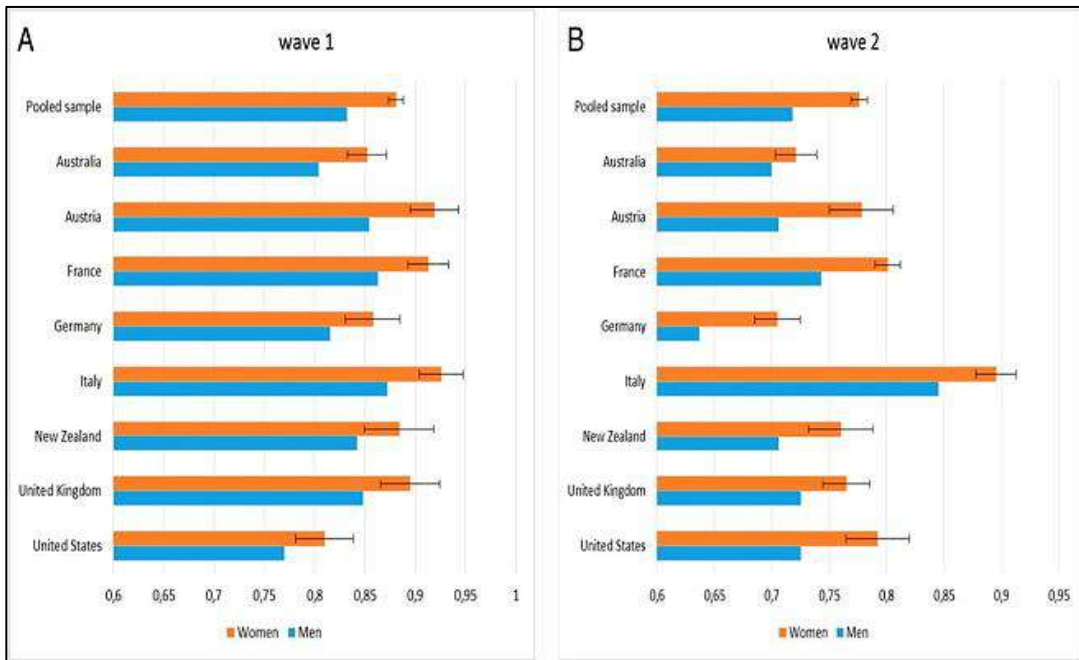
Fig: The difference of COVID-19 second wave and first wave worldwide.

- **Syndromatic difference between the waves of corona virus:**

In the midst of an enormous flood in novel Covid cases in the nation, there's a great deal of worry over the indications of Covid-19 and its seriousness in the second rush of the pandemic.

Considering this, the Indian Council of Medical Research Director General Dr. Balram Bhargava clarified the distinction in the seriousness of the manifestations saying that Coivd-19 side effects in this wave are significantly less than a year ago.

"On the off chance that you see the side effects, seriousness is less this time. In this wave, we have seen more instances of shortness of breath while in the last wave, manifestations like dry hack, joint torment, migraines were more," Dr Bhargava clarified, according to news organization ANI.

He additionally said that RT-PCR test is highest quality level of testing. "We measure two qualities or more, in this way, there is no possibility of missing location of any freak," he said over worries of infection freak strains and their recognition through RT-PCR.

Bhargava additionally said there is no distinction in the percentage of death between the principal wave and second wave.

He further said that solitary an insignificantly high extent of COVID-19 patients are of more youthful age and that the normal of patients in the main wave was 50 years and in this wave, it is 49 years. He additionally said that the more seasoned populace keeps on being more powerless against be conceded in the medical clinic in the momentum wave.

"From zero to 19 years – the thing that matters was 5.8 percent versus 4.2 percent, and in 20-40 years, the thing that matters was 25% versus 23%. There is a peripheral distinction in this. More than 70% were above or equivalent to 40 years old. A higher number of asymptomatic people got conceded for the current year, than a higher extent of patients conceded with shortness of breath," he said.

He additionally said that asymptomatic/gentle disease can be overseen at home and doesn't need hospitalization and furthermore added that ventilator necessity in second wave isn't high.

"There is no adjustment of the passing rate between the principal wave and the subsequent wave. Comparative patterns are being seen across every one of the states since this is a countrywide information of a public library information which has been

gathered of just hospitalized patients, so this is 10,000 hospitalized patients that are being investigated," added Dr. Bhargava.

The ICMR boss additionally thought that there was an enormous measure of laxity in regards to the pandemic and numerous occurrences of COVID-unseemly conduct were likewise seen. He additionally focused on that the RT-PCR test estimates at least two qualities in the body and there is zero chance of missing the recognition of a COVID-19 freak through the test.

"I might want to accentuate that the RT-PCR test that we are using, they measure at least two qualities and they never miss a test. We have consistently utilized at least two qualities for testing and thusly missing is totally unthinkable. It can track down any sort of freak since it estimates at least two qualities at various locales," he told ANI.

Dr. Bhargava further said that the pace of contagiousness of the 'twofold freak' found in India has not yet been set up.

Three fundamental variations from the United Kingdom, South Africa and Brazil have effectively been found in India.

As indicated by the Health Ministry, India announced 2,73,810 new COVID-19 cases, taking the absolute number of positive cases in the country to 1,50,61,919. There are right now 19,29,329 dynamic cases in the country as of Monday. The loss of life arrived at 1,78,769 with extra 1,619 fatalities.

Just now, upwards of 1,44,178 individuals recuperated from the infection. With this, the absolute number of recuperations arrived at 1,29,53,821 in India.
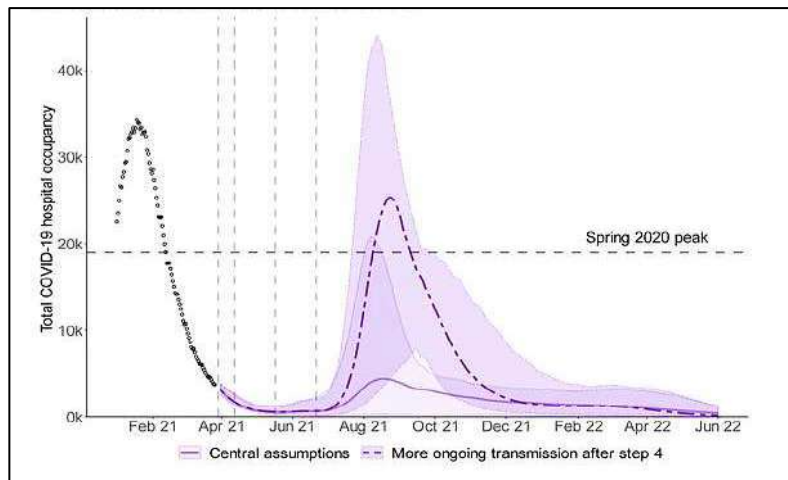
Fig: Corona virus cases in UK and hospital occupancy

- **Medical oxygen-based difference between waves of corona virus:**

In this wave, more instances of windedness have been seen while in the past one, side effects like dry hack, joint agony, cerebral pains were more, as indicated by the ICMR. The manifestations of joint throb, exhaustion, muscle hurt, loss of smell or sore throat are significantly less contrasted with the principal wave. In any case, windedness is higher in this wave, fundamentally raising the necessity of supplemental oxygen in the country.

➕ **First wave:**

Symptoms like dry hack, joint torment, migraines were more.

➕ **Hospitalized patients:**

41.7 % reporting shortness of breath.

➕ **Second wave:**

Shortness of breath is higher in this wave and so there is a higher requirement of oxygen.

➕ **Hospitalized patients:**

47.5 % reporting shortness of breath.
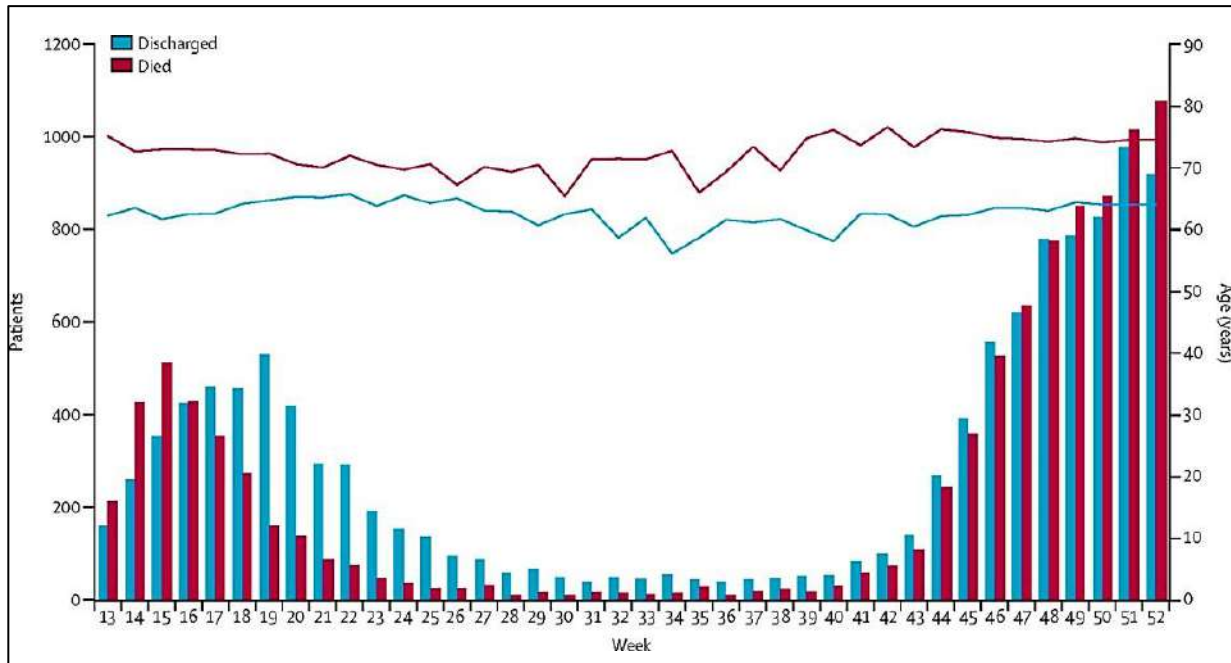
Fig: Major difference between the hospitalized patients in the first and second wave of COVID-19

- **Difference between the waves of corona virus based on infection in young individuals:**

Individuals between 30-45 years old testing positive continue as before as a year ago at 21%. No overabundance pace of youngsters testing positive.

   ↓ **First wave:**

People under 30 years old established 31% positive cases.

   ↓ **Second wave:**

People under 30 years old establish 32% of positive cases.

- **Difference between the waves of corona virus based on age:**

Just barely high extents of COVID-19 patients are of more youthful age and that of the normal time of patients. Over 70% were above or equivalent to 40 years old.

   ↓ **First wave:**

Average period of patients was 50 years.

   ↓ **Second wave:**

Average time of patients is 49 years.

- **Difference between the waves of corona virus based onDeath rate:**

The second wave of Covid-19 in India is 'more severe' than the first wave and there is no change in the death rate.

- **Difference between the waves of corona virus based onVirus itself: SARS-CoV-2:**

In the previous year, the infection has transformed many occasions over and there are different unidentified transformations; of them, some are of concern.

   ↓ **First wave:**

Original type of SARS-CoV-2

   ↓ **Second wave:**

   There is a twofold freak, in addition to the U.K., Brazilian, South African variations that have exhibited to have higher contagiousness. According to WHO creates a virus and its own replica or multiple replicas which is called mutation. The three most risky variations are US (B.1.1.1.7 variant), South Africa (B.1.1.

351) and Brazil (B.1.1.1.28.2.1 variant). Double mutation variant first known as cross conversion. According to the researchers 18 mutations in 7 genes have been observed as a result of mutation. As a result, the virus has become more powerful. Kalyani National institute of biomedical genomics has discovered a new genome sequence for this virus. This new variant has been named B.1.617. Another triple mutation was also found that was named as B.1.618. Changes in spike protein are usually observed here. The first appearance of this variant was found on 25 October. A genomic sequencing in March showed that the presence of this variant in the COVID samples are increasing. The corona virus also contains glycoprotein, a type of S1 and S2. S1 contains a lot of amino acids of which 69 to 70 are amino acids. As a result,he does not have to make two amino acids. As a result,he enters the receptor faster than his old incarnation.

- **The reason behind COVID-19 surge:**

Expressing the purposes for the unexpected spike in sure cases, he said that individual have shown a huge measure of laxity in after COVID-19 unseemly conduct and different unidentified change of the infection have additionally added to the flood. He said some changed infection strains from the UK, Brazil and South Africa are of worry as they showed to have higher contagiousness. 'We have likewise tracked down a twofold freak in India yet the higher contagiousness of this isn't set up,' he added.India so far has recorded more than 1,50,61,919 positive cases, out of which 1,29,53,821 have effectively recuperated and 1,78,769 have kicked the bucket. According to the most recent reports from MoHFW, in the previous 24 hours 2,73,810 new cases, 1,44,178 new recuperations and 1,619 passing's have been accounted for. At present, the absolute number of dynamic cases in India is 19,29,329.

- **COVID-19: First Wave vs. Second Wave:**

The first influx of the infection in quite a while had seen a spike in September 2020 and proceeded to decrease. Slice to December 2020, new instances of the contamination fired appearance up and today on 25th December, 2020, India is the second-most noticeably terrible hit country with 98,26,775 dynamic cases and an aggregate of 1,42,628 passing up until this point.

The second influx of the infection is being looked at as milder than the principal wave back in 2020. There are huge loads of inquiries around how the second floor of the COVID is unique in relation to the first wave in quite a while of side effects, spread and age profile and freak variations.

- **Symptoms:**
  - ❖ The first flood of the COVID included chills, fever, loss of smell and taste, body throb, and respiratory inconveniences.
  - ❖ The new indications detailed during the second rush of COVID-19 incorporate free movements, hearing weakness and pin eyes.

Symptoms	First wave	Second wave
Fever	94.1	94.5
Coughing	92.1	92.6
Shortness of breath	94.5	94.7
Runny or stuffy nose	53.5	55.8
Headache	70.3	72.7
Diarrhea	49.5	53.5
Loss of smell of test	75.7	78.9
Rash on the body	34.8	36.8
Sore throat	86.2	86.9

Table: Increase rate of the Nobel corona virus symptoms in the first and second wave.

Class a symptoms	Class b symptoms
Fever	Headache
Cough	Sore throat
Chills	Fatigue
Shortness of breath	Runny nose
Loss of smell and taste	Neustria, vomiting or diarrhea

- **Spread:**
  ❖ The principal wave of the infection was more inescapable topographically though the subsequent wave is more grouped. This implies the contamination during the subsequent wave is restricted to a lesser number of areas of interest yet with a higher number of cases in those very hotpots.

  ❖ The second wave, in contrast to the principal wave, is showing the quickest spread pace of COVID-19.

Number of Tests Occured For Identifying the New Cases
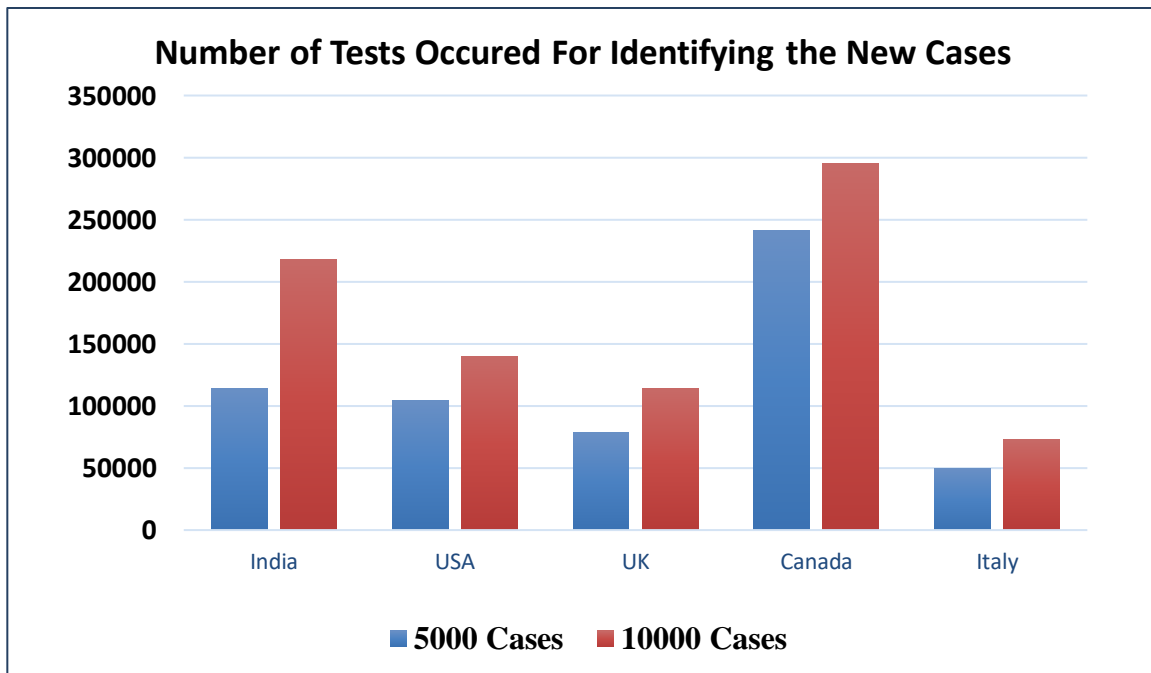
Fig: The number of tests concluded for COVID-19 analysis worldwide.

- **Age Profile:**

  ❖ In the primary wave, the death rate among more established individuals was higher however the subsequent wave is holding more youthful individuals under 45 years old.

  ❖ Maharashtra and Karnataka, the two most exceedingly awful hit states in the nation have detailed 50% of the cases among individuals under 45 years old.

  ❖ Also, specialists and specialists and the information by the public authority have shown that more kids are trying positive for the infection in the subsequent wave.

- **Mutant Variants:**

  The subsequent wave is accepted to observe a spike in the quantity of cases because of the twofold freak variation of COVID-19. Maharashtra has revealed 60% of twofold freak COVID-19 cases. Double mutation variant first known as cross conversion. According to the researchers 18 mutations in 7 genes have been observed as a result of mutation. As a result, the virus has become more powerful. Kalyani National institute of biomedical genomics has discovered a new genome sequence for this virus. This new variant has been named B.1.617. Another triple mutation was also found that was named as B.1.618. Changes in spike protein are usually observed here. The first appearance of this variant was found on 25 October. A genomic sequencing in March showed that the presence of this variant in the COVID samples are increasing. The corona virus also contains glycoprotein, a type of S1 and S2. S1 contains a lot of amino acids of which 69 to 70 are amino acids. As a result, he does not have to make two amino acids. As a result, he enters the receptor faster than his old incarnation.

  ➢ **Vaccine:**

  India chose to give crisis licensure to antibodies which are approved for use in the U.S., U.K., Europe and Japan or by the World Health Organization (WHO), an immunization deficiency is comforting in India and is battling to fulfill developing needs. Such unfamiliar antibodies from the initial 100 recipients are survived for 7 days and then are carried out in Country. Two Indian organizations – Serum Institute of India and Bharat Biotech are the two organizations inside

which antibodies were affirmed through one year for crisis use in India. Two diverse adenovirus-based vectors are contained in the Sputnik immunization. Each vector converting SARS antigen. One is used for the first and another one for the subsequent portion. Says Polly Roy "The two dosages make significant degrees of antibodies", Roy is aVirology Educator in the Department of Infection Biology at the London School of Hygiene and Tropical Medicine. She says "IN light of the utilization of two distinct vectors for two portions, this antibody might be more compelling".

Vaccine	Characters of viruses	Benefits
Sinovac	Whole virus vaccine	The benefit of a whole virus inactivated vaccine is including the fact that it's a well-established technology and to increase the immune system but low.
PfizerbioNtechmoderna	RNA or mRNA vaccine	Boast the immune system and the killer t-cells destroy the infected cells.
Sputnik v	Non replicating viral vector	Viral vector-based vaccination is another well-established technology that can help in triggering strong immune response m
Novavax	Protein subunit	The protein subunit vaccine is a well-established technology and can boost the immune response.
Covaxin	Inactivated vaccine	Covaxin is immune potential oralso known as vaccine adjuvants. And this vaccine increases the immune response in human
Covisheild	Adenovirus viral vectors	Protects against SARS COV -2 virus and increase immunity.

Conclusion:

From this examination we have tracked down a more prominent contrast between the two waves in the Covid. The examination is worldwide however there is a primary premise upon the COVID19 pandemic circumstance dependent on India. The investigation has centered upon the significant contrasts between the two floods of Covid pandemic. The examination appeared about the death rate unaltered in the two waves. Be that as it may, the infectivity has extreme contrast between the waves. The infectivity of first wave was similarly lower than that of the subsequent wave. Second wave additionally can taint the youngsters more. The subsequent wave has hereditary change in the Covid strains so it has greater chance contamination. It likewise can have the safe getaway. So, the RT-PCR may fizzle for certain instances of second wave disease. The distinction likewise present as per freak variation, period of patients, side effects, region contaminated, disease rate, manifestations, clinical oxygen interest, syndromatic contrast and a few more distinction.

References:

1. Africanews. COVID-19: Egypt confirms first coronavirus case in Africa. Coronavirus outbreak News. Al Jazeera. 2020. https://www. Aljazeera.com/news/2020/02/egypt-confirms-coronavirus-case-Africa-200214190840134.html (accessed June 14, 2020).

2. WHO. COVID-19 as a Public Health Emergency of International Concern (PHEIC) under the IHR. World Health Organization: Geneva, 2020. https://extranet.who.int/sph/covid-19-public-health-Emergency-international-concern-pheic-under-ihr (accessed June 14, 2020).

3. Africa CDC. Africa Joint Continental Strategy for COVID-19 Outbreak. 2020. https://africacdc.org/download/africa-joint-Continental-strategy-for-covid-19-outbreak/ (accessed May 10, 2020).

4. PERC. Partnership for Evidence-Based Response for COVID-19 (PERC). 2020.https://preventepidemics.org/covid19/perc/(accessed Dec 28, 2020).

5. Africa CDC. COVID-19 Pandemic Response Initiatives. 2020. https://africacdc.org/download/covid-19-pandemic-response-initiatives/ (accessed Dec 28, 2020).

6. Atalan A. 2020. Is the lockdown important to prevent the COVID-19 pandemic? Effects on psychology, environment and Economy-perspective. Annals of medicine and surgery 56, 38-42 https://doi.org/10.1016/j.amsu.2020.06.010.

7. Bontempi E. 2020. The Europe second wave of COVID-19 infection and the Italy "strange" situation. Environmental Research. In press.

8. Cacciapaglia G., Cot C., Sannino F. 2020. Second wave COVID-19 pandemics in Europe: a temporal playbook, Scientific Reports , 10(1),15514, https://doi.org/10.1038/s41598-020-72611-5.

9. Chang S., Pierson E., Koh P.W. et al. 2020. Mobility network models of COVID-19 explain inequities and inform Reopening. Nature. https://doi.org/10.1038/s41586-020-2923-3.

10. Chaudhry R., Dranitsaris G., Mubashir T., Bartoszko J., Riazi S. 2020. A country level analysis measuring the impact of Government actions, country preparedness and socioeconomic factors on COVID-19 mortality and related health Outcomes. Eclinicalmedicine. 100464. DOI: 10.1016/j.eclinm.2020.100464.

11. Coccia M. 2005. A taxonomy of public research bodies: a systemic approach, Prometheus, vol. 23, n. 1, pp. 63-82. DOI:10.1080/0810902042000331322.

12. Coccia M. 2015. Spatial relation between geo-climate zones and technological outputs to explain the evolution of Technology. Int. J. Transitions and Innovation Systems, vol. 4, nos. 1-2, pp. 5-21, http://dx.doi.org/10.1504/IJTIS.2015.074642.

13. Coccia M. 2016. The relation between price setting in markets and asymmetries of systems of measurement of goods, The Journal of Economic Asymmetries, vol. 14, part B, November, pp. 168-178, https://doi.org/10.1016/j.jeca.2016.06.001.

14. Coccia M. 2017. Asymmetric paths of public debts and of general government deficits across countries within and outside The European monetary unification and economic policy of debt dissolution, The Journal of Economic Asymmetries, Vol. 15, June, pp. 17-31, https://doi.org/10.1016/j.techfore.2010.02.003.

15. Coccia M. 2017a. The Fishbone diagram to identify, systematize and analyze the sources of general purpose technologies. Journal of Social and Administrative Sciences, vol. 4, n. 4, pp. 291-303, http://dx.doi.org/10.1453/jsas.v4i4.1518.

16. RECOVERY Collaborative Group. Lopinavir-ritonavir in patients admitted to hospital with COVID-19 (RECOVERY): a randomised, controlled, open-label, platform trial. Lancet. 2020; 396: 1345–1352. https://doi.org/10.1016/S0140-6736(20)32013-4 PMID: 33031764.

17. Lam S, Lombardi A, Ouanounou A. COVID-19: A review of the proposed pharmacological treatments. Eur J Pharmacol. 2020; 886: 173451. https://doi.org/10.1016/j.ejphar.2020.173451 PMID: 32768505.

18. COVID-19 RISK and Treatments (CORIST) Collaboration. Use of hydroxychloroquine in hospitalised COVID-19 patients is associated with reduced mortality: Findings from the observational multicentre Italian CORIST study. Eur J Intern Med. 2020; 82: 38–47. https://doi.org/10.1016/j.ejim.2020.08.019 PMID: 32859477.

19. Ip A, Ahn J, Zhou Y, Goy AH, Hansen E, Pecora AL, et al. Hydroxychloroquine in the treatment of outpatients with mildly symptomatic COVID-19: a multi-center observational study. BMC Infect Dis. 2020; 21:72. https://doi.org/10.1186/s12879-021-05773-w PMID: 33446136.

20. Ran J, Zhao S, Han L, Liao G, Wang K, Wang MH, et al. A re-analysis in exploring the associationBetween temperature and COVID-19 transmissibility: an ecological study with 154 Chinese cities. EurRespir J. 2020; 56: 2001253. https://doi.org/10.1183/13993003.01253-2020 PMID: 32631839.

21. Ran J, Zhao S, Han L, Chen D, Yang Z, Yang L, et al. The ambient ozone and COVID-19 transmissibilityIn China: A data-driven ecological study of 154 cities. J Infect. 2020; 81: e9–e11. https://doi.org/10.1016/j.jinf.2020.07.011 PMID: 32652165.

22. Ran J, Zhao S, Han L, Qiu Y, Cao P, Yang Z, et al. Effects of particulate matter exposure on the trans-Missibility and case fatality rate of COVID-19: A Nationwide Ecological Study in China. J Travel Med.2020; 27: taaa133. https://doi.org/10.1093/jtm/taaa133 PMID: 32779721.

23. Ajzenman N, Cavalcanti T, Da Mata D. More than words: leaders? Speech And risky behavior during a pandemic. SSRN. (2020). Doi: 10.2139/ssrn.35 82908. [Epub ahead of print].

24. Kochanczyk M, Grabowski F, Lipniacki T. Dynamics of COVID-19 pandemic ´At constant and time-dependent contact rates. Math Modell Nat Phenomena. (2020) 15:28. Doi: 10.1051/mmnp/2020011

25. Rowlett J, Karlsson CJ. Decisions and disease: the evolution of Cooperation in a pandemic. arXiv[Preprint].arXiv:200412446. (2020) Doi: 10.1038/s41598-020-69546-2.

26. Steinegger B, Arenas A, Gómez-Gardenes J, Granell C. Pulsating campaigns Of human prophylaxis driven by risk perception palliate oscillations Of direct contact transmitted diseases. Phys Rev Res. (2020) 2:023181. Doi: 10.1103/PhysRevResearch.2.023181.

27. Johnston MD, Pell B. A dynamical framework for modeling fear of Infection and frustration with social distancing in COVID-19 spread. arXiv[Preprint].arXiv:200806023. (2020).

28. Tellis GJ, Sood N, Sood A. Why did US governors delay lockdowns against COVID-19? Disease Science vs Learning, Cascades, and Political Polarization. SSRN. (2020). Doi: 10.2139/ssrn.3575004. [Epub ahead of print].

29. Hossain MM. Current status of global research on novel coronavirus disease (COVID-19): a bibliometric analysis and knowledge mapping. SSRN. (2020). Doi: 10.2139/ssrn.3547824. [Epub ahead of print].

30. Hethcote HW. The mathematics of infectious diseases. SIAM Rev. (2000) 42:599–653. Doi: 10.1137/S0036144500371907.

31. Anderson RM, May RM. Infectious Diseases of Humans: Dynamics and Control. Oxford: Oxford University Press (1992).

32. Lim, J.; Jeon, S.; Shin, H.Y.; Kim, M.J.; Seong, Y.M.; Lee, W.J.; Choe, K.W.; Kang, Y.M.; Lee, B.; Park, S.J.; et al. Case of the index patient who caused tertiary transmission of COVID-19 infection in Korea: The application of lopinavir/ritonavir for the treatment of COVID-19 infected pneumonia monitored by quantitative RT-PCR. J. Korean Med. Sci. 2020, 35. [CrossRef].

33. Wang, H.; Wang, S.; Yu, K. COVID-19 infection epidemic: The medical management strategies in Heilongjiang Province, China. Crit. Care 2020, 24, 107. [CrossRef].

34. Chan, K.W.; Wong, V.T.; Tang, S.C.W. COVID-19: An update on the epidemiological, clinical, preventive and therapeutic evidence and guidelines of integrative Chinese-Western medicine for the management of 2019 novel coronavirus disease. Am. J. Chin. Med. 2020, 13, 1–26. [CrossRef].

35. Chinese Association of Rehabilitation Medicine; Respiratory rehabilitation committee of Chinese Association of Rehabilitation Medicine. Cardiopulmonary rehabilitation group of Chinese society of physicai medicine and rehabilitation. Zhonghua Jie He He Hu Xi Za Zhi 2020, 43, E029. 40. Russell, C.D.; Millar, J.E.; Baillie, J.K. Clinical evidence does not support corticosteroid treatment for 2019-nCoV lung injury. Lancet 2020, 395, 473–475. [CrossRef].

36. Arabi, Y.; Mandourah, Y.; Al-Hameed, F.; Sindi, A.A.; Almekhlafi, G.A.; Hussein, M.A.; Jose, J.; Pinto, R.; Al-Omari, A.; Kharaba, A.; et al. Corticosteroid therapy for critically ill patients with

middle east respiratory syndrome. Am. J. Respir. Crit. Care Med. 2018, 197, 757–767. [CrossRef] [PubMed].

37. World Health Organization Clinical Management of Severe Acute Respiratory Infection When Novel Coronavirus (nCoV) Infection is Suspected. Available online: https://www.who.int/publications-detail/ clinical-management-of-severe-acute-respiratory-infection-when-novel-coronavirus-(ncov)-infection-issuspected (accessed on 28 March 2020).

38. Lee, N.; Chan, K.C.A.; Hui, D.S.; Ng, E.K.; Wu, A.; Chiu, R.W.; Wong, V.W.; Chan, P.K.; Wong, K.T.; Wong, E.; et al. Effects of early corticosteroid treatment on plasma SARS-associated Coronavirus RNA concentrations in adult patients. J. Clin. Virol. 2004, 31, 304–309. [CrossRef] [PubMed].

39. Gordon, C.J.; Tchesnokov, E.P.; Feng, J.Y.; Porter, D.P.; Gotte, M. The antiviral compound remdesivir potently inhibits RNA-dependent RNA polymerase from Middle East respiratory syndrome coronavirus. J. Biol. Chem. 2020, 295, 4773–4779. [CrossRef].

40. de Wit, E.; Feldmann, F.; Cronin, J.; Jordan, R.; Okumura, A.; Thomas, T.; Scott, D.; Cihlar, T.; Feldmann, H. Prophylactic and therapeutic remdesivir (GS-5734) treatment in the rhesus macaque model of MERS-CoV infection. Proc. Natl. Acad. Sci. USA 2020, 117, 6771–6776. [CrossRef].

41. Yao, X.; Ye, F.; Zhang, M.; Cui, C.; Huang, B.; Niu, P.; Liu, X.; Zhao, L.; Dong, E.; Song, C.; et al. In vitro antiviral activity and projection of optimized dosing design of hydroxychloroquine for the treatment of severe acute respiratory syndrome coronavirus 2 (SARS-CoV-2). Clin. Infect. Dis. 2020. [CrossRef].

42. Wang, M.; Cao, R.; Zhang, L.; Yang, X.; Liu, J.; Xu, M.; Shi, Z.; Hu, Z.; Zhong, W.; Xiao, G.; et al. Remdesivir and chloroquine effectively inhibit the recently emerged novel coronavirus (2019-nCoV) in vitro. Cell Res. 2020, 30, 269–271. [CrossRef].

43. Cortegiani, A.; Ingoglia, G.; Ippolito, M.; Giarratano, A.; Einav, S. A systematic review on the efficacy and safety of chloroquine for the treatment of COVID-19. J. Crit. Care 2020, 9441, 30390–30397. [CrossRef].

Source details

Feedback >   Compare sources >

European Journal of Molecular and Clinical Medicine

Formerly known as: New Horizons in Translational Medicine

Scopus coverage years: 2018, 2020

(coverage discontinued in Scopus)

Publisher: EJMCM, International House

E-ISSN: 2515-8260

Subject area: (Immunology and Microbiology: Applied Microbiology and Biotechnology)   (Immunology and Microbiology: Immunology)

(Biochemistry, Genetics and Molecular Biology: Molecular Medicine)   (Immunology and Microbiology: Microbiology)   View all ∨

Source type: Journal

View all documents >   Set document alert   🖫 Save to source list

CiteScore 2019
0.2   ⓘ

SJR 2019
0.152   ⓘ

SNIP 2022
0.000   ⓘ

CiteScore   CiteScore rank & trend   Scopus content coverage

Comprehensive Studies of Black Pepper and its Chemical Profiling

Article · January 2021

2 authors, including:

Tanmay Ghosh
Dinabandhu Andrews College university of calcutta
74 PUBLICATIONS   **211** CITATIONS

Comprehensive Studies of Black Pepper and its Chemical Profiling

TANMAY GHOSH[1]*, JOYDIP GHOSH[2]

[1] Department of Microbiology, Dinabandhu Andrews College, Baishnabghata, South 24 Parganas, Kolkata– 700084, West Bengal, India.

[2] Department of Microbiology Rabindra Mahavidyalaya, Champadanga, Hooghly, West Bengal – 712401 India.

Research Article

ABSTRACT

In a traditional systems use of medicinal plants have a great role. Medicinal plants have diverse pharmacological potential with very lesser or no side effect. Black pepper (*Piper niger* L.) is a natural medicinal plant used to treat many diseases. Here we have used ethanol, chloroform, and methanol extract of Black pepper of 50µg/ml, 100µg/ml, 200µg/ml, and 300µg/ml concentration. It is observed that 300µg/ml concentration of ethanol extract of Black pepper shows the high zone of inhibition. There are several phytochemical, found in Black pepper after observing in qualitative phytochemicals analysis. The phytochemicals are alkaloids, flavonoids, steroids, tannins, and saponins.

INTRODUCTION

The Plants have antimicrobial, antiviral, and antibacterial potential. Day by day the search on antimicrobial activities of plants increases with high expectation. Black pepper is a type of spice, scientific name Piper nigram, found in almost all over the world having various medicinal activities. A fresh mature Black pepper of approximately 5m in diameter contains a seed like a drupe. Black pepper is mainly cultivated in tropical regions, Vietnam is the world's largest source of Black pepper. It can maintain cholesterol levels, blood sugar, gut breath and can improve the brain. Here I have studied the antimicrobial effect of Black pepper.

MATERIAL AND METHODS

Collection of Plant Material:

Seed of Black Pepper was selected for the study of antibacterial activity and phytochemical analysis. The seed black pepper was collected from the market on Hooghly, West Bengal, India.

Taxonomical position of Black pepper:-

Kingdom: Plantae

Clade: Tracheophtyes

long Clade: Angiosperms

Clade: Mangnoliids

Order: Piperales

Family: *Piperaceae*

Genus: Piper

Species: *P. nigrum*

Fig 1: Black papper

Bacterial cultures:

To study the antibacterial effect here used Staphylococcus aureus as Gram-positive bacteria, Escherichia coli, and Salmonella typhi as Gram-negative bacteria.

Preparation of different extraction:

- **Ethanol extract:** 10 g of powdered plant material was dissolved into enough ethanol to make 40 ml of ethanolic extract (25% w/v). The procedure to make extract was same as procedure used for aqueous extract.

- **Chloroform extract:** 5gm of air-dried powder of leaves was mixed with 25ml of chloroform in a conical flask and then kept on a rotary shaker for 10mints. Then they were bound with tissue paper and a rubber band. Some holes were made so that air can pass through it and then kept in room temperature for 3-5 days for evaporating.

- **Methanol extract:** 5gm of air-dried powder of leaves was mixed with 25ml of methanol in a conical flask and then kept on a rotary shaker for 10mints. Then they were bound with tissue paper and a rubber band. Some holes were made so that air can pass through it and then take room temperature for 3-5 days for evaporating.

Preparation of extract concentration:

Four concentrations (50mg/ml, 100mg/ml, 200mg/ml and 300mg/ml) were made from each of the three extracts (Chloroform, Ethanol, Methanol extract). In every case, 3 gm of Extract was mixed with 10ml DMSO (Dimethyl Sulfoxide) to prepare 300 mg/ml stock concentration..

Microbiological assay:

- **Agar disc diffusion method:** The antibacterial screening of seed extract of black pepper was prepared by dissolving 3gm of each extract separately in 10ml Dimethyl Sulphoxide (DMSO). From this 50µg/ml, 100µg/ml, 200µg/ml, 300µg/ml concentration were taken for the analysis of antibacterial activity. A hollow tube was heated and pressed above the inoculated agar plate. It was removed immediately by making a well in the plate; two wells on each plate were made one each for DMSO control.

- **Disc diffusion method:** A single colony of the purified isolates was inoculated in 5 ml sterile peptone water and incubated at 37°C overnight. Thereafter, a loop full culture was diluted in 5 ml sterile phosphate-buffered saline and seeded into Muller Hinton agar. The antibiotic disc (Hi-Media) was placed on the surface of the agar and incubated overnight at 37°C. The zone of inhibition was recorded and a control sensitive culture was included in the experiment.

Medium: 3.8 g of Mueller Hinton Agar (MHA) was added with 100ml of distilled water. Then it autoclaved at 121^{0}C for 15 minutes. Poured it uniformly in Petri plates and then set the agar properly in the require temperature for future use.

Inoculums and Incubation: 0.1mg of bacterial culture was transferred in agar plate. Then the plate was stood for 5min, before it prepared for tested different concentrations. The seed extract of pepper was loaded in different concentrations into the agar plate. Then incubate with the bacterial culture at 37^{0}C for 24-48 hours in the incubator.

Phytochemical screening of spices:

- **Screening for alkaloids:** To 5 ml each of the spice extracts, 5 ml of aqueous hydrochloric acid was added on a steam bath at 60°C for 5 min. The spice extract was filtered with a 3 layered muslin cloth. In one ml of the filtrate, few drops of Draggendoff's reagent were added. The appearance of Blue-black turbidity was positive for alkaloids.

- **Screening for steroids:** 1 ml of extract was dissolved in 10 ml of chloroform and an equal volume of concentrated sulphuric acid was added by the sides of the test tube. The upper layer turns red and the sulphuric acid layer showed yellow with green fluorescence. This indicates the presence of steroids.

- **Screening for tannins:** 5ml of each extracts was stirred separately with 100 ml distilled water and filtered. One millilitre ferric chloride reagent was added to the filtrate. A blue-black or blue-green precipitate was an indication of the presence of tannin.

- **Screening for flavonoids:** 5 ml of dilute ammonia solution was added to the aqueous extract followed by the addition of 1 ml concentrated H_2SO_4. The appearance of yellow color indicated the presence of flavonoids.

- **Screening for saponins:** 5ml of each extracts were mixed with distilled water and shaken separately in a test tube. Frothing, which persists on warm heating was taken as preliminary evidence of the presence of the saponin.

Table 1- Phytochemical study of black pepper.			
Phytochemicals	**Chloroform**	**Methanol**	**Ethanol**
Alkaloids	+	-	+
Flavonoids	-	+	-
Tannins	-	-	-
Saponins	+	+	-
Steroids	-	+	+

RESULTS AND DISCUSSION

For the extraction of the active compounds of Black pepper seed, we used both polar and non-polar solvents. Using the Agar diffusion method the antibacterial activities can be determined by measuring the diameter of the growth inhibition zone. The extract of Black pepper using different solvents like benzene, methanol, ethanol, and chloroform were screened to study antibacterial activity against both Gram-positive and Gram-negative bacteria. By using Agar cup method antibacterial activity was tested on Muller Hinton Agar (MHA). Various concentrations of extracts were prepared.

Table 2- of black Antibacterial activity of Methanol extract pepper seeds against different bacteria			
concentration	Zone of inhibition		
	Staphylococcus aureus	*Escherichia Coli*	*Salmonella typhi*
300	20.2±1	27.1±2	18.8±1
200	18.3±2	22.4±1	16.4±2
100	17.2±1	19.8±2	15.5±1
50	15.1±2	16.5±1	13.6±2
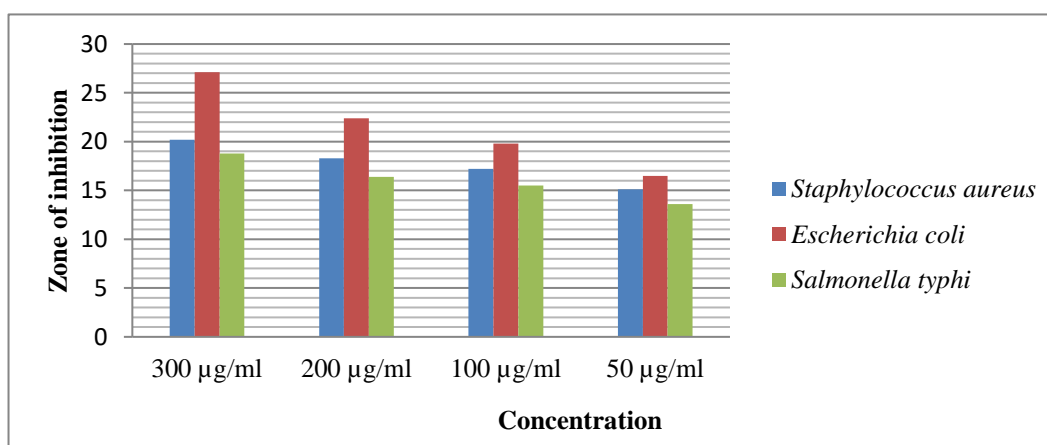
Fig 2: Antibacterial activity of Ethanol extract of black pepper seeds against different bacteria.

Table 3- Antibacterial activity of Ethanol extract of black pepper seeds against different bacteria			
concentration	Zone of inhibition		
	Staphylococcus aureus	*E. coli*	*Salmonella typhi*
300	38.0±1.0	33.0±2.0	32.4±1.0
200	33.0±2.0	32.1±1.0	28.3±2.0
100	27.3±1.0	26.3±2.0	25.0±1.0
50	24.8±22.0	22.2±0	19.6±2.0
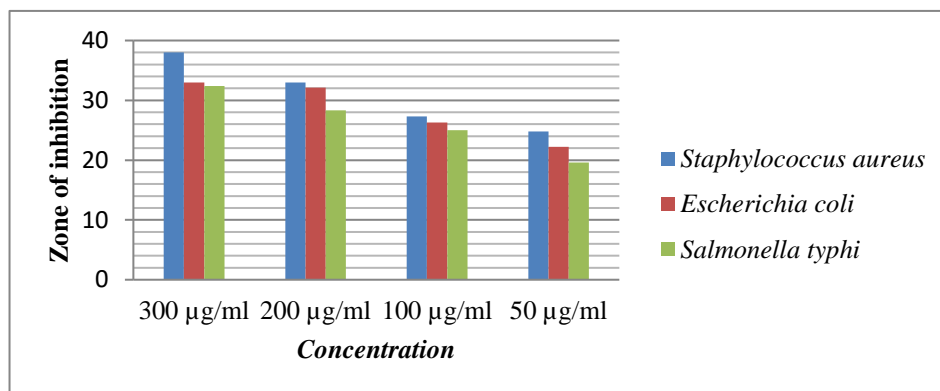
Fig 3: Antibacterial activity of Ethanol extract of black pepper seeds against different bacteria.

Table 4-Antibacterial activity of Chloroform extract of black pepper seeds against different bacteria.			
concentration	**Zone of inhibition**		
	Staphylococcus aureus	**E. coli**	**Salmonella typhi**
300	28.3±1.0	32.0±2.0	31.2±1.0
200	27.4±2.0	31.2±1.0	28.2±2.0
100	24.0±1.0	27.0±0	25.3±1.0
50	22.0±2.0	23.2±1.0	20.2±2.0
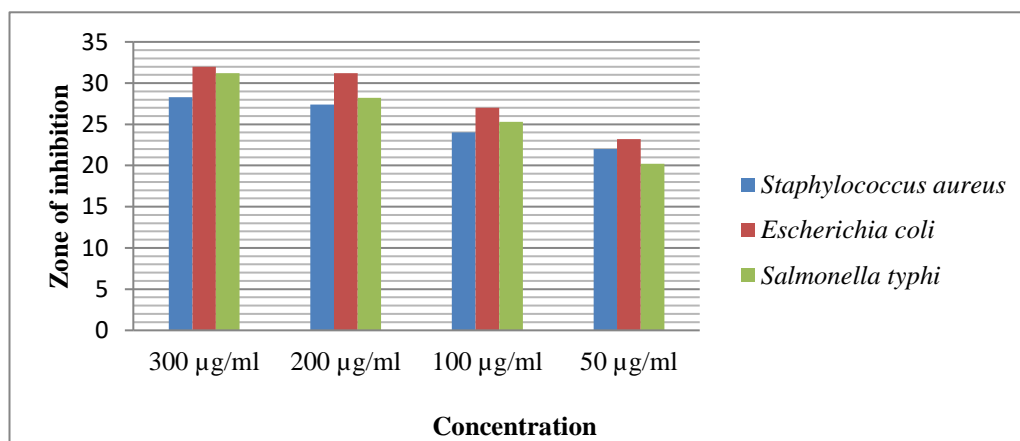
Fig: 4 -Antibacterial activity of Chloroform extract of black pepper seeds against different bacteria.

CONCLUSION

Black pepper extract has greater antibacterial activity. It was observed that Gram-positive bacteria are more susceptible than Gram-negative bacteria treated with Black pepper extract. After qualitative chemical analysis, we found alkaloid, flavonoid, tannins, saponins, and steroid from it. So, it is clear that we should be getting positive results by using Black pepper extract as an antibacterial agent.

REFERENCE

1. Akter S, Haque T, Irine EJ, Kabir MF, Ahmed S, Begum T (2015).Comparative antimicrobial activities of different species of Ixora. J. Pharma. Phytochem. 3(6):103-105 Miyazawa M, Hisama M (2003). Antimutagenic activity of phenylpropanoids from clove (*Syzygium aromaticum*). J. Agric. Food Chem. 51(22):6413-6422

2. Sonam C, Sharma K. and Uleria S.G. Antimicrobial Activity of some essential oils present status and future perspectives. Medicines. 2017; 4:58.

3. Srivastava KC, Malhotra N (1991). Acetyl eugenol, a component of oil of cloves (*Syzygium aromaticum* L.) inhibits aggregation and alters arachidonic acid metabolism in human blood platelets.

4. Davidson PM and Branen AL, Antimicrobial activity of non-halogenated phenolic compounds, J Food Prot, 1981, 44, 623-632.

5. S. S. Nathan, K. Kalaivani, and K. Murugan, "Effects of neemlimonoids on the malaria vector Anopheles stephensi Liston(Diptera: Culicidae)," Acta Tropica, vol. 96, no. 1, pp. 47–552005.

6. T. Kalaivani, E. Meiganam, N. Premkumpatoprotectivear, andR. Siva, "Studies on hepatoprotective properties of leaf extractsof Azadirachta indica A. Juss (Meliaceae)," EthnobotanicalLeaflets, vol. 13, no. 2, pp. 165–170, 2009.

7. Sharma, R. R (2012) preliminary Phytochemical screening of some indigenous medicinal plants leaves to extract theregulation of antibiotic activity. Sci, Res.,Rep. 2(3):307-310.

8. RinkyBisht, Sheetalchanyal, and Pavan Kumar Agarwal "Antimicrobial, and Phytochemical analysis of leaf extract of medicinal fruit plants ". Asian journal pharma Research. Volume. 9(4),pp. 131-136, 2006.

9. Louppe D. Timbers 1, Volume 7. Plant resources of tropical Africa. PROTA edition. 2008, p 265 & 266.

10. Little J.Common fuelwood crops: a handbook for their identification. McClain Printing Co: Parsons, WV. 1983.

11. Mistry KS, Sanghvi Z, Parmar G, Shah S. The antimicrobial activity of Azadirachta indica, Mimusops Elengi, Tinospora cardiofolia, Ocimum sanctum, and 2% chlorhexidine on common endodontic pathogens: An in vitro study. Eur J Dent. 2014;8(2):172-7.

12. Ghonmode WN, Balsaraf OD, Tambe VH, Saujanya KP, Patil AK, Kakde DD. Comparison of the antibacterial efficiency of neem leaf extracts, grape seed extracts, and 3% sodium hypochlorite against E. feacalis - An in vitro study. J Int Oral Health. 2013;5(6):61-6.

13. Elangovan A, Muranga J, Joseph E. Comparative evaluation of the antimicrobial efficacy of four chewing sticks commonly used in South India: An in vitro study. Indian J Dent Res. 2012;23(6):840.

14. Rao DS, Penmatsa T, Kumar AK, Reddy MN, Gautam NS, Gautam NR. Antibacterial activity of aqueous extracts of Indian chewing sticks on the dental plaque: Anin vitro study. J Pharm Bioallied Sci. 2014;6(Suppl):S140-S145.

15. Arumugam A, Agullo P, Boopalan T, Nandy S, Lopez R, Gutierrez C, Narayan M, Rajkumar L. Neem leaf extract inhibits mammary carcinogenesis by altering cell proliferation, apoptosis, and angiogenesis. Cancer Biology and Therapy. 2014; 15(1):26-34. DOI: 10.4161/cbt.26604

16. Priyadarsini RV, Murugan RS, Sripriya P, Karunagaran D, Nagini S. The neem limonoids azadirachtin and nimbolide induce cell cycle arrest and mitochondria-mediated apoptosis in human cervical cancer (HeLa)cells. Free Radical Research. 2010; 44(6):624-634. DOI: 10.3109/10715761003692503.

17. Mahapatra S, Young CYF, Kohli M, Karnes RJ, Klee EW, Holmes MW et al. Antiangiogenic effects and therapeutic targets of Azadirachta indica leaf extract in endothelial cells. Evidence-Based Complementary and Alternative Medicine. 2012; 2012:14. DOI: 10.1155/2012/303019.303019

18. Dhar R, Dawar H, Garg S, Basir SF, Talwar GP. Effect of volatiles from neem and other natural products the gonotrophic cycle and oviposition of Anopheles stephensi and An. culicifacies (Diptera: Culicidae). Journal of Medical Entomology. 1996; 33(2):195-201DOI: 10.1093/jmedent/33.2.195.

19. Nathan SS, Kalaivani K, Murugan K. Effects of neem limonoids on the malaria vector Anopheles stephensiListon (Diptera: Culicidae) Acta Tropical. 2005; 96(1):47-55. DOI: 10.1016/j.actatropica.2005.07.002.

UGC-CARE List

UGC-CARE List

You searched for **"2319-9857"**. Total Journals : **1**

Search: [ ]

Sr.No.	Journal Title	Publisher	ISSN	E-ISSN	UGC-CARE coverage years	Details
1	Research and Reviews: Journal of Agriculture and Allied Sciences	Research and Reviews	2319-9857	2347-226X	from June-2019 to April- 2022	Discontinued from April 2022

Showing 1 to 1 of 1 entries

Previous 1 Next

Home

○ UGC

🔍 Search

Evaluation of Phytochemical and Biochemical Profiling of Marine Red Algae *Gracilariacrassa*

[1]T.Parvathi, [2]M.Sathish, [3]Subhesh Saurabh Jha [4]Khongdet Phasinam, [5]L.Nivetha, [6]Tanmay Ghosh

[1,2.]Research Scholars, PG and Research Department of Botany, J.J.College of Arts and Science (Autonomous), Pudukkottai, Affiliated to Bharathidasan University, Trichy.

[3]Research Scholar, Department of Botany, Institute of Sciences; Banaras Hindu University

[4]Assistant Professor, Faculty of Food and Agricultural Technology, Pibulsongkram Rajabhat University, Phitsanulok, Thailand

[5]Assistant professor, Department of biotechnology, PSG College of Arts & Science, Coimbatore, Tamilnadu

[6]Assistant Professor, Department of Microbiology, Dinabandhu Andrews College, Baishnabghata, South 24 Parganas, Kolkata – 700084, West Bengal, India.

Abstract

The aim of the present study sought to evaluated that biochemical constituents like protein, carbohydrate, total lipids, total phenols and phytochemical were analyzed from the marine red algae *Gracilariacrassa.* The present observation *G.crassa* showed the flavonoids, alkaloid, phenol, chlorogenic acid and carbohydrates were presented all the extracts. The biochemical content, fatty acid profile and mineral compositions were also recorded from the *Gracilariacrassa* extract. In this study, the biochemical constituents such as total carbohydrate ($19.34\pm0.10\%$), total protein ($23.13\pm0.005\%$), total phenols (7.81 ± 0.23 mg/g) and total lipids ($0.27\pm0.5\%$) were observed from the extract of *G.crassa.* The fatty acid profile showed that the higher concentration of saturated fatty acid and poly unsaturated linoleic acids were recorded. In mineral composition, the Ca (135.4 ± 0.20 mg/100^{-1}) level was high when compared with other elements. In view of the results, the present study suggests that *G.crassa* contains important nutrients for human health and is possible natural functional foods.

Key words: phytochemical, fatty acid, *Gracilariacrassa,* protein, mineral and total lipids.

INTRODUCTION

Seaweeds are primitive non-flowering plants without true roots, stem and leaves. They grow in the intertidal, shallow and deep sea areas up to 180 meter depth and also in estuaries, backwaters and lagoons on solid substrates such as rocks, dead corals, pebbles, shells, mangroves, and other plants (Anantharaman*et al.,*2007). Seaweeds are classified as Rhodophyta (red algae), Phaeophyta (brown algae) and Chlorophyta (green algae) depending on their nutrient and chemical composition. It was estimated that about 90% of the species of marine plant are algae and about 50% of the global photosynthesis is contributed from algae

(Dhargalkar*et al.,* 2005).Seaweeds are considered as a source of bioactive compounds as they are able to produce a great variety of secondary metabolites characterised by a broad spectrum of biological activities. Compounds with antioxidant, antiviral, antifungal and antimicrobial activities have been detected in brown, red and green algae (Chew *et al.*, 2008). The environment in which seaweeds grow is harsh as they are exposed to a combination of light and high oxygen concentrations. These factors can lead to the formation of free radicals and other strong oxidising agents but seaweeds seldom suffer any serious photodynamic damage during metabolism. This fact implies that seaweed cells have some protective mechanisms and compounds (Matasukawa*et al.*, 1997). Many metabolites isolated from marine algae possess bioactive effects. The discovery of metabolites with biological activities, from macro algae, has increased significantly in the past three decades; on the other hand, seaweeds have recently received significant attention for their potential as natural antioxidants. Marine organisms are a rich source of structurally novel and biologically active metabolites (Perry *et al.,* 1991).

Seaweeds are very important natural resources from the oceans that are employed as human foods and animal feeds in their whole form, and as sources of polysaccharides (mainly alginates, carrageenans and agar), carotenoids, lipids, vitamins, minerals, dietary fiber, proline and amino acids for use in food and pharmaceutical industry (Debbarama*et al.,* 2016). Seaweeds have been included for a long time in the traditional diet of East Asian countries such as Japan, Korea and China; more recently, their presence in all forms in the diet of Western countries has been progressively increasing (Torres *et al.,* 2019). Sumitra Vijayaragavan *et al.,* (1980) analyzed the seasonal variations in biochemical composition of some seaweed from Goa coast. Muthuraman and Ranganathan, (2004) investigated protein, amino acids, total sugars and lipid contents of *Caulerpascalpelliformis, Cladophoravagabunda, Enteromorphacompressa, Halimedamacroloba, Ulvafasciata and Chaetomorphaantennina*. The biochemical composition of seaweeds differs and is affected by inflow of land sources, geographic area and season of the year and temperature of water (Jenson, 1993).

However, the nutrient profile of seaweeds such as Gracilaria is influenced by different factors such as seaweed species, habitat, maturity stage, season, water temperature and the sampling conditions and method employed in the determinations (Torres *et al.,* 2019). *Gracilariacrassa* is exclusively marine red algae. It varies in size and shape. They are either epiphyte, grow as crust on the rocks or shells as a large fleshy, and branched like thalli. There are several benefits arises from this species such as medical and food wise. In the present study, the phytochemical screening from marine red algae and evaluate their antimicrobial potential. Thus, the present study sought to evaluate the phytochemical screening and chemical composition of *Gracilariacrassa*from the Muttam coast of Palk Bay, Kanyakumari.

MATERIALS AND METHODS

Collection of seaweeds

The seaweed*Gracilariacrassa* was collected from coastal area of Muttam, Kanyakumari district, Tamil

Nadu, India. Macro algae samples were collected manually using transects method from the submerged marine rocks, soft substratum, during low tide in the intertidal and sub-tidal regions.After collection of sample, it was brought to the laboratory. Algal samples were washed in running tap water to remove any associated debris and then with the distilled water. After washing the samples were dried in a blotting paper for two weeks. After drying the sample was grinded in to powder form which was then stored in 4 °C for further studies. The algal specimen was identified at central salt and marine algal research station (CSMARS), Mandapam.

Preparation of extract

One gram of algal sample was extracted with 10 ml of different solvents systems such as methanol, chloroform and aqueous in a beaker for 24 hours at room temperature. Then the solvent portion was centrifuge at 5000rpm for 10minutes. The supernatant was collected from the centrifuge tube and the solvent were evaporated. Finally crude extract was obtained. The extracts were collected in separate plastic vials and stored in the refrigerator for further studies.

Phytochemical analysis

Phytochemical screening was carried out to assess the qualitative chemical composition of different solvent extracts using commonly employed precipitation and coloration to identify the major natural chemical groups such as alkaloids, saponin, phenols, carbohydrates, flavonoids, glycosides, coumarins, steroids, tannins, chlorogenic acid and anthocyanin were performed by the standard procedure as described by Harborne,1973.

Biochemical analysis

Estimation of Carbohydrate

The total carbohydrate content of the powdered *Gracilariacrassa* was estimated by phenol-sulphuric acid method (Dubois, *et al,* 1956). The Phenol - Sulfuric Acid method is an example of a colorimetric method that is widely used to determine the total concentration of carbohydrates present in foods. A clear aqueous solution of the carbohydrates to be analyzed is placed in a test-tube, then phenol and sulfuric acid are added. The solution turns a yellow-orange color as a result of the interaction between the carbohydrates and the phenol. The absorbance at 420 nm is proportional to the carbohydrate concentration initially in the sample. The sulfuric acid causes all non-reducing sugars to be converted to reducing sugars, so that this method determines the total sugars present. This method is non-stoichemetric and so it is necessary to prepare a calibration curve using a series of standards of known carbohydrate concentration.

Estimation of Protein

The total protein content in the crude extracts of *Gracilariacrassa*was estimated by Biuret method. Seaweeds powders 250 mg were taken in a test tube and 2 ml distilled water was added to it. The mixtures

were mixed thoroughly by shaking for 1 minute by CM 101 Cyclo mixer, REMI and 4 ml Biuret reagent (9 g of sodium potassium tartrate, 3 g of copper sulphate, 5H2O and 5g of potassium iodide, in 400 ml of 0.2N sodium hydroxide solution and make up the volume to 1000 ml) was added to each seaweeds solution which were incubated for 30 minutes in room temperature and after incubation, mixtures were centrifuged at 4000 rpm for 10 minutes, supernatants were collected and the observance of all supernatants were taken at 540 nm with UV/Vis Spectrophotometer (Goshev and Nedkov, 1979). Bovine serum albumin (BSA) solution was used as standard. From 0-10 mg/ml of different concentration of BSA solutions was prepared and from each working standard 1 ml of solutions was taken and 4 ml Biuret reagent were added to it and incubated for 30 minutes and observance of OD value was taken at 540 nm. The standard calibration curve was made by using the estimated absorbance at y axis and concentration at x axis. From this calibration standard curve protein content of seaweeds were estimated.

Estimation of total Lipids

The lipid content of the *Gracilariacrassa* was estimated by using chloroform methanol mixture as described by Folch *et al,* (1957). The extract of seaweed was homogenized with chloroform / methanol (2:1) to a final volume 20 times the volume of the sample. After dispersion, the whole mixture was agitated for 15-20 mins in an orbital shaker at room temperature. The homogenate was then centrifuged to recover the liquid phase. Then solvent was washed with 0.9% sodium chloride solution and vortexed for few seconds and the mixture was centrifuged at low speed (2000rpm) to separate the 2 phases. The upper layer was siphonized without mixing the whole preparation. The lower chloroform phase containing lipids was evaporated under vacuum using a rotary evaporator.

Estimation of total Phenol

Total phenolic compounds were determined in sample extracts using the Folin– Ciocalteu reagent (Dewanto *et al.,* 2002). An aliquot of 0.125 ml of diluted extracts were mixed with 0.5 ml of distilled water and 0.125 ml of the Folin–Ciocalteu reagent. After 6 min, 1.25 ml of Na2CO3 (7 %) and 1 ml of distilled water were added and the obtained preparation was mixed thoroughly then incubated. After 90 min, the absorbance was monitored at 760 nm and the results are expressed as mg of gallic acid equivalents per gramme of dry residue (mg GAE/g). The assay was done in triplicate.

Estimation of fatty acid

Fatty acids in the sample were identified and quantified methyl esters in NEON II gas chromatography instrument following the procedure outlined by Niller and Berger (1985).

Estimation of mineral content

For mineral composition, 100 mg ground dried samples were treated with 10 mL of concentrated HNO3

overnight (Santoso*et al.,* 2006). Thereafter, 2.5 mL concentrated $HClO_4$ and 250 μL H_2SO_4 were added to the samples followed by heating until no white smoke was emitted. One hundred milliliters of 2 % HCl was added in the digested sample and filtered with a 0.22-μm membrane filter. The samples were analyzed using inductively coupled plasma atomic emission spectroscopy (PerkinElmer, Optima 2000, USA).

RESULTS AND DISCUSSION

Phytochemical analysis

Preliminary phytochemical tests of *Gracilariacrassa* were done by using methanol, chloroform and water. The each extracts confirmed the presence of important active chemical constituents such as flavonoids, alkaloid, phenol, chlorogenic acid and carbohydrates. The saponinand tannin are presented in the methanol extract only and coumarine and anthocyanin were absent in all the extracts. Glycosides are presented in both chloroform and methanol extracts. The results of the phytochemical analysis are compiled in Table.1.Phytochemicals are naturally present in the seaweeds and are biologically significant and plays an essential role in defending themselves against various pathogenic microbes. The phytochemical screening of plants reveals the presence of primary and secondary metabolites that suggest the plant might be of medicinal orindustrial importance. Rajakumar and Alwin PremSingh (2017) reported that the methanol and aqueous extracts of *Gracilariaedulis*showed the presence of a number of metabolites such as alkaloids, saponin, phenols, terpenoids, proteins, flavonoids, glycosides, coumarins and tannins.The present observation *G.crassa*showed the flavonoids, alkaloid, phenol, chlorogenic acid and carbohydrates were presented all the extracts. This was correlated with the previous work done by Harold Peter (2011), reported that the whole plant extracts of *Canthiumparviflorum* revealed the presence of phytochemicals such as alkaloids, oils, flavanoids, gums, phenols, saponins, steroids, tannins and terpenoids. Flavonoids possess anti-allergic, anti-inflammatory, antiviral and antioxidant activities (Bbosa, 2010).

Biochemical analysis

The determined for various chemical constituents like, carbohydrate, protein, total lipids and total phenols were recorded in *G. crassa*are shown in the Table.2. The biochemical constituents such as total carbohydrate (19.34±0.10%), total protein (23.13±0.005%), total phenols (7.81±0.23 mg/g) and total lipids (0.27±0.5%) were observed from the extract of *G.crassa.* Among the biochemical constituents, the protein content was higher compared to other content. In previous study, Dhamotharan (2002) investigated the level of the total lipid and protein content in brown algae and found that the levels of lipid and protein were high in *stoechospernummarginatum* as compared to *padina*.Mumtaj (2015) reported that the protein contents differ according to the species and seasonal conditions. It is confirmed in this study brown algae *Turpanariagonaidae*showing maximum concentration of protein, DNA and amino acid and it will be followed by *Gracilariafolifera*and *Bryopsis*. Impellizzeri *et al.,*(1975) reported the occurrence of amino

acids and low-MW carbohydrates in 18 macroscopic marine algae belonging to the division *Rhodophyta,* class *Florideophyceae*. Both biotic and abiotic factors form the micro and macro environment of the organism and the strong or less perceivable variations in the environmental parameters influence such distinct differential amount of carbohydrates. Chemical composition of green, brown seaweeds and protein contents of red seaweeds of Sourashtra coast were reported by Dave *et al.,*(1977). Dhamotharan (2002) estimated the total phenol content in brown algae and found that the levels of total phenol content in *stoechospernummarginatum* (920μg/g dry wt.*)* is three folds that of padina (280 μg/g dry wt). Therefore, a number of studies have focused on the biological activities of phenolic compounds. As one of the major utilizable algal resources of the sea, they are known to contain carbohydrates, proteins, vitamins and minerals and micro nutrients (Chapman, 1980). The present observation *G.crassa*showed the higher concentration protein.

Fatty acid profile

The fatty acid profile was recorded in *G. crassa.* Among the fatty acid content, the omega fatty acid (0.9832±0.002%) was presented in higher and followed by linolenic acid (0.2834±0.0020%). The moderate amount of alpha linolenic acid (0.1184±0.0010%), margaric acid (0.1137±0.0010%) and oleic acid (0.1134±0.0010%) were also presented. The least composition moroctic acid (0.0096±0.0001%) was recorded (Table.3). Red seaweeds are particularly rich in SFAs and PUFAs which have nutritional applications that lead to their extensive use in food, feed, cosmetic, biotechnological and pharmaceutical applications (Kumari*et al.,* 2010).Variation in fatty acid content may also be due to the season of collection as well as other abiotic factors such as nutrition, salinity, light and temperature (Francavilla*et al.,* 2013). According to this work (Sakthivel and Devi, 2015), the most abundant fatty acids in both seaweeds were palmitic, stearic and α-linoleic acid acids. The same fatty acids were also found abundant in *G. changii* (Francavilla*et al.,* 2013).In the present study, omega fatty acid (0.9832±0.002%) was presented in higher and followed by linolenic acid (0.2834±0.0020%). The presence of this n-3 fatty acid in *Gracilaria*spp. is inconstant, because it was found in *G. gracilis* (Francavilla*et al.,* 2013), but it was not detected in *G. changii*(Chan and Matanjun,2017) or *G. edulis* (Sakthivel and Devi, 2015). Fatty acids overall profile obtained in this work were significantly different than 57.5% SFAs, 18.3% MUFAs and 18.4% PUFAs reported for *Gracilaria* sp. (Da Coasta*et al.,* 2017) or the 7.5% SFAs, 38.3% MUFAs and 51.2% PUFAs 18.4% reported for *Gracilariachangii* (Chan and Matanjun,2017).

Mineral content

The mineral such as, calcium, magnesium, iron, sodium, potassium, copper, zinc, phosphorus, manganese, chromium, lead, cadmium, iodine, nickel and molybdenum were estimated in *G.crassa* extract. Calcium (135.4±0.20 mg/100^{-1}) was the major mineral constituent in *G.crassa.* The moderate amount of potassium

$(34.43\pm0.152mg/100^{-1})$, sodium $(25.56\pm0.152mg/100^{-1})$ and phosphorus $(14.65\pm0.020mg/100^{-1})$ were also presented. The level of inc $(5.653\pm0.0153mg/100^{-1})$, iodine $(3.110\pm0.021mg/100^{-1})$, chromium $(2.440\pm0.200mg/100^{-1})$, magnesium $(2.343\pm0.015mg/100^{-1})$ and manganese $(1.960\pm0.0152mg/100^{-1})$ were also recorded. The least level of iron $(0.119\pm0.002mg/100^{-1})$, copper $(0.119\pm0.0012mg/100^{-1})$, lead $(0.454\pm0.200mg/100^{-1})$, cadmium $(0.214\pm0.201mg/100^{-1})$, molybdenum $(0.68\pm0.15mg/100^{-1})$ and nickel $(0.342\pm0.05mg/100^{-1})$ were observed (Table.4). Seaweeds are one of the richest sources of minerals and trace elements, because the cell-wall polysaccharides and proteins of seaweed contain sulfate, anionic carboxyl and phosphate groups which act as binding sites for metal retention (Ródenas de la Rocha *et al.,* 2009). With respect to the mineral content, *G.crassa* showed a higher content of Ca $(135.4\pm0.20\ mg/100^{-1})$ in previous work, seaweeds had a higher or similar content of minerals like Zn, Cu, Mg and Fe when compared with the content of *G. acerosa* (Syad et al., 2013), *G. edulis* (Sakthivel and Devi, 2015), *G. fisheri* and *G. tenuistipidatata* (Benjama and Masniyom*et al.,* 2012), with the exception of Mg in *G. edulis* which were lower than those found for other previous works as *G. changii*(Chan and Matanjun,2017). The ability of seaweeds to accumulate metals will depend on a variety of factors such as location, exposure, salinity, temperature, pH, light, nitrogen content, season, plant age, metabolic processes or the affinity of the plant for each element among others (Sánchez-Rodríguez *et al.,* 2001). In view of the present results, *G.crassa* contain an adequate amount of minerals, which suggests that these seaweeds could act as important sources of mineral supplements which are essential for human nutrition.

Taple.1 Preliminary phytochemical analysis of various solvents extract of *G.crassa*

S.No	Phytochemical content	Name of the test	Chloroform	Methanol	Aqueous
1	Alkaloid	Mayers test	+	+	+
		Dragendroffs test	+	+	+
		Wagner test	-	+	-
2	Saponin	Foam test	-	+	-
3	Flavonoids	Ammonia test	+	+	+
4	Phenol	Phenol reagent	+	+	+
5	Carbohydrate	Molish test	+	+	+
		Fehling test	-	-	-
		Benedicts test	-	-	-
6	Glycosides	Burchard test	+	+	-
7	Coumarins	NaCl test	-	-	-
8	Tannin	Lead acetate test	-	+	-

9	Chlorogenic acid	Ammonia test	+	+	+
10	Anthocyanin	NaOH test	-	-	-

Table.2 Biochemical analysis of *G.crassa*

S.No	Biochemical content	Composition (%)
1	Carbohydrates	19.34±0.10
2	Protein	23.13±0.05
3	Lipid	0.27±0.5
4	Phenol	7.81 mg/g

Table.3 Fatty acid profile of *G.crassa*

S. No	Fatty acid	Composition (%)
1	Palmitic acid	0.0816 ±0.1000
2	Margaric acid	0.1137±0.0010
3	Stearic acid	0.0834±0.010
4	Oleic acid	0.1134±0.0010
5	Linolenic acid	0.2834±0.0020
6	Alpha linolenic acid	0.1184±0.0010
7	Moroctic acid	0.0096±0.0001
8	Omega fatty acid	0.9832±0.002
9	DHA	0.0871±0.001
10	EPA	0.1948±0.003

Table.4 Mineral composition of *G.crassa*

S.No	Minerals	mg/100g^{-1}
1	Ca	135.4±0.20
2	Mg	2.343±0.015
3	Fe	0.119±0.002
4	Na	25.56±0.152
5	K	34.43±0.152
6	Cu	0.119±0.0012
7	Zn	5.653±0.0153
8	P	14.65±0.020
9	Mn	1.960±0.0152

10	Cr	2.440±0.200
11	Pb	0.454±0.200
12	Cd	0.214±0.201
13	I	3.110±0.021
14	Mo	0.68±0.15
15	Ni	0.342±0.05

CONCLUSION

The alga is rich source of omega fatty acid, calcium and phosphorus formed the major bulks in the minerals as well as in fatty acid content. The investigation revealed the richness of alga in protein and carbohydrate content; the lipid content being least. Thus, the overall observation of the present study suggests that shows nutritive biochemical properties and promising as a source of pharmacognosical value. Hence, it can be concluded that the *G.crassa* was used in food industry for nutritional purpose and pharmaceutical industry as a source of basic materials in the preparation of nutrient supplement products and fine chemical synthesis.

REFERENCES

1. Anantharaman P.G, Thirumaran and Balasubramanian T. 2007.Seaweed Farming: Alternative Livelihood. In Kannaiyan.S. and Venkataramanan (Eds). Biodiversity Conversation in Gulf of Manner Biosphere Reserve, National Biodiversity Authority, Chennai.

2. Bbosa, G. S. 2010. Medicinal Plants used by traditional Medicines Practitioners for the treatment of HIV/AIDS and related conditions in Uganda. *Journal of Ethnopharmacol*, 130: 43-53.

3. Benjama, O andMasniyom, P. 2012. Biochemical composition and physicochemical properties of two red seaweeds (*Gracilariafisheri* and *G. tenuistipitata)* from the Pattani Bay in Southern Thailand.Songklanakarin*J. Sci. Technol*. 34, 223–230

4. Chan, P.T andMatanjun, P. 2017. Chemical composition and physicochemical properties of tropical red seaweed, *Gracilariachangii*. *Food Chem*. 221, 302–310.

5. Chapman, D.J. (Ed.), 1980. Seaweed and their uses, 2nd edn. Chapman & Hall, New York,334.

6. Chew, Y. L., Lim, Y. Y., Omar, M. and Khoo, K. S. 1992.Antioxidant activity of three edible seaweeds from two areas in South East Asia. LWT 41: 1067-1072.

7. Da Costa, E, Melo, T, Moreira, A.S.P, Bernardo, C, Helguero, L, Ferreira, I, Cruz, M.T, Rego, A.M, Domingues, P, Calado, R. 2017. Valorization of lipids from Gracilaria sp.Through lipidomics and decoding of antiproliferative and anti-inflammatory activity.*Mar. Drugs*, 15, 62

8. Dave, M.J., Gany, S.K and Iyengar, R.R. 1977. Assessment of the possibility at seaweeds to be utilized as supplementary animal feed. CSMCRI, Bhavnagar Salt Res. Ind., 13(122): 33 40.

9. Debbarama, J,Rao, B.M, Murthy, L.N, Mathew, S,Venkateshwarlu, G andRavishankar, C. 2016. Nutritional profilingof the edible seaweeds *Gracilariaedulis, Ulvalactuca* and *Sargassum sp. Indian J. Fish*. 63, 81–87.

10. Dhamotharan R. 2002. An investigation on the bioactive principles of Padinatetrastromatica Hauck and Stoechospermummarginatum (C.AG) Kuetz.with respect to antimicrobial and biofertilizer properties. Ph.D Thesis, University of Madras, Chennai, Tamilnadu,

11. Dhargalkar VK andNeelam P. 2005. Science and Culture, 71 (3-4): 60-66.

12. DuBois, M., Gilles, K., Hamilton, J., Rebers, P. and Smith, F. 1956.Colorimetric Method forDetermination of Sugars and Related Substances. Analytical Chemistry, 28(3):350-356.

13. Folch, J., Lees, M. and Sloane-Stanley, G.H. 1957.A simple method for the isolation andpurification of total lipids from animal tissues.*J Biolchem*, 226(1): 497-509.

14. Francavilla, M,Franchi, M,Monteone, M andCaroppo, C. 2013. The red seaweed *Gracilariagracilis* as a multi products source.*Mar. Drugs*, 11, 3754–3776

15. Goshev, I and P. Nedkov. 1979. Extending the range of application of the biuret reaction: Quantitative determination of insoluble proteins. *Analytical Biochemistry* 95 (**2**):340-343.

16. Harborne, J.B. 1973. Phytochemical methods.Chapman & Hall, New York, 288.

17. Haroled Peter PL, Abraham Shajan, Godwin Blessing Issac A, Sanjoy Das and ArasanElayaraja. 2011. Preliminary phytochemical and antimicrobial screening of whole plant extracts of *Canthiumparviflorum* Lam. *International Journal of Phytopharmacy Research*, 2: 30-34.

18. Impellizzeri, G, Mangiafico, S, Oriente, G, Piatelli, M, Sciuto, S, Fattorusso, E, Magno, S, Santacroce, C andSica, D. 1975. Amino acids and low molecular weight carbohydrates of some marine red algae. Phytochemistry 14: 1549–1557.

19. Jensen, A. 1993.Present and future Needs for Alga and Algal products.Hydrobiology, 260/261: 15-21.

20. Kumari, P, Kumar, M, Gupta, V, Reddy, C.R.K and Jha, B. 2010. Tropical marine macroalgae as potential sources of nutritionally important PUFAs.*Food Chem*. 120, 749–757

21. Matsukawa, R, Dubinsky, Z, Kishimoto, E, Masaki, K, Masuda, Y, Takeuchi, T, Chihara, M, Yamamoto, Y, Niki, E and Karube, I. 1997. A Comparison of Screening Methods for Antioxidant Activity in Seaweeds.*Journal of AppliedPhycology*, **9**, 29-35.

22. Mumtaj. S. 2015. Study on the Biochemical Characterization of Marine Seaweeds of Mandabam Sea Coast. *Int.J.Curr.Microbiol.App.Sci*. 4(10): 273-281

23. Muthuraman, B. and R. Ranganathan.2004. Biochemical studies on some green algae of Kanyakumari coast. Seaweed Research and Utilisation, 26(1&2): 69-71.

24. Niller, S and Berger, T .1985. Bacteria identification by GC Hewlet Packard Application note oo. 228-241.

25. Perry, N. B, Blunt, J.W and Munro, M.H.G. 1991. A Cytotoxic and antifungal 1,4naphthaquinone and related compounds from a New Zealand alga *Landsburgiaquercifolia*. *J. Nat. Prod.,* 54: 978.

26. RajakumarR.andAllwinPrem Singh Y. 2017. Preliminary phytochemical and antimicrobial studies on the crude extract of red algae *GracilariaEdulis*against clinical isolates. *European Journal of Pharmaceutical and Medical Research,*4(07), 763-766.

27. Ródenas de la Rocha, S, Sánchez-Muniz, F.J, Gómez-Juaristi, M andMarín, M.T.L. 2009.Trace elements determination in edible seaweeds by an optimized and validated ICP-MS method. *J. Food Compos.*Anal. 22, 330–336

28. Sakthivel, R and Devi, K.P. 2015.Evaluation of physicochemical properties, proximate and nutritional composition of Gracilariaedulis collected from Palk Bay. Food Chem. 174, 68–74.

29. Sánchez-Rodríguez, I, Huerta-Diaz, M.A,Choumiline, E, Holguín-Quiones, O andZertuche-González, J.A. 2001.Elemental concentrations in different species of seaweeds from Loreto Bay, Baja California Sur, Mexico: Implications for the geochemical control of metals in algal tissue. Environ. Pollut. 114, 145–160.

30. Santoso J, Gunji S, Yoshie-Stark Y and Suzuki T. 2006.Mineral contents ofIndonesian seaweeds and mineral solubility affected by basiccooking.*Food SciTechnol* 12:59–66

31. SumitraVijayaraghavan, M. D. Rajagopal and M. V. M. Wafar, 1980.Variation in biochemicalcomposition of some seaweeds from Goa coast. Indian J. Mar. Sci., 961-63.

32. Syad, A.N,Shunmugiah, K.P andKasi, P.D. 2013. Seaweeds as nutritional supplements: Analysis of nutritional profile, physicochemical properties and proximate composition of G. acerosa and S. wightii. Biomed. Prev. Nut. 3, 139–144

33. Torres, P, Santos, J.P, Chow, F and dos Santos, D.Y. 2019.A comprehensive review of traditional uses,bioactivity potential, and chemical diversity of the genus Gracilaria (Gracilariales, Rhodophyta).*Algal Res.*37, 288–306.

Source details

Feedback >   Compare sources >

Annals of the Romanian Society for Cell Biology

Scopus coverage years: from 2009 to 2020

(coverage discontinued in Scopus)

Publisher: Universitatea de Vest Vasile Goldis din Arad

ISSN: 2067-3019   E-ISSN: 2067-8282

Subject area: (Biochemistry, Genetics and Molecular Biology: Physiology) (Biochemistry, Genetics and Molecular Biology: Molecular Biology)

(Biochemistry, Genetics and Molecular Biology: Cell Biology)

Source type: Journal

View all documents >   Set document alert   🖫 Save to source list

CiteScore 2020	ⓘ
0.6	

SJR 2020	ⓘ
0.101	

SNIP 2022	ⓘ
0.027	

CiteScore   CiteScore rank & trend   Scopus content coverage

Study on Phenological Diversity of Chlorophycean Algae with its Role in Environment

Sandipan Chatterjee[1], *TanmayGhosh [2]

[1]Department of Botany, SuriVidyasagar College, Suri, Birbhum – 731101, West Bengal, India.
[2]Department of Microbiology, Dinabandhu Andrews College, Baishnabghata, South 24 Parganas, Kolkata – 700084, West Bengal, India.
Corresponding Author: **TanmayGhosh (tanmay.tanmay.ghosh780@gmail.com)**

Abstract:
The River water algae can resist many environmental stresses. Usually they grow on water if the water is steady but the River water is also contaminated by series of natural reasons. Many genera can grow in the River water. The algae are identified by their shape, size, colour and morphological structure. The physiochemical status of the River water contributes to the phenology of Chlorophycean algae of the River Ganga in Kolkata. Maximum algal population was determined by testing the concentration of algae in the water of the Ganga River. Summer is the season when algal growths are seen at its peak but in the winter the concentration of those algal species are less. But the predominant two species are *Chlamydomonas* sp. and *Dunalliella*sp.
Key-words: Resist, Habitat, Terrestrial, Multicellular.

Introduction:
Algae are the diverse group of autotrophic organism, able to photosynthesis and having motile or non motile unicellular or multicellular forms. It is believed that although the chloroplasts have the single origin but all the algal groups are not originated from a single algal ancestor. Most algae have marine habitat but several algal species have terrestrial habitat as well. Most algae are found abundantly from desert sand to sea water to hot springs and glaciers of ice. They can be flagellated single celled organism or multicellular thallus type structure. The giant kelp of Eastern Pacific which is 60 meters long and deep dense forest like structure is also a type of algal growth itself. The aquatic ecosystems are also dependent on the algae. The primary producers of the ecosystem are algae. The fresh water fishes feed on algal food substances. So the fresh water food chains are highly dependent on algae. During stages of their lifecycle, fishes consume about 75% of algae. The BOD is often provided by the algal biomass of the water bodies. So algae are important to produce fishes in fisheries. The algae produce about 48% of oxygen of the world itself. The algal groups are producing single cell proteins (SCP) now days. The algal growth in the environment depends upon some conditions which are light, pH, temperature, hardness, salinity, phosphorus content, nitrate content and water current velocity for the growth of phytoplankton. Nutrients are the main factor for the growth of algal species. In the River like Ganga River the phosphorus content is predominantly found, which is certainly a trace element for the growth of algal species. Nitrogen is also found to be responsible for triggering a algal bloom. But this factor is more commonly studied in the case of salt sea water. The sources of water nutrients, important for algal growth are divided into two divisions by scientists. The first division is natural sources. And second division is artificial or man-made sources. Natural sources include the sources provided by nature as soil leach nutrients, atmospheric deposited nutrients and nutrients come with a certain water flow. The man-made sources are more complex and highly effective those may be manure, fertilizer, industrial effluents and human sewage. Among all the autotrophs algae secures its significant ranking by versatilities. It has excellent variation in structure. It possesses role in biodiversity and have wild variation of habitats. It is just not enough for algal qualities as there a lot of algal qualities. They have various thallus organizations. The periodic distribution is very hard for this organism which is referred to be phenology. Time to time the researchers has researched upon the algal diversity of Indian subcontinent. Systematic and classification of algae are overviewed by scientists on the basis of their morphology, cytology, biochemistry and recent aspects of biology. An attempt is made to focus on fresh water green algae or River water green algae. So the study is done on Ganga water algae of Kolkata.

Fig 1: Algal bloom in the Ganga River.

Materials and methods:
Sample collection:
Samples of fresh water algae were collected from the different locations as Babughat, James PrincepGhat and many more Ghats, which are located on the Ganga River. The samples were taken to laboratory. They were washed in mild warm water and cold water. The samples are also preserved in 4% formaldehyde. Mounts of the samples were also prepared.

Detection of algal diversity:
Detection of algal diversity was done by microscopic analysis of the specimen. The structure of algal samples was studied under microscope. And the identification was done on basis on the phylogenetic tree and they are also noted.

Determination of concentration of algal cells:
The algal cell concentration was determined by the direct microscopic count methods. The concentrations were calculated per ml of water. And in every season the abundance of algal species are calculated.

Results:
The Chlorophyceae an algal flora that has found to be appearing in the Ganga water have studied along. It was found that the microbes isolated were coming from several groups, genera and orders. Orders are below.

Order	Genera
*Chlorococcales*sp.	*Pediastrum, Chlorella, Scenedesmus, Hydrodictium*
Volvocales sp.	*Clamydomons, Duralliceae, Pandoria, Eudorina*
Ulotrichales sp.	*Enteromorpha*
Cladophorales sp.	*Cladophora*
Chaetophorales sp.	*Stigeoclonium*
Conjugales sp.	*Spirogyra, Zygnema, Cosmarium, Closterium*

From this study the predominant genera are 15 different genera of algae among which mostly found are *Dunalliella*sp. and *Clamydomons*sp. Those two genera are found in high concentration in every season in Ganga River water. In the month of January to March a mass growth in the algal biomass is seen significantly rising. While in the month of May to July the growth faced a decrease. And in the month of December the decrease turn into the lowest growth condition of those algal species. The peak was found in January in the case of algal growth. The abundance chart of algae in the Ganga River water of Kolkata expresses the weather advantage influence on the algal growth. Due to the nutrient availability and excess sunlight the algal growth is found most abundantly in the Ganga River water. But the winter available with nutrients lacks the sunlight to cause the lowest algae found there. The monsoon season have a speciality the new fresh rain water is available in the season. That new fresh water mostly washout some algae and

nutrients of the season. So the growth starts to decrease at this season. The population of *Chlorella* sp. was found significantly less across the whole year while other algal group's shows decrease and increase in the growth. We can see the serial decrease for almost every isolated algal group from January to December. That yearly change of algal growth is expressed by the study. The seasonal variations of those 15 algal species are included in the chat below.

Sl.	Algae	Jan	Feb	Mar	Apr	May	Jun	Jul	Aug	Sept	Oct	Nov	Dec
1	*Pediastrum*sp.	++	+	+++	-	-	++	+	-	-	+	-	-
2	*Scenedesmus* sp.	-	+++	+	-	+	-	-	+	+	-	-	-
3	*Chlorella* sp.	++	+	-	+	-	-	+++	-	-	+	-	-
4	*Hydrodictium* sp.	-	++	+	-	++	+	-	-	-	-	-	-
5	*Clamydomons* sp.	+++	-	+	++	-	-	+	++	-	-	++	+
6	*Duralliceae* sp.	+++	+	+	-	+	+	-	-	-	++	+	+
7	*Pandoria* sp.	++	+++	+	-	+	+	+	+	-	-	-	-
8	*Eudorina* sp.	-	++	+++	++	-	-	-	-	+	-	-	-
9	*Enteromorpha* sp.	+	+++	++	+	-	-	+	-	+	-	++	-
10	*Cladophora* sp.	++	+++	-	++	-	+	-	-	+	-	-	-
11	*Stigeoclonium* sp.	+++	++	-	+	-	++	-	-	-	-	-	-
12	*Cosmarium* sp.	+	+++	++	-	+	-	+	-	-	+	-	-
13	*Spirogyra* sp.	++	+	+	-	+	-	-	+	-	-	-	-
14	*Zygnema* sp.	+++	++	-	+	-	-	+	-	+	-	-	-
15	*Closterium* sp.	+	++	+++	+	-	++	-	+	-	+	-	-

This study is also shown the algal population mostly flourishes in the late winter mainly in early January. And this growth starts to decrease in the late monsoon. So the perfect time for the algal management for water is late winter and early summer. The remediation can't be done in the summer as the growth of plankton is high which may lead to hazards for the treatment. The seasonal changes of this growth also show that the temperature also effect on the microbial population specially the algal population.

Discussion:
The Kolkata is one of the religious and ancient places of West Bengal. It is a tourist spot also. The Kalighat made it famous religiously. The British capital was the Kolkata due to the easy transportation by Ganga River. The Ganga River is also one of the important causes of the economical importance of the place. The Ganga River is also responsible for agricultural and human resources of the region. But the River water is affected by human activities and pollution. Xenobiotic compounds along with several chemicals and bio fertilizers are mixed with the River water from industrial and agricultural sites. This causes the algal bloom in water. The algae grow upon the water for various causes. And this study shows the algal groups isolated from Ganga water are *Chlorococcales* sp., *Volvocales* sp., *Ulotrichales* sp., *Conjugales*sp.,*Chaetophorales* sp., and *Cladophorales* sp.. While summer predominant are *Chlamydomonas*sp. and *Duralliceaae*sp. The most common algae in water are *Chlamydomonas*sp. *and Duralliceaae*sp. The plankton status of the water indicates the physiochemical status of water.

Conclusion:

Algal diversity plays an important role in determining the quality of a water body. Here we have isolated Chlorophycean algae from the Ganga River. Algae forms may take over River and algal bloom highly interfere with the eco-system of River. Although it has an important role in food chain.Chlorophycean can tolerate high degree of pollution. It has been observed that quantity of algae vary season to season because of changes in temperature, pH and other physiological factors of water. In summer the concentration of Chlorophycean most and it gradually decreases up to winter when concentration of respective algal species are very loss. We can use these algae in agriculture field as nitrogen source and for waste water treatment also. It can help us more than its harm.

References:
1. Mohanty AK, Satpathy KK, Sahu G, Sasmal SK, Sahu BK, Panigrahy RC (2007) Red tide of Noctilucascintillans and its impact on the coastal water quality of the near–shore waters, off the Rushikulya River, Bay of Bengal. CurrSci 93:616–618.
2. Nagabhushanam AK (1967) On an unusually dense phytoplankton 'bloom' around Minicoy Island (Arabian Sea) and its effect on the local tuna fisheries. CurrSci 36:611–612.

3. Naik RK, Anil AC, Narale DD, Chitari RR, Kulkarni VV (2011a) Primary description of surface water phytoplankton pigment patterns in the Bay of Bengal. J Sea Res 65:435–441.
4. Naik RK, Hegde S, Anil AC (2011b) Dinoflagellate community structure from the stratified environment of the Bay of Bengal, with special emphasis on harmful algal bloom species. Environ Monit Assess 182:15–30.
5. Naik RK, Sarno D, Kooistra WHC, D'Costa PM, Anil AC, 2010. Skeletonema (Bacillariophyceae) in Indian waters: A reappraisal. Indian J Mar Sci 39(2):290–293.
6. Naqvi SWA, George MD, Narvekar PV, Jayakumar, DA, Shailaja MS, Sardesai S, Sarma VVSS, ShenoyDM, Naik H, Maheswaran PA, Krishnakumari K, Rajesh G, Sudhir AK, Binu MS (1998) Severe fish mortality associated with 'red tide' observed in the sea off Cochin. CurrSci 75:543–544.
7. Naqvi SWA, Jayakumar DA, Narvekar PV, Naik H, Sarma VVSS, D'Souza W, Joseph S, George MD (2000) Increased marine production of N2O due to intensifying anoxia on the Indian continental shelf. Nature 408:346–349.
8. Nayak BB, Karunasagar I (2000) Bacteriological and physico–chemical factors associated with Noctilucamilicans bloom along Mangalore, Southwest coast of Indian. Indian J Mar Sci 29:139–143.
9. O'Herald (2001) NIO discovers toxic algal off Goa. O'Herald Newspaper Goa, 29th October 2001 Padmakumar KB, Sanilkumar MG, Saramma AV (2007) A 'Red tide' caused by the diatom Coscinodiscus on the southwest coast of India. Harmful Algae News, An IOC Newsletter on toxic alage and algal blooms 35:14.
10. Padmakumar KB, Sanilkumar MG, Saramma AV, Sanjeevan VN, Menon NR (2008a) Microcystisaeruginosabloom on Southwest coast of India. Harmful Algae News, An IOC Newsletter on toxic alage and algal blooms 37:11–12.
11. Padmakumar KB, Sanilkumar MG, Saramma AV, Sanjeevan VN, Menon NR (2008b) "Green tide" of Noctilucamiliaris in the Northern Arabian Sea. Harmful Algae News, An IOC Newsletter on toxic alage and algal blooms 36:12.
12. Padmakumar KB, SreeRenjima G, Fanimol CL, Menon NR, Sanjeevan VN (2010a) Preponderance of heterotrophic Noctilucascintillans during a multi–species diatom bloom along the southwest coast of India. Int J OcOceanogr 4:5–63.
13. Padmakumar KB, Thomas LC, Salini TC, John E, Menon NR, Sanjeevan VN (2011) Monospecific bloom of noxious raphidophyteChattonella marina in the coastal waters ofSouth–West coast of India. Int J Biosci 1(1):57– 69.
14. Padmakumar NR, Smitha BR, Thomas LC, Fanimol CL, SreeRenjima G, Menon NR, Sanjeevan VN (2010b) Blooms of Trichodesmiumerythraeum in the South Eastern ArabianSea during the onset of 2009 Summer Monsoon. Ocean Sci J 45(3):51–157.
15. Smith, G.M. 1920. Phytoplankton of the Inland Lakes of Wisconsin part. I. Myxophyceae,

Phaeophyceae, Heterokontae and Chlorophyceae, Wisconsin Geological and Natural History Survey. Bull. 57 Sc. Ser. 12: 1-243.

16. Venkataraman, G. 1939. December. A systematic account of Some south Indian Diatoms, Proceeding of the Indian Academy of Sciences: Vol. X, No. 6: 293-368 pp.

17. Williamson, D. B. 1999. A proposed new desmids genus Cruiangulum and description of three new desmids species From rock pools in the Western C.

18. Whitton B A, 1969. Seasonal changes in the Phytoplankton of St. James Park lake, London, London Nat. 48: 14-39.

Source details

Feedback >   Compare sources >

Annals of the Romanian Society for Cell Biology

Scopus coverage years: from 2009 to 2020

(coverage discontinued in Scopus)

Publisher: Universitatea de Vest Vasile Goldis din Arad

ISSN: 2067-3019   E-ISSN: 2067-8282

Subject area: (Biochemistry, Genetics and Molecular Biology: Physiology)   (Biochemistry, Genetics and Molecular Biology: Molecular Biology)

(Biochemistry, Genetics and Molecular Biology: Cell Biology)

Source type: Journal

View all documents >   Set document alert   🖫 Save to source list

CiteScore 2020   ⓘ
0.6

SJR 2020   ⓘ
0.101

SNIP 2022   ⓘ
0.027

CiteScore   CiteScore rank & trend   Scopus content coverage

Computer-Aided Diagnostic System for Digital Mammography

Yang Xingyao[*]**, Muhammad Fayaz**[$]**, Tanmay Ghosh**[#]

[*]School of Information Science and Engineering, Xinjiang University Urumqi, Xinjiang, China
[$]University of Engineering and Technology, Peshawar, Pakistan
[#]Department of Microbiology, Dinabandhu Andrews college, Baishnabghata, South 24 Parganas West Bengal

Corresponding author
Khan Alamgir
School of Information Science and Engineering, Xinjiang University Urumqi, Xinjiang, China
EMAIL: JOHNALAM4@GMAIL.COM

1 - Abstract

In this work, Computer-Aided Detection (CADe) and Computer-Aided Diagnosis (CADx) systems are developed and tested using the public and freely available mammographic databases named MIAS and DDSM databases, respectively. CADe system is used to differentiate between normal and abnormal tissues, and it assists radiologists to avoid missing a breast abnormality. At the same time, CADx is developed to distinguish between normal, benign and malignant breast tissues, and it helps radiologists to decide whether a biopsy is needed when reading a diagnostic mammogram or not. Any CAD system is constituted of typical stages including preprocessing and segmentation of mammogram images, extraction of regions of interest (ROI), features removal, features selection and classification. In both proposed CAD systems, ROIs are selected using a window size of 32×32 pixels, then a total of 543 features from four different feature categories are extracted from each ROI and then normalized. After that, the selection of the most relevant features is performed using four different selection methods from MATLAB Pattern Recognition Toolbox v.5 (PRtool5) named Sequential Backward Selection (SBS), Sequential Forward Selection (SFS), Sequential Floating Forward Selection (SFFS) and Branch and Bound Selection (BBS) methods. We also utilized Principal Component Analysis (PCA) as the fifth method to reduce the dimensions of the features set. After that, we used different classifiers such as Support Vector Machines (SVM), K-voting Nearest Neighbor (K-NN), Quadratic Discriminant Analysis (QDA) and Artificial Neural Networks (ANN) for the classification. Both CAD systems have the same implementation stages but different output. CADe systems are designed to detect breast abnormalities while CADx system indicates the likelihood of malignancy of lesions. Finally, we independently compared the performance of all classifiers with each selection method in both modes. The evaluation of the proposed CAD systems is done using performance indices such as sensitivity, specificity, the area under the curve (AUC) of the Receiver Operating Characteristic (ROC) curves, the overall accuracy and Cohen-k factor. Both CAD systems provided encouraging results. These

results were different corresponding to the selection method and classifier.

2 - Key words

Digital Mammography; Breast Cancer; Computer-Aided Diagnosis; Machine Learning; Medical Image Processing.

3 - Introduction

Breast cancer is the abnormal growth of breast cells, which usually starts in the lobules of the inner lining of the milk ducts. Different types of breast cancer exist with different stages, truculence and genetic makeup. 10-years disease-free survival rates vary from 98% to 10% with the best treatment plan. Breast cancer treatment includes various strategies such as surgery, chemotherapy, hormone therapy and radiation. Breast cancer is still being a significant public healthcare problem among women, and it is the most common cancer around the world. The cause of this disease remains undetermined, and this makes primary prevention to be impossible. It is believed that early detection of breast cancer is the most promising way to lower the number of women suffering from it and this improves the chances to provide proper treatment options so that treatment will work with better results [2]. Among women in U.S., breast cancer is the most commonly diagnosed cancer besides skin cancer, and its death rates are the highest among other cancers besides lung cancer. In 2016, it is expected to diagnose approximately 246,660 new cases of invasive breast cancer in women, and the expected diagnosed cases of non-invasive breast cancer are 61,000 women

in the U.S. Also About 2,600 new patients of invasive breast cancer in men are expected to be discovered [3]. Mammography is a particular type of radiography, using low radiation levels to acquire images for a breast to diagnose a consequent exist of abnormal structures that imply a disease like cancer. The early detection of strange mammary pathologies like nonpalpable breast masses and calcifications is extremely important for successful cure of breast cancer patients. Mammography is the standard screening tool that is used to perform the task of breast cancer detection, and it results to reduce at least 30% in breast cancer deaths in the world [4], [5]. The benefit of mammography screening has undergone some recent contention since definite evidence relating mammography with mortality may not be proven. In contrast, an Institute of Medicine Report on Mammography suggests that using mammography screening for earlier detection of breast cancer may be an important factor in decreasing mortality from breast cancer in recent years [6]. The computer-based systems may provide a second supportive alternative in detecting breast abnormalities by completing the expert knowledge of radiologists, and two may help to make concise diagnostic decisions. Computer-aided diagnosis (CAD) is a diagnostic procedure performed by the help of computer algorithms. Computerized systems for such a purpose are called CAD systems. It has been proved that the radiologist's performance in diagnosing mammography images can be increasingly improved by assisting them with the results obtained by the CAD system. Therefore, motivations become keen to develop robust CAD systems to support

radiologists' ability in reading different mammograms accurately [7].

4 - Important contents

Recently, many CADe systems have been developed by research groups for detection and classification of breast abnormalities. In many systems, some typical stages should be performed to find suspicious breast lesions. The main steps of such a method are shown in figure 3.1. The implementation of the proposed CADe system is accomplished using digital mammograms from MIAS database. The preprocessing is the first stage of the CADe system by which the breast region is enhanced and segmented by applying image processing techniques to improve the quality and reduce the noise ratio of the mammogram. The next stage is the selection of a region of interest (ROI), where a group of suspicious ROIs are selected to further delineate or classify them as normal or abnormal lesions. The following stage is the feature extraction that aims to characterize the lesions to differentiate actual lesions from falsely detected candidates, where the selected ROI is used to calculate a set of features. After feature extraction comes to the feature selection step which is considered an essential part of any classification scheme where the success of classification task largely depends on the selected features and the extent of their role in the model. The final stage is the classification where the selected features are then inputted into a classifier. The classifier is trained to distinguish normal from abnormal lesions. The design and experimental verification of the proposed study are achieved through two main phases. The first phase is the training phase, while the other is the testing phase, with 50% of the database. In the training phase, the system is trained to differentiate between healthy and cancerous cases by inputting the selected features of predefined normal and malignant images to the classifier. Then, in the testing phase, we test the performance of the system by entering elements of a test image to evaluate the correctness degree of the system decision.
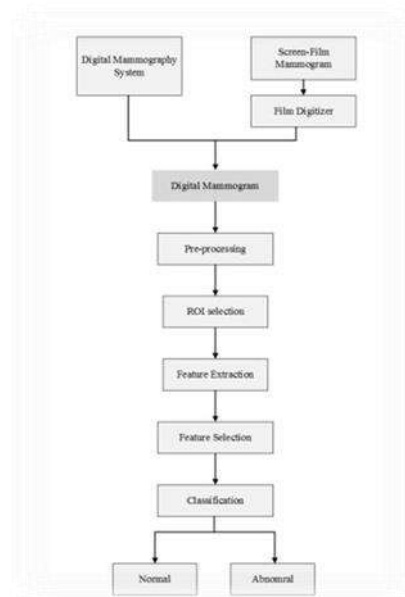
Figure 3.1: Block diagram of a generic CADe system

In future work, It is imperative to continue the development of CAD systems that can contribute in the study of the breast cancer, innovating techniques capable of assisting the radiology experts and helping to reduce their subjectivity and examination time. The proposed systems are suitable to continue working on, by using datasets with a large number of samples representing different cases, including various classes of breast tissue abnormalities especially micro calcifications, extracting new powerful textural features and using more robust

classification algorithms utilizing hybrid classifiers.

We can additionally use Enhancement of Mammography Images Using Peripheral Region Equalization

5 - Conclusions

Early detection of breast cancer is of great importance to increase the survival rate and improve the chances to provide proper treatment options so that treatment will work with better results. Mammography is the gold standard tool for the early detection of breast cancer. Still, the sensitivity of mammography is usually affected by the image quality and the radiologist's level of expertise. CAD systems have been developed to support radiologists' decision and thus decreasing the false positive rate. In this study, we proposed computer-aided detection (CADe) and computer-aided diagnosis (CADx) systems. Both systems have the same implementation techniques, but each system is designed to perform a different task. CADe system is used to detect the abnormalities in breast lesions while CADx system is intended to diagnose and determine the malignancy of the suspicious breast tissues. MIAS database was used to develop the CADe system, whereas the CADx system was designed using the DDSM database. The same combination of different features extracted from each ROI was used in both CAD systems. Also, both CADe and CADx systems have the same feature selection methods and classifiers.

In almost all mammography systems, during the acquisition of a mammogram, the breast is compressed between the compression paddle and the support table then taking an image of the compressed breast tissue. Due to the forces that are applied on the upper surface of the breast by the upper plate, the deformation of the breast will happen. When compression is used, the top plate is tilted, which results in variation in breast thickness up to 2 cm from the chest wall to the breast margin. Variation in breast thickness affects image analysis by its impact on the grey level values of the image at the peripheral area of the breast, which causes changes in contrast at the breast periphery [20]. The outer space of the chest always tends to have lower intensity than the central area of the breast. So, a radiologist typically must adjust a window level setting when reading different areas of the image to assess a copy of the entire breast. This process may make only portions of the image comparable at any one window level setting and increases the time it takes to read the image especial with a massive number of patients. Peripheral equalization (P.E.) method is a dedicated image processing technique improved for mammogram enhancement. It is used to enhance the visibility of the outer area of the breast to make image features visible in both central and peripheral regions of the chest with one window level setting. The technique is also referred to as peripheral enhancement or thickness correction. Fatty tissues in the interior and outer regions of the breast have similar grey level values after equalization [19]. Figure A.1 shows an example of the process of peripheral equalization.
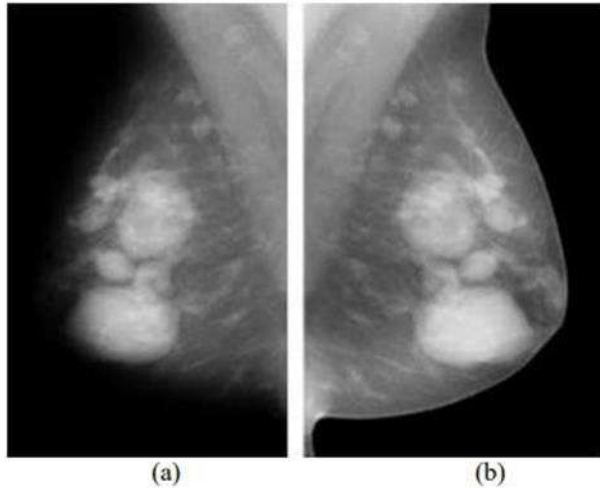
Figure A.1: Example of a corrected mammogram . (a): an MLO image. (b): The thickness corrected vision.

The peripheral enhancement technique proposed by Tao Wu et al. [8] is used as a preprocessing stage in our CAD systems. The general concept described here is to estimate the normalized thickness profile (NTP) of a breast from a mammogram image and enhance the peripheral area. The algorithm is described in detail as follows: The first step is the segmentation of a projection mammogram where segment the breast muscle or breast region from the background using adaptive threshold value computed using the Otsu thresholding. Separating a mammogram into breast and background regions can be done by Otsu' threshold value. A segmentation image (S.I.) was generated in which pixels were assigned a first value (e.g. amount of one) in a breast region and a second value (e.g. the value of zero) in the background region. Figure A.2 shows the segmentation step by Otsu thresholding for MIAS data set.
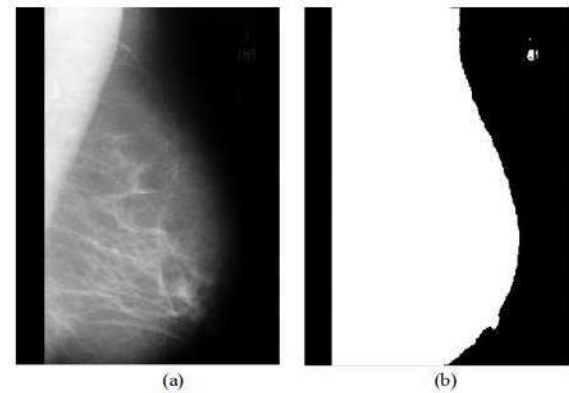
Figure A.2: Segmentation step of a mammogram (a): The original mammogram. (b): The mammogram image segmented by Otsu thresholding.

The second step is a blurred image (B.I.) generation. In this step, a two dimensional (2D) lowpass filter (LPF) was applied to the original image in the frequency domain to obtain a blurred vision, which primarily reflected variations in breast thickness. The Gaussian low-pass filter GLPF with cutoff frequency equal to 20 was used in this study. The filter function of GLPF in the frequency domain is:

$$H(u, v) = e^{-\frac{D(u,v)}{2D_0^2}},$$

(A.1)

1.   Multiply the input image f (x,y) by (−1) x+y to centre the transform.
2.   Compute F(u, v), the DFT of the image from step (1).
3.   Multiply F(u, v) by a filter function H (u, v).
4.   Compute the inverse DFT of the result in (3).
5.   Obtain the real part of the result in (4).

6.   Multiply the result in (5) by(-1) x+y. A perspective plot, image display of a Gaussian LPF function is shown in figure A.3.
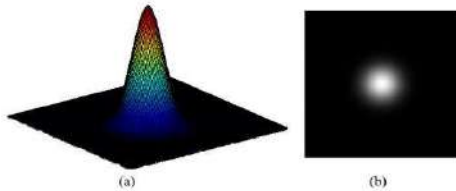
Figure A.3: Gaussian low-pass filter GLPF. (a): Perspective plot of a GLPF transfer function (3D). (b): Filter displayed as an image (2D).

6 - References

1. G. A. Sulik, Pink Ribbon Blues: How Breast Cancer Culture Undermines Women's Health. Oxford University Press, 2011.

2. H. D. Cheng and M. Cui, "Mass lesion detection with a fuzzy neural network," in 2003 IEEE International Conference on Acoustics, Speech, and Signal Processing (ICASSP '03), vol. 2, no. 6, p. II-849-52

3. American Cancer Society. Cancer Facts & Figures 2016. Atlanta: American Cancer Society; 2016.

4. M. P. Sampat, M. K. Markey, and A. C. Bovik, "Computer-Aided Detection and Diagnosis in Mammography," in Handbook of Image and Video Processing, Second Edi., vol. 10, no. 4, Elsevier, 2005, pp. 1195–1217.

5. M. Akay, Ed., Wiley Encyclopedia of Biomedical Engineering. Hoboken, NJ, USA: John Wiley & Sons, Inc., 2006.

6. R. A. Castellino, "Computer aided detection (CAD): an overview," Cancer Imaging, vol. 5, no. 1, pp. 17–19, Aug. 2005.

7. S. Yu and L. Guan, "A CAD system for the automatic detection of clustered microcalcifications in digitized mammogram films.," IEEE Trans. Med. Imaging, vol. 19, no. 2, pp. 115–26, Feb. 2000.

8. T. Wu, R. H. Moore, and D. B. Kopans, "Multi-threshold peripheral equalization method and apparatus for digital mammography and breast tomosynthesis." Google Patents, 27Jul-2010.

9. R. Sivaramakrishna and R. Gordon, "Detection of breast cancer at a smaller size can reduce the likelihood of metastatic spread: A quantitative analysis," Acad. Radiol., vol. 4, no. 1, pp. 8–12, Jan. 1997.

10. S. V. Rajkumar and L. C. Hartmann, "Screening Mammography in Women Aged 40- 49 Years," Medicine (Baltimore)., vol. 78, no. 6, pp. 410–416, Nov. 1999

11. . S. A. Feig and R. E. Hendrick, "Radiation risk from screening mammography of women aged 40-49 years.," J. Natl. Cancer Inst. Monogr., no. 22, pp. 119–24, 1997.

12. . R. a. Smith, A. C. von Eschenbach, R. Wender, B. Levin, T. Byers, D. Rothenberger, D. Brooks, W. Creasman, C. Cohen, C. Runowicz, D. Saslow, V. Cokkinides, and H. Eyre, "American Cancer Society Guidelines for the Early Detection of Cancer: Update of Early Detection Guidelines for Prostate, Colorectal, and Endometrial Cancers: ALSO: Update 2001--Testing for Early Lung Cancer Detection," CA. Cancer J. Clin., vol. 51, no. 1, pp. 38–75, Jan. 2001.

13. M. Elmanna and Y. Kadah, Computer Aided Diagnosis System for Digital Mammography. Germany: Scholars' Press, 2015.

14. American College of Obstetricians & Gynecologists, "Breast Cancer Screening. Practice Bulletin No. 122," Obs. Gynecol, vol. 118, pp. 372–82, 2011.

15. A. Qaseem, V. Snow, K. Sherif, M. Aronson, K. B. Weiss, and D. K. Owens, "Screening mammography for women 40 to 49 years of age: a clinical practice guideline from the American College of Physicians.," Ann. Intern. Med., vol. 146, no. 7, pp. 511–5, Apr. 2007.

16. "Recommendations on screening for breast cancer in average-risk women aged 40- 74 years," Can. Med. Assoc. J., vol. 183, no. 17, pp. 1991–2001, Nov. 2011.

17. "Mammomat Inspiration with PRIME Technology The reference in low-dose mammography." Siemens Healthcare GmbH, Germany, 2016.

18. R. Perez, Design of Medical Electronic Devices. Academic Press, 2002.

19. P. R. Snoeren and N. Karssemeijer, "Thickness Correction of Mammographic Images by Means of a Global Parameter Model of the Compressed Breast," IEEE Trans. Med. Imaging, vol. 23, no. 7, pp. 799–806, Jul. 2004.

20. X. H. Wang, W. F. Good, B. E. Chapman, Y.-H. Chang, W. R. Poller, T. S. Chang, and L. A. Hardesty, "Automated Assessment of the Composition of Breast Tissue Revealed on Tissue-Thickness-Corrected Mammography," Am. J. Roentgenol., vol. 180, no. 1, pp. 257–262, Jan. 2003.

21. D. Lavanya et al. / Indian Journal of Computer Science and Engineering (IJCSE) Analysis of feature selection with classification: Breast Cancer Datasets.

STUDY THE ROLE OF AMLA SEED IN MEDICINAL AND PHARMACOLOGICAL FIELD

Article · January 2021

1 author:

Tanmay Ghosh
Dinabandhu Andrews College university of calcutta
78 PUBLICATIONS **215** CITATIONS

STUDY THE ROLE OF AMLA SEED IN MEDICINAL AND PHARMACOLOGICAL FIELD

*Tanmay Ghosh[1],

[1]Department of Microbiology, Dinabandhu Andrews College, Baishnabghata, South 24 Parganas,

Kolkata – 700084, West Bengal, India.

[*Corresponding Author]

Abstract:

The main reason for this study is to investigate the antibacterial activities of Amla seed (*Phyllanthus emblica*) against some common bacteria. *Phyllanthus emblica* is a commonly known Indian fruit. In this study, we have used four bacteria such as *Escherichia coli*, *Pseudomonas aeruginosa*, *Staphylococcus aureus* and *Bacillus subtilis*. In this study, Amla seed was used for their antibacterial activity. Various extracts were prepared from the powder and used as ethanol, methanol, chloroform, benzene. The most activity is seen in the case of ethanol extracts. Also the flavonoids, tanins, alcoloids were also found in the amla. The results were stunning and showed us that the amla have a high level of inhibition towards Gram negative bacteria than Gram positive bacteria. It was found that the *Escherichia coli* were the highest inhibited organism by the ethyl extract of amla. The zone of inhibition were calculated and put over graphs for study. We studied four extraction (methanol, ethanol, chloroformed benzene) of four concentration (200, 100, 50 & 25) µg/ml. We observed that Escherichia coli showed the highest zone of inhibition (32.4±2 mm) of Ethanol extract of *Phyllunthus emblica* at 200 µg/ml concentration. *Staphylococcus aureus* showed a (24.3±2) mm zone of inhibition at 25 µg/ml concentration of Ethanol extract of *Phyllunthus emblica*. Finally, we conclude that the extracts of Amla seed are used as an antibiotic agent due to its sensitive inhibitory reaction against different bacteria.
Keywords: Investigate, Against, Antibacterial, Commonly.

Introduction:

Amla is the most effective and important fruit in India. *Phyllanthus emblica officinals* is (amla) belongs to the family *Phyllanthaceae*, species *emblica*. Amla is a small to medium sized delicious fruit. Amla is found in Uttar Pradesh, Tamil Nadu, and Rajasthan in India. All parts of amla were used in the treatment of various diseases. Amla used to treat many diseases such as diabetes, asthma, bronchitis, cough, and skin. Amla contains polyphonists and large amounts of vitamin C, calcium, Iron, essential amino acids, many other vitamins, minerals and anti-oxidants. Amla is the effective traditional herbal medicines which had been used to treat and manage diseases since ancient times. In this study, we were experimented with amla seed extract. Pharmacological research describes on amla reveal its analgesic. The extract of seed showed maximum zone of inhibition of antibacterial activity.

Fig 1: Amla Fruits

Method and materials:

Site of the experiment:

The whole experiment was carried out in the lab room 6 Rabindra Mahavidyalaya, Champadanga, West Bengal India.

Source of microorganisms:

Tested microorganisms *Escherichia coli and Pseudomonas aeruginosa, Bacillus subtilis, Staphylococcus aureus* were collected from Chandigarh in India.

Sources of materials:

The tested Amla was collected from the market of Champadanga, Hooghly, West Bengal, India.

Fig 2: *Phyllanthus emblica*

Methanol extraction:

The methanol extract was made by adding 10 grams of Amla seed powder in 20ml of 70% aqueous methionine (W/V), covered with filter paper kept on a rotary shaker for 24 hours and then kept in a dark area at room temperature for 2 to 3 days. The filtered supernatant was

collected and the solvent was evaporated to make the final volume of 400mg/ml of Amla seed methanol extract for the experiment.

Ethanol Extraction:

The ethanol extract was made by dissolving ten grams (5gms) of Amla seeds powder in 20 ml of ethanol and distilled water (82 W/V) covered with filter paper kept for 24 hours in a dark area at room temperature. The filtered supernatant was collected and the solvent was approved by incubating at room temperature for 48 hours to make a final volume 400 mg/ml of Amla seeds ethanol extract for the experiment.

Chloroform extract:

About 5 grams of Amla seeds powder were taken, then dispersed seed in 25 ml of solution , chloroform solution and shaken in a rotary shaker for 3 minutes, then closed with the paper and tightened with rubber band. Few holes were made in the paper to facilitate air circulation and room temperature maintained for 5 days.

Benzene Extraction:

To prepare benzene extraction, at first we took 5gms of dried powder of fruit extract of *Phyllanthus emblica* in a 100ml conical flask and added 25ml of benzene and shake them very carefully. Then they covered with a tissue paper tightly with a rubber band. At last, some small pores created above the tissue paper for passing air and evaporation. They transferred at room temperature for 48 hours.

Extract preparation:

20 gram to dry powder was dispersed in methanol, ethanol, chloroform in a conical flask and shaker in a rotary for 24 hours, then the supernatant was collected and the solvent was evaporated.

Sources of Antibiotics:

An antibiotic (Amphicilin) was collected from the nearby market of Champadanga, Hooghly, and West Bengal, India.

Preparation of extract concentration:

 We had prepared four extracts before. From this four extractions viz. Methanol, Ethanol, Acetone, and Benzene, using DMSO we prepared four different concentrations such as 50μg/ml, 100μg/ml, 200μg/ml, and 400μg/ml.

Method:

The antimicrobial screening of seed extract *Phyllanthus emblica* was dissolving of 3 gm of seed extract in 10ml Dimethyl Sulphoxide (DMSO). From 25mg/ml, 75mg/ml, 150mg/ml &

300mg/ml concentration was taken for the antibacterial activity. The hollow tube was heat and incubating agar plate. One DMSO was taken as control.

Medium:

At first, we take 3.8g of Mueller Hinton Agar (MHA) and added water then shaking very well. Then it autoclaved to at 15lbs and transferred to a sterile Petri plate and the agar plate which was at low temperature, (3 – 4-millimeter thickness) becomes cool.

Inoculums and Incubation:

0.1ml of microorganisms was transferred to the agar plate, and then they were allowed for 5 minutes before made various concentrations. Then the microorganisms cultures incubation at room temperature (37°C) for 24 – 48 hours.

Statistical analysis:

After incubation, we can see a clear zoon around the Petri plate which called "zone of inhibition". Then we measured the zone of inhibition using a zone reader. We take three nearly similar values of the zone of inhibition for each concentration of Amla seed extract. The obtained values were analyzing used SIGMAPLOT software (version – 14.0). The data of results were analyzed by using the "t" test.

Phytochemical estimation:

Extract preparation:

20 gm of air-dried powder was taken in 100 ml of each solvent (Methanol, Ethyl Acetate, Hexane, Benzene and Chloroform) in a conical flask, plugged with cotton wool, and then kept on a rotary shaker. After 24 hours the supernatant was collected and the solvent was evaporated.

Phytochemical studies:

The methods described by Harborne were used to test for the presence of the active ingredients in the test sample.

❖ **Test for steroids:**

A 10 ml of plant extract (methanol, ethyl acetate, hexane, benzene, chloroform) was evaporated to a dry mass and the mass is dissolved in 0.5 ml of chloroform. Acetic anhydride [0.5 ml] and 2 ml of concentrated sulphuric acid were added to the above.

❖ **Test for alkaloids:**

The plant extract (methanol, ethyl acetate, benzene, chloroform) [0.5 g] was stirred with 5 ml of 1% HCl on a steam bath. The solution obtained was

filtered and 1 ml of the filtrate was treated with two drops of Mayer's reagent. The two solutions were mixed and made up to 100ml with distilled water.

Fig 3: Amla

❖ **Test for tannins:**

About 1 g of plant extract powder was weighed into a beaker and 10 ml of distilled water added. The mixture was boiled for five minutes. Two drops of 5% $FeCl_3$ were then added.

❖ **Test for flavonoids:**

A few drops of 1% NH_3 solution is added to the plant extract [0.5 g] in a tube for observation of Yellow coloration.

❖ **Test for reducing sugar:**

To 0.5 ml of extract solution, 1 ml of water and 5 - 8 drops of Fehling's solutions were added at hot and Observed for brick red precipitate.

Table 1: Display of the presence/absence of different Phytochemicals in the seeds of *Phyllumthas emblica*

200Phytochemicals	Methanol	Ethanol	Chloroform	Benzene
Tannin	-	+	-	+
Alkaloid	+	-	-	-
Flavonoid	+	-	-	-
Phenolic	+	-	+	+
Steroid				
Saponin	-	-	-	+
Reducing Sugar	-	-	-	-

Results:

We used both polar as well as non-polar solvents for the extraction of active components from the seeds of the *Phyllunthas emblica* plant. The antibacterial activity of the *Phyllunthas emblica* was assessed using the agar well diffusion method by measuring the diameter of growth inhibition zones and its subsequent concentration was arranged.

Table 2: The antimicrobial activity of Ethanol extract against different bacteria				
Zone of inhibition (mm)				
Concentration (µg/ml)	*Escherichia coli*	*Pseudomenas aeruginosa*	*Bacillus subtilis*	*Staphylococcus aureus*
200 µg/ ml	32.4±2	27.2±1	26.3±1	24.3±2
100 µg/ml	27.7±1	25.4±1	23.4±2	21.3±3
50 µg/ ml	25.2±1	22.3±2	20.3±2	18.2±2
25 µg/ ml	22.4±2	17.1±0	15.2±3	13.2±4
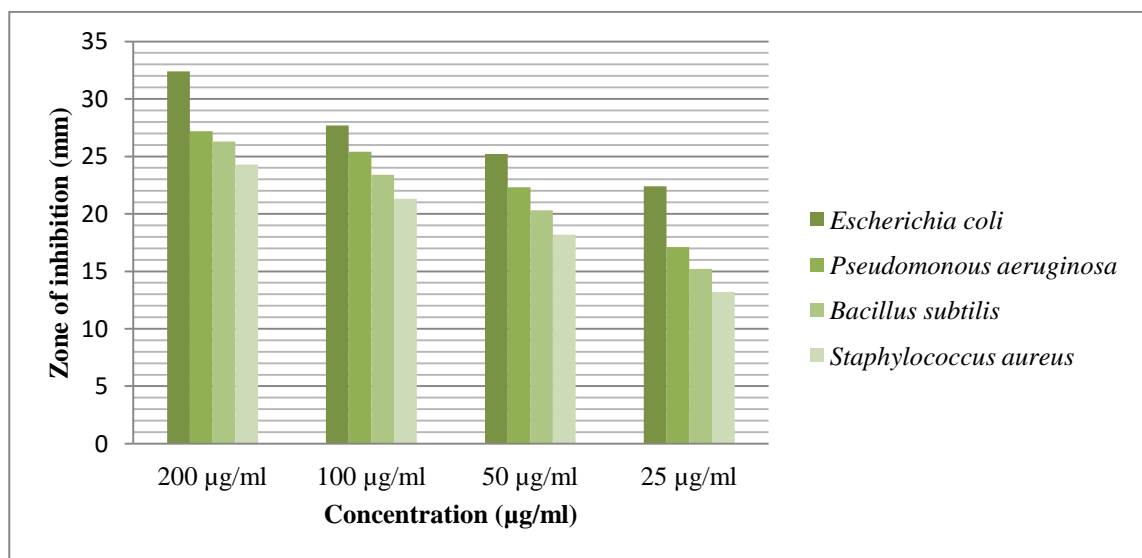
Fig 4: The antimicrobial activity of Ethanol extract against different bacteria.
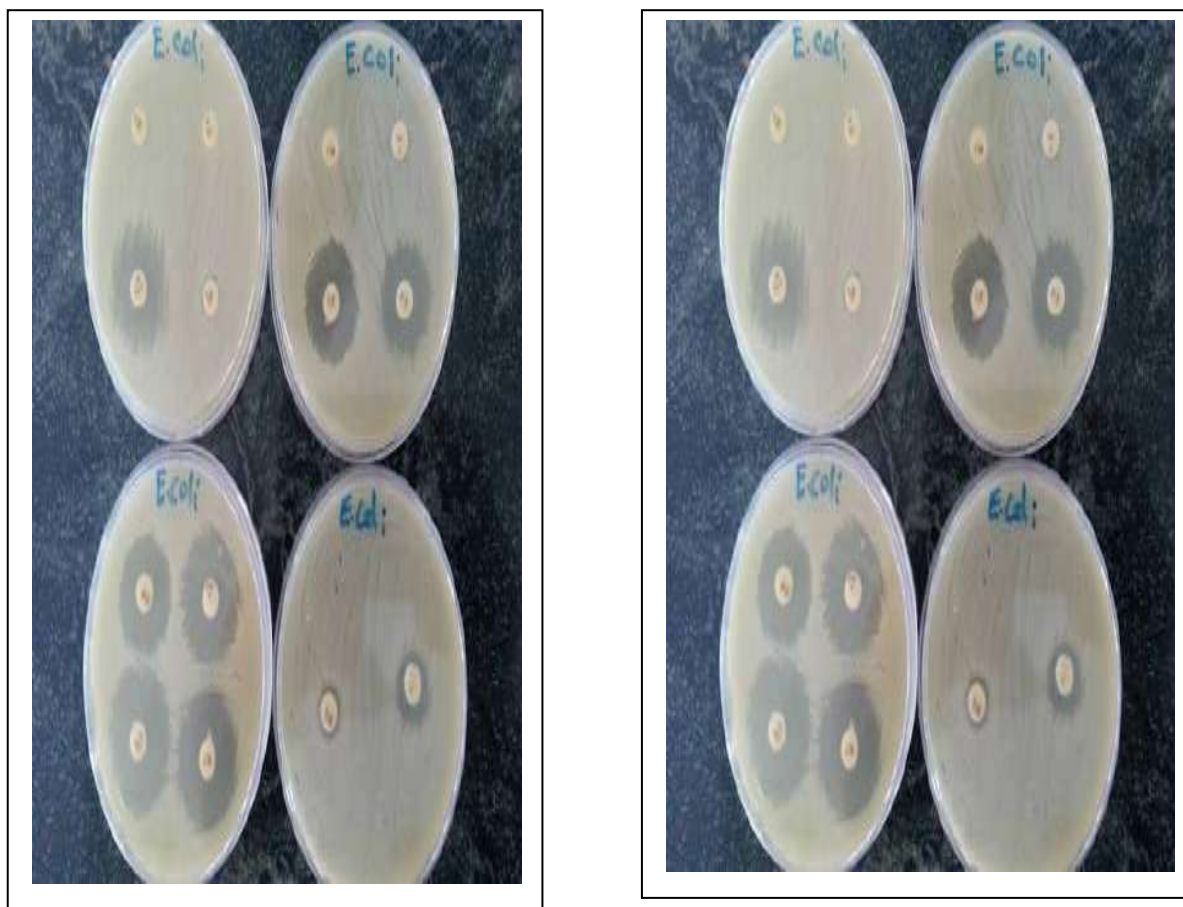
Fig 5: zone of inhibition of *E. coli*

Table 3: The antimicrobial able activity of chloroform extract against different bacteria				
Zone of inhibition (mm)				
Concentration Mg/ ml	*Escherichiaco*	*Pseudomonas aeruginosa*	*Bacillussub*	*Staphylococcus aureus*
200 µg/ml	30.2±3	28.1±1	25.2±3	22.3±2
100 µg/ml	27.1±2	23.4±2	23.1±2	20.4±2
50 µg/ml	24.3±2	19.9±1	21.3±2	19.3±2
25 µg/ml	21.2±2	16.6±2	19.2±2	17.2±2
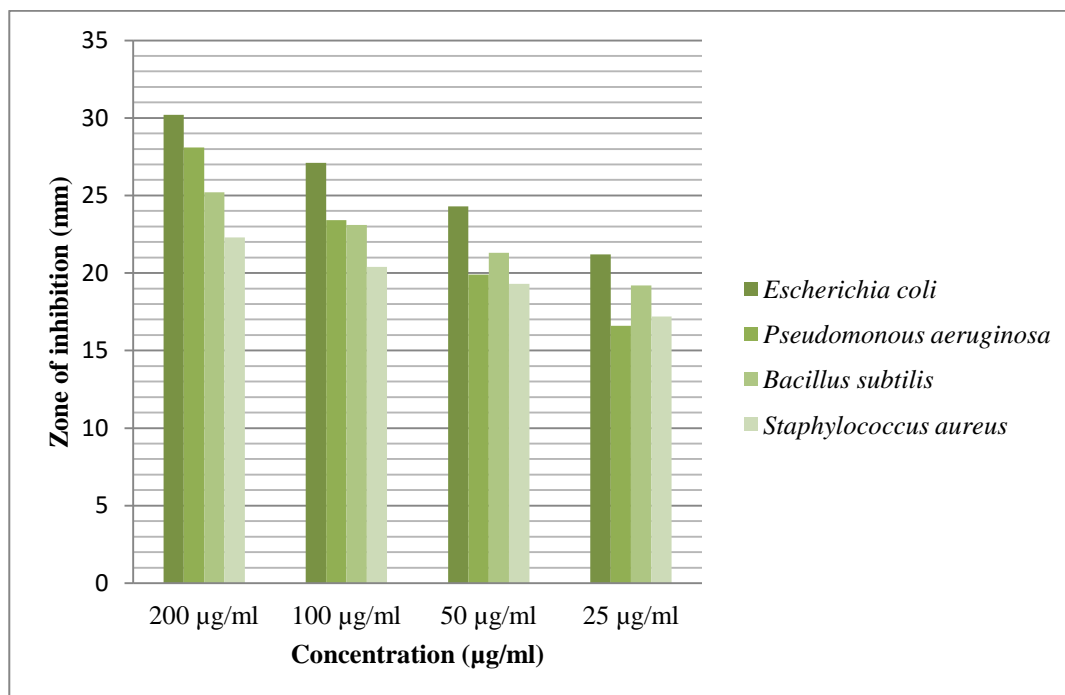
Fig 5: The antimicrobial activity of chloroform extract against different bacteria.

Table 4: The antimicrobial activity of Methanol extract against different bacteria				
Zone of inhibition				
Concentration	*Escherichia coli*	*Pseudomonas aeruginosa*	*Bacillus subtilis*	*Staphylococcus aureus*
200 µg/ ml	27.2±1	20.2±1	18.2±3	16.3±4
100 µ g/ml	23.5±2	19.4±2	16.2±1	15.3±2
50 µg/ml	22.5±1	17.5±1	15.3±2	13.2±2
25 µg/ml	19.7±2	14.7±2	13.4±2	11.2±3
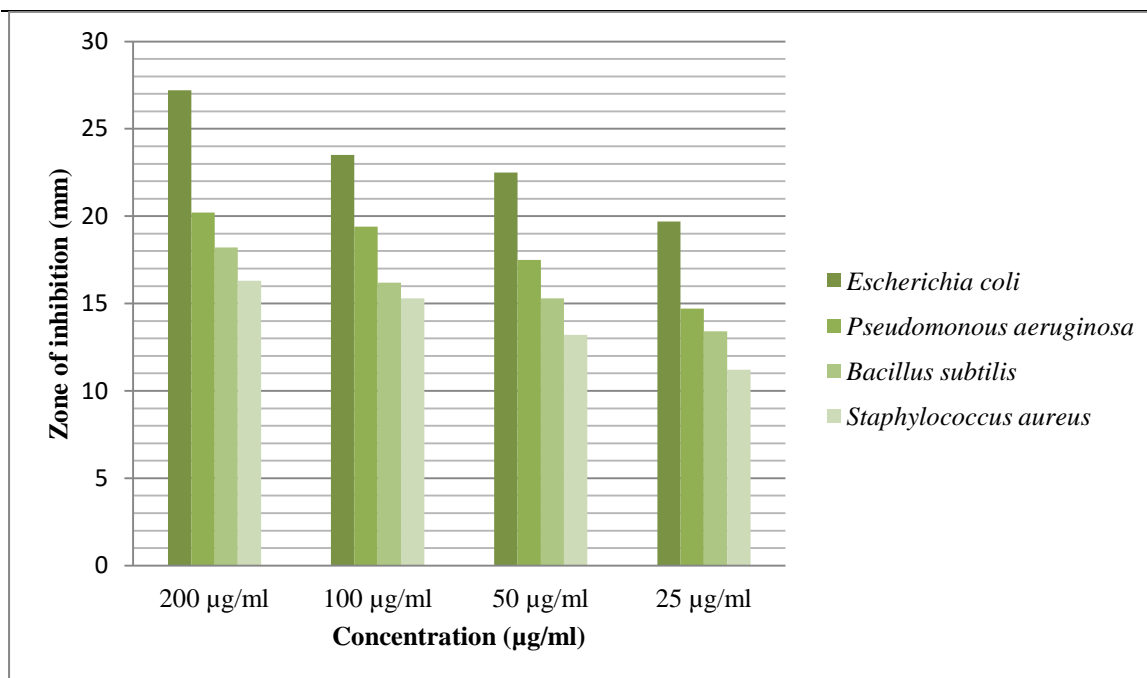
Fig 3: The antimicrobial activity of Methanol extract against different bacteria

Table 5: The antibacterial activity of Benzene extract against different bacteria				
Zone of inhibition				
Concentration µg/ ml	*Escherichia coli*	*Pseusomonas aeruginosa*	*Bacillus subtilis*	*Staphylococcus aureus*
200 µg/ ml	29.3±1	27.2±1	25.3±2	22.3±2
100 µg/ ml	26.2±2	23.5±2	23.4±2	20.4±2
50 µg/ ml	24.3±3	22.5±1	21.3±1	19.4±2
25 µg/ ml	21.2±2	19.7±2	19.2±3	16.5±3
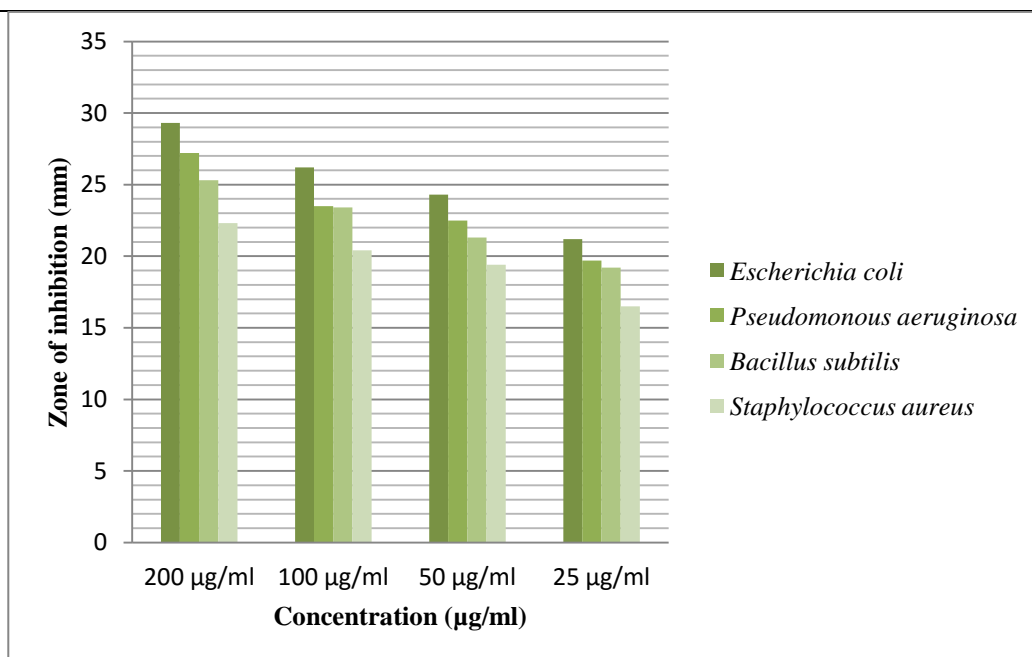
Fig 4: The antibacterial activity of Benzene extract against different bacteria.

Discussion:

The result showed that inhibition of Gram-negative bacteria more than Gram-positive after treated with Amla seed extract. So, the Gram-negative bacteria *Escherichia coli* showed a wide range of inhibitory zone and *Bacillus subtilis* and *Pseudomonas aeruginosa, Staphylococcus aureus* were showed less inhibitory zone. We studied four extractions (Methanol, Ethanol, Chloroform and Benzene) of four concentration (200, 100, 50 & 25) µg/ml. We observed that *Escherichia coli* showed the highest zone of inhibition (32.4±2 mm) of Ethanol extract of *Phyllunthus emblica* at 200 µg/ml concentration. *Staphylococcus aureus* showed a (24.3±2) mm zone of inhibition at 25 µg/ml concentration of Ethanol extract of *Phyllunthus emblica.* Finally, we conclude that the extracts of Amla seed are used as an antibiotic agent due to its sensitive inhibitory reaction against different bacteria.

Conclusion:

The study on Amla seed extract has many antibacterial activities on different bacteria. This fruit and its seed have medicinal value that helps in our health and others purpose. The seed extract was used in many medicinal and pharmaceutical fields. *Phyllunthus emblica* (amla) has an important role in Ayurveda medicine. Amla is possible food for industries. This food can prevent bacterial infection. Amla seed coat powder has hydration properties.

Future aspects:

There have big future aspects of research work with Amla seeds. *Phyllunthus emblica* should certainly find a place in the treatment of various bacterial infections. The results from the present study are very encouraging and indicate that this herb should be studied more

extensively to explore its potential in the treatment of infectious diseases as well. It was established that the fractions containing the high concentrations of oil inhibited the growth of microorganisms and results were compared with antibiotic penicillin commonly used therapeutically and they showed less strong inhibition for Gram-negative bacteria and pronounced inhibition for Gram-positive bacteria. *Phyllunthus emblica* shows significant activity because the seed contains many useful compounds such as (Methanol, Ethanol, Chloroform and Benzene) which of them have higher medicinal value especially in the treatment of diabetes and digestion, eruptions, and flatulence, protective agents. Various crude execonomical roles in our human society. The future of in vivo human studies determines the molecular traded essential oil made from seed in the entire world in many developed countries. It is also considered a valuable product in both the food and pharmaceutical industries.

References:

1. Baliga MS, Prabhu AN, Prabhu DA, Shivashankara AR, Abraham A, Patty PL,Antidiabetic and Cardioprotective Effects of Amla (*Emblica officinalisGaertn*) and its Phytochemicals: Preclinical observations, Bioactive Food as Dietary Interventions for Diabetes, 2013, 583-600.

2. Chatterjee A,Chattopadhyay S, Sandip K,Bandyopadhyay, Biphasic Effect of Phyllanthus Emblica L. Extract on NSAID-Induced Ulcer: An Anti-oxidative TrailWeaved with Immunomodulatory Effect, Evidence-Based Complementary and Alternative Medicine, 2011, 2010, 1-13.

3. YokozawaT,Kim HY, Kim HJ, Tanaka T, Sugino H, Okubo T, Chu D, Juneja LR, Amla (Emblica officinalisGaertn.) Attenuates Age-Related Renal Dysfunction by Oxidative Stress, Journal of Agricultural and Food Chemistry,55, 2007, 7744-52.

4. Vasudevan M, Parle M, Memory enhancing activity of Anwalachurna (Emblica officinalisGaertn.): An Ayurvedic preparation, Physiology &Behaviour, 91(1), 2007, 46–54.

5. Madhuri S, Studies on estrogen induced uterine and ovarian carcinogenesis and effect of ProImmu in rat, PhD thesis, Jabalpur, MP, RDVV, 2008.

6. Krishnaveni M, Mirunalini S, Chemopreventive efficacy of Phyllanthus emblica L. (amla) fruit extract on 7,12-dimethylbenz(a)anthracene-induced oral carcinogenesis – A dose–response study, Environmental Toxicology, and Pharmacology, 34(3), 2012, 801-10.

7. Adil MD, Kaiser P, Satti NK, Zargar AM, Vishwakarma RA, Nasdaq SA, Effect of Emblica Officinalis (fruit) against UVB-induced photo-aging in human skin fibroblasts, Journal of Ethnopharmacology, 132(1), 2010, 109-14.

8. Deep G, Dhiman M, Rao AR, Kale RK, Chemopreventive potential of Triphala (a composite Indian drug) on benzo(a)pyrene-induced fore stomach tumorigenesis in murine tumor model system, Journal of Experimental and, Experimental Clinical Cancer Research, 24(4), 2005, 555-63.

9. Varadacharyulu N, Damodara Reddy, PadmavathiP, Paramahamsa M, Modulatory role of Emblica Officinalis against alcohol-induced biochemical and biophysical changes in rat erythrocyte membranes, Food and Chemical Toxicology, 47, 2009, 1958-63.

10. Prakash D, Upadhyay G, Gupta C, Pushpangadan P, Singh KK, Antioxidant and free radical scavenging activities of some promising wild edible fruits, International Food Research Journal, 19 (3), 2012, 1109-16.

11. Nripendranath, Bibhabasu H, Rhitajit S, Santanu B, Comparative study of the antioxidant and reactive oxygen species scavenging properties in the extracts of the fruits of Terminaliachebula, Terminaliabelerica and Emblica Officinalis, BMC Complementary and Alternative Medicine,10, 2010, 1-15.

12. Santoshkumar J, DevarmaniMS, Sajjanar M, Pranavakumar MS, Dass P, A study of Anti-inflammatory activity of fruit of Emblica officinalis (Amla) in Albino rats,MedicaInnovatica, 2(1), 2013, 17-26.

13. Bhattacharya SK, Bhattacharya A, Sairam K, Ghosal S, Effect of Bioactive tannoid principles of Emblica Officinalis on ischemia-reperfusion-induced oxidative stress in rat heart,Phytomedicine, 9(2), 2002, 171-4.

14. Yi-Fei W, Ya-Feng W, Xiao-Yana W,Shea, Chui-Wena Q, Yi-Cheng L, Kitazatoc K, Qing-Duan Q, Yan W, Li-Yun Z, Jin-Hua Z, Chong-Rene Y, Qing L, Ying-June Z,Phyllaemblicin B inhibits Coxsackievirus B3 induced apoptosis and myocarditis, Antiviral Research, 84, 2009, 150-58.

15. Kumar, G.S., H. Nayaka, S.M. Dharmesh and P.V. Salimath, 2006. Free and bound phenolic antioxidants in amla (*Emblica officinalis*) and turmeric (*Curcuma longa*). J. Food Comp. Anal., 19: 446-452.

16. Liu, X., C. Cui, M. Zhao, J. Wang, W. Luo, B. Yang and Y. Jiang, 2008. Identification of phenolics in the fruit of emblica (*Phyllanthus emblica* L.) and their antioxidant activities. Food Chem., 109: 909-915.

17. Nosal ova G, Mokry J, Hasan KM, Antitussive activity of the fruit extract of Emblica officinalisGaertn, (Euphorbiaceae), Phytomedicine. 2003;10,583-9.

18. Chatterjee A, Chattopadhyay S, Sandip K,Bandyopadhyay, Biphasic Effect of Phyllanthus emblica L. Extract on NSAID-Induced Ulcer: An Anti-oxidative Trail Weaved with Immunomodulatory Effect, Evidence-Based Complementary and Alternative Medicine. 2011; 1-13.

19. YokozawaT,Kim HY, Kim HJ, Tanaka T, Sugino H, Okubo T, Chu D, Juneja LR, Amla (Emblica officinalisGaertn.) Attenuates AgeRelated Renal Dysfunction by Oxidative Stress, Journal of Agricultural and Food Chemistry. 2007; 55, 7744-52.

20. Krishnaveni M, Mirunalini S, Chemopreventive efficacy of Phyllanthus emblica L. (Amla) fruit extract on 7,12dimethylbenz (a) anthracene induced oral carcinogenesis – A dose– response study, Environmental Toxicology and Pharmacology. 2012; 34(3):801-10.

21. Adil MD, Kaiser P, Satti NK, Zargar AM, Vishwakarma RA, Tasduq SA, Effect of Emblica officinalis (fruit) against UVB-induced photoaging in human skin fibroblasts, Journal of Ethnopharmacology.2010; 132(1): 109-14.

UGC-CARE List

You searched for **"2277-5218"**. Total Journals : **1**

Search:

Sr.No.	Journal Title	Publisher	ISSN	E-ISSN	UGC-CARE coverage years	Details
1	New Horizons	Mehr Chand Mahajan DAV College for Women	2277-5218	NA	from June-2019 to April- 2021	Discontinued from April 2021

Showing 1 to 1 of 1 entries

Previous 1 Next

A REVIEW ON MUSHROOM BORNE MICROBES WITH THEIR HARMFUL AND BENEFICIAL ROLES *

Article · October 2020

2 authors:

Tanmay Ghosh
Dinabandhu Andrews College university of calcutta
74 PUBLICATIONS   **211** CITATIONS

SEE PROFILE

Mohan Kumar Biswas
Visva Bharati University
118 PUBLICATIONS   **521** CITATIONS

SEE PROFILE

A REVIEW ON MUSHROOM BORNE MICROBES WITH THEIR HARMFUL AND BENEFICIAL ROLES*

BY

Tanmay Ghosh✣
Department of Microbiology
Dinabandhu Andrews College
Baishnabghata, South 24 Parganas (South), Kolkata - 700 084, West Bengal, India

Mohan Kumar Biswas✣
Department of Plant Protection
Palli Siksha Bhavana
Visva - Bharti, Sriniketan, Birbhum, West Bengal

Abstract:-

Mushroom is quite renowned to us. It is used as food supplement with higher amount of vitamins, protein and other essential elements. All bioactive molecules are found in fungi. It is also found that several fungi have antimicrobial, anti inflammatory and antiviral properties also. Mushrooms are in the group of fungi. There are two types of mushroom edible and non edible mushroom. Inspite of being a good food mushroom also possess economical and medicinal role in human life. Now a day's mushroom is found in almost every country as food. But mushroom also contains some mycoflora. These mycofloras are referred to as mushroom borne mycoflora. Some of these mycofloras are very harmful for human and those fungi but some of them are also beneficial. In this total review we are trying to discuss about some of those mushroom borne mycoflora. Although the mushroom borne mycoflora are a new thing to be described property. There are some mushroom borne mycoflora described in this review.

Introduction:-

The mushroom borne mycoflora is a very new topic in the field of microbiology. The fungal mycoflora is often said to the fungi associated microbes. But there is some soil free living Bacteria who helps in the protection and growth of the mushroom but rarely found in the mushroom surface until mushroom blooming. Name of such microbes are *Pseudomonas* sp.*,* Mesophilic organisms*,* Solibacillus*,* Comamonas*,* Acinetobacter *and* Sphingomonas*.* These microbes also help in bio conversion of raw minerals for the mushroom. From green moulds several bacteria from the group of bacilli are found to have a suppression effect on the mycoparasites. Thus they protect the fungi from the mycoparasites. There are some bacteria as Proteobacteria, Bacteroidetes, Actinobacteria, Verrucomicrobia which have an important role in truffle maturation. There are also some harmful microbes in mushroom mycoflora as *Verticillium fungicola, Myceliophthora lutea, Chrysosporium liteum, Cladobotryum dendroides* who are responsible for mushroom disease as soft decay, COBWEB, mildew, Dry Bubble, Dingle

spot, brown spot, yellow mould and mat disease. This disease cause a high yield of mushroom loses. The microbes association with fungi are also found to be harmful for the human body sometimes. *Trichoderma aggressivum, Cladobotry iummycophilum* and the mushroom virus X are commonly found associated with mushrooms and causing a high yield loss of these mushrooms. From a study of Jamia Humdard University, Delhi in 2018 it was found that 11 predominant fungi were isolated from the Oyster mushroom (*Pleurotus* spp.) among which the predominant fungi are *Aspergillus flavus, Aspergillus niger, Penicillium spp, Rhizopus spp* and *Trichoderma harzianum*. In another study it was found that the packaged mushroom sometimes contains *Staphylococcus aureus* which produces the enterotoxins causing digestive disorder of human beings. This *Staphylococcus aureus* is majorly found in the mushroom of *Agaricus bisporus*. These mushrooms borne mycoflora are both contain good and bad effects over the world. Our study is to discuss about all this mushroom borne mycoflora. The mushroom borne mycofloras are divided into two groups – Beneficial mushroom borne mycoflora and Harmful mushroom borne mycoflora. The beneficial mushroom borne mycoflora include the mycoflora, helps the fungi to grow, bloom and uptake the nutrition. But the harmful mycoflora of mushroom causes the damage and lose of yield of mushroom. Some of the harmful mushroom mycoflora also causes the disease to both humans and mushrooms.

Some harmful mushroom mycoflora and their disease:-

1) ***Verticillium fungicola:-***

   It is bacteria that cause a high damage to the mushroom yield.

   Disease forms:-

   Dry bubble, fungal spot, and brown spot. This is the most common and serious fungal disease and if it is left uncontrolled disease can totally destroy the mushroom crop in 2 to 3 weeks. From India the first report of heavy incidence of dry bubble was found.

   Disease management and control:-

   I) The primary infection is controlled by the use of sterilized casin soil. Heat treatment of 63°C for 1hour can prevent the disease.

   ii) In laboratory trails V. malthousei was contrled by zineb on a large scale bercemazine b 80 used at 0.1 to 1.2% controlled the disease by 3 sprays,

   iii) Under laboratory condition use of leaf extract of *Cannabis sativus, Citrus sp., Euclipus sp., Datura* sp.
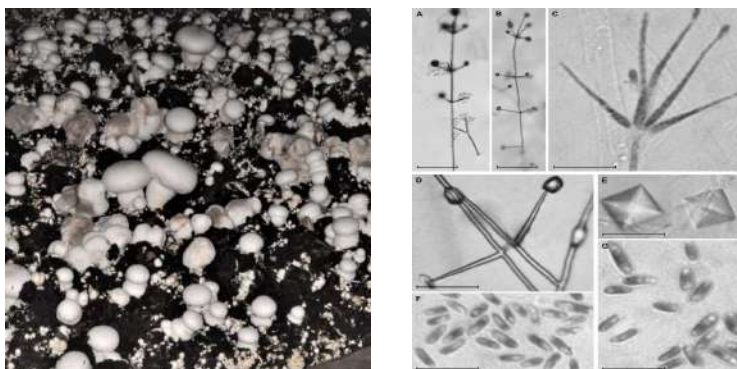
Fig 1: *Verticillium fungicola*

2) *Mycogone perniciosa* :-

It is another microbe of the mushroom.

Disease forms:-

Wet bubble, White mould. In white bottom mushroom the disease is formed by *Mycogone perniciosa*. It is a major disease in mushroom growing countries.

Disease management and control:

The aerated steam at 54.4°c for 25mins can eliminate this pathogen formaldehyde can also be used.

Benomyl spray 0.5 to 4g/m³ is reported effective for protecting the mushroom crop.

 Ag 13.6 and Ag 13.9 are found effective against this pathogen.

Fig 2: *Mycogone perniciosa*

Fig 3: White mould disease

Fig 4: Wet bubble disease

3) *Cladobotryum dendroides:-*

Disease forms:-

Soft decay, COBWEB, mildew. This disease caused extensive damage by causing soft decay or soft rot. The fruit body is damaged due to humidity.

Disease management and control:

Live stem sterilization or heat at 50°C for 4 hours effectively eliminate the pathogen and saves the mushroom.

Terraclor a chfmican can eradicate the pathogen even after the establishment of a good bond with the mushroom.

Cannabis, Sativas, Cumin, Resinus, Eucalyptus, Datura and citrus are found, which are effective against the pathogen.

Fig 5: *Cladobotryum dendroides*	Fig 6: COBWEB disease

4) **Trichoderma virid , T. hamantum, Penecillium cyclopium, Aspergillus sp. :-**
   These all microbes are put into the. Same category as they produce same type of disease.
   Disease formed:-
   Green mould, Trichoderma spot
   One of the most common and destructive disease of mushroom cultivation is green mould which is mainly caused by *Trichoderma viride, Penecillium cyclopium* and *Aspergillus* sp. mainly it is the disease of bottom mushroom.
   Disease management and control:-
   Proper pasteurisation and sterilization is found effective for the disease.
   2% formalin or baristin TBZ or treatment by zine b can control the disease.
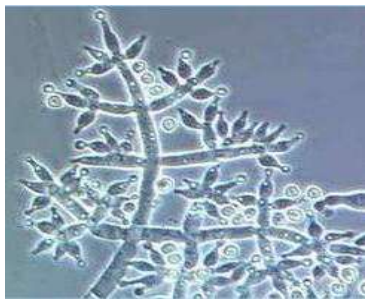
Fig 7: *Trichoderma virid*	Fig 8: *Penecillium cyclopium*	Fig 9: *Aspergillus* sp.

5) **Myceliophthora lutea, Chrysosporium liteum:-**
   Disease formed:-
   Mat disease and yellow mould. All those fungi produce yellow mycelial growth in both yellow mould and mat disease. In natural these diseases cause 5 to 30 %of yield loss of the common bottom fungi. In the maximum cases they can cause the yield loss of 29 to 85 % of the crop yield.
   Disease management and control:-
   Proper pasteurisation is essential for this disease cure. They can't tolerate the heat of 51°c for 6 hours or 54°c for 4 hours.
   Benomyl and blitox are found effective against these pathogens. Spraying the solution trice is found effective.
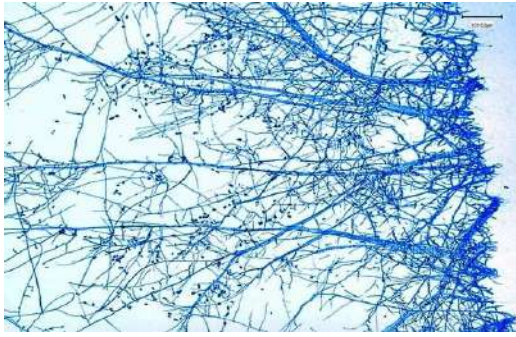
Fig 10: *Chrysosporium liteum*
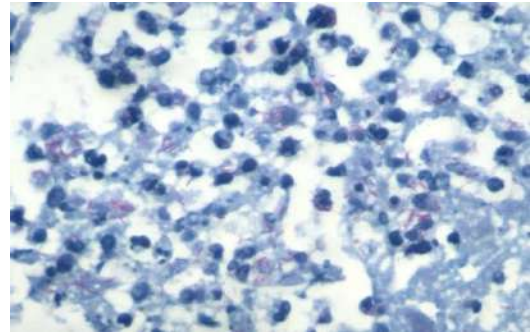
Fig 11: *Myceliophthora* sp.

6) *Cladobotrym apiculatum, C. Verticillatum, Gliocladium virens, Arthobotrys pleuroti, Cibirina fungicola*:-

These fungi are all attacking on the oyster mushroom.

Disease symptoms:-

- Small green irregular sunken spots on fruit body and soft rot or soft decay.
- Green spot, brown spot, pale yellow spot.
- Browning discolouration.

Disease management:-

The use of spray with bavistin and benomyl twice is found effective. Carbendazin and blitox are also found useful.
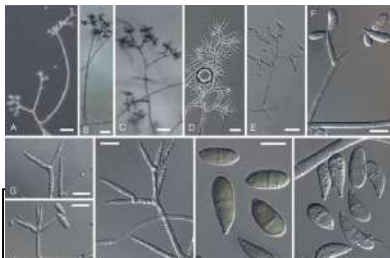
Fig 13: *Gliocladium virens*

Fig 14: Green spot disease
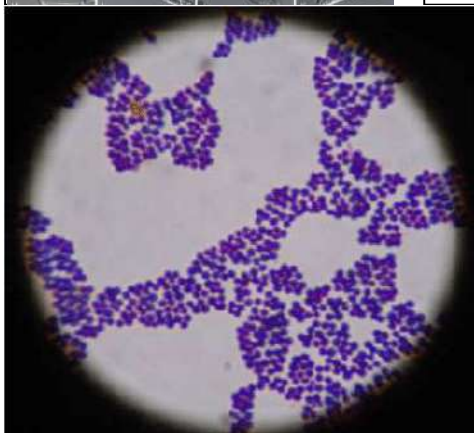
Fig 15: *Staphylococcus aureus*

Fig 16: Soft rot disease of Potatoes

7) *Staphylococcus aureus*:-

This bacterium is sometimes found in the packaged mushroom. Bacteria are responsible for the food poisoning in several cases. This bacterium mainly produces an enterotoxin in the edible mushroom. The bacteria are generally found on the surface of *Agaricus bisporus* if the packaging left air inside it. In the presence of low O_2 the bacteria produce the enterotoxin, and the major way to fight against it is to proper packaging of mushroom.

Some beneficial mushroom mycoflora is described below.

1) *Pseudomonas* **sp., Mesophilic organisms, Solibacillus, Comamonas, Acinetobacter and Sphingomonas:-**

These are the free living soil bacteria that are often found on the surface of some edible fungi. They help the mushroom from three ways - A) The microbes give protection to the fungi from mycoparasites so they can remain good, B) They often help the fungi to get nutrient by degrading complex organic molecules into the simple ones and C) Some microbes produce the signals that help the fungi to bloom or represent a fruiting body.

Fig 17: *Pseudomonas* sp.

Fig 18: Mesophilic organisms
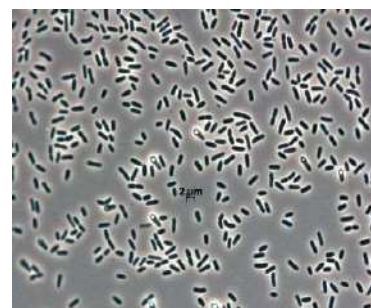
Fig 19: Solibacillus organisms
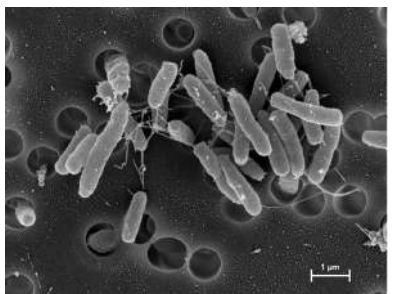
Fig 20: Comamonas organisms

Fig 21: Acinetobacter

Fig 22: Sphingomonas

2) **Proteobacteria, Bacteroidetes, Actinobacteria, Verrucomicrobia:-**

These microorganisms are often found associated with mushrooms. They help in a lot of way but most of them help in truffle maturation.

In the world of mushroom mycoflora there is still a vast plane to discover. They are information till now we can discuss throw our review.

Fig 23: Proteobacteria
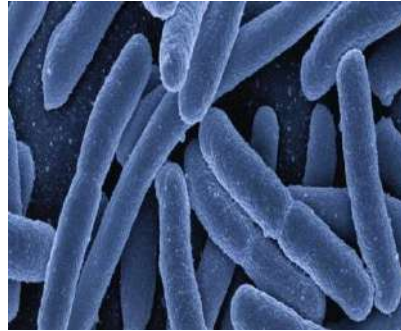
Fig 24: Bacteroidetes

Fig 25: Verrucomicrobia

Conclusion:-

In the world of mushroom mycoflora there are two type of mushroom mycoflora which could be found. They are beneficial and harmful mushroom mycoflora. The beneficial ones tried to enhance the mushroom crop production and help in fungal nutrition and protection, on the other hand the harmful mushroom mycoflora creates some disease and lowers the yield of the mushroom crop and produces some disease even in some humans. So from here we could conclude that there is a lot of mycoflora on the edible mushroom. And mushroom mycoflora have a serious impact on our daily lives. The earlier studies of the researchers have proven that the mushroom often carry mycoflora associated with them as *Pseudomonads* sp., Solibacillus, Comamonus, Actinobactor, Bacteroidetes, Actinobacteria, Verricomicrobial are found to be helpful to mushroom. So they are considered to be the good beneficial or healthy mushroom borne mycoflora. There are also some studies proving the presence of some particular mushroom borne mycoflora which not only reduce the mushroom yield but also decrease the nutritional quality of the mushroom. Even sometimes they cause disease to the person who consumes the mushroom. The particular mushrooms borne mycoflora are *Cladobotrym* sp., *Trichoderma* sp., *Aspergillus* sp., *Gliocladium* sp., *Arthobotrys* sp., etc. The mushroom borne mycoflora are found to be both beneficial and harmful. So there are a vast subject to be studied. In this review a short summary of some mushroom borne mycoflora is given.

Reference:-

1) Bailey, K.L., Boyetchko, S.M., Langle, T., 2010. Social and economic drivers shaping The future of biological control: A Canadian perspective on the factors affecting The development and use of microbial biopesticides. Biological Control 52, 221-229.

2) Sakula. A. 1967. Hlushroom worker's lung. – Br. Hied. J. 3: 31: 61-70. 705-7 10.

3) Bakker, P.A.H.M., De Boer, M., Zhang, K.,Van der Sluis, I., Van Loon, L.C., 2002a. Dose Response relationships for control of fusarium wilts byPseudomonas fluorescensRS111. IOBC/WPRS Bulletin 25, 107–110.

4) Pattanaik. P., Patra, A.K. and Pattanayak, N.B. (1998).

5) Serratiamarcescensce from oyster mushroom Spawn -a case study. JDairying Food and Home Sci. 17: 3-4.

6) Moorthy, V.K. and Mahanan, R.C. (1996). Seasonalvariation in contamination of spawn and yield ofPleurotussajor-caju (Fr.) Singer' in a commercialfarm in coastal Karnataka. Mushroom Res. 5: 23-28

7) Biserka, B.I. (1972). Dealing with microbial trouble Makers in commercial spawn production of *Agaricus bisporus* L. Mushroom Sci. 8: 305-31.

8) Baysal E, Peker H, Kemal M, Temiz A (2003). Cultivation of oyster mushroom on waste paper with Some added supplementary materials. Bioresource Technology; 89:95-97.

9) Chakravarty D K. et al. (1982). Relative efficacy of fungicides in the control of weed fungi in the beds of Oyster mushroom. Pesticides; 16: 19-20.

10) ChangChang S T (1990). Future trends in cultivation of alternative mushrooms. Mushr J; 215: 422-433.

11) Cha J S (2004). Pest Disease Management. Mushroom Growers Handbook. Mushroom World; 1.

12) Chhata L K and B B L Thakore (2010). Fungal competitors and their effect on yield of oyster mushroom (Pleurotusflorida). J. Mycol. Plant Pathol., 40: 103-105.

13) Das N and Mukherjee M (2007). Cultivation of Pleurotusostreatus on weed plants. Bio Resource Technology; 98: 2723-2726.

14) Meera Pandey and Tewari R P (1989). Air and substrate mycoflora associated at various stages of oyster Mushroom cultivation. Indian Phyto; 42:173-177.

15) Morris E Doyle, O Clancy, K J and Elliotl T J (1995). A profile of Trichoderma species II-mushroom Growing units. Science and cultivation of edible fungi; 2: 619-625.

16) Munshi N A and Ghani M Y (2003). Mushroom Industry in Kashmir Valley- Present status, Future Prospects and problems. SKUAST J of Re; 5: 1-19.

17) Antony-Babu, S., Deveau, A., Van Nostrand, J.D., Zhou, J., Le Tacon, F., Robin, C., et al. (2014) Black truffle-associatedBacterial communities during the development and matura-Tion of Tuber melanosporumascocarps and putative func-Tional roles. Environ Microbiol 16: 2831–2847.

18) Antunes, L.P., Martins, L.F., Pereira, R.V., Thomas, A.M.,Barbosa, D., Lemos, L.N., et al. (2016) Microbial communityStructure and dynamics in thermophilic composting viewedThrough metagenomics and metatranscriptomics. Sci Rep 6:38915.

19) Aslani, M.A., Harighi, B., and Abdollahzadeh, J. (2018)Screening of endofungal bacteria isolated from wild grow-Ing mushrooms as potential biological control agentsAgainst brown blotch and internal stipe necrosis diseases Of *Agaricus bisporus*. Biol Control 119: 20–26.

20) Bahram, M., Vanderpool, D., Pent, M., Hiltunen, M., andRyberg, M. (2018) The genome and microbiome of aDikaryotic fungus (Inocybeterrigena, Inocybaceae) rev-Ealed by metagenomics. Environ Microbiol Rep 10:155–166.

21) Benucci, G.M.N., and Bonito, G.M. (2016) The truffle micro-Biome: species and geography effects on bacteria associ-Ated with fruiting bodies of hypogeous Pezizales. MicrobEcol 72: 4–8

UGC-CARE List

UGC-CARE List

You searched for **"0022-3301"**. Total Journals : **1**

Search: [   ]

Sr.No.	Journal Title	Publisher	ISSN	E-ISSN	UGC-CARE coverage years	Details
1	The Journal of Oriental Research Madras (print only)	The Kuppuswami Sastri Research Institute	0022-3301	NA	from June-2019 to Present	View

Showing 1 to 1 of 1 entries

Previous   1   Next

Home

UGC

Search

Study of Antibacterial Activity of Chrysopogon zizanioids (vetiver) and its Anti-venom Potential Aspect

Article · April 2020

4 authors, including:

Tanmay Ghosh
Dinabandhu Andrews College university of calcutta
77 PUBLICATIONS **214** CITATIONS

SEE PROFILE

Mohan Kumar Biswas
Visva Bharati University
118 PUBLICATIONS **525** CITATIONS

SEE PROFILE

Study of Antibacterial Activity of *Chrysopogon zizanioids* (vetiver) and its Anti-venom Potential Aspect

Tanmay Ghosh[*1], **Mohan Kumar Biswas**[2], **Debokinandan Maity**[3] **and Pradyut Dutta**[4]

Department of Microbiology,
Dinabandhu Andrews College, Baishnabghata, South 24 Parganas (South), Kolkata - 700 084, West Bengal, India

A B S T R A C T

Chrysopogon zizanicides is a well-known medicinal plant use in several purpose. The plant extract of vetiver grass use as perfumery purpose, antibacterial agent, healing wound. This plant extract is very effective and safe. The vetiver root extracts are prepared by methanol, ethanol, chloroform, hexane solvents. The extract are evaporated and stored at 4°C in an airtight container. The antibacterial activity of vetiver roots extracts was determined. Here well diffusion method is used to determine the activity of vetiver root extract. The inhibitory concentration of the extracts 50 mg/ml, 100 mg/ml, 200 mg/ml, 400 mg/ml are tested by dilution broth method. The Ampicillin was used as positive control of bacteria. The DMSO (dimethyl sulfoxide) 10ml were used as blind control. The highest zone of inhibition was observed in 400 mg/ml vetiver roots methanol extract against *Staphylococcus aureus.* The lowest zone of inhibition observed in 50 mg/ml vetiver roots Chloroform extract against *Klebsiella pneumoniae.*

Key words: *Chrysopogon zizanioids, Klebsiella pneumoniae*, Antibacterial activity, Anti-venom potential

Vetiver is native to Indian and it founds in wild state of Indian's tropical area. The vetiver is improtant for various economic purposes including vetiver oil, extract from roots, and the roots are dug out from the wild resources of India and several countries Caribbean sea, Haiti, Island are the good source of vetiver oil in the world and also Java, Japan, China, India (Sangeeta and Stella 2012, Singh and Maheswari 1983). *Chrysopogon zizanioids* is scientific name, common name is vetiver and it is popularly known as Khus grass in India. The vetiver oil is used in medicine purposes and also in perfumery purposes. In India, roots are used for mats, hand fans, baskets and different types of things, which are used in our daily life (Jain 1991, Lavania 2003). Various part of this grass is used in various ailments such as burns, fever (Chomochalow 2001), epilepsy, scorpion sting (Fengche *et al*. 2003, Gaikwad *et al*. 2012),

snakebite (Yoganarasimhan 1996) etc. It is considered that the most effective step for snakebite victims is to immediate administration but use of plant extract against snake venom is more scientific for last 20 years. The plant extracts of vetiver having property to neutralize snake venom. This plant extract directly combated the enzyme of snake venom without cells of immune-system producing effector cells. The root extract used for headache and toothache to get a good effect. The leaf paste is used in lumbago, rheumatism. The leaf juice vapours have a great effect in malarial fever and the rots are used to relief from acidity. Vetiver oil is dark brown in colour and have earthy odour (Balasankar *et al*. 2013). Vetiver oils have different types of beauty and emotional effects. It helps in control the activity of sebaceous oil glands and this normalize the oily skin and clear acnes, and a good effect on cut, wound inflamed skin. It is used in depression (Trease and Evans 1989), insomnia, anxiety, stress (Sofowara 1993, Luqman *et al*. 2005), tension and nervousness to cure (Anon 1976). When it is in dilute state it smells like sandal oil.

[1*]Tanmay Ghosh, Department of Microbiology (tanmay.tanmay.ghosh780@gmail.com), Dinabandhu Andrews College, Baishnabghata, South 24 Parganas, (South), Kolkata - 700 084, West Bengal

[2]Department of Plant Protection, Palli Siksha Bhavana, Visva - Bharti, Sriniketan, Birbhum, West Bengal

[3,4]Department of Microbiology, Rabindra Mahavidyalaya, Champadanga, Hooghly, West Bengal

MATERIALS AND METHODS

Collection of plant

The plant material roots are collected from Damodar riverside, Pursurah, Hooghly, West Bengal, India and identified by Prof. Tanmay Ghosh, Champadanga, Hooghly, West Bengal, India. First roots were washed with cold water and then hot water. Then roots were dried at room temperature for 4 to 5 days. Then roots were crushed to fine powder by mixer grinder and store in air tight container.

Fig 1 Vetiver roots

Preparation of root extract

Chloroform extract: 6 gm of dried powder of roots was mixed with 18 ml of chloroform in a conical flask and shake for 10 minutes. Then the flask was bind with tissue paper and rubber band. Some holes were made for pass the air and then kept in room temperature for 2-4 days for evaporate.

Ethyl acetate extract: 6 gm of dried powder of roots was mixed with 18 ml ethyl acetate in a conical flask and then it shaken for 10 minutes. Then the flask is bind with tissue paper and rubber band. Some holes were made for air can pass through it and then kept in room temperature for 2-4 days for evaporate.
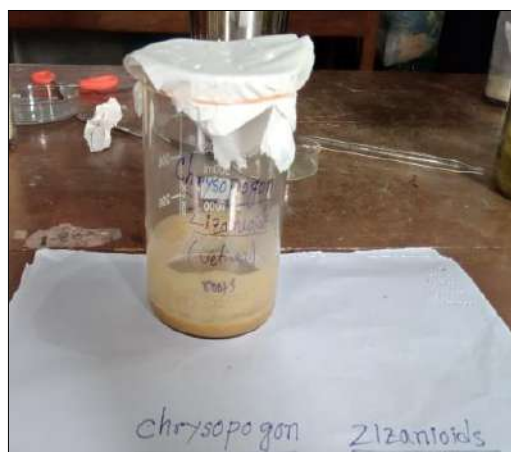
Fig 2 Methanol extract

Methanol extract: 6 gm of dried powder of roots was mixed with 18 ml methanol in a conical flask and shake for 10 minutes. Then the flask is bind with tissue paper and rubber band. Some holes were made for air can pass through

it and then kept in room temperature for 2-4 days for evaporate.

Hexane extract: 6 gm of dried powder of roots was mixed with 18 ml of Hexane in a conical flask and then it shaken for 10 minutes. Then the flask is bind with tissue paper and rubber band. Some holes were made for air can pass through it and then kept in room temperature for 2-4 days for evaporate.

Preparation of extract concentration: Four concentrations were made 50mg/ml, 100mg/ml, 200mg/ml, and 400mg/ml from each of the four-extract chloroform, ethyl acetate, methanol, and hexane. In every case, 4gm of extract was mixed with 10ml DMSO to prepare 400mg/ml stock concentration. Other three concentrations were made by adding extra DMSO with stock in other test tube.

Collection of bacterial cultures: The pathogenic bacterial cultures were brought from Microbial Type Culture Collection (MTCC) Chandigarh, India. The cultures are *Staphylococcus aureus* (MTCC 3159), *Bacillus subtilis* (MTCC 1825), *Salmonella typhi* (MTCC 3215), *Escherichia coli* (MTCC 3878), *Pseudomonas aeruginosa* (MTCC 6324), *Klebsiella pneumonia* (MTCC 5123). The cultures maintain in nutrient agar slants and stored in 4°C.

Collection of antibiotic: The antibiotic Ampicillin is collected from the Champadanga market, Hooghly, West Bengal.

Bacterial inoculum preparation: Bacterial inoculum was prepared by 0.1 ml of cultures was transferred to the agar plates and incubated at $37^{\circ C}$ for 4-5 hours.

Antimicrobial activity determination

Well diffusion method: Well diffusion method was carried on Muller Hinton agar plates. Petri plates were prepared by 20 ml of Muller Hinton agar and allowed to solidify for the use in susceptibility test against bacteria. Plates were dried and 0.1ml of inoculum was poured and spread and allow to dry. After the cork borer agar well made on agar plate and poured different concentration of extract into the well. The Ampicillin used as positive control and DMSO 0.10ml was used as negative or blind control. The plates were incubated at 37°C for 24 hours in incubator. The zone of inhibition were examine and measured (Cromwell *et al*. 1955, Rao and Suseela 2014).

Phytochemical estimation: The various solvent extracts (aqueous, ethanol, chloroform, methanol, hexane) are subjected to phytochemical screening to test the presence of metabolites such as carbohydrate, alkaloids, flavonoids, tannins, steroids, saponins, terpenoids and phlobatannins, proteins by using standard procedure (Hasan *et al*. 2009, Ates and Turgay 2009).

Carbohydrates test: Some drops of vetiver solvent extract are heated with Fehling's A and B solution.

Observed an orange red precipitate indicates the presence of carbohydrates.

Alkaloids test: Vetiver solvent extract was mixed with 2ml of Wagner's reagent. Observed a Reddish brown coloured precipitate which indicates the presence of alkaloids.

Flavonoids test: 4ml dilute ammonia solution was added to a portion of the crude extract followed by addition of concentrated H_2SO_4. The presences of flavonoids were observed in each extract as a result of yellow colouration. The yellow colouration disappeared on standing.

Steroids test: 2ml of acetic anhydride was added to 0.5 ml extract of plant sample with 2ml H_2SO_4. The colour will be changed from violet to blue or green in samples indicates the presence of steroids.

Saponins test: Roots extract was mixed with 4ml of distilled water in a test tube and it was shake well and add some drops of olive oil. The formation of stable foam, which observes to indicates the presence of saponins.

Terpenoids test: The 4ml of extract was mixed properly with 2ml of chloroform and 3ml of concentrated H_2SO_4 was carefully added along the sides of the test tube to from a layer. For the presence of terpenoids a reddish brown colour of interface was observe. That means it show positive result.

Phlobatannins test: To test the presence of pholobatannins each solvent extract was boiled with 2% aqueous HCl. It was observe that red precipitate, which ensure the presence of phlobatannins.

Proteins test: Add 3ml of Biuret reagent to 3ml of extract, shake well, and warm it on water bath. Observed a red or violet colour indicates the presence of proteins.

Table 1 Qualitative phytochemical analysis of *Chrysopogon zizanioids* extracts

Test	Aqueous	Ethanol	Chloroform	Methanol	Hexane
Carbohydrate	+	+	+	+	+
Alkaloids	+	+	-	+	-
Flavonoids	+	+	+	+	-
Steroids	+	+	+	+	-
Saponins	+	+	+	+	-
Terpenoids	+	+	+	+	-
Phlobatannins	-	-	-	-	-
Proteins	+	+	+	+	+

RESULTS AND DISCUSSION

The antibacterial activity of vetiver roots extract has been performed against six bacteria are *Staphylococcus aureus, Bacillus subtilis, Salmonella typhi, Escherichia coli, Pseudomonas aeruginosa, Klebsiella pnemoniae*. The test result shown on the bellow (Table 2).

Table 2 The antimicrobial activity of Methanol extract against different bacteria

Concentration	Zone of inhibition (mm)					
	Staphylococcus aureus	*Bacillus subtilis*	*Salmonella typhi*	*Escherichia coli*	*Pseudomonas aeruginosa*	*Klebsiella pneumoniae*
400 mg/ml	31.3 ± 1	31.2 ± 1	31.2 ± 1	31.2 ± 1	30.4 ± 1	30.0 ± 1
200 mg/ml	27.6 ± 1	27.0 ± 1	28.0 ± 1	28.4 ± 1	28.2 ± 1	28.2 ± 1
100 mg/ml	26.4 ± 1	22.5 ± 1	26.2 ± 1	26.2 ± 1	26.0 ± 1	26.2 ± 1
50 mg/ml	23.2 ± 2	22.2 ± 1	24.8 ± 2	24.8 ± 1	24.2 ± 1	24.2 ± 2
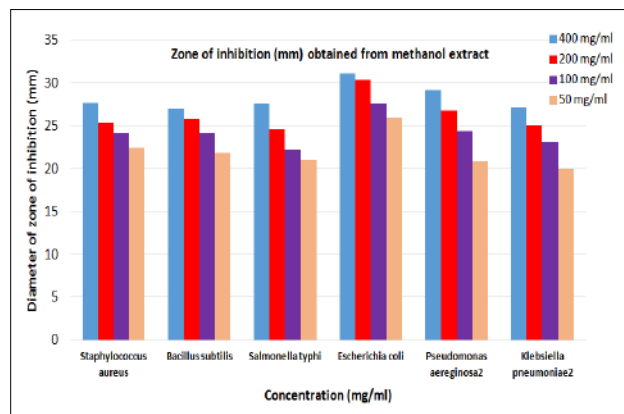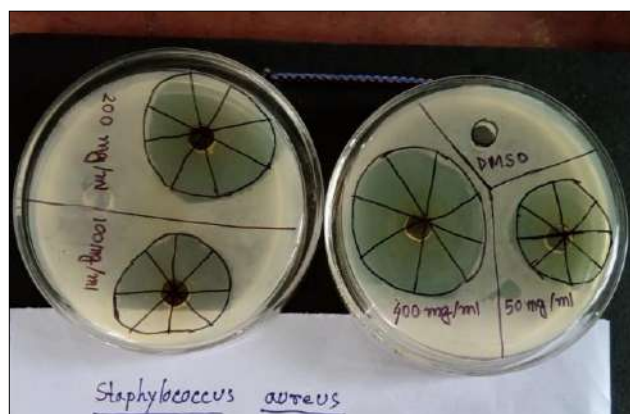
Fig 3 Zone of inhibition (mm) obtained from methanol extract *Staphylococcus aureus*

Staphylococcus aureus highest zone of inhibition was 31.3 ± 1mm at 400 mg/ml methanol extract and the lowest antibacterial activity shows on *Bacillus subtilis* zone of inhibition was 22.2 ± 1mm at 50 mg/ml methanol extract.

Table 3 The antimicrobial activity of chloroform extract against different bacteria

Concentration	Zone of inhibition (mm)					
	Staphylococcus aureus	*Bacillus subtilis*	*Salmonella typhi*	*Escherichia coli*	*Pseudomonas aeruginosa*	*Klebsiella pneumoniae*
400 mg/ml	28.0 ± 1	29.7 ± 1	29.2 ± 2	29.4 ± 2	28.8 ± 2	29.2 ± 1
200 mg/ml	26.5 ± 1	27.7 ± 1	28.0 ± 1	27.2 ± 1	27.2 ± 1	27.2 ± 1
100 mg/ml	23.7 ± 1	26.5 ± 1	27.1 ± 2	25.8 ± 2	26.2 ± 2	22.7 ± 2
50 mg/ml	23.2 ± 2	25.5 ± 1	24.0 ± 1	23.2 ± 1	24.2 ± 1	20.0 ± 1
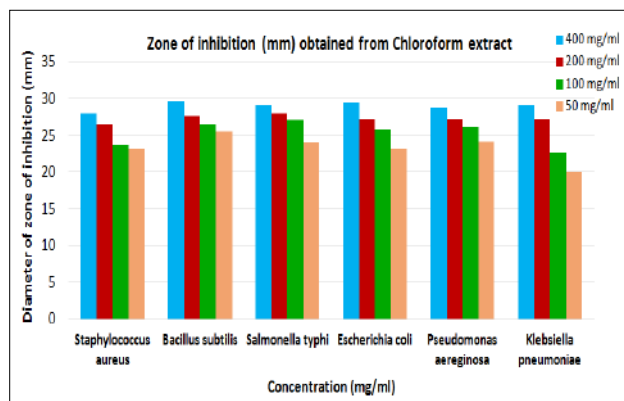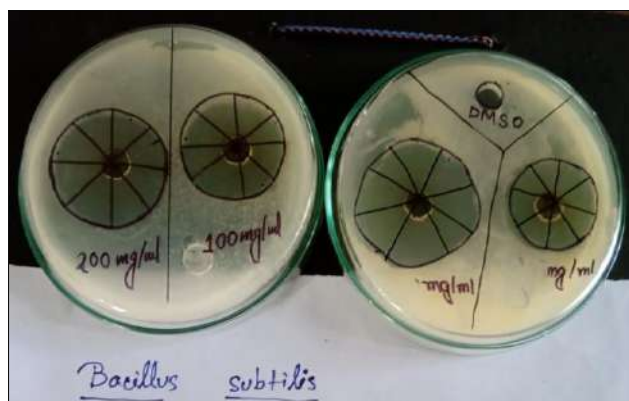
Fig 4 Zone of inhibition (mm) obtain from chloroform extracts of *Bacillus subtilis*

The highest antibacterial activity against *Bacillus subtilis* zone of inhibition was 29.7 ± 1mm at 400 mg/ml chloroform extract and the lowest activity shows on *Klebsiella pneumoniae* at 50 mg/ml zone of inhibition was 20.0 ± 1mm.

Table 4 The antimicrobial activity of ethanol extract against different bacteria

Concentration	Zone of inhibition (mm)					
	Staphylococcus aureus	*Bacillus subtilis*	*Salmonella typhi*	*Escherichia coli*	*Pseudomonas aeruginosa*	*Klebsiella pneumoniae*
400 mg/ml	28.7 ± 10	28.5 ± 1	28.8 ± 2	28.2 ± 1	28.2 ± 1	28.2 ± 2
200 mg/ml	25.8 ± 10	27.2 ± 1	26.0 ± 1	26.2 ± 1	24.4 ± 1	25.8 ± 2
100 mg/ml	23.4 ± 10	25.7 ± 1	25.0 ± 2	25.1 ± 2	22.4 ± 2	23.4 ± 1
50 mg/ml	21.2 ± 10	24.2 ± 1	24.4 ± 2	23.0 ± 1	20.4 ± 1	21.2 ± 1
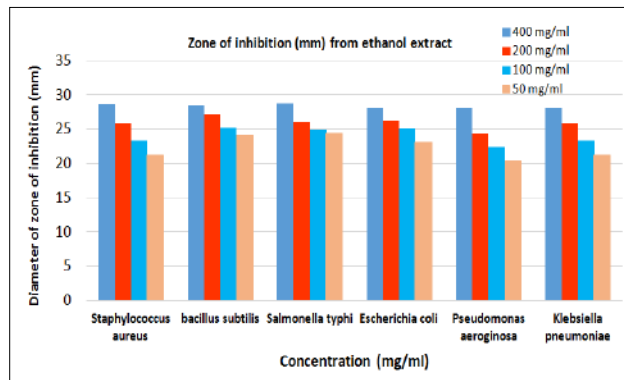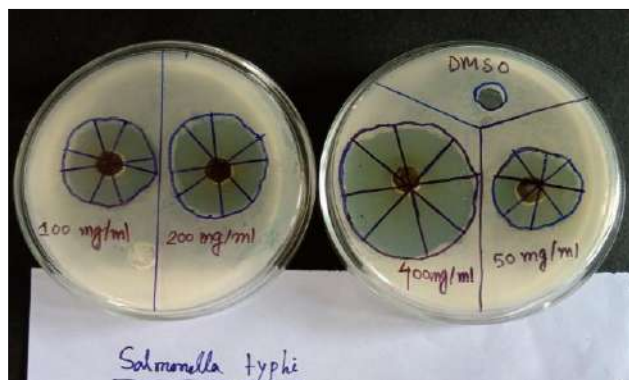
Fig 5 Zone of inhibition (mm) from ethanol extract of *Salmonella typhi*

The highest antibacterial activity against *Salmonella typhi* zone of inhibition was 28.8 ± 2mm at 400 mg/ml of ethanol extract and the lowest activity shows on *Pseudomonas aeruginosa* at 50 mg/ml zone of inhibition was 20.4 ± 1 mm.

Table 5 The antimicrobial activity of hexane extract against different bacteria

Concentration	Zone of inhibition (mm)					
	Staphylococcus aureus	*Bacillus subtilis*	*Salmonella typhi*	*Escherichia coli*	*Pseudomonas aeruginosa*	*Klebsiella pneumoniae*
400 mg/ml	27.7 ± 1	27.0 ± 1	27.6 ± 1	31.2 ± 2	29.2 ± 2	27.2 ± 1
200 mg/ml	25.4 ± 1	25.8 ± 1	24.6 ± 1	30.4 ± 2	26.8 ± 2	25.1 ± 1
100 mg/ml	24.2 ± 1	24.2 ± 2	22.2 ± 1	27.6 ± 1	24.4 ± 2	23.1 ± 1
50 mg/ml	22.4 ± 1	21.8 ± 1	21.0 ± 1	26.0 ± 1	20.8 ± 2	20.0 ± 1
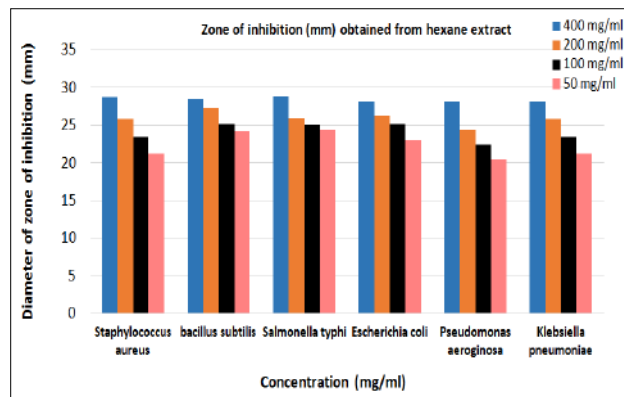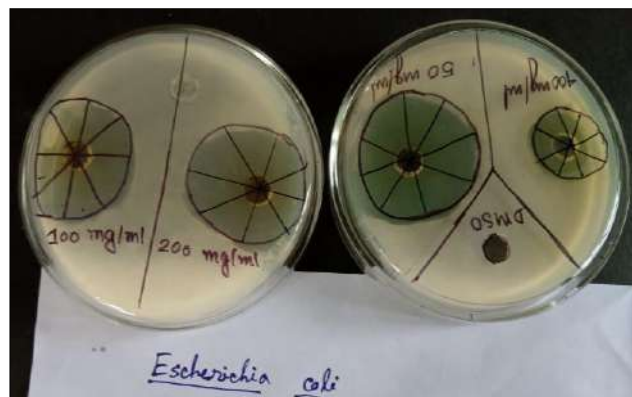
Fig 6 Zone of inhibition (mm) obtained from hexane extract of *Escherichia coli*

Vetiver roots extract of hexane 400 mg/ml shows the highest antibacterial activity against *Escherichia coli* zone of inhibition was 31.2 ± 2 mm and the lowest activity shows on *Klebsiella pneumonia* at 50 mg/ml zone of inhibition was 20.0 ± 1 mm.

From the (Table 1) found that vetiver roots extract of methanol 400 mg/ml concentration shows highest antibacterial activity against positive result namely bacteria was *Staphylococcus aureus* zone of inhibition was 31.3±1mm and the lowest antibacterial activity shows on *Bacillus subtilis* zone of inhibition was 22.2±1mm at 50 mg/ml methanol extract. From the (Table 2) found that vetiver roots extract of Chloroform 400mg/ml concentrations shows highest antibacterial activity against *Bacillus subtilis* zone of inhibition was 29.7±1mm and the lowest activity shows on *Klebsiella pneumoniae* at 50mg/ml zone of inhibition was 20.0±1mm. From the (Table 3) found that vetiver roots extract of Ethanol 400mg/ml shows highest antibacterial activity against *Salmonella typhi* zone of inhibition was 28.8±2mm and the lowest activity shows on *Pseudomonas aeruginosa* at 50mg/ml zone of inhibition was 20.4±1mm. From the (Table 4) found that vetiver roots extract of Hexane 400mg/ml shows the highest antibacterial activity against *Escherichia coli* zone of inhibition was 31.2±2mm and the lowest activity shows on *Klebsiella pneumonia* at 50mg/ml zone of inhibition was 20.0±1mm.

Anti-venom potential of Chrysopogon zizanioids (vetiver)

Chrysopogon zizanioids a grass of poaceae group having several medicinal role like antibacterial role use as perfume, wound healing and the most important factor is it have an anti-venom potential. There was few of active compound found from plant few of which shows anti-venom activity. Snake venom contains several neurotoxin enzyme, cardiotoxin, and peptide, protein of low molecular mass with specific chemical and biological activities. The different enzyme of snake decreases the WBC, RBC, platelets and haemoglobin of victim. It was observed that after treated with plant extract of vetiver orally the WBC, RBC, platelets and haemoglobin count increased. The plant extract of vetiver induced increased in antioxidant activities, regeneration, and reparative process of cellular membrane.

Plants contain natural substance that can promote health. From the study, it can be concluded that the vetiver root extract has the antibacterial activity. Different bacteria are treated with antibiotic Ampicillin by same concentration of plant extract. Plant extract inhibits the bacteria more than Ampicillin, this concentration was more effective than antibiotic so, we can use this extract for medicinal purpose for a good result. These methods are safe that may be applied to control the growth and spread out of microorganisms directly to the infection site and it is nontoxic for humans and gave an effective result in small concentrations. This could be further exploited by in vivo study to increase the overall activity. The presence of phytochemical compounds has antibacterial effects.

Plants are produces thousands of metabolites, many of them have medicinal uses. About 80-82% of the world, population depends upon the plant or plant extract, and this is a major source of health care. In this study, we are studying the effects of vetiver roots extract against human pathogenic bacteria such as *E. coli*, *Bacillus subtilis, Salmonella typhi* etc. Different part of this grass is used in various ailments such as burns, fever, epilepsy, scorpion sting, snakebite etc. The root extract used for headache and toothache. The leaf is used in lumbago, rheumatism. The leaf juice vapours have a great effect in malarial fever and the rots are used to relief from acidity. Vetiver roots extract

have antimicrobial effect on pathogenic bacteria. Vetiver oil prevents the growth of *Staphylococcus aureus*. It cause abortion, it show a good activity on nerve problems and circulating problems. If roots oil applied to the skin, its cure Lice, repelling insects and it is helps to tress free. Vetiver roots oil have Inhalation activity, and a good effects in Joint and muscle pain (rheumatism) and in trouble to sleeping (insomnia). Vetiver roots oil use for scalp and hair. The anti-inflammatory and antiseptic properties and helps in scalp ailments like eczema, psoriasis, and even dandruff. Vetiver oil has a high antioxidants power and helps in boosting immune system by removing various types of toxins from body and fighting free radicals. Vetiver oil helps to clear acne and acne marks too. The plant extract of *Chrysopogno zizanioids* is effective in neutralizing the toxic effect of envenomation. So in future, we can elucidate on it, research on it so that we can know more about the anti-venom activity of vetiver. We should found active compound that so anti-venom activity so that this plant extract can use in medicinal field.

LITERATURE CITED

Ananthanarayanan R and Paniker C K J. 2000. *Textbook of Microbiology*. 6th Edition. Orient Longman private limited. pp 7-22.

Anon V. 1976. *The Wealth of India*. Publication of Information Directorate, Council of Scientific and Industrial Research, New Delhi, India. **10**: 451-457.

Ates D A and Turgay E. Antimicrobial activities of various medicinal and commercial plant extracts. *Turkish Journal of Biology* **27**: 157-162.

Balasankar D, Vanilarasu K, Preetha P S, Rajeswari S, Umadevi M and Bhowmk D. 2013. Traditional and medicinal uses o vetiver. *Journal of Medicinal Plants Studies* **1**: 19-20.

Chomochalow N. 2001. The utilization of vetiver as medicinal and Aromatic plants with special reference to Thailand. PRVN, Tech Bull No2001/1 ORDPB Bangkok.

Cromwell B T, Peach K and Tracey M V. 1955. *Modern Methods of Plant Analysis*. Springer Verlag Berlin, Edition 1st. **3**: 373-374.

Dahiya P and Purkayastha S. 2012. Phytochemical analysis and antibacterial efficacy Dill seed oil against multi drag resistant clinical isolates. *Asian Journal of Pharmaceutical and Clinical Research* **5**: 62-64.

Fengche, Xiwang and Hyunjinkim. 2003. Antioxident, Antiocarcinogenic and Termiticidalactivites of vetiver oil. Department of Biochemistry and Genetics, Clemson University, SC-29634.

Gaikwad R S, Rajendra B K, Kulkarni A U, Gaikwad D R and Panchal V H. 2012. *In vitro* antimicrobial activity of crude extracts of Jatropha species. *Current Botany* **3**: 09-15.

Hasan A, Rahman S, Deeba F and Mahmud S. 2009. Antimicrobial activity of some plant extracts having hepatoprotective effects. *Journal of Medicinal Plant Research* **3**(1): 20-23.

Jain S K. 1991. *Dictionary of Indian Folk Medicine and Ethanobotany*. Deep Publication, New Delhi. pp 193-223.

Lavania U L. 2003. Vetiver root oil and its utilization. Tech Bulletin No 203/1, PRVN<ORDPB, Bangkok, Thailand.

Luqman S, Srivastava S, Darokar M P, Khanuja S P S. 2005. Pharma Biol43, 2005, 732-736.

Mishra S, Sharma S K, Mohapatra S and Chauhan D. 2013. An overview on *Vetiverzizanioies*. *Research Journal of Journal of Pharmaceutical Bio Chemistry Science* **4**: 777-780.

Rao R R and Suseela M R. 2014. *Vetiveria zizanioides* (LINN.) Nasha multipurpose eco-friendly grass of India. National Botanical Research Institute Lucknow, India. pp 439-442.

Sangeeta D and Stella D. 2012. Screening of antimicrobial activity of Vetiver extracts against certain pathogenic microorganisms. *International Journal of Pharma Bio Archeology* **3**: 197-203.

Singh K K and Maheswari J K. 1983. Traditional phytotherapi amongst the tribals of Varanasi district U.P. *Journal of Economical and Tax Botany* **4**: 829-838

Sofowara A. 1993. *Medicinal Plants and Traditional Medicine in Africa*. 2nd Edition. Ibadan (Nigeria): Spectrum Books Ltd.

Trease G E and Evans W C. 1989. *Pharmacognosy*. 13th Edition. London (UK): ELBS Oxford University Press.

Yoganarasimhan S N. 1996. *Medicinal Plants of India*. Karnataka: Interline Publishing. **1**: 359.

UGC-CARE List

UGC-CARE List

You searched for **"0976-1675"**. Total Journals : **1**

Search: [   ]

Sr.No.	Journal Title	Publisher	ISSN	E-ISSN	UGC-CARE coverage years	Details
1	Research Journal of Agricultural Sciences- An International Journal	Centre for Advanced Research in Agricultural Sciences	0976-1675	2249-4538	from September-2019 to Present	View

Showing 1 to 1 of 1 entries

Previous 1 Next

Home

○ UGC

🔍 Search

SAVITRIBAI PHULE PUNE UNIVERSITY

4. Date Palm: An Antimicrobial Agent with Its Nutritional Benefits

Tanmay Ghosh

Department of Microbiology, Dinabandhu Andrews College, Baishnabghata, South 24 Parganas, Kolkata – 700084, West Bengal, India.

ABSTRACT

Date palm trees are known as the population of the Eastern zone, give a portion of food for human antibiotic resistant. Most of the natural products have an antibacterial effect which use in clinical purpose. Date palm is an essential nourishing source in the Eastern zone. The extraction of Date seed powder was done by using hexane and ethyl acetate solvents. Date palm pits show antibacterial activities on two bacteria (Klebsiella pneumonia and Escherichia coli) and its function is reducing the side effect on neurotransmitter are that brain, hormone, testosterone, muscle of male albino rats. The proper aim of this study is to use the nuclei dates as an antimicrobial on Klebsiella pneumonia and Escherichia coli than the pursuit of perfect antibiotics. It was identified that the methanol extract of date seed contains alkaloids, carbohydrates, phenols, flavonoids, protein, amino acid, tannins, and anthraquinones except steroids, saponins, and cardiac glycoside. The metabolic extract of date seed has also shown moderate inhibition on the growth of Gram-positive and Gram-negative bacteria.

KEYWORDS

Resistant, Extraction, Neurotransmitter, Pursuit.

Introduction

Antibiotic resistance is a biggest threat to global health. Approximately 5 lakhs persons of the world are infected by drug-resistant tuberculosis and Human Immuno Deficiency Virus. The Date palm (Phoenix dactylifera L.) is one of the most noteworthy sources of food which have antibacterial potential. The percentage of reducing sugar is 88% in varieties and the percentage of non-reducing sugars is 3.82%. Dates are contemplated a tonic. The flower of the plant is used as economic source. Date palm cures male fertility by increasing sperm number and quality.

Dates (Phoenix dactylifera) are an important nutritional source in many countries of the world, because of the Dates containing different nutrients such as carbohydrates, vitamins, and minerals. Date palm flowering and fruiting were also valuable. All of the Dates accommodate the various qualitative and quantitative amounts of phytochemicals.

Natural phytochemicals, such as phenolic compounds, which need for human health, showed the most antioxidant activity. In addition to antioxidant activity that helps the study demonstrated the antibacterial activity of phenols and phenolic compounds. The seed powder is also used as a coffee replacement and as food involves.

The seed also yields essential fatty acids such as Palmitic acid, Stearic acid, Lauric acid, Oleic acid, and Linoleic acid. As Date Palm have different anticancer property, it is important to phytochemical analysis of Date Palm to find what agent is actually responsible for its function. The aim of the study is to profile to Date palm fruits and leaves and evaluate their functional significance such as antimicrobial activities to their nutritional benefits.

Taxonomic Position:

Kingdom: Plantae
Clade: Tracheophytes
Clade: Angiosperms
Clade: Monocots
Clade: Commelinids
Order: Articles
Family: Arecaceae
Genus: Phoenix
Species: P. dactylifera

Fig 1: Date Palm

Materials and Methods:

The Date seed was extracted by using Ethyl acetate and Hexane.

Collection of seeds:

Design Implementation

- The Date seed (Phoenix dactylifera) was selected for the study of antimicrobial activity and phytochemical analysis. The seeds were collected from the fruit market in Arambagh, West Bengal, India. Phoenix dactylifera seeds were collected. First seeds were washed with cold water and then with hot water. Then seeds were dried in room temperature at 37 degree Celsius for 7-10 days.

Then seeds were air dried and powdered. Date seed powder of 200g was added to 400ml hexane and incubated in a shaker at room temperature. After 24 h incubation, the solvent was filtered from the mixture and the powder was dried and used again for extraction using 400 ml ethyl acetate by incubating for 24 h in a shaken. The solvent was filtered and stored in a bottle.

Fig 2: Date Palm Seed

Fig 3: Seed Extracts of Date Palm

Site of Experiments:

The whole experiments were carried out in the laboratory room of Rabindra Mahavidyalaya, Champadanga, Hooghly, and West Bengal, India.

Collection of Microorganisms:

The tested microorganisms are Escherichia coli and Klebsiella pneumonia.

Preparation of Different Seed Extracts

Benzene Extract:

About 5 g of dried seeds were taken and powdered to store. Then dispersed in 25 ml of benzene solution and shake it for 10 minutes. Then used with paper and tied with the rubber band. Few holes were made in the paper air circulation and took it in room temperature at 370C, maintenance for 4 days.

Hexane Extract:

About 5 g of dried seeds were taken and powdered to store. Then dispersed in 25 ml of hexane solution and shake in for 10 minutes. Then used with paper and tied with the rubber band. Few holes were made in the paper air circulation and took it in room temperature at 370C, maintenance for 4 days.

Chloroform Extract:

About 5 g of dried seeds were taken and powdered to store. Then dispersed in 25 ml of chloroform solution and shake in for 10 minutes. Then used with paper and tied with the rubber band. Few holes were made in the paper air circulation and took it in room temperature at 370C, maintenance for 4 days.

Ethyl acetate Extract:

About 5 g of dried seeds were taken and powdered to store. Then dispersed in 25 ml of ethyl acetate solution and shake in for 10 minutes. Then used with paper and tied with the rubber band. Few holes were made in the paper air circulation and took it in room temperature at 370C, maintenance for 4 days.

Methanol Extract:

About 5 g of dried seeds were taken and powdered to store. Then dispersed in 25 ml of methanol solution and shake in for 10 minutes. Then used with paper and tied with the rubber band. Few holes were made in the paper air circulation and took it in room temperature at 370C, maintenance for 4 days.

Preparation of Extract Concentration:

Four extracts of Benzene, Chloroform, Hexane and Ethyl acetate of 50µg/ml, 100µg/ml, 200µg/ml and 400µg/ml concentration were mixed respectively by using DMSO to analyse the extract which were most effective to inhibit bacteria.

Microbiological Assay by Agar Disc Diffusion Method:

For antimicrobial screening of seed extract Phoenix dactylifera 3 gm of each extracts were dissolved in 10 ml Dimethyl Sulphoxide (DMSO) from 25µg/ml, 75µg/ml, 150µg/ml, and 300µg/ml concentration were taken for the antimicrobial activity. A hollow tube was heated and inoculated in the agar plate. It was removed as soon as possible by making a good plate each plate was for only one DMSO control.

Medium:

3.8 gm. of Mueller Hinton Agar (MHA) was added to 100ml of water and autoclaved at 1210C for 20 minutes at 15 lb./inch square and transferred to a sterile Petri dish and clotted the agar at low temperature.

Inoculum and Incubation:

Inoculate 1gm of culture in Agar plate for 5min then as per previous concentrations kept it at 370C temperature for 24-48 hours. Measured the diameter of zone of inhibition area accurately. As per this method made each extracts of required concentrations.

Phytochemical Estimation:

Extract Preparation:

20 gm. of dry powder was dispersed in methanol, ethyl acetate, hexane, benzene, and chloroform in a conical flask and shaken for 20 hours. Then the precipitation was collected.

Phytochemical Studies:

The methods described by air borne microorganisms were used to test for the presence of ingredients in the test sample.

Test of Steroids:

About 10 ml of seed extract (methanol, ethyl acetate, hexane, benzene, chloroform) was taken to dry mass, and the mass is dissolved in 0.5 ml of chloroform.

Test for Alkaloids:

The seed extract (methanol, ethyl acetate, hexane, benzene, chloroform) was mixed with 5ml of 1% HCL on a steam bath. The solvent was filtered, and 1 ml of the filtrate was treated with Mayer's reagent.

Test for Tannins: About 1 g of plant extract powder was baked and 10 ml of distilled water added. The mix up was boiled 10 minutes. Two drops of 5% FeCl3 were added.

Test for Flavonoids: A drop of NH solution is added to the seed extract in a test tube for observation of yellow colour.

Test for Reducing Sugar: To 0.5 ml extract solution, 1 ml of water and 8 drops of Fehling's solution were added at hot water and then red precipitation was observed.

Fig 4: Zone of Inhibition of Escherichia Coli Against Ethanol Extract

Phytochemicals	*Phoenix dactylifera L.*		
	Chloroform	**Methanol**	**Ethanol**
Alkaloids	-	-	-
Anthraquinones	-	++	-
Catechin	-	+++	+++
Flavonoids	-	-	-
Glycosides	-	+++	+++
Phenolic groups	-	++	+
Reducing sugars	-	+++	-
Saponins	-	+++	+++
Tannins	-	+++	+++
Terpenoids	++	-	-

Table 1: Antibacterial activity of the *Phoenix dactylifera* in different bacteria for hexane extract in different concentration				
Test Microorganism	**Concentration(µg/ml)**			
	100µg/ml	**50µg/ml**	**25µg/ml**	**12.5µg/ml**
Escherichia coli	27.25±2.0	22.25±2.0	18.25±2.0	17.25±2.0
Bacillus subtilis	28.5±3.0	27.25±2.0	21.25±2.0	18.5±3.0
Staphylococcus aureus	36.1±3.0	27.4±3.0	23.7±2.0	20.0±2.0
Klebsiellapneumonia	32.3±2.0	28.2±3.0	23.0±2.0	19.5±2.0
Pseudomonas aeruginosa	34.5±2.0	31.7±2.0	26.0±2.0	21.2±3.0
Salmonella enteritis	29.0±2.0	26.2±3.0	23.1±2.0	19.4±3.0
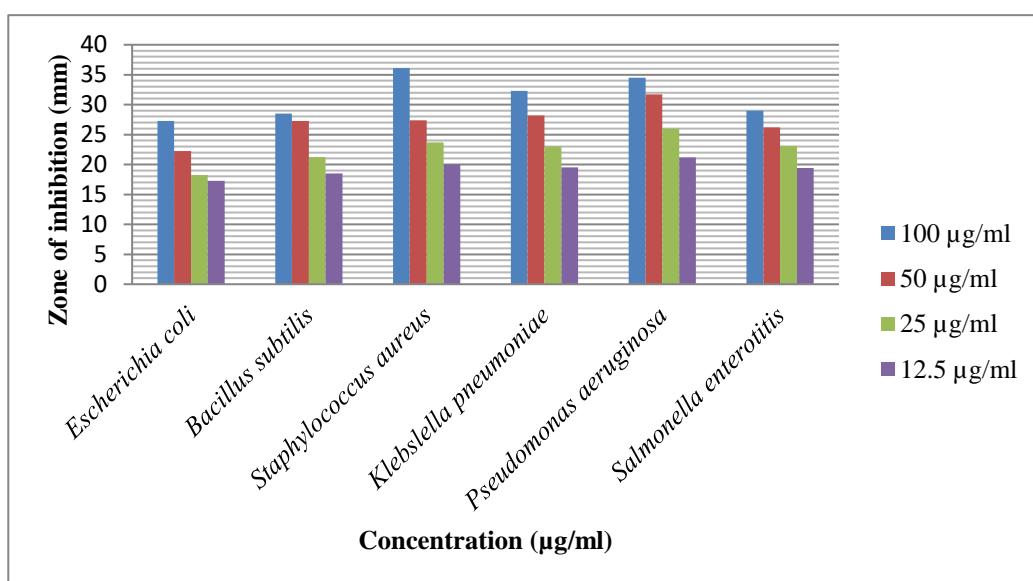
Fig 5: Antibacterial activity of the Phoenix dactylifera in different bacteria for hexane extracts in different concentration

Test microorganism	Concentration(µg/ml)			
	100 µg/ml	50 µg/ml	25 µg/ml	12.5 µg/ml
Escherichia coli	27.2±2.0	22.5±2.0	18.25±2.0	17.25±2.0
Bacillus subtilis	32.5±3.0	29..25±2.0	22.25±2.0	19.5±2.0
Staphylococcus aureus	35.1±3.0	29.4±3.0	26.7±2.0	21.0±0.0
Klebsiella pneumonia	32.3±2.0	28.0±2.0	25.0±2.0	22.5±2.0
Pseudomonas aeruginosa	32.5±2.0	30.7±2.0	28.0±2.0	21.2±3.0
Salmonella enteritis	33.0±2.0	30.2±3.0	28.1±2.0	18.4±3.0

Table 2: Antibacterial activity of the *Phoenix dactylifera* in different bacteria for chloroform extract in different concentration

Fig 6: Antibacterial activity of the Phoenix dactylifera in different bacteria for chloroform extract in different concentration.

Table 3: Antibacterial activity of the *Phoenix dactylifera* in different bacteria for benzene extract in different concentration				
Test microorganism	**Concentration(μg/ml)**			
	100 μg/ml	**50 μg/ml**	**25 μg/ml**	**12.5 μg/ml**
Escherichia coli	27.2±2.0	22.5±2.0	18.25±2.0	17.25±2.0
Bacillus subtilis	32.5±3.0	29..25±2.0	22.25±2.0	19.5±2.0
Staphylococcus aureus	35.1±3.0	29.4±3.0	26.7±2.0	21.0±0.0
Klebsiella pneumonia	32.3±2.0	28.0±2.0	25.0±2.0	22.5±2.0
Pseudomonas aeruginosa	32.5±2.0	30.7±2.0	28.0±2.0	21.2±3.0
Salmonella enteritis	33.0±2.0	30.2±3.0	28.1±2.0	18.4±3.0

Fig 7: Antibacterial activity of the Phoenix dactylifera in different bacteria for benzene extract in different concentration

Table 4: Antibacterial activity of the *Phoenix dactylifera* in different bacteria for ethyl acetate extract in different concentration				
Test microorganism	**Concentration(µg/ml)**			
	100 µg/ml	**50 µg/ml**	**25 µg/ml**	**12.5 µg/ml**
Escherichia coli	37.2±2.0	32.5±2.0	28.25±2.0	24.25±2.0
Bacillus subtilis	42.5±3.0	39.25±2.0	32.25±2.0	29.5±2.0
Staphylococcus aureus	44.1±3.0	39.4±3.0	36.7±2.0	33.4±0.0
Klebsiella pneumonia	41.3±2.0	38.0±2.0	35.0±2.0	32.5±2.0
Pseudomonas aeruginosa	35.3±2.0	33.7±2.0	28.0±2.0	25.2±3.0
Salmonella enteritis	43.0±2.0	35.2±3.0	33.1±1.0	29.9±3.0
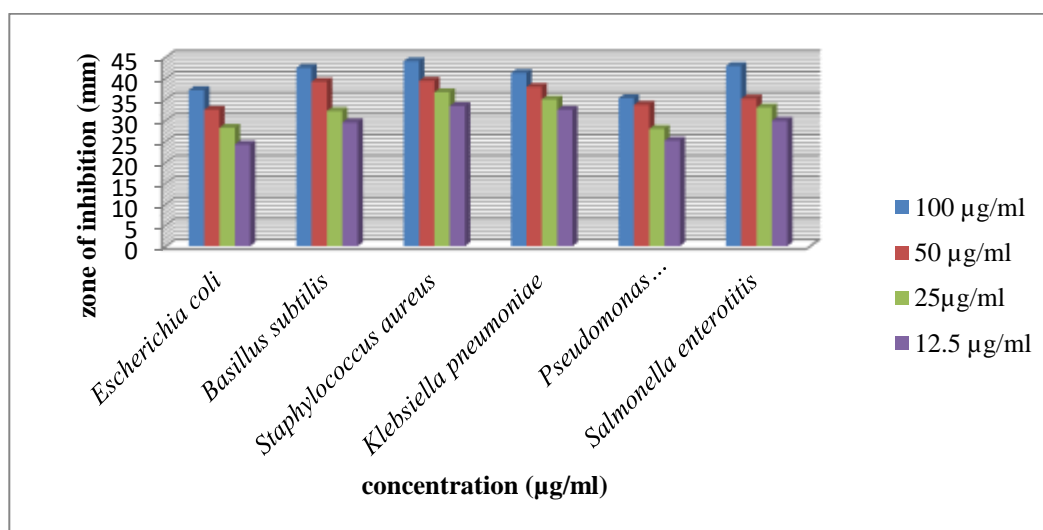
Fig 8: Antibacterial activity of the Phoenix dactylifera in different bacteria for ethyl acetate extract in different concentration

Conclusion:

Many plants, their fruits, and their seeds have many medicinal values that help in our health and other purposes. The study on Date seeds extract shows many antibacterial activities on different bacteria. The antibiotics treated to resist many bacteria, ampicillin, the plant extract as the same concentrations inhibit many bacteria. In this research, we observed the result of phytochemicals in my study. It is an inference that Phoenix dactylifera L. seed powders contain the chemical constituents like alkaloids, saponins, flavonoids, terpenoids, glycosides, steroids and phenolic compounds in this plant seed. However, it recommended that further work can be carried out to isolate the bioactive constituents in Phoenix dactylifera L.

Sing various extraction solvent with a view characteristics the presence of chemical such as the plant seed. This plant seed plays an important role in the fields of pharmaceutical and medicine and also treats infectious disease among the plant the best result respectively.

Future Aspects:

As plants have no side effects for human health, it can be used in treatment of many diseases. Date seeds are found useful in treating blood sugar related problems, diabetes, and related complications. According to recent research, Date seeds have shown potential for protective effects against early diabetic complications of both liver and kidney. Date seed oil is obtained from Date seeds through a Soxhlet extraction technique. Date seed oil is mainly composed of the four fatty acids namely oleic, linoleic, Lauric, and Palmitic acid. Listed below are some of the well-known health benefits of using Date seed oil. Some people use Date seeds as an additive to coffee. Add Date syrup into the warm water with lemon and drink as a tea or infused water. Try to make healthy bread spread. Just blend Date syrup with honey or Jaggery. Use this instead of jam.

Add Date powder into your smoothies or juices. Add Date palm seed powder into your baking dishes like cookies, cakes, etc. Add Date syrup while making the salad dressing for extra health benefits.

References:

1. Ali-Mohamed, A. Y., &Khamis, A. S. H. (2004). Mineral ion content of seeds of six cultivars of Bahraini date palm (Phoenix dactylifera). Journal of Agricultural and Food Chemistry, 52, 6522e6525.
2. Al-Farsi, M., & Lee, C. Y. (2008). Optimization of phenolic and dietary fiber extraction from date seeds. Food Chemistry, 108, 977e985.
3. Al-Farsi, M., Alasalvar, C., Morris, A., Baron, M., &Shahidi, F. (2005). Compositional and sensory characteristics of three native sun-dried dates (Phoenix dactylifera L.) varieties grown in Oman. Journal of Agricultural and Food Chemistry, 53, 7586e7591.
4. Al-Farsi, M., Alasalvar, C., Al-Abid, M., Al-Shoaily, K., Al-Amry, M., & Al-Rawahy, F. (2007). Compositional and functional characteristics of dates, syrups, and their by-products. Food Chemistry, 104, 943e947.
5. Al-Hooti, S., Sidhu, J. S., &Qabazard, H. (1998). Chemical composition of seeds dates fruit cultivars of the United Arab Emirates. Journal of Food Science and Technology, 35, 44e46.
6. Ali, B. H., Bashir, A. K., & Alhadrami, G. (1999). Reproductive hormonal status of rats treated with date pits. Food Chemistry, 66, 437e441.
7. Besbes, S., Blecker, C., Deroanne, C., Bahloul, N., Lognay, G., Drira, N., et al. (2004). Phenolic, tocopherol, and sterol profiles. Journal of Food Lipids, 11, 251e265.
8. Bouaziz, M. A., Besbes, S., Blecker, C., Wathelet, B., Deroanne, C., &Attia, H. (2008). Protein and amino acid profiles of Tunisian DegletNour and Aligdate palm fruit seeds. Fruits, 63, 37e43.
9. Caponio, F., Alloggio, V., & Gomes, T. (1999). Phenolic compounds of virgin olive oil: Influence of paste preparation techniques. Food Chemistry, 64, 203e209.

10. Devshony, S., Eteshola, A., &Shani, A. (1992). Characterization and some potential application of date palm (Phoenix dactilifera L.) seeds and seeds oil. Journal of American Oil Chemists Society, 69, 595e597.

11. Elgasim, E. A., Alyousef, Y. A., & Humeida, A. M. (1995). The possible hormonal activity of date pits and flesh fed to meat animals. Food Chemistry, 52, 149e152.

12. FAO (2010). Statistical Databases; http://faostat.fao.org, accessed October 24, 2010.

13. Guo, C., Yang, J., Wei, J., Li, Y., Xu, J., & Jiang, Y. (2003). Antioxidant activities of peel, pulp, and seed fractions of common fruits as determined by FRAP assay. Nutrition Research, 23, 1719e1726.

14. Hamada, J. S., Hashim, I. B., & Sharif, A. F. (2002). Preliminary analysis and potential uses of date pits in foods. Food Chemistry, 76, 135e137.

15. Hussein, A. S., Alhadrami, G. A., & Khalil, Y. H. (1998). The use of dates and date pits in broiler starter and finisher diets. Bioresource Technology, 66, 219e223.Costa LG, Giordano G, Furlong CE. Pharmacological and dietary modulators of paraoxonase

16. (PON1) activity and expression: the hunt goes on. Biochem Pharmacol. 2011; 81(3):337–44. doi:
10.1016/j.bcp.2010.11.008. [PMC free article] [PubMed] [CrossRef] [Google Scholar]

17. Costa LG, Richter RJ, Li WF, Cole T, Guizzetti M, Furlong CE. Paraoxonase (PON 1) as a biomarker of susceptibility for organophosphate toxicity. Biomarkers. 2003; 8(1):1–12. DOI: 10.1080/13547500210148315. [PubMed] [CrossRef] [Google Scholar]

18. Aviram M. Introduction to paraoxonases. J Lipids. 2012; 2012:1–3. doi: 10.1155/2012/687273. [PMC free article] [PubMed] [CrossRef] [Google Scholar]

19. Androutsopoulos VP, Kanavouras K, Tsatsakis AM. Role of paraoxonase 1 (PON1) in organophosphate metabolism: implications in neurodegenerative diseases. ToxicolApplPharmacol. 2011;
256(3):418–24. DOI: 10.1016/j.taap.2011.08.009. [PubMed] [CrossRef] [Google Scholar]

20. Al-Khayri, J., &Naik, P. (2017). Date palm micro propagation: Advances and applications. Ciência E Agrotecnologia, 41(4), 347–358. Doi:10.1590/1413-70542017414000217 [CrossRef], [Web of Science ®], [Google Scholar]

21. Al-Sayyed, H. F., Takruri, H. R., &Shomaf, M. S. (2014). The effect of date palm fruit (Phoenix dactilifera L.) on 7, 12-dimethylbenzene (α) anthracene (DMBA)-induced mammary cancer in rats. Research Opinions in Animal & Veterinary Sciences, 4(1), 11–18. [Google Scholar]

22. Barghini, P., Di Gioia, D., Fava, F., &Ruzzi, M. (2007). Vanillin production using metabolically engineered Escherichia coli under non-growing conditions. Microbial Cell Factories, 6, 1475–2859. DOI:10.1186/1475-2859-6-13 [CrossRef], [Web of Science ®], [Google Scholar]

23. Bellakhdar, J. (1997). Moroccan traditional pharmacopeia: Ancient Arabic medicine and popular knowledge. Paris Ibis Press (Eds). [Google Scholar]

24. El Hadrami, A., Daayf, F., & El Hadrami, I. (2011). Secondary metabolites of the date palm. In S. M. Jain, J. M.Al-Khayri, & D. V. Johnson (Eds.), Date palm biotechnology (pp. 653–674). Netherlands: Springer. [CrossRef], [Google Scholar]

25. Gaceb-Terrak, R. (2010). Contribution to the knowledge of interactions dates palm (Phoenix dactilifera L.) and the causal agent of beyond (Fusariumooxysporumfsp albinism by phytochemical analysis of lipids and phenylpropanoids. Ph.D. thesis,

University of Sciences and Technology HouariBoumediene,Algiers, Algeria. (in French) [Google Scholar]

26. Hazzouri, K. M., Flowers, J. M., Visser, H. J., Khierallah, H. S., Rosas, U., Pham, G. M., et al. (2015). Whole-genome re-sequencing of date palms yields insights into the diversification of a fruit tree crop. Nature Communications, 6, 8824. DOI:10.1038/ncomms9824 [CrossRef], [PubMed], [Web of Science ®], [Google Scholar]

27. Trigui, M., Hsouna, A. B., Tounsi, S., & Jaoua, S. (2013). Chemical composition and evaluation of antioxidant and antimicrobial activities of Tunisian Thymelaeahirsuta with special reference to its mode of action. Ind. Crop Production, 41, 150–157. DOI:10.1016/j.indcrop.2012.04.011 [CrossRef], [Web of Science ®], [Google Scholar]

28. WHO Global Strategy for Containment of Antimicrobial Resistance. (2001). [eBook] Worldhealthorganization. p.70.https://www.who.int/drugresistance/WHO_Global_Strategy_English.pdf [Google Scholar]

29. World Health Organization. (2018). Antimicrobial resistance. [online] http://www.who.int/news-room/fact-sheets/detail/antimicrobial-resistance [Google Scholar]

30. Doha, M. A, and Al-Okbi, S.Y. (2004). In vivo evaluation of the antioxidant and anti-inflammatory activity of different extracts of date fruits in adjuvant arthritis. Polish Journal of food and nutrition sciences. 13:397-402. Dunham, M.W., and Miya, T.S. (1967). A note on a simple apparatus for detecting neurological deficits in rats and mice. J Am Pharm Assoc Am Pharm Assoc (Baltim) 1967; 46:208-9. El-Moggy, S. A.; Abdel-Aziz, S. A.; Al-Shanawany, M. and Omar, A. (1991). The gonadotropic activity of Palmae in mature male rats. Alexandrina. J. Pharmac Sci.5:156-159.

31. Fayadh, J. M., and Al-Showiman, S.S. (1990). Chemical composition of date palm (Phoenix dactylifera L.). J.Chem.Soc.Pak., 12:84-103. Glowinski, J., and Iversen, L. L. (1966). Regional studies catecholamines in the rat brain .I. The disposition of [3H] norepinephrine, [3H] dopamine, and [3H] dopa in various regions of the brain. J. Neurochem., 13:655-669.

32. Gu, L.; Kelm, M. A.; Hammer stone, J. F.; Beecher, G.; Holden, J.; Haytowitz, D. and Prior, R.L. (2003). Screening of foods containing proanthocyanidins and their structural characterization using LCMS/ MS and histolytic degradation. J. Agric. Food Chem, 51: 7513-7521

33. Harris, H. F. (1900). On the rapid conversion of hematoxylin into haematin staining reactions. J.Appl.MicroscopicLab.Methods 3:777Hasenekoglu, (1990). Laboratory Techniques for Micro fungi, Atatürk University, Erzurum, Turkey, p .66. Hess, R. A.;

34. Buick D.; Lee K. H. (1997). A role for estrogens in the male reproductive system. Nature; 390: 509-12.

35. Hill, H. B. (1971). Principles of medical statistics, 9TH ed, Oxford Univ.

36. Ishida, O.; John, F.K. (2005). The anti-cancer activity of polysaccharide prepared from Libyan dates (Phoenix dactylifera L.) on ethanol-induced gastric ulcer in rats. J.Ethnopharmacol., 98:313-317.

37. Jassim, S.A.A, and Naji, M. A. (2007). In vitro Evaluation of the Antiviral Activity of an Extract of Date Palm (Phoenix dactylifera L.) Pits on a Pseudomonas Phage. Evidence-based Compl. and Alt. Medicine 70: 57-62.

38. Kostyuk, V. A; Potapovich A. I and Strigunova E. N. (2004). Experimental evidence that flavonoid metal complexes may act as mimics of superoxide dismutase. Arch BiochemBiophys; 428: 204-8.
39. Lee, G. Y; Jang, H. I.Hwang, I. G.; Rhee, M. S. (2009). Prevalence and classification of pathogenic Escherichia coli isolated from fresh beef, poultry, and pork in Korea. J. Food Microbiol. 134: 196-200.
40. Mahran, G.H.; Abdel-Wahab, S. M. and Attia, A. M. (1976). A phytochemical study of date palm pollen.Planta Med; 29: 171-5.
41. Mansouri, A.; Embarek, G.; Kokkalou, E. and Kefalas, P (2005). Phenolic profile and antioxidant activity of the Algerian ripe date palm fruit (Phoenix dactylifera). Food Chem. 89: 411-420
42. Miura, T.; Ohta, T.; Miura, C.I. and Yamauchi, K (2003). Complementary deoxyribonucleic acid cloning of spermatogonial stem cell renewal factor. Endocrinology; 144: 5504-10.
43. Mohamed, B.A.; Nabil, A.H., and Hanan, A.S. (2008). Protective effects of extract from dates (Phoenix Dactylifera L.) and ascorbic acid on thioacetamide-induced hepatotoxicity in rats.IranianJ.Pharm.Res. 7:193-201.
44. Nadkarni, K. M. (1976). Editor. Indian MateriaMedica Mumbai: Bombay Popular PrakashanPvt.Ltd.Narnia, K.; Li, M.; Jaroszynski. L. (2004). Stem cell-based therapeutically approach of male infertility by teratocarcinoma derived germ cells.
45. Hum Mol Genet; 13: 1451-60. Park, C.O. (1998). The effects of methylprednisolone on prevention of brain edema after experimental moderate diffuse brain injury in rats comparison between dosage, injection time, and treatment methods. Yonsei. Med. J. 39(5):395-403.
.

Research Journal of Agricultural Sciences Phytochemical Screening and In-vitro Evaluation of the Antibacterial Potential of Leaf Extract of Eucalyptus globulus against some Pathoge…

Article · March 2020

2 authors:

Sandipan Chatterjee
SURI VIDYASAGAR COLLEGE
21 PUBLICATIONS   372 CITATIONS

SEE PROFILE

Tanmay Ghosh
Dinabandhu Andrews College university of calcutta
77 PUBLICATIONS   214 CITATIONS

SEE PROFILE

Phytochemical Screening and *In-vitro* Evaluation of the Antibacterial Potential of Leaf Extract of *Eucalyptus globulus* against some Pathogenic Bacteria

Sandipan Chatterjee[1] and Tanmay Ghosh*[2]

[1]Department of Botany, Suri Vidyasagar College, Suri, Birbhum - 731 101, West Bengal, India
[2]Department of Microbiology,
Dinabandhu Andrews College, Baishnabghata, South 24 Parganas, (South), Kolkata - 700 084, West Bengal, India

A B S T R A C T

Plants are healthy and natural resource of life. In particular, medicinal plants are of great importance with endless therapeutic properties useful for curing various diseases with an advantage of being natural. The present study is to evaluate the qualitative estimation of phytochemicals and antimicrobial activity of ethyl acetate, hexane, chloroform, methanol extracts of leaves of *Eucalyptus globulus* against the following microorganisms: *Bacillus subtilis*; *Enterococcus faecalis*; *Staphylococcus aureus*; *Proteus vulgaris*; *Escherichia coli* and *Klebsiella pneumoniae*. The process was carried out by agar well diffusion method. The extracts were poured into the wells at different concentrations like 25mg/ml, 75mg/ml, 150mg/ml and 300mg/ml. After incubation zones of inhibition were observed. As the concentrations of extract increased the activity also increased and thus the zone of inhibition too increased. Among four extracts, zone of inhibition was best in ethyl acetate extract. In case of *Staphylococcus aureus*, the ethyl acetate extract (300 mg/ml) showed maximum zone of inhibition 46.0 ± 2.0mm, while in case of *Klebsiella pneumoniae*the hexane extract (25 mg/ml) showed minimum zone of inhibition 15.0 ± 0.0 mm. Ethyl acetate extract is more effective than other three extract. Hence *Eucalyptus globulus* can be used in developing drugs and medicines against various activities of bacteria. Study has also been shown the presence of various phytochemical constituents such astannin, saponin, glycosides, alkaloids, phenolic content in the leaf of *Eucalyptus globulus*. The *Eucalyptus globulus* oil has antimicrobial activity against different microorganisms and appears to be a viable alternative as germicidal agent hence, further investigation is recommended. Its antimicrobial activity was evaluated against six bacterial species, including food poisoning and spoilage bacteria and human pathogens. The results of the antibacterial activity tests revealed that the leaf extract of *E. globulus* has rather a strong antibacterial activity, especially against *Staphylococcus aureus.*

The spread of drug resistant pathogens is one of the most serious threats to successful treatment of microbial diseases and growing problem of antimicrobial resistance has become a important public health concern worldwide and especially in developing countries as a result of overuse and misuse of antibiotics (Ruifang *et al*. 2006). Many plants are used for different industrial purposes such as food, drugs, and perfumery manufacturing (Zarai *et al*.

2012). Their use has taken place since ancient times, and despite many of them were substituted by synthetic ones, the demand for natural products is increasing (Guillén *et al*. 1996). They have been shown to possess antibacterial, antifungal, antiviral, insecticidal and antioxidant properties (Burt 2004, Kordali *et al*. 2005). Aromatic and medicinal plants which push in the whole world have therapeutic virtues, because they produce certain bioactive molecules

*Corresponding author: Tanmay Ghosh, Department of Microbiology, Dinabandhu Andrews College, Baishnabghata, South 24 Parganas, Kolkata - 700 084, West Bengal
e-mail: tanmay.tanmay.ghosh780@gmail.com | **Contact:** +91- 9732188299

which react with other organisms in the environment, inhibiting bacterial or fungal growth. The molecules that can inhibit pathogens and have little toxicity to host cells are considered candidates for developing new antimicrobial drugs (Manika *et al*. 2013, Sheeba 2012). It has been used in folk medicine throughout the world as anti-inflammatory, analgesic and antipyretic remedies for the symptoms of respiratory infections, such as cold, flu, and sinus congestion (Rahimi-Nasrabad *et al*. 2012, Shahwar *et al*. 2012). Essential oils from Eucalyptus species have been approved as food additives, and the extracts also widely used in modern pharmaceutical, and cosmetic industries (Arfao *et al*. 2013). In addition, the oil possesses a wide spectrum of biological activity including antimicrobial, fungicidal, insecticidal/ insect repellent, herbicidal, acaricidal and nematicidal (Singla *et al*. 2014). *Staphylococcus aureus* is one of opportunistic pathogens that cause severe and life threatening infections in immune-compromised patients and is mainly responsible for post-operative wound infection, toxic shock syndrome and food poisoning (Bachir and Benali 2012, Chambers and Deleo 2009). The main purpose of this research article is to focus on the antimicrobial activities of *Eucalyptus globulus* and the mechanisms involved in the inhibition of these pathogenic microorganisms. Eucalyptus leaf extracts have been used to treat influenza, chest problems, and skin rashes while their vapor is inhaled to fight inflammation. They contain great amounts of essential oil up to 3.5% (w/w), which is used in medicine, aromatherapy and perfumes. The essential oil extracted from leaves of *Eucalyptus globulus* is known to be a rich source of traditional medicines and it is widely used to treat pulmonary tuberculosis, diabetes, asthma and also used as disinfectant, antioxidant agent, and antiseptic agent especially in the treatment of respiratory tract infections and certain skin diseases (Song *et al*. 2009). Eucalyptus essential oils is use to reduce mycelial growth and inhibit spore production and germination (Nezhad *et al*. 2009).

Taxonomy, botanical and ecological characteristics of the plant
Taxonomical position

Kingdom	:	Plantae
Clade	:	Angiosperms
Clade	:	Eudicots
Clade	:	Rosids
Order	:	Myrtales
Family	:	Myrtaceae
Genus	:	*Eucalyptus*
Species	:	*E. globulus*

Fig 1 *Eucalyptus globules* Plant

They have a wide distribution in tropical and sub-tropical areas, and are cultivated in many other climates (Salari *et al*. 2006). The Tasmanian blue gum, southern blue gum or blue gum Eucalyptus (*Eucalyptus globulus*), is an evergreen, typically grow from 30 to 55 m tall. The tallest currently known specimen in Tasmania is 90.7 m tall (MobileReference 2008), up to 200cmin diameter (Louppe

2008). Root system is deep and spreading. Bark smoothish, mottled gray, brown, and greenish or bluish, peeling in long strips, at base becoming gray, rough and shaggy, thick and finely furrowed; inner bark light yellow within thin green layer. Leaves alternate, drooping on flattened yellowish petioles 1.5-4 cm long, narrowly lanceolate, 10-30 cm long, 2.5–5cm wide, mostly curved, acuminate at tip, acute at base, entire, glabrous, thick, leathery, with fine straight veins and vein inside marlin, shiny dark green on both surfaces (Little 1983) (Fig 1). Flowers bisexual, regular, whitish; pedicel up to 8 mm long; flower buds top-shaped, divided into an oboconical, ribbed or smooth hypanthium, and flattened, hemispherical operculum having a short knob, stamens numerous, ovary inferior, 3-5 –celled (Louppe 2008). The fruits are woody and range from 1.5 to 2.5 cm in diameter. Numerous small seeds are shed through valves (numbering between 3 and 6 per fruit) which open on the top of the fruit. It produces roots throughout the soil profile, rooting several feet deep in some soils. They do not form taproots (MobileReference 2008). The Eucalyptus tree consists with fragrant foliage rich in oil glands and is an excellent source of commercially important eucalyptus oil that finds extensive use in pharmaceutical, perfumery and industry (Brooker and Kleinig 2006). The most important type of eucalyptus oil is the medicinal type derived primarily from *Eucalyptus globulus* Labill (Tasmanian blue gum) (Barceloux 2012).

MATERIALS AND METHODS

Selection and collection of herb material

The plant *Eucalyptus globulus* was selected for study of antibacterial activity and phytochemical analysis. The plant *Eucalyptus globulus* was collected randomly from the garden of Rabindra Mahavidyalaya, Champadanga, Hooghly, West Bengal, India. The identity of the plant specimen was confirmed by Prof. Tanmay Ghosh and Prof. Joydip Ghosh at the Department of Microbiology, Champadanga, Hooghly.

Preparation of herb material

First leaves were washed with cold water and then with hot water. The leaves were air-dried in the shade at the ambient temperature and stored in double-layer paper bags at the room temperature for 7-10 days, protected from the direct light, until further analysis. Then air dried leaves were crushed to fine powder by mixer grinder and store in air-tight bottles (Fig 2).

(A) Leaves ground to powder   (B) Extract obtained
Fig 2 Extract preparation

Preparation of different plant extract
Hexane extraction

5gm of air-dried powder of leaves was mixed with 30 ml of hexane in a conical flask and then kept on a rotary shaker for 15 mints. Then they were bind with tissue paper and rubber band. Some pores were made so that air can pass through it and then take room temperature for 3-5 days for evaporate.

Chloroform extraction

5gm of air-dried powder of leaves was mixed with 30 ml of chloroform in a conical flask and then kept on a rotary shaker for 15 mints. Then they were bind with tissue paper and rubber band. Some holes were made so that air can pass through it and then take room temperature for 3-5 days for evaporate.

Ethyl acetate extraction

5gm of air-dried powder of leaves was mixed with 30 ml of ethyl acetate in a conical flask and then kept on a rotary shaker for 15 mints. Then they were bind with tissue paper and rubber band. Some holes were made so that air can pass through it and then take room temperature for 3-5 days for evaporate.

Methanol extract

5gm of air-dried powder of leaves was mixed with 30 ml of methanol in a conical flask and then kept on a rotary shaker for 15 mints. Then they were bind with tissue paper and rubber band. Some holes were made so that air can pass through it and then take room temperature for 3-5 days for evaporate.

Preparation of extract concentration

Four concentrations (25mg/ml, 75mg/ml, 150mg/ml and 300mg/ml) were made from each of the four extracts (Benzene, Chloroform, Ethyl acetate, Methanol extract). In every case 3 gm of extract was mixed with 10ml DMSO (dimethyl sulfoxide) to prepare 300 mg/ml stock concentration. Then other three concentrations were made by adding extra DMSO with the Stock in other test tube.

Collection of microorganisms

Six bacterial species namely *Bacillus subtilis* (MTCC 441); *Enterococcus faecalis* (MTCC 439); *Staphylococcus aureus* (MTCC 737); *Proteus vulgaris* (MTCC 426); *Escherichia coli* (MTCC 443) and *Klebsiella pneumonia* (MTCC 432) were used in the present study. These strains of bacteria were purchased from Microbial Type Culture Collection (MTCC), Institute of Microbial technology (IM-TECH), Chandigarh, India. The bacterial strains were maintained in Muller Hinton Agar (MHA, pH-7.2) at 37°C.The stock culture slants were maintain at 4°C. Each culture was serially diluted ($10^{-1}–10^{-10}$) before spreading.

Collection of antibiotics

Two antibiotics, Ampicillin and Chloramphenicol were collected from a medical shop of Champadanga market, Hooghly, West Bengal.

Culture medium

3.8 g of Mueller Hinton Agar (MHA) was added to 100ml of distilled water and autoclaved at 121°C for 15 minutes at 15 lbs and poured in sterile petri plates up to a uniform thickness of approximately 4mm and the agar is allowed to set at ambient temperature and used.

Inoculums and incubation

0.1 ml of each bacterial culture was transferred to the respective agar plates. The inoculated plates were allowed to stand for 5 min, before making wells for different concentrations to be tested. The extracts of leaf of *Eucalyptus globulus* were loaded at different concentrations in the well on agar plate. Then bacterial cultures and incubated at 37°C for 24-48 hours in an incubator.

Testing of antimicrobial activity by agar well diffusion method

The antibacterial screening of leaf extract of *Eucalyptus globulus* was prepared by dissolving 3gm of each extract separately in 10ml Dimethyl Sulphoxide (DMSO). From this 25mg/ml, 75mg/ml, 150mg/ml, 300mg/ml concentration were taken for the analysis of antibacterial activity. Muller Hinton agar was use to check antimicrobial activity by well diffusion method. Autoclaved medium was poured in to petri plates in the laminar air flow hood. The microorganisms from 24 hrs old broth were spread on the cooled medium. A hollow tube of stainless steel borer of diameter 6-8 mm was heated and pressed above the inoculated agar plate. It was removed immediately by making a well in the plate. Eight plates were made for each microorganism and one wall (Two parts) made on each plate the entire surface at angle 180°. Two plate was for four type of concentration (25 mg/ml, 75 mg/m; 150 mg/ml, 300 mg/ml) of each extract of *Eucalyptus globulus*, two plate is for same type of concentration (as the leaf extract) of each type of antibiotic (Ampicillin, Chloramphenicol) and one for Control (by DMSO). Because we have to prove the extracts have large zone of inhibition than those antibiotics by this parallel study. These plates were incubated for 24-48 hrs.

Statistical analysis

After incubation the diameter of zone of inhibition around the well was measured using zone reader (Vennila and Udayakumar 2015). Corresponding 4 values of zones of inhibition for each concentration of *Eucalyptus globulus* extract were taken. The values so obtained were compared within the group (same concentration of extract) and with different groups (different concentrations of extract) for different bacteria and statistical analysis was done. Results obtained were analyzed statistically and values were expressed as Mean ± SD.

RESULTS AND DISCUSSION

The result of the present study showed significant antibacterial activity against each of six bacterial species namely *Bacillus subtilis* (MTCC 441); *Enterococcus faecalis* (MTCC 439); *Staphylococcus aureus* (MTCC 737);

Proteus vulgaris (MTCC 426); *Escherichia coli* (MTCC 443) and *Klebsiella pneumoniae* (MTCC 432). Crude extracts obtained from leaf of *Eucalyptus globulus* using different solvents like methanol, ethyl acetate, chloroform and hexane were screened for antibacterial activity against pathogenic bacteria.

In case of *Staphylococcus aureus*, the ethyl acetate extract (300 mg/ml) showed maximum zone of inhibition 46.0 ± 2.0 mm (Fig 3), while hexane extract (25 mg/ml) showed minimum zone of inhibition 18.0 ± 2.0 (Table 1).

Table 1 Antibacterial activity of various extract of *Eucalyptus globulus* against *Staphylococus aureus* (MTCC 737)

Concentrations (mg/ml)	Average zone (mm) of inhibition of various extract of*Eucalyptus globulus*			
	Ethyl Acetate	Methanol	Chloroform	Hexane
300	46.0 ± 2.0	43.2 ± 2.0	41.1 ± 1.0	39.0 ± 2.0
150	39.0 ± 1.0	37.1 ± 2.0	36.0 ± 2.0	33.1 ± 1.0
75	34.1 ± 1.0	32.0 ± 1.0	31.0 ± 1.0	27.2 ± 1.0
25	23.0 ± 2.0	20.2 ± 2.0	18.2 ± 1.0	18.0 ± 2.0
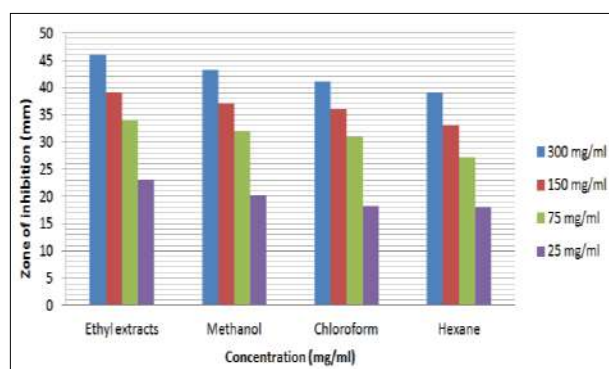
Fig 3 Antibacterial activity of ethyl acetate of *Eucalyptus globules* against *Staphylococus aureus*

In case of *Proteus vulgaris*, the ethyl acetate extract (300 mg/ml) showed maximum zone of inhibition45.0 ± 2.0 mm (Fig 4), while hexane extract (25 mg/ml) showed minimum zone of inhibition 19.2 ± 2.0 (Table 2).

Table 2 Antibacterial activity of various extract of *Eucalyptus globulus* against *Proteus vulgaris* (MTCC 426)

Concentrations (mg/ml)	Average zone (mm) of inhibition of various extract of *Eucalyptus globulus*			
	Ethyl Acetate	Methanol	Chloroform	Hexane
300	45.0 ± 2.0	44.0 ± 2.0	42.0 ± 2.0	37.0 ± 2.0
150	40 .1± 1.0	39.0 ± 1.0	37.2 ± 1.0	34.1 ± 1.0
75	36.0 ± 2.0	34.1 ± 1.0	33 .0 ± 1.0	31.0 ± 2.0
25	24.2 ± 2.0	22.0 ± 2.0	21.1 ± 2.0	19.2 ± 2.0
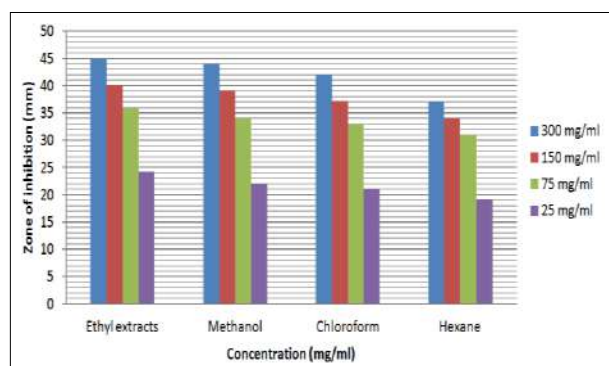
Fig 4 Antibacterial activity of ethyl acetate of *Eucalyptus globules* against *Proteus vulgaris*

In case of *Enterococcus faecalis*, the ethyl acetate extract (300 mg/ml) showed maximum zone of inhibition 43.0 ± 2.0 mm (Fig 5), while hexane extract (25 mg/ml) showed minimum zone of inhibition 17.0 ± 0.0 (Table 3).

Table 3 Antibacterial activity of various extract of *Eucalyptus globulus* against *Enterococcus faecalis* (MTCC 439)

Concentrations (mg/ml)	Average zone (mm) of inhibition of various extract of *Eucalyptus globulus*			
	Ethyl Acetate	Methanol	Chloroform	Hexane
300	43.0 ± 2.0	42.0 ± 0.0	40.2 ± 1.0	37.0 ±0.0
150	39.0 ± 1.0	36.2 ± 2.0	33.0 ± 0.0	31.2 ± 2.0
75	34.0 ± 0.0	32.0 ± 1.0	29.1 ± 2.0	27.1 ± 1.0
25	22.2 ± 1.0	20.0 ± 0.0	18.0 ± 1.0	17.0 ± 0.0
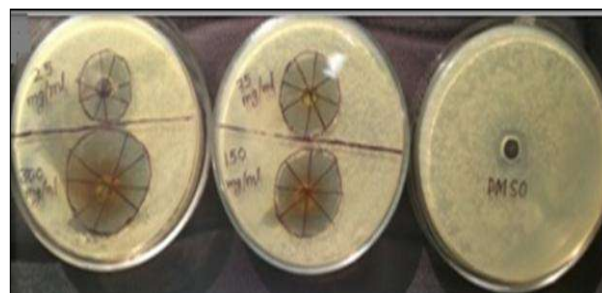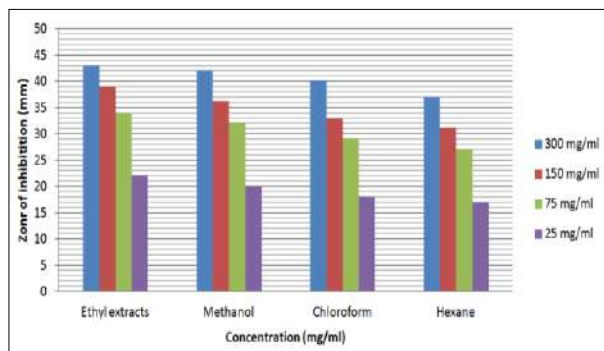
Fig 5 Antibacterial activity of ethyl acetate of *Eucalyptus globules* against *Enterococcus faecalis*

In case of *Escherichia coli*, the ethyl acetate extract (300 mg/ml) showed maximum zone of inhibition 42.0 ± 0.0 mm (Fig 6), while chloroform extract (25 mg/ml) showed minimum zone of inhibition 18.0 ± 0.0 (Table 4).

Table 4 Antibacterial activity of various extract of *Eucalyptus globulus* against *Escherichia coli*(MTCC 443)

Concentrations (mg/ml)	Average zone (mm) of inhibition of various extract of *Eucalyptus globulus*			
	Ethyl Acetate	Methanol	Chloroform	Hexane
300	42.0 ± 0.0	40.2 ± 1.0	36.0 ±0.0	34.0 ±0.0
150	35.2 ± 2.0	32.0 ± 0.0	29.2 ± 1.0	27.2 ± 1.0
75	34.1 ± 1.0	30.1 ± 2.0	28.1 ± 1.0	24.1 ± 2.0
25	21.0 ± 0.0	19.0 ± 1.0	18.0 ± 0.0	19.0 ± 0.0
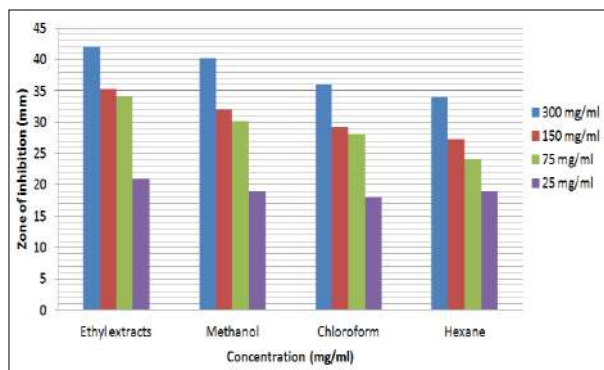
Fig 6 Antibacterial activity of ethyl acetate of *Eucalyptus globules* against *Escherichia coli*

In case of *Bacillus subtilis*, the ethyl acetate extract (300 mg/ml) showed maximum zone of inhibition 40.3 ± 1.0 mm (Fig 7), while hexane extract (25 mg/ml) showed minimum zone of inhibition 16.0 ± 0.0 (Table 5).

Table 5 Antibacterial activity of various extract of *Eucalyptus globulus* against *Bacillus subtilis* (MTCC 441)

Concentrations (mg/ml)	Average zone (mm) of inhibition of various extract of *Eucalyptus globulus*			
	Ethyl Acetate	Methanol	Chloroform	Hexane
300	40.3 ± 1.0	37.0 ±1.0	35.0 ±2.0	33.0 ±1.0
150	34.0 ± 0.0	31.2 ± 0.0	27.2 ± 0.0	25.2 ± 2.0
75	30.0 ± 0.0	27.1 ± 2.0	25.1 ± 1.0	23.1 ± 1.0
25	25.6 ± 1.0	19.0 ± 0.0	17.0 ± 0.0	16.0 ± 0.0
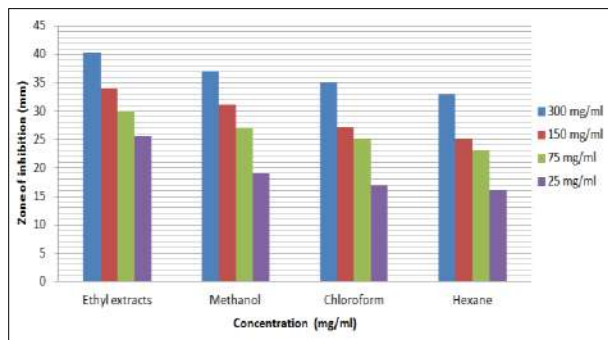
Fig 7 Antibacterial activity of ethyl acetate of *Eucalyptus globules* against *Bacillus subtilis*

Table 6 Antibacterial activity of various extract of *Eucalyptus globulus* against *Klebsiella pneumoniae* (MTCC 432)

Concentrations (mg/ml)	Average zone (mm) of inhibition of various extract of *Eucalyptus globulus*			
	Ethyl Acetate	Methanol	Chloroform	Hexane
300	36.5 ± 0.0	34.0 ±4.0	32.0 ± 3.0	30.0 ± 2.0
150	29.3 ± 3.0	27.2 ± 2.0	24.2 ± 2.0	22.2 ± 1.0
75	28.2 ± 2.0	24.1 ± 1.0	22.1 ± 2.0	19.1 ± 3.0
25	19.0 ± 2.0	15.0 ± 1.0	17.0 ± 3.0	18.0 ± 0.0
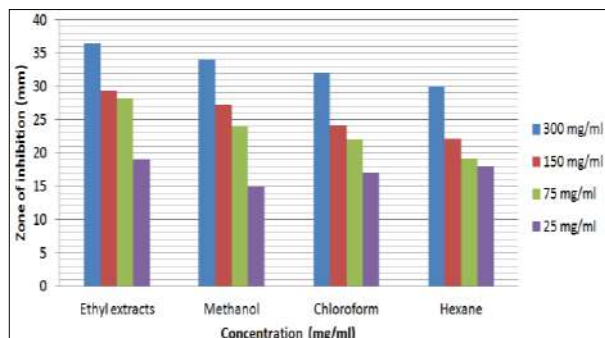
Fig 8 Antibacterial activity of ethyl acetate of *Eucalyptus globules* against *Klebsiella pneumoniae*

In case of *Klebsiella pneumoniae*, the ethyl acetate extract (300 mg/ml) showed maximum zone of inhibition 36.5 ±0.0 mm (Fig 8), while methanol extract (25 mg/ml) showed minimum zone of inhibition 15.0 ± 1.0 (Table 6). Mean zone of inhibition and standard deviation for each concentration and each bacterium was calculated for analysis.

In present investigation all the extracts of *Eucalyptus globulus* used for the study showed antimicrobial activity against Gram positive and Gram negative bacteria. Antibacterial activity was tested on Muller Hinton Ager (MHA) plates by agar cup method. Various concentrations of extracts were prepared. The whole process was tested against six species of bacteria, *Bacillus subtilis* (MTCC 441); *Enterococcus faecalis* (MTCC 439); *Staphylococcus aureus* (MTCC 737); *Proteus vulgaris* (MTCC 426); *Escherichia coli* (MTCC 443) and *Klebsiella pneumoniae* (MTCC 432) were taken for study. There was no zone of inhibition in the negative control by DMSO. The antibacterial efficacy of various solvent extracts of *Eucalyptus globulus* showed varied level of inhibition against the bacteria. The antibacterial activity of the various solvent extracts of leaf of *Eucalyptus globulus* against

bacterial isolates showed best results at the concentration of 300 mg/ml. *Eucalyptus globulus* leaves extract showed increasing zones of inhibition with increasing concentration against all bacteria. From the study, it can be concluded that the leaves extract of *Eucalyptus globulus* has the antibacterial activity. Each bacterium was treated with antibiotic ampicillin and chloramphenicol by same concentration as plant extract. Zones of inhibitions were larger in case of plant extract than antibiotics. Plant extract inhibits the bacteria more than ampicillin and chloramphenicol, this concentration was more effective than antibiotic so, we can use this extract for medicinal purpose for a good result. They are safe and sustainable methods that may be applied to control the growth of microorganisms directly to the infection site and nontoxic for humans and effective in small concentrations. Further investigations on the isolation and identification of bioactive components on the plant would help to ascertain its potency. This could be further exploited by in vivo study systems to increase the overall activity. The presence of phytochemical compounds exhibit antibacterial effects. Among four extracts Ethyl acetate is more effective and hexane is less effective. Highest antibacterial activity was observed against

Staphylococcus aureus (MTCC 737) and lowest antibacterial activity was observed against *Klebsiella pneumoniae* (MTCC 432).

Phytochemical estimation
Extract preparation

20 gm of air-dried powder was taken in 100 ml of each solvent (methanol, ethyl acetate, hexane, chloroform) in a conical flask, plugged with cotton wool and then kept on a rotary shaker. After 24 hours the supernatant was collected and the solvent was evaporated.

Phytochemical studies

The methods described by Harborne were used to test for the presence of the active ingredients in the test sample (Harborne and Baxter 1993).

Test for steroids

10 ml of plant extract (methanol, ethyl acetate, hexane, chloroform) was evaporated to a dry mass and the mass is dissolved in 0.5 ml of chloroform. Acetic anhydride [0.5 ml] and 2 ml of concentrated H_2SO_4 were added to before (Harborne and Baxter 1993).

Test for saponins

5 ml of the extract with 10 ml of water in a test tube was shaken for few minutes, and then a full mass of small bubbles formation was taken as an indication of the presence and absence of saponins.

Test for phenols

Equal volume of the extract was added to equal volume of $FeCl_3$, a deep bluish green solution was taken as a positive test for the presence of phenols.

Test for alkaloids

The plant extract (methanol, ethyl acetate, hexane, chloroform) [0.5 g] was stirred with 5 ml of 1% HCl on a steam bath. The solution obtained was filtered and 1 ml of the filtrate was treated with two drops of Mayer's reagent. The two solutions were mixed and made up to 100ml with distilled water (Harborne and Baxter 1993, Evans and Trease 1988).

Test for tannins

About 1 g of plant extract powder was weighed into a beaker and 10 ml of distilled water added. The mixture was boiled for five minutes. Two drops of 5% $FeCl_3$ were then added (Iyengar 1995).

Test for flavonoids

A few drops of 1% NH_3 solution is added to the plant extract [0.5 g] in a tube for observation of yellow coloration (Priyadarsini and Rani 2011).

Test for glycosides

5 ml of extract plus 25 ml of dilute H_2SO_4 were poured into a test tube. The mixture was boiled for 15 min, cooled and neutralized with 10% NaOH and 5 ml of Fehling A and B was added. Brick red precipitate is a positive test for the presence of glycosides.

Table 7 Display the presence/absence of different phytochemicals in the leaf of *Eucalyptus globulus*

Phytochemicals	Ethyl acetate	Hexane	Chloroform	Methanol
Tannin	+	+	+	+
Alkaloid	+	+	-	+
Flavonoid	+	+	+	+
Phenols	+	+	+	-
Steroid	+	+	+	+
Saponin	+	-	+	+
Glycosides	+	+	-	+

Traditional medicinal practice has been known for centuries in many parts of the world for the treatment of various diseases (Priyadarsini and Rani 2011). The use of antibiotics has revolutionized the treatment of various enteric bacterial infections. The result of phytochemical analysis of this plant showed that all the tested extracts have bioactive substances which display antimicrobial activity. For instance, tannins are known to be made up of phenols and phenolic compounds that have been used as disinfectant. Due to differences in geographical location of these plants, the phytochemical constituent can be greatly affected (Perianayagam and Pillai 2006). However, their indiscriminate use has led to an alarming increase in antibiotic resistance among microorganism, thus necessitating the need for development of novel antimicrobials. The present study may conclude that the leaves of *Eucalyptus globulus* possess various phytochemicals like alkaloid, saponin, flavonoid, protein and tannin in a high quality and possess various bioactive properties. Through the world *Eucalyptus globulus* is well recognized in different pharmacological practices and the presence of high quantities of those bioactive phytochemicals may attribute to its medicinal value. The bio-inductive study will be helpful for improving the yield of these metabolites. All this information leads us to conclude that leaves of *Eucalyptus globulus* harbours immense qualities and can future prove a pivotal role in the field of phytochemical research and developing drugs and medicines.

Future aspect

Scientific research and inventions have always been the thrust of mankind and is largely responsible for the standard of living he has today. Natural resources of a country are of primary importance for the economic development. Plants were in existence even before man came into existence. The importance of plants in the medical treatment cannot be overestimated. Hence, the global knowledge about Indian herbals will hopefully be enhanced by information on the evidence-base of these plants. The emerging field of herbal products industry holds a great potential to the economic development of the Indian region. There is an increasing trend of using plants as a source of food, medicine and perfumes. In conclusion, the results obtained in this study

indicated that the traditional plant, *Eucalyptus globulus* generally used as potential source for useful drugs like anti-inflammatory, anticancer, antimicrobial, insectifuge, nematicide, anticoronary, wound healing, hepatoprotective activities demonstrated broad spectrum antibacterial activity against bacterial isolates of both Gram negative and Gram-positive bacteria. So, further research is needed to isolate, identify, characterize and elucidate the structure of these bioactive compounds responsible for medicinal values of *Eucalyptus globulus*.

LITERATURE CITED

Arfao A T, Nola M, Djimeli C L, Nougang M E and Fokou J B. 2013. Cultivability of *Salmonella typhi*, *Vibrio cholerae* and enteropathogenic *E.coli* in water microcosm in the presence of *E. microcorys* leaves extract: effect of the concentration of leaves extract and incubation temperature. *International Journal of Research and Bioscience* **2**(4): 32-46.

Bachir R and Benali M. 2012. Antibacterial activity of the essential oils from the leaves of *Eucalyptus globulus* against *Escherichia coli* and *Staphylococcus aureus*. *Asian Pacific Journal of Tropical Biomedicine* 2012: 739-742.

Barceloux D G. 2012. *Medical Toxicology of Natural Substances: Foods, Fungi, Medicinal Herbs, Plants, and Venomous Animals*. John Wiley and Sons Edition.

Brooker M I H and Kleinig D A. 2006. *Field Guide to Eucalyptus*. Vol. 1. South-eastern Australia. Bloomings: Melbourne.

Burt S A. 2004. Essential oils: their antibacterial properties and potential applications in foods: A review. *Inter Journal of Food Microbiology* **94**: 223-253.

Chambers H F and Deleo F R. 2009. Waves of resistance: *Staphylococcus aureus* in the antibiotic erq. *Nat Review in Microbiology* **7**(9): 629-641.

Evans W C and Trease G E. 1988. Tratado de farmacognosia, 12th Eds. Nuev Federal University of Paraná, Caixa Postal 5336, CEP 80040-980.

Guillén M D, Cabo N and Burillo J. 1996. Characterization of the essential oils of some cultivated aromatic plants of industrial interest. *Journal of Science and Food Agriculture* **70**: 359-363.

Harborne J B and Baxter H. 1993. *Phytochemical Dictionary*. Taylor and Francis Washington DC, 1765.

Iyengar M A. 1995. *Study of Crude Drugs*. Manipal Power Press, Manipal, India. pp **8**: 2.

Kordali S, Kotan R, Mavi A, Cakir A, Ala A and Yildirim A. 2005. Determination of the chemical composition and antioxidant activity of the essential oil of *Artemisia dracunculus* and of the antifungal and antibacterial activities of Turkish *Artemisia absinthium*, *A. dracunculus*, *Artemisia santonicum* and *Artemisia spicigera* essential oils. *Journal of Agriculture and Food Chemistry* **53**: 9452-9458.

Little E L Jr. 1983. *Common fuel wood crops: A handbook for their identification*. McClain Printing Co: Parsons, WV.

Louppe D. 2008. *Timbers 1*. Plant resources of tropical Africa. PROTA Edition. **7**: 265-266.

Manika N, Chanotiya C S, Negi M P S and Bagchi G D. 2013. Capious shoots as a potential source for the production of essential oil in *Eucalyptus globulus*. *Industrial Crops and Products* **46**: 80-84.

MobileReference. 2008. The illustrated *Encyclopedia* of trees and shrubs: An essential guide to trees and shrubs of the world.

Nezhad F M, Zeigham H, Mota A, Sattari M and Yadegar A. 2009. Antibacterial activity of *Eucalyptus* extracts on Methicillin resistance *Staphylococcus aureus*. *Research Journal of Biological Sciences* **4**(8): 905-908.

Perianayagam J B, Sharma S K and Pillai K K. 2006. Anti-inflammatory activity of *Trichodesma indicium* root extract in experimental animals. *Journal of Ethnopharmacology* **104**: 410-414.

Priyadarsini I and Rani V. 2010. Traditional medicinal knowledge in India- An appraisal. *Socio-Economic Voices Report*. Dec 2010-Jan 2011.

Rahimi-Nasrabad M, Ahmadi F and Batooli H. 2012. Essential oil composition of *Eucalyptus procera* Dehnh. leaves from central Iran. *National Production Research* **26**(7): 637-642.

Ruifang Z, Karen E, Vincent R and Richard J Z. Antibiotic resistance as a global threat: Evidence from China, Kuwait and the United States. *Globalization Health* **2**: 6.

Salari M H, Amine G, Shirazi M H, Hafezi R and Mohammadypour M. 2006. Antibacterial effects of *Eucalyptus globulus* leaf extract on pathogenic bacteria isolated from specimens of patients with respiratory tract disorders. *Clinical Microbiology and Infection* **12**(2): 194-196.

Shahwar D, Raza M A, Bukhari S and Bukhari G. 2012. Ferric reducing antioxidant power of essential oils extracted from *Eucalyptus* and *Curcuma* species. *Asian Pacific Journal of Tropical Biomed* **2**(Suppl 3): S1633-S1636.

Sheeba E. 2010. Antibacterial activity of *Scilanum surattense* burm. *Food Journal of Science and Engineering Technology* **6**(1): 1-4.

Singla N, Thind R K and Mahal A K. 2014. Potential of *Eucalyptus* oil as repellent against house rat, *Rattus rattus*. *Science World Journal* 2014; doi: 10.1155/2014/249284.

Song A, Wang Y and Liu Y. 2009. Study on the chemical constituents of the essential oil of the leaves of *Eucalyptus globules* Labill from China. *Asian Journal of Traditional Medicine* **4**: 134-140.

Vennila and Udayakumar B M R J. 2015. *British Microbiology Research Journal* **5**(1): 83-93.

Zarai Z, Chobba I B, Mansour R B, Békir A, Gharsallah N and Kadri A. 2012. Essential oil of the leaves of *Ricinus communis* L. *In vitro* cytotoxicity and antimicrobial properties. *Lipids in Health and Disease* **11**: 102.

UGC-CARE List

You searched for **"0976-1675"**. Total Journals : **1**

Search: [   ]

Sr.No.	Journal Title	Publisher	ISSN	E-ISSN	UGC-CARE coverage years	Details
1	Research Journal of Agricultural Sciences- An International Journal	Centre for Advanced Research in Agricultural Sciences	0976-1675	2249-4538	from September-2019 to Present	View

Showing 1 to 1 of 1 entries

Previous 1 Next

Home

UGC

Search

SAVITRIBAI PHULE PUNE UNIVERSITY

Edible Mushroom: A Newish Arm in Medical and Agricultural Field

Article · October 2020

2 authors:

Tanmay Ghosh
Dinabandhu Andrews College university of calcutta
74 PUBLICATIONS   **211** CITATIONS

SEE PROFILE

Mohan Kumar Biswas
Visva Bharati University
118 PUBLICATIONS   **521** CITATIONS

SEE PROFILE

Edible Mushroom: A Newish Arm in Medical and Agricultural Field

*Tanmay Ghosh[1], **Mohan Kumar Biswas**[2]

[1]*Department of Microbiology,*
Dinabandhu Andrews College, Baishnabghata, South 24 Parganas (South), Kolkata - 700 084, West Bengal, India
[2]*Department of Plant Pathology, Palli Siksha Bhavana, Visva - Bharti, Sriniketan, Birbhum, West Bengal*

Abstract: A mushroom, also called toadstool, is a fruiting body of fungus that bears spore and they are very freshly. Normally mushrooms grow above ground or on its food source. There are over 50000 species of mushrooms, besides this yeasts and molds are also consisted of it. Among these 50000 species 1.2% is toxic and most of others are utilized in medicinal purpose. Most of mushroom species are tough, gelatinous and woody and posses a nasty smell with very bad taste. Only 20 varieties have good flavor. The most widely cultivated mushrooms are button mushrooms, Pleurotus mushrooms, shiitakes, wood ears and common mushrooms. It commonly helps as a correct diet food, controls and modulates many functions in human body, besides it maintained the state of good health, and reduces the risk of many diseases. Medicinal edible mushrooms have been valued as natural source of various important compounds. Mushrooms are rich source of mineral constituents, phosphorous and particularly potassium, magnesium, and various vitamins such as vitamins B2, B3, B12, D, E, and C. The mushrooms can be a source of heavy metals, radioactive substances, etc. They also used as laxative, antibiotic, cholesterol-lowering etc. Mushrooms are used to preventing and treating high risk of stroke, diabetes, cancers, etc. We also knows that mushrooms contain many bio-active compounds such as phenols, polyphenols, polysaccharides, terponoids, selenium, sodium and organic acid which are responsible for treating diseases and beneficial to the skin and hair. There are many mushroom production industries. Now a day's disposal of industrial by products is a great problem in the whole world because they pollute the environment, but the organic disposal materials from mushrooms by-products are very important compounds, which may be used in agriculture as bio fertilizer due to their functional and nutritional properties. This review indulges a clear knowledge about the manifold uses and procedures of mushroom farming. In the financially poor areas malnutrition related diseases are very common. Mushroom revolution because for mushrooms cultivation there is no need of proper cultivating field and medicine as it can grow on waste materials.

Key-words: Poisonous, Agriculture, Nutritional, Laxative.

Introduction:
Mushrooms, the obvious umbrella-shaped, spore-bearing fruiting body of a macro fungi (not vegetables), that grow on the food source that is cellulose [1]. Mushrooms are usually composed of a stipe (stem), a pileus (cap), and lamellae (gills). They did not make their own food due to lack of Chlorophyll. They absorb nutrients from decaying materialfrom environment, but when they grow commercially, they cultivated on substrate containing various components [2]. In India, the evincible climate changing area, to a great challenge because the quantity of agricultural land is limited even this is decreasing day by day for industrial purposes and like in other cases. The word mushroom has been used in a variety of ways at different times and in different countries. For having delicious flavour mushrooms are also used as an ingredient of gourmet cuisine through all over the world due to their nutritive and medicinal values and also used as delicious food components [3]. In World, there are different types of mushrooms like white button mushrooms, crimino mushrooms, and Oyster mushrooms. Three types of mushrooms are grown in India such as white button mushrooms, milky mushrooms, and Oyster mushrooms [4]. In India mushrooms produced 35% of total

production. There is very good scope in mushroom cultivation in West Bengal. With growing number of Chinese restaurants in large cities like Kolkata, Durgapur, and Siliguri demand for mushroom is increasing day by day. Mainly button and oyster mushroom has demand in West Bengal.*Pleurotus* sp.commonly known as Oyster Mushroom is cultivated in many countries of the world. China being the biggest mushroom producer around the world, *Pleurotus sp.*are found mainly in valley, Druas and Jammu. This mushroom can grow as a wide range of temperature. Mushrooms are richest sources of vegetables (21% to 30% protein, mineral elements Ca, Na, P, K and less amount of fat 0.35% - 0.65% dry wt. and starch 0.02% dry wt.). Mushroom considered as a healthy food. It contains low calories, high protein, vitamins and minerals etc. Mushrooms have medicinal values which enhance immune system. Mushroom contains various phytochemical compounds like flavonoids, phenolic compounds, Polysaccharides, vitamin, alkaloids, purine, lectin, saponins, and glycopeptides etc. which possess antifungal, antibacterial, antioxidant, and antiviral properties [5]. Mushrooms are suitable for diabetic and heart patients because of their low starch and cholesterol content [6]. Mushrooms extracts have a great pharmaceutical role in cancer therapy due to their anti cancer properties [7]. The polysaccharide content mushrooms are used as anti cancer drug [8]. Recently some bioactive molecules including anti-tumour agent, anti-allergic, anti-diabetic agent found in some species of mushrooms [9]. The mushroom by products also used in different field like food products, animal feed, Bio fertilizer, energy production, bioremediation, and bio based materials [10]. Polysaccharides from edible mushrooms are used in pharmaceutical as well as nutraceuticals and functional food [11]. Spent Mushroom Substrate (SMS) has an utilization as organic fertilizer in agricultural and horticultural purposes. Besides this its extra cellular enzymes are able to degrade many pollutants, so it is also used in bioremediation [12]. The SMS is used in fermentation process, such as bio-ethanol production and can be brunt to produce energy and suitable feedstock for biogas production [13]. Mushrooms as an effective food are used in me as a proofed nutritional supplement to boost immunity, thus the term considers the applications of mushroom, reviewing the current study of various aspects of mushrooms towards food, medicine, minerals, drugs and etc. In this present research topic, we discussed about the important medicinal and agricultural value of edible mushrooms and their uses in different fields.

Figure: Oyster Mushrooms.

Figure: White Button Mushrooms.

Figure: Shiitake Mushrooms.

Figure: Brown Cap Mushrooms.

Figure: White milky Mushrooms.

Figure: Black Ear Mushrooms.

Taxonomic Position:
Kingdom- Fungi.
Division- Basidiomycota.
Class- Agaricomycetes.
Order- Agaricales.

Different types of edible mushrooms:

SL. No.	Common variety	Scientific Name
1.	Button, European/Temperate	*Agaricus bisporus*
2.	Button/Edulis/Hot Weather Mushroom	*Agaricus bitorqius*
3.	Common Oyster Mushroom	*Pleurotus ostreatus*
4.	Oyster Mushroom	*Pleurotus abolonus*

5.	Paddy straw/Chinese/tropical mushroom	*Valvariella volvacea, V. Diplosia*
6.	Black Ear mushroom	*Auricularia polytricha*
7.	White milky mushroom	*Colocybe indica*
8.	Brown cap /giant mushroom	*Stropharia rugso annulata*
9.	Shiitake mushroom	*Lentinus edodes*
10.	Bear head Mushroom	*Hericium erinaceus*
11.	Wood ear Mushroom	*Auricularia aurcula*
12.	Silver ear mushroom	*Tremella fuciformis*
13.	Ling zhi	*Ganoderma lucidum*
14.	Enoki	*Flammulina velutips*

Nutrional aspects:

Nutrition	Amount of Nutrients in 1 cup of Mushrooms
Energy(calorie)	21.1
Protein(g)	3.0
Calcium (g)	2.9
Carbohydrates (g)	3.1,including 1.9gm of sugar.
Iron(g)	0.5
Magnesium (g)	8.6
Phosphorus (mg)	82.6
Potassium (mg)	305
Sodium (mg)	4.8
Zinc(mg)	0.5

Copper(mcg)	305
Selenium (mcg)	8.9
Vitamin C (mg)	2.0
Vitamin D (mg)	0.2
Folate(mcg DFE)	16.3
Choline(mg)	16.6
Niacin (mg)	3.5

Carbohydrate:

Mushrooms contain mannitol (0.95%), reducing sugar (0.28%), glycogen (0.59%), and hemi-cellulose(0.91) % as well as pentose, hexose, methyl pentose, sugar alcohol, sugar acids, Ami no sugar, disaccharides, etc. as carbohydrate content[14]. The carbohydrate content is varied in different types of mushrooms. There is no starch content in mushrooms, so it is an important food component for diabetic patient. Mushrooms uptake helps to reduce daily insulin requirements in the patient's body and also stabilized the glucose level of blood in the body [15].

Protein:

Protein is an important component for human health and proper growth. Mushrooms are the best protein source rather than others vegetables. Usually mushroom contains 20-40% protein on dry basis [16]. *Volvariella volvacea* contain 4.98% protein which is the most protein containing mushrooms species comparison with others. On the basis of dry weight, they usually contain 19.3%, wheat 13.2%, soybean 39.1%, and milk 25.2% as compared to 19-35% protein. [17].

Fat:

Mushrooms contain very low fat as compared to carbohydrates and proteins. The fat remain in the mushrooms are subordinatesbyunsaturated fatty acids, mainly linoleic acids [18]. Unsaturated fatty acids are essential for our diet, but saturated fatty acids present in animal's fats are dangerous to human health. The fat contain of mushrooms is representative of free fatty acids, mono-glycerides, di-glycerides, tri-glycerides, sterols, sterol esters and phospholipids, and about 72% of total unsaturated fatty acids are found in mushrooms [19]. Shiitake mushrooms contain 76% of fat, is the most unsaturated fatty acids containing mushrooms species. Due to high percentage of linoleic acids, mushrooms are very significant foods.

Vitamin:

Mushrooms are a good source of several essential vitamins like thiamine, riboflavin, niacin, biotin, and vitamin-C [20]. Mushrooms are one of the best sources of vitamin B, but poor in vitamin A, D and E [21]. Folic acid and vitamin B12 are present in mushrooms but absent in Vegetative foods [22].

Minerals: Mushrooms contain very essential minerals constituents like calcium, potassium, phosphorus, sodium etc.

Values in Medicinal sites:

From the earlier, fungi have been used for numerous health benefits. Contain biochemical compounds that present in fungi are beneficial for human health. Large numbers of edible mushrooms species have been shown to have some immune modulator, therapeutic and antineoplastic properties, as well as in prevention and treatment of diseases for health. Many types of edible mushrooms contain vitamin B that is a very powerful antioxidant, which is called selenium that improve preventive measures and prevent cells and tissue damage. Although, we also know that different types of specific biochemical compounds which are polysaccharides, tri-terpenoids, glycol-protein, alkaloids, phenolics, flavonoids, carotenoids, fats, tocopherols,

volatile, lectins, enzymes, minerals, ascorbic and organic acid and immuno modulating compounds which are responsible for improving human health in different way. The edible mushroom is a good effective substance for human health such as antifungal, antiviral, antibacterial, antiinflammatory, antitumor, hepatoprotective, hypotensive, antidiabetic, hypolipedmic etc. application. In the pharmaceutical significant properties of edible mushrooms are regulations of bryophyllum, maintences of homeostasis, improvement of life threatening diseases – cancer, heart diseases, cerebral stroke and cure or prevention of different types of diseases.We also well know about a numbers of edible mushroom species are use same medicinal purpose such as, *Amanita muscaria* used therapeutically as a powder, *Amanita phalloids* used against cholera and intermittent fever, *Psllocybe mexicana* used to treatment of mental disorders etc. Now a day, we also know that *P. citrinopileatus* fruiting body extracts examine anti-thyperlipidamic effects and some microorganism tested some mushroom extracts such as *P. cornucopia* is the most effective antigenatoxic and bio-antimutagenic activities on *Salmonella typhimurium* and *Escherichia coli* etc. Recently responded those Oyster mushrooms are highly nutritious for us and used to antioxidant, antifamatory, and antitumor activities.So, we also well know that increasing recognition of edible mushroom species are completely fighting for different types of diseases. Medicinal values of the important mushroom are given below.

Medicinal values of some important mushroom:

Mushrooms	Compounds	Medicinal Properties
Ganoderma lueidum	Ganoderic acid	1. Augmentsimmune system 2. Liver protection
	Beta glycan	1. Antibiotic properties 2. Inhibits cholesterol synthesis
Lentinula edodes	Eritadenine	Low cholesterol
A. bioporous	Lectins	Enhance insulin secretion
P. sahar caju	Lavostatin	Lower cholesterol
G. frondosa	Acidic polysaccharides	Decrease blood glucose
	Lectins	Decrease blood glucose
Flammulina velutipes	Ergothioneine	Antioxidant
	Proflamin	Anti-cancer activity
Trametes versicolor	Polysaccharide-K (kresin)	1. Decrease immune system 2. Depression
Cordyceps sinen	Cardycepin	1. Cure lung infections 2. Hypoglycemic activity 3. Cellular health properties

1. **Good for Heart:**
   The edible mushrooms have little fat with high proportion of unsaturated fatty acids, cholesterol free, moderate amounts of fiber, and consequently it is the relevant choice for heart patients and treating cardiovascular diseases. Minimal sodium with rich potassium in mushroom enhances salt balance and maintaining blood circulation in human being. Hence, mushrooms are suitable for people suffering from high blood pressure. Some edible mushrooms are stern to decrease cholesterol levels such as *Lentinula*, *Pleurotus* sp. etc., that prevents heart attack. Otherwise some edible mushrooms contains nutrients that can help to prevent cells from sticking to blood vessel wells and forming plaque build-up then helps to protect the heart by maintaining healthy blood presser and circulation.

2. **Prevents cancer:**
   Compounds restricting tumor activity are found in some mushrooms, but only a limited number have undergone clinical trials. All forms of edible mushrooms and white button mushrooms in particular, can prevent prostate and breast cancer by protecting our cells against DNA damage but also inhibiting tumor formation. The drug known as polysaccharide- K (kresin) is isolated from *Trametes versicolor,* which is used as a leading cancer drug. Some edible mushrooms like *Lentinula edodes*, *Tramtes versicolor* and *Agaricus bisporus* used to clinically validate and some mushrooms are also useful in the treatment and management of neurodegenerative disease such as Alzheimer.

3. **Low caloric food:**
   Due to lower caloric values of mushroom, mushroom is ideal food for diabetic patients. It also contains little fat and sugar with no starch. The lean proteins that present in mushroom can burn cholesterol. So, it is an recommendable food for peoples with heavy weight.

4. **Anti- aging property:**
   Mushroom contains several polysaccharides that can scavenge superoxide free radicals. It can slow down the aging process by its anti-aging properties. Ergothioneine is a specific antioxidant found in *Flamulina velutipes* and *Agaricus bisporus* that are good for eyes, kidneys, bone marrow, liver and skin.

5. **Regulates digestive system:**
   In addition to the fiber extracted from mushrooms, oligosaccharides act as pre-biological in the gut and so they anchor useful bacteria in the colon. This dietary fiber helps in the digestive process and the healthy functioning of the intestinal system.

Value in Agricultural sites:

Mushrooms have different prices in agriculture. There is huge potential for food application in mushroom by-products. However, there is a lack of proper studies about the polysaccharides obtained from edible mushrooms. Maybe some researches have been done on use of mushroom by-products as animal feed. In the animal sector, the main by-products used for feeding are in solid fermentation feed. According to the available studies, the by-products of mushrooms complement the benefits of animal feed supply related to animal quality, economic realities and environmental concerns. Waste from mushroom production is considered to have different advantages, the same production facility is used for lower collection cost and it contains many inorganic pets, p. Contains K, MG and C and can be used as ash fertilizer from biomass waste. Also, the other use in agriculture is bioremediation, biological treatments, and energy production, bio-based material etc.

Conclusion:

Mushrooms have been associated with mankind and profound biochemicals. Since ancient times, people have probably swallowed wild mushrooms with delicious for their taste and pleasant aroma. The above review of polish and foreign literature shows that in the global market and currently play a significant

economic role. Recently, the consumption of mushroom increases with high rates, edible mushroom containing proteins are greater than animal protein. Edible mushrooms are rich in fiber, Vit-B, Vit-C, low fat with higher proportion of polyunsaturated fatty acid. Mushroom contain large amount of carbohydrates (4.5%) with no starch. Mushroom by-products are also use in various fields. Several bioactive compounds present in mushroom by-product have agricultural benefits. There is a good demand of mushroom by-product in agricultural site. So, mushroom cultivation should increase industrial application, SMS i.e. spent mushroom substrate can be used as animal feed, fertilizer after processing in industry. For example, in the case of enzymes most studies are focused on SMS and fermentation broths are not well studied for the extraction and properties of these compounds. Animal feed, fertilizers, consequent development, biochemicals and bio-based materials as well as energy production are areas that have been explored in the past years with promising and highly attractive results. Bio-based substances form an emerging field, which indicates the huge potential of SMS and mycelium in the development of novel bio-substances with SP space with sustainable practice and very attractive properties. Notification of articulated error fills the concept of economy.

Reference:

1. Bilal Ahmad Wani, R. H. Bodha and A. H. Wani; "Nutritional and medicinal importance of mushrooms"; Journal of Medicinal Plants Research Vol. 4(24), pp. 2598-2604, 18 December, 2010.
2. Mary Jo Feeney, MS, RDN, FADA, FAND,Amy Myrdal Miller, MS, RDN,PeterRoupas, PhD; "Mushrooms-Biologically Distinct and Nutritionally Unique"; Nutrition Today, Volume 49, Number 6, November/December 2014.
3. Suresh Chandra and Samsher; "Nutritional and medicinal aspects of edible mushrooms"; HIND AGRI-HORTICULTURAL SOCIETY,Vol.2 No.2 July 2006 : (647-651).
4. Bilal Ahmad Wani, R. H. Bodha and A. H. Wani; "Nutritional and medicinal importance of mushrooms"; Journal of Medicinal Plants Research Vol. 4(24), pp. 2598-2604, 18 December, 2010.
5. Bilal Ahmad Wani, R. H. Bodha and A. H. Wani; "Nutritional and medicinal importance of mushrooms"; Journal of Medicinal Plants Research Vol. 4(24), pp. 2598-2604, 18 December, 2010.
6. Bilal Ahmad Wani, R. H. Bodha and A. H. Wani; "Nutritional and medicinal importance of mushrooms"; Journal of Medicinal Plants Research Vol. 4(24), pp. 2598-2604, 18 December, 2010.
7. Seema Patel,ArunGoyal; "Recent developments in mushrooms as anti-cancer therapeutics: A review"; 3 Biotech (2012) 2:1–15.
8. Bilal Ahmad Wani, R. H. Bodha and A. H. Wani; "Nutritional and medicinal importance of mushrooms"; Journal of Medicinal Plants Research Vol. 4(24), pp. 2598-2604, 18 December, 2010.
9. Seema Patel, ArunGoyal; "Recent developments in mushrooms as anti-cancer therapeutics: A review"; 3 Biotech (2012) 2:1–15.
10. FilipaAntunes , Sara Marçal , OludemiTaofiq , Alcina M. M. B. Morais ,Ana Cristina Freitas, Isabel C. F. R. Ferreira and Manuela Pintado; "Valorization of Mushroom By-Products as a Source of Value-Added Compounds and Potential Applications"; Molecules 2020, 25, 2672.
11. FilipaAntunes , Sara Marçal , OludemiTaofiq , Alcina M. M. B. Morais ,Ana Cristina Freitas, Isabel C. F. R. Ferreira and Manuela Pintado; "Valorization of Mushroom By-Products as a Source of Value-Added Compounds and Potential Applications"; Molecules 2020, 25, 2672.
12. FilipaAntunes , Sara Marçal , OludemiTaofiq , Alcina M. M. B. Morais ,Ana Cristina Freitas, Isabel C. F. R. Ferreira and Manuela Pintado; "Valorization of Mushroom By-Products as a Source of Value-Added Compounds and Potential Applications"; Molecules 2020, 25, 2672.
13. FilipaAntunes , Sara Marçal , OludemiTaofiq , Alcina M. M. B. Morais ,Ana Cristina Freitas, Isabel C. F. R. Ferreira and Manuela Pintado; "Valorization of Mushroom By-Products as a Source of Value-Added Compounds and Potential Applications"; Molecules 2020, 25, 2672.
14. Suresh Chandra and Samsher; "Nutritional and medicinal aspects of edible mushrooms"; HIND AGRI-HORTICULTURAL SOCIETY,Vol.2 No.2 July 2006 : (647-651).

15. Suresh Chandra and Samsher; "Nutritional and medicinal aspects of edible mushrooms"; HIND AGRI-HORTICULTURAL SOCIETY,Vol.2 No.2 July 2006 : (647-651).

16. Seema Patel • ArunGoyal; "Recent developments in mushrooms as anti-cancer therapeutics: A review"; 3 Biotech (2012) 2:1–15.

17. Bilal Ahmad Wani*, R. H. Bodha and A. H. Wani; "Nutritional and medicinal importance of mushrooms"; Journal of Medicinal Plants Research Vol. 4(24), pp. 2598-2604, 18 December, 2010.

18. Bilal Ahmad Wani*, R. H. Bodha and A. H. Wani; "Nutritional and medicinal importance of mushrooms"; Journal of Medicinal Plants Research Vol. 4(24), pp. 2598-2604, 18 December, 2010.

19. Suresh Chandra and Samsher; "Nutritional and medicinal aspects of edible mushrooms"; HIND AGRI-HORTICULTURAL SOCIETY,Vol.2 No.2 July 2006 : (647-651).

20. Suresh Chandra and Samsher; "Nutritional and medicinal aspects of edible mushrooms"; HIND AGRI-HORTICULTURAL SOCIETY,Vol.2 No.2 July 2006 : (647-651).

21. Bilal Ahmad Wani*, R. H. Bodha and A. H. Wani; "Nutritional and medicinal importance of mushrooms"; Journal of Medicinal Plants Research Vol. 4(24), pp. 2598-2604, 18 December, 2010.

22. Suresh Chandra and Samsher; "Nutritional and medicinal aspects of edible mushrooms"; HIND AGRI-HORTICULTURAL SOCIETY,Vol.2 No.2 July 2006: (647-651).

SAVITRIBAI PHULE PUNE UNIVERSITY

≡ **UGC-CARE List**

- Home
- ◯ UGC
- 🔍 Search ‹

UGC-CARE List

You searched for **"0975-1386"**. Total Journals : **1**

Search: [   ]

Sr.No.	Journal Title	Publisher	ISSN	E-ISSN	UGC-CARE coverage years	Details
1	Wesleyan Journal of Research	Bankura Christian College	0975-1386	NA	from June-2019 to January- 2023	Discontinued from Jan 2023

Showing 1 to 1 of 1 entries

Previous 1 Next

A long-term seasonal analysis on the relationship between LST and NDBI using Landsat data

Subhanil Guha [a], Himanshu Govil [a,*], Neetu Gill [b], Anindita Dey [c]

[a] *Department of Applied Geology, National Institute of Technology Raipur, Chhattisgarh, India*
[b] *Chhattisgarh Council of Science and Technology, Raipur, Chhattisgarh, India*
[c] *Department of Geography, Nazrul Balika Vidyalaya, Guma, West Bengal, India*

ARTICLE INFO

ABSTRACT

Urbanization is necessary for the worldwide rapidly growing population to achieve a better living standard. Change of land surface feature is the key consequence of urbanization and it promotes a rise of land surface temperature (LST). The present article analyzes the seasonal variability of LST-normalized difference built-up index (NDBI) relationship on various land surface in Raipur City of India by collecting sixty-four Landsat images of four specific seasons from 1991–92, 1995–96, 1999–00, 2004–05, 2009–10, 2014–15, and 2018–19. Land surface composition and seasonal difference noticeably affect the LST distribution and LST-NDBI correlation. The LST always builds positive correlation with NDBI. The post-monsoon season indicates the strongest (0.72) LST-NDBI correlation, followed by the monsoon (0.69), pre-monsoon (0.67), and winter (0.57). The LST-NDBI correlation is strong on green vegetation; strong to moderate on built-up and open land; and moderate on water bodies. This research work recommends that the environmentalists and urban planners should consider the remaining open spaces for a better ecological condition.

1. Introduction

In modern era, fast urbanization fosters the land conversion processes and rapid rise of surface temperature in a very short duration (Du et al., 2016; Guha et al., 2020a; Liu et al., 2018). Satellite image can detect these land surface changes successfully by using their thermal infrared (TIR), visible and near-infrared (VNIR), and shortwave infrared (SWIR) bands (Guha, 2016; Guha et al., 2018a, 2018b; 2018c; Alexander, 2020). These VNIR, SWIR, and TIR band based several spectral indices are frequently used in various environmental domains (Govil et al., 2020a, 2020b; Guha et al., 2017; He et al., 2019; Guha and Govil, 2019, 2020). Different types of land use/land cover (LULC) in heterogeneous urban area response differently in TIR band of satellite data (Shigeto, 1994; Ferelli et al., 2018; Fatemi and Narangifard, 2019; Guha et al., 2020b, c; Nimish et al., 2020; Sultan and Satyanarayana, 2020).

TIR region of electromagnetic spectrum has a huge potential in determining the characteristics of land surface dynamics in any natural environment along with the VNIR and SWIR regions (Alexander, 2020). Land surface temperature (LST) plays a major role to analyze the biogeochemical processes acted over the earth surface cover (Govil et al., 2019; Guha et al., 2019, 2020d, e; Hao et al., 2016). Spatial

variation of LST is mainly due to the variation of the reflectance and roughness of land surface (Grimm et al., 2008). Generally, green vegetation and water bodies present low LST, whereas built-up area, bare rock surface or dry soil reflects high LST (Guha et al., 2020a, b, d, e; Li et al., 2017). Thus, LST related studies are very important in urban and land use planning (Li et al., 2017). Normalized difference built-up index (NDBI) is an important spectral index that significantly correlates to LST (Guha et al., 2018a). Generally, the nature of LST-NDBI relationship in a region is positive and is controlled by several factors, such as humidity, vegetation, air pollution, rock surface, dry or wet soil, heterogeneous man-made materials, etc. (Guha et al., 2019, 2020b).

Several recent studies evaluate LST-NDBI correlation on different types of LULC in tropical environment (Guha et al., 2018a; Alexander, 2020; Balew and Korme, 2020; Son et al., 2020). However, the seasonal analysis of the LST-NDBI relationship in tropical India is rare. The strength of LST-NDBI correlation changes due to the seasonal changes of climatic components. Change in season and LULC types regulate the value of NDBI. Thus, a long-term analysis of LST-NDBI relationship in different seasons is very significant for the development of any kind of environmental planning in an urban landscape as it provides a long reliable nature of information. The present study conducts on Raipur in

---
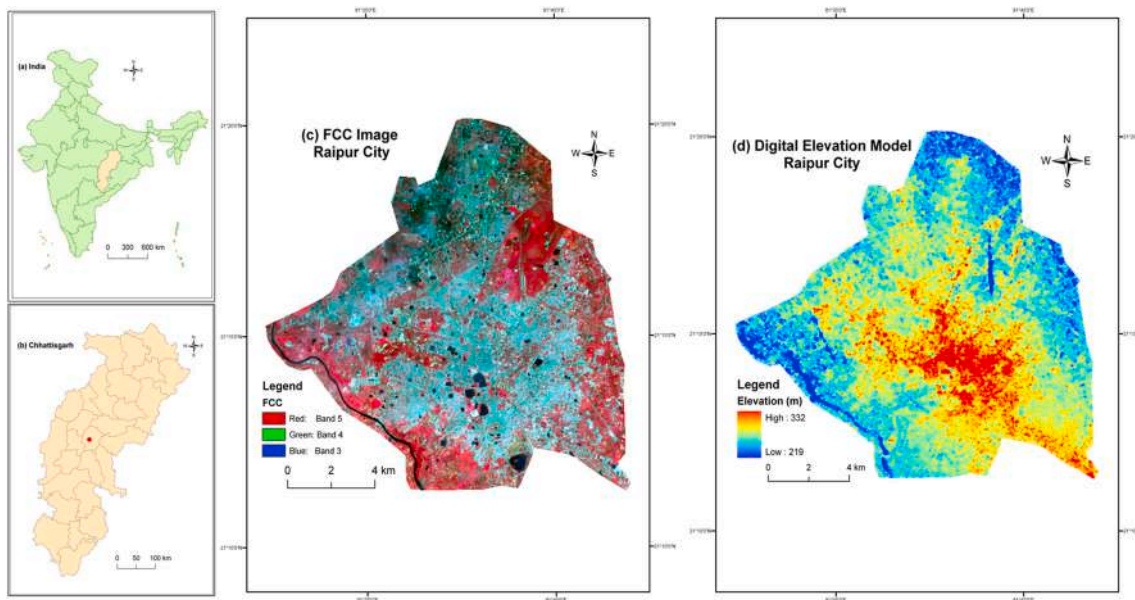
Fig. 1. Location of Raipur City: (a) India (b) Chhattisgarh (c) FCC image of Raipur City (d) DEM of Raipur City.

Table 1
Climate data for Raipur City (1981–2012) (Source: IMD).

Weather Elements	January	February	March	April	May	June	July	August	September	October	November	December
Maximum Temp (°C)	31.5	34.8	39.8	43.2	45.2	44.4	36.1	33.7	34.4	37.7	32.5	30.8
Minimum Temp (°C)	8.6	11.3	15.7	19.7	22.2	21.6	21.2	21.7	21.3	16.8	11.6	8.9
Mean Temp (°C)	20.7	23.4	28.9	32.3	34.7	31.7	27.8	27.2	27.8	27.6	23.1	20.3
Mean Monthly Rainfall (mm)	13.7	13.4	11.9	8.9	30.3	221.1	326.9	299.9	200.5	50.4	9.8	6.6
Average Relative Humidity (%)	47	35	28	22	27	52	76	79	73	59	51	49

tropical India, as the city avoids the direct effect of humid maritime climate due to its landlocked position. The study examines the nature and trend of the LST-NDBI relationship on different types of LULC and their seasonal variation. The study will be effective for future city to make the city more sustainable.

2. Study area and data

Fig. 1 shows the research place (Raipur City of India) of the present research work. Fig. 1(a) presents the outline map of India where Chhattisgarh State is located in the middle part (Source: Survey of India (SOI)). Fig. 1(b) presents the outline map of Chhattisgarh State with districts (Source: SOI). Fig. 1(c) represents the false colour composite (FCC) image of Raipur City from recent Landsat 8 data (Date: November 7, 2018) where blue, green, and red bands of the image are filtered by the green, red, and infrared bands, respectively (Source: United States Geological Survey (USGS)). Fig. 1(d) indicates the digital elevation model (DEM) (Date: October 11, 2011) of Raipur City using Advanced Spaceborne Thermal Emission and Reflection Radiometer (ASTER) DEM data (Source: USGS). The city extends from 21°11′22″N to 21°20′02″N and from 81°32′20″E to 81°41′50″E. The total area of the city is approximately 164.23 km^2. The only big river of the area is Mahanadi. The south of the city is covered by dense forests. Geologically, the city is very stable. According to India Meteorological Department (IMD), Raipur is under the savannah type of climate. Table 1 presents the climatic data of Raipur from 1981 to 2012 (Source: IMD). May is the hottest month followed by April, June, and March. July is the rainiest month followed by August, June, and September. October and November are the post-monsoon months experience a pleasant weather condition. December (the coldest month), January, and February are the winter months. The pre-monsoon and winter months (including November)

remain dry compared to the monsoon and post-monsoon months.

USGS Data Centre provides the Thematic Mapper (TM), Enhanced Thematic Mapper Plus (ETM+), and Operational Land Imager/Thermal Infrared Sensor (OLI/TIRS) sensors of Landsat data for this study. Table 2 provides the detailed information about the used Landsat satellite sensors. The pixel size of the VNIR and SWIR bands of TM, ETM+, and OLI/TIRS data is 30 m. The original pixel sizes of the TIR bands of different Landsat sensors vary with each other (120 m for TM, 60 m for ETM+, and 100 m for OLI/TIRS data) and lower than the VNIR and SWIR bands. The USGS data centre provides these Landsat datasets after resampling the original TIR bands with lower resolution to a common platform of higher resolution (30 m) for direct comparative study. The resolution of all the VNIR, SWIR, and TIR bands must be equal for any kind of numerical operation.

Table 2 provides the specification of the sixty-three selected Landsat datasets of different sensors (TM, ETM+, and OLI/TIRS) from different seasons used in the present study.

3. Methodology

3.1. LST estimation from Landsat sensor

The present study applied mono-window algorithm for LST estimation process (Qin et al., 2001). Several separate equations (Yang and Que, 1996; Carlson and Replay, 1997) are part of this algorithm.

3.2. Extraction of different types of LULC by using NDBI

NDBI (Zha et al., 2003) is an automatic choice as a spectral index to perform a reliable and authentic LST-built-up area relationship in a city. It always provides a strong to moderate positive correlation (Zha et al.,

Table 2
Specification of Landsat data sets from 1991–92 to 2018-19.

Landsat scene ID	Date of acquisition	Time (UTC)	Path/Row	Sun elevation (°)	Sun azimuth (°)	Cloud cover (%)	Earth-Sun distance (astronomical unit)
1991–1992							
LT51420451991077ISP00	18-Mar-91	04:17:34	142/044	48.58	118.92	0.00	0.99
LT51420451991093ISP00	03-Apr-91	04:17:46	142/044	53.04	111.64	0.00	0.99
LT51420451991141ISP00	21-May-91	04:18:39	142/044	59.93	87.09	1.00	1.01
LT51420451991269ISP01	26-Sep-91	04:20:03	142/044	52.47	123.30	13.00	1.00
LT51420451991285BKT02	12-Oct-91	04:20:12	142/044	42.22	131.85	6.00	0.99
LT51420451991317ISP00	13-Nov-91	04:20:19	142/044	41.53	142.35	1.00	0.99
LT51420451992016ISP00	16-Jan-92	04:20:22	142/044	35.26	139.03	3.00	0.98
LT51420451992032BKT01	01-Feb-92	04:20:27	142/044	37.41	135.03	0.00	0.98
LT51420451992048ISP00	17-Feb-92	04:20:15	142/044	40.89	130.26	4.00	0.98
1995–1996							
LT51420451995104ISP01	14-Apr-95	04:05:06	142/044	52.75	103.75	0.00	1.00
LT51420451995344BKT00	10-Dec-95	03:56:47	142/044	33.01	139.15	0.00	0.98
LT51420451996027ISP00	27-Jan-96	04:00:14	142/044	33.31	132.27	0.00	0.88
LT51420451996267ISP00	23-Sep-96	04:14:16	142/044	51.81	120.64	2.00	1.00
LT51420451996283ISP00	09-Oct-96	04:15:07	142/044	48.92	129.53	0.00	0.99
LT51420451996299ISP00	25-Oct-96	04:15:55	142/044	45.37	136.48	5.00	0.99
LT51420451996315ISP00	10-Nov-96	04:16:41	142/044	41.61	141.11	7.00	0.99
1999–2000							
LE71420451999315SGS00	11-Nov-99	04:49:00	142/044	45.72	149.96	0.00	0.99
LE71420452000030SGS00	30-Jan-00	04:48:55	142/044	41.46	142.31	0.00	0.98
LE71420452000094SGS00	03-Apr-00	04:48:35	142/044	59.72	118.62	0.00	1.00
LE71420452000126SGS00	05-May-00	04:48:20	142/044	65.97	98.50	0.00	1.00
LE71420452000270SGS00	26-Sep-00	04:46:33	142/044	57.21	131.59	6.00	1.00
LE71420452000350SGS00	15-Dec-00	04:46:31	142/044	38.94	150.22	0.00	0.98
2004–2005							
LT51420452004081BKT00	21-Mar-04	04:35:14	142/044	53.26	121.40	0.00	0.99
LT51420452004113BKT00	22-Apr-04	04:36:01	142/044	61.43	104.47	1.00	1.00
LT51420452004145BKT00	24-May-04	04:36:54	142/044	64.25	86.72	0.00	1.00
LT51420452004161BKT00	09-Jun-04	04:37:23	142/044	63.98	81.78	9.00	1.01
LT51420452004273BKT00	29-Sep-04	04:40:16	142/044	55.47	131.40	9.00	1.00
LT51420452004289BKT00	15-Oct-04	04:40:36	142/044	51.63	139.65	4.00	0.99
LT51420452004321BKT00	16-Nov-04	04:41:11	142/044	43.41	148.58	0.00	0.98
LT51420452004337BKT00	02-Dec-04	04:41:33	142/044	40.14	149.58	0.00	0.98
LT51420452004353BKT00	18-Dec-04	04:41:52	142/044	38.12	148.74	0.00	0.98
LT51420452005019BKT00	19-Jan-05	04:42:17	142/044	38.92	143.21	0.00	0.98
LT51420452005035BKT00	04-Feb-05	04:42:29	142/044	41.74	139.16	0.00	0.98
2009–2010							
LT51420452009062KHC01	03-Mar-09	04:42:22	142/044	49.04	130.64	0.00	0.99
LT51420452009078KHC00	19-Mar-09	04:42:44	142/044	54.10	124.40	2.00	0.99
LT51420452009094BKT00	04-Apr-09	04:43:05	142/044	58.86	116.70	0.00	1.00
LT51420452009110BKT00	20-Apr-09	04:43:24	142/044	62.67	107.39	0.00	1.00
LT51420452009126BKT00	06-May-09	04:43:42	142/044	65.03	97.25	0.00	1.00
LT51420452009142KHC00	22-May-09	04:44:00	142/044	65.88	88.22	1.00	1.00
LT51420452009174KHC00	23-Jun-09	04:44:35	142/044	64.96	80.76	0.00	1.00
LT51420452009286KHC00	13-Oct-09	04:46:12	142/044	53.04	140.48	0.00	0.99
LT51420452009302BKT00	29-Oct-09	04:46:20	142/044	48.72	146.41	0.00	0.99
LT51420452009350KHC00	16-Dec-09	04:46:44	142/044	38.90	150.21	1.00	0.99
LT51420452010033KHC00	02-Feb-10	04:46:59	142/044	41.92	140.89	0.00	0.98
LT51420452010049KHC00	18-Feb-10	04:47:02	142/044	45.89	136.27	7.00	0.98
2014–2015							
LC81420452014076LGN01	17-Mar-14	04:56:36	142/044	55.95	129.38	0.00	0.99
LC81420452014092LGN01	02-Apr-14	04:56:19	142/044	60.91	121.72	0.00	0.99
LC81420452014140LGN01	20-May-14	04:55:38	142/044	68.56	90.40	5.46	1.01
LC81420452014156LGN01	05-Jun-14	04:55:45	142/044	68.38	83.30	0.02	1.01
LC81420452014316LGN01	12-Nov-14	04:56:21	142/044	46.22	152.46	7.59	0.98
LC81420452014364LGN01	30-Dec-14	04:56:09	142/044	39.34	150.83	0.41	0.98
LC81420452015015LGN01	15-Jan-15	04:56:09	142/044	40.22	147.71	0.01	0.98
LC81420452015031LGN01	31-Jan-15	04:56:04	142/044	42.76	143.86	0.01	0.98
LC81420452015047LGN01	16-Feb-15	04:55:55	142/044	46.67	139.41	0.01	0.98
2018–2019							
LC81420452018071LGN00	12-Mar-18	04:55:43	142/044	54.19	131.16	2.10	0.99
LC81420452018087LGN00	28-Mar-18	04:55:36	142/044	59.29	124.07	0.01	0.99
LC81420452018135LGN00	15-May-18	04:55:08	142/044	68.27	93.32	0.30	1.01
LC81420452018167LGN00	16-Jun-18	04:55:01	142/044	67.74	81.10	2.31	1.01
LC81420452018279LGN00	06-Oct-18	04:55:53	142/044	56.39	140.40	0.06	0.99
LC81420452018295LGN00	22-Oct-18	04:55:59	142/044	51.96	147.33	0.02	0.99
LC81420452018311LGN00	07-Nov-18	04:56:03	142/044	47.49	151.56	0.22	0.99
LC81420452018359LGN00	25-Dec-18	04:55:59	142/044	39.40	151.57	0.01	0.98
LC81420452019042LGN00	11-Feb-19	04:55:52	142/044	45.33	140.84	0.00	0.98
LC81420452019058LGN00	27-Feb-19	04:55:48	142/044	49.94	135.93	4.27	0.99

Table 3

Description of NDBI and its threshold values used for extracting the various types of LULC.

Acronym	Description	Formulation	References	Threshold limits of NDBI for extracting different LULC types		
				Vegetation	Water bodies	Built-up area and bare land
NDBI	Normalized difference built-up index	$\frac{SWIR1 - NIR}{SWIR1 + NIR}$	Zha et al. (2003)	<0	0–0.1	>0.1

Table 4

Total area (km^2) under different types of LULC.

Year	Green area	Urban settlement and open area	Water area
1991–92	140.38	21.16	2.69
1995–96	130.23	31.72	2.29
1999–00	117.74	44.59	1.89
2004–05	112.41	49.68	2.14
2009–10	90.69	71.59	1.95
2014–15	81.63	81.28	1.32
2018–19	63.58	99.53	1.12

2003) in any season. Built-up area is the most important land surface feature for an urban environment and it controls the LST a lot. Apart from this, the nature of the same built-up area cannot change largely with time or season. Moreover, the spatial expansion of built-up area is a very common event in any type of global, regional or local city. Thus, the significance of NDBI is gradually increasing in the LST related studies conducted in an urban environment (Chen et al., 2006). The SWIR1 and NIR bands of Landsat sensor determine NDBI (Table 3). The two extremes of NDBI values are −1 and + 1. The built-up area increases with the increase of the positive NDBI. NDBI value ranges between 0.1 and 0.3 shows the built-up area, whereas NDBI >0.25 shows the bare lands (Table 3). NDBI is also used to extract other LULC types, e.g., vegetation (NDBI < 0), and water bodies (0 < NDBI < 0.1) (Table 3). The post-monsoon images are suitable for the generation of LULC maps due to less pollution. The previously mentioned threshold limits of NDBI (Guha et al., 2017) generate different types of LULC and the maximum likelihood classification validates the results. The average overall accuracy for all the images is 92.14%, whereas the value of kappa statistic is 0.87.

4. Results and discussion

4.1. Extraction of LULC types using NDBI

Table 4 represents the total area under different LULC categories. Water area is the most stable LULC type in the study area. Green area decreases in a very significant amount (76.80 km^2) from 1991–92 to 2018–19, whereas the settlement and open area increases at a very high rate (78.37 km^2 in 27 years) due to rapid land conversion.

From Fig. 2 (LULC maps) it is clear that the northwest portion of the city was urbanized rapidly from 1991–92 to 2004–05, and after 2004–05, the green areas drastically reduced due to conversion into built-up area. Only the eastern and the southwestern parts have some urban vegetation.

4.2. LST and NDBI: seasonal distribution

Table 5 shows the seasonal distribution of LST. The winter months indicate the lowest mean LST values for all the years, whereas the pre-monsoon months show the highest mean LST. The post-monsoon months have the mean LST value nearer to the winter, while monsoon months have a slightly high value of mean LST than the post-monsoon months.

The pre-monsoon months (Fig. 3) have the maximum LST followed by monsoon (Fig. 4), post-monsoon (Fig. 5), and winter (Fig. 6) months. The northwest and southeast sections reflect a low percentage of urban vegetation and high LST value (Fig. 2). The vegetation (decreased) and built-up land (increased) changes significantly with time. The correlation coefficient values of the linear correlation between the LST-NDBI relationships are positive (for any year or season). The post-monsoon season has the strongest mean correlation coefficient value (0.72), followed by the monsoon (0.69), pre-monsoon (0.67), and winter (0.57) season.

It is seen from Fig. 3 that in 2018–19, more than 90% of the area in
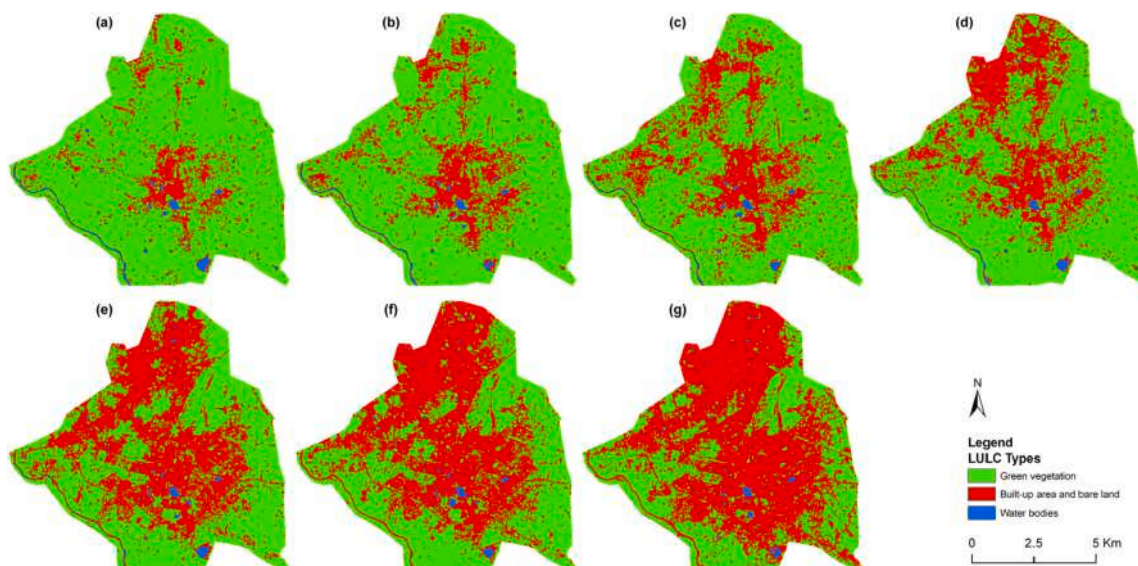
Fig. 2. NDVI threshold-based LULC maps: (a) 1991–92 (b) 1995–96 (c) 1999–00 (d) 2004–05 (e) 2009–10 (f) 2014–15 (g) 2018-19.

Table 5

Temporal and seasonal variation of LST values, and correlation coefficient of LST-NDBI relationship.

Season	Year of acquisition	LST (°C)				Correlation coefficients for LST-NDBI relationship
		Min.	Max.	Mean	Std.	
Pre-monsoon	1991–92	24.25	35.22	31.54	1.30	0.64
	1995–96	24.54	41.07	34.64	1.89	0.76
	1999–00	26.36	41.57	36.38	1.89	0.81
	2004–05	27.37	43.32	38.01	2.05	0.72
	2009–10	25.39	41.84	36.67	2.25	0.64
	2014–15	26.97	39.68	34.40	1.65	0.67
	2018–19	25.50	38.70	33.14	1.68	0.58
	Average	*27.98*	*44.21*	*37.88*	*1.94*	*0.71*
Monsoon	1991–92	22.38	30.83	25.74	1.41	0.83
	1995–96	19.28	30.01	24.09	1.33	0.74
	1999–00	17.62	31.23	24.18	1.34	0.82
	2004–05	22.16	29.97	26.11	0.96	0.66
	2009–10	21.94	38.38	33.06	2.40	0.54
	2014–15	26.43	36.63	31.70	1.16	0.43
	2018–19	25.49	34.98	31.08	1.13	0.69
	Average	*24.61*	*36.64*	*30.94*	*1.52*	*0.76*
Post-monsoon	1991–92	20.17	29.38	24.32	1.65	0.82
	1995–96	19.85	28.20	23.70	1.30	0.81
	1999–00	24.36	36.38	29.17	1.91	0.79
	2004–05	23.46	34.46	28.01	1.58	0.69
	2009–10	22.59	34.45	27.51	1.54	0.72
	2014–15	19.44	28.31	23.47	1.12	0.54
	2018–19	24.31	34.09	28.08	1.30	0.71
	Average	*23.62*	*35.15*	*28.56*	*1.53*	*0.79*
Winter	1991–92	18.37	28.33	23.29	1.15	0.70
	1995–96	18.38	25.61	21.79	0.98	0.59
	1999–00	19.74	34.30	26.54	1.71	0.66
	2004–05	19.27	29.27	24.07	1.15	0.56
	2009–10	18.82	27.79	23.31	1.15	0.55
	2014–15	19.95	30.62	25.13	1.35	0.52
	2018–19	20.33	30.14	24.37	1.18	0.44
	Average	*21.28*	*33.14*	*26.67*	*1.33*	*0.57*
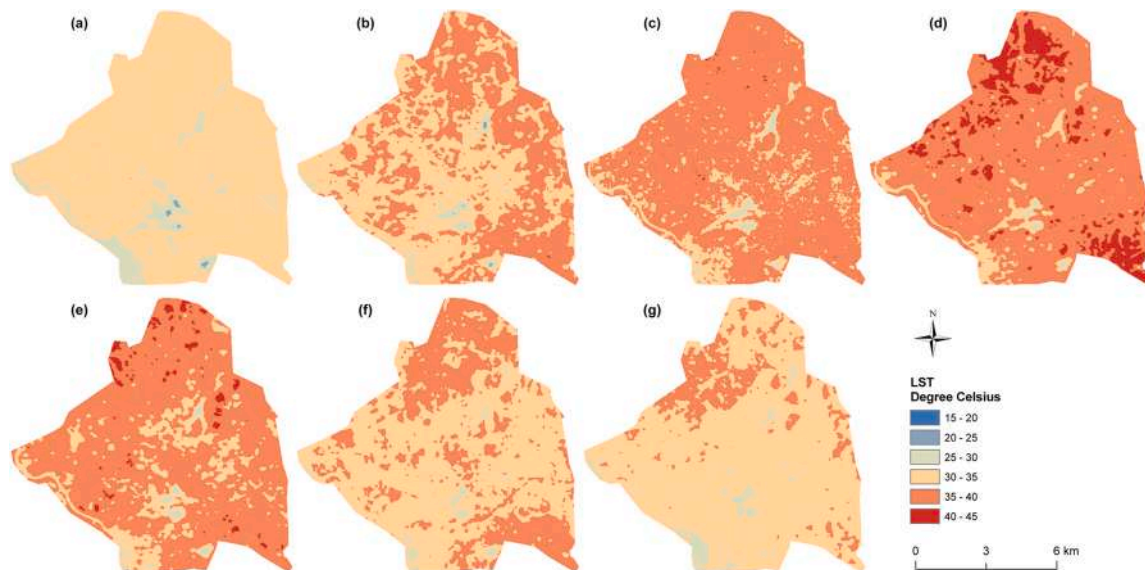
Fig. 3. Mean LST in pre-monsoon season: (a) 1991–92 (b) 1995–96 (c) 1999–00 (d) 2004–05 (e) 2009–10 (f) 2014–15 (g) 2018-19.

the pre-monsoon season was above 30 °C LST. A different result was seen in the winter season, where area above 40 °C LST was almost none. In 1991–92 an 1995–96, almost 90% of the area was below 25 °C LST in the winter season (Fig. 6). Monsoon (Fig. 4) and post-monsoon (Fig. 5) seasons indicate a moderate range of LST.

Fig. 7 shows the seasonal variation of minimum, maximum, and mean LST for individual years and their average values. Pre-monsoon season clearly indicates the highest LST. The overall trend of LST is increasing. However, from 2009–10, the trend of LST in pre-monsoon

season is slightly inverse. It is mainly due to some atmospheric instability. Table 6 presents the temporal and seasonal change in mean LST for the whole city. In terms of total gain in mean LST, monsoon months reflect the best result.

4.3. Validation of the estimated LST

In the present study, Moderate Resolution Imaging Spectroradiometer (MODIS) data derived LST validates the Landsat data derived
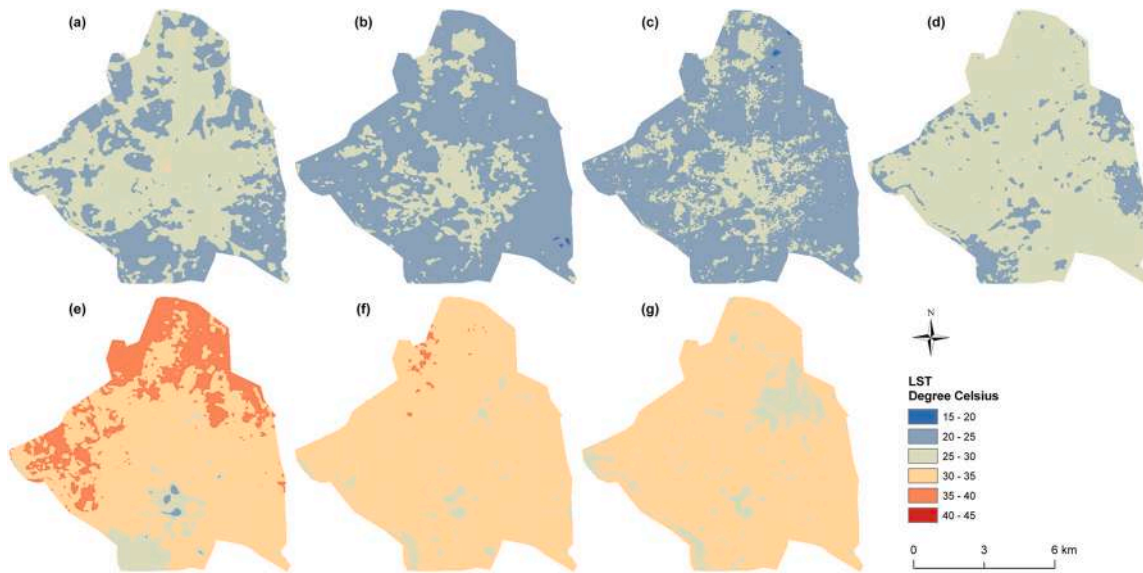
Fig. 4. Mean LST in monsoon season: (a) 1991–92 (b) 1995–96 (c) 1999–00 (d) 2004–05 (e) 2009–10 (f) 2014–15 (g) 2018-19.
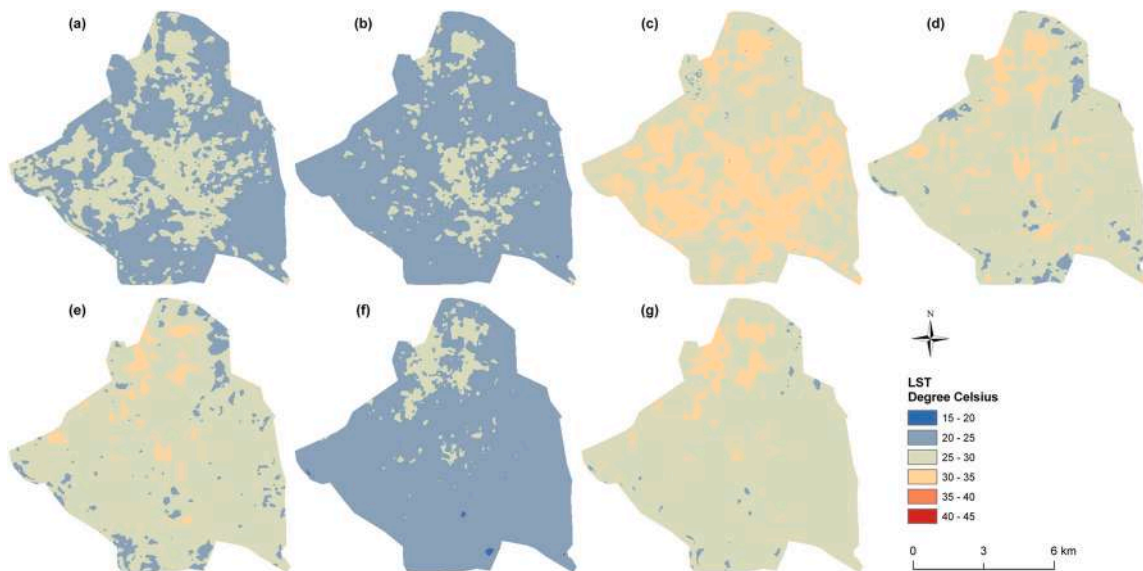
Fig. 5. Mean LST in post-monsoon season: (a) 1991–92 (b) 1995–96 (c) 1999–00 (d) 2004–05 (e) 2009–10 (f) 2014–15 (g) 2018-19.

LST. This validation process was performed from 2004-05 session due to the unavailability of suitable MODIS data sets in 1999–00 session or earlier period. The passing time of MODIS and Landsat sensor is different for a specific region. The MODIS-LST and Landsat-LST correlation is mainly area based rather than pixel based. As the MOD11A1 data derived LST (1000 m resolution) is much lower than the spatial resolution of Landsat data derived LST (100 m resolution), the area based validation of the result was performed instead of pixel based validation. This correlation has been performed on the basis of sample study. Pearson's linear correlation method was applied in the study. A significant correlation coefficient values for all season is noticed after using the one-tail Student's t-test (Table 7).

4.4. Seasonal variation on LST-NDBI relationship

Fig. 8(a–d) shows the seasonal variation of LST-NDBI relationships on different LULC types. Here, three types of LULC are considered, i.e., (1) vegetation, (2) water bodies, and (3) built-up and open area. On vegetation, the correlation is strongly positive for any season. NDBI is a built-up index that extracts built-up area invariably. Thus, the LST-NDBI relationship is strongly positive on the built-up area. On water bodies, the relationship is moderate positive. The pre-monsoon season (Fig. 8 (a)) produces a strong positive LST-NDBI correlation on the settlement area and a moderate positive relationship on vegetation and water bodies. In the monsoon season, the relationship is strong to moderate positive on built-up and green area, and moderate positive on water bodies (Fig. 8 (b)). The post-monsoon season has a stable and strong positive correlation (correlation coefficient > 0.50) for any LULC categories throughout the period (Fig. 8 (c)). The strongest correlation builds on green vegetation. In winter, the relationship is moderate positive (Fig. 8 (d)). Green vegetation shows the best LST-NDBI correlation, followed by water bodies. Bare lands reflect the least correlation in the winter season because at that time dry soil and exposed rock surface get cooler than vegetation and water bodies.

Fig. 9 represents a generalized view of the overall seasonal variation of LST-NDBI relationships. The relationship is positive and very stable.
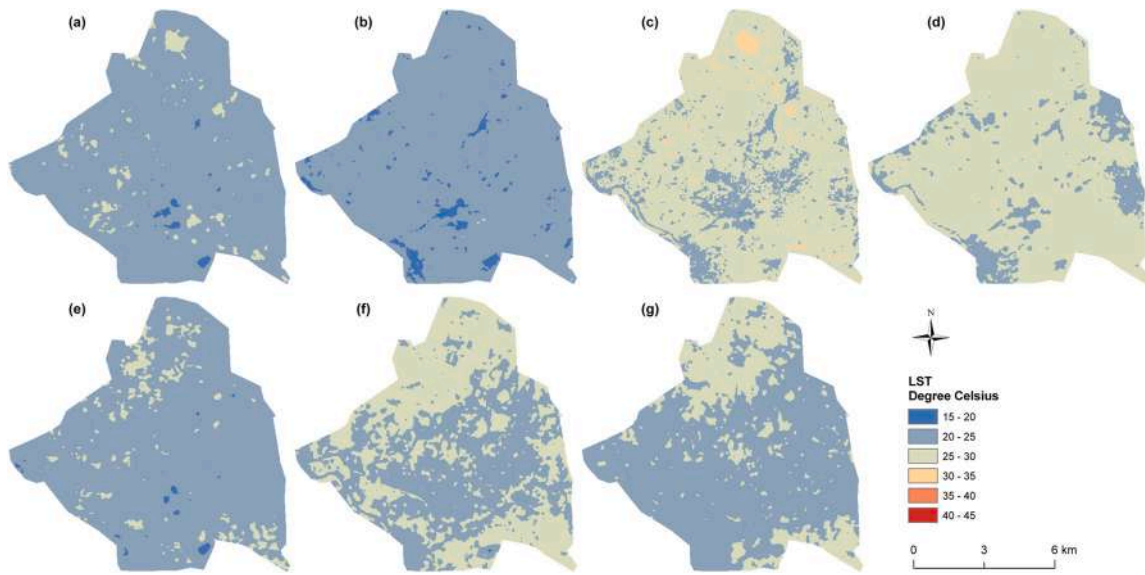
Fig. 6. Mean LST in winter season: (a) 1991–92 (b) 1995–96 (c) 1999–00 (d) 2004–05 (e) 2009–10 (f) 2014–15 (g) 2018-19.
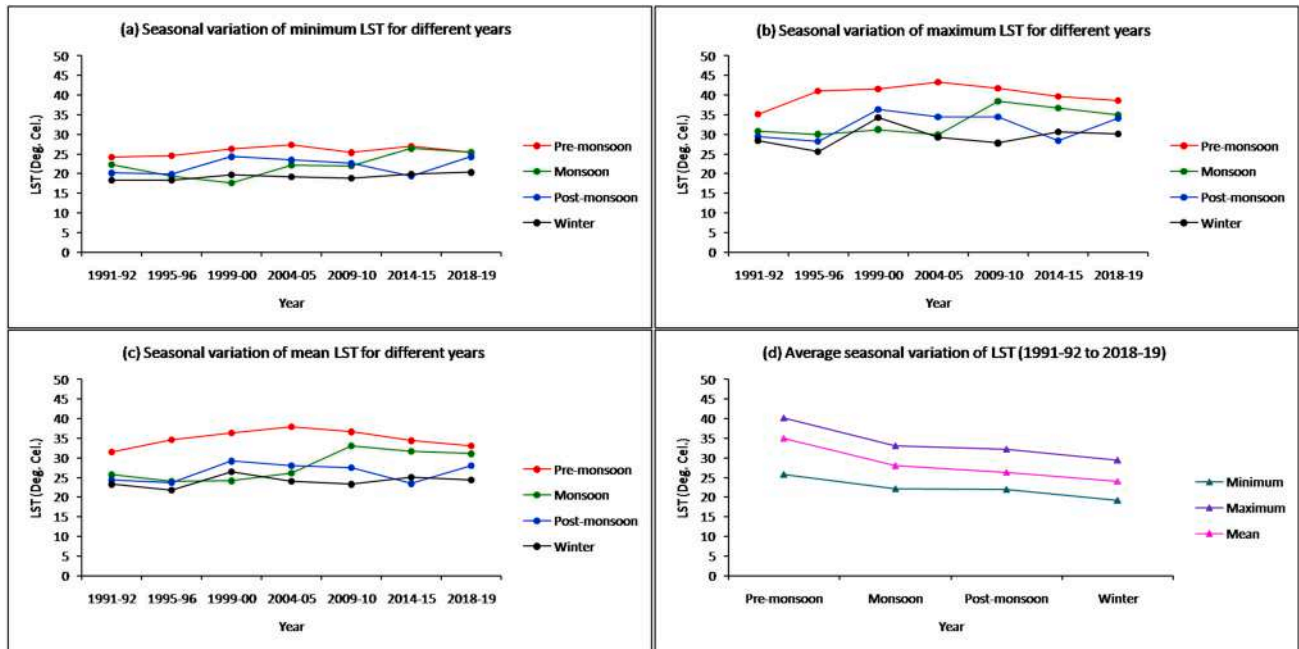
Fig. 7. Seasonal variation of LST (^{o}C): (a) minimum LST for individual years (b) maximum LST for individual years (c) mean LST for individual years (d) average of minimum, maximum, and mean LST for total period of study.

Table 6
Temporal and seasonal change in mean LST (^{o}C) for the whole study area.

Season	1991-92 to 1995-96	1995-96 to 1999-00	1999-00 to 2004-05	2004-05 to 2009-10	2009-10 to 2014-15	2014-15 to 2018-19	1991-92 to 2018-19	Average
Pre-monsoon	2.90	1.74	1.63	−1.34	−2.27	−1.26	1.60	0.49
Monsoon	−1.65	0.09	1.93	6.95	−1.36	−0.62	5.34	1.53
Post-monsoon	−0.62	5.47	−1.16	−0.50	1.34	−4.04	4.76	0.75
Winter	−1.50	4.75	−2.47	−0.76	1.82	−0.76	1.08	0.31
Sum	−0.87	12.05	−0.07	4.35	−0.47	−6.68	12.78	
Average	−0.22	3.01	−0.02	1.09	−0.12	−1.67	3.19	

ARTICLE IN PRESS

S. Guha et al.   Quaternary International xxx (xxxx) xxx

Table 7
Correlation coefficients (0.05 significance level) between Landsat-LST and MODIS-LST.

Season	Year of acquisition	Correlation coefficients
Pre-monsoon	2004–05	0.75
	2009–10	0.74
	2014–15	0.66
	2018–19	0.65
Monsoon	2004–05	0.77
	2009–10	0.71
	2014–15	0.69
	2018–19	0.72
Post-monsoon	2004–05	0.81
	2009–10	0.79
	2014–15	0.71
	2018–19	0.80
Winter	2004–05	0.62
	2009–10	0.65
	2014–15	0.62
	2018–19	0.68

The post-monsoon reveals the best correlation among all the four seasons. Dry atmosphere (winter season) reduces the strength of correlation, while the wet seasons (post-monsoon and monsoon) enhance the strength of the LST-NDBI correlation. Moreover, the strength of LST-NDBI correlation reduces with time (highest in 1991–92 and lowest in 2018–19).

The present study indicates a very strong and stable LST-NDBI correlation for the last 28 years. The result is reliable and significant compared to the other similar studies. A strong positive LST-NDBI correlation was found in Fuzhou City, China using Landsat data (Zhang et al., 2009). Balew and Korme (2020) found a positive correlation in Bahir Dar City, Ethiopia, where LST was decreased in the later period. A moderate to high positive correlation (up to 0.6) between LST and NDBI was observed in Melbourne City, Australia (Jamei et al., 2019). The LST-NDBI correlation was also strong positive ($R^2 > 0.72$) in San Salvador City of El Salvador (Son et al., 2020). Chen and Zhang (2017) showed the strong positive nature of the correlation coefficient of the LST-NDBI relationship in a study performed in Kunming, China. Rosa dos Santos et al. presented a strong positive LST-NDBI correlation. Chen et al. (2013) established a LST-NDBI correlation in Wuhan City, China for spring (0.639), summer (0.717), autumn (0.807), and winter (0.762) which is very much similar to the result found in the current research.

5. Conclusion

The current study analyzes the temporal and seasonal relationship of LST and NDBI in Raipur City, India using sixty-four Landsat data sets
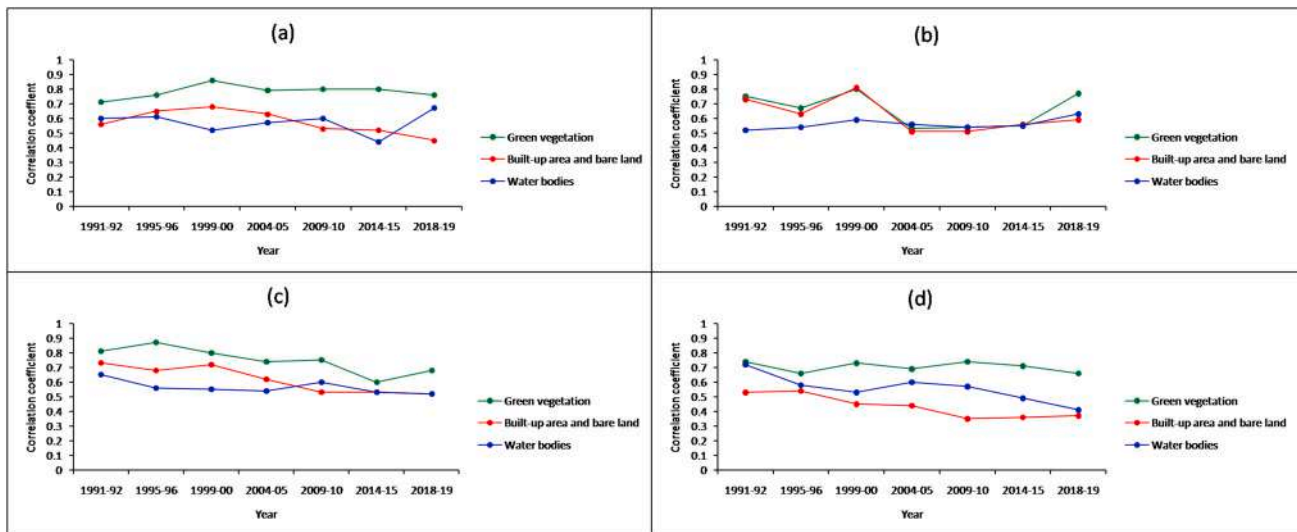
Fig. 8. Seasonal variation of the LST-NDBI relationship on different types of LULC: (a) pre-monsoon (b) monsoon (c) post-monsoon (d) winter.
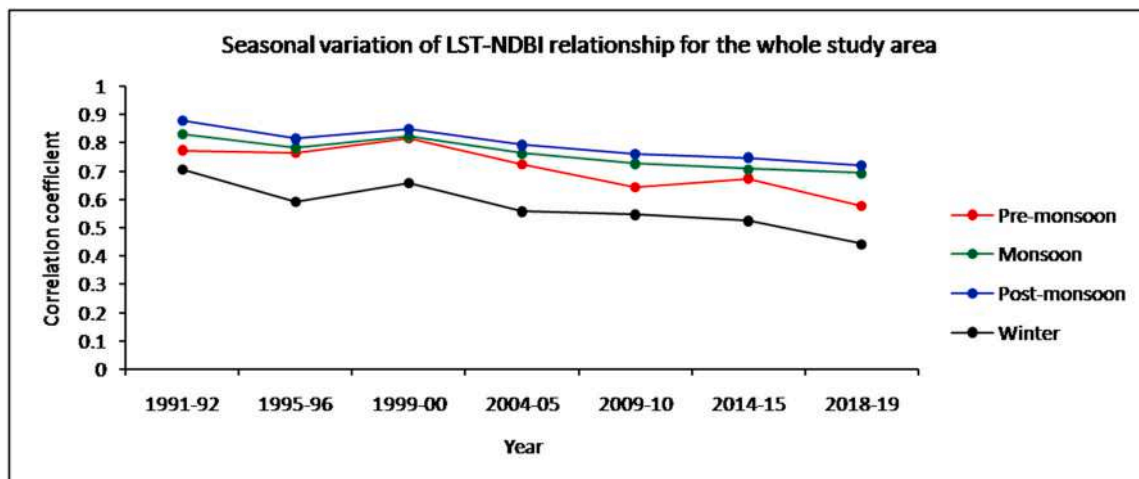
Fig. 9. Long-term seasonal variation of the LST-NDBI correlation.

from 1991–92, 1995–96, 1999–00, 2004–05, 2009–10, 2014–15, and 2018–19. In general, the results show that LST positively correlates NDBI, irrespective of any season. The correlation is strong in the post-monsoon and monsoon, strong to moderate in pre-monsoon and moderate in winter. The LST-NDBI relationship varies for specific LULC types. Among the various LULC categories, the green vegetation presents the strongest correlation. In the winter season, water bodies show a better correlation. Both the changed and unchanged area suffers from the increasing trend of LST. Moreover, the study also reflects the increasing trend of the LST with the urbanization, which can be a serious threat for plants, animals, and human health systems.

Declaration of competing interest

Acknowledgment

References

Alexander, C., 2020. Normalised difference spectral indices and urban land cover as indicators of land surface temperature (LST). Int. J. Appl. Earth Obs. Geoinf. 86, 102013. https://doi.org/10.1016/j.jag.2019.102013.

Balew, A., Korme, T., 2020. Monitoring land surface temperature in Bahir Dar city and its surrounding using Landsat images. Egypt. J. Remote Sens. Space Sci. https://doi.org/10.1016/j.ejrs.2020.02.001.

Carlson, T.N., Ripley, D.A., 1997. On the relation between NDVI, fractional vegetation cover, and leaf area index. Remote Sens. Environ. 62, 241–252. https://doi.org/10.1016/S0034-4257(97)00104-1.

Chen, L., Li, M., Huang, F., Xu, S., 2013. Relationships of LST to NDBI and NDVI in wuhan city based on landsat ETM+ image. In: 2013 6th International Congress on Image and Signal Processing. CISP, Hangzhou, pp. 840–845, 2013.

Chen, X.L., Zhao, H.M., Li, P.X., Yi, Z.Y., 2006. Remote sensing image-based analysis of the relationship between urban heat island and land use/cover changes. Remote Sens. Environ. 104 (2), 133–146. https://doi.org/10.1016/j.rse.2005.11.016.

Chen, X., Zhang, Y., 2017. Impacts of urban surface characteristics on spatiotemporal pattern of land surface temperature in Kunming of China. Sustain. Cities Soc. 32, 87–99. https://doi.org/10.1016/j.scs.2017.03.013.

Du, S., Xiong, Z., Wang, Y., Guo, L., 2016. Quantifying the multilevel effects of landscape composition and configuration on land surface temperature. Remote Sens. Environ. 178, 84–92.

Fatemi, M., Narangifard, M., 2019. Monitoring LULC changes and its impact on the LST and NDVI in district 1 of shiraz city. Arab. J. Geosci. 12, 127. https://doi.org/10.1007/s12517-019-4259-6.

Ferrelli, F., Huamantinco, M.A., Delgado, D.A., Piccolo, M.C., 2018. Spatial and temporal analysis of the LST-NDVI relationship for the study of land cover changes and their contribution to urban planning in Monte Hermoso, Argentina. Doc. Anal. Geogr. 64 (1), 25–47. https://doi.org/10.5565/rev/dag.355.

Guha, S., 2016. Capability of NDVI technique in detecting mangrove vegetation. Int. J. Adv. Biol. Res. 6 (2), 253–258.

Govil, H., Guha, S., Dey, A., Gill, N., 2019. Seasonal evaluation of downscaled land surface temperature: a case study in a humid tropical city. Heliyon 5 (6), e01923. https://doi.org/10.1016/j.heliyon.2019.e01923.

Govil, H., Guha, S., Diwan, P., Gill, N., Dey, A., 2020a. Evaluation of ASTER TIR data-based lithological indices in parts of Madhya Pradesh and Chhattisgarh state, India. In: Sharma, N., Chakrabarti, A., Balas, V. (Eds.), Data Management, Analytics and Innovation, Advances in Intelligent Systems and Computing, vol. 1042. Springer, Singapore, pp. 161–169. https://doi.org/10.1007/978-981-32-9949-8_12.

Govil, H., Guha, S., Diwan, P., Gill, N., Dey, A., 2020b. Analyzing linear relationships of LST with NDVI and MNDISI using various resolution levels of landsat 8 OLI/TIRS data. In: Sharma, N., Chakrabarti, A., Balas, V. (Eds.), Data Management, Analytics and Innovation, Advances in Intelligent Systems and Computing, vol. 1042. Springer, Singapore, pp. 171–184. https://doi.org/10.1007/978-981-32-9949-8_13.

Grimm, N.B., Faeth, S.H., Golubiewski, N.E., Redman, C.L., Wu, J., Bai, X., Briggs, J.M., Grimm, N., 2008. Global change and the ecology of cities. Science 319, 756–760.

Guha, S., Govil, H., 2019. Evaluation of ASTER TIR data-based lithological indices in malanjkhand copper mines of Madhya Pradesh, India. B. Appl. Earth Sci. 129 (1), 3–8. https://doi.org/10.1080/25726838.2019.1684018.

Guha, S., Govil, H., 2020. An assessment on the relationship between land surface temperature and normalized difference vegetation index. Environ. Dev. Sustain. https://doi.org/10.1007/s10668-020-00657-6.

Guha, S., Govil, H., Besoya, M., 2020e. An investigation on seasonal variability between LST and NDWI in an urban environment using Landsat satellite data. Geomat. Nat.

Haz. Risk. 11 (1), 1319–1345. https://doi.org/10.1080/19475705.2020.1789762, 1789762.

Guha, S., Govil, H., Dey, A., Gill, N., 2018a. Analytical study of land surface temperature with NDVI and NDBI using Landsat 8 OLI/TIRS data in Florence and Naples city, Italy. Eur. J. Remote Sens. 51 (1), 667–678. https://doi.org/10.1080/22797254.2018.1474494.

Guha, S., Govil, H., Dey, A., Gill, N., 2020b. A case study on the relationship between land surface temperature and land surface indices in Raipur City, India. Geografisk Tidsskrift-Danish J. Geogr. 120 (1), 35–50. https://doi.org/10.1080/00167223.2020.1752272.

Guha, S., Govil, H., Diwan, P., 2019. Analytical study of seasonal variability in land surface temperature with normalized difference vegetation index, normalized difference water index, normalized difference built-up index, and normalized multiband drought index. J. Appl. Remote Sens. 13 (2), 024518 https://doi.org/10.1117/1.jrs.13.024518.

Guha, S., Govil, H., Tripathi, M., Besoya, M., 2018b. Identification of rocks and their quartz content in Amarkantak, India using ASTER TIR data. Int. Arch. Photogram. Rem. Sens. Spatial Inf. Sci. XLII-5 https://doi.org/10.5194/isprs-archives-XLII-5-255-2018, 2018 ISPRS TC V Mid-term Symposium "Geospatial Technology – Pixel to People", 20–23 November 2018, Dehradun, India.

Guha, S., Govil, H., Tripathi, M., Besoya, M., 2018c. Evaluating Crosta technique for alteration mineral mapping in Malanjkhand copper mines, India. Int. Arch. Photogram. Rem. Sens. Spatial Inf. Sci. XLII-5 https://doi.org/10.5194/isprs-archives-XLII-5-251-2018, 2018 ISPRS TC V Mid-term Symposium "Geospatial Technology – Pixel to People", 20–23 November 2018, Dehradun, India.

Guha, S., Govil, H., Gill, N., Dey, A., 2020a. Analysing the capability of NCI technique in change detection using high-and medium-resolution multispectral data. In: Geoecology of Landscape Dynamics. Springer, Singapore, pp. 133–147. https://doi.org/10.1007/978-981-15-2097-6_10.

Guha, S., Govil, H., Diwan, P., 2020d. Monitoring LST-NDVI relationship using premonsoon landsat datasets. Adv. Meteorol. 4539684. https://doi.org/10.1155/2020/4539684.

Guha, S., Govil, H., Gill, N., Dey, A., 2020c. Analytical study on the relationship between land surface temperature and land use/land cover indices. Ann. GIS 26 (2), 201–216. https://doi.org/10.1080/19475683.2020.1754291.

Guha, S., Govil, H., Mukherjee, S., 2017. Dynamic analysis and ecological evaluation of urban heat islands in Raipur city, India. J. Appl. Remote Sens. 11 (3), 036020. https://doi.org/10.1117/1.JRS.11.036020.

Hao, X., Li, W., Deng, H., 2016. The oasis effect and summer temperature rise in arid regions-case study in Tarim Basin. Sci. Rep. 6, 35418. https://doi.org/10.1038/srep35418.

He, B.J., Zhao, Z.Q., Shen, L.D., Wang, H.B., Li, L.G., He, B.J., 2019. An approach to examining performances of cool/hot sources in mitigating/enhancing land surface temperature under different temperature backgrounds based on landsat 8 image. Sustain. Cities Soc. 44, 416–427.

Jamei, Y., Rajagopalan, P., Sun, Q.C., 2019. Spatial structure of surface urban heat island and its relationship with vegetation and built-up areas in Melbourne, Australia. Sci. Total Environ. 659, 1335–1351. https://doi.org/10.1016/j.scitotenv.2018.12.308.

Liu, H., Zhan, Q., Yang, C., Wang, J., 2018. Characterizing the spatio-temporal pattern of land surface temperature through time series clustering: based on the latent pattern and morphology. Rem. Sens. 10, 654.

Li, W.F., Cao, Q.W., Kun, L., Wu, J.S., 2017. Linking potential heat source and sink to urban heat island: heterogeneous effects of landscape pattern on land surface temperature. Sci. Total Environ. 586, 457–465. https://doi.org/10.1016/j.scitotenv.2017.01.191.

Nimish, G., Bharath, H.A., Lalitha, A., 2020. Exploring temperature indices by deriving relationship between land surface temperature and urban landscape. Remote Sens. Appl. Soc. Environ. 18, 100299. https://doi.org/10.1016/j.rsase.2020.100299.

Qin, Z., Karnieli, A., Barliner, P., 2001. A mono-window algorithm for retrieving land surface temperature from landsat TM data and its application to the Israel-Egypt border region. Int. J. Rem. Sens. 22 (18), 3719–3746. https://doi.org/10.1080/01431160010006971.

Shigeto, K., 1994. Relation between vegetation, surface temperature, and surface composition in the Tokyo region during winter. Remote Sens. Environ. 50, 52–60. https://doi.org/10.1016/j.scs.2019.101846.

Son, N.T., Chen, C.F., Chen, C.R., 2020. Urban expansion and its impacts on local temperature in San Salvador, El Salvador. Urban Clim. 32, 100617. https://doi.org/10.1016/j.uclim.2020.100617.

Sultana, S., Satyanarayana, A.N.V., 2020. Assessment of urbanisation and urban heat island intensities using landsat imageries during 2000 – 2018 over a sub-tropical Indian City. Sustain. Cities Soc. 52, 101846.

Yang, J., Qiu, J., 1996. The empirical expressions of the relation between precipitable water and ground water vapor pressure for some areas in China. Sci. Atmos. Sin. 20, 620–626.

Zhang, Y., Odeh, I.O.A., Han, C., 2009. Bi-temporal characterization of land surface temperature in relation to impervious surface area, NDVI and NDBI, using a sub-pixel image analysis. Int. J. Appl. Earth Obs. Geoinf. 11 (4), 256–264. https://doi.org/10.1016/j.jag.2009.03.001.

Zha, Y., Gao, J., Ni, S., 2003. Use of normalized difference built-up index in automatically mapping urban areas from TM imagery. Int. J. Rem. Sens. 24 (3), 583–594. https://doi.org/10.1080/01431160304987.

Subhanil Guha is pursuing his Ph.D. degree in Remote Sensing and GIS from the Department of Applied Geology, National Institute of Technology Raipur, India. He received his B.Sc. and M.Sc. degree in Geography from University of Calcutta, West Bengal, India. He also received P.G. Diploma in Geoinformatics from IIRS, Dehradun, India and

ITC, Enschede, The Netherlands. His research interests include applications of thermal infrared remote sensing in various fields of geography, environment, and geology.

Himanshu Govil received his B.Sc., M.Sc. and Ph.D. degree in Geology from Aligarh Muslim University, Aligarh, Uttar Pradesh, India. He also received his P.G. Diploma in Geoinformatics from IIRS, Dehradun, India and ITC, Enschede, The Netherlands. Since 2015, he has been working as an assistant professor in the Department of Applied Geology at National Institute of Technology Raipur, India. His research interests include applications of hyperspectral and thermal infrared remote sensing in mineral exploration and geological mapping.

Neetu Gill received her B.A., M.A., and Ph.D. degree in Geography from Mahatma Jyotiba Phule Rohilkhand University, Bareilly, Uttar Pradesh, India. She also received her P.G.

Diploma in Remote Sensing and GIS from Indian Institute of Remote Sensing, Dehradun, India. Currently, she is working in Chhattisgarh Council of Science and Technology, Raipur, India. Her research interests include applications of remote sensing in various fields of geography and environment.

Anindita Dey received her B.Sc. degree in Geography from University of Calcutta, West Bengal, India and M.A. degree in Geography from Guru Ghasidas University, Chhattisgarh, India. She also received her P.G. Diploma in Geoinformatics from West Bengal University of Technology, India. Currently, she is working as a faculty member in the Department of Geography at Nazrul Balika Vidyalaya, Guma, West Bengal, India. Her research interests include applications of remote sensing in geography and urban land use.

Source details

Feedback >   Compare sources >

Quaternary International

Scopus coverage years: from 1989 to Present

Publisher: Elsevier

ISSN: 1040-6182

Subject area: (Earth and Planetary Sciences: Earth-Surface Processes)

Source type: Journal

View all documents >   Set document alert   💾 Save to source list

CiteScore 2022   ⓘ
5.6

SJR 2022   ⓘ
0.856

SNIP 2022   ⓘ
0.995

CiteScore   CiteScore rank & trend   Scopus content coverage
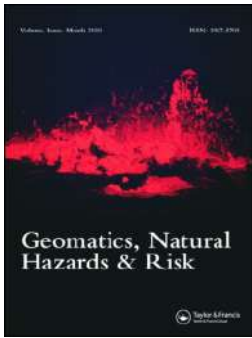
An investigation on seasonal variability between LST and NDWI in an urban environment using Landsat satellite data

Subhanil Guha , Himanshu Govil & Monika Besoya

Published online: 17 Jul 2020.

Submit your article to this journal ☑

View related articles ☑

View Crossmark data ☑

Taylor & Francis
Taylor & Francis Group

An investigation on seasonal variability between LST and NDWI in an urban environment using Landsat satellite data

Subhanil Guha ⓘD, Himanshu Govil ⓘD and Monika Besoya ⓘD

Department of Applied Geology, National Institute of Technology Raipur, Chhattisgarh, India

ABSTRACT

The urban landscape is considered the most complex and heterogeneous landscape among the different land surface features. It rises the land surface temperature (LST) to a large extent compared to the surrounding rural body. This investigation deals with the seasonal variability between LST and normalized difference water index (NDWI) on the different land surfaces in Raipur, India by using sixty-four Landsat images from 1991–92 to 2018–19. The results show that the post-monsoon season indicates the best correlation (0.42) between LST and NDWI, followed by the monsoon (0.34), pre-monsoon (0.25) and winter (0.04). The water bodies reflect a moderate negative correlation of LST-NDWI in all the four seasons (−0.49 in pre-monsoon, −0.33 in monsoon, −0.31 in post-monsoon and −0.45 in winter). On green vegetation, this LST-NDWI correlation is strongly positive in pre-monsoon (0.67) season, moderate positive in monsoon (0.43) and post-monsoon (0.50) seasons, and weak negative in winter (0.25) season. The built-up area and bare lands build a weak positive correlation of LST-NDWI in all the four seasons (0.24 in pre-monsoon, 0.21 in monsoon, 0.27 in post-monsoon and 0.15 in winter). This study can be beneficial for land use planning and management of any city under a similar physical environment.

1. Introduction

Land surface temperature (LST) extensively contributes in determining the ecological health of modern urban environment (Foley et al. 2005; Patz et al. 2005; Huang et al. 2009; Du et al. 2016; Grimn et al. 2008; Liu et al. 2018). The urbanization is a man-induced fast process stands on mainly the land conversion and urban area expansion (Guha et al. 2020a). Satellite image helps us in monitoring these rapid urban changes by visible and near-infrared (VNIR), shortwave infrared (SWIR) and thermal infrared (TIR) bands (Chen et al. 2006; Mondal et al. 2011; Das et al. 2013; Ghobadi et al. 2014; Guha 2016; Alexander 2020). The normalized difference remote sensing indices

CONTACT Subhanil Guha ✉ subhanilguha@gmail.com

are invariably used in detecting several environmental changes in urban landscape (Chen et al. 2006; Guha, Govil, Dey et al. 2018, 2020; Govil et al. 2019; Guha and Govil 2019, 2020; He et al. 2019). Apart from the LST estimation, TIR region of electromagnetic spectrum is also very useful in identifying land surface related changes in any region and is significantly applied in almost every sector of earth science domain (Wen et al. 2017; Ferelli et al. 2018; Guha et al. 2018a, 2018b; Alexander 2020; Govil et al. 2020a, 2020b; Nimish et al. 2020; Sultan and Satyanarayana 2020).

Spatial variation of LST is mainly due to the variation of the reflectance and roughness of land surface (Grimm et al. 2008). Generally, green vegetation and water bodies present low LST, whereas built-up area, bare rock surface, or dry soil reflects high LST (Li et al. 2017; Guha et al. 2020b; Guha, Govil, and Diwan 2020). Thus, LST related studies are very important in urban and land use planning and development.

Many tropical and sub-tropical regions or cities around the world reflect various types of analysis on LST, such as Kuwait City of Kuwait (Uddin et al. 2010), Banda Aceh City of Indonesia (Achmad et al. 2010), Lusaka City of Zambia (Simwanda and Murayama 2018), Seoul Metropolitan area of South Korea (Priyankara et al. 2019), Surabaya of Indonesia (Handayani et al. 2019), Addis Ababa of Ethiopia (Dissanayake et al. 2019a), Lagos City of Nigeria (Dissanayake et al. 2019b). Estoque worked on some tropical Southeast Asian cities (e.g. Baguio and Manila in Philippines, Jakarta of Indonesia, Bangkok of Thailand) to demonstrate the UHI effect clearly (Estoque and Murayama 2016, 2017; Estoque et al. 2017). Simwanda et al. (2019) attempted on four rapidly growing tropical African cities (Lusaka of Zambia, Nairobi of Kenya, Addis Ababa of Ethiopia and Lagos of Nigeria) to analyse the effect of surface UHI. Moreover, Ranagalage, Dissanayake et al. (2018) and Ranagalage, Estoque, Zhang, et al. (2018) quantified the urban volume and LST in Tsukuba and Tsuchiura cities of Japan. Hence, urban planning with a high ratio of vegetation and water bodies is a prime condition for LST reduction. The scenario becomes worse in the urban environment of Indian sub-continent, where LST rise is a regular and strong phenomenon. Humid climate, high density of population, high level of different types of pollution, irregular nature of monsoon rainfall, severe heat wave in summer months, unplanned road and settlement in urban area, expansion of urban area, unhygienic lifestyle, lower quality of transport system, increasing slum area, etc. act as positive catalysts for rising up the LST. Recently, some important research works on LST were conducted in most of the Indian sub-continent countries like India, Pakistan and Sri Lanka (Senanayake et al. 2013; Guha et al. 2017, 2019; Ranagalage et al. 2017; Arshad et al. 2019; Ranagalage, Estoque, Handayani, et al. 2018; Ranagalage and Murayama 2018; Dissanayake et al. 2019c; Govil et al. 2019; Mehmood and Butt 2019; Ranagalage et al. 2019; Imran and Mehmood 2020). Normalized difference water index (NDWI) is the most popular index for the extraction of water body that is invariably applied in land use and LST related studies (McFeeters 1996, 2013; Chen et al. 2006; Weng and Quattrochi 2006; Essa et al. 2012; Chen et al. 2013; Yuan et al. 2017). Generally, the nature of LST-NDWI relationship in an urban area is non-linear and insignificant which is controlled by several factors, such as humidity, vegetation, wetland, bare land, air pollution, rock surface, dry or wet soil, heterogeneous man-made materials, etc. (McFeeters 1996; Ghobadi et al. 2014).
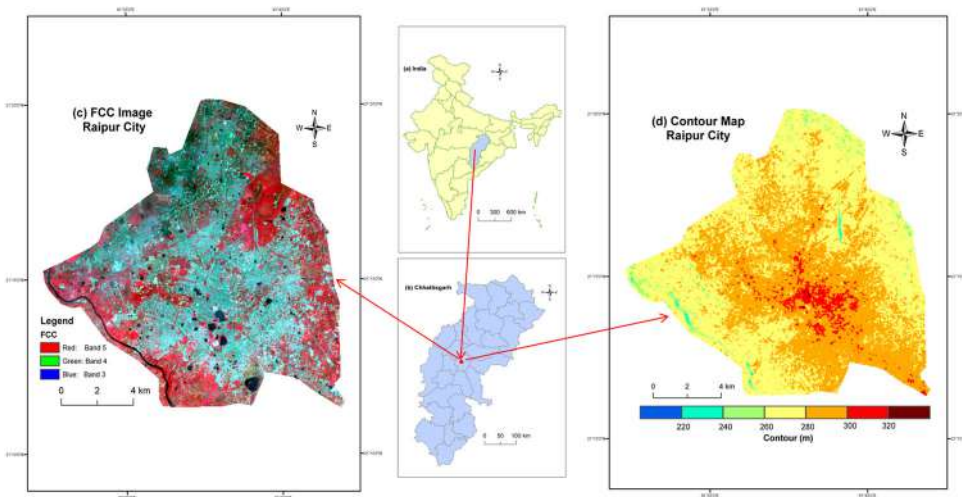
Figure 1. Location of Raipur City: (a) India, (b) Chhattisgarh, (c) FCC image of Raipur City and (d) Contour map of Raipur City [Source: USGS and Survey of India].

In many current research articles, the relationship between LST and NDWI have been constructed using TIR remote sensing (Chen et al. 2006; Ezzine et al. 2014; Debnath et al. 2018; Zhang et al. 2017; Choudhury et al. 2019; Feng et al. 2018; German et al. 2018; Govil et al. 2019; Wu et al. 2019). But, the seasonal analysis of the LST-NDWI relationship in tropical India is rare. The nature of LST and NDWI is changed due to the seasonal changes of evaporation, precipitation, moisture content, air temperature, etc. Thus, a continuous assessment of LST-NDWI relationship is very important in the tropical environment of Indian sub-continent.

The entire research work was conducted in Raipur City of Central India as it is not influenced by the humid maritime or dry extreme climatic condition. The study examines the nature and trend of the effect of LST on NDWI and the LST-NDWI relation on different types of LULC and their seasonal variation. The key objectives of the current research are (1) seasonal assessment of LST and NDWI, and (2) seasonal investigation of LST-NDWI relationship as a whole and on different LULC types. The study will be effective for future town and country planners for better environmental planning.

2. Study area and data

Figure 1 shows the research place (Raipur City of India) of the present research work. Figure 1(a) presents the outline map of India where Chhattisgarh State is located in the middle part (Source: Survey of India). Figure 1(b) presents the outline map of Chhattisgarh State with districts (Source: Survey of India). Figure 1(c) represents the false colour composite (FCC) image of Raipur City prepared from a recent Landsat data (Date: 7 November 2018 (Source: United States Geological Survey (USGS)). Figure 1(d) indicates the contour map of Raipur City prepared from Advanced Spaceborne Thermal and Reflection Radiometer (ASTER) digital elevation model (DEM) data (Date: 11 October 2011 (Source: USGS)) . The city extends from

21°11′22″N to 21°20′02″N and from 81°32′20″E to 81°41′50″E. The total area of the city is approximately 164.23 km². According to India Meteorological Department (IMD), Raipur is under the tropical savannah type of climate. Mean monthly temperature ranges from 12 °C (December) to 42 °C (May). May is the hottest month (average temperature 35 °C) followed by April (average temperature 33 °C), June (average temperature 32 °C) and March (average temperature 29 °C). July is the rainiest month (average rainfall 327 mm) followed by August (average rainfall 300 mm), June (average rainfall 221 mm) and September (average rainfall 200 mm). October and November are the post-monsoon months experience a pleasant weather condition. December (the coldest month: average temperature 20 °C), January (average temperature 21 °C) and February (average temperature 24 °C) are the winter months. November to April remain almost dry (average rainfall <50 mm) compared to the June to September (average rainfall >200 mm).

Table 1 shows the band-wise general description of Landsat satellite sensors. During the entire period of the present study, 21, 8, 14 and 21 level-1 Landsat images have been selected for pre-monsoon, monsoon, post-monsoon and winter seasons, respectively (Table 2). All the data are freely available from the USGS Data Centre. The VNIR, and SWIR bands of Landsat 5 Thematic Mapper (TM), Landsat 7 Enhanced Thematic Mapper Plus (ETM+) and Landsat 8 Operational Land Imager (OLI) and Thermal Infrared Sensor (TIRS) data have a spatial resolution of 30 m. TIR band 10 (100 m resolution) of OLI/TIRS data was recommended due to its better calibration (Guha, Govil, Dey, et al. 2018) and it was resampled to 30 m × 30 m pixel size by USGS Data Centre. TM data has only one TIR band (band 6) of 120 m resolution which was resampled to 30 m × 30 m pixel size by the USGS Data Centre. ETM + data has TIR band (band 6) of 60 m resolution and it was resampled to 30 m × 30 m pixel size by USGS Data Centre.

3. Methodology

In this study, level-1 data of Landsat TM, ETM + and OLI/TIRS sensors were used. Radiometric correction, geometric correction and resampling are the required pre-processing steps for using these Landsat level-1 images. LST was retrieved through the TIR bands of Landsat data sets (band 6 for TM and ETM + data, whereas band 10 for OLI/TIRS data). Green and NIR bands are required for NDWI generation, while red, NIR and TIR bands are needed in generating LST. Finally, the derived LST and NDWI images of the same season and same year were combined, e.g. the TM data of 18 March 1991, 3 April 1991 and 21 May 1991 were combined to obtain the final product of pre-monsoon image for 1991–92. Following these steps, a total of twenty-eight combined images (four seasonal images for seven separate years) were generated.

3.1. Image pre-processing and atmospheric correction

The TIR bands of different Landsat sensors were resampled at 30 m resolution using the nearest neighbour algorithm to match the VNIR bands. Atmospheric correction of the data was done by the following steps:

Table 1. Band and wavelength information about various types of Landsat sensors (Source: USGS).

Landsat 5 TM			Landsat 7 ETM+			Landsat 8 OLI/TIRS		
Bands	Wavelength (μm)	Resolution (m)	Bands	Wavelength (μm)	Resolution (m)	Bands	Wavelength (μm)	Resolution (m)
Band1-Blue	0.45–0.52	30	Band1-Blue	0.45–0.52	30	Band1-Ultra Blue	0.435–0.451	30
Band2-Green	0.52–0.60	30	Band2-Green	0.52–0.60	30	Band2-Blue	0.452–0.512	30
Band3-Red	0.63–0.69	30	Band3-Red	0.63–0.69	30	Band3-Green	0.533–0.590	30
Band4-NIR	0.76–0.90	30	Band4-NIR	0.77–0.90	30	Band4-Red	0.636–0.673	30
Band5-SWIR1	1.55–1.75	30	Band5-SWIR1	1.55–1.75	30	Band5-NIR	0.851–0.879	30
Band6-TIR	10.40–12.50	120*(30)	Band6-TIR	10.40–12.50	60**(30)	Band6-SWIR1	1.566–1.651	30
Band7-SWIR2	2.08–2.35	30	Band7-SWIR2	2.09–2.35	30	Band7-SWIR2	2.107–2.294	30
			Band8-Pan	0.52–0.90	15	Band8-Pan	0.503–0.676	15
						Band9-Cirrus	1.363–1.384	30
						Band10-TIR1	10.60–11.19	100***(30)
						Band11-TIR2	11.50–12.51	100***(30)

*TM band 6 was acquired at 120 m resolution, but products are resampled by USGS to 30 m pixels.
**ETM+ band 6 is acquired at 60 m resolution, but products are resampled by USGS to 30 m pixels.
***TIRS bands 10 and 11 are acquired at 100 m resolution, but products are resampled by USGS to 30 m pixels.

Table 2. Description of used Landsat data sets.

Landsat scene ID	Date of acquisition	Time (UTC)*	Path/Row	Sun elevation (°)	Sun azimuth (°)	Cloud cover (%)	Earth–Sun distance (astronomical unit)	Resolution of VNIR and SWIR bands (m)	Resolution of TIR bands (m)
Pre-monsoon season									
LT51420451991077ISP00	18-Mar-91	04:17:34	142/044	48.58	118.92	0.00	0.99	30	120
LT51420451991093ISP00	03-Apr-91	04:17:46	142/044	53.04	111.64	0.00	0.99	30	120
LT51420451991141ISP00	21-May-91	04:18:39	142/044	59.93	87.09	1.00	1.01	30	120
LT51420451995104ISP01	14-Apr-95	04:05:06	142/044	52.75	103.75	0.00	1.00	30	120
LE71420452000094SGS00	03-Apr-00	04:48:35	142/044	59.72	118.62	0.00	1.00	30	60
LE71420452000126SGS00	05-May-00	04:48:20	142/044	65.97	98.50	0.00	1.00	30	60
LT51420452004081BKT00	21-Mar-04	04:35:14	142/044	53.26	121.40	0.00	0.99	30	120
LT51420452004113BKT00	22-Apr-04	04:36:01	142/044	61.43	104.47	1.00	1.00	30	120
LT51420452004145BKT00	24-May-04	04:36:54	142/044	64.25	86.72	0.00	1.00	30	120
LT51420452009062KHC01	03-Mar-09	04:42:22	142/044	49.04	130.64	0.00	0.99	30	120
LT51420452009078KHC00	19-Mar-09	04:42:44	142/044	54.10	124.40	2.00	0.99	30	120
LT51420452009094BKT00	04-Apr-09	04:43:05	142/044	58.86	116.70	0.00	1.00	30	120
LT51420452009110BKT00	20-Apr-09	04:43:24	142/044	62.67	107.39	0.00	1.00	30	120
LT51420452009126BKT00	06-May-09	04:43:42	142/044	65.03	97.25	0.00	1.00	30	120
LT51420452009142KHC00	22-May-09	04:44:00	142/044	65.88	88.22	1.00	1.00	30	120
LC81420452014076LGN01	17-Mar-14	04:56:36	142/044	55.95	129.38	0.00	0.99	30	100
LC81420452014092LGN01	02-Apr-14	04:56:19	142/044	60.91	121.72	0.00	0.99	30	100
LC81420452014140LGN01	20-May-14	04:55:38	142/044	68.56	90.40	5.46	1.01	30	100
LC81420452018071LGN00	12-Mar-18	04:55:43	142/044	54.19	131.16	2.10	0.99	30	100
LC81420452018087LGN00	28-Mar-18	04:55:36	142/044	59.29	124.07	0.01	0.99	30	100
LC81420452018135LGN00	15-May-18	04:55:08	142/044	68.27	93.32	0.30	1.01	30	100
Monsoon season									
LT51420451991269ISP01	26-Sep-91	04:20:03	142/044	52.47	123.30	13.00	1.00	30	120
LT51420451996267ISP00	23-Sep-96	04:14:16	142/044	51.81	120.64	2.00	1.00	30	120
LE71420452000270SGS00	26-Sep-00	04:46:33	142/044	57.21	131.59	6.00	1.00	30	60
LT51420452004161BKT00	09-Jun-04	04:37:23	142/044	63.98	81.78	9.00	1.01	30	120
LT51420452004273BKT00	29-Sep-04	04:40:16	142/044	55.47	131.40	9.00	1.00	30	120
LT51420452009174KHC00	23-Jun-09	04:44:35	142/044	64.96	80.76	0.00	1.00	30	120
LC81420452014156LGN01	05-Jun-14	04:55:45	142/044	68.38	83.30	0.02	1.01	30	100
LC81420452018167LGN00	16-Jun-18	04:55:01	142/044	67.74	81.10	2.31	1.01	30	100
Post-monsoon season									
LT51420451991285BKT02	12-Oct-91	04:20:12	142/044	42.22	131.85	6.00	0.99	30	120
LT51420451991317ISP00	13-Nov-91	04:20:19	142/044	41.53	142.35	1.00	0.99	30	120
LT51420451996283ISP00	09-Oct-96	04:15:07	142/044	48.92	129.53	0.00	0.99	30	120

Table 2. Continued.

Landsat scene ID	Date of acquisition	Time (UTC)*	Path/Row	Sun elevation (°)	Sun azimuth (°)	Cloud cover (%)	Earth–Sun distance (astronomical unit)	Resolution of VNIR and SWIR bands (m)	Resolution of TIR bands (m)
LT51420451996299ISP00	25-Oct-96	04:15:55	142/044	45.37	136.48	5.00	0.99	30	120
LT51420451996315ISP00	10-Nov-96	04:16:41	142/044	41.61	141.11	7.00	0.99	30	120
LE71420451999315SGS00	11-Nov-99	04:49:00	142/044	45.72	149.96	0.00	0.99	30	60
LT51420452004289BKT00	15-Oct-04	04:40:36	142/044	51.63	139.65	4.00	0.99	30	120
LT51420452004321BKT00	16-Nov-04	04:41:11	142/044	43.41	148.58	0.00	0.98	30	120
LT51420452009286KHC00	13-Oct-09	04:46:12	142/044	53.04	140.48	0.00	0.99	30	120
LT51420452009302BKT00	29-Oct-09	04:46:20	142/044	48.72	146.41	0.00	0.99	30	120
LC81420452014316LGN01	12-Nov-14	04:56:21	142/044	46.22	152.46	7.59	0.98	30	100
LC81420452018279LGN00	06-Oct-18	04:55:53	142/044	56.39	140.40	0.06	0.99	30	100
LC81420452018295LGN00	22-Oct-18	04:55:59	142/044	51.96	147.33	0.02	0.99	30	100
LC81420452018311LGN00	07-Nov-18	04:56:03	142/044	47.49	151.56	0.22	0.99	30	100
Winter season									
LT51420451992016ISP00	16-Jan-92	04:20:22	142/044	35.26	139.03	3.00	0.98	30	120
LT51420451992032BKT01	01-Feb-92	04:20:27	142/044	37.41	135.03	0.00	0.98	30	120
LT51420451992048ISP00	17-Feb-92	04:20:15	142/044	40.89	130.26	4.00	0.98	30	120
LT51420451995344BKT00	10-Dec-95	03:56:47	142/044	33.01	139.15	0.00	0.98	30	120
LT51420451996027ISP00	27-Jan-96	04:00:14	142/044	33.31	132.27	0.00	0.88	30	120
LE71420452000030SGS00	30-Jan-00	04:48:55	142/044	41.46	142.31	0.00	0.98	30	60
LE71420452000350SGS00	15-Dec-00	04:46:31	142/044	38.94	150.22	0.00	0.98	30	60
LT51420452004337BKT00	02-Dec-04	04:41:33	142/044	40.14	149.58	0.00	0.98	30	120
LT51420452004353BKT00	18-Dec-04	04:41:52	142/044	38.12	148.74	0.00	0.98	30	120
LT51420452005019BKT00	19-Jan-05	04:42:17	142/044	38.92	143.21	0.00	0.98	30	120
LT51420452005035BKT00	04-Feb-05	04:42:29	142/044	41.74	139.16	0.00	0.98	30	120
LT51420452009350KHC00	16-Dec-09	04:46:44	142/044	38.90	150.21	1.00	0.99	30	120
LT51420452010033KHC00	02-Feb-10	04:46:59	142/044	41.92	140.89	0.00	0.98	30	120
LT51420452010049KHC00	18-Feb-10	04:47:02	142/044	45.89	136.27	7.00	0.98	30	120
LC81420452014364LGN01	30-Dec-14	04:56:09	142/044	39.34	150.83	0.41	0.98	30	100
LC81420452015015LGN01	15-Jan-15	04:56:09	142/044	40.22	147.71	0.01	0.98	30	100
LC81420452015031LGN01	31-Jan-15	04:56:04	142/044	42.76	143.86	0.01	0.98	30	100
LC81420452015047LGN01	16-Feb-15	04:55:55	142/044	46.67	139.41	0.01	0.98	30	100
LC81420452018359LGN00	25-Dec-18	04:55:59	142/044	39.40	151.57	0.01	0.98	30	100
LC81420452019042LGN00	11-Feb-19	04:55:52	142/044	45.33	140.84	0.00	0.98	30	100
LC81420452019058LGN00	27-Feb-19	04:55:48	142/044	49.94	135.93	4.27	0.99	30	100

*IST = UTC + 0530 (IST = Indian standard time, UTC = Coordinated universal time).

Table 3. Description of NDWI.

Acronym	Description	Formulation	References
NDWI	Normalized difference water index	$\frac{Green-NIR}{Green+NIR}$	McFeeters (1996, 2013)

i. Conversion of digital number (DN) into spectral reflectance:

$$\rho\lambda \;=\; M\rho \; \text{X} \; Qcal \;+\; A\rho \tag{1}$$

where, $\rho\lambda$ is the spectral reflectance at top-of-atmosphere (TOA) without correction for solar angle (Unit less), $Qcal$ is the level-1 pixel value in DN, $M\rho$ is the reflectance multiplicative scaling factor for the band, $A\rho$ is the reflectance additive scaling factor for the band.

ii. Correction of spectral reflectance at top-of-atmosphere ($\rho\lambda$) with local sun elevation angle (θs):

$$\rho'\lambda \;=\; \rho\lambda/\sin\;(\theta s) \tag{2}$$

iii. For TIR band of Landsat data, a similar calibration equation is used:

$$L\lambda \;=\; ML \; \text{X} \; Qcal \;+\; AL \tag{3}$$

where, $L\lambda$ is the spectral radiance at TOA, $Qcal$ is the level-1 pixel value in DN, ML is the radiance multiplicative scaling factor for the band and AL is the radiance additive scaling factor for the band.

3.2. Retrieving LST from Landsat data

In this study, the mono-window algorithm has been applied to retrieve LST from multi-temporal Landsat satellite images (Qin et al. 2001; Guha et al. 2017) where three necessary parameters are ground emissivity, atmospheric transmittance and effective mean atmospheric temperature. Several individual equations are part of this mono-window algorithm to determine LST.

These equations are briefly mentioned as given below: (1) conversion of the DN values of TIR band to spectral radiance (Markham and Barker 1985); (2) conversion of this radiance data into degree Celsius (Coll et al. 2010); (3) conversion of the spectral radiance to at-sensor brightness temperature (Wukelic et al. 1989; Chen et al. 2006); (4) determination of normalized difference vegetation index (NDVI) (Tucker 1979); (5) determination of fractional vegetation from NDVI (Carlson and Ripley 1997); (6) determination of land surface emissivity by fractional vegetation (Sobrino et al. 2001, 2004); (7) determination of water vapour content (Yang and Qiu 1996;); (8) determination of total atmospheric transmittance (Qin et al. 2001; Sun et al. 2010); (9) computation of the effective mean atmospheric transmittance of Raipur (Qin et al. 2001; Sun et al. 2010); (10) retrieval of LST using Landsat data (Qin et al. 2001).

Table 4. Accuracy assessment of LULC types (1991–92 to 2018–19).

	LULC types	1991–92	1995–96	1999–00	2004–05	2009–10	2014–15	2018–19
User accuracy (%)	Vegetation	95.65	100.00	95.00	88.24	100.00	100.00	90.91
	Built-up area/bare land	88.89	90.00	90.00	77.78	93.33	94.74	86.96
	Water bodies	100.00	83.33	100.00	100.00	84.62	87.50	83.33
Producer accuracy (%)	Vegetation	100.00	100.00	95.00	88.24	92.31	100.00	83.33
	Built-up area/bare land	88.89	81.82	90.00	87.50	93.33	94.74	90.91
	Water bodies	88.89	90.91	100.00	71.43	91.67	87.50	83.33
Overall accuracy (%)		95.00	92.50	97.50	85.00	92.50	95.00	87.50
kappa coefficient		0.91	0.88	0.96	0.76	0.89	0.92	0.78

Table 5. Total area (km^2) under different types of LULC during the study period.

Year	Vegetation	Built-up area/ bare land	Water
1991–92	140.38	21.16	2.69
1995–96	130.23	31.72	2.29
1999–00	117.74	44.59	1.89
2004–05	112.41	49.68	2.14
2009–10	90.69	71.59	1.95
2014–15	81.63	81.28	1.32
2018–19	63.58	99.53	1.12

3.3. Determination of NDWI

The current reserach work applied NDWI (McFeeters 1996, 2013) as a robust normalized difference spectral index for determining the relationship with LST. NDWI is determined by the green and near-infrared (NIR) bands. For, TM and ETM + data, band 2 is used as green band and band 4 is used as NIR band, respectively. For OLI/ TIRS data, band 3 and band 5 are used as green and NIR bands, respectively (Table 3). The value of NDWI ranges between −1 and +1. Generally, the negative value of NDWI indicates the built-up area and bare land those have no water surfaces, whereas the positive NDWI value shows water and vegetation surface (McFeeters 1996, 2013).

3.4. LULC classification and accuracy assessment

The Raipur City were classified into three different LULC categories including vegetation, built-up area/bare land and water bodies at seven different years (1991–92, 1995–96, 1999–00, 2004–05, 2009–10, 2014–15 and 2018–19) using the maximum likelihood classification algorithm. 400 sample points were generated in each year to cover these three types of LULC. Google earth history images, topographical maps (Source: Survey of India) and LULC maps (Source: Directorate of Town and Country Planning, Chhattisgarh) of Raipur City were used for reference study. After that, user accuracy, producer accuracy, overall accuracy, and kappa coefficient were calculated by using confusion matrix.

Table 4 presents the results of accuracy assessment for LULC classification for the year 1991–92, 1995–96, 1999–00, 2004–05, 2009–10, 2014–15 and 2018–19, separately. The overall accuracies are 95.00%, 92.50%, 97.50%, 85.00%, 92.50%, 95.00% and 87.50%, and the kappa coefficients are 0.91, 0.88, 0.96, 0.76, 0.89, 0.92 and 0.78,
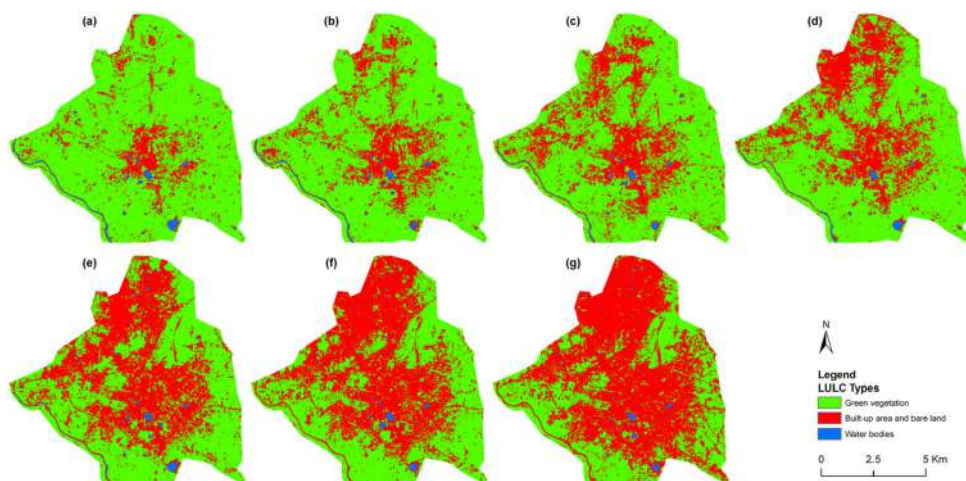
Figure 2. Classified LULC maps: (a) 1991–92, (b) 1995–96, (c) 1999–00, (d) 2004–05, (e) 2009–10, (f) 2014–15 and (g) 2018–19. Source: Author.

Table 6. Temporal and seasonal variation of LST values and Pearson's linear correlation coefficient values of LST-NDWI relationship (significant al 0.05 level).

Season	Year of acquisition	LST (°C)				Correlation coefficients for LST-NDWI relationship
		Min.	Max.	Mean	Std.	
Pre-monsoon	1991–92	24.25	35.22	31.54	1.30	0.13
	1995–96	24.54	41.07	34.64	1.89	0.12
	1999–00	26.36	41.57	36.38	1.89	0.33
	2004–05	27.37	43.32	38.01	2.05	0.29
	2009–10	25.39	41.84	36.67	2.25	0.26
	2014–15	26.97	39.68	34.40	1.65	0.29
	2018–19	25.50	38.70	33.14	1.68	0.35
	Average	*25.76*	*40.20*	*34.96*	*1.81*	0.25
Monsoon	1991–92	22.38	30.83	25.74	1.41	0.26
	1995–96	19.28	30.01	24.09	1.33	0.36
	1999–00	17.62	31.23	24.18	1.34	0.48
	2004–05	22.16	29.97	26.11	0.96	0.28
	2009–10	21.94	38.38	33.06	2.40	0.31
	2014–15	26.43	36.63	31.70	1.16	0.33
	2018–19	25.49	34.98	31.08	1.13	0.36
	Average	*22.18*	*33.14*	*27.99*	*1.39*	0.34
Post-monsoon	1991–92	20.17	29.38	24.32	1.65	0.35
	1995–96	19.85	28.20	23.70	1.30	0.45
	1999–00	24.36	36.38	29.17	1.91	0.26
	2004–05	23.46	34.46	28.01	1.58	0.34
	2009–10	22.59	34.45	27.51	1.54	0.47
	2014–15	19.44	28.31	23.47	1.12	0.49
	2018–19	24.31	34.09	28.08	1.30	0.55
	Average	*22.02*	*32.18*	*26.32*	*1.48*	0.42
Winter	1991–92	18.37	28.33	23.29	1.15	0.05
	1995–96	18.38	25.61	21.79	0.98	−0.03
	1999–00	19.74	34.30	26.54	1.71	−0.08
	2004–05	19.27	29.27	24.07	1.15	−0.03
	2009–10	18.82	27.79	23.31	1.15	0.11
	2014–15	19.95	30.62	25.13	1.35	0.03
	2018–19	20.33	30.14	24.37	1.18	0.21
	Average	*21.28*	*33.14*	*26.67*	*1.33*	*0.57*

Figure 3. Spatial distribution of LST in pre-monsoon season: (a) 1991–92, (b) 1995–96, (c) 1999–00, (d) 2004–05, (e) 2009–10, (f) 2014–15 and (g) 2018–19. Source: Author.

Figure 4. Spatial distribution of LST in monsoon season: (a) 1991–92, (b) 1995–96, (c) 1999–00, (d) 2004–05, (e) 2009–10, (f) 2014–15 and (g) 2018–19. Source: Author.

respectively, for the year 1991–92, 1995–96, 1999–00, 2004–05, 2009–10, 2014–15 and 2018–19. The average value of overall accuracy and kappa coefficient for the seven separate years are 92.14% and 0.87, respectively. Thus, the present research successfully achieves the required accuracy assessment for LULC classification (Lea and Curtis 2010; Nigatu et al. 2014).

3.5. Generation of LST-NDWI relationship on different LULC categories

LST-NDWI relationship of the selected Landsat datasets were generated on three specific LULC types in the study area, i.e. water, vegetation and built-up area/bare land. Finally, the seasonal and temporal variations of these LST-NDWI relationships were analysed.

4. Results and discussion

4.1. Estimated area under different LULC categories

The total area under different LULC categories was shown in Table 5. Water bodies are the most stable LULC type in the study area. Green vegetation was decreased in a very significant amount (76.80 km^2) from 1991–92 to 2018–19. At the same time, the built-up area/bare land was increased at a very high rate (78.37 km^2 in 27 years) due to rapid conversion of land.

Figure 2 shows the false colour composite (FCC) images of the post-monsoon Landsat images of different years. Generally, the monsoon and post-monsoon seasons enhance the greenness of an area. Here, the post-monsoon images are considered for the generation of LULC maps. In 1991–92, the built-up area/bare land were mainly found in the central part of the Raipur City. The northwest portion of the city was rapidly urbanized from 1991–92 to 2004–05 as the percentage of urban vegetation was declined due to the conversion into built-up areas. After 2004–05, the green areas
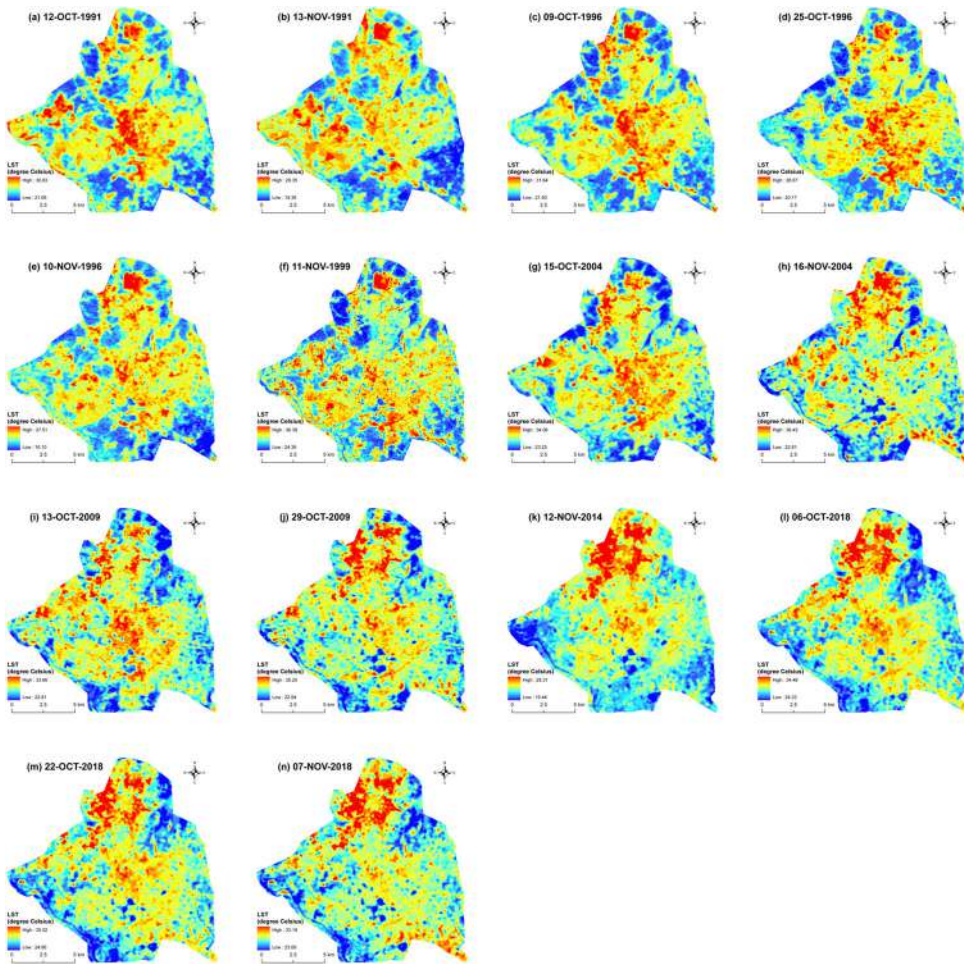
Figure 5. Spatial distribution of LST in post-monsoon season: (a) 1991–92, (b) 1995–96, (c) 1999–00, (d) 2004–05, (e) 2009–10, (f) 2014–15 and (g) 2018–19. Source: Author.

were reduced at an alarming rate as most of the parts of the city were converted into bare land/built-up area. Only the eastern and the southwestern parts were covered by urban vegetation.

4.2. Characteristics of the spatial distribution of LST and NDWI

Table 6 presents the values of LST for different years. The winter season indicates the lowest mean LST values for all the years, whereas the highest mean LST values are found in the pre-monsoon seasons during the entire time span. From 1991–92 to 2018–19, the mean LST has increased in every season. The post-monsoon season has the mean LST value nearer to the winter season, while monsoon season has a slightly high value of mean LST than the post-monsoon season. The correlation coefficient values of Pearson's linear correlation between the LST and NDWI for the entire period are moderate positive to weak negative. The post-monsoon season has the
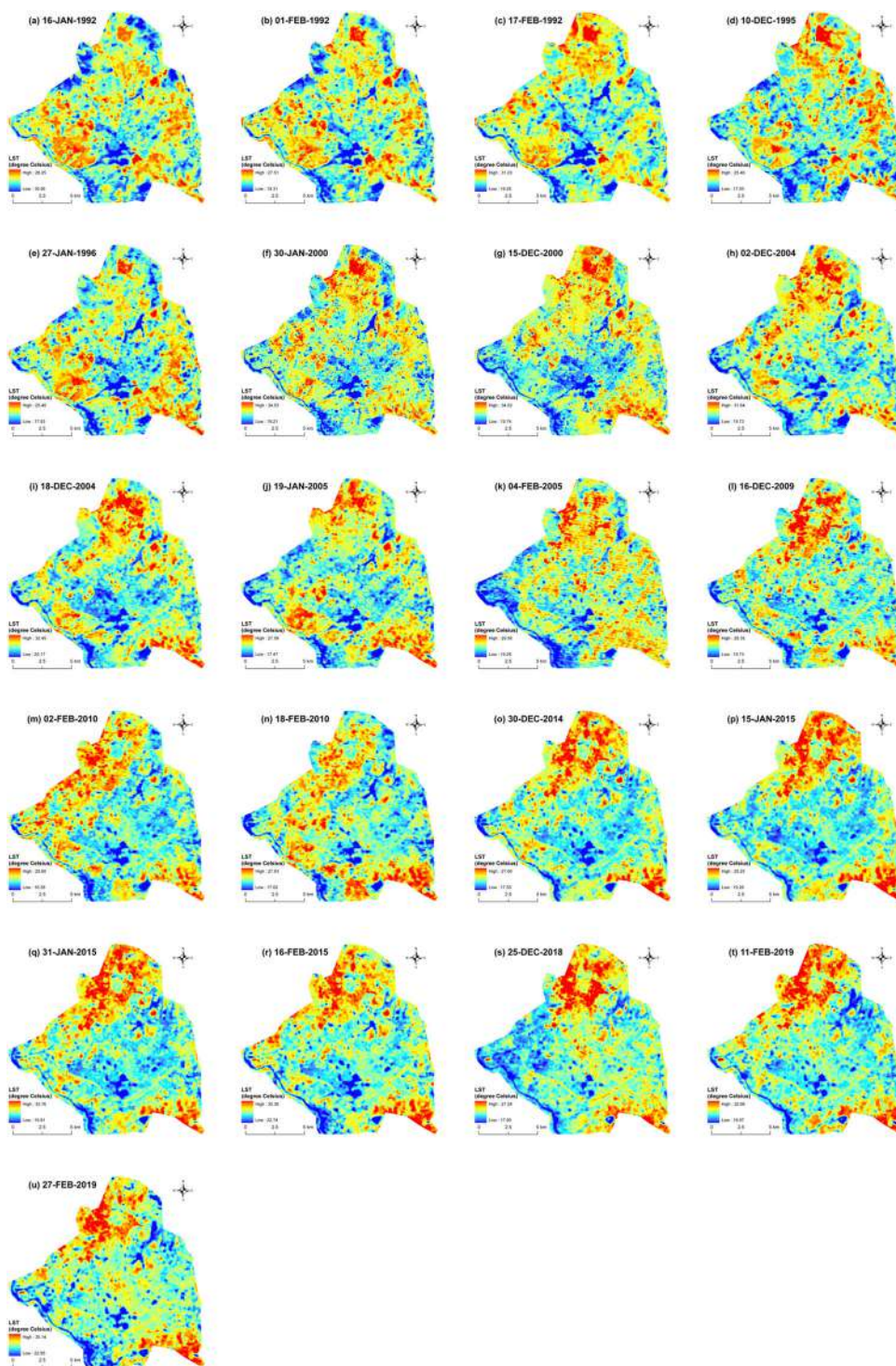
Figure 6. Spatial distribution of LST in winter season: (a) 1991–92, (b) 1995–96, (c) 1999–00, (d) 2004–05, (e) 2009–10, (f) 2014–15 and (g) 2018–19. Source: Author.
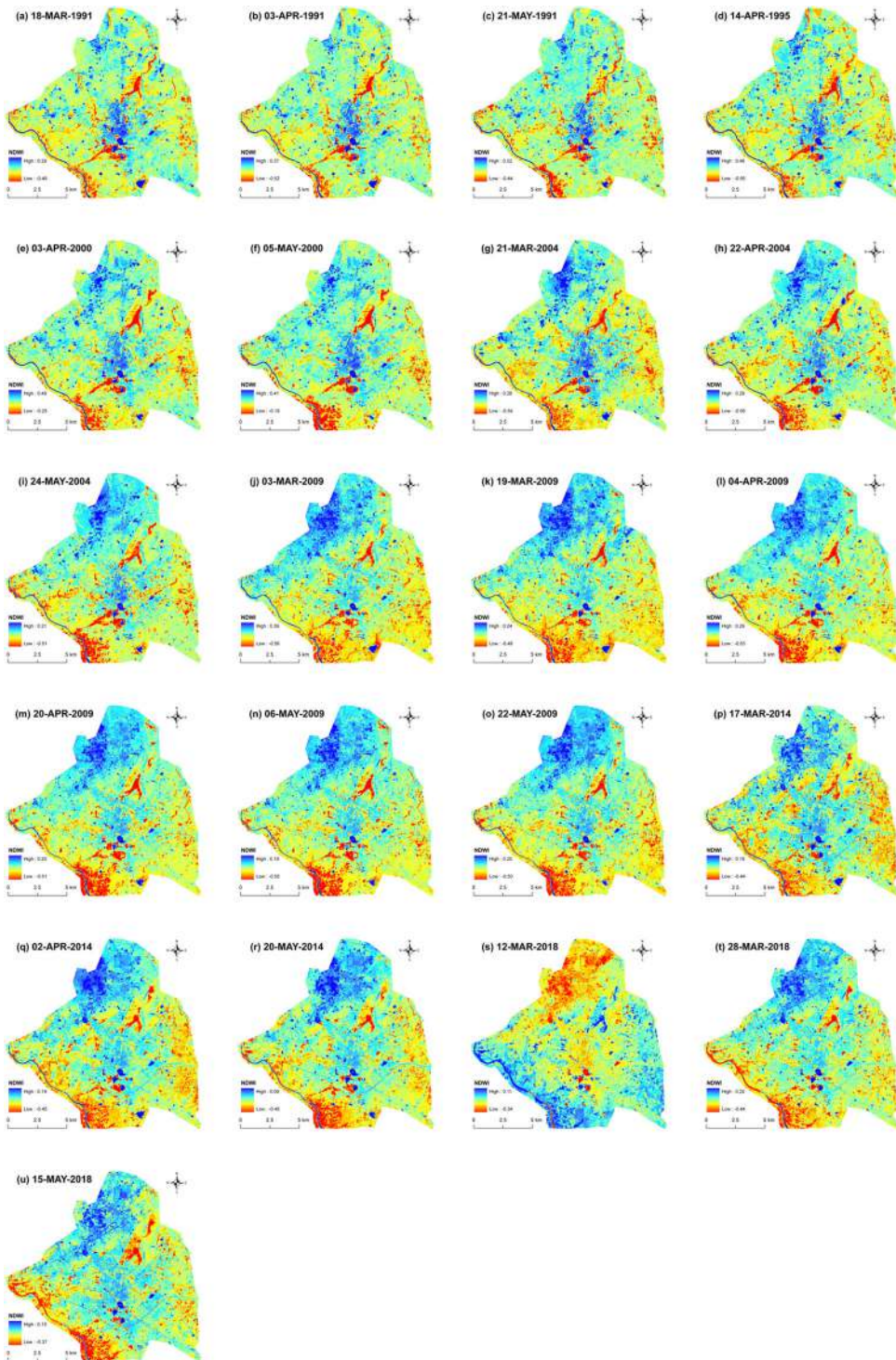
Figure 7. Spatial distribution of NDWI in pre-monsoon season: (a) 1991–92, (b) 1995–96, (c) 1999–00, (d) 2004–05, (e) 2009–10, (f) 2014–15 and (g) 2018–19. Source: Author.
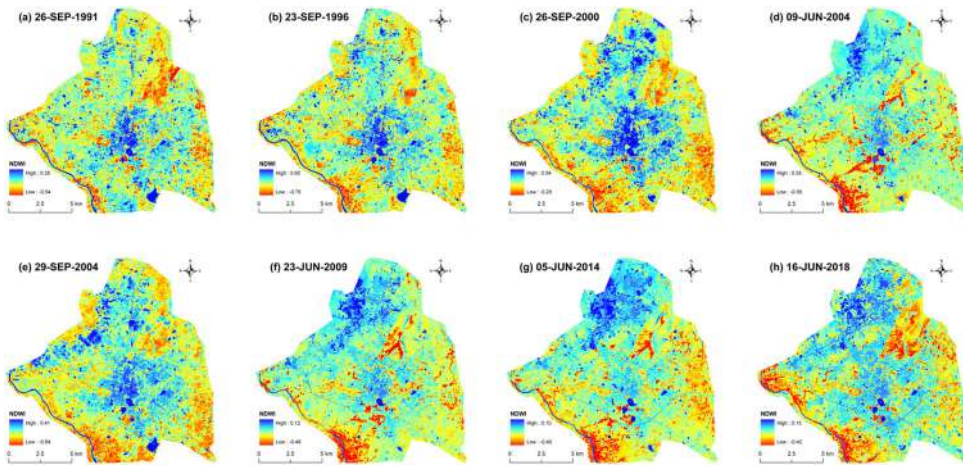
Figure 8. Spatial distribution of NDWI in monsoon season: (a) 1991–92, (b) 1995–96, (c) 1999–00, (d) 2004–05, (e) 2009–10, (f) 2014–15 and (g) 2018–19. Source: Author.

strongest mean (mean value of 1991–92, 1995–96, 1999–00, 2004–05, 2009–10, 2014–15 and 2018–19) correlation coefficient value (0.42), followed by the monsoon (0.34), pre-monsoon (0.25) and winter (0.04) season.

In the present study, LST and NDWI values of each and every single satellite image were determined and the average LST and NDWI values for each season of a single year were also generated. Figures 3–6 show the LST maps of pre-monsoon, monsoon, post-monsoon and winter season, respectively, whereas Figures 7–10 show the NDWI maps of the corresponding seasons. The figures reveal an inverse spatial relationship between LST and NDWI in some parts of the city (e.g. the southeast section shows high LST and low NDWI), whereas most of the areas show positive relationship (e.g. the southwest part has low LST and low NDWI for all the seasons, while the northwest part has high LST and high NDWI). The pre-monsoon season satellite images (Figure 3) have the highest mean LST followed by the satellite images of monsoon (Figure 4), post-monsoon (Figure 5) and winter (Figure 6) seasons. The northwest and southeast parts of the study area exhibit high LST. These parts also have a low percentage of urban vegetation and a high percentage of built-up area and bare land (Figure 2). It shows that the proportion of vegetation was reduced and the built-up area was increased significantly during the time.

Figures 11 and 12 present the seasonal distribution of mean LST and mean NDWI, respectively. These images are composed of the combined images of different months of same season for separate year. The letter 'a', 'b', 'c', 'd', 'e', 'f' and 'g' stand for the year 1991–92, 1995–96, 1999–00, 2004–05, 2009–10, 2014–15 and 2018–19, respectively. Besides, the number '1' '2', '3' and '4' stand for pre-monsoon, monsoon, post-monsoon and winter seasons, respectively. Thus, the term 'a1' indicates the pre-monsoon image of 1991–92; 'a2' indicates the monsoon image of 1991–92; and so on. Figure 11 shows that generally, LST is decreased from the pre-monsoon season to winter season and from 1991–92 to 2018–19, but the trend is not gradual. The conversion of other lands into the built-up area and bare land influences a lot on the
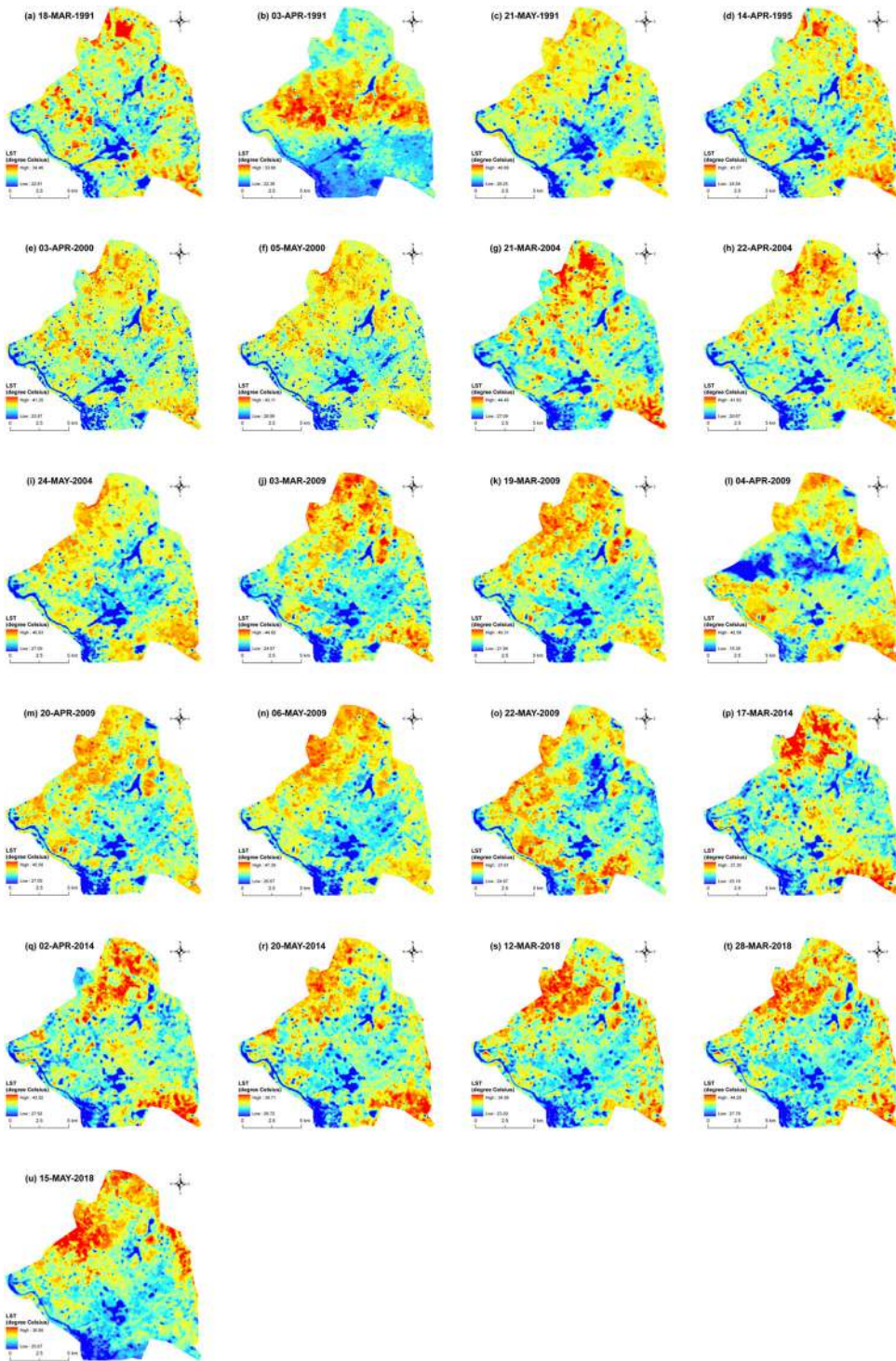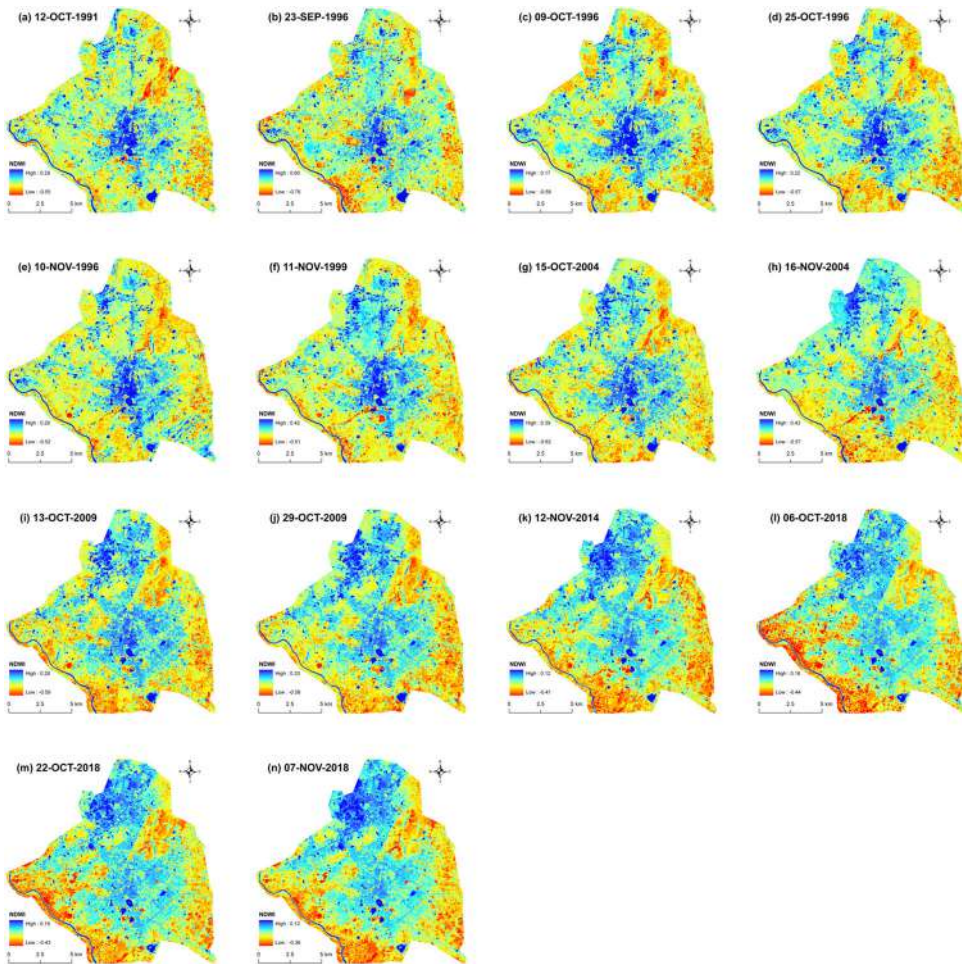
Figure 9. Spatial distribution of NDWI in post-monsoon season: (a) 1991–92, (b) 1995–96, (c) 1999–00, (d) 2004–05, (e) 2009–10, (f) 2014–15 and (g) 2018–19. Source: Author.

mean LST of the city. Both the changed and unchanged built-up area and bare land suffer from the increasing trend of LST. The pre-monsoon season has the maximum average value of mean LST (34.96 °C) followed by monsoon (27.99 °C), post-monsoon (26.32 °C) and winter (24.07 °C). The northwest and southeast parts of the study area exhibit the high LST. These parts also have a low percentage of urban vegetation and high percentage of built-up area and bare land. It shows that the proportion of vegetation has been reduced significantly with time. It is seen that throughout the time, more than 90% of the area in the pre-monsoon season was above 27 °C LST. A different result was seen in the winter season, where 35 °C LST is the maximum upper limit during the entire span.

Figure 12 shows that there is no such variations occur in the temporal or seasonal values of NDWI.
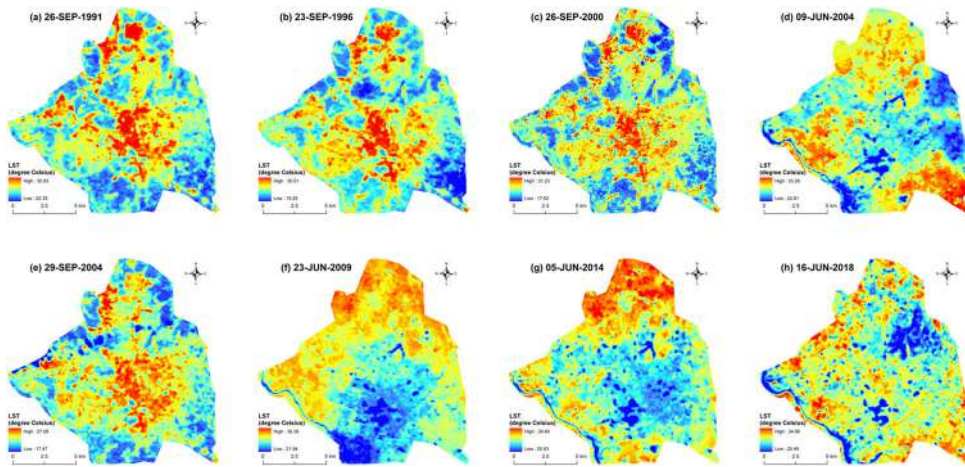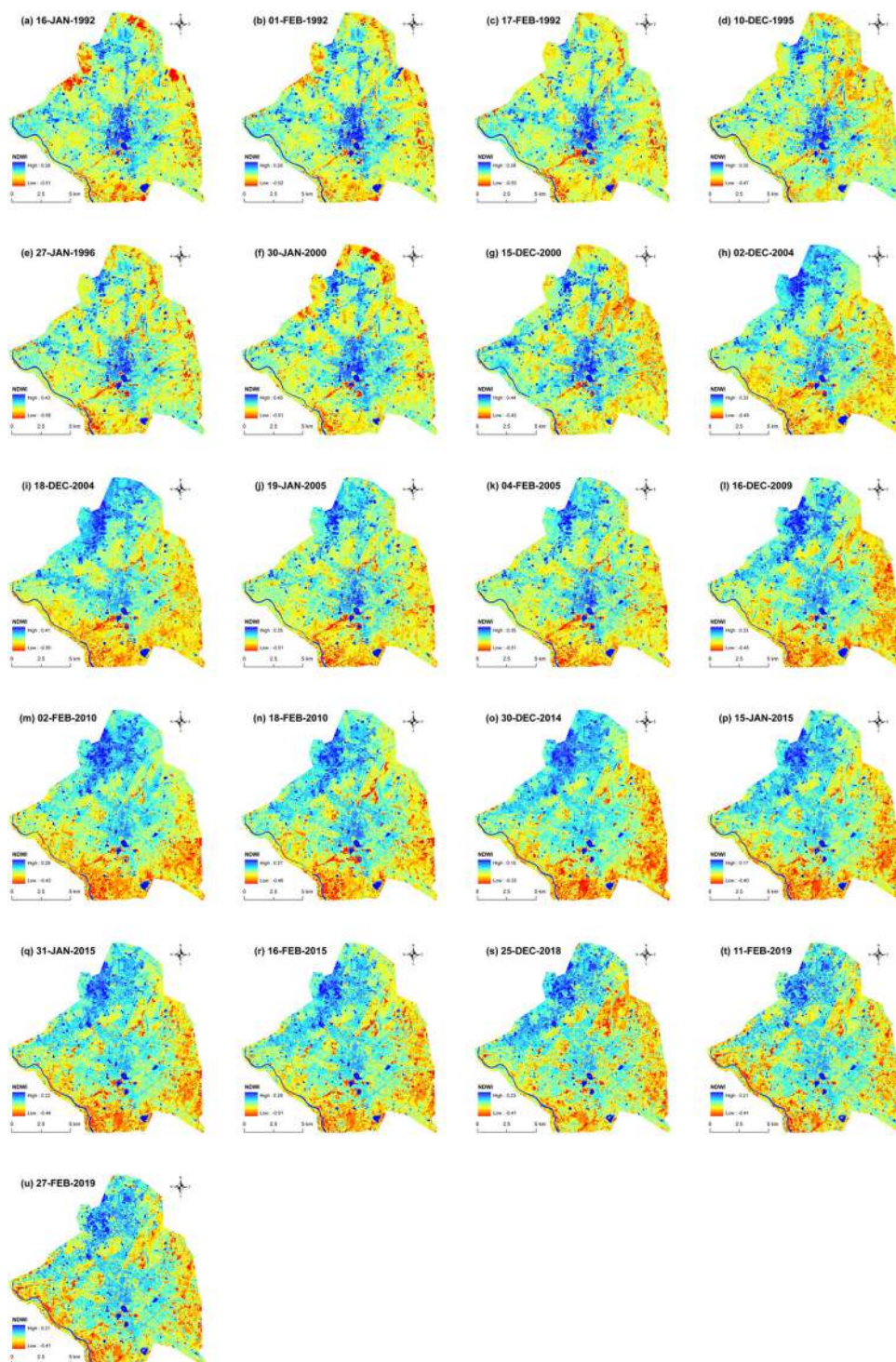
Figure 10. Spatial distribution of NDWI in winter season: (a) 1991–92, (b) 1995–96, (c) 1999–00, (d) 2004–05, (e) 2009–10, (f) 2014–15 and (g) 2018–19. Source: Author.
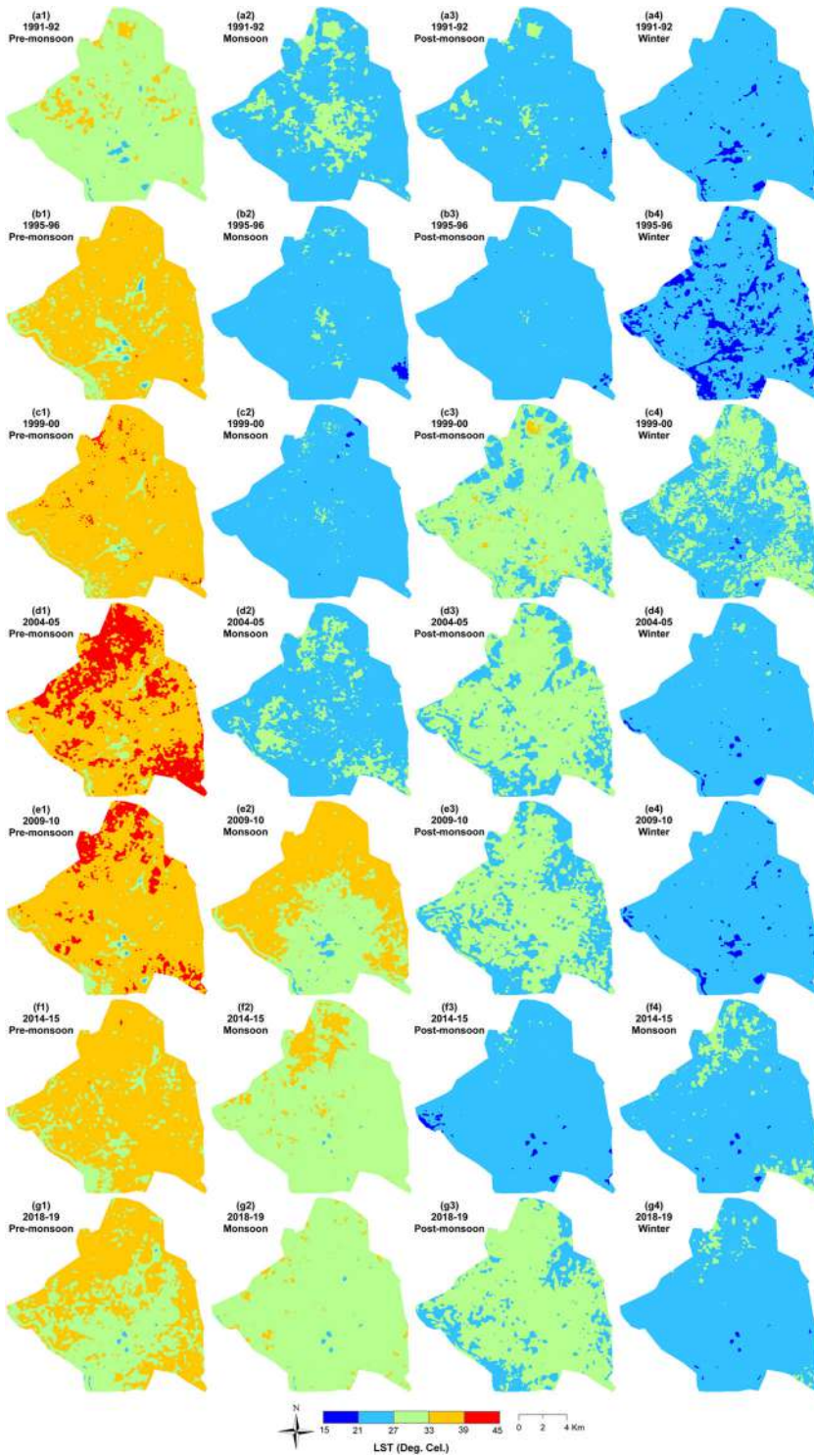
Figure 11. Seasonal distribution of mean LST: (a1–a4) 1991–92, (b1–b4) 1995–96, (c1–c4) 1999–00, (d1–d4) 2004–05, (e1–e4) 2009–10, (f1–f4) 2014–15 and (g1–g4) 2018–19. Source: Author.
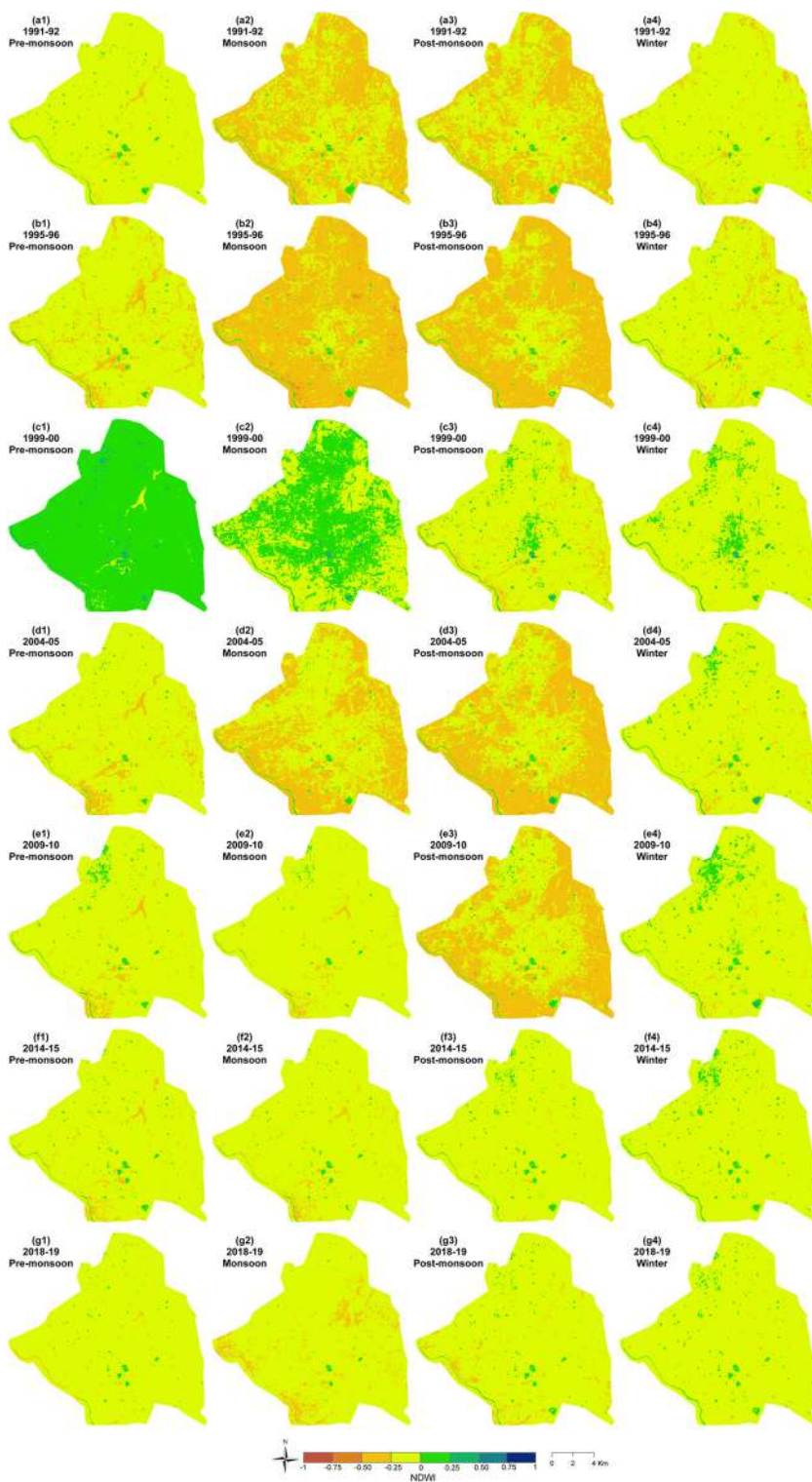
Figure 12. Seasonal distribution of mean NDWI: (a1–a4) 1991–92, (b1–b4) 1995–96, (c1–c4) 1999–00, (d1–d4) 2004–05, (e1–e4) 2009–10, (f1–f4) 2014–15 and (g1–g4) 2018–19. Source: Author.
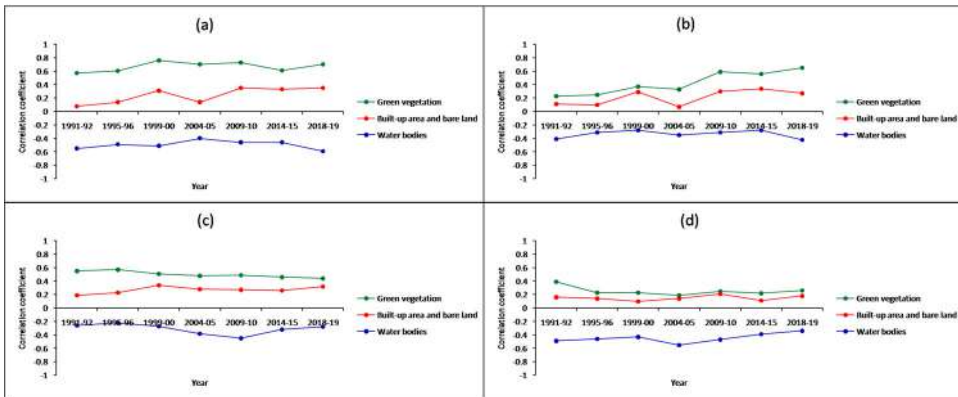
Figure 13. Seasonal variation of the LST-NDWI relationship on different types of LULC (a) pre-monsoon, (b) monsoon, (c) post-monsoon and (d) winter (significant at 0.05 level). Source: Author.

4.3. Relationship between LST and various types of LULC

The LST of the study area significantly depends upon the LULC types. Generally, the area with green vegetation has low LST value; the built-up areas and bare lands have moderate to high LST value, and the water bodies are characterized by a low to moderate range of LST. In the pre-monsoon season, the built-up area and bare land have comparatively high LST than the other LULC types. But in the winter season, these areas have comparatively low to moderate LST due to low emissivity. Green areas and water areas are characterized by a relatively stable range of low LST values.

4.4. Seasonal variation on LST-NDWI relationship

Figure 13(a–d) shows the seasonal variation of LST-NDWI relationships on different LULC types in winter, pre-monsoon, monsoon and post-monsoon season, respectively. Here, only three types of LULC are considered, i.e. (1) vegetation, (2) water bodies and (3) built-up area and bare land. On water bodies, the LST-NDWI relationship is moderate negative for any season. NDWI is a water index that is frequently used in water body extraction. On the bare land and built-up area of the study area, the correlation is a weak positive for all four seasons. On green vegetation, the relationship is strong (pre-monsoon) to moderate (monsoon, post-monsoon and winter (weak moderate)) positive. The pre-monsoon season (Figure 13(a)) has a strong positive LST-NDWI correlation on the green vegetation (0.67), a weak positive correlation on bare land with built-up area (0.24) and a moderate negative correlation on green vegetation (−0.49). In the monsoon season, the correlation is moderate positive on green vegetation (0.43), weak positive (0.21) on bare land and built-up area, whereas the correlation is moderate negative (−0.43) on water bodies (Figure 13(b)). The post-monsoon season has a moderate to strong positive correlation (0.50) on green vegetation, a weak positive correlation (0.27) on bare land and built-up area and has a moderate negative correlation (−0.31) on water bodies (Figure 13(c)). In winter (Figure 13(d)), the LST-NDWI correlation is weak positive (0.25) on green vegetation,
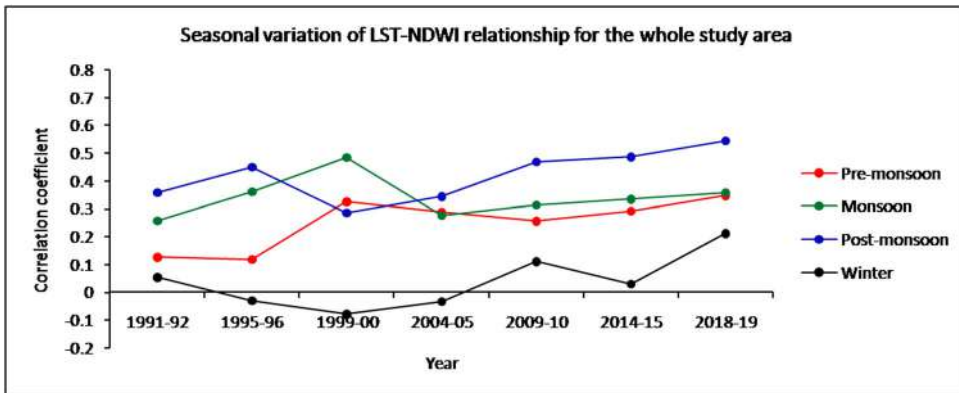
Figure 14. Seasonal variation of the LST-NDWI relationship (significant at 0.05 level). Source: Author.

weak positive (0.15) on built-up area and bare lands. Water bodies have a moderate negative (−0.45) correlation in the winter season.

Figure 14 represents a generalized view of the overall seasonal variation of LST-NDWI relationships. The correlation is positive in the three seasons except the winter where it is mostly negative along with some positive values. It can be concluded from Figure 14 that the post-monsoon season reveals the best correlation, followed by the monsoon and pre-monsoon seasons. There is practically no such relationship found in the winter season. Dry seasons (winter and pre-monsoon) reduce the strength of the correlation, while the wet seasons (post-monsoon and monsoon) enhance the strength of the LST-NDWI correlation.

The present study indicates that LST builds an insignificant and non-linear correlation with NDWI in Raipur City, India from 1991–92 to 2018–19 in four different seasons. The result is reliable and significant compared to the other similar studies using Landsat data. A variable negative LST-NDWI linear correlation was found in the dry barren land of Northwest India and adjoining area of Pakistan, where the LST and NDWI values are highly variable with the nature of rock compositions (Das 2018). NDWI and LST built a non-linear correlation when considering the whole urban area in Wuhan City of China (Wu et al. 2019). In Banda Aceh City of Indonesia, LST built a negative correlation with NDWI from 1988 to 2018 (Achmad et al. 2019). Choudhury et al. (2019) showed a negative correlation of LST-NDWI relationship on the water bodies of Asansol-Durgapur Development Region, India. NDWI and LST built a negative relationship in a dry barren land like Kuwait Desert (Uddin et al. 2010). LST and NDWI produce a negative correlation on the water bodies of Nanchang City, China (Zhang et al. 2017). A significant negative relationship was found between LST and NDWI on the water bodies in Shenzhen City, China (Chen et al. 2006). The present results show a significant and stable negative correlation (−0.49, −0.34, −0.31 and −0.45 in pre-monsoon, monsoon, post-monsoon and winter seasons, respectively) between LST and NDWI on the water bodies throughout the period.

5. Conclusion

The present study investigates the temporal and seasonal relationship of LST and NDWI in Raipur City, India using sixty-four Landsat data sets of four different seasons for 1991–92, 1995–96, 1999–00, 2004–05, 2009–10, 2014–15 and 2018–19. In general, the results show that relationship between LST and NDWI is non-linear. The correlation is moderate positive in the post-monsoon (0.42) and monsoon (0.34) seasons, whereas it is found weak positive in pre-monsoon (0.25) and winter (0.03). The presence of high moisture content in the air and plants is the main responsible factor for high positivity. The LST-NDWI relationship varies for specific LULC types. The water bodies reflect a moderate negative correlation of LST-NDWI in all the four seasons (−0.49 in pre-monsoon, −0.34 in monsoon, −0.31 in post-monsoon and −0.45 in winter). On green vegetation, this LST-NDWI correlation is also strong positive in pre-monsoon (0.67), moderate positive in monsoon (0.43) and post-monsoon (0.50), weak positive in winter (0.25). The built-up area and bare land generate a weak positive correlation of LST-NDWI in all the four seasons (0.24 in pre-monsoon, 0.21 in monsoon, 0.27 in post-monsoon and 0.15 in winter). All the four seasons have very insignificant and non-linear correlation for all LULC types (0.14 in pre-monsoon, 0.10 in monsoon, 0.15 in post-monsoon and −0.02 in winter). The high percentage of urban vegetation and urban water bodies can promote the ecological health of a rapidly growing city like Raipur. The LST-NDWI correlation found in the present study (non-linear) is slightly different from the correlation (negative) built in the desert cities and town those are mostly under dry climate. However, the study will be an effective one for the future town and country planners in such cities of tropical humid areas of Indian sub-continent those are having higher temperatures than the surrounding rural or farmland areas.

Disclosure statement

No potential conflict of interest was reported by the author(s).

ORCID

Subhanil Guha 🔾 http://orcid.org/0000-0002-2967-7248
Himanshu Govil 🔾 http://orcid.org/0000-0002-3433-8355
Monika Besoya 🔾 http://orcid.org/0000-0003-3397-4285

References

Achmad, A., Zainuddin, Muftiadi M. 2019. The relationship between land surface temperature and water index in the urban area of a tropical city. IOP Conf Ser. Earth Environ Sci. 365: 012013.
Alexander C. 2020. Normalised difference spectral indices and urban land cover as indicators of land surface temperature (LST). Int J Appl Earth Obs Geoinf. 86:102013.
Arshad A, Zhang W, Zaman MA, Dilawar A, Sajid Z. 2019. Monitoring the impacts of spatio-temporal land-use changes on the regional climate of city Faisalabad, Pakistan. Ann GIS. 25(1):57–70.

Carlson TN, Ripley DA. 1997. On the relation between NDVI, fractional vegetation cover, and leaf area index. Remote Sens Environ. 62(3):241–252.

Chen XL, Zhao HM, Li PX, Yi ZY. 2006. Remote sensing image-based analysis of the relationship between urban heat island and land use/cover changes. Remote Sens Environ. 104(2): 133–146.

Chen L, Li M, Huang F, Xu S. 2013. Relationships of LST to NDBI and NDVI in Wuhan City based on Landsat ETM + image. 2013 6th International Congress on Image and Signal Processing (CISP), Hangzhou, 2013, pp. 840–845.

Choudhury D, Das K, Das A. 2019. Assessment of land use land cover changes and its impact on variations of land surface temperature in Asansol-Durgapur Development Region. Egypt J Remote Sens Space Sci. 22(2):203–218.

Coll C, Galve JM, Sanchez JM, Caselles V. 2010. Validation of Landsat-7/ETM + thermal-band calibration and atmospheric correction with ground-based measurements. IEEE Trans Geosci Remote Sensing. 48(1):547–555.

Das DN, Mondal A, Guha S. 2013. Change in mangrove forest cover and deltaic islands in sundarban areas of West Bengal: a temporal analyses using NCI technique on LANDSAT TM5 data. Clim Change Environ. Sundaresan J, Sreekesh S, Ramanathan AL, Scientific Publisher, 113-127.

Das S. 2018. Characterization of surface geological material in northwest India and adjoining areas of Pakistan using normalized difference water index, land surface temperature and silica index. J Indian Soc Remote Sens. 46(10):1645–1656.

Debnath M, Syiemlieh HJ, Sharma MC, Kumar R, Chowdhury A, Lal U. 2018. Glacial lake dynamics and lake surface temperature assessment along the Kangchengayo-Pauhunri Massif, Sikkim Himalaya, 1988–2014. Remote Sens Appl Soc Environ. 9:26–41.

Dissanayake D, Morimoto T, Murayama Y, Ranagalage M. 2019a. Impact of landscape structure on the variation of land surface temperature in Sub-Saharan region: a case study of Addis Ababa using Landsat data (1986–2016). Sustainability. 11(8):2257.

Dissanayake D, Morimoto T, Murayama Y, Ranagalage M, Handayani HH. 2019b. Impact of urban surface characteristics and socio-economic variables on the spatial variation of land surface temperature in Lagos City, Nigeria. Sustainability. 11(1):25.

Dissanayake D, Morimoto T, Ranagalage M, Murayama Y. 2019c. Land-use/land-cover changes and their impact on surface urban heat islands: case study of Kandy City, Sri Lanka. Climate. 7(8):99.

Du S, Xiong Z, Wang Y, Guo L. 2016. Quantifying the multilevel effects of landscape composition and configuration on land surface temperature. Remote Sens Environ 178:84–92.

Essa W, Verbeiren B, Van der Kwast J, Van de Voorde T, Batelaan O. 2012. Evaluation of the DisTrad thermal sharpening methodology for urban areas. Int J Appl Earth Obs Geoinf. 19: 163–172.

Estoque RC, Murayama Y. 2016. Quantifying landscape pattern and ecosystem service value changes in four rapidly urbanizing hill stations of Southeast Asia. Landscape Ecol. 31(7): 1481–1507.

Estoque RC, Murayama Y. 2017. Monitoring surface urban heat island formation in a tropical mountain city using Landsat data (1987–2015). ISPRS J Photogramm Remote Sens. 133: 18–29.

Estoque RC, Murayama Y, Myint SW. 2017. Effects of landscape composition and pattern on land surface temperature: an urban heat island study in the megacities of Southeast Asia. Sci Total Environ. 577:349–359.

Ezzine H, Bouziane A, Ouazar D. 2014. Seasonal comparisons of meteorological and agricultural drought indices in Morocco using open short time-series data. Int J Appl Earth Obs Geoinf. 26:36–48.

Feng Y, Li H, Tong X, Chen L, Liu Y. 2018. Projection of land surface temperature considering the effects of future land change in the Taihu Lake Basin of China. Global Planet Change. 167:24–34.

Foley JA, DeFries R, Asner GP, Barford C, Bonan G, Carpenter SR, Chapin FS, Coe MT, Daily GC, Gibbs HK, et al. 2005. Global consequences of land use. Science. 309:570–574.

Ferrelli F, Huamantinco MA, Delgado DA, Piccolo MC. 2018. Spatial and temporal analysis of the LST-NDVI relationship for the study of land cover changes and their contribution to urban planning in Monte Hermoso, Argentina. Doc Anal Geogr. 64(1):25–47.

German A, Espinosa MO, Abril M, Scavuzzo CM. 2018. Exploring satellite based temporal forecast modelling of Aedes aegypti oviposition from an operational perspective. Remote Sens Appl Soc Environ. 11:231–240.

Ghobadi Y, Pradhan B, Shafri HZM, Kabiri K. 2014. Assessment of spatial relationship between land surface temperature and land use/cover retrieval from multi-temporal remote sensing data in South Karkheh Sub-basin, Iran. Arab J Geosci. 8(1):525–537.

Govil H, Guha S, Dey A, Gill N. 2019. Seasonal evaluation of downscaled land surface temperature: a case study in a humid tropical city. Heliyon. 5(6):e01923.

Govil H, Guha S, Diwan P, Gill N, Dey A. 2020a. Evaluation of ASTER TIR Data-Based Lithological Indices in Parts of Madhya Pradesh and Chhattisgarh State, India. In: Sharma N, Chakrabarti A, Balas V, editors. Data management, analytics and innovation. Advances in intelligent systems and computing. Vol. 1042. Singapore: Springer. p. 161–169.

Govil H, Guha S, Diwan P, Gill N, Dey A. 2020b. Analyzing linear relationships of LST with NDVI and MNDISI using various resolution levels of Landsat 8 OLI/TIRS data. In: Sharma N, Chakrabarti A, Balas V, editors. Data management, analytics and innovation. Advances in intelligent systems and computing. Vol. 1042. Singapore: Springer. p. 171–184.

Grimm NB, Faeth SH, Golubiewski NE, Redman CL, Wu J, Bai X, Briggs JM, Grimm N. 2008. Global change and the ecology of cities. Science. 319(5864):756–760.

Guha S. 2016. Capability of NDVI technique in detecting mangrove vegetation. Int J Adv Biol Res. 6(2):253–258.

Guha S, Govil H. 2019. Evaluation of ASTER TIR data-based lithological indices in Malanjkhand Copper Mines of Madhya Pradesh. India. Appl Earth Sci. 129(1):3–8.

Guha S, Govil H. 2020. An assessment on the relationship between land surface temperature and normalized difference vegetation index. Environ Dev Sustain.

Guha S, Govil H, Dey A, Gill N. 2018. Analytical study of land surface temperature with NDVI and NDBI using Landsat 8 OLI/TIRS data in Florence and Naples city, Italy. Eur J Remote Sens. 51(1):667–678.

Guha S, Govil H, Dey A, Gill N. 2020. A case study on the relationship between land surface temperature and land surface indices in Raipur City, India. Geogr Tidsskr. 120(1):35–50. https://doi.org/10.1080/00167223.2020.1752272

Guha S, Govil H, Diwan P. 2019. Analytical study of seasonal variability in land surface temperature with normalized difference vegetation index, normalized difference water index, normalized difference built-up index, and normalized multiband drought index. J Appl Remote Sens. 13(2):024518. https://doi.org/1010.1117/1.JRS.13.024518.

Guha S, Govil H, Diwan P. 2020. Monitoring LST-NDVI relationship using Premonsoon Landsat datasets. Adv Meteorol. 2020:1–15.

Guha S, Govil H, Dey A, Gill N. 2020a. Analysing the capability of NCI technique in change detection using high- and medium-resolution multispectral data. In: Sahdev S, Singh R, Kumar M (eds) Geoecology of landscape dynamics. Advances in Geographical and Environmental Sciences. Springer, Singapore. p. 133–147.

Guha S, Govil H, Gill N, Dey A. 2020b. Analytical study on the relationship between land surface temperature and land use/land cover indices. Ann GIS. 26(2):201–216.

Guha S, Govil H, Mukherjee S. 2017. Dynamic analysis and ecological evaluation of urban heat islands in Raipur city. J Appl Remote Sens. 11(03):1. https://doi.org/10.1117/1.JRS.11.036020

Guha S, Govil H, Tripathi M, Besoya M. 2018a. Identification of rocks and their quartz content in Amarkantak, India using ASTER TIR data. The International Archives of the Photogrammetry, Remote Sensing and Spatial Information Sciences, Volume XLII-5, 2018 ISPRS TC V Mid-term Symposium; November 2018; Dehradun, India. p. 255–223.

Guha S, Govil H, Tripathi M, Besoya M. 2018b. Evaluating Crosta technique for alteration mineral mapping in Malanjkhand copper mines, India. The International Archives of the Photogrammetry, Remote Sensing and Spatial Information Sciences, Volume XLII-5, 2018 ISPRS TC V Mid-term Symposium "Geospatial Technology – Pixel to People; November 2018; Dehradun, India. p. 20–23.

Handayani HH, Murayama Y, Ranagalage M, Liu F, Dissanayake D. 2018. Geospatial analysis of horizontal and vertical urban expansion using multi-spatial resolution data: a case study of Surabaya, Indonesia. Remote Sens. 10(10):1599.

He BJ, Zhao ZQ, Shen LD, Wang HB, Li LG, He BJ. 2019. An approach to examining performances of cool/hot sources in mitigating/enhancing land surface temperature under different temperature backgrounds based on landsat 8 image. Sustain Cities Soc. 44:416–427.

Huang S, Taniguchi M, Yamano M, Wang CH. 2009. Detecting urbanization effects on surface and subsurface thermal environment—a case study of Osaka. Sci Total Environ. 407: 3142–3152.

Imran M, Mehmood A. 2020. Analysis and mapping of present and future drivers of local urban climate using remote sensing: a case of Lahore. Arab J Geosci. 13(6):278.

Lea C, Curtis AC. 2010. Thematic accuracy assessment procedures, Natural Resource Report NPS/NRPC/NRR—2010/204 NPS 999/10. Fort Collins, CO: U.S. Department of the Interior, National Park Service, Natural Resource Program Center.

Li WF, Cao QW, Kun L, Wu JS. 2017. Linking potential heat source and sink to urban heat island: heterogeneous effects of landscape pattern on land surface temperature. Sci Total Environ. 586:457–465.

Liu H, Zhan Q, Yang C, Wang J. 2018. Characterizing the spatio-temporal pattern of land surface temperature through time series clustering: based on the latent pattern and morphology. Remote Sens. 10:654

Markham BL, Barker JK. 1985. Spectral characteristics of the LANDSAT thematic mapper sensors. Int J Remote Sens. 6(5):697–716.

McFeeters SK. 1996. The use of the Normalized Difference Water Index (NDWI) in the delineation of open water features. Int J Remote Sens. 17(7):1425–1432.

McFeeters SK. 2013. Using the Normalized Difference Water Index (NDWI) within a geographic information system to detect swimming pools for mosquito abatement: a practical approach. Remote Sens. 5(7):3544–3561.

Mehmood R, Butt MA. 2019. Appraisal of urban heat island detection of Peshawar using land surface temperature and its impacts on environment. J Indian Soc Remote Sens. 47(6): 1091–1096.

Mondal A, Guha S, Mishra PK, Kundu S. 2011. Land use/land cover changes in Hugli Estuary using Fuzzy C-Mean algorithm. Int J Geomat Geosci. 2(2):613–626.

Nimish G, Bharath HA, Lalitha A. 2020. Exploring temperature indices by deriving relationship between land surface temperature and urban landscape. Remote Sens Appl Soc Environ. 18:100299

Nigatu W, Dick ØB, Tveite H. 2014. GIS based mapping of land cover changes utilizing multi-temporal remotely sensed image data in Lake Hawassa watershed, Ethiopia. Environ Monit Assess. 186(3):1765–1780.

Patz JA, Campbell-Lendrum D, Holloway T, Foley JA. 2005. Impact of Regional Climate Change on Human Health. Nat Cell Boil 438:310–317.

Priyankara P, Ranagalage M, Dissanayake D, Morimoto T, Murayama Y. 2019. Spatial process of surface urban heat island in rapidly growing Seoul metropolitan area for sustainable urban planning using Landsat Data. Climate. 7(9):110.

Qin Z, Karnieli A, Berliner P. 2001. A mono-window algorithm for retrieving land surface temperature from Landsat TM data and its application to the Israel-Egypt Border Region. Int J Remote Sens. 22(18):3719–3746.

Ranagalage M, Dissanayake D, Murayama Y, Zhang X, Estoque RC, Perera E, Morimoto T. 2018. Quantifying surface urban heat island formation in the world heritage tropical mountain city of Sri Lanka. ISPRS J Geo Inf. 7(9):341.

Ranagalage M, Estoque RC, Murayama Y. 2017. An urban heat island study of the Colombo metropolitan area, Sri Lanka, based on Landsat data (1997–2017). ISPRS J Geo Inf. 6(7):189.

Ranagalage M, Estoque R, Handayani H, Zhang X, Morimoto T, Tadono T, Murayama Y. 2018. Relation between urban volume and land surface temperature: a comparative study of planned and traditional cities in Japan. Sustainability. 10(7):2366.

Ranagalage M, Estoque RC, Zhang X, Murayama Y. 2018. Spatial changes of urban heat island formation in the Colombo District, Sri Lanka: implications for sustainability planning. Sustainability. 10(5):1367.

Ranagalage M, Murayama Y. 2018. Measurement of urban built-up volume using remote sensing data and geospatial techniques. Tsukuba Geoenviron Sci. 14:19–29.

Ranagalage M, Murayama Y, Dissanayake D, Simwanda M. 2019. The impacts of landscape changes on annual mean land surface temperature in the tropical mountain city of Sri Lanka: a Case study of Nuwara Eliya (1996–2017). Sustainability. 11(19):5517.

Senanayake IP, Welivitiya W, Nadeeka PM. 2013. Remote sensing based analysis of urban heat islands with vegetation cover in Colombo city, Sri Lanka using Landsat-7 ETM + data. Urban Clim. 5:19–35.

Simwanda M, Murayama Y. 2018. Spatiotemporal patterns of urban land use change in the rapidly growing city of Lusaka, Zambia: implications for sustainable urban development. Sustain Cities Soc. 39:262–274.

Simwanda M, Ranagalage M, Estoque RC, Murayama Y. 2019. Spatial analysis of surface urban heat islands in four rapidly growing African cities. Remote Sens. 11(14):1645.

Sobrino JA, Jimenez-Munoz JC, Paolini L. 2004. Land surface temperature retrieval from Landsat TM5. Remote Sens Environ. 90(4):434–440. doi.org/10.1016/j.rse.2004.02.003

Sobrino JA, Raissouni N, Li Z. 2001. A comparative study of land surface emissivity retrieval from NOAA data. Remote Sens Environ. 75(2):256–266. (00)00171-1

Sultana S, Satyanarayana ANV. 2020. Assessment of urbanisation and urban heat island intensities using landsat imageries during 2000–2018 over a sub-tropical Indian City. Sustain Cities Soc. 52:101846.

Sun Q, Tan J, Xu Y. 2010. An ERDAS image processing method for retrieving LST and describing urban heat evolution: a case study in the Pearl River Delta Region in South China. Environ Earth Sci. 59:1047–1055.

Tucker CJ. 1979. Red and photographic infrared linear combinations for monitoring vegetation. Remote Sens Environ. 8(2):127–150.

Uddin S, Al Ghadban AN, Al Dousari A, Al Murad M, Al Shamroukh D. 2010. A remote sensing classification for land-cover changes and micro-climate in Kuwait. Int J SDP. 5(4):367–377.

Wen LJ, Peng W, Yang H, Wang H, Dong LJ, Shang X. 2017. An analysis of land surface temperature (LST) and its influencing factors in summer in western Sichuan Plateau: a case study of Xichang City. Remote Sens Land Res. 29(2):207–214.

Weng Q, Quattrochi D. 2006. Thermal remote sensing of urban areas: an introduction to the special issue. Remote Sens Environ. 104(2):119–122.

Wu C, Li J, Wang C, Song C, Chen Y, Finka M, Rosa DL. 2019. Understanding the relationship between urban blue infrastructure and land surface temperature. Sci Total Environ. 694:133742.

Wukelic GE, Gibbons DE, Martucci LM, Foote HP. 1989. Radiometric calibration of Landsat Thematic Mapper thermal band. Remote Sens Environ. 28:339–347.

Yang J, Qiu J. 1996. The empirical expressions of the relation between precipitable water and ground water vapor pressure for some areas in China. Sci Atmos Sinica. 20:620–626.

Yuan X, Wang W, Cui J, Meng F, Kurban A, De Maeyer P. 2017. Vegetation changes and land surface feedbacks drive shifts in local temperatures over Central Asia. Sci Rep. 7(1):3287.

Zhang X, Estoque RC, Murayama Y. 2017. An urban heat island study in Nanchang City, China based on land surface temperature and social-ecological variables. Sustain Cities Soc. 32:557–568.

Source details

Feedback ›   Compare sources ›

Geomatics, Natural Hazards and Risk

Open Access ⓘ

Scopus coverage years: from 2010 to Present

Publisher: Taylor & Francis

ISSN: 1947-5705   E-ISSN: 1947-5713

Subject area: (Earth and Planetary Sciences: General Earth and Planetary Sciences) (Environmental Science: General Environmental Science)

Source type: Journal

View all documents ›   Set document alert   💾 Save to source list

CiteScore 2022
7.3   ⓘ

SJR 2022
0.813   ⓘ

SNIP 2022
1.184   ⓘ

CiteScore   CiteScore rank & trend   Scopus content coverage

COVID-19 lockdown effect on land surface temperature and normalized difference vegetation index

Subhanil Guha & Himanshu Govil

Published online: 30 Apr 2021.

Submit your article to this journal ⏎

Article views: 589

View related articles ⏎

View Crossmark data ⏎

Taylor & Francis
Taylor & Francis Group

COVID-19 lockdown effect on land surface temperature and normalized difference vegetation index

Subhanil Guha [ID] and Himanshu Govil [ID]

Department of Applied Geology, National Institute of Technology Raipur, Chattisgarh, India

ABSTRACT

Coronavirus disease (COVID-19) has changed the human lifestyle just like a disaster in 2020. Many people died throughout the world due to its severe attack. Lockdown is the most common term used in today's life to prevent the adverse effect of COVID-19. However, during the lockdown period, a significant improvement in the urban environment was noticed in almost every part of the world. During the lockdown period, the decrease in the number of running vehicles and moving people on the road lowers the pollution level and it has a direct positive impact on the urban environment. The study examines the changes found in land surface temperature (LST) and normalized difference vegetation index (NDVI) during the lockdown period in Raipur city, India with the earlier periods (2013–19) to compare the environmental status. The results indicate that the LST is reduced and NDVI is increased significantly during the lockdown period, and the negativity of the LST-NDVI correlation is increased remarkably. The study also shows a better ecological status of the city during the lockdown period. The study is useful for environmental strategists and urban planners.

1. Introduction

COVID-19 has been spread by severe acute respiratory syndrome coronavirus-2 which has affected more than 219 countries and territories till 3 March 2021. Over 115.365 million total cases of COVID-19 patients were reported so far among whose 2.562 million people were died (https://www.worldometers.info/coronavirus). The most affected countries are the United States of America, India, Brazil, Russia, the United Kingdom, France, Spain, Italy, Turkey, Germany, Colombia, Argentina, Mexico, Poland, Iran, South Africa, Ukraine, Indonesia, Peru, Czechia, and the Netherlands. In each of these countries, at least 1 million people have been affected by the virus. The whole world is looking for its vaccine or suitable medicine for a long time which is still not available in the market. The World Health Organization

CONTACT Subhanil Guha ✉ subhanilguha@gmail.com

(WHO) and the government of individual countries have repeatedly presented several preventive methods to restrict the spreading of this disease. Lockdown is the most popular and effective method among them. As the common people of different countries did not maintain the basic steps to protect themselves from the severe effect of COVID-19, the lockdown was very necessary to stop the contamination process. In the lockdown process, people are compelled to stay at home without any emergency or medical purpose. Academic institutions, public and private offices, restaurants, banks, public and private transports, factories, shops, etc. are entirely closed at the time of proper lockdown.

The lockdown process slows down the environmental pollution and develops a less polluted ecologically rich society (Bashir et al. 2020; Chakraborty and Maity 2020; Garg et al. 2020; Gupta et al. 2020; Mandal and Pal 2020; Mollalo et al. 2020; Öcal et al. 2020; Pandey et al. 2020a, 2020b; Saadat et al. 2020; Şahin 2020; Sharma et al. 2020; Shi et al. 2020; Yunus et al. 2020; Zambrano-Monserrate et al. 2020). The restricted transportation system and industrial activities reduce the air pollution level and enhance air quality. The vegetation grows at a fast rate without any kind of interruption. The immediate positive effect of this lockdown on the environment was noticed in the reduction of air temperature and land surface temperature (LST) (Shi et al. 2020; Yunus et al. 2020). Some valuable studies were conducted in the Indian context to show the improvement of air quality during the lockdown period in India (Chauhan and Singh 2020a, 2020b; Garg et al. 2020; Singh and Chauhan 2020a, 2020b).

LST primarily depends on the land surface composition and solar radiation (Guha et al. 2018; Peng et al. 2016). The vegetation surface generates a low amount of LST, whereas the man-made concrete land surface reflects a high amount of LST (Li et al. 2017). Hence, LST has a broad impact on the planning and development of land utilization management systems (Guha and Govil 2020a, 2020b, 2020c). Normalized difference vegetation index (NDVI) is widely considered as the most significant remote sensing index that regulates the variation of LST (Chen et al. 2006). The LST and NDVI normally generate an inverse correlation (Chen et al. 2006). The improvement of air pollution and the increase of moisture in air predominantly increase the strength of the LST-NDVI correlation (Govil et al. 2019, 2020).

The complete lockdown process in India was started on 25 March 2020 and ended on 31 May 2020. It was broken into four phases as follows:
First Phase: 25 March 2020 − 14 April 2020
Second Phase: 15 April 2020 − 3 May 2020
Third Phase: 4 May 2020 − 17 May 2020
Fourth Phase: 18 May 2020 − 31 May 2020

After the lockdown phases, unlock phases were started and it is still going. The unlock phases were broken into the following phases till 28 February 2021:
Unlock Phase 1.0: 1 June 2020 − 30 June 2020
Unlock Phase 2.0: 1 July 2020 − 31 July 2020
Unlock Phase 3.0: 1 August 2020 − 31 August 2020
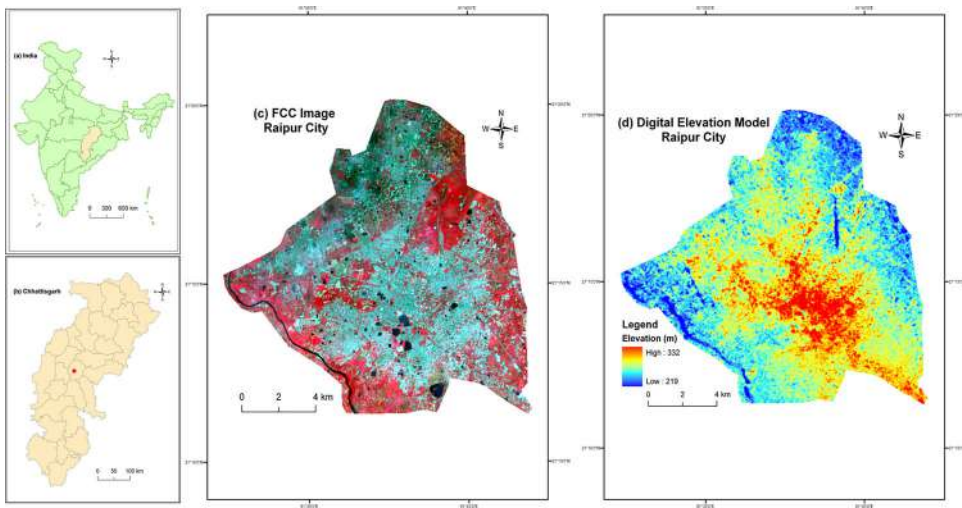
Figure 1. Location map of Raipur city: (a) India (b) Chhattisgarh (c) FCC image of the city (d) DEM of the city.

Unlock Phase 4.0: 1 September 2020 − 30 September 2020
Unlock Phase 5.0: 1 October 2020 − 31 October 2020
Unlock Phase 6.0: 1 November 2020 − 30 November 2020
Unlock Phase 7.0: 1 December 2020 − 30 December 2020
Unlock Phase 8.0: 1 January 2021 − 31 January 2021
Unlock Phase 9.0: 1 February 2021 − 28 February 2021
Unlock Phase 10.0: 1 March 2021 − 31 March 2021 (ongoing)

The key objective of the case study is to examine the immediate effect during the lockdown period in Raipur city of India on the LST, NDVI, and LST-NDVI relationship. Another objective is to evaluate the effect of lockdown on the thermal comfort level of the city. The study can be appraised for future urban planners to develop better environmental planning and management system.

2. Study area

Figure 1 shows the geographical location of Raipur city of India which extends from 21°11′22″N to 21°20′02″N and from 81°32′20″E to 81°41′50″E. The city covers an area of around 165 km^2. Figure 1(a) presents the outline map of India where Chhattisgarh State is located in the middle part (http://www.surveyofindia.gov.in). Figure 1(b) presents the outline map of Chhattisgarh State with districts (http://www. surveyofindia.gov.in). Figure 1(c) represents the false colour composite (FCC) image of Raipur city (https://raipur.gov.in) from recent Landsat 8 OLI/TIRS data of 18 May 2020 (https://www.earthexplorer.usgs.gov). Figure 1(d) indicates the digital elevation map (DEM) of Raipur city produced by the ArcGIS software using the last available ASTER DEM data of 11 October 2011 (https://www.earthexplorer.usgs.gov). The city is characterised by the tropical dry and wet type of climate (http://www.imdraipur. gov.in). The mean monthly temperature ranges from 12 to 42 °C. May presents the

highest average temperature (35 °C), while December presents the lowest average temperature (20 °C). The highest average rainfall (327 mm) is observed in July. March, April, and May are considered as the summer or pre-monsoon months.

3. Materials and methods

In the study, level-1 eighteen Landsat 8 OLI/TIRS data for April and May from 2013 to 2020 were obtained from the United States Geological Survey (USGS) Data Centre (https://www.earthexplorer.usgs.gov). Red, NIR, and TIR bands were required for the research work. The spatial resolution of band 4, band 5, and band 10 of OLI/TIRS data are 30, 30, and 100 m, respectively. The original TIR band 10 was resampled into 30 m spatial resolution by the USGS data centre using the cubic convolution resampling method for further application. The entire research work was performed by using the ArcGIS 9.3 software (https://www.esri.com). The spatial analyst tools of ArcGIS software were used for the raster calculations, correlation analysis, and LST analysis. The following sub-sections are included in the whole methodology section: (1) estimation of LST, (2) determination of NDVI.

3.1. Estimation of LST

LST was estimated from OLI/TIRS sensor by using the mono-window algorithm (MWA) (Qin et al. 2001; Sekertekin and Bonafoni 2020; Wang et al. 2015, 2019). The MWA requires three essential parameters like surface emissivity, atmospheric transmittance, and effective mean atmospheric temperature for LST determination. Although OLI/TIRS data has two TIR bands, band 10 is appropriate for the LST retrieval method as band 11 has larger uncertainty (Barsi et al. 2014; Montanaro et al. 2014).

Equation (1) converts the pixel values of the TIR band into spectral radiance (Zanter 2019).

$$L_\lambda = M_L . Q_{CAL} + A_L \qquad (1)$$

where L_λ= TOA spectral radiance (Wm^{-2}sr^{-1}mm^{-1}), M_L = band-specific multiplicative rescaling factor, A_L= band-specific additive rescaling factor, Q_{CAL}= quantized and calibrated standard product pixel values.

Equation (2) converts the pixel values directly into spectral reflectance (Zanter 2019).

$$\rho_\lambda = \frac{M_\rho . Q_{CAL} + A_\rho}{\sin \theta_{SE}} \qquad (2)$$

where ρ_λ= spectral reflectance, M_ρ = band-specific multiplicative rescaling factor, A_ρ= band-specific additive rescaling factor, Q_{CAL}= quantized and calibrated standard product pixel values, θ_{SE}= local sun elevation angle.

Equation (3) converts the spectral radiance into at-sensor brightness temperature (Wukelic et al. 1989):

$$T_b = \frac{K_2}{\ln\left(\frac{K_1}{L_\lambda} + 1\right)} \tag{3}$$

where T_b = brightness temperature (Kelvin), L_λ= spectral radiance (Wm^{-2} sr^{-1} mm^{-1}), K_1 and K_2 are calibration constants. For OLI/TIRS data, K_1= 774.89, K_2= 1321.08 (Wm^{-2} sr^{-1} mm^{-1}).

Equation (4) determines the fractional vegetation of each pixel (Carlson and Ripley 1997):

$$F_v = \left(\frac{NDVI - NDVI_{min}}{NDVI_{max} - NDVI_{min}}\right)^2 \tag{4}$$

where F_v= fractional vegetation, $NDVI_{min}$= minimum NDVI value, $NDVI_{max}$= maximum NDVI value.

Equations (5–6) show the relationship among ε, ε_v, ε_s, Fv, and $d\varepsilon$ (Sobrino et al. 2004).

$$d\varepsilon = (1 - \varepsilon_s)(1 - F_v)F\varepsilon_v \tag{5}$$

$$\varepsilon = \varepsilon_v F_v + \varepsilon_s(1 - F_v) + d\varepsilon \tag{6}$$

where ε= land surface emissivity, $d\varepsilon$= effect of the geometrical distribution of the natural surfaces and internal reflections, ε_v= vegetation emissivity, ε_s= soil emissivity, Fv= fractional vegetation.

Equation (7) calculates the land surface emissivity (Sobrino et al. 2004).

$$\varepsilon = 0.004 \times F_v + 0.986 \tag{7}$$

where ε = land surface emissivity, F_v = fractional vegetation.

Equation (8) calculates the water vapour content (Yang and Qiu 1996):

$$w = 0.0981 \times \left[10 \times 0.6108 \times \exp\left(\frac{17.27 \times (T_0 - 273.15)}{237.3 + (T_0 - 273.15)}\right) \times RH\right] + 0.1697 \tag{8}$$

where w = water vapour content (g/cm^2), T_0 = near-surface air temperature (Kelvin), RH = relative humidity (%). These atmospheric parameters were provided by the Meteorological Centre, Raipur.

Equation (9) estimates the atmospheric transmittance of Raipur (Qin et al. 2001):

$$\tau = 1.031412 - 0.11536w \tag{9}$$

where τ= total atmospheric transmittance, w = water vapour content (g/cm^2).

Equation (10) estimates the effective mean atmospheric transmittance of Raipur (Qin et al. 2001):
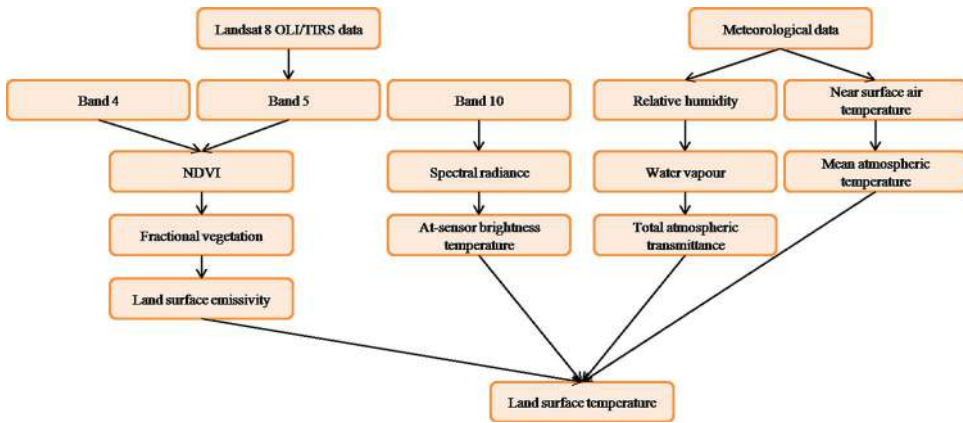
Figure 2. Flowchart of the methodology.

$$T_a = 17.9769 + 0.91715T_0 \tag{10}$$

where T_a= mean atmospheric temperature, T_0= near-surface air temperature.

Equations (11–12) computes the internal parameters C and D and Eq. (13) retrieves LST from OLI/TIRS data (Qin et al. 2001):

$$C = \varepsilon\tau \tag{11}$$

$$D = (1 - \tau)[1 + (1 - \varepsilon)\tau] \tag{12}$$

$$T_s = \frac{[a(1 - C - D) + (b(1 - C - D) + C + D)T_b - DT_a]}{C} \tag{13}$$

where ε = land surface emissivity, τ = total atmospheric transmittance, C and D are internal parameters based on atmospheric transmittance and land surface emissivity, T_s = land surface temperature, T_a = mean atmospheric temperature, T_b = at-sensor brightness temperature, $a = -67.355351$, $b = 0.458606$.

3.2. Determination of NDVI

The study used NDVI (Tucker 1979) as a significant remote sensing index to estimate the impact of the changing environment on LST.

Equation (14) expresses the formula of NDVI:

$$NDVI = NIR-Red/NIR + Red \tag{14}$$

For OLI/TIRS data, NIR and red bands are bands 5 and 4, respectively. The value of NDVI lies between −1 (the extreme negative value) and +1 (the extreme positive value). The negative NDVI values generally indicate water bodies, whereas high positive NDVI values correspond to green and healthy vegetation covers. Values near to 0 or slightly positive indicate sealed areas or barren lands.

Table 1. Comparison of LST and LST-NDVI correlation (significant al 0.05 level) in April and May from 2013 to 2020 using Landsat 8 OLI/TIRS data [Data during the lockdown period have been shown as bold italic font].

Date of acquisition	Time (UTC)[a]	Cloud cover (%)	LST (°C)				NDVI				Correlation coefficients for LST-NDVI relationship
			Min.	Max.	Mean	SD	Min.	Max.	Mean	SD	
April											
2013-Apr-08	04:59	0	29	47	41	2.58	−0.17	0.55	0.11	0.61	−0.46
2014-Apr-02	04:56	0	28	43	36	1.99	−0.13	0.52	0.14	0.07	−0.45
2015-Apr-05	04:55	0	27	43	37	2.08	−0.13	0.49	0.12	0.06	−0.45
2016-Apr-23	04:55	0	30	49	43	2.27	−0.16	0.55	0.13	0.07	−0.47
2017-Apr-10	04:55	0	27	44	38	2.18	−0.14	0.48	0.11	0.06	−0.51
2017-Apr-26	04:55	2	29	49	42	2.57	−0.19	0.59	0.12	0.07	−0.47
2020-Apr-02	*04:55*	*0*	*26*	*43*	*35*	*2.09*	*−0.12*	*0.55*	*0.19*	*0.09*	*−0.57*
2020-Apr-18	*04:55*	*1*	*27*	*38*	*33*	*1.48*	*−0.09*	*0.52*	*0.17*	*0.07*	*−0.53*
May											
2013-May-01	04:57	0	28	42	37	1.72	−0.13	0.56	0.13	0.06	−0.48
2013-May-17	04:58	2	28	46	40	2.22	−0.12	0.52	0.12	0.06	−0.44
2014-May-20	04:55	5	26	39	35	1.72	−0.07	0.45	0.12	0.05	−0.41
2015-May-07	04:55	0	27	40	35	1.81	−0.09	0.49	0.14	0.05	−0.42
2015-May-23	04:55	9	25	42	36	2.26	−0.07	0.43	0.12	0.05	−0.35
2016-May-25	04:55	0	28	41	37	1.65	−0.07	0.47	0.12	0.05	−0.38
2017-May-12	04:55	0	29	43	38	1.89	−0.17	0.55	0.14	0.06	−0.29
2018-May-15	04:55	0	30	44	37	1.92	−0.09	0.40	0.13	0.05	−0.46
2019-May-18	04:55	0	29	45	40	2.12	−0.18	0.51	0.12	0.06	−0.44
2020-May-04	*04:55*	*3*	*29*	*41*	*35*	*1.67*	*−0.16*	*0.57*	*0.18*	*0.08*	*−0.53*

[a]IST = UTC + 0530 (IST = Indian standard time, UTC = coordinated universal time).

The total methodology of the present study is shown by a simple flowchart in Figure 2.

4. Results and discussion

Table 1 represents the values of LST, NDVI, and the LST-NDVI correlation coefficients before 2020 and during the lockdown period of 2020 due to COVID-19. The effects have been discussed separately as follows:

4.1. Effect of lockdown on LST

The minimum LST values in the earlier images of April month (28.64, 27.92, 27.30, 30.22, 27.35, and 29.47 °C) were quite higher compared to the minimum LST values in the lockdown images of April month (26.21 and 27.08 °C). The maximum LST values also show similar result (47.38, 43.52, 43.34, 49.45, 44.58, 49.39 °C LST in the earlier images and 43.30, 38.38 °C LST during the lockdown period). The mean LST values during the lockdown period of April month (35.10 and 33.47 °C) were quite lower compared to the mean LST values in the lockdown images of April month (40.88, 36.61, 36.79, 42.97, 38.37, and 42.06 °C). The average value of the mean LST of April during the lockdown period (34.29 °C) is 5.3 °C lower than the earlier years (39.61 °C). Like April, a similar type of result regarding LST is found in May also. The average value of the mean LST of May during the lockdown period (35.49 °C) is 2.30 °C lower than the earlier years (37.59 °C). The result indicates a positive change during the lockdown phase. It is mainly because of the low concentration of the population and various types of vehicles on the road. The reduction of transport and
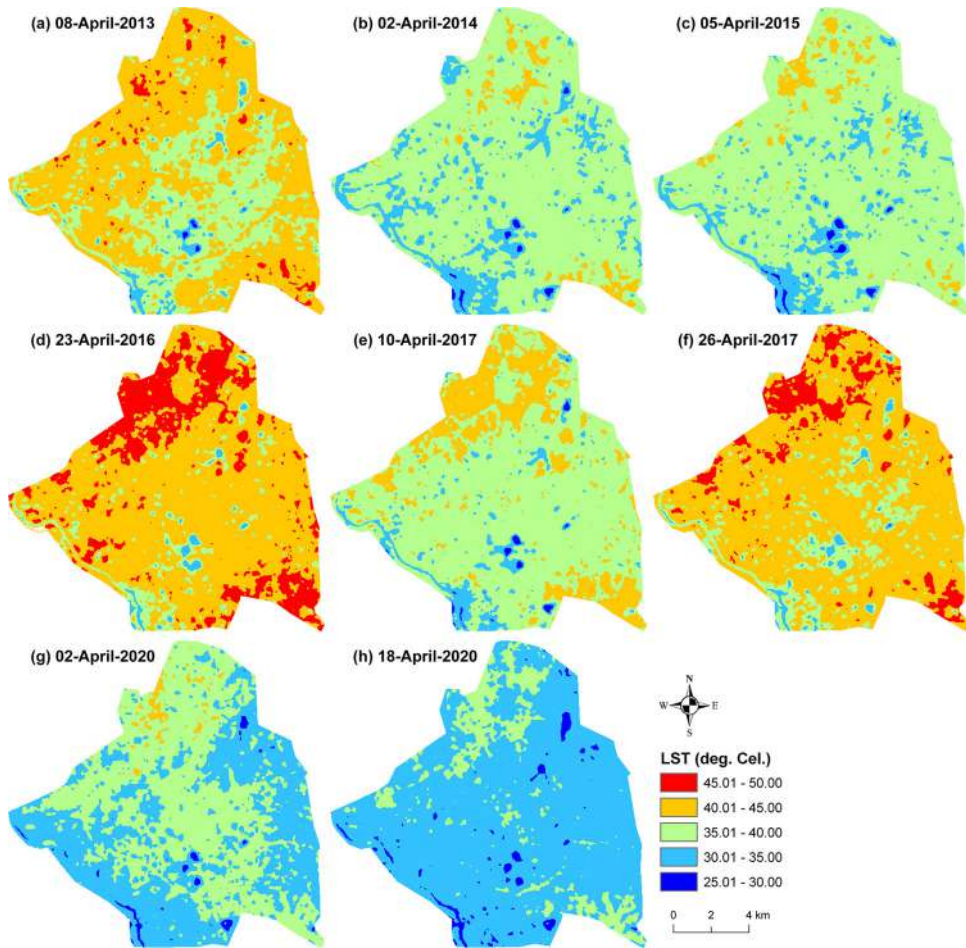
Figure 3. Spatial distribution of LST in April: (a–f) 2013–17 (earlier period); (g–h) 2020 (lock-down period).

industrial pollutants performs a crucial role in the reduction of mean LST during the lockdown period in Raipur City.

Figures 3 and 4 shows the spatial distribution of LST of Raipur city of April and May from 2013 to 2020. During the lockdown period, LST was reduced throughout the area. In 2020, LST reduced significantly spatially from west to east and from south to north. It shows a nice result for our environment. The health status of vegetation covers increased prominently and pollution levels decreased at a significant rate. It helps to decrease the LST directly.

4.2. Effect of lockdown on NDVI

Figures 5 and 6 present the NDVI distribution map for April and May from 2013 to 2020. The lockdown phases had a great effect on NDVI. The three dates (2 April 2020, 18 April 2020, and 4 May 2020) of the lockdown phase show a higher value of mean NDVI (0.19, 0.17, and 0.18 on 2 April 2020, 18 April 2020, and 4 May 2020,
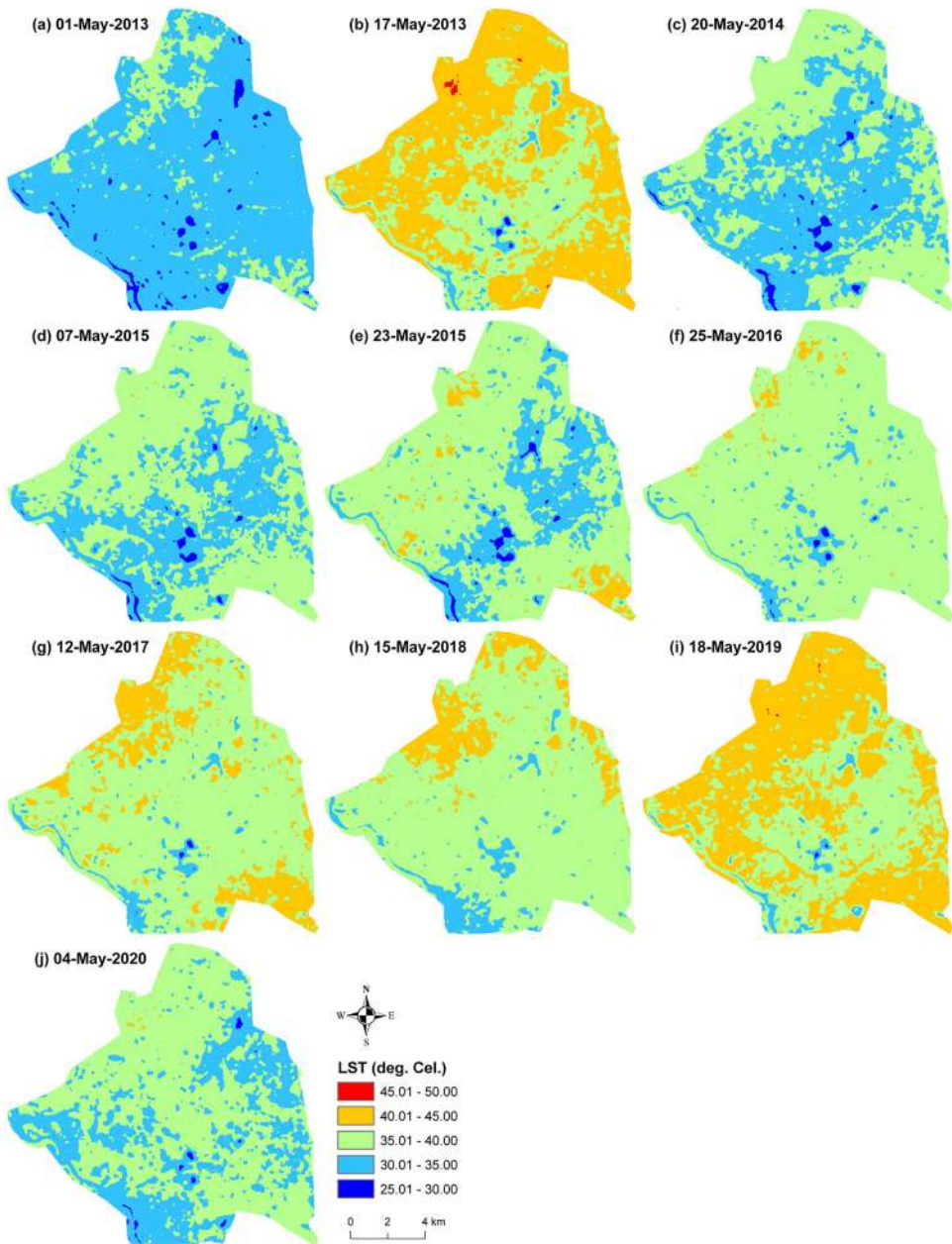
Figure 4. Spatial distribution of LST in May: (a–i) 2013–19 (earlier period); (j) 2020 (lockdown period).

respectively) than the images of earlier years (Table 1). The low level of pollution and the health status of vegetation not impacted by anthropic disturbance (emission, traffic, industrial activities, etc.) reflect an increase in NDVI. It is very clear from Figures 4(g, h), and 5(j) that overall NDVI values were enhanced in the southwest and northeast portions of the area during the lockdown period. It is a positive sign of the lockdown period.
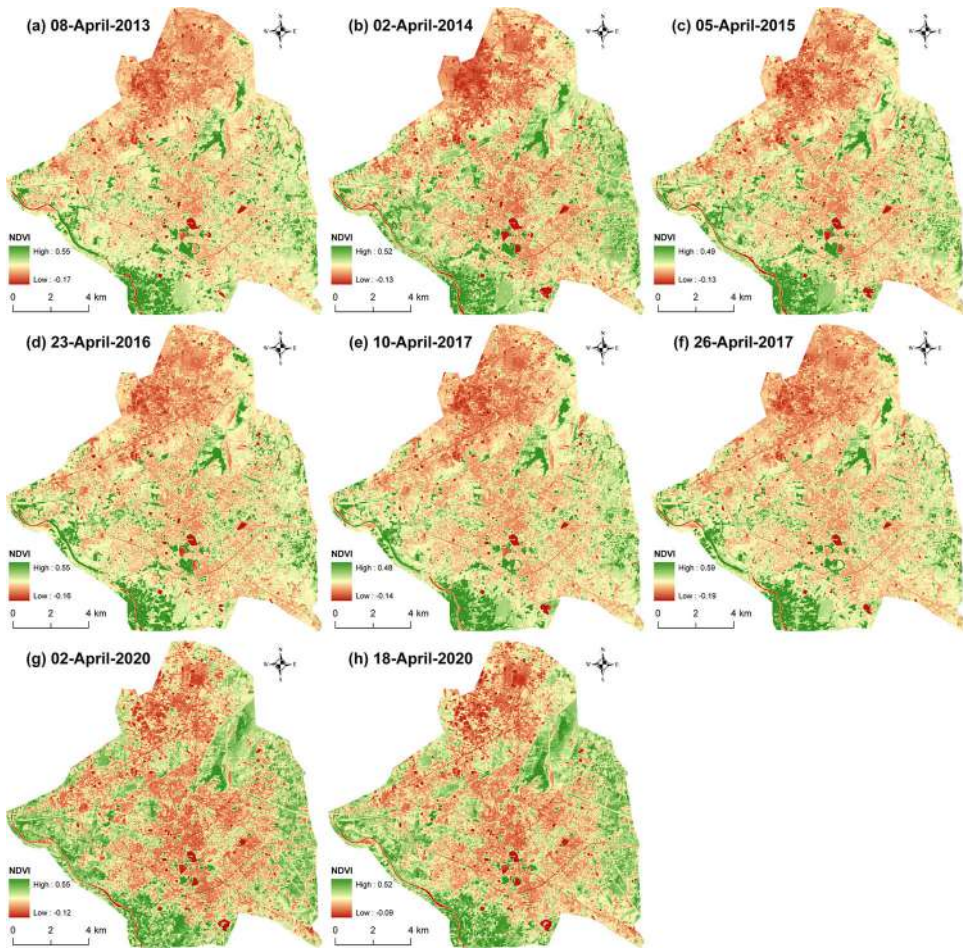
Figure 5. Spatial distribution of NDVI in April: (a–f) 2013–17 (earlier period); (g–h) 2020 (lock-down period).

4.3. Effect of lockdown on LST-NDVI relationship

The LST–NDVI relationship was analyzed by applying Karl Pearson's linear correlation coefficient method. These correlation coefficients were negative throughout the research period (2013–2020). A two-tailed test was performed at a significance level of 0.05 for the correlation analysis. Table 1 shows a clear picture of the correlation analysis in both April and May. In April 2020 (lockdown period), the correlation coefficients were −0.57 (2 April 2020) and −0.53 (18 April 2020). These numerical figures are quite higher than the earlier years, e.g. −0.46 in 8 April 2013, −0.45 in 2 April 2014, −0.45 in 5 April 2015, −0.47 in 23 April 2016, −0.51 in 10 April 2017, −0.47 in 26 April 2017. The average LST-NDVI correlation coefficient of the lockdown period for April month was −0.55 that was higher than the average of the earlier years (−0.47).

The result was almost similar in May. In May 2020 (lockdown period), the correlation coefficient was −0.53 (4 May 2020). It is higher than the earlier years, e.g. −0.48 in 1 May 2013, −0.44 in 17 May 2013, −0.41 in 20 May 2014, −0.42 in 7 May
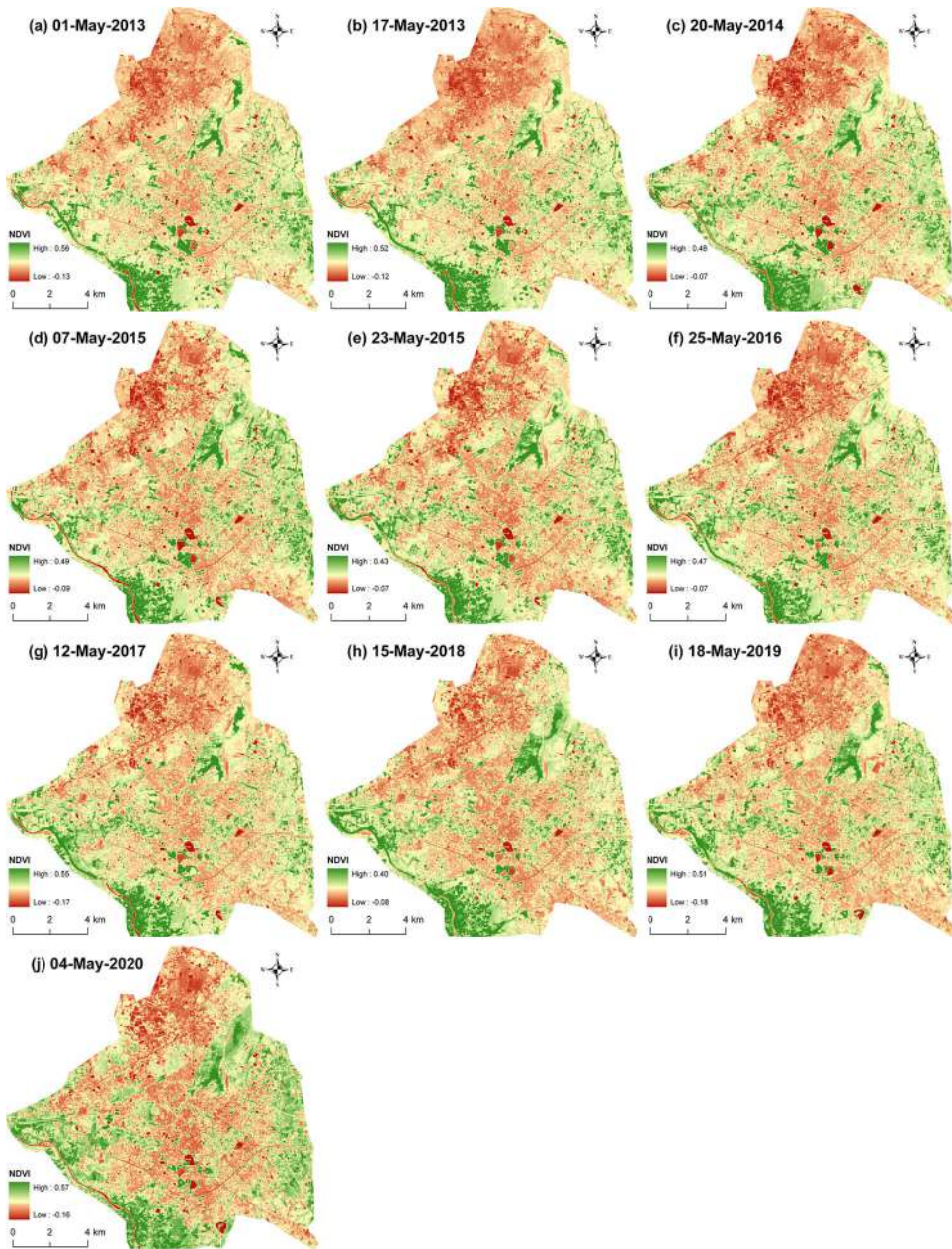
Figure 6. Spatial distribution of NDVI in May: (a–i) 2013–19 (earlier period); (j) 2020 (lock-down period).

2015, −0.35 in 23 May 2015, −0.38 in 25 May 2016, −0.29 in 12 May 2017, −0.46 in 15 May 2018, −0.44 in 18 May 2019. The LST-NDVI correlation coefficient of the lockdown period for May month was −0.53 that was much higher than the average of the earlier years (-0.41). This analysis presents a positive impact of COVID-19 on our natural environment as the lockdown period enhances the LST-NDVI correlation coefficient. It was the combined result of a decrease in LST and an increase in NDVI.
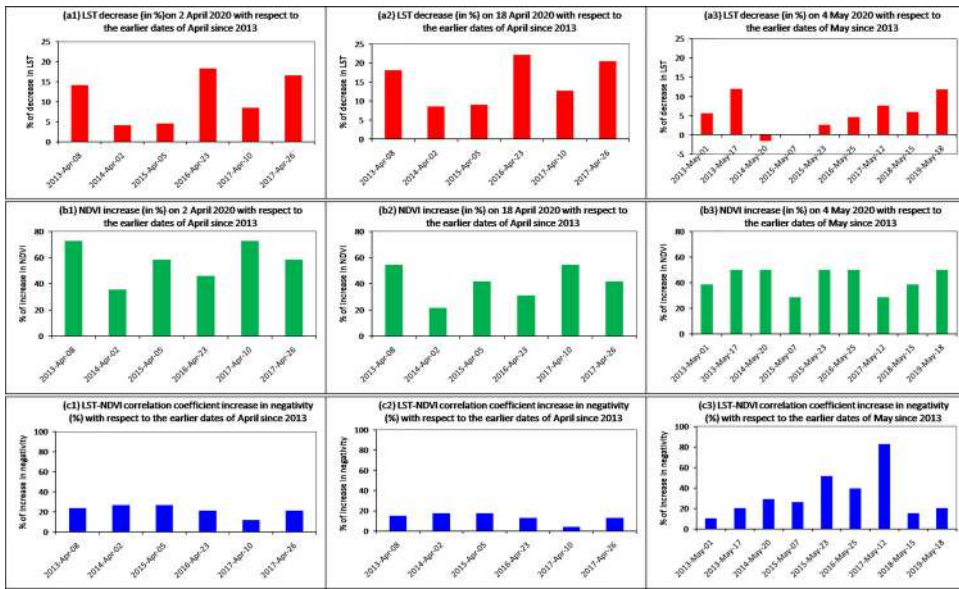
Figure 7. Comparison of LST and NDVI between lockdown period and the earlier dates: (a1–a3) Decrease of LST (in %); (b1–b3) Increase of NDVI (in %); (c1–c3) Increase of negativity in LST-NDVI correlation (in %).

It can be considered that if the pollution level is controlled like the lockdown period, the negativity of the LST-NDVI correlation must be increased and a better environmental system can be achieved.

Figure 7 shows the comparison between the LST and NDVI values and their correlation between the lockdown period of 2020 and the earlier years since 2013. In the lockdown period, LST decreases at a high percentage than the previous years (up to 22% in April and up to 12% in May) (Figure 7(a1–a3)). It is clear that the value of NDVI increases up to 73% in April and up to 50% in May in the lockdown period compared to the previous years due to the interrupted growth of green vegetation (Figure 7(b1–b3)). Thus, a negative LST-NDVI correlation was observed throughout the entire period. But, the strength of this negative correlation or the negativity of the correlation was increased at a high percentage, e.g. up to 27% in April and up to 83% in May (Figure 7(c1–c3)). It was a great achievement of the lockdown period in the natural environment.

4.4. Effect of lockdown on the thermal comfort level of the city

Some thermal comfort indices are available for evaluating the ecological quality of urban life. In this study, the urban thermal field variance index (UTFVI) was used for the evaluation of the thermal comfort level of Raipur city during the lockdown period. UTFVI is calculated using the Eq. 15 (Guha et al. 2017):

$$UTFVI = \frac{T_s - T_{mean}}{T_{mean}} \qquad (15)$$

Where, $UTFVI =$ Urban Thermal Field Variance Index

Table 2. The threshold limits of UTFVI.

UTFVI	UHI phenomenon	Ecological evaluation index
<0.000	None	Excellent
0.000–0.005	Weak	Good
0.005–0.010	Middle	Normal
0.010–0.015	Strong	Bad
0.015–0.020	Stronger	Worse
>0.020	Strongest	Worst
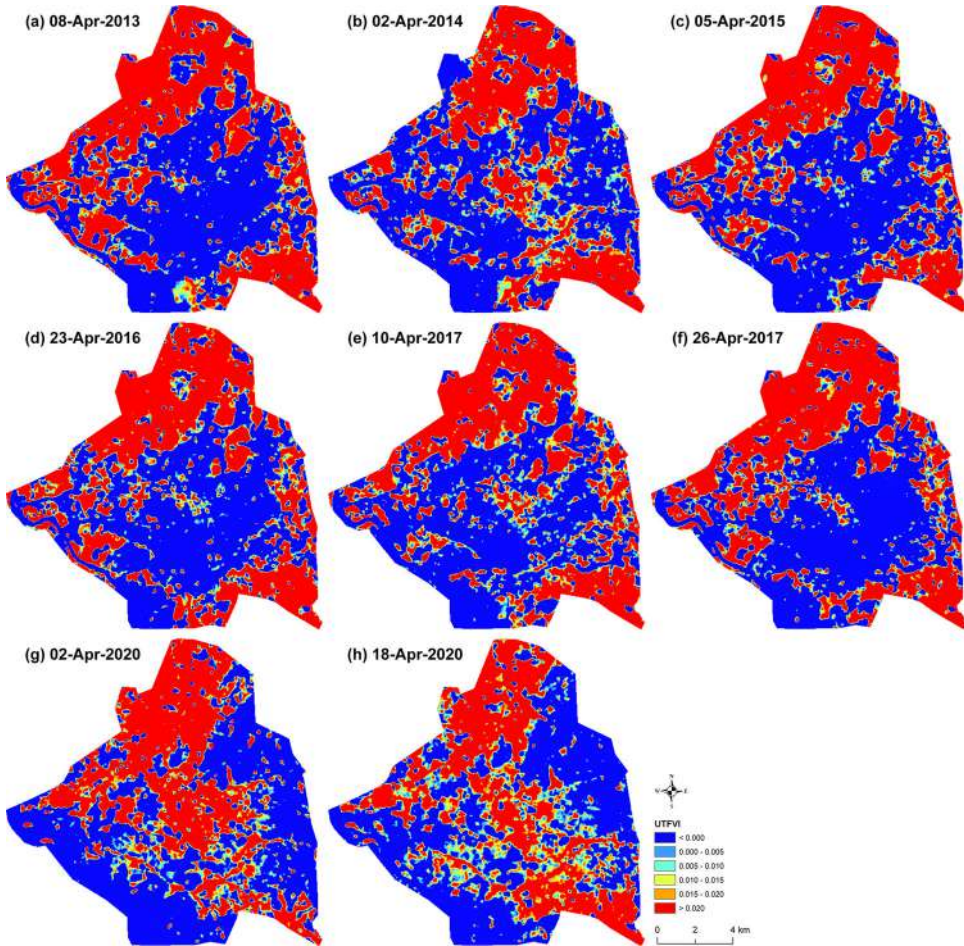
Figure 8. Spatial distribution of UTFVI in April: (a–f) 2013–17 (earlier period); (g–h) 2020 (lockdown period).

T_s = LST (°C)

T_{mean} = Mean LST (°C)

The UTFVI values of Raipur city were divided into six following categories (Table 2).

Figures 8 and 9 present the spatial distribution map of UTFVI for April and May, respectively. Table 3 shows the percentage of area under different UTFVI categories for each image. The city has two extreme categories for ecological evaluation: the
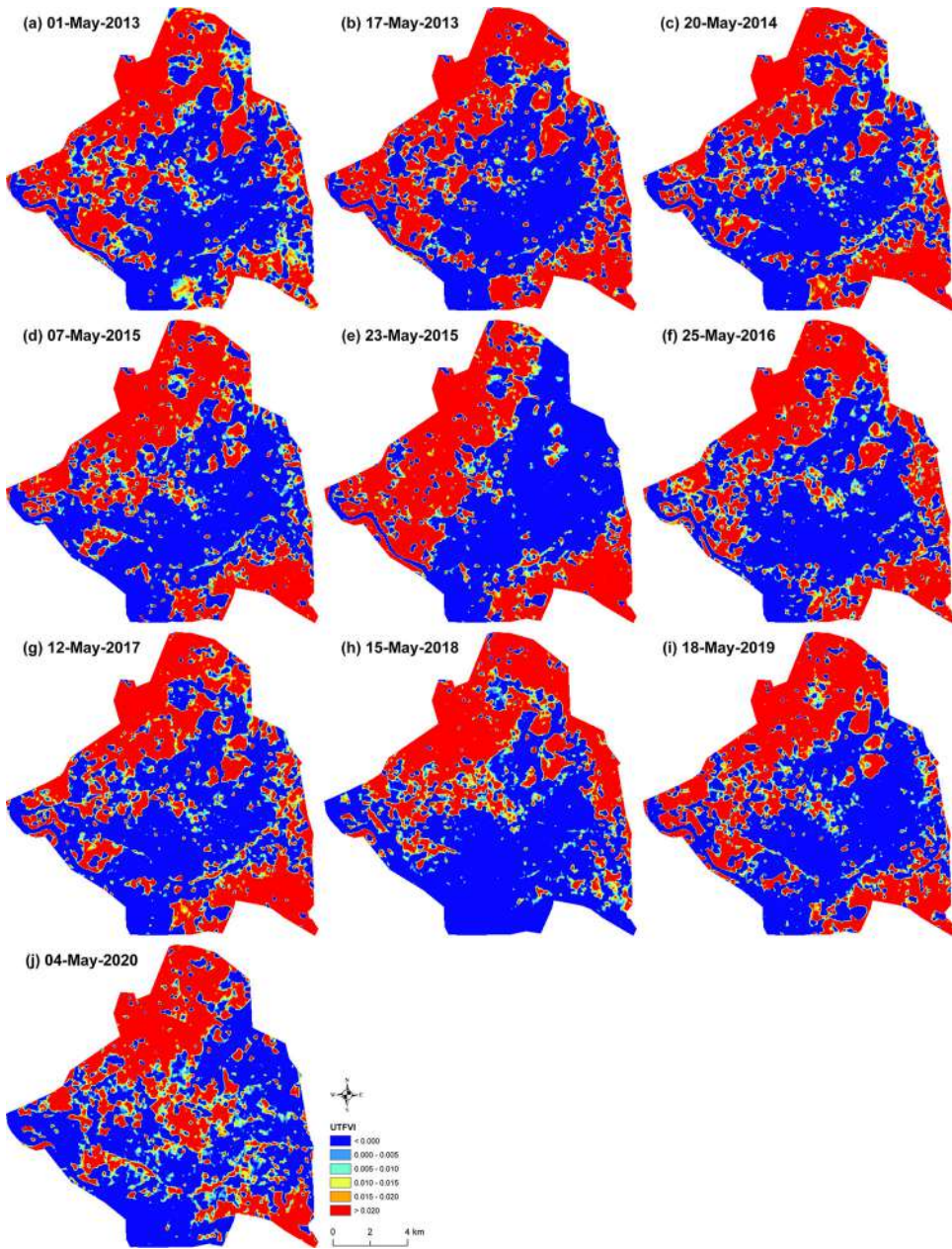
Figure 9. Spatial distribution of UTFVI in May: (a–i) 2013–19 (earlier period); (j) 2020 (lockdown period).

excellent category (UTFVI < 0) and the worst category (UTFVI > 0.020). Most of the areas of Raipur (> 45% during the entire period) having an excellent thermal condition (UTFVI < 0) where vegetation and water bodies are present in a high ratio. The central and southwest portions experience excellent thermal conditions. However, the worst category (UTFVI > 0.020) of the ecological evaluation index also exists in a large portion (>31% during the entire period) in the northwest, north,

Table 3. Area (%) under various ranges of UTFVI [Data during the lockdown period have been shown as bold italic font].

Date of acquisition	UTFVI <0.000	UTFVI 0.000–0.005	UTFVI 0.005–0.010	UTFVI 0.010–0.015	UTFVI 0.015–0.020	UTFVI >0.020
April						
2013-Apr-08	47.34	2.96	3.06	3.17	3.11	40.36
2014-Apr-02	48.59	4.27	3.77	4.09	3.37	35.91
2015-Apr-05	49.83	3.93	3.81	3.61	3.48	35.34
2016-Apr-23	47.60	3.59	3.57	3.62	3.45	38.17
2017-Apr-10	46.58	4.61	4.40	4.34	4.04	36.03
2017-Apr-26	48.73	3.27	3.15	3.29	3.24	38.32
2020-Apr-02	*49.31*	*4.90*	*4.88*	*4.31*	*4.29*	*32.31*
2020-Apr-18	*45.55*	*5.56*	*5.97*	*5.81*	*5.20*	*31.91*
May						
2013-May-01	45.06	4.99	5.05	4.95	4.89	35.06
2013-May-17	46.42	3.29	3.49	3.39	3.63	39.78
2014-May-20	48.26	4.33	4.10	4.02	4.08	35.21
2015-May-07	49.02	4.11	3.99	3.75	3.67	35.48
2015-May-23	49.47	2.91	2.89	2.79	2.75	39.19
2016-May-25	48.19	4.13	4.19	3.96	4.03	35.50
2017-May-12	48.23	4.33	4.10	4.02	4.09	35.23
2018-May-15	49.15	4.37	3.85	3.57	3.42	35.64
2019-May-18	48.89	4.20	3.95	3.69	3.54	35.73
2020-May-04	*48.54*	*5.71*	*5.37*	*4.73*	*4.24*	*31.41*

east, and southeast parts. Here, most of the lands are impervious (either bare land with exposed rock surface or under built-up areas).The normal thermal condition (0.005 < UTFVI < 0.010) is found in some small patches surrounding the vegetation and water areas while the worse condition (0.015 < UTFVI < 0.020) exists around the areas of the built-up class.

During the lockdown period, the area under the worst ecological condition (<33% of the total area) has been decreased at a significant rate than the previous years. However, all the satellite images of the previous periods include areas belonging to the worst ecological condition and exceeding >35%. The climatic conditions remain almost unchanged throughout the period and no precipitation has occurred during this time. Only the percentage of relative humidity is increased during the lockdown period due to reduced air pollution (Table 4). Besides, Figure 10 and Table 5 show that the built-up area is increased (27.42%) and the area covered by vegetation is decreased (26.73%) during this total period of study. Hence, it may be stated that the city has experienced a better ecological and thermal condition during the lockdown period.

5. Conclusion

The study examines the value of LST, NDVI, and LST-NDVI correlation coefficient to compare the environmental condition of Raipur city in the lockdown period and the earlier times. A total of eighteen Landsat 8 OLI/TIRS data of April (eight) and May (ten) months from 2013 to 2020 were used for this investigation. The results show that the value of LST reduced and the value of NDVI increased in the lockdown period (25 March 2020 − 31 May 2020) due to the sudden stop of industrial and transport activities in Raipur. The negativity of the LST-NDVI correlation was also increased significantly during the lockdown period. It shows that the natural

Table 4. Description of some meteorological components [Data during the lockdown period have been shown in bold italic font].

Date of acquisition	Rainfall (mm)	Air temperature (°C)	Air pressure (mbar)	Relative humidity (%)	Wind speed (km/h)
April					
2013-Apr-08	0	34	1007	24	0
2014-Apr-02	0	33	1007	28	4
2015-Apr-05	0	33	1006	27	6
2016-Apr-23	0	36	1003	22	6
2017-Apr-10	0	34	1010	12	5
2017-Apr-26	0	36	1006	20	5
2020-Apr-02	0	34	1009	57	2
2020-Apr-18	0	32	1008	44	4
May					
2013-May-01	0	36	1004	40	12
2013-May-17	0	39	1000	20	6
2014-May-20	0	33	1006	31	10
2015-May-07	0	32	1008	38	12
2015-May-23	0	35	1000	18	12
2016-May-25	0	36	1000	30	7
2017-May-12	0	35	1009	41	4
2018-May-15	0	34	1007	49	6
2019-May-18	0	38	1005	26	6
2020-May-04	0	32	1007	46	4

Table 5. Total area (km^2) under different types of LULC in 2013 and 2020.

Date of acquisition	Green vegetation	Built-up area and bare land	Water bodies
08 April 2013	82.13	80.78	1.32
18 April 2020	60.18	102.93	1.12
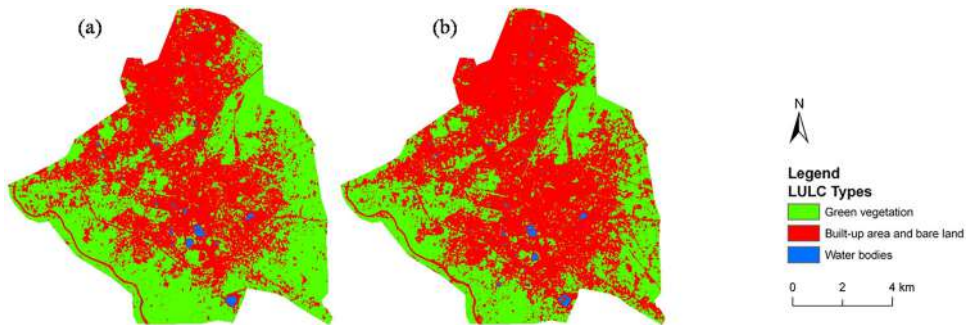
Figure 10. LULC map of Raipur city: (a) 2013, (b) 2020.

environment becomes less polluted and ecologically more comfortable compared to the previous years and before the lockdown period.

The study is very much useful for urban planners as the results depict the positive impact of the lockdown period on the land surface of Raipur city and surrounding areas. As green areas and water bodies are the main responsible land covers for the generation of low LST zones, city planners should focus more on the land conversion process. The urban planners should convert the existing bare lands into vegetation and water surface. To conserve the ecological condition, tree plantation is quite necessary along the roads, commercial buildings, and residential apartments.

Acknowledgements

Disclosure statement

ORCID

Subhanil Guha 🆔 http://orcid.org/0000-0002-2967-7248
Himanshu Govil 🆔 http://orcid.org/0000-0002-3433-8355

References

Barsi JA, Schott JR, Hook SJ, Raqueno NG, Markham BL, Radocinski RG. 2014. Landsat-8 Thermal Infrared Sensor (TIRS) vicarious radiometric calibration. Remote Sens. 6(11): 11607–11626. DOI: 10.3390/rs61111607.

Bashir MF, Ma B, Bilal Komal B, Bashir MA, Tan D, Bashir M. 2020. Correlation between climate indicators and COVID-19 pandemic in New York, USA. Sci Total Environ. 728: 138835. DOI: 10.1016/j.scitotenv.2020.138835.

Carlson TN, Ripley DA. 1997. On the Relation between NDVI, fractional vegetation cover, and leaf area index. Remote Sens Environ. 62(3):241–252.

Chakraborty I, Maity P. 2020. COVID-19 outbreak: migration, effects on society, global environment and prevention. Sci Total Environ. 728:138882. DOI: 10.1016/j.scitotenv.2020.138882.

Chauhan A, Singh RP. 2020a. Decline in PM2.5 concentrations over major cities around the world associated with COVID-19. Environ Res. 187:109634. DOI: 10.1016/j.envres.2020.109634.

Chauhan A, Singh RP. 2020b. Effect of lockdown on HCHO and trace gases over India during March 2020. Aerosol Air Qual Res. DOI: 10.4209/aaqr.2020.07.0445.

Chen XL, Zhao HM, Li PX, Yi ZY. 2006. Remote sensing image-based analysis of the relationship between urban heat island and land use/cover changes. Remote Sens Environ. 104(2): 133–146. DOI: 10.1016/j.rse.2005.11.016.

Garg V, Aggarwal SP, Chauhan P. 2020. Changes in turbidity along Ganga River using Sentinel-2 satellite data during lockdown associated with COVID-19. Geomat Nat Haz Risk. 11(1):1175–1195. DOI: 10.1080/19475705.2020.1782482.

Govil H, Guha S, Dey A, Gill N. 2019. Seasonal evaluation of downscaled land surface temperature: A case study in a humid tropical city. Heliyon 5(6): e01923. DOI: 10.1016/j.heliyon.2019.e01923

Govil H, Guha S, Diwan P, Gill N, Dey A. 2020. Analyzing Linear Relationships of LST with NDVI and MNDISI Using Various Resolution Levels of Landsat 8 OLI/TIRS Data. In: Sharma N., Chakrabarti A., Balas V. (eds) Data Management, Analytics and Innovation. Advances in Intelligent Systems and Computing, vol 1042. Springer, Singapore, pp. 171–184. DOI: 10.1007/978-981-32-9949-8_13

Guha S, Govil H. 2020a. An assessment on the relationship between land surface temperature and normalized difference vegetation index. Environ Dev Sustain. 23(2):1944–1963. DOI: 10.1007/s10668-020-00657-6.

Guha S, Govil H. 2020b. Seasonal impact on the relationship between land surface temperature and normalized difference vegetation index in an urban landscape. Geocarto Int. DOI: 10.1080/10106049.2020.1815867.

Guha S, Govil H. 2020c. Land surface temperature and normalized difference vegetation index relationship: a seasonal study on a tropical city. SN Appl Sci. 2:1661. DOI: 10.1007/s42452-020-03458-8.

Guha S, Govil H, Dey A, Gill N. 2018. Analytical study of land surface temperature with NDVI and NDBI using Landsat 8 OLI/TIRS data in Florence and Naples city, Italy. Eur J Remote Sens. 51(1):667–678.

Guha S, Govil H, Mukherjee S. 2017. Dynamic analysis and ecological evaluation of urban heat islands in Raipur city. J Appl Remote Sens. 11(03):1. DOI: 10.1117/1.JRS.11.036020.

Gupta S, Raghuwanshi GS, Chanda A. 2020. Effect of weather on COVID-19 spread in the US: a prediction model for India in 2020. Sci Total Environ. 728:138860. DOI: 10.1016/j.scitotenv.2020.138860.

https://www.earthexplorer.usgs.gov.

https://www.esri.com.

http://www.imdraipur.gov.in.

https://raipur.gov.in.

http://www.surveyofindia.gov.in.

https://www.worldometers.info/coronavirus.

Li WF, Cao QW, Kun L, Wu JS. 2017. Linking potential heat source and sink to urban heat island: heterogeneous effects of landscape pattern on land surface temperature. Sci Total Environ. 586:457–465. DOI: 10.1016/j.scitotenv.2017.01.191.

Mandal I, Pal S. 2020. COVID-19 pandemic persuaded lockdown effects on environment over stone quarrying and crushing areas. Sci Total Environ. 732:139281. DOI: 10.1016/j.scitotenv.2020.139281.

Montanaro M, Gerace A, Lunsford A, Reuter D. 2014. Stray light artifacts in imagery from the Landsat 8 Thermal Infrared Sensor. Remote Sens. 6(11):10435–10456. DOI: 10.3390/rs61110435.

Mollalo A, Vahedi B, Rivera KM. 2020. GIS-based spatial modeling of COVID-19 incidence rate in the continental United States. Sci Total Environ. 728:138884. DOI: 10.1016/j.scitotenv.2020.138884.

Öcal A, Cvetković VM, Baytiyeh H, Tedim FMS, Zečević M. 2020. Public reactions to the disaster COVID-19: a comparative study in Italy, Lebanon, Portugal, and Serbia. Geomat Nat Haz Risk. 11(1):1864–1885. DOI: 10.1080/19475705.2020.1811405.

Pandey AP, Singh AP, Bansal BK, Suresh G, Prajapati SK. 2020a. Appraisal of seismic noise scenario at national seismological network of India in COVID-19 lockdown situation. Geomat Nat Haz Risk. 11(1):2095–2122. DOI: 10.1080/19475705.2020.1830187.

Pandey AP, Suresh G, Singh AP, Sutar AK, Bansal BK. 2020b. A widely felt Tremor (ML 3.5) of 12 April 2020 in and around NCT Delhi in the backdrop of prevailing COVID-19 pandemic lockdown: analysis and observations. Geomat Nat Haz Risk. 11(1):1638–1652. DOI: 10.1080/19475705.2020.1810785.

Peng J, Xie P, Liu Y, Ma J. 2016. Urban thermal environment dynamics and associated landscape pattern factors: a case study in the Beijing Metropolitan Region. Remote Sens Environ. 173:145–155.

Qin Z, Karnieli A, Berliner P. 2001. A mono-window algorithm for retrieving land surface temperature from landsat TM data and its application to the Israel-Egypt Border Region. Int J Remote Sens. 22(18):3719–3746.

Saadat S, Rawtani D, Hussain CM. 2020. Environmental perspective of COVID-19. Sci Total Environ. 728:138870. DOI: 10.1016/j.scitotenv.2020.138870.

Şahin M. 2020. Impact of weather on COVID-19 pandemic in Turkey. Sci Total Environ. 728:138810. DOI: 10.1016/j.scitotenv.2020.138810.

Sekertekin A, Bonafoni S. 2020. Land surface temperature retrieval from landsat 5, 7, and 8 over rural areas: assessment of different retrieval algorithms and emissivity models and tool-box implementation. Remote Sens. 12(2):294.

Sharma S, Zhang M, Anshika Gao J, Zhang H, Kota SH. 2020. Effect of restricted emissions during COVID-19 on air quality in India. Sci Total Environ. 728:138878. DOI: 10.1016/j.sci-totenv.2020.138878.

Shi P, Dong Y, Yan H, Zhao C, Li X, Liu W, He M, Tang S, Xi S. 2020. Impact of temperature on the dynamics of the COVID-19 outbreak in China. Sci Total Environ. 728:138890. DOI: 10.1016/j.scitotenv.2020.138890.

Singh RP, Chauhan A. 2020a. Impact of lockdown on air quality in India during COVID-19 pandemic. Air Qual Atmos Health. 13(8):921–928. DOI: 10.1007/s11869-020-00863-1.

Singh RP, Chauhan A. 2020b. Impact of lockdown associated with COVID-19 on atmospheric pollution in India. Climatological, Meteorological, and Environmental Factors in the COVID-19 Pandemic, AGU, 4–6 August 2020.

Sobrino JA, Jimenez-Munoz JC, Paolini L. 2004. Land surface temperature retrieval from Landsat TM5. Remote Sens Environ. 90(4):434–440.

Tucker CJ. 1979. Red and photographic infrared linear combinations for monitoring vegetation. Remote Sens Environ. 8(2):127–150.

Wang F, Qin Z, Song C, Tu L, Karnieli A, Zhao S. 2015. An improved mono-window algorithm for land surface temperature retrieval from Landsat 8 thermal infrared sensor data. Remote Sens. 7(4):4268–4289.

Wang L, Lu Y, Yao Y. 2019. Comparison of three algorithms for the retrieval of land surface temperature from Landsat 8 images. Sensors. 19(22):5049.

Wukelic GE, Gibbons DE, Martucci LM, Foote HP. 1989. Radiometric calibration of Landsat Thematic Mapper thermal band. Remote Sens Environ. 28:339–347.

Yang J, Qiu J. 1996. The empirical expressions of the relation between precipitable water and ground water vapor pressure for some areas in China. Sci Atmos Sin. 20:620–626.

Yunus AP, Masago Y, Hijioka Y. 2020. COVID-19 and surface water quality: Improved lake water quality during the lockdown. Sci Total Environ. 731:139012. DOI: 10.1016/j.scitotenv.2020.139012.

Zambrano-Monserrate MA, Alejandra Ruano M, Sanchez-Alcalde L. 2020. Indirect effects of COVID-19 on the environment. Sci Total Environ. 728:138813. DOI: 10.1016/j.scitotenv.2020.138813.

Zanter KL. 2019. 8 (L8) Data Users Handbook. EROS: Sioux Falls, SD, USA.

Source details

Feedback >   Compare sources >

Geomatics, Natural Hazards and Risk

Open Access ⓘ

Scopus coverage years: from 2010 to Present

Publisher: Taylor & Francis

ISSN: 1947-5705   E-ISSN: 1947-5713

Subject area: (Earth and Planetary Sciences: General Earth and Planetary Sciences) (Environmental Science: General Environmental Science)

Source type: Journal

View all documents >   Set document alert   🖫 Save to source list

CiteScore 2022
7.3   ⓘ

SJR 2022
0.813   ⓘ

SNIP 2022
1.184   ⓘ

CiteScore   CiteScore rank & trend   Scopus content coverage

ⓘ   Improved CiteScore methodology   ✕

CiteScore 2022 counts the citations received in 2019-2022 to articles, reviews, conference papers, book chapters and data

papers published in 2019-2022, and divides this by the number of publications published in 2019-2022. Learn more >

Annual assessment on the relationship between land surface temperature and six remote sensing indices using landsat data from 1988 to 2019

Subhanil Guha & Himanshu Govil

Taylor & Francis
Taylor & Francis Group

Check for updates

Annual assessment on the relationship between land surface temperature and six remote sensing indices using landsat data from 1988 to 2019

Subhanil Guha [ID] and Himanshu Govil [ID]

Department of Applied Geology, National Institute of Technology Raipur, Raipur, India

ABSTRACT

The study focused on deriving the LST of the Raipur City of India and generating the relationships of LST with six selected remote sensing indices, like MNDWI, NDBaI, NDBI, NDVI, NDWI, and NMDI. The entire study was performed by using 210 cloud-free Landsat data of different months from 1988 to 2019. The LST retrieval mono-window algorithm was applied in the study. Based on Pearson's linear correlation coefficient (r), the study finds that LST builds a strong positive correlation ($r = 0.65$) with NDBI, a moderate positive correlation ($r = 0.30$) with NDBaI, a weak positive correlation with NDWI ($r = 0.19$), a strong negative relation with NMDI ($r = -0.54$), and a moderate negative correlation ($r = -0.38$) with MNDWI and NDVI. These relationships were consistent and stronger in earlier years. The LST-NDBI correlation is the most consistent ($CV = 9.09$), while the LST-NDBaI correlation is the most variable ($CV = 60.21$).

1. Introduction

Land surface temperature (LST) analysis is extensively considered as an important parameter in urban planning and management as the dynamic land surface can enhance the variability of LST distribution in the mixed urban landscape (Arnfield 2003; Amiri et al. 2009; Rinner and Hussain 2011; Mirzaei 2015; Zhao et al. 2016; Guha and Govil 2020). Recently, the intensity of LST in some global cities is increasing rapidly (Zhou et al. 2011; Zhang et al. 2013; Chun and Guldmann 2014; Coseo and Larsen 2014; Kim and Guldmann 2014; Peng et al. 2016; Dai et al. 2018). Different kinds of land surface (green body, water, built-up area, bare land) indices were frequently used to assess and monitor the dynamic response of LST with mixed urban land (Rizwan et al. 2008; Li et al. 2011; Song et al. 2014; Kuang et al. 2015; Guha et al. 2020a, 2020b). The existing spectral indices were used to build the relationship between LST and different types of LULC in various land surfaces (Huang et al. 2015; Jovanović et al. 2015; Mbuh et al. 2019; Majumder et al. 2020; Piyoosh and Ghosh 2020; Guha et al. 2020c).Thus, the scholars tried to analyze the variation of LST in urban areas using remote sensing techniques (Govil et al. 2019, 2020). The analysis of long-term LST-remote sensing indices relationship for any

Indian city was less studied. This study is simply based on the LST-remote sensing indices relationships for Raipur City, India. The six following selected remote sensing indices were used in the present study, i.e., modified normalized difference water index (MNDWI), normalized difference bareness index (NDBaI), normalized difference built-up index (NDBI), normalized difference vegetation index (NDVI), normalized difference water index (NDWI), and normalized multi-band drought index (NMDI).

The goals of the study are: (1) to assess the annual trend of LST and six remote sensing indices in Raipur City using Landsat images from 1988 to 2019; and (2) to investigate the variability of LST-remote sensing indices relationships during the period. These LST-remote sensing indices relationships can be used as significant indicators for future urban and environmental planning in a rapidly growing tropical city.

2. Study area and data sources

The present study has been conducted over Raipur City of Chhattisgarh, India (Figure 1). Figure 1(a) presents the outline map of India where Chhattisgarh State is located in the middle part (http://www.surveyofindia.gov.in). Figure 1(b) presents the outline map of Chhattisgarh State with districts (http://www.surveyofindia.gov.in). Figure 1(c) represents the false colour composite (FCC) image of Raipur City from recent Landsat data. Figure 1(d) indicates the contour map of Raipur (Date: 11 October 2011) of Raipur City (https://www.earthexplorer.usgs.gov). Raipur extends from $21^{\circ}11'22''$ N to $21^{\circ}20'02''$ N latitude and from $81^{\circ}32'20''$ E to $81^{\circ}41'50''$ E. The elevation of Raipur is ranged between 219-322 m. Under a Savannah type of climate, the city enjoys four typical seasons (https://www.mausam.imd.gov.in). March, April, and May are considered as pre-monsoon months; June, July, August, and September are considered as monsoon months; October and November are considered as post-monsoon months; and December, January, and February are considered as winter months. The annual average temperature of Raipur City is approximately 23-30 °C. According to the census of India, Raipur is the 45th largest city in India and the largest city of Chhattisgarh. The demographic profile of Raipur City is characterized by a total population of 1010087, a sex ratio of 945, and a literacy
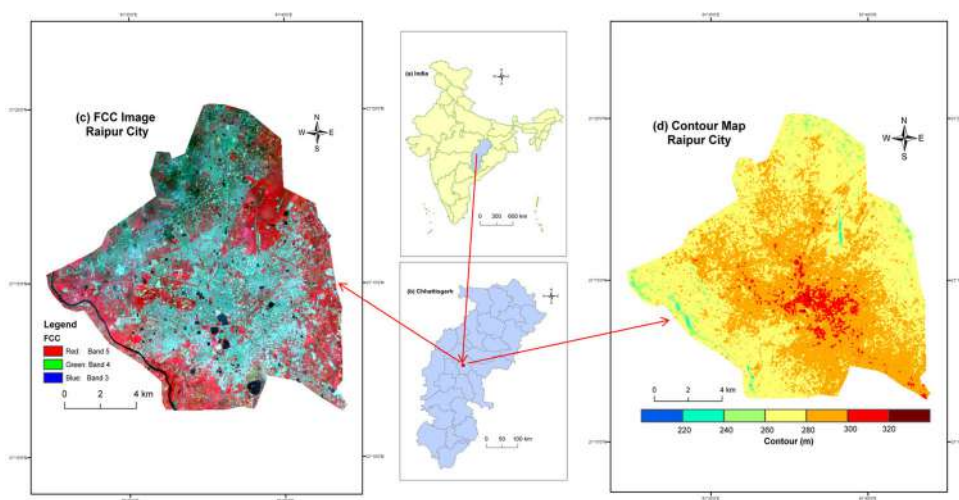
Figure 1. Location of the study area: (a) India (b) Chhattisgarh (c) FCC image of Raipur City (d) Contour Map of Raipur City.

rate of 86.45% (https://www.censusindia.gov.in). The city has a very high density of population (4500/km^2 in 2011) and a high growth rate (61.27 during 2001-2011). Raipur is often considered a smart city and one of the fastest-growing cities in India in terms of area and population. The city has been completely transformed in the last 10-15 years.

A total of two hundred and ten cloud-free Landsat satellite images of different sensors from 1988 to 2019 were selected to conduct the entire study. There is no Landsat satellite image available in 1997 and 2012. Thus, the analysis is skipped for these two aforesaid years. These data sets were freely procured from the United States Geological Survey (http://earthexplorer.USGS.gov). Green, red, near-infrared (NIR), shortwave infrared (SWIR), and thermal infrared (TIR) bands were used in generating LST, MNDWI, NDBaI, NDBI, NDVI, NDWI, and NMDI. LST was retrieved through TIR bands of Landsat data sets [band 6 for Landsat 5 Thematic Mapper (TM) and Landsat 7 Enhanced Thematic Mapper Plus (ETM+) data, whereas band 10 for Landsat 8 Operational Land Imager (OLI)/Thermal Infrared Sensors (TIRS) data]. The whole study was performed by using ArcGIS 9.3 software.

3. Methodology

3.1. Determination of different remote sensing indices

Different remote sensing indices are applied to extracting different types of land use/land cover (LULC). In any urban area, the major LULC categories are vegetation, water bodies, dry and wet soil, bare land, and built-up area. Thus, these six remote sensing indices MNDWI, NDBaI, NDBI, NDVI, NDWI, and NMDI were selected for the present study as these indices can be used to extract vegetation, water bodies, built-up area, soil, and bare land by using their threshold values (Chen et al. 2006). MNDWI (Xu 2006) is used to enhance the water bodies among the other land surfaces and it is inversely related to LST. NDBaI (Zhao and Chen 2005) is generally used for bare land detection and is positively correlated to LST values. NDBI (Zha et al. 2003) is another remote sensing index applied for detecting built-up land and is also correlates positively with LST. NDVI (Tucker 1979) is a vegetation index used frequently in several fields of remote sensing study including LST derivation. It generally builds an inverse correlation with LST. NDWI (McFeeters 1996) is widely used for the extraction of the water surface and it normally generates a non-linear relationship with LST. NMDI (Wang and Qu 2007) is used to identify the dry and wet soil and is negatively correlated to LST. These six remote sensing indices (Table 1) were applied in the present study to assess their long-term annual relationship with LST.

Table 1. Description of MNDWI, NDBaI, NDBI, NDVI, NDWI, and NMDI.

Acronym	Description	Formulation	References
MNDWI	Modified Normalized difference water index	Green-SWIR/Green + SWIR	Xu 2006
NDBaI	Normalized difference bareness index	SWIR-TIR/SWIR + TIR	Zhao and Chen 2005
NDBI	Normalized difference built-up index	SWIR-NIR/SWIR + NIR	Zha et al. 2003
NDVI	Normalized difference vegetation index	NIR-Red/NIR + Red	Tucker 1979
NDWI	Normalized difference water index	Green-NIR/Green + NIR	McFeeters 1996
NMDI	Normalized multi-band drought index	[NIR-SWIR1 + SWIR2)]/ [NIR+(SWIR1 + SWIR2)]	Wang and Qu 2007

3.2. Retrieving LST from landsat thermal band

Many LST retrieval methods are applicable for different satellite sensors. The mono-window algorithm (Qin et al. 2001; Yang et al. 2014; García-Santos et al. 2018; Wang et al. 2019; Sekertekin and Bonafoni 2020), single-channel algorithm (Jiménez-Muñoz and Sobrino 2003; Jiménez-Muñoz et al. 2009; Coll et al. 2012; Chatterjee et al. 2017), split-window algorithm (McMillin 1975; Price 1984; Becker and Li 1990; Rozenstein et al. 2014), and radiative transfer equation (Yu et al. 2014; Zhu et al. 2020) are the main well-known LST retrieval algorithms using Landsat thermal bands (Weng 2001; Weng and Yang 2004; Zhang et al. 2016). Despite giving a good result, the radiative transfer equation cannot be applicable without *in situ* parameters of atmospheric profile at the satellite pass. Although the split-window algorithm gives the accurate result, it was not used in the study as only band 10 of Landsat 8 OLI/TIRS data was selected for LST generation due to its better calibration (Barsi et al. 2014). The mono-window algorithm and single-channel algorithm also provide good results. In this study, the mono-window algorithm was applied to retrieve LST from multi-temporal Landsat satellite images. Ground emissivity, atmospheric transmittance, and effective mean atmospheric temperature -these three parameters are needed to derive the LST using the mono-window algorithm. At first, the original TIR bands (100 m resolution for Landsat 8 OLI/TIRS data, 120 m resolution for Landsat 5 TM data, and 60 m resolution for Landsat 7 ETM + data) were resampled into 30 m by USGS data centre for further application.

The TIR pixel values are firstly converted into radiance from digital number (DN) values. Radiance for TIR bands of Landsat 5 TM data and Landsat 7 ETM + data are obtained using Eq. (1) (https://www.earthexplorer.usgs.gov):

$$L_\lambda = \left[\frac{L_{MAX\lambda} - L_{MIN\lambda}}{QCAL_{MAX} - QCAL_{MIN}} \right] * [Q_{CAL} - QCAL_{MIN}] + L_{MIN\lambda} \tag{1}$$

where, L_λ is Top of Atmosphere (TOA) spectral radiance ($Wm^{-2}sr^{-1}mm^{-1}$), Q_{CAL} is the quantized calibrated pixel value in DN, $L_{MIN\lambda}$ ($Wm^{-2}sr^{-1}mm^{-1}$) is the spectral radiance scaled to $QCAL_{MIN}$, $L_{MAX\lambda}$ ($Wm^{-2}sr^{-1}mm^{-1}$) is the spectral radiance scaled to $QCAL_{MAX}$, $QCAL_{MIN}$ is the minimum quantized calibrated pixel value in DN and $QCAL_{MAX}$ is the maximum quantized calibrated pixel value in DN. $L_{MIN\lambda}$, $L_{MAX\lambda}$, $QCAL_{MIN}$, and $QCAL_{MAX}$ values are obtained from the metadata file of Landsat 5 TM data and Landsat 7 ETM + data. Radiance for Landsat 8 TIR band is obtained from Eq. (2) (Zanter 2019):

$$L_\lambda = M_L.Q_{CAL} + A_L \tag{2}$$

where, L_λ is the TOA spectral radiance ($Wm^{-2}sr^{-1}mm^{-1}$), M_L is the band-specific multiplicative rescaling factor from the metadata, A_L is the band-specific additive rescaling factor from the metadata, Q_{CAL} is the quantized and calibrated standard product pixel values (DN). All of these variables can be retrieved from the metadata file of Landsat 8 data.

For Landsat 5 and Landsat 7 data, the reflectance value is obtained from radiances using Eq. (3) (USGS):

$$\rho_\lambda = \frac{\pi.L_\lambda.d^2}{ESUN_\lambda.\cos\theta_s} \tag{3}$$

where, ρ_λ is unitless planetary reflectance, L_λ is the TOA spectral radiance ($Wm^{-2}sr^{-1}\mu m^{-1}$), d is Earth-Sun distance in astronomical units, $ESUN_\lambda$ is the mean solar exo-atmospheric spectral irradiances ($Wm^{-2}\mu m^{-1}$) and θ_s is the solar zenith angle in degrees. $ESUN_\lambda$ values for each band of Landsat 5 and Landsat 7 data can be obtained

from the handbooks of the related mission. θ_s and d values can be attained from the metadata file.

For Landsat 8 data, reflectance conversion can be applied to DN values directly as in Eq. (4) (Zanter 2019):

$$\rho_\lambda = \frac{M_\rho . Q_{CAL} + A_\rho}{\sin \theta_{SE}} \qquad (4)$$

where, M_ρ is the band-specific multiplicative rescaling factor from the metadata, A_ρ is the band-specific additive rescaling factor from the metadata, Q_{CAL} is the quantized and calibrated standard product pixel values (DN) and θ_{SE} is the local sun elevation angle from the metadata file.

Eq. (5) is used to convert the spectral radiance to at-sensor brightness temperature (Wukelic et al. 1989; Chen et al. 2006):

$$T_b = \frac{K_2}{\ln\left(\frac{K_1}{L_\lambda} + 1\right)} \qquad (5)$$

where, T_b is the brightness temperature in Kelvin (K), L_λ is the spectral radiance in $Wm^{-2}sr^{-1}mm^{-1}$; K_2 and K_1 are calibration constants. For Landsat 8 data, K_1 is 774.89, K_2 is 1321.08 ($Wm^{-2}sr^{-1}mm^{-1}$). For Landsat 7 data, K_1 is 666.09, K_2 is 1282.71 ($Wm^{-2}sr^{-1}mm^{-1}$). For Landsat 5 data, K_1 is 607.76, K_2 is 1260.56 ($Wm^{-2}sr^{-1}mm^{-1}$).

The land surface emissivity ε, is estimated from Eq. (6) using the NDVI Thresholds Method (Sobrino et al. 2001, 2004).

$$\varepsilon = \varepsilon_v F_v + \varepsilon_s(1-F_v) + d\varepsilon \qquad (6)$$

where, ε is land surface emissivity, ε_v is vegetation emissivity, ε_s is soil emissivity, Fv is fractional vegetation, $d\varepsilon$ is the effect of the geometrical distribution of the natural surfaces and internal reflections that can be expressed by Eq. (7):

$$d\varepsilon = (1-\varepsilon_s)(1-F_v)F\varepsilon_v \qquad (7)$$

where, ε_v is vegetation emissivity, ε_s is soil emissivity, Fv is fractional vegetation, F is a shape factor whose mean is 0.55, the value of $d\varepsilon$ maybe 2% for mixed land surfaces (Sobrino et al. 2004).

The fractional vegetation F_v, of each pixel, is determined from the NDVI using Eq. (8) (Carlson and Ripley 1997):

$$F_v = \left(\frac{NDVI - NDVI_{min}}{NDVI_{max} - NDVI_{min}}\right)^2 \qquad (8)$$

where, (a)$NDVI<0.2$ for bare soil; (b)$NDVI>0.5$ for vegetation; (c)$0.2<=NDVI<=0.5$ for mixed land with bare soil and vegetation (Sobrino et al. 2001, 2004).

Finally, the land surface emissivity ε can be expressed by Eq. (9):

$$\varepsilon = 0.004 * F_v + 0.986 \qquad (9)$$

where, ε is land surface emissivity, Fv is fractional vegetation.

Water vapour content is estimated by Eq. (10) (Li 2006):

$$w = 0.0981 * \left[10 * 0.6108 * \exp\left(\frac{17.27 * (T_0 - 273.15)}{237.3 + (T_0 - 273.15)}\right) * RH\right] + 0.1697 \qquad (10)$$

where, w is the water vapour content (g/cm^2), T_0 is the near-surface air temperature in Kelvin (K), RH is the relative humidity (%). These parameters of atmospheric profile are

Table 2. Atmospheric transmittance for four standard atmospheric conditions.

Atmospheric profiles	Water Vapour (w) in g/cm^2	Atmospheric transmittance (τ)
High temperature	0.4-1.6	$\tau = 0.974290 - 0.080076w$
High temperature	1.6-3.0	$\tau = 1.031412 - 0.11536w$
Low temperature	0.4-1.6	$\tau = 0.982007 - 0.09611w$
Low temperature	1.6-3.0	$\tau = 1.053710 - 0.14142w$

obtained from the Meteorological Centre, Raipur (http://www.imdraipur.gov.in). Atmospheric transmittance is determined for Raipur City using Eq. (11) and Table 2 (Qin et al. 2001; Sun et al. 2010):

$$\tau = 1.031412 - 0.11536w \qquad (11)$$

where, τ is the total atmospheric transmittance, w is the water vapour content (g/cm^2).

The effective mean atmospheric temperature of Raipur was also determined from Table 3 (Qin et al. 2001; Sun et al. 2010):

Raipur City is located in the tropical region. Thus, Eq. (12) is applied to compute the effective mean atmospheric transmittance of Raipur (Qin et al. 2001; Sun et al. 2010):

$$T_a = 17.9769 + 0.91715T_0 \qquad (12)$$

LST is retrieved from Landsat 5 TM and Landsat 8 OLI/TIRS satellite data by using Eq. (13-15) (Qin et al. 2001):

$$T_s = \frac{[a(1 - C - D) + (b(1 - C - D) + C + D)T_b - DT_a]}{C} \qquad (13)$$

$$C = \varepsilon\tau \qquad (14)$$

$$D = (1 - \tau)[1 + (1 - \varepsilon)\tau] \qquad (15)$$

where, ε is the land surface emissivity, τ is the total atmospheric transmittance, C and D are internal parameters based on atmospheric transmittance and land surface emissivity, T_b is the at-sensor brightness temperature, T_a is the mean atmospheric temperature, T_0 is the near-surface air temperature, T_s is the land surface temperature, $a = -67.355351$, $b = 0.458606$.

4. Results and discussion

4.1. Spatial-temporal distribution of LST

The spatial distribution maps of LST derived from various Landsat data sets were shown in Figure 2. The annual mean LST values from 1988 to 2019 were generated (Table 4). The mean LST value of a total of thirty-two years is 29.17 °C. It is only the average mean LST value estimated from the available cloud-free data. As the data of all months for one single year was not available the trend of LST cannot be determined properly. The high LST value was found in the northwest and southeast Raipur.

4.2. Spatial distribution of MNDWI, NDBaI, NDBI, NDVI, NDWI, and NMDI

All the six remote sensing indices (MNDWI, NDBaI, NDBI, NDVI, NDWI, and NMDI) including their mean values were generated using the VNIR, SWIR, and TIR bands of Landsat data sets. Figure 3 presents the mean annual MNDWI values from 1988 to 2019. The high MNDWI values were found in the northwest and southeast parts of the city. Figure 4 presents the mean annual NDBaI values for the period. The

Table 3. Effective mean atmospheric temperature for four standard atmospheres..

Standard atmosphere	Effective mean atmospheric temperature (T_a) in Kelvin
For USA 1976	$T_a = 25.9396 + 0.88045T_0$
For tropical	$T_a = 17.9769 + 0.91715T_0$
For mid-latitude summer	$T_a = 16.0110 + 0.92621T_0$
For mid-latitude winter	$T_a = 19.2704 + 0.91118T_0$
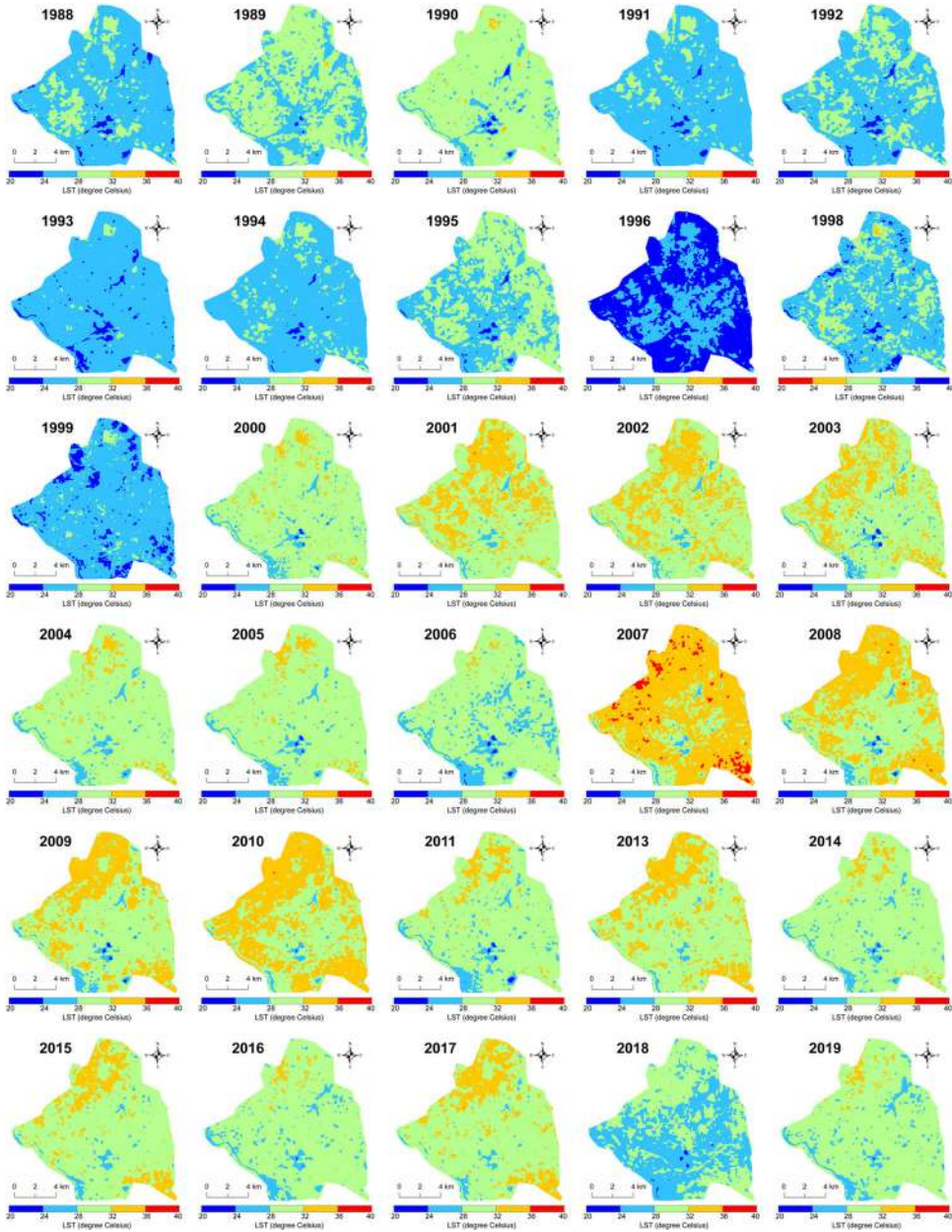
Figure 2. Spatial distribution of mean LST (1988–2019).

Table 4. Mean annual values of LST, MNDWI, NDBaI, NDBI, NDVI, NDWI, and NMDI (1988–2019).

Date of acquisition	Mean LST	Mean MNDWI	Mean NDBaI	Mean NDBI	Mean NDVI	Mean NDWI	Mean NMDI
1988	26.72	−0.37	−0.22	0.20	0.14	−0.17	0.08
1989	28.22	−0.39	−0.17	0.25	0.09	−0.16	0.06
1990	29.50	−0.39	−0.22	0.26	0.10	−0.14	0.06
1991	26.79	−0.29	−0.29	0.13	0.15	−0.17	0.10
1992	26.84	−0.38	−0.24	0.20	0.11	−0.19	0.08
1993	25.86	−0.39	−0.24	0.22	0.09	−0.18	0.07
1994	27.01	−0.39	−0.21	0.24	0.07	−0.16	0.06
1995	28.06	−0.39	−0.28	0.22	0.11	−0.18	0.07
1996	23.45	−0.32	−0.33	0.06	0.25	−0.26	0.14
1998	27.30	−0.34	−0.34	0.17	0.15	−0.18	0.09
1999	25.93	−0.23	−0.37	0.08	0.12	−0.15	0.17
2000	30.00	−0.13	−0.16	0.16	−0.07	0.03	0.18
2001	31.39	−0.23	−0.20	0.17	0.02	−0.06	0.14
2002	31.24	−0.11	−0.20	0.20	−0.11	0.08	0.16
2003	30.80	−0.12	−0.19	0.23	−0.17	0.12	0.16
2004	30.06	−0.34	−0.31	0.16	0.13	−0.19	0.11
2005	30.10	−0.34	−0.28	0.19	0.08	−0.15	0.09
2006	29.04	−0.31	−0.31	0.16	0.10	−0.15	−0.03
2007	32.31	−0.33	−0.27	0.21	0.04	−0.12	0.09
2008	31.65	−0.30	−0.34	0.19	0.05	−0.11	0.10
2009	31.06	−0.25	−0.31	0.18	0.07	−0.13	0.13
2010	31.99	−0.29	−0.30	0.19	0.04	−0.11	−0.18
2011	29.89	−0.31	−0.33	0.16	0.10	−0.15	0.11
2013	31.34	−0.09	−0.43	−0.02	0.11	−0.11	−0.10
2014	29.74	−0.09	−0.41	−0.02	0.12	−0.12	−0.18
2015	30.66	−0.10	−0.42	−0.01	0.12	−0.11	0.30
2016	29.36	−0.08	−0.44	−0.03	0.12	−0.11	0.31
2017	30.73	−0.08	−0.44	−0.01	0.10	−0.10	0.30
2018	28.50	−0.07	−0.42	−0.03	0.11	−0.10	0.31
2019	29.40	−0.08	−0.44	−0.03	0.12	−0.12	0.31
1988-2019	29.17	−0.25	−0.30	0.13	0.08	−0.12	0.11

southeast section of the study area is characterized by barren land where NDBaI values are higher. Figure 5 shows the mean annual NDBI values. The higher NDBI values are concentrated in the southeast and northwest parts which are under the built-up area or bare surface. Figure 6 is related to the distribution of mean annual NDVI values. The southwest and northeast portions of the area with higher vegetation density present the high NDVI values. Figure 7 shows the mean annual NDWI values during the entire span of the study. The NDWI values are higher in the water areas that are sparsely concentrated in the central and south-eastern parts. The high values of NMDI are observed in the south-central part (Figure 8). The average annual values of MNDWI, NDWI, and NMDI were slightly increased in the later years, whereas the average annual values of NDBaI and NDBI were slightly increased in the later years compared to the earlier years. Actually, the mean values of LST and six spectral indices for all the available Landsat images have been used in an individual year. It is possible that in a particular year, most of the images are available from a specific season. Hence, the mean value of LST or spectral indices of a particular year may be significantly low or high compared to the other years and it is reflected in the final resultant figures. The mean annual value of MNDWI, NDBaI, NDBI, NDVI, NDWI, and NMDI were −0.25602, −0.30945, 0.139069, 0.086088, −0.12566, and 0.112952, respectively during the entire period of study.

Figure 9 shows the mean LST values from 1988 to 2019. In the early years, the mean LST values are much lesser. From 2001, the values have risen significantly. After 2013, the
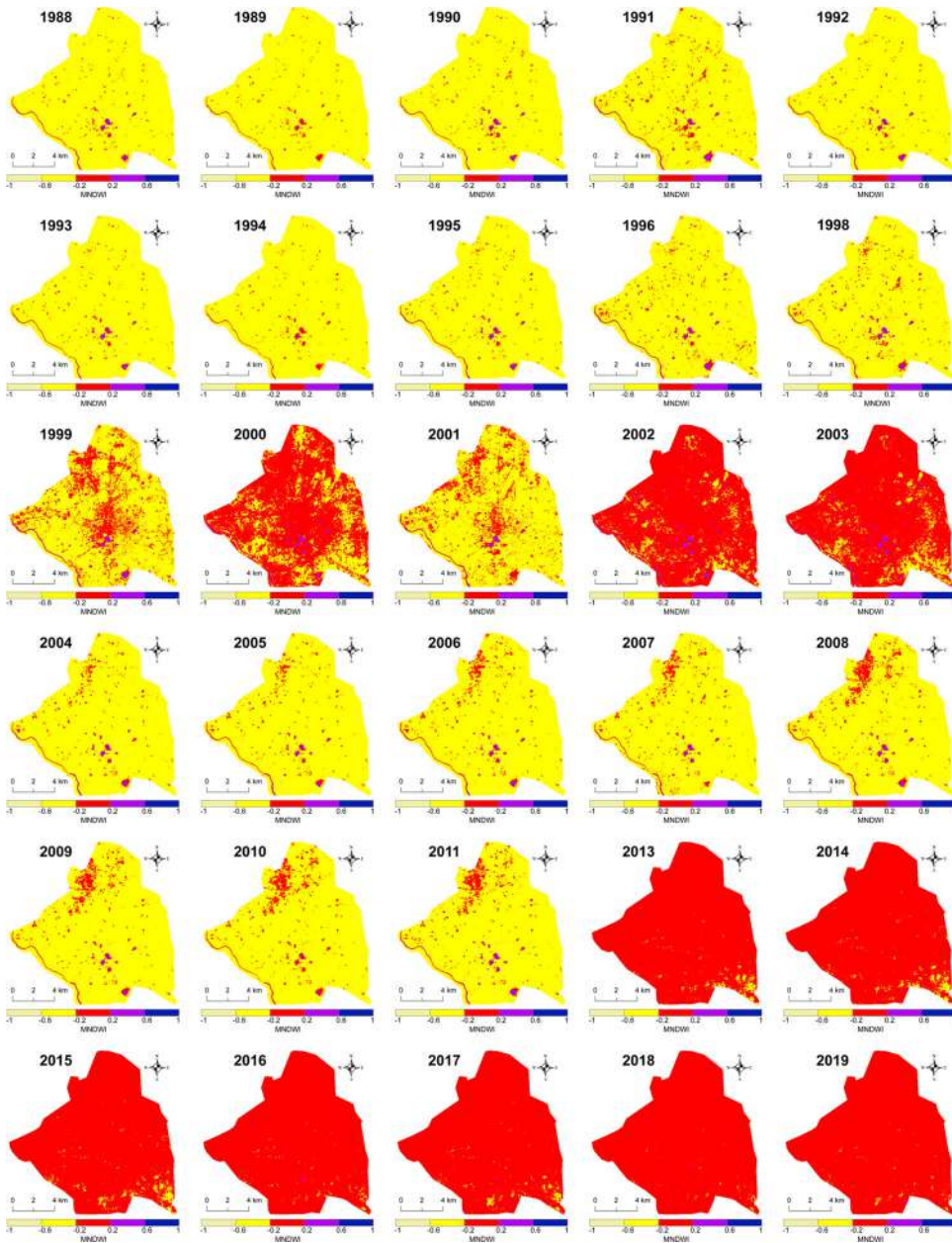
Figure 3. Spatial distribution of mean MNDWI (1988–2019).

values have declined. However, it should be remembered that the LST values were estimated by using the available satellite data.

The mean values of the spectral indices from 1988 to 2019 were shown in Figure 10. The NDBI, NDVI, and NDWI values are more stable than the MNDWI, NDBaI, and NMDI. After 2013, more deviation was seen in the mean NDBI, MNDWI, NDBaI, and NMDI values. It means that Landsat 8 data has more fluctuation in the reflectance values of SWIR bands compared to the Landsat 5 and Landsat 7 satellite sensors. Figure 11 shows the year-wise change in mean LST (1988-2019). In the earlier periods, the trend
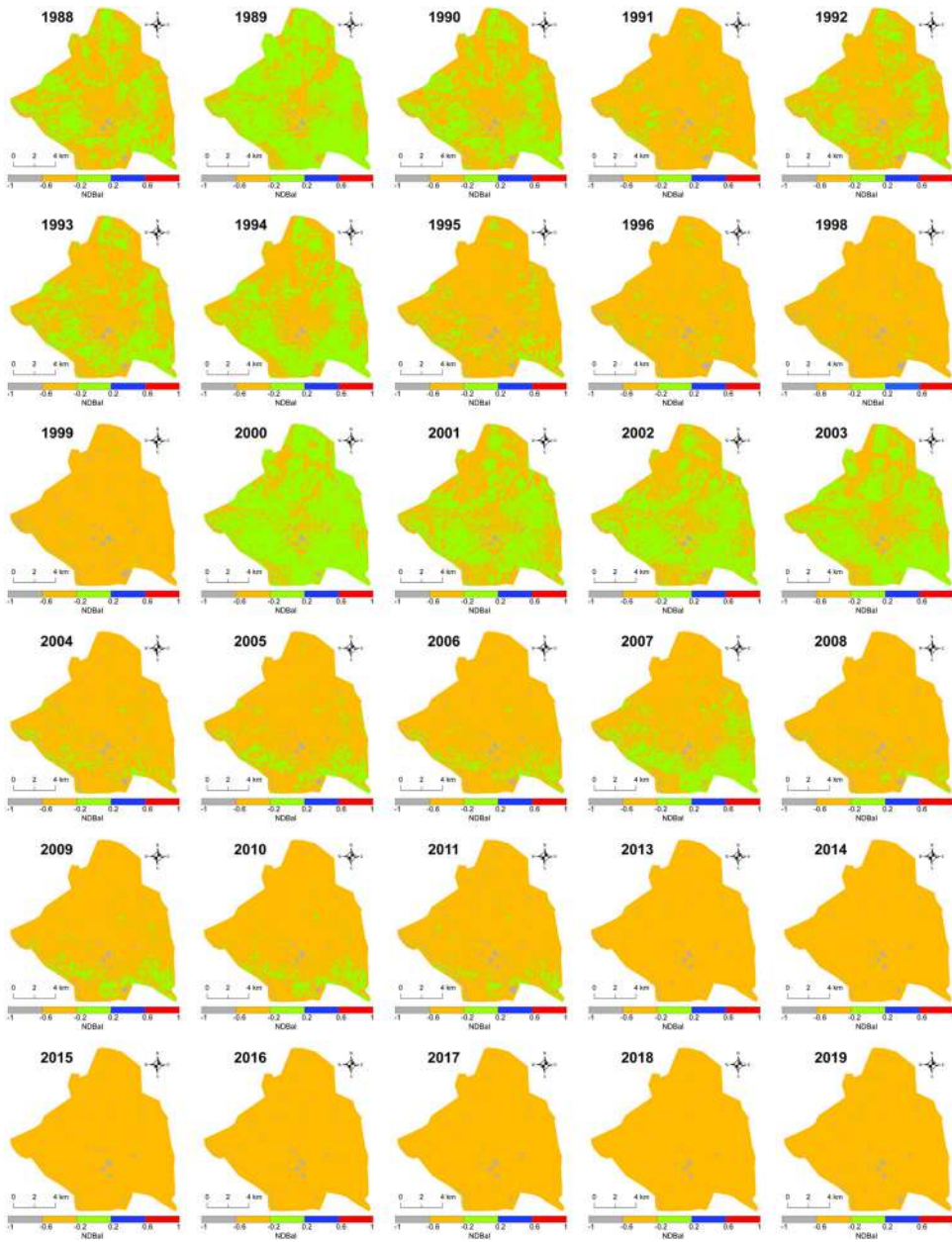
Figure 4. Spatial distribution of mean NDBaI (1988–2019).

was almost rising while it was almost falling from 2002 to 2006. After 2006, the trend of LST was falling and rising in every alternate year.

Figure 12 presents the year-wise change in the values of the spectral indices from 1988 to 2019. The NMDI values are more fluctuating than the other spectral indices. In the earlier and the later periods, the spectral indices have very little deviation compared to the middle years. Especially, for the last four years, all the spectral indices are very stable.

Figure 5. Spatial distribution of mean NDBI (1988–2019).

4.3. Estimation of the variability of LST-MNDWI, LST-NDBaI, LST-NDBI, LST-NDVI, LST-NDWI, and LST-NMDI relationships

Table 5 represents the annual average correlation coefficients (*r*) of Pearson's linear correlation method between LST and six remote sensing indices by using the student's two-tailed test (0.05 significance level). LST builds a negative correlation with MNDWI, NDVI, and NMDI, while it builds a positive correlation with NDBI, NDBaI, and NDWI (Table 5). The annual mean *r* was determined between LST and six remote sensing indices. Here, the LST-NDBI correlation builds the best positive ($r = 0.65$) among the six
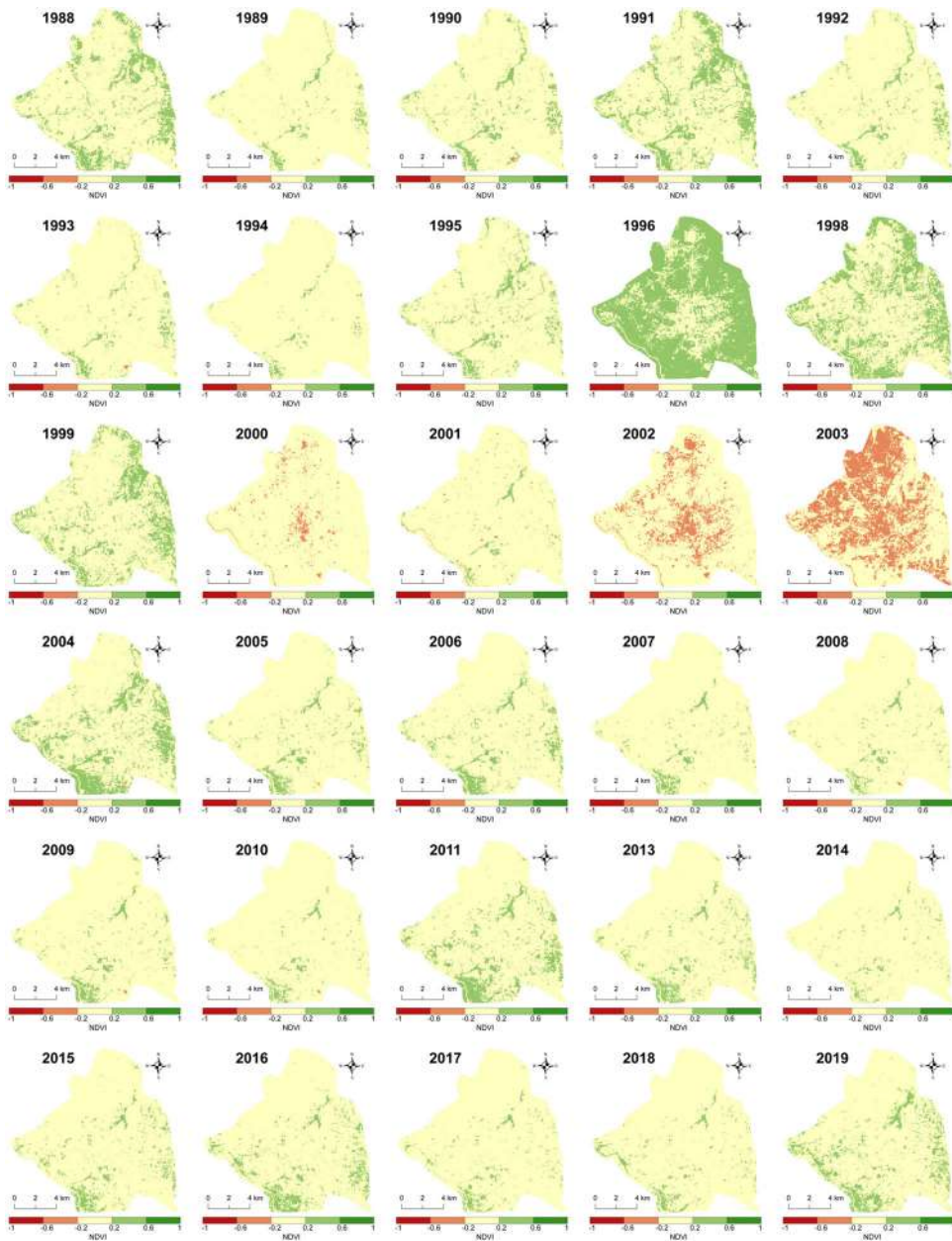
Figure 6. Spatial distribution of mean NDVI (1988–2019).

LST-remote sensing indices correlation analyses because NDBI values are increased with the expansion of the built-up area which is the reason for high LST generation. LST-NMDI builds a strong negative correlation ($r = -0.54$) as the higher NMDI value in an urban area is responsible for low LST. LST-NDVI and LST-MNDWI reflect a moderate negative correlation ($r = -0.38$) as the high NDVI indicates the high green areas and low LST. A moderate positive correlation ($r = 0.30$) is found between LST and NDBaI as in the mixed urban area. NDBaI is used for the extraction of bare and semi-bare lands of a particular region. Only NDWI presents a weak positive correlation ($r = 0.19$) and it is also
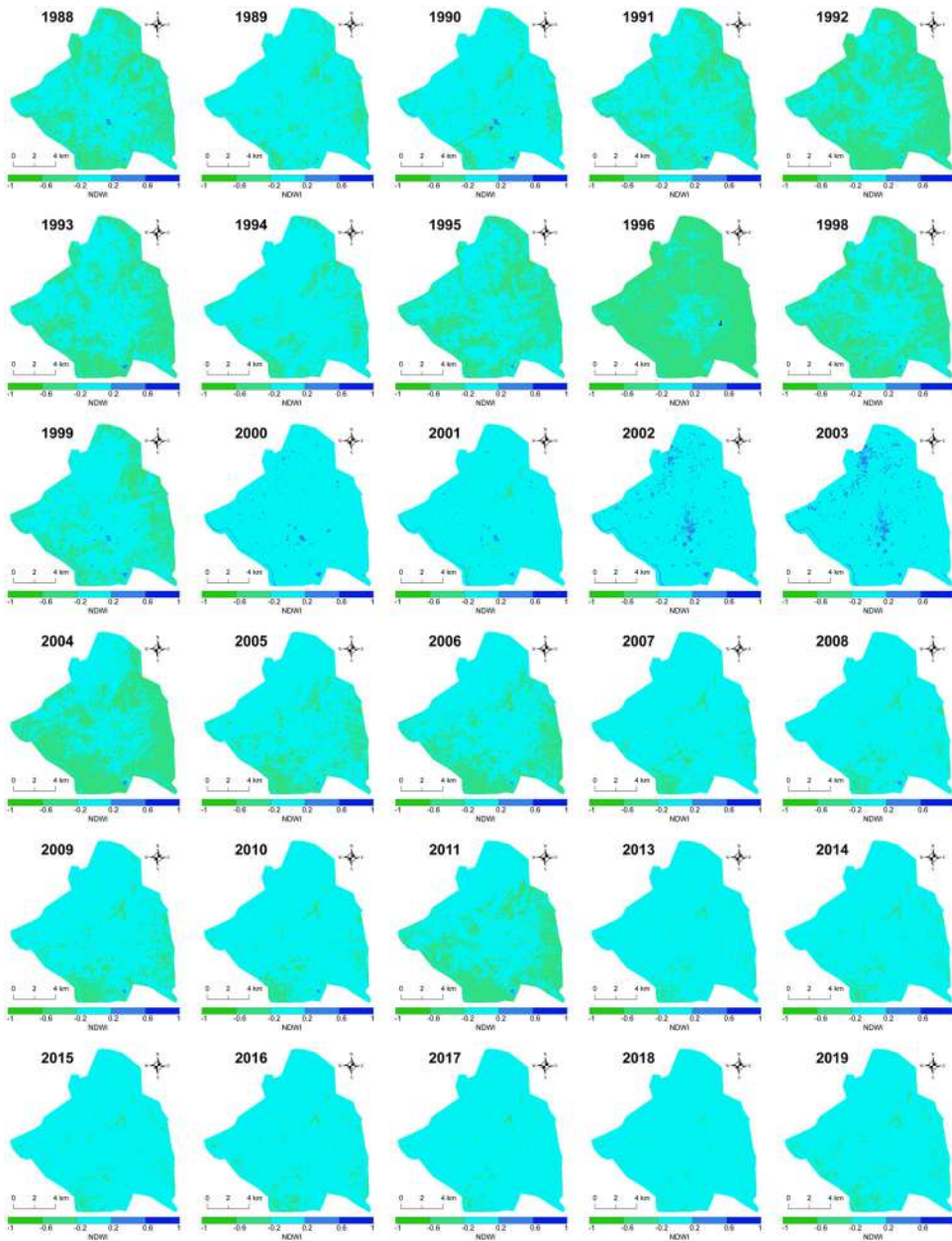
Figure 7. Spatial distribution of mean NDWI (1988–2019).

too inconsistent. In this urban area, the bare and semi-bare lands are mainly composed of various kinds of mixed heterogeneous materials. Among these, some materials (rock fragments, mineral grains, dry soil, or artificial set-up) enhances the LST, whereas other materials (wet soil, biotic components, marshy wetlands, or wastelands) reduces the LST.

Figure 13 and Table 5 show a long-term LST-remote sensing indices annual relationship. The figure depicts that LST builds a strong and stable negative correlation ($r = -0.54$) with NMDI. The negativity is gradually decreasing from the early years to the later years. LST builds a moderate negative correlation ($r = -0.38$) with NDVI and
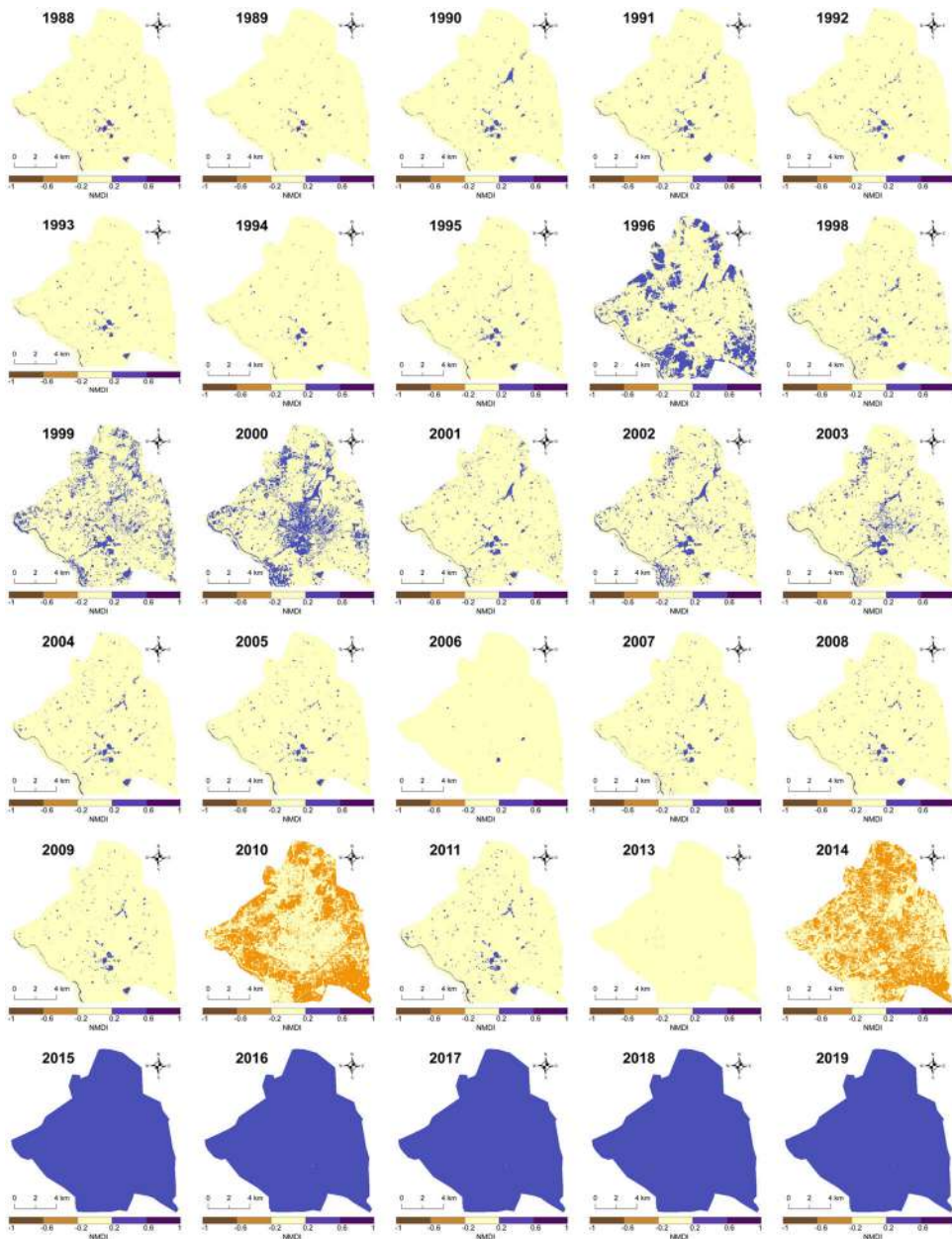
Figure 8. Spatial distribution of mean NMDI (1988–2019).

MNDWI. The negativity of the LST-MNDWI correlation decreases with time, while LST-NDVI shows a comparatively stable correlation. A strong and very stable positive correlation ($r = 0.65$) is found between LST and NDBI. LST builds a moderate positive correlation ($r = 0.30$) with NDBaI and a weak positive correlation ($r = 0.19$) with NDWI. But, the nature of these relationships is different from each other. In LST-NDBaI correlation positivity decreases with time, whereas positivity increases in LST-NDWI correlation.
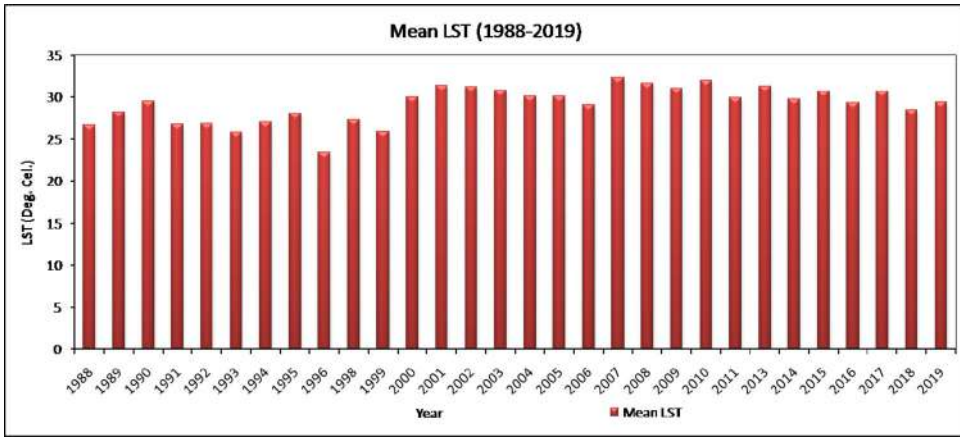
Figure 9. Mean values of LST from 1988 to 2019.
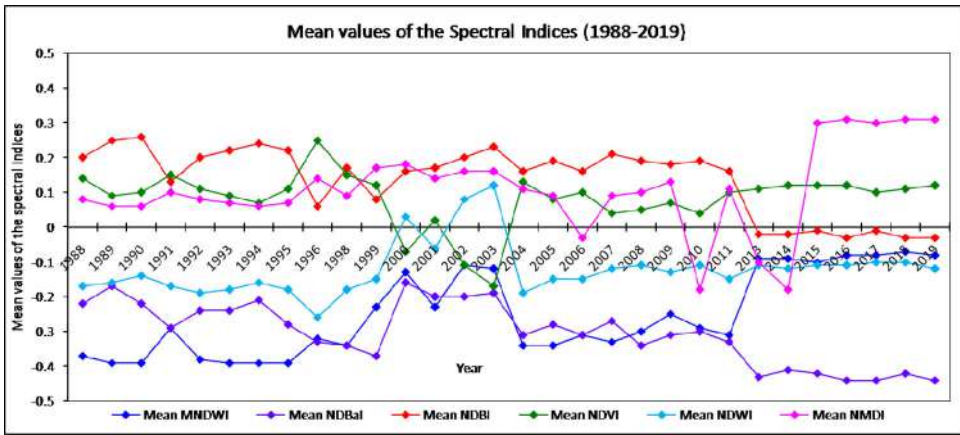
Figure 10. Mean values of the spectral indices from 1988 to 2019.
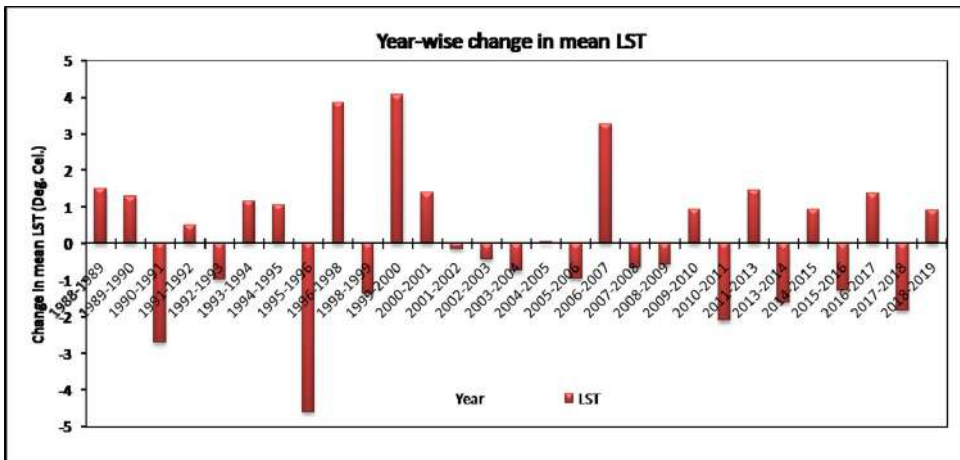
Figure 11. Year-wise change in mean LST from 1988 to 2019.
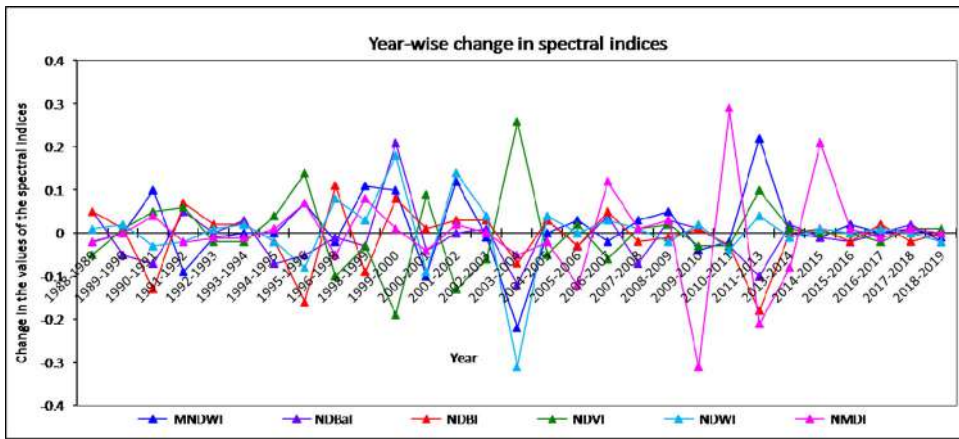
Figure 12. Year-wise change in the values of the spectral indices from 1988 to 2019.

Table 5. Mean annual correlation coefficients (*r*) of LST-remote sensing indices correlation analyses from 1988 to 2019 (0.05 level of significance).

Date of acquisition	LST-MNDWI	LST-NDBal	LST-NDBI	LST-NDVI	LST-NDWI	LST-NMDI
1988	−0.47	0.47	0.66	−0.38	0.11	−0.53
1989	−0.40	0.33	0.60	−0.34	0.09	−0.49
1990	−0.52	0.50	0.72	−0.42	0.16	−0.64
1991	−0.51	0.44	0.68	−0.35	0.16	−0.59
1992	−0.50	0.47	0.65	−0.35	0.12	−0.58
1993	−0.48	0.44	0.68	−0.34	0.09	−0.56
1994	−0.47	0.43	0.65	−0.38	0.12	−0.53
1995	−0.47	0.43	0.61	−0.24	0.01	−0.52
1996	−0.47	0.55	0.77	−0.52	0.34	−0.69
1998	−0.43	0.43	0.61	−0.23	0.03	−0.48
1999	−0.43	0.49	0.63	−0.29	0.10	−0.50
2000	−0.53	0.51	0.75	−0.47	0.19	−0.60
2001	−0.44	0.47	0.77	−0.58	0.39	−0.63
2002	−0.52	0.51	0.77	−0.51	0.28	−0.60
2003	−0.52	0.41	0.70	−0.43	0.18	−0.57
2004	−0.36	0.31	0.65	−0.39	0.21	−0.52
2005	−0.37	0.29	0.64	−0.37	0.19	−0.50
2006	−0.34	0.25	0.64	−0.37	0.20	−0.54
2007	−0.42	0.29	0.68	−0.40	0.18	−0.57
2008	−0.36	0.21	0.62	−0.30	0.14	−0.50
2009	−0.26	0.12	0.61	−0.42	0.27	−0.46
2010	−0.32	0.16	0.63	−0.36	0.21	−0.58
2011	−0.21	0.10	0.62	−0.43	0.31	−0.42
2013	−0.23	0.07	0.60	−0.43	0.25	−0.58
2014	−0.23	0.06	0.59	−0.33	0.22	−0.58
2015	−0.26	0.06	0.60	−0.33	0.21	−0.49
2016	−0.20	0.08	0.59	−0.37	0.26	−0.46
2017	−0.22	0.04	0.57	−0.34	0.23	−0.44
2018	−0.23	0.09	0.60	−0.36	0.23	−0.45
2019	−0.14	0.03	0.60	−0.43	0.34	−0.46
1988-2019	−0.38	0.302343	0.65	−0.38	0.19	−0.53

The variability and consistency of the relationships between LST and six remote sensing indices were measured by using the standard deviation (*SD*) and coefficient of variation (*CV*). Table 6 presents the variability of these LST-remote sensing indices relationships. High values of SD and CV indicate the high variability or low consistency of the data and vice-versa.
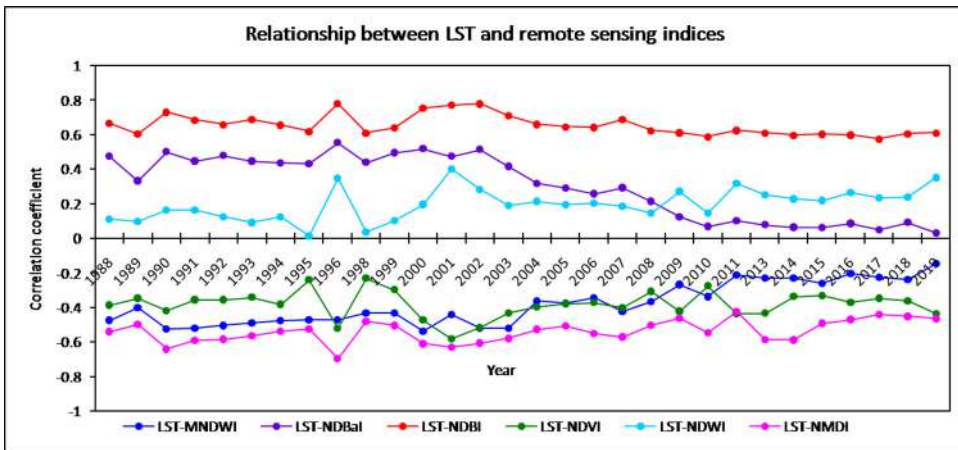
Figure 13. Annual assessment on LST-remote sensing indices relationship (1988 to 2019) (0.05 level of significance).

Table 6. Variability of LST-remote sensing indices relationship (1988–2019).

1988-2019	LST-MNDWI	LST-NDBaI	LST-NDBI	LST-NDVI	LST-NDWI	LST-NMDI
Mean	−0.38192	0.302343	0.653648	−0.3839	0.196367	−0.53852
Standard deviation (SD)	0.118983	0.182046	0.059413	0.078485	0.091089	0.065217
Coefficient of variation (CV)	31.15	60.21	9.09	20.44	46.39	12.11

It is clear from the table that LST-NDBI ($CV = 9.09$) and LST-NMDI ($CV = 12.11$) relationships were the most consistent among the six relationships. It is mainly because the NDBI and NMDI are more consistent in an urban environment. LST-NDVI, LST-MNDWI, and LST-NDWI have moderate variability as NDVI, NDWI, and MNDWI varies moderately with the season. LST-NDBaI ($CV = 60.21$) is the most variable relationship among the LST and six remote sensing indices due to the high spatiotemporal and seasonal variability of NDBaI in any urban area.

The study reflects the relationship between LST and the various spectral indices to take new action in environmental planning and management of any city. The area has a positive correlation promotes the LST whereas the area with a negative correlation reduces the LST. Hence, the environmental planners should select the areas with positive correlation and must take the necessary actions to convert them in the areas where the correlation will be negative. In this way, the fallow or barren lands can be converted into parks, wetlands, or artificial water bodies. Forest or dense vegetation must be protected and social forestry can be introduced at a large scale. Most of the industrial and commercial activities must be restrained in particular areas located far away from the dense residential places. A specific area of the city should be allotted as wasteland. Thus, the correlation between LST and the spectral indices significantly determines the vulnerable area of the city and the ecological health of the city could be improved by converting these vulnerable places into vegetation and water bodies.

5. Conclusion

In this paper, two hundred and ten cloud-free Landsat datasets from 1988 to 2019 were used to determine the relationship of LST with six remote sensing indices (MNDWI, NDBaI, NDBI, NDVI, NDWI, and NMDI) in Raipur City. The mono-window algorithm was applied for retrieving LST using two hundred and ten multi-temporal Landsat images

of different sensors. The correlation coefficients vary from strong positive ($r = 0.65$ for LST-NDBI) to moderate positive ($r = 0.30$ for LST-NDBaI) and weak positive ($r = 0.19$ for LST-NDWI), and from strong negative ($r = -0.54$ for LST-NMDI) to moderate negative ($r = -0.38$ for LST-NDVI and LST-MNDWI). LST-NDBI correlation was the most consistent ($CV = 9.09$) and the LST-NDBaI correlation was the most variable ($CV = 60.21$) among the six LST-remote sensing indices correlation during the entire study period. The study will be helpful for the urban planning and management division of Raipur City.

Acknowledgment

Disclosure statement

ORCID

Subhanil Guha 🆔 http://orcid.org/0000-0002-2967-7248
Himanshu Govil 🆔 http://orcid.org/0000-0002-3433-8355

References

Amiri R, Weng Q, Alimohammadi A, Alavipanah SK. 2009. Spatial-temporal dynamics of land surface temperature in relation to fractional vegetation cover and land use/cover in the Tabriz urban area, Iran. Remote Sens Environ. 113(12):2606–2617.

Arnfield J. 2003. Two decades of urban climate research: a review of turbulence, exchanges of energy and water, and the urban heat island. Int J Climatol. 23(1):1–26.

Barsi J, Schott J, Hook S, Raqueno N, Markham B, Radocinski R. 2014. Landsat-8 thermal infrared sensor (TIRS) vicarious radiometric calibration. Remote Sens. 6(11):11607–11626.

Becker F, Li Z-L. 1990. Towards a local split window method over land surfaces. Int J Remote Sens. 11(3):369–393.

Carlson TN, Ripley DA (1997) On the Relation between NDVI, Fractional Vegetation Cover, and Leaf Area Index. Remote Sens Environ 62: 241-252. doi:10.1016/S0034-4257(97)00104-1

Chatterjee RS, Singh N, Thapa S, Sharma D, Kumar D. 2017. Retrieval of land surface temperature (LST) from landsat TM6 and TIRS data by single channel radiative transfer algorithm using satellite and ground-based inputs. Int J Appl Earth Obs Geoinf. 58:264–277.

Chen XL, Zhao HM, Li PX, Yi ZY (2006) Remote sensing image-based analysis of the relationship between urban heat island and land use/cover changes. Remote Sens Environ 104(2): 133–146. doi:10.1016/j.rse.2005.11.016

Chun B, Guldmann JM. 2014. Spatial statistical analysis and simulation of the urban heat island in high-density central cities. Landsc Urban Plann. 125:76–88.

Coll C, Valor E, Galve JM, Mira M, Bisquert M, García-Santos V, Caselles E, Caselles V. 2012. Long-term accuracy assessment of land surface temperatures derived from the advanced along-track scanning radiometer. Remote Sens Environ. 116:211–225.

Coseo P, Larsen L. 2014. How factors of land use/land cover, building configuration, and adjacent heat sources and sinks explain Urban Heat Islands in Chicago. Landsc Urban Plann. 125:117–129.

Dai Z, Guldmann JM, Hu Y. 2018. Spatial regression models of park and land-use impacts on the urban heat island in central Beijing. Sci Total Environ. 626:1136–1147.

García-Santos V, Cuxart J, Martínez-Villagrasa D, Jiménez MA, Simó G. 2018. Comparison of three methods for estimating land surface temperature from Landsat 8-TIRS sensor data. Remote Sens. 10(9):1450.

Govil H, Guha S, Dey A, Gill N. 2019. Seasonal evaluation of downscaled land surface temperature: A case study in a humid tropical city. Heliyon. 5(6):e01923.

Govil H, Guha S, Diwan P, Gill N, Dey A. 2020. Analyzing linear relationships of LST with NDVI and MNDISI using various resolution levels of Landsat 8 OLI/TIRS data. In: Sharma N, Chakrabarti A, Balas V, editors. Data management, analytics and innovation. Advances in intelligent systems and computing. Vol. 1042. Singapore: Springer; p. 171–184. https://doi.org/10.1007/978-981-32-9949-8_13.

Guha S, Govil H, Besoya M. 2020c. An investigation on seasonal variability between LST and NDWI in an urban environment using Landsat satellite data. Geomat Nat Hazards Risk. 11(1):1319–1345.

Guha S, Govil H, Dey A, Gill N. 2020a. A case study on the relationship between land surface temperature and land surface indices in Raipur City, India. Geogr Tidss-Danish J Geogr. 120(1):35–50.

Guha S, Govil H, Gill N, Dey A. 2020b. Analytical study on the relationship between land surface temperature and land use/land cover indices. Ann GIS. 26(2):201–216.

Guha S, Govil H. 2020. Seasonal impact on the relationship between land surface temperature and normalized difference vegetation index in an urban landscape. Geocarto Int. doi:10.1080/10106049.2020.1815867

Huang W, Zeng Y, Li S. 2015. An analysis of urban expansion and its associated thermal characteristics using Landsat imagery. Geocarto Int. 30(1):93–103.

Jiménez-Muñoz JC, Cristobal J, Sobrino JA, Soria G, Ninyerola M, Pons X, Pons X. 2009. Revision of the single-channel algorithm for land surface temperature retrieval from Landsat thermal-infrared data. IEEE Trans Geosci Remote Sensing. 47(1):339–349.

Jiménez-Muñoz JC, Sobrino JA. 2003. A generalized single channel method for retrieving land surface temperature from remote sensing data. J Geophys Res. 108(D22):4688.

Jovanović D, Govedarica M, Sabo F, Sladić D, Ristić A. 2015. Spatial analysis of high-resolution urban thermal patterns in Vojvodina, Serbia. Geocarto Int. 30(5):483–505.

Kim JP, Guldmann JM. 2014. Land-use planning and the urban heat island. Environ Plann B Plann Des. 41(6):1077–1099.

Kuang W, Liu Y, Dou Y, Chi W, Chen G, Gao C, Yang T, Liu J, Zhang R. 2015. What are hot and what are not in an urban landscape: quantifying and explaining the land surface temperature pattern in Beijing. Landscape Ecol. 30(2):357–373.

Li J (2006) Estimating land surface temperature from Landsat-5 TM. Remote Sens Technol Appl 21: 322–326.

Li J, Song C, Cao L, Zhu F, Meng X, Wu J. 2011. Impacts of landscape structure on surface urban heat islands: A case study of Shanghai, China. Remote Sens Environ. 115(12):3249–3263.

Majumder A, Kingra PK, Setia R, Singh SP, Pateriya B. 2020. Influence of land use/land cover changes on surface temperature and its effect on crop yield in different agro-climatic regions of Indian Punjab. Geocarto Int. 35(6):663–686.

Mbuh MJ, Wheeler R, Amanda C. 2019. Spatiotemporal analysis of urban heat island intensification in the city of Minneapolis-St. Paul and Chicago Metropolitan Areas Using Landsat Data from 1984 to 2016. Geocarto Int. doi:10.1080/10106049.2019.1655802

McFeeters SK (1996) The use of the Normalized Difference Water Index (NDWI) in the delineation of open water features. Int J Remote Sens 17(7): 1425–1432. doi:10.1080/01431169608948714

McMillin LM. 1975. Estimation of sea surface temperaturesfrom two infrared window measurements with different absorption. J Geophys Res. 80(36):5113–5182.

Mirzaei PA. 2015. Recent challenges in modeling of urban heat island. Sustain Cities Soc. 19:200–206.

Peng J, Xie P, Liu Y, Ma J. 2016. Urban thermal environment dynamics and associated landscape pattern factors: a case study in the Beijing metropolitan region. Remote Sens Environ. 173:145–155.

Piyoosh AK, Ghosh SK. 2020. Analysis of land use land cover change using a new and existing spectral indices and its impact on normalized land surface temperature. Geocarto Int. doi:10.1080/10106049.2020.1815863

Price JC. 1984. Land surface temperature measurements from the split window channels of the NOAA 7 advanced very high resolution radiometer. J Geophys Res. 89(D5):7231–7237.

Qin ZH, Karnieli A, Berliner P. 2001. A mono-window algorithm for retrieving land surface temperature from Landsat TM data and its application to the Israel–Egypt border region. Int J Remote Sens. 22(18):3719–3746.

Rinner C, Hussain M. 2011. Toronto's urban heat island exploring the relationship between land use and surface temperature. Remote Sens. 3(6):1251–1265.

Rizwan AM, Leung DYC, Chunho L. 2008. A review on the generation, determination and mitigation of the urban heat island. J Environ Sci. 20(1):120–128.

Rozenstein O, Qin Z, Derimian Y, Karnieli A. 2014. Derivation of land surface temperature for Landsat-8 TIRS using a split window algorithm. Sensors (Basel)). 14(4):5768–5780.

Sekertekin A, Bonafoni S. 2020. Land surface temperature retrieval from landsat 5, 7, and 8 over rural areas: assessment of different retrieval algorithms and emissivity models and toolbox implementation. Remote Sens. 12(2):294.

Sobrino JA, Raissouni N, Li Z (2001) A comparative study of land surface emissivity retrieval from NOAA data. Remote Sens Environ 75(2): 256–266. doi:10.1016/S0034-4257(00)00171-1

Sobrino JA, Jiménez-Muñoz JC, Paolini L (2004) Land surface temperature retrieval from Landsat TM5. Re-mote Sens Environ 9: 434–440. doi:10.1016/j.rse.2004.02.003

Song J, Du S, Feng S, Guo L. 2014. The relationships between landscape compositions and land surface temperature: quantifying their resolution sensitivity with spatial regression models. Landsc Urban Plann. 123:145–157.

Sun Q, Tan J, Xu Y (2010) An ERDAS image processing method for retrieving LST and describing urban heat evolution: A case study in the Pearl River Delta Region in South China. Environ Earth Sci 59: 1047–1055. doi:10.1007/s12665-009-0096-3

Tucker CJ. 1979. Red and photographic infrared linear combinations for monitoring vegetation. Remote Sens Environ. 8(2):127–150.

Wang L, Lu Y, Yao Y. 2019. Comparison of three algorithms for the retrieval of land surface temperature from landsat 8 images. Sensors. 19(22):5049.

Wang L, Qu JJ. 2007. NMDI: A normalized multi-band drought index for monitoring soil and vegetation moisture with satellite remote sensing. Geophys Res Lett. 34(20):L20405.

Weng Q, Yang S. 2004. Managing the adverse thermal effects of urban development in a densely populated Chinese city. J Environ Manage. 70(2):145–156.

Weng Q. 2001. A remote sensing-GIS evaluation of urban expansion and its impact on surface temperature in Zhujiang Delta, China. Int J Remote Sens. 22(10):1999–2014.

Wukelic GE, Gibbons DE, Martucci LM, Foote HP (1989) Radiometric calibration of Landsat Thematic Mapper thermal band. Remote Sens Environ 28: 339–347. doi:10.1016/0034-4257(89)90125-9

Xu H. 2006. Modification of normalized difference water index (NDWI) to enhance open water features in remotely sensed imagery. Int J Remote Sens. 27(14):3025–3033.

Yang L, Cao Y, Zhu X, Zeng S, Yang G, He J, Yang X. 2014. Land surface temperature retrieval for arid regions based on Landsat-8 TIRS data: A case study in Shihezi. J Arid Land. 6(6):704–716.

Yu X, Guo X, Wu Z. 2014. Land surface temperature retrieval from Landsat 8 TIRS—comparison between radiative transfer equation-based method, split window algorithm and single channel method. Remote Sens. 6(10):9829–9852.

Zanter K (2019) Landsat 8 (L8) Data Users Handbook; EROS: Sioux Falls, SD, USA.

Zha Y, Gao J, Ni S. 2003. Use of normalized difference built-up index in automatically mapping urban areas from TM imagery. Int J Remote Sens. 24(3):583–594.

Zhang H, Qi ZF, Ye XY, Cai YB, Ma WC, Chen MN. 2013. Analysis of land use/land cover change, population shift, and their effects on spatiotemporal patterns of urban heat islands in metropolitan Shanghai, China. Appl Geogr. 44:121–133.

Zhang Z, He G, Wang M, Long T, Wang G, Zhang X, Jiao W. 2016. Towards an operational method for land surface temperature retrieval from Landsat 8 data. Remote Sens Lett. 7(3):279–288.

Zhao HM, Chen XL. 2005. Use of normalized difference bareness index in quickly mapping bare areas from TM/ETM+, in IEEE Int. Geosci Remote Sens Symp. 3(25–29):1666–1668.

Zhao M, Cai H, Qiao Z, Xu X. 2016. Influence of urban expansion on the urban heat island effect in Shanghai. Int J Geogr Inf Sci. 30(12):2421–2441.

Zhou WQ, Huang G, Cadenasso ML. 2011. Does spatial configuration matter? Understanding the effects of land cover pattern on land surface temperature in urban landscapes. Landsc Urban Plan. 102(1): 54–63.

Zhu X, Duan S-B, Zhao W, Wu H, Leng P, Gao M, Zhou X. 2020. Retrieval of land surface temperature with topographic effect correction from Landsat 8 thermal infrared data in mountainous areas. IEEE Trans Geoscie Remote Sens.doi:10.1109/TGRS.2020.3030900

Source details

Feedback >   Compare sources >

Geocarto International

Open Access ⓘ

Scopus coverage years: from 1986 to Present

Publisher: Taylor & Francis

ISSN: 1010-6049   E-ISSN: 1752-0762

Subject area: (Social Sciences: Geography, Planning and Development) (Environmental Science: Water Science and Technology)

Source type: Journal

View all documents >   Set document alert   💾 Save to source list

CiteScore 2022
4.3   ⓘ

SJR 2022
0.655   ⓘ

SNIP 2022
1.260   ⓘ

CiteScore   CiteScore rank & trend   Scopus content coverage

Research Article

Monitoring LST-NDVI Relationship Using Premonsoon Landsat Datasets

Subhanil Guha [ID], Himanshu Govil, and Prabhat Diwan

Department of Applied Geology, National Institute of Technology Raipur, Raipur, India

Correspondence should be addressed to Subhanil Guha; subhanilguha@gmail.com

The present study monitors the interrelationship of land surface temperature (LST) with normalized difference vegetation index (NDVI) in Raipur City of India using premonsoon Landsat satellite sensor for the season of 2002, 2006, 2010, 2014, and 2018. The results describe that the mean LST of Raipur City is gradually increased with time. The value of mean NDVI is higher in the area below mean LST compared to the area above mean LST. The value of mean NDVI is also higher in Landsat 8 data than Landsat 5 and Landsat 7 data. A strong negative LST-NDVI correlation is observed throughout the period. The correlation coefficient is higher in the area above mean LST and lower in the area below mean LST. The value of the correlation coefficient is decreased with time. The mixed urban landscape of the city is closely related to the changes of LST-NDVI relationship. These results provide systematic planning of the urban environment.

1. Introduction

Thermal infrared (TIR) bands of satellite images often regulate the biogeochemical actions of the Earth surface features [1–4]. Land surface temperature (LST) determination from TIR bands is very important as it depends on the land surface material and varies from time to time [5]. Fast urbanization rapidly changes the characteristics of the surface components [6]. Natural vegetation is one of the most significant features that control the variation of LST distribution [7]. The most commonly used vegetation index is normalized difference vegetation index (NDVI) which is significantly applied in the computation of LST [8–11]. There are so many factors like climate, types of vegetation, land use, urbanization, etc., that influence the LST-NDVI correlation [12–14].

A number of research scholars recently attempted to build the LST-NDVI correlation [12, 15–17]. Some previous attempts were spatiotemporal in nature and were mainly conducted on the big cities like Tokyo, Shanghai, Chongqing, Shijiazhuang, Rome, Shiraz, Melbourne, Bangkok, Monte Hermoso, Beijing, Islamabad [18–27], etc.

But, the discussion based on the LST-NDVI correlation in an Indian city in premonsoon season was rare.

The surface configurations naturally control the spatial and temporal resolution of any satellite sensor [28]. Generally, LST builds an inverse relationship with vegetation [29]. NDVI acts as a determining factor of LST [30], and some studies used the LST-NDVI correlation to evaluate the distributional pattern of LST [31–36]. A lot of recent studies assess the LST-NDVI correlation in multidimensional approach [2, 32, 37–48].

Many recent research works conducted on the Indian context describe the LST-NDVI correlation [49–54]. To discuss the spatial-temporal variation of LST-NDVI correlation in the premonsoon season, Raipur, a smart and rapidly growing Indian city, was selected. The study reflects the following specific objectives:

(1) Describe the spatiotemporal distribution of LST and NDVI in the premonsoon months.

(2) Analyze the LST-NDVI correlation in the premonsoon months.
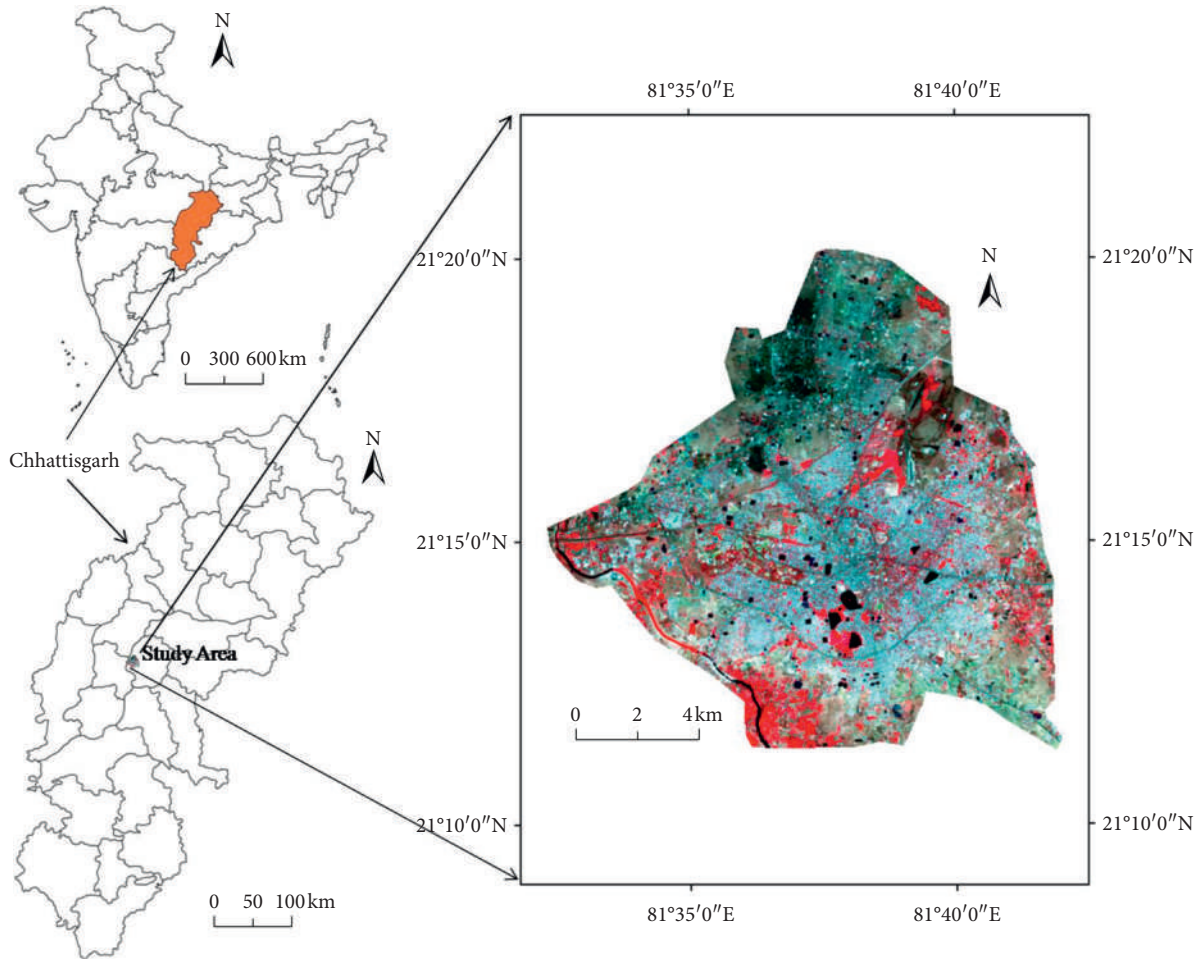
FIGURE 1: Location of the study area.

TABLE 1: Description of Landsat data from different sensors.

Date of acquisition	Satellite sensor	Time	Path/row	Cloud cover (%)
25-Apr-2002	Landsat 7 ETM+	04:44:54	142/044	0.00
11-May-2002	Landsat 7 ETM+	04:44:54	142/044	5.00
28- Apr-2006	Landsat 5 TM	04:48:00	142/044	2.00
15-Jun-2006	Landsat 5 TM	04:48:12	142/044	4.00
07-Apr-2010	Landsat 5 TM	04:47:02	142/044	0.00
23-Apr-2010	Landsat 5 TM	04:46:59	142/044	0.00
25-May-2010	Landsat 5 TM	04:46:51	142/044	0.00
17-Mar-2014	Landsat 8 OLI_TIRS	04:26:36	142/044	0.00
02-Apr-2014	Landsat 8 OLI_TIRS	04:26:19	142/044	0.00
20-May-2014	Landsat 8 OLI_TIRS	04:25:38	142/044	5.46
05-Jun-2014	Landsat 8 OLI_TIRS	04:25:45	142/044	0.02
12-Mar-2018	Landsat 8 OLI_TIRS	04:55:43	142/044	2.10
28-Mar-2018	Landsat 8 OLI_TIRS	04:55:36	142/044	0.01
15-May-2018	Landsat 8 OLI_TIRS	04:55:08	142/044	0.30
16-Jun-2018	Landsat 8 OLI_TIRS	04:55:01	142/044	2.31

2. Study Area and Data

Raipur, the capital and the largest city of Chhattisgarh, India, was selected as the study area which extends between $21°11'22''N$ to $21°20'02''N$ and $81°32'20''E$ to $81°41'50''E$ with an elevation of 280–310 m (Figure 1). The average annual temperature of the city is around 27–30°C. The entire work conducted on the hot and dry premonsoon months

TABLE 2: Derivation of normalized difference vegetation index (NDVI).

Acronym	Description	Formulation	Reference
NDVI	Normalized difference vegetation index	$(NIR − Red)/(NIR + Red)$	[60]
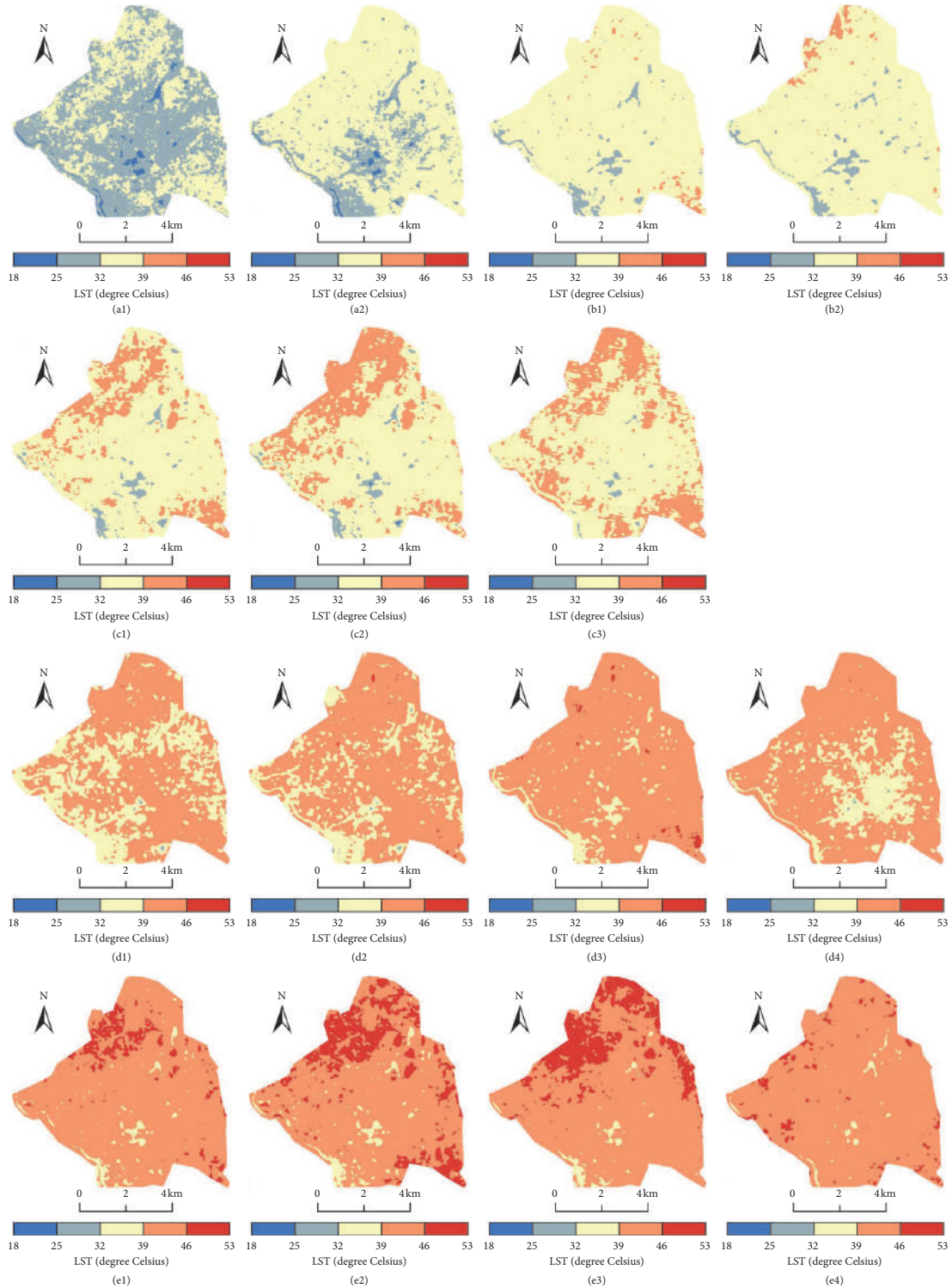
FIGURE 2: Variation in the distribution of LST (°C): (a1-a2) 2002, (b1-b2) 2006, (c1–c3) 2010, (d1–d4) 2014, and (e1-e4) 2018.

TABLE 3: Temporal variations in the distribution of LST (oC) (2002–2018).

Date	LST (minimum)	LST (maximum)	LST (mean)	LST (standard deviation)
Mean 2002	22.08	36.56	31.91	1.82
Mean 2006	25.83	41.83	35.62	2.06
Mean 2010	25.82	43.35	37.42	2.22
Mean 2014	31.26	47.27	40.49	2.03
Mean 2018	33.98	50.40	43.53	2.11
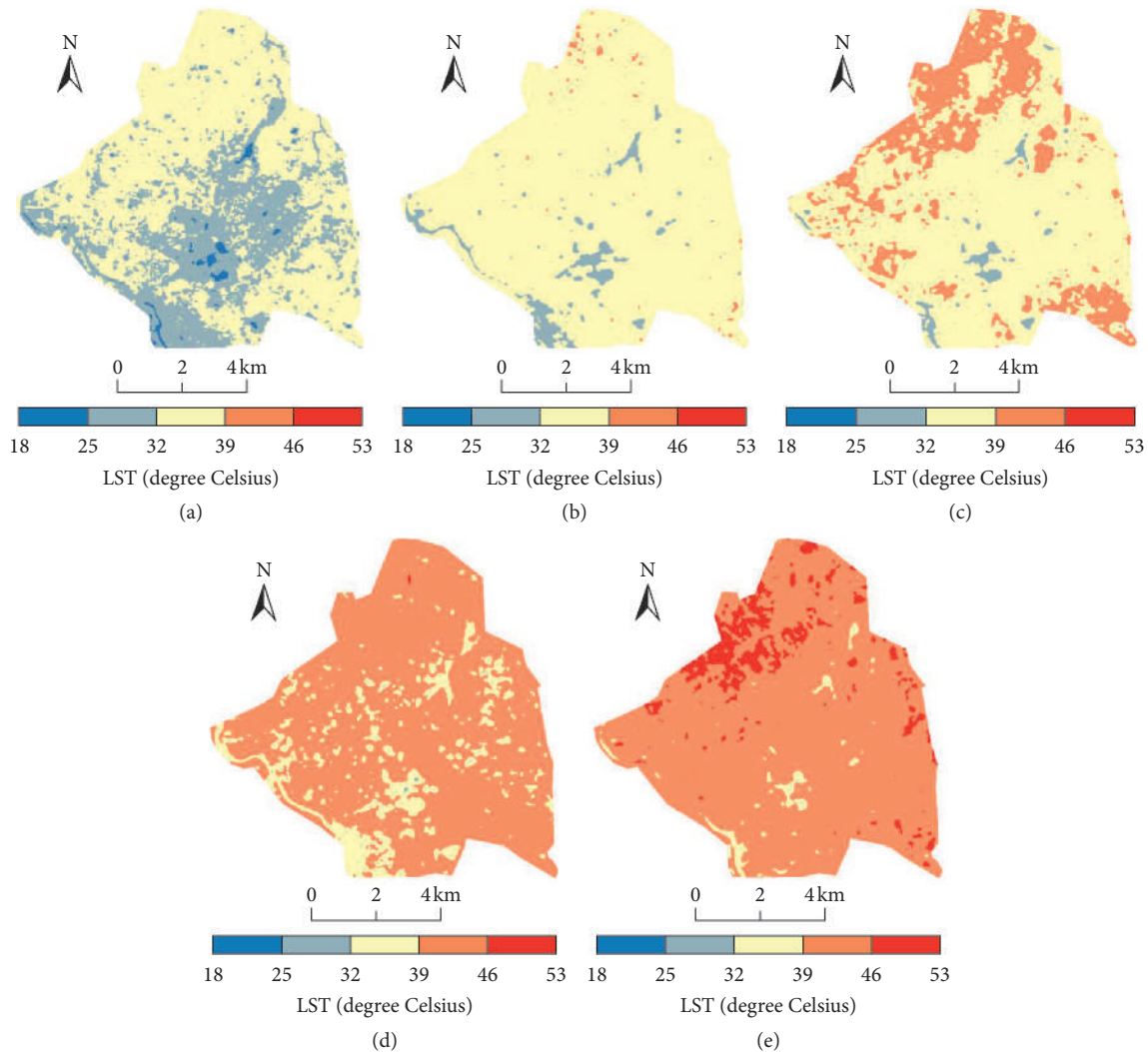
FIGURE 3: Distribution of mean LST ($^{\circ}$C): (a) 2002 (b) 2006 (c) 2010 (d) 2014 (e) 2018.

(March, April, May, and June). The range of the maximum temperature of the premonsoon months lies between 40–45°C. The total population of Raipur is 1,010,087. Literacy rate and sex ratio are 86.45% and 945, respectively.

Five Landsat 5 Thematic Mapper (TM), two Landsat 7 Enhanced Thematic Mapper Plus (ETM+), and eight Landsat 8 Operational Land Imager (OLI)/Thermal Infrared Sensors (TIRS) data of premonsoon seasons with four years interval were freely downloaded from the United States Geological Survey website (https://earthexplorer.usgs.gov) to use in the present study (Table 1). Different types of

Landsat satellite sensors overpass the Raipur City of India between 04:25 and 04:56 Greenwich Mean Time (09:55 to 10:26 AM Indian Standard Time). The data were obtained with maximum illumination which is needed in LST related study. ArcGIS 9.3 software was used to conduct the entire computation.

3. Methodology

Geometric correction, radiometric correction, and resampling are the required preprocessing steps for using the

TABLE 4: Correlation coefficients between Landsat and MODIS sensors derived mean LST.

Acquisition date (Landsat data)	Acquisition date (MODIS data)	Correlation coefficient
25-Apr-2002	25-Apr-2002	0.72
11-May-2002	11-May-2002	0.68
28- Apr-2006	29- Apr-2006	0.75
15-Jun-2006	17-Jun-2006	0.79
07-Apr-2010	06-Apr-2010	0.71
23-Apr-2010	22-Apr-2010	0.78
25-May-2010	24-May-2010	0.67
17-Mar-2014	16-Mar-2014	0.79
02-Apr-2014	01-Apr-2014	0.76
20-May-2014	19-May-2014	0.64
05-Jun-2014	04-Jun-2014	0.72
12-Mar-2018	13-Mar-2018	0.62
28-Mar-2018	27-Mar-2018	0.68
15-May-2018	12-May-2018	0.70
16-Jun-2018	15-Jun-2018	0.73

TABLE 5: Temporal variations in the distribution of NDVI for whole Raipur City (2002–2018).

Date of acquisition	NDVI (minimum)	NDVI (maximum)	NDVI (mean)	NDVI (standard deviation)
Mean	−0.23	0.56	0.00	0.07
Mean	−0.19	0.52	0.09	0.08
Mean	−0.21	0.50	0.02	0.06
Mean	−0.11	0.48	0.14	0.07
Mean	−0.12	0.44	0.12	0.06

Landsat images. LST was determined by using the TIR bands (band 6 for TM and ETM + data, and band 10 for OLI and TIRS data).

3.1. Image Preprocessing and Atmospheric Correction.
The satellite data acquired from Landsat sensors were subset to limit the data size. The thermal infrared bands of Landsat sensors were resampled at 30 m resolution using the nearest neighbour algorithm to match the optical bands. Atmospheric correction of the satellite data was performed by the following steps.

For optical bands of Landsat data, the following equation is used to converting a Digital Number into spectral reflectance:

$$\rho\lambda = M\rho \times Q_{cal} + A\rho, \qquad (1)$$

where $\rho\lambda$ is the spectral reflectance at top-of-atmosphere (TOA) without correction for solar angle (Unitless), Q_{cal} is the Level 1 pixel value in Digital Number (DN), $M\rho$ is the reflectance multiplicative scaling factor for the band (REFLECTANCE_MULT_BAND_n from the metadata), and $A\rho$ is the reflectance additive scaling factor for the band (REFLECTANCE_ADD_BAND_N from the metadata). The $\rho\lambda$ is corrected with local sun elevation angle θs by the following equation:

$$\rho'\lambda = \frac{\rho\lambda}{\sin(\theta s)}. \qquad (2)$$

For TIR band of Landsat data, a similar calibration equation is used:

$$L\lambda = ML \times Q_{cal} + AL, \qquad (3)$$

where $L\lambda$ is the spectral radiance at TOA in $Wm^{-2}sr^{-1}mm^{-1}$, Q_{cal} is the Level 1 pixel value in Digital Number (DN), ML is the radiance multiplicative scaling factor for the band (RADIANCE_MULT_BAND_n from the metadata), and AL is radiance additive scaling factor for the band (RADIANCE_ADD_BAND_n from the metadata).

3.2. LST Estimation Using Landsat Satellite Sensors.
In the present study, the LST was determined by using the monowindow algorithm [55] in which the three necessary elements are atmospheric transmittance, ground emissivity, and effective mean atmospheric temperature.

The original TIR bands of Landsat datasets were resampled into 30 m. The equations are as follows:

$$L_{\lambda} = \text{RadianceMultiBand} \times DN + \text{RadianceAddBand}, \qquad (4)$$

where L_{λ} is spectral radiance ($Wm^{-2}sr^{-1}mm^{-1}$).

$$T_b = \frac{K_2}{\ln((K_1/L_{\lambda}) + 1)}, \qquad (5)$$

where T_b is the at-sensor brightness temperature (Kelvin); K_2 and K_1 are calibration constants for Landsat datasets.
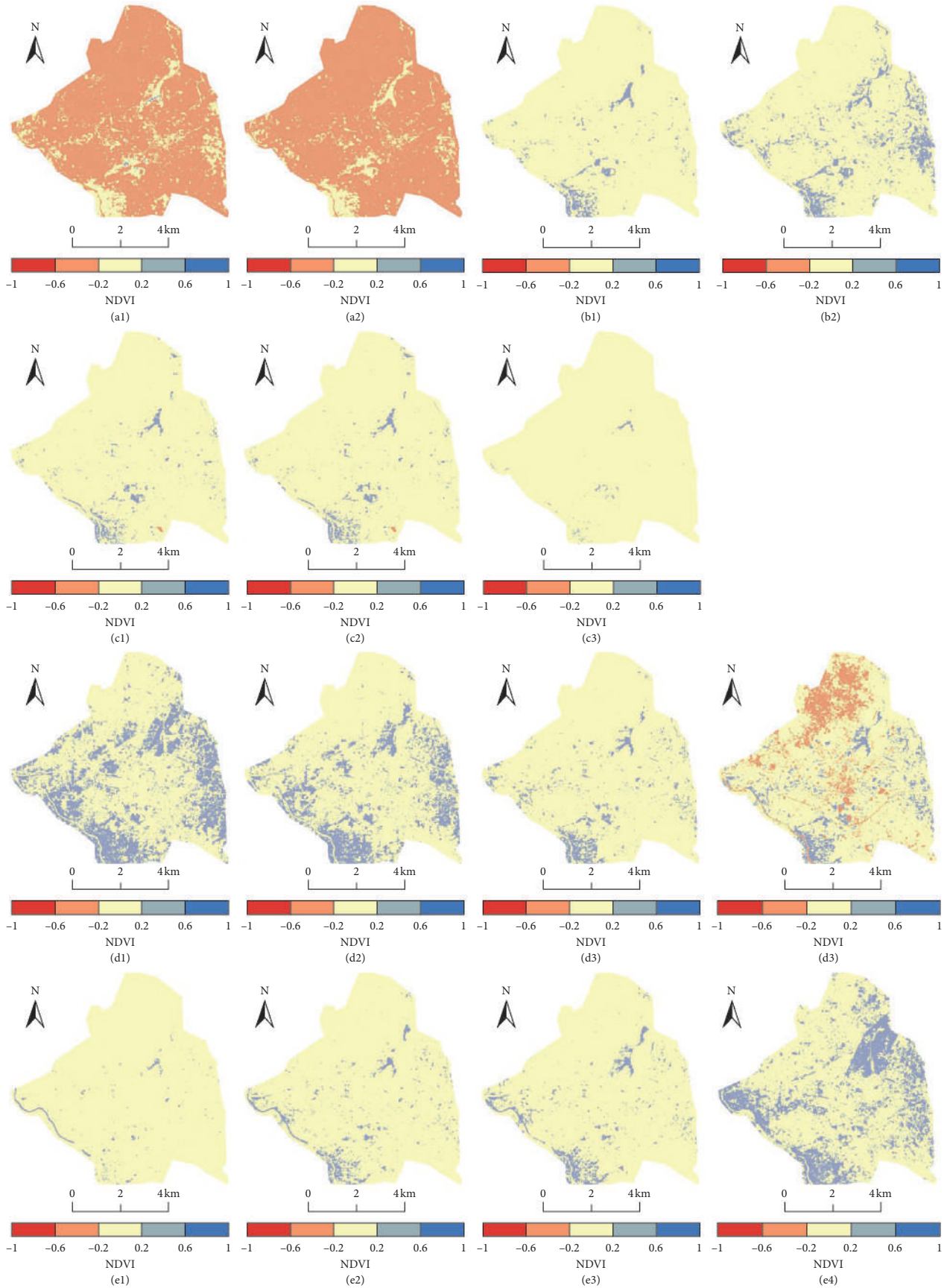
Figure 4: Variation in the distribution of NDVI: (a1-a2) 2002 (b1-b2) 2006 (c1-c3) 2010 (d1-d4) 2014 (e1-e4) 2018.
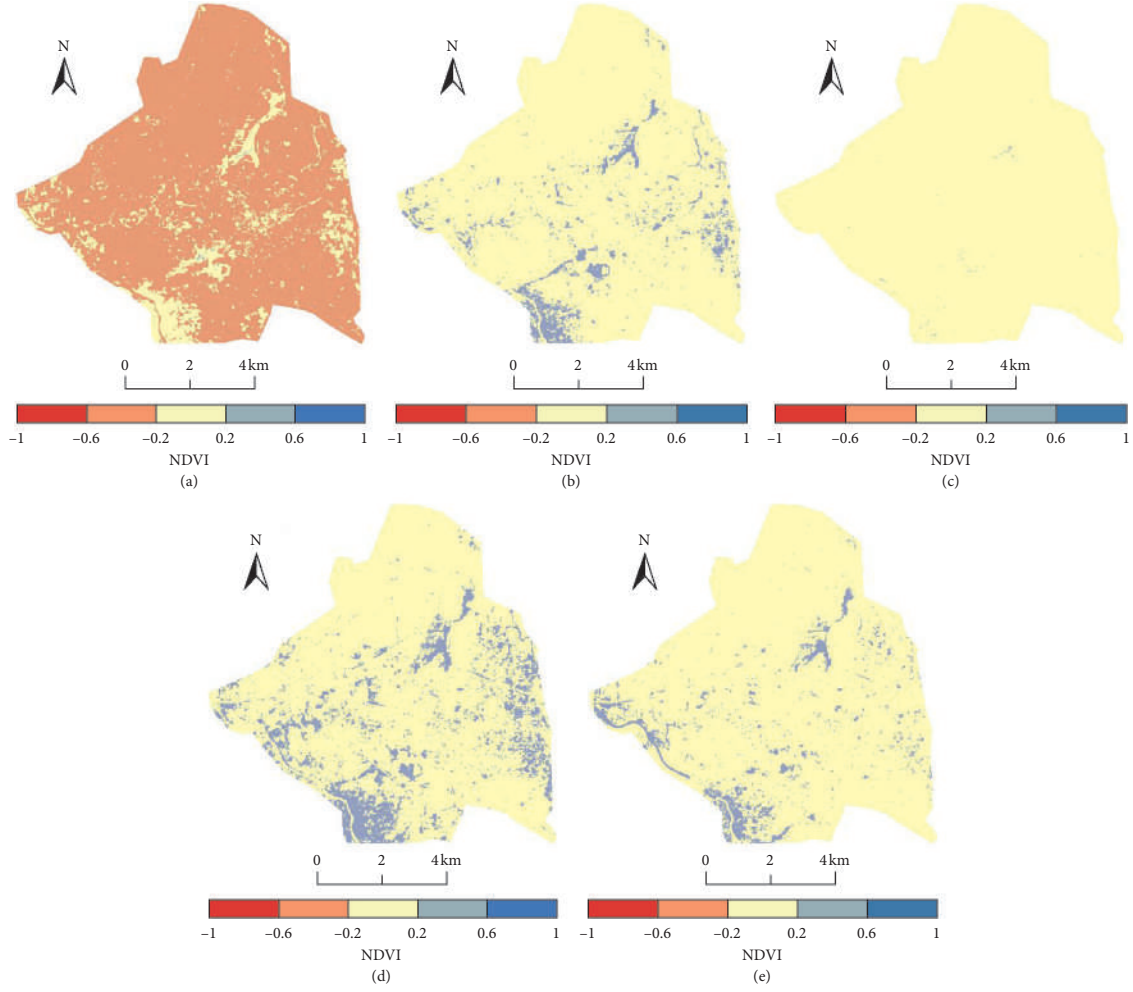
FIGURE 5: Distribution of mean NDVI: (a) 2002, (b) 2006, (c) 2010, (d) 2014, and (e) 2018.

$$F_v = \left(\frac{\text{NDVI} - \text{NDVI}_{\min}}{\text{NDVI}_{\max} - \text{NDVI}_{\min}} \right)^2, \quad (6)$$

where $\text{NDVI}_{\min}$ is the minimum value (0.2) of NDVI for bare soil pixel and $\text{NDVI}_{\max}$ is the maximum value (0.5) of NDVI for healthy vegetation pixel.

$d\varepsilon$ is the geometric distribution effect for the natural surface and internal reflection. The value of $d\varepsilon$ may be 2% for mixed and elevated land surfaces.

$$d\varepsilon = (1 - \varepsilon_s)(1 - F_v) F \varepsilon_v, \quad (7)$$

where ε_s is soil emissivity; F_v is fractional vegetation; F is a shape factor (0.55); and ε_v is vegetation emissivity.

$$\varepsilon = \varepsilon_v F_v + \varepsilon_s (1 - F_v) + d\varepsilon, \quad (8)$$

where ε is land surface emissivity. The value of ε is calculated by the formula given below:

$$\varepsilon = 0.004 \times F_v + 0.986. \quad (9)$$

Water vapour content is determined by the following equation:

$$w = 0.0981 \times \left[10 \times 0.6108 \times \exp\left(\frac{17.27 \times (T_0 - 273.15)}{237.3 + (T_0 - 273.15)} \right) \right. $$
$$\left. \times \text{RH} \right] + 0.1697, $$

$$(10)$$

where w is water vapour content (g/cm^2); T_0 is near-surface air temperature (Kelvin); RH is relative humidity (%). The information on these parameters was provided by the Meteorological Centre, Raipur.

$$\tau = 1.031412 - 0.11536w, \quad (11)$$

where τ is the total atmospheric transmittance.

The effective mean atmospheric transmittance of Raipur City was determined as follows [33]:

FIGURE 6: The area above mean LST (pink portion) and the area below mean LST (black portion): (a1-a2) 2002, (b1-b2) 2006, (c1–c3) 2010, (d1–d4) 2014, and (e1–e4) 2018.
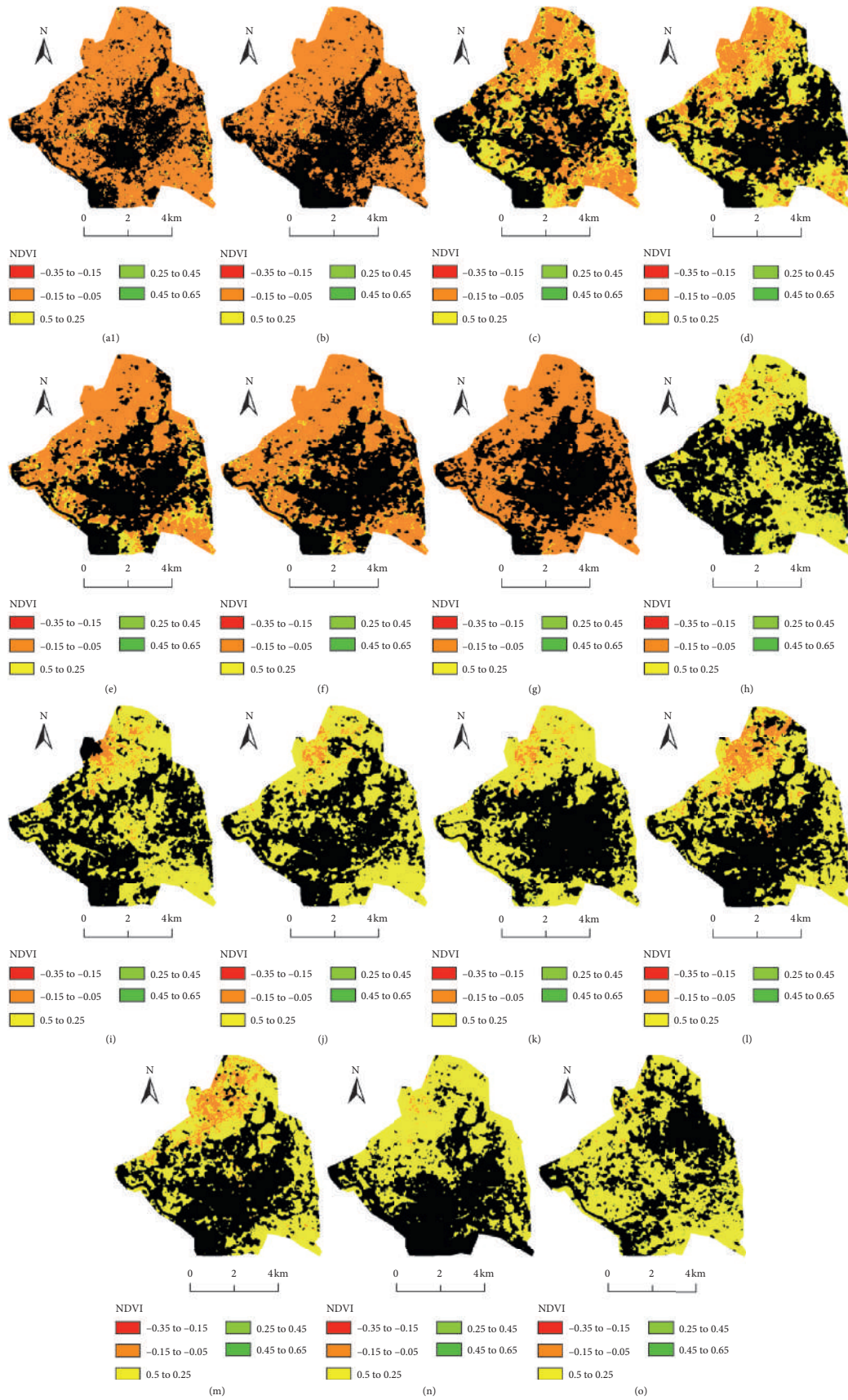
FIGURE 7: NDVI in the area above mean LST: (a-b) 2002, (c-d) 2006, (e–g) 2010, (h–k) 2014, and (l–o) 2018. The black portion of the maps shows the area below mean LST.

TABLE 6: Temporal variations of NDVI in the area above mean LST (2002–2018).

Year	NDVI (minimum)	NDVI (maximum)	NDVI (mean)	NDVI (standard deviation)
Mean 2002	−0.14	0.21	−0.02	0.03
Mean 2006	−0.09	0.34	0.06	0.05
Mean 2010	−0.18	0.30	0.01	0.04
Mean 2014	−0.03	0.39	0.12	0.05
Mean 2018	−0.08	0.34	0.11	0.04

$$T_a = 17.9769 + 0.91715T_0,$$

$$T_s = \frac{[a(1 - C - D) + (b(1 - C - D) + C + D)T_b - DT_a]}{C},$$

$$C = \varepsilon\tau,$$

$$D = (1 - \tau)[1 + (1 - \varepsilon)\tau],$$

$$\text{(12)}$$

where T_a is mean atmospheric temperature and T_s is land surface temperature; $a = -67.355351$ and $b = 0.458606$.

3.3. NDVI Estimation Using Landsat Sensors.

Many previous research works applied various remote sensing indices to extract various land use classes [8, 18, 23, 24, 33, 34, 49, 56]. Here, only NDVI was applied to correlate with LST. NDVI can be used to estimate other LULC types along with green vegetation [33, 57–60]. Red and NIR bands of Landsat data are used to determine NDVI (Table 2).

4. Results and Discussion

4.1. Spatiotemporal Contrast in the Distribution of LST.

Figure 2 presents the distribution of LST in the premonsoon months from 2002 to 2018 with a four years interval (Table 3). The average of annual mean LST value lies between 31.91°C (2002) and 43.53°C (2018). The north-west and the southeast parts of the study area, which are under open bare land, experience higher LST values. The lower values of LST are observed in central regions of the city because of the presence of park, scattered trees, wetlands, and water bodies (Figure 3).

4.2. Validation of the Result by Using Other Satellite Data.

Any satellite retrieved LST needs a proper validation with an *in situ* measurement or other satellite retrieved LST [2]. Here, MODIS data were used to validate the values of LST. As MODIS and Landsat sensors cannot pass over the same region in a particular date, MOD11A1 data (resolution—1 km) of the following particular dates (Table 4) were used to validate for the resulting LST. These particular dates were free from any cloud coverage or precipitation. TIR bands of MODIS sensor (1 km) and Landsat sensors (120 m, 120 m, and 100 m for Landsat 5, 7, and 8 sensors, respectively). Landsat and MODIS sensors provide a slightly different value of LST due to water vapour content, resampling method, and different passing time of the sensors

[56]. After performing the downscaling process, a significant correlation coefficient was found between the Landsat derived mean LST and corresponding MODIS derived mean downscaled LST (Table 4).

4.3. Variation in NDVI Distribution for Multitemporal Landsat Data.

Red and NIR bands are required to derive the formula of NDVI [60]. Table 5 represents the value of NDVI for the Landsat satellite images during the study period. Figure 4 presents the spatial and temporal status of NDVI for the whole study area, date-wise and year-wise. Southwest and northeast portions of the city reflect higher NDVI values due to high percentage of green vegetation. The average values of maximum NDVI were gradually decreased (0.56 in 2002, 0.52 in 2006, 0.50 in 2010, 0.48 in 2014, and 0.44 in 2018) since the beginning of the study. It means that vegetation was lost at a substantial rate. The spatial distribution of LST and NDVI exhibits an opposite direction (Figure 5).

4.4. Spatiotemporal Distribution of NDVI during the Entire Period.

Figure 6 shows the area above mean LST (pink part) and the area below mean LST (black part) for every single image during the period of study. Figure 7 and Table 6 represent the temporal variation in the NDVI distribution values for the area has more than mean LST during the entire period. The black portion of the maps shows the area below mean LST (Figure 7). Generally, it seems to have an increase in NDVI values with time. But, there is no such particular pattern of increase of NDVI. 2014 and 2018 have greater NDVI values (maximum and mean NDVI) than the earlier years.

Figure 8 and Table 7 represent the temporal variation in the spatial distribution of NDVI values in the area below mean LST. The black portion of the maps shows the area above mean LST (Figure 8). A steady decreasing trend has been observed in the values of mean NDVI. The value of maximum NDVI is much higher in the area below mean LST than in the area above mean LST.

Figure 9 shows the graphical presentation of the spatial and temporal change of mean NDVI for the area having less than mean LST, the area having more than mean LST, and the whole area of the city. The overall trend is increasing in nature. In 2006, the mean NDVI values were more than in 2002. The values were reduced again in 2010. From 2010 to 2014, a high slope was found in mean NDVI values. In 2014 and 2018, the trend line was quite stable. It is clear from Figure 9 that mean NDVI values are higher for Landsat 8
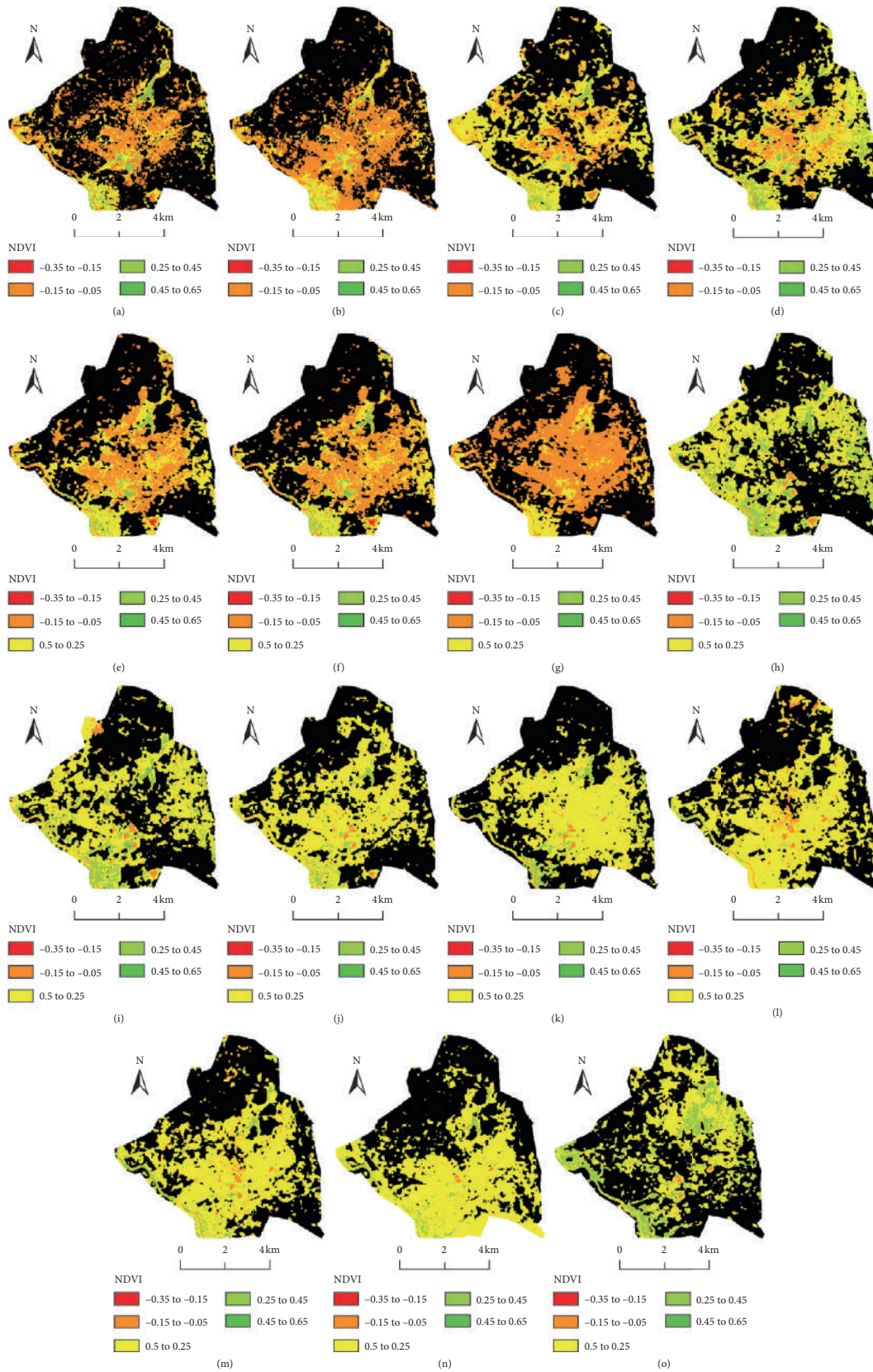
FIGURE 8: NDVI in the area below mean LST: (a-b) 2002, (c-d) 2006, (e–g) 2010, (h–k) 2014, and (l–o) 2018. The black portion of the maps shows the area above mean LST.

TABLE 7: Temporal variations of NDVI in the area below mean LST (2002–2018).

Date of acquisition	NDVI (minimum)	NDVI (maximum)	NDVI (mean)	NDVI (standard deviation)
Mean	−0.23	0.57	0.04	0.10
Mean	−0.19	0.52	0.11	0.09
Mean	−0.21	0.50	0.04	0.08
Mean	−0.11	0.48	0.17	0.07
Mean	−0.12	0.44	0.14	0.06
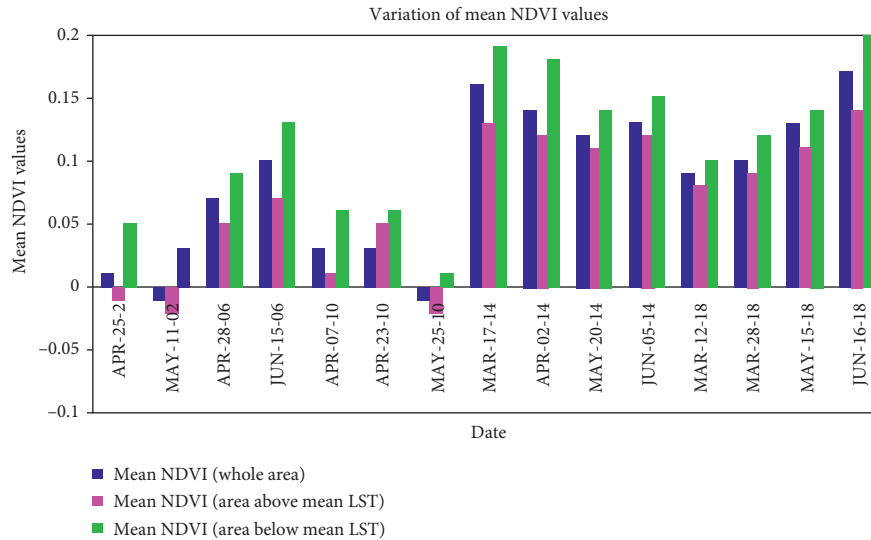
FIGURE 9: Temporal variation of mean NDVI for each satellite image.
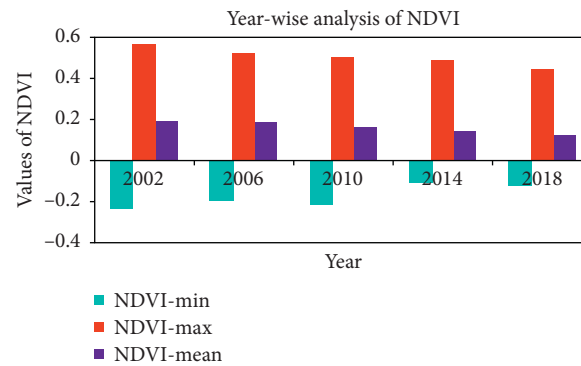
FIGURE 10: Year-wise analysis of NDVI.

data, whereas these values were lower for Landsat 5 or Landsat 7 data. This variation of mean NDVI in different Landsat sensors is mainly due to the configuration of the sensors as the spectral resolution of NIR band of Landsat 8 data (0.851–0.879 μm wavelength) is different from the NIR band of Landsat 5 data (0.760–0.900 μm wavelength) or Landsat 7 data (0.770–0.900 μm wavelength). Further, the year-wise analysis of NDVI has been shown in Figure 10. The diagram shows that the values of maximum NDVI are gradually decreasing with time, whereas the values of minimum NDVI and mean NDVI are increasing. The result is quite significant as it reflects the loss of urban vegetation within the entire time period.

4.5. LST-NDVI Correlation in the Whole City, Above Mean LST Areas, and Below Mean LST Area. LST builds a strong to moderate stable negative correlation with NDVI in the whole Raipur City during the study period. Figure 11 shows a date-wise correlation. The LST-NDVI correlation is moderate to strong negative for the whole area, whereas the correlation does not show any specific pattern for below mean LST zones and above mean LST zones, separately. Figure 12 shows a year-wise correlation. The negativity was almost gradually decreased with time. In the area above mean LST, this correlation is moderately negative and it is stable as these regions mainly cover a high proportion of urban vegetation. In the area below mean LST, LST builds a
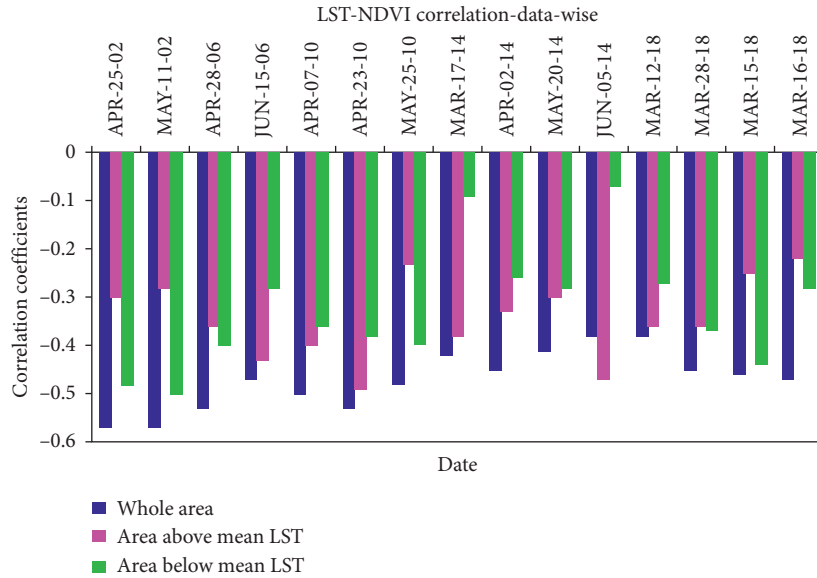
FIGURE 11: Date-wise LST-NDVI correlation analysis.
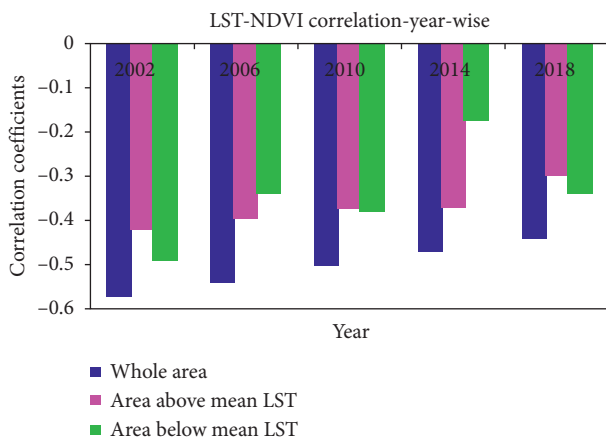
FIGURE 12: Year-wise LST-NDVI correlation analysis.

moderate to weak correlation with NDVI and some fluctuations are present in this relationship due to the different land compositions.

5. Conclusion

The present study monitors the LST-NDVI correlation using different Landsat satellite sensors of the premonsoon season for a specific time interval. Mean LST was a significant measurement for the study as it performs in the area above mean LST as well as in the area below mean LST along with the whole Raipur City. From 2002 to 2018 premonsoon months, the LST was increased by 11.62°C. The LST-NDVI correlation was negative for the study area throughout the period. For Landsat 8 data, mean NDVI values are higher than the other Landsat sensors and thus, the mean NDVI values become higher in recent times. The area below mean LST has a weaker correlation than the area above mean LST. The strength of the correlation was reduced gradually with

time. Future urban and environmental planning in the premonsoon season can be implemented using the spatio-temporal variation of LST-NDVI relationship.

Data Availability

The data used to support the findings of this study are included within the article.

Conflicts of Interest

The authors declare that they have no conflicts of interest.

References

[1] H. Govil, S. Guha, P. Diwan, N. Gill, and A. Dey, "Evaluation of ASTER TIR data-based lithological indices in parts of Madhya Pradesh and Chhattisgarh State, India," in *Data Management, Analytics and Innovation*, N. Sharma, A. Chakrabarti, and V. Balas, Eds., vol. 1042, Springer, Advances in Intelligent Systems and Computing, pp. 161–169, Springer, 2020a.

[2] S. Guha and H. Govil, "An assessment on the relationship between land surface temperature and normalized difference vegetation index," *Environment, Development and Sustainability*, 2020.

[3] X. Hao, W. Li, and H. Deng, "The oasis effect and summer temperature rise in arid regions-case study in Tarim Basin," *Scientific Reports*, vol. 6, no. 1, p. 35418, 2016.

[4] C. J. Tomlinson, L. Chapman, J. E. Thornes, and C. Baker, "Remote sensing land surface temperature for meteorology and climatology: a review," *Meteorological Applications*, vol. 18, no. 3, pp. 296–306, 2011.

[5] G. L. Hou, H. Y. Zhang, Y. Q. Wang, Z. H. Qiao, and Z. X. Zhang, "Retrieval and spatial distribution of land surface temperature in the middle part of Jilin province based on MODIS data," *Scientia Geographica Sinica*, vol. 30, pp. 421–427, 2010.

[6] W. Li, Q. Cao, K. Lang, and J. Wu, "Linking potential heat source and sink to urban heat island: heterogeneous effects of

landscape pattern on land surface temperature," *Science of The Total Environment*, vol. 586, pp. 457–465, 2017.

[7] X. L. Yuan, W. Wang, J. Cui, F. Meng, A. Kurban, and P. De Maeyer, "Vegetation changes and land surface feedbacks drive shifts in local temperatures over Central Asia," *Scientific Reports*, vol. 7, no. 1, p. 3287, 2017.

[8] S. Guha, H. Govil, A. Dey, and N. Gill, "Analytical study of land surface temperature with NDVI and NDBI using Landsat 8 OLI and TIRS data in Florence and Naples city, Italy," *European Journal of Remote Sensing*, vol. 51, no. 1, pp. 667–678, 2018.

[9] A. S. Hope and T. P. McDowell, "The relationship between surface temperature and a spectral vegetation index of a tallgrass prairie: effects of burning and other landscape controls," *International Journal of Remote Sensing*, vol. 13, no. 15, pp. 2849–2863, 1992.

[10] Y. Julien, J. A. Sobrino, and W. Verhoef, "Changes in land surface temperatures and NDVI values over Europe between 1982 and 1999," *Remote Sensing of Environment*, vol. 103, no. 1, pp. 43–55, 2006.

[11] R. C. G. Smith and B. J. Choudhury, "On the correlation of indices of vegetation and surface temperature over South-Eastern Australia," *International Journal of Remote Sensing*, vol. 11, no. 11, pp. 2113–2120, 1990.

[12] Y. Ghobadi, B. Pradhan, H. Z. M. Shafri, and K. Kabiri, "Assessment of spatial relationship between land surface temperature and land use/cover retrieval from multi-temporal remote sensing data in South Karkheh Sub-basin, Iran," *Arabian Journal of Geosciences*, vol. 8, no. 1, pp. 525–537, 2014.

[13] C. Qu, J. H. Ma, Y. Q. Xia, and T. Fei, "Spatial distribution of land surface temperature retrieved from MODIS data in Shiyang River Basin," *Arid Land Geography*, vol. 37, pp. 125–133, 2014.

[14] Y. Zhou, T. M. Shi, Y. M. Hu, and M. Liu, "Relationships between land surface temperature and normalized difference vegetation index based on urban land use type," *Chinese Journal of Ecology*, vol. 30, pp. 1504–1512, 2011.

[15] Z. N. Li, D. Sibo, T. Bohui et al., "Review of methods for land surface temperature derived from thermal infrared remotely sensed data," *Journal of Remote Sensing*, vol. 20, pp. 899–920, 2016.

[16] D. Stroppiana, M. Antoninetti, and P. A. Brivio, "Seasonality of MODIS LST over Southern Italy and correlation with land cover, topography and solar radiation," *European Journal of Remote Sensing*, vol. 47, no. 1, pp. 133–152, 2014.

[17] L. J. Wen, P. Wenfu, Y. Huarong, W. Huaiying, D. Lijun, and S. Xue, "An analysis of land surface temperature (LST) and its influencing factors in summer in Western Sichuan Plateau: a case study of Xichang City," *Remote Sensing for Land and Resources*, vol. 29, no. 2, pp. 207–214, 2017.

[18] S. Bonafoni, "Spectral index utility for summer urban heating analysis," *Journal of Applied Remote Sensing*, vol. 9, no. 1, Article ID 096030, 2015.

[19] R. C. Estoque, Y. Murayama, and S. W. Myint, "Effects of landscape composition and pattern on land surface temperature: an urban heat island study in the megacities of Southeast Asia," *Science of The Total Environment*, vol. 577, pp. 349–359, 2017.

[20] M. Fatemi and M. Narangifard, "Monitoring LULC changes and its impact on the LST and NDVI in district 1 of Shiraz city," *Arabian Journal of Geosciences*, vol. 12, no. 4, p. 127, 2019.

[21] F. Ferrelli, M. A. Huamantinco Cisneros, A. L. Delgado, and M. C. Piccolo, "Spatial and temporal analysis of the LST-NDVI relationship for the study of land cover changes and their contribution to urban planning in Monte Hermoso, Argentina," *Documents d'Anàlisi Geogràfica*, vol. 64, no. 1, pp. 25–47, 2018.

[22] Y. Jamei, P. Rajagopalan, and Q. C. Sun, "Time-series dataset on land surface temperature, vegetation, built up areas and other climatic factors in top 20 global cities (2000–2018)," *Data in Brief*, vol. 23, p. 103803, 2015.

[23] K. Liu, X. Zhang, X. Li, and H. Jiang, "Multiscale analysis of urban thermal characteristics: case study of Shijiazhuang, China," *Journal of Applied Remote Sensing*, vol. 8, no. 1, Article ID 083649, 2014.

[24] X. Luo and W. Li, "Scale effect analysis of the relationships between urban heat island and impact factors: case study in Chongqing," *Journal of Applied Remote Sensing*, vol. 8, no. 1, Article ID 084995, 2014.

[25] S. Naeem, C. Cao, M. M. Waqar, C. Wei, and B. K. Acharya, "Vegetation role in controlling the ecoenvironmental conditions for sustainable urban environments: a comparison of Beijing and Islamabad," *Journal of Applied Remote Sensing*, vol. 12, no. 1, Article ID 016013, 2018.

[26] K. Shigeto, "Relation between vegetation, surface temperature, and surface composition in the Tokyo region during winter," *Remote Sensing of Environment*, vol. 50, no. 1, pp. 52–60, 1994.

[27] W. Z. Yue, X. J. Hua, and X. L. Hua, "An analysis on eco-environmental effect of urban land use based on remote sensing images: a case study of urban thermal environment and NDVI," *Acta Ecologica Sinica*, vol. 26, pp. 1450–1460, 2006.

[28] H. K. Zhang, B. Huang, M. Zhang, K. Cao, and L. Yu, "A generalization of spatial and temporal fusion methods for remotely sensed surface parameters," *International Journal of Remote Sensing*, vol. 36, no. 17, pp. 4411–4445, 2015.

[29] J. A. Voogt and T. R. Oke, "Thermal remote sensing of urban climates," *Remote Sensing of Environment*, vol. 86, no. 3, pp. 370–384, 2003.

[30] S. N. Goward, Y. Xue, and K. P. Czajkowski, "Evaluating land surface moisture conditions from the remotely sensed temperature/vegetation index measurements: an exploration with the simplified simple biosphere model," *Remote Sensing of Environment*, vol. 79, no. 2–3, pp. 225–242, 2002.

[31] H. Govil, S. Guha, A. Dey, and N. Gill, "Seasonal evaluation of downscaled land surface temperature: a case study in a humid tropical city," *Heliyon*, vol. 5, no. 6, Article ID e01923, 2019.

[32] H. Govil, S. Guha, P. Diwan, N. Gill, and A. Dey, "Analyzing linear relationships of LST with NDVI and MNDISI using various resolution levels of Landsat 8 OLI and TIRS data," in *Data Management, Analytics and Innovation*, N. Sharma, A. Chakrabarti, and V. Balas, Eds., vol. 1042, Springer, Advances in Intelligent Systems and Computing, pp. 171–184, Springer, 2020b.

[33] S. Guha, H. Govil, A. Dey, and N. Gill, "A case study on the relationship between land surface temperature and land surface indices in Raipur City, India," *Geografisk Tidsskrift-Danish Journal of Geography*, pp. 1–16, 2020a.

[34] S. Guha, H. Govil, N. Gill, and A. Dey, "Analytical study on the relationship between land surface temperature and land use/land cover indices," *Annals of GIS*, 2020b.

[35] G. Gutman and A. Ignatov, "The derivation of the green vegetation fraction from NOAA/AVHRR data for use in numerical weather prediction models," *International Journal of Remote Sensing*, vol. 19, no. 8, pp. 1533–1543, 1998.

[36] Q. Weng, D. Lu, and J. Schubring, "Estimation of land surface temperature-vegetation abundance relationship for urban

heat island studies," *Remote Sensing of Environment*, vol. 89, no. 4, pp. 467–483, 2004.

[37] B. Hao, M. Ma, S. Li et al., "Land use change and climate variation in the three gorges reservoir catchment from 2000 to 2015 based on the google earth engine," *Sensors*, vol. 19, no. 9, p. 2118, 2019.

[38] Q. Hassan, C. Bourque, F.-R. Meng, and R. Cox, "A wetness index using terrain-corrected surface temperature and normalized difference vegetation index derived from standard MODIS products: an evaluation of its use in a humid forest-dominated region of eastern Canada," *Sensors*, vol. 7, no. 10, pp. 2028–2048, 2007.

[39] K. Li and Z. Yu, "Comparative and combinative study of urban heat island in Wuhan city with remote sensing and CFD simulation," *Sensors*, vol. 8, no. 10, pp. 6692–6703, 2008.

[40] H. Liu and Q. Weng, "Scaling effect of fused ASTER-MODIS land surface temperature in an urban environment," *Sensors*, vol. 18, no. 11, p. 4058, 2018.

[41] P. Mohammad, A. Goswami, and S. Bonafoni, "The impact of the land cover dynamics on surface urban heat island variations in semi-arid cities: a case study in Ahmedabad city, India, using multi-sensor/source data," *Sensors*, vol. 19, no. 17, p. 3701, 2019.

[42] S. A. Nowicki, R. D. Inman, T. C. Esque, K. E. Nussear, and C. S. Edwards, "Spatially consistent high-resolution land surface temperature mosaics for thermophysical mapping of the mojave desert," *Sensors*, vol. 19, no. 12, p. 2669, 2019.

[43] H. Qi, F. Huang, and H. Zhai, "Monitoring spatio-temporal changes of terrestrial ecosystem soil water use efficiency in Northeast China using time series remote sensing data," *Sensors*, vol. 19, no. 6, p. 1481, 2019.

[44] O. Rozenstein, Z. Qin, Y. Derimian, and A. Karnieli, "Derivation of land surface temperature for landsat-8 TIRS using a split window algorithm," *Sensors*, vol. 14, no. 4, pp. 5768–5780, 2014.

[45] Y. Shi, Y. Xiang, and Y. Zhang, "Urban design factors influencing surface urban heat island in the high-density city of Guangzhou based on the local climate zone," *Sensors*, vol. 19, no. 16, p. 3459, 2019.

[46] L. Slawsky, L. Zhou, S. Roy, G. Xia, M. Vuille, and R. Harris, "Observed thermal impacts of wind farms over northern Illinois," *Sensors*, vol. 15, no. 7, pp. 14981–15005, 2015.

[47] H. Sun, B. Zhou, and H. Liu, "Spatial evaluation of soil moisture (SM), land surface temperature (LST), and LST-derived SM indexes dynamics during SMAPVEX12," *Sensors*, vol. 19, no. 5, p. 1247, 2019.

[48] J. Zhang and Y. Wang, "Study of the relationships between the spatial extent of surface urban heat islands and urban characteristic factors based on landsat ETM+ data," *Sensors*, vol. 8, no. 11, pp. 7453–7468, 2008.

[49] S. Guha, H. Govil, and S. Mukherjee, "Dynamic analysis and ecological evaluation of urban heat islands in Raipur city, India," *Journal of Applied Remote Sensing*, vol. 11, no. 3, Article ID 036020, 2017.

[50] N. Kikon, P. Singh, S. K. Singh, and A. Vyas, "Assessment of urban heat islands (UHI) of Noida City, India using multi-temporal satellite data," *Sustainable Cities and Society*, vol. 22, pp. 19–28, 2016.

[51] D. Kumar and S. Shekhar, "Statistical analysis of land surface temperature-vegetation indexes relationship through thermal remote sensing," *Ecotoxicology and Environmental Safety*, vol. 121, pp. 39–44, 2015.

[52] A. Mathew, S. Khandelwal, and N. Kaul, "Investigating spatial and seasonal variations of urban heat island effect over Jaipur city and its relationship with vegetation, urbanization and elevation parameters," *Sustainable Cities and Society*, vol. 35, pp. 157–177, 2017.

[53] A. Mathew, S. Khandelwal, and N. Kaul, "Spatio-temporal variations of surface temperatures of Ahmedabad city and its relationship with vegetation and urbanization parameters as indicators of surface temperatures," *Remote Sensing Applications: Society and Environment*, vol. 11, pp. 119–139, 2018.

[54] P. Singh, N. Kikon, and P. Verma, "Impact of land use change and urbanization on urban heat island in Lucknow city, Central India. A remote sensing based estimate," *Sustainable Cities and Society*, vol. 32, pp. 100–114, 2017.

[55] Z. Qin, A. Karnieli, and P. Berliner, "A mono-window algorithm for retrieving land surface temperature from Landsat™ data and its application to the Israel-Egypt border region," *International Journal of Remote Sensing*, vol. 22, no. 18, pp. 3719–3746, 2001.

[56] S. Guha, H. Govil, and P. Diwan, "Analytical study of seasonal variability in land surface temperature with normalized difference vegetation index, normalized difference water index, normalized difference built-up index, and normalized multiband drought index," *Journal of Applied Remote Sensing*, vol. 13, no. 2, Article ID 024518, 2019.

[57] S. Guha and H. Govil, "Evaluation of ASTER TIR data-based lithological indices in Malanjkhand copper mines of Madhya Pradesh, India," *Applied Earth Science*, vol. 129, no. 1, pp. 3–8, 2019.

[58] Y. Ke, J. Im, J. Lee, H. Gong, and Y. Ryu, "Characteristics of Landsat 8 oli-derived NDVI by comparison with multiple satellite sensors and in-situ observations," *Remote Sensing of Environment*, vol. 164, pp. 298–313, 2015.

[59] T. Purevdorj, R. Tateishi, T. Ishiyama, and Y. Honda, "Relationships between percent vegetation cover and vegetation indices," *International Journal of Remote Sensing*, vol. 19, no. 18, pp. 3519–3535, 1998.

[60] C. J. Tucker, "Red and photographic infrared linear combinations for monitoring vegetation," *Remote Sensing of Environment*, vol. 8, no. 2, pp. 127–150, 1979.

Source details

Feedback ⟩   Compare sources ⟩

Advances in Meteorology

Open Access ⓘ

Scopus coverage years: from 2012 to Present

Publisher: Hindawi

ISSN: 1687-9309   E-ISSN: 1687-9317

Subject area: (Earth and Planetary Sciences: Geophysics)   (Environmental Science: Pollution)   (Earth and Planetary Sciences: Atmospheric Science)

Source type: Journal

View all documents ⟩   Set document alert   💾 Save to source list

CiteScore 2022
4.6   ⓘ

SJR 2022
0.598   ⓘ

SNIP 2022
1.042   ⓘ

CiteScore   CiteScore rank & trend   Scopus content coverage

Land surface temperature and normalized difference vegetation index relationship: a seasonal study on a tropical city

Subhanil Guha[1] · Himanshu Govil[1]

Abstract

Land surface temperature (LST) and its relationship with normalized difference vegetation index (NDVI) are significantly considered in environmental study. The aim of this study was to retrieve the LST of Raipur City of tropical India and to explore its seasonal relationships with NDVI. Landsat images of four specific seasons for three particular years with fourteen years time interval were analyzed. The result showed a gradual rising (3.63 °C during 1991–2004 and 1.54 °C during 2004–2018) of LST during the whole period of study. The mean LST value of three particular years was the lowest (27.21 °C) on green vegetation and the highest (29.81 °C) on bare land and built-up areas. The spatial distribution of NDVI and LST reflects an inverse relationship. The best (− 0.63) and the least (− 0.17) correlation were noticed in the post-monsoon and winter seasons, respectively, whereas a moderate (− 0.45) correlation were found both in the monsoon and pre-monsoon seasons. This LST-NDVI correlation was strong negative (− 0.51) on vegetation surface, moderate positive on water bodies (0.45), and weak positive on the built-up area and bare land (0.14). In summary, the LST is greatly controlled by surface characteristics. This study can be used as a reference for land use and environmental planning in a tropical city.

Keywords Landsat · LST · NDVI · Tropical city

1 Introduction

Urbanization accelerates the ecological stress by warming the local or global cities for a large extent [1–6]. Presently, many urban areas are suffering with a huge land conversion and resultant new heat zones [7–9]. Remote sensing techniques are significantly effective in detecting the land use/land cover (LULC) change and its consequences [10]. Several satellite sensors are capable to identify these change zones by using their visible and near-infrared (VNIR) and shortwave infrared (SWIR) bands [11]. Apart from the conventional LULC classification algorithms, some spectral indices are used in detecting specific land features. Normalized difference vegetation index (NDVI) can be considered as the most applied spectral index in this scenario [12]. Recently, thermal infrared (TIR) bands are also used by generating some indices for different types of LULC extraction [13–15]. These remote sensing indices are used significantly in several application fields like rocks and mineral mapping, forest mapping, agricultural monitoring, LULC mapping, hazard mapping, urban heat island mapping and monitoring, among others [14, 16–19].

Land surface temperature (LST) retrieved from several remotely sensed data is widely used in the detection of urban heat island and ecological comfort zone [20–23]. LST can change significantly in a vast homogeneous land surface or even inside a relatively small heterogeneous urban area [14, 24, 25]. Different types of LULC response differently in TIR band and consequently LST largely varies in an urban environment [26–44]. The LULC types are mainly changed by land conversion process [10]. Thus, time is an important factor in LST monitoring. These spatial and temporal data of LST is also varied with the

---

seasonal changes as sun elevation and sun azimuth are changed with seasons. Hence, the seasonal variation of LST is quite important in any LULC related study.

NDVI is a dominant factor in LST derivation processes and is used invariably in any LST related study [45–49]. NDVI is directly used in the determination of land surface emissivity and thus is a significant factor for LST estimation [50, 51]. It also determines the LULC categories by its optimum threshold limits in different physical environment [14]. Being a vegetation index, NDVI depends largely on seasonal variation [12]. Hence, LST is also regulated by the change of seasons. Thus, seasonal evaluation of LST and NDVI is an important task in LST mapping and monitoring, especially in an urban landscape.

The relationship of LST with NDVI is quite interesting and it attracts the remote sensing scientists from several directions [52–55]. The nature and strength of this relationship heavily depend on space and time. Generally, in the tropical environment the LST-NDVI relationship is negative [56–58]. The negativity of the relationship is determined by the changing type of LULC over time. Thus, spatial and temporal changes in this relationship are observed on different types of LULC. Apart from the spatial and temporal changes, seasonal variation of LST-NDVI relationship is a very important study in any mixed urban land surface.

Several studies are available on the seasonal analysis of LST-NDVI relationship. Many tropical cities are a part of these studies. Many valuable research articles found on LST-NDVI relationships in the Chinese landscape [59–67]. Some studies were also performed in Indian urban landscape [35, 36, 68–71].These studies found that LST builds a negative relationship with NDVI and this negativity can change with season. Wet season reflects a stronger negative correlation than dry season as the moisture content is more in the wet season [72]. This relationship can also change with the change of land surface types. Vegetation surface builds a strong correlation and the strength is reduced on bare land surface, built-up surface, and water surface.

The present study calculates the LST and NDVI from Landsat datasets of four different seasons (winter, pre-monsoon, monsoon, and post-monsoon) in Raipur City of India using a total of 12 Landsat satellite images for 1991, 2004, and 2018. Meanwhile, the LULC map has been obtained by suitable threshold values of NDVI. The main aims of the study were (1) to analyze the seasonal variation of spatial distribution pattern of the LST in the study area, (2) to determine the seasonal variation of LST-NDVI relationship for whole of the city, and (3) to explore the seasonal variation of LST-NDVI relationship on different LULC types.

2 Study area and data

Figure 1 shows the study area (Raipur City of India) of the present research work including the false colour composite (FCC) image of and digital elevation model (DEM) image. Raipur is one of the fastest-growing smart cities in India. The latitudinal and longitudinal extent of the city is from 21°11′22″ N to 21°20′02″ N and from 81°32′20″ E to 81°41′50″ E. The total area of the city is approximately 164.23 km². The only big river is Mahanadi which flows along the eastern boundary of Raipur. The southern part of the city is covered by dense forests. Geologically the city is very stable. According to India Meteorological Department (IMD) (https://mausam.imd.gov.in) [75], the study area is under a tropical wet and dry climate with four typical seasons (pre-monsoon, monsoon, post-monsoon, and winter). May is the hottest month followed by April, June, and March. July is the rainiest month followed by August, June, and September. October and November are the post-monsoon months experience a pleasant weather condition. December (the coldest month), January, and February are the winter months. The pre-monsoon and winter months (including November) remain dry compared to the monsoon and post-monsoon months.

Four Landsat 8 Operational Land Imager (OLI) and Thermal Infrared Sensors (TIRS) data of 2018; four Landsat 5 Thematic Mapper (TM) data of 2004; and four Landsat 5 TM data of 1991 have been freely downloaded from the United States Geological Survey (USGS) (https://earthexplorer.usgs.gov) Data Centre (Table 1). Landsat 8 TIRS dataset has two TIR bands (bands 10 and 11) in which band 11 has uncertainty in calibration. Thus, only TIR band 10 (100 m resolution) has been recommended for the present study. The TIR band 10 has been resampled to 30 m × 30 m pixel size with cubic convolution method by the USGS. Landsat 5 TM data has only one TIR band (band 6) of 120 m resolution which has also been resampled to 30 m × 30 m pixel size with cubic convolution method by the USGS. The spatial resolution of visible to near infrared (VNIR) bands of the two types of Landsat datasets is 30 m.

3 Methodology

3.1 Retrieving LST from Landsat data

In this study, the mono-window algorithm was applied to retrieve LST from multi-temporal Landsat satellite sensors [1, 76–79] where three necessary parameters are ground emissivity, atmospheric transmittance, and effective mean atmospheric temperature. At first, the original TIR bands (100 m resolution for Landsat 8 OLI/TIRS data,
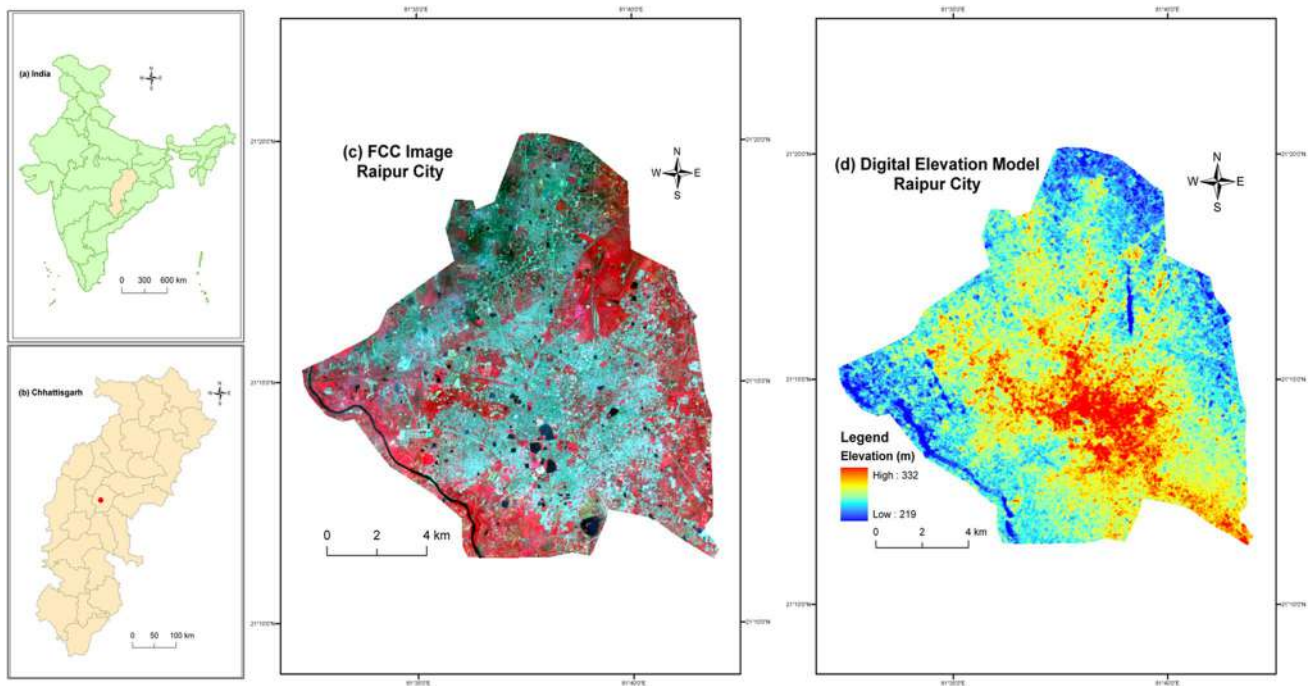
Fig. 1 Location of the study area: **a** India **b** Chhattisgarh **c** FCC image of Raipur City **d** DEM image of Raipur City (*Source*: https://earthexplorer.usgs.gov [73] and http://www.surveyofindia.gov.in [74])

Table 1 Specification of Landsat data sets (*Source*: USGS)	Season	Date of acquisition	Path-row	Resolution of VNIR bands (m)	Resolution of TIR bands (m)
	Pre-monsoon	18-Mar-1991	142–045	30	120
		22-Apr-2004	142–045	30	120
		28-Mar-2018	142–045	30	100
	Monsoon	26-Sep-1991	142–045	30	120
		09-Jun-2004	142–045	30	120
		16-Jun-2018	142–045	30	100
	Post-monsoon	12-Oct-1991	142–045	30	120
		15-Oct-2004	142–045	30	120
		22-Oct-2018	142–045	30	100
	Winter	14-Feb-1991	142–045	30	120
		02-Dec-2004	142–045	30	120
		08-Feb-2018	142–045	30	100

120 m resolution for Landsat 5 TM data) were resampled into 30 m by USGS data centre for further application.

The TIR pixel values are firstly converted into radiance from digital number (DN) values. Radiance for TIR band of Landsat 5 TM data is obtained using Eq. (1) (USGS):

$$L_{\lambda} = \left[\frac{L_{MAX\lambda} - L_{MIN\lambda}}{QCAL_{MAX} - QCAL_{MIN}} \right] * \left[Q_{CAL} - QCAL_{MIN} \right] + L_{MIN\lambda}$$

(1)

where L_{λ} is Top of Atmosphere (TOA) spectral radiance (Wm^{-2} sr^{-1} mm^{-1}), Q_{CAL} is the quantized calibrated pixel value in DN, $L_{MIN\lambda}$ (Wm^{-2} sr^{-1} mm^{-1}) is the spectral radiance scaled to $QCAL_{MIN}$, $L_{MAX\lambda}$ (Wm^{-2} sr^{-1} mm^{-1}) is the

spectral radiance scaled to $QCAL_{MAX}$, $QCAL_{MIN}$ is the minimum quantized calibrated pixel value in DN and $QCAL_{MAX}$ is the maximum quantized calibrated pixel value in DN. $L_{MIN\lambda}$, $L_{MAX\lambda}$, $QCAL_{MIN}$, and $QCAL_{MAX}$ values are obtained from the metadata file of Landsat TM data. Radiance for Landsat 8 TIR band is obtained from Eq. (2) [80]:

$$L_\lambda = M_L \cdot Q_{CAL} + A_L \tag{2}$$

where L_λ is the TOA spectral radiance (Wm^{-2} sr^{-1} mm^{-1}), M_L is the band-specific multiplicative rescaling factor from the metadata, A_L is the band-specific additive rescaling factor from the metadata, Q_{CAL} is the quantized and calibrated standard product pixel values (DN). All of these variables can be retrieved from the metadata file of Landsat 8 data.

For Landsat 5 data, the reflectance value is obtained from radiances using Eq. (3) (USGS):

$$\rho_\lambda = \frac{\pi \cdot L_\lambda \cdot d^2}{ESUN_\lambda \cdot \cos\theta_s} \tag{3}$$

where ρ_λ is unitless planetary reflectance, L_λ is the TOA spectral radiance (Wm^{-2} sr^{-1} μm^{-1}), d is Earth-Sun distance in astronomical units, $ESUN_\lambda$ is the mean solar exoatmospheric spectral irradiances (Wm^{-2} μm^{-1}) and θ_s is the solar zenith angle in degrees. $ESUN_\lambda$ values for each band of Landsat 5 can be obtained from the handbooks of the related mission. θ_s and d values can be attained from the metadata file.

For Landsat 8 data, reflectance conversion can be applied to DN values directly as in Eq. (4) [80]:

$$\rho_\lambda = \frac{M_\rho \cdot Q_{CAL} + A_\rho}{\sin\theta_{SE}} \tag{4}$$

where M_ρ is the band-specific multiplicative rescaling factor from the metadata, A_ρ is the band-specific additive rescaling factor from the metadata, Q_{CAL} is the quantized and calibrated standard product pixel values (DN) and θ_{SE} is the local sun elevation angle from metadata file.

Equation (5) is used to convert the spectral radiance to at-sensor brightness temperature [81, 14]:

$$T_b = \frac{K_2}{\ln\left(\frac{K_1}{L_\lambda} + 1\right)} \tag{5}$$

where T_b is the brightness temperature in Kelvin (K), L_λ is the spectral radiance in Wm^{-2} sr^{-1} mm^{-1}; K_2 and K_1 are calibration constants. For Landsat 8 data, K_1 is 774.89, K_2 is 1321.08 (Wm^{-2} sr^{-1} mm^{-1}). For Landsat 5 data, K_1 is 607.76, K_2 is 1260.56 (Wm^{-2} sr^{-1} mm^{-1}).

The land surface emissivity ε, is estimated using the NDVI Thresholds Method [51, 82].

In NDVI Threshold Method, there are three following equations:

a. $NDVI < 0.2$ for bare soil;
b. $NDVI > 0.5$ for vegetation;
c. $0.2 <= NDVI <= 0.5$ for mixed land with bare soil and vegetation.

In the last case, ε is estimated from Eq. (6):

$$\varepsilon = \varepsilon_v F_v + \varepsilon_s(1 - F_v) + d\varepsilon \tag{6}$$

where ε is land surface emissivity, ε_v is vegetation emissivity, ε_s is soil emissivity, Fv is fractional vegetation, $d\varepsilon$ is the effect of the geometrical distribution of the natural surfaces and internal reflections that can be expressed by Eq. (7):

$$d\varepsilon = (1 - \varepsilon_s)(1 - F_v)F\varepsilon_v \tag{7}$$

where ε_v is vegetation emissivity, ε_s is soil emissivity, Fv is fractional vegetation, F is a shape factor whose mean is 0.55, the value of $d\varepsilon$ may be 2% for mixed land surfaces [51].

The fractional vegetation F_v, of each pixel, is determined from the NDVI using Eq. (8) [50]:

$$F_v = \left(\frac{NDVI - NDVI_{min}}{NDVI_{max} - NDVI_{min}}\right)^2 \tag{8}$$

where $NDVI_{min} = 0.2$ and $NDVI_{max} = 0.5$.

Finally, the land surface emissivity ε can be expressed by Eq. (9):

$$\varepsilon = 0.004 * F_v + 0.986 \tag{9}$$

where ε is land surface emissivity, Fv is fractional vegetation.

Water vapour content is estimated by Eq. (10) [29, 83]:

$$w = 0.0981 * \left[10 * 0.6108 * \exp\left(\frac{17.27 * (T_0 - 273.15)}{237.3 + (T_0 - 273.15)}\right) * RH\right] + 0.1697 \tag{10}$$

where w is the water vapour content (g/cm^2), T_0 is the near-surface air temperature in Kelvin (K), RH is the relative humidity (%). These parameters of atmospheric profile are the average values of 14 stations around Raipur which are obtained from the Meteorological Centre, Raipur (http://www.imdraipur.gov.in) [84] and the Regional Meteorological Centre, Nagpur (http://www.imdnagpur.gov.in [85]). Atmospheric transmittance is determined for Raipur City using Eq. (11) [76, 86]:

$$\tau = 1.031412 - 0.11536w \tag{11}$$

where τ is the total atmospheric transmittance, ε is the land surface emissivity.

Raipur City is located in the tropical region. Thus, Eq. (12) is applied to compute the effective mean atmospheric transmittance of Raipur [76, 86]:

$$T_a = 17.9769 + 0.91715T_0 \qquad (12)$$

LST is retrieved from Landsat 5 TM and Landsat 8 OLI/TIRS satellite data by using Eqs. (13–15) [76]:

$$T_s = \frac{[a(1 - C - D) + (b(1 - C - D) + C + D)T_b - DT_a]}{C} \qquad (13)$$

$$C = \varepsilon\tau \qquad (14)$$

$$D = (1 - \tau)[1 + (1 - \varepsilon)\tau] \qquad (15)$$

where ε is the land surface emissivity, τ is the total atmospheric transmittance, C and D are internal parameters based on atmospheric transmittance and land surface emissivity, T_b is the at-sensor brightness temperature, T_a is the mean atmospheric temperature, T_0 is the near-surface air temperature, T_s is the land surface temperature, $a = -67.355351, b = 0.458606$.

3.2 Extraction of different types of LULC by using the threshold limits of NDVI

NDVI can extract different types of LULC by using the optimum threshold values [14, 87–89]. This threshold values can differ with respect to the differences in physical environment. The NDVI threshold limits were applied on the post-monsoon images to extract the different LULC types accurately. Table 2 presents the suitable threshold limits of NDVI used for extracting the vegetation (> 0.2), water bodies (< 0), built-up area/bare land (0–0.2) in the study area.

4 Results and discussion

4.1 Accuracy assessment for LULC classification

The maximum likelihood classification method was applied to validate NDVI threshold based LULC classification. The overall accuracy values of the LULC classification were 95.00%, 85.00%, and 87.50% in 1991, 2004, and 2018, respectively. The kappa coefficients for the LULC

classification were 0.91, 0.76, and 0.78 in 1991, 2004, and 2018, respectively. The kappa coefficient value of > 0.75 reflects the compatibility of the classification method [90]. In the present study, the average overall accuracy and average kappa coefficient were 89.17% and 0.82, respectively. Thus, the NDVI threshold method based LULC classification was significantly validated.

4.2 Extraction of LULC types using NDVI

Figure 2 shows the FCC images and LULC maps of the post-monsoon Landsat images of 1991, 2004, and 2018. Generally, the post-monsoon images reduce the level of air pollution due to the presence of high moisture content in the air and these images also enhance the greenness of an area. Thus, the post-monsoon images are generally considered for the generation of LULC maps. LULC maps were generated using the threshold limits of NDVI for different types of LULC by using ArcGIS software (https://www.esri.com/) [91]. In 1991, built-up area and bare land are mainly found in the northwest and middle portions of the city. Land conversion accelerates the decrease of vegetal covered area especially during 2004-2018. The major segment of vegetation is mainly found in the east and southwest parts of the city.

4.3 Characteristics of the spatial distribution of LST and NDVI

Table 3 shows the LST and NDVI values for different multi-date satellite data. The pre-monsoon image (Fig. 3) has the maximum values of mean LST (29.50 °C in 1991, 36.80 °C in 2004, and 37.90 °C in 2018) followed by monsoon (Fig. 4) image (25.74 °C in 1991, 29.23 °C in 2004, and 31.08 °C in 2018), post-monsoon (Fig. 5) image (24.99 °C in 1991, 27.56 °C in 2004, and 29.01 °C in 2018), and winter (Fig. 6) image (23.99 °C in 1991, 25.17 °C in 2004, and 26.91 °C in 2018). The mean LST of the city is increased by 8.40 °C in the pre-monsoon season, 5.34 °C in the monsoon season, 4.02 °C in the post-monsoon season, and 2.92 °C in the winter season during the whole time span (1991–2018). In the case of NDVI, the maximum value is decreased gradually with time (Figs. 3, 4, 5 and 6). Seasonally, the highest values of NDVI are observed in the post-monsoon images followed by the

Table 2 NDVI used for extracting different types of LULC [14]

Acronym	Description	Formulation	References	Threshold limits of NDVI for extracting different LULC types		
				Vegetation	Water bodies	Built-up area and bare land
NDVI	Normalized difference vegetation index	$\frac{NIR-Red}{NIR+Red}$	[87]	> 0.2	< 0	[0–0.2]
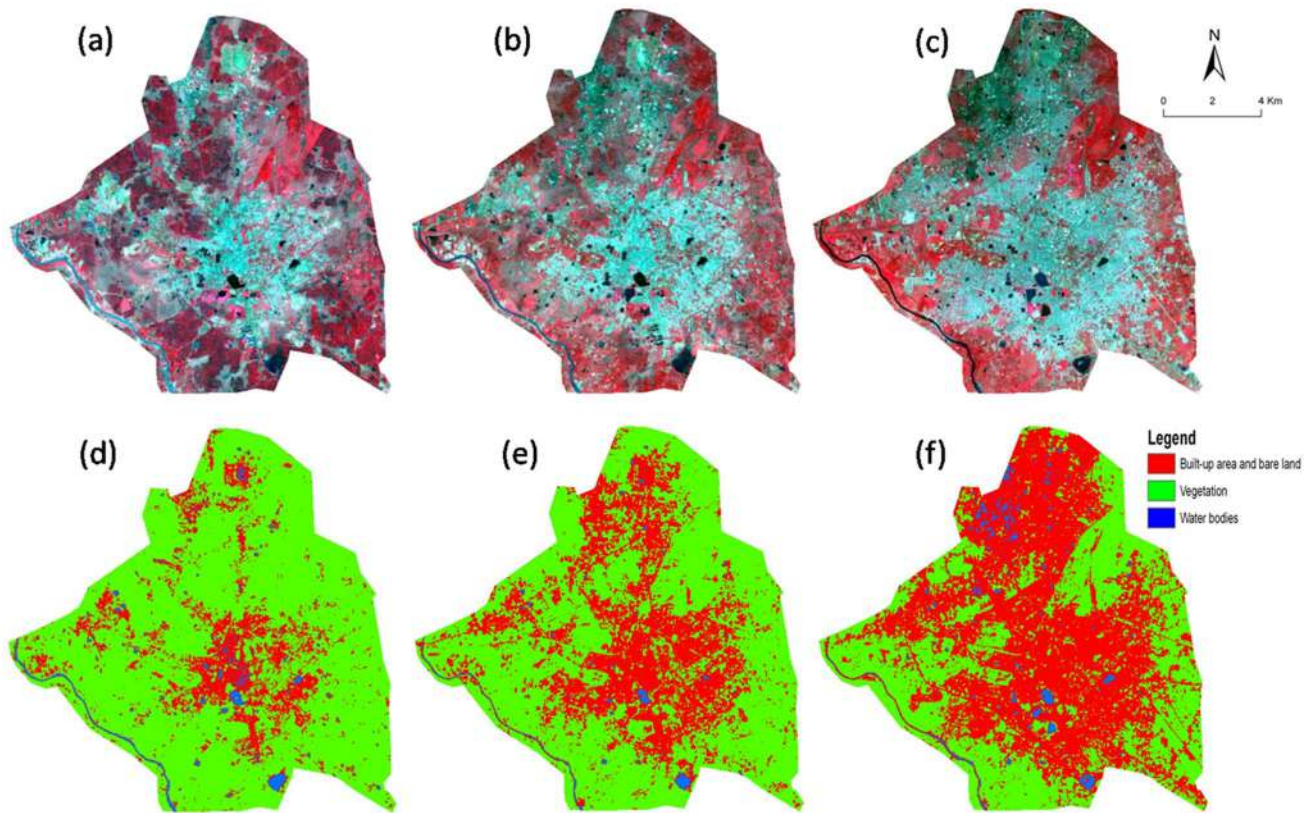
Fig. 2 FCC satellite images of post-monsoon season: **a** 14-OCT-1991 **b** 15-OCT-2004 **c** 22-OCT-2018; LULC maps in post-monsoon season: **d** 12-OCT-1991 **e** 15-OCT-2004 **f** 22-OCT-2018

Table 3 Temporal and seasonal variation of LST, NDVI, and LST-NDVI relationship (1991–2018)

Season	Date of acquisition	LST (°C)				NDVI				Correlation coefficient for LST-NDVI
		Min.	Max.	Mean	Std.	Min.	Max.	Mean	Std.	
Pre-monsoon	18-MAR-1991	22.81	34.46	29.50	1.27	−0.31	0.57	0.09	0.07	−0.40
	22-APR-2004	26.67	41.83	36.80	1.94	−0.32	0.59	0.07	0.08	−0.51
	28-MAR-2018	27.78	44.28	37.90	2.25	−0.16	0.50	0.10	0.06	−0.45
Monsoon	26-SEP-1991	22.38	30.83	25.74	1.41	−0.22	0.61	0.29	0.10	−0.48
	09-JUN-2004	22.81	33.26	29.23	1.58	−0.32	0.60	0.06	0.08	−0.41
	16-JUN-2018	25.49	34.98	31.08	1.13	−0.15	0.48	0.17	0.07	−0.47
Post-monsoon	12-OCT-1991	21.06	30.83	24.99	1.86	−0.27	0.64	0.32	0.11	−0.63
	15-OCT-2004	23.25	34.06	27.56	1.75	−0.41	0.70	0.31	0.15	−0.63
	22-OCT-2018	24.86	35.52	29.01	1.36	−0.14	0.48	0.18	0.08	−0.63
Winter	14-FEB-1991	14.71	30.01	23.99	2.21	−0.35	0.64	0.12	0.08	−0.12
	02-DEC-2004	19.73	31.64	25.17	1.34	−0.31	0.54	0.08	0.08	−0.20
	08-FEB-2018	21.99	32.53	26.91	1.30	−0.16	0.46	0.08	0.05	−0.18

monsoon, pre-monsoon, and winter images. The figures show that the proportion of vegetation is gradually reduced with time and NDVI is inversely related to LST.

4.4 Relationship between LST and LULC

The LST of the study area is significantly dependent upon the LULC types. Actually, this NDVI-threshold based emissivity method is not suitable for LST extraction of water
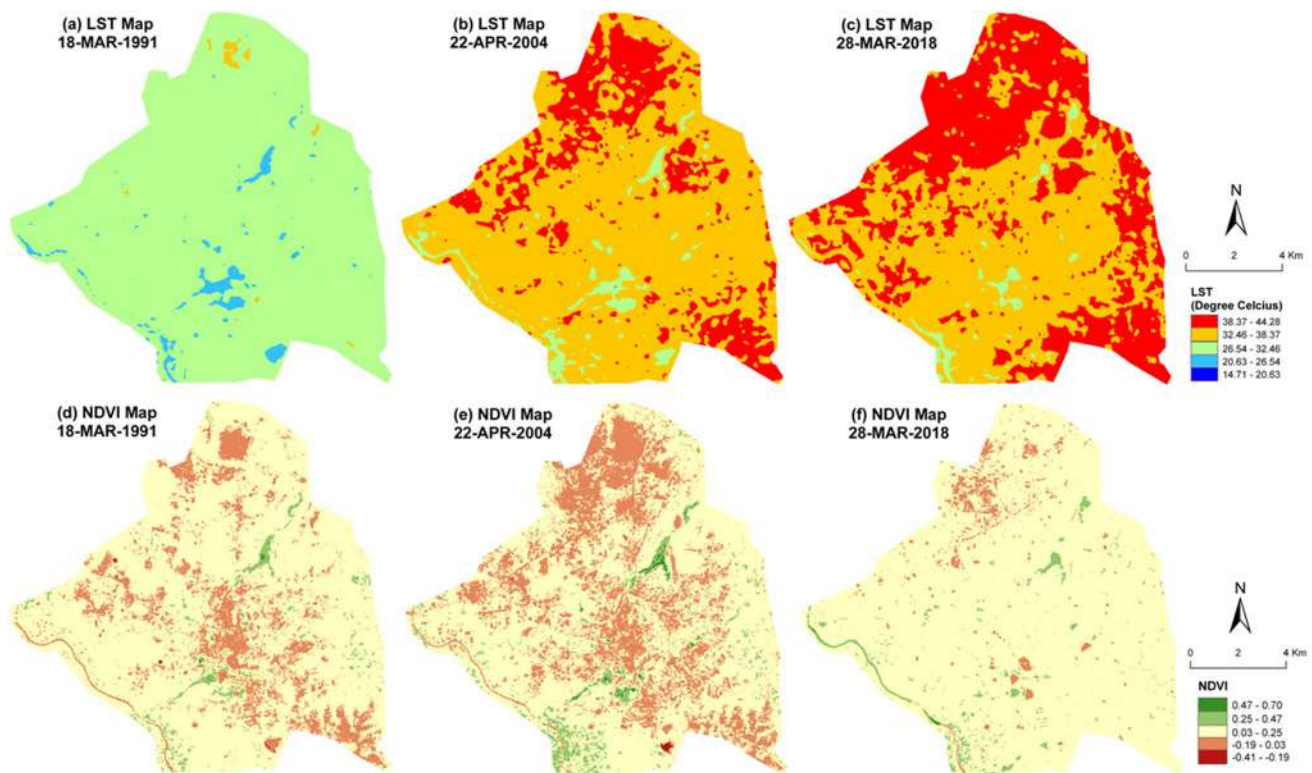
Fig. 3 Spatial distribution of LST in pre-monsoon season: **a** 18-MAR-1991 **b** 22-APR-2004 **c** 28-MAR-2018; spatial distribution of NDVI in pre-monsoon season: **d** 18-MAR-1991 **e** 22-APR-2004 **f** 28-MAR-2018

bodies. However, the present results show that the area with green vegetation has low LST value, whereas the built-up areas and bare lands have moderate to high LST value. In pre-monsoon season, built-up area and bare land has comparatively high LST than the other LULC types. But in the winter season, these areas have comparatively low to moderate LST due to low emissivity. The green areas and water areas are characterized by a relatively stable range of LST.

4.5 LST variation with the change in LULC types

Table 4 presents the temporal changes in LST with the changes in LULC types. Only the post-monsoon images of 1991, 2004, and 2018 were considered for this analysis. Generally, the land is converted into the built-up area or bare land from the other types of LULC, e.g., vegetation or water bodies. No such exceptional cases are seen in Raipur City during the entire period. Built-up area and bare land are increased while vegetation and water bodies are decreased significantly. The mean LST of the built-up area and bare land is increased from 1991 to 2004 (4.23 °C in post-monsoon season) and from 2004 to 2018 (1.49 °C in post-monsoon season), irrespective of any season. The green area gains 4.66 °C mean LST when it is converted

into the built-up area and bare land between 1991 and 2018, and gained 2.20 °C mean LST between 2004 and 2018. The converted land from water bodies to the built-up area and bare land gains 2.49 °C during 1991–2018 and 0.96 °C mean LST during 2004–2018, respectively. Furthermore, the unchanged built-up area and bare land have also witnessed an increase in LST during the entire time span (2.79 °C mean LST from 1991 to 2018 and 0.83 °C mean LST from 2004 to 2018). Hence, the results indicate significantly to the trend of climate change.

4.6 Seasonal variation on LST-NDVI relationship

Table 3 presented the seasonal variation of mean LST values. Winter images indicate the lowest mean LST for 1991, 2004, and 2018. The highest mean LST values are found in the pre-monsoon images for all the three years. From 1991 to 2004, mean LST has been increased in every season. From 2004 to 2018, mean LST has been increased again for all the seasons. Post-monsoon images have mean LST value nearer to winter images while monsoon images have a slightly high value of mean LST than the post-monsoon images. Figure 7a–d show the seasonal variation of LST-NDVI relationships on different LULC types in pre-monsoon, monsoon, post-monsoon, and winter
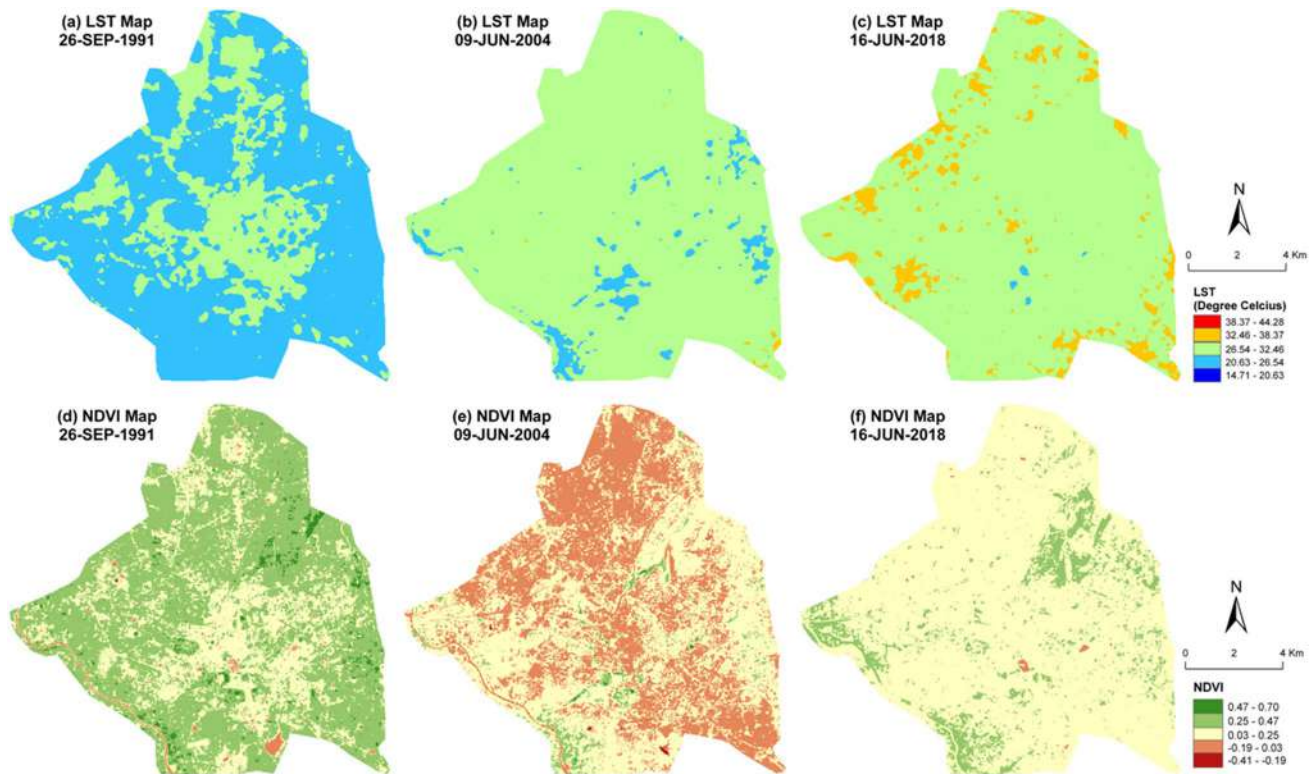
Fig. 4 Spatial distribution of LST in monsoon season: **a** 26-SEP-1991 **b** 09-JUN-2004 **c** 16-JUN-2018; spatial distribution of NDVI in monsoon season: **d** 26-SEP-1991 **e** 09-JUN-2004 **f** 16-JUN-2018

season, respectively. Here, only three types of LULC were considered, i.e., (1) vegetation, (2) water bodies, and (3) built-up area and bare land. On vegetation, the LST-NDVI relationships were negative, irrespective of any season. Only winter season (Fig. 7d) has weak negative regression, while the other three seasons (Fig. 7a–c) have moderate to strong negative regression. Since, NDVI is a vegetation index the LST-NDVI relationship is strongly effective on vegetation. On water bodies, the relationship is positive (weak to moderate). In the post-monsoon season (Fig. 7c), the relationship is weak to moderate. In the rest of the three seasons (Fig. 7a–d), the relationship is moderate. On the built-up area and bare land, the relationship is not so much significant. All four seasons (Fig. 7a–d) indicate weak regression as the surface materials become more heterogeneous in nature. Figure 7e represents a generalized view of the overall seasonal variation of LST-NDVI relationships. The relationship is negative, irrespective of any season. In winter, the relationship was weak negative (− 0.12 in 1991, − 0.2 in 2004, and − 0.20 in 2018). The pre-monsoon and monsoon season built a moderately

negative LST-NDVI relationship. In the pre-monsoon season, the correlation coefficient values of LST-NDVI relationship were − 0.40 (1991), − 0.51 (2004), and − 0.45 (2018). In post-monsoon season, these correlation coefficient values were − 0.48 in 1991, − 0.41 in 2004, and − 0.47 in 2018. The post-monsoon season built a stable and strong negative correlation. The correlation coefficient values of LST-NDVI relationship were − 0.63 for all the 3 years. Hence, the post-monsoon season reveals the best correlation among the four seasons. It was mainly due to the high intensity of moisture and chlorophyll content in green vegetation. Dry atmosphere reduces the strength of correlation, whereas the wet seasons (post-monsoon and monsoon) enhance the strength of correlation.

Liang et al. [92], Ghobadi et al. [27], and Guha et al. [24] observed a negative LST-NDVI relationship in their study. A significant positive linear LST-NDVI relationship was observed between LST and NDVI [93]. In Shanghai City, Yue et al. [56] showed a negative LST-NDVI relationship and it varied on different LULC types. Sun and Kafatos [94] stated that LST-NDVI correlation was positive in winter
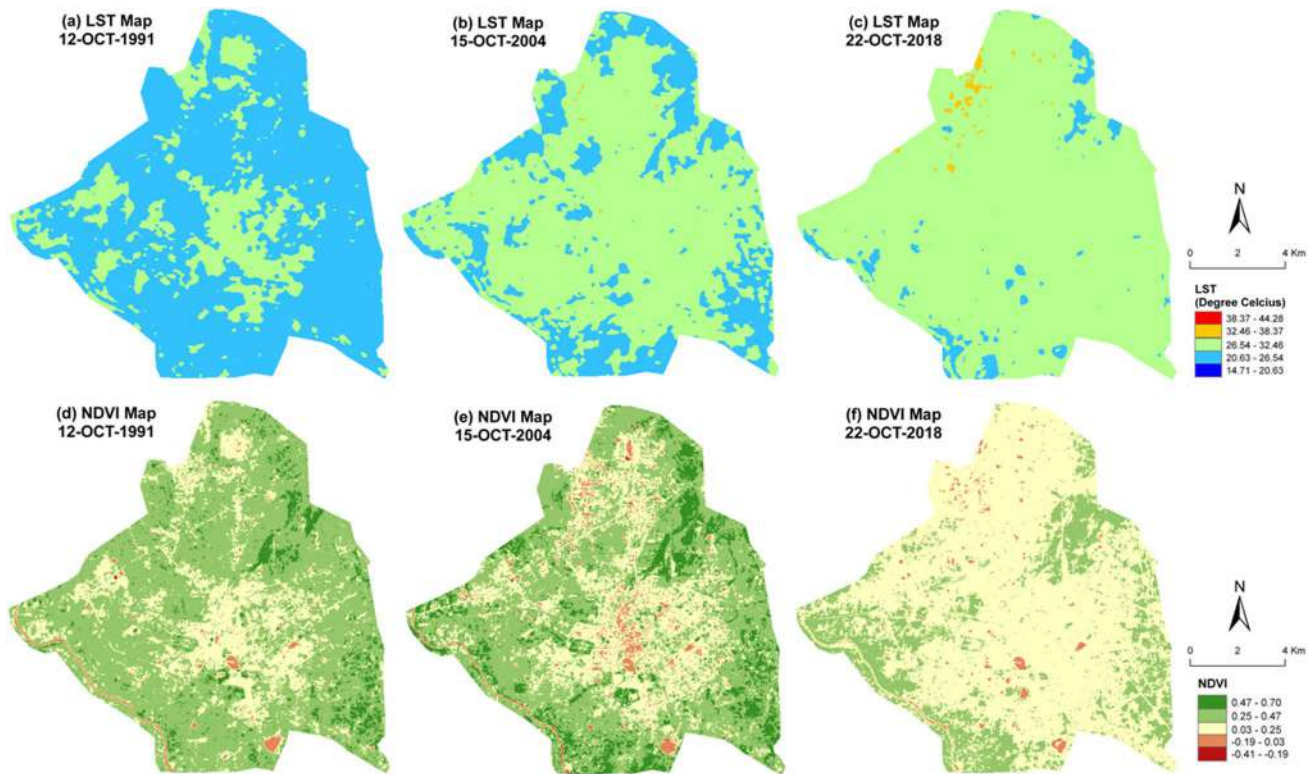
Fig. 5 Spatial distribution of LST in post-monsoon season: **a** 12-OCT-1991 **b** 15-OCT-2004 **c** 22-OCT-2018; spatial distribution of NDVI in post-monsoon season: **d** 12-OCT-1991 **e** 15-OCT-2004 **f** 22-OCT-2018

season, while it was negative in summer season. This relationship was also negative in Mashhad, Iran [57]. The relationship was strong negative in Berlin City for any season [95]. This correlation tends to be more negative with the increase of surface moisture [96–99]. The present study also found that the LST-NDVI correlation is negative, irrespective of any season. The value of correlation coefficient is inversely related to the surface moisture content, i.e., negativity of the relationship increases with the increase of surface moisture content.

5 Conclusion

The present study analyzes the spatial, temporal, and seasonal relationship of LST and NDVI in a tropical city of India using 12 Landsat data sets of four different seasons

(winter, pre-monsoon, monsoon, and post-monsoon) for 1991, 2004, and 2018. The mono-window algorithm was applied in deriving LST. In general, the results showed that LST is inversely related to NDVI, irrespective of any season. In the post-monsoon season, the relationship was strong negative (-0.63), while it was found weak negative (-0.17) in winter. A moderate range of negativity (-0.45) was noticed in pre-monsoon and monsoon season. The presence of healthy green plants and high moisture content in the air are the main responsible factors for high negativity. The LST-NDVI relationship varies for specific LULC types. The green area presents a strong negative (-0.51) regression, while the built-up area and bare land presents a weak positive regression (0.14). The relationship is moderately positive (0.45) on water bodies. On vegetation, the LST-NDVI relationship was highly negative in the pre-monsoon (-0.65), monsoon (-0.52), and post-monsoon (-0.58) seasons, while it was weak negative (-0.28)
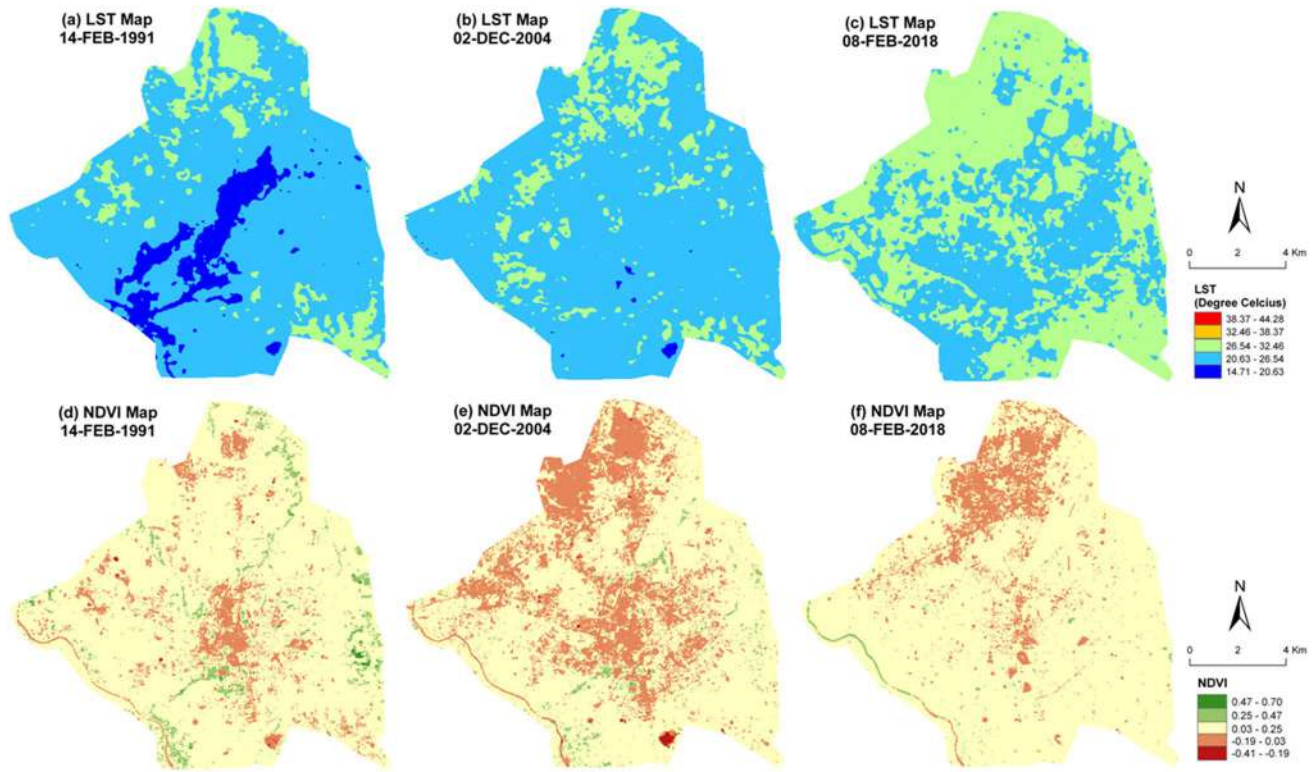
Fig. 6 Spatial distribution of LST in winter season: **a** 14-FEB-1991 **b** 02-DEC-2004 **c** 08-FEB-2018; spatial distribution of NDVI in winter season: **d** 14-FEB-1991 **e** 02-DEC-2004 **f** 08-FEB-2018

Table 4 Change in mean LST (°C) with the conversion of different types of LULC into the built-up area/bare land

Conversion of different LULC into built-up area/bare land	1991–2018			2004–2018		
	1991	2018	1991–2018	2004	2018	2004–2018
Vegetation	25.02	29.68	4.66	27.32	29.52	2.20
Water bodies	26.29	28.87	2.49	26.78	27.74	0.96
Built-up area/bare land	27.25	30.04	2.79	29.14	29.97	0.83
Total	25.51	29.74	4.23	28.25	29.74	1.49

in the winter season. The mean LST of the study area was increased by 5.16 °C during 1991–2018. The conversion of other lands into the built-up area and bare land influences a lot on the mean LST of the city. Both the changed and unchanged built-up area and bare land suffer from the increasing trend of LST. This result significantly presents the influence of climate change in Raipur City.
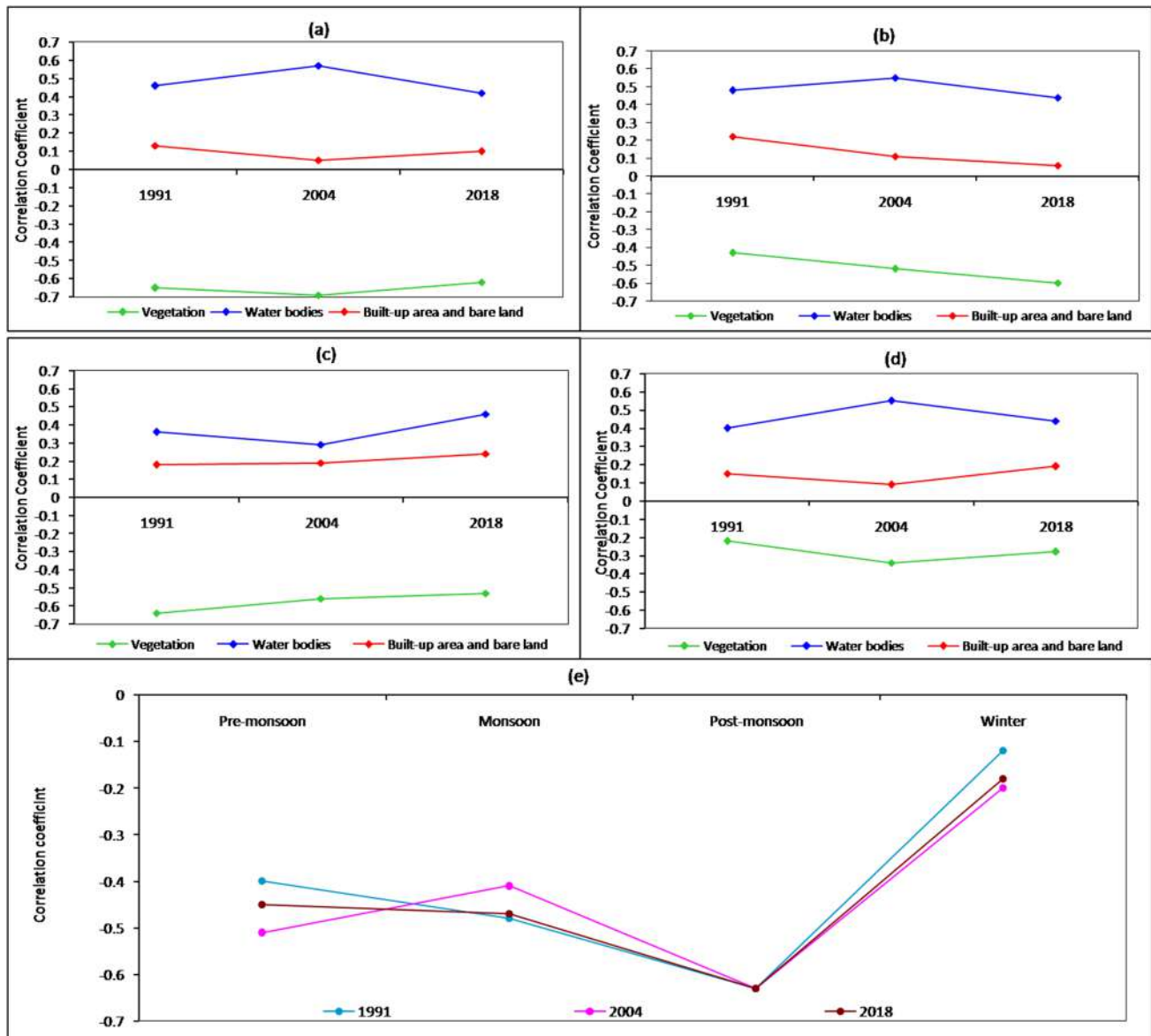
Fig. 7 Seasonal variation of LST-NDVI relationship on different types of LULC: **a** pre-monsoon **b** monsoon **c** post-monsoon **d** winter **e** overall

Compliance with ethical standards

Conflict of interest No potential conflict of interest was reported by the authors.

References

1. Foley JA, DeFries R, Asner GP, Barford C, Bonan G, Carpenter SR, Chapin FS, Coe MT, Daily GC, Gibbs HK et al (2005) Global consequences of land use. Science 309:570–574
2. Fu P, Weng Q (2016) A time series analysis of urbanization induced land use and land cover change and its impact on land surface temperature with landsat imagery. Remote Sens Environ 175:205–214
3. Grimm NB, Faeth SH, Golubiewski NE, Redman CL, Wu J, Bai X, Briggs JM, Grimm N (2008) Global change and the ecology of cities. Science 319:756–760
4. Liu H, Zhan Q, Yang C, Wang J (2018) Characterizing the spatio-temporal pattern of land surface temperature through time series clustering: based on the latent pattern and morphology. Remote Sens 10:654

5. Liu Y, Peng J, Wang Y (2018) Efficiency of landscape metrics characterizing urban land surface temperature. Landsc Urban Plan 180:36–53

6. Peng J, Ma J, Liu Q, Liu Y, Hu Y, Li Y, Yue Y (2018) Spatial-temporal change of land surface temperature across 285 cities in China: an urban-rural contrast perspective. Sci Total Environ 635:487–497

7. Patz JA, Campbell-Lendrum D, Holloway T, Foley JA (2005) Impact of regional climate change on human health. Nat Cell Boil 438:310–317

8. Huang S, Taniguchi M, Yamano M, Wang CH (2009) Detecting urbanization effects on surface and subsurface thermal environment—a case study of Osaka. Sci Total Environ 407:3142–3152

9. Zhou D, Xiao J, Bonafoni S, Berger C, Deilami K, Zhou Y, Frolking S, Yao R, Qiao Z, Sobrino JA (2019) Satellite remote sensing of surface urban heat islands: progress, challenges, and perspectives. Remote Sens 11:48

10. Guha S, Govil H, Dey A, Gill N (2020) A case study on the relationship between land surface temperature and land surface indices in Raipur City, India. Geogr Tidsskr. https://doi.org/10.1080/00167223.2020.1752272

11. Govil H, Guha S, Diwan P, Gill N, Dey A (2020) Analyzing linear relationships of LST with NDVI and MNDISI using various resolution levels of landsat 8 OLI and TIRS data. In: Sharma N, Chakrabarti A, Balas V (eds) Data management, analytics and innovation. Advances in intelligent systems and computing, vol 1042. Springer, Singapore, pp 171–184. https://doi.org/10.1007/978-981-32-9949-8_13

12. Guha S, Govil H (2020) An assessment on the relationship between land surface temperature and normalized difference vegetation index. Environ Dev Sustain. https://doi.org/10.1007/s10668-020-00657-6

13. Kalnay E, Cai M (2003) Impact of urbanization and land-use change on climate. Nat Cell Boil 423:528–531

14. Chen XL, Zhao HM, Li PX, Yi ZY (2006) Remote sensing image-based analysis of the relationship between urban heat island and land use/cover changes. Remote Sens Environ 104(2):133–146

15. Peng J, Jia J, Liu Y, Li H, Wu J (2018) Seasonal contrast of the dominant factors for spatial distribution of land surface temperature in urban areas. Remote Sens Environ 215:255–267

16. Berger C, Rosentreter J, Voltersen M, Baumgart C, Schmullius C, Hese S (2017) Spatio-temporal analysis of the relationship between 2D/3D urban site characteristics and land surface temperature. Remote Sens Environ 193:225–243

17. Du S, Xiong Z, Wang Y, Guo L (2016) Quantifying The Multilevel Effects Of Landscape Composition And Configuration On Land Surface Temperature. Remote Sens Environ 178:84–92

18. Peng J, Xie P, Liu Y, Ma J (2016) Urban thermal environment dynamics and associated landscape pattern factors: a case study in the beijing metropolitan region. Remote Sens Environ 173:145–155

19. He BJ, Zhao ZQ, Shen LD, Wang HB, Li LG, He BJ (2019) An approach to examining performances of cool/hot sources in mitigating/enhancing land surface temperature under different temperature backgrounds based on landsat 8 image. Sustain Cities Soc 44:416–427

20. Weng Q (2009) Thermal Infrared Remote Sensing for Urban Climate and Environmental Studies: methods, Applications, and Trends. ISPRS J Photogramm Sens 64:335–344

21. Fu P, Weng Q (2015) Temporal dynamics of land surface temperature from landsat TIR time series images. IEEE Geosci Sens Lett 12:1–5

22. Hao X, Li W, Deng H (2016) The oasis effect and summer temperature rise in arid regions-case study in Tarim Basin. Sci Rep 6:35418. https://doi.org/10.1038/srep35418

23. Tran DX, Pla F, Latorre-Carmona P, Myint SW, Caetano M, Kieu HV (2017) Characterizing the relationship between land use land cover change and land surface temperature. ISPRS J Photogramm Sens 124:119–132

24. Guha S, Govil H, Diwan P (2019) Analytical study of seasonal variability in land surface temperature with normalized difference vegetation index, normalized difference water index, normalized difference built-up index, and normalized multi-band drought index. J Appl Remote Sens 13(2):024518. https://doi.org/10.1117/1.JRS.13.024518

25. Hou GL, Zhang HY, Wang YQ, Qiao ZH, Zhang ZX (2010) Retrieval and spatial distribution of land surface temperature in the middle part of jilin province based on MODIS data. Sci Geogr Sin 30:421–427

26. Shigeto K (1994) Relation between vegetation, surface temperature, and surface composition in the Tokyo region during winter. Remote Sens Environ 50:52–60

27. Ghobadi Y, Pradhan B, Shafri HZM, Kabiri K (2014) Assessment of spatial relationship between land surface temperature and land use/cover retrieval from multi-temporal remote sensing data in South Karkheh Sub-basin, Iran. Arab J Geosci 8(1):525–537. https://doi.org/10.1007/s12517-013-1244-3

28. Stroppiana D, Antoninetti M, Brivio PA (2014) Seasonality of MODIS LST over Southern Italy and correlation with land cover, topography and solar radiation. Eur J Remote Sens 47:133–152

29. Li ZN et al (2016) Review of methods for land surface temperature derived from thermal infrared remotely sensed data. J Remote Sens 20:899–920

30. Estoque RC, Murayama Y, Myint SW (2017) Effects of landscape composition and pattern on land surface temperature: an urban heat island study in the megacities of Southeast Asia. Sci Total Environ 577:349–359

31. Wen LJ et al (2017) An analysis of land surface temperature (LST) and its influencing factors in summer in western Sichuan Plateau: a case study of Xichang City. Remote Sens Land Res 29:207–214

32. Zhao ZQ, He BJ, Li LG, Wang HB, Darko A (2017) Profile and concentric zonal analysis of relationships between land use/land cover and land surface temperature: case study of Shenyang, China. Energ Build 155:282–295. https://doi.org/10.1016/j.enbuild.2017.09.046

33. Ferrelli F, Huamantinco MA, Delgado DA, Piccolo MC (2018) Spatial and temporal analysis of the LST-NDVI relationship for the study of land cover changes and their contribution to urban planning in Monte Hermoso, Argentina. Doc Anal Geogr 64(1):25–47. https://doi.org/10.5565/rev/dag.355

34. Mahato S, Pal S (2018) Changing land surface temperature of a rural Rarh tract river basin of India. Remote Sens Appl Soc Environ 10:209–223. https://doi.org/10.1016/j.rsase.2018.04.005

35. Mathew A, Khandelwal S, Kaul N (2018) Spatio-temporal variations of surface temperatures of Ahmedabad city and its relationship with vegetation and urbanization parameters as indicators of surface temperatures. Remote Sens Appl Soc Environ 11:119–139. https://doi.org/10.1016/j.rsase.2018.05.003

36. Sannigrahi S et al (2018) Analyzing the role of biophysical compositions in minimizing urban land surface temperature and urban heating. Urban Climate. https://doi.org/10.1016/j.uclim.2017.10.002

37. Fatemi M, Narangifard M (2019) Monitoring LULC changes and its impact on the LST and NDVI in District 1 of Shiraz City. Arab J Geosci 12:127. https://doi.org/10.1007/s12517-019-4259-6

38. Filho WLFC, De Barros Santiago D, De Oliveira-Júnior JF, Da Silva Junior CA (2019) Impact of urban decadal advance on land use and land cover and surface temperature in the city of Maceió, Brazil. Land Use Policy 87:104026. https://doi.org/10.1016/j.landusepol.2019.104026

39. Mushore TD, Dube T, Manjowe M, Gumindogab W, Chemuira A, Rousta I, Obindi J, Mutanga O (2019) Remotely sensed retrieval of Local climate zones and their linkages to land surface temperature in Harare metropolitan city, Zimbabwe. Urban Clim 27:171–259. https://doi.org/10.1016/j.uclim.2018.12.006

40. Mushore TD, Odindi J, Dube T, Matongera TN, Mutanga O (2017) Remote sensing applications in monitoring urban growth impacts on in-and-out door thermal conditions: a review. Remote Sens Appl Soc Environ 8:83–93. https://doi.org/10.1016/j.rsase.2017.08.001

41. Mushore TD, Odindi J, Dube T, Mutanga O (2017) Prediction of future urban surface temperatures using medium resolution satellite data in Harare metropolitan city, Zimbabwe. Build Environ 122:397–410. https://doi.org/10.1016/j.buildenv.2017.06.033

42. Ullah S, Ahmad K, Sajjad RU, Abbasi AM, Nazeer A, Tahir AA (2019) Analysis and simulation of land cover changes and their impacts on land surface temperature in a lower Himalayan region. J Environ Manag 245:348–357. https://doi.org/10.1016/j.jenvman.2019.05.063

43. Nimish G, Bharath HA, Lalitha A (2020) Exploring temperature indices by deriving relationship between land surface temperature and urban landscape. Remote Sens Appl Soc Environ 18:100299. https://doi.org/10.1016/j.rsase.2020.100299

44. Sultana S, Satyanarayana ANV (2020) Assessment of urbanisation and urban heat island intensities using landsat imageries during 2000 – 2018 over a sub-tropical Indian City. Sustain Cities Soc 52:101846. https://doi.org/10.1016/j.scs.2019.101846

45. Smith RCG, Choudhury BJ (1990) On the correlation of indices of vegetation and surface temperature over south-eastern Australia. Int J Remote Sens 11:2113–2120

46. Hope AS, McDowell TP (1992) The relationship between surface temperature and a spectral vegetation index of a tall grass prairie: effects of burning and other landscape controls. Int J Remote Sens 13:2849–2863

47. Julien Y, Sobrino JA, Verhoef W (2006) Changes in land surface temperatures and NDVI values over Europe between 1982 and 1999. Remote Sens Environ 103:43–55

48. Yuan XL et al (2017) Vegetation changes and land surface feedbacks drive shifts in local temperatures over Central Asia. Sci Rep 7:3287. https://doi.org/10.1038/s41598017034322

49. Mondal A, Guha S, Mishra PK, Kundu S (2011) Land use/Land cover changes in Hugli Estuary using Fuzzy C-Mean algorithm. Int J Geomat Geosci 2(2): 613–626

50. Carlson TN, Ripley DA (1997) On the relation between NDVI, fractional vegetation cover, and leaf area index. Remote Sens Environ 62:241–252. https://doi.org/10.1016/S0034-4257(97)00104-1

51. Sobrino JA, Jimenez-Munoz JC, Paolini L (2004) Land surface temperature retrieval from Landsat TM5. Remote Sens Environ 9:434–440. https://doi.org/10.1016/j.rse.2004.02.003

52. Gutman G, Ignatov A (1998) The derivation of the green vegetation fraction from NOAA/AVHRR data for use in numerical weather prediction models. Int J Remote Sens 19(8):1533–1543. https://doi.org/10.1080/014311698215333

53. Goward SN, Xue YK, Czajkowski KP (2002) Evaluating land surface moisture conditions from the remotely sensed temperature/vegetation index measurements: an exploration with the simplified simple biosphere model. Remote Sens Environ 79:225–242. https://doi.org/10.1016/S0034-4257(01)00275-9

54. Voogt JA, Oke TR (2003) Thermal remote sensing of urban climates. Remote Sens Environ 86:370–384. https://doi.org/10.1016/S0034-4257(03)00079-8

55. Weng QH, Lu DS, Schubring J (2004) Estimation of land surface temperature-vegetation abundance relationship for urban heat island studies. Remote Sens Environ 89:467–483. https://doi.org/10.1016/j.rse.2003.11.005

56. Yue W, Xu J, Tan W, Xu L (2007) The relationship between land surface temperature and NDVI with remote sensing. Application to Shanghai Landsat 7 ETM+ data. Int J Remote Sens 28:3205–3226. https://doi.org/10.1080/01431160500306906

57. Gorgani SA, Panahi M, Rezaie F (2013) The relationship between NDVI and LST in the Urban area of Mashhad, Iran. In: International conference on civil engineering architecture and urban sustainable development. November, Tabriz, Iran

58. Govil H, Guha S, Dey A, Gill N (2019) Seasonal evaluation of downscaled land surface temperature: a case study in a humid tropical city. Heliyon 5(6):e01923. https://doi.org/10.1016/j.heliyon.2019.e01923

59. Cui L, Wang L, Qu S, Singh RP, Lai Z, Jiang L, Yao R (2019) Association analysis between spatiotemporal variation of vegetation greenness and precipitation/temperature in the Yangtze River Basin (China). Environ Sci Pollut Res 25(22):21867–21878. https://doi.org/10.1007/s11356-018-2340-4

60. Cui L, Wang L, Qu S, Singh RP, Lai Z, Yao R (2019) Spatiotemporal extremes of temperature and precipitation during 1960–2015 in the Yangtze River Basin (China) and impacts on vegetation dynamics. Theor Appl Climatol 136(1–2):675–692. https://doi.org/10.1007/s00704-018-2519-0

61. Gui X, Wang L, Yao R, Yu D, Li C (2019) Investigating the urbanization process and its impact on vegetation change and urban heat island in Wuhan, China. Environ Sci Pollut Res 26(30):30808–30825. https://doi.org/10.1007/s11356-019-06273-w

62. Qu S, Wang L, Lin A, Yu D, Yuan M, Li C (2020) What drives the vegetation restoration in Yangtze River basin, China: climate change or anthropogenic factors? Ecol Indic 108:105724. https://doi.org/10.1016/j.ecolind.2019.105724

63. Qu S, Wang L, Lin A, Zhu H, Yuan M (2018) What drives the vegetation restoration in Yangtze River basin, China: climate change or anthropogenic factors? Ecol Indic 90:438–450. https://doi.org/10.1016/j.ecolind.2018.03.029

64. Yao R, Cao J, Wang L, Zhang W, Wu X (2019) Urbanization effects on vegetation cover in major African cities during 2001–2017. Int J Appl Earth Obs 75:44–53. https://doi.org/10.1016/j.jag.2018.10.011

65. Yao R, Wang L, Huang X, Chen J, Li J, Niu Z (2018) Less sensitive of urban surface to climate variability than rural in Northern China. Sci Total Environ 628–629:650–660. https://doi.org/10.1016/j.scitotenv.2018.02.087

66. Yao R, Wang L, Huang X, Niu Z, Liu F, Wang Q (2017) Temporal trends of surface urban heat islands and associated determinants in major Chinese cities. Sci Total Environ 609:742–754. https://doi.org/10.1016/j.scitotenv.2017.07.217

67. Yuan M, Wang L, Lin A, Liu Z, Qu S (2020) Vegetation green up under the influence of daily minimum temperature and urbanization in the Yellow River Basin, China. Ecol Indic 108:105760. https://doi.org/10.1016/j.ecolind.2019.105760

68. Kumar D, Shekhar S (2015) Statistical analysis of land surface temperature-vegetation indexes relationship through thermal remote sensing. Ecotox Environ Safe 121:39–44. https://doi.org/10.1016/j.ecoenv.2015.07.004

69. Kikon N, Singh P, Singh SK, Vyas A (2016) Assessment of urban heat islands (UHI) of Noida City, India using multi-temporal satellite data. Sustain Cities Soc 22:19–28. https://doi.org/10.1016/j.scs.2016.01.005

70. Singh P, Kikon N, Verma P (2017) Impact of land use change and urbanization on urban heat island in Lucknow city, Central India. A remote sensing based estimate. Sustain Cities Soc 32:100–114. https://doi.org/10.1016/j.scs.2017.02.018

71. Mathew A, Khandelwal S, Kaul N (2017) Investigating spatial and seasonal variations of urban heat island effect over Jaipur city and its relationship with vegetation, urbanization and elevation parameters. Sustain Cities Soc 35:157–177. https://doi.org/10.1016/j.scs.2017.07.013

72. Guha S, Govil H, Gill N, Dey A (2020) Analytical study on the relationship between land surface temperature and land use/land cover indices. Ann GIS 26(2):201–216. https://doi.org/10.1080/19475683.2020.1754291

73. https://www.earthexplorer.usgs.gov

74. http://www.surveyofindia.gov.in

75. https://www.mausam.imd.gov.in

76. Qin Z, Karnieli A, Barliner P (2001) A mono-window algorithm for retrieving land surface temperature from landsat TM data and its application to the Israel–Egypt border region. Int J Remote Sens 22(18):3719–3746. https://doi.org/10.1080/01431160010006971

77. Wang F, Qin Z, Song C, Tu L, Karnieli A, Zhao S (2015) An improved mono-window algorithm for land surface temperature retrieval from Landsat 8 thermal infrared sensor data. Remote Sens 7(4):4268–4289

78. Wang L, Lu Y, Yao Y (2019) Comparison of three algorithms for the retrieval of land surface temperature from Landsat 8 images. Sensors 19(22):5049

79. Sekertekin A, Bonafoni S (2020) Land surface temperature retrieval from landsat 5, 7, and 8 over rural areas: assessment of different retrieval algorithms and emissivity models and toolbox implementation. Remote Sens 12(2):294

80. Zanter K (2019) Landsat 8 (L8) Data users handbook; EROS: Sioux Falls, SD, USA

81. Wukelic GE, Gibbons DE, Martucci LM, Foote HP (1989) Radiometric calibration of landsat thematic mapper thermal band. Remote Sens Environ 28:339–347

82. Sobrino JA, Raissouni N, Li Z (2001) A comparative study of land surface emissivity retrieval from NOAA data. Remote Sens Environ 75(2):256–266

83. Yang J, Qiu J (1996) The empirical expressions of the relation between precipitable water and ground water vapor pressure for some areas in China. Sci Atmos Sinica 20:620–626

84. http://www.imdraipur.gov.in

85. http://www.imdnagpur.gov.in

86. Sun Q, Tan J, Xu Y (2010) An ERDAS image processing method for retrieving LST and describing urban heat evolution: a case study in the Pearl River Delta Region in South China. Environ Earth Sci 59:1047–1055

87. Tucker CJ (1979) Red and photographic infrared linear combinations for monitoring vegetation. Remote Sens Environ 8(2):127–150

88. Purevdorj TS, Tateishi R, Ishiyama T, Honda Y (1998) Relationships between percent vegetation cover and vegetation indices. Int J Remote Sens 19:3519–3535

89. Ke YH, Im J, Lee J, Gong HL, Ryu Y (2015) Characteristics of landsat 8 oli-derived NDVI by comparison with multiple satellite sensors and in-situ observations. Remote Sens Environ 164:298–313. https://doi.org/10.1016/j.rse.2015.04.004

90. Nigatu W, Dick ØB, Tveite H (2014) GIS based mapping of land cover changes utilizing multi-temporal remotely sensed image data in lake Hawassa watershed. Ethiopia. Environ Monit Assess 186(3):1765–1780. https://doi.org/10.1007/s10661-013-3491-x

91. https://www.esri.com

92. Liang BP, Li Y, Chen KZ (2012) A research on land features and correlation between NDVI and land surface temperature in Guilin City. Remote Sens Tech Appl 27:429–435

93. Cao L, Hu HW, Meng XL, Li JX (2011) Relationships between land surface temperature and key landscape elements in urban area. Chin J Ecol 30:2329–2334

94. Sun D, Kafatos M (2007) Note on the NDVI-LST relationship and the use of temperature-related drought indices over North America. Geophys Res Lett. https://doi.org/10.1029/2007GL031485

95. Marzban F, Sodoudi S, Preusker R (2018) The influence of land-cover type on the relationship between LST-NDVI and LST-T_{air}. Int J Remote Sens 39(5):1377–1398. https://doi.org/10.1080/01431161.2017.1462386

96. Lambin EF, Ehrlich D (1996) The surface tenperature-vegetation index space for land use and land cover change analysis. Int J Remote Sens 17:463–487. https://doi.org/10.1080/01431169608949021

97. Moran MS, Clarke TR, Inouie Y, Vidal A (1994) Estianting crop water-deficit using the relation between surface air-temperature and spectral vegetation index. Remote Sens Environ 49:246–263. https://doi.org/10.1016/0034-4257(94)90020-5

98. Sandholt I, Rasmussen K, Andersen J (2002) A simple interpretation of the surface temperature/vegetation index space for assessment of surface moisture status. Remote Sens Environ 79:213–224. https://doi.org/10.1016/s0034-4257(01)00274-7

99. Prehodko L, Goward SN (1997) Estimation of air temperature from remotely sensed surface observations. Remote Sens Environ 60:335–346. https://doi.org/10.1016/S0034-4257(96)00216-7

100. Coll C et al (2010) Validation of Landsat-7/ETM + thermal-band calibration and atmospheric correction with ground-based measurements. IEEE Trans Geosci Remote Sens 48(1):547–555

101. Guha S, Govil H, Mukherjee S (2017) Dynamic analysis and ecological evaluation of urban heat islands in Raipur city, India. J Appl Remote Sens 11(3):036020. https://doi.org/10.1117/1.JRS.11.036020

102. Guha S, Govil H, Diwan P (2020) Monitoring LST-NDVI Relationship Using Premonsoon Landsat Datasets. Adv Meteorol 2020:4539684. https://doi.org/10.1155/2020/4539684

103. Guha S, Govil H, Dey A, Gill N (2018) Analytical study of land surface temperature with NDVI and NDBI using Landsat 8 OLI/TIRS data in Florence and Naples city, Italy. Eur J Remote Sens 51(1):667–678. https://doi.org/10.1080/22797254.2018.1474494

104. Guha S, Govil H (2020) Seasonal impact on the relationship between land surface temperature and normalized difference vegetation index in an urban landscape. Geocarto Int. https://doi.org/ 10.1080/10106049.2020.1815867

Source details

Feedback ›   Compare sources ›

SN Applied Sciences

Open Access ⓘ

Scopus coverage years: from 2019 to 2023

Publisher: Springer Nature

E-ISSN: 2523-3971

Subject area: (Engineering: General Engineering) (Earth and Planetary Sciences: General Earth and Planetary Sciences)

(Physics and Astronomy: General Physics and Astronomy) (Environmental Science: General Environmental Science)   View all ⌄

Source type: Journal

View all documents ›   Set document alert   💾 Save to source list

CiteScore 2022	ⓘ
5.3	

SJR 2022	ⓘ
0.424	

SNIP 2022	ⓘ
0.898	

CiteScore   CiteScore rank & trend   Scopus content coverage

Dynamic seasonal analysis on LST-NDVI relationship and ecological health of Raipur City, India

Subhanil Guha

Submit your article to this journal ⤤

Article views: 244

View related articles ⤤

View Crossmark data ⤤

Taylor & Francis
Taylor & Francis Group

🔓 OPEN ACCESS | ✓ Check for updates

Dynamic seasonal analysis on LST-NDVI relationship and ecological health of Raipur City, India

Subhanil Guha 🔴

Department of Applied Geology, National Institute of Technology, Raipur, India

ABSTRACT

Land surface temperature (LST) is a significant component of the ecological health of any city and the LST is closely related to the normalized difference vegetation index (NDVI). The present study evaluates the seasonal variability of the relationship of LST with NDVI by using a large dataset of Landsat sensors for different seasons from 1991–92 to 2018–19. Pearson's correlation coefficient technique was used to obtain the LST-NDVI relationship. The study also compares the ecological and thermal status of the city by applying the urban thermal field variance index (UTFVI). The results found that the mean LST increased considerably. The post-monsoon season produces the best correlation (−0.59), followed by the monsoon season (−0.53), pre-monsoon season (−0.45), and winter season (−0.22). Apart from this relationship, the ecological status of the city has also been estimated. Almost an equal portion of lands are under the excellent and worst categories of ecological condition. This study is beneficial for future ecological planning in any tropical city.

Introduction

In the twenty-first century, urban expansion and growth is responsible to generate urban heat islands or high LST zones inside the city (Fu and Weng 2016; Liu, Peng, and Wang 2018; Peng et al. 2018a). Massive land conversion increases the LST (Zhou et al. 2019; Guha, Govil, and Diwan 2020). Different wavelength zones of the electromagnetic spectrum efficiently generate various spectral indices to detect the different categories of land surface materials (Guha and Govil 2021). VNIR, SWIR, and TIR bands efficiently detected the land surface characteristics (Das, Mondal, and Guha 2013; Govil et al. 2019). Various spectral indices can take an important role in extracting surface features. NDVI is a vegetation index frequently used in vegetation mapping, land use/land cover (LULC) mapping, town planning, LST monitoring, etc. (Mondal et al. 2011; Du et al. 2016; Peng et al. 2016; Berger et al. 2017; Peng et al. 2018b).

LST deals with the urban heat island effect and it changes significantly in an urban area (Hao, Li, and Deng 2016; Tran et al. 2017). Various land features influence LST differently (Shigeto 1994; Estoque, Murayama, and Myint 2017; Zhao et al. 2017; Mahato and Pal 2018; Mushore et al. 2019). Land conversion process changes the intensity of LST (Wen et al. 2017; Guha and Govil 2020). Seasonal analysis of LST is quite essential in urban ecological studies as vegetation changes with season.

The LST-NDVI correlation analysis influences LST related research work (Smith and Chowdhury 1990;

Guha, Govil, and Diwan 2020). NDVI also classifies the LULC features by its optimum threshold limits in diverse physical environments (Chen et al. 2006). Seasonal variability changes LST, NDVI, and also LST-NDVI correlation analysis. The LST-NDVI correlation is quite fascinating in remote sensing studies (Gutman and Ignatov 1998; Goward, Xue, and Czajkowski 2002). This LST-NDVI correlation is mostly negative that is observed in many recent studies performed in the mixed urban areas (Alexander 2020; Chi et al. 2020; Neinavaz et al. 2020; Nse, Okoliea, and Nse 2020). However, the negativity varies with the change in LULC types.

Many LST-NDVI correlation-related research works are available in the tropics and sub-tropics (Kikon et al. 2016; Qu et al. 2018, 2020; Cui et al. 2019a, 2019b; Gui et al. 2019; Guha and Govil 2021). The correlation appears stronger in the wet season (Guha and Govil 2020). A long seasonal investigation between LST and NDVI is necessary for any sustainable town planning in tropical cities (Li et al. 2017). However, the LST-NDVI correlation on different LULC categories are not so much discussed for any Indian tropical city. The long-term ecological status of any Indian city was also need to evaluate.

The present study highlights the seasonal changes in the LST-NDVI correlation as a whole and on various types of land surface covers in Raipur using 64 Landsat satellite images. The primary focuses of the study are (1) to determine the seasonal variation of LST as a whole and on different land surface materials, (2) to

---

investigate the seasonal variability of LST-NDVI correlation, and (3) to determine the long-term ecological and thermal status of the city.

Study area and data

Raipur, the study area, is currently the capital of Chhattisgarh, and it ranks 45 in India by population. The total study area extends from 21°11′22″N to 21°20′02″N and from 81°32′20″E to 81°41′50″E with an average elevation of around 275 m. Figure 1(a), 1(b), 1(c), and 1(d) show the outline map of India, outline map of Chhattisgarh, false color composite (FCC) image of Raipur city, and contour map of Raipur City, respectively. The city covers an area of approximately 165 km^2. The climate of the city is considered as dry and wet savannah climate (https://www.mausam.imd.gov.in). Four types of seasons are observed in Raipur, i. ethat is, monsoon, pre-monsoon, post-monsoon, and winter. The mean annual temperature ranges from 12°C (December) to 42°C (May). The pre-monsoon or summer months are usually hot and remain almost dry. The temperature often rises above 45°C in April and May. May is the hottest month (average temperature 35°C) followed by April (average temperature 33°C), June (average temperature 32°C), and March (average temperature 29°C). July is the rainiest month (average rainfall 327 mm) followed by August (average rainfall 300 mm), June (average rainfall 221 mm), and September (average rainfall 200 mm). October and November are the post-monsoon months that experience a pleasant weather condition with comparatively low temperature and high to the moderate moisture content in the air. The presence of a high density of green vegetation adds an extra flavor in Raipur during the monsoon and the post-monsoon seasons. December (the coldest month: average temperature 20°C), January (average temperature 21°C), and February (average temperature 24°C) come under the winter season. November to April remains almost dry (average rainfall <50 mm) compared to the June to September (average rainfall >200 mm). There are too many small patches of mixed sandy, loamy, and black soil formed in the study area. The south-eastern part of the city is mainly associated with dry bare soil with rocky weathered residuals that give a high amount of LST. The central part of the city has numerous small and medium-sized water areas.

Nine Landsat 5 data from 1991 to 1992, seven Landsat 5 data from 1995 to 1995, six Landsat 7 data from 1999 to 1900, eleven Landsat 5 data from 2004 to 2005, 13 Landsat 5 data from 2009 to 2010, nine Landsat 8 data from 2014 to 2015, and 10 Landsat 8 data from 2018 to 19 were procured from the United States Geological Survey (USGS) Data Center (https://www.earthexplorer.usgs.gov). The present study used the band 10 of Landsat 8 data as to it has a better calibration (Barsi et al. 2014). All the TIR bands from different Landsat sensors were resampled by the USGS data provider applying the cubic convolution method.

Methodology

Retrieving LST from landsat data

Mono-window algorithm (Qin, Karnieli, and Barliner 2001; García-Santos et al. 2018), single-channel algorithm (Jiménez-Muñoz and Sobrino 2003; Jiménez-Muñoz et al. 2009; Coll et al. 2010; Chatterjee et al. 2017), split-window algorithm (McMillin 1975;
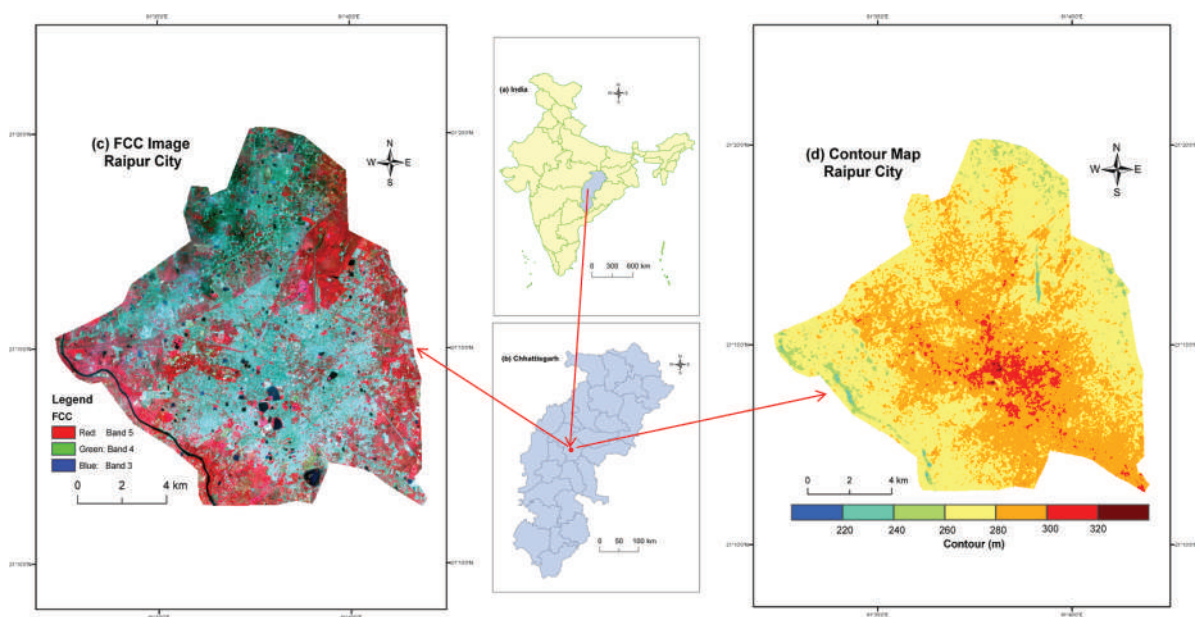

Figure 1. Location of the study area (Raipur City, India): (a) Chhattisgarh State in India (b) Raipur City in Chhattisgarh (c) FCC image of Raipur City (d) Contour Map of Raipur City.

Rozenstein et al. 2014), etc. are the main LST retrieval algorithm from Landsat thermal bands. In the present study, the reliable mono-window algorithm derives LST from three different Landsat sensors.

At first, the cubic convolution resampling process converts the original TIR bands (100 m resolution for Landsat 8 data, 120 m resolution for Landsat 5 data, and 60 m resolution for Landsat 7 data) into 30 m for further application. The entire procedure includes the following methods:

The TIR pixel values are firstly converted into radiance from digital number (DN) values. Radiance for TIR bands of Landsat 5 TM data and Landsat 7 ETM+ data are obtained using Eq. (1) (USGS):

$$L_\lambda = \left[\frac{L_{MAX\lambda} - L_{MIN\lambda}}{QCAL_{MAX} - QCAL_{MIN}} \right] * [Q_{CAL} - QCAL_{MIN}] + L_{MIN\lambda} \tag{1}$$

where L_λ is Top of Atmosphere (TOA) spectral radiance (Wm^{-2}sr^{-1}mm^{-1}), Q_{CAL} is the quantized calibrated pixel value in DN, $L_{MIN\lambda}$ (Wm^{-2}sr^{-1}mm^{-1}) is the spectral radiance scaled to $QCAL_{MIN}$, $L_{MAX\lambda}$ (Wm^{-2}sr^{-1}mm^{-1}) is the spectral radiance scaled to $QCAL_{MAX}$, $QCAL_{MIN}$ is the minimum quantized calibrated pixel value in DN and $QCAL_{MAX}$ is the maximum quantized calibrated pixel value in DN. $L_{MIN\lambda}$, $L_{MAX\lambda}$, $QCAL_{MIN}$, and $QCAL_{MAX}$ values are obtained from the metadata file of Landsat 5 TM data and Landsat 7 ETM+ data. Radiance for Landsat 8 TIR band is obtained from Eq. (2) (Zanter 2019):

$$L_\lambda = M_L . Q_{CAL} + A_L \tag{2}$$

where L_λ is the TOA spectral radiance (Wm^{-2}sr^{-1}mm^{-1}), M_L is the band-specific multiplicative rescaling factor from the metadata, A_L is the band-specific additive rescaling factor from the metadata, Q_{CAL} is the quantized and calibrated standard product pixel values (DN). All of these variables can be retrieved from the metadata file of Landsat 8 data.

For Landsat 5 and Landsat 7 data, the reflectance value is obtained from radiances using Eq. (3) (USGS):

$$\rho_\lambda = \frac{\pi . L_\lambda . d^2}{ESUN_\lambda . \cos \theta_s} \tag{3}$$

where ρ_λ is unitless planetary reflectance, L_λ is the TOA spectral radiance (Wm^{-2}sr^{-1}μm^{-1}), d is Earth-Sun distance in astronomical units, $ESUN_\lambda$ is the mean solar exo-atmospheric spectral irradiances (Wm^{-2}μm^{-1}) and θ_s is the solar zenith angle in degrees. $ESUN_\lambda$ values for each band of Landsat 5 and Landsat 7 data can be obtained from the handbooks of the related mission. θ_s and d values can be attained from the metadata file.

For Landsat 8 data, reflectance conversion can be applied to DN values directly as in Eq. (4) (Zanter 2019):

$$\rho_\lambda = \frac{M_\rho . Q_{CAL} + A_\rho}{\sin \theta_{SE}} \tag{4}$$

where M_ρ is the band-specific multiplicative rescaling factor from the metadata, A_ρ is the band-specific additive rescaling factor from the metadata, Q_{CAL} is the quantized and calibrated standard product pixel values (DN) and θ_{SE} is the local sun elevation angle from the metadata file.

Eq. (5) is used to convert the spectral radiance to at-sensor brightness temperature (Wukelic et al. 1989; Chen et al. 2006):

$$T_b = \frac{K_2}{\ln(\frac{K_1}{L_\lambda} + 1)} \tag{5}$$

where T_b is the brightness temperature in Kelvin (K), L_λ is the spectral radiance in Wm^{-2}sr^{-1}mm^{-1}; K_2 and K_1 are calibration constants. For Landsat 8 data, K_1 is 774.89, K_2 is 1321.08 (Wm^{-2}sr^{-1}mm^{-1}). For Landsat 7 data, K_1 is 666.09, K_2 is 1282.71 (Wm^{-2}sr^{-1}mm^{-1}). For Landsat 5 data, K_1 is 607.76, K_2 is 1260.56 (Wm^{-2}sr^{-1}mm^{-1}).

The land surface emissivity ε, is estimated from Eq. (6) using the NDVI Thresholds Method (Sobrino, Raissouni, and Li 2001; Sobrino, Jimenez-Munoz, and Paolini 2004).

$$\varepsilon = \varepsilon_v F_v + \varepsilon_s (1 - F_v) + d\varepsilon \tag{6}$$

where ε is land surface emissivity, ε_v is vegetation emissivity, ε_s is soil emissivity, F_v is fractional vegetation, $d\varepsilon$ is the effect of the geometrical distribution of the natural surfaces and internal reflections that can be expressed by Eq. (7):

$$d\varepsilon = (1 - \varepsilon_s)(1 - F_v) F \varepsilon_v \tag{7}$$

where ε_v is vegetation emissivity, ε_s is soil emissivity, F_v is fractional vegetation, F is a shape factor whose mean is 0.55, the value of $d\varepsilon$ maybe 2% for mixed land surfaces (Sobrino, Jimenez-Munoz, and Paolini 2004).

The fractional vegetation F_v, of each pixel, is determined from the NDVI using Eq. (8) (Carlson and Repley 1997):

$$F_v = \left(\frac{NDVI - NDVI_{min}}{NDVI_{max} - NDVI_{min}} \right)^2 \tag{8}$$

where (a) NDVI < 0.2 for bare soil; (b) NDVI > 0.5 for vegetation; (c) 0.2 < = NDVI < = 0.5 for mixed land with bare soil and vegetation (Sobrino, Raissouni, and Li 2001; Sobrino, Jimenez-Munoz, and Paolini 2004).

Finally, the land surface emissivity ε can be expressed by Eq. (9):

$$\varepsilon = 0.004 * F_v + 0.986 \tag{9}$$

where ε is land surface emissivity, F_v is fractional vegetation.

Water vapor content is estimated by Eq. (10) (Yang and Que 1996):

$$w = 0.0981$$
$$* \left[10 * 0.6108 * \exp\left(\frac{17.27 * (T_0 - 273.15)}{237.3 + (T_0 - 273.15)} \right) * RH \right]$$
$$+ 0.1697$$

(10)

where w is the water vapor content (g/cm^2), T_0 is the near-surface air temperature in Kelvin (K), RH is the relative humidity (%). These parameters of atmospheric profile are obtained from the Meteorological Center, Raipur (http://www.imdraipur.gov.in). Atmospheric transmittance is determined for Raipur City using Eq. (11) (Qin, Karnieli, and Barliner 2001; Sun, Tan, and Xu 2010):

$$\tau = 1.031412 - 0.11536w \quad (11)$$

where τ is the total atmospheric transmittance, w is the water vapor content (g/cm^2).

Raipur City is located in the tropical region. Thus, Eq. (12) is applied to compute the effective mean atmospheric transmittance of Raipur (Qin, Karnieli, and Barliner 2001; Sun, Tan, and Xu 2010):

$$T_a = 17.9769 + 0.91715T_0 \quad (12)$$

LST is retrieved from Landsat 5, 7, and 8 satellite data by using Eq. (13–15) (Qin, Karnieli, and Barliner 2001):

$$T_s = \frac{[a(1 - C - D) + (b(1 - C - D) + C + D)T_b - DT_a]}{C}$$

(13)

$$C = \varepsilon\tau \quad (14)$$

$$D = (1 - \tau)[1 + (1 - \varepsilon)\tau] \quad (15)$$

where ε is the land surface emissivity, τ is the total atmospheric transmittance, C and D are internal parameters based on atmospheric transmittance and land surface emissivity, T_b is the at-sensor brightness temperature, T_a is the mean atmospheric temperature, T_0 is the near-surface air temperature, T_s is the land surface temperature, $a = -67.355351$, $b = 0.458606$.

Determination of ecological status by urban thermal field variance index (UTFVI)

The study has applied the UTFVI (Nichol 2005) for determining the ecological status of Raipur City in different seasons during the study span. The Eq. 16 computes the UTFVI.

$$UTFVI = \frac{T_s - T_{mean}}{T_{mean}} \quad (16)$$

where $UTFVI$ = Urban Thermal Field Variance Index
T_s = LST (^oC)
T_{mean} = Mean LST (^oC)

Various categories of LULC extraction using NDVI threshold method

NDVI, the most popular vegetation index (Tucker 1979) was used in the present research for determining the seasonal correlation with LST. The value of NDVI ranges from −1.0 to +1.0. Positive NDVI indicates the presence of green vegetation. Greenness increases with the increase of the positive NDVI. But, this threshold limit of NDVI varies according to different climatic conditions. NDVI is used to extract various LULC categories (Chen et al. 2006). Generally, the wet season has more NDVI values compared to the dry season. Here, the post-monsoon images generate LULC maps as it maintains the ratio of wetness and dryness. In the present study, various threshold limits of NDVI present various categories of LULC (Table 1). The estimated threshold limit of NDVI depends on the physical environment of any region. NDVI > 0.2 shows vegetation, NDVI < 0 shows water and 0 < NDVI < 0.2 shows built-up and bare surface. The maximum likelihood classification method validates the NDVI threshold-based classified LULC categories.

LST-NDVI correlation on various categories of LULC

The present study used Pearson's correlation coefficient method to analyze the relationship between LST and NDVI. The value of the correlation coefficient (r) ranges from −1 to +1. The −1 value of r represents a perfect negative correlation whereas the +1 value of r represents a perfect positive correlation. The 0 value of r represents neutral correlation. The LST-NDVI correlation develops on various LULC categories. Each LULC category generates a separate correlation coefficient value for LST-NDVI relationship. The study also evaluates the seasonal variability of the LST-NDVI correlation.

Results and discussion

Accuracy assessment for the classification of various land surface materials

The maximum likelihood classification algorithm classifies Raipur City into various land surface materials for

Table 1. Description and threshold values of NDVI in LULC classification.

Acronym	Description	Formulation	References	Threshold limits of NDVI for extracting different LULC types		
				Vegetation	Water bodies	Built-up area and bare land
NDVI	Normalized difference vegetation index	$\frac{NIR-Red}{NIR+Red}$	Tucker 1979	> 0.2	< 0	0–0.2

1991–92, 1995–96, 1999–00, 2004–05, 2009–10, 2014–15, and 2018–19. The NDVI threshold method-based extracted LULC data is used as the reference data. The values of overall accuracy are 95.00%, 92.50%, 97.50%, 85.00%, 92.50%, 95.00%, and 87.50% in 1991–92, 1995–96, 1999–00, 2004–05, 2009–10, 2014–15, and 2018–19, respectively. The Kappa coefficient values are 0.91, 0.88, 0.96, 0.76, 0.89, 0.92, and 0.78 in 1991–92, 1995–96, 1999–00, 2004–05, 2009–10, 2014–15, and 2018–19, respectively. According to Nigatu, Øb, and Tveite (2014), the classification is satisfied if Kappa coefficient is > 0.75. The average overall accuracy is 92.14% and the average Kappa coefficient is 0.87. Thus, the maximum likelihood classification method significantly validates the NDVI threshold method-based LULC classification.

Spatial distribution of different types of LULC

Figure 2(a) presents the spatiotemporal changes of LULC of Raipur City from 1991–92 to 2018–19. Green vegetation decreases in a very high proportion while the settlement and barren land increase at a very high rate due to rapid land conversion.

Figure 2(b) shows the percentage of changed LULC during the study period. The annual rate of conversion for waterbodies and vegetation from 1991–92 to 2018–19 is 2.08% and 1.85%, respectively. However, in the same period, the settlement and barren land expands at a high percentage of the annual rate (13.23%). An alarming annual growth of bare land/built-up (49.95% between 1991–92 and 1995–96, 40.57% between 1995–96 and 1999–00, 11.42% between 1999–00 and 2004–05, 44.10% between 2004–05 and 2009–10, 13.53% between 2009–10 and 2014–15, and 19.99% between 2014–15 and 2018–19) was observed during the whole span. This rapid conversion of urban land is mainly due to the massive pressure for population growth and migration (Parvaze and Nasser 2012; Guha, Govil, and Mukherjee 2017; Ray et al. 2020).

LST and NDVI distribution

There is a prominent seasonal variation occurred in the mean LST values (Table 2). The lowest and highest values of the mean LST are noticed in the winter and pre-monsoon season, respectively.

Figure 3(a-d) shows the seasonal change in the minimum, maximum, and mean values of LST for the entire study period. The pre-monsoon season shows the highest LST and winter season has the lowest LST. Before 2009–2010, the trend of LST is increasing. However, 2009–2010 onwards, the LST is slightly
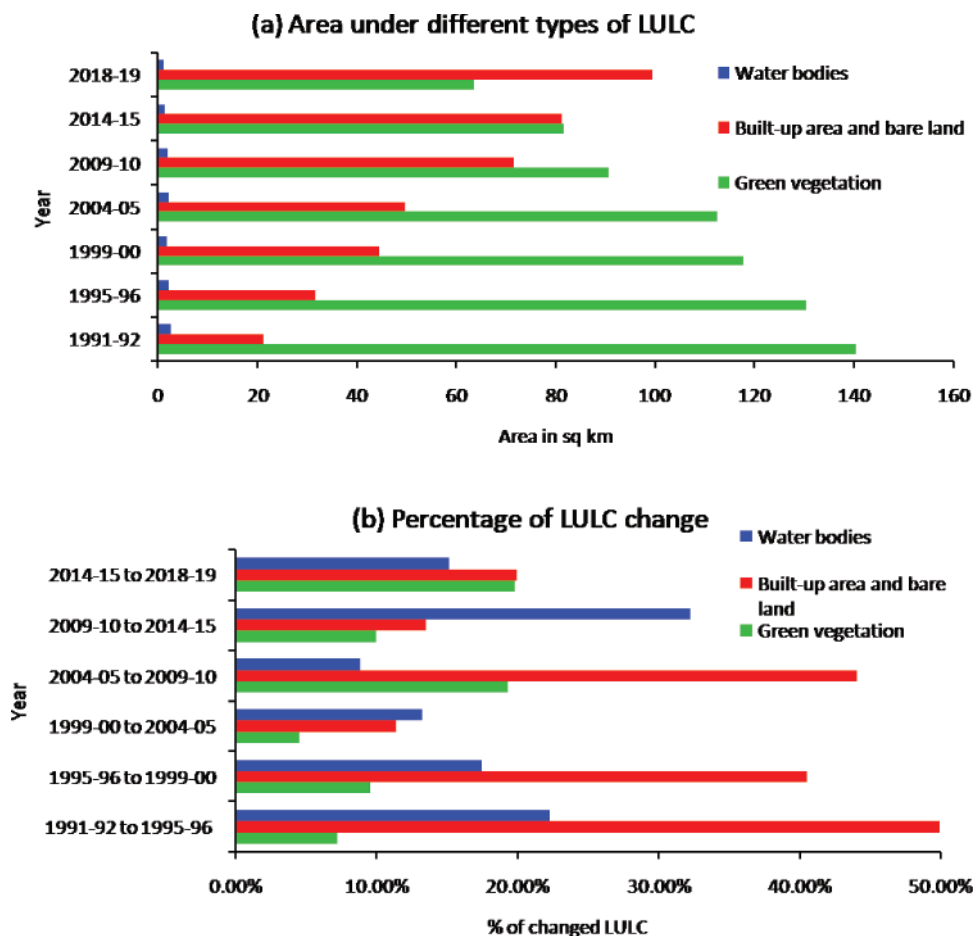

Figure 2. Change in LULC (191–92 to 2018–19): (a) area under different types of LULC (b) percentage of changed LULC.

Table 2. Seasonal variability of LST and the LST-NDVI correlation coefficient.

Season	Year of acquisition	LST (°C)				Correlation coefficients for LST-NDVI correlation
		Min.	Max.	Mean	Std.	
Pre-monsoon	1991–92	24.25	35.22	31.54	1.30	−0.36
	1995–96	24.54	41.07	34.64	1.89	−0.38
	1999–00	26.36	41.57	36.38	1.89	−0.58
	2004–05	27.37	43.32	38.01	2.05	−0.49
	2009–10	25.39	41.84	36.67	2.25	−0.47
	2014–15	26.97	39.68	34.40	1.65	−0.43
	2018–19	25.50	38.70	33.14	1.68	−0.43
	Average	25.76	40.20	34.96	1.81	−0.45
Monsoon	1991–92	22.38	30.83	25.74	1.41	−0.48
	1995–96	19.28	30.01	24.09	1.33	−0.55
	1999–00	17.62	31.23	24.18	1.34	−0.64
	2004–05	22.16	29.97	26.11	0.96	−0.55
	2009–10	21.94	38.38	33.06	2.40	−0.52
	2014–15	26.43	36.63	31.70	1.16	−0.48
	2018–19	25.49	34.98	31.08	1.13	−0.47
	Average	22.18	33.14	27.99	1.39	−0.53
Post-monsoon	1991–92	20.17	29.38	24.32	1.65	−0.51
	1995–96	19.85	28.20	23.70	1.30	−0.59
	1999–00	24.36	36.38	29.17	1.91	−0.69
	2004–05	23.46	34.46	28.01	1.58	−0.59
	2009–10	22.59	34.45	27.51	1.54	−0.58
	2014–15	19.44	28.31	23.47	1.12	−0.53
	2018–19	24.31	34.09	28.08	1.30	−0.62
	Average	22.02	32.18	26.32	1.48	−0.59
Winter	1991–92	18.37	28.33	23.29	1.15	−0.24
	1995–96	18.38	25.61	21.79	0.98	−0.20
	1999–00	19.74	34.30	26.54	1.71	−0.29
	2004–05	19.27	29.27	24.07	1.15	−0.17
	2009–10	18.82	27.79	23.31	1.15	−0.22
	2014–15	19.95	30.62	25.13	1.35	−0.14
	2018–19	20.33	30.14	24.37	1.18	−0.25
	Average	19.26	29.43	24.07	1.23	−0.22

decreased due to atmospheric instability and plantation program. A clear fluctuation in mean LST was noticed since the beginning of the study. Overall, the LST increases in the given duration of the research. Land conversion raises the LST values. The monsoon season gain most of the LST.
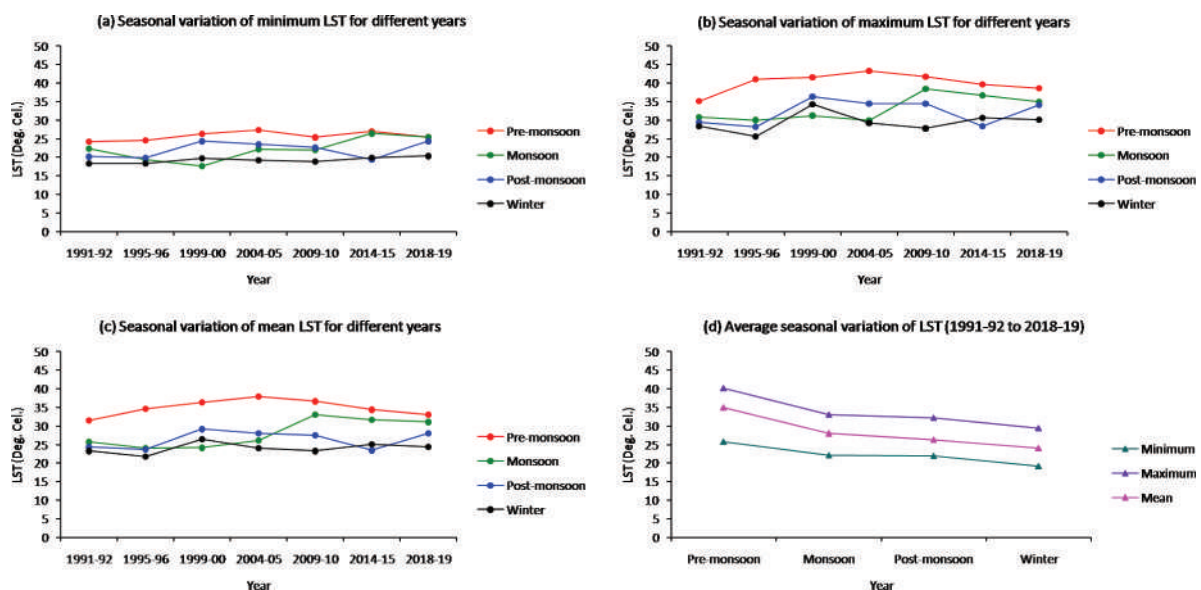
Figure 4 shows the map of spatiotemporal and seasonal distributions of mean LST throughout the study. The high LST zones are formed in the northwest and southeast sections where vegetation is less compared to the bare land/built-up area. Throughout the time, more than 85% of the area was above 27°C LST in the pre-monsoon period.

Figure 5 reflects the map of seasonal distribution of NDVI. The spatial relationship of LST with NDVI is easy to understand in Figures 5 and 6. The high NDVI is related to the healthy and green plants that reduce the intensity of LST. The NDVI value was found higher in the earlier images. In the middle period, the NDVI value decreased due to tree felling and land conversion. The NDVI value develops a significant rising trend in recent years. After taking some initiation of social forestry by the government and many non-government sectors, the city becomes ecologically rich, and the NDVI values increase gradually. Consequently, some governmental activities control the rising trend of LST in many parts of the city, which promotes even a reverse tendency of LST in the last few years. It can be a remarkable achievement for the city planners.

Relationship of land surface materials with LST

The temporal changes of LST depend on various categories of land surface materials. Green area and water area decrease the LST, while bare land/built-up surface increases LST. Consequently, the built-up/bare land surfaces increase, while vegetation and water surface decrease in a significant amount. Land conversion is the main responsible factor for the seasonal change of mean LST. As a result, the mean LST significantly increased (1.60°

Figure 3. Seasonal variability of LST values: (a) minimum (b) maximum (c) mean (d) average of minimum, maximum, and mean.
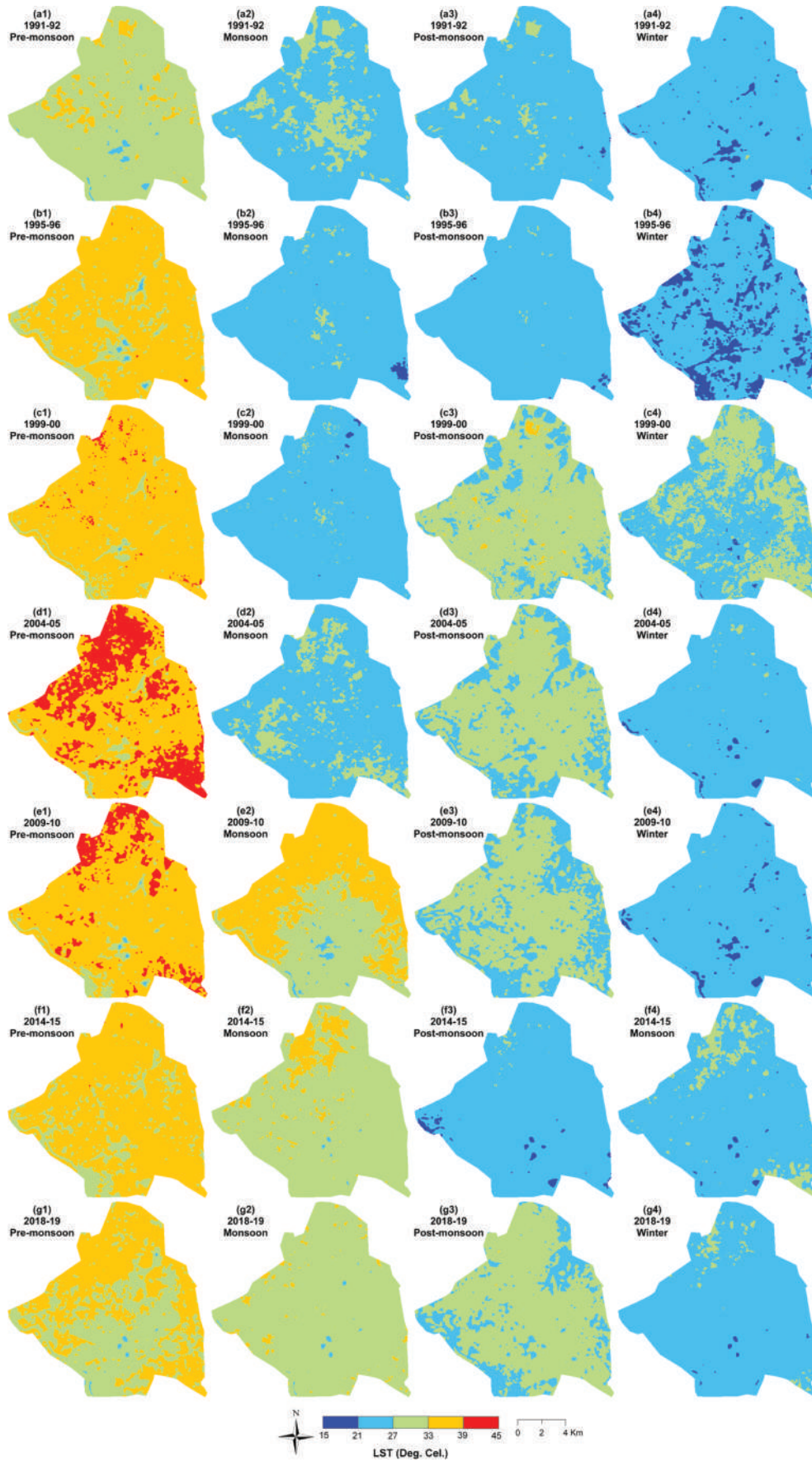
Figure 4. Spatiotemporal and seasonal distribution map of LST.
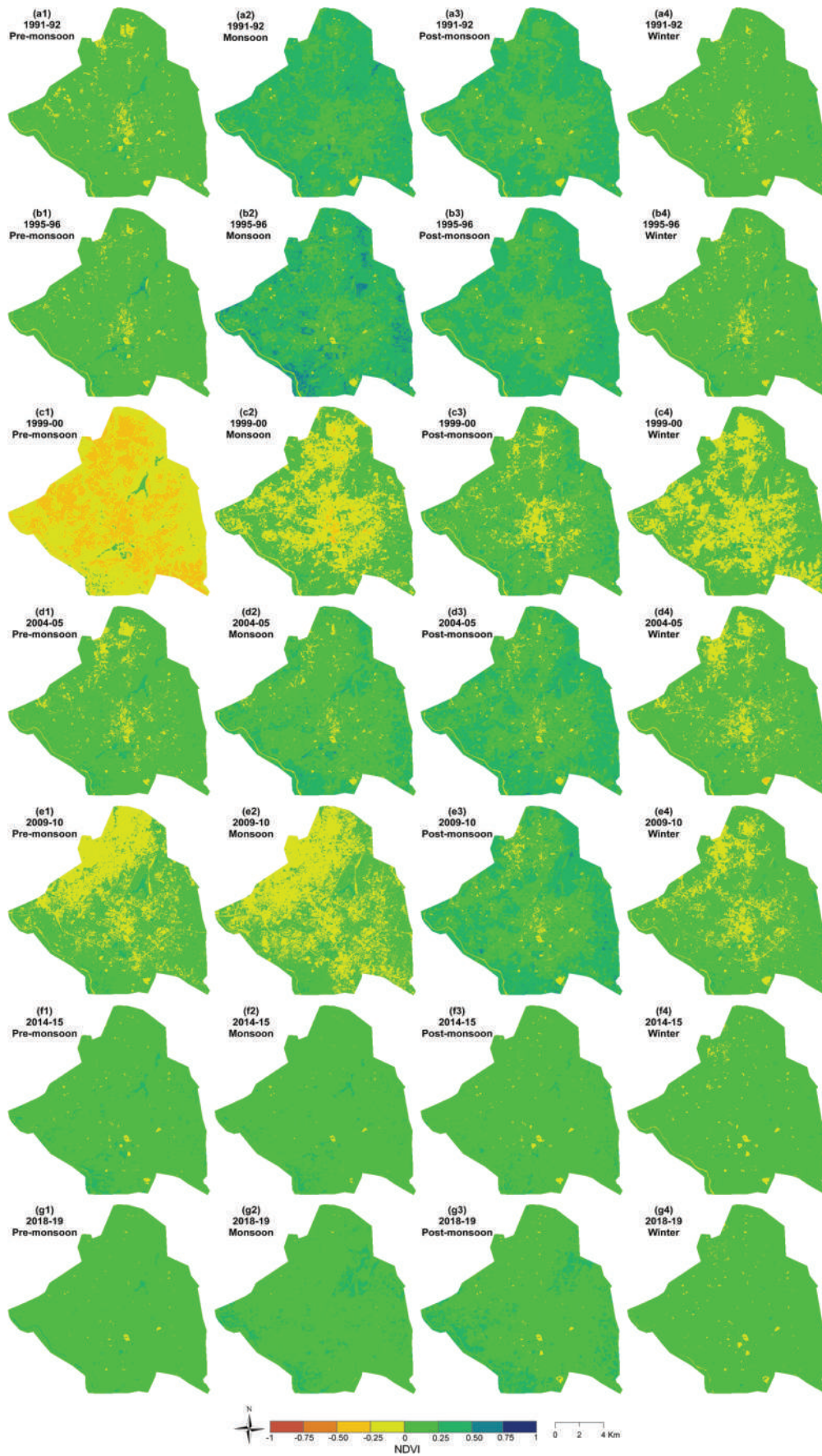
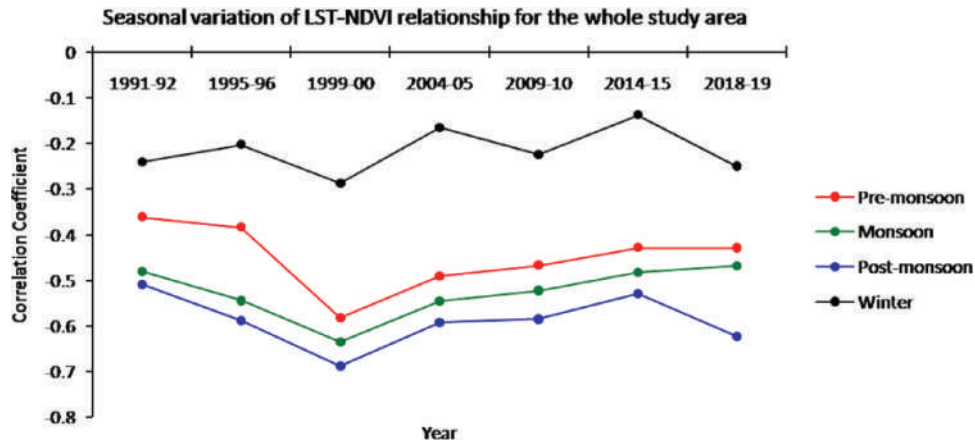**Figure 5.** Spatiotemporal and seasonal distribution map of NDVI.

Figure 6. Seasonal variability of LST-NDVI correlation: overall view.

Table 3. The threshold of ecological evaluation index.

UTFVI	UHI phenomenon	Ecological evaluation index
<0.000	None	Excellent
0.000–0.005	Weak	Good
0.005–0.010	Middle	Normal
0.010–0.015	Strong	Bad
0.015–0.020	Stronger	Worse
>0.020	Strongest	Worst

C in pre-monsoon, 5.34°C in monsoon, 4.76°C in post-monsoon, and 1.08°C in winter season) from 1991–92 to 2018–19.

Seasonal fluctuation on LST-NDVI correlation

Figure 6 represents a negative correlation between LST and NDVI. The correlation is weak negative (minimum, maximum, and mean correlation coefficients are −0.14, −0.29, and −0.22, respectively) in winter due to the dryness of the weather. The pre-monsoon season has a moderate negative (minimum, maximum, and mean

correlation coefficients are −0.36, −0.58, and −0.45, respectively) LST-NDVI correlation because of the moderate humidity in air and plant. The correlation is moderate to strong negative (minimum, maximum, and mean correlation coefficients are −0.47, −0.64, and −0.53, respectively) in monsoon because of the wet weather condition. The correlation is strong negative (minimum, maximum, and mean correlation coefficients are −0.51, −0.69, and −0.59, respectively) in post-monsoon season throughout the study period because the percentage of water vapor also remains high in the post-monsoon season and plants look healthy due to high ratio of chlorophyll content. Thus, the post-monsoon and monsoon seasons generate a more stable and stronger correlation compared to the winter season. The results show that the wetness of the season enhances the strength of the LST-NDVI correlation.

The LST-NDVI correlation was negative in several recent studies performed in Shanghai, China (Yue et al. 2007); in Mashhad, Iran (Gorgani, Panahi, and Rezaie 2013); in Berlin, Germany (Marzban, Sodoudi, and
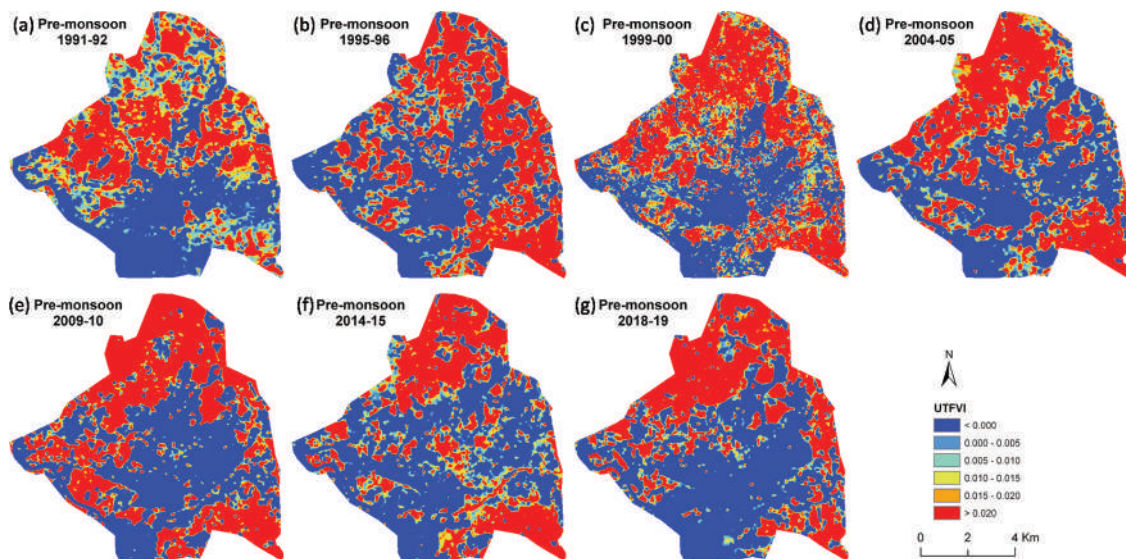

Figure 7. Thermal status of Raipur City in pre-monsoon season using UTFVI: (a) 1991–92 (b) 1995–96 (c) 1999–00 (d) 2004–05 (e) 2009–10 (f) 2014–15 (g) 2018–19.

Figure 8. Thermal status of Raipur City in monsoon season using UTFVI: (a) 1991–92 (b) 1995–96 (c) 1999–00 (d) 2004–05 (e) 2009–10 (f) 2014–15 (g) 2018–19.

Preusker 2018); in Aarhus, Denmark (Alexander 2020); in Uyo, Nigeria (Nse, Okoliea, and Nse 2020); in Yellow River Delta, China (Chi et al. 2020); in Bavarian Forest National Park, Germany (Neinavaza, Skidmorea, and Darvishzadeha 2020). The presence of surface moisture reduces the intensity of LST (Lambin and Ehrlich 1996). The present research also shows a negative correlation.

Ecological and thermal status of Raipur City

One additional aim of the study was to estimate the thermal and ecological status of Raipur City. The thermal status of Raipur City was based on the values of UTFVI those are categorized into six ecological evaluation indices (Table 3). The areas with high UTFVI values show low NDVI and vice-versa.

Figures 7, 8, 9, and 10 indicate that Raipur City has two extreme categories for ecological and thermal status: the excellent category (UTFVI < 0) and the worst category (UTFVI > 0.020) for each and every season. Almost half of the areas of Raipur City (approximately 40–45% during the entire periods) have an excellent thermal condition (i.e., UTFVI < 0). These areas have abundant green fields and waterbodies. Mainly, the central and southwest portions experience such thermal condition. However, the worst category (i.e., UTFVI > 0.020) of the ecological evaluation index also exists in a large portion (approximately 35–45% for all of the satellite data) of the city. The northwest and southeast parts fall under the worst category. Here, most of the lands are impervious (bare land with exposed rock surface or built-up areas). The good and normal categories of ecological condition (0.000 < UTFVI

Figure 9. Thermal status of Raipur City in post-monsoon season using UTFVI: (a) 1991–92 (b) 1995–96 (c) 1999–00 (d) 2004–05 (e) 2009–10 (f) 2014–15 (g) 2018–19.
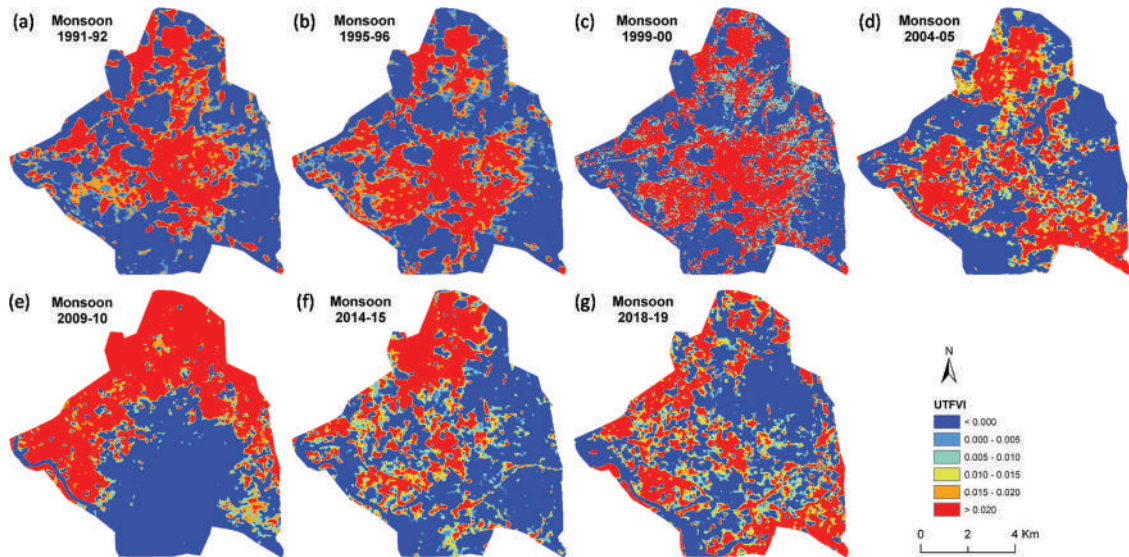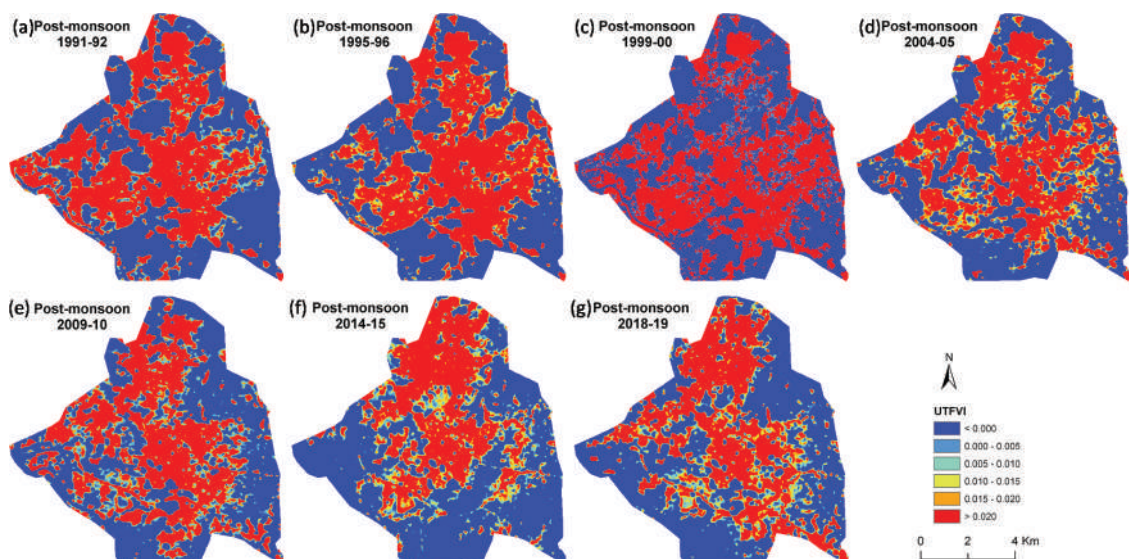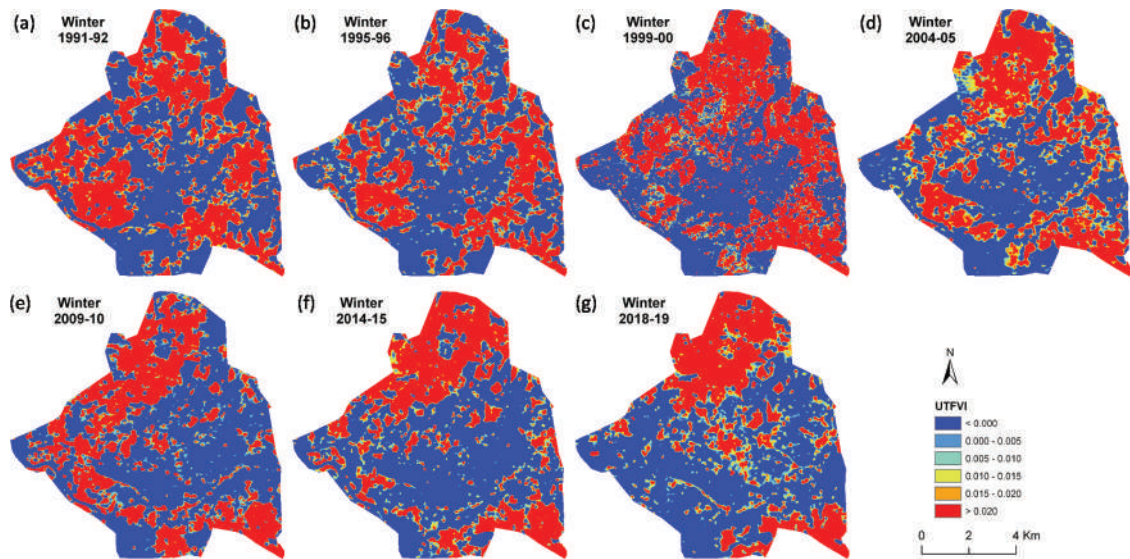
Figure 10. Thermal status of Raipur City in winter season using UTFVI: (a) 1991–92 (b) 1995–96 (c) 1999–00 (d) 2004–05 (e) 2009–10 (f) 2014–15 (g) 2018–19.

< 0.010) are found with some small patches surrounding the areas with excellent condition while the bad and worse categories (0.010 < UTFVI < 0.020) exist around the areas of the built-up class. The pre-monsoon season shows the highest worst categorized area while the monsoon and post-monsoon seasons show the lowest percentage of area having excellent condition. The area under the excellent category has slightly increased from 1991–92 to 2018–19 due to proper ecological planning and environmental management.

Conclusion

The present research concludes that the LST is negatively correlated to NDVI for all four seasons. The correlation is strong to moderate in post-monsoon (−0.59) and monsoon (−0.53), moderate in pre-monsoon (−0.45), and weak to moderate in winter (−0.22). Wet season shows a strong correlation, while dry season shows a weak correlation. The mean LST of the city significantly increased during the research period (1.60°C in the pre-monsoon, 5.34°C in monsoon, 4.76°C in post-monsoon, and 1.08°C in winter). The result appreciably shows the influence of LULC change and climate change. Moreover, the thermal status of the city is quite interesting. Almost an equal portion of lands are under the excellent and worst categories of ecological condition. A stable ecological healthy status can be achieved through a suitable environmental planning and management system.

Acknowledgments

Disclosure of potential conflicts of interest

ORCID

Subhanil Guha http://orcid.org/0000-0002-2967-7248

References

Alexander, C. 2020. "Normalised Difference Spectral Indices and Urban Land Cover as Indicators of Land Surface Temperature (LST)." *International Journal of Applied Earth Observation and Geoinformation* 86: 102013. doi:10.1016/j.jag.2019.102013.

Barsi, J., J. Schott, S. Hook, N. Raqueno, B. Markham, and R. Radocinski. 2014. "Landsat-8 Thermal Infrared Sensor (TIRS) Vicarious Radiometric Calibration." *Remote Sensing* 6 (11): 11607–11626. doi:10.3390/rs61111607.

Berger, C., J. Rosentreter, M. Voltersen, C. Baumgart, C. Schmullius, and S. Hese. 2017. "Spatio-Temporal Analysis of the Relationship between 2D/3D Urban Site Characteristics and Land Surface Temperature." *Remote Sensing of Environment* 193: 225–243. doi:10.1016/j.rse.2017.02.020.

Carlson, T. N., and D. A. Ripley. 1997. "On the Relation between NDVI, Fractional Vegetation Cover, and Leaf Area Index." *Remote Sensing of Environment* 62 (3): 241–252. doi:10.1016/S0034-4257(97)00104-1.

Chatterjee, R. S., N. Singh, S. Thapa, D. Sharma, and D. Kumar. 2017. "Retrieval of Land Surface Temperature (LST) from Landsat TM6 and TIRS Data by Single Channel Radiative Transfer Algorithm Using Satellite and Ground-based Inputs." *International Journal of Applied Earth Observation and Geoinformation* 58: 264–277. doi:10.1016/j.jag.2017.02.017.

Chen, X. L., H. M. Zhao, P. X. Li, and Z. Y. Yi. 2006. "Remote Sensing Image-based Analysis of the Relationship between Urban Heat Island and Land Use/cover Changes." *Remote Sensing of Environment* 104 (2): 133–146.

Chi, Y., J. Sun, Y. Sun, S. Liu, and Z. Fu. 2020. "Multi-temporal Characterization of Land Surface Temperature and Its Relationships with Normalized Difference Vegetation Index and Soil Moisture Content in the Yellow River Delta, China." *Glob Ecol Conserv* 23: e01092122. doi:10.1016/j.gecco.2020.e01092.

Coll, C., J. M. Galve, J. M. Sanchez, and V. Casseles. 2010. "Validation of Landsat-7/ETM+ Thermal-band Calibration and Atmospheric Correction with Ground-based Measurements." *IEEE Transactions on Geoscience and Remote Sensing* 48 (1): 547–555. doi:10.1109/TGRS.2009.2024934.

Cui, L., L. Wang, S. Qu, R. P. Singh, Z. Lai, L. Jiang, and R. Yao. 2019a. "Association Analysis between Spatiotemporal Variation of Vegetation Greenness and Precipitation/temperature in the Yangtze River Basin (China)." *Environmental Science and Pollution Research* 25 (22): 21867–21878. doi:10.1007/s11356-018-2340-4.

Cui, L., L. Wang, S. Qu, R. P. Singh, Z. Lai, and R. Yao. 2019b. "Spatiotemporal Extremes of Temperature and Precipitation during 1960–2015 in the Yangtze River Basin (China) and Impacts on Vegetation Dynamics." *Theoretical and Applied Climatology* 136 (1–2): 675–692. doi:10.1007/s00704-018-2519-0.

Das, D. N., A. Mondal, and S. Guha. 2013. "Change in Mangrove Forest Cover and Deltaic Islands in Sundarban Areas of West Bengal: A Temporal Analyses Using NCI Technique on LANDSAT TM5 Data." *Climate Change and Environment, Scientific Publisher* 113–127.

Du, S., Z. Xiong, Y. Wang, and L. Guo. 2016. "Quantifying the Multilevel Effects of Landscape Composition and Configuration on Land Surface Temperature." *Remote Sensing of Environment* 178: 84–92. doi:10.1016/j.rse.2016.02.063.

Estoque, R. C., Y. Murayama, and S. W. Myint. 2017. "Effects of Landscape Composition and Pattern on Land Surface Temperature: An Urban Heat Island Study in the Megacities of Southeast Asia." *Science of the Total Environment* 577: 349–359. doi:10.1016/j.scitotenv.2016.10.195.

Fu, P., and Q. Weng. 2016. "A Time Series Analysis of Urbanization Induced Land Use and Land Cover Change and Its Impact on Land Surface Temperature with Landsat Imagery." *Remote Sensing of Environment* 175: 205–214. doi:10.1016/j.rse.2015.12.040.

García-Santos, V., J. Cuxart, D. Martínez-Villagrasa, M. A. Jiménez, and G. Simó. 2018. "Comparison of Three Methods for Estimating Land Surface Temperature from Landsat 8-TIRS Sensor Data." *Remote Sensing* 10 (9): 1450. doi:10.3390/rs10091450.

Gorgani, S. A., M. Panahi, and F. Rezaie. 2013. "The Relationship between NDVI and LST in the Urban Area of Mashhad." In *Iran. International Conference on Civil Engineering Architecture and Urban Sustainable Development. November*. Iran: Tabriz.

Govil, H., S. Guha, A. Dey, and N. Gill. 2019. "Seasonal Evaluation of Downscaled Land Surface Temperature: A Case Study in A Humid Tropical City." *Heliyon* 5 (6): e01923. doi:10.1016/j.heliyon.2019.e01923.

Goward, S. N., Y. K. Xue, and K. P. Czajkowski. 2002. "Evaluating Land Surface Moisture Conditions from the Remotely Sensed Temperature/Vegetation Index Measurements: An Exploration with the Simplified Simple Biosphere Model." *Remote Sensing of Environment* 79 (2–3): 225–242. doi:10.1016/S0034-4257(01)00275-9.

Guha, S., and H. Govil. 2020. "Land Surface Temperature and Normalized Difference Vegetation Index Relationship:

A Seasonal Study on a Tropical City." *SN Applied Sciences* 2 (10): 1661 (2020). doi:10.1007/s42452-020-03458-8.

Guha, S., and H. Govil. 2021. "Annual Assessment on the Relationship between Land Surface Temperature and Six Remote Sensing Indices Using Landsat Data from 1988 to 2019." *Geocarto International* 1–20. doi:10.1080/10106049.2021.1886339.

Guha, S., H. Govil, and P. Diwan. 2020. "Monitoring LST-NDVI Relationship Using Premonsoon Landsat Datasets." *Advances in Meteorology* 2020: 4539684. doi:10.1155/2020/4539684.

Guha, S., H. Govil, and S. Mukherjee. 2017. "Dynamic Analysis and Ecological Evaluation of Urban Heat Islands in Raipur City, India." *Journal of Applied Remote Sensing* 11 (3): 036020. doi:10.1117/1.JRS.11.036020.

Gui, X., L. Wang, R. Yao, D. Yu, and C. Li. 2019. "Investigating the Urbanization Process and Its Impact on Vegetation Change and Urban Heat Island in Wuhan, China." *Environmental Science and Pollution Research* 26 (30): 30808–30825. doi:10.1007/s11356-019-06273-w.

Gutman, G., and A. Ignatov. 1998. "The Derivation of the Green Vegetation Fraction from NOAA/AVHRR Data for Use in Numerical Weather Prediction Models." *International Journal of Remote Sensing* 19 (8): 1533–1543. doi:10.1080/014311698215333.

Hao, X., W. Li, and H. Deng. 2016. "The Oasis Effect and Summer Temperature Rise in Arid Regions-case Study in Tarim Basin." *Scientific Reports* 6 (1): 35418. doi:10.1038/srep35418.

http://www.imdraipur.gov.in

https://www.earthexplorer.usgs.gov

https://www.mausam.imd.gov.in

Jiménez-Muñoz, J. C., J. Cristóba, J. A. Sobrino, G. Soria, M. Ninyerola, and X. Pons. 2009. "Revision of the Single-channel Algorithm for Land Surface Temperature Retrieval from Landsat Thermal-infrared Data." *IEEE Transactions on Geoscience and Remote Sensing* 47 (1): 339–349. doi:10.1109/TGRS.2008.2007125.

Jiménez-Muñoz, J. C., and J. A. Sobrino. 2003. "A Generalized Single Channel Method for Retrieving Land Surface Temperature from Remote Sensing Data." *Journal of Geophysical Research: Atmospheres* 108 (D22): 4688. doi:10.1029/2003JD003480.

Kikon, N., P. Singh, S. K. Singh, and A. Vyas. 2016. "Assessment of Urban Heat Islands (UHI) of Noida City, India Using Multi-temporal Satellite Data." *Sustainable Cities and Society* 22: 19–28. doi:10.1016/j.scs.2016.01.005.

Lambin, E. F., and D. Ehrlich. 1996. "The Surface Temperature-Vegetation Index Space for Land Use and Land Cover Change Analysis." *International Journal of Remote Sensing* 17 (3): 463–487. doi:10.1080/01431169608949021.

Li, W. F., Q. W. Cao, L. Kun, and J. S. Wu. 2017. "Linking Potential Heat Source and Sink to Urban Heat Island: Heterogeneous Effects of Landscape Pattern on Land Surface Temperature." *Science of the Total Environment* 586: 457–465. doi:10.1016/j.scitotenv.2017.01.191.

Liu, Y., J. Peng, and Y. Wang. 2018. "Efficiency of Landscape Metrics Characterizing Urban Land Surface Temperature." *Landscape and Urban Planning* 180: 36–53. doi:10.1016/j.landurbplan.2018.08.006.

Mahato, S., and S. Pal. 2018. "Changing Land Surface Temperature of a Rural Rarh Tract River Basin of India." *Remote Sens Appl Soc Environ* 10: 209–223. doi:10.1016/j.rsase.2018.04.005.

Marzban, F., S. Sodoudi, and R. Preusker. 2018. "The Influence of Land-cover Type on the Relationship

between NDVI–LST and LST- T Air." *International Journal of Remote Sensing* 39 (5): 1377–1398. doi:10.1080/01431161.2017.1462386.

McMillin, L. M. 1975. "Estimation of Sea Surface Temperatures from Two Infrared Window Measurements with Different Absorption." *Journal of Geophysical Research* 80 (36): 80–82. doi:10.1029/JC080i036p05113.

Mondal, A., S. Guha, P. K. Mishra, and S. Kundu. 2011. "Land use/Land Cover Changes in Hugli Estuary Using Fuzzy C-Mean Algorithm." *Int J Geomat Geosci* 2 (2): 613–626.

Mushore, T. D., T. Dube, M. Manjowe, W. Gumindogab, A. Chemuira, I. Rousta, J. Obindi, and O. Mutanga. 2019. "Remotely Sensed Retrieval of Local Climate Zones and Their Linkages to Land Surface Temperature in Harare Metropolitan City, Zimbabwe." *Urban Climate* 27: 259–271. doi:10.1016/j.uclim.2018.12.006.

Neinavaza, E., A. K. Skidmorea, and R. Darvishzadeha. 2020. "Effects of Prediction Accuracy of the Proportion of Vegetation Cover on Land Surface Emissivity and Temperature Using the NDVI Threshold Method." *International Journal of Applied Earth Observation and Geoinformation* 85: 101984. doi:10.1016/j.jag.2019.101984.

Nichol, J. E. 2005. "Remote Sensing of Urban Heat Islands by Day and Night." *Photogram Eng Remote Sens* 19: 1639–1649.

Nigatu, W., D. Øb, and H. Tveite. 2014. "GIS Based Mapping of Land Cover Changes Utilizing Multi-Temporal Remotely Sensed Image Data in Lake Hawassa Watershed, Ethiopia." *Environmental Monitoring and Assessment* 186 (3): 1765–1780. doi:10.1007/s10661-013-3491-x.

Nse, O. U., C. J. Okoliea, and V. O. Nse. 2020. "Dynamics of Land Cover, Land Surface Temperature and NDVI in Uyo City, Nigeria." *Sci Afr* 10: e00599. doi:10.1016/j.sciaf.2020.e00599.

Parvaze, A. L., and A. R. Naseer. 2012. "Internal-Migration of Chhattisgarh: Socio-Economic Aspect." *IOSR Journal of Business and Management* 4 (3): 46–49. doi:10.9790/487X-0434649.

Peng, J., J. Jia, Y. Liu, H. Li, and J. Wu. 2018a. "Seasonal Contrast of the Dominant Factors for Spatial Distribution of Land Surface Temperature in Urban Areas." *Remote Sensing of Environment* 215: 255–267. doi:10.1016/j.rse.2018.06.010.

Peng, J., J. Ma, Q. Liu, Y. Liu, Y. Hu, Y. Li, and Y. Yue. 2018b. "Spatial-Temporal Change of Land Surface Temperature across 285 Cities in China: An Urban-Rural Contrast Perspective." *Science of the Total Environment* 635: 487–497. doi:10.1016/j.scitotenv.2018.04.105.

Peng, J., P. Xie, Y. Liu, and J. Ma. 2016. "Urban Thermal Environment Dynamics and Associated Landscape Pattern Factors: A Case Study in the Beijing Metropolitan Region." *Remote Sensing of Environment* 173: 145–155. doi:10.1016/j.rse.2015.11.027.

Qin, Z., A. Karnieli, and P. Barliner. 2001. "A Mono-Window Algorithm for Retrieving Land Surface Temperature from Landsat TM Data and Its Application to the Israel-Egypt Border Region." *International Journal of Remote Sensing* 22 (18): 3719–3746. doi:10.1080/01431160010006971.

Qu, S., L. Wang, A. Lin, D. Yu, M. Yuan, and C. Li. 2020. "What Drives the Vegetation Restoration in Yangtze River Basin, China." *Climate Change or Anthropogenic Factors? Ecol Indic* 108: 105724. doi:10.1016/j.ecolind.2019.105724.

Qu, S., L. Wang, A. Lin, H. Zhu, and M. Yuan. 2018. "What Drives the Vegetation Restoration in Yangtze River Basin, China." *Climate Change or Anthropogenic Factors? Ecol Indic* 90: 438–450. doi:10.1016/j.ecolind.2018.03.029.

Ray, J., F. Naaz, P. Khasnobis, and R. Majumder. 2020. "Internal Migration and Inclusive Development: Insights from the Field." In *Development Challenges of India after Twenty Five Years of Economic Reforms. India Studies in Business and Economics*, edited by N. K. Mishra. Singapore: Springer. doi:10.1007/978-981-15-8265-3_22.

Rozenstein, O., Z. Qin, Y. Derimian, and A. Karnieli. 2014. "Derivation of Land Surface Temperature for Landsat-8 TIRS Using a Split Window Algorithm." *Sensors* 14 (4): 5768–5780. doi:10.3390/s140405768.

Shigeto, K. 1994. "Relation between Vegetation, Surface Temperature, and Surface Composition in the Tokyo Region during Winter." *Remote Sensing of Environment* 50 (1): 52–60. doi:10.1016/0034-4257(94)90094-9.

Smith, R. C. G., and B. J. Choudhury. 1990. "On the Correlation of Indices of Vegetation and Surface Temperature over South-eastern Australia." *International Journal of Remote Sensing* 11 (11): 2113–2120. doi:10.1080/01431169008955164.

Sobrino, J. A., J. C. Jimenez-Munoz, and L. Paolini. 2004. "Land Surface Temperature Retrieval from Landsat TM5." *Remote Sensing of Environment* 9 (4): 434–440. doi:10.1016/j.rse.2004.02.003.

Sobrino, J. A., N. Raissouni, and Z. Li. 2001. "A Comparative Study of Land Surface Emissivity Retrieval from NOAA Data." *Remote Sensing of Environment* 75 (2): 256–266. doi:10.1016/S0034-4257(00)00171-1.

Sun, Q., J. Tan, and Y. Xu. 2010. "An ERDAS Image Processing Method for Retrieving LST and Describing Urban Heat Evolution: A Case Study in the Pearl River Delta Region in South China." *Environmental Earth Sciences* 59 (5): 1047–1055. doi:10.1007/s12665-009-0096-3.

Tran, D. X., F. Pla, P. Latorre-Carmona, S. W. Myint, M. Caetano, and H. V. Kieu. 2017. "Characterizing the Relationship between Land Use Land Cover Change and Land Surface Temperature." *ISPRS* Journal of Photogrammetry and Remote Sensing 50: 119–132. doi:10.1016/j.isprsjprs.2017.01.001.

Tucker, C. J. 1979. "Red and Photographic Infrared Linear Combinations for Monitoring Vegetation." *Remote Sensing of Environment* 8 (2): 127–150. doi:10.1016/0034-4257(79)90013-0.

Wen, L., W. Peng, H. Yang, H. Wang, L. Dong, and H. Shang. 2017. "An Analysis of Land Surface Temperature (LST) and Its Influencing Factors in Summer in Western Sichuan Plateau: A Case Study of Xichang City." *Remote Sens Land Res* 29 (2): 207–214. doi:10.6046/gtzyyg.2017.02.30.

Wukelic, G. E., D. E. Gibbons, L. M. Martucci, and H. P. Foote. 1989. "Radiometric Calibration of Landsat Thematic Mapper Thermal Band." *Remote Sensing of Environment* 28: 339–347. doi:10.1016/0034-4257(89)90125-9.

Yang, J., and J. Qiu. 1996. "The Empirical Expressions of the Relation between Precipitable Water and Ground Water Vapor Pressure for Some Areas in China." *Sci Atmos Sinica* 20: 620–626.

Yue, W., J. Xu, W. Tan, and L. Xu. 2007. "The Relationship between Land Surface Temperature and NDVI with Remote Sensing. Application to Shanghai Landsat 7 ETM + Data." *International Journal of Remote Sensing* 28 (15): 3205–3226. doi:10.1080/01431160500306906.

Zanter, K. 2019. Landsat 8 (L8) Data Users Handbook. :Sioux Falls, SD, USA: EROS.

Zhao, Z. Q., B. J. He, L. G. Li, H. B. Wang, and A. Darko. 2017. "Profile and Concentric Zonal Analysis of Relationships between Land Use/land Cover and Land Surface Temperature: Case Study of Shenyang, China." *Energy and Buildings* 155: 282–295. doi:10.1016/j.enbuild.2017.09.046.

Zhou, D., J. Xiao, S. Bonafoni, C. Berger, K. Deilami, Y. Zhou, S. Frolking, R. Yao, Z. Qiao, and J. A. Sobrino. 2019. "Satellite Remote Sensing of Surface Urban Heat Islands: Progress, Challenges, and Perspectives." *Remote Sensing* 11 (1): 48. doi:10.3390/rs11010048.

Source details

Feedback >   Compare sources >

Ecosystem Health and Sustainability

Open Access ⓘ

Scopus coverage years: from 2015 to Present

Publisher: American Association for the Advancement of Science

ISSN: 2096-4129   E-ISSN: 2332-8878

Subject area: (Agricultural and Biological Sciences: Ecology, Evolution, Behavior and Systematics)   (Environmental Science: Ecology)

(Environmental Science: Management, Monitoring, Policy and Law)

Source type: Journal

[View all documents >]   [Set document alert]   💾 Save to source list

CiteScore 2022   ⓘ
6.6

SJR 2022   ⓘ
1.023

SNIP 2022   ⓘ
1.277

CiteScore   CiteScore rank & trend   Scopus content coverage

Studies on the influence of large earthquakes (M>7) upon 9 kHz sferics recorded from Kolkata

Dr. S. Barui

Assistant professor & HOD, Department of Electronics, Dinabandhu Andrews College, Kolkata-700084, India

Abstract - **The outcome of the analyses of some significant observations in the records of VLF sferics over Kolkata (Lat. 22.56º N, Long. 88.5º E) at 9 kHz during the occurrences of large earthquake on August 14, 2021 will be presented here. Discrete spike-type signals are obtained as the precursors of this earthquake with magnitude M>7. The number of spikes and their intensities are found to vary irregularly and reached their maximum value on the day of occurrence. It then decreases gradually and finally ceased.**

Index Terms - **Earthquake, ionospheric perturbation, precursory effects, seismo-eletromagnetism.**

I.INTRODUCTION

Seismo-electromagnetic emissions are observed in ULF-ELF-VLF bands in the seismically active zones prior to the incidence of any large earthquake (Fuzinawa and Takahashi 1995; Hayakawa 2010; Sorokin *et al.*, 2007). During any large earthquake, electromagnetic radiations, chemical and gaseous particle emanations would cause ionospheric effects that modulate the electric charge distribution. These incidents are taken as the signatures of lithosphere-atmosphere-ionosphere coupling influencing the conductivity, electron density fluctuations, changes in temperature and ionic composition of the lower atmosphere (Boskova *et al.,* 1994). There is rapid enhancement in the occurrences of H_2, CO_2, CH_4 along with the increase of atmospheric radioactivity connected to the emissions of elements like radon, radium, uranium and their decay products (Biagi *et al.* 2009; Yasuok *et al.* 2012).

The August 14, 2021, Haiti earthquake was the deadlier earthquake that killed more than 2,248 people as of September 7, 2021 and injured above 12,000 people. At least 136,800 buildings were damaged or destroyed. It occurred at 12:29:09 UTC as well as at 08:29:09 Haiti local time on August 14, 2021. The strength is M 7.2 with its epicenter at Lat. 18.408^0 N, Long. 73.475^0 W, about 150 km west of the Capital, Port-an-Prince.The depth of the epicenter of the main shock is 10 km.

In this paper, the results of some significant observations at 9 kHz recorded over Kolkata (Lat. 22.56º N, Long. 88.5º E) by VLF receivers during this earthquake will be presented.

II. OBSERVATIONAL RESULTS

We detected the effects of the large earthquakes upon 9 kHz sferics from several days prior to the day of occurrence which continued for some days during the post-earthquake period.

The fractional change in the mean signal amplitude became higher in the nighttime than the daytime. For higher reflection height, the VLF signals have lower attenuation. The reduction of signal strength is due to higher attenuation at the earth-ionosphere wave guide. The variations in signal amplitude due to solar flares during the occurrence of lightning, electron density perturbation in the lower ionosphere cannot affect the decrease in daily mean amplitude and these are neglected in comparison to earthquake associated effects. Storm effects on VLF propagation show some decrease of the VLF phase and amplitude at nighttime during the main phase of storm. The parameters, eg, surface temperature; radon emanation may influence the conductivity of the lower ionosphere leading to the modification of atmospheric electric field.

In the seismoactive region surrounding the place of occurrences of the earthquakes at Haiti (Lat. 18.408^0 N, Long. 73.475^0 W), because of lithosphere-ionosphere coupling and perturbation of temperature on the earth's surface, the atmospheric medium is further excited that move towards the ionosphere. By

this, electromagnetic emissions from lithosphere propagate upwards modifying the ionosphere.

Various features are observed from the continuous records of VLF sferics at 9 kHz near Kolkata. Spiky variations at 9 kHz records are noticed during the occurrences of the earthquakes on August 14, 2021 having magnitudes M=7.2 with 10 K.m. depth at the epicenter. Fig. 1 shows the time series graph of sferics on April 01, 2021 at 9 kHz recorded at Kolkata in a normal day where no spiky variations are observed. The normal day means meteorologically and geophysically clear day and there is no occurrence of any earthquake having M>5. The figure shows the diurnal variations with sunrise and sunset effects. The commencement time of spikes is several hours earlier than the commencement of the earthquakes or around the time of their occurrences. The number of spikes per hour, i.e., the intensity of spikes varies with the earthquake. The spiky variations for the strong earthquake have been considered for analyses during August 7 – August 21, 2021.
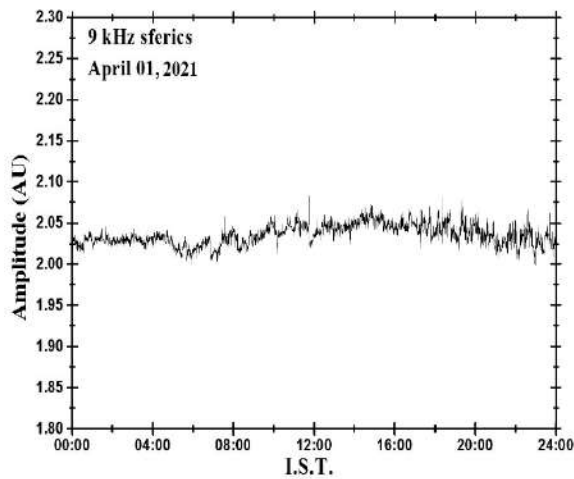

Fig.1: Normal day record of 9 kHz sferics signal observed near Kolkata of April 01, 2021, a meteorologically clear day.

Figure 2 represents the time-series graphs of amplitude of 9 kHz signals at different dates before and after the day of occurrence of the earthquake. It is seen that the commencement of spike events occurs some days prior to the strong earthquake and then decrease gradually. The variation in spike heights and the variation of total number of spikes per hour increase with the approach of the day of occurrence and reached their maximum values.
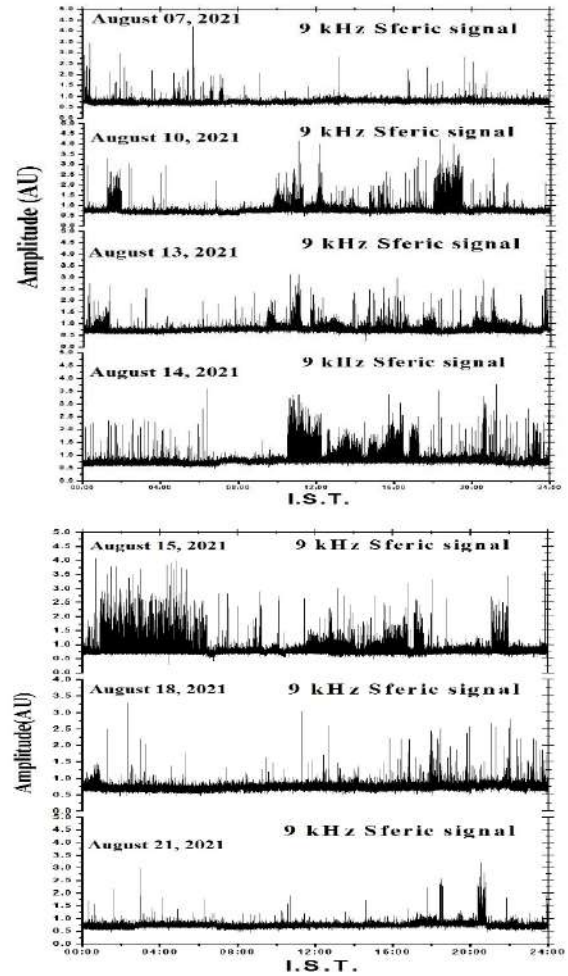

Fig.2: Diurnal variation of 9 kHz sferics signal observed near Kolkata.

The variations gradually reduce during the post earthquake period and finally ceased. In the time scale, the spikes occurred in the duration of the order of a few minutes. The experimental site is situated at a distance of 70 km from Kolkata, free from big and small industries, and dense locality. So, the occurrences of man-made and other industrial noises were absent. The power supply system for the receiver is thoroughly checked and no fault or any leakage was detected. So, the nature of the spikes does not depend on any of those causes. Also, the nature of the spikes and their characteristic separations are completely different from the local thunderstorm transient variations or from any other effects, e.g., solar flare, meteor shower, geomagnetic storms (De *et al.,* 2010). Total number of spikes per hour as observed during the month of August, 2021 for 7 days are represented by bar diagram in Fig. 3. The amplitude is maximum for the earthquake with large M value. The bars with

different heights indicate the precursory and post seismic effects. The diurnal pattern observed in Fig. 1 is absent in the records of the earthquake occurrence dates (Fig. 2).
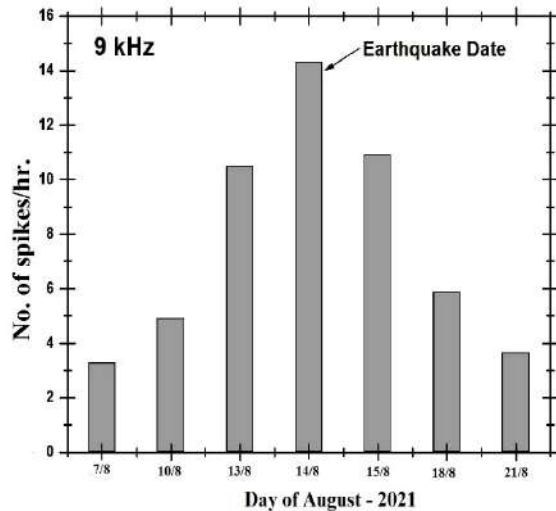

Fig.3: Variation of number of spike per hour on 9 kHz due to strong earthquakes.

III. CONCLUSION

Some characteristic features of large earthquake have been analyzed from the recorded data. Some of their aspects are shown in Fig. 2. The night time intensity and the number of occurrence of spikes are found to be much higher than the day time (Kumar *et al.,* 2013). The signal is characterized by spiky variations commencing several hours prior to the occurrence of earthquake. The nearer the epicenters from the receiver, the higher is the amplitudes of spikes. The amplitude of spikes is very much dependent on the magnitude of the earthquake.

During any large earthquake, there will be coupling between lithosphere–atmosphere and ionosphere through some probable channels, e.g., chemical channel, acoustic channel and electromagnetic (EM) channel. From chemical channel, there will be water elevation, gas emanation/radon emanation, changes in geophysical parameters which introduce chemical/conductivity changes in air resulting in a modification of the atmospheric electric field perturbing the plasma density in the ionosphere. Acoustic channel introduces excitation of atmospheric oscillations that propagate up to the ionosphere thereby modifying the ionospheric density. EM channel is supposed to introduce VLF emission,

ionizations, electric charge redistribution above the surface of the earth by which anomalous electric field would be generated producing large-scale irregularities. Anomalous field propagates into the inner magnetosphere and interacts with energetic particles. These particles precipitate into the lower ionosphere initiating direct heating, liberation of exo-electrons, and/or ionization of the ionosphere by seismo-ELF–VLF waves. These are detected as precursors of any vast earthquake of large M-value.

Although any quantitative relation between the observed signals and the earthquake source parameters are lacking (Pham and Geller 2002), the claim of background noise also fails to comply with the time-series records of any observed signals during the occurrence of large earthquake.

REFERENCES

[1] Biagi, P. F., Castellana, L., Maggipinto, T., Loiacono, D., Schiavulli, L., Ligonzo, T., Fiore, M., Suciu, E., and Ermini, A. (2009), A pre seismic radio anomaly revealed in the area where the Abruzzo earthquake (M=6.3) occurred on 6 April 2009, Nat. Hazards Earth Syst. Sci., 9, 1551-1556.

[2] Boskova, J., Smilauer, I., Triska, P., and Kudela, K. (1994), Anomalous behaviour of plasma parameters as observed by the Intercosmos-24 satellite prior to the Irianian earthquake of 20 June 1990, Studia geophysica et geodaetica, 38, 213-220.

[3] De, S. S., De, B. K., Bandyopadhyay, B., Paul, S., Haldar, D. K., Bhowmick, A., Barui, S., and Ali, R. (2010), Effects on atmospherics at 6 kHz and 9 kHz recorded at Tripura during the India–Pakistan border earthquake, Nat. Hazards Earth Syst. Sci., 10, 843-855.

[4] Fuzinawa, Y., and Takahashi, K. (1995), Paper presented at IUGG Meeting Boulder, Colorado, 2–4 July 1995.

[5] Hayakawa, M., Kasahara, Y, Nakamura, T., Muto, F., Horie, T., Maekawa, S., Hobara, Y., Rozhnoi, A. A., Solivieva, M, and Molchanov, O. A. (2010), A statistical study on the correlation between lower ionospheric perturbations as seen by subionospheric VLF/LF propagation and earthquakes, J. Geophys. Res., 115, A09305, doi.: 10.1029/2009JA015143.

[6] Kumar. A., Kumar. S., Hayakawa. M., and Menk. F. (2013), Subionospheric VLF perturbations observed at low latitude associated with earthquake from Indonesia region, J. Atmos. Sol.-Terr. Phys., 102, 71-80.

[7] Pham, V. N., and Geller, R. J. (2002), Comment on "Signature of pending earthquake from electromagnetic anomalies" by K. Eftaxias et al., Geophys. Res. Lett., 29, doi.:10.1029/ 2002 GL015328.

[8] Sorokin, V. M., Yaschenko, A. K., and Hayakawa, M. (2007), A perturbation of DC electric field caused by light ion adhesion to aerosols during the growth in seismic-related atmospheric radioactivity, Nat. Hazards Earth Syst. Sci., 7, 155-163.

[9] Yasuok, Y., Isikaw, T., Nagahama, H., Kawada, Y., Omori, Y., Tokonami, S., and Shinogi, M. (2012), Radon anomalies prior to earthquakes. In M. Hayakawa(Ed.), The Frontier of Earthquake Prediction Studies (pp. 410-427). Tokyo, Japan: Nihon-senmontosho-Shuppan.